NIST Special Publication 847
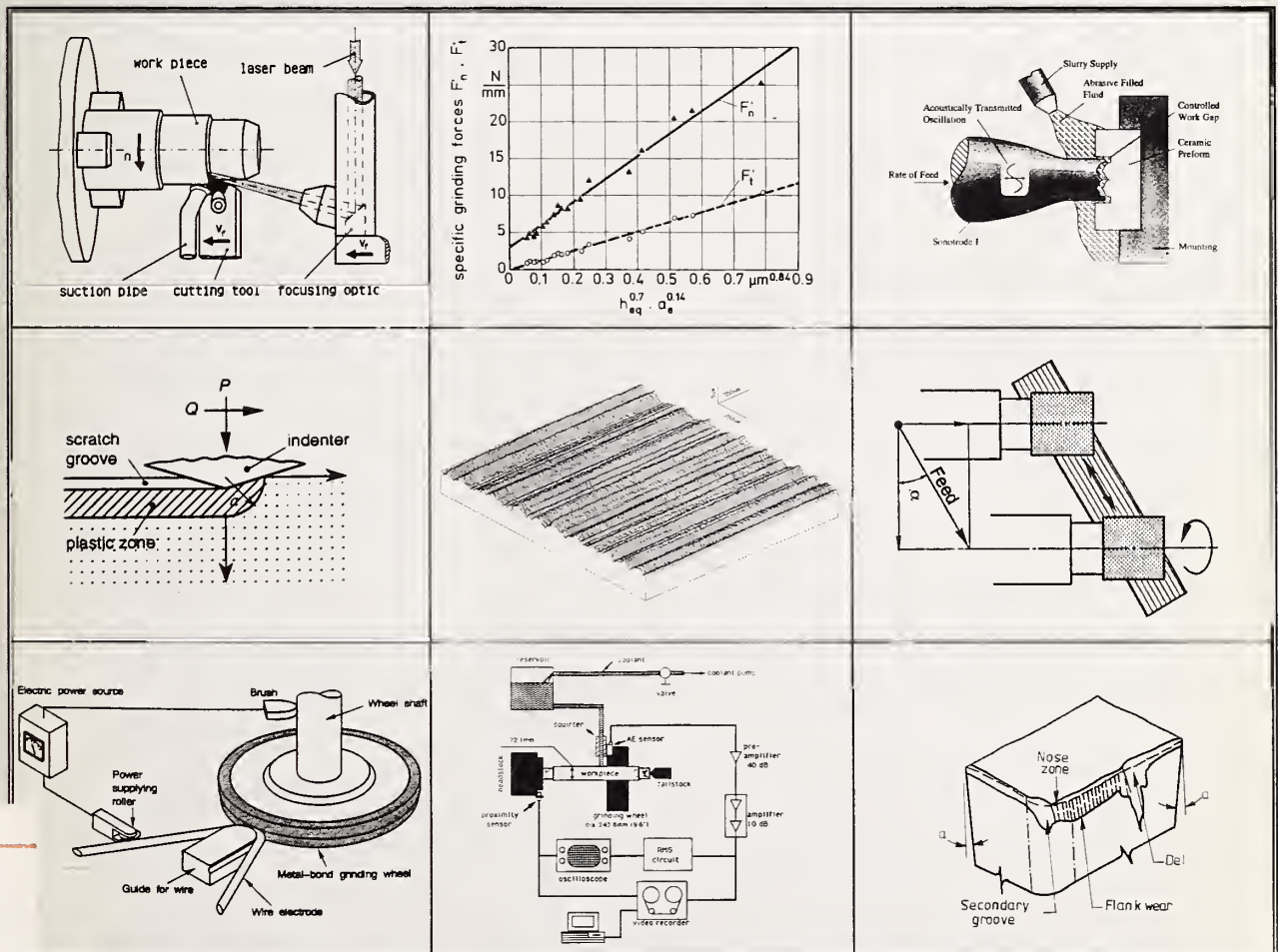
Machining of Advanced Materials

Proceedings of the International Conference on Machining of Advanced Materials
July 20-22, 1993
Gaithersburg, Maryland

Said Jahanmir, Editor

*T*he National Institute of Standards and Technology was established in 1988 by Congress to "assist industry in the development of technology . . . needed to improve product quality, to modernize manufacturing processes, to ensure product reliability . . . and to facilitate rapid commercialization . . . of products based on new scientific discoveries."

NIST, originally founded as the National Bureau of Standards in 1901, works to strengthen U.S. industry's competitiveness; advance science and engineering; and improve public health, safety, and the environment. One of the agency's basic functions is to develop, maintain, and retain custody of the national standards of measurement, and provide the means and methods for comparing standards used in science, engineering, manufacturing, commerce, industry, and education with the standards adopted or recognized by the Federal Government.

As an agency of the U.S. Commerce Department's Technology Administration, NIST conducts basic and applied research in the physical sciences and engineering and performs related services. The Institute does generic and precompetitive work on new and advanced technologies. NIST's research facilities are located at Gaithersburg, MD 20899, and at Boulder, CO 80303. Major technical operating units and their principal activities are listed below. For more information contact the Public Inquiries Desk, 301-975-3058.

Technology Services
- Manufacturing Technology Centers Program
- Standards Services
- Technology Commercialization
- Measurement Services
- Technology Evaluation and Assessment
- Information Services

Electronics and Electrical Engineering Laboratory
- Microelectronics
- Law Enforcement Standards
- Electricity
- Semiconductor Electronics
- Electromagnetic Fields[1]
- Electromagnetic Technology[1]

Chemical Science and Technology Laboratory
- Biotechnology
- Chemical Engineering[1]
- Chemical Kinetics and Thermodynamics
- Inorganic Analytical Research
- Organic Analytical Research
- Process Measurements
- Surface and Microanalysis Science
- Thermophysics[2]

Physics Laboratory
- Electron and Optical Physics
- Atomic Physics
- Molecular Physics
- Radiometric Physics
- Quantum Metrology
- Ionizing Radiation
- Time and Frequency[1]
- Quantum Physics[1]

Manufacturing Engineering Laboratory
- Precision Engineering
- Automated Production Technology
- Robot Systems
- Factory Automation
- Fabrication Technology

Materials Science and Engineering Laboratory
- Intelligent Processing of Materials
- Ceramics
- Materials Reliability[1]
- Polymers
- Metallurgy
- Reactor Radiation

Building and Fire Research Laboratory
- Structures
- Building Materials
- Building Environment
- Fire Science and Engineering
- Fire Measurement and Research

Computer Systems Laboratory
- Information Systems Engineering
- Systems and Software Technology
- Computer Security
- Systems and Network Architecture
- Advanced Systems

Computing and Applied Mathematics Laboratory
- Applied and Computational Mathematics[2]
- Statistical Engineering[2]
- Scientific Computing Environments[2]
- Computer Services[2]
- Computer Systems and Communications[2]
- Information Systems

[1]At Boulder, CO 80303.
[2]Some elements at Boulder, CO 80303.

Machining of Advanced Materials

Proceedings of the International Conference on Machining of Advanced Materials
July 20-22, 1993
Gaithersburg, Maryland

Said Jahanmir, Editor

Ceramics Division
Materials Science and Engineering Laboratory
National Institute of Standards and Technology
Gaithersburg, MD 20899

U.S. Department of Commerce
Ronald H. Brown, Secretary
National Institute of Standards and Technology
Arati Prabhakar, Director

PREFACE

Advanced materials, such as ceramics and composites, are being increasingly used in various applications. The high cost associated with machining and damage generated during machining are major impediments to the implementation of these materials. In some cases, current machining methods cannot be used and innovative techniques or modifications of existing methods are needed.

The present volume contains papers presented at the International Conference on Machining of Advanced Materials, held at the National Institute of Standards and Technology, Gaithersburg, Maryland, July 20-22, 1993. The goal of this conference was to strengthen communication and technology transfer among researchers and engineers involved in various aspects of machining as related to ceramics and composites. The following topics are included in these proceedings:

- traditional and nontraditional machining and finishing techniques,

- mechanisms of material removal,

- nondestructive evaluation and characterization of machining damage,

- effect of machining damage on performance and properties,

- sensors for in-process measurement of surface quality,

- special cutting tools and cutting/grinding fluids for advanced materials,

- new machine tool designs,

- novel concepts for machining of advanced materials, and

- machining of advanced materials for specialized applications, including biological implants.

Planning for the conference began in January 1992. Following the preparation of a preliminary program, several acknowledged leaders involved in research and technology development in machining of advanced materials were consulted to determine if such a conference was warranted. Since the response was positive, two committees were organized to assist in the planning and execution of the conference. The call-for-paper was mailed to more than 4000 engineers and research scientists worldwide with interest in the conference topic, and was published in Ceramic Industry, Mechanical Engineering, and Ceramic Bulletin. A total of 115 abstracts were received. Following review, 91 abstracts were accepted based on their technical content and compatibility with the goal of the conference. A total of 58 manuscripts were submitted to NIST. These papers were subjected to a thorough and critical review, and a total of 48 manuscripts were accepted. The revised manuscripts sent to NIST in a camera-ready format are included in this volume.

To accommodate the large number of papers without having parallel sessions, the papers were divided into oral presentations and posters. In addition to the published papers in these proceedings, 15 other presentations were included without publication.

This conference was co-sponsored by the National Institute of Standards and Technology - Ceramics Division, the National Science Foundation - Materials Processing and Manufacturing Program, and the U.S. Navy - Manufacturing Technology Program. The support and encouragement received from Steve Freiman, Bruce Kramer, and Phil Nanzetta are gratefully appreciated.

The members of the Organizing Committee and the Advisory Committee, listed on the following page, provided much needed expertise and assistance in formulating the plans and bringing the conference together.

This conference was endorsed by Ceramic Industry, the American Society of Mechanical Engineers, and the American Ceramic Society. These organizations assisted in publicizing the conference. I am grateful to Pat Janeway, Mildred DeVita, Shiv Kapoor, Paul Holbrook, and Ron Barks for their efforts and endorsement of the conference.

I am indebted to Kathy Kilmer and Lori Phillips of the NIST Conference Office, who made all the detailed arrangements for the conference. Many thanks to Vanessa Williams for her assistance in preparing the conference program and assembling the proceedings.

Said Jahanmir
National Institute of Standards
and Technology

COVER ILLUSTRATION

The cover illustrations were taken from the papers published in these proceedings. These illustrations indicate the broad coverage of topics presented in the conference.

DISCLAIMER

Information on product names, manufacturers, or suppliers are included in this report for clarification. This does not imply endorsement of the products or services by the National Institute of Standards and Technology.

TABLE OF CONTENTS

EFFECT OF GRINDING ON STRENGTH

PRECISION MACHINING

FREE ABRASIVE MACHINING

TURNING AND MILLING

LASER AND ELECTRICAL DISCHARGE MACHINING

GRINDING OF TECHNICAL CERAMICS

MACHINING OF CERAMIC COMPONENTS: PROCESS-TECHNOLOGICAL POTENTIALS

W. KONIG and A. WAGEMANN
Fraunhofer Institute of Production Technology, Aachen, Germany

In the production of ceramic components machining in the green state bears many advantages according to flexibility and economy. This holds true especially for small lot sizes when compared to forming processes like moulding and pressing. But unfortunately in the ceramic industry, in most cases, the process design in green machining is based only on experience. Therefore, approaches will be presented for an economic and quality consistent green machining process by applying the potentials of modern machine tools and cutting tools like PCD.

The situation is different in the area of fine machining of ceramics where numerous approaches have been presented in recent years towards optimizing the machining processes, which are already applied in industry such as grinding and lapping. From these investigations, limits can be derived with respect to process performance and quality.

Improvement of flexibility, economy and quality in fine machining is connected with the development of new ceramic machining technologies. Potentials will be illustrated for grinding with increased cutting speed and for electro discharge machining of conductive ceramics.

Introduction

A close-up look at the production of ceramic parts reveals that manufacturing cost and flexibility are determined less by the material used, or by processing, but rather by shaping. This process comprises not only the actual initial shaping (injecting, casting, pressing) but also green and white machining and finish-machining after sintering as shown in Fig. 1.

The technique of machining ceramic components before sintering offers a great potential to make shaping more flexible and less cost-intensive (1, 2). Green machining, in the case of small to medium quantities, permits the shaping process to be both flexible and economical in comparison with other shaping processes as the unit tool costs are lower. The deployment of geometrically simpler semi-finished products permits good levels of homogenity and distribution of density to be achieved in the green part, and thus high part quality after sintering. It also allows high levels of accuracy to be obtained in the sintered parts. This is of vital importance as after sintering, only a small amount of material must be removed in order to obtain the final geometry required; thus, shortening effectively the very time consuming and costly finish-machining step.

Finish-machining of the functional surfaces of a part is, however, unavoidable in most cases. The difficulties involved in machining sintered ceramics can result in up to 90 % of the part costs being incurred during this stage. A number of investigations have, therefore, already been undertaken into the common finishing methods such as grinding and lapping with a view to making finish machining more economical and,
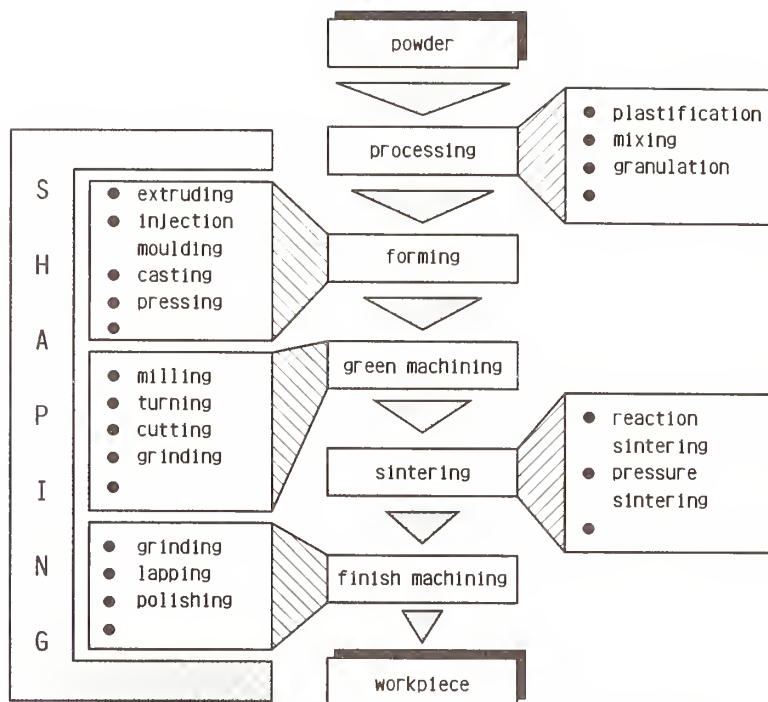
Fig. 1: Production steps of ceramic components

The diagram shows the production flow:

powder → processing → forming → green machining → sintering → finish machining → workpiece

SHAPING (vertical label on left):
- extruding
- injection moulding
- casting
- pressing

(connected to forming)

- milling
- turning
- cutting
- grinding

(connected to green machining)

- grinding
- lapping
- polishing

(connected to finish machining)

processing (right side):
- plastification
- mixing
- granulation

sintering (right side):
- reaction sintering
- pressure sintering

at the same time, more reliable in terms of quality.

The main technological potential offered by further improvements lies in the deployment of innovative machining methods. High speed grinding, electro-discharge machining and laser-assisted turning will be presented here as examples.

Green Machining

Green machining of small numbers of units in order to produce more flexibly at lower cost is an approach already adopted by the ceramics industry. Research shows, however, that there is little, if any, systematic understanding of the process design necessary for green machining. Company know-how is based mainly on experience; the technological reserves have not been tapped to a sufficient degree.

Technological reserves (Fig. 2) are not limited to the area of process control, i.e. the selection of machining parameters and the partition of machining steps. The use of suitably designed

tools and tool geometries specially adapted to the material is important, particularly for drilling or milling. Another factor of fundamental significance is the selection of the cutting tool material, or rather, of its exact specification. The example in Fig. 2 illustrates clearly the degree to which tool life and tool costs and, therefore, manufacturing costs can be influenced by the selection of cutting material.

A major problem which arises in green machining is the low level of strength of the material and the resultant problems in clamping and handling the parts (3). Clamping devices commonly used in metal working are frequently used to hold the parts. These devices, however, have major disadvantages with regards to the transfer of force and sensitivity. The use of vacuum clamping or flexible clamping elements offers options for improvement.

The situation concerning the machine tools available is similar to that of clamping devices. Here too, machine design and components are not adapted to meet the special requirements of green

4

Fig. 2: Technological potentials

The figure contains the following labels:

turning of pre-sintered SiC

flank wear: 0,25 mm; 0,20; 0,15; 0,10; 0,05; 0

cutting length l_c: 10 20 30 100 200 m 300

Technological Potentials

- process strategy
- tools
- new cutting materials
- ceramic adapted systems
  for clamping and handling
- adapted machine tool
  and peripherie

$v_c = 50$ $v_c = 100$ f α_o γ_o λ_s κ_r ε_r r_ε
[m/min] [m/min] [mm/r] [mm]

				α_o	γ_o	λ_s	κ_r	ε_r	r_ε
▲	△	0,1	HM K10	6°	0°	0°	90°	60°	0,8
●		0,1	PCD	6°	0°	0°	72,5°	35°	0,8
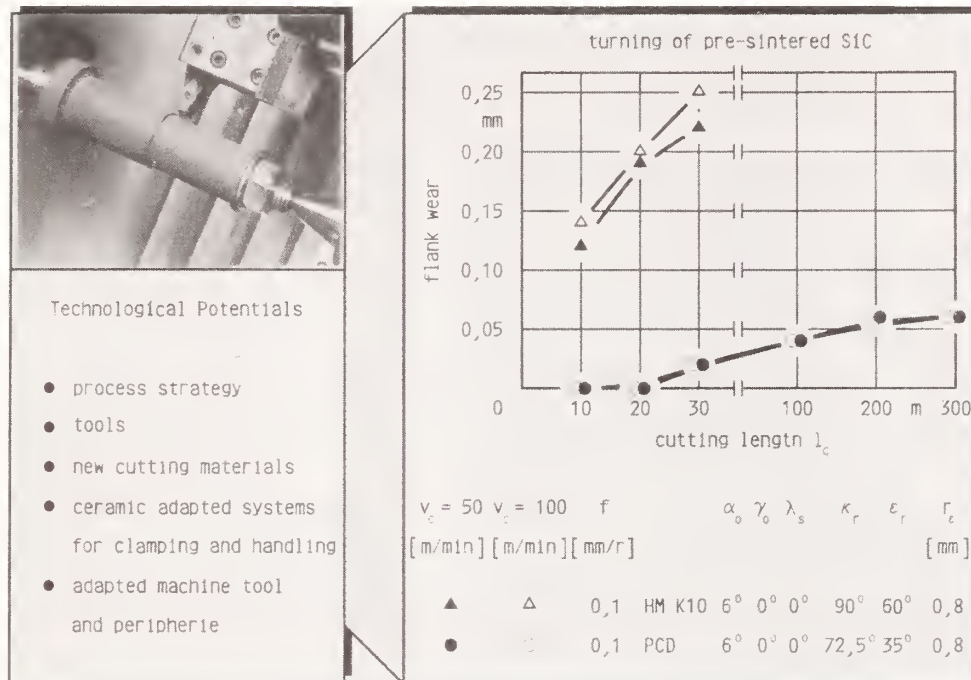
machining. The high abrasion of the particles removed, calls for corresponding designs to ensure the protection of the bearing and guide parts of the machine tool. Additionally, the use of modern cutting tool materials such as polycrystalline diamond (PCD) makes very high cutting rates and spindle speeds necessary.

Extraction and, in certain cases, separation and re-use of the materials extracted (i.e. chips) represents another important area in connection with green machining (4). At first sight, this appears trivial, but even extraction of the particles removed, directly at the point of cut presents a problem when modern machine tools are in use due to a lack of space.

Some of the potentials indicated can be considered independently of the material to be machined (machine design and periphery, clamping tools), whereas the other areas are determined largely by the composition or the properties of the green material (in this context the term "green material" also shall include materials, which are pre-sintered to increase their strength). Consequently, knowledge of material-specific behaviour is vital to the determination of the machining parameters. In order to be able to define a machining strategy, it is, therefore advisable to have a method of characterisation of the machinability. It would then be possible to draw up definitions of ranges in which machining can be carried out profitably.

Two examples will now be presented of an approach which permits appropriate ranges for feed rate and infeed to be defined effectively in the context of turning. Figure 3 defines the variables, used in the following to describe the turning process.

The test, referred to in the following as cone turning test involves turning off cylindrically a pre-turned cone made of the material in question so that the infeed changes in the course of the cut. The relationship between infeed and surface quality is now instantly identifiable for each feed rate. In the case of pre-sintered SiC (Fig. 4), it emerges, for example, that surface quality deteriorates with diminishing infeed. In practice this means that the concluding finish cut, which is appropriate in some other cases, actually

5

results here in lower surface quality.   When this interrelationship is considered for
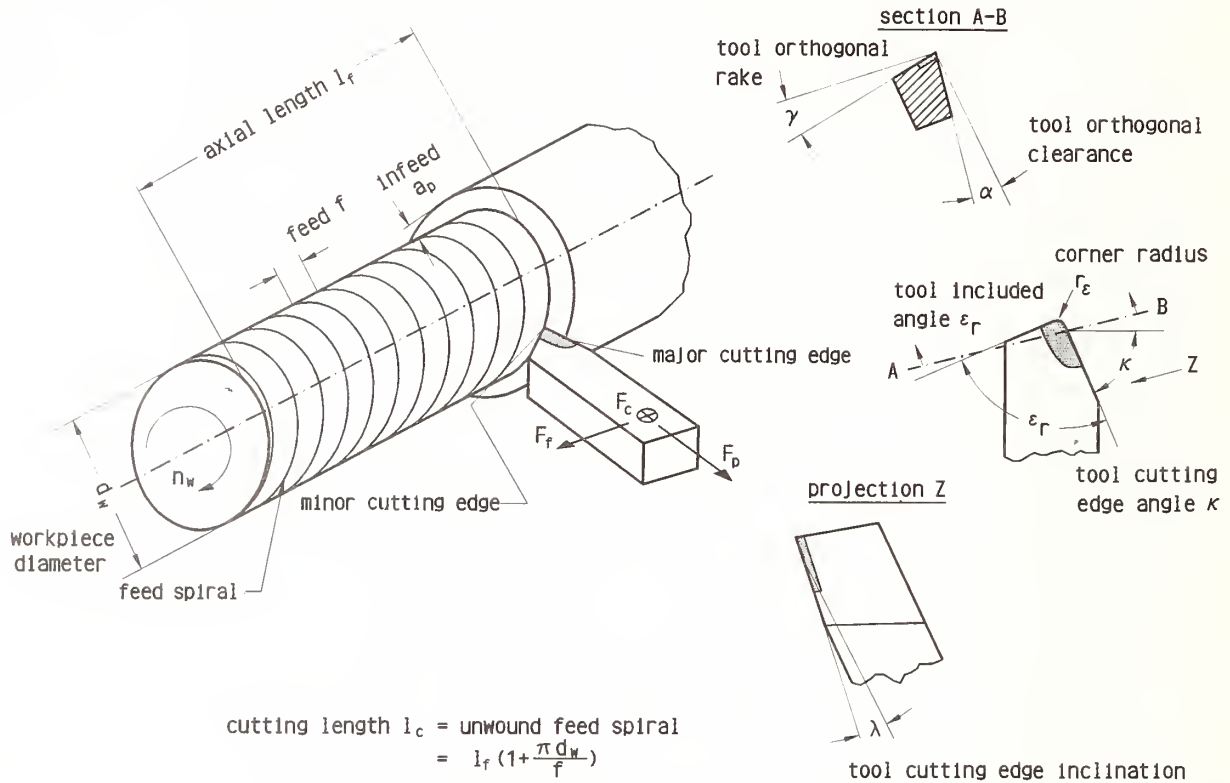
Fig. 3: Characteristics of turning process and -tool
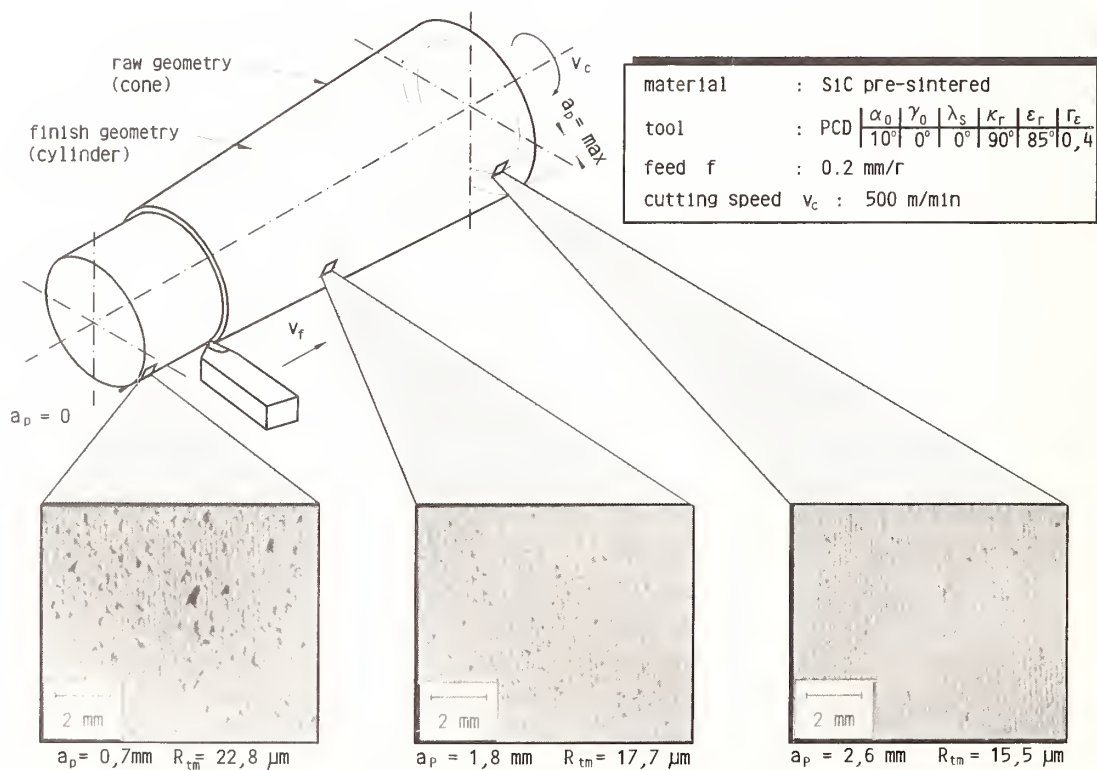
Fig. 4: Cone turning test at pre-sintered SiC

6

various feed rates (Fig. 5), it becomes clear that the infeed required, increases with feed and that there is a feed range in which the infeed is not critical (in Fig. 5 for f = 0.1 mm/rev).

machining process. In contrast, when Al_2O_3 is machined, short chips are formed due to the approximately 8 % proportion of binder in the green part. Material removal is characterised here
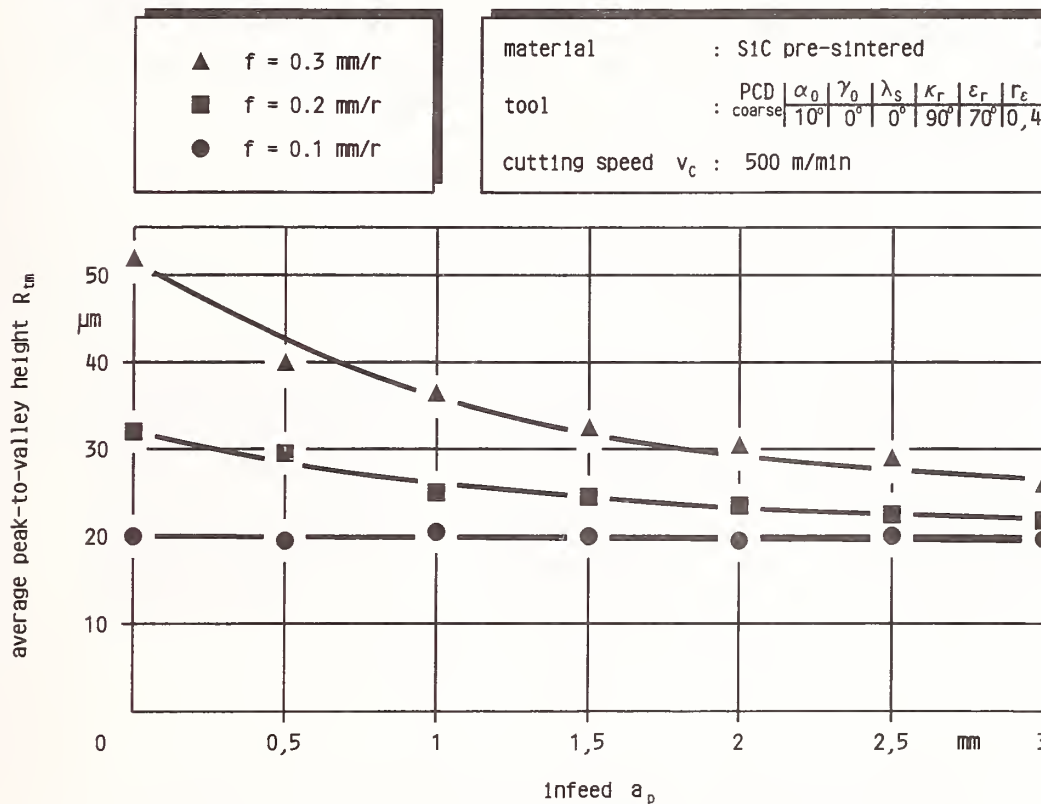
Fig. 5: At pre-sintered SiC the roughness decreases with increasing infeed

Monomer-cast Al_2O_3 behaves quite differenly. This material has very favourable properties as regards green machining since it combines high strength with almost plastic chip formation as is shown in the detailed photo in Fig. 6, on the left. Here too, there is a clear interdependency between infeed and surface quality which is, however, exactly the reverse to that in the case of the SiC shown. The almost ductile chip formation is conducive to the achievement of a surface without any spalling, the roughness of which is characterised only by feed grooves.

It seems likely that the completely different dependencies between infeed and surface quality obtainable are attributable to the fundamentally different chip formation mechanisms. Pre-sintered SiC is susceptible to brittle fracture and unconnected particles are removed in the

less by brittle fracture than by ductile chip formation.

The two examples described, indicate that the cone turning test is a simple means of defining favourable ranges for the parameters feed and infeed and can thus supply standards for process design. Besides feed and infeed, cutting speed is an important influencing variable in the machining process.

In contrast to feed and infeed, cutting speed exerts little influence on surface quality. By increasing the cutting speed, the proportion of cutting time of the machining process can be reduced without impairing the quality.

The reduction in cutting time is not the only benefit to be gained from increased cutting speed. Higher cutting speed also results in reduced tool

7

raw geometry
(cone)

finish geometry
(cylinder)

n

a_p = max

v_f

a_p = 0

material	: Al_2O_3, green state						
tool	: PCD	α_0	γ_0	λ_s	κ_r	ε_r	r_ε
		$10°$	$0°$	$0°$	$90°$	$85°$	$0,4$
feed f	: 0,2 mm/r						
cutting speed v_c	: 500 m/min						

0.5 mm   0.5 mm   0.5 mm

a_p = 0,05 mm R_{tm} = 4,2 µm a_p = 1,0 mm R_{tm} = 5,9 µm a_p = 1,95 mm R_{tm} = 10,4 µm
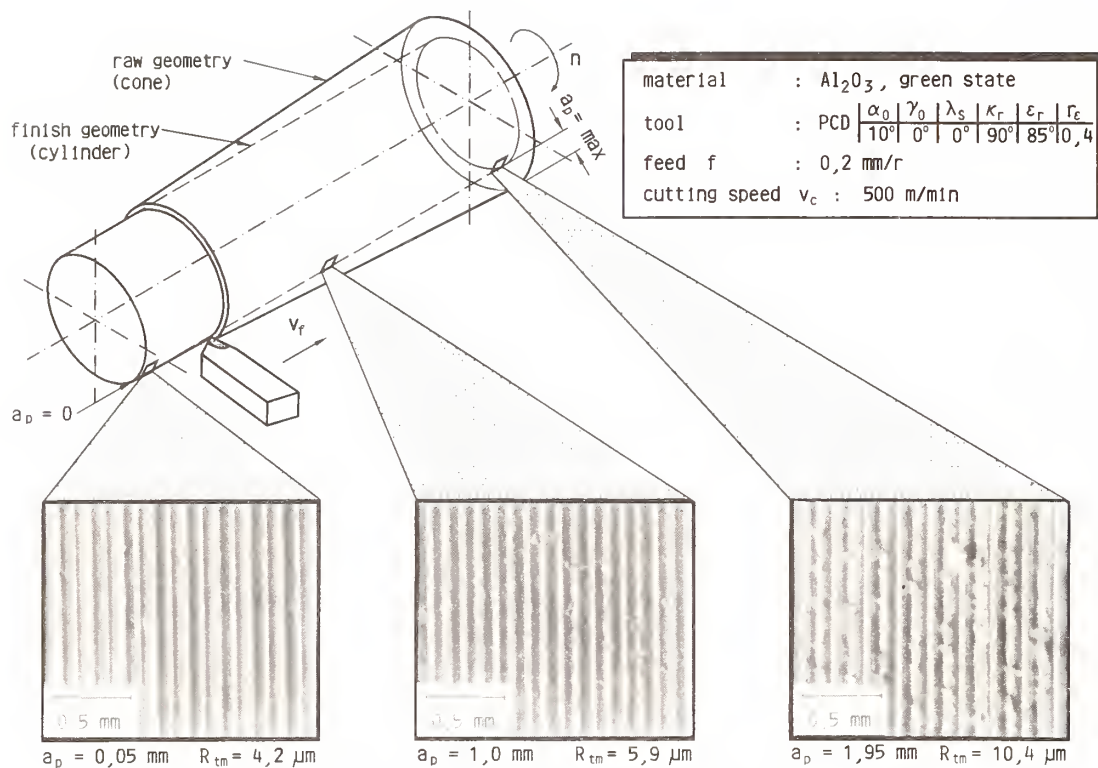
Fig. 6: Cone turning test at monomer-cast Al_2O_3

● v_c = 60 m/min
■ v_c = 100 m/min
▲ v_c = 200 m/min

material	: SiC pre-sintered						
tool	: PCD	α_0	γ_0	λ_s	κ_r	ε_r	r_ε
	coarse	$4°$	$0°$	$0°$	$100°$	$70°$	0
feed f	: 0.2 mm/r						
infeed a_p	: 2 mm						
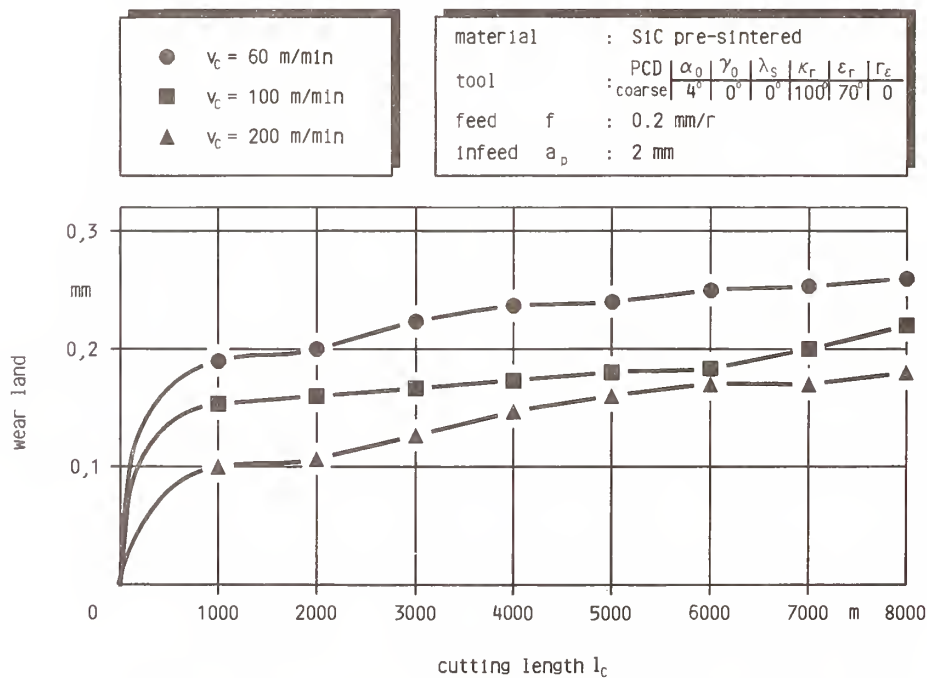
Fig. 7: The tool wear decreases with higher cutting speed

wear. It should be noted at this point, however, that the level to which cutting speed can be raised is limited by the machinery currently available and by the strength of the material

(stress caused by centrifugal forces).

The interrelationships so far described relate only to the influenece of process parameters. Other means of influencing the process behaviour are tool design and the selection of cutting tool materials. The comparison of different cutting materials in Fig. 2 shows tool life of approximately 30 m for pre-sintered SiC. In the case of PCD, as shown in Fig. 7, tool life is prolonged by a factor of 100 while cutting edge wear remains unchanged. Additionally, as previously described, substantially higher cutting speeds can be reached thus further cutting costs. Despite its higher purchase price, PCD is likely to prove economically viable as a cutting material for this application.

type of bonding phase offers an additional means of influencing wear via the cutting tool material.

Another way of exerting influence on tool life is by adapting the tool geometry, in particular that of the tool corner radius since this is the area most affected by wear. Evidence of this is provided by a comparison of two tools made of identical material but with different cutting edge geometries. A sharp cutting edge corner is subjected to particularly high stress and, therefore, demonstrates considerably more pronounced levels of wear than the rest of the cutting edge. As shown in Fig. 9, the greatest level of wear appears at the corner of the cutting edge. In the case of a tool with a corner radius, the stress exerted on the corner is distributed along the circumference of the corner radius. The
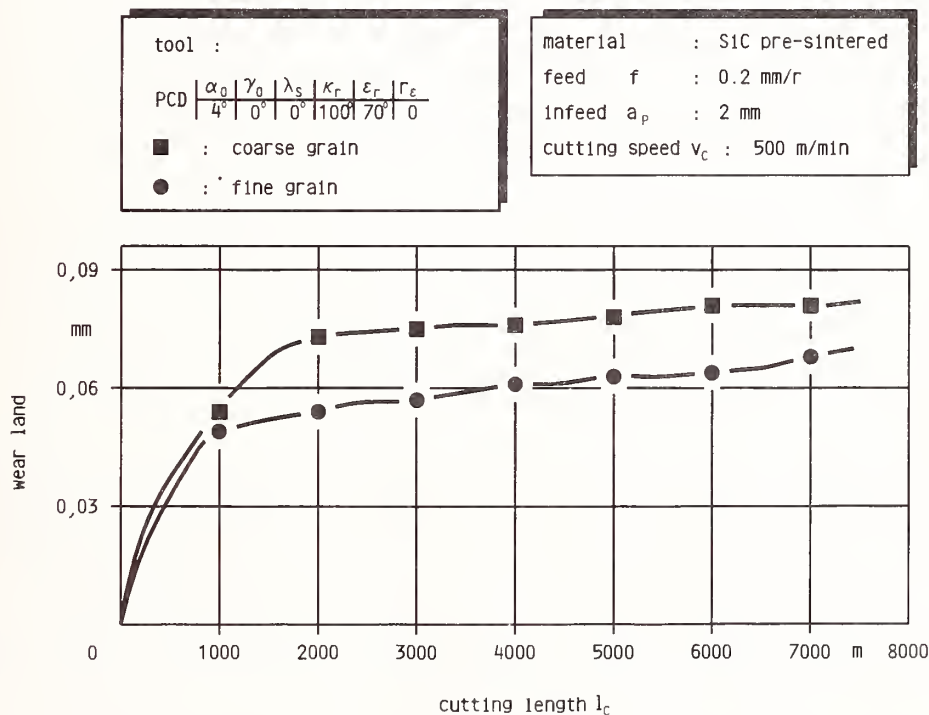
Fig. 8: Tool wear is influenced by PCD-grain size

The decision as to the cutting material to be used involves the selection of a group of cutting tool materials as well as its exact specification. The wear curves plotted in Fig. 8 show that in the case of PCD, tool life can be influenced by the grain size used. Finer diamond grain result in better tool life behaviour. In the case of PCD, the

cutting edge and corner, therefore, demonstrate uniformly low signs of wear.
This relationship is of major importance since a tool which has a corner radius does not suffer much from shifting of the cutting edge; the dimensional accuracy of the workpiece is consequently high.

9

These interdependencies show that when the technique of green machining is applied, analysis of the cutting process in conjunction with the use of modern tools and machine tools adapted to the requirements of green machining offers considerable potential for more flexible and more economical production of ceramic components.

While these mechanisms can be set by the creep feed grinding process in surface grinding operations, this variant cannot be applied to the ubiquitous peripheral grinding operations. The cutting forces which occur as a result of the increased contact length in peripheral creep feed-grinding are so high that a workpiece either can

tool :

PCD coarse	α_0	γ_0	λ_s	κ_r	ε_r
	10°	0°	0°	90°	85°

● edge radius r_ε = 0,4 mm
■ edge radius r_ε = 0 mm

material : SiC pre-sintered
feed   f   : 0,2 mm/r
infeed a_p : 2 mm
cutting speed v_c : 200 m/min
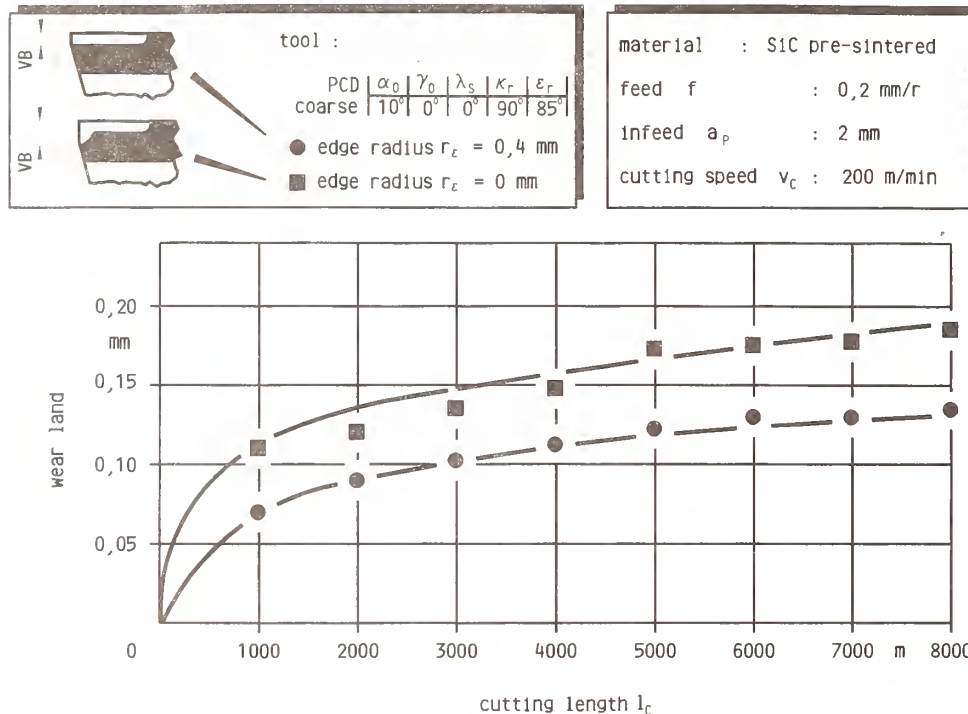
Fig. 9: The flank wear is substantially determined by the corner radius

High Speed Grinding
Comprehensive investigations into the grinding of ceramic have shown that by ensuring favourable cutting conditions at the individual cutting edge when grinding advanced ceramic, it is possible to effect a process with minimum surface damage.

Depending on material and the process parameters, removal can be mainly ductile or brittle. While brittle material removal is more favourable in terms of energy, as grinding can be carried out with low cutting forces, predominantly ductile material removal is currently believed to be necessary in order to obtain high part quality. This is achieved by ensuring small chip thickness at the individual cutting edge and a relatively large rounded tip radius of the cutting edge.

no longer be held between centers or is destroyed. In general, very strong workpiece deformation occurs due to the high cutting forces. This results in time-consuming finishing operations in order to obtain the level of dimensional and form accuracy required.

Chip thickness can, therefore, be reduced only via the following process parameters:
- higher diamond concentration
- smaller diamond grain size
- increased cutting speed
- reduced workpiece rotational speed
in the case of peripheral grinding at a constant material removal rate.

With regards to tool specification and workpiece rotational speed, changes can be made only

within certain ranges. Tools with fine grains (D < 91 µm) cannot be used for roughing as the diamond grains would become overstressed and would break off. It is very difficult to dress tools which are too highly concentrated (> C 100) as the increased number of diamond grains offers considerable resistance to the dressing tool.

Reduced workpiece rotational speed results in high infeed per revolution in plunge grinding operations. The effect of this is increased contact distance, and thus, a higher number of cutting edges engaging at one time. At a constant removal rate, this transition to creep feed grinding results in forces which are too high and, therefore, in substantial form deviation.

Our own investigations into high speed grinding of ceramic support the findings related to enhanced surface quality initially derived theoretically, as Fig. 10 shows using traverse grinding as an example.

This result is independent of tool type. While use of tool-type A (resin-bonded) is approved up to a cutting speed of only 63 m/s, when higher cutting speeds are required, the best surface qualities can be obtained using tool type-D (vitrified bonded) at v_c = 100 m/s. These surface qualities correspond approximately to those of dressed functional surfaces in spite of the relatively high removal rate. Tool wear is not increased in comparison with conventional grinding conditions.
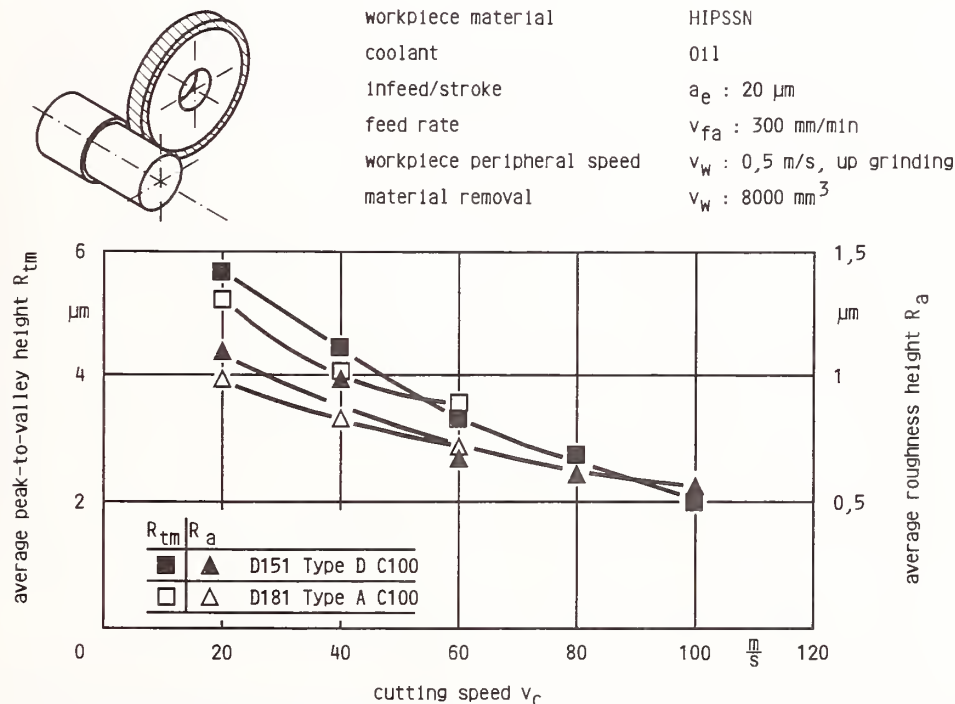
Fig. 10: Higher cutting speeds permit improved surfaces

In contrast, theoretically at least, higher cutting speed permits decreased chip thickness and, at the same time, lower cutting force, at a constant material removal rate. Higher cutting speed results in reduced chip thickness at a constant material removal rate and thus in lower forces on the individual grain.

Increased cutting speed from the currently standard range of 20 - 50 m/s to up to 150 m/s, however, requires grinding wheels specially designed for such speeds and adapted grinding machines. In terms of the grinding machine, this means the use of spindle and balancing systems for higher rotational speeds and stronger machine protection. This does not pose any major

problems due to the steadily expanding application of CBN (Cubic Boron Nitride) high speed grinding, but does, in general, mean higher machine costs.

The tool itself, however, is a critical factor. Initially the problem lies in the higher thermal stress to which the diamond is subjected by the high cutting speeds. Additionally, the centrifugal force exerted by high rotational speed, subjects the diamond layer to high stress levels. This poses problems particularly for the multi-layer diamond tools.

Knowledge of the radial expansion occurring when CNC-machines are used is, however, extremely important. Due to safety regulations geometrical reference values are frequently determined when the machine is at a standstill. At a cutting speed of 120 m/s an absolute change in geometrical dimensions of 30 μm is caused.

High speed grinding is beneficial especially when CNC machines are used. The high removal rates obtainable using this method reduce the machining time. This is of major significance where high machine hourly rates are concerned.

material	AlMg45MuF27
outside wheel diameter	d_s : 500 mm
inside wheel diameter	d_1 : 203,2 mm
wheel width	b_s : 10 mm
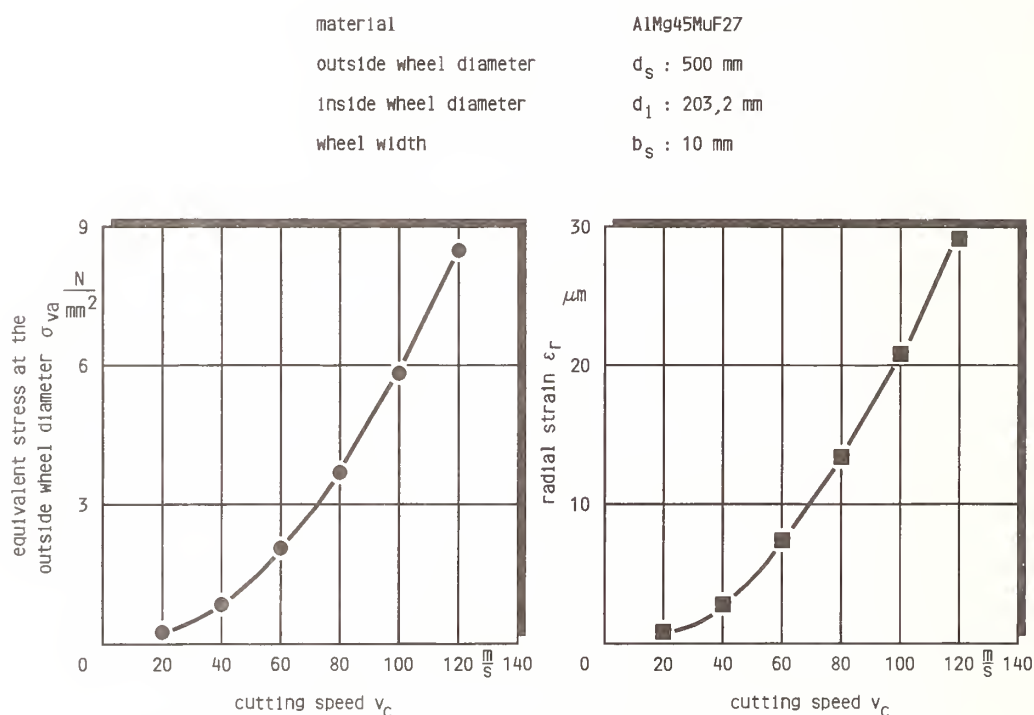
Fig. 11: Higher cutting speed causes increased radial tool strain

An appraisal of the radial strain and of the equivalent stress on the outer diameter of a conventional grinding wheel to be used for machining ceramic illustrates the problem (Fig. 11). A mathematical model was used for this purpose (5). The equations on which the calculations rest, are based on the two-dimensional equilibrium analysis of the forces occurring in a co-rotational frame.
In this example, the model indicates that the stress to which the outer diameter of the tool is subjected to centrifugal force is negligible.

Electro Discharge Machining
Complex moulds or holes either cannot be manufactured at all using industrially established methods such as grinding or lapping, or can be manufactured only in time-consuming, expensive operations. The deployment of electro discharge machining, which has already proved its worth in the manufacture of tools in the metal working industry, is a viable option in such cases. Although this method requires the material to have some degree of conductivity (6), it is independent of the material's mechanical

characteristics (6).

The thermal material removal process effected by EDM is characterised by the removal of material in a solid, liquid or gaseous state. The energy required for the cutting operation is supplied in the form of temporary electrical discharges (arc). The material removal process occurs in a dielectric fluid (Fig. 12) which serves on one hand as an insulator between workpiece and tool and on the other as a means of removing the particles caused by the removal operation.

surface cut by electro discharge machining (7). The free silicon between the SiC grains is removed and whole grains break out as a result. The reason for this is the high conductivity of the free silicon. This encourages the base of the plasma channel to form on the Si-bonding phase and to result in material removal there.

The roughness achievable can be influenced mainly via the impulse frequency of the discharges. Due to a rise in the contamination of the work gap, the higher impulse frequency
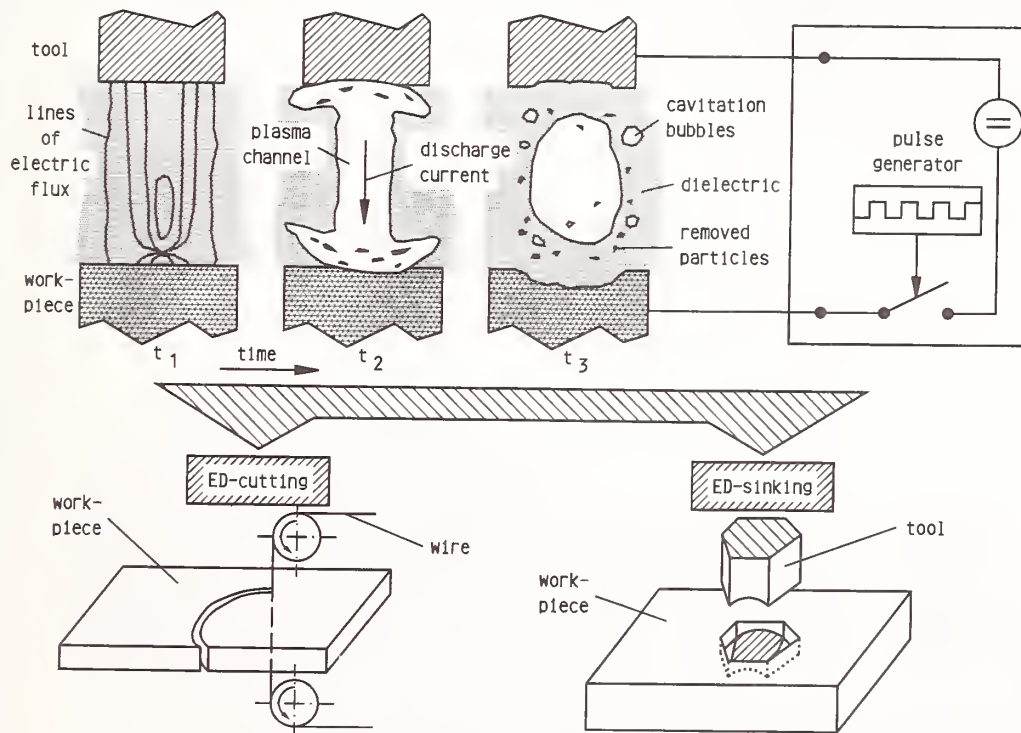
Fig. 12: Principle of Electro Discharge Machining

In general, a distinction can be drawn between electro discharge-sinking and electro discharge-cutting (Fig. 12). Electro discharge cutting has already been mastered to a high level and is, therefore, the most suitable for industrial application. This method permits prismas and holes of any contour with flank inclination angles of up to 30° to be manufactured.

Silicon-infiltrated silicon carbide, is by virtue of its 10 - 15 % ratio of free silicon particularly suitable for electro discharge machining. Figure 13 shows the polished cross-section of a SiSiC

results in enhanced re-ignition conditions for the arc and thus in more pronounced removal of the Si phase, or rather, in increased roughness. The rate of discharge and impulse duration are of less importance to surface roughness. However the risk of thermally induced crack formation causing damage to the surface rises with increasing impulse duration.

Electro-discharge machining also exerts influence on part strength. Machining tests show that bending strength changes with roughness. Investigations into other machining methods
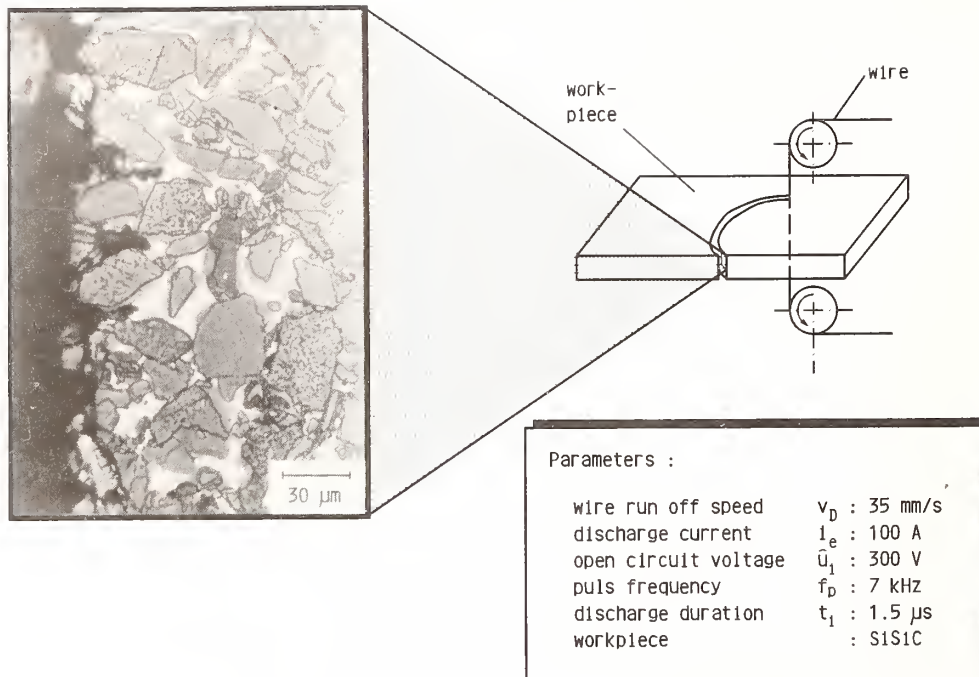
Fig. 13: Relief of ED-cut SiSiC surface
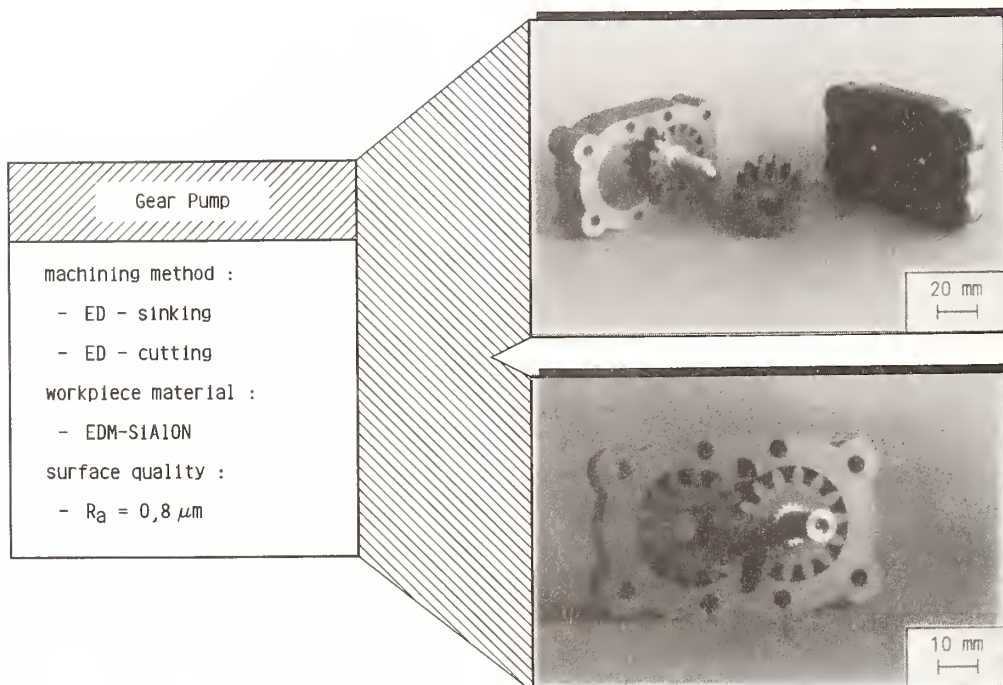
Fig. 14: ED-cut gear pump

show, however, that it may not be concluded that any correlation exists between roughness and strength. Strength and Weibull modulus levels are low in comparison with creep feed grinding or lapping. The Weibull modulus can, however, be increased to a value of 40 with a uniform degree

of strength by trimming the contours at low impulse frequency (8).

The gear pump in Fig. 14 is an example of the excellence this method has to offer. However it has not yet established itself industrially for the machining of ceramics. In view of the fact that this method permits the economically viable manufacture of parts and batch sizes which cannot otherwise be manufactured economically, any deterioration in workpiece properties which may arise from the adjustment of the electric conductivity is acceptable.

Laser Assisted Machining

Provided due account is taken of the strength behaviour of ceramic which is dependent on temperature, it is possible to machine sintered parts with a defined cutting edge. In the case of silicon nitride, there are amorphous areas at the grain boundary of the largely crystalline structure which result in a softening of the material at a temperature of approximately 1100°C. This permits the heated material to be machined in a turning operation, for example.

suitable for use as a source of energy to heat the material. The laser beam is connected via an optic on the second carriage of a lathe. The beam is thereby directed onto the shearing zone via the tool cutting edge. A CBN turning tool carries out the cutting operation.

When suitable machining parameters are selected, surface qualities are achieved comparable to those obtained in grinding operations. Even cracks, which would be expected to form as a consequence of the thermal stress on the part during the process have not, to date, been in evidence.

Laser-assisted turning offers advantages over the established grinding operations - particularly in the manufacture of parts with complex geometries since it is much easier to use suitable forming tools and to change tools. The interrelationships explained, indicate that the technology of laser-assisted hot machining can be successfully deployed even in hard machining operations involving ceramic components.
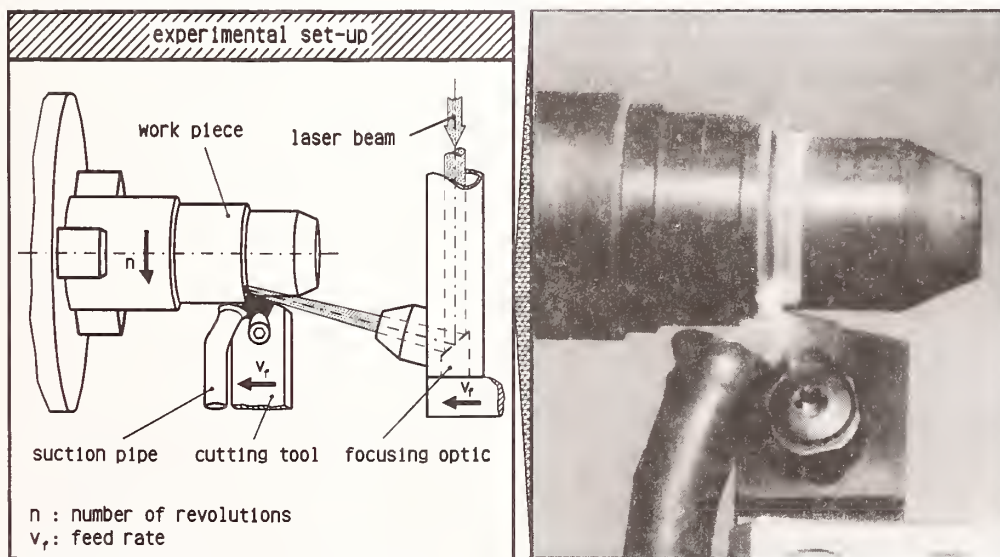
Fig. 15: Principle of Laser Assisted Turning

Figure 15 shows a design of a machine suitable for such applications (9). The very high energy density, good dosability and the narrow heat-affected zone of a laser make it eminently

Summary

The examples of different methods given, show that in the field of shaping, there is considerable room for improvement in terms of both quality

15

and economic viability in green machining and finish machining operations after sintering. As regards green machining, the lack of a systematic understanding of the process is the greatest drawback. Additionally, the tools and machine tools used are insufficiently adapted to the requirements of green machining.

The area of finish machining has already been the subject of a number of research studies and has advanced continuously. It should be noted that processes such as high speed grinding, electro discharge machining and laser-assisted turning, for example hold out prospects of the deployment of innovative machining technologies as well as of continued optimization of industrially established methods.

Literature

1. W. König, E. Verlemann, A. Wagemann, "Zeitgemäße Konzepte für die Keramik-fertigung, "Fortschrittsberichte der DKG, Vol. 7, No. 4, pp. 27-39, 1993

2. D.L. Halcomb, M. C. Rey, "Ceramic Cutting Tools for Machining Unsintered Compacts of Oxide Ceramics," Ceramic Bulletin, Vol. 61, No. 12, 1982

3. W. König, A. Zaboklicki, "Laserunter-stütztes Drehen von Keramik," vorge-sehen zur Veröffentlichung in VDI-Z, No. 7, 1993

4. G. Spur, "Keramikbearbeitung," C. Hanser Verlag, München, Wien 1989

5. W. König, F. Ferlemann, "CBN-Schleifscheiben für 500 m/s Schnitt-geschwindigkeit," IDR, No. 4, pp. 222-251, 1990

6. W. König, D.F. Dauw, G. Levy, U. Panten, "EDM, "A Future Step Towards the Machining of Ceramics," CIRP Annals, Vol.37, No. 2, 1988

7. W. König et al., "Qualitätssichere Endbearbeitung in der Serienfertigung keramischer Bauteile," Abschlußbericht zum BMFT Projekt Nr. 03M2011B 0, Aachen 1989

8. U. Panten, "Funkenerosive Bearbeitung von elektrisch leitfähigen Keramiken," Dissertation RWTH Aachen 1990

9. W. Spang, "Mechanische Bearbeitung von Hochleistungskeramik," Internationale Zeitschrift für Technik und Wirtschaft, Vol. 43, No. 2, 1989

HIGHLY EFFICIENT FINISHING OF CERAMICS BY HELICAL SCAN GRINDING

K. SUZUKI
Nippon Institute of Technology, Saitama, Japan

T. UEMATSU
Toyama Prefectural University, Toyama, Japan

T. NAKAGAWA
University of Tokyo, Tokyo, Japan

A highly efficient finishing method in grinding of ceramics has been developed. In this method, named "Helical Scan Grinding", a straight wheel or a mounted wheel is fed at an angle from the direction of grinding velocity. Such motion can be realized easily on an NC grinding machine. This method has a feature that a wheel with coarse diamond grains can be used in finish grinding, leading to high efficiency finishing. Experiments showed that surface roughness was improved with the angle. When a cermet workpiece was ground with a mounted diamond wheel of mesh size 100/120, while the surface finish was Rmax=4.2μm(maximum peak to valley height) in the normal grinding or at an angle of 0 degree, the surface finish in the helical scan grinding at an angle of 45 degree was Rmax=0.6μm, about one seventh of that in the normal grinding. The helical scan grinding produced similar effects on silicon nitride, silicon carbide, and hard metals. This method is applicable to both flat and curved surfaces, and also to polishing of stainless steel with a wheel type abrasive brush.

1. INTRODUCTION

Ceramic materials have many superior properties; it is expected that they will play an important roll in the field of mechanical parts in near future. In fact, some kinds of engineering ceramics have already been used successfully in, for example, automobiles and machine tools. It is well known that machining of ceramic materials is very difficult. Usually, they are machined on a grinding machine with diamond grinding wheels; but the efficiency is extremely low. The efficiency has been improved by adoption of rapid feed deep grinding and by the development of a grinding center(1).

Recent studies on grinding of ceramics are directed to obtain very smooth surfaces. Conventional methods of obtaining smooth surfaces are to use grinding wheels with small abrasive grains. But, the efficiency is not sufficiently high enough to meet the demands.

In this paper, a highly efficient finish grinding method named "helical scan grinding method", which utilizes an inclined spindle or special movement on an NC grinding machine, is described.

2. HELICAL SCAN GRINDING METHOD

Finish grinding has conventionally been carried out in the following manner: ①by adopting a grinding wheel with fine abrasive grains, ②by adopting slow feed speed, and ③by adopting small depth of cut. But, stock removal rate by this approach is inevitably very low. The proposed "helical scan grinding" can be implemented to obtain better surface finish at high rates of stock removal. This method is realized by inclining a wheel axis relative to feed direction, as shown in Figure 1(a), which results in reduction of actual distance between adjacent abrasive grains. Accordingly, this method has a feature

17

that a wheel with coarse grains can be used in finish grinding, leading to high efficiency finishing.

3. EXPERIMENTAL SETUP AND CONDITIONS

For realizing the proposed finish grinding method, a specially designed machine tool with an inclinable spindle is necessary. But currently, such a grinding machine is not available. In the present experiments a horizontal machining center was used to yield the same effect as an inclined spindle. A straight wheel or a mounted wheel was fed, as shown in Figure 1(b), so as to form an angle between the feed direction and the direction of grinding velocity by utilizing two-dimensional movement of an NC machine tool.

Metal bonded diamond grinding wheels were used because they have a sufficient strength to endure high axial grinding forces. Workpiece materials were cermet, silicon nitride, silicon carbide, tungsten carbide and aluminium oxide. Grinding fluid was chemical soluble type grinding fluid(dilution:1/50).

4. RESULTS AND DISCUSSION

4.1 Influence of Helix Angle

Figure 2 shows the effect of the helical scan grinding method in grinding cermet material with a rather coarse wheel(SD100) having D=30mm in diameter and 20mm in length. Figure 3 illustrates photographs and profile curves of surfaces ground at different helix angles. Judging from the photographs, the surface finish seems to be rather worse. But the roughness proved that the helical scan grinding improved surface finish significantly. Grinding by a normal method, with helix angle $\alpha=0°$, resulted in a surface roughness of Rmax=4.2μm(maximum peak to valley height). However, grinding by the helical scan grinding method with helix angle of $\alpha=45°$, improved the surface roughness to Rmax=0.6μm. This indicates that the helical scan grinding method could yield 7 times superior surface finish. Though much improvemenon in surface roughness has been achieved in the proposed method, micro waviness is observed on the surface in certain conditions. This
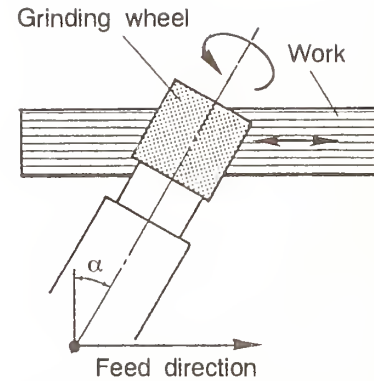
(a)Inclined spindle method
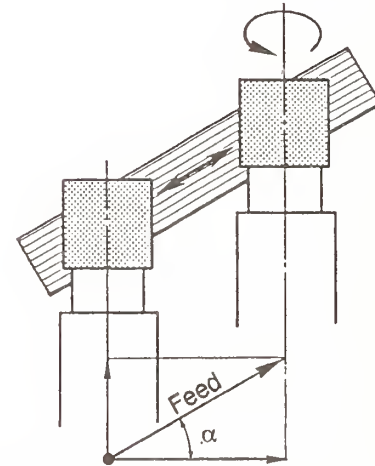
(b)Helical scan grinding on NC machine

Fig.1 Schematic principle of helical scan grinding method.
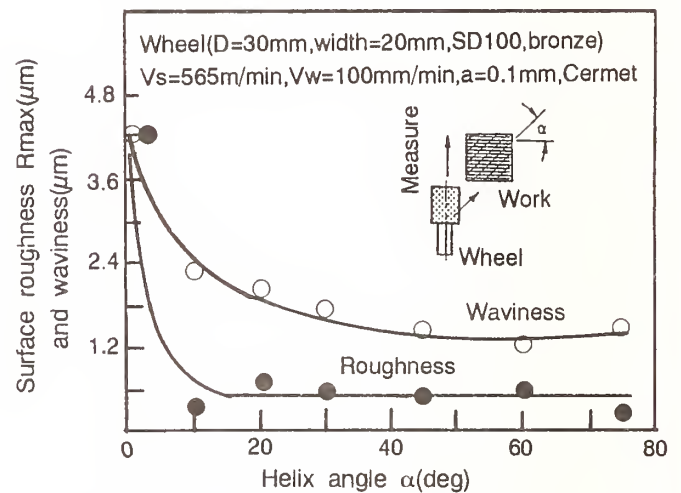
Fig.2 Improvement of surface roughness in helical scan grinding.

phenomenon may be due to the lack of straightness of the wheel along its axis. However, waviness is better than conventional grinding.

18

Figure 4 shows a relation between feed speed Vw and surface roughness ground by helical scan grinding at a helix angle of $\alpha=45°$ and depth of cut a=0.1mm. Figure 5 shows a relation between depth of cut and surface roughness at $\alpha=45°$ and Vw=100mm/min. The smaller the depth of cut or/and feed speed, the smaller the surface roughness and waviness. It is worth noting that such a smooth surface with Rmax=0.3μm was obtained inspite of the coarse grain wheel with 100 mesh size.

4.2 Helical Scan Traverse Grinding Method

In grinding of a wide surface, traverse grinding is usually used. Here the helical scan grinding method was adopted in traverse grinding. Figure 6 shows the surface profile curves obtained by grinding in three different grinding methods, i.e., conventional grinding, helical scan grinding($\alpha=45°$) and traverse helical scan grinding($\alpha=45°$, traverse pitch p=0.2mm) for the cermet material with 100 mesh diamond wheel. The waviness was successfully reduced in traverse grinding, though surface roughness in both helical scan grinding methods improved to almost the same extent.

Figure 7 shows the result of the three grinding methods for cermet with a straight grinding wheel(D=125mm, b=13.5mm, SD200). In this case, the surface roughness by helical scan method is Rmax=0.3μm, whereas it is higher at Rmax=1.8μm in conventional grinding. Both helical scan grinding methods show little waviness with almost the same surface roughness values, probably because straightness of the wheel was good by an appropriate trueing by "on-machine electrodischarge trueing method"(2).

4.3 Influence of Workpiece Material

As a next step, the helical scan grinding method was applied to sintered tungsten carbide(WC), silicon nitride, silicon carbide, and aluminium oxide. For the former three materials, the helical scan grinding method yielded remarkable effect in improving surface roughness. But in case of aluminium oxide, the improvement of surface roughness was
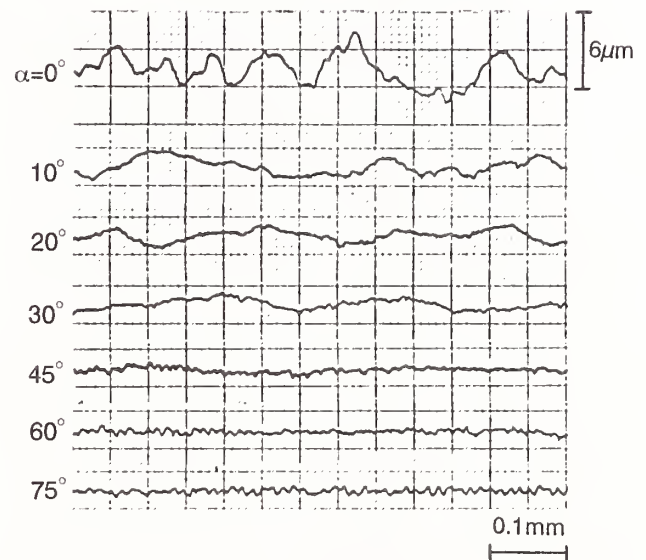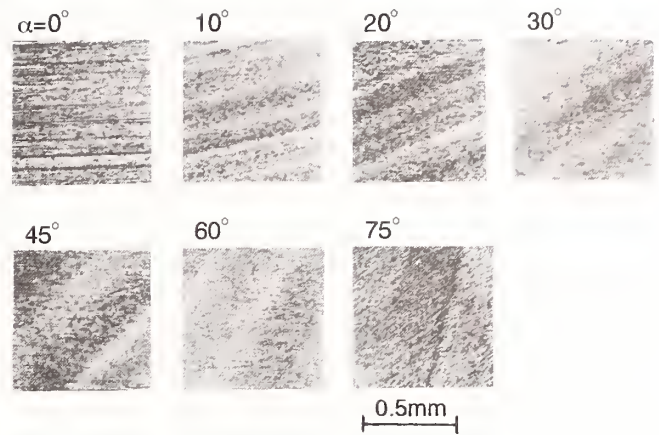
Fig.3   Surface appearance and profile curves in helical scan grinding.
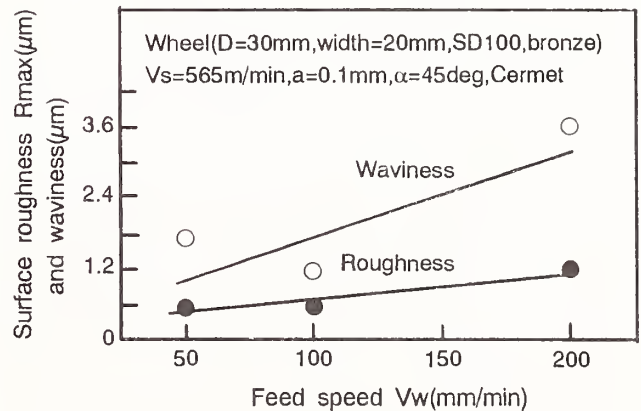
Fig.4   Relation between roughness, waviness and feed speed.

only by a factor of two, which was rather a small improvement compared with the other materials. This result indicates that the effect of the helical scan grinding method in improving surface roughness may depend on the workpiece material.

4.4 Application to Finishing of Curved Surface

Automobile parts made of ceramics are increasing. They often require rather smooth surface finish. Here, the helical scan grinding method was applied to finish grinding of the curved surface of rocker arm pads made of hot pressed silicon nitride.

A straight wheel(D=150mm,b=15mm,SD400) was fed on a machining center along an NC-programmed 3D curved path to make a curved surface with a certain helix angle. Under conditions of helix angle of 45° and feed speed of 50mm/min, a satisfactory curved surface with roughness under Rmax=0.6μm was obtained.

5. CONCLUSIONS

The proposed helical scan grinding method proved to be effective for realizing high efficiency finish grinding of ceramics and cermets with a diamond wheel of coarse grain size. Surface roughness was improved by increasing the helix angle; at a helix angle of 45 degree, it was about seven times better than in ordinary grinding. It was also found that the proposed method can be successfully applied to grinding of curved surfaces. It is expected that various other applications of the helical scan grinding method will be found for attaining high efficiency finishing.

[REFERENCES]
(1)T.Nakagawa, K.Suzuki, and T.Uematsu, "Highly Efficient Grinding of Ceramics and Hard Metals on Grinding Center," Annals of the CIRP 35/1, pp.205 – 210, 1986.

(2)K.Suzuki, T.Uematsu and T.Nakagawa, "On-machine Trueing/Dressing of Metal Bond Grinding Wheels with Electro-Discharge Machining," Annals of the CIRP 36/1, pp.115 – 118, 1987.
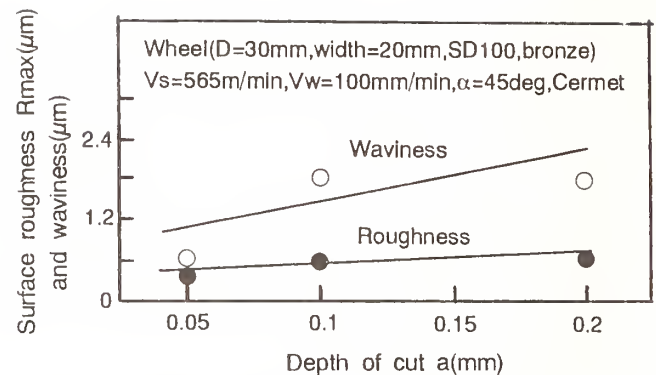
Fig.5 Relation between roughness, waviness and depth of cut.
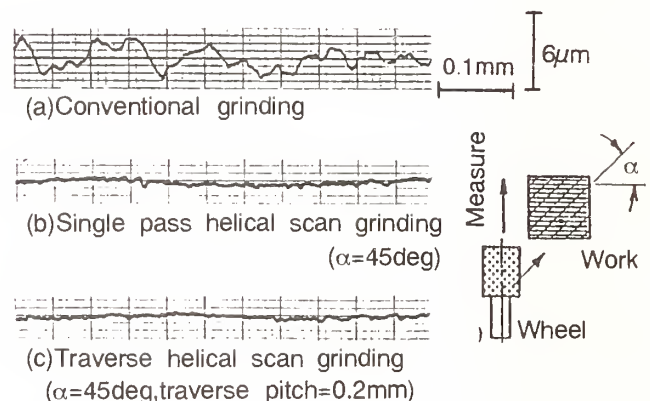
Fig.6 Decrease of waviness in traverse helical scan grinding.(Mounted wheel,D=30mm, b=20mm,SD100,cermet)
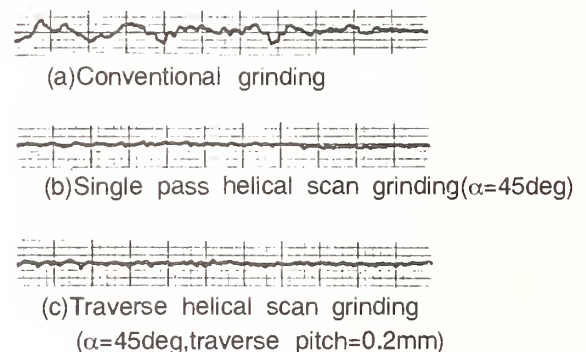
Fig.7 Surface profile curves in helical scan grinding with a straight wheel. (D=125mm,b=13.5mm,SD200,cermet)

GRINDING OF CERAMIC MATERIALS: A MODEL FOR ENERGY CONSUMPTION AND FORCE TRANSFORMATION

S. X. LIANG and O. F. DEVEREUX
University of Connecticut, Storrs, CT

A simple model is introduced for relating grinding forces to operational equipment parameters: The normal force on the wheel is assumed proportional to the normal component of the velocity of the workpiece relative to the wheel, and the tangential force on the wheel is assumed essentially frictional and, thus, proportional to the normal force. Both force components are shown to be proportional to the product of the workpiece velocity and the depth of cut. Comparably simple expressions are derived for average normal and tangential stress at the grinding interface and for specific grinding energy. The normal and tangential forces are related to measured horizontal and vertical force components via the effective locus of application of these forces on the wheel, i.e., by an angle ϕ from the vertical which is shown to be closely represented by $2\beta/3$, where β is the angle subtended by the grinding interface. Experiments on silicon carbide using an instrumented surface grinder with a resin-bonded diamond wheel and a synthetic coolant showed excellent correspondence to this model over a wide range of table feed rates and grinding depths.

Introduction

The economic use of ceramic materials in applications traditionally reserved for metals and alloys is often restricted by their shaping and finishing, processes normally performed by grinding. Methods for study of ceramic grinding include a "machining" approach, entailing analysis of grinding forces, grinding energy and chip formation (1), and an indentation mechanics approach, in which grinding is modelled as a multiplicity of individual indentations or individual abrasive grain scratches. (1, 2, 3) In a mechanistic study of grinding the independent variables necessarily relate to force components at the grinding interface, while the parameters amenable to measurement are different, e.g., force components experienced by the table, and those subject to control are still different, e.,g., depth of cut and table feed rate in the case of a simple surface grinding operation. The development of a simple model relating these sets of parameters is an important aspect of this study in that it permits an association of material failure conditions with simple machine parameters.

Analysis of Grinding Forces

Grinding behavior may be correlated with the normal and tangential force components at the arc of contact between the wheel and workpiece, as distinguished from the horizontal and vertical force components that are amenable to measurement but not directly relevant to the process. The normal force component may be associated with the penetration load applied to the abrasive grains; the tangential component with the friction of grain/workpiece contact and a pseudo-viscous effect of the chip-laden coolant. In this model the normal force is assumed proportional to the normal component of the velocity of the workpiece relative to the wheel, V_w, and the frictional component of the tangential force to be proportional to the normal

Figure 1: Definition of parameters at the wheel/workpiece interface.

force component. Thus, for the increment of contact arc defined by the angles θ and $\theta + d\theta$, shown in Figure 1,

$$dF_n = c_n \cdot V_w \cdot \sin\theta \cdot r \cdot d\theta \qquad (1)$$

and

$$dF_t = c_t \cdot V_w \cdot \sin\theta \cdot r \cdot d\theta \qquad (2)$$

where F_n and F_t are the normal and tangential force components, r is the wheel radius and c_n and c_t are constants. (The corresponding force components per unit width are given by $F_n' \equiv F_n/b$ and $F_t' \equiv F_t/b$ where b is the wheel width or specimen width, whichever is smaller.) The wheel contacts the workpiece over the range $0 \leq \theta \leq \beta$ where, if a is the depth of cut, β is defined by

$$\cos\beta = \frac{r - a}{r} \qquad (3)$$

and, therefore,

$$\sin\beta = \left[1 - \left(1 - \frac{2a}{r} + \frac{2a^2}{r^2}\right)\right]^{1/2} \qquad (4)$$

or

$$\sin\beta \approx \beta \approx \left(\frac{2a}{r}\right)^{1/2} \qquad (5)$$

for small a. Integrating equations (1) and (2) over the range $0 \leq \theta \leq \beta$,

$$F_n = c_n \cdot \int_0^\beta V_w \cdot r \cdot \sin\theta \cdot d\theta$$

$$= c_n \cdot V_w \cdot r \cdot (1 - \cos\beta) = c_n \cdot V_w \cdot a \qquad (6)$$

and

$$F_t = c_t \cdot \int_0^\beta V_w \cdot r \cdot \sin\theta \cdot d\theta$$

$$= c_t \cdot V_w \cdot r \cdot (1 - \cos\beta) = c_t \cdot V_w \cdot a \qquad (7)$$

We may define corresponding values of the average grinding stress, σ_n and σ_t, as the normal and tangential components of the grinding force per unit width divided by the length of grinding arc:
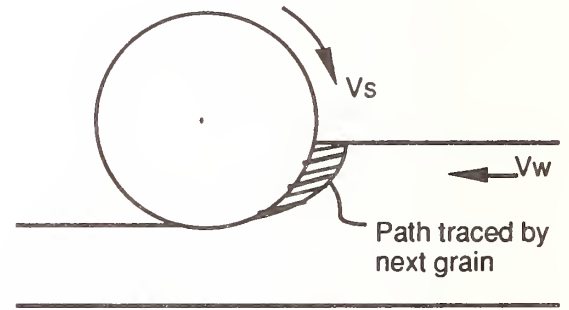
(Figure 2a)
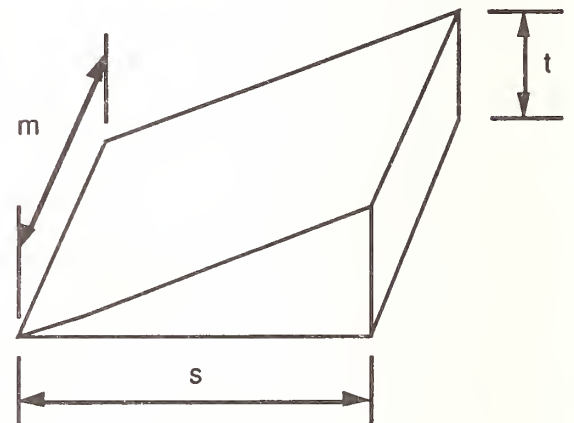
(Figure 2b)

Figure 2: Idealized chip geometry.

$$\sigma_n = \frac{F_n'}{r \cdot \beta} = \frac{c_n \cdot V_w \cdot a}{r \cdot b \cdot \beta} \qquad (8)$$

and

$$\sigma_t = \frac{F_t'}{r \cdot \beta} = \frac{c_t \cdot V_w \cdot a}{r \cdot b \cdot \beta} \qquad (9)$$

where β is expressed in radians. Substituting from equation (5),

$$\sigma_n = \frac{c_n \cdot V_w}{b} \cdot \left(\frac{a}{D_s}\right)^{1/2} \qquad (10)$$

and

$$\sigma_t = \frac{c_t \cdot V_w}{b} \cdot \left(\frac{a}{D_s}\right)^{1/2} \qquad (11)$$

where $D_s \equiv 2 \cdot r$ is the wheel diameter.

The grinding energy is related to the geometry of the chips formed during grinding. These may be idealized by the shape depicted in Figure 2, with a maximum thickness given by the grain depth of cut, t, which in turn may be inferred from Figure 2. The horizontal velocity of the workpiece into the wheel, V_w, may be resolved into normal and tangential components, $V_w \cdot \sin\beta$ and $V_w \cdot \cos\beta$, respectively. The thickness of a given chip is defined by the time interval h/V_s, where V_s is the peripheral velocity of the wheel and h is the circumferential distance between adjacent abrasive grains, during which the relative movement of the wheel into the workpiece, i.e., in the normal direction, is given by

$$t = \frac{h}{V_s} \cdot V_w \cdot \sin\beta \qquad (12)$$

$$= h \cdot \frac{V_w}{V_s} \cdot \left(\frac{2a}{r}\right)^{1/2} \qquad (13)$$

The length of the chip side, s, is given by

$$s = r \cdot \beta \qquad (14)$$

Substituting the material removal rate, $Z_w \equiv V_w \cdot a \cdot b$, t may be expressed

$$t = \frac{2h}{V_s \cdot b} \cdot \frac{Z_w}{(D_s \cdot a)^{1/2}} \qquad (15)$$

We might anticipate that the specific energy of the grinding process, U, defined by

$$U \equiv \frac{\text{Energy consumption rate}}{\text{Material removal rate}} = \frac{E}{Z_w} \qquad (16)$$

would increase with decreasing chip thickness. As a first approximation in dealing with brittle materials we may neglect plastic deformation energy and treat the energy consumption, E, as the sum of the fracture energy,

$$E_{frac} = n \cdot A_1 \cdot \gamma \qquad (17)$$

and the frictional energy

$$E_{fric} = F_n \cdot \mu \cdot V_s \qquad (18)$$

or

$$E = n \cdot A_1 \cdot \gamma + F_n \cdot \mu \cdot V_s \qquad (19)$$

and

$$U = \frac{n \cdot A_1 \cdot \gamma}{Z_w} + \frac{F_n \cdot \mu \cdot V_s}{Z_w} \qquad (20)$$

where n is the number of chips created in unit time; A_1, the surface area of one chip; γ, the surface tension; and μ, the relevant coefficient of friction between the workpiece and an abrasive grain.

The rate of chip formation may be approximated by the area of the wheel which passes through the workpiece per unit time, $V_s \cdot b$, times the density of particles on the wheel surface, h^{-2}, or

$$n = \frac{V_s \cdot b}{h^2} \qquad (21)$$

The surface area of the chip, as depicted in Figure 2, may be approximated by that of the lateral surfaces, i.e., the contribution of the edges may be neglected. Furthermore, we may approximate the width of the chip by the abrasive particle size, m. Thus, the area A_1 is given by

$$A_1 = 2 \cdot r \cdot \beta \cdot m \qquad (22)$$

Substituting equations (6), (21) and (22) along with β

23
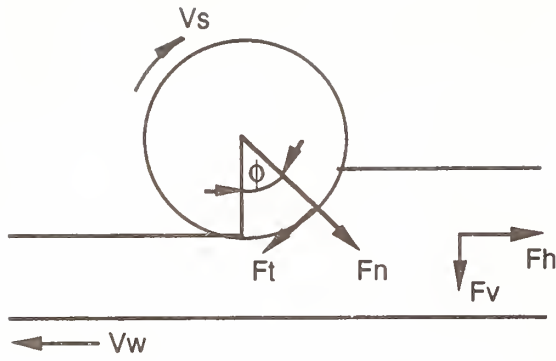
a. Down Feed Grinding
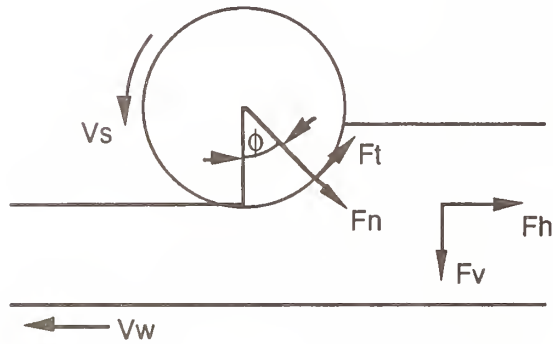
b. Up Feed Grinding

Figure 3: Force relationships in up feed and down feed grinding.

$= \sin\beta = 2(a/D)^{1/2}$ into equation (20), we have

$$U = \frac{4 \cdot V_s \cdot r \cdot b \cdot m \cdot \gamma}{h^2 \cdot Z_w} \cdot \left(\frac{a}{D_s}\right)^{1/2} + \frac{C_n \cdot V_w \cdot a \cdot \mu \cdot V_s}{Z_w}$$

$$= \frac{4 \cdot V_s \cdot r \cdot b \cdot m \cdot \gamma}{h^2 \cdot Z_w} \cdot \left(\frac{a}{D_s}\right)^{1/2} + \frac{C_n \cdot \mu \cdot V_s}{b} \quad (23)$$

or, in terms of table feed rate,

$$U = \frac{4 \cdot V_s \cdot r \cdot m \cdot \gamma}{h^2 \cdot V_w \cdot (D_s \cdot a)^{1/2}} + \frac{C_n \cdot \mu \cdot V_s}{b} \quad (24)$$

Equations (23) and (24) allow us to express several basic dependencies. At constant depth of cut:

$$U = C'' V_w^{-1} + C' \quad (25)$$

At constant table feed rate:

$$U = C''' a^{-1/2} + C' \quad (26)$$

At constant material removal rate:

$$U = C^{iv} a^{1/2} + C' \quad (27)$$

Transformation of Force Coordinates

Grinding force is usually measured as the vertical and horizontal components of the force, using a three-component dynamometer placed beneath the workpiece. We have defined the normal and tangential grinding stress values, σ_n and σ_t, which may be integrated along the grinding arc, yielding effective net force components, F_n and F_t. In conventional grinding, which is characterized by a small depth of cut, little error is entailed in equating these components with the vertical and horizontal force components, respectively, but appreciable error may be seen when the depth of cut is large as in creep feed grinding. The relationships between the measured vertical and horizontal components and the defined normal and tangential components for up feed and down feed grinding are apparent in Figure 3. Clearly

$$F_t = F_h \cdot \cos\phi + F_v \cdot \sin\phi \quad (28)$$

and

$$F_n = F_v \cdot \cos\phi - F_h \cdot \sin\phi \quad (29)$$

for down feed grinding, and

$$F_t = F_h \cdot \cos\phi - F_v \cdot \sin\phi \quad (30)$$

and

$$F_n = F_v \cdot \cos\phi + F_h \cdot \sin\phi \quad (31)$$

for up feed grinding, where ϕ defines the effective locus of application of F_t and F_n.

The value of ϕ is a function of the distribution of normal and tangential stresses at the grinding interface. In this work we have assumed the normal force to be

24

proportional to the normal component of the velocity of the workpiece relative to the wheel, and the tangential force to be proportional to the normal force. These relationships are given by equations (1) and (2):
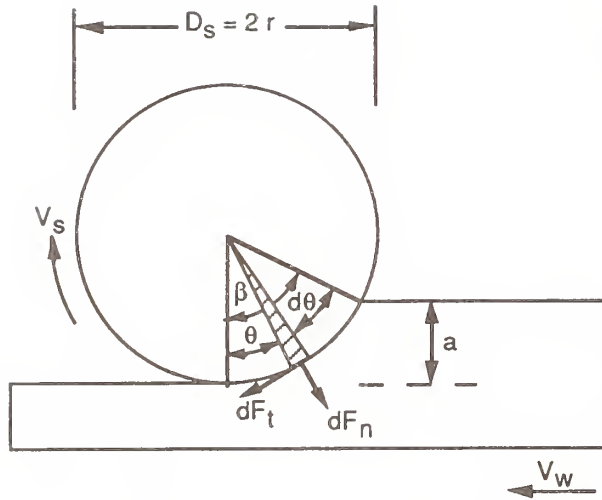
$$dF_n = c_n \cdot V_w \cdot \sin\theta \cdot r \cdot d\theta \qquad (1)$$

and

$$dF_t = c_t \cdot V_w \cdot \sin\theta \cdot r \cdot d\theta \qquad (2)$$

Thus, with reference to Figure 1, the horizontal (x) and vertical (y) components of these force increments are given by

$$dF_{nx} = c_n \cdot V_w \cdot r \cdot \sin^2\theta \cdot d\theta \qquad (32)$$

$$dF_{ny} = c_n \cdot V_w \cdot r \cdot \sin\theta \cdot \cos\theta \cdot d\theta \qquad (33)$$

and

$$dF_{tx} = c_t \cdot V_w \cdot r \cdot \sin\theta \cdot \cos\theta \cdot d\theta \qquad (34)$$

$$dF_{ty} = c_t \cdot V_w \cdot r \cdot \sin^2\theta \cdot d\theta \qquad (35)$$

The respective force components are, thus,

$$F_{nx} = c_n \cdot \int_0^\beta V_w \cdot r \cdot \sin^2\theta \cdot d\theta$$
$$= \frac{c_n \cdot V_w \cdot r}{2} \left[\beta - \frac{\sin(2\beta)}{2} \right] \qquad (36)$$

$$F_{ny} = c_n \cdot \int_0^\beta V_w \cdot r \cdot \sin\theta \cdot \cos\theta \cdot d\theta$$
$$= \frac{c_n \cdot V_w \cdot r}{2} \sin^2\beta \qquad (37)$$

$$F_{tx} = c_t \cdot \int_0^\beta V_w \cdot r \cdot \sin\theta \cdot \cos\theta \cdot d\theta$$
$$= \frac{c_t \cdot V_w \cdot r}{2} \sin^2\beta \qquad (38)$$

$$F_{ty} = c_t \cdot \int_0^\beta V_w \cdot r \cdot \sin^2\theta \cdot d\theta$$
$$= \frac{c_t \cdot V_w \cdot r}{2} \left[\beta - \frac{\sin(2\beta)}{2} \right] \qquad (39)$$

Clearly

$$\tan\phi = \frac{F_{ty}}{F_{tx}} = \frac{F_{nx}}{F_{ny}} = \frac{\beta - \frac{1}{2}\sin(2\beta)}{\sin^2\beta} \qquad (40)$$

Expanding the trigonometric functions, this reduces to

$$\phi \approx \frac{2}{3}\beta \qquad (41)$$

As the next term in the expansion is $-2\beta^3/15$, this approximation is of the order of 10% in error at $\beta = 0.7$ radians $= 40°$.

Empirical Confirmation of Model

Experimental System

Grinding tests were performed on sintered silicon carbide specimens, 0.0254m long x 0.00635m wide x 0.0127m high (1 in x 0.2 in x 0.5 in), with a density of 3.1 g/cm^3, a Knoop hardness of 2800 kg/mm^2, an elastic modulus of 410 GPa and a fracture toughness of 4.6 MPa$\cdot$m$^{1/2}$. Tests were performed with a surface grinder with a static stiffness of $11 \cdot 10^6$ N/m. To permit a range of table feed rates the original hydraulic feed table was replaced with roller bearing slide-way with a travel length of 0.1 m (4 in.), a load capacity of 1607 N (360 lb.), and a straight line accuracy of 2.8×10^{-6} m (0.00011 in.). The table was driven by a stepping motor with a resolution of 12,800 steps/revolution, a static torque of 0.55 Nm, a velocity range of 0.01 - 50 rev/s in either direction and an acceleration range of 0.01 - 1000 rev/s^2. The wheel was a resin bonded diamond wheel with a diameter, D_s, of 0.1778 m (7 in.); a width, b, of 0.00635 m (0.25 in.); and an abrasive concentration of 25 volume percent of 170/200 mesh, medium grade diamond. The wheel operated at a peripheral speed, V_s, of 24.2 m/s; it was trued with a single point diamond using a 2.54×10^{-6} m (0.1 mil) depth of cut, a transverse feed rate of 4.32×10^{-3} m/s (0.17 in/s) and a runout of 5.08×10^{-6} m (0.2 mil), and was dressed with

25
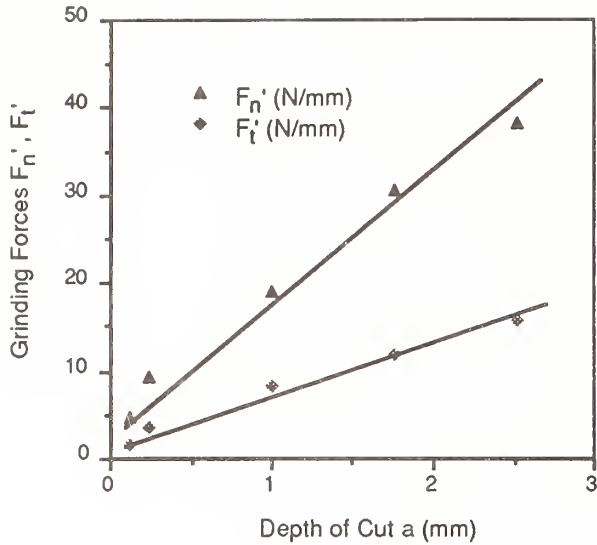
Figure 4: Grinding force per unit width vs. depth of cut, a, at constant table feed rate,

$V_w = 3.38$ mm/s (8 in/min).
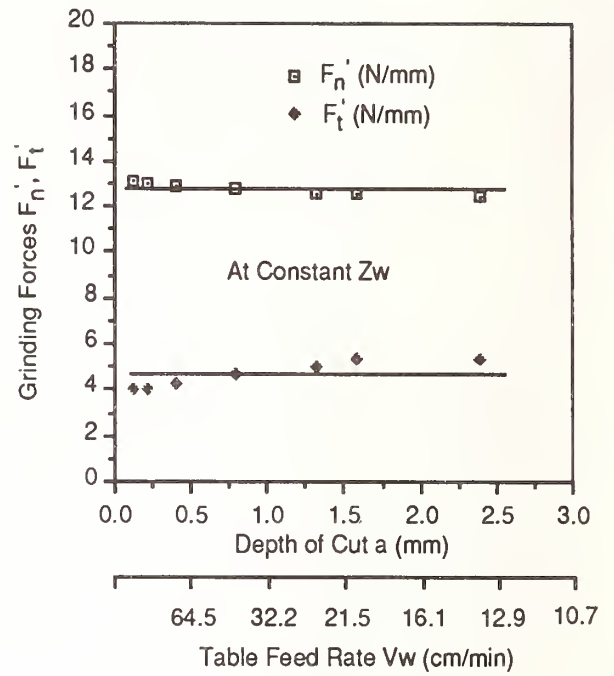
Figure 6: Grinding force per unit width vs. depth of cut, a, and table feed rate, V_w, at constant material removal rate,

$Z_w \equiv V_w \cdot a \cdot b = 34.2$ mm^3/s (0.125 in^3/min).
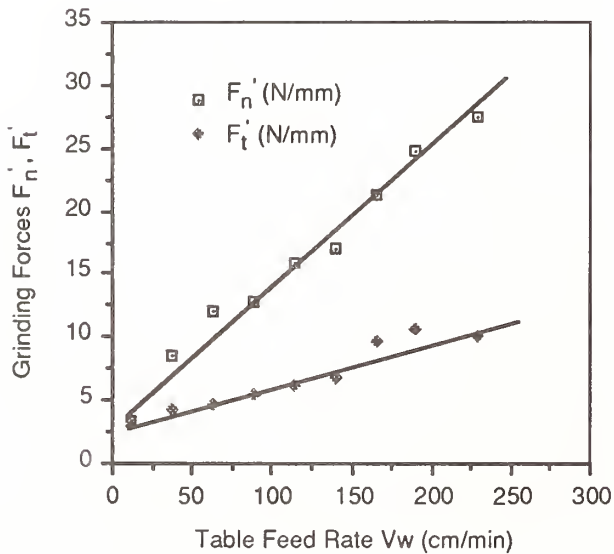
Figure 5: Grinding force per unit width vs. table feed rate, V_w, at constant depth of cut,
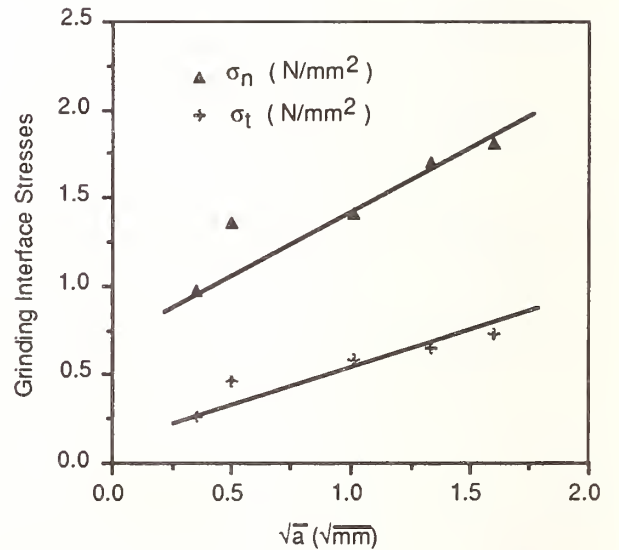
a = 0.5 mm (20 mil).

Figure 7: Grinding stress vs. depth of cut, $a^{1/2}$, at constant table feed rate,

$V_w = 3.38$ mm/s (8 in/min)

26
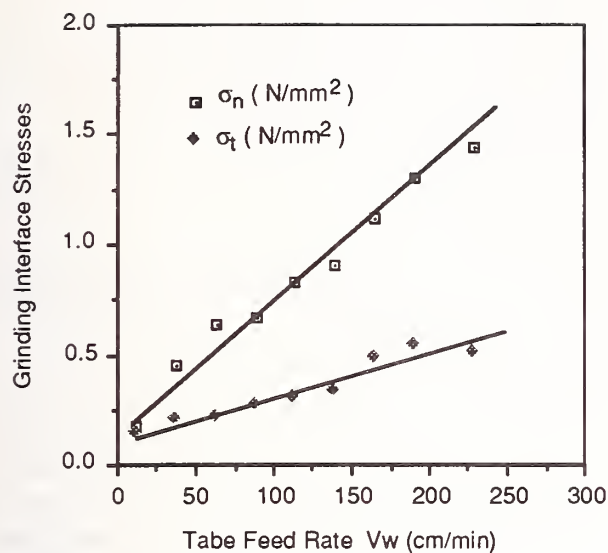
Figure 8: Grinding stress vs. table feed rate, V_w , at constant depth of cut
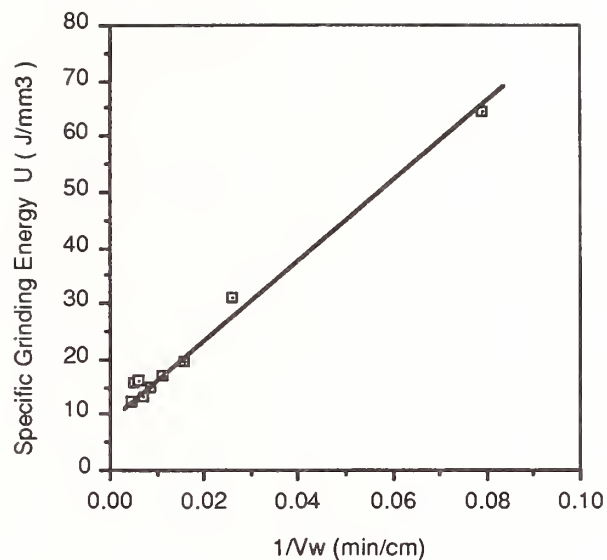
a = 0.5 mm (20 mil).

Figure 10: Specific grinding energy, U, vs. V_w^{-1} at constant depth of cut,

a = 0.5 mm (20 mil).
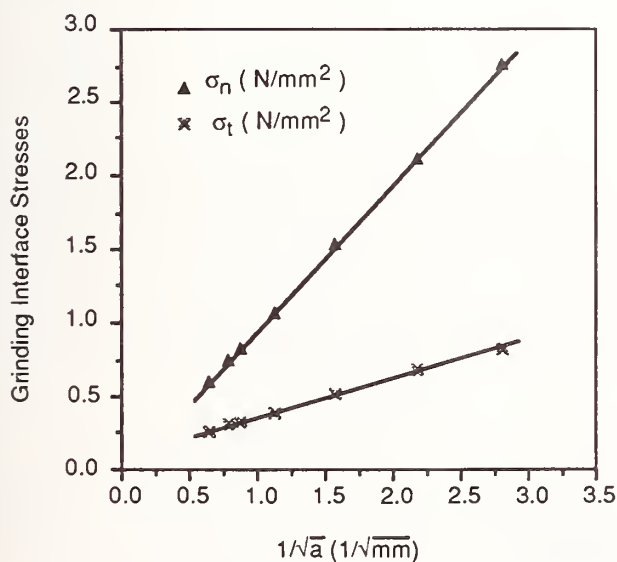
Figure 9: Grinding stress vs. depth of cut, $a^{-1/2}$, at constant material removal rate,

Z_w = 34.2 mm³/s (0.125 in³/min).
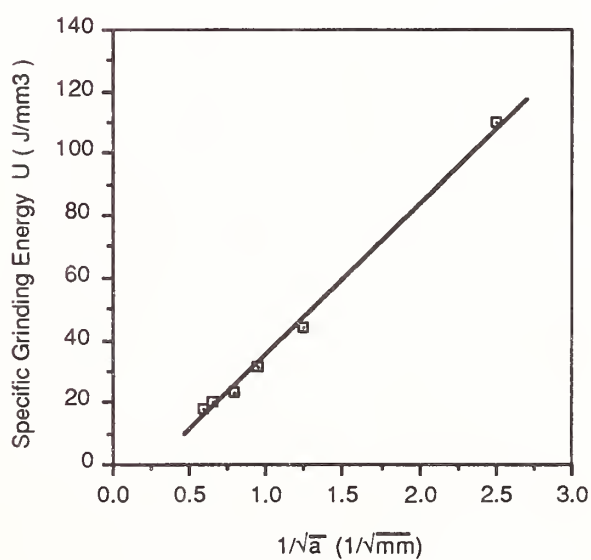
Figure 11: Specific grinding energy, U, vs. $a^{-1/2}$ at constant table feed rate,

V_w = 3.38 mm/s (8 in/min).

27

Figure 12: Specific grinding energy, U, vs. $a^{1/2}$ at
constant material removal rate,
Z_w = 34.2 mm³/s (0.125 in³/min).
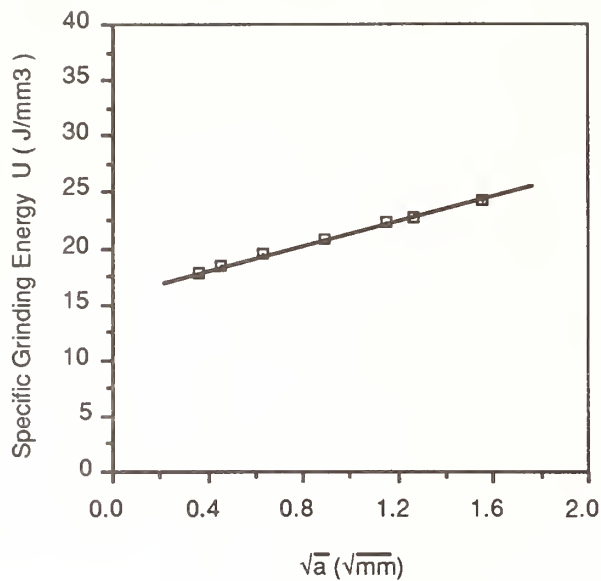
an alundum rod. A synthetic coolant was applied at a rate of 0.0631 L/s (1 gallon/min) at 6.895x10⁵ Pa (100 psi) and 24°C. Three components of grinding force were measured with a dynamometer employing a piezoelectric transducer. Specific energy, in N•m/m³, was determined as

$$U \equiv \frac{F_t \cdot V_s}{V_w \cdot a \cdot b} \qquad (42)$$

Slide-way control and data acquisition were provided by an on-line computer.

Observations

The experimental work on silicon carbide described in the foregoing section provides empirical support for the simple force model presented in this manuscript. For example, Figure 4 shows a correlation of the basic assumptions of the model as described in equations (6) and (7) with empirical observation, i.e., a linear relation between both normal and tangential force, F_n' and F_t' and depth of cut, a, at constant table feed rate, V_w.
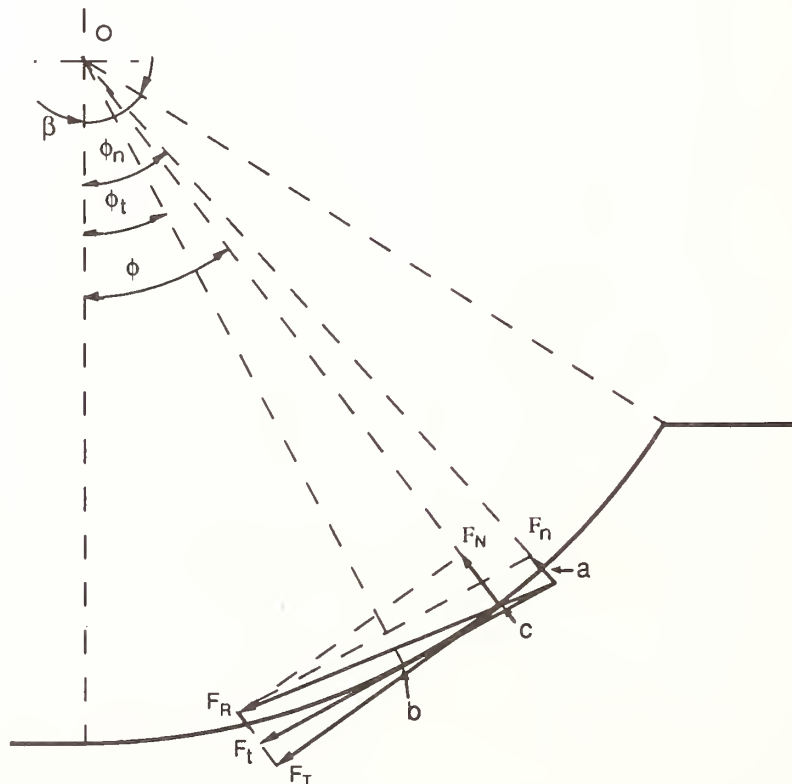
Figure 13: Parameters for determining the effective locus of
application of the resultant force, F_R.

28

Figure 5 shows the linear relation, also assumed in equations (6) and (7), between the forces, F_n' and F_t' and V_w at constant a. The correlation of grinding force with depth of cut and table feed rate is shown in Figure 6 at constant material removal rate, $Z_w \equiv V_w \cdot a \cdot b$. The corresponding correlation of normal and tangential grinding stress, σ_n and σ_t, as described in equations (10) and (11), is given in Figures 7, 8 and 9. Similarly, equation (25) predicts a linear relation between specific (grinding) energy, U, and V_w^{-1} at constant depth of cut, shown experimentally in Figure 10; a linear relation between U and $a^{-1/2}$ at constant V_w, shown in Figure 11; and a linear relation between U and $a^{1/2}$ at constant Z_w, shown in Figure 12.

Discussion

The foregoing model represents two simple assumptions that appear to be appropriate for the grinding of brittle materials, i.e., that the normal stress is proportional to the normal component of the velocity of the workpiece relative to the wheel, and that the tangential stress is proportional to the normal stress and thus arises from frictional causes. The proportionality inherent in this model also causes the resultants of the normal and tangential forces to be applied at the same locus,

$$\phi = \frac{2}{3}\beta \tag{41}$$

Although the model is, to a considerable extent, justified by the correlations shown in Figures 4 through 12, it clearly represents an extreme in grinding behavior. Another extreme might be represented by "plowing," in which the tangential force may be modelled as that due to a Newtonian viscosity. In this case the previous expression for the normal force may be retained,

$$dF_n = c_n \cdot V_w \cdot \sin\theta \cdot r \cdot d\theta \tag{1}$$

but now

$$dF_t = c_t \cdot r \cdot d\theta \tag{43}$$

i.e., the tangential force component is independent of position along the grinding arc. The horizontal (x) and vertical (y) components of these force increments are given by

$$dF_{nx} = c_n \cdot V_w \cdot r \cdot \sin^2\theta \cdot d\theta \tag{32}$$

$$dF_{ny} = c_n \cdot V_w \cdot r \cdot \sin\theta \cdot \cos\theta \cdot d\theta \tag{33}$$

and

$$dF_{tx} = c_t \cdot r \cdot \cos\theta \cdot d\theta \tag{44}$$

$$dF_{ty} = c_t \cdot r \cdot \sin\theta \cdot d\theta \tag{45}$$

The respective force components for this model are, thus,

$$F_{nx} = c_n \cdot \int_0^\beta V_w \cdot r \cdot \sin^2\theta \cdot d\theta$$

$$= \frac{c_n \cdot V_w \cdot r}{2}\left[\beta - \frac{\sin(2\beta)}{2}\right] \tag{36}$$

$$F_{ny} = c_n \cdot \int_0^\beta V_w \cdot r \ \sin\theta \cdot \cos\theta \cdot d\theta$$

$$= \frac{c_n \cdot V_w \cdot r}{2}\sin^2\beta \tag{37}$$

$$F_{tx} = c_t \cdot \int_0^\beta r \cdot \cos\theta \cdot d\theta$$

$$= c_t \cdot r \cdot \sin\beta \tag{46}$$

$$F_{ty} = c_t \cdot \int_0^\beta r \cdot \sin\theta \cdot d\theta$$

$$= c_t \cdot r\left(1 - \cos\beta\right) \tag{47}$$

Clearly the locus of application of the normal force is unchanged, that is,

$$\tan\phi_n = \frac{F_{nx}}{F_{ny}} = \frac{\beta - \frac{1}{2}\sin(2\beta)}{\sin^2\beta} \tag{40'}$$

and

$$\phi = \frac{2}{3}\beta \tag{41}$$

shown as point a in Figure 13. In accord with its lack

29

of dependence on the angle θ, however, the effective site of application of the tangential force is the average value of θ along the contact arc,

$$\tan\phi_t = \frac{F_{ty}}{F_{tx}} = \frac{1 - \cos\beta}{\sin\beta} = \tan\frac{\beta}{2} \qquad (48)$$

or

$$\phi_t = \frac{\beta}{2} \qquad (49)$$

shown as point b in Figure 13. Being applied at different loci, the net normal and tangential forces are not orthogonal. The effective locus of application, ϕ, of the resultant force F_R is shown as point c in Figure 13, where F_R may be resolved into orthogonal components F_N and F_T. Clearly

$$\frac{\beta}{2} \le \phi \le \frac{2\beta}{3} \qquad (50)$$

with the actual value being determined by the material and machine parameters c_n, c_t and V_w.

As with any body, the forces acting upon the grinding wheel may be represented as a translational force, F_R and a torque, T. Since the normal force, expressed either as F_n or F_N, is by definition radial and passes through the axis of rotation, the torque applied to the wheel is clearly given by

$$T = F_t \cdot r = F_T \cdot r \qquad (51)$$

i. e., from equation (43)

$$F_T = F_t = c_t \cdot r \cdot \beta \qquad (52)$$

The normal force, F_N, at the locus of application, ϕ, is determined by

$$F_R^2 = F_N^2 + F_T^2 = (F_{nx} + F_{tx})^2 + (F_{ty} - F_{ny})^2 \qquad (53)$$

Resolution of equation (53) is facilitated by expanding the trigonometric functions of equations (36), (37), (46) and (47) and keeping only those terms of order 3 or less:

$$F_{nx} \approx \frac{c_n \cdot V_w \cdot r}{3} \cdot \beta^3 \qquad (54)$$

$$F_{ny} \approx \frac{c_n \cdot V_w \cdot r}{2} \cdot \beta^2 \qquad (55)$$

$$F_{tx} \approx c_t \cdot r \cdot \left(\beta - \frac{\beta^3}{6}\right) \qquad (56)$$

$$F_{ty} \approx \frac{c_t \cdot r}{2} \cdot \beta^2 \qquad (57)$$

Substituting and discarding terms of order β^6,

$$F_N \approx \frac{r \cdot \beta^2}{6} \cdot (9c_n^2 \cdot v_w^2 + 6c_n \cdot c_t \cdot v_w - 3c_t^2)^{\frac{1}{2}} \qquad (58)$$

The angle ϕ may be determined through balancing force components at the effective locus of application:

$$F_N \cdot \sin\phi + F_T \cdot \cos\phi = F_{nx} + F_{tx} \qquad (59)$$

$$F_T \cdot \sin\phi - F_N \cdot \cos\phi = F_{ty} - F_{ny} \qquad (60)$$

Multiplying equation (59) by F_N and equation (60) by F_T and adding:

$$\sin\phi = \frac{F_N \cdot (F_{nx} + F_{tx}) + F_T \cdot (F_{ty} - F_{ny})}{F_N^2 + F_T^2} \approx \phi \qquad (61)$$

where F_N, F_{nx}, F_{ny}, F_T, F_{tx} and F_{ty} are given by equations (58), (54), (55), (52), (56) and (57), respectively. Equation (61) is seen to approach the limits expressed by equation (50); that is

$$\lim_{c_t \to 0} \phi = \frac{2}{3} \cdot \beta \qquad (62)$$

$$\lim_{c_n \to 0} \phi = \frac{\beta}{2} \qquad (63)$$

Brach et al. (5) studied the relationship between F_t and F_h in cases in which the ratio of depth of cut to wheel diameter was large (or the normal force on the wheel was large compared to the tangential component). Using the trigonometric relationships between F_h and F_v, and F_t and F_n, with data obtained in the sawing of granite they empirically found $\phi = 0.69\beta$ in up feed grinding and $\phi = 0.54\beta$ in down feed grinding. Ohishi (6) used $\phi = 0.5\beta$ as the effective point of application of the resultant force and and found this to be consistent with observations on the grinding of a

bearing steel, while Shafto (7) found empirically that $\beta/2 \leq \phi \leq 2\beta/3$ for a nickel alloy and $\phi = 0.7\beta$ for tool steels.

In practice the value of ϕ may depend on such parameters as the sharpness of the grinding wheel, the coolant used and the grinding mode (up feed or down feed). Also, while for brittle materials the value should be close to $2\beta/3$, for ductile materials where the grinding may be characterized by plowing the value of ϕ may approach 0.5β. However, uncertainty in the point of resultant force application does not yield comparable uncertainty in the values of F_t and F_n. From equations (28) and (29)

$$dF_t = (-F_h \cdot \sin\phi + F_v \cdot \cos\phi) \cdot d\phi \qquad (64)$$

and

$$dF_n = (-F_v \cdot \sin\phi - F_n \cdot \cos\phi) \cdot d\phi \qquad (65)$$

or, if ϕ is quite small,

$$dF_t \approx F_v \cdot d\phi \qquad (66)$$

and

$$dF_n \approx -F_h \cdot d\phi \qquad (67)$$

In our experiments the depth of cut, a, was of the order of $2.5 \times 10^{-4} \sim 2.5 \times 10^{-3}$ m (0.01" ~ 0.1"). Using the wheel radius, r = 0.089 m (3.5"), and equation (3) the angle β varied from 0.076 radians to 0.24 radians. Taking the latter case and assuming a maximum value for ϕ, $\phi = 2\beta/3 = 0.16$ radians, a 10% uncertainty in ϕ would yield an uncertainty in the force components of $\Delta F_t = 0.016F_v$ and $\Delta F_n = -0.016F_h$.

Summary

The importance of using F_t instead of F_h in the calculation of spindle power consumed is well known, especially for creep feed grinding of brittle materials. However, we typically are able to measure F_h and F_v, not F_t and F_n; values of the latter parameters can be determined only if the effective locus of application, c, of the resultant force can be estimated. In our model we assumed that F_t behaved as a frictional force, i.e., $F_t \propto F_n$ and determined that $\phi = 2\beta/3$, where β is the angle subtended by the wheel/workpiece interface. This assumption enables a simple calculation of F_t and F_n

via equations (28) and (29) or (30) and (31), and with the additional assumption that the normal force, F_n, is proportional to the normal velocity of the workpiece relative to the wheel the specific grinding energy is expressed by equation (23) or (24). Certain dependences of force and energy on process parameters such as depth of cut and table feed rate are inherent in this model. Experiments with surface grinding of polycrystalline silicon carbide showed a general confirmation of these relationships, thus providing experimental support to the model. If proportionality between F_t and F_n cannot be assumed as in the case of ductile materials, the net tangential force and net normal force no longer have the same locus of application. In this case the angle ϕ is still defined and may be determined, but its dependence on process parameters is considerably more complex.

References

1. S. Malkin, and J.E. Ritter, "Grinding Mechanisms and Strength Degradation for Ceramics," Winter Annual Meeting of ASME, Chicago, pp. 57-72, 1988.

2. H.K. Tonshoff, and H. Trumpold, "Evaluation of Surface Layers of Machined Ceramics," CIRP Reports and News, Vol. 38, No. 2, pp. 699-708, 1989.

3. H.K. Tonshoff, and R. Telle, "Chip Formation and Material Removal in Grinding of Ceramics," 4th International Grinding Conference, SME, MR 90-539, 1990.

4. Alfred Lammer, "Surface Topography and Strength of Ceramic Materials after Grinding," 4th International Grinding Conference, SME, MR 90-541, 1990.

5. K. Brach, D.M. Pai, E. Ratterman, and M.C. Shaw, "Grinding Force and Energy," J. of Eng. for Industry, Vol. 110, pp. 25-31, 1988.

6. Susumu Ohishi, "Study of Creep Feed Grinding," PhD Thesis, Tokyo Metropolitan University, Japan, 1984.

7. G.R. Shafto, "Creep Feed Grinding," PhD Thesis, University of Bristol, England, 1974.

Nomenclature

a	depth of cut
A_1	surface area of one chip
b	grinding interface width
c_n, c_t	characteristic parameters of wheel and workpiece
C', C''	constants
C''', C^{iv}	constants
D_s	wheel diameter
E	energy consumption rate
F_n	normal force on grinding interface
F_t	tangential force on grinding interface
F_n'	normal grinding force per unit width
F_t'	tangent grinding force per unit width
F_h	horizontal force on table
F_v	vertical force on table
F_N	normal resultant force on wheel
F_T	tangent resultant force on wheel
F_R	resultant force on wheel
h	average distance between two adjacent abrasive grains
m	average abrasive particle size
n	rate of chip production
r	radius
s	length of chip side
t	maximum grain depth of cut
U	specific grinding energy
μ	coefficient of friction between the wheel and the workpiece
V_w	table feed rate
V_s	peripheral speed of the wheel
Z_w	material removal rate
β	angle subtended by the grinding interface
θ	angle between 0 and β
ϕ	effective locus of application of F_R
ϕ_t	effective locus of application of F_T
ϕ_n	effective locus of application of F_N
σ_n	normal stress applied on the grinding interface
σ_t	shear stress applied on the grinding interface
γ	surface tension

ON PERFORMANCE OF METAL-BONDED SINGLE-LAYER DIAMOND ABRASIVE TOOL

A. K. CHATTOPADHYAY and H. E. HINTERMANN
CSEM, Neuchatel, Switzerland

The dependance of performance of metal-bonded single-layer diamond abrasive tools on the topography of working surface is reported in this paper. The behaviour of such monolayer diamond abrasive tools continued to change irreversibly during grinding of aluminium oxide primarily because of grit wear. The rate of increase in normal force and power was higher for tools with a smaller grit size in comparison to that for tools with a larger grit size. On the other hand, single-layer diamond abrasive tool having low and uniform bond level demonstrated distinct advantage in offering steady behaviour while grinding GG40 cast iron at a high depth of cut. The normal force and the spindle power remained virtually constant for tools with a larger grit size over a long grinding span. However, these two parameters recorded higher values and a slow increase with cumulative infeed for tools with a smaller grit size. But, a material like cast iron could cause premature failure of such diamond tools, even having a wide and uniform grit spacing, through loading when bond level was high.

1. Introduction

The remarkable properties of diamond such as high wear resistance and excellent cutting edge stability are being used creatively to fabricate tools having different geometries with just a single-layer of diamond grit bonded to a metal substrate by a galvanic or a brazed metal layer. The essential feature of such single-layer tool is large diamond exposure compared to coventional composite type metal-bond wheel, which results in free-cutting action.

However, it is contended that grit protrusion of galvanically bonded tool may not always be sufficient to avoid intensive bond-chip or bond-work interactions causing force and heat build-up and loading. This problem can be further aggravated by the presence of "nodules" which refers to galvanic nickel build-up in the space between the grits (1). In contrast, in brazed tools the very nature of bonding is supposed to keep a low bond level in the space between the grit thus, allowing large chip clearance space, efficient coolant flow and cool cutting action (1). A recently developed vacuum sintering process also permits the use of high protrusion of diamond grit in the single-layer tool unlike the galvanically bonded counterpart (2). It has been further revealed that commercially fabricated brazed tools do not necessarily provide high diamond exposure as claimed by the manufacturer because of accumulation of brazed material in the space between the grit during brazing (3). On the other hand, control of bond level and maintenance of its uniformity which determines the initial topography of the working surface depends on various constructional as well as process parameters of fabrication (3, 4, 5). The performance of a single-layer tool depends largely on the initial topography of the working surface but may be significantly influenced by the work material characteristics and cutting conditions.

The principal objective of the the present investigation was to evaluate the dependence of performance of brazed metal-bonded monolayer diamond abrasive tools on the topography of its working surface in grinding of an oxide ceramic and cast iron.

2. Test Procedure

Brazed bonded monolayer diamond grinding wheels with a cup shape were used on a tool and cutter grinder to conduct experiment in face grinding mode. Diamond grit were of two sizes viz. D251 (250/212 μm mesh) and D126 (125/106 μm mesh). The diameter and width of working surface of the wheel were 75 mm and 5 mm, respectively.

Table 1 Different types of diamond abrasive tools

Tool	Grit size	Grit protrusion, μm	Characteristic feature
Type A	D251	185-205	Metal-bonded single-layer
Type B	D126	80-95	Metal-bonded single-layer
Type C	D126	50-60	Metal-bonded single-layer
Type D	D126	30-40	Metal-bonded composite type
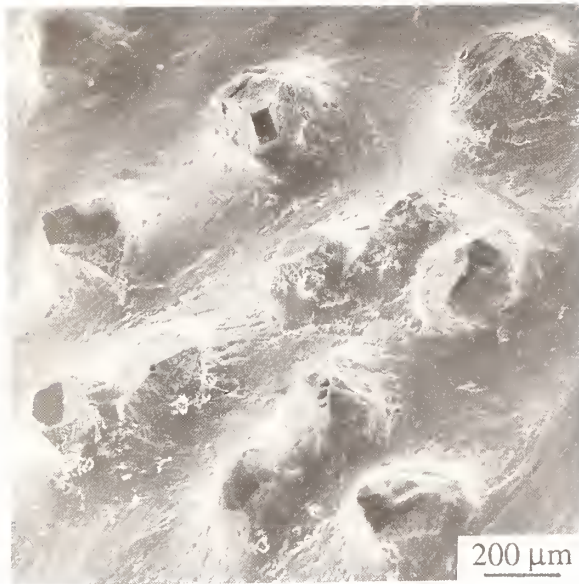
Fig. 1 Surface topography of diamond abrasive tool of Type A.

Fig. 3 Surafce topography of diamond abrasive tool of Type C.

Fig. 2 Surface topography of diamond abrasive tool of Type B.
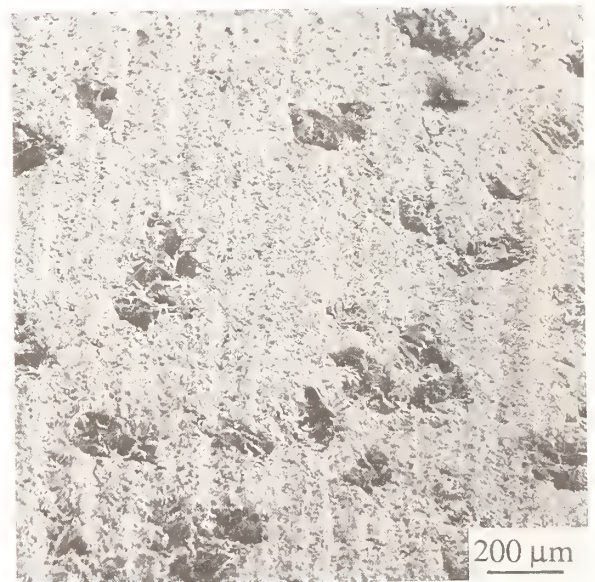
Fig. 4 Surface topography of diamond abrasive tool of Type D.
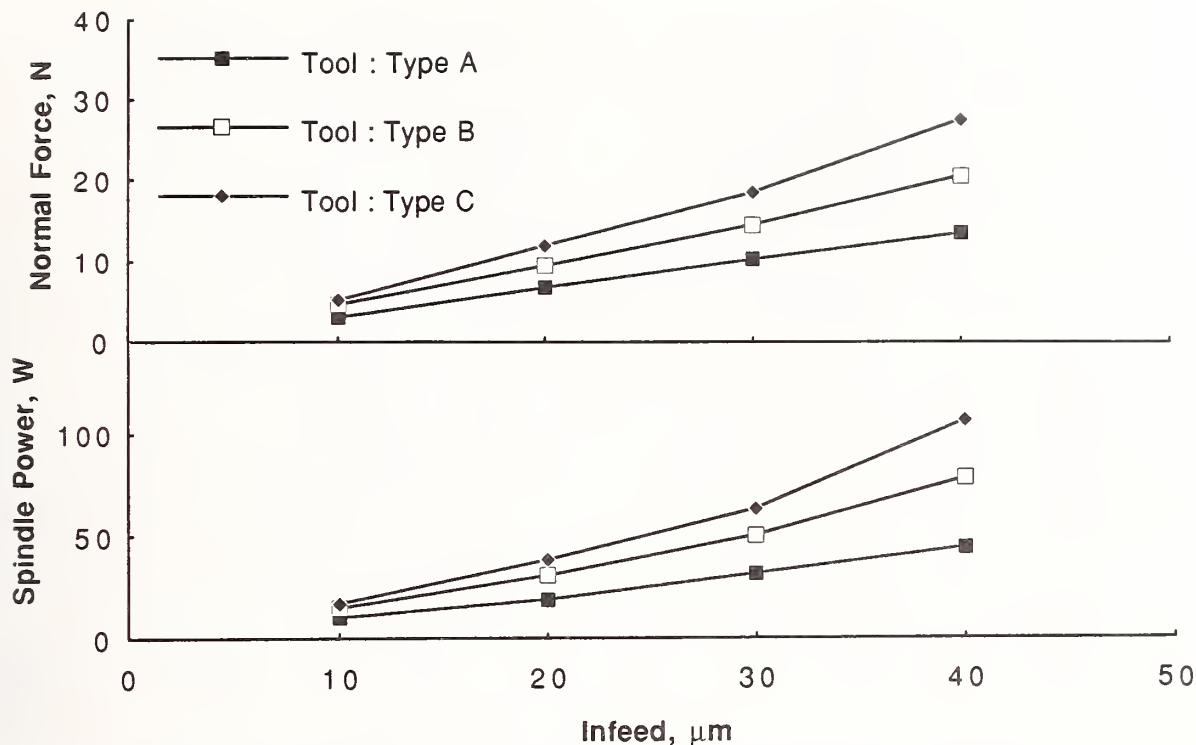
Fig. 5 Normal force and spindle power versus infeed for abrasive tools of Type A, B and C in dry grinding of oxide ceramic.

The normal force and the power drawn by the spindle during grinding were recorded, using a piezoelectric dynamometer and a wattmeter connected to a two channel recorder. SEM observations were made on the wheel surface before and after grinding tests. Representative chip samples of the work materials were collected during grinding and also observed under SEM.

The work materials were as follows : sintered aluminium oxide (hardness : 1200 $HV_{1.0}$, density : 3.925 gm/cm^3) and GG40 cast iron (hardness : 184 $HV_{1.0}$)

The workpieces were round bars of 12 mm diameter, the end face of which was ground. The grinding conditions were as follows : wheel speed, 30 m/s; table speed, 2 m/min; infeed, 10, 20, 30, 40 µm; environment, dry and wet (5% soluble oil).

3. Results

Designation of the diamond wheels used in the present investigation along with their grit size and grit protrusion are indicated in Table 1. Surface topography of a brazed monolayer diamond tool (designated as Type A) with grit size D251 is shown in Fig. 1. The grit can be seen to be

effectively wetted by the bonding matrix. The relative height between the tip of grains and mean bond base was found to be in the order of 185-205 µm. Figure 2 visualizes a brazed single-layer diamond tool (designated as Type B) with grit size D126. In this case the grit protrusion was found to be in the order of 80-95 µm. Figure 3 shows the surface of another brazed monolayer diamond wheel (designated as Type C) which was very similar to the wheel of Type B in terms of grit size, distribution pattern and density but differing in bond level. It can be easily observed that bond level was higher than that used in the wheel of Type B. This tool showed grit protrusion of the order of 50-60 µm.

To understand clearly the role bond level or crystal exposure, a composite type metal bonded diamond wheel (designated as Type D) with grit size D126 was also included. Figure 4 reveals the surface of the same obtained after truing and dressing. This was done to expose the crystals which formed a composite structure with the metal matrix. Numerous cutting points were generated on the crystals after dressing. Truing and dressing of the cup metal bonded diamond wheel were performed according to the recommendation of the wheel manufacturer (6).

35
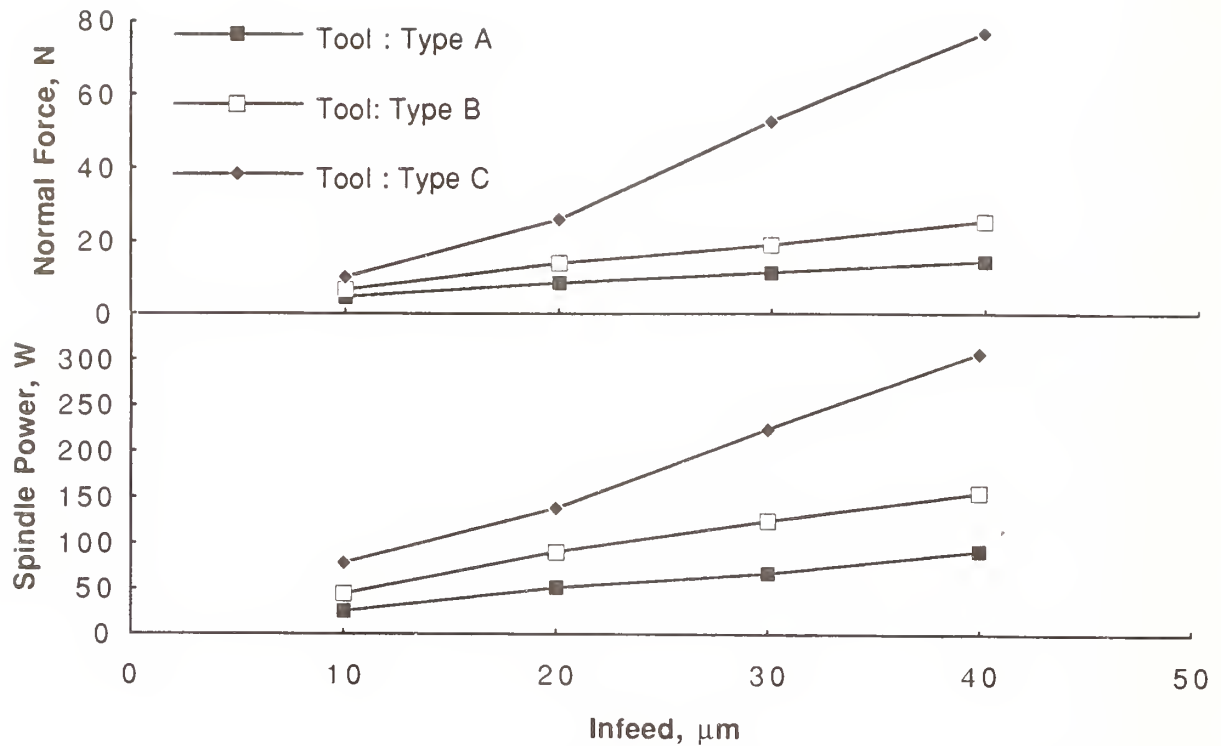
Fig. 6 Normal force and spindle power versus infeed for abrasive tools of Type A, B and C in dry grinding of cast iron.

Figure 5 shows that the normal force and spindle power were always smaller for wheel of Type A in comparison to wheels of Type B and C. Diamond wheel of Type B with a larger grit protrusion, however, showed lower magnitude of force and power in comparison to similar tool (Type C) but with smaller grit protrusion. This difference was more pronounced at higher infeed values.

Figure 6 shows the variation of normal force and spindle power with infeed during dry grinding of cast iron by diamond tools of Type A, B and C. The tool of Type A again developed lower normal force and required lower spindle power in comparison to tools of type B and C. The fact which draws attention was disproportionate increase of normal force and spindle power at relatively high infeed values for the Type C tool. Comparing Figures 5 and 6 one can arrive at the conclusion that spindle absorbed more power in grinding cast iron than in aluminium oxide ceramic.

The wheel of Type D was ineffective in dry grinding of cast iron. This is quite evident from Fig. 7. With infeed of 10 μm, the normal force and spindle power was as high as 23N and 138 W, respectively. At 20 μm infeed, these two parameters escalated to 95N and 540W just after

34 grinding passes. Figures 6 and 7 together indicate that during wet grinding of cast iron, tool of Type D exhibited higher force and power at all infeeds in comparison that exhibited by the wheel of Type C even under dry grinding. Again, this difference was more evident at higher infeed values. Figure 7 further reveals that the force and power absorbed during dry grinding of ceramic by tool of Type D were far below that absorbed during dry or wet grinding of cast iron by the same tool. Figure 7 also shows that the normal force and spindle power could be effectively reduced for tool of Type D in grinding ceramic through application of cutting fluid. Such reduction of force and power was of particular relevance when grinding is conducted at high infeed.

To understand the difference in performance between wheels of Type A and B in grinding oxide ceramic and cast iron, tests were conducted for a long duration with 40 μm infeed.

Figure 8 shows that the force and spindle power increased with cumulative infeed and rate of increase was higher for tool of Type B (grit size D126) in comparison to the tool of Type A (grit size D251) and gap between the force and power curves continued to widen as is evident from the
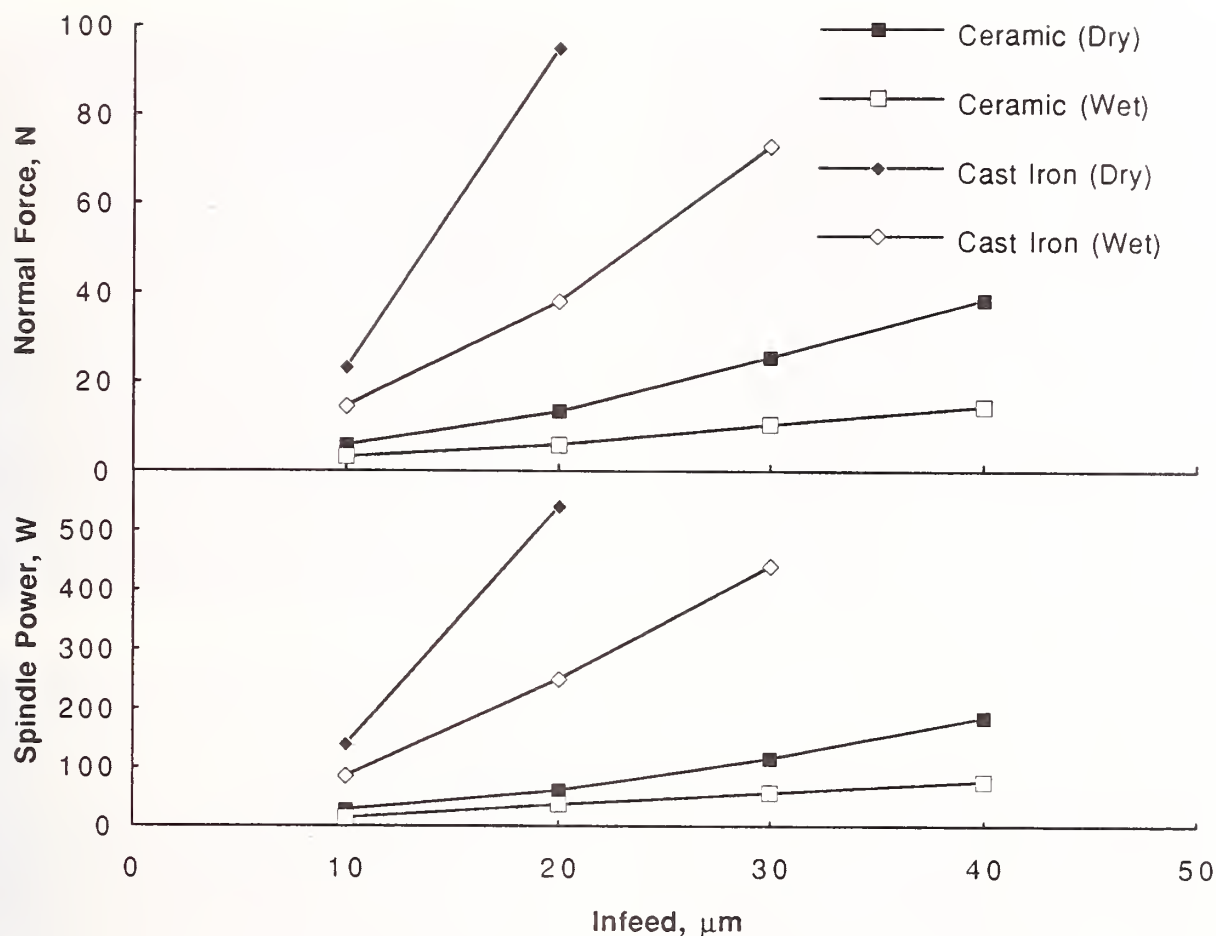
Fig. 7 Normal force and spindle power versus infeed for abrasive tool of Type D.

same figure. Figure 9 on the other hand indicates that normal force and power drawn by the spindle during grinding of cast iron by tool of Type A remained virtually constant with cumulative infeed. The same figure further reveals that these two parameters recorded higher values and slow increase with cumulative infeed for tool of Type B.

Figures 10 (a) and (b) show the types of chips produced during grinding of oxide ceramic and cast iron. Ceramic was ground mainly through formation of fine powder-like chips as a result of crushing. Cast iron, though formed fragmental chips, underwent some degree of plastic deformation before fracture as can be seen from Fig. 10 (b). The size of cast iron chips was much higher than those produced in grinding of ceramic.

Figure 11 shows topography of wheel of Type A after removing 76 mm from the ceramic bar. The grit appear to be mostly worn flat. Grit fracture or grit pull out was also not evident. The powder-like chips did not cause any wheel loading. Figure

12 reveals a different topography of the same wheel of Type A after removing 76 mm from the cast iron bar. The active grit appear to have a fractured surface in total contrast to what can be seen in Fig. 11. However, there was no sign of macrofracture of grit which takes place at the bond level. Similarly grit pull out or wheel loading was also not evident. Wheel loading did not occur in wheel of Type B while grinding cast iron but Fig. 13 clearly establishes the limitation of Type C wheel while grinding cast iron only because of loading. Micrographs of figure 13 clearly reveals heavily deformed chips of cast iron adhered to the surface of Type C wheel during grinding at 40 µm infeed.

4. Discussions

The difference in requirments of normal force and spindle power for monolayer diamond tools with different grit sizes may be related to increased number of cutting points of the tools with smaller grit sizes. But variation in bond level in tools with two different grit sizes could also influence performance. Single-layer diamond

37
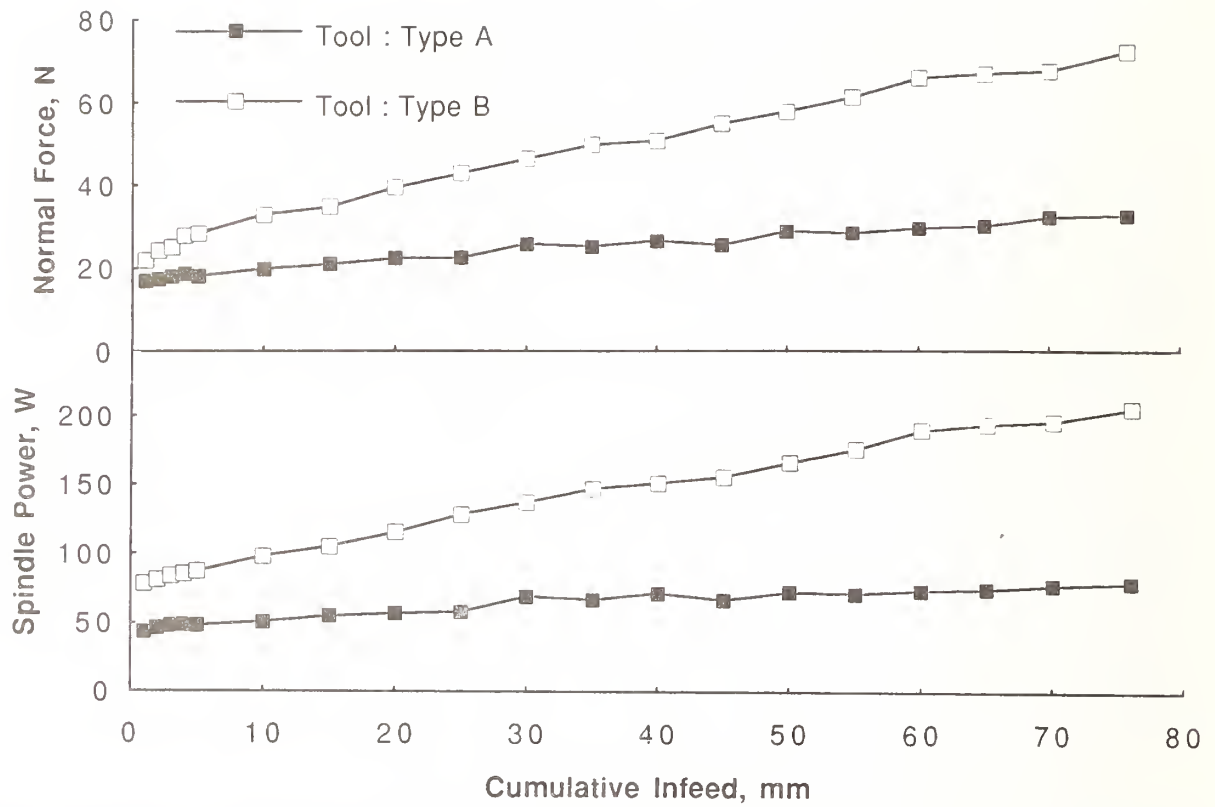
Fig. 8 Normal force and spindle power versus cumulative infeed for abrasive tools of Type A and B in dry grinding of oxide ceramic.
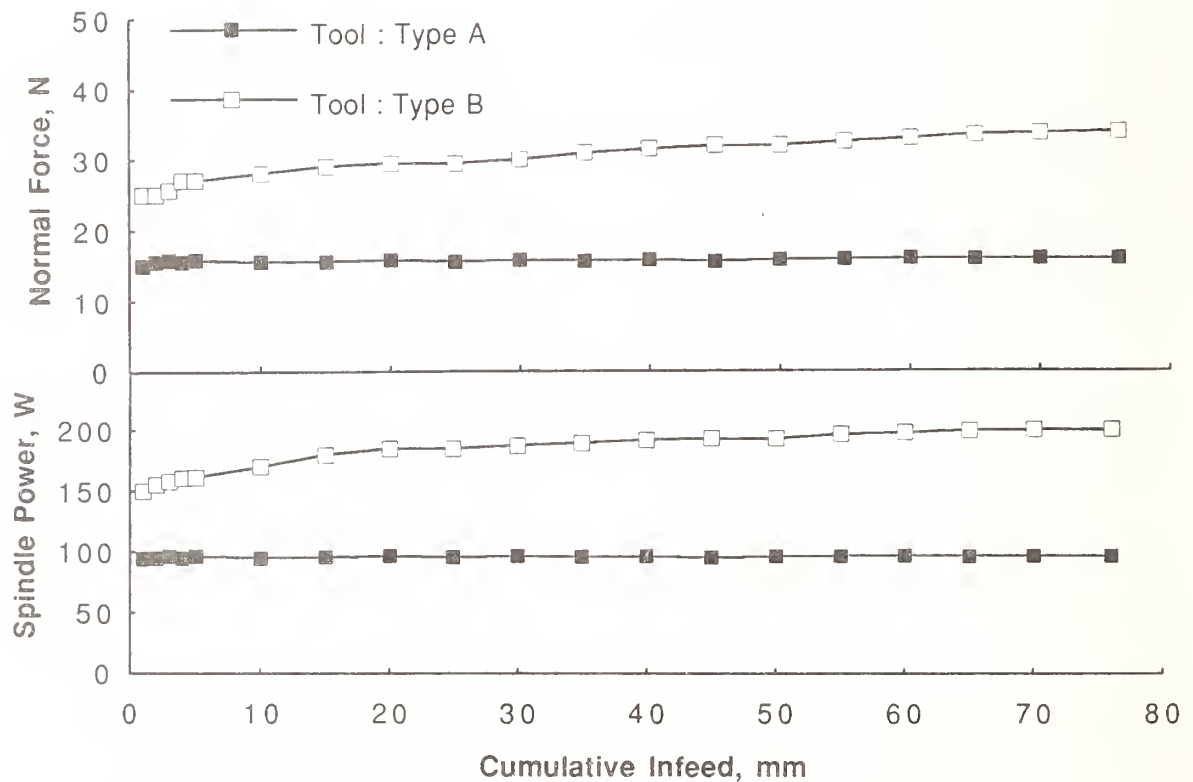
Fig. 9 Normal force and spindle power versus cumulative infeed for abrasive tools of Type A and B in dry grinding of cast iron.

38

25 µm

(a)

50 µm
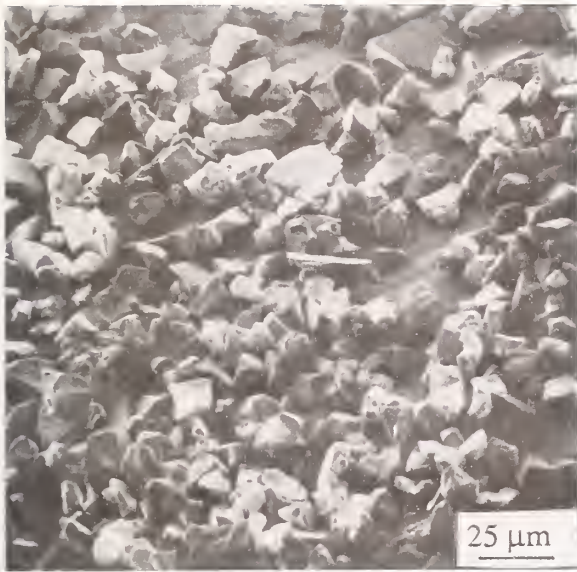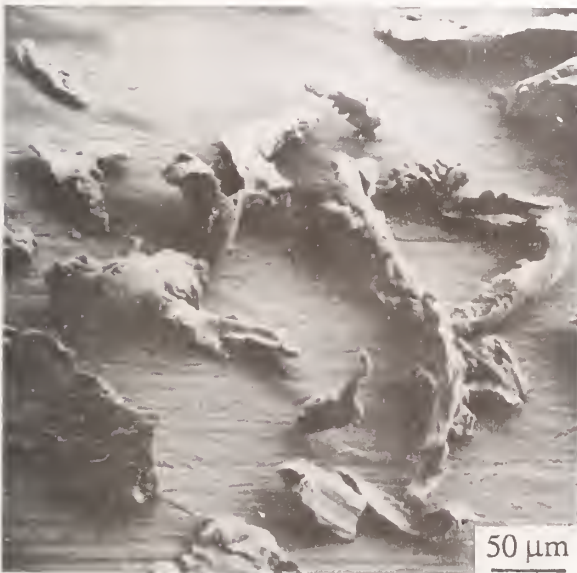
(b)

Fig. 10 Types of chip produced during grinding of (a) oxide ceramic and (b) cast iron.

200 µm

Fig. 11 Surface topography of abrasive tool of Type A after dry grinding of oxide ceramic.


200 µm
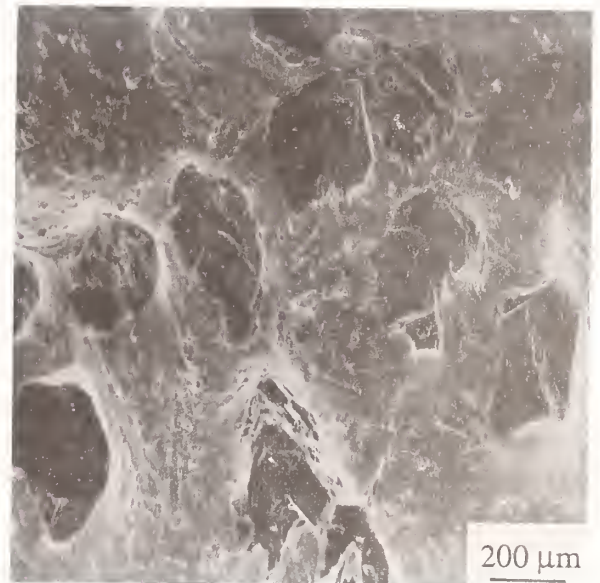
Fig. 12 surface topography of abrasive tool of Type A after dry grinding of cast iron.

tools with same grit size and similar density of distribution performed differently because of a wide variation in bond-chip and bond-work interactions. A high bond level could have an overidding influence.

Performance of an abrasive wheel also depends on the workmaterial characteristics. The spindle power which directly reflects tangential force was rather high for cast iron and more than for ceramic. As mentioned earlier ceramic was ground mainly through crushing where as cast iron underwent some degree of plastic deformation before formation of fragmented chips. The plastic deformation mainly accounted for the differences in spindle power and tangential force between ceramic and cast iron grinding. Apart from this severity of bond-chip interactions, bond-work interactions could influence the response of the wheel during grinding of ceramic and cast iron. Chip accommodation was easier with powder-like chips of ceramic than with relatively "large" fragmented

39

Fig. 13 SEM micrographs showing loading of abrasive tool of Type C in dry grinding of cast iron.

chips of cast iron under identical conditions of grinding. Similar observations (7,8) were also made during grinding of various materials, which varied widely in terms of ductility.

In ceramic grinding attritious wear was the major grit wear caused by progressive grit abrasion by the oxide ceramic resulting in rounding-off of the cutting points and development of wear flats on a large proportion of grit. Such change in grit geometry led to an increase in normal force developed during penetration of the work material and the energy required to remove material during grinding. Flatening of the cutting points could also increase friction at the grit-workpiece interface. In cast iron grinding, grit fracture was the major cause of wear. Such controlled brake down of the grit kept the wheel rather sharp and normal force and spindle power were virtually constant for tools with grit size D251 and increased very slowly for tool with grit size D126. Diamond abrasive tools with grit size D126 and high bond level experienced a premature failure in grinding cast iron at high infeed because of chip accommodation problems. Because of high bond level, cast iron chips were squeezed in the space between the bond and the workpiece and adhered to the tool surface. Such unfavourable change in wheel topography caused escalation of force and power to very high values.

5. Conclusions

1. Single-layer diamond abrasive tool did not suffer from grit pull out during grinding of oxide ceramic. Also, there was no evidence of chip accommodation problem with fine powder-like chips of oxide ceramic even at high infeed. However, the behaviour of such tool continued to change with passage of grinding time. This occured because of attritious wear of the diamond grit, caused by aluminium oxide resulting in rounding off of sharp points and generation of wear flats.

2. The rate of increase of normal force and spindle power was higher for tool with smaller grit size (D126) than that for tool with larger grit size (D251).

3. The bond level or crystal exposure has a predominant influence on the performance of an abrasive tool in grinding those materials which tend to stick to the wheel surface.

4. Comparative evaluation of single-layer brazed diamond wheel with coventional metal bond wheel may be made in grinding those materials which may not create a critical chip storage problem but, may cause irreversible change in the wheel behaviour through rapid wear of the single-layer diamond crystals.

6. References

1. L. M. Peterman, "Diamond Tooling in Non-Metallics", Proc. Superabrasive 85 Conference, Chicago, Illinois, pp. 1-12, 1985.

2. E. D. Kizikov, "Vaccum Technology for Diamond Toolmaking", Industrial Diamond Review, Vol. 1, pp. 20-23, 1991.

3. A. K. Chattopadhyay, L. Chollet, H. E. Hintermann, "On Performance of Brazed Bonded Monolayer Diamond Grinding Wheel", Annals CIRP, Vol. 40/1, pp. 347-350, 1991.

4. A. K. Chattopadhyay, L. Chollet H. E. Hintermann, "Experimental Investigation on Induction Brazing Of Diamond with Ni-Cr Hardfacing Alloy under Argon Atmosphere", Journal of Materials Science, Vol. 26 pp. 5093-5100, 1991.

5. H. E. Hintermann, A. K. Chattopadhyay, "New Generation Superabrasive Tool with Monolayer Configuration", Diamond and Related Materials, Vol. 1, pp. 1131-1143, 1992.

6. Tyrolit (Austria), Technical Information on Diamond and CBN.

7. D. M. Pai, E. Ratterman, M. C. Shaw, "Grinding Swarf", Wear, Vol. 131, pp. 329-339, 1989.

8. A. K. Chattopadhyay, L. Chollet, H. E. Hintermann, "On Performance of Chemically Bonded Single Layer CBN Grinding Wheel", Annals CIRP, Vol. 39/1, pp. 309-312, 1990.

A SYSTEMS APPROACH FOR GRINDING OF CERAMICS

K. SUBRAMANIAN, P. D. REDINGTON, and S. RAMANATH
Norton Company, Worcester, MA

Every manufacturing process involves four key elements: machine tool, work material, processing tool, and operational factors. These four input elements are related to output of the manufacturing process through process interactions. This systems description is also applicable for the grinding process. Through careful understanding of the input elements, their role in process interactions and the consequent output behavior, significant progress has been made in the grinding of ceramics. Several of the features of input elements, i.e., machine tool, diamond wheels, work material, and operational factors influence the process interactions, which result in plastic deformation and/or brittle fracture. The grinding system for ceramics is optimized when brittle fracture is minimized and plastic deformation is maximized by simultaneously controlling several of the input elements. Successful use of this systems approach for grinding of ceramics has resulted in production viable grinding of ceramics. A description of this systems approach is followed by several examples. These technical results will be useful if they are accompanied by recognition of key cost elements and their control. A total cost approach to this end is also described with examples.

Introduction:

Every manufacturing process involves four key elements: machine tool, work material, processing tool and operational factors. These four input elements are related to output of the manufacturing process through process interactions. This systems description of the grinding process is shown in Figure 1. Each of the input elements are composed of large number of variables. It is nearly impossible to characterize each of these variables to the last detail. Further, such approach is expensive and time consuming. However, it is critical that the role of each input variable is assessed in terms of the process interactions: cutting, ploughing, rubbing/sliding, at least qualitatively. Quantitative assessment of such microscopic interactions are difficult, but should be pursued whenever possible, using macroscopic or measurable process interactions such as forces and energy. These process interactions in turn influence the output of

the grinding system, which may be described in technical terms or as system output, when economic factors are also included. Thus every grinding operation in a systems approach becomes a process of simultaneously manipulating selected few input variables in order to maximize the cutting component of the process interactions and minimize the tribological components: ploughing and rubbing/-sliding in order to achieve the desired output results. Through careful understanding of the input elements, their role in process interactions and the consequent output behavior, significant progress has been made in the grinding of ceramics. After careful understanding of the technical elements of the grinding process, it is also necessary to apply them systematically through attention to a few strategic elements of the total cost. This paper attempts to highlight some of the results achieved in these areas.

Grindability of Ceramics vs. Metals:

Ceramics include a wide range of materials with their thermophysical properties dependent on the type, composition, microstructure, and the processing methods. In this regard, ceramics are a family of materials, just as we recognize metals as a family of materials. Once we recognize this commonality, many of the principles applicable to abrasive finishing of metals—an industry with over 100 years of history—become applicable to the abrasive machining of ceramics. However, for the same properties considered (thermal conductivity, Young's modulus, high temperature resistance, fracture toughness, etc.), metals and ceramics fall into distinctly different ranges. If we recognize these differences, then the principles of abrasive machining of metals can be modified for successful abrasive machining of ceramics. [1]

The strength of ceramic material varies widely, depending on the material chosen. Even for a given material, like silicon nitride, for example, the strength depends on the sintering aids used and the sintering methods (pressureless sintering, hot pressing, hot isostatic pressing (HIP), etc.) applied. In this regard, the ceramic materials are analogous to metals in which the composition, microstructure, and strength influence their grindability. Table 1 compares typical properties of selected ceramic materials with those of metals and a typical polymer.

In general, ceramic materials have higher stiffnesses (Young's modulus, E) than metals. This would imply that elastic deformation of ceramic materials during grinding would be less than metals for the same applied grinding forces. This is indeed true, and as a result, ceramic materials can be machined to closer tolerances, more precise geometry, superior finish, and better flatnesses and parallelism than is possible for metals. This principle is the basis for choosing ceramic materials over metals in precision instrument parts, machine tool beds or ways, as well as for gage blocks.

Ceramics are generally more chemically stable than metals. Hence the burn sometimes observed on metals during grinding is rarely observed on ceramic materials. Furthermore, the hot hardness and recovery hardness of metals are
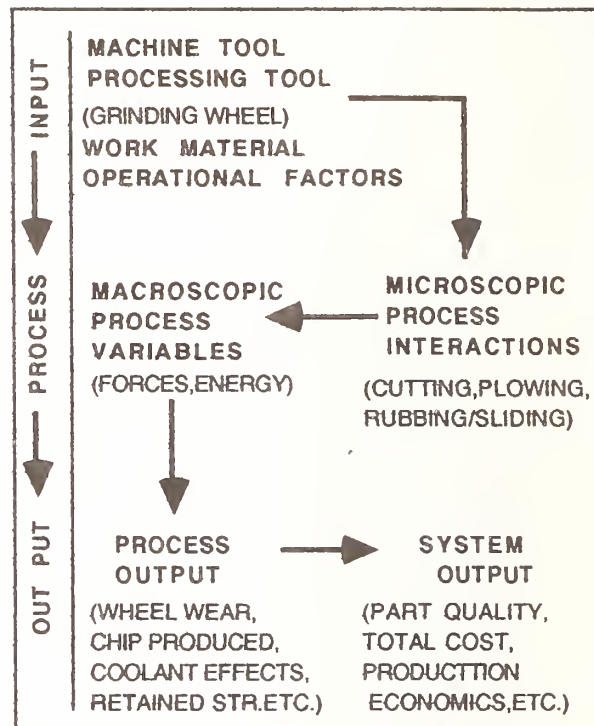
FIGURE 1
A SYSTEMS APPROACH FOR
PRODUCTION GRINDING

much lower than those of ceramics. In other words, any large scale thermal softening that aids in the grinding of metals may be rarely counted on in the grinding of ceramics.

Thermal conductivity of ceramic materials varies widely. This property determines the ability to conduct heat away from the grinding zone. Poor thermal conductivity in metals such as Titanium and Inconel can lead to high temperatures and great difficulty in grinding. Similarly, it is more difficult to grind poorly conducting ceramics and the problem becomes worse when they are also poor in thermal shock resistance.

One characteristic that significantly distinguishes ceramics from metals is their low fracture toughness. With all the above similarities between metals and ceramics in mind, it would appear that it is possible to achieve successful grinding of ceramics if the generation and propagation of cracks during the grinding process can be minimized.

44

Mechanisms of Material Removal in the Grinding of Ceramics:

Recognizing the low fracture toughness of ceramics, models have been proposed which describe initiation and propagation of microcracks during the grinding of ceramics. These models are generally described as "Indentation Fracture" models. [2,3,4] It has also been proposed that ductile deformation of ceramics takes place under extremely small depth of cut. This model described as "ductile regime grinding" assumes occurrence of plastic deformation only and seeks to achieve this condition using extremely low material removal rates. [5,6] Under practical production grinding conditions, it would appear that both these models operate, dependent on the force per grain, volume removed per abrasive particle, size of the abrasive particle, etc. [7] The description of the occurrence of both brittle fracture and plastic deformation and their optimization to achieve desired production rate and part quality is shown in Figure 2. Several of the features of input elements, i.e., machine tool, diamond wheels, work material, and operational factors influence these process interactions, i.e., brittle fracture vs. plastic deformation. The ceramic grinding system description and the input/output relations are shown in Figure 3. Referring to Fig. 2, it would appear that the mechanisms of material removal in the grinding of ceramic material are associated with both plastic deformation and brittle fracture. It may be nearly impossible to isolate one mechanism or the other unless extreme grinding conditions are chosen. These are identified as "coarse grinding" (where brittle fracture mechanism dominates) and "fine or ductile regime grinding" (where plastic deformation mechanism dominates). The consequence of such choices are low strength and poor reliability in the case of "coarse grinding" and extremely small material removal rate, high forces and specific energy in the case of "fine or ductile regime grinding". Referring to the process interactions described in Figure 1, it may be envisioned that plastic deformation is desirable to increase the cutting component. However, excessive deformation may result in inefficient cutting process accompanied by excessive ploughing and rubbing/sliding components. While brittle fracture may be a means of generating surfaces at the lowest forces and ener-

TABLE 1
PHYSICAL AND MECHANICAL PROPERTIES OF SELECTED CERAMICS, METALS AND A TYPICAL POLYMER

MATERIAL	Density (g/cm³)	Melting/ Decomposition Temperature (°C)	Thermal Conductivity W/m.K
CERAMICS			
Aluminum oxide	3.4-4.0	2050	27
Silicon Carbide	3.0-3.2	2500	63-155
Silicon nitride	3.2-3.5	1900	9-30
Zirconium oxide	5.8	2500	2
Ferrite	5.0-6.0	2000	8
Fused Quartz	2.2	1670	1.4
METALS			
Inconel 718	8.1	1400	12.4
Tool steel 52100	7.84	1500	52
bearing steel	7.85	1500	30-40
Aluminum	2.2	660	204
POLYMER			
Polyethylene	1.1	120	0.32

MATERIAL	Coefficient of Thermal Expansion (10^{-6}/k)	Tensile strength (MPa)	Modulus of Elasticity (CPa)
CERAMICS			
Aluminum oxide	8	205-550	385
Silicon Carbide	4-5	415-550	420
Silicon nitride	3	620-1100	305
Zirconium oxide	9-10	965-1380	140
Ferrite	7.5	140-170	205
Fused Quartz	0.55	110	77
METALS			
Inconel 718	7	1240-1405	215
Tool steel 52100	7	1405-2000	210
bearing steel	11	415-550	210
Aluminum	13	275-550	70
POLYMER			
Polyethylene	167	7-20	3.5

45

gy, it is certainly not desirable where highest strength and reliability are required. Thus optimizing the ceramic grinding system becomes a process of maximizing the cutting component through plastic deformation, while minimizing the grinding forces and energy input. This can be accomplished through a careful and simultaneous selection of input parameters identified in Figures 2 and 3. While this approach is common with metal grinding, the additional factor in ceramics grinding will be the control of force per grain. Under such process interactions, selection of suitable grinding cycle including rough and finish grinding steps is a matter of trade off between process economics and surface characteristics desired. There are several examples of the successful use of this systems approach for grinding of ceramics. Few of these results are described here.

Applications of the Systems Approach for Grinding of Ceramics:

Production Viable Grinding: Table 2 describes the results towards production viable grinding of ceramics. Material removal rates (MRR) of 1-30mm^3/mm/sec (.1-3 in^3/min/in) are now routinely achieved; the higher MRR are used for rough grinding processes while the lower values are used for finish grinding.[8] Such MRR, if they are achieved using coarse abrasive particles (100μ or larger), predominantly result in brittle fracture with poor surface quality (low strength and poor surface finish). Finer abrasive grains can be successfully used to achieve the high MRR' mentioned earlier, if the machine tool has rigidity and power to transmit the forces and energy required. This may, on occasion, also require unique wheel design to overcome the limitations of part geometry and fixturing.

Mirror Finish Grinding: Plastic deformation dominated grinding of ceramics using fine abrasive particles often permit controlled finishing of ceramic surfaces. As a result, extremely smooth surfaces have been produced in various grinding modes (e.g.) surface grinding, cylindrical grinding, creep feed grinding. For example, mirror finish grinding of ceramics in external cylindrical grinding has resulted in finish of the order of 7nm (.3μ inches) in hot pressed Silicon Nitride[9]. Such superior finish is often dependent on the work material grain size, uniformity and strength.

INPUT		
M/C TOOL		
LOW	**VIBRATION**	LARGE
PROCESSING TOOL		
SMALL	**GRAIN SIZE**	LARGE
SMALL	**GRAIN TIP RADIUS**	LARGE
WORK MATERIAL		
SMALL	**GRAIN SIZE**	LARGE
HIGH	**FRACTURE TOUGHNESS**	LOW
OPERATIONAL FACTORS		
LARGE	**CUTTING VELOCITY**	SMALL
SMALL	**DEPTH OF CUT**	LARGE
SMALL	**CHIP THICKNESS**	LARGE
PROCESS VARIABLES		
SMALL	**FORCE PER GRAIN**	LARGE
LARGE	**SPECIFIC ENERGY**	SMALL
LARGE	**GRINDING FORCE**	SMALL
OUT PUT		
HIGH	**PART STRENGTH**	LOW
FINE	**SURFACE FINISH**	POOR
GOOD	**EDGE CHIPPAGE**	POOR
LOW	**MATERIAL REMOVAL RATE**	HIGH

FIGURE 2
GRINDING OF CERAMICS
(GOVERNING MECHANISMS
AND CONTROL VARIABLES)

Pull out or localized removal of work material while mirror finish grinding is an evidence of inhomogeneity in grinding forces caused by limitations in one of the four input elements.

Grinding from Solid: When the grinding system is integrated as described earlier, with attention to process interactions that minimize the force per grain, high MRR grinding conditions can be used to grind components of complex geometry from simple solid shapes. Figure 4 shows several components that were ground from simple shaped raw material blanks.

Figure 4a shows four fluted end mill ground from a solid cylindrical rod of 16mm diameter. The entire end mill was finished in 35 minutes, which compares well with 5 to 15 minutes required for grinding steel end mills from cylindrical blanks. The details of grinding conditions are shown in Figure 4a. Figure 4b shows a spring produced by helical slot grinding on a hollow tube.

Figure 4c shows a rod plunge ground from a nominal size of 10 to 15mm to less than 1mm diameter. This was carried out through a plunge cylindrical grinding process using a vitrified bonded diamond wheel. The details of grinding conditions are shown in Figure 4c. Such thin sections are difficult to produce in the grinding of metals. However, ceramic materials due to their higher stiffness do not deflect as much and hence, can be machined to achieve extremely thin sections or small cross-sections (if brittle fracture during grinding is minimized) through the systems approach. Figure 4d shows a range of parts, most of which are produced from simple shaped unfinished blanks.

Microgrinding of Ceramics: The principles of controlled chip formation in finishing of ceramics can be extended to emulate precision finishing processes used in metal components. Hyperlap is a fixed abrasive finishing process in which grinding wheels operating at low velocities replace loose abrasive lapping. This results in higher MRR achievable in the grinding processes while maintaining flatness and parallelism achievable in lapping processes. This technology has been extended in the finishing of ceramics using a process called Microgrinding. Sometimes this application is also described as Flat Honing[10]. Table 3 shows some of the results achieved in microgrinding of ceramics on a variety of work materials. In addition to the obvious productivity and quality advantages, this process is environmentally benign as simple cool-
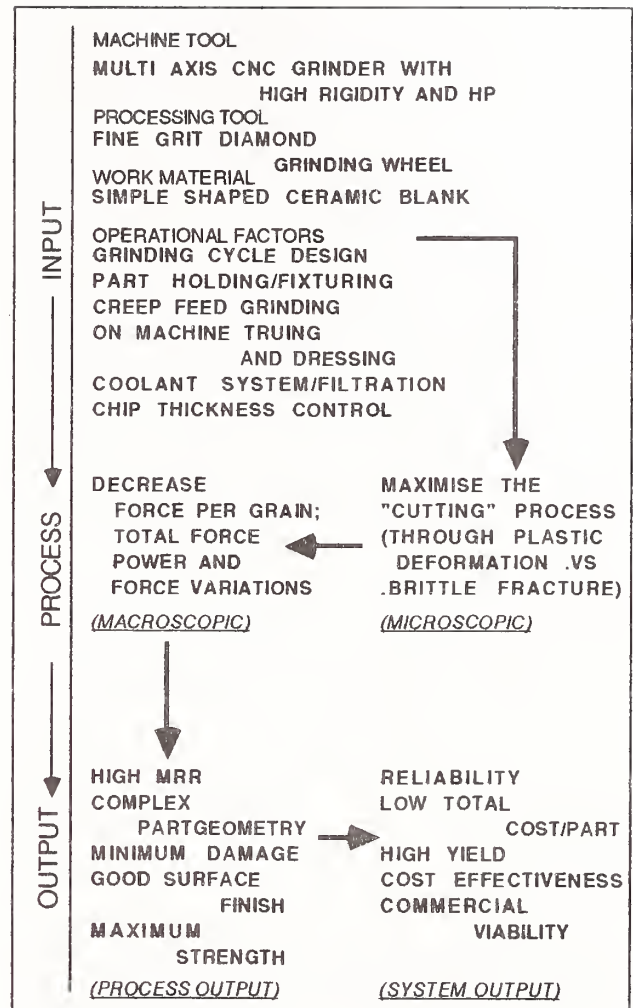
FIGURE 3
SYSTEMS DESCRIPTION FOR THE
PRECISION GRINDING OF CERAMICS

TABLE 2
PRODUCTION VIABLE CERAMICS GRINDING

	Past	Now
Material Removal Rate		
(mm³/sec/mm)	.1-1.0	1-30
(cu.in/min./in.)	0.01-0.1	0.1-3
Surface Finish		
(μm)	.750-1.27	.0075-.125
(microinch)	30-50	.3-5
Cycle Time:		
6 Hours --> 1 Hour		
Hrs --> 35 min.		
48 Min --> less than 10 min.		

47

ants or water can be used without the need for lapping fluids. Also oil bearing abrasive slurry need not be disposed of in microgrinding processes as none is required!

TABLE 3
MICROGRINDING/FLAT HONING CASE STUDIES

CASE NO.	MATERIAL	WHEEL	MRR (mm³/sec)	Ra (μm)	FLAT-NESS TOLE-RANCES (μm)	THICK-NESS TOLE-RANCES (μm)
				SURFACE FINISH		
1	SAPPHIRE	320 GRIT VITRIFIED BOND	38X10³	.50	5-10	2.5

Result: 5 TO 10 TIMES FASTER COMPARED TO LAPPING WITH CONVENTIONAL ABRASIVES

| 2 | SILICON NITRIDE | 320 GRIT VITRIFIED BOND | 55 | .20 | 2.5 | 2.5 |

Result: 5 TIMES FASTER COMPARED TO LAPPING WITH CONVENTIONAL ABRASIVES

| 3 | SILICON CARBIDE | 320 GRIT METAL BOND | 27 | .25 | 2.5 | 2.5 |

Result: 3 TIMES FASTER COMPARED TO LAPPING WITH CONVENTIONAL ABRASIVES

| 4 | ALUMINA/ TiC | 600 GRIT VITRIFIED BOND | 2.2 | .125 | NO CHIPPING AT 200X | – |

| 5 | FERRITE | 320 GRIT METAL BOND | 55 | .40 | 2.5 | 2.5 |

Note:
Work Material: See Table
Machine: Double Sided Lapping/Grinding Machine
Wheel: 800mm Dia; See Table for grit size and bond type
OPERATIONAL PARAMETERS:
Wheel Speed: 1 to 5m/sec at O.D.
Work Speed: 0.1 to 5m/sec
Coolant: Mineral Oil (or) Water Based Coolants

Total Cost Approach for Grinding of Ceramics:

Having briefly looked at the technical results of the systems approach for ceramic grinding, let us now briefly review some economic aspects. There are several recent publications which address this subject [11,12,13]. Our objective here is to highlight the key cost controlling elements and how to attack them strategically.

Every ceramic component starts with the ceramic raw material, which in most cases, will be in powder form. The amount of ceramic material used to produce one component is termed as the material cost. This powder is often processed in one or more ways to achieve the unfinished blank. These processes may be hot pressing, hot isostatic pressing, sintering, etc. We shall call these "Ceramic Processing" and the cost associated with this as the ceramic processing cost. The unfinished blank may then be finished often using grinding or other abrasive processes such as ultrasonic machining. The cost associated with this, we will call as the "Finishing Cost". Thus the total cost of a ceramic component (Fig. 5) will be:

$$\text{Total Cost} = \text{Finishing Cost} + \text{Ceramic Processing Cost} + \text{Material Cost} \qquad (1)$$

In reality, these elements of costs are not independent. "Yield" is defined as the fraction of the total number of parts produced to arrive at one good or usable component. Yield in every processing step influences the total cost. The yield becomes increasingly critical as we move from raw material to finished part. When a part is rejected at the finishing stage, the total cost of a good part produced increases not only due to the loss in the finishing, but also due to all other costs incurred up to this time. This compounding effect is shown in the equation below:

$$\text{Total Cost} = \frac{\text{Finishing Cost}}{(\text{Y.Fin.})} + \frac{\text{Ceramic Processing Cost}}{(\text{Y.Fin.}) \times (\text{Y.Proc.})}$$
$$+ \frac{\text{Material Cost}}{(\text{Y.Fin.}) \times (\text{Y.Proc.})} \qquad (2)$$

where,
Y.Fin. = Yield in the finishing process
Y.Proc. = Yield in the ceramic processing operation.

Finishing Cost consists of the cost of machining, inspection, set up or fixturing. Thus:

$$\text{Finishing Cost} = \text{Machining Cost} + \text{Inspection Cost} + \text{Set Up or Fixturing Cost} \qquad (3)$$

as illustrated in Fig. 6.

FIGURE 4a
CERAMIC END MILLS FINISHED BY GRINDING
OF SOLID CYLINDRICAL BLANKS
Work Material: Hipped Silicon Nitride
Machine: 5 axis CNC Grinder
Wheel: SD320R100 BXL6145
OPERATIONAL PARAMETERS:
Wheel Speed: 35 m/sec
Work Speed: 50 mm/min
Depth of Cut: Roughing: 2.5mm
              Finishing: 0.25mm
Coolant: 100% oil applied at 2001/min;
         .828 MPa

FIGURE 4c
THIN DIAMETER CERAMIC RODS GENERATED
FROM STANDARD CYLINDRICAL RODS BY
PLUNGE GRINDING
Work Material: See Figure
Machine: Okuma CNC Grinder
Wheel: SD320l150 VX223C
OPERATIONAL PARAMETERS:
Wheel Speed: 45 m/sec
Work Speed: 5.0 m/min at O.D.
Depth of Cut: .05 mm/rev
Coolant: Water Soluble Oil
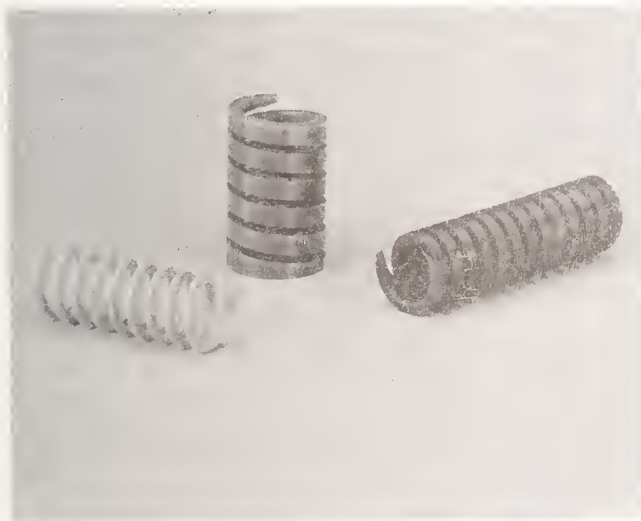
FIGURE 4b
CERAMIC SPRINGS GROUND FROM HOLLOW
TUBES USING SUITABLE GRINDING METHODS
Work Material: Zirconia
Machine: CNC Grinder
Wheel: SD180R100 BXL6145
OPERATIONAL PARAMETERS:
Wheel Speed: 35 m/sec
Work Speed: .6 mm/min
Depth of Cut: .37mm
Coolant: 100% oil applied at 2001/min;
         .828 MPa

FIGURE 4d
A SELECTION OF COMPLEX GEOMETRY
CERAMIC PARTS WITH SURFACES GENERATED
BY DIAMOND GRINDING PROCESSES

Let us now focus on machining costs, and it consists of components due to machine tool, labor, abrasive tools and overhead costs. Thus:

Machining Cost = Machine Tool Cost + Labor Cost
$$+ \text{ Overhead Cost } + \text{ Tool Cost} \qquad (4)$$

The Machine Tool, Labor and Overhead Costs are directly linked to the time it takes to produce one part, called the cycle time. Thus:

Machine Tool Cost (M.T.C.) = Machine Rate ($/hr) x Cycle Time $\quad$ (5)

Labor Cost (L.C.) = Labor Rate ($/hr) x Cycle Time $\qquad$ (6)

Overhead Cost (OHC) = Burden Rate ($/hr) x Cycle Time $\qquad$ (7)

Tool Cost = Abrasive Wheel Cost/No. of Parts
$$\text{Machined per Wheel} \qquad (8)$$

Since cycle time has a profound impact on the finishing cost, let us look into its components briefly. It is defined as the time consumed in finishing per part. Thus:

Cycle Time = Total Time Consumed (T)/No. of Parts machined
$$\text{in Time T. (N)} \qquad (9)$$

Total Time (T) = Set up time + Inspection Time + Grinding Time $\quad$ (10)

Grinding Time = Wheel/Work Contact Time + Wheel
$$\text{Preparation Time} \qquad (11)$$

Wheel preparation time is required for truing and dressing. Part load and unload time is included in the set-up time.

Grinding time directly influences the number of parts machined per wheel mentioned in equation 8. Thus cycle time indirectly influences the tool cost as well.

The above equations describe the elements of costs and their inter-relationship in the manufacture of ceramic components. Attempts to minimize each cost element individually is tedious and often futile. It is imperative to recognize the key cost elements and attack them strategically. This approach cannot be solely based on economics, but a rather careful combination of economic and technical factors will be required. In the following, few of our experiences are described:

Yield in the finishing process, described in equation 2 would appear to be a key cost controlling element.

TOTAL COST PER PART=

MATERIAL COST+
CERAMIC PROCESS COST+
FINISHING COST
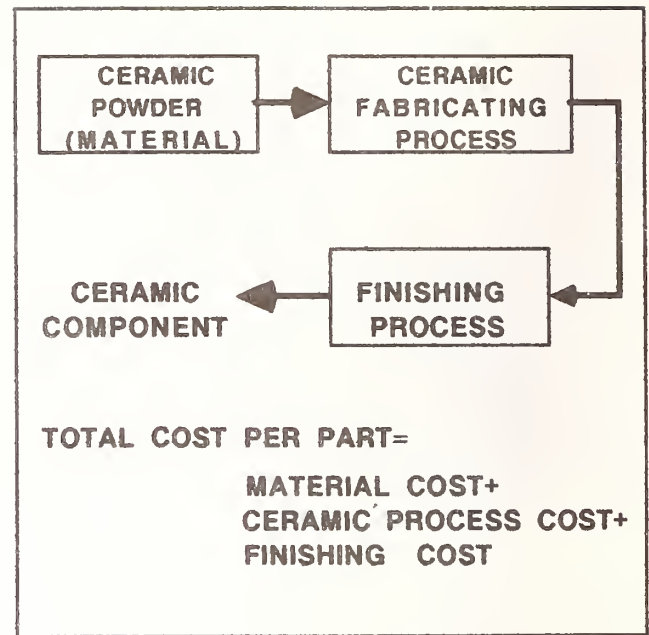
FIGURE 5
COMPONENTS OF COST FOR A CERAMIC PART

TABLE 4
INFLUENCE OF CERAMIC PROCESS AND
FINISHING PROCESS YIELD ON THE TOTAL COST

CASE	Ceramic Process Yield (%)	Finishing Process Yield (%)	Material Cost	Process Cost	Finishing Cost	Total Cost
Hypothetical	100	100	5	5	10	20
Actual						
(a)	20	100	25	25	10	60
(b)	100	20	25	25	50	100
(c)	20	20	125	125	50	300
Step 1	100	100	6	6	12	24
Step 2	100	100	7	4	4	15

Note: All costs are in relative units. As an example in the hypothetical case, the total material cost (20 units) consists of 25% in material cost (5 units), 25% in process cost (5 units) and 50% in finishing cost (10 units). Subsequent examples are illustrated as modifications using the hypothetical case as the reference or base. The above table is based on our experience in a wide range of advanced ceramic components grinding.

Step 1: Yield in the finishing process is optimized through systems approach to grinding which includes modifications to the geometry of the unfinished blank and ceramic processing steps.

Step 2: Step 1 is followed by changes in component design (without altering the function) that lower the ceramic process cost and accelerate the finishing process.

50

Table 4 shows a hypothetical case and three situations which represent the range of realistic conditions commonly observed. While the exact values are not critical, the trends are important. The total cost noted in our examples (a), (b) and (c) represent the range of costs quoted for ceramic components, which are 3 to 15 times that of ideal or anticipated future costs for ceramic components. However, it is possible to systematically attack these total costs using step 1 and step 2 also demonstrated in Table 4. Figure 4 shows actual cases where step 1 has been demonstrated successfully.

TABLE 5
TWO STEP APPROACH TO
REDUCE FINISHING COST

	PRESENT	STEP 1	STEP 2
SET UP			
	• SEVERAL TO MANY SET UPS. • POOR FIXTURING • LACK OF MULTI--AXIS MACHINING CAPABILITY • LIMITED PROCESS PLANNING OR WHEEL DESIGN.	• SINGLE OR FEW SET UPS • GOOD FIXTURE DESIGN • MULTI AXIS CNC MACHINES USED • CAREFULLY DESIGNED PROCESS PLAN AND WHEEL DESIGN.	• SAME AS STEP1 • PART DESIGN PERMITS RAPID SET UP.
INSPECTION			
	• MULTIPLE SET UPS REQUIRE REPEATED INSPECTION FOR GEOMETRIC ACCURACY AND CUMULATIVE ERRORS. • SMALL STOCK WITH NEAR NET SHAPE AND ABSENCE OF LOCATING SURFACES REQUIRE FREQUENT INSPECT-ION.	• SINGLE OR FEW SET UPS REDUCE CUMULATIVE ERRORS AND INSPECTION TIME. • MACHINE TOOL ACCURACY AND PRECISION USED TO BUILD CLOSE TOLERANCE IN THE PART REDUCING INSPECTION TIME.	• SAME AS STEP 1. • PART DESIGN PERMITS RAPID INSPECTION AND REDUCED INSPECTION.
MACHINING			
	• PART DESIGN LESS TOLERANT FOR VARIATIONS IN THE MACHINING PROCESS • PART DESIGN NOT CONDUCIVE FOR RAPID MACHINING. • PART DESIGN NOT SUITABLE FOR SINGLE STEP OR MULTI AXIS MACHINING.	• SAME AS PRESENT	• PART DESIGN MODIFIED TO PROVIDE LOCATING SURFACES FOR MACHINING REFERENCE. • SIMPLE SOLID SHAPE WITH CONSISTANCY • RAPID MACHI--NING METHODS
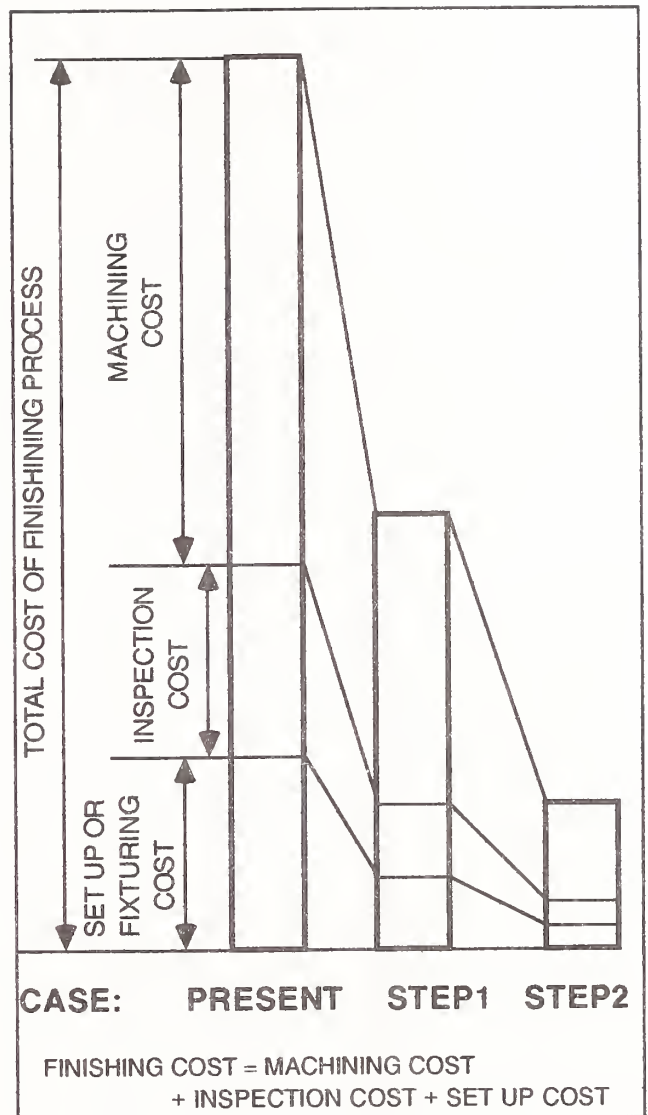
FIGURE 6
TOTAL COST APPROACH TO
REDUCE THE FINISHING COST

Through this and other examples, it has been learned that the yield can be maximized by careful understanding of the grinding interactions and optimizing them using the systems approach described in Figures 2 and 3. Finishing cost and cycle time are two other elements which require close scrutiny in the total cost approach. Finishing cost can often be minimized by controlling the inspection and set-up costs. This is pursued simultaneously with cycle time reduction using the understanding of grinding process interactions described earlier. These approaches for total cost reduction are shown in Figure 6 and Table 5. While some of these steps may appear to be obvious, it is critical that these steps

CYCLE
TIME(HRS.)

FINISHING
RATE($/HR.)
RELATIVE
UNITS

YIELD
(%)

FINISHING
COST($/PART)
RELATIVE
UNITS
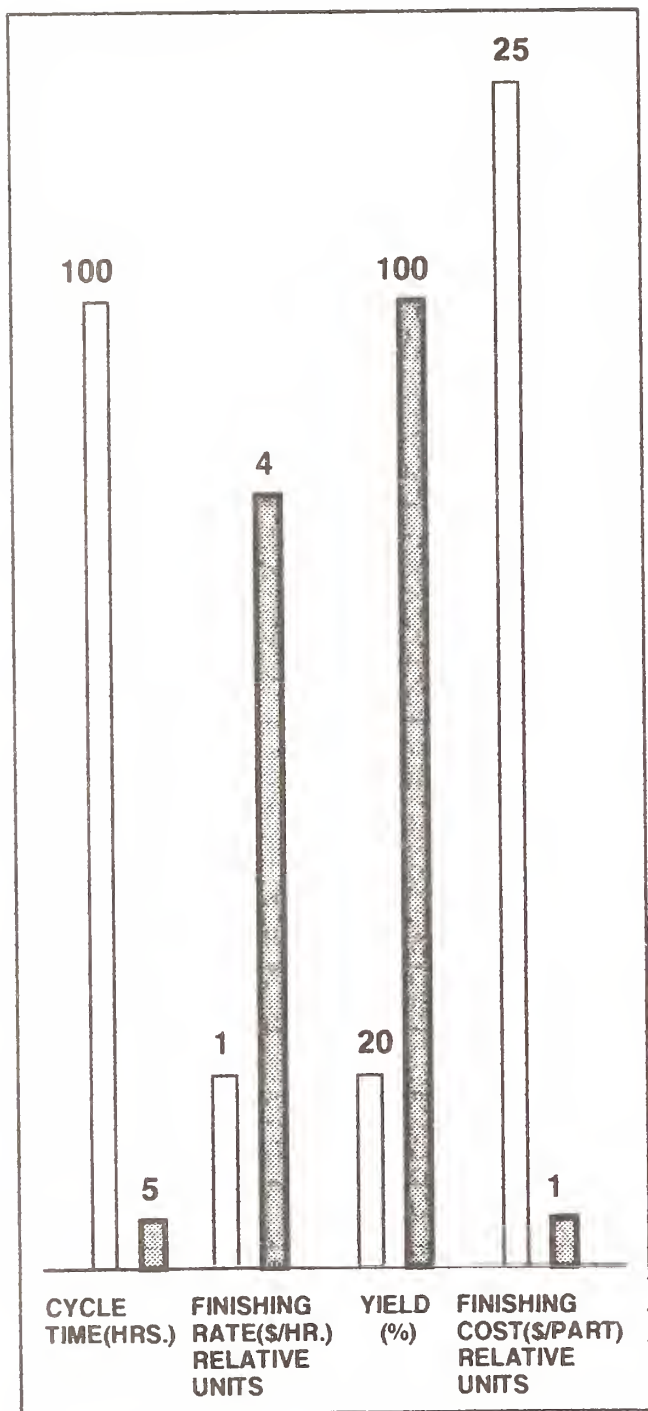
☐ PAST

▒ AFTER SYSYETMS APPROACH
INCLUDING TOTAL COST CONSIDERATIONS

FIGURE 7
COST BENEFITS BASED ON
THE SYSTEMS APPROACH

are pursued rigorously in order to find early commercialization of the advanced and emerging materials. Figure 7 illustrates an actual case where the cycle time is dramatically reduced and the yield is improved, thus decreasing the total cost by a factor of 25. In order to achieve these results, state-of-the-art grinding system is required which increases the finishing rate (machine rate + labor rate + burden rate) by a factor of 4. However, such increases are totally justified with high return on investment or short payback period, because of increased throughput (cycle time reduction) and finishing cost reduction. In addition, the component also exhibited higher strength and reliability during performance tests.

Surprisingly, methods to lower finishing costs are also associated with sound finishing practices necessary to achieve reliable grinding of high strength parts! Thus cost effective finishing of ceramics to achieve low total cost per part would appear to be concurrent with reliable finishing methods for ceramics.

Summary:

It has been described earlier in this paper that machine tools, diamond wheels, work materials and operational factors play a key role in the grinding of ceramics. Integrating these four key elements into a grinding system has been shown to be required both for technical reasons as well as economic or total cost considerations. The biggest challenge in the introduction of advanced materials like ceramics is the difficulty in bringing about such system integration based on sound technical reasoning and economic considerations. The risks, uncertainties and cost avoidance considerations, always seem to dominate over reasonable technical experiences whenever new manufacturing systems are to be implemented.

Grinding, like any manufacturing process, is an interdisciplinary effort, often requiring expertise in each of the four input areas, i.e., machine tool, wheel, work material and operational factors. Integrating the grinding system is far more effective when expertise in these four elements are brought together. Such interdisciplinary efforts facilitate systems integration far more than individual and interconnected efforts. Indeed such interdisciplinary and cooperative effort decreases the risks and

52

uncertainties. Several redundant costs are avoided or eliminated in this process. Such effort makes the total cost approach -- where changes in materials and ceramic processes are acceptable to increase finishing yield and decrease total cost -- practical to implement. There are attempts to bring about inter-industry collaboration of machine tool builders, ceramic manufacturers or users and wheel manufacturers to achieve the necessary integrations of grinding systems for ceramic components[14, 15]. Widespread efforts to achieve such system integration through sound technical and economic reasoning will be necessary to achieve early commercialization of ceramic components.

List of References

1. K. Subramanian and S. Ramanath, "Principles of Abrasive Machining Processes", Section 5, Vol. 4, Ceramics and Glasses, ASM Hand Book, 1991.

2. B.R. Lawn, A.A. Evans, and D.B. Marshall, Elastic/Plastic Indentation Damage in Ceramics: The Median/Radial Crack System, J. Am. Ceram. Soc., Vol. 63 (No. 9-10), 1980, p. 574-581.

3. I. Inasaki, Grinding of Hard and Brittle Materials, Ann. CIRP, Vol. 36 (No. 2), 1987, p. 463-471.

4. R.W. Rice and J.J. Mecholsky, The Nature of Strength Controlling Machining Flaws in Ceramics, The Science of Ceramic Machining and Surface Finishing II, Special Publication 562, National Bureau of Standards, 1976, p. 351-378.

5. M. Miyashita, Ultraprecision Centerless Grinding of Brittle Materials, First Annual Precision Engineering Conference, North Carolina State University, Raleigh, 1985.

6. T.A. Bifano, T.A. Dow, and R.O. Scattergood, "Ductile Regime Grinding: A New Technology for Machining Brittle Materials", Proceedings of the Intersociety Symposium on Machining of Advanced Ceramic Materials and Components, ASME, 11/12/1988, pp. 113-120.

7. K. Subramanian and S. Ramanath, "Mechanisms of Material Removal in the Grinding of Ceramics", Proceedings of the Symposium on Precision Machining: Technology and Machine Development and Improvement, ASME Publication, PED-Vol. 58, 1992.

8. R.N. Kopp, et.al, "Progress in the Finishing of Technical/Advanced/Fine/Electronic Ceramics", SME Paper No. M91-178, 1991.

9. Unpublished internal research results, Norton Company.

10. J.H. Indge, "Double Sided Precision Abrasive Machining of Ceramic Materials", SME Paper No. EM90-139, 1989.

11. S. Jahanmir, et. al, "Ceramic Machining: Assessment of Current Practice and Research Needs in the United States", NIST Special Publication 834, June 1992.

12. S. Das and T.R. Curlee, "The Cost of Silicon Nitride Powder and the Economic Viability of Advanced Ceramics", American Ceramic Society Bulletin, Vol. 71, No. 7, 7/1992, pp. 1103-1111.

13. K. Subramanian and P.D. Redington, "Total Cost Approach for Ceramic Component Development", Ceramic Engineering and Science Proceedings, American ceramic Society, Vol. 14, #1-2, 1993, pp. 309-320.

14. K. Subramanian and P.D. Redington, "Ceramic Machining Technology Center -An Innovative Approach for Precision Production Grinding", SME Paper No. EM91-256.

15. "The Challenges of Ceramic Machining Continue", Edited by Laurel M. Sheppard, American Ceramic Society Bulletin, Vol. 17, No. 11, November 1992, pp. 1590-1603.

THE ROLE OF MATERIAL AND GRINDING PARAMETERS IN GRINDING OF ALUMINA FIBER-REINFORCED ALUMINUM ALLOYS

H. CHANDRASEKARAN and J. O. JOHANSSON
Swedish Institute for Metals Research, Stockholm, Sweden

Results from a grinding study of Al_2O_3 short fiber reinforced Al-alloy MMC is presented in this paper. Variants of MMC material were tested for a range of grinding conditions and abrasive wheel types. Grinding forces and surface finish were measured and qualitative study of the ground surfaces using optical and scanning electron microscopy was also carried out. While the grinding conditions appear to play only a limited role upon the measured surface finish, the abrasive type on the other hand displayed great influence. These indicate that the measured surface finish parameters do not reflect the true state of the surface. Force considerations and qualitative surface studies revealed the overall superiority of diamond and cubic boron nitride wheels over the conventional abrasives. The two important features, namely disturbance of the near surface fibers and the development of micro-cavities along the contour of the fibers in the grinding plane observed by us could have critical implication upon the surface integrity of these MMC materials.

1. INTRODUCTION

In the course of the past few years the class of materials identified as metal matrix composites (MMC) consisting of high-performance reinforcements in a metallic matrix have increased in their range. The main attraction of these materials is the possibility of tailoring the mechanical and physical properties between those of the reinforcement and the metallic matrix. The cost of the materials are dictated by the matrix, reinforcement and the manufacturing process used. In this context alumna/silicon carbide fibre/particle based aluminium composites using some type of pressure infiltration or melt mixing appear to be cost competitive (1). Accordingly these may be expected to find specific applications in such light weight wear resistant parts as valve gear and other engine components.

However, these intended applications primarily in the automobile industry would require some machining. Existing information on the machinability of aluminium alloy composites reinforced with Al_2O_3 fibres/particles based upon chip forming operations like turning and drilling (3, 4, 5 and 6) indicate that the composite materials could present machining difficulties, often intriguing from some points of view. Tool wear is often abrasive, demanding highest tool hardness. Another problem is the quality of machined surfaces and sub-surface damages accentuated with the increasing wear of the cutting tool (3) and grinding might be the answer (2) then.

However, information about the *grindability* of MMC is very limited. Hence as a first step it was proposed to collect fundamental information on the grindability of these materials such as cutting forces and surface finish, when grinding some standard Al alloy composites reinforced with short alumina fibres.

The abrasive wheel types as well as the grinding conditions were varied to cover a broad range of parameters at this stage. Instead of the traditional grindability studies based upon the grinding coefficient or G factor (relationship between the volumes of ground material to worn abrasive wheel), the focus was directed towards the understanding the grindability of these materials from energetic and wheel-work combinations point of view as relevant to the surface integrity aspects. This involves a study of the contact phenomenon between the abrasive grit and the hard alumina fibers, as well as the soft Al alloy matrix.

2. EXPERIMENTAL PROCEDURE
2.1 ALUMINIUM ALLOY COMPOSITES

The work material for the grinding tests was produced using the "squeeze casting", a technique in which molten Al-2Mg alloy was allowed to infiltrate an alumina preform of required shape under suitable temperature and pressure within a closed preheated mould (7), resulting in short cylinders of 60 mm diameter and 40 mm high. Accordingly Al-2Mg alloy with respectively 10 and 26 vol.% alumina fibers was the principal test material. Nominal properties of the composites used in our grinding tests are shown in Table 1.

Table 1 Properties of the Al alloy composites

.No Property	Material variants		
	Al-2Mg		Al-9Si-3Cu
	10% fiber	26% fiber	30% fiber
1. Yield stress (MPa)	98	163	-
2. Ultimate tensile stress (MPa)	187	263	200
3. Vickers hardness (GPa)	1.20	1.40	1.52

|25 μm|
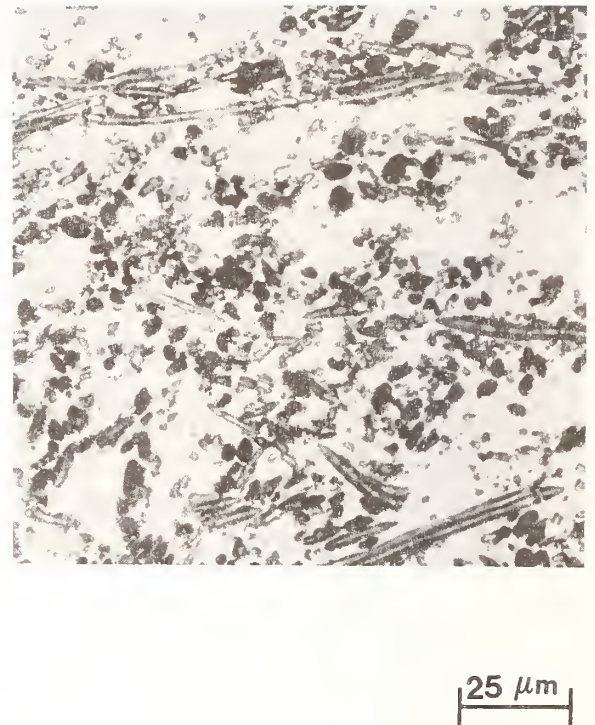
Fig.1   Microstructure of 26% fibre MMC material (axial section).
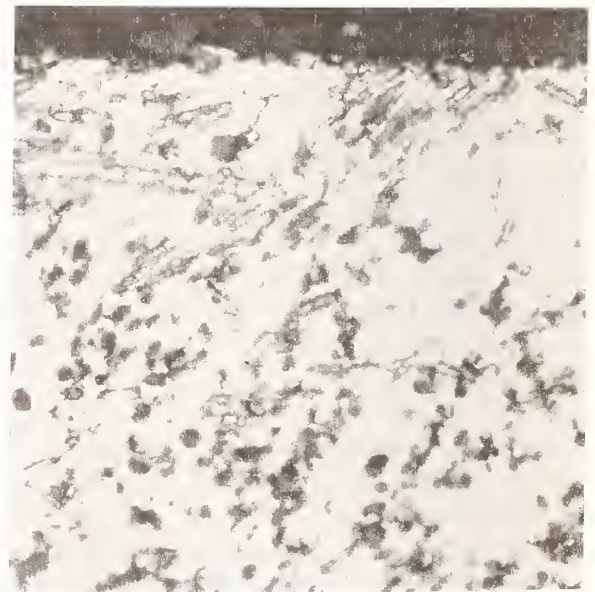
Fig.2   Microstructure of 26% fibre MMC material (tangential section).

The manufacturer´s specifications (7) indicate a mean fibre diameter of 3 mm and a length of ~ 3.5 mm in the preforms, which in all probability gets broken during the processing of the cylinders. The mechanical properties indicated in Table.1 correspond to the favourable radial direction of the cylinder. Detailed study of fibre morphology reported by van Hille et al (8) for this type of composites indicates that about 60% of the cumulative fibre population has an orientation of 0° ~ 20° with respect to the ideal horizontal or 0° plane, the rest occupying other positions. Normal to the axis of the cylinder the fibers may be expected to be randomly oriented although fibre bundling is often noticed (8). Typical microstructure (axial and radial sections)of the MMC material is shown in Figs.1-2.

2.2 GRINDING WHEELS

From traditional grinding practice aluminium and its alloys being soft materials are often ground with SiC abrasives, while ceramics (the fiber material in our MMC) are generally ground with diamond wheels. Hence for composite material containing both hard and soft phases, investigations involving a broad range of the abrasive types used in modern applications was considered. Understanding the relative interaction between the composite material and the grinding wheels based upon different type of abrasives was the motivating factor, not the choice of the optimal grinding wheel for the composites under investigation. Accordingly representative wheels, based upon alumina (Al_2O_3), silicon carbide (SiC), cubic boron nitride (CBN) and synthetic diamond (SD) abrasives from the same manufacturer was used. Here the grinding wheel choice namely grain size, type of bond and the degree of compaction was based upon manufacturers recommendations and what was considered as comparable wheels for standard surface grinding applications to produce similar type of surface quality. All the wheels are intended for the same peripheral grinding speed (~ 30 m/sec.). The specifications of the wheel for the proposed surface grinding tests are shown in Table 2.

Table 2.   Grinding wheel specifications

.No	Abrasive	Mesh size	Bond	Specification
1.	Al_2O_3	60	vitrified	43 A60 J6 VM
2.	SiC	60	vitrified	C60 I VM
3.	CBN (75% conc.)	126	phenolic	B126 R75 B-2
4.	Diamond (75% conc.)	126	phenolic	SDN126 R75 B2A-3

Obviously the mesh size specification and the number of active grains per unit area of the grinding wheel are somewhat different for these two groups of wheels, and this should be considered when comparing their grinding performance in terms of material removal mechanisms. However, from the point of view of application, these wheels are expected to perform in a similar fashion.

3. GRINDING TESTS
3.1 TEST DESCRIPTION

All the grinding tests were carried out in a horizontal surface grinding machine with a constant coolant (5% emulsion in water) flow of about ~14 lit/min. The cylindrical work pieces were held in a V block type fixture and the circular faces were ground using the down feeding of the abrasive wheel. The dimensions of the Al_2O_3,and SiC grinding wheels were the same, namely 356 mm diameter and 50 mm width, while the cubic boron nitride and synthetic diamond wheels had the same diameter, but a width of 12 mm only. Hereafter the above four type of abrasive wheels will be designated respectively as A60, S60, CBN and SDN. The machine spindle speed of 1815 rpm gave a peripheral speed of 33.8 m/sec. Only plunge feeding of the wheel and up-grinding mode of the traversing table was used in all these tests. To minimize the effects of non-uniform table speeds long stroke lengths (compared to ground length) were used. The exact time for the test grinding strokes was used to estimate the true table speed.

The idea behind the selection of parameters for the grinding test was the possibility of ob-

taining grinding forces and surface finish information as functions of
* the type of abrasive grit used
* the different levels of fiber content in a given Al alloy matrix and
* the wheel depth of cut and the table speed.
In the context of the grinding parameter selection, the relative role of the dimensions of the fiber (its diameter and length) and its concentration in a given composite and the distribution density of the abrasive grains in the grinding wheels would be of interest. Accordingly, wheel depth of cut was varied between 5 and 30 µm, while table speed was varied between 7 and 25 m/min.

The grinding wheels were balanced and trued with each change of wheel. This actually involves in the case of CBN and SDN, wheel *balancing*, followed by *truing* the mounted grinding wheel on the machine using a rotating diamond wheel dresser to eliminate radial run-out and finally *opening* of the wheel structure using Al_2O_3 sticks. The Al_2O_3 and SiC wheels were trued using multi diamond dresser stick. During the grinding tests with A60 and S60 wheels dressing was carried out anew for each test run.

3.2 MEASUREMENT OF GRINDING FORCES

For grinding tests with a wheel depth of cut a =10 µm, and a table speed of Vw = 15 m/min identified as the reference condition, the grinding forces were measured for all the combinations of abrasive wheels and composite variants. With the MMC specimens mounted on a three component piezo-electric force platform the grinding forces were measured during a single up-grinding pass. The output of the dynamometer was monitored through a charge amplifier, while for signal storage and subsequent analysis, a multi-channel digital memory oscilloscope with built-in hard copy out-put was used. The force measuring system with a natural frequency of about 4.7 KHz in the radial direction may be considered sufficient to identify phenomenon associated with the rotational frequency of the grinding wheel (~30 Hz) such as vibrations, run-out and non-uniformities on the wheel surface. Reliable identification of the action of individual abrasive grains as they move over the matrix and fibres,

would however require a measuring system with much higher natural frequencies.
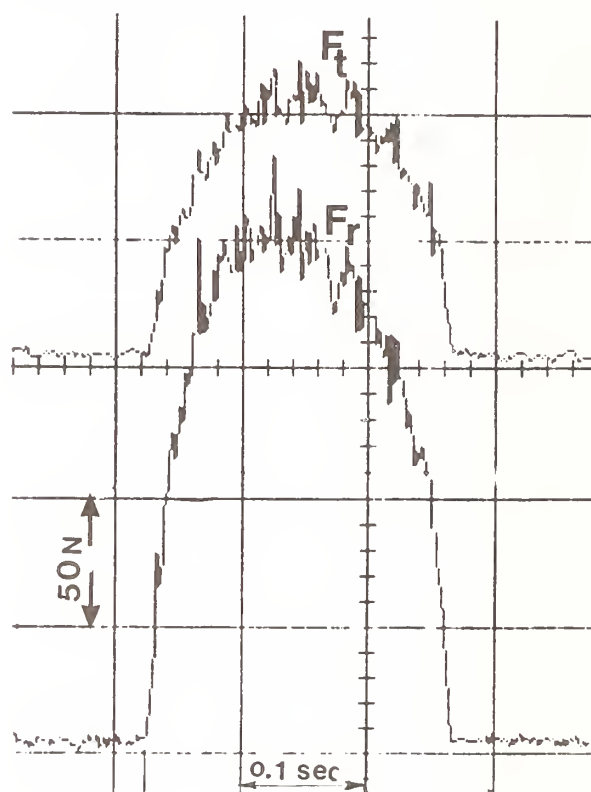
Fig. 3   Trace of grinding forces
(F_t and F_r) A60 wheel-10% fiber MMC
a=10 µm; V_w =15 m/min

The typical trace of the radial F_r and the tangential F_t components of the grinding forces recorded by the oscilloscope is shown in Fig. 3. Since the true wheel depth of cut associated with a single abrasive grain is a process variable, the measured total grinding forces also display scatter. The difference in the wheel composition as well as the substantial difference in wheel width (and hence damping) between the conventional and superabrasives wheels resulted in greater force fluctuations especially with CBN wheels. Subsequently, in all measurements for any given wheel-work combination, the maximum mean measured forces were normalized with respect to the maximum ground width.

58

The consolidated results relating grinding forces to the abrasive wheel types and grinding conditions (wheel depth of cut and table speed) when grinding MMC with different fiber contents are shown in Figs.4-5. Normalized information relating the grinding energy to the abrasive types and the grinding conditions are shown in Fig. 6, while the variation of grinding force ratio μ ($=F_t/F_r$) as a function of the abrasives used, fibre content and grinding conditions are shown in Fig. 7.
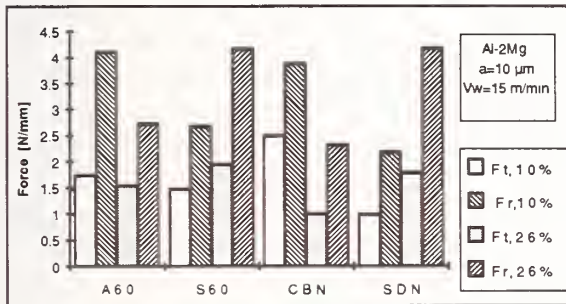
Fig.4   Grinding (reference conditions) forces for 10% and 26% fiber MMC.
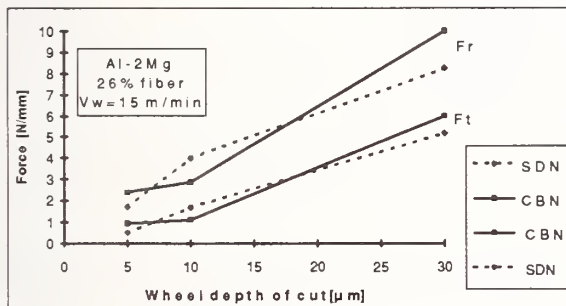
Fig.5a   Variation of grinding forces with wheel depth of cut **a** for 26% fiber MMC.
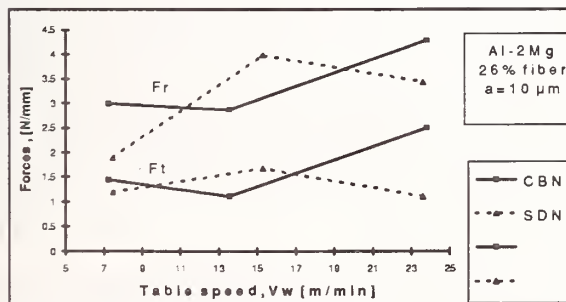
Fig.5b   Variation of grinding forces with table speed V_w for for 26% fibre MMC.
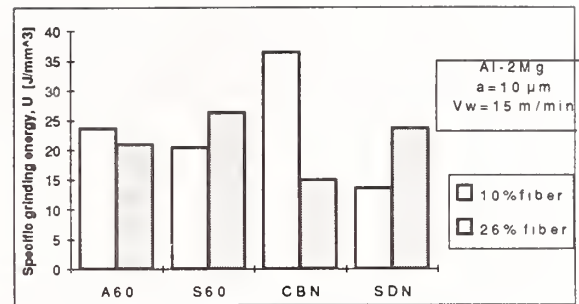
Fig.6   Specific grinding energy (reference conditions) for 10 and 26% fiber MMC with different abrasives.

3.3 SURFACE FINISH IN GRINDING

Grinding is often required to fulfil tolerance and quality requirements and thus it is essential to relate these features to the MMC material (matrix alloy and fiber content), the abrasive medium and the grinding conditions used. With this aim the ground surfaces were analysed using a non-contact surface finish measuring system, using infrared laser beam. All the traditional s urface finish parameters such as Ra (centre line average), Rz (peak to valley depth) and Rp(mean peak distance from centre line) were measured.
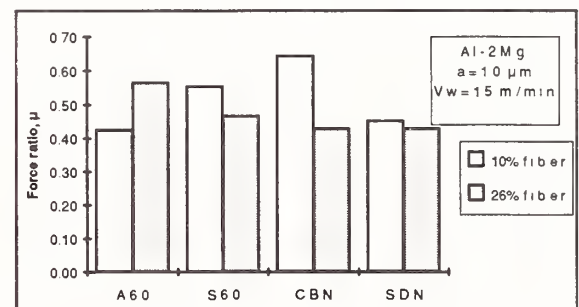
Fig.7   Force ratio μ (= Ft /Fr) when grinding (reference conditions) 10 and 26% fibre MMC with 4 abrasives.

The probable modes of surface build-up during grinding, the indirect influence of the abrasives (grain sharpness) and the degree of fiber damage/delamination could also be understood to some extent from such topographic information.

59
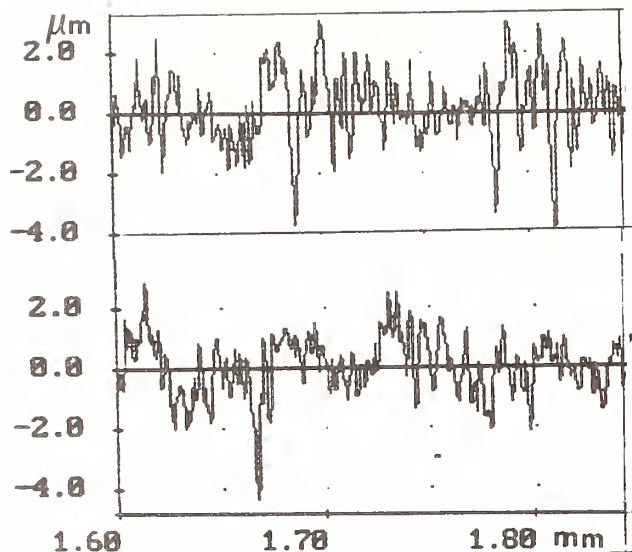
Fig.8 Trace of ground (reference
condition) surface of 26% fibre MMC
as recorded by non-contact laser
measuring system.
a) A60 wheel   b) SDN wheel.

For each grinding condition the surface finish across the grinding direction was measured at three places and the average was used in subsequent evaluations. Based upon the traditional Ra value alone, the ground MMC surfaces may be considered to be good. Differences arise from the MMC composition and the abrasive types used for grinding, rather than from the grinding conditions. Trace of a MMC surface profiles after grinding tests is shown in Fig.8. The consolidated results relating the measured surface finish parameters Ra, and Rz to the abrasive types and grinding conditions (wheel depth of cut and table speed) when grinding MMC with 26% fiber content are shown in Figs.9-10. The influence of grinding conditions upon Ra is marginal with some improvement with increasing wheel depth of cut (Figs. 9a and 10a), but an exactly contrary behaviour was observed with increasing table speed (Figs. 9b and 10b).

a) Variation of Ra

a) Variation of Ra

b) Variation of Rz.

b) Variation of Rz.

Fig.9 Variation of surface finish as
a function of wheel depth of cut for
26% fibreMMC when grinding with
different abrasives.
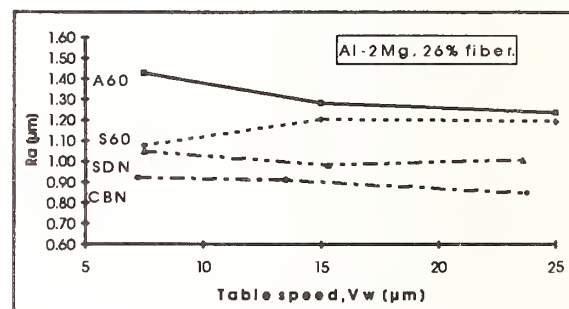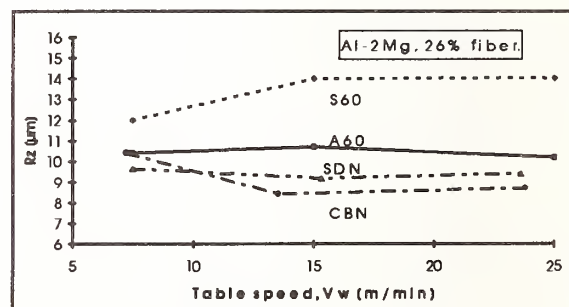
Fig.10 Variation of surface finish as a function of table speed for 26% fiber MMC using different abrasives.

The deeper scratches denoted by Rz exhibit even less sensitivity to grinding depth and table speed in this context. The best measured surface finish correspond to CBN and SDN grinding and the worst to grinding with A60 wheels, while grinding with the S60 wheels often resulted in intermediate values of finish.
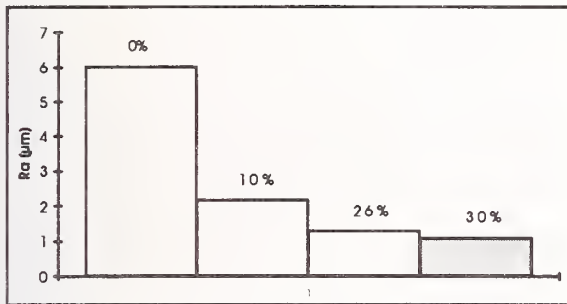
a) Variation of Ra
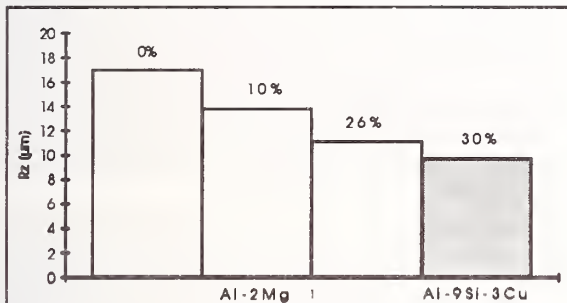
b) Variation of Rz

Fig.11 Influence of fibre content upon surface finish when grinding with A60 wheels; a=10 µm, V_w=15 m/min.

The influence of increasing content of the hard fiber in Al alloy MMC upon the surface finish (Ra) is shown in Fig. 11a corresponding to reference grinding conditions using A60 wheel. The poor surface finish associated with the fiber free matrix alloy improves appreciably with increasing fiber content, tapering off around a fibre content of about 30%. Similar influence upon Rz values (Fig. 11b) appears to be less sensitive to fiber content.

Another general effect of the grinding process upon the surface properties of the MMC material is the resulting hardness. It is conceivable that during the grinding process, due to the interaction of the abrasive grit with the matrix and fib-

er the surface fiber content could be affected. To verify such a hypothesis the micro hardness measurement of the ground surfaces was carried out using a 50 grams load. Figure12 shows the hardness variation over the surface (at ten different points) ground with different grinding wheels at the reference condition. The mean ground surface hardness for the Al-2Mg alloy MMC was around 125 HV, and as could be seen from the figure the influence of the abrasive type upon resulting hardness appears to be small and was confirmed to be statistically not significant.
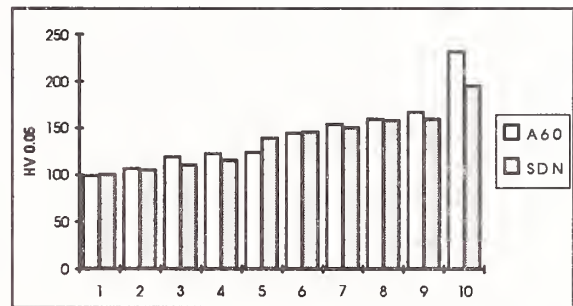
Fig.12 Scatter in the surface microhardness (10 measurements) of 26% fiber Al-2Mg alloy MMC ground (reference conditions) with A60 and SDN abrasives.

3.4. SEM STUDIES

A useful method for judging the qualitative aspects of wheel-work interaction in grinding is the direct observation of ground surfaces in the scanning electron microscope. Accordingly, unetched surfaces of ground MMC were investigated in SEM both in the topographic mode (SE) as well as in the back scattered (BS) mode. The degree of surface disturbance associated with the conventional and super abrasives, when grinding hard fiber reinforced MMC material could be seen in Fig. 13, showing the typical surfaces ground by A60, S60 and SDN wheels. SDN exhibits the best quality, while S60 exhibits grooves with some adhesion. In general. grinding with conventional abrasives is characterized by adhered and disturbed surface with a few clean scratch marks, CBN by a number of clean scratch marks with occasional adhesion and SDN with a large number of clean scratch marks with hardly any adhesion.

61

The chips are hardly in the form of fine filament like chips normally associated with steel grinding (9), due to the constant interruption by the hard fibres and consequent grit fracture-/dislodgement.

Figures 14 to 17 show the typical appearance of 26% fibre Al-2Mg MMC ground with conventional and super abrasives. At this fiber content the Al_2O_3 wheel has the disadvantage of both insufficient hardness of grit (almost the same as that of the fiber) and a rather brittle bond (vitrified) along with contiguous grit configuration. Although there is enough chip space, this is unable to accommodate the material removed.

Fig.13 Typical view (SEM) of the surface of 26% fiber Al-2Mg MMC ground with.
a) A60 wheel b) S60) wheel c) SDN).
wheel.
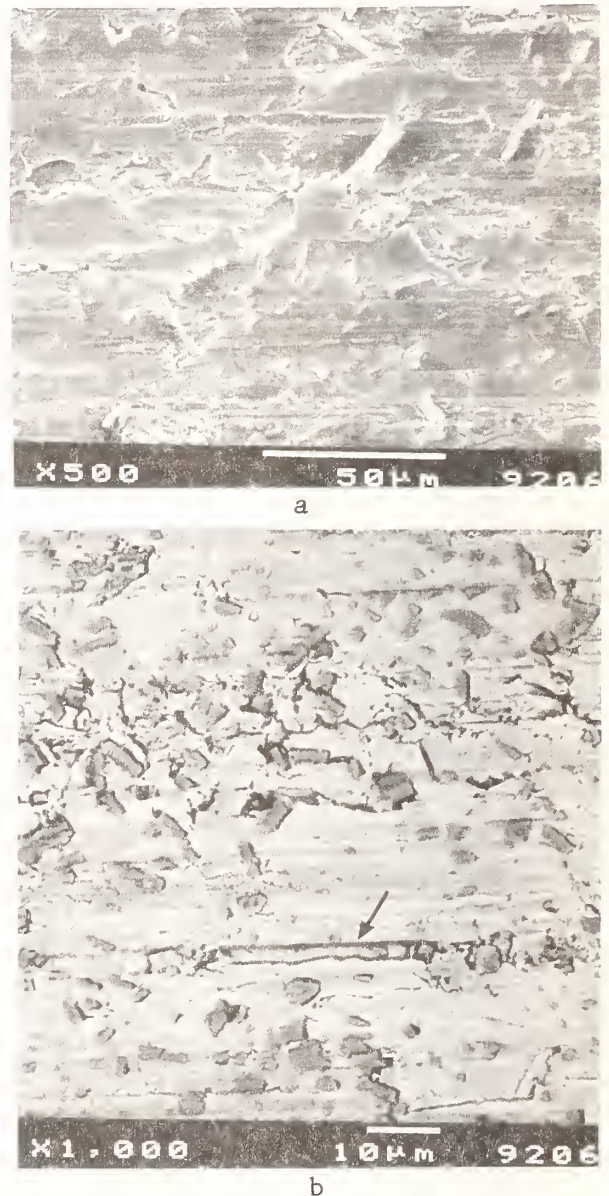
Fig.14 Typical view (SEM) of the surface of 26% fiber Al-2Mg MMC ground with A60 wheel; a=10 μm, V_w=15 m/min
a) general appearance, b) detail of a single disturbed fiber from (a) in the back scattered (BS) mode showing clearly the matrix (light) and the fibers (grey).

The normal forces increase and the heat concentrating on the work material (due to the poor thermal properties of the A60 wheel), results in the physical movement of individual fiber in the grinding direction (Fig. 14) as well as fiber displacement, due to the inability of the grit to cut clean through the fibers.
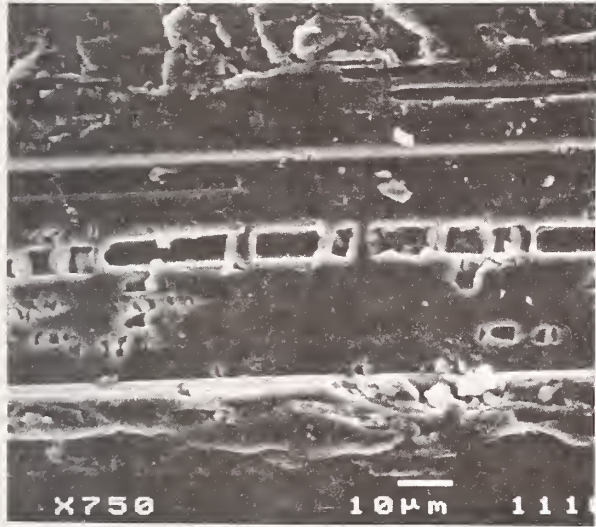
a
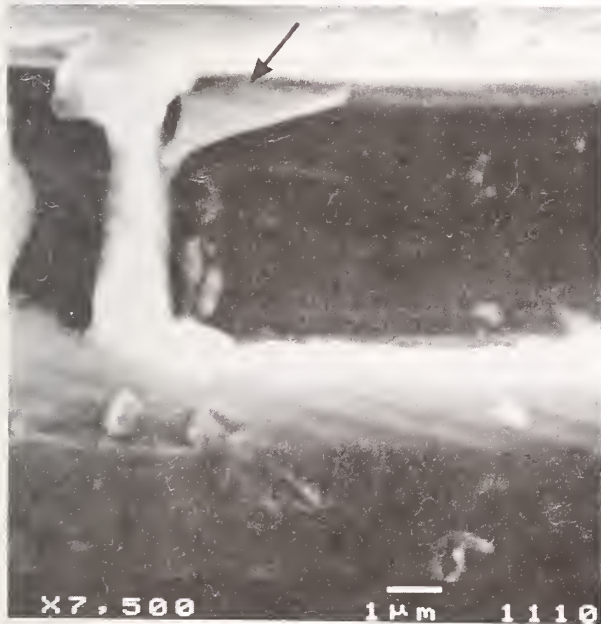
b

Fig.15 SEM view of surface ground with S60 wheel; other conditions as in Fig. 14.
a) abrasive groove and exposed fiber parallel to the grinding direction,
b) enlarged view (BS mode) of the fiber from (a) showing fracture fiber fracture (see arrow).

With the marginally harder SiC grit the true interaction between the grit and fibre is more complex as shown for a single fiber, which happens to lie exactly parallel to the grinding direction. Individual grit could however, cut clean through the MMC material and get damaged mid way (Fig. 15). The generation of the groove in turn results in the exposure of more fibres. We further notice that the presence of even small fibers is accompanied by cavity formation around the contour of the fibers. This feature appears to be *a characteristic of grinding MMC material* as this was observed even in the case of favourable grinding with the super abrasives.

In the case of super abrasives, the available chip space is favourable (large areas of shallow depth), and as long as this is not filled, there is no problem. The extent to which the harder and sharper fine grit points of CBN could work through the MMC material is readily seen in Fig.16a. Large pull out and disturbance of fibers was rarely seen here, but again around the contour of each surface fiber worked by the grits, cavity formation was observed. These could be very small (Fig. 16b).

A closer scrutiny of the bottom of individual grooves from SDN grinding (Fig. 17) displays that the hard and sharp diamond grit could effectively decapitate individual fibres and the remnant trace hardly reveals large scale cavity formation associated with the other abrasives, although the fiber section could be seen (Fig. 17b).

4. DISCUSSION OF TEST RESULTS
4.1 GRINDING FORCES

The force results show that as a function of grinding depth of cut and table speed (Fig. 4) these are similar to the surface grinding of metals, namely increase in forces with wheel depth of cut. Unlike the influence of the wheel depth of cut, an increase in table speed increases the true thickness of cut removed by individual abrasives only marginally. Consequently, the influence of table speed appears to be negligible upon the smaller F_t force, while some marginal influence could be seen upon the larger F_r force. This was especially true for the CBN and SDN wheels. The measured

Further, the distribution of the abrasives in the CBN and SDN wheels is characterized by individual grains surrounded by the organic bond, while in the case of the conventional wheels the grits occupy contiguous regions separated by similar regions of the vitrified bond. These differences may be expected to affect chip packing in grinding which in turn affects the measured grinding forces (10). Thus the adhesive behaviour of the wheels would be affected both due to the intrinsic properties of the abrasives as well as by their physical configuration. Al_2O_3 wheels display the worst combination (lowest grit hardness and maximum material pick-up) and the diamond the best (highest grit hardness and minimal material pick-up), and the SiC and CBN wheels come in between.

In a similar manner, the measured grinding forces as a function of the abrasive types could be somted into two distinct groups, based upon the relative role of the reinforcing fiber content. SiC and SDN wheels displayed an increase in forces with an increased fiber content, while this was quite the contrary with Al_2O_3 wheel. All these effects were appreciable in the case of the larger radial force F_r. We have to keep in mind here that an increase in the content of alumina fiber results in two different effects, namely an increase in the hard phase as well as a decrease in the matrix phase having greater influence upon adhesion. Accordingly an abrasive displaying minimal adhesive affinity to the matrix alloy and at the same time hard enough to cut through the alumina fiber (~2000 HV) would be the most successful. The basic physical properties of the four abrasive types used in our tests is shown in Table 3.

From this table we can see that SiC, CBN and diamond all have greater hardness than that of alumina fiber. Diamond with its excellent low friction properties along with the highest hardness thus exhibits the best capability and this could be readily seen from the small forces especially for 10% fiber MMC (Fig.4).

Similar behaviour could be observed in the case of S60 wheels. Both these abrasives are able to

grind and thus with increasing fiber content the forces also increase.

Table 3. Physical properties of the abrasives used

Properties	Abrasive types			
	A60	S60	CBN	SDN
Composition	Al_2O_3	SiC	BN	C
Dens. ρ (gm/cm³)	3.92	3.21	3.48	3.52
Knoop hardness (GPa)	~21	26	42~46	56~102
Therm. cond. λ (W/m C)	6	55	200~700	600~2000
Therm. exp. α (10⁶/deg.C)	86	45	48	15
Oxid. resistance (deg.C)	1750	1500	1400	800

In chip forming operations like turning, an increase in fibre content results in the increase of material defects, resulting in energywise favourable shearing in the shear plane, and mesured forces decrease (11). In the case of A60 wheel, with increasing fiber content the grit loss increases; thus material removal does not take place, and the measured forces come down. The role of radial force to sustain and influence actual metal removal is well known in the case of grinding metals (10), and thus the poor grinding performance of A60 wheels is accompanied by a reduction in the radial force F_r with increasing fiber content.

4.2 GRINDING ENERGY AND HEAT GENERATION

The influence of the grinding conditions could be normalized using the parameter of nominal material removal rate (a .V_w). The grinding forces are marginally affected by the metal removal rate to start with. Subsequently, however, as the relative role of force ratio changes, the effect of material removal rate upon forces increases. This effect appears to be similar for both CBN and SDN (Fig. 5). Ultimately the effects of grinding conditions influencing both the grinding forces and the nominal rate of material removal is expressed by the concept of specific grinding energy U (J/mm³). The value of U may be expressed as

$$U = (F_t . V_g) / (a.W_g V_w) \qquad (1)$$

forces for a given grinding condition using different types of abrasives appears to be more complex. Here, eventhough the abrasive wheels are nominally comparable in terms of performance, both the abrasive distribution per unit area of wheel as well as the type of bonds (vitrified for the A60 and S60 wheels, but phenolic for CBN and SDN) differ.

a

a

b

h
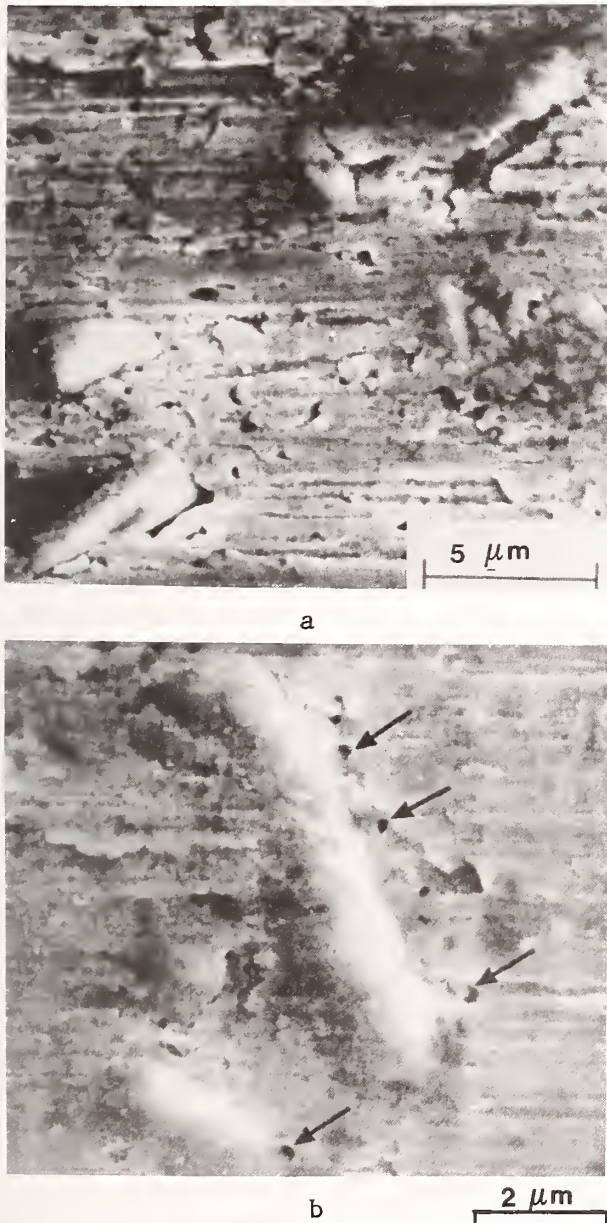
Fig.16 SEM view of surface ground with CBN wheel; other conditions as in Fig. 14.
a) fine scratches in matrix and two fibers with their contours exposed
b) region around another fibre showing a series of micro-cavities (arrows) along the fiber contour.
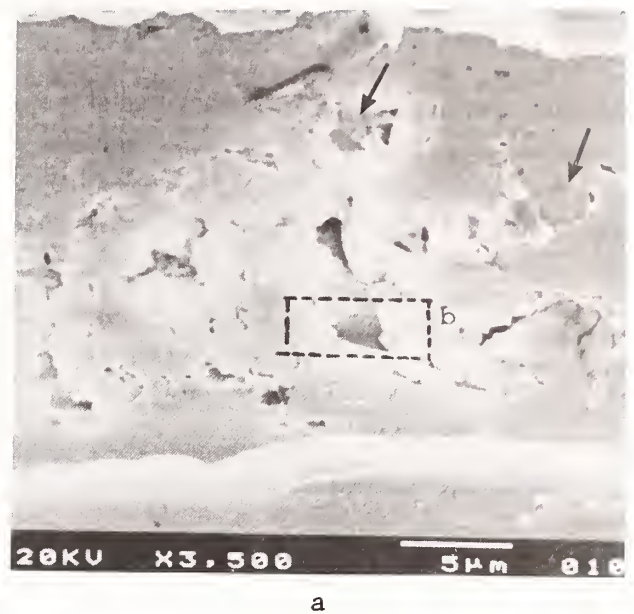
Fig.17 SEM view of surface ground with SDN wheel; other conditions as in Fig. 14.
a) abrasive track and exposure of fibers (arrows)
b) detail from (a) showing the section of a single fiber due to its decapitation by diamond grit

where V_g and V_w correspond to wheel and work velocity, while a and W_g correspond to wheel depth and width of grinding. Of this total energy, some part is carried away by the grinding swarf, approximated by Malkin (10) as a percentage of the maximum possible energy associated with chip formation namely the energy for melting a unit volume of material U_c. The remaining energy available for heating the work material U_w may be expreesed as

$$U_w = U - 0.45 U_c$$

$$= \left[(F_t \cdot V_g)/(a \cdot W_g \, V_w) - 0.45 \, U_c \right] \qquad (2)$$

The parameter U is also convenient in comparing the grinding behaviour of materials in general. For 10% fibre Al-2Mg MMC material this energy decreases progressively (Fig. 5) in the sequence A60 S60 and SDN, indicating thereby the cutting efficiency of the diamond grit. With increasing fibre content S60 and diamond display a small increase in the energy requirements, while the A60 wheel being unable to grind, exhibits only a marginal change. The role of wheel depth of cut in this context appears to be marginal, while higher table speeds result in smaller energy requirements. These correspond to CBN and SDN grinding of 26% fibre Al-2Mg MMC material. Thus an enhancement of material removal rate through increased wheel depth of cut appears to be advantageous, if the abrasive is hard enough and the bond could take the load.

Good correlation has been reported (10) between the theoretical prediction and experimental data concerning the surface temperatures associated with the grinding of carbon steels using an analysis in which the energy available for heating (U_w) is used to calculate temperature rise based upon the approximation of a moving heat source on a half-space. It is proposed to use similar approximation for estimating the surface temperature during the grinding of fibre reinforced MMC material also. In the absence of reliable thermal properties of the MMC material with the two fiber content, as a first approximation we shall use the properties of the matrix alloy in our temperature computations.

Based upon the measured grinding force (F_t) and the velocities of the grinding wheel (V_g) and the workmaterial (V_w), the wheel depth of cut a, and the width of cut W_g, and thereby the grinding energy (Ug assumed to be uniformly distributed over the wheel work contact length), we can express the maximum temperature rise (θ_{max}) of the ground surface (10) as

$$\theta_{max} = \frac{1.12 \cdot \alpha^{1.2} \cdot a^{0.75} \cdot V_w^{0.5} \left[U - 0.45 U_c \right]}{\lambda \cdot d_e^{0.25}} \qquad (3)$$

where α and λ are respectively the thermal diffusivity and thermal conductivity of the matrix material and d_e is the equivalent diameter (= D, the grinding wheel diameter in surface grinding). Using eq.(3) the temperature rise associated with the grinding of the Al-2Mg MMC with respectively 10% and 26% fibre content using the four type of grinding wheels A60, S60, CBN and SDN was calculated. The influence of the wheel depth of cut a upon the temperature rise when grinding 26% fibre MMC material with CBN and SDN wheels is shown in Fig. 18, while consolidated results for all combinations for the reference grinding conditions are shown in Fig. 18.
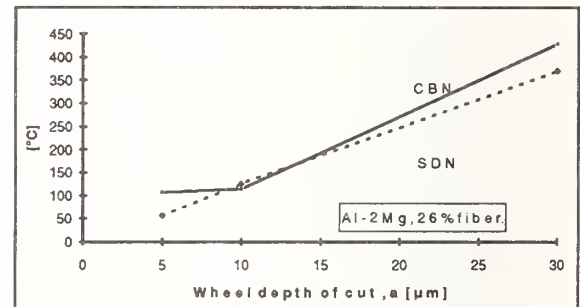
Fig.18a Calculated maximum surface tempeature as a function of wheel depth of cut during the grinding of 26% fiber MMC material.

The temperature rise for the reference conditions appears to be nominal for most wheel-work combinations, being the order of 80-250°C. As may be expected the lowest temperature rise corresponds to the grinding of 10% fiber MMC with SDN wheels. With 26% fiber MMC materials S60 and CBN wheels display a rise of 180°C, while for SDN this is somewhat less ~150°C.

In terms of grinding conditions the wheel depth of cut a appears to have the greatest effect showing up to 450°C rise during CBN grinding (Fig. 17a) and somewhat less for diamond grinding.
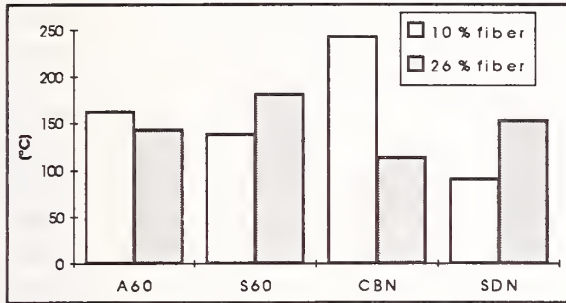
Fig.18b Calculated maximum surface temperature in Al-2Mg MMC material when grinding with different wheel types at reference grinding conditions.

4.3 THERMAL EFFECTS ON FIBER

An indirect effect of heating of the MMC material during grinding is the associated unfavourable stress build-up due to the large difference in the thermal expansion behaviour of the matrix and fiber materials (this being respectively 24 and 8 x 10^{-6}/°C). Using the simple model for the axial stress σ_m in the matrix (parallel to the fibre direction) brought about by a strain mismatch due to a change in temperature $\Delta\theta$ proposed in (12), and the concept of force equilibrium we can write

$$\sigma_m = -\left\{\frac{\left[E_m\Delta\theta(\alpha_m - \alpha_f)\right]}{1 + (v_mE_m / v_fE_f)}\right\} \qquad (4)$$

$$\Sigma F = (\sigma_m A_m + \sigma_f A_f) \qquad (5)$$

where F is the resultant force, σ, E, v, correspond respectively to axial stress, elastic module and volume fraction of phases and the suffixes m and f denote the matrix and fiber material. Substituting the appropriate values of E_m =70 and E_f = 300 GPa in the above equations along with the other relevant values and solving for σ_f, we can estimate the resulting tensile stress level in the fibers as a function of temperature rise (Table 4) estimated earlier.

Table 4. Probable axial tensile stress in fibers due to temperature rise in grinding.

Vol. % of fiber	Stress in MPa		
	100°C	200°C	θ_{max}(427°C)
10%	325	650	-
26%	190	380	810

The indicated maximum fiber stress of 810 MPa is appreciable considering the tensile strength of alumina fibers (~2000 MPa) reported by the manufacturer (7). Thus there appears to be an immanent possibility that during grinding in addition to the mechanical action of the grit, thermal effects could affect fiber fracture. Such effects should be observable especially in the case of long fibres lying parallel to the grinding direction experiencing the combined action of mechanical and thermal stresses.

4.4 MATERIAL REMOVAL MECHANISMS IN GRINDING

The observation of the ground surfaces along with the evaluated surface parameters and grinding forces could be used to get an idea about the actual nature of material removal during the grinding of the fiber reinforced MMC materials. If the abrasive grit is hard and sharp enough, then it can slice clean through the MMC material, as exemplified by SDN and CBN wheels. Recent analysis of energy partition in grinding using single grit model and the appropriate thermal properties (13) do indicate appreciable similarities between CBN and SDN. In such a situation the only other basic difference between these two abrasives could be the friction between the grinding chip and the individual abrasive grit exhibited by these two materials. Further, forces associated with CBN grit are notoriously sensitive to the correct truing and opening of these wheels, and thus along with the advantages of temperatures, diamond turns out to be the better among the two.

When the abrasive makes a clean cut the actual separation of the material in the form of a chip is associated with cavity formation as shown schematically in Fig. 19.
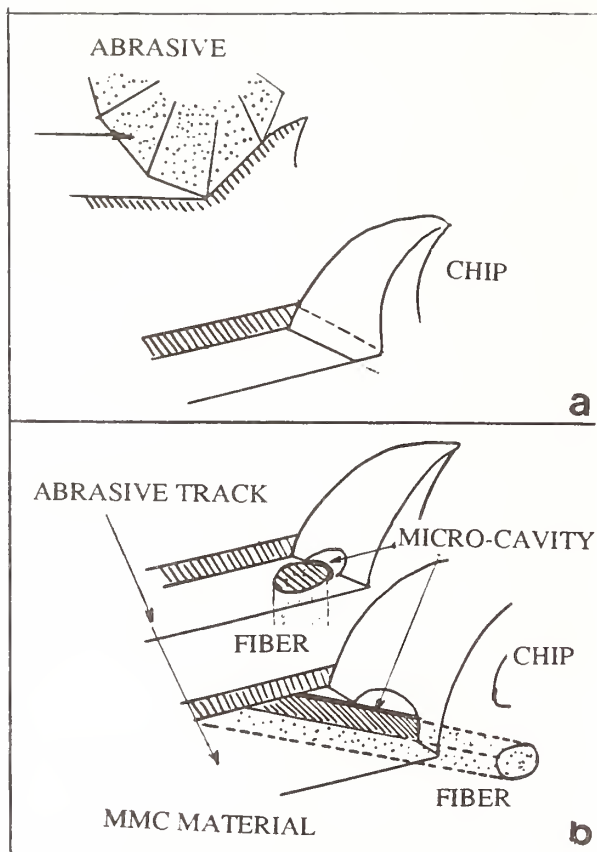
Fig.19 Schematic view of chip separation stage during the grinding of fiber reinforced MMC material.
a) region with no fiber
b) fiber rich region showing the evolution of micro-cavities for two different fiber orientations.

This is due to the large difference in the flow properties of the matrix and fiber material. At the instant of chip separation, the brittle fiber fractures easily, while the soft and ductile matrix continues to deform and fail in the ductile mode. The extent and size of these cavities are dependent upon the relation between the width of cut of individual grits and the material present here. Further, the degree of wettability between the fibers and the matrix has a central role in this context. In fiber free regions cavity formation is less probable. If major part of this width is associated with the hard fiber (single or a group) then a series of cavities along the width corresponding to the brittle fiber will arise (Fig.19b). If the fibers are locat-

ed normal to the grinding plane, cavity formation will be minimal during the grinding of fiber reinforced MMC, while if these were located perpendicular to the grinding direction, this could result in severe cavity formation in the ground material. In a practical case like ours where a majority of fibres are oriented at an angle (< 20° to the grinding plane as mentioned in §2.2) the extent of concomitant cavity formation associated with the fibrers and grinding would be in between. While from pure strength point of view these defects associated with the projected length of fibers in the grinding plane are not critical by themselves, if corrosion and fatigue control component failure, then the grinding mode and its optimization would be very critical to the performance of MMC product.

4.5. ROLE OF FIBRE-ABRASIVE INTERACTION

The exact nature of interaction between the abrasive grit and the hard fibers are not easily observed in the present study. However we can indirectly conclude that in the absence of hard and sharp abrasive grits as in the case of A60 wheels, major part of the measured grinding energy is due to the grit ploughing and bond to matrix adhesion (as a consequence of grit fracture), rather than chip formation. This is clear from the quality of the ground surface, especially that of Ra value as function of fiber content (Fig. 12). Unlike Rz (characteristic of scratch depth) value, Ra is very much affected in this context. The situation is similar in the case of SiC grits.

In the case of CBN and SDN grinding, evidence from single grit *in-situ* studies in SEM using diamond grits (14) indicate that fracture of fibres perpendicular to the scratch direction to occur when a specific normal load is reached. Based upon the reported (14) normal forces corresponding to fiber fracture (0.2 N) and the geometry of the observed width of track (~ 25 μm) we can estimate a fracture stress level of about 2036 MPa, comparable to the tensile strength of the fiber material. In our grinding tests, the speeds are much higher and the abrasive track widths vary from 20 to 50 μm (Figs 14 and 16). This would mean that fiber fracture could easily take place as is also supported by the SEM studies. Further the

is also supported by the SEM studies. Further the thermal effects could also contribute appreciably to this feature. The sum total of these factors is the high probability of severe fiber fracture in grinding.Thus the original fiber length in the pre-form (3~4 mm long) undergoes continuous frac-turing during the different manufacturing stages of the MMC material, including the finishing opera-tion like grinding. An important implication of this phenomenon is that the physical distribution of fibres on the service surface after a manufactur-ing step like grinding could be different from the original.

5. CONCLUSIONS

Based upon this very first attempt some conclusions on the grinding of this class of mate-rials as well as on some aspects of the surface integrity of ground MMC materials could be made. These will be enumerated now.

1. Super abrasive wheels are to be preferred in the grinding of alumina fiber reinforced Al alloys. In general grinding wheel using synthetic diamond grits results in superior surfaces irrespective of the fiber volume content and the type of aluminium alloy used. CBN based wheels could also be effective, but are associated with more exacting wheel preparation.
2. Increase in the alumina fiber content in the MMC material results in the increase of grinding forces when the abrasive used are hard and sharp enough as is the case with SiC and super abra-sives.
3. When the abrasive grits of sufficient hardness and sharpness is used (as is the case with SDN wheels), the role of the grinding parameters (wheel depth of cut and table speed) have only a marginal influence upon the measured surface finish parameters.
4. Both considerations of mechanical loading of the fibers under grinding as well as thermal con-siderations indicate that even under successful grinding conditions, fracture of individual alu-mina fibers in the MMC material into smaller bits to be highly probable. Diamond grits, however often preferentially decapitate the hard fibers.
5. Surface studies also indicate that grinding of these fiber reinforced MMC materials is charac-terized by the presence of a large number of con-comitant micro-cavities corresponding to the pro-jected contours of individual fibers in the plane of grinding.

ACKNOWLEDGEMENTS

REFERENCES
1.   D. Richter, "Commercial Alternatives in Metal Matrix Composites, Advan. Mat. Techno-logy International, ed. David Whittaker, Sterling Pub.,London 1992.
2.   M.Ebisawa, M. Hara, T. Hayashi and H.Usio, "Production Process of Metal Matrix Composite (MMC) Engine Block, SAE paper No.910835, 1991
3.   C.T. Lane, "Machining Characteristics of Particle Reinforced Aluminium, Proc.of Conf. "Fabrication of Particulate Reinforced Metal Composites"-Sept.17-19, Montreal, Canada, pp.204-210, 1990
4.   G. A. Chadwick, and P. J. Heath, "Machining of Metal Matrix Composites", Metals and Materials, Feb. pp.73-76, 1990
5.   A. R. Chambers, and S. E. Stephens, "Machining of Al-5Mg Reinforced with 5 vol.% Saffil and 15 vol.% SiC", Material Sci. and Engg., A135, pp.287-290, 199
6.   J. Monaghan, J and P. O. O´Reilly, "The Drilling of Al/SiC Metal Matrix Composite, J. of Material. Process. Technology, 33, pp. 569-487, 1992.
7.   P. Johansson, S. Savage, A. Sjöberg,and N. Bäckström, "Magnesium Metal Matrix Com-posites by Squeeze Casting Experiments, Swedish Institute for Metals Research Report No. IM-2522. 1989
8.   D. van Hille, S. Bengtsson, and R. Warren, "Quantitative Metallographic Study of the Fibre Morphology in Short Alumina Fibre Reinforced Aluminium Alloy Matrix", Compos. Sci. and Technol., 35, pp. 195-20, 1989

9.   D. M. Pai, E. Ratterman, and M. Shaw,1989), "Grinding Swarf", <u>Wear</u>, 131, p.329-339, 1989

10.   S. Malkin, Grinding of metals, Theory and Application", <u>J. of App. Metal Working</u>, vol.3 No. 2, pp. 95-109, 1984.

11.   C. H. Andersson, J. E. Stahl, and M. Andersson, "Plastic Deformation and Machining Properties of Some Low Volume Fraction Short Fibre Reinforced Metal Matrix Copmposite Material", Proc of 9the RISØ Int. Symposium on Behaviour. of Ceramic and Metallic.Composites., ed. S. I. Andersen, H. Lilholt, and O. B. Pedersen, Denmark, 1988

12.   G. S. Daehn, and G. Gonzalez-Doncel, "Deformation of Whisker Reinforced Metal Matrix Composites under Changing Temperature Conditions", <u>Metallurgical Trans. A</u>, 20a, Nov.pp-2355-2368, 1989.

13.   T. Matsuo, S. Toyoura, E. Oshima, E. and Y. Ohbuchi, Y. "Effects of Grain Shape on Cutting Force in Superabrasive Single-grit Tests", <u>Ann.of CIRP</u>, 38/1, pp.323-326, 1989

14.   A. Alahelisten, M. Olsson and S. Högmark, "Tribological Properties of an Aluminium Alloy Matrix Composite", Proc. of Nordic Tribology Conference, Copenhagen,1990

ELASTIC STRESS FIELDS CAUSED BY SLIDING MICROINDENTATION OF BRITTLE MATERIALS

Y. AHN, T. N. FARRIS, and S. CHANDRASEKAR
Purdue University, West Lafayette, IN

An analytical model of the stress field caused by sliding microindentation of brittle materials is developed. The complete stress field is treated as the superposition of applied normal and tangential forces with a sliding blister approximation of the localized inelastic deformation occurring just underneath the indenter. It is shown that lateral cracking is produced by the sliding blister stress field and that median cracking is caused by the applied contact forces. The model is combined with experimental volume change measurements to show that the relative magnitude of tensile stresses governing lateral crack and median crack growth varies with the magnitude of the applied load. This prediction is consistent with the different regimes of cracking observed under a sliding pointed indenter in soda-lime glass and other brittle solids.

1 Introduction

Microscopic observations of machined ceramic surfaces show that brittle fracture contributes substantially to material removal in stock removal and coarse finishing processes. A careful examination of the fractures in machined ceramics reveals striking similarities with fractures about quasi-static and sliding indentations produced by sharp indenters in brittle solids. It was, therefore, decided to develop a model for characterizing the stress fields produced by sliding, sharp indenters in brittle solids. The model that has been developed is an extension of that proposed by Yoffe [1] to describe the stress fields and fractures generated under a quasi-static indentation by a pointed indenter in brittle materials. We begin with a review of the deformation produced under a pointed indentation and a discussion of the Yoffe model.

When a sharp indenter is quasi-statically applied onto the surface of a brittle solid, the classical theory relating the hardness to the yield stress of metals [2] no longer applies since yielding no longer occurs at a constant maximum shear stress or at a constant volume [3]. A large body of experimental observations has shown that in brittle materials, the volume of material displaced by the penetration of the indenter is accommodated by compaction or shear deformation, or both, and this may occur either uniformly or irregularly. In silicate glasses, which have a relatively open structure, the displaced material is most readily accommodated by compaction within a zone underneath the indenter. However, in soda-lime glasses and in most ceramics shear deformation dominates with some compaction also taking place underneath the

71

indenter. The experimental model used by Yoffe to describe the deformation underneath a sharp conical indenter in soda-lime glass is based on the work of Peter [4], amongst others, who showed that the mean contact pressure under a sharp indenter remains constant and relatively independent of the indenter geometry. This model assumes that as a conical indenter is applied to the solid surface yielding initially occurs in a hemi-spherical bowl under the indenter and continues until the yielded zone attains its stable preferred state for that pressure. As the indenter is loaded further, no additional flow occurs within this bowl, but fresh yielding takes place in an adjoining thin hemi-spherical shell. This process continues and "it is as if a set of nested hemi-spherical bowls separated by plastic filler were forced down in turn, one within the other, and become locked in the positions shown in Figure 1(a) [1]." The yielding process occurs through a combination of shear deformation and compaction within the yielded zone. Part of the material displaced by the indenter is accommodated by compaction within the yielded zone while the remaining material is pushed into the surroundings causing a volume change. At the end of the indentation process, the elastic half-space is left with an over-large hemi-spheroid fixed in a hemi-spherical cavity on its surface. This misfit leads to a residual stress in the region outside of the cavity. Consequently, as the material reacts to this residual stress, cracking may occur within the solid.

The "blister" field proposed by Yoffe [1] was for describing the development of cracks below a conical indenter acting on a brittle solid. Yoffe assumed that the inelastic zone underneath the indenter is hemi-spherical in shape with a radius equal to the contact radius (Figure 1a). The stress distribution in the surrounding elastic zone was obtained as the superposition of two stress fields—the Boussinesq field for the point force which idealized the indentation pressure distribution and a doublet force system which idealized the localized inelastic deformation. The doublet force system for the blister field consisted of superposition of a point center of expansion in an infinite elastic solid with an additional doublet to satisfy the free surface normal stress boundary condition. Such a doublet force system leads to a volume increase of the inelastic deformation zone that must be taken up by com-
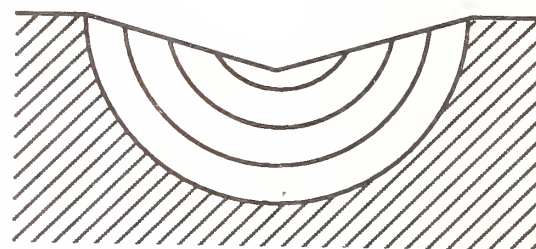
(a)
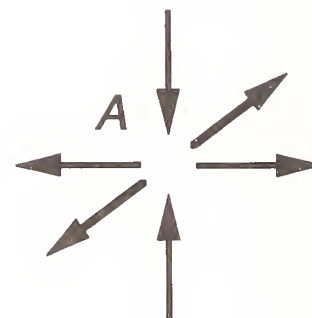
(b)

Figure 1: (a) Indentation by yielding of successive bowls and (b) force doublet used for blister field

paction or elastic deformation of the remainder of the solid. The volume increase is a measure of the "strength" of the blister field. The strength of the blister field varies with the applied force; this variation is characterized by a material property which has thus far defied a precise estimation. Qualitatively, Yoffe's model has predicted the origin and growth of radial, median, and lateral crack systems quite well. It's only disadvantage is from a quantitative point of view as a procedure for determining the strength of the blister field for various indenter geometries is not yet available.

Models to describe the sliding indentation fracture process in ceramics have not yet evolved to a stage where the inelasticity under the indenter is accounted for completely [5, 6, 7]. This is in large part due to the difficulty introduced by a lack of information concerning the constitutive behavior of ceramics in large hydrostatic compressive stress fields such as that existing underneath a microindentation. It seems that a reasonable first step for modeling the sliding indentation stress fields would be to extend Yoffe's work on static indentation to the sliding situation. This extension should include the load-history effects of inelastic deformation left behind by the sliding indenter and the elastic effects due to the frictional force.

In this paper Yoffe's blister field is extended to model sliding microindentation stress fields. The extension of the blister field is called the sliding blister field and its derivation is detailed in Section 2. In Section 3, the predictions of this theory are compared to the experimental observations of Ahn et al [8] of fractures around sliding indentations. The paper concludes with a brief discussion of the experimentally observed cracking that is explained qualitatively by the sliding blister field model.

2 Derivation of Sliding Blister Stress Fields

A schematic illustration of the sliding microindentation geometry and the location of the inelastic deformation zone is shown in Figure 2. The pointed indenter is loaded normal to the surface by the load P acting in the z-direction and tangentially by the friction force Q acting in the x-direction. As we are interested in details of the stress field outside of the plastic zone, for simplicity we use the Boussinesq and Cerruti solutions
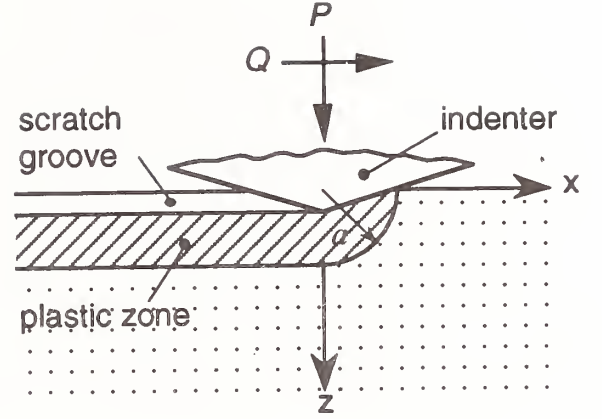
Figure 2: Schematic side view of sliding microindentation and moving coordinate system

for concentrated point forces rather than the actual contact pressure distribution acting between the indenter and specimen surface. It is assumed that the inelastic deformation occurs in a region whose boundary in front of the sliding indentation takes the shape of one fourth of a sphere with radius a equal to the half-width of the groove. Behind the indenter this zone takes the shape of a half cylinder of radius a and length equal to the total sliding distance. In the following, the well known solutions for the concentrated normal and tangential loading of a half space is given followed by the sliding blister field solution.

Recalling the coordinate system of Figure 2, the Boussinesq field for the concentrated normal force P acting normal to the surface of a semi-infinite half-space at the origin is [9]

$$\sigma_x^n = \frac{P}{2\pi}\left[\frac{1-2\nu}{r^2}\left\{\left(1-\frac{z}{\rho}\right)\frac{x^2-y^2}{r^2}+\frac{zy^2}{\rho^3}\right\} -\frac{3zx^2}{\rho^5}\right] \tag{1}$$

$$\sigma_y^n = \frac{P}{2\pi}\left[\frac{1-2\nu}{r^2}\left\{\left(1-\frac{z}{\rho}\right)\frac{y^2-x^2}{r^2}+\frac{zx^2}{\rho^3}\right\} -\frac{3zy^2}{\rho^5}\right] \tag{2}$$

$$\tau_{xy}^n = \frac{P}{2\pi}\left[\frac{1-2\nu}{r^2}\left\{\left(1-\frac{z}{\rho}\right)\frac{xy}{r^2}-\frac{xyz}{\rho^3}\right\} -\frac{3xyz}{\rho^5}\right] \tag{3}$$

$$\sigma_z^n = -\frac{3P}{2\pi}\frac{z^3}{\rho^5} \tag{4}$$

$$\tau_{yz}^n = -\frac{3P}{2\pi}\frac{yz^2}{\rho^5}, \qquad \tau_{zx}^n = -\frac{3P}{2\pi}\frac{xz^2}{\rho^5} \tag{5}$$

where $r^2 = x^2 + y^2$ and $\rho^2 = x^2 + y^2 + z^2$ define the distance from the load to the field point in the xy plane and the total distance, respectively, and ν is Poisson's ratio. The corresponding stress components due to the concentrated tangential force Q acting at the origin in the positive x-direction are given by [9]

$$\sigma_x^t = -\frac{Q}{2\pi}\left[\frac{3x^3}{\rho^5} - (1-2\nu)\left\{\frac{x}{\rho^3} - \frac{3x}{\rho(\rho+z)^2}\right.\right.$$
$$\left.\left. + \frac{x^3}{\rho^3(\rho+z)^2} + \frac{2x^3}{\rho^2(\rho+z)^3}\right\}\right] \tag{6}$$

$$\sigma_y^t = -\frac{Q}{2\pi}\left[\frac{3xy^2}{\rho^5} - (1-2\nu)\left\{\frac{x}{\rho^3} - \frac{x}{\rho(\rho+z)^2}\right.\right.$$
$$\left.\left. + \frac{xy^2}{\rho^3(\rho+z)^2} + \frac{2xy^2}{\rho^2(\rho+z)^3}\right\}\right] \tag{7}$$

$$\tau_{xy}^t = -\frac{Q}{2\pi}\left[\frac{3xy^2}{\rho^5} + (1-2\nu)\left\{\frac{y}{\rho(\rho+z)^2}\right.\right.$$
$$\left.\left. - \frac{x^2y}{\rho^3(\rho+z)^2} - \frac{2x^2y}{\rho^2(\rho+z)^3}\right\}\right] \tag{8}$$

$$\sigma_z^t = -\frac{Q}{2\pi}\frac{3xz^2}{\rho^5} \tag{9}$$

$$\tau_{yz}^t = -\frac{Q}{2\pi}\frac{3xyz}{\rho^5}, \qquad \tau_{zx}^t = -\frac{Q}{2\pi}\frac{3x^2z}{\rho^5} \tag{10}$$

The superscripts n and t denote normal and tangential loading, respectively. The loads applied to the indenter are supported by these elastic stresses which decay as $1/\rho^2$ as $\rho \to \infty$.

In addition to the stresses due to the loading of the indenter, there are stresses induced in the elastic zone due to the misfit of the deformation occurring in the inelastic zone. Here we focus on these stresses which are referred to as residual stresses since they remain in the elastic zone after the indenter slides away. Since the sliding indentation is performed quasi-statically, the residual stresses can be treated as a superposition of the static indentation residual stresses continuously formed by distributing Yoffe's blister field. That is, the inelastic deformation due to Yoffe's blister field accumulates behind the sliding indenter.

We shall therefore begin with the blister field derived by Yoffe [1] to describe quasi-static (normal) indentation residual stresses. Yoffe's blister field is made up of the doublet force system shown in Figure 1(b) which consists of the superposition of two full-space elastic stress systems. These two systems are a center of dilatation, three orthogonal doublets, and a doublet of twice this strength applied in opposite sense perpendicular to the surface of the half-space. The resulting stress system, two outward double forces in the surface plane and an inward double force of equal magnitude perpendicular to it, satisfies the free surface condition along the surface of the half-space. The stress components of the resulting blister field are [1]

$$\frac{\sigma_x^b}{2A} = \left[\frac{(1-2\nu)(x^2+2y^2)}{r^2\rho^3} + \frac{(-5+4\nu)x^2}{\rho^5}\right.$$
$$\left. - \frac{(1-2\nu)(2x^2+3y^2)z^2}{r^2\rho^5} + \frac{15x^2z^2}{\rho^7}\right] \tag{11}$$

$$\frac{\sigma_y^b}{2A} = \left[\frac{(1-2\nu)(2x^2+y^2)}{r^2\rho^3} + \frac{(-5+4\nu)y^2}{\rho^5}\right.$$
$$\left. - \frac{(1-2\nu)(3x^2+2y)^2z^2}{r^2\rho^5} + \frac{15y^2z^2}{\rho^7}\right] \tag{12}$$

$$\frac{\sigma_z^b}{2A} = -\left[\frac{1-2\nu}{\rho^3} + \frac{2(4+\nu)z^2 - (1-2\nu)r^2}{\rho^5}\right.$$
$$\left. - \frac{15z^4}{\rho^7}\right] \tag{13}$$

$$\frac{\tau_{xy}^b}{2A} = -\left[\frac{(1-2\nu)xy}{r^2\rho^3} + \frac{(5-4\nu)xy}{\rho^5}\right.$$
$$\left. - \frac{(1-2\nu)xyz^2}{r^2\rho^5} - \frac{15xyz^2}{\rho^7}\right] \tag{14}$$

$$\frac{\tau_{yz}^b}{2A} = -\left[\frac{6yz}{\rho^5} - \frac{15yz^3}{\rho^7}\right] \tag{15}$$

$$\frac{\tau_{zx}^b}{2A} = -\left[\frac{6xz}{\rho^5} - \frac{15xz^3}{\rho^7}\right] \tag{16}$$

where A is the strength of the blister field.

To superpose the blister field as the indenter slides, the strength of the blister field per unit sliding length, B, is defined as $A = B(\xi)d\xi$. Thus, defining a function f such that

$$\sigma_x^b \equiv Af_\sigma(x, y, z),$$

the residual stress due to the sliding blister field is

$$\sigma_x^r = \int_a^b B(\xi)f_\sigma(x-\xi, y, z)d\xi.$$

where the indenter slides from $x = a$ to $x = b$. The remaining residual stresses are calculated us-

ing the same procedure. The experimental config-
uration of interest corresponds to sliding the in-
denter over a length, large compared to the con-
tact size, and examination of the stresses near the
indenter's present location. This special case cor-
responds to $B(\xi) = B$, a constant, $a = -\infty$, $b = 0$,
in which integration leads to the following residual
stress field:

$$
\frac{\sigma_x^r}{2B} = -\frac{2\nu(y^2 - z^2)}{(y^2 + z^2)^2} + \frac{x}{(y^2 + z^2)\rho^5} \times (2\nu x^4 y^2
$$
$$
-2x^2 y^4 + 6\nu x^2 y^4
$$
$$
-2y^6 + 4\nu y^6 - 2\nu x^4 z^2 - 4x^2 y^2 z^2
$$
$$
+2\nu x^2 y^2 z^2 - 3y^4 z^2 + 6\nu y^4 z^2
$$
$$
-2x^2 z^4 - 4\nu x^2 z^4 + z^6 - 2\nu z^6) \qquad (17)
$$

$$
\frac{\sigma_y^r}{2B} = -\frac{2y^2(y^2 - 3z^2)}{(y^2 + z^2)^3} + \frac{x}{(y^2 + z^2)^3 \rho^5} \times (2x^4 y^4
$$
$$
+6x^2 y^6 - 2\nu x^2 y^6
$$
$$
+4y^8 - 2\nu y^8 - 6x^4 y^2 z^2 - 7x^2 y^4 z^2
$$
$$
-6\nu x^2 y^4 z^2 - 2y^6 z^2 - 8\nu y^6 z^2
$$
$$
-12x^2 y^2 z^4 - 6\nu x^2 y^2 z^4 - 15y^4 z^4
$$
$$
-12\nu y^4 z^4 + x^2 z^6 - 2\nu x^2 z^6
$$
$$
-8y^2 z^6 - 8\nu y^2 z^6 + z^8 - 2\nu z^8) \qquad (18)
$$

$$
\frac{\sigma_z^r}{2B} = \frac{2z^2(z^2 - 3y^2)}{(y^2 + z^2)^3} + \frac{xz^2}{(y^2 + z^2)^3 \rho^5} \times (6x^4 y^2
$$
$$
+15x^2 y^4 + 9y^6
$$
$$
-2x^4 z^2 + 10x^2 y^2 z^2 + 12y^4 z^2 - 5x^2 z^4
$$
$$
-3y^2 z^4 - 6z^6) \qquad (19)
$$

$$
\frac{\tau_{xy}^r}{2B} = -y\frac{2(1-\nu)x^2 + 2(1-\nu)y^2 - z^2 - 2\nu z^2}{\rho^5}
$$

$$
\frac{\tau_{yz}^r}{2B} = -4yz\frac{y^2 - x^2}{(y^2 + z^2)^3} + \frac{xyz}{(y^2 + z^2)^2 \rho^5} \times (4x^4 y^2
$$
$$
+10x^2 y^4 + 6y^6 - 4x^4 z^2 + 3y^4 z^2
$$
$$
-10x^2 z^4 - 12y^2 z^4 - 9z^6) \qquad (20)
$$

$$
\frac{\tau_{zx}^r}{2B} = -\frac{z(2x^2 + 2y^2 - z^2)}{\rho^5} \qquad (21)
$$

In the above expressions for the residual stress
field, the origin is located at the present indenter
location (Figure 2).

Lastly, the complete stress field is obtained by
superposing the elastic field and the residual stress
field as

$$
\sigma = \sigma^n + \sigma^t + \sigma^r, \quad \tau = \tau^n + \tau^t + \tau^r.
$$

As is shown in the next section, qualitatively dif-
ferent stress distributions are expected for different
relative values of P, Q, and B.
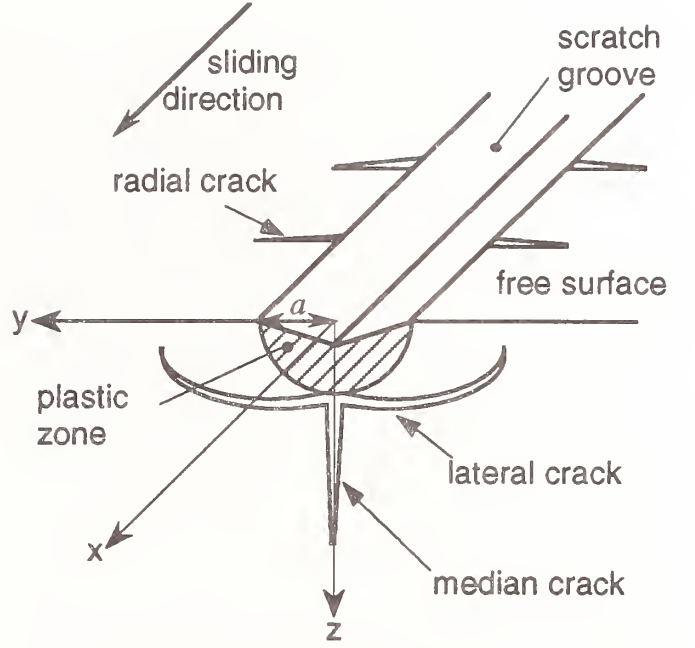
Figure 3: Schematic view of cracking induced by
sliding microindentation of brittle solids

Table 1: Classification of deformation patterns in
soda-lime glass under a sliding Vickers indenter [8]

Normal load (N)	Deformation pattern
$0 \sim 0.05$	No crack
$0.05 \sim 0.8$	Median cracking
$0.8 \sim 3$	Median and lateral cracking with lateral crack growth to the surface at higher loads
$3 \sim 6$	Median cracking and crushed scratch track

3 Results and Discussion

With the derivation of the sliding indentation
stress field in place, it is now possible to analyze
observations of the microcracking about scratches
in brittle solids made by Swain [5], Misra and
Finnie [6], and Ahn et al [8]. Figure 3 shows a
schematic view of the crack patterns which have
emerged from the studies, most of which have been
carried out at light loads in soda-lime glass, silicon,
polycrystalline alumina, and Ni-Zn ferrite. The
typically observed crack patterns are median, lat-
eral, and chevron(radial) cracks. The load regimes
at which the various cracks occur in soda-lime glass
are summarized in Table 1.

As noted earlier, all of these cracks are usually
observed to initiate at or close to the boundary be-

tween the inelastic deformation zone and the surrounding elastic solid. The subsequent growth of these cracks occurs in the elastic region. Therefore, it will be assumed that these cracks are initiated and propagated by tensile stresses which occur in the elastic material immediately adjoining the inelastic zone. The stress fields are now examined in detail to determine whether the peak tensile stresses are consistent with the occurrence of experimentally observed cracking. Under this assumption, the occurrence of the median crack is thus related to $\sigma_y(x, 0, a)$, the lateral crack to $\sigma_z(x, 0, a)$, and the radial crack to $\sigma_x(x, a, 0)$. Therefore, the magnitudes of these stresses are now compared to predict which crack patterns are most likely to occur at a given load. The calculations will refer to detailed experimental observations in soda-lime glass. Hence its Young's modulus, E = 70 GPa, and Poisson's ratio, $\nu = 0.25$, are used in Equations (1-21) the ensuing calculations.

3.1 Residual Stress

The consequences of the residual stress field produced by sliding indentation are examined first. Figure 4 shows the calculated residual normal stress distributions at several locations along the x-axis in soda-lime glass. For comparison to subsequent plotting of the complete stress field, the residual stresses are nondimensionalized using $P/2a^2$ (the average contact pressure) and plotted for the case $B/P = 0.005$. The stresses correspond to the indenter having moved from $x = -\infty$ to $x = 0$, its present location. The residual stress field will approximate the complete stress field for large negative values of x/a. The residual stress $\sigma_z^r(x, 0, a)$ is tensile behind the sliding indenter. On the other hand, the normal stresses $\sigma_y^r(x, 0, a)$ and $\sigma_x^r(x, a, 0)$, are compressive almost everywhere behind the indenter. Furthermore, their magnitudes are much smaller than that of σ_z. The tensile nature of $\sigma_z^r(x, 0, a)$ behind the indenter is a possible cause of lateral cracking in a plane perpendicular to the z-axis in the wake of the indenter. Such lateral cracking was commonly observed by Ahn et al [8] at normal loads in the range of $0.8 \sim 3$ Newtons.

The residual stress field is in plane strain in the $y - z$ plane once the indenter has receded sufficiently far away from that point, i.e. for sufficiently large negative values of x/a. Figure 5 shows
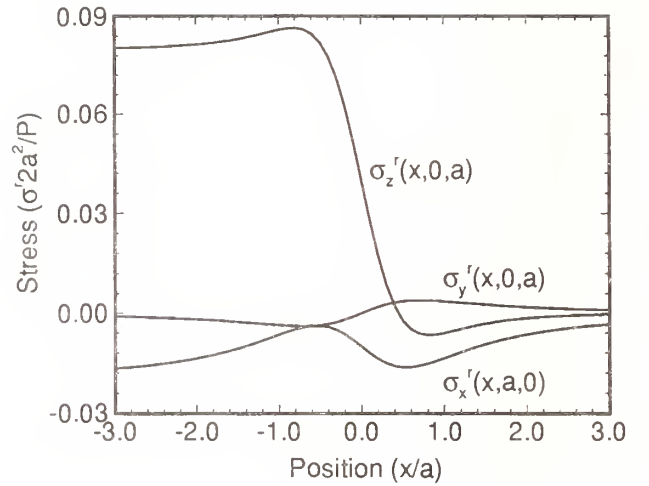
Figure 4: Residual normal stress distribution at the edge of the plastic zone (B/P = 0.005)

the residual stress distribution in this plane strain field. The normal stress $\sigma_z^r(-2a, y, a)$ reaches its maximum tensile value at $y = 0$ which is consistent with lateral crack initiation behind the indenter. If the growth of this crack is determined by the maximum local tensile stress, then the direction of crack propagation may be also predicted using the residual shear stress in Figure 5. The sign of the shear stress for $|y| < a$ is consistent with lateral crack growth that begins parallel to the $x - y$ plane subsequently turning slightly out the plane and growing towards the surface as indicated schematically in Figure 2. The fact that σ_y^r is tensile away from $y = 0$ is also consistent with lateral crack growth towards the surface. These conclusions are drawn from the assumption that the crack grows perpendicular to the maximum principal stress. However, the stress results alone do not explain well why the observed lateral crack is much longer than the width of the scratch. A more detailed fracture mechanics analysis that includes the effect of the cracking on the stress field is required to fully explain the lateral crack growth behavior. Such an analysis using three dimensional boundary elements is presently underway.

3.2 Complete Stress Field

The complete stress field requires the normal (P) and tangential forces (Q) which are related by

$$Q = \mu P$$
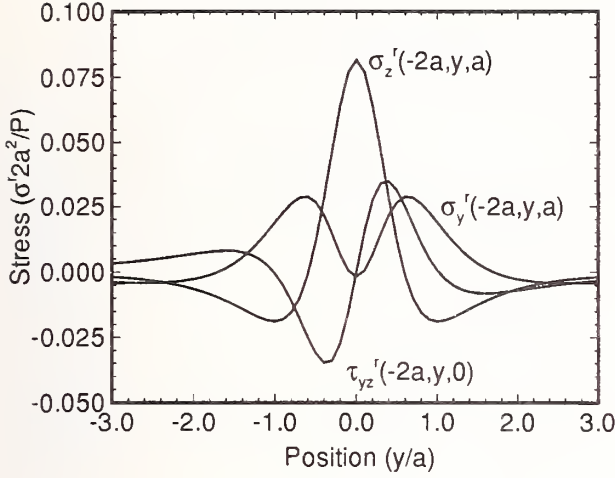
Figure 5: Plane strain residual normal and shear stress distributions versus position perpendicular to the scribing direction (B/P = 0.005)

Figure 6: Complete normal stress distributions at the edge of the plastic zone (B/P = 0.0025)

where μ is the coefficient of friction. When sliding a Vickers diamond indenter against soda-lime glass at extremely slow speeds (5 mm/min) and at low loads (0.1~4 N), Ahn et al [8] measured $\mu = 0.13 \pm 0.033$. Thus, to compare the stress field with crack observations the following calculations use $\mu = 0.13$. Figures 6 and 7 shows trends in the complete normal stress field acting in the uncracked body at the locations where the median, lateral, and radial cracks are observed to occur. In particular, the stresses are given for two ratios of B/P. The normal stress σ_y has its maximum at $x \approx 0$ so that median cracking is expected just underneath the indenter. The normal stress σ_x has a maximum at $x \approx -1.3a$. Thus radial cracks could be initiated at a distance behind the moving indenter. In the range of $x \leq \sim -2a$, the normal stress σ_z maintains its maximum value, so that lateral cracking is expected to occur in the residual stress field. For $B/P < \sim 0.005$ (see Figure 6), the maxima of the tensile stress σ_x and σ_z are smaller than that of σ_y. Thus median cracking only is expected. For $B/P > \sim 0.005$, the maximum value of the normal stress σ_x is still small but the maximum value of σ_z is greater than that of σ_y. Therefore, in this case, it is expected that a median crack first occurs under the moving indenter followed by formation of a lateral crack after the sliding indenter has passed. There could, therefore, be a time delay in emergence of lateral cracking after median cracking. Indeed, it is commonly observed in sliding

indentation experiments that there is considerable lateral crack growth after the indentation process is completed.

The stress field can be observed more completely through the contour plots of Figures 8-11. The contours are given for the elastic zone only to emphasize that the sliding blister field does not model the details inside the inelastic zone. Figures 8-9 show that the lateral cracks initiate at the base of the inelastic zone behind the indenter. Figures 10-11 indicate that the median crack is induced underneath or ahead of the indenter primarily by the applied loads rather than the blister field stresses.

In conclusion, the tensile stresses which determine the various types of cracking are $\sigma_z(-2a, 0, a)$ for lateral cracking, $\sigma_y(0, 0, a)$ for median cracking, and $\sigma_x(-1.3a, a, 0)$ for radial cracking. Furthermore, the formation of median cracking alone is generally expected only for small values of B/P i.e. when the strength of the residual stress field, B, is small or P is large. Also it can be said that lateral cracking will also occur when the residual stress field becomes significant compared to the stress field due to the applied loading.

4   Sliding Blister Field Strength

The stress fields derived from the sliding indentation model depends on the factor B which may be termed, by analogy with Yoffe's blister field con-
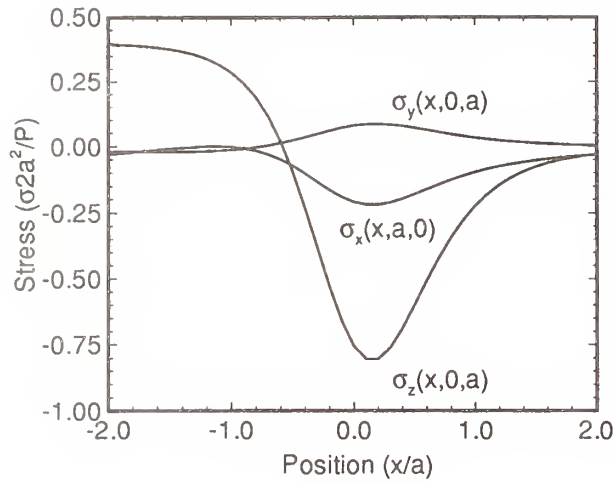
Figure 7: Complete normal stress distributions at the edge of the plastic zone (B/P = 0.025)
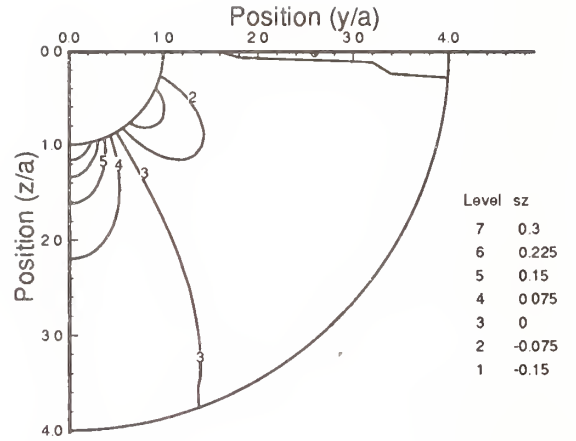
Figure 9: Complete stress contour $\sigma_z 2a^2/P$, x=-3a, B=0.025 P
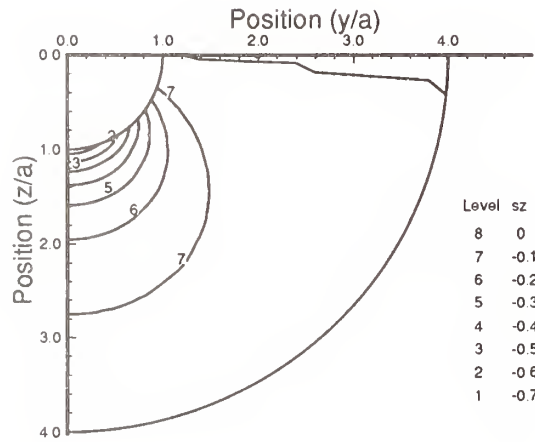
Figure 8: Complete stress contour $\sigma_z 2a^2/P$, x=0, B=0.025 P
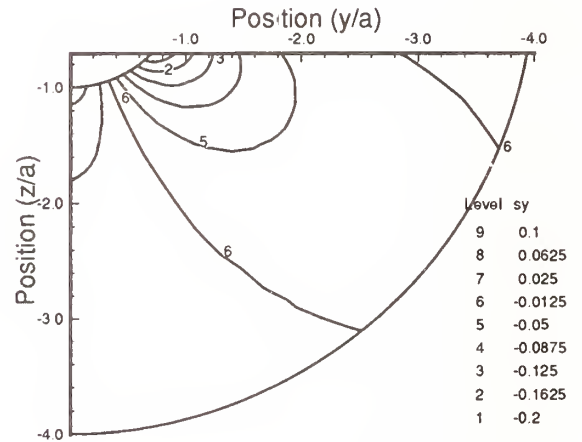
Figure 10: Complete stress contour $\sigma_y 2a^2/P$, x=0, B=0.0025 P
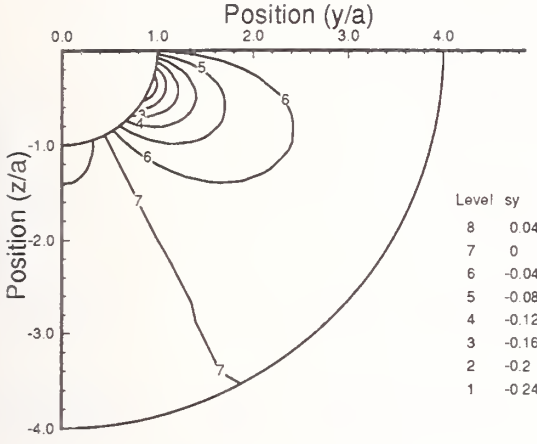
Figure 11: Complete stress contour $\sigma_y 2a^2/P$, x=0, B=0.025 P

stant, A, as the strength of the sliding indentation blister field. At present there exists no well defined experiment which can be used to unambiguously obtain the values of A or B. Next B is estimated from certain experimental observations. This estimated value of B is then used to calculate the stress field explicitly.

Bridgman and Simon [3] showed that most glasses do undergo a certain amount of compaction under stress. For calculating B, it will be assumed that any compaction of the glass which occurs under the sliding indenter is completely accommodated within the plastic zone. Furthermore, the remaining volume of material displaced by the indenter is assumed to be pushed out of the plastic zone. For static indentation with a sharp indenter, the increase in volume of any hemi-sphere of radius ρ ($\rho > a$, a = plastic zone radius) is independent ρ and the volume change is given by

$$\Delta V = 2\pi A \frac{1-2\nu}{3G} \tag{22}$$

where A is the strength of the doublet producing the static indentation blister field and G is the shear modulus. Figure 12 shows a schematic of a typical profile taken across a scratch track in glass produced by a sliding Vickers indenter at light loads ($\sim 0.05 - 0.1N$). See Ahn et al [8] for actual scratch profiles. Small humps appear on either side of the scratch track, which in the absence of any cracking around the indentation, is mostly due to upward flow of the material. Such a profile suggests that some of the material displaced
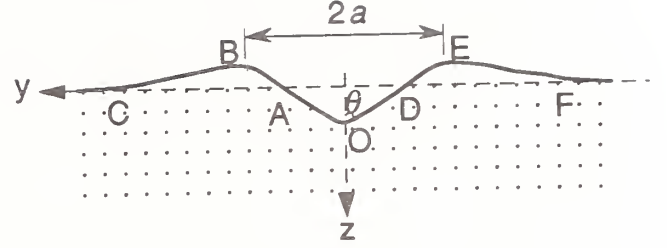
Figure 12: Sketch of surface profile across a scratch track made by a sliding Vickers indenter in soda-lime glass (load $\sim$ 0.05-1 N). The ratio of vertical to horizontal magnification is 5:1

by the indenter is also accommodated by this upward flow. The upward plastic flow factor, F_P, is defined, using Figure 12, as

$$F_P = \frac{\triangle OAD - (\triangle ABC + \triangle DEF)}{\triangle OBE} \tag{23}$$

where $\triangle OAD$ is the area of the triangle having vertices O, A, and D. While estimating B, it is necessary to also account for this upward flow of the material.

By analogy with the static indentation blister field, we can estimate the increase in volume around an infinitely long scratch due to the sliding indentation blister field as

$$\lim_{l\to\infty} \int_{-l}^{l} B\Delta V(x-\xi, y, z)d\xi =$$

$$\lim_{l\to\infty} \left[\left(\frac{2a^2 l}{\tan\theta} + \frac{2a^3}{3\tan\theta} \right) \right.$$

$$\left. - \left(\pi a^2 l + \frac{8\pi a^2}{3} \right) \frac{\delta V_c}{V} \right] F_p \tag{24}$$

where $\delta V_c/V$ is the compaction ratio for glass and F_p is the upward plastic flow factor. The terms in the first parenthesis of the right hand side of Equation (24) represent the impression volume of the sliding indentation and the terms in the second parenthesis represent the original volume of plastic

deformation zone. The parameters a and θ are defined in Figure 12.

Combining Equations (22) and (24) gives

$$B = \frac{3Ga^2}{2\pi(1-2\nu)}\left(\frac{1}{\tan\theta} - \frac{\pi}{2}\frac{\delta V_c}{V}\right)F_p \qquad (25)$$

and B can now be estimated if the compaction ratio $(\delta V_c/V)$ and F_P are known.

The value of compaction ratio for soda-lime glass can be estimated using a curve fit of the data of Cheng and Finnie [10] for the compaction of soda-lime glass under hydrostatic pressure. Their equation is

$$\frac{\delta V_c}{V}(\%) = \frac{0.951 - 0.729p + 1.934p^2 + 0.260p^3}{(1+p)^2} \qquad (26)$$

where p is the applied hydrostatic pressure in GPa. In order to estimate the values of a, θ, and F_p, experimental measurements of the width $(2a)$ and depth $(a/\tan\theta)$ of a scratch track in soda-lime glass were carried out for various applied loads (0.05 to 0.8 N). From the experimental data the half width of the track, a (μm), can be expressed as a function of P (N) as

$$a = 9.48P^{0.57} \qquad (27)$$

The average value of θ was obtained from Talysurf profiles of a number of scratch tracks as $83.6° \pm 1.46$. Using the profilometric measurements, the average value of F_P was estimated as 0.055.

We are now in a position to evaluate B as a function of normal load P. This variation is shown in Figure 13. The value of B increases monotonically with applied load P. Due to the nature of the increase in B with P shown in Figure 13, it is expected that the strength of the residual stress field eventually dominates the Boussinesq and Cerutti stress fields at large normal loads P. This is clearly evident in Figure 14. At low loads $(<\sim 0.6$ N) the stress $\sigma_y(0,0,a)$ is the dominant tensile stress so that median cracking is expected in a plane perpendicular to the y-axis. This is consistent with the absence of lateral cracks in this regime. But for $P >\sim 0.6N$ the tensile stress $\sigma_z(-2a,0,a)$ becomes more significant. This is consistent with the observation of both median and lateral cracks in this load regime in Ahn et al [8]. It is hard to anticipate radial cracking because the tensile stress
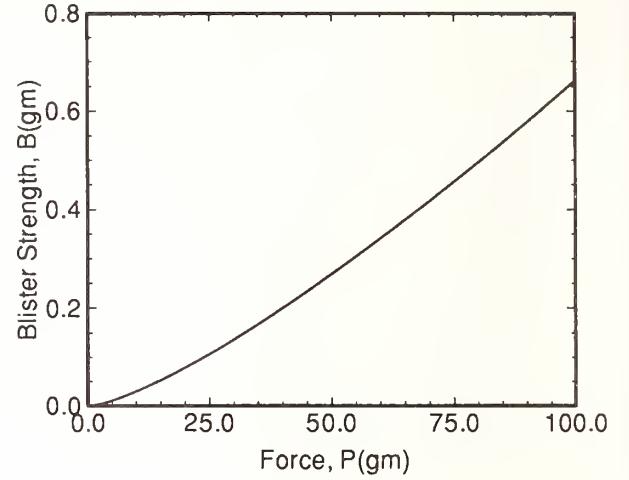
Figure 13: Strength of residual stress field as a function of applied load

$\sigma_x(-1.3a,0,a)$ is always much smaller than the remaining stresses, $\sigma_y(0,0,a)$ and $\sigma_z(-2a,0,a)$. Perhaps this explains why the radial cracks were only occasionally seen in soda-lime glass and, even when they were observed, the length of the radial cracks were quite small.

The analytical predictions are in close the experimental classification summarized in Table 1. It must be noted, however, that perturbations in the stress field due to energy dissipation by one or more crack systems have been largely ignored. Also, it is at present difficult to explain the crushed scratch track produced in the load range of $3-6N$ in soda-lime glass using the analysis.

5   Conclusion

The stress field produced by a sliding sharp indenter in brittle solids has been derived from an extension of Yoffe's model for static microindentation. Numerical results are illustrated and compared with experimental observations. The strength of the residual stress field has been evaluated as a function of the normal load has been discussed. It has been shown that the present analytical model provides reasonably good descriptions of the crack patterns observed around sliding indentations in brittle materials. In particular, the analysis accounts for the occurrence of lateral cracking under sliding indenters above an experimentally observed threshold load. These conclusions are presently be-
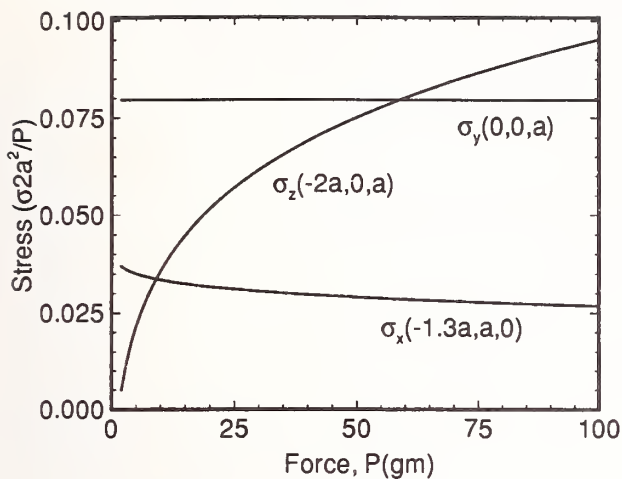
Figure 14: Tensile stress at crack location as a function of applied load

ing further addressed through inclusion of the blister field stresses in a complete fracture mechanics analysis.

References

[1] E.H. Yoffe, "Elastic Stress Fields Caused by Indenting Brittle Materials," *Philosophical Magazine A*, **46**, (4) pp 617–628, 1982.

[2] D. Tabor, *The Hardness of Metals,* Oxford University Press, 1951.

[3] P.W. Bridgman and I. Simon, "Effects of Very High Pressure on Glass," *Journal of Applied Physics*, **24** (4) pp 405–413, 1953.

[4] K.W. Peter, "Densification and Flow Phenomena of Glass in Indentation Experiments," *Journal of Noncrystalline Solids*, **5**, pp 103–115, 1970.

[5] M.V. Swain, "Microfracture about Scratches in Brittle Solids," *Proceedings of the Royal Society A*, **366**, pp 575–597, 1979.

[6] A. Misra and I. Finnie, "On the Scribing and Subsequent Fracturing of Silicon Semiconductor Wafers," *Journal of Materials Science*, **14**, pp 2567–74, 1979.

[7] S.Y. Chen, T.N. Farris, and S. Chandrasekar, "Sliding Microindentation Fracture of Brittle Materials," *STLE Tribology Transactions*, **34** (2) pp 161–168, 1991.

[8] Y. Ahn, S. Chandrasekar, and T.N. Farris, "Deformation Observations about Sliding Microindentation in Soda-Lime Glass and Ni-Zn Ferrite," *Journal of Applied Mechanics*, 1993, Submitted.

[9] K.L. Johnson, *Contact Mechanics*, Cambridge, Cambridge, 1985.

[10] W. Cheng, E. Ling, and I. Finnie, "Median Cracking of Brittle Solids Due to Scribing with Sharp Indenters," *Journal of the American Ceramic Society*, **73** (3) pp 580–586, 1990.

ON-MACHINE ELECTRO-DISCHARGE TRUEING FOR METAL BOND DIAMOND GRINDING WHEELS FOR CERAMICS

K. SUZUKI
Nippon Institute of Technology, Saitama, Japan

T. UEMATSU and T. YANASE
Toyama Prefectural University, Toyama, Japan

T. NAKAGAWA
University of Tokyo, Tokyo, Japan

This paper describes a new method for effective and precise trueing and/or dressing for metal-bond grinding wheels on a grinding machine by utilizing electro-discharge machining. A simplified trueing unit with an electrode mounted on the table of an NC grinding machine makes highly efficient and precise trueing and/or dressing possible to the metal-bond superabrasive wheels mounted on the spindle of the machine. The wheels trued by this method showed a higher grinding ratio and lower grinding forces than the wheels trued by a conventional method.

1. INTRODUCTION

Superabrasive grinding wheels, such as diamond or CBN wheels, are generally used in the grinding of hard-to-grind materials such as cemented carbide, high speed steel, and ceramics. Such superabrasive wheels require trueing and dressing before use to eliminate wheel eccentricity as a result of mounting on the spindle, and to provide sharp cutting edges on the abrasive particles. Trueing is also carried out to provide a desired shape on a wheel or to correct a dulled profile. But the trueing of superabrasive wheels is rather difficult especially in the case of metal bond grinding wheels. Metal bond wheels have several good features such as high grinding ratio and ability of high efficiency grinding; but their use requires the development of efficient and precise trueing methods. This paper describes a newly developed trueing method, which uses electro-discharge machining on a grinding machine, for metal bond superabrasive wheels.

2. PRINCIPLE AND FEATURES OF "ON-MACHINE ED TRUEING METHOD"

Trueing of conventional grinding wheels are carried out easily with diamond dressers. But the trueing of superabrasive wheels are rather
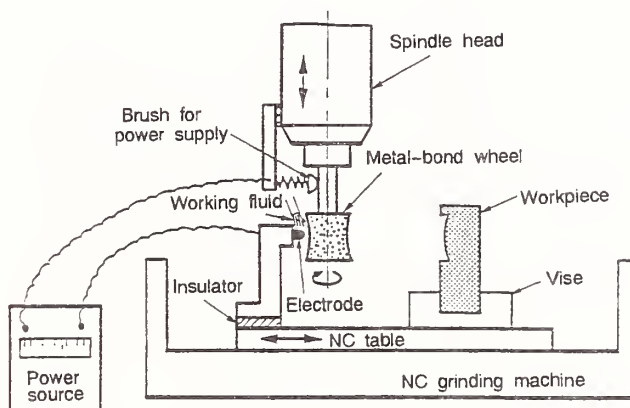
Fig.1 Schematic illustration of on-machine ED trueing/dressing method(1).

difficult. Among three kinds of diamond grinding wheels, i.e., resinoid, vitrified and metal bond wheels, trueing of metal bond wheels is the most difficult because of the toughness of the matrix material. The authors have developed a new trueing method named "On-machine electro-discharge(ED) trueing method" for metal bond diamond or CBN wheels(1).

In this method, trueing is performed on a grinding machine by utilizing electro-discharge machining between an electrode on the table and a metal bond wheel mounted on the spindle of an NC grinding machine as shown

in Figure 1.   The expected features of the method are as follows;

(1)Applicable to all metal bond wheels and electrically conductive resinoid wheels.
(2)Precise trueing owing to on-machine method.
(3)Precise trueing of small wheels and/or thin wheels with negligibly small applied forces.
(4)Dressing of wheels by adopting finishing ED conditions.
(5)Profile trueing by using NC movement of a grinding machine.
(6)ED trueing with chemical solution grinding fluids.
(7)Automatic trueing operation.

3. ON-MACHINE WIRE ED TRUEING

The most important factor in the on-machine ED trueing is how to prevent electrode wear, which reduces the trueing accuracy.   One solution for suppressing the electrode wear is to adopt appropriate ED conditions; but, this approach is difficult. Another solution is to use a wire electrode like a wire EDG method(2).

Figure 2 shows a schematic arrangement of the on-machine wire ED trueing method.   In an actual set-up a wire electrode runs along a ceramic guide mounted on the trueing unit on the NC table of the grinding machine as shown in Figure 3.   It is possible to use conventional cutting or grinding fluids as the dielectric fluid for the ED trueing.

The main features of the on-machine wire ED trueing are as follows;

(1)Accurate trueing/dressing is possible because of no wire electrode wear.
(2)Trueing for a profiled wheel is possible by utilizing NC movement of the grinding machine, and no profiled electrode is necessary.

4. ON-MACHINE ED TRUEING WITH A BLOCK ELECTRODE

4.1 Principle and Procedure

ED trueing with a block electrode is more preferable than the method with a wire electrode from the view point of the trueing efficiency.   But there exists a problem of electrode wear in the case of the block electrode.

To solve this problem, an on-machine
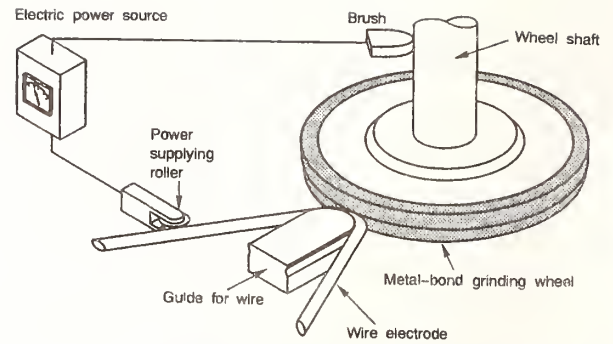
Fig.2   Schematic illustration of on-machine wire ED trueing/dressing method(3).
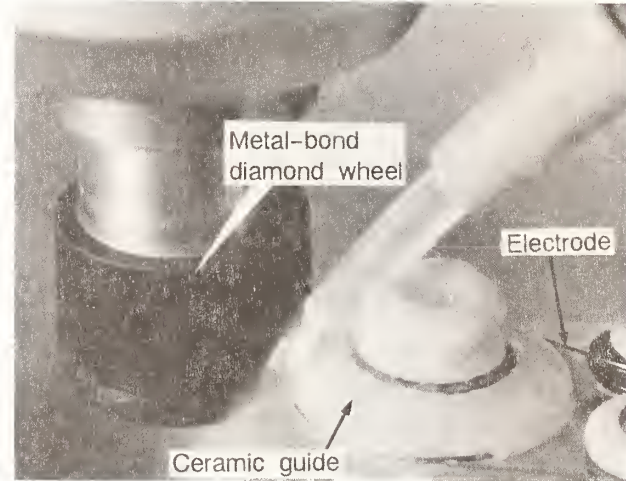
Fig.3   A state of on-machine wire ED trueing of a metal-bond diamond wheel(D=30mm)(3).
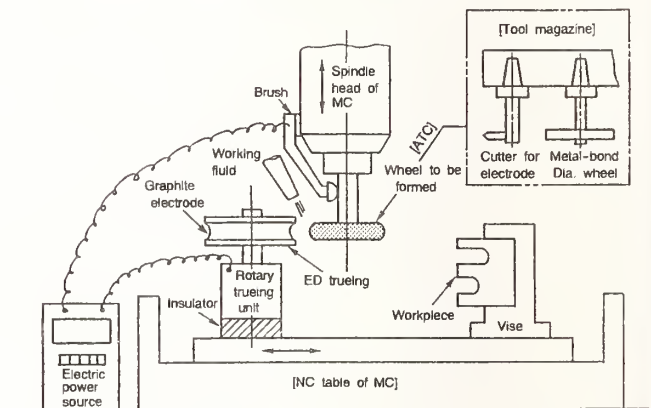
Fig.4   Arrangement of equipments for the on-machine ED trueing with a block electrode on an NC grinding machine.

electrode forming method has been developed by using NC movement and automatic tool changing function(ATC) of a grinding machine(3,4).   Procedure of the on-machine ED trueing method combined with the on-machine electrode forming method is as follows(Figures 4 and 5):

(a)Forming of electrode   (b)On-machine ED trueing   (c)Correction of worn electrode   (d)Finish ED trueing(dressing)
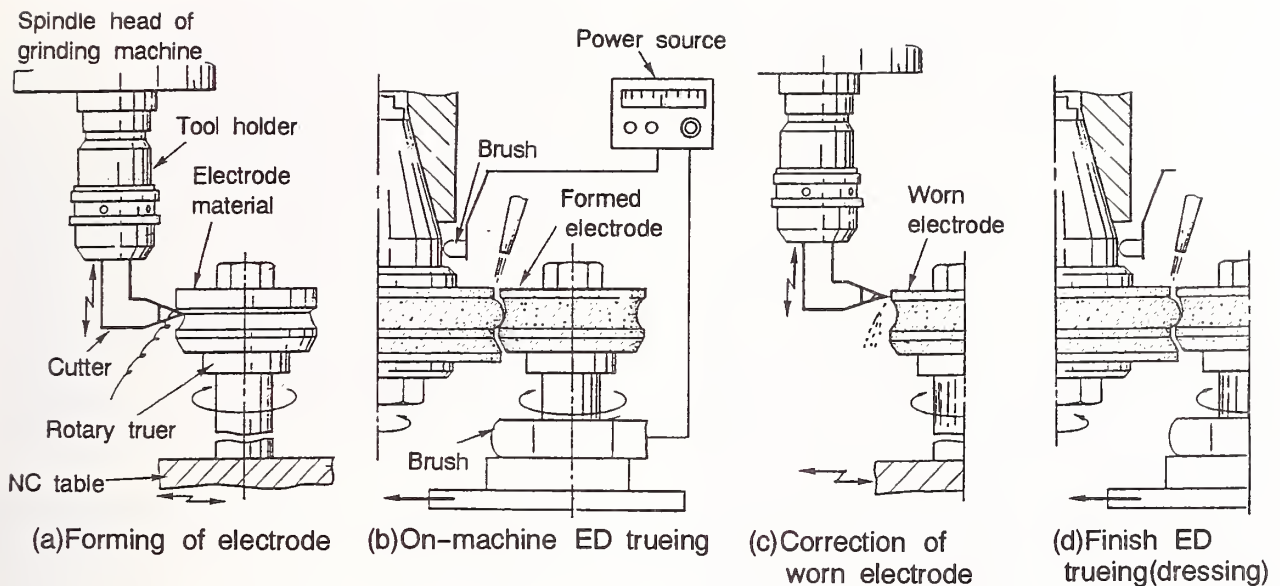
Fig.5 Procedure of the on-machine ED trueing method with on-machine electrode forming.

(1)A turning or cutting tool is selected from a tool magazine and is mounted on a spindle of a grinding machine.

(2)Rotating graphite electrode which is set on the NC table is machined with the selected cutting tool to provide a desired geometry(Fig.5a).

(3)By the help of ATC a grinding wheel is mounted on the spindle instead of the cutting tool.

(4)ED trueing is conducted between the formed graphite electrode and the grinding wheel(Fig.5b).

(5)When the wear of the electrode becomes larger, the electrode is machined again to provide the accurate shape(Fig.5c).

(6)Final trueing is conducted with a finishing ED condition(Fig.5d).

4.2 Advantages by "On-machine Electrode Forming"

The on-machine electrode forming method provides the following advantages:

(1)The shape of a block electrode, for a rather complicated profiled wheel, is
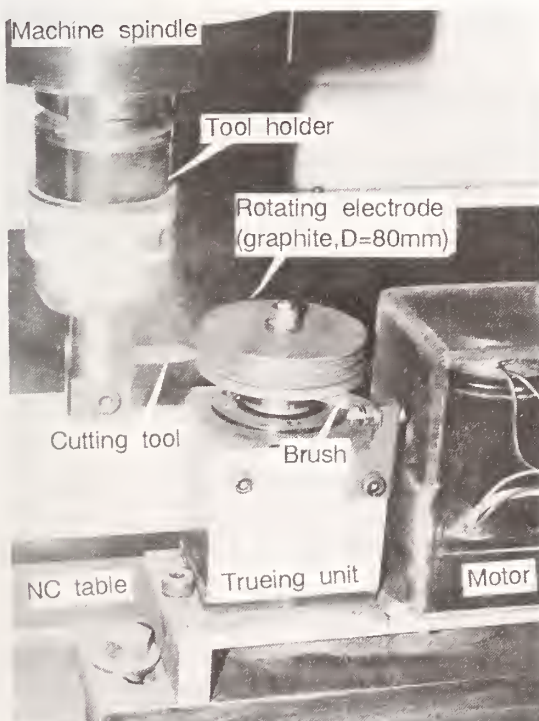
Fig.6   Machining of a graphite electrode (D=80mm) to provide a desired shape(3).
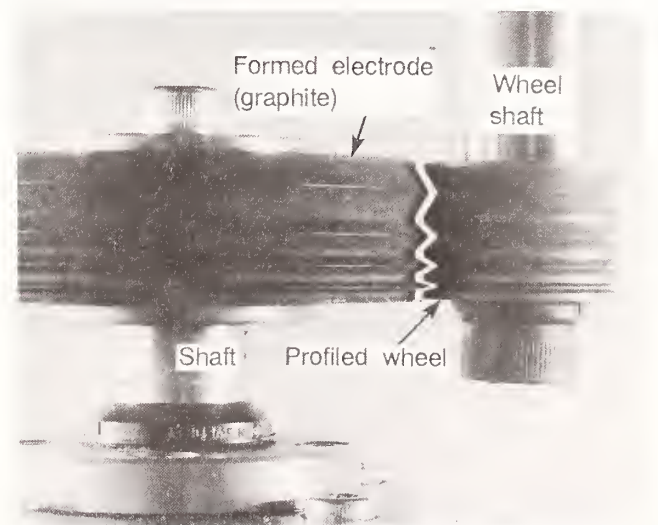
Fig.7   Profiled metal bond diamond grinding wheel(D=30mm) by the on-machine ED trueing.

generated accurately and efficiently with an NC program on a grinding machine.

(2)Dulled shape of the block electrode, due to wear, is corrected with a cutting tool mounted on a spindle of an NC grinding machine.

4.3 Form Trueing

Figure 6 shows the machining setup for providing a desired shape on a graphite electrode. Figure 7 shows s profiled grinding wheel after on-machine ED trueing. It took only about 15 minutes to form the wheel from the original cylindrical shape. With the profiled grinding wheel, it is possible to carry out profile grinding of work materials set on the table of a grinding machine immediately. Figure 8 shows a ceramic sample with a complicated shape ground with profiled wheels.

4.4 Trueing Efficiency

The effects of trueing conditions such as no-load voltage, settled peak current, and duty factor on the trueing efficiency, and the electrode wear were investigated with bronze bond diamond grinding wheels. The diameter of the wheel is 30mm and the width of trueing is 5mm. The electrode was fed automatically toward the grinding wheel so as to keep the gap distance constant. The trueing efficiency was expressed by the feeding speed f_d of the electrode. The following observations were made.

(1)f_d increased with the increase of E_0(no-load voltage), and it reached 0.18mm/min in the case of E_0=150V.

(2)f_d increased with Ip(settled peak current), and it reached 0.41mm/min in the case of Ip=45A(Figure 9).

(3)f_d increased with the increase of pulse on-time τ_{on} and decrease of off-time τ_{off}. And the wear of the electrode(ε) decreased with the increase of τ_{on} and decrease of τ_{off}(Figure 10).

(4)Positive polarity provided higher trueing efficiency and low electrode wear.

(5)Graphite was better than copper and brass, when chemical solution grinding fluid was used as the dielectric fluid.

(6)Relative rotational speed of the electrode and the grinding wheel had only a minor
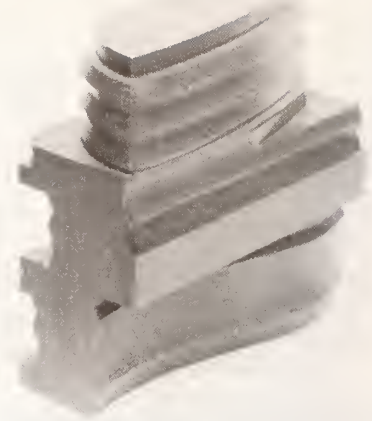
Fig.8 Silicon nitride ceramics ground with profiled wheels made by the on-machine ED trueing.
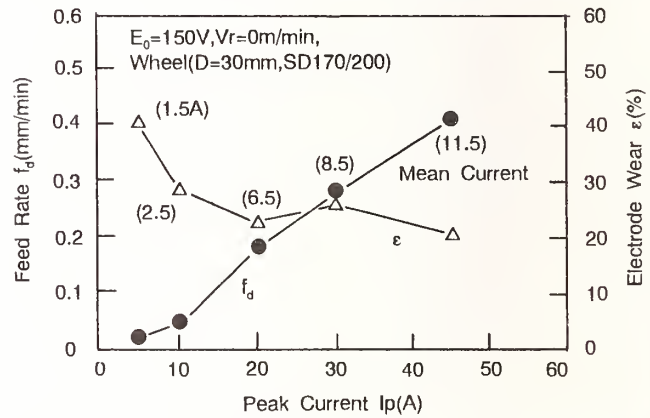
Fig.9 Relation between settled peak current and trueing efficiency.
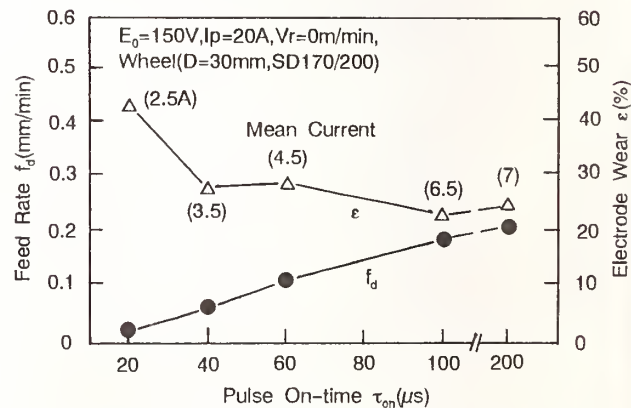
Fig.10 Relation between pulse on-time τ_{on} and trueing efficiency.

effect. But the small relative speed provided better trueing efficiency and less electrode wear(Figure 11).

4.5 Wheel Surface after ED Trueing/Dressing

Figure 12 shows the surface of a diamond wheel after ED trueing/dressing. It is observed that the diamond abrasives protrude sufficiently with no deterioration and are grasped firmly by the metal matrix. Similarly dressed surfaces were obtained for CBN wheels.

4.6 Grinding Ability of the Wheel

The grinding ability of a wheel dressed by ED technique was compared with that of a wheel dressed with a conventional WA(white fused alumina) stickstone(Figure 13). The grinding force for sintered silicon nitride ceramics was considerably lower in the case of the ED dressed wheel. The grinding ratio GR became higher by selecting an appropriate ED condition(smaller pulse width in this case). These tendencies were observed just in the same manner in grinding cemented carbide.

4.7 Dimensional Accuracy in ED Trueing

Dimensional accuracy in ED trueing was investigated by forming a typical shape as shown in Figure 14, which includes some peaks with various angles, a height of 2mm and a radius of 0.2mm. The accuracy was expressed in the form of the error between an electrode and a workpiece ground with a formed wheel. When the electrode was not reformed in the course of trueing process, the error was rather large, for example the error of the height was 0.1mm. But by reforming the electrode once or twice, the error was reduced to a great extent. The errors after two reforming cycles were under 0.01mm in height, $0.03 \sim 0.08$mm in radius, and $-0.04 \sim -0.38°$ in angle. Figure 15 shows a formed electrode(graphite), a trued wheel(metal−bond, SD600) and a ground sample(alumina ceramic).

5. DEVELOPMENT OF POWER SOURCE
5.1 Servo Control of Gap Distance

The gap distance between the electrode and the wheel has to be kept constant for stable and efficient ED trueing. For this purpose a simple control circuit was connected between the ED power source and the feed rate override function of the NC grinding machine as shown in Figure 16. The electrode on the table is fed intermittently toward the wheel with a feed rate of 100, 20 or 0% of
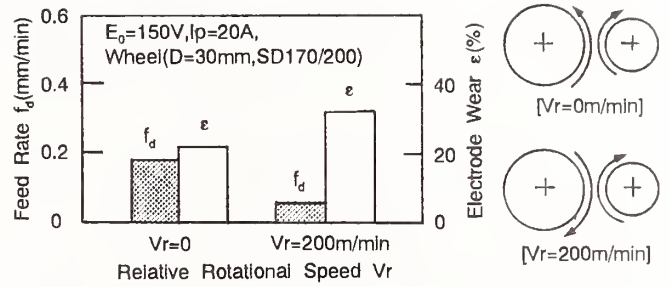
Fig.11 Effect of relative rotational speed between an electrode and a grinding wheel.
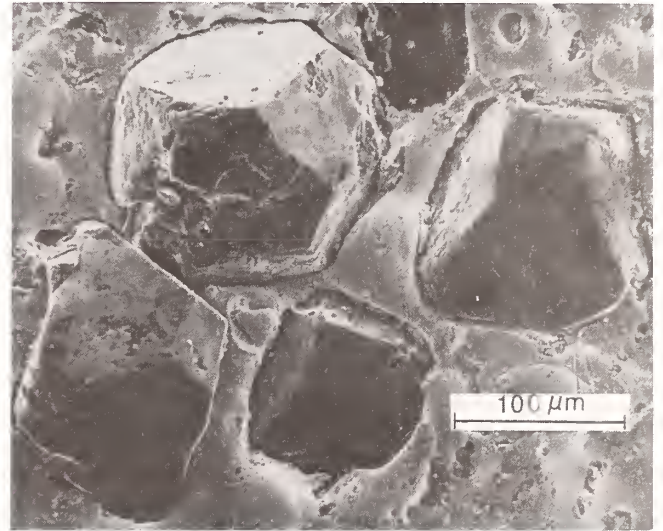
Fig.12 Surface of a diamond grinding wheel after ED trueing.
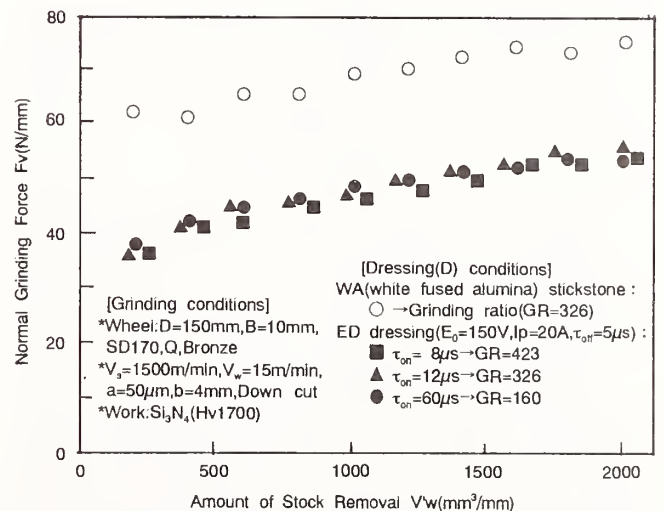
Fig.13 The grinding ability of the wheel dressed by the ED method in grinding silicon nitride ceramics.
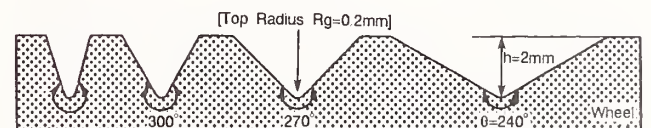
Fig.14 Shape for investigation of trueing accuracy.

programmed feed rate depending on the detected gap voltage. This servo control system was confirmed to work satisfactorily.

5.2 Power Source for ED Trueing

Conventional EDM power source can be used for the on-machine ED trueing, but it is not always advantageous. A rather compact and inexpensive power source was specially designed for ED trueing. Table 1 lists the main specifications of this power source. The above mentioned servo control circuit for gap distance is also included in the power source.

6. CONCLUSIONS

The authors proposed a new on-machine ED trueing method for metal bond superabrasive wheels, and investigated the effect of the method. The wire ED trueing makes precise trueing and dressing of profiled wheels possible by using the NC movement of a grinding machine; but the trueing efficiency is not so high. On the other hand, the ED trueing method with a block electrode combined with the on-machine electrode forming method showed superior features:

(1)Extremely high trueing efficiency
(2)Realization of profile trueing
(3)Correction of a worn grinding wheel on the machine
(4)Automatic trueing
(5)Sufficient projection of abrasive particles(=low grinding force)
(6)Provision of higher grinding ratio(=long tool life)

The on-machine ED trueing method requires a simple electrode unit and a simple electric power source.

[REFERENCES]

1. K.Suzuki, et al.,"Proposal of Electro-Discharge Trueing with Twin-Electrode," Proc. of Autumn Conf. of JSPE, pp.575-578, 1985(in Japanese).
2. T.Masuzawa et al., Annals of the CIRP 34/1, pp.431-434, 1985.
3. K.Suzuki, T.Uematsu, and T.Nakagawa, "On-machine Trueing/Dressing of Metal Bond Grinding Wheels with Electro-Discharge Machining," Annals of the CIRP 36/1, pp.115-118, 1987.
4. K.Suzuki, T.Uematsu et al.,"Recent Advances in the Grinding of Ceramics and Hard Metals," Proc. of Hard Metal Conf., England, pp.1-16, 1988.
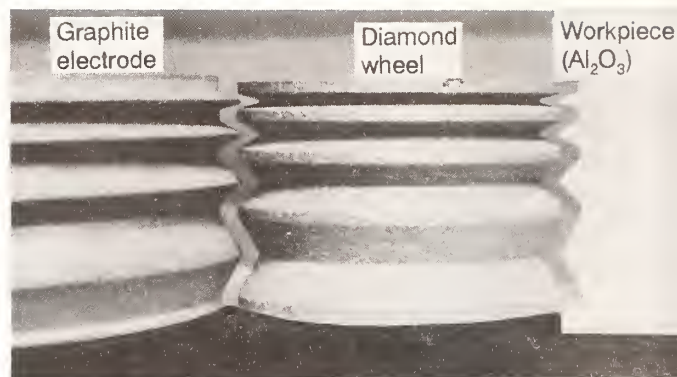
Fig.15 Sample of formed electrode, trued wheel and ground workpiece.(Metal-bond diamond wheel,D=30mm,b=30mm,SD600)
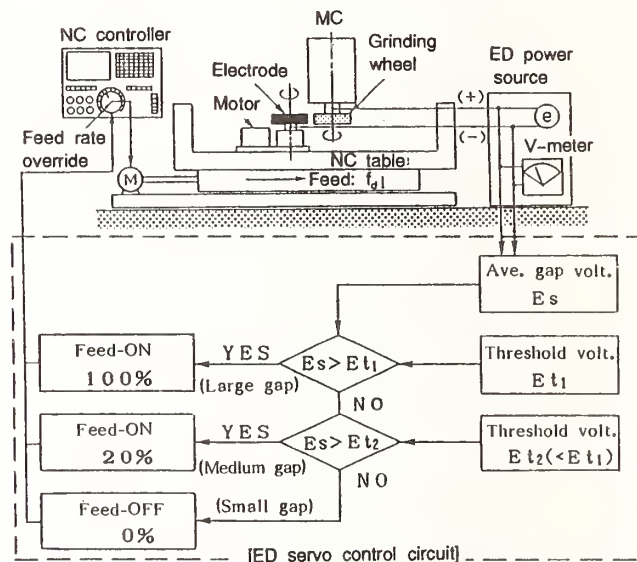
Fig.16 Control circuit for on-machine ED trueing.

Table 1 Specifications of ED power source.

Capacity	3kVA
Size & Weight	W600xD600xH800mm,90kgf
Monitor	Volt.& Amp.-meter, Override level meter
No-load Voltage	E_0=60 - 150V
Peak Current	Ip=2 - 75A
Pulse Width	On-time τ_{on} =1 - 200μs, Off-time τ_{off}=3 - 100μs
Condition-set	(1)Manual-set,(2)Pre-set, (3)External set
Safety Device	Automatic power-off device

CERAMIC GRINDING WITH SELF-SHARPENING DIAMOND WHEELS

R. S. HAHN
Hahn Engineering, Auburn, MA

The sharpness of resin-bonded diamond wheels was observed to increase 20-fold when the wheels were subjected to normal-force intensities of 30 to 50 N/mm. Once briefly subjected to those levels, the wheel would cut 15 to 20 times faster than the "as-dressed" wheel at moderate (lower) force levels. The resin bond wears very rapidly at the high-force intensities, causing wheel-regenerative chatter to occur. Accordingly, the "chatter-free-grind time" (CFGT) is short at the high-force level. In order to obtain reasonably long CFGTs it is necessary to operate the wheel at force levels that are high enough to give good stock-removal rates, yet not so high as to cause frequent wheel dressing to remove the wheel-regenerative chatter. The use of normal-force grinding controls to measure the wheelwork-machine time constant, the system stiffness, the work-removal parameter, and normal-force thresholds are described.

INTRODUCTION:

The grinding of ceramics and difficult to grind materials confronts many companies. The selection of grinding wheels and the grinding machine input variables to obtain a satisfactory manufacturing process is often difficult to achieve.

The development of a satisfactory grinding manufacturing process can be facilitated by distinguishing grinding process variables from grinding machine variables and identifying the important grinding process variables. Grinding machine variables, such as wheelspeed, workspeed, feedrate, depth of dress etc., are well understood. Grinding process variables, such as wheel sharpness, wheelwear rate, threshold normal stress, wheel breakdown stress, workpiece damage thresholds, surface finish and self-excited chatter characteristics need to be quantitatively measured and controlled.

WHEEL-WORK CHARACTERISTIC CHART:

Figure 1 illustrates a cylindrical grinding machine executing a plunge grinding operation. Upon feeding the cross slide at the rate $\bar{v}f$, the normal force between wheel and work at the moment of contact is zero. As the slide feeds, the "springs" in the system compress, building up the normal force and causing the wheel and work to mutually machine each other. The time rate of change of the workpiece radius $\bar{v}w$, of the wheel $\bar{v}s$, and the machine deflection $\dot{x}$, equals the feedrate $\bar{v}f$, thus:

$$\bar{v}w + \bar{v}s + \dot{x} = \bar{v}f \quad (1)$$

The volumetric rates of stock removal Z'w and wheelwear Z's per unit width of cut are:

$$Z'w=3.14*Dw*\bar{v}w \quad (2)$$

$$Z's=3.14*Ds*\bar{v}s \quad (3)$$

where
    Dw is the work diameter
    Ds is the wheel diameter

The stock removal rate Z'w and wheelwear rate Z's are plotted in Figure 2 against the normal force per unit width F'n, for AISI 52100 steel. A rubbing zone, a plowing zone, and a cutting zone are clearly recognizable(1). The rubbing-plowing and the plowing-cutting transition forces F'th, F'pc are indicated. The slope of the stock removal curve Z'w is generally a straight line for metals and is called the work removal parameter WRP. That parameter reflects the sharpness of the grinding wheel and the workpiece resistance to abrasion. In the grinding of metals, as the wheel becomes dull, the WRP falls and F'no and F'pc increase.

Figure 3 shows a plot of Z'w vs F'n for a 120 grit resin bonded diamond wheel grinding the ID of a Zirconia ring. The wheel was first dressed using a diamond dressing disc. Then grinding tests were made at increasing force levels, producing the concave upward curve in Fig. 3, followed by decreasing force levels producing the straight descending line with slope of .25 cumm/s*N. The numbers at each data point indicate the specific energy in joules/cumm.

Figure 4 is a similar plot for a 320 grit diamond wheel, again showing a concave upward characteristic for increasing forces. However, when grinding tests at decreasing force levels were attempted, wheel-regenerative chatter occurred as indicated by the letter "c". Also shown on Fig. 4 is the wheelwear as obtained by micrometer measurement of the wheel diameter before and after each grinding test. It is seen that the wheelwear is negligible except at the highest force level where wheel-regenerative chatter tends to occur. Wheel-regenerative chatter is a phenomenon associated with wheelwear and is discussed in the section below.

The concave upward characteristic for increasing forces may be explained in two ways; i.e. (1) by erosion of the resin bond to expose diamond grits, thereby sharpening the wheel, and/or (2) by increasing the dominance of the brittle fracture mode of material removal. However, the straight line characteristic for decreasing force levels indicates that a significant sharpening of the wheel has occurred. In addition, the used surface of the wheel sparkles brightly as the

result of the exposed diamonds. The possibility of micro fissures propagating deeply into the surface seems unlikely since 1 mm of stock was removed for each decreasing force data point. Therefore, it can be concluded that brief exposure of the wheel to high normal stresses will sharpen the wheel but wheel-regenerative chatter will quickly develop. (The average normal stress can be found by pressing the wheel statically against the workpiece and measuring the contact length under a given normal force and applying a small correction for the wheel-depth-of-cut. The normal stress corresponding to 44 N/mm in Fig. 4 was 28 N/sqmm (see Appendix).

CHATTER-FREE GRIND TIME:

Many commercial production grinding operations operate under conditions of dynamic instability. That means that self-excited vibrations will eventually develop. Those may be of the work-regenerative or the wheel-regenerative type. In the tests described here wheel-regenerative chatter prevailed. This type of chatter is analogous to the development of a "corduroy dirt road", wherein the pulsating forces between an automobile wheel and the road surface cause a propagation of a wavy-road surface to develop.
As pulsating forces occur between wheel and workpiece, a wavy surface on the periphery of the wheel tends to develop.

Figure 5 presents the chatter block diagram for cylindrical plunge grinding machines (2). Associated with the wheel-regenerative loop involving vs, is the "wheelwear stiffness Ks" representing the ratio of normal force to depth of wheelwear per wheel revolution.

Although the chatter theory is based on linear systems and considers Ks to be a constant, the wheelwear stiffness for vitreous and resin-bonded wheels is strongly nonlinear and Ks drops rapidly at high normal stress levels. Since the stability criterion in Fig 5 is usually not satisfied in commercial grinding machines, the growth of vibration amplitude is represented in Fig 6, where the chatter-free grind time indicates when the amplitude reaches an unacceptable limit. The chatter-free grind time can readily be determined in many cases, audibly , depending on the natural frequencies of the system. For the system described in Table 1, the chatter frequency occurs somewhat above the wheelhead spindle natural frequency, depending upon the normal force, and was in the region of 2000 Hz. For the point at 44 N/mm in Fig 4, the chatter-free grind time was about 5 s. Once the chatter has developed it is impossible to stop it without retruing the wheel. For the point at 44 N/mm in Fig 3 chatter did not develop in the 10 s grind time nor did it at the lower decreasing force grinds, where about 1 mm of stock was removed for each grind test. The 120 grit wheel evidently is less prone to chatter than the 320 grit wheel.

In grinding steel the chatter-free grind time is a very strong function of the stock removal rate Z'w (4) as shown in Fig 7 for two different spindle stiffnesses (3). A similar behavoir is expected in grinding ceramic materials. Although frequent truing of aluminium oxide wheels to remove the wheel-regenerative wavy surface is acceptible and is common practice, the truing of diamond wheels must be relatively

infrequent due to their much higher cost. Since the dominant parameter governing chatter growth rate is the "wheelwear stiffness Ks" and its functional relationship with normal stress, it is important to determine the operating normal stress that yields the desired chatter-free grind time.

FORCE GRINDING:

On conventional feed rate grinding machines the cross slide is fed at given feed rates. Normal forces are induced at the wheel-work interface. Those forces may be large or small depending on the sharpness of the grinding wheel and/or hardness of the workpiece and are determined by the WRP. As the wheel dulls, the induced force increases for a given feed rate and may cause microstructural damage to the workpiece. Those forces also vary in fast production grinding cycles with incoming stock variations. The deflections in the wheel-work system are directly related to variations in the normal force through the system stiffness, and result in size errors even though the CNC slides are positioned to a high degree of accuracy.

By introducing normal force sensors into the machine and driving the feed slide to generate prescribed force levels, deflections can be maintained constant, deflection errors can be eliminated, the sharpness of the grinding wheel can be monitored, and the wheel can be operated at optimum normal stress levels consistent with chatter-free grind time, wheelwear rate, and workpiece damage.

A normal-force-sensing CNC for internal grinding was used in the grinding tests. In addition to executing force cycles, the control can also capture grinding-process parameters. A set of typical parameters are shown in Table 1.

CONCLUSION

The use of normal force sensors in combination with computerized data acquisition and control provide improved performance for high precision grinding operations. Force control permits the wheel to be subjected to the appropriate normal stress level, consistent with wheelwear rates, chatter-free grinding times, surface integrity, and cycle time. Force sensing can be applied to monitor wheel sharpness to reduce workpiece damage and can be used to compensate for deflections in the wheelwork system to eliminate errors.

REFERENCES:

1. R.I.King, R.S.Hahn, "Handbook of Modern Grinding Technology", Chapman and Hall, New York, N.Y. 1986.

2. R.Snoeys, D.Brown, "Dominating Parameters in Grinding Wheel and Workpiece Regenerative Chatter", Proceedings of the 10th International Machine Tool Design and Research Conference, pp325-348, Pergamon Press, 1969.

3. R.P.Lindsay, "Chatter-Free Grind Time of high and low conformity Grinding Systems", unpublished report, 1972.

4. K.Srinivasan, "Application of the Regeneration Spectrum Method to Wheel Regenerative Chatter in Grinding", Trans. of ASME, Journal of Engineering for Industry, vol. 104, pp.46-54,February 1982.

APPENDIX:

To calculate the average
normal stress, the wheel-work
contact area is required. This
is obtained by coating the work
piece with a thin film of
Prussian Blue pigment and
pressing the wheel against the
"Prussian-blued" workpiece, and
axially rubbing it a small
distance, to determine the
contact length le. That length
may be modified because of the
"wheel depth of cut h".

The geometrical length of
contact lg, where elastic
deflection of wheel and work are
negligible, is given by (1):

lg= $\sqrt{Deq * h}$ (4)

where
Deq = Dw * Ds/(Dw +/- Ds)   (5)
      Dw = Work diameter
      Ds = Wheel diameter
          use + for OD grinding
              - for ID grinding
and
      h = $\bar{v}w$/Workspeed   (6)

If   lg <= le/2

   contact length = le   (7)
else
   contact length = le/2 + lg (8)

TABLE 1 COMPUTER-CAPTURED GRINDING PARAMETERS

    Rough grinding force(N)..................300
    Rough grinding velocity $\bar{v}w$(um/s).......31.9
    Normal force at final size(N).............0
    Normal threshold force Fth(N).............2
    Number of revolutions to round up.......111
    System stiffness(N/mm)..................1385
    Wheel-Work-Machine Time constant (s)... 4.5
    Remaining stock (um).....................72
    Final runout (um).........................0

93

TABLE 2   TEST CONDITIONS

```
Operation   ID grind
Work speed Nw = 6.7 rps
Wheel speed Ns = 173 rps
GMN high freq. motorized wheelhead 7.5 kw
Servo motor driven workhead
Workpiece  Zirconia Ring 92mm OD.76mm ID. 27mm wide
Coolant White & Bagley Heavy Duty Soluable #2213 5%sol
Dresser Wheel Truing Metal Bond Diamond 28mm OD x 3mm
Dresser Cross Axis to Wheel Axis
Grinding Wheels SD120-R100B56-1/8
                SD320-R150BXL6145-1/8
```
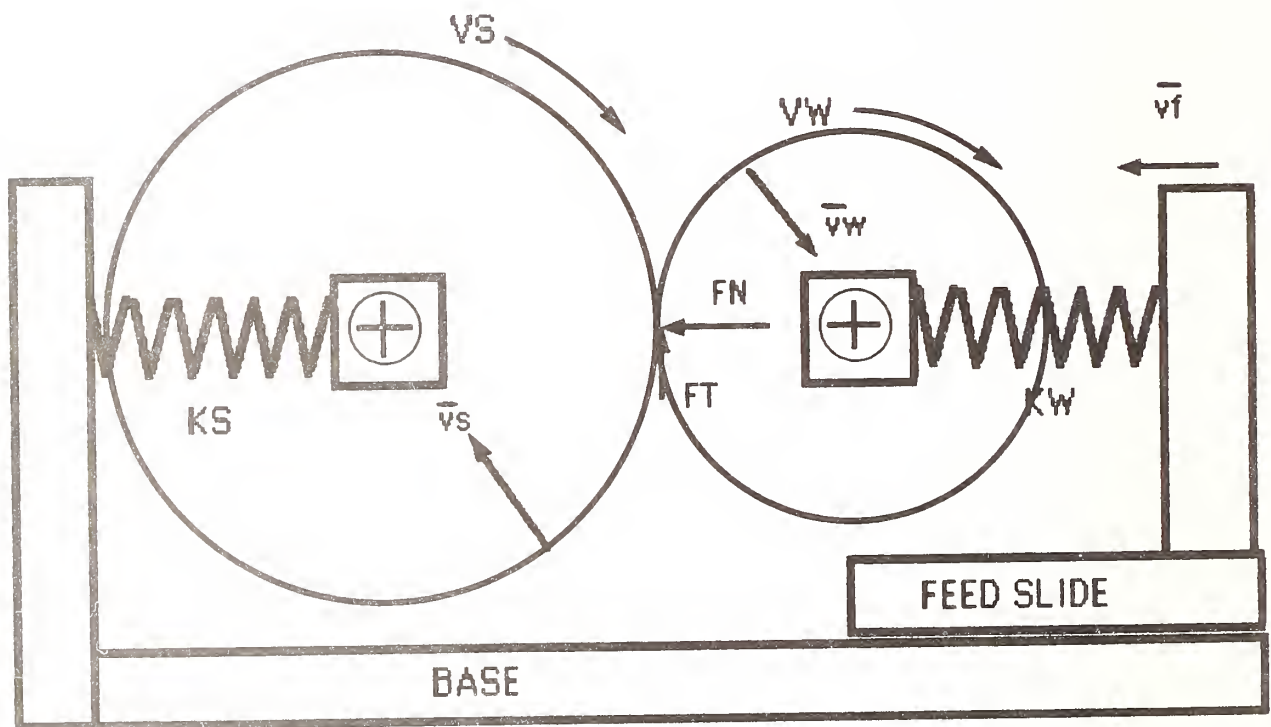
Fig 1. Wheel-work grinding system where
$\bar{v}f$ is the cross slide feedrate
$\bar{v}w$ is the radial stock removal rate
$\bar{v}s$ is the radial wheelwear rate
Vs is the wheel peripheral speed
Vw is the work peripheral speed
Fn is the normal component of force
Ft is the tangential component of force
Ks is the stiffness of wheel support
Kw is the stiffness of work support
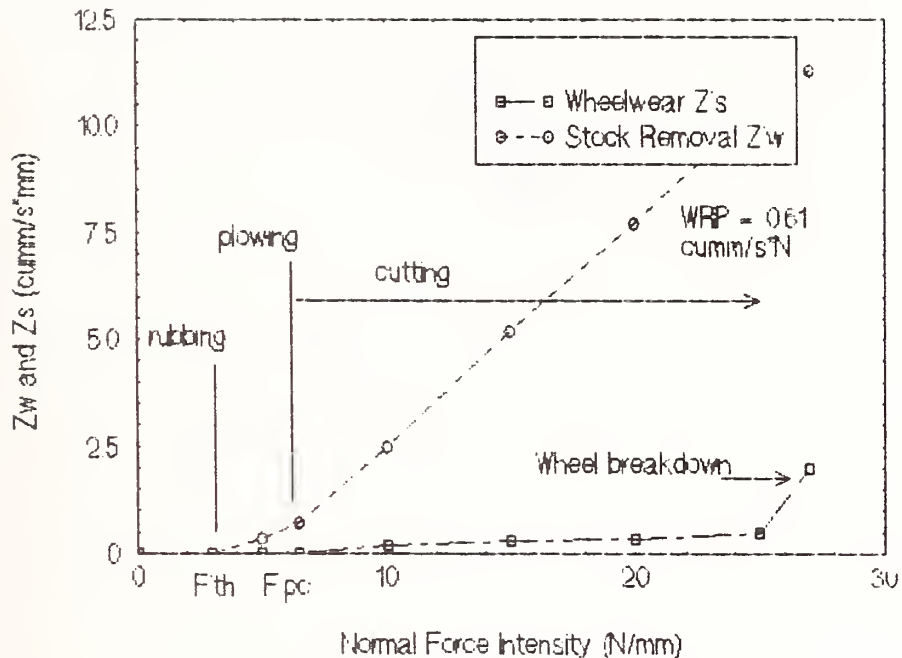
Fig 2. Wheel-work Characteristic Chart where
        Z'w is the volumetric stock removal rate for unit width
        Z's is the volumetric wheelwear rate for unit width
        WRP(work removal parameter) is the slope of Z'w vs F'n
        F'n is the normal force per unit width
        F'th is the threshold force per unit width
        F'pc is the ploughing-cutting transition

        for the following conditions:
            wheel..............................A80K4
            Dress lead(mm/rev)..............   .075
            Dress depth(um)....................... 5
            Wheelspeed(m/s)....................... 60
            Workspeed(m/s).................... 1.25
            Coolant..................Cim Cool 5 star
            Work material........AISI 52100 @ 60 Rc

NORMAL-STRESS-SHARPENING OF RESIN-BOND DIAMOND WHEELS
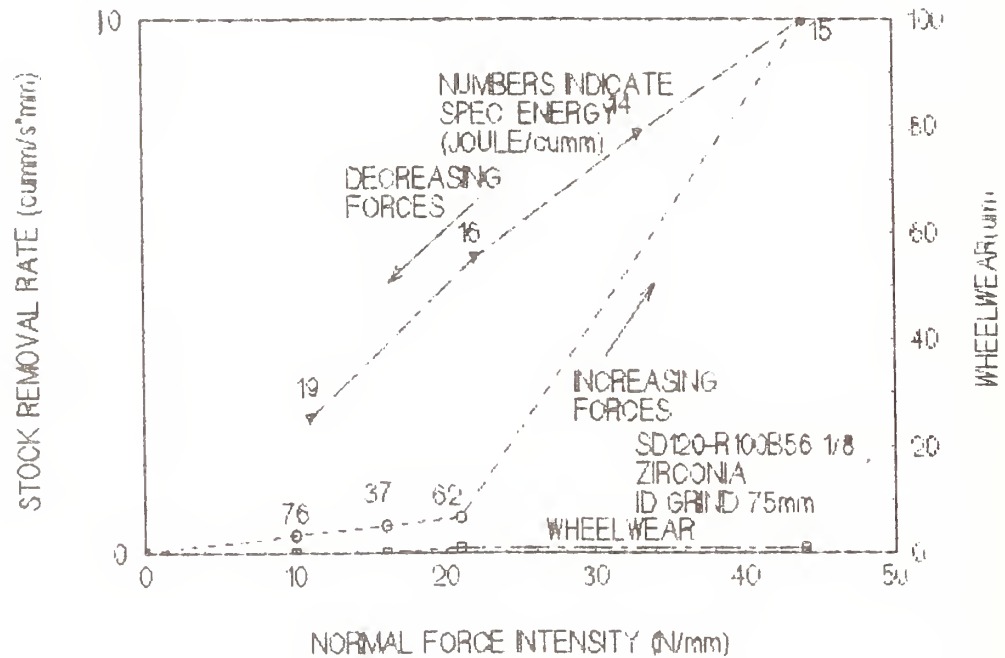
Fig 3. Normal stress sharpening of resin-bonded diamond wheel
showing the stock removal rate Z w vs Normal force per
unit width for increasing force levels followed by
decreasing force levels. The cumulative wheelwear
is also shown. The numbers over each data point
give the specific energy in joules/cumm.
Wheel.....55mm OD by 21mm wide.....SD120-R100B56-1/8
Workpiece...........ID Grind 75mm bore Zirconia Ring
Width of cut(mm)................................ 10

STOCK REMOVAL RATE (cumm/s*mm)

WHEELWEAR (um)

C INDICATES
CHATTER

12

16

DECREASING
FORCES

13

21

NUMBERS INDICATE
SPECIFIC ENERGY
(JOULES/cumm)
SD320R
ZIRCONIA
ID GRIND
60mm

34

INCREASING
FORCES

50

43

66   99

95   111

WHEELWEAR

NORMAL FORCE INTENSITY (N/mm)

Fig 4. Same conditions as Fig 3 except that chatter occurred
with the finer grit wheel as indicated for the points
marked with "C"   The numbers over each
data point give the specific energy in joules/cumm.
Wheel.....55mm OD by 21mm wide....SD320-R100B56-1/8

Y

$Y = A \exp(+at)$

a1   a2   a3

acceptable limit

time

chatter-free grind time
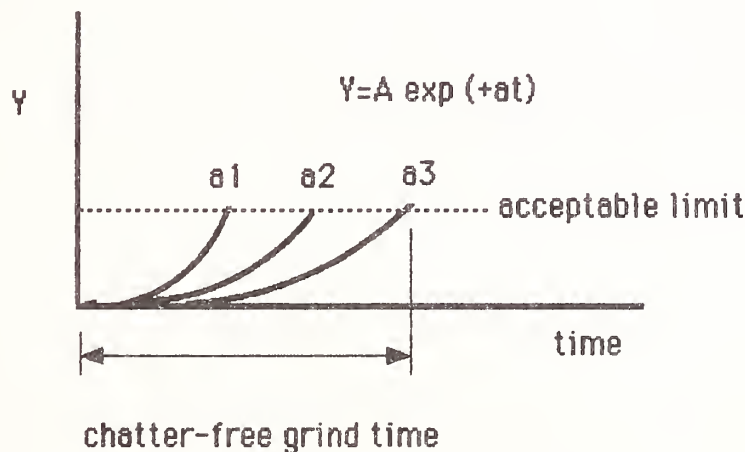
Fig 6. Illustration of the chatter growth rate and the
chatter-free-grinding time for an unstable system

STABILITY CRITERION

$$Kd/Kw + Kd/Ks + 2Kd/K1 > 1$$

Fig 5. Chatter block diagram for cylindrical grinding machines
relating the regenerative feedback effect of wheelwear
and/or wavy work surface to the dynamic system
parameters and the stability criterion where
G(s) is the normalized dynamic compliance
Km is the static stiffness of the wheel-work system
Kd is the minimum dynamic stiffness of the system
Kw is the work cutting "stiffness"
Ks is the wheelwear wear "stiffness"
K1 is the wheel-work contact stiffness
        see Snoeys and Brown ref (2)

Fig 7. Chatter-free-grind time vs Stock-removal rate
for internal grinding with two wheel-supporting
arbors of different static stiffness.

CHEMOMECHANICAL EFFECTS OF BORIC ACID IN CORE-DRILLING OF ALUMINA

S. JAHANMIR and H. LIANG*

National Institute of Standards and Technology, Gaithersburg, MD

Interactions between chemical compounds added to cutting fluids and the workpiece surface in the cutting zone can have pronounced effects on the material removal process during abrasive machining. These interactions can influence the coefficient of friction, the wear of the abrasive grit, and the mechanical properties of the workpiece, thus affecting the machining rate. Experiments were conducted on sapphire and polycrystalline alumina to evaluate the chemomechanical effects of boric acid mixed with distilled water. The machining tests were performed on a precision drill with metal-bonded diamond core-drills. Following the experiments, the drilled surfaces and the diamond particles in the drill were examined by scanning electron microscopy to elucidate the material removal process. The results indicated that addition of boric acid to distilled water increases the rate of drilling of polycrystalline alumina by a factor of two. But, boric acid was found to be ineffective in improving the drilling rate of single crystal alumina, i.e., sapphire. Based on the results it is postulated that boric acid interacts with the amorphous oxide grain boundary phase in polycrystalline alumina promoting intergranular fracture; thereby, increasing the drilling rate.

Introduction

In abrasive machining processes such as grinding, material removal occurs at the contact between the abrasive cutting points and the workpiece surface. The abrasive particle is forced to penetrate the workpiece as the workpiece and the particle are moved relative to each other and parallel to the surface. In this interaction, the workpiece surface undergoes elastic and plastic deformation, followed by fracture of small particles or chips from the surface. Depending on the contact conditions and the mechanical properties of the workpiece, chips are generated by plastic flow and/or brittle fracture [1].

The purpose of this paper is to elucidate the effect of boric acid added to distilled water in abrasive machining of alumina. This compound is used in cutting and grinding fluids for friction reduction, corrosion protection, and as bactericides and fungi cides [2-9]. In these applications, boric acid is mixed with various compounds such as sodium tetraborate, sodium tripolyphosphate, hydrofluoric acid, triethanolamine, ammonium fluorosilicate, and hexamethylenetetramine. It is not clear whether it is the boric acid or a compound formed by reaction of boric acid and other chemicals that produce a positive result with these fluids. Therefore, in our study boric acid was used as a single additive in distilled water in experiments using metal-bonded diamond core-drills to determine the basic mechanisms by which this compound influences the cutting process in ceramics. In materials capable of plastic deformation, for example, metals, chips are formed by shear in a ductile mode. However, in ceramic materials, which exhibit a limited ductility, chips are formed by plastic deformation and/or brittle fracture. Whether the chips are formed by brittle fracture or by plastic deformation depends on the penetration depth and the material's susceptibility to plastic flow as well as the environment [10-13].

Two models have been proposed to describe the chip formation process in ceramic materials. The

* Research Associate, University of Maryland, College Park, MD 20742

model proposed by Evans and Marshall [10] is based on the formation and propagation of median cracks (vertical to the surface) formed at the boundary between the elastic and plastic zones and the lateral cracks (parallel to the surface) formed as a result of residual stresses during unloading. In the crushing model proposed by Larchuk [14], material removal is described as an unstable fracture process, which involves propagation of cracks at origins distributed throughout the stressed region. The basic difference between the two models is that in the latter a large number of fragments are separated from the surface.

The fluid environment used in abrasive machining can have a large influence on the removal process [1]. These include temperature and friction control, swarf (or debris) removal, modification of the workpiece mechanical properties, influences on the wear and fracture of the abrasives, and reduction of swarf transfer to the wheel.

Several publications have considered the chemomechanical effects, i.e., combined mechanical and chemical interactions, during drilling of ceramics, stones and glasses [15-18]. Arguments about the effects of the fluid on diamond abrasive and the workpiece were focused on how the chemicals affect the mechanical properties such as hardness, material properties such as surface potential [19], and friction and wear of the diamond abrasives [20].

Generally, the chemomechanical effects of the cutting fluids in drilling involve more than one mechanism. For instance, Swain et al. [15] studied the effects of surface-active environments on hardness and drilling rate of polycrystalline alumina. They found that the hardness of alumina was lower in the presence of ethanol than in pentanol. The material removal process in ethanol, therefore, involved substantial plastic flow preceding or accompanying intergranular fracture. Plastic flow was less evident, however, in pentanol, a more brittle behavior and large conchoidal fragments were observed. The drilling rate of rotary diamond-studded bits were greatest in pentanol when the material was hardest and, presumably, most brittle.

In ductile-regime grinding, Bifano et al. [13] found an opposite result that alcohols with a small number of carbon atoms promote embrittlement and increase the machining rate of glass. Cuthrell [17] postulated that the observed higher drilling rates in ceramics are primarily the result of the embrittling effect of hydrogen ions from liquid or gaseous environments. Cooper [19], however, found that the effect of liquids on drilling hard stone was that of a reduction of diamond wear rather than a·direct effect

on the stone itself. Cooper and Berlie [20] reported a significant improvement in the drilling rate upon alternating the substitution of a series of normal alcohols (propanol, pentanol, and octanol) for water as the drilling fluid. The results were interpreted to reflect a reduction in wear of the diamond particles in the drill bit.

Considering that previous publications described the role of boric acid in reduction of friction in sliding tests [21-23], we had postulated that boric acid would reduce the friction coefficient at the tool/workpiece interface. The reduction in friction and the resultant lower temperatures at the diamond/workpiece interface, would reduce the wear rate of the diamond abrasives, and increase the drilling rate by maintaining sharp cutting points. However, we found that the chemomechanical effects of boric acid are complex and involve an embrittlement effect rather than affecting the wear of the diamond abrasives.

Experimental Procedure

A high-purity polycrystalline alumina (99.8%) was used in the experiments. The properties of this material (Coors AD 998) are listed in Table 1. The

Table 1. Composition and properties of polycrystalline alumina

Composition (%wt)	<0.1% SiO_2, 0.03% Na_2O, 0.02% TiO_2, 0.01% K_2O, balance of Al_2O_3
Grain size (μm)	3
Porosity (%)	0.2
Vicker's hardness (GPa)	15.0
Elastic modulus (GPa)	345
Compressive strength (MPa)	2071
Flexure strength (MPa)	331
Thermal conductivity (W/mK)	29.4
Indentation fracture toughness (MPa.m$^{1/2}$)	3.2
Thermal expansion coefficient (°C^{-1})	6.7 x 10^{-6}

specimens were in the form of circular disks with a diameter of 10 mm and a thickness of 3 mm. The disks were cut from a cylindrical rod and were used in the drilling experiments. In order to evaluate the effect of grain boundaries in the process of material removal, a limited number of tests were conducted on single crystal alumina or sapphire. In these tests the sapphire was oriented such that the (1010) plane was parallel to the flat disk surface.

Pure orthoboric acid, H_3BO_3 (99.99% wt), was added to distilled water at 4 %wt concentration. Boric acid is a white and pearlescent solid which is soluble in water up to 6.35% wt. Two commercial cutting fluids, designated A and B, were also tested for comparison with the boric acid solution. Fluid A is a low-foaming synthetic, whereas fluid B is a semisynthetic fluid. These two fluids were selected for drilling because they are used in grinding of ceramics. Table 2 lists the properties of the two fluids and boric acid.

A precision drill was used for performing the drilling experiments. The drilling setup is shown in the schematic diagram in Figure 1. In this setup, a pump is used to circulate the cutting fluid from a 4 liter reservoir through the core-drill using a water swivel. The fluid reservoir and all tubing were made from plastics. A clamp was fabricated to fix the alumina sample to the specimen holder, which was enclosed in a fluid tank. Both the specimen holder and the tank were made from stainless steel to eliminate corrosion and other possible chemical reactions.

The rotational speed of the drill could be adjusted to obtain three speeds (the maximum surface speeds are listed in the parentheses): 2100 rpm (0.70 m/s), 3770 rpm (1.25 m/s), and 5500 rpm (1.83 m/s). Metal-bonded core-drills with an outside diameter of 6.35 mm and a wall thickness of 0.13 mm were used. A new drill had an approximately 9.5 mm long diamond section, consisting of 30% vol natural diamond (100 mesh or 150 μm) in a bronze matrix bonded to a steel drill shank.

To define an optimum set of conditions for the drilling tests and to characterize the effect of rotational speed and applied load, tests were first performed in distilled water under various loads and speeds. The normal load on the drill was varied from 23.0 to 46.1 N. Following these preliminary tests, further testing with the boric acid solution and commercial fluids were conducted at a load of 33.3 N (contact pressure of 132 KPa) and a rotational speed of 2100 rpm (0.7 m/s) to avoid rapid wear of the diamond particles.

The following testing sequence was used to reduce the experimental uncertainties due to the differences in the condition of the drills, i.e., the number and distribution as well as sharpness of the diamond particles engaged in cutting during drilling. First, the alumina was drilled for 15 s using distilled water, and the hole depth was measured by a dial indicator (with a precision of 0.01 mm) at the completion of the first cycle. This was followed by a second cycle in which the test fluid was substituted

Table 2. Characteristics of cutting fluids

	Fluid A	Fluid B	Boric Acid Solution
Concentration in water	2% vol	1.2% vol	4% wt
pH of test fluid	9	9	6
Solubility in water	100% vol	100% vol	6.35% wt
Boiling point of compound (°C)	100	100	300
Freezing point of compound(°C)	-4	0	170
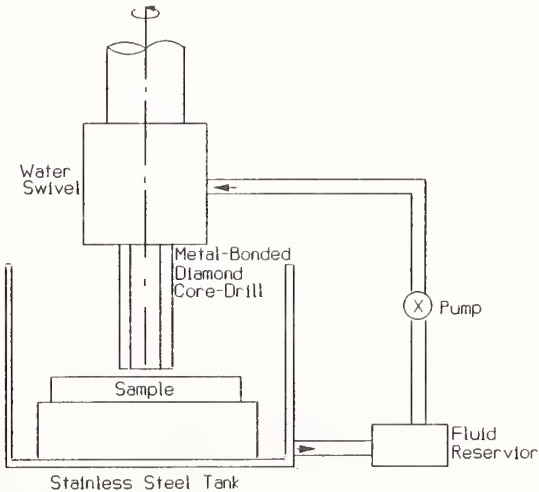
Figure 1. Schematic diagram of the drilling setup.

for water in drilling the same hole for another 15 s. The hole depth was measured after each cycle. The sequence of drilling alternating between water and test fluid was continued for a total duration of 60-180 s. Following these tests, the drilling rate for each cycle was obtained by dividing the measured hole depth by the drilling time. The relative change in the drilling rate was obtained by comparing the drilling rate for the test cycle in which the test fluid was used with the preceding cycle where only water was used.

During the drilling test, a 1 cm^3 sample of the cutting fluid was drawn from the stainless steel tank for the analysis of the debris. The fluid samples were centrifuged for 45 min to separate the debris. This step was followed by three subsequent washing cycles in the centrifuge. The debris was then retrieved in a distilled water solution, and the water was allowed to evaporate at room temperature. The collected debris was coated with a thin film of gold for examination in the SEM.

Prior to drilling a new hole, the drill was dressed by drilling a porous silicon carbide dressing stick. Depending on the wear of the diamond particles, a dressing time of 10 to 30 s was used. The drills were then examined under an optical microscope to check the diamond particles and to ensure that the wear flat areas were removed by dressing.

A few tests were performed with a short test time to allow observation of the material removal process. Prior to these tests, the polycrystalline alumina samples were polished with a series of diamond pastes of decreasing size from 30 to 0.25 μm. In these tests, the drill was engaged for only a few seconds to generate a small track on the alumina workpiece.

After the drilling tests, the diamond drill, the drilled surfaces and the debris were examined under an optical and a scanning electron microscope to elucidate the material removal process.

Experimental Results

a) Preliminary Tests in Distilled Water

A series of tests were performed in distilled water to determine the basic characteristics of the drilling process. Each test was performed for 60 s on a new polycrystalline alumina surface, and the hole depth was measured following the test. Figure 2 shows that the drilling rate of a new drill decreases with the number of drilled holes. The rapid decrease in the drilling rate is indicative of wear of the diamond particles. The figure shows that as the drill is dressed with a silicon carbide dressing stick for 30 s, the drilling rate increases; but it does not return to the initial high value.

Figure 3 shows the distribution of the diamond particles in a used drill as observed in the SEM. Figure 4 shows an optical micrograph of a section of a used drill. In this micrograph, the diamond particles that are highly reflective and appear bright have been worn. It was determined that less than 10% of the diamond particles were involved in cutting during drilling. A worn diamond particle is shown in the SEM micrographs of Figure 5, which indicates that wear of the diamond occurs by micro-scale fracture and attrition (i.e., tribochemical oxidation reaction). Since the wear flat is very smooth, it is reflective in an optical microscope. No evidence for large scale fracture of the diamond particles were found.

The main function of dressing is to sharpen the diamond particles, to remove the bond, and increase the clearance between the drill and the workpiece for an effective drilling. Examination of the diamond particles in a dressed drill in the optical microscope showed that the wear flat had disappeared after dressing. The distance between the metal bond and the diamond particles engaged in cutting was measured in an optical microscope by focusing on the diamond particles and the bond and measuring the height difference. The average height of the diamond particles after a few drilling tests was 10 ± 5 μm. In a worn drill, the clearance was reduced to less than 1 μm; and by dressing, the average height value was almost restored.

The drilling rate was found to be a function of both the applied load and the rotational speed, as shown in Figures 6 and 7. In these tests, the drills were not dressed; and the test sequence is identified by the numbers next to the data points in the figure. The data points for the first three tests are not shown since the condition of the drill changes rapidly at the beginning of the test (see Fig. 2). Figures 6 and 7 show that the drilling rate increases as the speed is increased. However, the effect of load appears to depend on the speed.

At 2100 rpm, the drilling rate increases monotonically with load. However, at the higher speed of 3770 rpm the drilling rate decreases after reaching a maximum. The reduction in the drilling rate observed at the high speed and high load, must be due to accelerated wear of the diamond particles under these conditions.
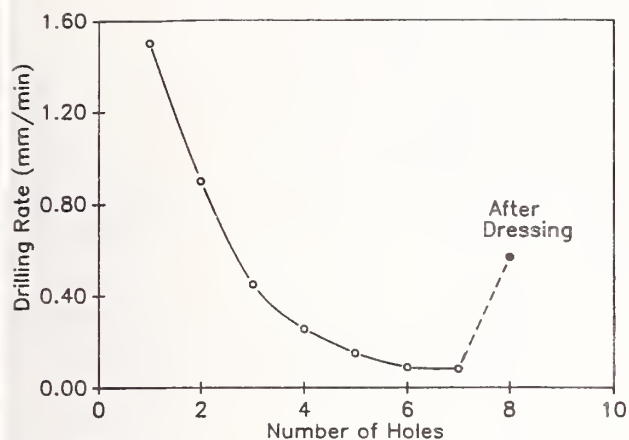
Figure 2. Reduction of drilling rate by the number of holes drilled in water (Load: 33.3 N, surface speed: 0.7 m/s, Test duration: 60s).
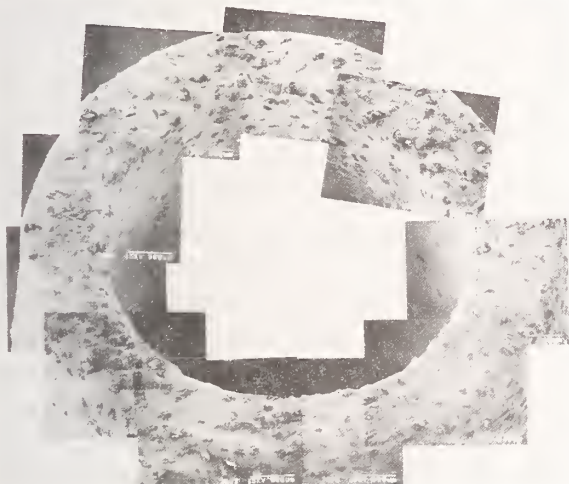
Figure 3. SEM micrograph showing the distribution of diamond particles in a used drill.
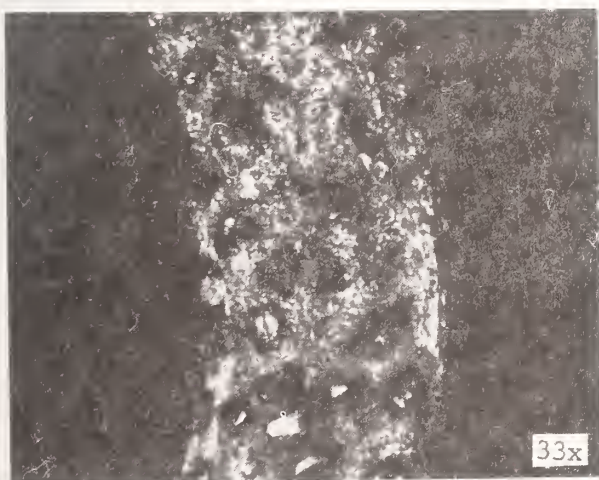
Figure 4. Optical micrograph of a section of used drill showing the worn diamond particles.
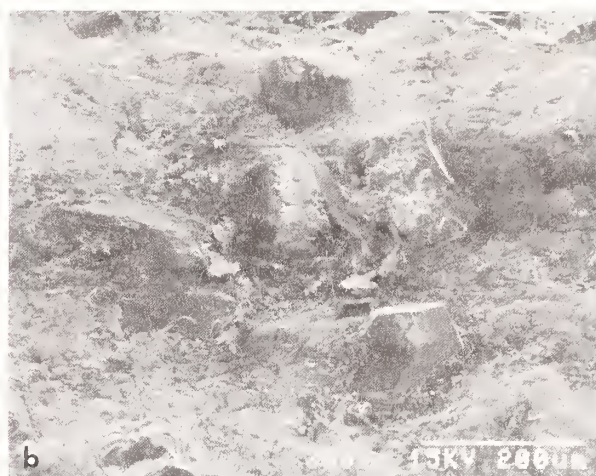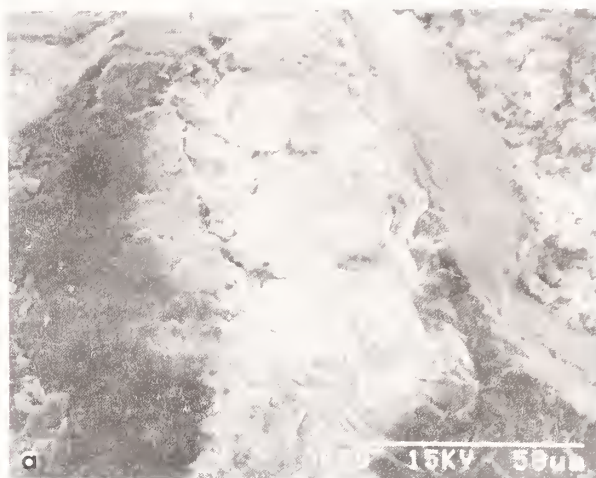
Figure 5. SEM micrographs showing the diamond particles after drilling: (a) the diamond particles in the center of the micrograph has been subjected to wear, and (b) the worn diamond.
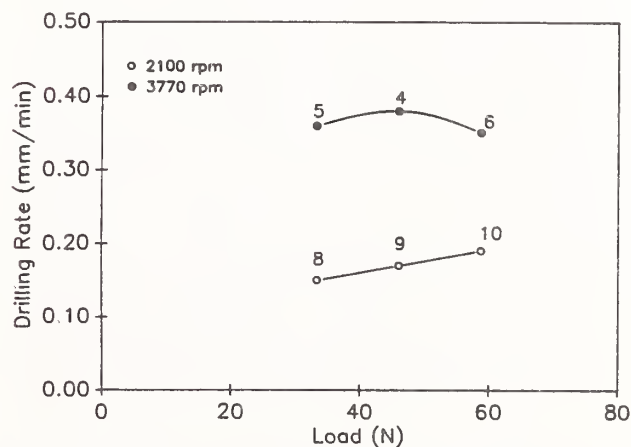
Figure 6. Effects of load and rotational speed on the drilling rate of polycrystalline alumina in water (Test duration: 60 s).
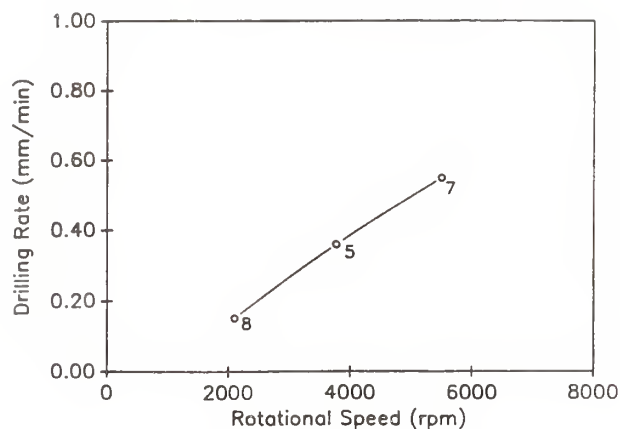
Figure 7. Effect of rotational speed on the drilling rate of polycrystalline alumina in water (Load: 33.3 N, Test duration: 60 s).
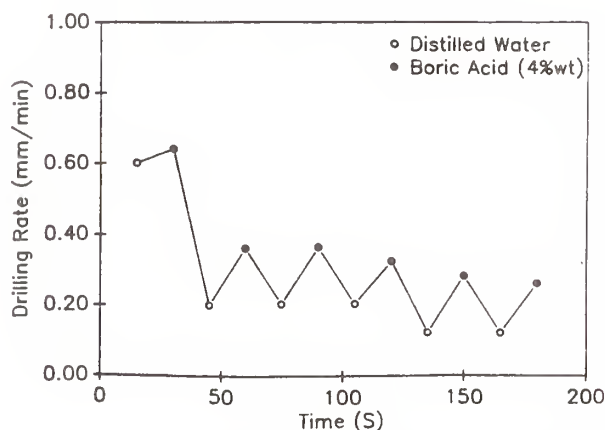
Figure 8. Drilling rate of polycrystalline alumina in distilled water and boric acid solution (Load: 33.3 N, Surface speed: 0.7 m/s).

---

b) Effect of Boric Acid on Drilling Rate

Based on the results of drilling tests in distilled water, a load of 33.3 N and a rotational speed of 2100 rpm (0.7 m/s) were used to avoid excessive wear on the diamond particles. Also, the drills were dressed prior to starting a new hole to provide a uniform drill condition. Figure 8 shows the drilling rate against the drilling time for a number of drilling cycles alternating between distilled water and 4% wt boric acid in distilled water. The figure clearly shows that the drilling rate of polycrystalline alumina increases on replacing the distilled water with the boric acid solution. The results for 11 test cycles are tabulated in Table 3, which shows that the boric acid solution increases the drilling rate by an average of 103% over the drilling rate measured in water.

The test results on the two commercial cutting fluids, shown in Figures 9 and 10, clearly indicate that the effect of these fluids on the drilling rate is small compared to the boric acid solution. The average values for the change in drilling rate for the commercial fluids, listed in Table 3, are 6% and -18%. Considering the standard deviations, also listed in the Table, it can be concluded that the commercial fluids are ineffective in increasing the drilling rate.

The test results obtained in drilling of sapphire in water and the boric acid solution, in Figure 11, are contrary to the results observed on polycrystalline alumina. Figure 11 shows that boric acid is ineffective in increasing the drilling rate of sapphire. This provides a possible clue for the mechanism by which boric acid solution increases the drilling rate of polycrystalline alumina. An interaction between the grain boundaries in polycrystalline alumina and boric acid is speculated as a factor in the material removal process.

c) Mechanisms of Material Removal

In order to elucidate the material removal process in drilling and to discern the effect of boric acid on the process, the drilled surfaces were examined in the SEM. Observations on the sides of cylindrical surfaces of the holes provided strong evidence for material removal by intergranular crack propagation, as seen in Figure 12. Surfaces drilled in water and those drilled in the boric acid solution, have the same appearance, essentially a fractured surface with occasional plastic grooves. The bottom of the drilled holes, were also similar, showing no difference between the surfaces drilled in water and those drilled in boric acid solution, shown in Figure 13. The bottom surfaces, however, have a different appearance than the cylindrical surfaces. Although, there is ample evidence for intergranular fracture, the bottom surfaces (Fig. 13) are covered with numerous debris, some of which have been plastically deformation.

A possible difference between the surface drilled in water and the one drilled in the boric acid solution is in the number of fine debris observed on the bottom surface. Although somewhat subjective, the number of fine debris in Figure 13 (a) for the boric acid solution is lower than that observed in Figure 13 (b) for water. In fact, the distilled water appeared cloudy after the tests; but became clear in a few hours. However, the boric acid solution remained cloudy after the tests. This indicates a possible dispersion of fine debris in the boric acid

Table 3. Drilling rate for the three cutting fluids

Cutting Fluids	% Increase in Drilling Rate Over Water
Boric acid (4% wt)	103 ± 42
Fluid A (1.2% vol)	6 ± 19
Fluid B (2% vol)	-18 ± 26

Figure 11. Drilling rate of sapphire for a number of drilling cycles in distilled water and boric acid solution (Load: 33.3 N, Surface speed: 0.7 m/s).
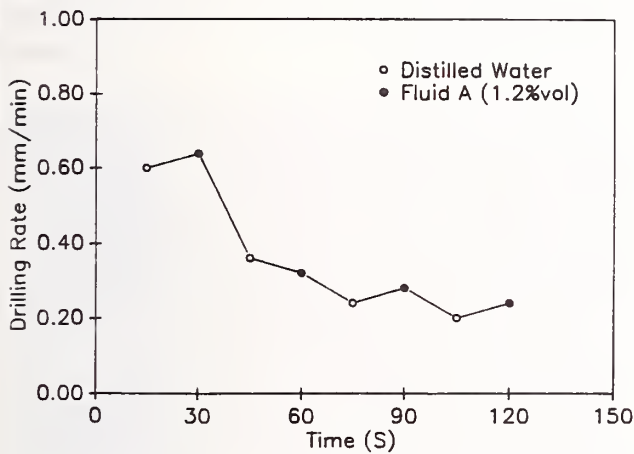
Figure 9. Drilling rate of polycrystalline alumina for a number of drilling cycles in distilled water and Fluid A (Load: 33.3 N, Surface speed: 0.7 m/s).
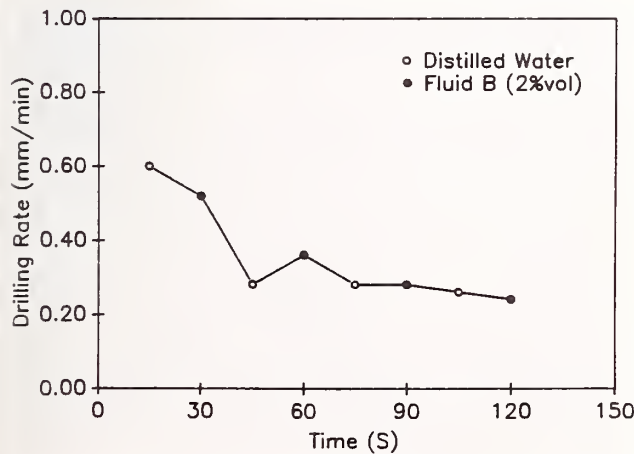
Figure 10. Drilling rate of polycrystalline alumina in distilled water and fluid B (Load: 33.3 N, Surface speed: 0.7 m/s).

Figure 12. SEM micrographs of the cylindrical surfaces of holes drilled: (a) in distilled water, and (b) in boric acid solution (Load: 33.3 N, Surface speed: 0.7 m/s).

107

solution. Since the unused boric acid solution is clear, and stays clear when stored, these observations provide a second clue for the mechanism of boric acid solution; mainly, dispersion of fine debris.

The debris, or swarf, collected after the drilling tests, are as shown in Figure 14. The debris appear to have a bimodal size distribution; one at 3 to 4 μm and the other much less than 1 μm. It is also found from Figure 14 that the debris size in water is somewhat smaller than that collected from the boric acid solution. The larger particle size in the boric acid solution, suggests a more efficient material removal process in that solution than in water.

d) Results of Short Drilling Tests

Since the drilling process is complex, it is difficult to identify the material removal mechanism by examination of the drilled surfaces and the debris.

Therefore, a series of short tests were conducted on polished surfaces to characterize the removal process at the initiation of drilling. In these tests, the drill was engaged with polished surfaces of polycrystalline alumina and sapphire only for a few seconds; and the surfaces were examined in the SEM. The micrographs in Figure 15 show the typical appearance of the polycrystalline alumina surfaces after short tests in distilled water and in the boric acid solution. In distilled water, the surface has been subjected to plastic deformation by the diamond particles, and several deep scratches are evident in Figure 15 (a). In contrast to this observation, the surface of the sample tested in the boric acid solution in Figure 15 (b) shows evidence for intergranular fracture rather than plastic deformation. Although, both surfaces contained regions of plastic deformation and intergranular fracture, the difference

Figure 13. SEM micrographs of the bottom surfaces of the holes in polycrystalline alumina: (a) in distilled water, and (b) in boric acid solution.
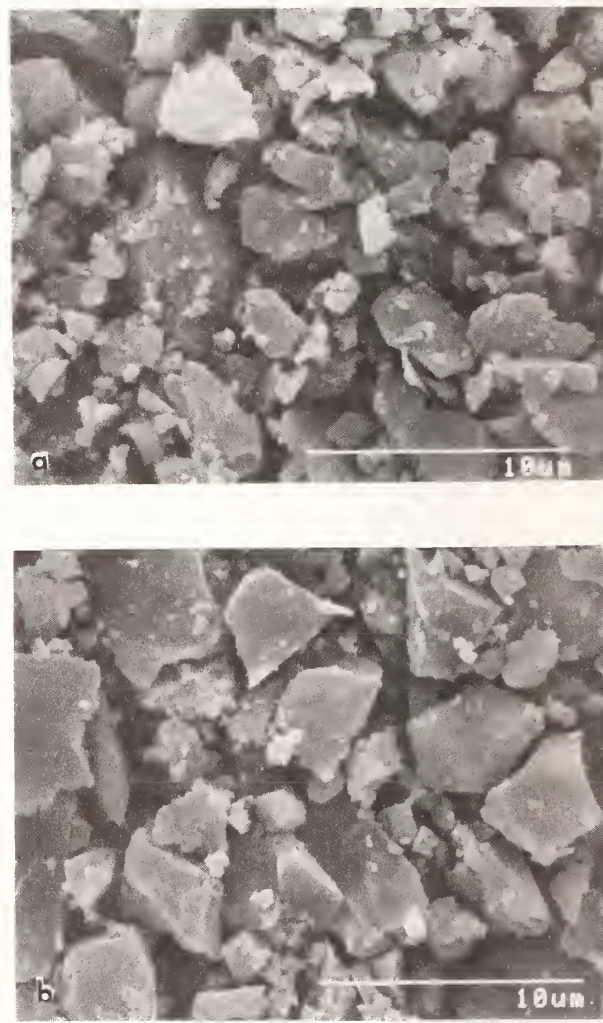
Figure 14. SEM micrographs of the debris collected after drilling polycrystalline alumina: (a) from distilled water, and (b) from boric acid solution.

108

in the two micrographs in Figure 15 are representative of the surfaces in the short tests. Based on the short tests, it is therefore concluded that considerable plastic deformation precedes fracture in water; but the material removal process in the boric acid solution primarily consists of intergranular fracture. This implies that the increase in drilling rate with boric acid is related to an interaction between the boric acid and the grain boundaries in the polycrystalline alumina. This conclusion is partially supported by the fact that the boric acid solution did not increase the drilling rate of sapphire.

Two short tests were conducted on a sapphire surface to compare the effect of boric acid solution with water. Typical drilled surfaces are shown in Figure 16. The sapphire surfaces contain evidence for plastic deformation, i.e., plowing marks, and

cleavage fracture. The surface appearance for both cases are similar, which indicates that boric acid had no observable effect on the removal process in sapphire.

Discussion

The results presented in this paper clearly show that addition of boric acid to distilled water increases the material removal rate in drilling of polycrystalline alumina. The subsequent SEM examinations of the drilled surfaces, in short as well as longer tests, suggested that an interaction between boric acid and the grain boundaries in polycrystalline alumina may contribute to the material removal process by enhancing intergranular fracture. The implication of
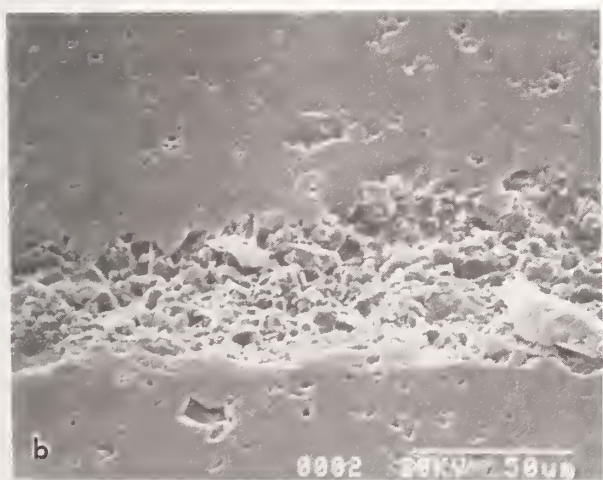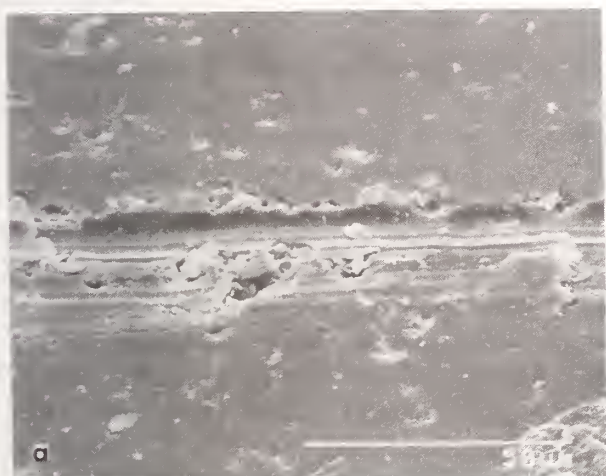
Figure 15. SEM micrographs of the alumina surfaces after short drilling tests: (a) in distilled water, and (b) in boric acid solution.
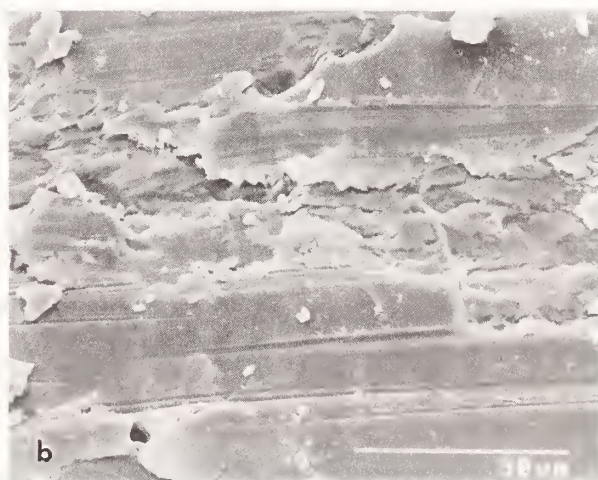
Figure 16. SEM micrographs of the sapphire surfaces after short drilling test: (a) in distilled water, and (b) in boric acid solution.

these observations and other possible interactions between boric acid and alumina are described in this section.

Several publications have shown that boric acid can be used as a solid lubricant to reduce the friction coefficient of two sliding surfaces [21-23]. In these experiments either boric acid or boric oxide powder is used to form a coating on the sliding surfaces. In the latter case, reaction of the boric oxide coating with the moisture in the air environment forms boric acid on the surface [22,23]. The observed low friction coefficient of boric acid was assumed to be related to its layered triclinic crystal structure with weak bonding between the layers. During sliding, these layers are aligned parallel to the direction of relative motion and, once so aligned, can slide over one another with relative ease to provide a low coefficient of friction [22,23].

Boric acid is also used as an additive in metal cutting fluids to reduce friction, increase corrosion resistance, and control microbial degradation. In these formulations, boric acid is always used in combination with several other compounds, such as amines, fatty acids, and alcohols [2-9]. Recent machining experiments have shown the addition of boric acid to distilled water, without the addition of any other compounds, can reduce the cutting force by 20 to 50%, depending on the cutting conditions [24]. In one test, a reduction by as much as 96% was observed when turning a polycrystalline alumina using a PCD (polycrystalline diamond) tool insert. Similarly, boric acid was found to be effective in milling of a glass-ceramic dental material using a high-speed steel end mill [25]. The effectiveness of boric acid in these experiments was used as an indication that boric acid either deposits on the surfaces or reacts with the workpiece under the high loads and temperatures encountered in the cutting zone. By analogy, a similar mechanism was anticipated in drilling.

To evaluate the possibility of reaction between alumina and boric acid, we should first examine the state of boric acid in water. Aqueous solutions of orthoboric acid H_3BO_3 are only very slightly acidic (pH = 6 at 4% wt]. H_3BO_3 is considered to be a very weak monobasic acid by hydroxide ion binding; i.e.,

$$H_3BO_3 + 2H_2O = B(OH)_4^- + H_3O^+.$$
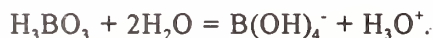
(The simple orthoborate ion, BO_3^{3-}, does not exist in aqueous solutions.) [26] The following reaction may be possible between alumina and boric acid under

the high pressures and high temperatures in the cutting zone:

$$Al_2O_3 + H_3BO_3 + 3H_2O = Al(B(OH)_4)_3 + Al(OH)_3.$$
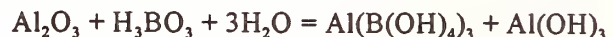
Recent investigations have shown that aluminum hydroxide $Al(OH)_3$ when formed by hydrolysis on alumina sliding surfaces can decrease the friction coefficient and the wear rate of alumina [27-29]. However, aluminum hydroxide can form in either water or the boric acid solution. Therefore, formation of aluminum borate $Al(B(OH)_4)_3$ rather than the aluminum hydroxide on the alumina surface during machining may have an influence on the removal process. Similar to sodium borate, this compound is possibly a surfactant and can be used as a detergent/dispersant additive in aqueous solutions [26]. It is not clear whether aluminum borate can provide lubrication and a lower friction, but it is expected to be softer than alumina. Therefore, by analogy with other solid lubricants, it could act as a lubricant. Although this reduction in friction could explain the lower cutting forces observed in turning and milling [24-25], it cannot be used as a direct explanation for the observed increase in the drilling rate.

SEM examinations of the drilled surfaces and the results obtained on sapphire, suggested an interaction between boric acid and grain boundaries in polycrystalline alumina. The particular polycrystalline alumina used for this study contains an amorphous grain boundary phase consisting of a mixture of SiO_2, Na_2O, TiO_2, and K_2O, with the first two having the highest concentration (see Table 1). Studies on environmentally assisted fracture of oxide glasses [30,31] have shown that the rate of crack growth is controlled by the chemical activity of the active species in the environment as well as by the stress intensity at the crack tip. For example, Michalske and Freiman[32] have described a specific chemical mechanism by which strained Si-O bonds in amorphous silica react with OH$^-$ ions in water to increase the rate of crack growth. In fact, White et al. [33] have obtained direct evidence showing an increased crack propagation rate in basic aqueous solutions as the pH is increased. As another example, Weiderhorn and Johnson [34] observed definite effects of hydrogen ion activity on crack growth in silica and other glasses, suggesting that OH$^-$ and H$^+$ ions may show a different stress-dependent reaction rate than H_2O. These observations on the environmentally assisted fracture of amorphous oxides that similar effects may occur during machining of polycrystalline ceramics containing an amorphous oxide grain boundary phase.

Several reactions may be possible between boric acid and the oxide grain boundary constituents. Identification of these reactions is beyond the scope of this paper, and requires a detailed examination. Nevertheless, reaction between the boric acid and the grain boundaries in alumina that can increase the rate of crack growth is a plausible explanation for the observed increase in the material removal rate in drilling and the decrease in cutting force in turning and milling. In the former machining operations, enhanced crack growth in the presence of boric acid can decrease the cutting forces since material removal may occur with less plastic deformation.

Another possible chemical effect that might enhance drilling is the formation of surfactants such as aluminum borate, sodium borate, aluminum hydroxide, and silicon hydroxide, etc., which can be beneficial in the removal of the debris from the cutting zone during drilling. The debris must pass through a small clearance between the bronze bond and the exposed diamond particles. If the debris agglomerate and form particles larger than the clearance of about 10 μm, then the diamond particles may be pushed away from the workpiece surface and reduce the drilling rate. In this respect, another important function of a drilling fluid is enhanced corrosion of the metal bond. If bond corrosion can be controlled to remove a sufficient amount of bond material and increase the clearance, then drilling could be more efficient. This effect for boric acid was not examined in the present study, but it needs to be examined in the future.

Conclusions

Based on the test results in drilling of single and polycrystalline alumina with bronze-bonded diamond core drills, the following conclusions can be made:

1) Addition of 4% wt boric acid to distilled water increases the rate of drilling of polycrystalline alumina by a factor of 2.

2) Boric acid is ineffective in improving the drilling rate of single crystal alumina.

3) The results suggest that interactions between boric acid and the amorphous oxide grain boundary phase in polycrystalline alumina promotes intergranular fracture.

References

[1] S. Jahanmir, L. Ives, A. Ruff, and M. Peterson, "Ceramic Machining: Assessment of Current Practice and Research Needs in the United States," Nation Institute of Standards and Technology Special Publication 834, June, 1992.

[2] C. S. Sulhan, "Stable Cutting Fluid," U.S. Patent No. 2,999,064, 1961.

[3] A. P. Rawlinson and J. White, "Soluble Oil Giving Cutting Fluid on Emulsification with Water Omits Conceptional Coupling Agent and Biocide," EP Patent No. 120,665, 1984.

[4] D. Schuster, "Corrosion Inhibiting Piperazine Derivatives Containing Boron," DE Patent No. 1,620,447, 1975.

[5] Z. Jin, S. Peng, X. Huang, S. Guan, C. Liu, and H. Xu, "High Speed Cutting Steel Production Involves Adding Dropwise Mixture of Formamide, Ethanol, Thiourea, and Boric Acid," CN Patent No. 85,100,129, 1986.

[6] V. V. Yakusheva, "Lubricant for Mechanical Treatment of Metals," SU Patent No. 1,482,934, 1989.

[7] K. K. Johnson, "Water Soluble Grinding Agent Composition Containing Reaction Products of Alkanolamine and Boric Acid and Glycol," JP Patent No. 61,081,477, 1986.

[8] W. Ritschel and H. Lorke, "Boric Acid, Di-ethanolamine and Monoethanolamine Condensate used in Aqueous Corrosion Protective Solution," DE Patent No. 3,304,164, 1984.

[9] W. T. Branneen, G. D. Burt, and R. A. McDonald, "Phosphite Amine Lubricant for Metal Working and Machining," U.S. Patent No. 4,965,002, 1990.

[10] A. G. Evans and D. B. Marshall, "Wear Mechanisms in Ceramics," Fundamentals of Friction and Wear of Materials, D. D. Rigney (Ed.), ASME Press, New York, NY, pp. 439-452, 1981.

[11] M. C. Shaw, H. G. Shafer, and M. Adler, "Chip Formation in Single Point Diamond Turning," Am. Soc. Prec. Eng. Meeting, Rochester, NY, September, 1990.

[12] K. Subramanian, "Advanced Ceramic Components; Current Methods and Future Needs for Generations of Surfaces," Intersociety Symposium on Machining of Advanced Ceramic Materials for Components, R. E. Barks, K. Subramanian, and K. E. Ball (Eds.), Am. Cer. Soc., Westerville, OH, pp. 10-32, 1987.

[13] T. G. Bifano, D. Depiero, and D. Golini, "Ductile-Regime Grinding of Brittle Materials," Ultraprecision in Manufacturing Engineering, M. Weck and R. Hartel (Eds.), Springer-Berlag, New York, NY, pp. 22-40, 1988.

[14] T. J. Larchuk, J. C. Conway, Jr., and H. P. Kirchner, "Crushing as a Mechanism of Materials Removal During Abrasive Machining," J. Am. Cer. Soc., Vol. 68, No. 4, pp. 209-215, 1985.

[15] V. Swain, R. M. Latanision, and A. R. C. Westwood, "Further Studies on Environment-Sensitive Hardness and Machinability of Al_2O_3," J. Am. Cer. Soc., Vol. 58, No. 9-10, pp. 372-376, 1975.

[16] T. G. Bifano, D. DePiero, and D. Golini, "Chemomechanical Effects in Ductile-Regime Machining of Glass," Precision Engineering, American Ceramic Society, in press.

[17] R. E. Cuthrell, "The Effect of Chemical Environments on the Fracture of Ceramic Surfaces," B. J. Hockey and W. R. Rice (Eds.), National Bureau of Standards Special Publication 562, U.S. Government Printing Office, Wash. D.C., pp. 139-145, 1979.

[18] L. H. Robinson, "Effect of Hardness Reducers on Failure Characteristics of Rock," Soc. Petr. Eng. J., pp. 295-300, September, 1967.

[19] G. A. Cooper, "Some Observations on Environmental Effects when Diamond Drilling," The Science of Ceramic Machining and Surface Finishing II., B. J. Hockey and W. R. Rice (Eds.), National Bureau of Standards Special Publication 562, U.S. Government Printing Office, Wash. D.C., pp. 115-138, 1979.

[20] G. A. Cooper and J. Berlie, "On the Influence of Finishing Fluid During Diamond Grinding," J. Matls. Sci., Vol. 11, pp. 1771-1775, 1976.

[21] M. B. Peterson, S. L. Murray, and J. J. Florek, "Consideration of Lubricants for Temperatures above 1000F," ASLE Trans., Vol. 2, pp. 225-234, 1960.

[22] A. Erdermir, G. R. Fenske, and R. A. Erck, "Study of the Formation and Self-lubrication Mechanisms of Boric Acid Films on Boric Oxide Coatings," Surface and Coatings Technology, Vol. 43/44, pp. 588-596, 1990.

[23] A. Erdemir, R. A. Erck, and J. Robles, "Relationship of Hertzian Contact Pressure to Friction Behavior of Self-lubrication Boric Acid Films," Surface and Coatings Technology, Vol. 49, pp. 435-438, 1991.

[24] G. M. Zhang, T. W. Hwang, D. K. Anand, and S. Jahanmir, "Tribological Interaction in Machining Aluminum Oxide Ceramics," Proceedings of Navy Tribology Workshop, U.S. Naval Academy, Annapolis, MD, pp. 9-13, 1992.

[25] E. D. Rekow, G. M. Zhang, V. P. Thompson, and S. Jahanmir, "Factorial Design Technique to Investigate the Effect of Machine Tool Parametes and Machining Environment on Surface Finish," J. Dent. Research, IADR Abstract 570, 1993.

[26] J. C. Bailar, H. J. Emeleus, R. Nyholm, and A. F. Trotman-Dickenson, (Eds.), Comprehensive Inorganic Chemistry, Vol. 1, Pergamon Press, 1973.

[27] X. Dong, S. Jahanmir, and S. M. Hsu, "Tribological Characteristics of α-Al_2O_3 at Elevated Temperature," J. Am. Cer. Soc., Vol. 74 No. 5, pp. 1036-1044, 1991.

[28] R. S. Gates, S. M. Hsu, and E. E. Klaus, "Tribochemical Mechanism of Alumina with Water," Tribo. Trans., Vol. 32, pp. 357-363, 1989.

[29] M. G. Gee and X. S. Matharu, "The Measurements of Sliding Friction and Wear at High Temperature," Int. J. High Tech. Ceram., Vol. 4, pp. 319-331, 1989.

[30] S. W. Freiman, "Effects of Chemical Environments on Slow Crack Growth in Glasses and Ceramics," J. Geophysical Res., Vol. 89, No. B6, pp. 4072-4076, 1984.

[31] S. M. Widerhorn, Fracture of Ceramics, National Bureau of Standards Special Publication 303, U.S. Government Printing Office, Wash. D.C., pp. 217-241, 1969.

[32] T. A. Michalske and S. W. Freiman, "A Molecular Interpretation of Stress Corrosion in Silica," Nature, Vol. 295, pp. 511-512, 1982.

[33] G. S. White, S. W. Freima, S. M. Wiederhorn, and T. D. Coyle, "Effects of Counterions on Crack Growth in Vitreous Silica," J. Am. Ceram. Soc., Vol. 70, No. 12, pp. 891-895, 1987.

[34] S. W. Wiederhorn and H. Johnson, "Effect of Zeta Potential on Crack Propagation in Glass in Aqueous Solutions," J. Am. Ceram. Soc. Vol. 55, No. 7-8, pp. 342, 1975.

CHARACTERIZATION OF MACHINED
SURFACES

ULTRASONIC MEASUREMENT OF SURFACE AND SUBSURFACE STRUCTURE IN CERAMICS

J. A. SLOTWINSKI, N. N. HSU, and G. V. BLESSING
National Institute of Standards and Technology, Gaithersburg, MD

An effort is underway to detect near-surface damage using nondestructive ultrasonic methods. A sharply focused ultrasonic transducer was used to generate short-duration pulses in water and to receive echoes from the surface of the submerged sample. Direct-reflected and mode-converted interface wave echoes were separable in the time domain echo waveforms. Amplitude scans were taken with software controlled X-Y scanning stages capable of 0.1 μm resolution. The surface topography of ground silicon nitride (Si_3N_4) samples had a prominent affect on the direct-reflected echo amplitude. It is a principal goal of this program to distinguish this topographical structure from subsurface damage by studying the amplitude and velocity of various echo modes. In addition to Si_3N_4 samples, glass samples have been investigated for reference purposes.

INTRODUCTION

The intrinsic properties of ceramics make them prime candidates for many applications ranging from ball bearings to engine components. Unfortunately, the grinding processes in preparing ceramic materials may cause subsurface cracks which can lead to failure when the material is under stress. Destructive methods such as modulus of rupture tests yield quantitative statistical information, such as the average stress at which failure occurs in specific material lots. This, however, yields limited information about the extent and location of damage. At present there is simply no nondestructive method for detecting subsurface damage in a process-control application. Ultrasonics provides a rapid, nondestructive method of material defect detection which may prove applicable to the on-line detection of subsurface damage in ceramic materials.

In the pulse-echo ultrasonic technique, the amplitude of the return echoes provides information about the sample's surface roughness [1,2] and possibly the near-surface structure [3]. It is the goal of this work to study the amplitude behavior of certain ultrasonic echo modes from ground ceramic samples in order to distinguish between surface roughness and possible subsurface damage or structure.

EXPERIMENTATION

Ultrasonic Technique

The general ultrasonic system is shown in Figure 1. The nucleus of this system is the ultrasonic transducer. The transducer converts high-voltage excitations, occurring several thousand times a second, into short (< 0.1 μs) ultrasonic pulses. These pulses travel through a fluid coupling, such as water, to the specimen of interest, whence some of the ultrasonic energy returns back to the transducer. The returning

Figure 1: General ultrasonic system arrangement.
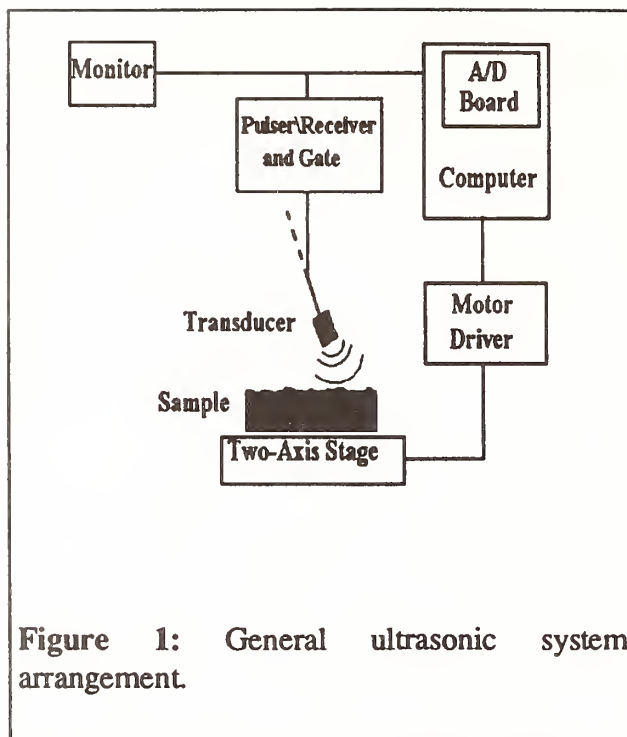
ultrasonic energy is then converted back into an electrical signal, which is displayed on an oscilloscope and/or recorded for analysis.

In this work a broadband sharply focused 50 MHz F/0.8 transducer is used to transmit and receive ultrasonic signals in conjunction with a pulser/receiver unit. At its focus this transducer has a nominal half-amplitude beamwidth of 35 μm as determined by pulse-echo measurements while scanning perpendicular to a razor blade edge. This is in agreement with pertinent ultrasonic beam-profile models [4]. In this study, a gated peak detector acquires specific amplitude values from the reflected ultrasonic signal as the sample of interest is scanned. Different wave modes, each providing possibly distinct information about the interrogated sample, can be gated separately. The amplitude data are then read and recorded by a personal computer through an analog to digital converter (A/D) board.

The same software which acquires the data also controls movement of the sample by means of X-Y scanning stages. These stages are designed for high-precision positioning, with a resolution of 0.1 μm. The computer code allows for different scanning rates and step sizes, and is capable of raster scans. This enables efficient examination of the samples' entire surface region.

The three ultrasonic arrangements considered in this experimentation are illustrated in Figure 2. The first case (a) is that of an ultrasonic beam focused on the surface of the target. Here the ultrasonic pulses react primarily to the surface structure, but may also be sensitive to near-surface damage. In the second case (b) the ultrasound is focused just below the surface of the target (i.e., defocused), where the sensitivity to subsurface structure such as cracks and porosity increases. The final case (c) involves the generation of a surface wave only. Here ultrasonic pulses strike the target surface at a critical angle θ_c, as determined by Snell's law of refraction, and propagate along the material interface as a surface wave. This mode radiates acoustic energy away from the interface into the coupling fluid as it propagates and is therefore

Figure 2: Sensor/sample orientations: (a) Normal incidence, surface focus; (b) Normal incidence, subsurface focus; and (c) Non-normal incidence, surface wave.
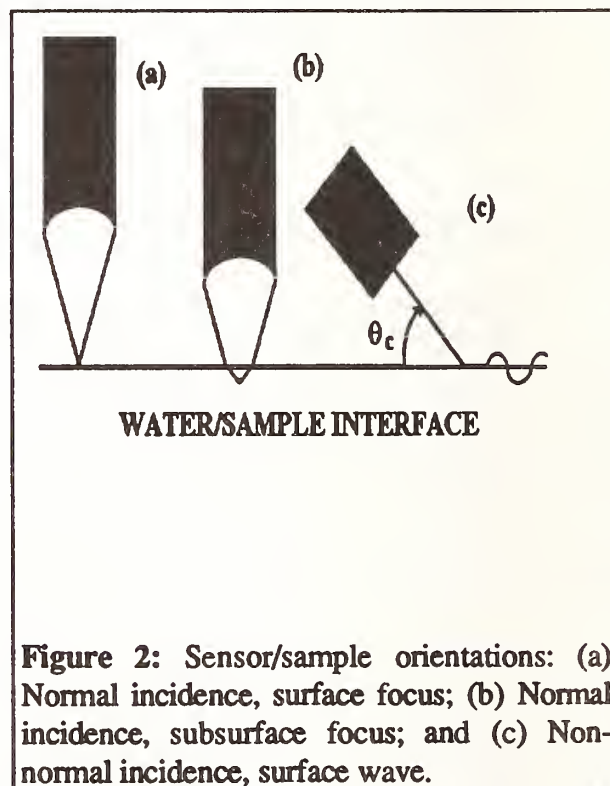
often referred to as a "leaky wave." (This phenomenon is the ultrasonic equivalent of the optical evanescent wave.) For a 50 MHz carrier signal this wave has a penetration depth on the order of 100 μm in Si_3N_4.
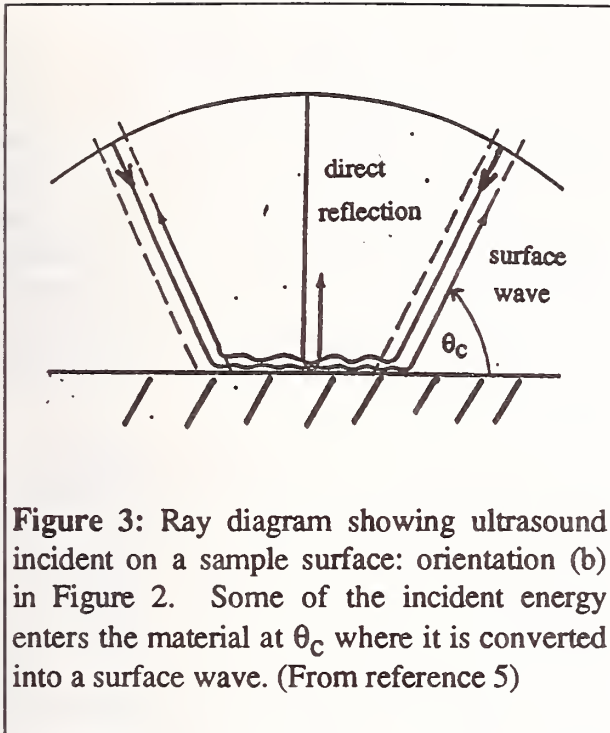
Figure 3: Ray diagram showing ultrasound incident on a sample surface: orientation (b) in Figure 2. Some of the incident energy enters the material at θ_c where it is converted into a surface wave. (From reference 5)

When the transducer is focused on the sample surface, only the direct-reflected longitudinal mode is present. For the defocused situation, however, both longitudinal and surface modes may be observed. In this case a portion of the wave energy is incident on the sample at θ_c, generating a surface wave by mode conversion (Figure 3) [5].

Often it is difficult to empirically distinguish between these two signal pulses. To aid in this, a numerical Green's function calculation was used for proper mode identification [6]. For Si_3N_4 the numerical results predict a leaky wave that is phase-reversed compared to the direct reflection. This was experimentally verified by observing the separation of the mode-converted and direct-reflection waves when the transducer was defocused in a controlled manner. Figure 4 shows the time separation between the direct reflection and the leaky wave for incident ultrasound on Si_3N_4. The top trace shows the direct reflection echo waveform when the sample surface is located at the transducer's focus. The three subsequent traces show the echo waveforms for various defocused positions as the transducer is moved closer to the sample surface. As the transducer is increasingly defocused the leaky

wave propagates over a larger surface path, resulting in increased time separation between it and the direct reflection.

Samples

The ceramics tested were sintered reaction-bonded silicon nitride (Si_3N_4) samples, possessing a density of 3.2 g/cm^3. They were subjected to varying grinding conditions which could in turn be expected to yield varying degrees of subsurface damage. This report focuses on two ground samples which were prepared in highly distinct manners, in an effort to search for contrasting features. The different grinding parameters are shown in Table I [7]. The first sample was conventionally ground, followed by one or two spark-out passes. The second sample was prepared by creep-feed grinding. (These two samples are hereafter referred to as "lightly" and "harshly" ground, respectively.)

The different grinding conditions resulted in different surface roughnesses. The lightly and harshly ground samples possessed average surface roughness values (R_a) equal to 0.3 and 0.5 μm $\pm$ 0.02 μm, respectively. (The average surface roughness value is defined as the average deviation of the surface contours from a plane through their median value.) The ground surfaces had somewhat regular surface periodicities (grinding groove spacing) of about 40 μm.
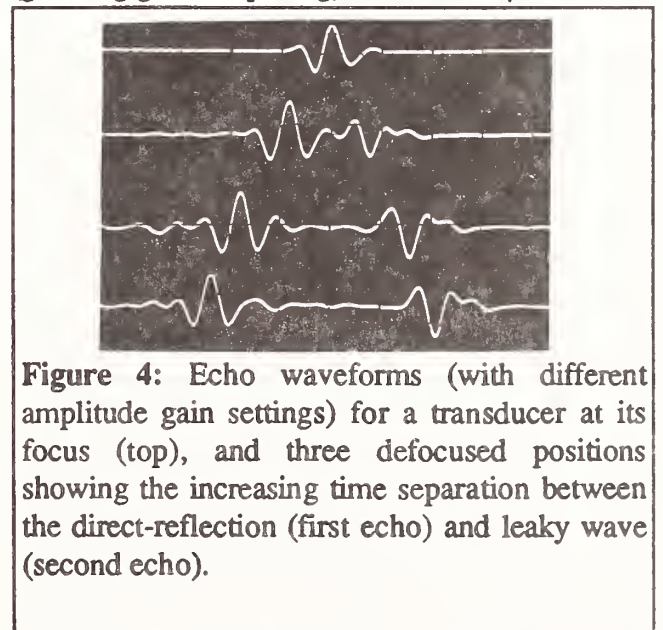
Figure 4: Echo waveforms (with different amplitude gain settings) for a transducer at its focus (top), and three defocused positions showing the increasing time separation between the direct-reflection (first echo) and leaky wave (second echo).

A separate, lightly ground sample from the same material batch was polished to a sufficient depth to remove all topographical surface features and possible near-surface structure. This sample had an $R_a = 0.04 \pm 0.01$ µm. It was used as a material reference.

Table I: Grinding Conditions

Condition	conventional	creep-feed
Grinding Wheel	320 grit 150 conc.	80 grit 100 conc.
Grinding Fluid	Emulsion plus 1-2 spark-out passes	Emulsion 20:1
Table Speed (m/min)	15.2	1.52
Cross Feed (mm/pass)	4.00	4.50
Down Feed (mm)	0.0051	0.2540
Volume Removal Rate (mm^3/min)	310	1737

RESULTS

Numerous ultrasonic echo amplitude

scans were made on the various samples, with the transducer beam focused in some cases on the surface, and in other cases below the surface (i.e., defocused). In all cases the center ray of the incident ultrasound was normal to the surface. The same transmitter energy settings and nominally the same receiver gain were used in the scans. This allows direct comparison between the scans. Representative scans are presented first for the ultrasonic beam focused on the sample surfaces.

Figure 5 is echo amplitude data taken in 10 µm steps over a 1 mm scan length on the polished Si_3N_4 sample surface. While this scan was parallel to the original grinding direction, it is representative of all scans parallel and perpendicular to that direction. The lack of significant echo amplitude variation is to be expected for the ultrasonic wavelength of 30 µm interacting on this polished surface. We also note that the observed amplitude variation in Figure 5, with a measured standard deviation of ± 1.2 mV about the mean value of 382.3 mV, is equivalent to the system electrical noise level. This noise level is principally generated by the gated peak detector output.

Figures 6 and 7 are representative scans taken parallel and perpendicular, respectively, to the grinding direction on the lightly ground sample. The scan length was again 1 mm, in 10 µm steps. The noticeably large loss of signal, centered at the 0.2 mm position in the parallel scan, is of uncertain origin. Possibilities are an inclusion or a grinding wheel artifact. Two

Figure 5: Highly polished silicon nitride echo amplitude scan.
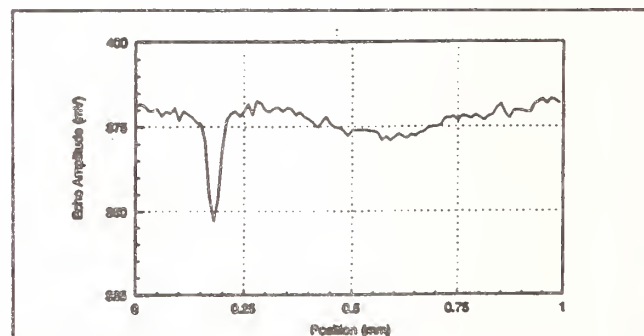
Figure 6: Echo amplitude scan on lightly ground silicon nitride taken parallel to grinding grooves.

features that we can explain in the parallel scan are the same baseline system noise as observed in Figure 5, and the gentle rolling character of the baseline attributed to crossing a groove or peak along the grinding direction. In the perpendicular scan of Figure 7, the mean echo amplitude level is nominally the same as in Figure 6, but with much greater baseline structure due to crossing the grooves of variable height.
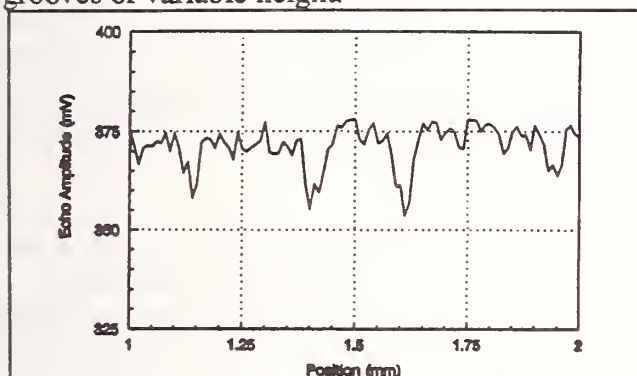
Figure 7: Echo amplitude scan on lightly ground silicon nitride taken perpendicular to grinding grooves.

Figure 8, a data scan taken perpendicular to the grooves of the harshly ground sample, possesses two features of interest for comparison to Figure 7. The first is a mean amplitude of 355.4 mV, which is lower than that of the smoother-surface lightly ground sample. The second is a standard deviation of ± 9.9 mV, which is larger than that of the lightly ground sample. These can be explained in terms of the different
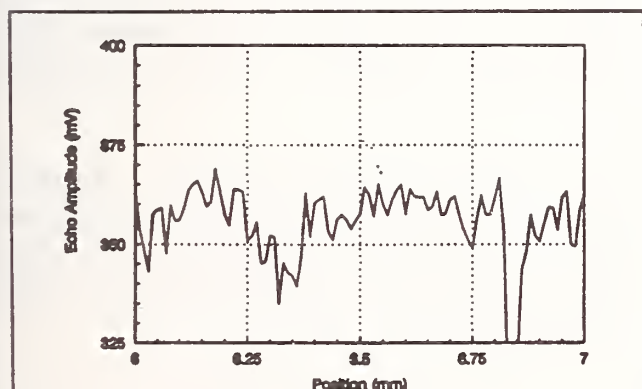
Figure 8: Echo amplitude scan on harshly ground silicon nitride taken perpendicular to grinding grooves.

surface roughnesses of the two samples. More of the incident ultrasound is scattered away and/or extinguished due to phase cancellations in the grooves for a rough surface than for a smooth surface [1,2].

Longitudinal scans were also performed with the ultrasonic beam focused just below the surface of the ceramic samples, in an attempt to enhance sensitivity to subsurface structure. The echo amplitude scans with subsurface focusing at depths of 10, 20, and 30 μm were done on the lightly polished sample in a direction parallel to the grinding grooves. The recorded scans gave no indication of subsurface structure.

As mentioned previously, a leaky surface mode is also present when the transducer is defocused. Leaky wave scans on the lightly ground sample were done in a direction parallel to the grinding grooves. The leaky wave did not show any signal amplitude variation. This result, which seems rather innocent at first, is significant for the following reason: the leaky wave did not show any variation due to the inevitable crossing of grinding grooves. (It is virtually impossible to align the samples such that no grooves are traversed, due to the beam and groove geometry.) This suggests that the leaky wave mode is not as sensitive to surface roughness as the focused longitudinal wave.

A glass slide, ostensibly free of subsurface damage, was scanned to help verify this reduced sensitivity to surface roughness. The slide had smooth and rough (frosted) surface regions with R_a=0.03 ± 0.01 μm and R_a=3.2 ± 0.5 μm respectively, as determined by contacting stylus. Neither region had a discernible surface periodicity. There was no leaky wave amplitude variation on the smooth region and a 10% amplitude variation on the rough region. This is compared to the case where the ultrasonic beam was focused on the surface, which resulted in no amplitude variation on the smooth region, but a 60% amplitude variation on the rough region. From this we conclude that the leaky wave is less sensitive than the reflected longitudinal wave to surface roughness. This agrees with other results [8] which show that defocused ultrasound is relatively insensitive to surface roughness.

Following ultrasonic testing, cross sections of the ceramic samples were polished, revealing comparable subsurface features at the lightly and harshly ground surfaces. In cross section, the ground surfaces exhibited fracture-like structure to a depth of about 10 μm. This was observed at optical magnifications of 250 and 1000X.

CONCLUSIONS

A sensitivity of pulsed ultrasound to the surface topography of various grinding/polishing conditions has been observed on Si_3N_4 ceramic samples. At an ultrasonic carrier frequency approaching 50 MHz, corresponding to a wavelength of about 30 μm in a water coupling medium, wave scattering mechanisms affecting the echo amplitude of the reflected pulse easily discriminated amongst the ground surfaces. The surface roughnesses ranged from 0.04 μm R_a on the highly polished sample to about 0.5 μm R_a on a harshly ground sample. If the surface grinding features of these silicon nitrides could be demonstrably related to their material quality, ultrasonic wave scattering would provide a means for effective quality control. Furthermore, this sensor technique, which is both rapid and nondestructive, can be applied in-process.

An effort was also made to study subsurface material structure by monitoring the amplitude of surface waves generated when defocusing the highly focused F/0.8 transducer. No distinguishing signatures were observed between any of the samples that could not be attributed to surface roughness.

ACKNOWLEDGMENTS

REFERENCES

[1] G.V. Blessing and D.G. Eitzen, "Ultrasonic Sensor for Measuring Surface Roughness," Proceedings of the International Congress on Optical Science and Engineering, pp. 281-289, 1989.

[2] G.V. Blessing, D.G. Eitzen, H.M. Ryan, and J.A. Slotwinski, "Surface Micrometrology Using Ultrasound," Proceedings of the 1990 IEEE Ultrasonics Symposium, Vol. 2, pp. 1047-1052, 1990.

[3] K. Yamanaka, Y. Enomoto, and Y. Tsuya, "Acoustic Microscopy of Ceramic Surfaces," IEEE Transactions on Sonics and Ultrasonics, Vol. SU-32, No. 2, pp. 313-319, 1985.

[4] G.S. Kino, Acoustic Waves: Devices, Imaging, and Analog Signal Processing, (Prentice-Hall, Inc. NJ) p. 185, 1987.

[5] R.S. Gilmore, K.C. Tam, J.D. Young, and D.R. Howard, "Acoustic Microscopy from 10 to 100 MHz for Industrial Applications," Phil. Trans. R. Soc. Lond., Vol. 320, pp. 215-235, 1986.

[6] N.N. Hsu, S.E. Fick, and G.V. Blessing, "Green's Function of a Liquid/Solid Interface and Ultrasonic Materials Testing," Proceedings of the 1992 IEEE Ultrasonics Symposium, Vol. 1, pp. 395-398, 1992.

[7] S. Jahanmir, T.J. Strakna, G.D. Quinn, R.N. Kopp, S.C. Yoon, and K.V. Kumar "Effect of Grinding on Strength and Surface Integrity of Silicon Nitride Part II," Proceedings of the International Conference on Machining of

Advanced Materials, Gaithersburg, MD, July 20-22, 1993.

[8]   P. Reinholdtsen and B.T. Khuri-Yakub, "The Effects of Surface Roughness on Subsurface Defect Detection Using Acoustic Microscopy," Review of Progress in Quantitative NDE, Vol. 5A, pp. 485-491, 1985.

SURFACE CHARACTERIZATION OF ULTRASONIC MACHINED CERAMICS WITH DIAMOND IMPREGNATED SONOTRODE

H. DAM, S. JENSEN, and P. QUIST
Danish Technological Institute, Taastrup, Denmark

In this article a new ultrasonic machining process is presented. The tool is a diamond impregnated sonotrode, which is split at the end, so that it makes both lateral and longitudinal vibrations. Machining experiments were performed with glass, alumina and partially stabilized zirconia (PSZ). Material removal rates were highest for glass and alumina, at approximately 600 mm^3/min with R_a-values ranging from 1.6 to 2.1 μm. The material removal mechanism for glass and alumina was microfracture. The best surface quality was obtained with PSZ, but material removal rates were low. The material removal mechanism was controlled by plastic deformation.

1. INTRODUCTION

One of the major limitations in the use of ceramics, compared to other materials, is the relatively high cost of machining. This has been stated in several reports [1].

To solve these problems there are generally two ways:

1) - reduce or eliminate the need for machining by producing near net-shape components.

2) - develop new machining processes or improve or optimize the already existing methods.

In this paper, a new process for ultrasonic machining is presented, and the material removal rates are given. Further the machined surfaces were characterized to explain the material removal mechanisms.

2. DESCRIPTION OF PROCESS

Ultrasonic machining was developed during the 1950's for 2 and 3 dimensional machining of hard and brittle materials [2].

The conventional ultrasonic machining process uses an abrasive slurry of water and boron carbide. During processing the tool (sonotrode) hammers the abrasive particles against the workpiece surface; thus, creating a shape corresponding to the geometry of the sonotrode. The main advantage of the process is that the machining forces are low and complex geometries are possible. However, the material removal rates are rather low and the tolerances are hard to control. Therefore, attempts have been made to combine diamond grinding with ultrasonic machining. The first known experiments with diamond impregnated tools were made by Legge [3,4], and the process turned out to be versatile regarding both deep hole drilling and end mill facing. One of the latest attempts in this development has been the use of different ultrasonic

vibration modes with diamond impregnated tools. These have been reported by Kunabe [5], and it was concluded that torsional ultrasonic vibration is suitable for high precision core drilling while longitudinal ultrasonic vibration is suitable for core drilling with high material removal rates.

The tool used in these experiments uses a sonotrode which converts the longitudinal ultrasonic action into a mixed lateral and longitudinal vibration mode, see Figure 1. The working principle of the sonotrode is therefore basically like a tuning fork.
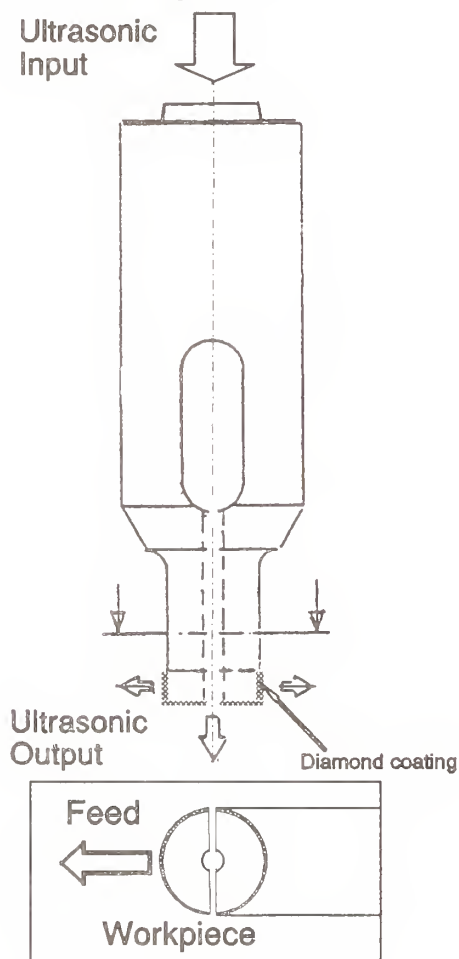
Fig. 1 Sonotrode for ultrasonic machining according to the tuning fork principle

With this process, it is possible to perform a milling process in hard and brittle materials.

3. DESCRIPTION OF EQUIPMENT

The equipment used in this series of experiments is described in the following sections.

3.1 Machine tool
The experiments were performed on an ultrasonic milling machine.

The main characteristics for this machine tool are ultrasonic frequency 19.5 - 20.5 KHz, amplitudes of 10 - 23 μm, ultrasonic power of 2 KW, spindle rotation of 0-5000 rpm, full 4 axis CNC control.

Further a force measurement system using piezoelectric sensors is built in. This system was used for measuring the machining forces.

3.2 Sonotrode
The sonotrode is shown on figure 2.1. Its most important dimensions and specifications are:

Length	130 mm
Top diameter	50 mm
Cutting diameter	24 mm

Diamond impregnation: Electrolytical coating with 181 μm as mean grain size.

3.3 Materials
The materials were commercial qualities of glass, alumina (99.7%) and partially stabilised zirconia (PSZ). The stabilising element in PSZ was magnesium oxide. The material data are shown in the table below.

Table 1　　Material data for the ceramics used in the experiments

Material	Glass	Alumina	PSZ
Density (g/cm^3)	2,5	3,9	5,8
Flexural Strength (MPa)	50	300	500
K_{IC} (MPa$\sqrt{m}$)	0,7	4,5	9
Hardness Knoop (Mpa)	7000	23000	17000

3.3 Analysis Equipment

The surface roughness measurements were performed using a surface profilometer with a pick up radius of 5 μm. A complete description of the equipment and the results of the roughness measurements are available in [6].

For the qualitative characterisation of the surfaces a Scanning Electron Microscope, SEM was used.

4. TEST PROCEDURE

Samples with a size of 50 x 24 mm were cut from three materials by diamond cutting. The samples were then glued to the base plate with sealing wax.

Three series of experiments were performed.

1　　machining of alumina to find feasible machining parameters

2　　rough machining, where the resultant machining forces were kept at the same level for all 3 materials.

3　　finish machining, where the feed rates were at the same level for all 3 materials. Furthermore, a series of "high feed finishing" were made with alumina and glass with increased feed.

The general machining parameters are shown in table 2.

Table 2　　General machining parameters

Spindle speed	3000 RPM
Frequency	20,2 kHz
Amplitude (input)	19 μm
Cooling	Internally through spindle and externally directly on tool.
Coolant	Water with rust inhibitor

5. RESULTS

5.1 Selection of feasible machining parameters

In these experiments the depths of cut (vertical) and the feeds (horisontal) were varied. At depths of cut at 2 mm there were heavy low frequency vibrations of the tool. If the feed was sufficiently low (5 mm/min), the low frequency vibrations disappeared, but instead the tool made half circular machining tracks as shown on figure 2.
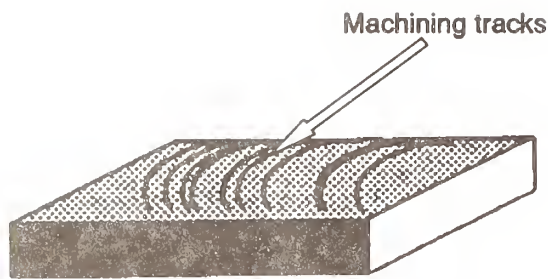
Fig. 2 Principal drawing of machining tracks appearing at to high feeds and depths of cut.

With the objective to increase the material removal rate and avoid both machining tracks and low frequency vibrations it was found that the highest material removal rates could be obtained at relatively low depths of cut ≤ 0.5 mm and high feeds ≥ 50 mm/min for glass and alumina. For PSZ the feeds had to be even lower ≤ 7 mm/min to avoid machining tracks.

5.2 Material removal rates and surface qualities for roughened and finished samples

The machining parameters for the roughing and finishing series are shown in Tables 3,4 and 5.

The forces in the tables were calculated as the resultant of the machining forces in x, y, and z directions.

Table 3 Machining parameters for rough machining keeping resultant machining forces at same level

Material	Feed (mm/min)	Depth of cut (mm)	F (N)
Glass	60	0,5	24
Alumina	50	0,5	24
PSZ	7	0,5	22

Table 4 Machining parameters for finishing, keeping feeds at the same level

Material	Feed (mm/min)	Depth of cut (mm)	F (N)
Glass	4	0,2	8
Alumina	4	0,2	8
PSZ	4	0,05	

Table 5 Machining parameters for high feed finishing

Material	Feed (mm/min)	Depth of cut (mm)	F (N)
Glass	30	0,2	9,4
Alumina	30	0,2	17,3

The resulting material removal rates are shown on figure 3.
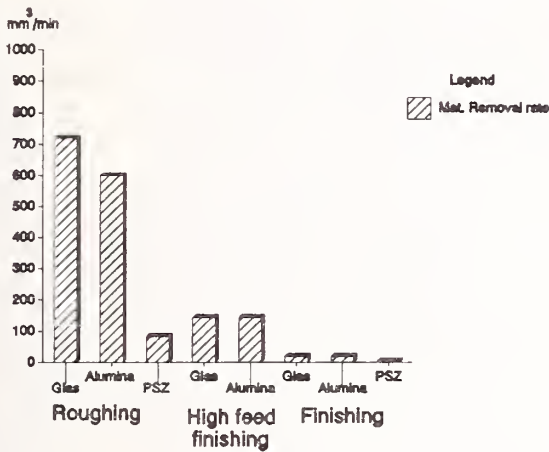
Fig. 3 Material removal rates

From figure 3 it can be seen that the material removal rates are very high for both glass and alumina, while PSZ has a rate 6 -7 times smaller at the same machining force. A problable explanation for this is that the fracture toughness of PSZ is much higher than alumina and it thus requires a larger amount of energy to remove material from the surface. Because the machining force and the spindle speed is kept constant, the only way to obtain a larger energy input per volume of removed material, is to slow down the feed.

The roughness measurements were performed at the bottom surface. The two most common roughness parameters are R_a and R_z. R_a is a measure for the arithmetic mean height of the surface profile. Let the function f(x) describe the height of the profile at the position x. R_a can then be found by integrating f(x) with respect to x over the measuring length l_m as shown below.

$$R_a = \frac{1}{l_m} \int_{x=0}^{x=l_m} f(x)\, dx$$

R_z is the mean height of the 5 highest peaks in the surface profile. It is comparable to R_{max} (maximum peak height), but it is less influ-

enced by statistical deviations, because it is taken as a mean of 5 peaks.
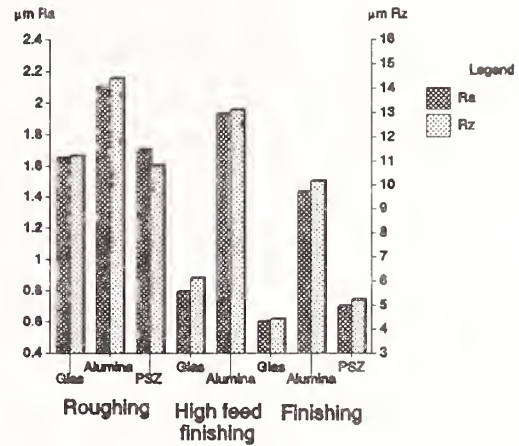
Fig. 4   Roughness parameters at the bottom of the machined surfaces.

If the surface roughness parameters are observed it can be seen that they decrease when feed and depths of cut are lowered. This was what could be expected. However if, the roughness parameters for alumina are observed they are generally higher. Furthermore it can be seen that a decrease in cutting depth and feed rate has much less effect on the surface quality, than for glass and PSZ.

If the surface roughness are described according to the new ISO standard, which is the same as DIN 4776 [7], a more detailled picture of the surface can be given.

In this standard three different roughness parameters are defined; R_{pk}, R_{vk} and R_k. They are derived from the Abott curve, which describes the distibution of peaks and valleys in the roughness profile as shown on fig. 5.
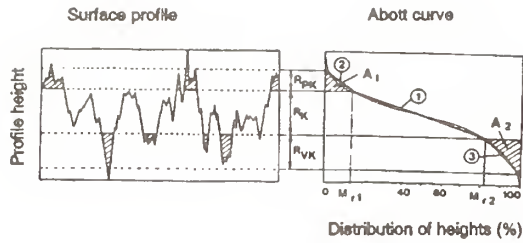
Fig. 5 Definition of R_{pk}, R_k and R_{vk} according to [7].

The exact definition of the three parameters are given in [7], but they can be interpreted as follows:

R_k is the depth of the roughness profile when the highest peaks and the lowest valleys are excluded. It is a measure for the bearing ratio, so that a low R_k means a high bearing ratio.

R_{pk} (the reduced peak height) is the height of the triangle with the shaded area, A_1. From a tribological point of view it gives a measure for the "running in" characteristic for the surface.

R_{vk} (the reduced valley height) is the height of the triangle with the shaded area A_2. If the surface is lubricated, R_{vk} gives a measure for the volume of lubricant on the surface.

The roughness parameters are shown in figure 6.
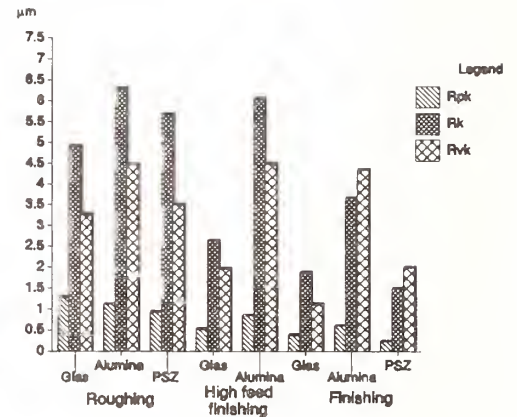
Fig. 6 Roughness parameters according to DIN 4776 for machined surfaces.

For alumina it can be seen that the reduced valley height R_{vk} is almost the same for all machining rates, while both R_k and R_{pk} are reduced in finishing. This indicates that there is a constant contribution from, for instance, porosities or grain pull-out. From a tribological point of view a low R_k has a high priority because it gives a higher bearing ratio. The best properties concerning friction coefficient and wear can therefore be expected with PSZ because it has a lower R_k and R_{pk} than any of the other materials.

For qualitative characterisation of the machined surfaces a SEM-investigation was performed. For PSZ and glass, two representative pictures are shown on figures 7 and 8.

130

Feed
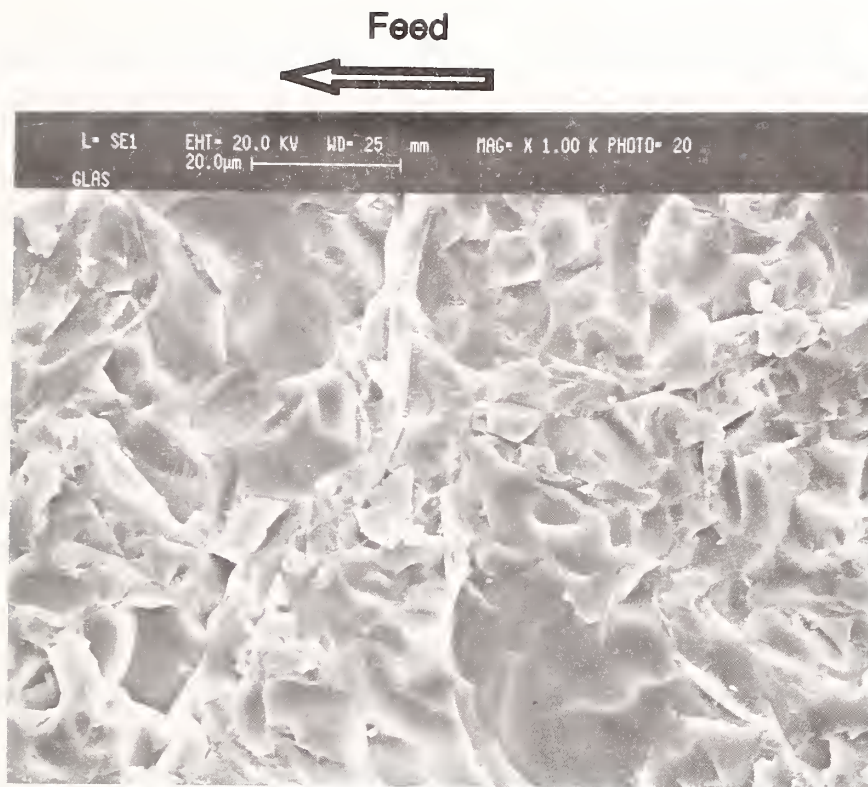
Fig. 7 Glass ultrasonic machined with impregnated diamonds (finish machining).

Feed
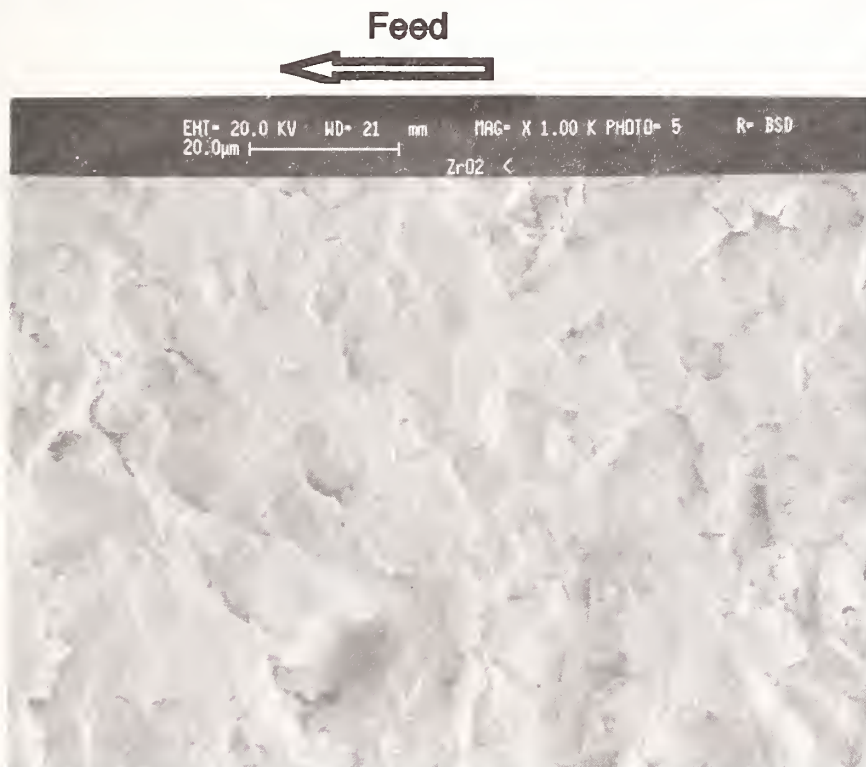
Fig. 8 PSZ ultrasonic machined with impregnated diamonds (finish machining).

Although the materials are machined under practically the same conditions and their R_a and R_z values are almost the same, there is a large difference in the structure of the surfaces. Glass is characterised by having sharp features and no machining marks. The PSZ

surface consits of flat plateaus with thin marks primarily perpendicular to the direction of feed which is indicated by the arrow. From this it can be concluded that the material removal mechanism for glass is brittle fracture. For PSZ the material removal mechanism is primarily plastic deformation and cutting, because the single ceramic grains are cut without leaving sharp edges.

6 DISCUSSION

If this new ultrasonic machining process is compared with other ceramic machining processes the closest "competitor" is rough grinding. The material removal rates and the surface qualities are practically at the same levels. However, because the resultant machining forces are at least one order of magnitude smaller there is a potential that the risk for machining damage and cracks is lowered. At the same time the generation of heat during processing is expected to be smaller. As a temperature gradient at the surface generally gives rise to tensile residual stresses the risk for such stresses will be lowered.

The successor for this series of experiments will therefore include an NDT analysis and a determination of the strength of the machined samples.

P.t several machines with a rotating ultrasonic vibrating spindle are commercially available. With longitudinal vibrations these machines perform well in deep hole drilling (z-axis) movement. Sonotrodes with lateral vibrations as the one described in this article perform well in x and y direction. A combination of these two machining processes would therefore reveal an interesting alternative for ceramic prototyping and complicated geometries.

CONCLUSION

An investigation of a new ultrasonic machining process using a diamond impregnated sonotrode with both lateral and longitudinal vibrations has been performed.

The primary material removal mechanism were based at microfracturing in alumina and glass, while the material removal in PSZ was based on plasticity.

The surface qualities obtained are comparable to rough grinding but machining forces are an order of magnitude lower. However, the effect of this on damages in the subsurface zone still needs to be investigated.

In summary ultrasonic machining with a split sonotrode combined with ultrasonic machining with diamond impregnated sonotrodes reveals an interesting alternative for future ceramic machining.

References

[1] S. Jahanmir, L.K.Ives, A.W. Ruff and M.B. Peterson
"Ceramic Machining: Assesment of Current Practice and Research Needs in the United States."
NIST-Special Publication 834, June 1992

[2] R. Schmeig
"Die ultraschallbearbeitung von Hochleistungskeramik."
Keramische Zeitschrifft, No 10, P. 515-27, 1985

[3] P. Legge
"Machining without Abrasive Slurry."
Ultrasonics, London, 4, p. 157-62, July 1966

[4] P. Legge
"Ultrasonic Drilling with a Diamond Impregnated Probe"
Ultrasonics, London, 4, p. 1, Jan. 1964

[5]   Junichiro Kunabe, Masahiko Jin, and
       Akifumi Nishio
"Precision Drilling of Ceramics by Ultrasonic
Superposition Vibration Cutting."
Journal of the Japan Society of Precision
Engineering
Vol 55, No 2, p. 366-71 1989

[6]   Zia Afreedi and Jan Efsen
"Ultrasonic Machining of Ceramic Materials"
(in danish),
Report from Institute of Manufacturing
Engineering, Technical University of Den-
mark November 1992

[7]   Deutsche Industrie Norm 4776 (DIN
       4776)
       "Measurement of Surface Roughness"
       May 1990

MEASUREMENT OF RESIDUAL STRESSES IN MACHINED CERAMICS USING THE INDENTATION TECHNIQUE

Y. AHN, S. CHANDRASEKAR, and T. N. FARRIS
Purdue University, West Lafayette, IN

Machining produces surface residual stresses which significantly influence the strength and fatigue resistance of ceramic components. As new methods are developed for machining ceramics, a quick and reliable technique for measurement of residual stresses would be valuable in assessing the viability of the new machining method from a residual stress perspective. The residual stresses on ground and polished (i.e. machined) surfaces of soda-lime glass, Ni-Zn ferrite, and silicon nitride have been measured using an indentation technique with a Vickers indenter. In this technique, the surface extent of the median/radial cracks produced by the Vickers indenter in machined and in annealed ceramics are measured. These are then combined with a fracture mechanics model to estimate the surface residual stresses in the machined ceramics. In order to determine the validity of the indentation technique for estimating machining residual stresses, these stresses were also measured using an X-ray diffraction and a deflection method. The residual stress values determined using the indentation technique in the machined ceramics were found to be reasonably close to those obtained from the X-ray diffraction and deflection methods. Since it is relatively simple and easily applied, the indentation technique appears to be a potentially promising method for evaluating residual stresses in machined ceramics.

1 Introduction

About seventy years ago, Griffith [1, 2] postulated the existence of microscopic and submicroscopic flaws (i.e. cracks) to explain the low measured strength values of glass compared to its theoretical strength. Since then it has become well established that the flaws generated at localized contacts between hard rigid particles and solid surfaces are an important cause of strength degradation in brittle solids.

One method of reducing the harmful effects of microscopic flaws is to induce compressive stresses in the surface. This has been accomplished to varying degrees by using different techniques: ion exchange and thermal tempering processes in soda-lime glass [3, 4]; chemical strengthening in alumina and glass ceramics by the formation of low thermal expansion solid solution surface layers at high temperatures [5]; and stress-induced phase transformation of metastable tetragonal zirconia to the monoclinic phase in partially stabilized zirconia (PSZ) [6]. Not only is the load for crack initiation considerably increased in the presence of surface compression but also if the generated cracks remain fully encased within the surface compressive layers, the strength of a ceramic containing surface compressive stresses is greater than that of the annealed ceramic [7, 8].

Recent work has shown that diamond grinding produces compressive residual stresses in ceramic surfaces [6, 7, 8]. However, the grinding process also introduces flaws in the surface and the strength of a ground ceramic is controlled by a combination of the residual stress and flaw dis-

135

Table 1: Compressive Residual Stresses (MPa) in Soda-Lime Glass and Ni-Zn Ferrite [12]

Material	Measurement Technique			
	Inden-tation	Deflec-tion	X-ray	Op-tical
Toughened Soda-Lime Glass	56±22 (Knoop) 60±5 (Vickers) 82±28 (cone)	85±11	not appli-cable	85.5
Lapped Ni-Zn Ferrite	69.5±15 (Vickers)	45±11	56±9	not appli-cable

Figure 1: (a) Schematic diagram of a side view of the cracks generated in soda-lime glass beneath a pointed indenter. In (b) are shown the surface traces of the half-penny median cracks: fc, full-penny median crack; hc, half-penny crack; lc, lateral crack; and 2c, the surface extent of the median crack. In the figure, the shallow radial cracks are not shown. These are usually normal to the indented surface but they do not contain the load axis [11].

tributions [7]. The potentially wide ranging structural applications for ceramics has highlighted a need for simple measurement techniques which could be used to estimate the residual stresses and flaw sizes produced by machining.

While there are a number of techniques available for the measurement of residual stresses, the indentation technique offers a particularly simple way of determining residual stresses in brittle materials [9, 10]. In this technique, the indentation cracking produced by a spherical or pointed (e.g. Vickers or Knoop) indenter is analyzed. Figure 1 is a schematic of the cracks typically generated by a pointed indenter in glass. Recently, the residual stresses in toughened glasses and lapped Ni-Zn ferrite ceramics have been measured using the pointed indentation technique [11, 12, 13]. The measurements in the glasses [11, 12, 13] were made using a Vickers, Knoop, or 90° WC conical indenter while with ferrite, a Vickers indenter was used [12]. In these studies, an independent estimate of the residual stress was also obtained using X-ray diffraction, a deflection method, or an optical photoelastic technique. The indentation, X-ray diffraction, and deflection methods are described in detail in Section 2. Table 1, from Reference [12], summarizes some of the measurement results. The studies showed that the measured values of the residual stress in glass and Ni-Zn ferrite estimated using the indentation technique compared well with those obtained using the other methods (see Table 1).

It was decided, therefore, to explore the validity

136

of the pointed indentation technique using a Vickers indenter for determining residual stresses in machined (i.e. ground and polished) ceramic surfaces. The residual stresses in machined surfaces of hot-pressed silicon nitride (Si_3N_4), soda-lime glass, and Ni-Zn ferrite determined using the pointed indentation technique were found to be quite close to the values obtained using other techniques such as X-ray diffraction or a deflection method. These results and the techniques used to obtain them are the subject of this paper.

2 Background: Residual Stress Measurement

It is appropriate to begin with a review of the residual stress measurement techniques used in the present investigation.

2.1 Pointed Indentation Technique

Recently, Chaudhri and Phillips [11] and Chandrasekar and Chaudhri [12] have compared the indentation cracking patterns of annealed and thermally tempered soda-lime glass using pointed (i.e. Vickers, Knoop, and a 90^0 cone) indenters and have estimated the residual compressive surface stresses. In the case of Vickers indentation-induced radial/median cracking, they estimated the residual surface stresses using the following relationship

$$\sigma_c = \frac{\chi}{1.16c^2}(P^* - P) \qquad (1)$$

where P^* and P are the loads which produce cracks of the same radius c in the tempered glass containing a compressive residual stress of magnitude σ_c and in the annealed glass, respectively, and χ is an indenter constant. Equation (1) is derived using linear elastic fracture mechanics. For the Vickers indenter the value of χ can be obtained from the analysis of Lawn and Fuller [14] as

$$\chi = \frac{1}{\pi^{3/2}\tan 68^0} \qquad (2)$$

Alternatively, an empirical estimate for χ can be obtained from a calibration test as follows

Using dimensional energy arguments, it can be shown that in a material which is free of residual stress an equation of the form

$$\chi\frac{P}{c^{3/2}} = K_{I_C} \qquad (3)$$

is valid for cracks formed during loading with pointed indenters [15]. The value of χ can now be determined if K_{I_C} for the material is known from an independent fracture toughness test such as the single-edge notched beam (SENB) test and the variation of crack radius, c, with indenter load, P, is measured for the specific indenter and material in an indentation experiment. Previously, both a calibrated value for χ [12] and an analytical estimate for χ (for a Vickers indenter) obtained using Equation (2) [11] have been used for residual stress measurement.

It should be noted that the indentation technique provides measurement of the local residual stress, that is, the stress over a small volume of size on the order of the indentation volume. Also, in the derivation of Equation (1), the residual stress is assumed to be constant over this volume.

2.2 Deflection Method

The deflection or curvature method [16] enables the measurement of the average in-plane residual stresses in a solid surface and their variation within the subsurface. The method employs a rectangular parallelepiped specimen which contains the residual stresses to be estimated. One face of the specimen, viz. the reference surface, is polished flat and its curvature is measured (at this stage it should be close to zero). Then a layer of uniform thickness is removed from the face opposite to the reference face; we denote this as the test face. The test face contains residual stresses which are to be determined. The layer is removed by a process (e.g. chemical etching, electropolishing, fine polishing with soft abrasives) that does not in itself induce any significant residual stresses. The removal of this layer causes a change in the principal curvatures of the reference face. These are then determined by profilometry of the reference face, by means of a strain-gauge rosette mounted on the reference face, or by optical interferometry on the reference face. The residual stress in the test face is then given by [17]

$$\begin{aligned}
\sigma_1(z, w_0) &= \frac{E}{6(1-\nu^2)}\left\{z^2\left[\frac{dC_1}{dz} + \nu\frac{dC_2}{dz}\right]\right. \\
&+ 4z[C_1(z) + \nu C_2(z)] \\
&+ 2(w_0 - 3z)[C_1(w_0) + \nu C_2(w_0)] \\
&\left. - 2\int_z^{w_0}[(C_1(z) + \nu C_2(z)]\,dz\right\} \quad (4)
\end{aligned}$$

where the test surface is at z=0, $\sigma_1(z, w_0)$ is a principal stress at depth z below the surface, w_0 is the initial plate thickness before etching, $C_1(z)$ and $C_2(z)$ are the principal curvatures of the reference face after a depth z of the material has been removed from the test face, $C_1(w_0)$ and $C_2(w_0)$ are the initial curvatures of the reference face before any etching, and E and ν are, respectively, the Young's modulus and Poisson's ratio of the specimen material.

The remaining principal stress $\sigma_2(z, w_0)$ can be obtained by interchanging the subscripts 1 and 2 in Equation (4). A further layer is then removed from the test surface and the residual stresses determined again as before. In this way, the residual stress distribution in the specimen is obtained. The measured residual stress values are average values of the stresses in planes parallel to the specimen surface.

2.3 X-ray Diffraction

In ceramic polycrystals, residual stresses can be determined using an X-ray diffraction technique in which the change in lattice spacing resulting from residual stresses is measured. Comprehensive reviews of the technique are available, see for example Hilley et. al. [18] and James and Cohen [16]. The technique requires a polycrystalline sample so that diffraction from a given set of (hkl) planes can be studied. The presence of residual stresses in the specimen causes the diffraction angle corresponding to the above planes to be changed. This is a consequence of the change in the lattice spacing of the (hkl) planes due to the residual stresses. From the measured change in the lattice spacing, the amount of strain is calculated. Using isotropic elasticity and knowing the X-ray elastic constant, $E/(1+\nu)$, for the direction normal to the (hkl) plane (in cubic crystals this would be the [hkl] direction), the residual stress can be determined from the strains thus measured. The X-ray elastic constant can be calculated from a knowledge of single crystal compliance constants [19] or obtained from direct calibration measurements of the lattice strain under an applied stress. If the X-ray beam diameter is only a few millimeters across, point-to-point determination of surface residual stresses can be made in specimens of size greater than ~10 mm. Furthermore, by removing surface layers, as in the case of the deflection method, the

Table 2: Material Properties

Property	Soda-Lime Glass	Ni-Zn Ferrite	Si$_3$N$_4$
E(GPa)	70	191	300
ν	0.25	0.2	0.26
ρ(gm/cc)	2.5	5.3	3.22
H(GPa)	5.5	7.3	16.7
K_{I_C}(MPa$\sqrt{m}$)	0.75	0.8	4.0

sub-surface residual stress distribution can be obtained [6].

3 Experimental Procedure

Three blocks each of soda-lime glass, Ni-Zn ferrite, and HP-Si$_3$N$_4$ (NC-132, Norton Co.) ceramics were prepared by grinding and polishing. Table 2 lists some relevant mechanical properties of the specimen materials which will henceforth be referred to as ceramics. Two of the blocks were of size $25 \times 12.5 \times 2.5$ mm while the third block was $\sim 25 \times 12.5 \times 12.5$ mm. The 25×12.5 mm faces on each of the blocks of ferrite and Si$_3$N$_4$ were machined by first grinding with a 600 grit size resin-bonded, diamond wheel and subsequently polished with 3 μm and 0.5 μm diamond paste. The grinding depth of cut was 5 μm and the wheel surface speed was 36 m/sec. In the case of the soda-lime glass blocks, the polishing was carried out using a 6 μm cerium oxide powder. In each case the deformed layer produced by grinding was not completely removed by the polishing process. Care was taken to ensure that all the three blocks of a given material were finished under nominally identical conditions. However, no consideration was given to ensuring that the specimen preparation procedures conformed to those used in industry. This latter aspect does not detract from the objectives of the study.

The residual stresses produced by machining (i.e. grinding and polishing) on the 25×12.5 mm face of the blocks were measured using the pointed indentation, X-ray diffraction (only with ferrite and Si$_3$N$_4$), and deflection methods. The pointed indentation technique was used with the $25 \times 12.5 \times 12.5$ mm blocks while the X-ray diffraction and deflection methods were used to determine the residual stresses in the $25 \times 12.5 \times 2.5$

mm blocks.

3.1 Pointed Indentation Technique

The ground and polished (25 × 12.5 mm) faces of the soda-lime glass, Ni-Zn ferrite, and HP-Si$_3$N$_4$ blocks contain residual stresses induced by machining. The machined faces were indented with a Vickers indenter on a conventional micro-hardness testing machine. The indentation loads were typically between 10 and 300 Newtons. In a typical test, the maximum indentation load was applied in 15 to 25 seconds and was maintained for a duration of 15 seconds before unloading. The blocks were examined using optical and scanning electron microscopy after unloading to determine the length $2c$ of the surface trace of the median/radial cracks (see Figure 1) and the indentation diagonal $2a$. Figure 2 is an optical micrograph showing the surface traces of the typical median/radial cracks in annealed Si$_3$N$_4$ produced by a Vickers indenter. The lengths AA and BB of the cracks in Figure 2 correspond to the length $2c$ of Figure 1, while the length CC in Figure 2 corresponds to the indentation diagonal ($2a$) of Figure 1. The sub-surface shape and extent of the cracks in Si$_3$N$_4$ (Figure 2) were not determined. Figure 3 shows a side view of the typical median/radial crack system in annealed soda-lime glass produced by a Knoop indenter. The photograph was taken in transmitted light. Here the length AA (which corresponds to the length $2c$ of Figure 1), is actually the diameter of a half-penny median crack and not the surface trace of of shallow radial cracks.

After several indentations had been made in each of the blocks and the various measurements (i.e. indentation diagonal and crack length) completed, the ferrite and silicon nitride blocks were annealed in an inert atmosphere of argon at 800°C for one and one-half hours to relieve the machining induced residual stresses. In the case of the soda-lime glass block, the annealing was carried out in air at 520°C for two hours. After annealing, the Si$_3$N$_4$ blocks were lightly polished using 0.5 μm diamond paste while the soda-lime glass and ferrite blocks were lightly polished using cerium oxide and magnesium oxide powders, respectively. Such polishing procedures have been found to induce a negligible amount of residual stress. The polished surfaces of the annealed blocks were again indented with a Vickers indenter at several differ-ent points using a range of indenter loads and the surface traces of the cracks were measured. The crack lengths thus obtained corresponded to surfaces which were nominally devoid of any residual stresses. The difference in the crack lengths measured on the ground and polished (machined) specimen surfaces, and the annealed specimen surfaces (free of residual stress) were used with Equation (1) to obtain the residual stress induced by the machining (i.e. grinding and polishing) in the ceramics.

3.2 Deflection and X-ray Diffraction Methods

Measurements of the residual stresses were carried out in the machined Ni-Zn ferrite and silicon nitride blocks using the deflection and X-ray diffraction methods. With the machined soda-lime glass blocks, the measurements were made using the curvature method alone.

In the deflection method, the principal curvatures of the reference face were determined by using a Talysurf 10 (Rank Taylor Hobson Inc.) profilometer to trace the reference face and by measuring the chordal rise over a fixed length. The principal curvatures of the reference face were also measured after layers of depth 4 μm and 8 μm were removed from the test face by polishing. Mechanochemical polishing with a 7 volume percent solution of orthophosphoric acid in water and 0.05 μm iron oxide abrasive powder was used for layer removal in ferrite and HP-Si$_3$N$_4$ while a 0.05 μm magnesium oxide powder was the polishing abrasive used on soda-lime glass. It is important that this layer removal process does not in itself introduce substantial residual stresses compared to the stresses being measured; past unpublished results have shown that each of the polishing agents used above induces less than 8 MPa surface residual stress in the soda-lime glass and the Ni-Zn ferrite. From the measured curvatures and the values of the elastic constants for soda-lime glass, Ni-Zn ferrite, and Si$_3$N$_4$ (Table 2), the residual stresses in the machined surface and at a depth of 4 μm from the machined surface were obtained using Equation (4). A piecewise linear fit of the curvature versus depth data was used in the calculation of the derivatives and integrals in Equation (4).
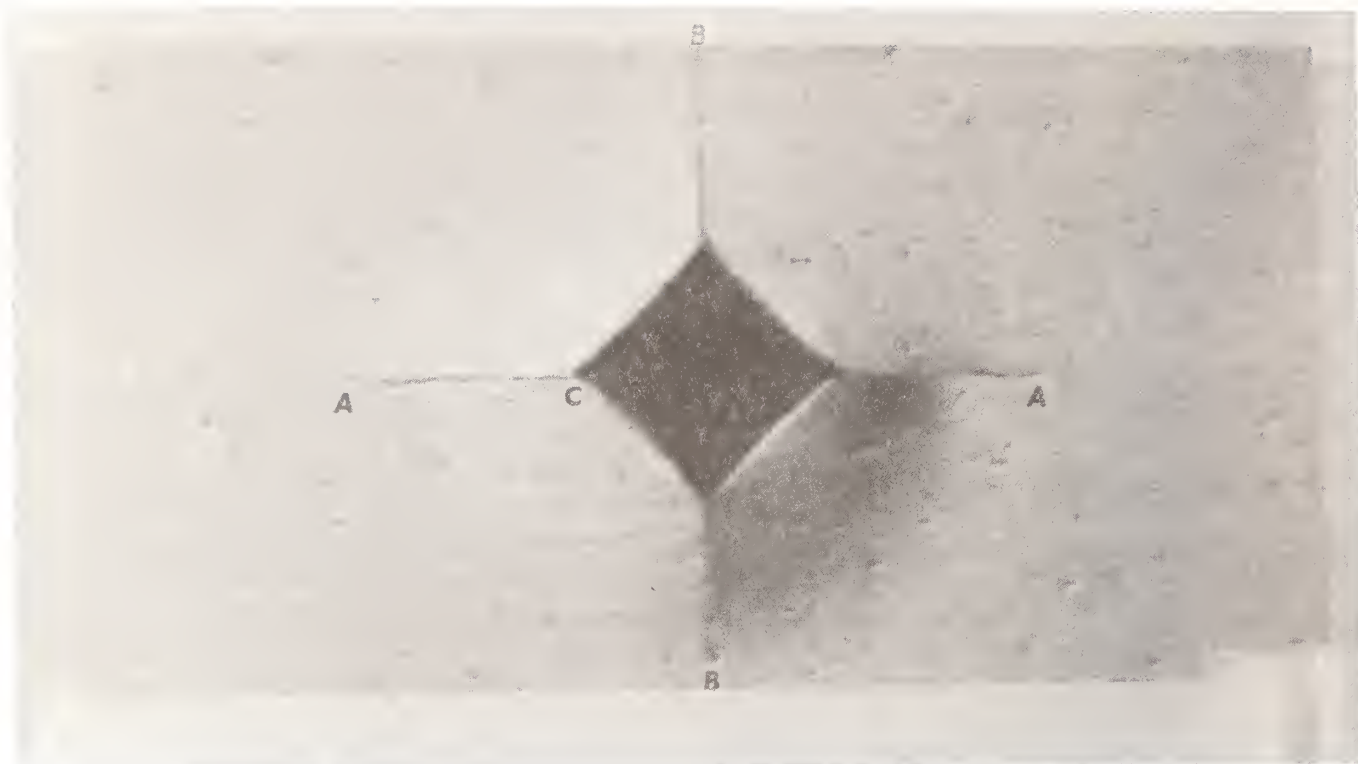
Figure 2: Optical micrograph of surface trace of a median/radial crack in HP-Si$_3$N$_4$ produced by a Vickers indenter (Load = 30 kg).
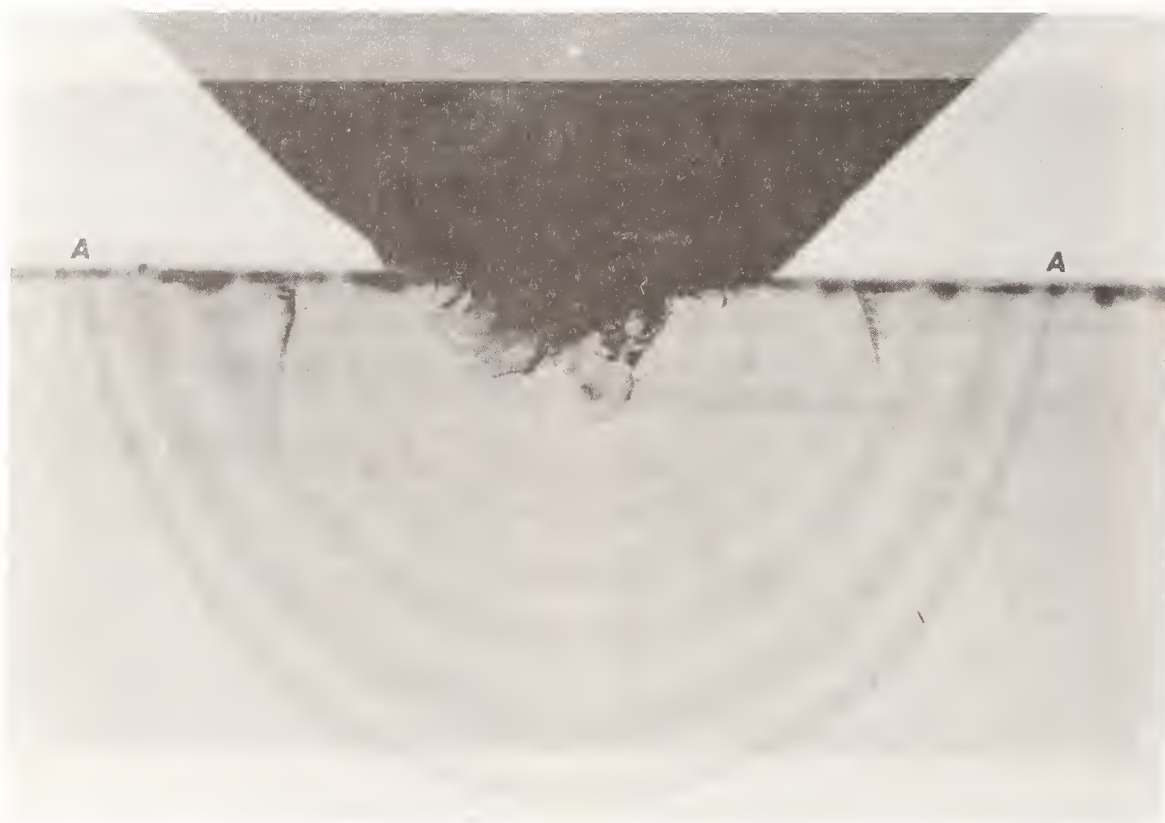
Figure 3: Photograph of a half-penny median crack in soda-lime glass produced by a pointed indenter. The photograph was taken in transmitted light through the sides of the glass block whilst the load is applied.

X-ray diffraction was carried out using Cr-radiation ($\lambda = 0.2291\,\eta m$) with a spot diameter of 3 mm as it has a much smaller penetration depth than does Cu radiation. The (119) and (323) peaks were selected for the observations in Ni-Zn ferrite and Si_3N_4 respectively. The diffraction angle θ was measured to an accuracy of 0.0125 degrees using a diffractometer and the residual stress was determined by the method described in Section 2.3. By translating the ceramic specimens, the surface residual stress was determined at three points in the ferrite and Si_3N_4 specimens. Similarly, the residual stress at a depth of $4\mu m$ from the surface was measured in both of the ceramics after removing surface layers by mechanochemical polishing (as in the deflection method).

Calibration experiments were conducted to determine the X-ray elastic constants, $E/(1+\nu)$, corresponding to the (119) and (323) planes in Ni-Zn ferrite and Si_3N_4 respectively. Details of the calibration method can be found in Chandrasekar and Chaudhri [12]. The measurements gave values of 150 ± 11 GPa, (119) plane in Ni-Zn ferrite, and 268 ± 14 GPa, (323) plane Si_3N_4, for the X-ray elastic constants.

4 Residual Stress Results

4.1 Indentation Technique

The residual stresses were obtained from indentation crack length measurements as follows. Figures 4, 5, and 6 show the variation of $c^{3/2}$ with load, P, for annealed soda-lime glass, Ni-Zn ferrite, and Si_3N_4, respectively. Here c is the radius of the surface trace of the median/radial crack (see Figure 1) produced by the Vickers indenter. The solid lines in Figures 4, 5, and 6 are a least-squares fit of the experimental data assuming that the relationship between P and $c^{3/2}$ is linear [14]. From the slopes of these straight lines and the values of K_{Ic} for the three materials (Table 2) the indenter constant (χ) was obtained using Equation (3) for each of the three materials. The values of χ for soda-lime glass, Ni-Zn ferrite, and Si_3N_4 thus estimated from the calibration experiments are listed in Table 3. The calibrated values of χ for all three ceramics (Table 3) are within 20 percent of the analytical value for χ (≈ 0.0725) estimated using Equation (2) for the Vickers indenter. The cali-

Table 3: Calibrated Values for the Indenter Constant χ

Material	χ
Soda-lime glass	0.0695
Ni-Zn ferrite	0.085
Silicon nitride	0.071
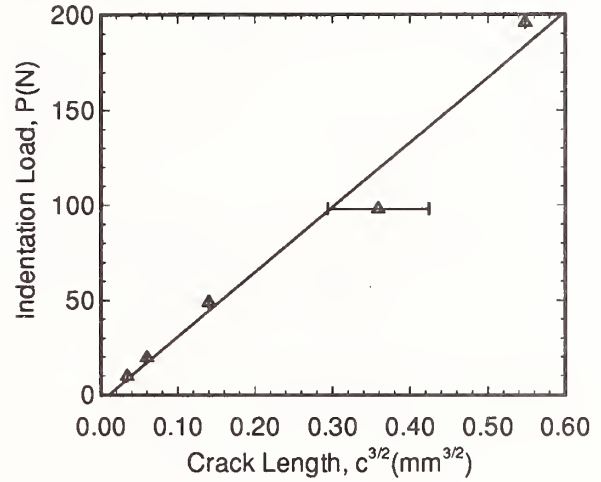
Figure 4: The variation of crack length with load in annealed soda-lime glass (maximum error bar is shown)

brated values of χ are used in the estimation of the residual stresses.

Figures 7, 8, and 9 show the variation of $(P^* - P)$ with c^2 for soda-lime glass, Ni-Zn ferrite, and Si_3N_4, respectively. The figures were obtained by combining the measurements of the crack lengths shown in Figures 4, 5, and 6 with similar measurements carried out on the machined surfaces of soda-lime glass, Ni-Zn ferrite, and Si_3N_4. The straight lines in Figures 7, 8, and 9 are a least squares fit of the data; that the data should be on a straight line is predicted analytically by Equation (1). The coefficients of regression for this least-square fit are given in Table 4. Using the slope $(P^* - P)/c^2$ of the straight lines in Figures 7, 8, and 9 (see Table 4) in Equation (1) together with the appropriate value of χ for each of the three materials from Table 3, we obtain the surface compressive residual stress (σ_c) in the machined surfaces of ceramics. The residual stress (σ_c) values are listed in Table 4. These residual stresses are caused by the localized plastic defor-
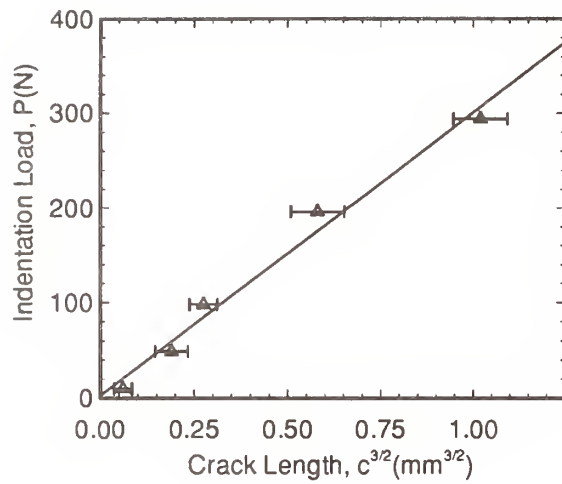
Figure 5: The variation of crack length with load in annealed Ni-Zn ferrite
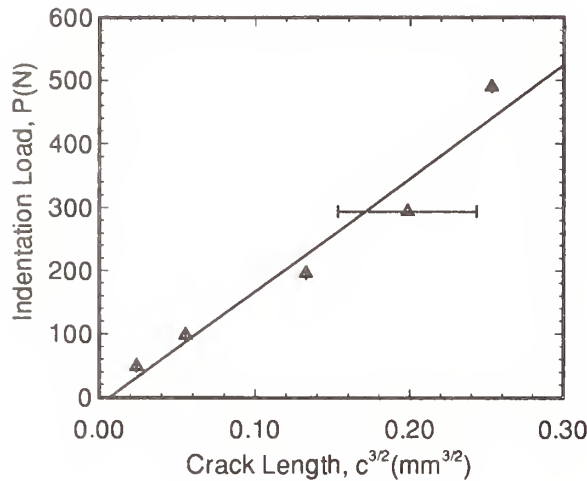
Figure 6: The variation of crack length with load in annealed Si_3N_4 (maximum error bar is shown)

Material	Slope $\frac{P^*-P}{c^2}$ (MPa)	R^2 Regression Coefficient	σ_c (MPa)
Soda-lime glass	464.7	0.96	27.8
Ni-Zn ferrite	1170.0	0.93	85.6
Si_3N_4	1951.3	0.99	119.1
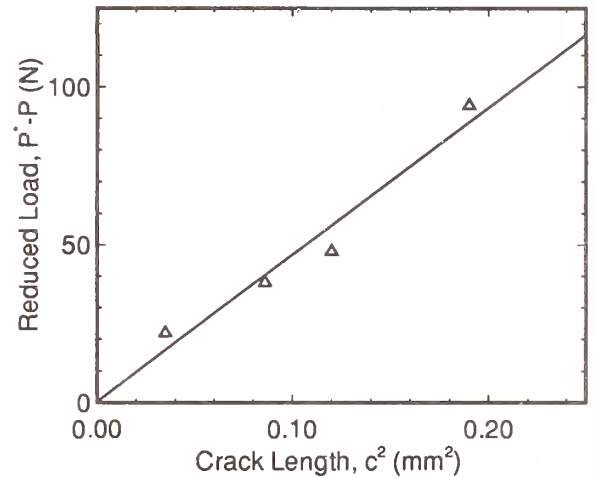
Figure 7: The variation of $P^* - P$ with c^2 in machined soda-lime glass (P^*, P, and c are defined near Equation 1)

mation of the ceramic materials during grinding and polishing.

4.2 Deflection Method

The measurements of curvature showed that the reference surfaces of the machined ceramics and glass were ellipsoids with the two principal curvatures differing by less than 8 percent. This corresponds to a state of equiaxial stress in planes parallel to the surface. Here equiaxiality of residual stress in a plane implies that the stress is equal in all directions in the plane since these planes are principal planes due to the symmetric geometry of grinding and polishing.

The surface compressive residual stress in the machined soda-lime glass block was determined as 21.0 ± 8 MPa; it decreased to a value of 11.0 ± 7.5

Figure 8: The variation of $P^* - P$ with c^2 in machined Ni-Zn ferrite (P^*, P, and c are defined near Equation 1)

Table 5: Summary of Residual Stress Measurements in Machined Surfaces (MPa)

	Material		
Technique	Soda-Lime Glass	Ni-Zn Ferrite	Si_3N_4
Indentation (surface)	27.8	85.6	119.1
Deflection (surface)	21±8	62±18	87±22
Deflection (subsurface)	11±7.5	35±14.5	59±13
X-ray (surface)	-	68±16	82±24
X-ray (subsurface)	-	43.0±14.5	49±17.0

All residual stresses are compressive.
The subsurface values were measured at a depth of 4 μm below the machined surface.

MPa at a distance of 4 micrometers from the surface, see Table 5. The decreases in the residual stress values were even greater with the Ni-Zn ferrite and Si_3N_4. In the case of the Ni-Zn ferrite, the surface residual compressive stress was 62.0±18 MPa while at a depth of 4 μm below the surface the compressive residual stress had a value of 35±14.5 MPa. The corresponding values for the compressive residual stress in the Si_3N_4 block were 87.0±22 MPa at the surface and 59.0±13 MPa at a depth of 4μm below the surface. The residual stress values are summarized in Table 5.

4.3 X-ray Diffraction

X-ray diffraction measurements of the residual stress were carried out in the machined Ni-Zn ferrite and Si_3N_4 blocks. The measured values of the residual stresses at the surface and at a depth of 4μm below the surface are given in Table 5. It is seen from Table 5 that these stress values are close to those obtained using the deflection method.

Figure 9: The variation of $P^* - P$ with c^2 in machined Si_3N_4 (P^*, P, and c are defined near Equation 1)

5 Discussion

The X-ray diffraction and deflection measurements of the residual stress have shown that in all of the machined ceramics, the surface residual stress is compressive (Table 5). The magnitude of the sur-

143

face residual stress produced by grinding and polishing is seen to be greatest in Si_3N_4 and smallest in glass. The measured surface residual stress of ~ 90 MPa in Si_3N_4 compares well with values of 110-140 MPa reported recently for this stress in polished Si_3N_4 [20]. An examination of the subsurface residual stress values in Table 5 shows that the stress gradients near the machined surface are quite steep, typically of the order of 3-8 MPa per micrometer.

It is interesting to compare the surface residual stress values in the machined ceramics estimated using the indentation technique with those obtained using deflection and X-ray diffraction methods. From Table 5 it can be seen that with all three ceramics, the indentation technique gives surface residual stress values which are reasonably close (within 30 percent) to those obtained using the X-ray diffraction and deflection methods. Both the indentation technique and the X-ray diffraction method estimate the localized residual stresses, while the deflection method estimates the average in-plane residual stress in planes parallel to the specimen surface.

It is now worthwhile to consider some of the reasons for the differences in the residual stress values determined using the indentation technique and the X-ray diffraction and deflection methods in Table 5. The analysis leading to Equations (1-3) used with the indentation technique [9, 10, 14, 15] assumes that penny/half-penny median cracks form during loading of the specimen by the indenter. Also, it is assumed that residual stress gradients near the indented surface are not steep. The X-ray diffraction and deflection method measurements have shown that with all of the machined ceramics, the residual stresses vary rapidly near the machined surface. There are also uncertainties pertaining to the formation and the shape of the cracks emanating from the corners of the Vickers-indentations (henceforth these cracks will be referred to as corner cracks). From in-situ observations of Vickers-indentation cracking, Chandrasekar and Chaudhri [12] have shown that in soda-lime glass, the corner cracks are surface traces of half-penny median cracks. This has also been confirmed by serial sectioning of the Vickers indents along planes parallel to the indented surfaces (unpublished work). Similar serial sectioning of the Vickers indents in Ni-Zn ferrite has shown

that for indentation loads exceeding 40 N, the corner cracks in ferrite are of the half-penny, median type. The shapes of the corner cracks in Si_3N_4 and in ferrite (at loads less than 40 N) are as yet unresolved.

As to when the various cracks form in the different ceramics, median cracks have been observed to form around Vickers indentations during unloading in annealed soda-lime glass when the maximum indentation load was less than 30-40 N [12]. In these cases there was no cracking during loading. When the maximum indentation load exceeded 40 N, median cracks were observed to form during loading [12]. It is quite possible that, given the magnitude of the indentation loads used in this study (e.g. Figure 4), some of the median cracks formed during unloading in the soda-lime glass. It is not yet established as to when median/radial cracks form in Si_3N_4 and Ni-Zn ferrite polycrystals. However, Lankford [21, 22] has observed from acoustic emission measurements that shallow surface radial (not median) cracks form during the loading of a Vickers indenter in polycrystalline SiC and Al_2O_3 at loads as small as 0.1-0.25 N. This could probably occur with Si_3N_4 and ferrite as well. Another point to be noted is that in the derivation of Equations (1-3), it is assumed that only one median crack is formed. The presence of more that one median/radial crack as is commonly observed with Vickers indentations could have an effect on the stress-intensity factors at the median/radial crack tips due to the interaction between various cracks [23].

Based on the above observations, it would be unreasonable to expect significantly better agreement between the residual stress values determined using the indentation technique and those measured using the X-ray diffraction and deflection methods. However, since the pointed indentation technique is simple and can be rapidly applied, it appears to be an attractive technique for measuring residual stresses produced by machining in brittle materials.

6 Conclusion

The residual stresses in machined soda-lime glass, Ni-Zn ferrite, and Si_3N_4 are measured using the pointed indentation technique with a Vickers indenter. For comparison, measurements of the

residual stresses in these machined ceramics have also been carried out using the deflection method and an X-ray diffraction technique (only with ferrite and Si_3N_4). The measured values of the residual stress estimated using the pointed indentation technique were found to be reasonably close (within 30 percent) to the values obtained from the deflection and X-ray diffraction measurements.

The absence of a detailed model for the indentation crack systems, the existence of steep residual stress gradients near the machined surface and uncertainties in the value of the indenter constant χ (Equation 2) prevent the indentation technique measurements from agreeing more closely with the residual stress values determined using the X-ray diffraction and deflection methods. However, due to the simplicity and ease of application of the indentation technique, it appears to be a potentially useful method for determining residual stresses in machined ceramic surfaces.

References

[1] A.A. Griffith, "The Phenomena of Rupture and Flow in Solids," *Philosophical Transactions of the Royal Society (London)*, **221**, pp 163–198, 1921.

[2] A.A. Griffith, "The Theory of Rupture," In *Proceedings of the First International Congress of Applied Mechanics*, pp 163–198, 1924.

[3] O.S. Narayanswamy and R. Gardon, "Calculation of Residual Stresses in Glass," *Journal of the American Ceramic Society*, **52**, pp 554–558, 1969.

[4] M.J.C. Hill and I.W. Donald, "Stress Profile Characteristics and Mechanical Behavior of Chemically Strengthened Lithium Magnesium Aluminosilicate Glasses," *Glass Tech*, **30** (4) pp 123–127, 1989.

[5] H.P. Kirchner, R.M. Gruver, and R.E. Walker, "Chemical Strengthening of Polycrystalline Alumina," *Journal of the American Ceramic Society*, **51** (5) pp 251, 1968.

[6] D.J. Green, F.F. Lange, and M.R. James, "Factors Influencing Residual Surface Stresses due to a Stress-Induced Phase Transformation," *Journal of the American Ceramic Society*, **66** (9) pp 623–629, 1983.

[7] R. Samuel, S. Chandrasekar, T.N. Farris, and R.H. Licht, "The Effect of Residual Stresses on the Fracture of Ground Ceramics," *Journal of the American Ceramic Society*, **72** (10) pp 1960–1966, 1989.

[8] D.P. Stinton, "Assessment of the State of the Art in Machining and Surface Preparation of Ceramics," Technical Report ORNL/TM-10791, Oak Ridge National Laboratory, Oak Ridge, TN, 1977.

[9] M.V. Swain, J.T. Hagan, and J.E. Field, "Determination of the Surface Residual Stresses in Tempered Glasses by Indentation Fracture Mechanics," *Journal of Materials Science Letters*, **12**, pp 1914–1917, 1977.

[10] D.B. Marshall and B.R. Lawn, "An Indentation Technique for Measuring Stresses in Tempered Glass Surfaces," *Journal of the American Ceramic Society*, **60** (1-2) pp 86–87, 1977.

[11] M.M. Chaudhri and M.A. Phillips, "Quasi-static Indentation Cracking of Thermally Tempered Soda-Lime Glass with Spherical and Vickers Indenters," *Philosophical Magazine A*, **62** (1) pp 1–27, 1990.

[12] S. Chandrasekar and M.M. Chaudhri, "Indentation Cracking in Soda-lime Glass and Ni-Zn Ferrite under Knoop and Conical Indenters and Residual Stress Measurements," *Philosophical Magazine A*, 1993. In-Press.

[13] R. Tandon and D.J. Green, "Indentation Behavior of Ion-exchanged Glasses," *Journal of the American Ceramic Society*, **73** (4) pp 970–977, 1990.

[14] B.R. Lawn and E.R. Fuller, "Equilibrium Penny-like Cracks in Indentation Fracture," *Journal of Materials Science*, **10**, pp 2016–2024, 1975.

[15] P. Ostojic and R. McPherson, "Review of Indentation Fracture Theory: Its Development; Principles; and Limitations," *International Journal of Fracture*, **33** (4) pp 297–312, 1987.

[16] M.R. James and J.B. Cohen, *Treatise on Materials Science and Technology*, pp 1–62. Academic Press, New York, 1980. Ed. H. Herman.

[17] R.G. Treuting and Jr. W.T. Read, "A Mechanical Determination of Biaxial Residual Stress in Sheet Materials," *Journal of Applied Physics*, **22** (2) pp 130–134, 1951.

[18] M.E. Hilley, J.A. Larson, J.F. Jatczak, and R.E. Ricklefs, *SAE Report J7849*, Society of Automotive Engineers, Warrendale, PA, 1971.

[19] J.F. Nye, *Physical Properties of Crystals*, Clarendon Press, Oxford, 1957.

[20] H. Kishimoto, A. Veno, H. Kawamoto, and S. Kondau, "X-ray Residual Stress Measurement of Sintered Si_3N_4," *Journal of the Society of Materials Science (Japan)*, **36** (407) pp 810–816, 1987.

[21] J. Lankford, "Threshold Microfracture during Elastic-plastic Indentation of Ceramics," *Journal of Materials Science*, **16** pp 1177–1182, 1981.

[22] J. Lankford and D.L. Davidson, "The Crack-initiation Threshold in Ceramic Materials Subject to Elastic-plastic Indentation," *Journal of Materials Science*, **14**, pp 1662–1668, 1979.

[23] L.M. Keer, T.N. Farris, and J.C. Lee, "Knoop and Vickers Indentation in Ceramics Analyzed as a Three-Dimensional Fracture," *Journal of the American Ceramic Society*, **69** (5) pp 392–396, 1986.

DETECTION OF SUBSURFACE DEFECTS IN MACHINED SILICON NITRIDE CERAMICS BY OPTICAL SCATTERING METHODS

W. A. ELLINGSON, D. M. AYAZ, M. P. BRADA, and W. O'CONNELL
Argonne National Laboratory, Argonne, IL

Silicon nitride (Si_3N_4) materials from two manufacturers, in the form of flexure test bars with surface finishes that were ground and polished (.03 μm Ra) and unidirectionally ground (.07 μm Ra) and contained simulated subsurface defects were studied by optical Fourier scattering methods. Subsurface defects were obtained by either ultrasonically drilling 750–μm–diameter holes to within 75-105 μm of the surface or by grinding slots parallel to and 75-105 μm below the surface. Because of the unique optical transmission properties of many ceramic materials, including those in this study, subsurface defects, such as those likely to be caused by machining–induced damage, may be detected by appropriate optical methods. In this study s–polarized He-Ne laser light (λ = 0.6328 μm) was used as the light source. Specular reflections were detected by an optical Fourier method that incorporates cross-polarization. Analysis of the scattered laser light was accomplished with a CCD-array camera, an eight-bit A/D converter, and a PC with locally written software. Results show that subsurface defects simulated in this study can be detected and that, for the surface finishes studied, changes in signal-to-noise ratio are observable.

INTRODUCTION

The life of elements that are subject to rolling–contact fatigue, such as bearings, can be significantly shortened if surface or subsurface defects are present. Ceramic rolling elements, especially ball bearings, are rapidly being developed for commercial applications [1-4]. Currently, because of their mechanical and physical properties, silicon nitride (Si_3N_4) ceramics are the materials of choice and offer several advantages over steel counterparts. These advantages include greater stiffness, operating speed, corrosion resistance, and thermal stability [4]. Further, the primary failure mode of Si_3N_4 bearings is spallation, the least harmful mode of failure [5-6].

Ceramic bearings are usually classified into two types: (1) hybrid bearings that include a ceramic rolling element and steel races or (2) all-ceramic bearings, which have ceramic rolling elements and ceramic races. The machining operations are typically different for each ceramic component [7,8]. The bearings are usually machined from hot-pressed "blanks," which are then hot-isostatically pressed (HIP'd) and finally lapped to finishes on the order of <.05 μm Ra. The races on the other hand are often ground with surface finishes <.1 – .2 μm Ra. Either of these machining operations has the potential to introduce surface and subsurface defects. However, subsurface defects could also be inherently present in the material and not affect machining but still impact fatigue life. Nondestructive testing methods, which can be reliably applied to map surface and near-surface defects would be significantly beneficial, primarily if the data generated could be correlated to life

prediction models. One nondestructive characterization method that has been extensively studied for metal surfaces (typically optical surfaces) is optical scattering [9-12]. Optical scattering occurs whenever a beam of light is incident upon a surface. Fundamental geometric optics predicts that, for a perfect reflector, the angle of reflection will be equal to the angle of incidence. However, if the surface on which the light is incident is transparent or semi–transparent, a component of the beam will be internally transmitted (except at the critical angle). Certain Si_3N_4 ceramics are partially transparent at selected wavelengths. Figure 1 shows a schematic diagram of an incident optical beam on a partially transparent material. A reflected beam, a transmitted optical beam, scattered light, and subsurface optical scatterers are present. However, many features on a scattering surface, particularly a machined ceramic surface, can cause scatter. These are shown schematically in Fig. 2, which shows a range of surface roughness, surface particulate, cutting–oil residues, and subsurface defects of different shape, orientation, and location.

Fig. 2. Schematic diagram showing different sources of optical scatter from a semi–transparent or transparent material, including a range of surface roughness.

It is important that we develop non–destructive methods that can discriminate between surface effects and subsurface defects. One such method, the method chosen for this study, involves the use of optical scattering and selected optical insertion and detector systems; a polarized incident laser light and a polarization analyzer are present in the detector. This is often referred to in the literature as a cross–polarization method. Figure 3 shows a schematic diagram relating the polarized direction of the laser light to the surface of a material, as well as incident and reflected beams. The material surface under study is in the x-y plane. For detection of subsurface defects surface scatter can be considered the noise and subsurface scatter the signal.

To improve the signal–to–noise (S/N) rati when detecting subsurface defects, on must either remove the surface effects c enhance the scatter caused by surfac topography by removing subsurface scatt effects. This is accomplished by selectir appropriate source and detectc polarization. In addition, the numeric aperture used in the detector system i important, because the reflected–light an scattered–light vectors are slightly differer (see Fig. 3).

Fig. 1. Schematic diagram of the optical scattering components for a semi-transparent poly-crystalline ceramic.
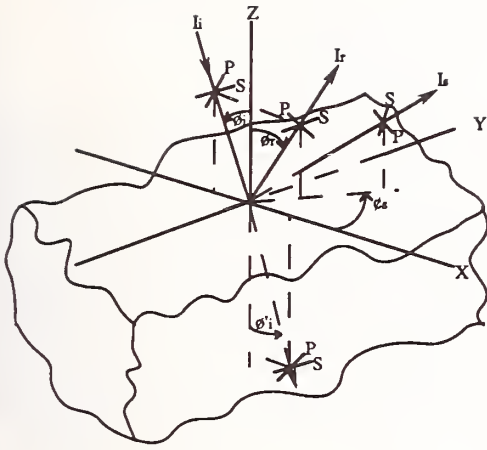
Fig. 3. Schematic diagram showing
polarization direction relative
to the material surface.

To understand scattered light, several
detector schemes have been studied by
previous researchers [13]. Total integrated
scatter (TIS) has usually been with a
He-Ne laser, optical components to filter
the beam, a detector to collect the total
scattered light over 2π steradians, and two
detectors specifically to detect specularly
and directly scattered light. Figure 4
shows a schematic diagram of a typical TIS
system. Note that no polariza-tion
analyzers are in place. TIS is related to
surface finish [11] as follows:

$$TIS = \frac{V_s}{V_{s+\Delta s}} \cong \left(\frac{4\pi\delta}{\lambda}\right)^2 ,$$

where

V_s = Voltage of detector for
scattered light only

$V_{s+\Delta s}$ = Voltage of detector for
scattered light plus
specularly scattered light

δ = rms surface roughness, μm

λ = Wavelength of incident
light, μm
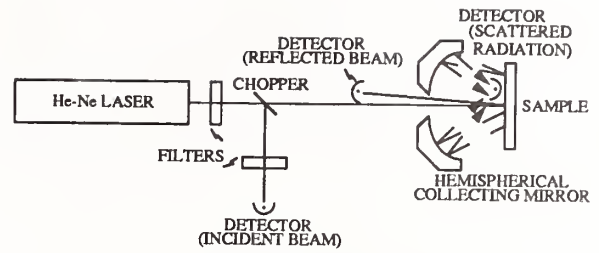
Fig. 4. Schematic diagram of the basic
components of an instrument for
measuring total integrated scatter.

Another method, angle-resolved scattering
(ARS), usually includes a He-Ne laser, but
incorporates optical components in the
input optics that provide a way to set
polarization, and an analyzing polarizer in
the detector, which is mounted on a
rotating stage to detect angular-dependent
scatter. Figure 5 shows a schematic
diagram of the basic components of an
ARS instrument. According to Bennett
and Matteson [11], little data are available
to relate ARS to surface roughness.
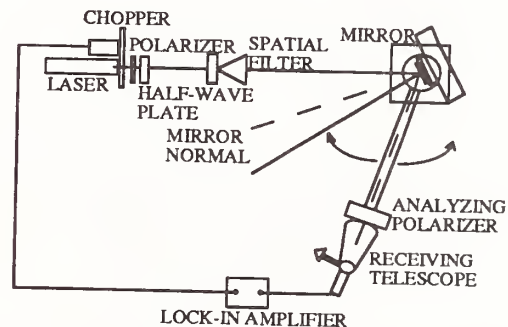
Fig. 5. Schematic diagram of basic
components of instrument
for measuring angle-resolved
scattering.

Probably the most robust analytical
approach to scattering distribution
developed to date is the bidirectional-
scatter distribution function (BSDF), first
proposed by Nicodemus et al., [14] in
1977. Variations of this function are
BRDF, BTDF, and BVDF, for reflective,
transmissive, and volume scattering,

respectively. All these variations, however, are considered subsets of BSDF, which is usually quantified in radiometric terms as the quotient of the scattered surface radiance divided by the incident surface radiance [9,11]. In Fig. 6, the scattered surface radiances is the light flux scattered per unit surface area per unit solid angle, i.e.,

$$S = \left(\frac{dp}{A}\right)\left(\frac{1}{\text{projected solid angle}}\right)$$

$$\text{in} \quad \frac{\text{watts}}{\text{mm}^2},$$

where

the projected solid angle = $(d\Omega_S)(\cos\theta_S)$.
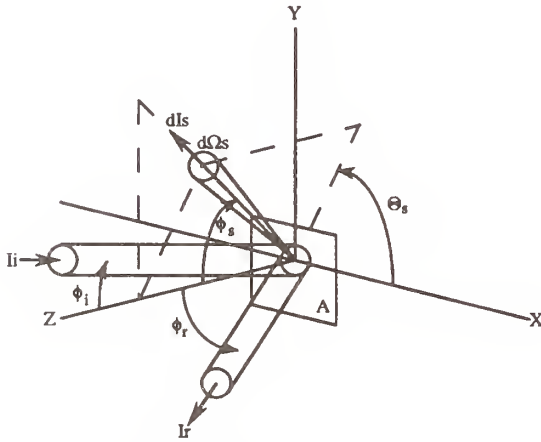
Fig. 6.   Schematic diagram showing the geometry for the definition of the bidirectional scatter distribution function.

The incident surface irradiance is the light flux on the surface per unit of illuminated surface area [11], i. e.,

Incident surface irradiance I =

$$\frac{Pi}{A} \quad \text{in watts / mm}^2.$$

Thus,

$$\text{BRDF} \quad = \quad \frac{S}{I} \quad = \quad \frac{dP/A}{Pi/A} \cdot \frac{1}{d\Omega_S \cos\theta_S} \quad =$$

$$\frac{1}{Pi}\left(\frac{dP}{d\Omega_S \cos\theta_S}\right).$$

Because the BRDF accounts for differences in reflected light, it will be modified as a function of the position of any analyzing polarizer and the type of scatterer. Thus, one should be able to discriminate subsurface defects from surface effects if the polarization effects of subsurface defects are large enough and the optical properties of the material are appropriate.

Optical Fourier transform theory [15] predicts that scatter patterns from surfaces will not be random. This is illustrated in Fig. 7, which shows predicted Fourier components of light scattered from various types of surfaces. Combining these theories suggests that coupling Fourier optics with an analyzing polarizer in the detector system would make it possible to detect and characterize subsurface defects, providing that polarization effects attributed to the defects are large enough and that the material has appropriate optical transmission characteristics.

In this study, we have found that, for two types of Si_3N_4 ceramics, the optical transmission properties are such that depths >100 μm of material can be penetrated at λ = 0.63 μm and that, for the two simulated types of defects, i.e., voids (by drilled holes) and parallel cracks (by saw cuts), the polarization effects are sufficient to allow detection if the surface finish is ground (<.07 μm Ra) or ground and polished (<.03 μm Ra).

TEST PROCEDURE

Specimens

In the test procedure, flexure test bars 3 x 5 x 25 mm of two HIP'd Si_3N_4 materials were produced and then machined by either a grinding procedure or a grinding procedure followed by polishing. Four bars were made of each material. Two of each were ground and polished and two were ground only. In each group, ground
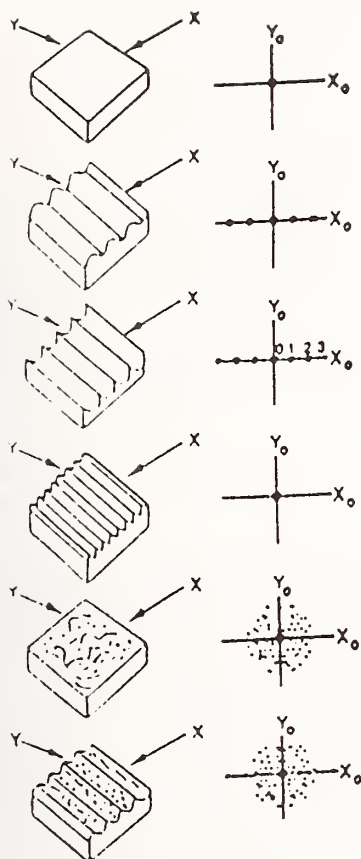
Fig. 7. Schematic diagram showing predicted two-dimensional Fourier transform plane of light scattered off various types of surfaces: (a) perfect flat, (b) periodic (sinewave), (c) periodic (d) periodic (saw tooth), (e) random, and (f) periodic plus random.

and polished or ground only, ultrasonically drilled non-through holes, 750 μm in diameter, were drilled perpendicular to the machined surface from the side opposite to the machined surfaces. Thus, the machined surface appeared defect free. A series of two to four holes, ≈2-4 mm apart, were drilled so that the defect depth below the machined surface ranged from 50 to 200 μm. Similarly, slots were cut in bars so that 50–200 μm of material remained.

Test equipment

The hybrid optical detector system used in this study is schematically illustrated in Fig. 8, which shows that a horizontally

polarized 35 mw He-Ne laser is followed by a λ/2 plate to allow polarization of the light to selected angles. A spatial filter with a 6.3 μm pinhole and 24 mm collimator is used together with a 95–cm focal length plano-convex lens to focus the light on a spot. The spot size was ≈1 mm in diameter. The detector system consisted of a polarization analyzer, a 110–mm diameter, 155–mm focal length double convex lens, an image display plate and a 512 x 512 charge–coupled–device (CCD)–array TV camera coupled to a lens with remotely controllable zoom and iris. The output of the CCD camera was fed to an eight-bit A/D board of a PC that was loaded with image software locally modified to perform digital image subtraction.

EXPERIMENTAL SET-UP
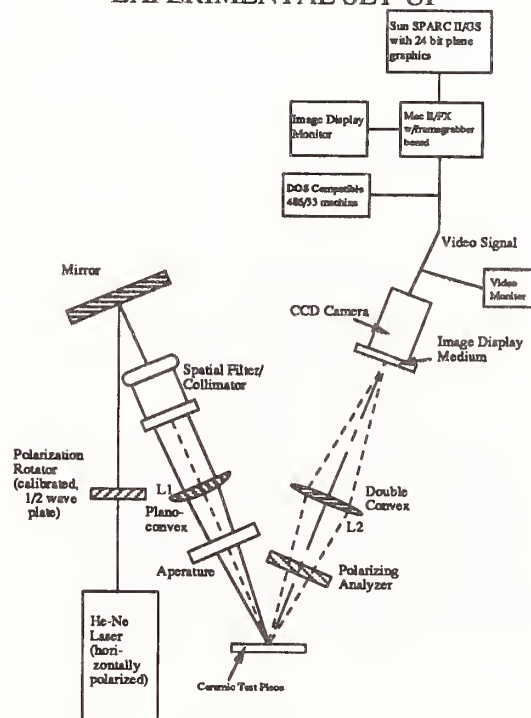
Fig. 8. Schematic diagram of experimental optical system used to study surface and subsurface defects.

The test specimens were mounted on a rotate-translate stage equipped with stepper motors. Thus, a specimen could be translated at constant incidence angle or rotated to change the angle of incidence (hence reflection). Although the entire optical system was mounted on a 1.3 x 2.7 x .3 m solid granite vibration–isolated

151

optical bench, we found that it was unnecessary to isolate the optical table.

Procedure

After each specimen was carefully mounted, the polarization analyzer was set so that almost total extinction of light occurred. This angle changed slightly with each finish type. Four to six optical Fourier transform images were taken at locations on the samples away from the intentional defects. These images were then averaged in the computer. This averaged data set was stored in the computer memory. By virtue of the modified software, we could set the computer so that image subtraction from "live video" from the CCD camera occurred. What this implies is that as the specimen was translated and subsequent images were displayed on the computer monitor, if these images did not substantially deviate from the "average image", the result would be a blank (or totally dark) image. However, if any subsequent image would deviate from the "average image" within the limits of the detection system, then only that "difference image" would appear. Such "difference images" were obtained by careful step-wise scanning of each ceramic test piece. The size of the step could be varied from 50 μm to over 1 mm by the translation stage. By using this method, and digitally storing scanned images, analysis of the difference images by digital image processing methods could be performed. At the present time, this analysis consists primarily of gray-scale histogram analysis to establish differences in the images that can be used to establish defect detection sensitivity.

RESULTS AND DISCUSSION

At the time we began these studies, we did not know if the optical transmission properties of the selected polycrystalline ceramics would allow sufficient penetration to allow detection of subsurface defects. Thus, we determined the initial optical transmission properties of the selected materials.

To obtain initial optical transmission properties, step wedges of both ground and polished and unidirectionally ground materials with step thicknesses of 100, 200, 400 and 600 μm were used with laser light of $\lambda = 0.6328$ μm. The results demonstrated sufficient optical transmission to begin an initial subsurface detection experiment. Previously available optical transmission data were for single-crystal Si_3N_4 and these data show that there is a wide window of optical transmission. However, no data were available for optical transmission properties of polycrystalline Si_3N_4.

Although the microstructure of each material is quite different, as shown in Fig. 9, these microstructures (obtained by polishing and etching) are typical for Si_3N_4. Notably, each material has elongated 3–5–μm grains and grains with diameters up to 1 μm. Although quoted as having a grain size <0.5 μm by some producers, the Si_3N_4 grains have high aspect ratios and these microstructures will need to be well defined for light scattering studies, especially for detection of subsurface defects.

All experimental data reported here were obtained by using an incidence angle (off surface normal) of 20°. This was the smallest angle achievable with the test equipment. Optical Fourier scatter patterns were obtained on all specimens and are similar to theoretically predicted patterns for randomly rough or unidirectionally roughened surfaces. Typical patterns obtained are shown in Fig. 10 for both a ground and polished specimen (Ra = 0.03 μm) and a unidirectionally ground specimen (Ra = 0.07 μm). These images can be compared to those shown conceptually in Fig. 7. With the experimental equipment used, no significant differences between ceramic materials specimens were verified. However, we observed experimental suggestions of differences that we have not had time to thoroughly study at this time.

For artifical subsurface defects (drilled holes), using the "difference image" method, we could easily detect 75– and 105–μm–deep defects on either the ground and polished or ground specimens. This was observable in real-time during live video subtraction and was verified by

histogram analysis. A typical example of our results is shown in Fig. 11, which shows optical Fourier transform difference images of specimens with no defects, a 75–μm–deep defect, and a 102–μm–deep defect on one of the ground and polished specimens. What is notable in these difference images is that the "no–defect image" is not totally black. This is thought to be caused by local differences in microstructure, as noted in Fig. 9. Microstructural differences may give rise to changes in polarization of scattered light, which would then pass the analyzing polarizer and be detected.

Fig. 10. Typical experimentally obtained optical Fourier transform scatter patterns obtained away from subsurface defect for (a) ground and polished and (b) unidirectionally ground only specimens of polycrystalline Si_3N_4. Note that the images show the significant differences in surface theoretically predicted in Fig. 7.

Fig. 9. Microstructure of two Si_3N_4 ceramics, used in this study: (a) material A, and (b) material B.
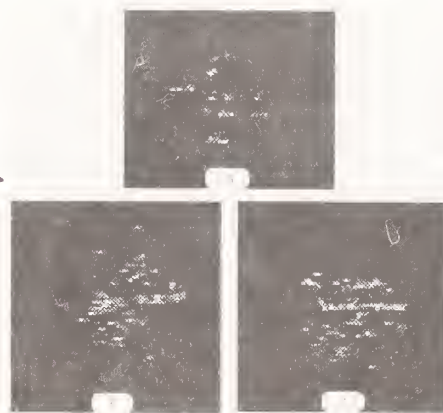
Fig. 11. Typical optical Fourier transform difference images (100 x 100 pixel) experimentally obtained on ground and polished (0.03 μm Ra) specimens with drilled–hole simulated defects: (a) No defect, (b) 75–μm–deep defect, and (c) 102–μm–deep defect.

For synthesized defects, a different scatter pattern is seen. The differences are manifested in both a large number of high-amplitude components (intensity of white spots) and Fourier component distribution as shown in Figs. 11b and c. These

153

differences are quantified in Fig. 12, which shows typical histograms of the gray–scale values of the resulting total difference images.

To understand the histograms in Fig. 12, we study the number of pixels with intensity values less than 138 (0 is white, 255 is black). The reason for this is that lower gray–scale values indicate larger quantities of light passing through the analyzing polarizer than in the no–defect average image. Thus, we see significant differences between the 75–μm–deep defect and the 102–μm–deep defect. This is as expected, because of the more significant attenuation (scatter) for deeper defects. Further, if one carefully examines the different images of Fig. 11, it is clear that the higher spatial frequency components of the 102–μm–deep defect have less intensity than the high spatial frequency components of the 75–μm–deep defect. Thus, analysis of these components, unless totally defect–size dependent, may provide a method to establish depth sensitivity. Similar results were obtained on other ground and polished specimens.

Figure 13 shows the experimentally obtained optical Fourier transform difference images for a ground specimen (Ra = .07 μm). As with the ground and polished specimens, we see distinct high–frequency components with much greater intensity (brightness), for regions of the bar with a defect than for regions without a defect, and further, the intensity is greater for the 75–μm–deep defect than for the 102–μm–deep defect.

This observation is quantified by examination of the histograms shown in Fig. 14. Once again, the highest brightness is observed for the specimen with the 75–μm defect.

For the synthesized crack defect specimens, only the edge of the cut could be detected by the scatter. This is currently thought to be caused by the repeated internal reflections within the cut cavity itself, which reduces the power of any light scattered back to the detector.
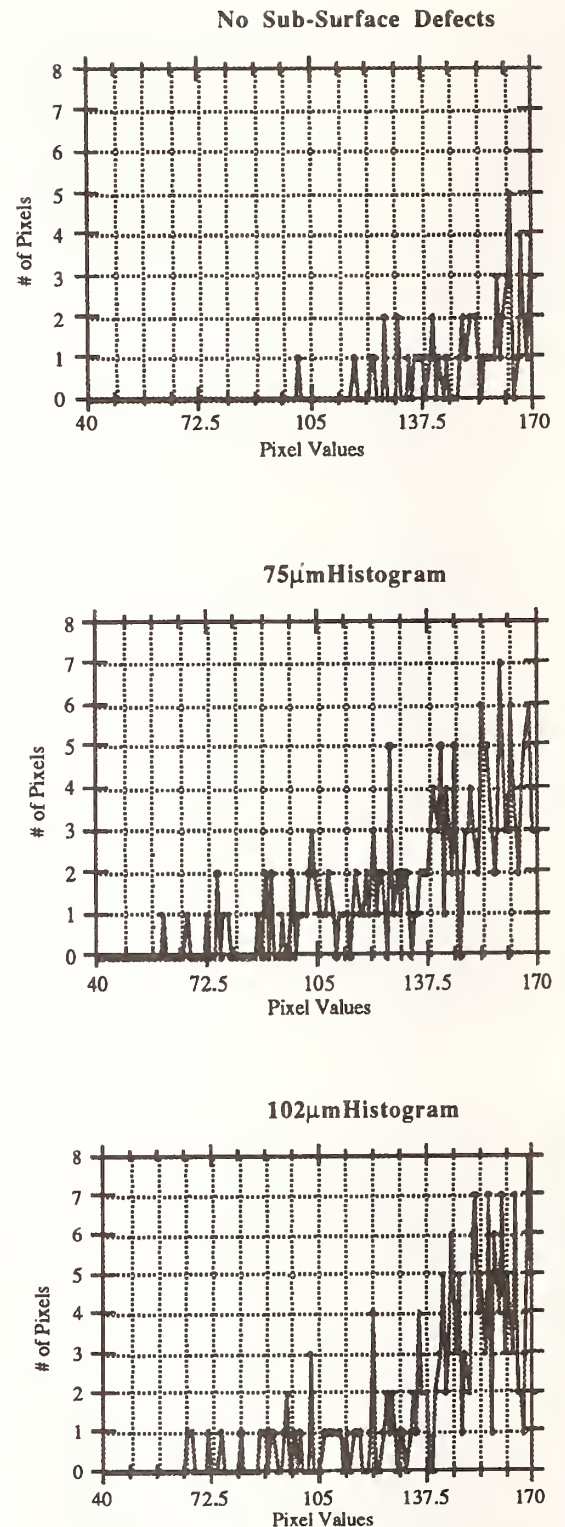
Fig. 12. Histograms of the gray scales of the optical Fourier difference images shown in Fig. 11 for ground and polished specimens (0.03 μm Ra) with drilled–hole simulated defects: (a) No defects, (b) 75–μm–deep defect, (c) 102–μm deep defect

154
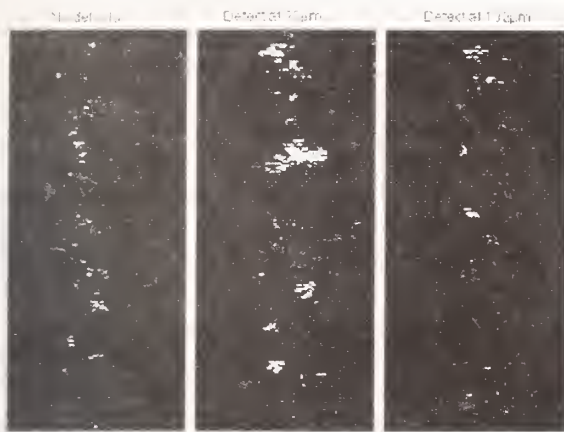
Fig. 13. Typical optical Fourier transform difference images experimentally obtained on ground specimens (0.07 μm Ra) with drilled–hole simulated defects: (a) no defect, (b) 75–μm–deep defect, (c) 102–μm–deep defect.

DISCUSSION AND SUMMARY

Optical scattering by a hybrid cross-polarization, Fourier-optics method has been used to detect subsurface defects, in the form of simulated voids, in ground and polished and unidirectionally ground Si_3N_4 specimens. Detection of subsurface defects is possible because of the optical transmission properties of polycrystalline Si_3N_4. Specimens from two sources were studied. The grain sizes of these specimens were found to be quite large, with diameters of 1 μm and aspect ratios of 3-5. For He-Ne lasers, $\lambda = 0.63$ μm, this means that the scatterer is as much as 10 times the wavelength of the light used. We have not yet studied grain size effects on scatter and only limited machined surface variations have been attempted. These defect and grain-size effects must be separated if possible. The impact of grain size will need to be carefully studied because it is likely that subsurface, machining-induced damage will be grain-size dependent. Further, it is not clear exactly what effect angle of incidence has on detection sensitivity, even though Fan and Huynh [16] and Cuthbert and Huyeh [17] have recently studied some of these aspects. Our current work studied scattering with a 20° angle of incidence and this also must be optimized.
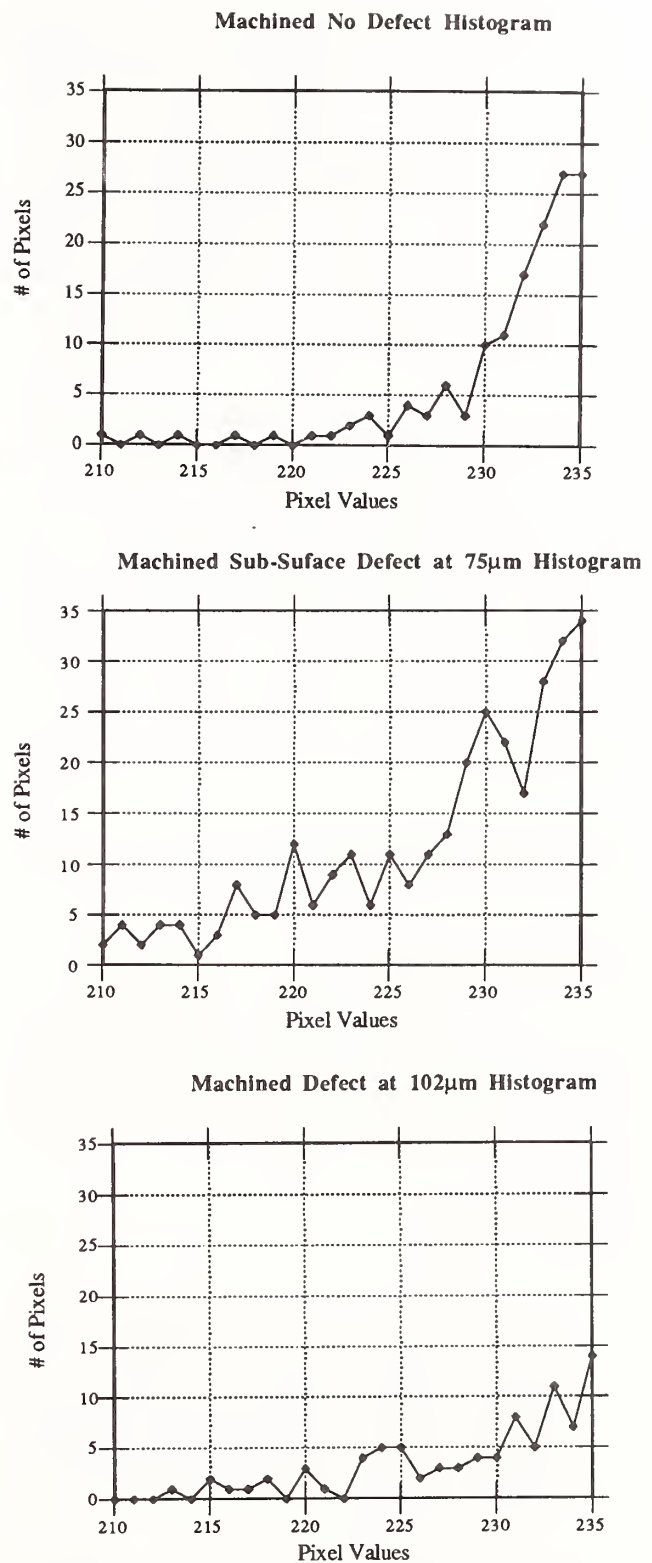
Fig. 14. Histograms of gray scales of the optical Fourier difference images for drilled–hole simulated defects shown in Fig. 13 (0.07 μm Ra): (a) No defects, (b) 75–μm–deep defect, (c) 102–μm–deep defect

In addition, the effect on polarization of surface characteristics of ceramics developed by different machining methods must be established. Bennett and Mattesan [11] and Stover [9] have indicated that greater penetration of semi-transparent materials will be possible if other than s-polarized light is used, because s-polarization maximizes reflection and minimizes transmission. Clearly, this needs to be examined in more detail.

Because of their complex curvature, ball bearings will have to be rotated rather than translated for surface studies. For full 4π–steradian coverage, methods to spin the balls must be developed; this is considered possible at the present time. For most ceramic races, the fatigue life will mainly be influenced by the contact points below the balls. Because bearing races are cylindrical, optical scatter details are not currently thought to present significant problems, and will be addressed in the future.

This method appears capable of detecting subsurface microcracking as well.

ACKNOWLEDGMENT

REFERENCES

1. Y. Nishihara, H. Nakashima, N. Tsushima, and S. Ito, "Factors that Affect Rolling contact Fatigue Life of Ceramics and Rolling Contact Fatigue Life of Ceramic Balls and Rollers," ASME paper 90–GT–377, Brussels, Belgium, 1990.

2. H. Takebayashi, T. M. Johns, K. Rukkaku, and K. Tanimoto, "Performance of Ceramic Bearings in High-Speed Turbine Application," Society of Automotive Engineers, paper 901629, Milwaukee, WI, Sept. 1990.

3. E. V. Zaretsky, "Ceramic Bearings for Use in Gas Turbine Engines," ASME J. of Engineering for Gas Turbines and Power, Vol. 111, No. 1, pp. 146-157, 1989.

4. J. F. Chudecki, "Ceramic Bearings – Applications and Performance Advantages in Industrial Applications," SAE Technical Paper Series 891904, 1989.

5. S. A. Horton, "Detection of Surface Defects in Ceramic Rolling Elements," proceedings of the 4th International Congress on Materials for Advanced Heat Engines, Goteborg, Sweden, 1991, Elsevier App. Sci., pp. 897-904.

6. R.T. Cundill, "Material Selection and Quality for Ceramic Rolling Elements," ibid., pp. 905-912.

7. S. Jahanmir, L. K. Ives, A. W. Ruff, and M. B. Peterson, "Ceramic Machining: Assessment of Current Practice and Research Needs in the United States," National Institute for Science and Technology, Special Publication 834, June 1992.

8. S. Jahanmir (editor), Ceramic Bearing Technology, National Institute for Science and Technology Special Publication 824, November 1991.

9. J. C. Stover, Optical Scattering Measurement and Analysis, McGraw–Hill, New York, 1990.

10. T. V. Vorburger and E. C. Teague, "Optical Techniques for On-line Measurement of Surface Topography," Precision Engineering, Vol. 3, No. 2, pp. 61-83, 1981.

11. J. M. Bennett and L. Mattson, Introduction to Surface Roughness and Scattering, Optical Society of America, Washington, DC, 1989.

12. B. Ruffing and J. Anschutz, "Surface Roughness Measurement by 2-D Digital Correlation of Speckle Images," Society of Photo-Optical Instrumentation Engineers, Vol. 814, pp. 105-112, 1987.

13. M. Shiraishi, "Scope of In-process Measurement, Monitoring and Control Techniques in Machining Process: Part 1. In-process Techniques for Tools," Precision Engineering, Vol. 10, No. 4, pp. 179-189, 1988.

14. F. E. Nicodemus, J. C. Richmond, J. J. Hsia, I. W. Ginsberg, and T. Limperis, Geometric Considerations and Nomenclature for Reflectance, U.S. National Bureau of Standards (NBS) Monograph 160, U.S. Department of Commerce, 1977.

15. J. W. Goodman, Introduction to Fourier Optics, McGraw-Hill, New York, 1968.

16. Y. Fan and V. M. Huynh, "Investigation of Light Scattering from Rough Periodic Surfaces: Numerical Solutions," Optics and Laser Technology, Vol. 24, No. 3, pp. 145–150, 1992.

17. L. Cuthbert and V. M. Huynh, "Statistical Analysis of Optical Fourier Transform Patterns for Surface Texture Assessment," Measurement Science and Technology, Vol. 3, No. 8, pp. 740–745, 1992.

CHATTER AND SURFACE PATTERN DETECTION FOR CYLINDRICAL GRINDING USING A FLUID COUPLED ACOUSTIC EMISSION SENSOR

Y. P. CHANG and D. A. DORNFELD
University of California, Berkeley, CA

An acoustic emission (AE) sensor setup has been designed to monitor the cylindrical grinding process using the coolant fluid as the signal transmission media. Modifications have been made in the coolant flow path to compensate for the problem of coolant flow instability inherent in a fluid coupling setup. Experiments have been conducted to evaluate the effectiveness of this setup on monitoring grinding chatter and grinding patterns. The root mean square energy of AE is used as the primary sensor signal characteristic. Successful detection of chatter vibration has been achieved through this setup. Defection of workpiece surface patterns existing prior to grinding has been investigated.

INTRODUCTION

Grinding is usually used as a finishing process in manufacturing. Therefore, the workpiece quality (surface pattern, roughness, and roundness) produced by the grinding process is critical to the quality of the product, and damage to the workpiece caused by abnormalities in the grinding process is very often irreversible. Since it is often difficult or practically impossible to predict these abnormalities much attention has been paid to the use of sensors for process feedback[1-4] and control[5].

Originally applied to the destructive testing of structures, acoustic emission (AE) has became a monitoring technique in manufacturing due to its sensitivity to process parameters. Active research in AE has shown the strong potential of this technique in manufacturing process monitoring [6]. Successful applications of AE for grinding processes have been developed in monitoring contact and spark-out, wheel dressing, wheel wear, chatter detection, workpiece surface roughness, and process parameter variations [7-13]. A fundamental study of AE in grinding was conducted by Dornfeld and Cai [7], in which the sensitivity of AE for detecting contact/noncontact between wheel/workpiece was established. Research has been performed on AE for monitoring wheel loading conditions [7-8], and wheel dressing conditions [10-11], and to predict wheel life in different grinding processes. With respect to monitoring of surface properties, Inasaki has investigated the influence on AE amplitude due to the change in workpiece surface roughness [8]. And several studies were done on correlating the AE signal to the work surface finish in turning process [14-17].

This study differs from earlier research in accessing surface roughness in grinding with AE [12] in that it determines the feasibility of using AE to observe the repetitive 2-D patterns generated on the work surface during cylindrical grinding. The attempt here is to establish a relationship between the in-process AE signal with those patterns on the work surface. Surface roughness values will be used to quantify the work surface characteristics.

EXPERIMENTAL SETUP

The design of the AE instrumentation in the present setup, which is different from that used in previous work [12], is shown in Figure 1, and is aimed at solving the problem of coolant flow noise. The instability of the output flow rate from the coolant pump, and the interaction between grinding wheel and coolant fluid have been the major contributors to coolant flow noise generation. In this work, a fluid reservoir has been incorporated into the coolant flow path, as indicated in Figure 1. This reservoir acts as two filters removing the flow rate instability (since the output flow rate is determined by the inlet diameter, outlet diameter, and fluid height in the reservoir and not directly related to the output of coolant pump) and minimizing the bubbles in the output flow of the coolant pump.

To avoid interaction between the coolant and the grinding wheel, the coolant stream is directed just adjacent to the grinding wheel. In this way the stream has minimum interaction with the grinding wheel (preferred from the sensor point of view) while still giving a satisfactory cooling effect for the process. The cutting signal generated at the cutting point travels through the workpiece and coolant to the AE transducer mounted on the coolant supply tube.

Figure 1 illustrates the setup on a cylindrical grinding machine. The diameter of the aluminum oxide grinding wheel is 9.6 in. (243.8mm); the workpiece is made of 1045 steel with the size of 72.1mm dia. and 304.8mm length. The grinding wheel speed is 1720rpm, and workpiece speed is 200rpm. The feed rate (grinding table speed) is 20in/min (508mm/min). And the typical value of depth of cut is 0.0005in. (0.0127mm). A broadband transducer is used to detect the AE signals, which pass through a cascade of preamplifier and main amplifier providing a total gain of 50 dB. The amplified AE signals were recorded by a modified video recorder. A proximity transducer was installed on the head stock spindle to measure the rotational speed of the work-
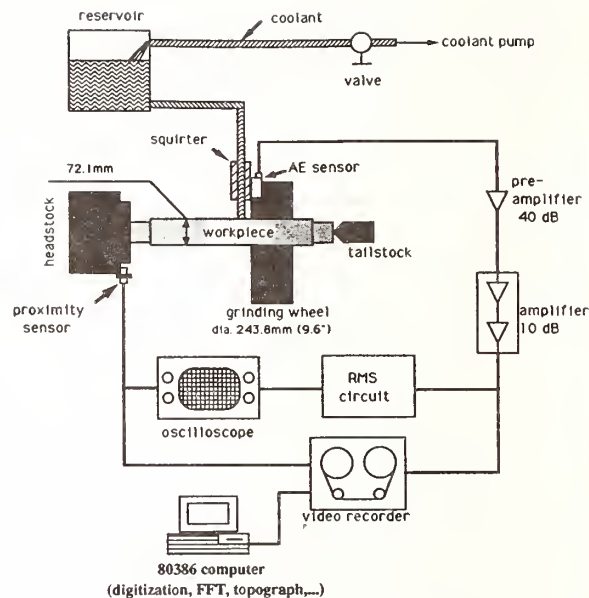
Fig.1 The Set-Up for Grinding Experiments with AE Sensor

piece. The signal from the proximity transducer also acts as the base line for positioning the AE signal on the workpiece surface. This signal was recorded on the audio channel of the video recorder. Both the AE root mean square (rms) energy signal and the proximity sensor signal were monitored on a digital oscilloscope. Digitization of the signals for analysis (calculation of Fast Fourier Transfer and rms) were performed on a personal computer.

The surface profile measurements were done by a stylus surface measurement instrument connected to a personal computer. Measurement of surface roughness along the axial direction of the cylindrical workpiece was straightforward since the instrument was designed to measure "flat" surfaces. For measurement along the periphery of the workpiece, the surface profile at 15 degrees to the center axis was measured and the peripheral profile approximated by geometrical calculations.

CHATTER DETECTION

The chattering phenomenon investigated in this study can be classified as self-excited grinding vibration. The vibration can be a

160

result of many factors including flexibility of workpiece-wheel structure, repetitive roundness error of the wheel/workpiece, which gives periodic variation on the depth of cut, and wheel wear. In this study, the wheel wear condition is the major cause of chatter.

At the beginning of each chatter experiment, the grinding wheel is dressed. Several cutting passes are conducted with one sparkout pass following each cutting pass. As the cutting passes continue, the wheel becomes progressively more loaded. The loaded wheel contributes additional thrust force components to the wheel/workpiece interaction in addition to the cutting force from the fresh wheel, which acts on the workpiece tangential to the workpiece circumference. This thrust is repetitive since the grinding wheel is rotating at a constant speed. As the wheel loading increases, the repetitive thrust will have an increasing magnitude, and the magnitude of the machine resonant frequency excited by the thrust will also increase. This phenomenon has been referred to as "chatter growth". The chattering noise is audible when it reaches a certain magnitude. The experiment is halted when the chatter noise is first detected by the technician operating the experiment to prevent machine damage.

Figure 2 shows the frequency spectrum of the root-mean-square energy, AE_{rms}, for five consecutive cutting passes. The sparkout passes conducted after each cutting pass have not been included in the figure. These sparkout passes are used to clean up the workpiece surface without any infeed of the grinding wheel. The chattering disappears in these sparkout passes.

The "chatter growth" phenomenon can be easily observed in the AE_{rms} signal at the frequency of 417.5Hz (Fig.2). According to other research results, an increase in depth of cut (radial engagement) gives a larger AE_{rms} signal level [7] and more severe chatter vibration. The exponential trend of the signal growth would have been more dramatic had the depth of cut not been reduced for different cutting passes.
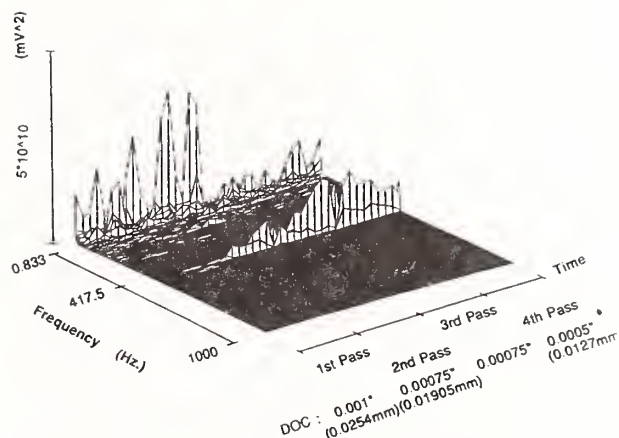
Fig.2 FFT of AE_{rms} for consecutive Cutting Cycles

The workpiece surface profile after the fifth pass in Figure 2 has been preserved and measured. There are chatter marks along the circumferential direction, which can be easily observed. Visually counting the marks (approximate 126 chatter marks can be spotted on the workpiece) with a workpiece rotation frequency of 3.15Hz the chatter frequency is calculated to be at 396.9 Hz, which is close to the resonant frequency of the AE_{rms} signal.
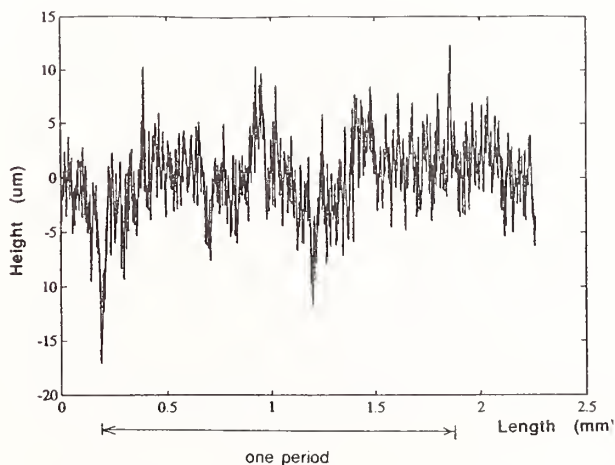
Fig.3 Surface Profile along the Workpiece Circumference

Figure 3 is the measurement result of the surface profile in the circumferential direction. The length for one period of chatter mark is calculated to be 1.8 mm. The average peak-to-valley height for the chatter marks is 30 μm. Since generating this surface resulted in

a significant AE signal level, seen in Figure 2, and from the signal growth in the same figure, chatter vibrations with smaller peak-to-valley heights are detectable by AE. Figure 4 shows the AE_{rms} for a less severe chatter vibration and the generated surface profile with peak-to-valley height at an average of 20 μm.

To examine the similarity between AE_{rms} and chatter marks, the AE signal has been filtered by a band pass finite impulse response (FIR) filter at 417.5 Hz. The filtered signal is then synchronized with work rotation using the proximity sensor signal. Finally this synchronized signal is mapped to a two dimensional contour plot to show the AE signal patterns. Figure 5a shows the 3-D plot of AE_{rms} after filtering and synchronization. Figure 5b illustrates the blow up of figure 5a in 2-D contour plot, which clearly shows the patterns contained in the signal. It is observed that the AE signal pattern is similar to the chatter marks on the work surface.

DETECTION OF WORK-PIECE SURFACE PATTERNS

This is a preliminary approach to detecting workpiece surface patterns generated during grinding by using the AE signal. In this approach, surface patterns have been artificially generated on the workpiece before the grinding process. The workpiece is then ground and AE signals recorded to determine the sensitivity of the AE signal to the existing patterns of the surface profile. The first group of experiments qualitatively tested the feasibility of this approach, while in the second group of experiments a quantitative test was attempted.

Two or three strips with a coarse surface roughness were generated on the workpiece surface along the axial direction by manual filing, as indicated in Figure 6. Figures 7- 9 show the 1-D, 2-D, and 3-D views of the AE_{rms} after synchronization to work rotation for the case with two strips on the workpiece. As illustrated in Figure 7 there are two signal spikes in each period of workpiece rotation. When all
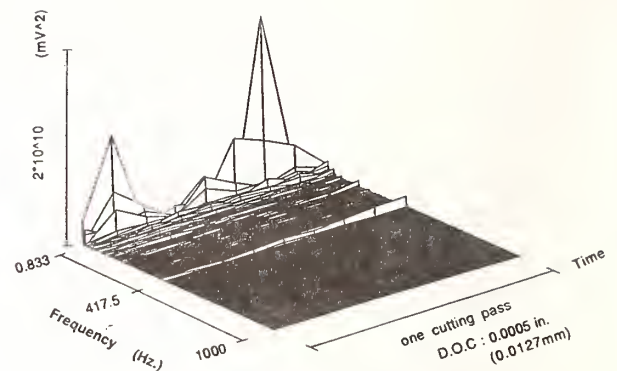
Fig.4 FFT of AE_{rms} for Less Severe Chatter
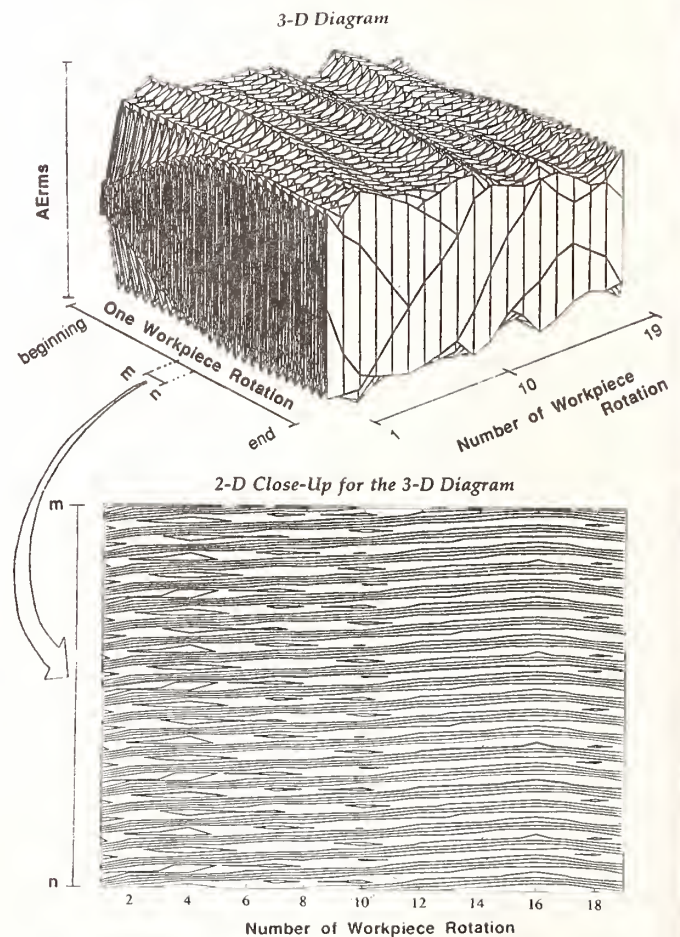
Fig.5 AE_{rms} Signal at the Chatter Frequency

162

the workpiece rotation periods for the cutting pass were joined in the 2-D contour plot, as in Figure 9, it can be observed that the AE_{rms} forms two strips along the axial direction of the workpiece. These strips are at the equivalent location to those physically on the workpiece. Figure 9 gives a three dimensional view of the AE signal, in which the strips contained in the signal can be clearly observed. Similar results were obtained for the case of three surface strips.
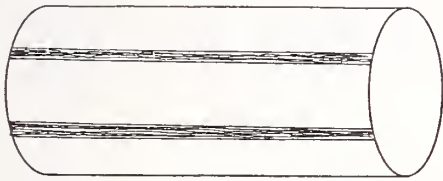
Fig.8 2-D Diagram of AE_{rms} for Workpiece with 2 Strip Patterns

Fig.6 Simulated Grinding Patterns on the Workpiece
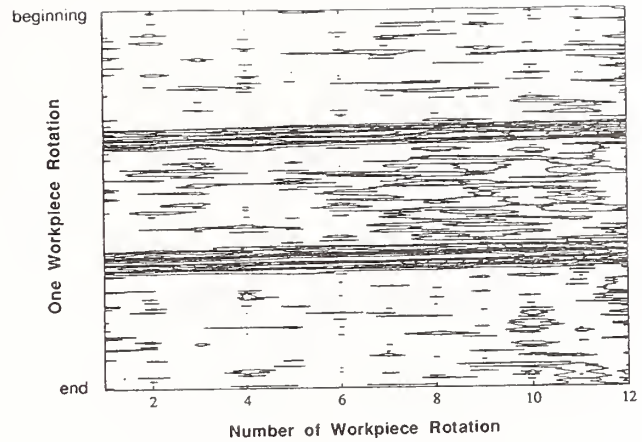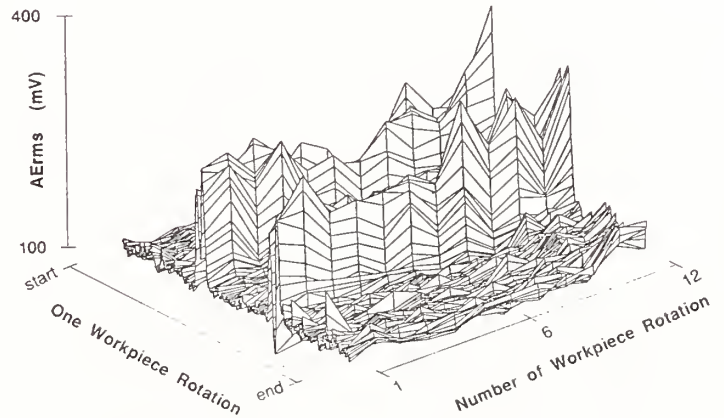
Fig.9 3-D Diagram of AE_{rms} for Workpiece with 2 Strip Patterns

In another set of experiments, quantification of the signal sensitivity was attempted. Three slots were machined on the workpiece surface by slitting saws. The width of the slots are 0.008 in. (0.203mm), 0.030 in. (0.762mm), and 0.040 in. (1.016mm). The slots lay along the axial direction on the workpiece surface at constant increments (120 degrees apart on the circumference). Figure 10 is a typical 1-D signal representation from a cutting pass for this workpiece. Signal spikes similar to previous experiment results were observed. The 2-D contour plot of the signal, as depicted in Figure 11, reflects the pattern of the slots with equivalent locations. Consecutive cutting passes were performed on the workpiece, with depth of cut varying at some passes, to gradually remove

Fig.7 1-D Diagram of AE_{rms} for Workpiece with 2 Strip Patterns
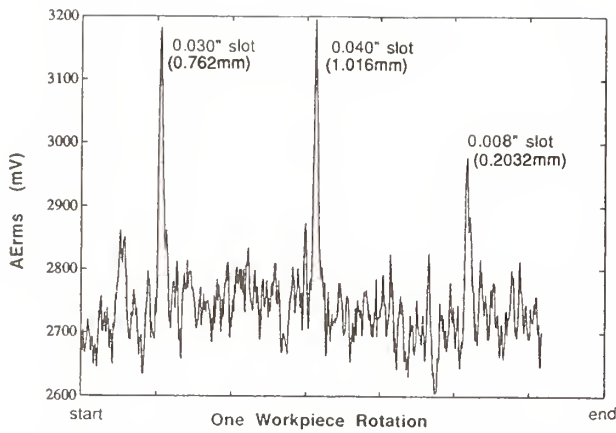
Fig.10 1-D Diagram of AE_{rms} for Workpiece with 3 Slots
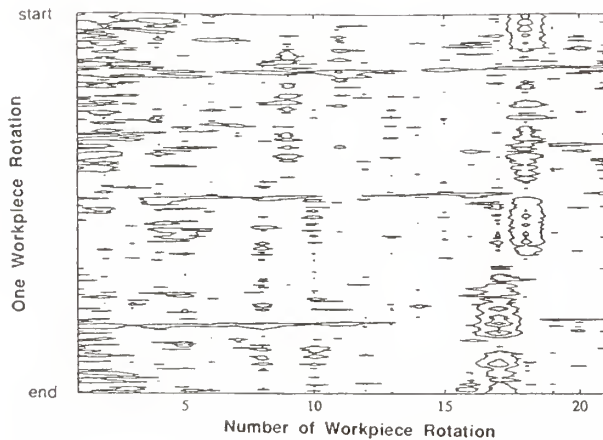
Fig.11 2-D Diagram of AE_{rms} for Workpiece with 3 Slots

the slots in the workpiece. The signal patterns for different passes were investigated.

The average mean and standard deviation (STD) of AE_{rms} were plotted in Figures 12 and 13. The average AE_{rms} mean, Fig. 12, reflects the variation in depth of cut but not the dimensions of the slots. This results from the fact that the change in metal removal rate introduced by the slots is so small that it does not affect the average value for the whole cutting pass. From Figure 13, two levels of standard deviation value were observed. For the first 11 cutting passes, when all the slots were present existing, the standard deviation values were at a higher level. During the 12th and 13th cutting passes where part of the slots

were removed, the level for standard deviation started to drop. Finally, for the 14th to 16th cutting passes where no slots existing on the workpiece, the standard deviation stayed at a lower level which was approximately 50 mV below the higher level. This figure, however, only gives information about pattern existence in a macroscopic view. To understand the existence of individual slots, the AE_{rms} signal corresponding to each slot was investigated.
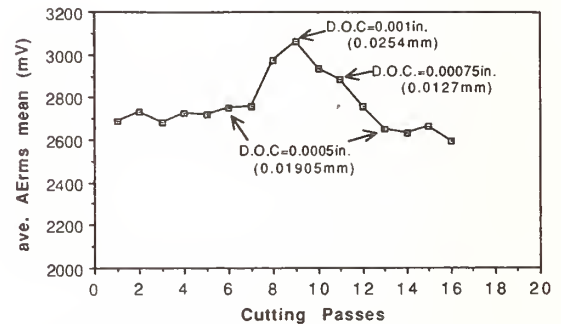
Fig.12 Ave. AE_{rms} Mean for Different Cutting Passes
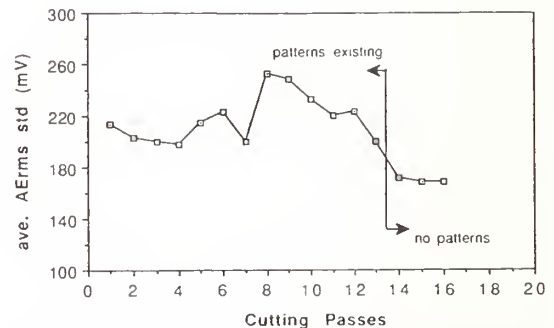
Fig.13 Ave. AE_{rms} Standard Deviation for Different Cutting Passes

Figure 14 is the 1-D signal diagram from the last cutting pass where no slots existed on the workpiece before grinding. The signal positions corresponding to the three slots are indicated on the diagram. It can be observed that the signals at these positions are the same as others, which is very different compared to the spikes they generated in Figure 10. It is, therefore, reasonable to assume that the signal generated by the slots are among the most spiky for the whole cutting pass. The "spikiness" of the AE_{rms} signal generated by the

164

slots were characterized by the deviation of the spike from the mean of the cutting pass signal. If the assumption is correct, the deviations should be bounded by a certain value related to the standard deviation of the cutting pass signal.
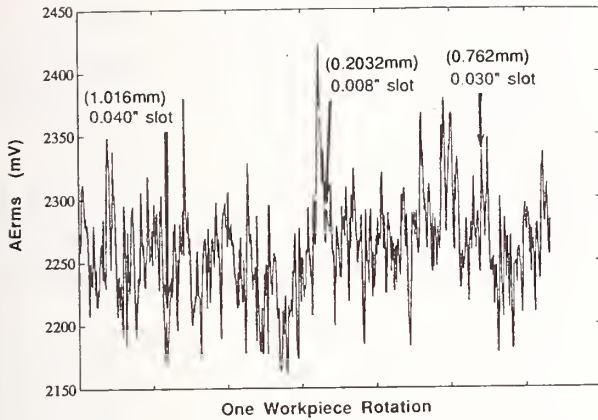
Fig.14 1-D Diagram of AE_{rms} for Workpiece with no Slots (previous location of slots shown by arrow)

To verify the assumption, the deviations were compared with the average standard deviation for each slot in every cutting pass. As illustrated in Figure 15, there were two levels of deviation values for each slot - the higher one for slot existence and the lower one for slot when removed. Through visual inspection between each cutting pass, it was recorded that after the 11th cutting pass, the 0.030 in. (0.762mm) slot was completely removed. And after the 12th cutting pass, the 0.008 in. (0.203mm) slot was also completely removed. At the end of the 13th cutting pass, all three slots were completely removed. From the correlation of this observation and the signal levels in Figure 15, it was concluded that the assumption was correct.

To utilize the assumption for slot existence detection, a threshold value is necessary to divide the spikes from other signals in the cutting pass. The threshold value of signal deviation was set to be 2.2 standard deviations based on the experiment results. It is assumed that a normal distribution describes the AE_{rms} from regular cutting passes on workpieces with no
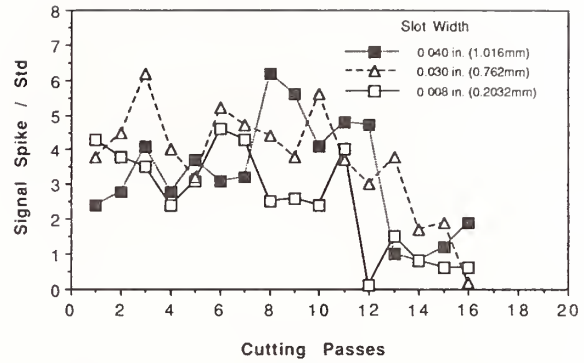
Fig.15 Ration of Spike Level over Standard Deviation for Different Cutting Passes

repetitive patterns. The 2.2 standard deviation threshold implies that the signal spikes generated by the slots on the workpiece will always fall among the highest 2.3 percent of the signals for the cutting pass.

CONCLUSIONS

The detection of grinding chatter and workpiece surface patterns has been studied using a refined fluid coupled acoustic emission sensor setup. It was shown that the AE_{rms} signal was able to pick up the chatter vibration generated through the grinding process. The chatter growth phenomenon was captured in the frequency spectrum of AE_{rms} during several cutting passes. Simulated grinding patterns on the workpiece were detected by the variation of the multi-dimensional AE_{rms} signal spikes. A suitable threshold of the variation for indicating surface defects has been determined to be 2.2 times standard deviation.

This technique is presently under evaluation in an industrial cylindrical grinding operation. The objective of that evaluation is to determine whether or not process instabilities (chatter) and the resulting surface degradation can be detected in process using acoustic emission sensing. Signal levels exceeding a threshold would indicate generation of surface defects and the grinding machine controller could respond by a change in feed rate or cycle stop to alert operators.

References

[1] Gao, Y. and Jones, B. 1992, "An Integrated Sensor System for Size and Roundness Control in Plunge Grinding", Int. J. Mach. Tools Manufact., Vol. 32, No. 3, pp. 281-290.

[2] Shiraishi, M. 1988, "Scope of In-Process Measurement, Monitoring and Control Techniques in Machining Processes- Part 1: In Process Techniques for Tools", Precision Engineering, Vol. 10, No. 4, pp.179-189.

[3] Shiraishi, M. 1989, "Scope of In-Process Measurement, Monitoring and Control Techniques in Machining Processes- Part 2: In Process Techniques for Workpiece", Precision Engineering, Vol. 11, No. 1, pp.27-37.

[4] Shiraishi, M. 1989, "Scope of In-Process Measurement, Monitoring and Control Techniques in Machining Processes- Part 3: In Process Techniques for Cutting Processes and Machine Tools", Precision Engineering, Vol. 11, No. 1, pp.39-47.

[5] Gao, Y. Jones, B. and Webster, J. 1992, "An Integrated Size and Roundness Adaptive Control System for the Plunge Grinding Process", Int. J. Mach. Tools Manufact., Vol. 32, No. 3, pp.291-303.

[6] Dornfeld, D. A. 1992, "Application of Acoustic Emission Techniques in Manufacturing", Proc. 11th Int'l Acoustic Emission Symposium, JSNDI, Fukuoka, Japan, pp.1-15.

[7] Dornfeld, D. A. and Cai, H. G. 1984, "An Investigation of Grinding Processes with Acoustic Emission", Trans. ASME, J. Eng. Industry, Vol. 106, no. 1, pp. 28-33.

[8] Wakuda, M. and Inasaki, I. 1991, "Detection of Malfunctions in Grinding Processes", Proc. 4th World Meeting of Acoustic Emission, ASNT, Boston, MA, pp. 494-501.

[9] Inasaki, I. 1991, "Monitoring and Optimization of Internal Grinding Process", Annals CIRP, Vol. 40, no. 1, pp. 359-362.

[10] Inasaki, I. and Okamura, K. 1985, "Monitoring of Dressing and Grinding Processes with Acoustic Emission Signals", Annals CIRP, Vol. 34, no. 1, pp. 277-280.

[11] Konig, W. and Meyen, H. P. 1990, "AE in Grinding and Dressing: Accuracy and Process Reliability", Proc. 4th International Grinding Conference, Technical Paper MR90-526, SME, Detroit, Michigan.

[12] Chang, Y. P. Diniz, A. E. and Dornfeld, D. A. 1992, "Monitoring the Grinding Process through Acoustic Emission Using a Squirter", Proc. Japan-USA Symposium on Flexible Automation, ASME, San Francisco, CA, pp. 335-340.

[13] Blum, T. and Dornfeld, D. A. 1990, "Grinding Process Feedback using Acoustic Emission", Proc. 4th International Grinding Conference, Technical Paper MR90-525, SME, Detroit, Michigan.

[14] Diniz, A. E. Liu, J. J. and Dornfeld, D. A. 1992, "Correlating Tool Life, Tool Wear, and Surface Finish Roughness by Monitoring Acoustic Emission in finish Turning", Wear.

[15] Blum, T. Suzuki, I. and Inasaki, I. 1988, "Development of a Condition

Monitoring System for Cutting Tools
using an Acoustic Emission Sensor",
Bulletin Japan Soc. Prec. Eng'g, 22, 4,
pp. 304-308.

[16] Dalpiaz, G. 1991, "Monitoring Workpiece
Quality Deterioration in Turning by AE
Analysis", Proc. 4th World Meeting on
Acoustic Emission, ASNT, Boston, MA.,
pp. 479-486.

[17] Diniz, A. E. Liu, J. J. and Dornfeld, D.
A. 1991, "Monitoring the Surface Rough-
ness Through AE in Finish Turning",
Proc. 4th Meeting on Acoustic Emission,
ASNT, Boston, MA., pp. 487-493.

EFFECT OF GRINDING ON STRENGTH

HIGH EFFICIENCY GRINDING OF STRUCTURAL CERAMICS

H. G. WOBKER and H. K. TONSHOFF
University of Hannover, Hannover, Germany

Advanced structural ceramics, such as silicon nitride or alumina, are attractive for many advanced applications due to their high strength at elevated temperatures, wear resistance and chemical stability. During the sintering process ceramics undergo a volumetric shrinkage and thus are far from meeting high demands on their form and size accuracy. To meet these demand in most cases grinding with diamond tools is necessary as a finishing process. The cost associated with this manufacturing step may reach up to 60 % of the total cost thereby diminishing the competiveness of ceramic parts. The paper presents an approach in grinding of these materials, based on the model of the equivalent chip thickness in grinding. The correlation between the chip thickness and the subsurface damage is used for the process layout. Thereby it is possible to reduce machining time effectively and to avoid effects of the grinding process on materials strength.

0   Introduction

Advanced structural ceramics such as silicon nitride or alumina are attractive for many advanced applications due to their high strength at elevated temperatures, resistance to chemical degradation, wear resistance, and low density. Despite these advantages there are considerable impediments to the introduction of advanced ceramics. With current technology fabrication costs are high, compared to other materials and component reliability is uncertain. The cost of machining can be as high as 90 percent of the total cost of some high precision components; and damage produced during machining can produce premature failure due to crack growth under stress. Thus apart from suitable material properties safe and economic machining is another prerequisite for a wider use of structural components (1-4).

1   Aim of the study and experimental details

Although advances have been made in near-net shape technology, machining in the fired condition remains to be the predominant process for the manufacturing of structural ceramics. In order to achieve high quality surfaces and high geometric accuracy the last step in manufacturing of ceramic components is grinding with diamond wheels. However, cutting, grinding, and polishing operations were found to leave subsurface cracks and

residual stresses in the surface layer of, brittle materials (Fig. 1) (1-3). The strength degration effect of microcracks in the surface of ceramics can easily be understood by equations of fracture mechanics. The stress necessary to propogate a microcrack is given in equation 1 (5),

$$\sigma_B = K_{Ic} \cdot Y \cdot \frac{1}{\sqrt{c}} \qquad /1/$$

While K_{Ic} is the fracture toughness of the material, Y refers to the crack geometry and c gives the crack length. If we assume a semicircle-shaped crack with a radius c = 50 µm, the bending strength of silicon nitride ceramic will be reduced by at least 30 percent.

It is obvious that compressive stresses acting at the flaw crack tips can increase strength by suppressing crack growth
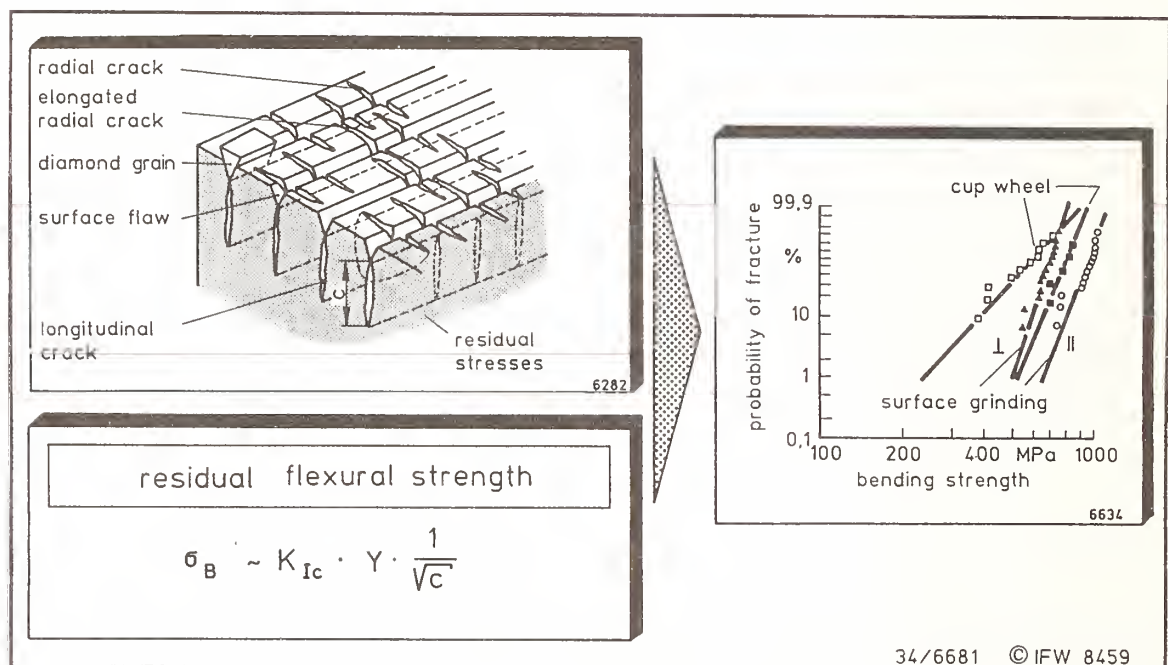
Fig. 1: Influence of machining on the strength of brittle materials

under stress. The interaction of flaws of different size, orientation and length and residual stresses is the origin for the effect of grinding on bending strength and fracture probability of ceramics. Fig. 1 shows strength values obtained from conventional surface and cup wheel ground silicon nitride (6).

The present study intends to investigate the interaction between machining conditions in grinding and the induced stresses

and microcracks in order to achieve an optimized process design in terms of productivity and product quality.

This paper reports on investigations conducted on alumina reinforced with dispersed zirconia and on hot isostatic pressed silicon nitride. The materials properties are given in Table I. The ceramics were ground with diamond cup wheels of different grit size and concentration in order to achieve flat

surfaces of different roughness and states of surface integrity. Residual machining stresses were evaluated by using x-ray diffractometry. For the variation of the penetration depth of the x-rays copper, chromium and titanium anode x-ray tubes were used (7). The bending strength of the ground samples were evaluated by four-point bending tests. For each grinding condition a set of 40 samples was tested.

Table I: Material Properties

	Al_2O_3/ZrO_2	$Si_3N_4-Y_2O_3$
Vickers hardness (HV 0,5)	2000	1500
Flexural strength (σ_{4bB}) MPa	600	750
Youngs modulus (E) GPa	380	280
Poissions ratio (μ)	0.24	0.26
Weibulls Modulus (m)	10	15
Fracture toughness (K_{Ic}) MPa · $m^{0.5}$	5.8	6.0

The grinding experiments were conducted with resin bonded diamond cup wheels of 350 mm diameter and D15 - D181 (15 µm-181 µm) grit size. Tangential, normal and radial forces were measured and recorded. Castrol "Honilo" grinding oil with a viscosity of 4.15 mm^2/s (at 40 °C) containing phosphorus additives was supplied to workpiece/wheel interface as coolant using a single high pressure jet.

2   Results

2.1   Forces and wheel wear in grinding

Grinding damage in brittle materials orginating from mechanical loads is mainly due to the grinding normal force F_n. Initial grinding test were therefore carried out to identify the influence of machine settings on grinding forces and wheel wear. As the true grit load can not be measured, the average normal grinding force per unit wheel width F_n' is used to compare the different grinding conditions. For the

comparision and explanation of results a term called grit depth of cut is introduced which refers to a theoretically value the average depth of cut of a cutting point during machining. The grit depth of cut, or undeformed chip thickness h_{cu}, in face grinding is given by equation 2 (8).

$$h_{cu} = \left[\frac{2}{C \cdot r} \left(\frac{v_{fa}}{v_c} \right) \right]^{\frac{1}{2}} \qquad (2)$$

Where C is the number of cutting edges per unit area, r the chip width to thickness ratio, v_c the cutting speed and v_{fa} the axial feed speed.

For the test described in this part forces and wheel wear were measured after approximately V'_w = 600 mm^3/mm of stock had been removed. The wheels were dressed and profiled after each grinding cycle with SiC-wheels mounted on a rotary brake truer.

From Fig. 2 the influence of different wheel speeds on the grinding forces and the surface roughness can be observed. With increasing wheel speed the grinding forces gradually decrease. Higher wheel speeds at a constant material removal rate lead to a reduction of the grit depth of cut resulting in lower grinding forces.

From Fig. 3 the effect of the axial table feed speed in grinding of silicon nitride on grinding forces and surface roughness can be derived. In general, higher feed speeds should lead to higher grinding forces due to an increase in grit depth of cut. However an increase of the material removal rate by means of the feed speed v_{fa} in grinding of silicon nitride results in lower grinding forces. This indicates that the diamond grits are prevented from blunting at higher depth of cut and short grinding cycles.
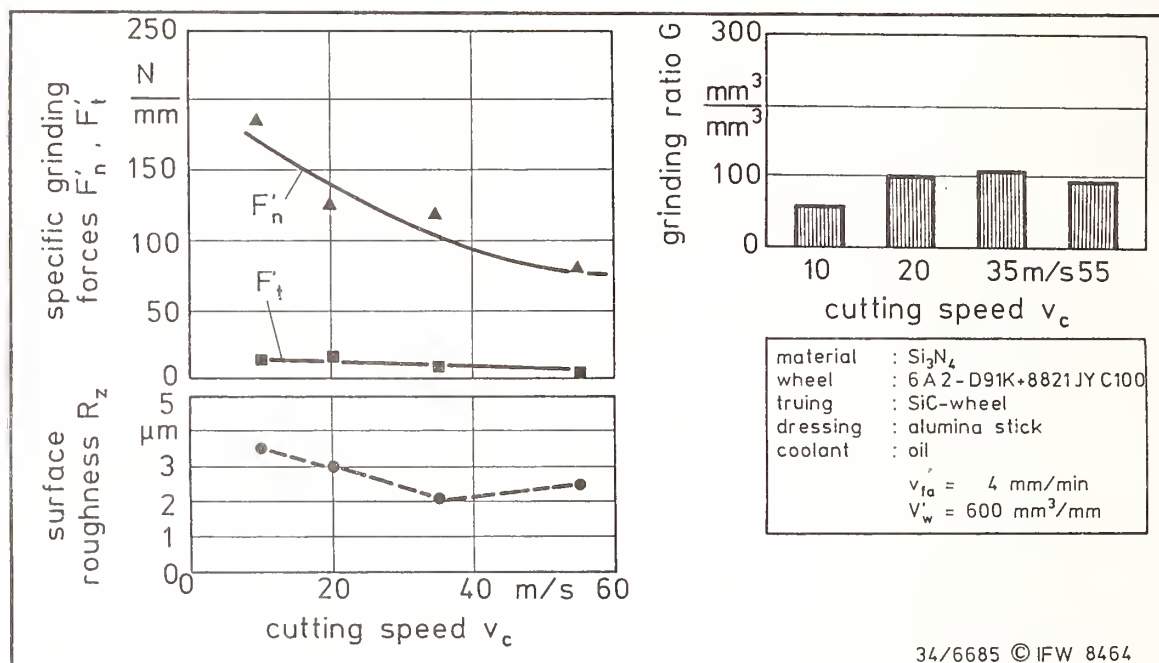
Fig. 2: Grinding forces at different cutting speeds

Consequently it is possible to increase efficiency of the grinding operation without any loss in accuracy.

Following general grinding technology, the use of "coarser" grit diamond wheels should result in lower grinding forces and a detoriation of the surface roughness of the ground parts due to the increased depth of cut. Fig. 4 shows results obtained from grinding using wheels of grit size D15-D181 at a constant material removal rate Q'_W. For the wheels with grit size D15-D91 the tendency is as expected, the forces decrease, simultaneously the surface roughness increases. However, comparing the results of the D91 wheel with those obtained with the D181 wheel the tendency is reversed. It appears to be possible to achieve surface roughness of the ground parts as good as those with the D46 wheel. This tendency can be explained by the number of cutting points per unit wheel surface. A coarser grit often show more than one cutting point (8),

therefore the total number of cutting points per unit wheel surface is higher compared to fine meshed wheels. The increase of the grinding forces observed with the coarse wheel supports this assumption.

All in all it can be stated that it is possible to maintain surface quality even with coarser wheels provided adapted truing and dressing cycles are applied.

Apart from grinding forces and surface roughness wheel wear in grinding of ceramics is another important factor. A comparison of G-ratios (i.e. stock removal/wheel wear) obtained in grinding of silicon nitride is given in Figure 4. From Figure 4 it appears that finer grit wheels wear relatively rapidly. Especially the DI81 wheel shows a good performance, due to its higher mecanical and thermal wear resistance.

174
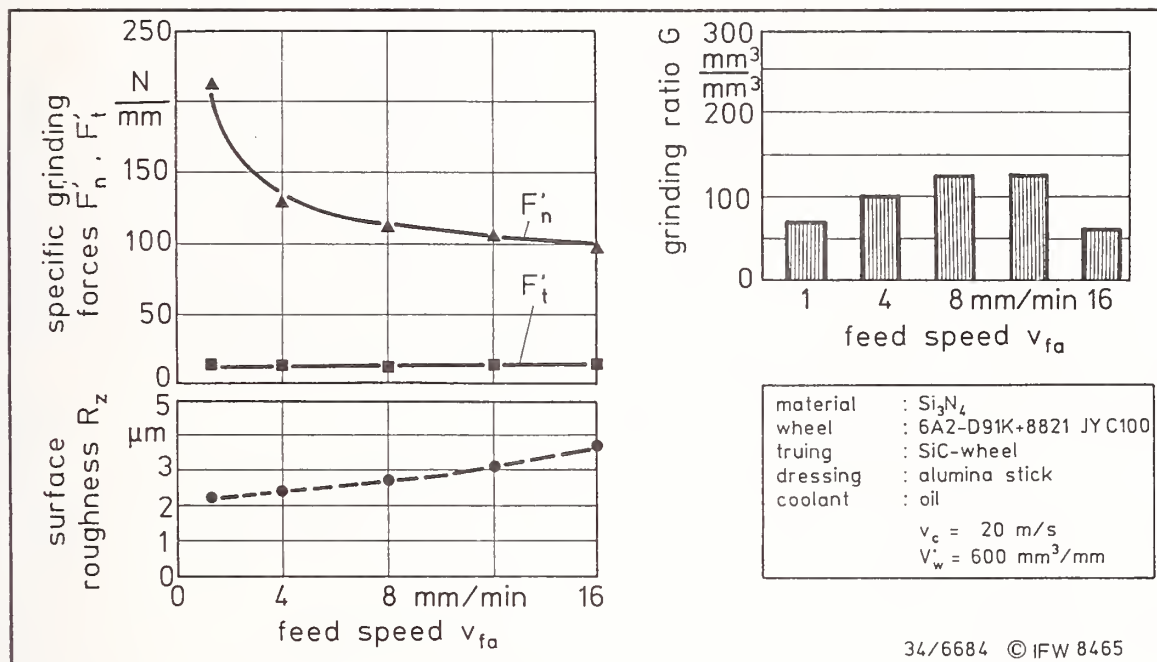
Fig. 3: Grinding forces versus axial feed speed
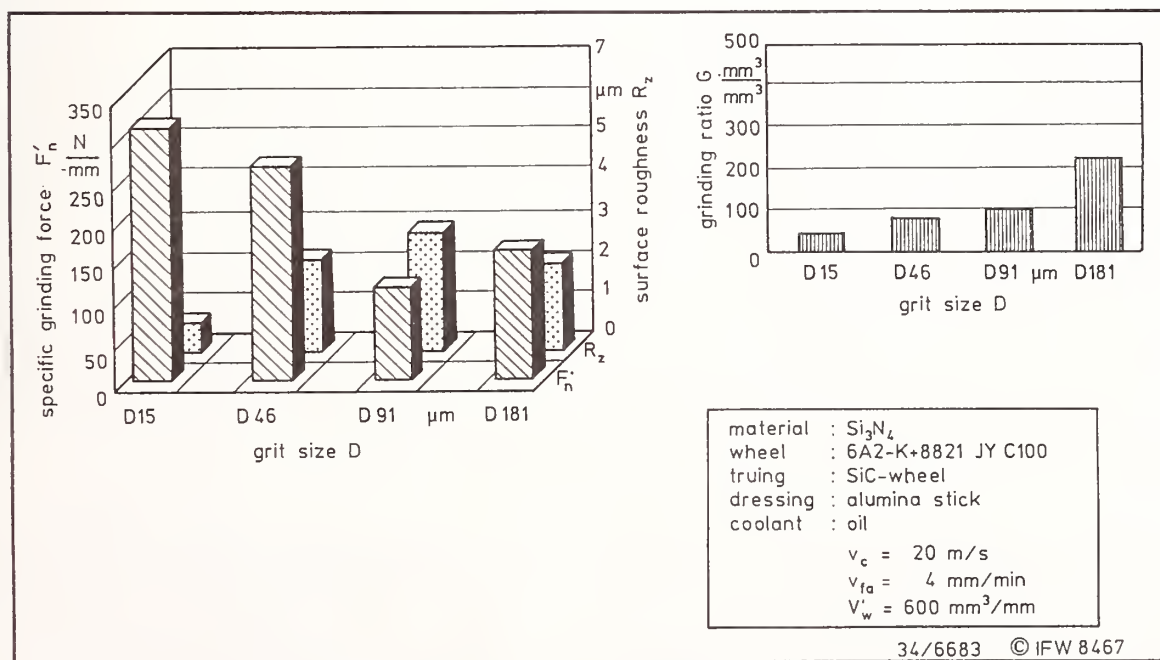
Fig. 4: Grinding forces and G-ratios for different grit sizes

The various grinding tests have demonstrated so far some potentials for an increase of efficiency in grinding of ceramics. However, the effect of the different machine settings and the wheel specifications on the workpiece quality i.e. residual stresses and subsurface damage, needs to be evaluated in order to maintain workpiece quality.

3.2 Residual stresses

For the exact description of the state of residual stresses in ground surfaces it is necessary to determine the stress depth profile and the orientation of the main stress direction. From metallic materials it is known that non-directional processes like a thermal influence produce no preferred orientation of the residual stresses. In contrast processes with a defined direction, like cutting or grinding are known to produce a distinctive orientation between residual stresses and the direction of cut. This is also true for residual stresses in ceramics as Fig. 5 demonstrates. The measurements revealed that the main stress direction is oriented perpendicular to the direction of cut, whereas a minimum is found in the direction of cut. The measurements were realized on the (030) lattice plane of the $Al_2O_3/10 \% ZrO_2$ ceramic.

The directional dependence of stresses in the surface layer correlates with the mechanical effects of the cutting edges. The largest amount of plastic deformation
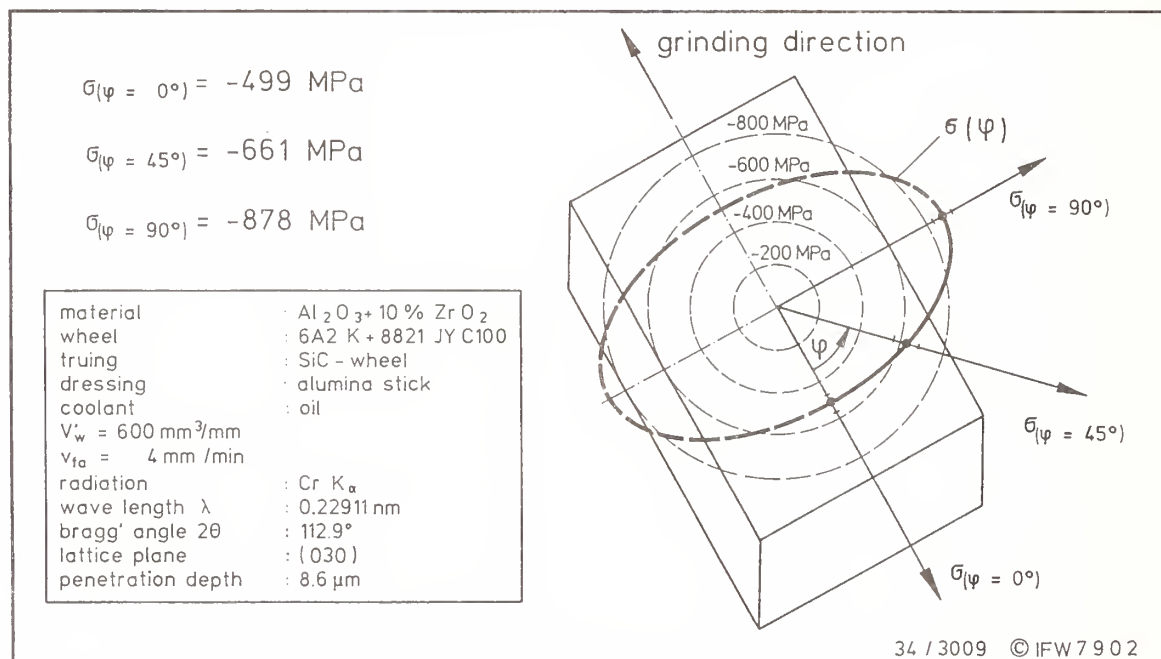
Fig. 5: Influence of the machining direction on residual stresses

is found perpendicular to the cutting direction. The material remaining in the cutting path is deformed plastically to a smaller extent due to crushing effects during material removal.

The penetration depth of x-rays depends on their wave length. It is defined as the value where the primary intensity is reduced to 1/e, or 37 percent of the initial value. In ceramics the layer of residual stresses extend well below the surface and

there are high stress gradients within the penetration depth of the radiation. Three different radiations where used to measure the stress versus depth profile in ground material. A typical profile found is shown in Fig. 6. The penetration depth of copper-K_α radiation in the Al_2O_3/ZrO_2 ceramic is about 17 µm at the (226) lattice plane and 21 µm at the (416) plane. Due to their longer wave length the use of chromium or titanium radiation reduces the penetration depth to 8 µm at the (030) plane and 4 µm at (113) plane respectively. Directly underneath the surface, high compressive stresses are found.

Figure 7 shows the effect of different cutting speeds on residual stresses in ground silicon nitride. The stresses decrease with increasing wheel speed in grinding. This corresponds to the alteration of the grinding forces which can be explained by the reduced grit depth of cut at high wheel speeds (4). Again, a comparison of stress values measured with chromium and copper radiation

indicates the existance of stress gradients in the subsurface layer.

To evaluate the influence of different wheel specifications on residual stresses, wheels of different grit size and concentration were compared (Fig. 8). All tests were conducted with diamond cup wheels at different cutting speeds. All wheel specifications tested showed the same tendency of lower compressive stresses at higher cutting speeds. Furthermore, at a defined cutting speed a coarser wheel with fewer cutting edges (i.e. coarser grit size or lower concentration) showed higher compressive stresses.

The reduction of cutting edges causes an increase of the grit depth of cut. With a higher grit depth of cut the forces acting at a single cutting point increase and thereby causing higher mechanical loading of the subsurface. With higher mechanical loading an increased plastic deformation and higher compressive stresses are likely.
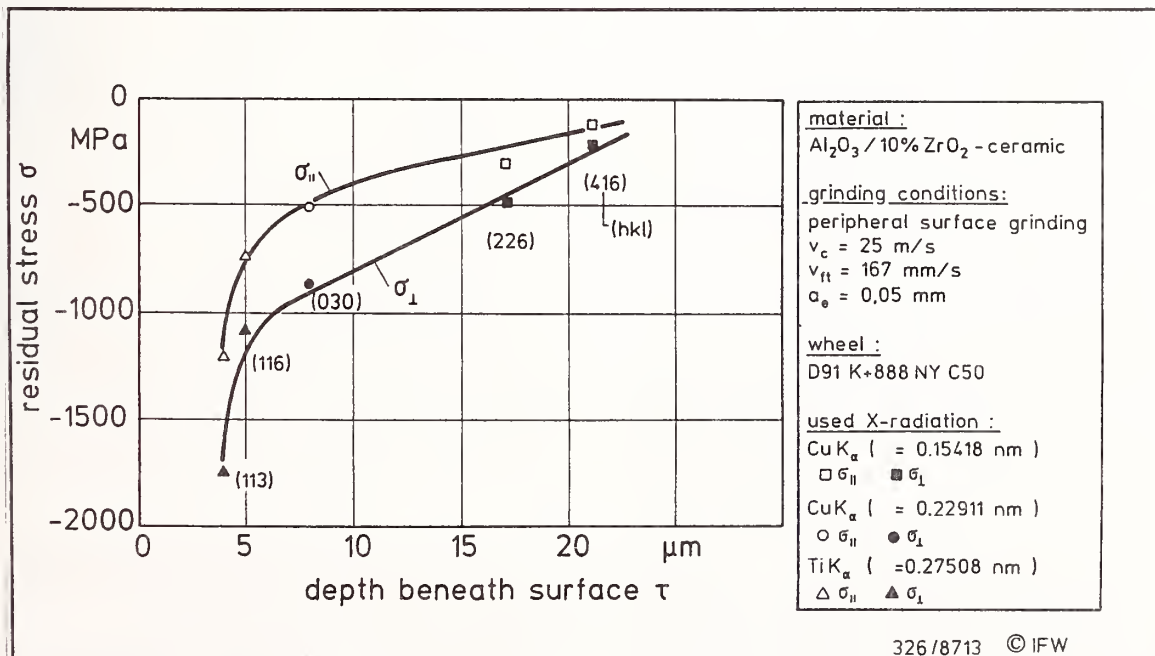
Fig. 6: Stress versus depth profile in ground Al_2O_3/ZrO_2 ceramic
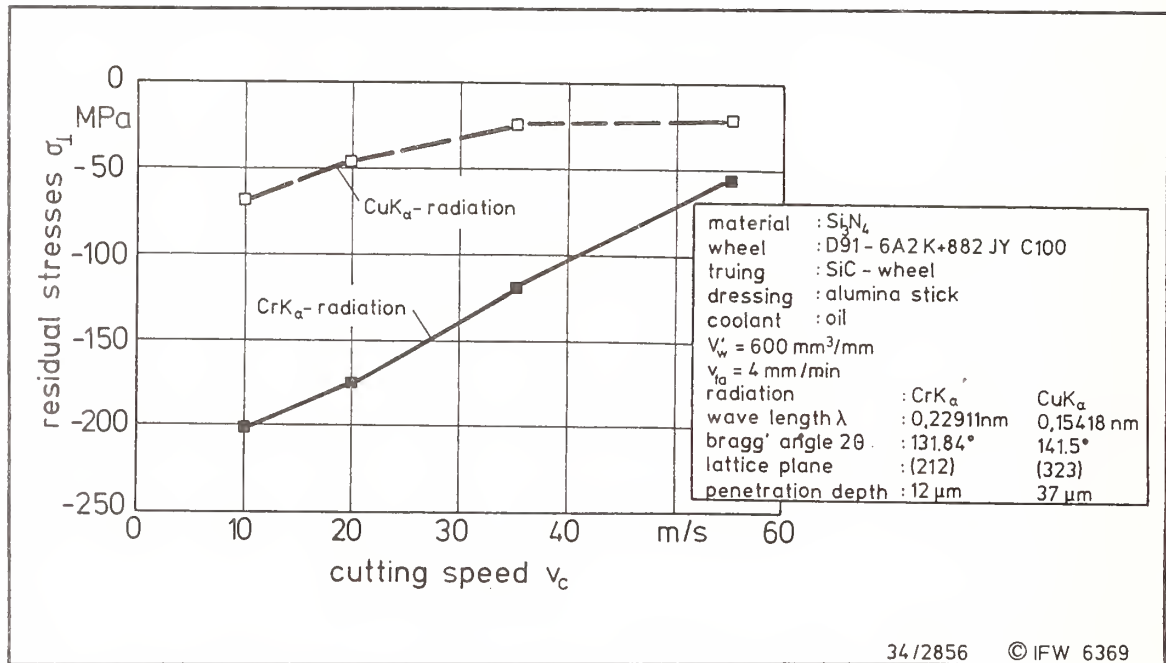
Fig 7: Influence of cutting speed on residual stresses

Within Fig 7:

residual stresses $\sigma_\perp$ / MPa

CuK_α – radiation

CrK_α – radiation

material	: Si_3N_4	
wheel	: D91 – 6A2 K+882 JY C100	
truing	: SiC – wheel	
dressing	: alumina stick	
coolant	: oil	
V'_w = 600 mm³/mm		
v_{fa} = 4 mm /min		
radiation	: CrK_α	CuK_α
wave length λ	: 0,22911nm	0,15418 nm
bragg' angle 2θ	: 131.84°	141.5°
lattice plane	: (212)	(323)
penetration depth	: 12 µm	37 µm

cutting speed v_c

34/2856   © IFW 6369
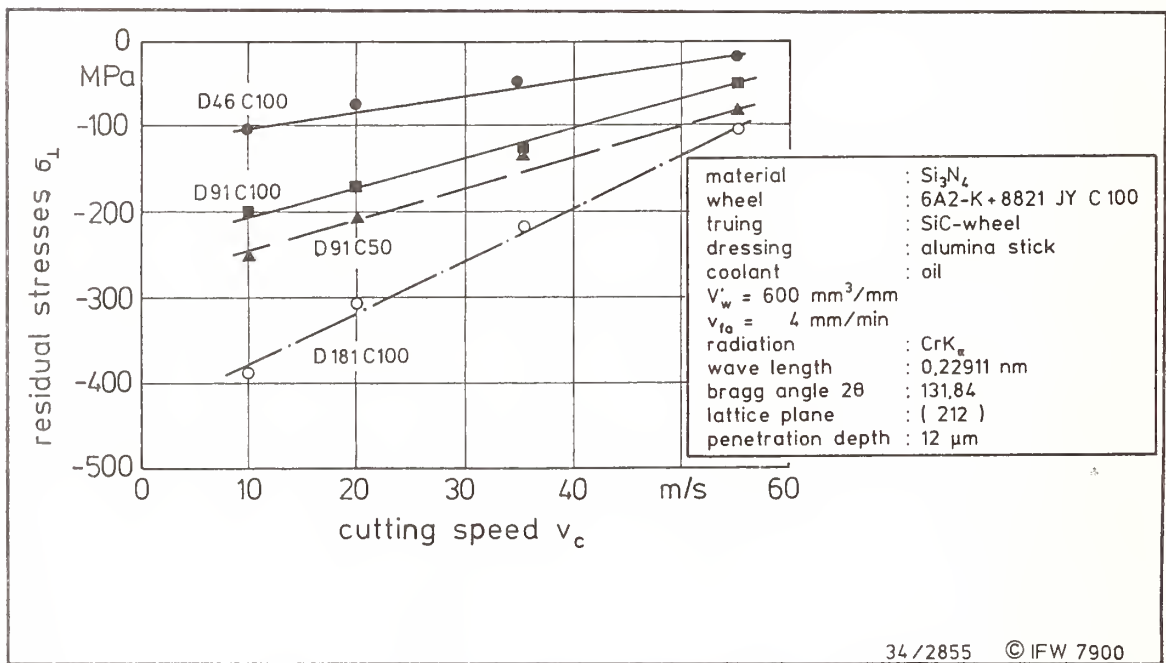
Fig. 8: Residual stresses in silicon nitride for different wheel specifications

Within Fig 8:

residual stresses $\sigma_\perp$ / MPa

D46 C100

D91 C100

D91 C50

D 181 C100

material	: Si_3N_4
wheel	: 6A2-K + 8821 JY C 100
truing	: SiC–wheel
dressing	: alumina stick
coolant	: oil
V'_w = 600 mm³/mm	
v_{fa} = 4 mm/min	
radiation	: CrK_α
wave length	: 0,22911 nm
bragg angle 2θ	: 131,84
lattice plane	: (212)
penetration depth	: 12 µm

cutting speed v_c

34/2855   © IFW 7900

178
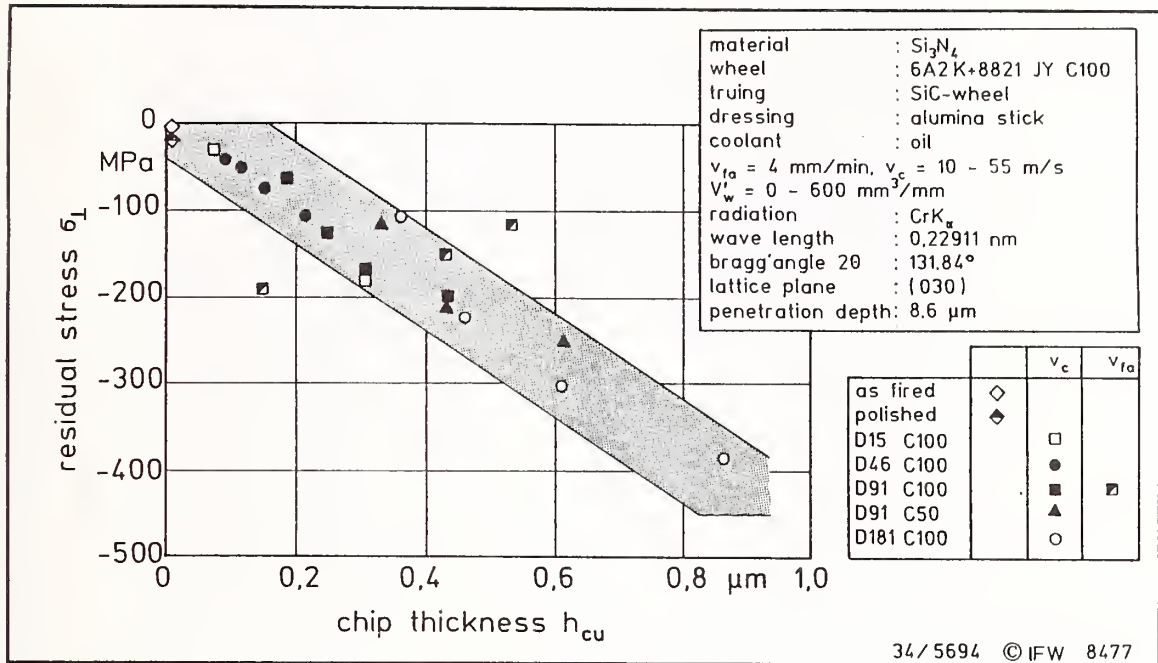
Fig. 9: Residual stresses in silicon nitride versus the chip thickness h_{cu}

In Fig. 9 the residual stresses found in grinding silicon nitride are plotted versus the undeformed chip thickness h_{cu} for different wheel specifications; cutting and feed speeds. Residual stresses are compressive in all cases and show an almost linear correlation with the chip thickness h_{cu}. Starting from a low state of stress for the polished material the compressive stresses increase at higher h_{cu} values. For the coarsest wheel, at a wheel speed of 10 m/s, the maximum stress was observed at -400 MPa. The good correlation between the residual stresses and the chip thickness supports the assumption that residual stresses in ceramics are mainly caused by the plastic deformation of the material by the cutting edges.

3.3 Grinding and strength of ceramics

In addition to residual stresses depend on the machining process subsurface microcracks may be generated in grinding of ceramics . Flaws are responsible for the premature failure of ceramics. For an appropriate process layout in view of the workpiece quality knowledge about the influence of the machining process on materials strength is a decisive factor.

Fracture of ceramics originate from machining flaws as well as from material intrinsic failures. The determined strength values are generally depend on the specimen size and number. In this investigation the bending strength of silicon nitride samples with dimensions 25.4 x 8 x 4 mm was tested via 4-point bending test. The measured strength and Weibull modulus have been corrected to give values independent of the specimen number by means of the Maximum- Likelihood-method. The grit size of the diamond wheels, the cutting speed and the feed speed were changed to produce groups of samples with different states of surface integrity. The achieved variation in the grit depth of cut is again characterized by the parameter h_{cu}. The influence of grinding conditions on bending strength and Weibull's modulus is shown in Fig. 10.
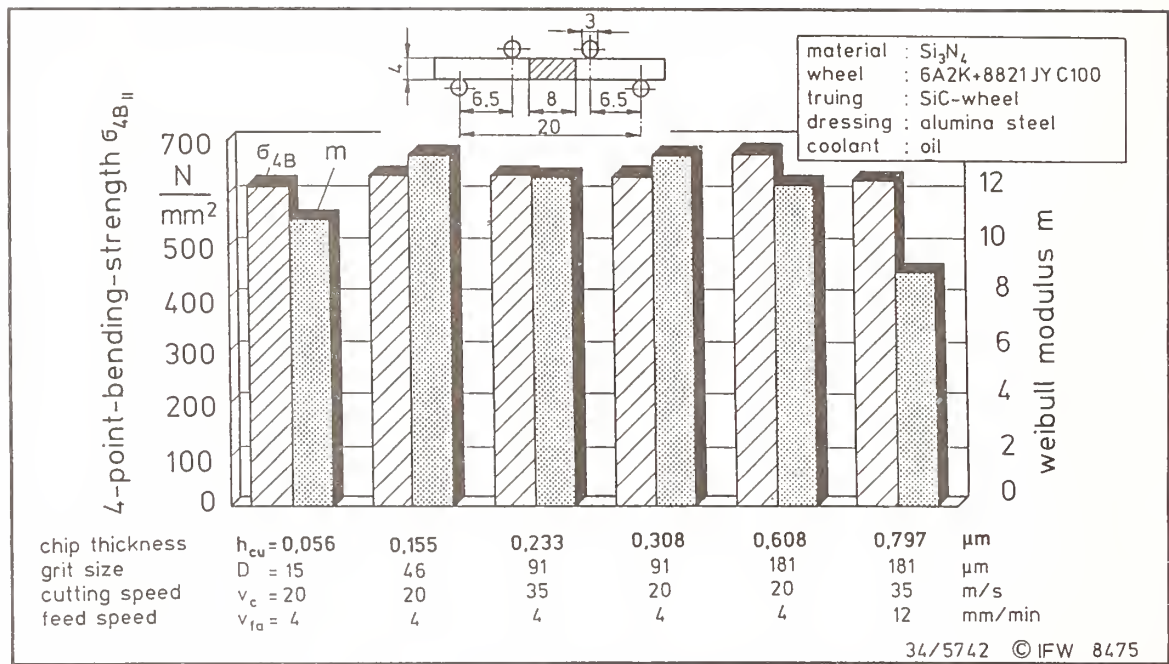
Fig. 10: Influence of grinding conditions on bending strength and fracture
probability of silicon nitride
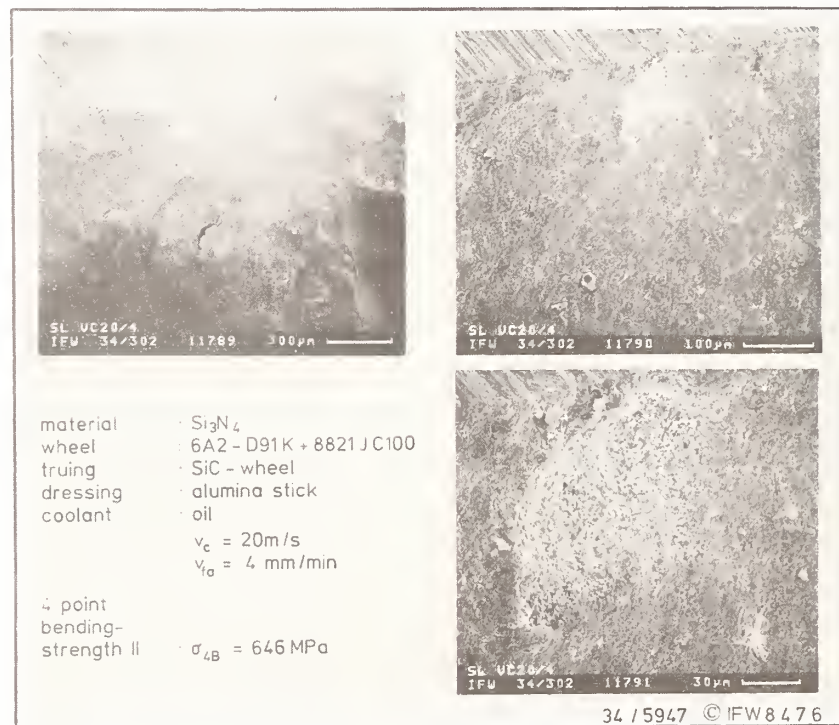
Fig. 11: Intrinsical material flaw in silicon nitride

material Si_3N_4
wheel   6 A 2 – D 181 K + 8821 JYC100
truing   SiC – wheel
dressing   alumina stick
coolant   oil
                v_c = 35 m/s
                v_{fa} = 12 mm/min

4 point
bending –
strength II σ_{4B} = 724 MPa

34 / 5946   © IFW 8479
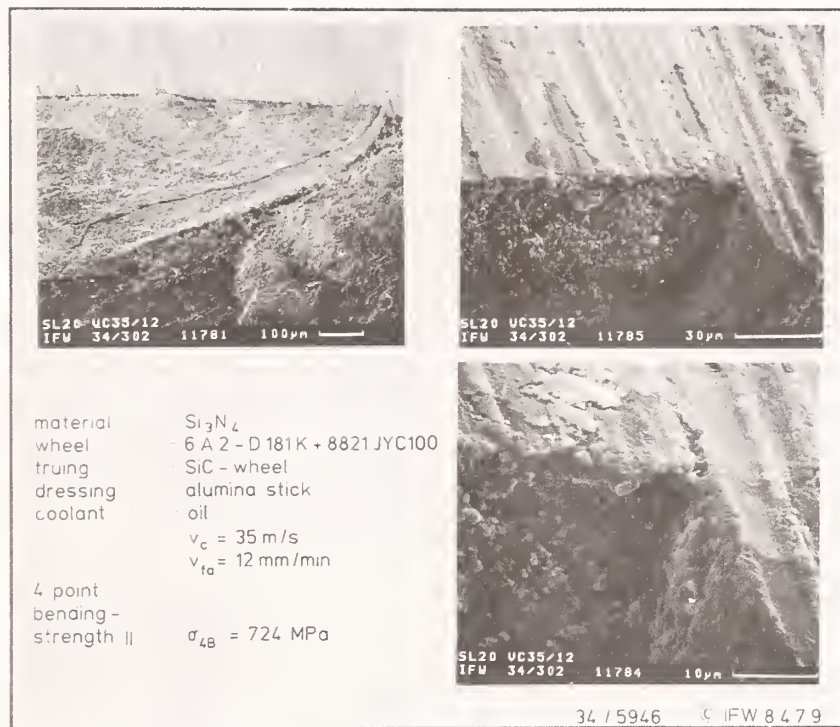
Fig. 12: Machining damage in silicon nitride

Strength values remain on the same level almost independent of the parameter variation. At high values of h_{cu} a decrease of the Weibull's modulus and successively a slight decrease of bending strength indicates an influence of machining. The reason for the almost unimpared strength of the material at low grit depth of cut is the presence of volume defects. The defects act as crack sources thereby limiting materials strength. These material intrinsic failures lead to a bending strength unaffected by the machining conditions, Fig. 11.

The decrease of Weibull modulus and of bending strength at large values of h_{cu} points to an influence of machining. At high grit depth of cut flaws (Fig. 12) are generated in the surface near region which exceed the dimensions of intrinsic failures causing an increase in fracture probability. This grit depth of cut should not be exceeded in grinding to avoid any decrease fracture strength or component reliability. Furthermore these results indicate that the grinding seems to flaw size exceed the thickness of the layer under compressive stresses. This may explain why no strength increasing effect of compressive stresses were found.

3.4 Optimization of the process

From this study it has become apparent that it is possible to optimize conventional ceramic grinding processes which are characterized by low cutting speeds, low infeed speeds and the use of fine-grained diamond wheels. For efficient grinding of ceramics the workpiece material properties have to be considered for process layout. Because of the brittleness of ceramics, parameters must be chosen that avoid grinding damage. This can be accieved by evaluating the critical depth of cut for the

material. Based on this parameters the process design towards an high efficiency can be made considering three basic process parameters. To reduce wheel wear in grinding a coarse type of grit should be applied (D l51-D l81). High wheel speeds are capable of limiting grinding forces. High feed speeds can be used to reduce machining time and attritious grit wear.
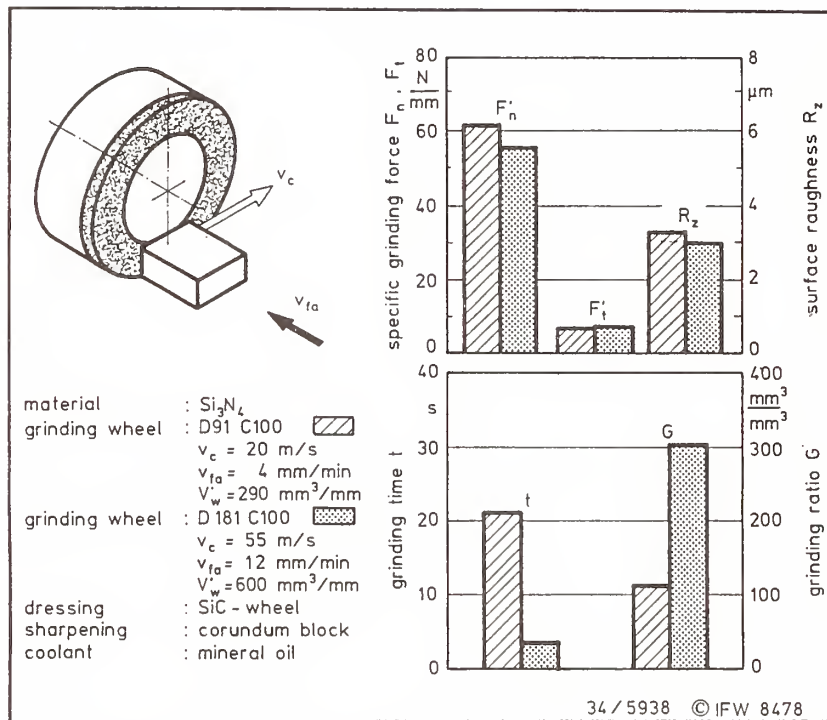
Fig. 13: Optimizing the grinding process

Grinding of silicon nitride cutting tool inserts may serve as an example for a comparision of a conventional process and one optimized with respect to the achieved results (Fig. 13). A conventional process in industry was substituted by an adapted process with optimized process parameters. The adaptation of the process parameters wheel speed, feed speed, and wheel specification were done based on the critical grit depth of cut of the material. The application of this technology reduces cycle time drastically by more than 60%. In addition the wheel wear is reduced to a third.

Grinding forces and surface roughness are maintained. If such process design is applied a considerable increase in efficiency in machining of advanced ceramics is possible.

References

(1)   Tönshoff, H.K.; Brinksmeier, E.; Wobker, H.-G.: "Evaluation of Surface   Layers of Machined Ceramics, Annals of CIRP Vol. 38/2, pp. 699-708, 1989

(2) Marshall, D.B.; Evans, A.G.; el. al.:
     "The Nature of Machining Damage in
     Brittle Materials", Proc. of Roy Soc.A,
     385, pp. 461-475, 1983

(3) Hakulinen, M.: "Residual Strength of
     Ground Hot Isostatically Pressed
     Silicon Nitride", Journal of nat.
     science, 20, pp, 1049-1060, 1985

(4) Tönshoff, H.K.; Roth, P.: "Chip
     Formation and Material Removal in
     Grinding of Ceramics" Proc. 4th. Int.
     Grinding Conf. Dearborn,
     9.-11.10.90, MR 90-539, pp. 1-18,
     1990

(5) Rosmanith, H.P.: "Fracture
     Mechanics", Springer Verlag,
     Heidelberg, 1982

(6) Allor, R.L.; Baker. R.R.: Effect of
     grinding Variables on Strength of Hot
     Pressed Silicon Nitride, ASME Paper
     83-GT-203, 1983

(7) Brinksmeier, E.; Siemer, H.; Wobker,
     H.-G.: Requirements on Non-
     destructive Testing Methods after
     Machining of Ceramics", 3rd. Int.
     Symposiom on Nondestructive
     Testing, DG28 P, Saarbrücken,
     3.-6.10.1988

(8) Malkin, S., "Grinding technology",
     Ellis Horwood Limited City, 1989

(9) Wobker, H.-G., "Schleifen
     keramischer Schneidstoffe", Dr.-Ing.
     Diss. Universität Hannover,1992

EFFECTS OF CERAMIC MICROSTRUCTURAL CHARACTER ON MACHINING DIRECTION - STRENGTH ANISOTROPY

R. W. RICE

W. R. Grace & Co., Columbia, MD

A literature review as well as substantial new experimental data are used to better define important microstructural parameters impacting the effects of machining direction on room temperature uniaxial flexural strength of ceramics. It is shown that grain size has a pronounced effect, with fine grain bodies showing the greatest strength anisotropy; i.e. strengths are commonly ~50% for flexure bars ground perpendicular versus bars ground parallel with the tensile axis. However, as grain size increases, this strength anisotropy first decreases, approaching zero at intermediate grain size (e.g., 20-50 µm) then increases again as grain size further increases, extrapolating to the range found for single crystals (which vary due to the effects of crystal orientation and machining direction relative to the tensile axis and preferred fracture planes). These observations are consistent with machining flaw sizes being approximately constant as a function of microstructure for a given machining condition, such that at intermediate grain size, flaw sizes approach the grain size, which then becomes a constraint on the ultimate flaw size until grain sizes are sufficiently large that failure occurs before flaws grow to the size of the grains. It is also shown that relatively fine homogeneous porosity has no significant effect on strength anisotropy from machining direction. However, increasing the pore, pore cluster or other defect sizes reduces strength anisotropy as a result of machining direction, with the anisotropy becoming zero when the scale of such defects is $\geq$ that of machining flaws so such defects dominate failure. Grain size effects on the anisotropy are nearly universal, i.e. most ceramics fall within a limited band as a function of grain size when effects of other sources of failure, e.g. pore clusters, are eliminated. Some ceramic particulate composites, whisker toughened Al_2O_3 and microcracking materials showed possible evidence of intrinsic reduction of strength anisotropy as a function of machining direction, mainly in toughened ZrO_2 materials.

1. Introduction

This author accidentally discovered the effect of machining direction on uniaxial flexure (σ) strength while studying surface finish effects on ceramics. Unusually wide strength scatter of machined polycrystalline Al_2O_3 bars was found to separate into two groups showing normal scatter, with the average strengths of the two groups differing by nearly a factor of two. More detailed evaluation revealed that the two groups correlated exactly with which direction the tensile surface of test bars had been machined relative to the bar axis. This had come about as a result of the machinist accidentally rotating the rectangular plate from which the bars were subsequently cut 90° when he turned it over to grind the second side after grinding the first side so one side of the test bars were ground perpendicular, the other parallel with the bar axis. This strength anisotropy with machining direction discovery led to a detailed study of strength anisotropy as a function of machining direction relative to the tensile axis for a wide variety of ceramic materials ranging from glassy carbon and soda lime glass to single crystals (Al_2O_3, $MgAl_2O_4$), polycrystalline oxides (Al_2O_3, MgO, ZrO_2, and $MgAl_2O_4$) and non-oxides (B_4C, SiC and Si_3N_4).[1] Limited tests also revealed similar, but somewhat less effects as a result of sanding with SiC abrasive paper. Examination of the literature revealed a precursor observation by Mould and Southwick,[2] who noted (as an aside to static fatigue studies) that

abrading glass specimens with 150 grit, emery cloth perpendicular to the tensile axis, resulted in strengths averaging ~50% lower than for abrasion parallel with the axis of subsequent flexure testing. Also, in the same time frame as the present author's initial work, Kirshner et al[3] independently showed strengths of small (~3.6 mm dia.) extruded rods of a commercial, sintered, 96% Al_2O_3 (G ~5µm) were lower when the rods were circumferentially scratched with a single point diamond versus axial scratching (Fig. 1A). The strength difference

increased with increasing load on the diamond, due mainly to an initially faster strength decrease of circumferentially scratched specimens. An approximately constant strength differential was reached at higher loads where strengths of circumferentially scratched rods were ~45% of those for axially scratched σ. Greater depth of cut (i.e. of infeed) of the diamond point rapidly decreased strengths (Fig. 1B).
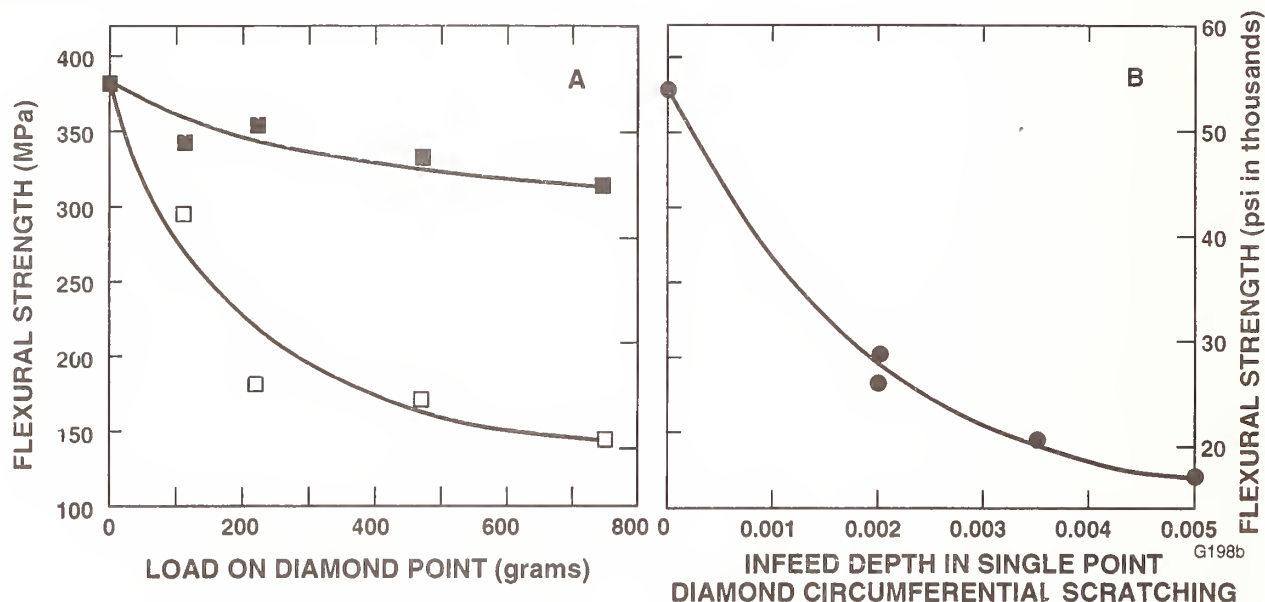
Fig. 1   Strength data of Kirchner et al[3] for extruded, 96% Al_2O_3 rods tested at 22°C as a function of scratching with a single point diamond. A) Data for scratching circumferentially (open squares) or axially (solid squares) as a function of load on the single point diamond, B) Data for circumferential scratching as a function of depth of diamond cut (infeed).

Subsequently, this author extended his work to include another silicate glass as well as a sulfide glass, stoichiometric $MgAl_2O_4$ crystals (versus previous Al_2O_3-rich $MgAl_2O_4$ crystals) and a TiC crystal.[4]   Several investigators subsequently confirmed substantial strength anisotropy as a result of machining direction in various high-strength Si_3N_4 bodies over a limited range of typical machining parameters (e.g. see refs. 5 and 6 as examples). The present author and colleagues showed this strength anisotropy arose primarily, if not exclusively, from differences in the geometry of flaws generated parallel to the machining direction versus that generated perpendicular with the machining direction.[7-10]   The depth of both flaw populations tends to be similar and does not change significantly with grain size (G) (including single crystals, i.e. G=∞).   However, while flaws generated perpendicular to the abrasive direction (which

dominate failure for stressing parallel to the machining direction) typically have an approximately half-penny shape, those generated parallel to the abrasive direction (which dominate failure for stressing perpendicular to the machining direction) typically have a substantially elongated shape. Thus, flaw depth to half length ratios were less for failure initiating flaws from machining perpendicular versus parallel with the bar axis.

Much more recently, some work has been done to address important parameters affecting this strength anisotropy. Thus, Ota and Miyahara[11,12] report greater strength reductions for dense Si_3N_4 as a result of changing diamond grinding wheel grit size, due mainly to greater strength reductions for grinding perpendicular to the bar (and hence tensile) axis than for grinding parallel with it. Their work differs some from, but is basically similar to, work of

Kirschner et al[3] (Fig. 1) and Anderson and Bratton[5] (Fig. 2). Rice and Mecholsky [8] showed diamond sawing resulted in similar but somewhat more severe strength anisotropy effects (while earlier studies have shown similar though possibly somewhat less effects of sanding versus grinding).[1] It was also clearly shown that failure of diamond sawn specimens occurred from flaws associated with more serious sawing scratches. More recently, Rice has shown that: 1) the strength anisotropy as a result of machining direction is a significant function of grain size, with a definite anisotropy minimum at intermediate grain size[13] (e.g., see Figs. 3-5); and 2) relatively fine homogeneous porosity by itself has no significant effect on strength anisotropy as a result of machining direction.[14]
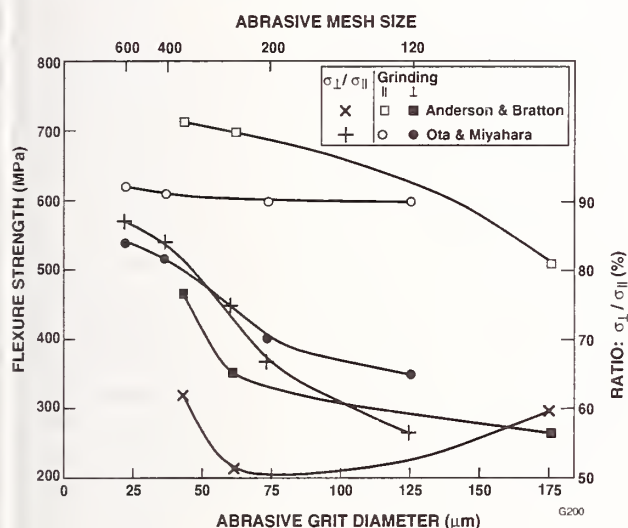
Fig. 2   Room temperature strengths of dense Si_3N_4 samples for machining perpendicular and parallel with the tensile axis and the ratio of the strength-ground perpendicular to that ground parallel with the tensile axis as a function of abrasive grit size. Data after Anderson and Bratton[5] and Ota and Miyahara.[11,12]

This paper further extends data on the effects of grain size and porosity on the strength anisotropy as a result of machining direction, including a broader range of material compositions and microstructures. Further, significant extension occurs as a result of evaluating effects of ceramic toughening failure mechanisms on the strength anisotropy from machining. Thus, in contrast to previous studies being limited to "monolithic" ceramics, a number of ceramic composites including various particulate composites with different toughening mechanisms as well as some whisker composites are evaluated. Ramification and application of these results are also discussed.

2.   Experimental Procedure

A variety of experimental and commercial materials (Table 1) were cut into bars ground parallel (on one side) and perpendicular (on the other side) relative to the bar length and subsequent tensile axis. Following sawing, all grinding was done with a 400 grit resin bonded diamond wheel with 100% concentration, (15.2 cm. dia. 1.3 cm in width) operated at 3,000 rpm (i.e., a surface speed of 143 m/s) with an in-feed rate ~7.6 cm/sec and 8µm depth of cut per pass, using a synthetic coolant.* Such grinding typically involved ~30 passes with a cross feed of ~ 8mm at the end of each pass. Because of the variable size samples available, resultant bar dimensions were also varied, but typically falling in the range of width to thickness ratios of 1.5-2. Three-point flexure testing in air at 22°C was utilized with fixed steel supports and spans of 1.25-2.0 cm and typical span to thickness ratios of 5-7. Subsequent to testing, extensive fractography was carried out to determine fracture initiation location, flaw character and microstructure. Keeping the key bar test ratios ~ constant as well as the extensive fractography minimizes limited effects of varying bar and test dimensions. Further, the primary focus of this paper is the relative difference in strength** for the same bars ground parallel with the tensile axis on one side and perpendicular on the other side.

3.   Experimental Results and Discussion

Both the strength and fractography results are summarized in Table 1.** The present Al_2O_3, MgO, ZrO_2, $MgAl_2O_4$, and B_4C*** results further document and extend previously shown grain size effects on strength anisotropy** as a function of

_____

* Doall Kleen Kool synthetic #01958.
** Throughout the rest of this paper, the measure of strength anisotropy will be the variation of the ratio of the strength tested perpendicular to the machining direction ($\sigma\perp$) to that tested parallel to the machining direction ($\sigma\parallel$) from a value of 1 or 100%. This is similar to using the difference in strengths, e.g. $\sigma\parallel$-$\sigma\perp$.
*** Note that greater scatter in the CeO_2 and especially the B_4C data is due to grain size variations in some of these bodies as well as less definition of grains in the 100% transgranular fracture (e.g. see Fig. 8).

187

machining direction. Thus, the greatest strength anisotropy ($\sigma\perp/\sigma\|$ of ratios) of 40-60% occurs at fine grain size, with less anisotropy as grain size increases, approaching zero (i.e. $\sigma\perp/\sigma\|$ ratios of ~100%) at intermediate grain size, then increasing to the single crystal values as grain size further increases (Figs. 3-5)). That a minimum anisotropy occurs at intermediate grain size is shown clearly by the Al_2O_3, $MgAl_2O_4$ (Fig. 3), MgO, and cubic zirconia (CZ, Fig. 4) and B_4C (Fig. 5) data, i.e. where there is more data at both moderate and larger grain sizes and for single crystal orientations relative to stressing and machining directions (their average is appropriate for comparison to polycrystalline behavior.) Similarly limited results for the other normally single phase materials support this trend, e.g., the boron[15] results (where SEM examination showed no grain structure, but it is reported to be ~2μm[15]). Thus, except for some materials showing less anisotropy, most materials follow a common trend, and, in fact, fall within a limited band (e.g. Figs. 3-5). The possibly somewhat lower strength anisotropy observed in this study (e.g. Fig. 3) versus the previous studies of this author is consistent with reduced strength anisotropy (i.e. higher $\sigma\perp/\sigma\|$ ratios) with less severe machining conditions, mainly due to less reduction in strength for machining perpendicular to the tensile axis (e.g. this author's previous studies utilized a removal depth of ~50μm per pass vs. 8μm here).

The rationale for plotting the ratio of the strength (σ) for grinding perpendicular versus that parallel with the bar axis as a function of $G^{-\frac{1}{2}}$ is to emphasize the relationship of the grain size dependence of this machining effect to the basic σ-$G^{-\frac{1}{2}}$ behavior of ceramic materials. It has been extensively shown elsewhere that ceramics failing from flaws follow a two-branch behavior on a σ-$G^{-\frac{1}{2}}$ plot.[13,16] In the large grain size regime, there is a substantial grain size dependence of strength, but at intermediate grain size this switches to either a zero or, much more commonly, a modest grain size dependence of strength. The underlying mechanism of this behavior arises from flaw sizes from machining typically not changing much with grain size. Thus, in the fine grain size regime, one has flaws which are substantially larger than the grain size, while in the large grain size regime flaws reach catastrophic failure before they grow to the grain size. Thus, the two branches of the σ-$G^{-\frac{1}{2}}$ behavior intersect when the flaw size is approximately equal to the grain size. The fact that the strength ratio for grinding perpendicular versus parallel with the tensile axis reaches a maximum (i.e. minimum anisotropy) at intermediate grain size (e.g. 20-50 μm) is

consistent with this mechanism. This implies that as the flaw size and grain size approach one another as the grain size becomes a constraint to flaw dimensions for the more elongated flaws associated with specimens failing from machining flaws as a result of machining perpendicular to the tensile axis. Some fractographic support for this observation has been previously presented, and is provided by this study as discussed further later.[9,13]

This study further shows that relatively fine, homogeneous porosity has no obvious effect on strength anisotropy as a function of machining direction. However, increasing heterogeneity of porosity increasingly reduces intrinsic machining-strength anisotropy (e.g. from finer grain sizes). Thus, comparison of various bodies of B, Al_2O_3, MgO and $MgAl_2O_4$, with generally fine (e.g. <1μm) homogeneous pores showed no significant strength anisotropy differences from other bodies of the same material with much less porosity (Table 1, Figs. 3, 4). For examples of somewhat homogeneous porosity see Figs. 6 & 7. As the size of the pores or pore clusters increased, the strength anisotropy as a function of machining direction decreased, becoming zero (i.e. $\sigma\perp/\sigma\| = 1$) when the pores or clusters became the flaws, e.g. CeO_2 (Fig. 8), ZrO_2 (Fig. 9), B (Figs. 10, 11), and aluminum titanate-zirconium titanate (AT-ZT) composites. These trends are further illustrated by the actual strength-porosity data (Figs. 12, 13). Materials with more (but not perfectly) homogeneous porosity show nearly (but not completely) parallel trends for strengths from parallel ($\sigma\|$) and perpendicular ($\sigma\perp$) grinding vs. porosity (e.g. Al_2O_3, Fig. 12), those with intermediate homogeneity of porosity less parallelness of $\sigma\|$ and $\sigma\perp$ vs. porosity (e.g. $MgAl_2O_4$, Fig. 12), and those with low homogeneity of porosity still less parallelness of the two strength-porosity curves e.g. B, Fig. 13. In all cases, the reduced parallelness is due to a reduced slope for the strengths of perpendicular bars vs. porosity.

A key question is whether the reduction in strength anisotropy from machining direction is due to interaction of the machining flaws with the pores to cause failure or due to the pores acting independently as sources of failure, hence overriding the machining effect. The above strength-porosity results (Figs. 12,13) can be interpreted as implying that strength anisotropy decreases due to increasing machining flaw-porosity intersections as pore size and heterogeneity increases. This is supported by the reduction in parallelness of the parallel and perpendicular ground strength vs. porosity curves as

Table 1

Flexure Strengths of Ceramics Ground Perpendicular
vs. Parallel to the Tensile Axis

Material	Procedure/ Source[1]	G (μm)[2]	P(%)[3]	w, t, Span[4] (mm)	$\sigma\perp$ [5] $\sigma\|$	$\frac{\sigma\perp}{\sigma\|}$% [5]	Fracture Origins[6]
I. Oxides							
Al_2O_3	HP (LA)/B (A-1-39)	4	0.5	5.0, 2.5, 15.0	(6) 330±20 (5) (8) 370±30 (7)	90	5SLG, 1CLG 7SLG, 1CLG
Al_2O_3	HP (LA)/B (A-3-30)	1	1.5	"	(5) 310±40 (11) (5) 620±100 (16)	51	2MF, 2MF? 3C, 1ILG &P's
Al_2O_3	HP (LA)/B (A-3-1)	0.7	6.0	"	(5) 250±30 (14) (6) 585±105 (18)	42	4MF 2C, 1IPA, 1IPA-LG, 1SPA
Al_2O_3	HP (LA)/B (A-3-39)	1	16.5	"	(5) 230±75 (32) (4) 335±145 (44)	69 (51)	3LSP, 2MF 2 LSP, 1IPA
Al_2O_3	HP (LB)/B (A-3-11)	1.5	1.0	"	(7) 320±30 (10) (5) 640±100 (16)	80	3MF, 2MF?, 1I-SP 2MF?, 1C, 1C?
Al_2O_3	HP (LB)/B (A-3-42)	2	0.8	"	(7) 415±40 (10) (7) 640±105 (16)	65 (59)	5MF, 2MF? 3C, 3MF?
Al_2O_3	HP (LB)/B (A-3-44)	1	1.2	"	(7) 295±70 (23) (6) 465±120 (26)	63 (63)	4MF, 2MF?, 1IPA? IC, 1I-SPA, 1ILG
Al_2O_3	(P-88) S/Diamonite	5		5.2, 2.5, 19.0	(5) 310±30 (10) (4) 380±30 (9)	80	1MF? none identified
Al_2O_3	(P-88) S/Diamonite	5		5.2, 2.4, 19.0	(5) 305±35 (12) (5) 315±35 (12)	98	porous areas? "
Al_2O_3	S (GE (Lucalox)	30	~0	5.2, 2.5, 12.7	(6) 260±35 (14) (6) 275±30 (11)	90	none identified "
CeO_2	S/Boeing	~30	6.0	5.1, 2.5, 15.2	(5) 80±10 (10) (5) 80±10 (9)	95 (99)	5SPA 3SPA, 1SPA+LG, 1C
CeO_2	S/Boeing	~30	6.6	2.4, 1.5, 12.7	(4) 95±10 (10) (4) 120±45 (39)	80	All SPA "
MgO	HP/Boeing	0.6	~0	4.0, 1.8, 12.7	(5) 185±10 (12) (5) 340±55 (16)	54 (51)	4MF? 4C, 1MF?
MgO	HP/Boeing (M-5-14)	0.5	4.5	5.5, 2.6, 12.7	(3) 105±15 (15) (3) 165±30 (18)	62	none found none found
$MgAl_2O_4$	S/Boeing (M-5-13)	8	26	5.3, 2.5, 15.2	(6) 120±20 (18) (6) 130±10 (9)	89	none identified " "
$MgAl_2O_4$	S/Ohio State	~10	~3	4.9, 2.4, 12.7	(4) 225±25 (11) (4) 265±30 (11)	85	2SP, 2SPA 1SP, 1IPA?
ZrO_2+5 w/o Y_2O_3	Crystal from skull melting	∞	0	3.5, 1.5, 15.2	(6) 1710±235 (14) (5) 1740±255 (15)	98	1MF, 1C 2MF
ZrO_2+20 w/o Y_2O_3	•	∞	0	4.2, 2.2, 15.2	(5) 195±50 (26) (5) 235±35 (15)	83	4MF 5MF

189

Material	Procedure/Source[1]	G (μm)[2]	P(%)[3]	w, t, Span[4] (mm)	$\sigma\perp$[5] $\sigma\|$	$\dfrac{\sigma\perp}{\sigma\|}$[5] %	Fracture Origins[6]
ZrO$_2$+11.2 w/o Y$_2$O$_3$	HP/Zyttrite (WPAFB)	~4	~1	5.3, 2.6, 15.2	(5) 230±20 (80) (5) 275±50 (18)	37	2PD, 1MF, 1MF? 2SPA?, 1MF
ZrO$_2$+2.9 w/o CaO	S/Zircoa-C	30 (15-60)	~7	5.1, 2.6, 15.2	(6) 170±15 (8) (6) 165±10 (6)	101	none detected "
ZrO$_2$+2.8 w/o MgO	S/Zircoa-1027	~4	~5	5.8, 2.9, 20.3	(5) 300±25 (9) (5) 320±25 (8)	95	none detected "
ZrO$_2$+6 w/o Y$_2$O$_3$	S/Union Carbide	~0.5	~2	5.8, 1.7, 15.2	(4) 365±85 (25) (3) 545±65 (12)	67 (73)	1SA, 1SP, 1SPA 1I-SP, 1SPA
ZrO$_2$+~3 m/oY$_2$O$_3$	S/Kyocera	3	~●	5.2, 2.6, 15.2	(6) 60±5 (8) (6) 60±5 (15)	104	none detected "
ZrO$_2$+~10 w/o mixed stabilizers	S/Diamonite Zirmonite 1000	2	~5	5.2, 2.5, 19.0	(6) 710±65 (9) (5) 670±110 (16)	105	3SPA, 1CPA, 1C 3SP, 1IP, 1MF?
ZrO$_2$+~10 w/o mixed stabilizers	S-HIP/ Diamonite Zirmonite 1000	2	1-2	4.7, 2.3, 12.7	(6) 850±35 (4) (6) 835±50 (6)	102	1C, ISPA, ISP?, 1I-SP, 1MF?. 1C, ISPA, 1IS-SPA

II. Non Oxides

  •   B, Borides

Material	Procedure/Source[1]	G (μm)[2]	P(%)[3]	w, t, Span[4] (mm)	$\sigma\perp$[5] $\sigma\|$	$\dfrac{\sigma\perp}{\sigma\|}$[5] %	Fracture Origins[6]
Boron	HP (383)	--	3.2	5.1, 2.3, 12.7	(4) 460±140 (30) (4) 540±130 (25)	88 (67)	3MF, 1C 2MF, 1MF?, 1MF-P
Boron	HP (560)	--	4.5	"	(5) 340±20 (6) (4) 440±85 (19)	77	3MF, 2MF? 2MF, 1MF-P, 1C
Boron	HP (566)	--	9.8	"	(5) 320±30 (10) (5) 390±100 (26)	82 (68)	3MF, 1SP, 1C 2MF, 1SPA, 1C
Boron	HP (594)	--	21	"	(5) 245±35 (13) (3) 240±30 (12)	101	1SPA, 1CVC?, CPA, 1IJPA,1IPA, 1I-SPA, 1C-IPA
Boron	HP (584)	--	29	"	(5) 190±100 (26) (3) 190±70 (38)	98	1C?, 1SP? 1SP, 1I-SP?
TiB$_2$	S/PPG (1900)	3	2	4.8, 2.3, 15.2	(1) 343 (1) 249	73	1C? 1MF?
TiB$_2$	S/PPG (1900)	3	2	3.4, 1.3, 12.7	(7) 430±60 (14) (7) 385±65 (16)	112	1PD, 1SPA, 1IPA, 1MF?,1C? 3I-SP, 1C
TiB$_2$	HP Ceradyne	--	~0	2.5, 5.3, 15.2	(5) 150±85 (58) (4) 135±65 (48)	115	None found None found
TiB$_2$	S/PPG (2100)	5	~0	5.2, 3.2, 17.8	(5) 355±30 (8) (4) 340±20 (6)	105	None found None found
TiB$_2$	S/PPG (2250)	150	~0	5.2, 2.6, 15.2	(3) 47±7 (15) (3) 49±3 (6)	98	None found None found

  •   C, Carbides

Material	Procedure/Source[1]	G (μm)[2]	P(%)[3]	w, t, Span[4] (mm)	$\sigma\perp$[5] $\sigma\|$	$\dfrac{\sigma\perp}{\sigma\|}$[5] %	Fracture Origins[6]
Graphite	/Unknown - Reactor Grade	20	21	5.0, 2.5, 15.2	(5) 30±3 (10) (4) 33±1 (40)	90	None found None found

Material	Procedure/Source[1]	G (µm)[2]	P(%)[3]	w, t, Span[4] (mm)	$\sigma\perp$[5] / $\sigma\parallel$	$\frac{\sigma\perp}{\sigma\parallel}$%[5]	Fracture Origins[6]
Graphite	/POCO	1-2	16	5.2, 2.6, 15.2	(8) 130±4 (3) (8) 133±4 (3)	90	3C, 2C? 1C, 3C?
B₄C	HP/Union Carbide	5-40	~0	12.7, 5.3, 1.8	(8) 225±85 (38) (8) 345±135 (39)	66 (54)	2MF, 1PD, 1C 1SPA, 1MF, 1C, 1C-LG
B₄C	HP/Union Carbide HT	20-100	~1	12.7, 4.3, 1.8	(8) 305±80 (27) (8) 340±55 (17)	84 (80)	3MF, 1MF?, 1SPA 1SPA, 1MF?
B₄C	HP/Carborundum	5-10	~0	"	(8) 360±20 (6) (7) 450±80 (18)	80	2MF, 1C? 2C, 1C? 1MF?
B₄C	HP/ESK	10	~0	"	(8) 275±25 (9) (8) 300±35 (11)	93 (93)	1SPA, 1CPA, 1MF 1SPA, 1IPA, 1LG
B₄C	HP/ESK, HT	10	~0	"	(6) 390±100 (25) (7) 435±80 (18)	93 (93)	1C, 1MF, 1MF+LG, 1LG 1LG, 1IPA
B₄C	HP/FMI	2	~0	4.2, 1.5, 12.7	(3) 305±50 (16) (3) 500±120 (24)	90	1MF, 1SP, 1C?, 1SLG? 2C
B₄C	S/FMI	~50	~7	3.1, 1.2, 12.7	(6) 190±15 (8) (6) 190±10 (5)	100	1SP?, 1I-SP? 1SP?, 1SPA?
B₄C	HP/Borid Prod.	~15	~0	4.5, 2.1, 1.3	(4) 415±20 (5) (4) 570±50 (8)	73	2MF, 1C? 2MF, 1PD, 1C
SiC	HP/Cercom	5	~0	5.1, 2.4, 12.7	(6) 495±55 (11) (6) 530±45 (9)	94	3C?, 1IP?, 1MF? 4C?, 1MF?
TiC	HP/Ceradyne	20	~1	5.2, 2.5, 12.7	(5) 365±80 (22) (4) 405±75 (18)	90	None found None found
ZrC	HP/Ceradyne	15	~2	5.3, 2.5, 15.2	(4) 260±25 (10) (3) 265±20 (8)	98	1MF, 1C?, 1SPD?, 1CPA? 1CP?, 1IPA?, 1IPD?
• Nitrides							
AlN	S/Dow	4	~1	6.1, 3.1, 20.3	(7) 320±30 (10) (8) 335±35 (11)	96	none detected " "
AlN	HP/Grace	15	~0	4.2, 1.7, 12.7	(6) 235±20 (8) (7) 260±15 (5)	90	none detected " "
BN	HP/Union Carbide	0.5 thick 3 dia.	~1	4.9, 2.3, 12.7	(6) 70±6 (8) (6) 85±15 (17)	82	none detected " "
Si₃N₄	S/Diamonite	~0.5	~2	4.9, 2.5, 19.0	(5) 640±40 (6) (4) 914±65 (6)	70	4MF? 1SPA, 1I-SPA; 1IPA
Si₃N₄	"	~4	~7	4.6, 2.7, 12.7	(5) 340±20 (6) (5) 335±45 (14)	102	2CP, 1I-SLG's, 1SP, 1PD 2C, 1C?, 1IP, 1SPA, 1C-LG-P?
Si₃N₄	HP/Diamonite (SN2)	4	~2	4.6, 2.8, 12.7	(6) 370±55 (15) (6) 425±25 (6)	88 (92)	Specific origins not detected
III. Composites							

Material	Procedure/Source[1]	G (μm)[2]	P{%}[3]	w, t, Span[4] (mm)	$\sigma\perp$[5] $\sigma\parallel$	$\dfrac{\sigma\perp}{\sigma\parallel}$%[5]	Fracture Origins[6]
Al$_2$O$_3$+ 27v/o TiB$_2$	HP/Grace		~0	11.5, 5.7, 12.7	(5) 600±30 (6) (5) 555±60 (11)	108	LAl$_2$O$_3$ G clusters? "
Al$_2$O3+ 42v/o TiC	HP/Grace		~0	"	(4) 360±30 (8) (4) 365±40 (12)	99	All PA's? "
Al$_2$O$_3$+TiC ~20v/o	HP/Valeron	1-2	~0	5.8, 1.8, 12.7	(5) 390±50 (12) (5) 560±60 (11)	70	3MF? 2C?, 1PD?
MgAl$_2$O$_4$+3 1v/o SiC	HP/Grace		~0	"	(4) 275±20 (7) (4) 300±40 (13)	91	All PA's? "
TiO$_2$+25% Al$_2$O$_3$	HP/Ceradyne	20		5.0, 2.3, 15.2	(4) 125±5 (4) (4) 140±15 (9)	91	All probable PA's
Pyroceram	F/Corning	0.5-3	~0	5.2, 2.6, 15.2	(5) 165±5 (3) (5) 220±40 (17)	75	1MF? 2C, 1MF?
Al$_2$O$_3$+26 w/o ZrO$_2$	S/Diamonite Zirmonite 200	2-3 (ZrO$_2$ 0.5-1)	~6	5.2, 2.4, 19.0	(3) 450±20 (4) (4) 390±145 (37)	115 (90)	1TSP?, 1SP, 1SPA 1C
Al$_2$O$_3$+26 w/o ZrO$_2$	S/Diamonite Zirmonite 200		~ 6	5.2, 2.6, 19.0	(5) 510±45 (9) (5) 555±55 (10)	92	2SA, 2SP, 1SPA 3SA, 1MF?
Al$_2$O$_3$+26 w/o ZrO$_2$	S/Diamonite Zirmonite 200	1 (ZrO$_2$ ~ 0.5)		"	(2) 605±10 (2) (6) 625±105 (16)	96 (92)	2MF? 2SP, 2MF?, 1I-CP
Al$_2$O$_3$+26 w/o ZrO$_2$	S-HIP/Diamonite Zirmonite 200	4	~●	5.2, 2.5, 12.7	(6) 830±95 (11) (6) 900±200 (22)	92 (87)	2SP, 1IP, 1MF? 3IP, 1SP, 1MF?
Al$_2$O$_3$+7 w/o SiCw	HP/Cercom (Disk)	~2	~0	5.1, 1.9, 12.7	(4) 610±50 (8) (4) 715±125 (18)	85	1ILG? 2C?, 1SLG?
Al$_2$O$_3$+25 v/o SiCw	HP/Cercom (Plate)	~1	~0	5.1, 1.7, 12.7	(5) 420±40 (10) (5) 560±55 (10)	75	1I-SLG, 1C?, 1PD? 2C?, 1SLG?
70AT-30ZT[7] (A)	S/Grace	4	~●	5.2, 2.4, 12.7	(6) 75±6 (7) (6) 75±6 (8)	96	none found
60AT-40ZT[7] (B)	S/Grace	2-10	7	5.2, 2.4, 12.7	(6) 85±6 (8) (6) 95±7 (8)	89	none found
40AT-60ZT[7] (D)	S/Grace	4	23	5.2, 2.5, 12.7	(6) 65±6 (9) (6) 65±6 (9)	96	none found

Footnotes:

(1)   F = fused (i.e., melted), HP = hot pressed, S = sintered, HIP = hot isostatically pressed.

(2)   Average diameter of grains measured on a fracture surface.

(3)   P = porosity.

(4)   w = bar width, t = bar thickness, span = test span in 3-point flexure.

(5) $\sigma\perp$ = average strength for grinding perpendicular to bar axis shown over average strength ground parallel to bar axis ($\sigma\parallel$). First number (in ()) is the number of tests averaged, next is the average strength and standard deviation, both rounded to the nearest 5 MPa (unless <10 MPa), and the last number (in ()) is the coefficient of variation. Note that the data were measured in psi units, so conversion to MPa and

192

rounding to the nearest 5 MPa may give slightly different coefficients of variations than shown (from the original psi), and from the $\sigma\perp/\sigma\|$ ratio. $\sigma\perp\backslash\sigma\|$ ratios in ( ) are corrected values due to unusually low strengths or failure from gross defects.

(6)   Fracture origin designations: Locations: C=from (rounded) corner of fracture, i.e., rounded bar edge; I = interior of bar, i.e. not at surface, S = bar surface, I-S = source not at, but sufficiently close to the surface to be uncertain whether it was an internal or surface (connected) origin. Types: LG = large grain; MF = machining flaw; P = Pore (P's = a few pores); PA = porous area (i.e., cluster of pores). Possible combinations shown by - or &, and uncertainty is designated by ?.

(7)   AT = aluminum titanate, ZT = zirconium titanate.
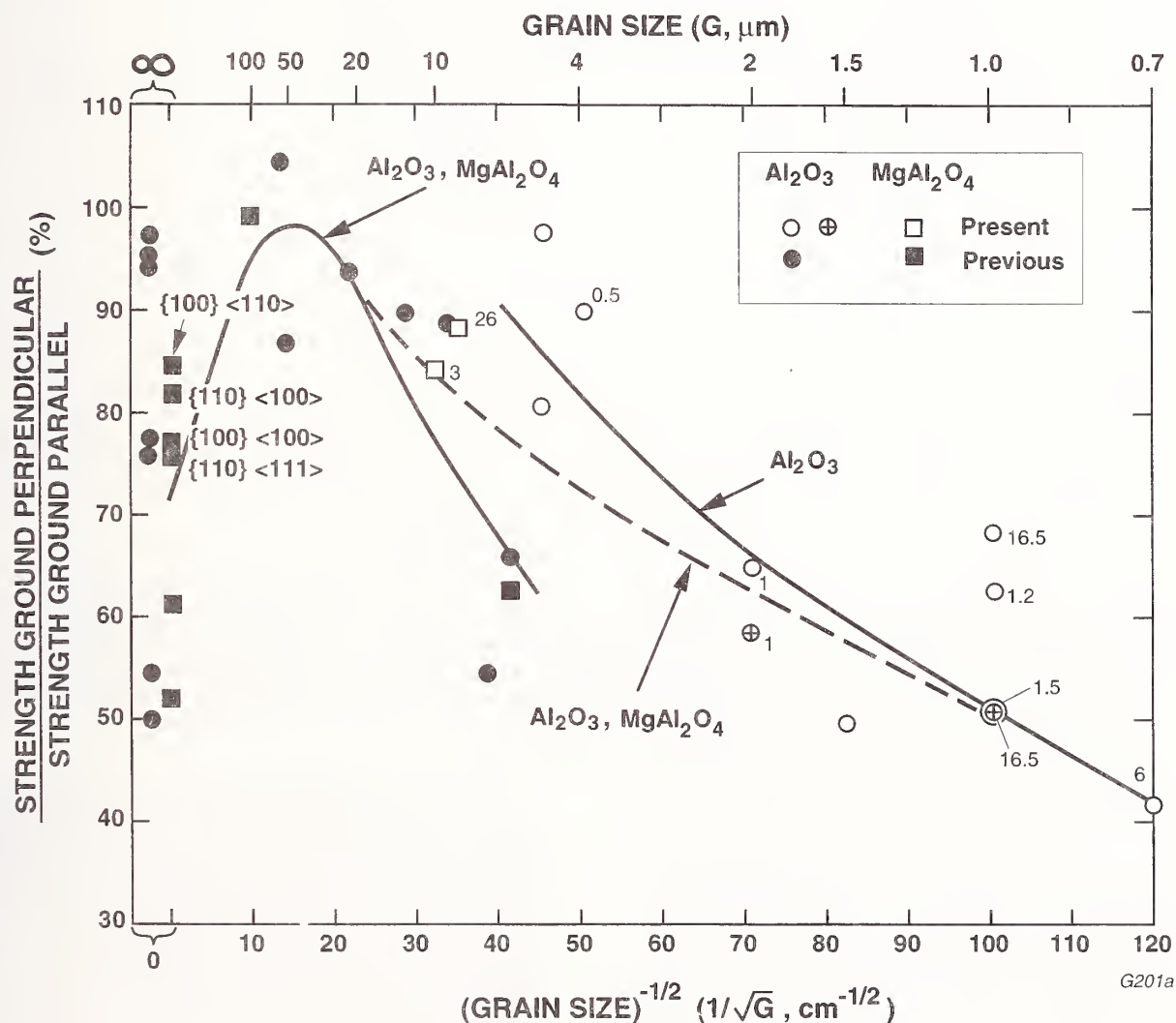
Fig. 3   Strength anisotropy, i.e. the ratio of the strength (at 22°C) ground perpendicular versus parallel with the tensile axis, as a function, the inverse square root of grain size for Al_2O_3 and $MgAl_2O_4$. Note strengths for several orientations for crystals of each of the two materials, specific orientations are shown for stoichiometric Czochralski-grown $MgAl_2O_4$; all other crystal data points are for different orientations cut from Vernuil-grown boules of each material. Data for both the present study and previous studies[1,4] are shown. Numbers adjacent to some data points are the volume % porosity where ≥0.5%. Note the trend lines shown for the materials, including a possible single trend for both materials (e.g. the dashed line), which are consistent with those of most other materials (Figs. 4 & 5).

·193
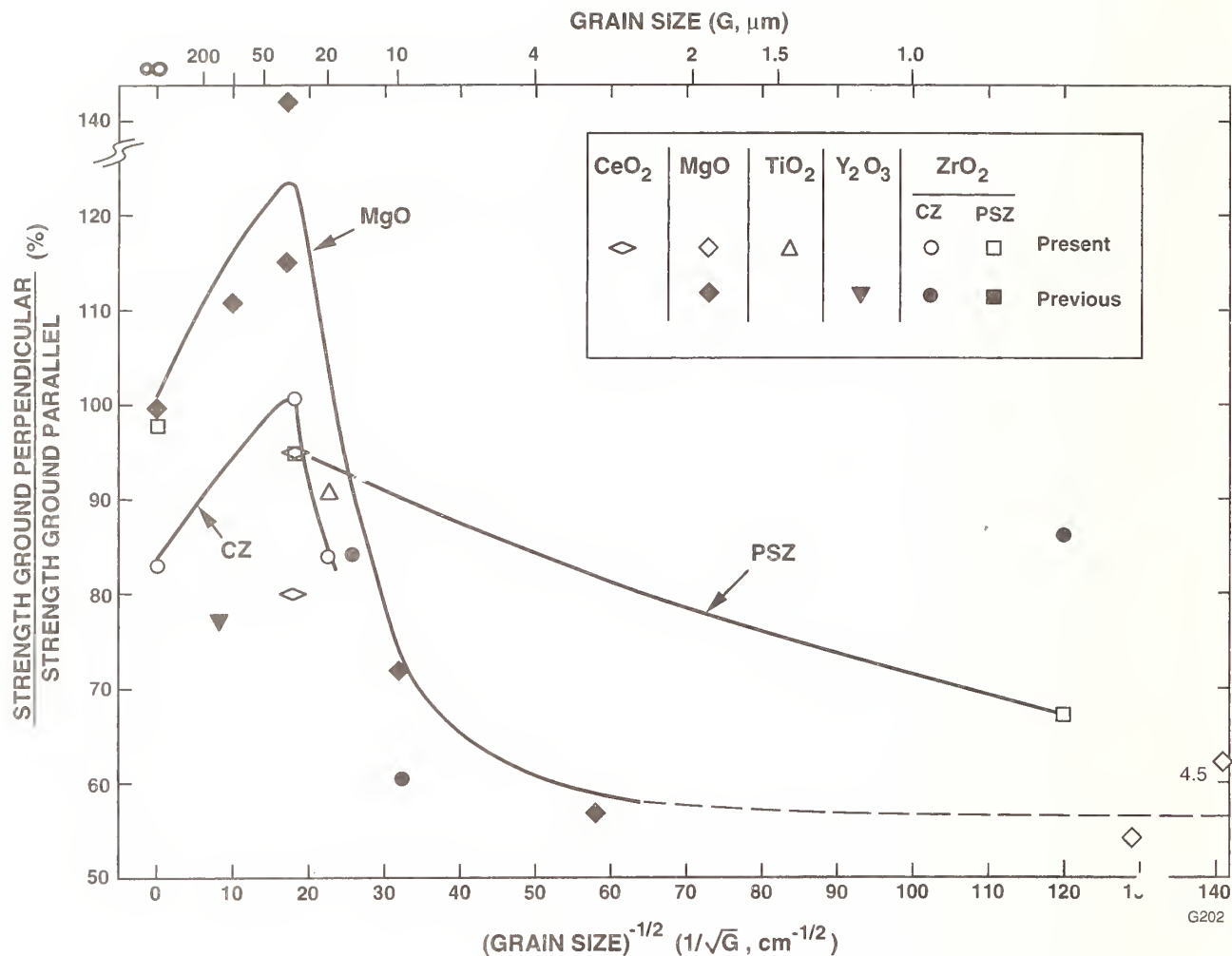
Fig. 4 Ratio of the strength (at 22°C) of other oxides ground perpendicular versus parallel with the tensile axis as a function of the inverse square root of grain size. Both current and previous data shown, including new data for both fully and partially stabilized ZrO_2 single crystals. Data for both the present study and previous studies[1,4] are shown. Numbers adjacent to some data points are the volume % porosity. Trend lines shown for some of these materials. Note the peak of the MgO data at intermediate grain size being >100% is attributed to surface work hardening effects.[13]

porosity heterogeneity increases. While the fractography results are clearly not unequivocal, they both directly and indirectly indicate that at least part of the reduction of strength anisotropy as a function of machining direction results from interaction of the machining flaws with the larger pores or pore clusters available for failure. First, where machining flaws were found in Al_2O_3 of different levels of porosity they were similar (Figs. 14, 15). Second, some strength anisotropy is typically observed, even in sample populations in which failure is predominantly associated with isolated larger pores or pore clusters. Although machining flaws generally could not be specifically identified in most porous samples, they must be interacting with the pores, since the pores themselves show no basis for providing strength anisotropy in contrast to

machining flaws clearly having this effect. Further, previous cases of specific interactions of machining flaws with larger pores have been shown in glass[17] and polycrystalline specimens.[8] It is also true that some of the materials of this study having pore clusters as a major factor in their fracture initiation had large grain size, e.g. particularly clear for the case of CeO_2 (e.g., Fig. 8). This may also have been a factor in the PSZ material (Zircoa 1027, while specific fracture origins were not identified in the samples of this study, previous studies of this material have shown fairly frequent initiation from grain boundaries with pores).[18] In these cases where pore clusters dominated failure initiation, it is still quite probable that the grain structure was limiting the ultimate size of the flaws even where the pore clusters were the initial flaws or a major portion
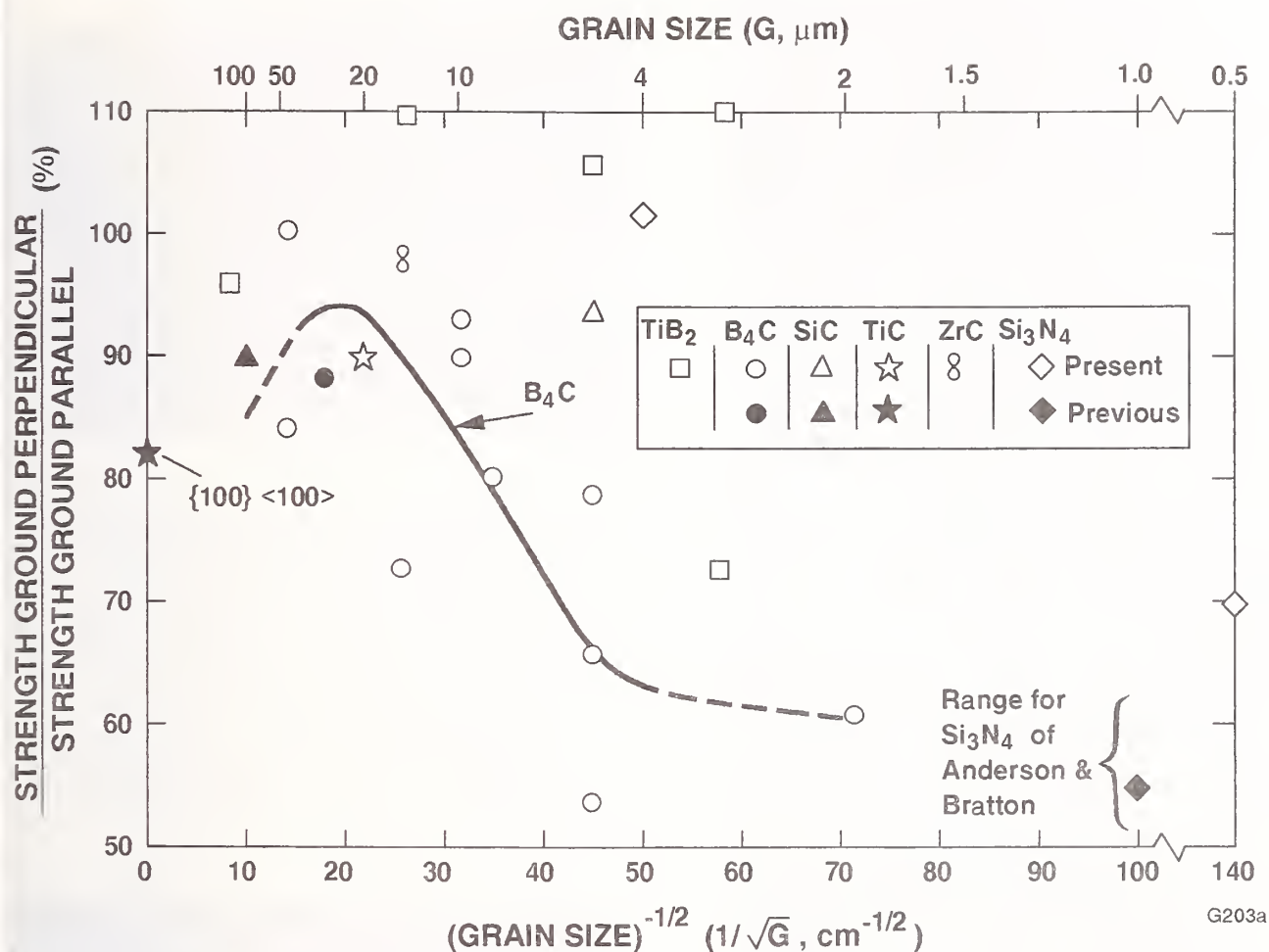
GRAIN SIZE (G, μm)

Fig. 5 Room temperature strength anisotropy of non-oxide specimens ground perpendicular versus parallel with their tensile axis as a function of the inverse square root of grain size. Data for both the present study and previous studies[1,4] are shown Note the TiC single- and poly-crystal data and that the B₄C trend line would also be consistent with the other non-oxide materials (as well as most oxides, Figs. 3,4).
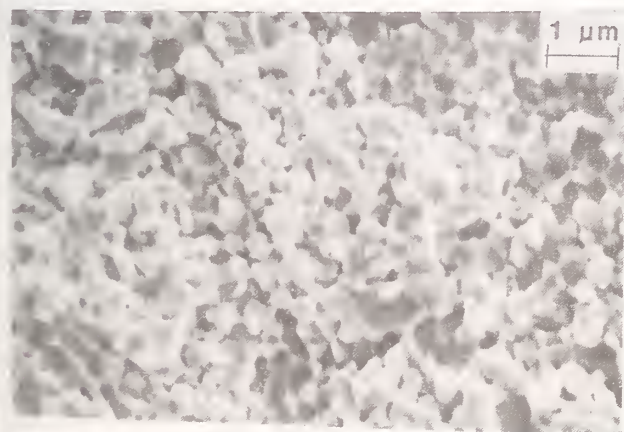
Fig. 6 Example of reasonably homogeneous porosity in fine grain hot pressed Al₂O₃. SEM of specimen A-3-39 of Table 1 having ~16.5% porosity.

of them (i.e., in combination with machining flaws). Thus, these materials further support the concepts of intermediate grain sizes limiting flaw sizes.

Next, consider the strength anisotropy due to different machining directions in composite materials with differing toughening mechanisms. All of these appear to suggest less strength anisotropy than would typically be expected for their average grain or particle sizes. However, in the case of most hot-pressed oxide-non oxide composites (Table 1), fracture origins appear to be predominantly either larger Al_2O_3 grain clusters (see Fig. 21) or porous areas (which, in the case of Al_2O_3-TiC were often associated with isolated graphite flakes or clusters of these), in both cases consistent with previous development and evaluation of these materials.[19]

Fig. 8 Example of heterogeneous porosity at the fracture origin of a ceria sample. Fracture initiated from the collection of larger pores in the bottom center of a photograph. This specimen failed at 93 MPa. Total porosity in these samples was approximately 30%. Clusters of porosity dominated failure of this material as shown in Table 1. However, this particular sample shows a somewhat greater degree of concentration and consolidation of pores than was true in some other samples.
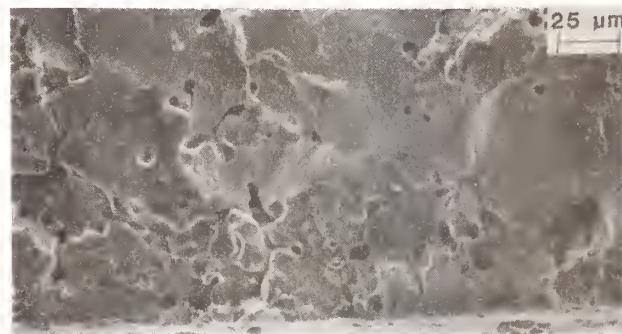
Fig. 9 Sample of heterogeneous porosity in CaO-PSZ. Failure initiated in this Zircoa-C specimen from the porosity near the tensile surface (bottom of the photograph) at a fracture stress of 165 MPa. Failure initiation from such clustered pores (which also typically limited grain sizes in the immediate region, as in this photo) was common for this material. Note larger grains from which failure did not initiate, e.g., in the bottom right area of the photo).

Fig. 7 Examples of somewhat homogeneous porosity in $MgAl_2O_4$. A) lower magnification SEM photo showing a somewhat homogeneous distribution of larger pores, many of which are not sufficiently large in size to be failure-causing flaws themselves and they are sufficiently sparse to not necessarily be frequent sources of failure. B) higher magnification SEM showing finer-scale pores, i.e. approximately the same or less than the grain size. These photos are of the $MgAl_2O_4$ (SMA1-7) with ~26% porosity.

196

Fig. 10 Example of extreme porosity heterogeneity causing failure in a highly porous hot pressed boron. This sample (584 of Table 1) failed at 215 MPa from the large pore and surrounding finer porosity in approximately the center of the photo. While this set of samples contained ~21% porosity, typically much of it was quite heterogeneous such that larger pores or pore clusters dominated failure initiation in this material, as was the case in this specimen as well as more generally shown in Table 1.
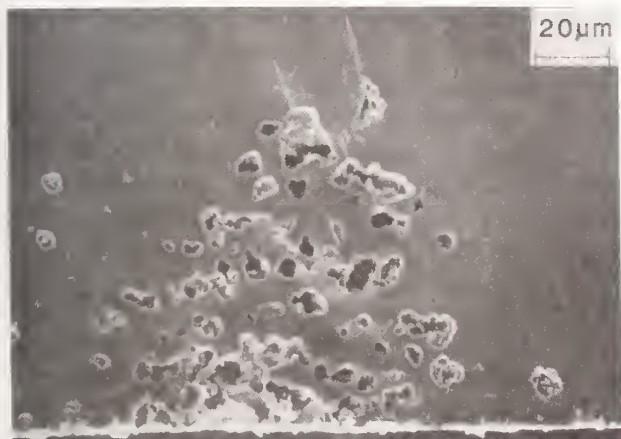
Fig. 11 Example of substantial porosity heterogeneity in a hot pressed boron sample of intermediate porosity (9.8%). This sample (566 of Table 1) failed at 353 MPa from the pore cluster shown.
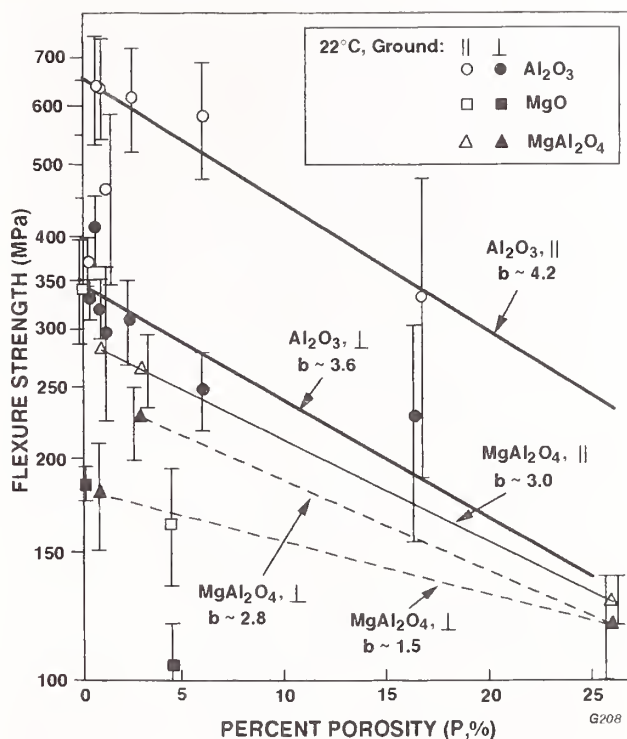
Fig. 12 Strengths for parallel and perpendicular ground Al_2O_3 (G~0.7-4μm) and $MgAl_2O_4$ (G~6-8μm) samples vs. porosity. Note these two materials show respectively nearly, and less, parallelness of the two sets of curves consistent with less porosity homogeneity in $MgAl_2O_4$ than Al_2O_3.
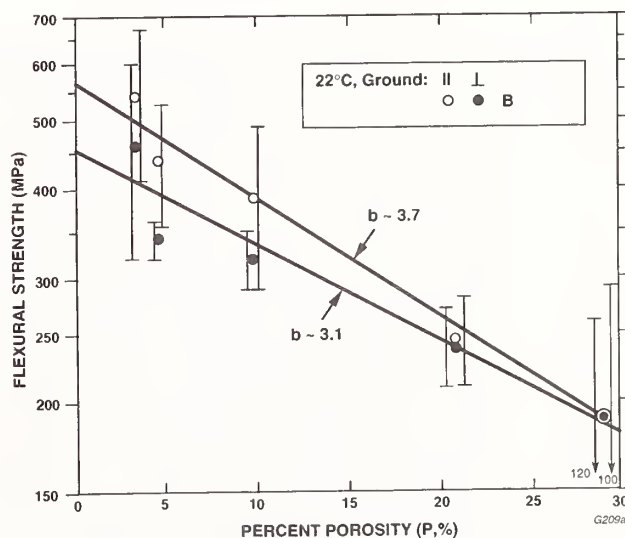
Fig. 13 Strengths for parallel and perpendicular ground boron vs. porosity. Note substantial lack of parallelness of the two curves consistent with the substantial heterogeneity of the porosity.

197
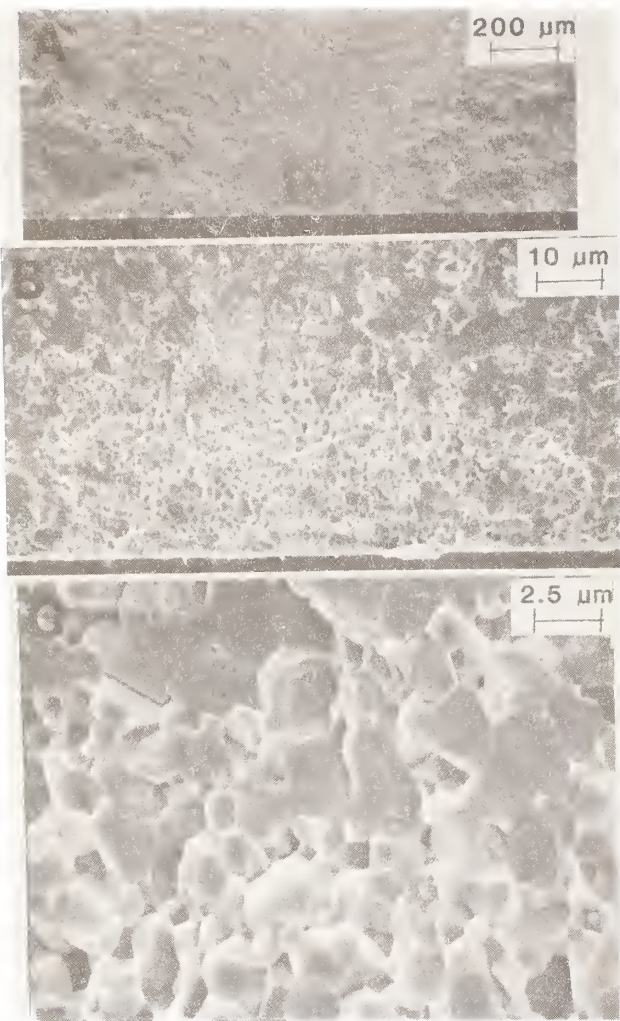
Fig. 14 Example of the failure initiation from a machining flaw in fine grain, nearly dense Al$_2$O$_3$. A) and B) show respectively finer and higher magnifications of the failure initiating flaw from machining perpendicular to the tensile axis (specimen A-3-42, 0.8% porosity). C) shows higher magnification of the demarcation between the original flaw (bottom half, all intergranular fracture) and the area of failure (top half, mixed inter- and transgranular fracture). The demarcation between total intergranular failure in the original flaw versus substantial transgranular failure beyond this was characteristic of most of the Al$_2$O$_3$ studied. A primary exception was extremely fine grain size materials where there was little or no transgranular failure. The failure stress was 387 MPa. K$_{IC}$ calculated from the failure stress and the flaw dimensions was ~3.0 MPam$^{1/2}$, which corrected to P=0 via e^{-4p} gives 3.1 MPam$^{1/2}$.
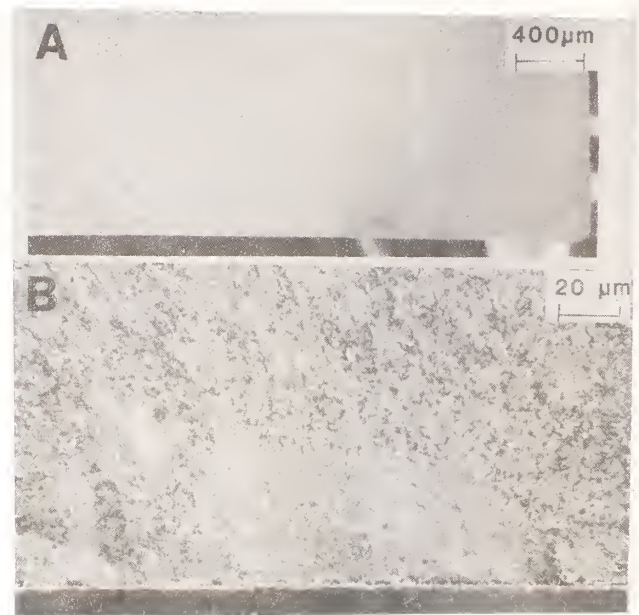
Fig. 15 Example of failure initiation from a machining flaw in a more porous (P=16.5%) Al$_2$O$_3$ body. A) shows a lower, and B) a higher magnification of the failure initiation flaw. This sample failed at 280 MPa, yielding a K$_{IC}$ of 2.2 MPam$^{1/2}$, which corrected to P=0 via e^{-4b} gives 4.2 MPam$^{1/2}$.

An important exception is the commercial hot pressed (and more homogeneous) Al$_2$O$_3$-TiC showing substantial anisotropy. Porous areas also appear to be the source of failure in the finer,* and especially the coarser grain graphite and the TiO$_2$-Al$_2$O$_3$ composites and hence a possible explanation for the limited strength anisotropy, as could possible microcracking due to the larger TiO$_2$ and graphite grains. Similarly, the AT-ZT composites which have low thermal expansion due to microcracking, exhibit quite limited strength anisotropy as a result of

---

* Note, however, that heterogeneity in the porosity of the finer grain graphite clearly did not appear to be extreme, questioning whether it was the total reason for very little strength anisotropy. Whether the soft character, or other factors such as twinning or microcracking play a role in its reduced anisotropy is unknown. Some measurable anisotropy in BN question this, but tests on dense materials, e.g. CVD graphite and BN (though complicated by preferred orientation and colony structures) could be useful.

machining direction, especially in view of their fine grain size, as noted earlier. While it may be tempting to attribute the limited strength anisotropy due to microcracking, it is equal or, quite probably more likely, that this is due to the substantial porosity in view of considerable heterogeneity in both pore spatial distribution and size. However, the limited strength anisotropy in Pyroceram may be somewhat less than might be expected for the grain size(s) of this material and no processing defects were evident nor expected in this material. Finally, the two hot pressed Al_2O_3-SiC whisker composites may also indicate some modest reduction in strength anisotropy as a function of machining relative to pure Al_2O_3 of the same grain size of the alumina matrix. However, note the trend for the strength anisotropy in these two bodies (and the commercial hot pressed Al_2O_3-TiC) to follow trends expected from the Al_2O_3 matrix grain size.

Trends are similar for various ZrO_2-toughened materials. Processing defects (mainly pores) were the common source of failure in most of the Al_2O_3-ZrO_2 composites which might explain their very limited σ anisotropy as a function of machining direction. HIPing these increased strengths and reduced the severity, but not the frequency, of such processing defects as fracture origins, modestly increasing the strength anisotropy. Similar results were obtained with various partially stabilized polycrystalline ZrO_2 materials. However, these showed more evidence of a possible intrinsic reduction in strength anisotropy. There are clearly other factors limiting strength anisotropy in some of these materials. Thus, the larger grain size and grain boundary pores of the sintered PSZ are also likely an important factor in the limited strength anisotropy as noted earlier. Also, one TZP material was extremely weak (apparently due to moisture degradation during actual use of the component from which the material was obtained). More generally, pores were a common factor in failure, including in the HIPed TZP, thus limiting strength anisotropy as in other materials. However, three factors suggest some intrinsic strength anisotropy reduction in zirconia toughened zirconia materials. First and most significant are the single crystal results, where partially stabilized ZrO_2 shows higher strength and ~0 strength anisotropy versus lower strength and higher strength anisotropy in fully stabilized ZrO_2 crystals. Porosity and grain size are not factors in these crystals (both sets of which are believed to have ~<110> tensile axes). Second, there is clearly more evidence of strength anisotropy in the TZP materials, especially at finest grain size (though less than in other materials at the same grain size).

Third, HIPing of TZP, though reducing the severity of pore origins, did not significantly increase strength anisotropy. Surface transformation and resultant surface compressive stresses in those materials[20] would be a likely explanation of such effects in ZrO_2 toughened materials since such surface stresses would likely inhibit flaw elongation. Greater effects indicated in TZP versus Al_2O_3-ZrO_2 bodies would be consistent with this, since such surface stresses should be greater in the former.

While the materials of this study did not yield nearly as extensive clear fractography results as some of the materials in earlier study,[8] these results nonetheless are consistent with the flaws from machining causing failure due to machining perpendicular to the tensile axis being more elongated relative to those causing failure as a result of machining parallel with the tensile axis of the test bars (Table 2). Thus, the flaw depth to half length ratios were typically less for grinding perpendicular versus parallel. The one possible exception was B_4C, where less differentiation in flaw anisotropy is expected because of the larger average grain size (and less definitive determination of grain size, as noted earlier). Examples of machining flaws are shown in Figs. 14-18, corner flaws (Fig. 19), and failure from large grains (Figs. 20, 21). Where flaws were definitive enough for calculating a K_{IC} (e.g. Figs. 14-18), values were consistent with previous data.[21,22]

Two issues regarding parameters effecting the strength anisotropy as a function of machining direction require further consideration. The first is the effect of machining parameters such as abrasive grit size (Fig. 2). Results of both Anderson and Bratton[5] and Ota and Miyahara[11,12] provide strength anisotropy data for machining parallel and perpendicular as a function of abrasive grit diameter. However, there is some disagreement in the trends. This may reflect differences in rate of material removal, as well as possibly of sample microstructure. Thus, further work is needed to better define how the anisotropy changes as a function of both machining and material parameters. Some work has been conducted to assess intermediate angles of machining relative to the tensile axis (showing a nearly linear transition between σ⊥ and σ∥).[23] The second aspect is the effect of specimen size relative to grinding wheel width. With typical strength test specimens, as used in this and most other studies, specimen width is often substantially less than that of the grinding wheel, such that in grinding parallel with the tensile axis the grinding wheel will typically more than cover

TABLE 2

Machining Flaw Depth to Half Length Ratio

Material[1]	G (μm)	Flaw Ratio $\sigma\perp$[3]	Flaw Ratio $\sigma\|$[3]
B	--	0.5±0.3 (15)	0.6±0.2 (15)
Al_2O_3	<2	0.5±0.3 (21)	0.8±0.3 (1)
B_4C	5-50	0.6±0.3 (13)	0.5±0.2 (8)
CZ xl	∞	0.1 (1)	0.3 (1)

1) B = boron, CZ xl - cubic zirconia crystal.

2) G = grain size. Although the G of the B was not seen in examinations of this study, it has been reported to be ~ 2μm.[15]

3) $\sigma\perp$ and $\sigma\|$ are respectively for specimens tested perpendicular and parallel to the machining direction. Number of values averaged shown in ( ).

the complete bar width. On the other hand, in grinding perpendicular to the bar axis, multiple adjacent passes of the wheel over the bar are required. This thus results in a number of regions in which the machining of the specimen occurred at or near the edge of the grinding wheel, where abrasive interactions with the workpiece may be different than under the main part of the grinding wheel. A few trials have previously been made with substantially larger test specimens, such that possible edge effects of grinding wheels would be experienced in both grinding parallel and perpendicular to the tensile axis.[8] However, these were not definitive since other (e.g., processing) defects became an increasing factor in the failure as specimen size was increased. Thus, it is still uncertain at this stage whether or not machining flaws associated with abrasive-workpiece interactions near the edge of the wheel may be different from those occurring from abrasive particles well away from the wheel edges, hence another area for further investigation.

Finally, three points should be noted. First, the strength anisotropy is quite important in the

design and manufacture of many components. Second, the flaw shape factors that underly this anisotropy are an important probe to help identify mechanism of failure, e.g. strength-grain size relations as emphasized here. However, other uses should be feasible, e.g. probing effects of surface stresses, e.g. as indicated for MgO and TZP here. Third, the grain size trends appear to be very common, if not universal, when effects of other sources of failure are removed.
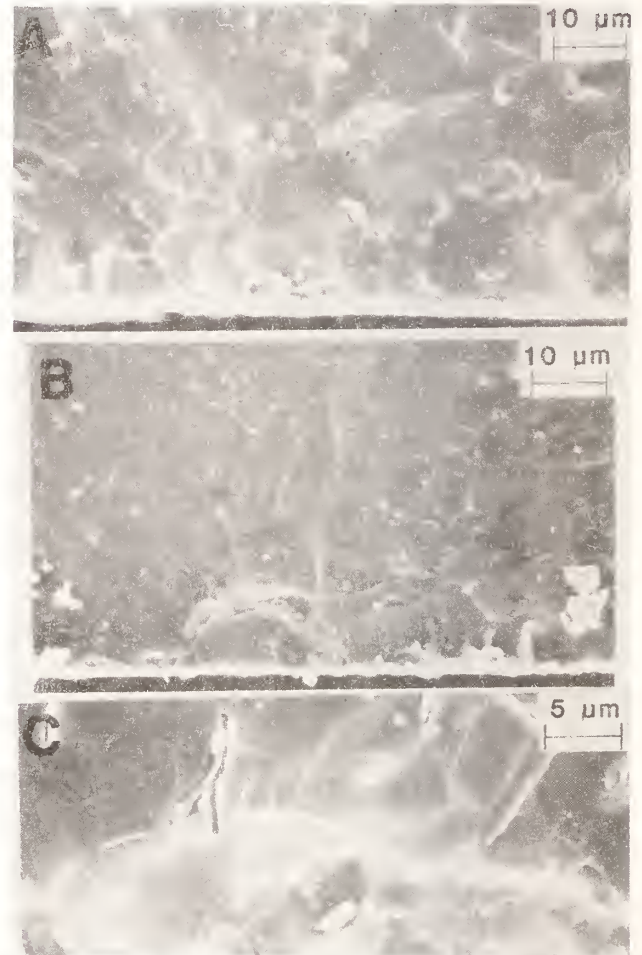
Fig. 16 Samples of machining flaws in B_4C. Representative SEM photos of machining flaws causing failure in test bars (typically approximately the bottom center of the photograph). The samples, their failure stresses and the fracture toughnesses calculated from their failure stress and flaws are as follows: A) Carborundum, 370 MPa, K_{IC} ~1.8 MPa m$^{1/2}$; B) Union Carbide heat treated, 266 MPa, K_{IC} ~1.7 MPa m$^{1/2}$; C) ESK, 354 MPa, K_{IC} ~4 MPa m$^{1/2}$. All samples represent failure from flaws from machining perpendicular to the tensile axis. Note the essentially exclusive transgranular failure and that the grain structure is not especially well defined.

200
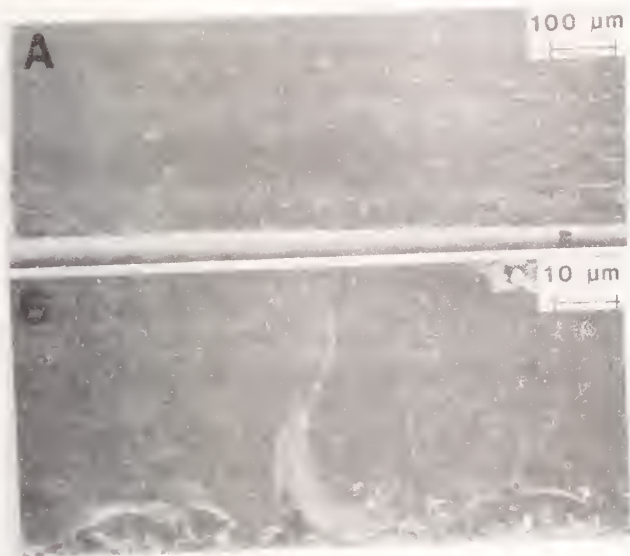
Fig. 17 Example of failure initiation from a machining flaw from grinding perpendicular to the tensile axis in hot pressed boron. A) and B) are respectively lower and higher magnifications of the failure initiation, with B) showing details of the elongated machining flaw from grinding perpendicular to the tensile axis. Sample 383, failure stress 340 MPa. K_{IC} calculated from the failure stress and flaw character ~1.9 MPa m$^{\frac{1}{2}}$ (correcting for the 3.2% porosity using e^{-4P} would increase the fracture toughness to ~2.2 MPa m$^{\frac{1}{2}}$ for P=O. Note the absence of any indication of grain structure in this material.
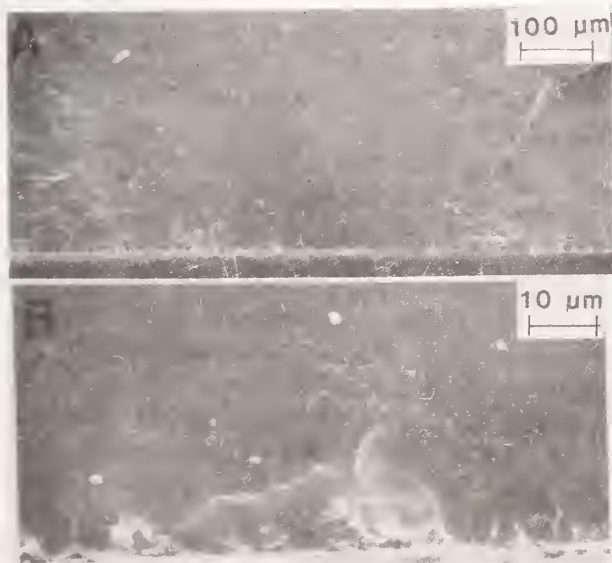
Fig. 18 Example of a failure initiating flaw for machining parallel with the tensile axis of a hot pressed boron. A) lower magnification

and B) higher magnification of the failure initiating flaw. Note the less-elongated character of this flaw relative to that shown in Fig. 17. Specimen was from the batch designated 560, with a failure stress of 437 MPa. The K_{IC} calculated from the failure stress and flaw character is ~1.7 MPam$^{\frac{1}{2}}$ (correction for the ~4.5% porosity versus e^{-4P} would raise this to ~2 MPa m$^{\frac{1}{2}}$ at P=O.
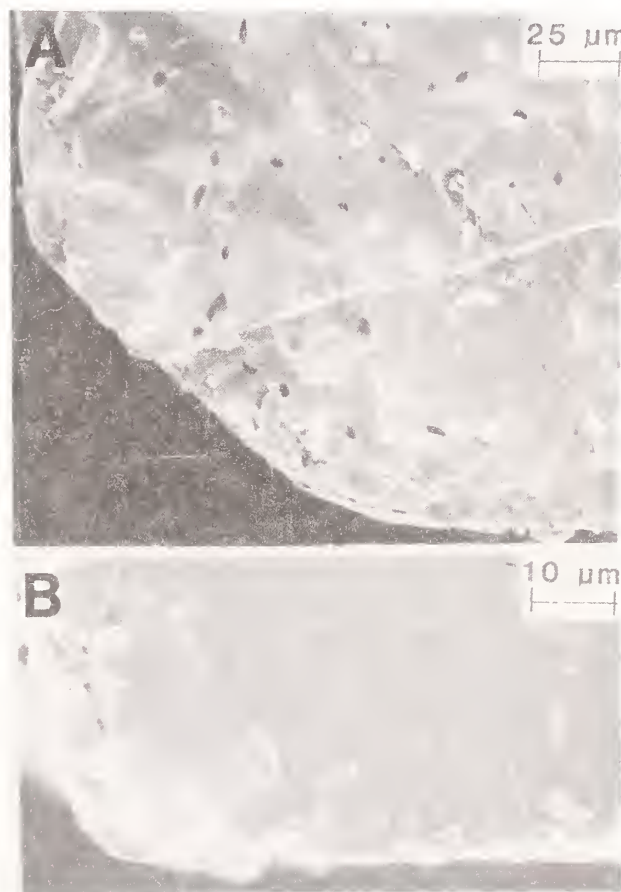
Fig. 19 Samples of corner failures. A) a ceria sample (failure stress 74 MPa). Note that while the failure markings clearly show failure initiation from the rounded corner, specific size and character of the flaw causing failure cannot be delineated. B) a hot pressed boron (560) failing at 460 MPa. Note a reasonably well-defined flaw extending in from the corner of this material which was generally much better for showing specifics of flaw character.

201
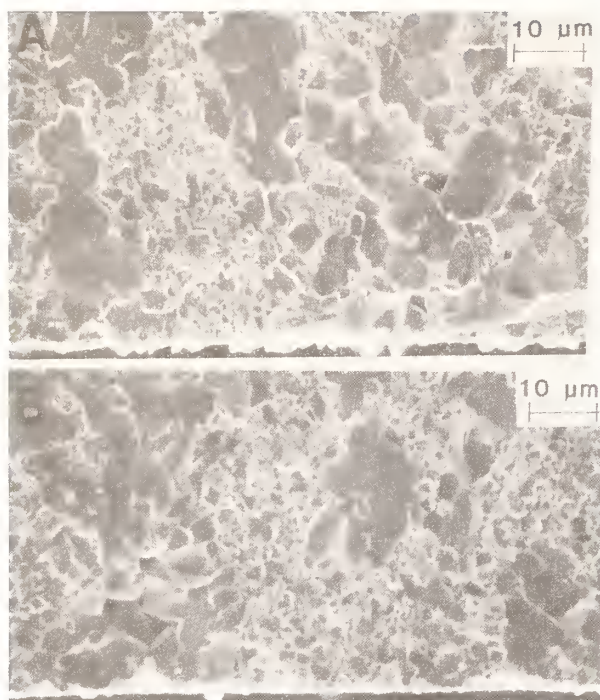
Fig. 20 Examples of larger grain clusters at probable fracture origins in Al_2O_3+27 v/o TiB_2 samples. A) and B) represent two probable fracture origin areas in this composite material. Note the hetero-geneous distribution of larger Al_2O_3 grain clusters, some of which are often associated with one or two moderately sized pores, e.g., the lower left-hand area of photo B).
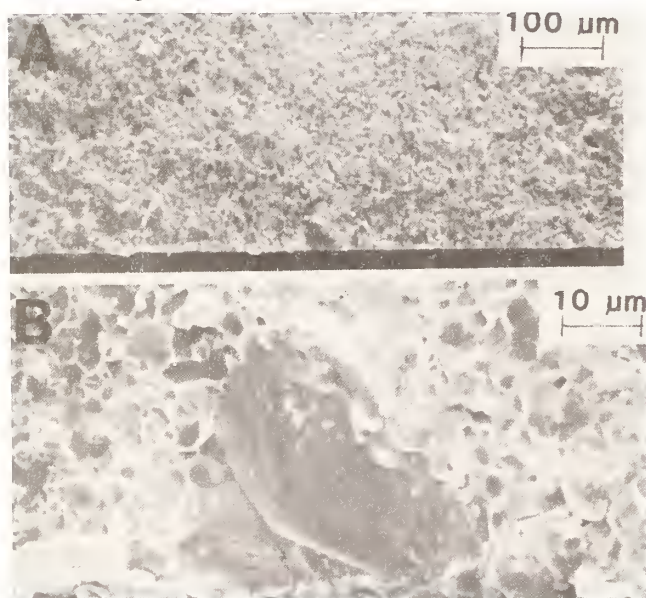
Fig. 21 Example of failure initiation from larger grains in hot pressed Al_2O_3. A) and B) represent respectively lower and higher magnifications of the large grain fracture origin in a sample (A-1-39) failing at 396 MPa. Note that using the large grain as the failure flaw size yields a K_{IC} of ~2.7 MPa m$^{1/2}$.

4. Summary and Conclusions

Substantial further data on the strength anisotropy as a function of grain size at room temperature for grinding parallel or perpendicular with the tensile axis of specimens has been provided. This includes a much broader range of materials in terms of composition, crystal structures, microstructures, and fracture mechanisms. This clearly reinforces and extends previous findings showing that grain size is a major variable in this effect. The greatest anisotropy occurs at fine grain size (or in amorphous materials) and decreases as grain size increases, rising to ~ zero anisotropy, i.e. limited or no difference, for strength ground perpendicular versus parallel with the tensile axis of bars at intermediate grain sizes (e.g., 20 to 80 µm). It then increases again, extrapolating to the range of single crystal values (which vary with crystal orientation relative to machining direction due, for example, to orientation of preferred fracture planes relative to abrasive motions and resultant stress directions). Fractography corroborates previous findings that a major factor in the machining strength anisotropy, i.e. lower strengths from machining perpendicular to the tensile axis versus machining parallel with the tensile axis, is greater elongation of flaws formed parallel vs. perpendicular to the machining direction (which dominate failure respectively for stressing perpendicular and parallel to the machining direction). The concept of the minimum strength anisotropy being due to the grain size constraining the flaws, hence first and more extensively constraining elongated flaws from perpendicular machining, is further supported. Thus, data shows a minimum in anisotropy at intermediate grain size unless greater anisotropy at larger, and especially finer, grain size are reduced or overridden by heterogeneous larger grains, porosity or other processing defects (e.g. as shown by fractography).

This study also further reinforces results showing that fine homogeneous porosity has little or no effect on strength anisotropy as a function of machining direction. However, the presence of larger pores or pore clusters which are frequent origins of failure can significantly reduce the machining anisotropy by being alternate sources of failure to the machining flaws, or combining with machining flaws, thus also limiting anisotropy. Finally, evaluations of the machining anisotropy in various ceramic composites indicate that some of these may provide some intrinsic limitations on strength anisotropy as a function of machining direction, with the most probable of these being TZP materials. However, even in these materials, both

grain size and porosity also have some impact on strength anisotropy similar to other materials.

REFERENCES

1. R.W. Rice, "The effect of grinding direction on the strength of ceramics," NBS Special Pub. 348, The Science of Ceramic Machining and Surface Finishing, Eds. S.J. Schneider Jr. and R.W. Rice, pp. 365-76, U.S. Govt. Printing Office, Washington, D.C. (Issued May 1972).

2. R.E. Mould, and R.D. Southwick, "Strength and static fatigue of abraded glass under controlled ambient conditions: II, Effect of various abrasions and the universal fatigue curve," J. Am. Cer. Soc. [42], 582-92 (1959).

3. H.P. Kirchner, R.M. Gruver, and R.E. Walker, "Strength effects resulting from simple surface treatments," NBS Special Pub. 348, The Science of Ceramic Machining and Surface Finishing, Eds. S.J. Schneider Jr. and R.W. Rice, pp. 353-63, U.S. Govt. Printing Office, Washington, D.C. (Issued May 1972).

4. R.W. Rice, "Machining of Ceramics" in "Ceramics for high-performance applications," Proc. of the Second Army Materials Technology Conference, Eds. J.J. Burke, A.E. Garum, and R.N. Katz, pp. 287-343, Metals & Ceramics Info. Center, Columbus, Ohio (1978).

5. C.A Anderson and R.J. Bratton, "Effect of surface finish on the strength of hot pressed silicon nitride," NBS Special Publication 562, The Science of Ceramic Machining and Surface Finishing II, B.J. Hockey and R.W. Rice, Eds., pp. 463-474 U.S. Government Printing Office, Washington, D.C. (1979).

6. D.W. Richerson, J.J. Schuldies, T.M. Yonushonis, and K.M. Johansen, "ARPA/ Navy Ceramic Engine Materials and Process Development Summary," Ceramics for High Performance Applications II, Proc. of the Fifth Army Materials Technology Conference, Eds. J.J. Burke, E.N. Lenoe and R.N. Katz., pp. 625-650, Metals & Ceramics Info. Center, Columbia, Ohio (1978).

7. J.J. Mecholsky, S.W. Freiman, and R.W. Rice, "Effect of grinding on flaw geometry and fracture of glass, J. Am. Cer. Soc. [60] 3-4 (1977).

8. R.W Rice, and J.J. Mecholsky, Jr., "The nature of strength controlling machining flaws in ceramics," NBS Special Publication 562, The Science of Ceramic Machining and Surface Finishing II, B.J. Hockey and R.W. Rice, Eds., pp. 351-78, U.S. Government Printing Office, Washington, D.C. (1979).

9. R.W. Rice, "Machining flaws and the strength grain size behavior of ceramics," Ibid., pp. 429-452.

10. R.W. Rice, J.J. Mecholsky, Jr., and P.F. Becher, "The effect of grinding direction on flaw character and strength of single crystal and polycrystalline ceramics," J. Mat. Sci. 16 (1981) 853-862.

11. Ota, Minoru and Miyahara, Katsutoshi, "The influence of grinding on the flexural strength of ceramics," Soc. of Manufacturing Engineers, MR90-538, paper presented at 4th International Grinding Conference, Dearborn, MI (1990).

12. K. Subramanian, and S. Ramanath, "Principles of abrasive machining," Engineered Materials Handbook Vol. 4, pp. 315-28, The Materials Information Society (1991).

13. R.W. Rice, "Correlation of machining-grain size effects on tensile strength with tensile strength-grain size behavior," J. Am. Cer. Soc. in press, (1992).

14. R.W. Rice, "Effects of porosity on strength anisotropy due to machining direction," (to be published).

15. D.R. Petrak, R. Ruh, and G.R. Atkins, "Mechanical properties of hot-pressed boron suboxide and boron, Am. Cer. Soc. Bull.

53[8], pp. 569-573 (1974).

16. R.W. Rice, "Microstructure dependence of mechanical behavior of ceramics," Treatise on Materials and Technology, Vol. II, Ed. R.K. McCrane, pp. 199-381, Academic Press, Inc., New York (1977).

17. R.W. Rice, "Pores as fracture origins in ceramics," *J. Mat. Sci.* **19** pp. 895-914 (1984).

18. R.W. Rice, K.R. McKinney, and R.P. Ingel, "Grain boundaries, fracture, and heat treatment of commercial partially stabilized zirconia," *J. Am. Cer. Soc.* **64** [12] C-175 - C-177 (1981).

19. C.P. Cameron, J.H. Enloe, L.E. Dolhert, and R.W. Rice, "A comparison of reaction vs. conventionally hot-pressed ceramic composites," *Ceram. Eng. Sci. Proc.* **11**[9-10], pp. 1190-1202 (1990).

20. J.S. Reed, and A-M. Lejus, "Affect of Grinding and Polishing on Near-Surface Phase Transformations in Zirconia," Mat. Res. Bull. **[12]**, pp. 949-54 (1977).

21. R.W. Rice, R.C. Pohanka, and W.J. McDonough, "Effect of stresses from thermal expansion anisotropy, phase transformations, and second phases on the strength of ceramics," *J. Am. Cer. Soc.*, [63], 11-12 (Nov.-Dec. 1980).

22. R.W. Rice, "Effects of thermal expansion mismatch stresses on the room-temperature fracture of boron carbide," *J. Am. Cer. Soc.* [10] 3116-18 (1990).

23. I. Tomayasu "Grinding characteristics and material strength after grinding of fine ceramics," Toyoda Machine Works, Ltd.

DIAMOND GRINDING OF SILICON NITRIDE CERAMIC

J. E. MAYER, JR. and G. P. FANG
Texas A&M University, College Station, TX

Diamond grinding of hot pressed silicon nitride (HPSN) ceramic material is the main focus of this paper. The object of this work is to achieve high overall removal rates while at the same time providing high strength in the final ground product. Grinding wheels with different diamond grit sizes have been explored. Results reported include surface characterization of the ground surface, transverse rupture strength data, and grinding flaw detection results. Key findings are: All finish ground surfaces showed surface damage (pitting) over the range of wheel grit sizes employed (5.1 to 249 microns). For longitudinally ground test bars, there is no apparent loss of strength as the grit depth of cut increases for the range investigated (0.085 to 0.281 microns). For transversely ground test bars, there is a decrease in strength as the grit depth of cut increases beyond a critical value. For diamond grinding of HPSN ceramic this critical value appears to be about 0.160 microns.

1. Introduction

Advanced ceramics, such as silicon nitride and silicon carbide, have the potential for broader use in structural applications such as heat engines which would greatly increase their efficiency; however, the strength variability and machining cost must be improved before this can take place (1-4). This paper is directed at providing ceramics which are ground with improved strength while at the same time achieving efficient grinding rates.

The conventional ceramic machining operation for final shaping and finishing is diamond grinding. Material removed by this process is usually by a microfracturing process (5-10). This fracturing process induces microcracks in the finished surface. The induced microcracks range down to 5-20 microns (11). These flaws result in variable strength of the produced components which causes the unreliable strength reputation. Grinding parameter investigations can improve the induced flaw situation. Parameters can be selected which result in less microfracturing, and thus can lead to higher strength of the ground ceramic material.

The main focus of this paper is diamond grinding of hot pressed silicon nitride (HPSN) ceramic material. Grinding wheels with different diamond grit sizes were used to grind transverse rupture strength bars. Grinding direction was in both the longitudinal direction and transverse to the bar length. These specimens were employed to obtain transverse rupture strength data (12-13) and to characterize the ground surfaces by use of scanning electron microscope (SEM) and profilometer. The grit surface density of the grinding wheels was measured by means of an optical microscope sighting on the grit flats; and this data was employed to compute the grit depth of cut. In this paper, the relationships of grit depth of cut and grind direction with strength and surface characteristics of the ground specimen for HPSN are discussed. Grit depth of cut to achieve high strength in the ceramic during grinding (10,14-19) is also discussed.

An investigation into methods to detect flaws (microcracks) induced by grinding of ceramics is being conducted utilizing surface monitoring techniques. Flaws (microcracks) in the range of 5-20 microns, which are of typical interest

regarding grinding cracks in ceramics (11), are the target size for these techniques. The flaw detection methods and progress in this investigation are discussed in this paper.

2.   Experimental Procedure

2.1   Machining

HPSN bars were obtained with approximately 0.508 mm (0.020 in) oversize all around to allow for the grind stock required in MIL-STD-1942(MR) (12-13). MIL-STD-1942(MR) was followed because it is a tighter specification than ASTM-C1161-91. These bars were all cut from one hot pressed billet. In this research, the bars were rough ground for the first 0.457 mm (0.018 in) and then finish ground for the final 0.0508 mm (0.002 in) in accordance with MIL-STD-1942(MR). The final bar dimensions were 3.00 mm x 4.00 mm x 45.0-50.0 mm (0.118 in x 0.158 in x 1.75-2.00 in), which are the dimensions required for the transverse rupture strength tests.

Resinoid-bonded diamond wheels with different grit sizes which were employed in this research are shown in Table 1. These wheels have 150 concentration and uncoated diamond. The outer diameter of the wheel is 152.4 mm (6 in) and the width and thickness of the diamond layer are 3.175 mm (0.125 in). The grit surface density was measured in this research by means of an optical microscope sighting on the grit flats.

A commercial surface grinder with microprocessor control on the wheel depth of cut was used in this research. The wheel depth of cut could be controlled at a unit of 1.27 microns (0.00005 in). The following grinding parameters were held constant at the indicated values: wheel speed = 24.69 m/s (4860 ft/min), table feed for roughing = 11.18 mm/s (26.4 in/min), table feed for finishing = 7.62 mm/s (18.0 in/min), and crossfeed = 1.59 mm (0.0625 in). The wheel depth of cut for roughing was 0.0254 mm (0.001 in) and for finishing 0.00254 mm (0.0001 in), except for the 5.1 micron grit wheel which used a 0.00127 mm (0.00005 in) wheel depth of cut for finishing. The same wheel was employed for roughing and finishing in the case of each grit size, except for the 5.1 micron grit wheel where the 50.8 micron grit wheel was used for roughing. The specific material removal rates for roughing and finishing conditions are shown in Table 2. For strength tests, five bars were prepared at each grinding condition with the grind direction longitudinal to the length of the bar, and another set of five bars were ground transverse to the bar length in order to determine the effect of grind direction on the strength. A water miscible synthetic grinding fluid was used in these experiments. The grinding wheels were trued with a commercial diamond roll truing device and were dressed with aluminum oxide dressing sticks. Truing and dressing procedures were standardized and were those recommended by the diamond grinding wheel supplier.

Table 1. Grit Size of Diamond Grinding Wheels

Wheel	Mean Grit Size		Grit Surface Density	
	microns	inches	No./mm^2	No./in^2
D4/8MIC-R150BXL6145-1/8	5.1	0.0002	49.91	32,200
SDG320-R150BXL6145-1/8	50.8	0.0020	27.59	17,800
SDG180-R150BXL6145-1/8	87.5	0.0035	11.66	7,520
SDG110-R150BXL6145-1/8	152	0.0060	8.324	5,370
SDG100-R150BXL6145-1/8	249	0.0098	6.402	4,130

Table 2. Specific Material Removal Rates

Grind Type	mm^3/s · mm	in^3/min · in
Roughing	0.284	0.0264
Finishing	0.0194	0.0018
Finishing (5.1 micron grit wheel only)	0.00968	0.0009

2.2 Surface Analysis

A scanning electron microscope (SEM) was utilized to characterize the ground surfaces for all of the grinding wheels. Magnifications employed were either 1500X or 3500X. Magnification of 7500X was used to investigate grinding swarf, and 10,000X was employed to illustrate plastic deformation on the ground surface. A contacting surface profilometer was utilized to measure the surface finish of the ground specimens.

2.3 Strength Testing

Transverse rupture strength tests were performed in accordance with MIL-STD-1942(MR) (12-13) on all bars ground in this research. The test fixture shown in Figure 1 was employed in these strength tests and the fixture was loaded by means of a universal test machine. A total of five bars were tested for each grinding condition to establish the transverse rupture strength. The range of strengths and the Weibull characteristic strength were utilized to present the results in this investigation.

2.4 Flaw Detection

The overall research plan includes attempts to detect flaws (microcracks) induced by grinding via various non-destructive surface monitoring techniques. The first two methods being investigated are the nuclear magnetic resonance imaging (NMRI) technique (20) and a thermal acoustic surface wave (Thermal Acousto Photonic NDE (TAP-NDE)) technique (21-25).

3. Experimental Results and Discussion

3.1 Grit Depth of Cut

The controlling factor in determining the material removal mechanism is believed to be the grit depth of cut, t, which is illustrated in Figure 2 (16-17,26-27).
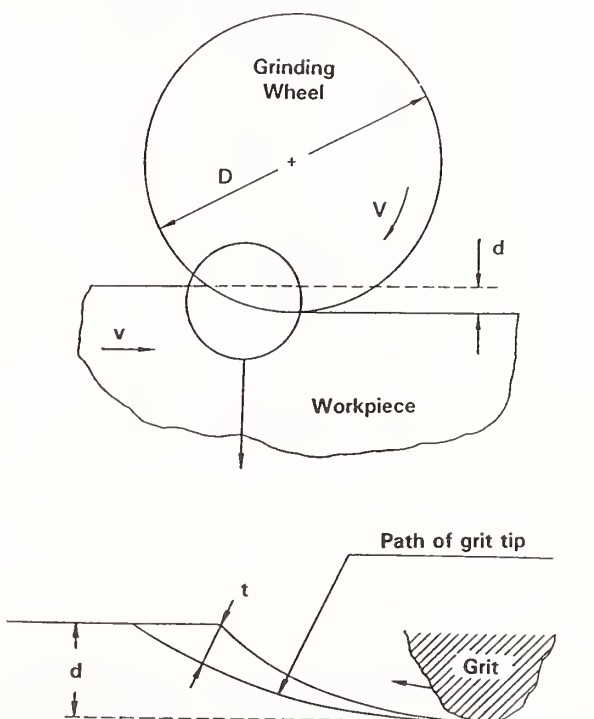

Figure 2. Illustration of the Surface Grinding Process Showing Various Process Variables.
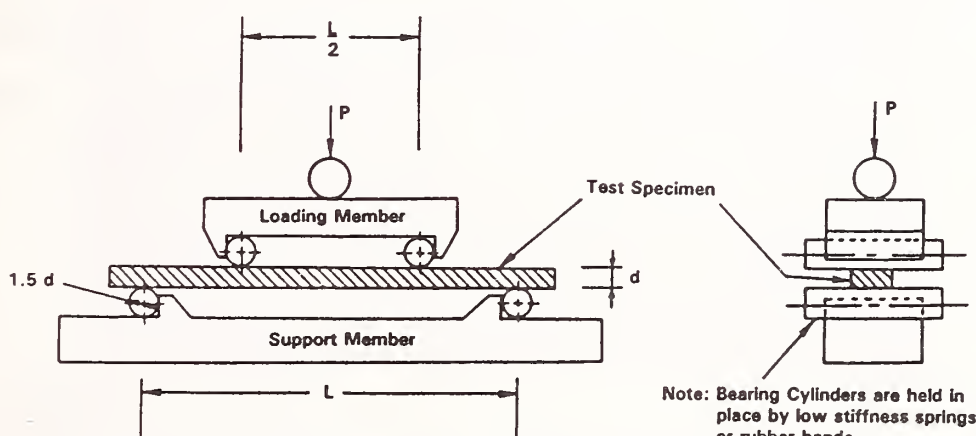
Figure 1. Four-Point Transverse Rupture Strength Test Fixture.

207

The value of t depends on both machine and wheel parameters and can be computed from the following expression (28):

$$t = \sqrt{\frac{4v}{VCr}\sqrt{\frac{d}{D}}} \qquad (1)$$

where t is grit depth of cut (maximum undeformed chip thickness)

C is the number of active cutting points per unit area of the wheel periphery (grit surface density)

r is the ratio of chip width to average undeformed chip thickness

V is wheel peripheral speed

v is workpiece speed (table speed)

d is wheel depth of cut

D is wheel diameter

The value of r is reported to be in the range of 10-20 (28); r is assumed to be equal to ten in this paper which should give a conservative value for t, i.e. the computed value of t may be larger than the actual value. The value of C was determined by means of an optical microscope sighting the grit flats after grinding with the wheel. The values of C so determined are shown in Table 1. The values of t for the grinding conditions employed in this research were computed using Equation (1) and are reported in Table 3, listed by diamond grit size. The values of grit depth of cut, t, shown in Table 3 will be utilized to help explain the surface characteristics and strength results.

for each of the grinding conditions, i.e. for each wheel grit size. These micrographs are shown in Figure 3. All of the SEM micrographs in Figure 3(a) - 3(f) show surface damage (pitting) and a combined ductile and fracture mode grinding (16,19,29); however, the trend is toward less damage and more ductile mode appearance as the diamond grit size becomes smaller, i.e. as the grit depth of cut becomes smaller. In this paper, the pitting is assumed to be caused by a fracturing process; and surface areas which are smooth and without pits are assumed to have been produced by a ductile material removal process, i.e. by plastic deformation. None of the micrographs, not even for the largest grit size Figure 3(e)-3(f), show evidence of extreme brittle fracture as observed when grinding glass as illustrated in Figure 4. This can be explained by the much higher fracture strength of HPSN compared to glass.

For the 5.1 micron grit wheel, a SEM micrograph was also made after the first 25.4 microns (0.001 inch) depth was removed during finish grinding. Figure 5 shows this 25.4 microns (0.001 inch) finish depth SEM micrograph. All other SEM micrographs of the ground surface were made after completion of finish grinding, i.e. after 50.8 microns (0.002 inches) depth was removed by finish grinding. By comparing Figure 5 with Figure 3 (a), one can observe the surface at the halfway point in finish grinding relative to that at the endpoint of finish grinding. Figure 5 exhibits greater surface damaged area than Figure 3 (a). The surface damage in Figure 5 was probably

Table 3. Grit Depth of Cut, t

Mean Grit Size		Computed t Values			
		Roughing		Finishing	
microns	inches	microns	micro-inches	microns	micro-inches
5.1	0.0002	--	--	0.0845	3.33
50.8	0.0020	0.2910	11.46	0.1351	5.32
87.5	0.0035	0.4478	17.63	0.2079	8.19
152	0.0060	0.5299	20.86	0.2460	9.69
249	0.0098	0.6041	23.78	0.2805	11.04

3.2   Surface Characteristics

Scanning electron microscope (SEM) micrographs were made of the finish ground surface

induced initially by the roughing grind wheel (50.8 micron grit) and is being removed by the 5.1 micron grit wheel during finish grinding.
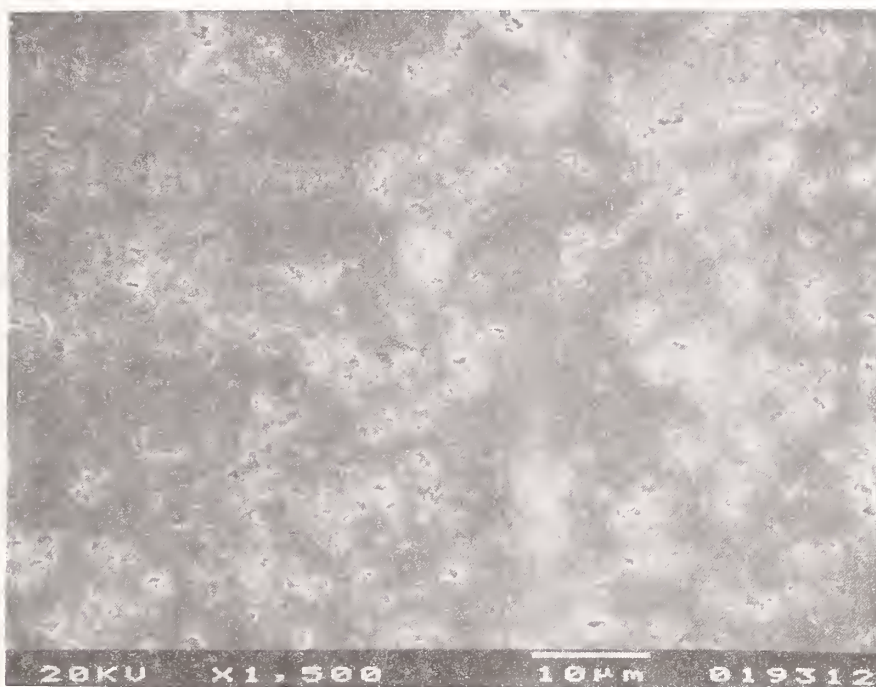
3 (a) 5.1 Micron Diamond Grit Size.
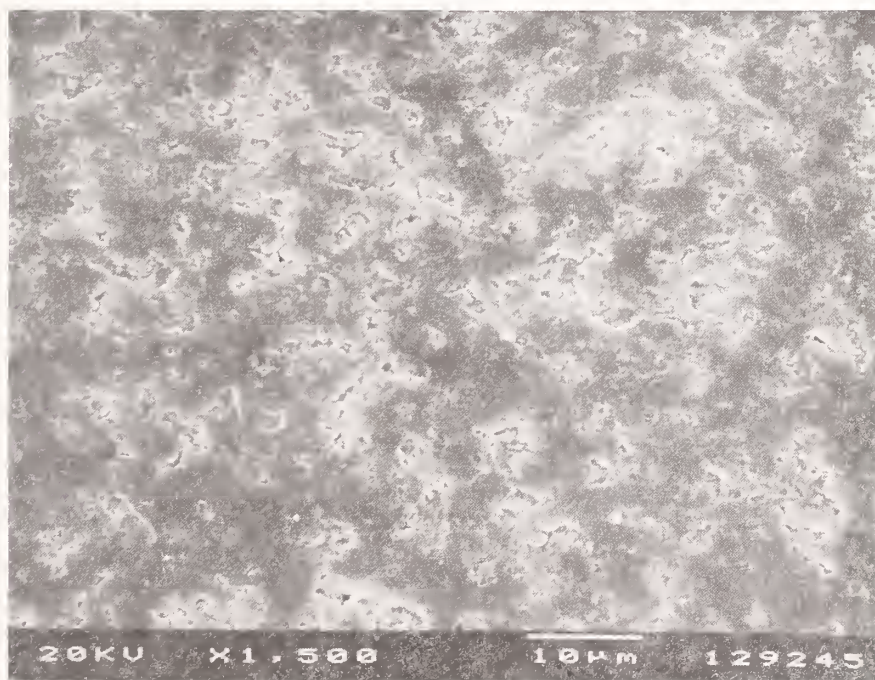
3 (b) 50.8 Micron Diamond Grit Size.
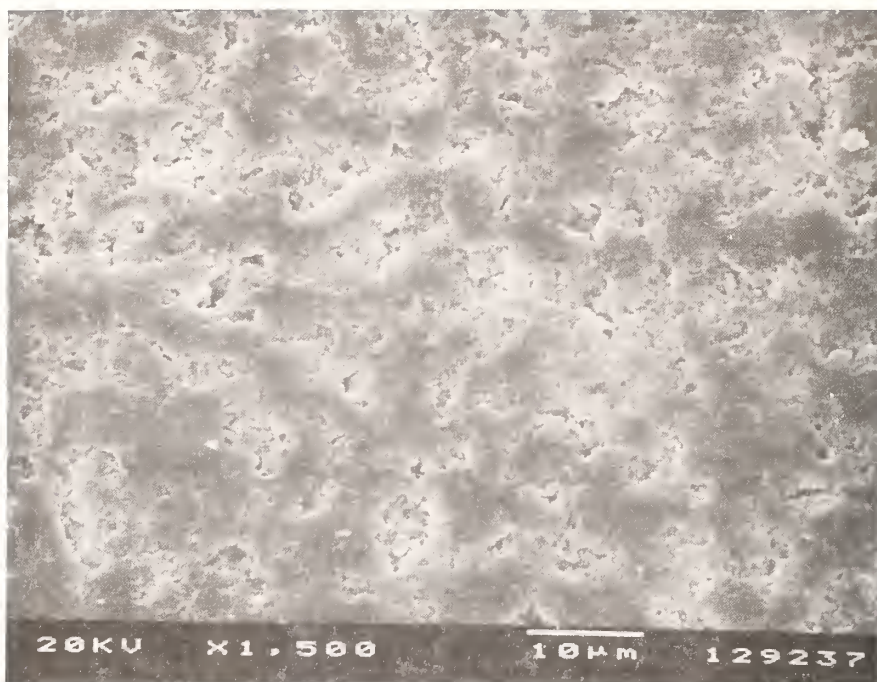
3 (c) 87.5 Micron Diamond Grit Size.
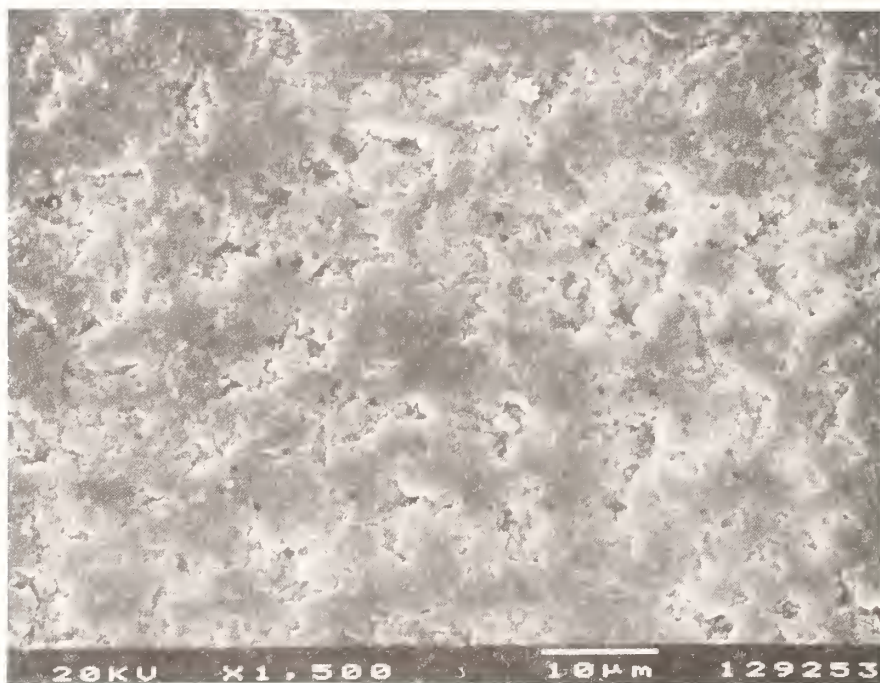
3 (d) 152 Micron Diamond Grit Size.
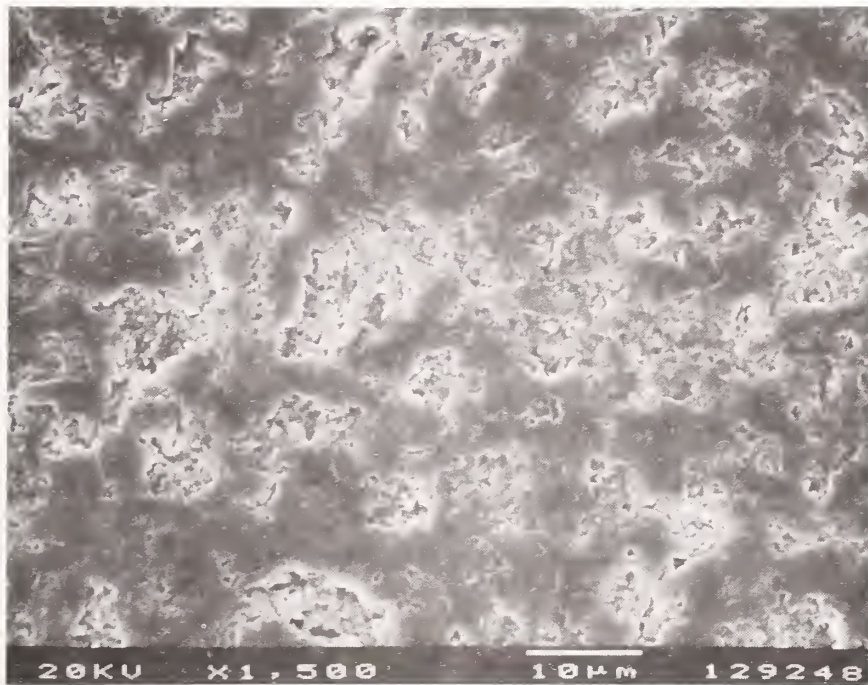
3 (e) 249 Micron Diamond Grit Size.
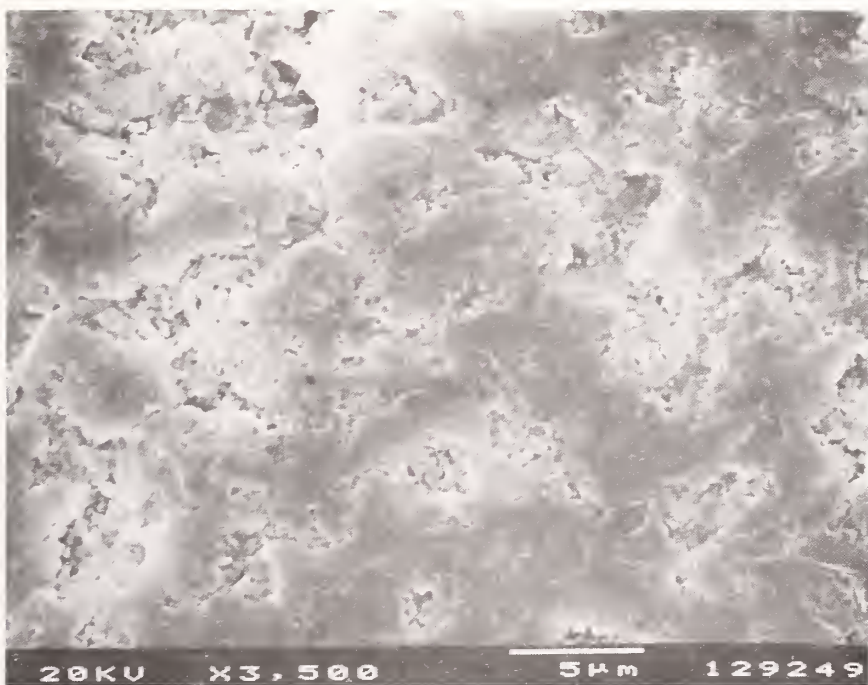
3 (f) 249 Micron Diamond Grit Size (Higher Magnification).

Figure 3. SEM Micrograph of Finish Ground Surfaces.
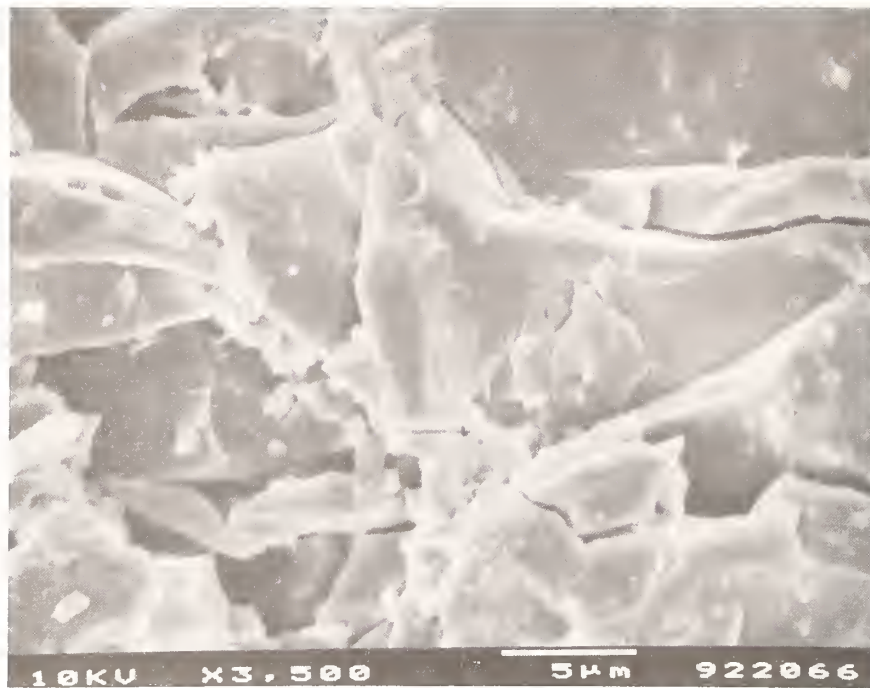
Figure 4. SEM Micrograph of Ground Glass Surface (102 Micron Diamond Grit Size).
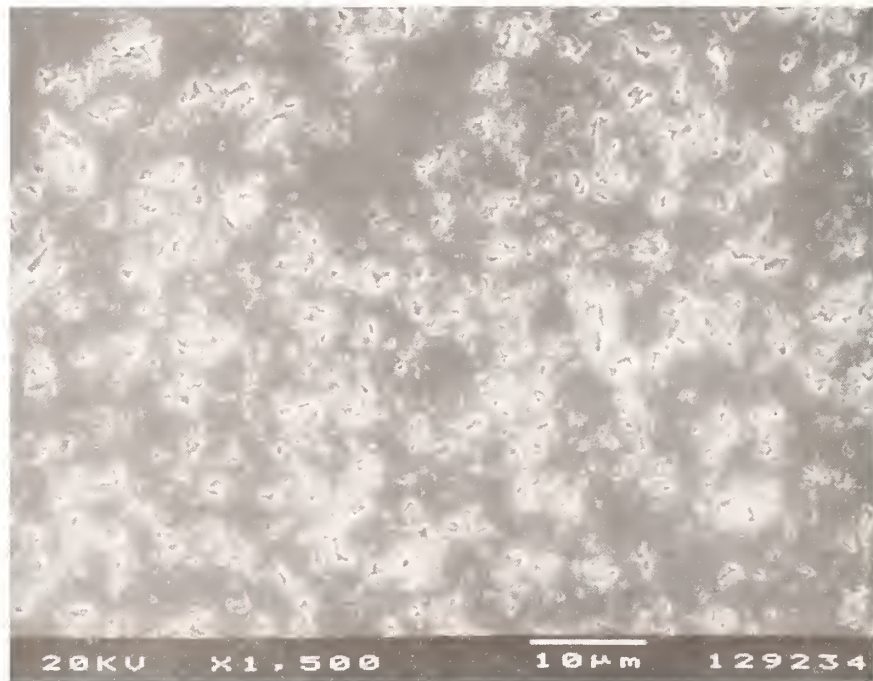
Figure 5. 5.1 Micron Diamond Grit Size (at halfway point in finish grinding).

212

The percentage of surface damaged area (total pitted area relative to total surface area) was measured by means of optical image processing of the SEM micrographs for the ground surfaces produced with the 5.1 micron grit wheel up through the 249 micron grit wheel. SEM micrographs with 750X magnification were employed for these measurements. The results are listed in Table 4. The percent area values in Table 4 are the average of five different locations on the ground surface. Table 4 indicates that the percent surface damaged area ranges from about 3% to 25% as the wheel grit size ranges from 5.1 microns to 249 microns.

Table 4.   Percentage of Surface Damaged Area

| Mean Grit Size | | Percent Damaged |
microns	inches	(Pitted) Area
5.1	0.0002	2.83
50.8	0.0020	11.91
87.5	0.0035	16.56
152	0.0060	23.85
249	0.0098	24.91

Figure 6 shows SEM micrographs of grinding swarf and Figure 7 a grinding groove under higher magnification. The swarf was collected by employing fresh coolant, collecting coolant coming from the wheel during grinding, depositing a coolant drop on a SEM stud, and letting air dry. In Figure 6, Sample A and Sample B are SEM micrographs taken at different locations in the grinding swarf. Figure 8 shows the bulk structure of the HPSN which was obtained by etching the ground surface with 49% hydrofluoric acid for 2 hours at room temperature. From a comparison of the swarf in Figure 6, the surface area region next to the grinding groove in Figure 7, and the damaged areas in Figure 3 with the bulk structure in Figure 8, it appears that the material removal mechanism in the damaged areas is by fracturing out HPSN grains or clumps of grains.

6 (a)   Sample A.

213
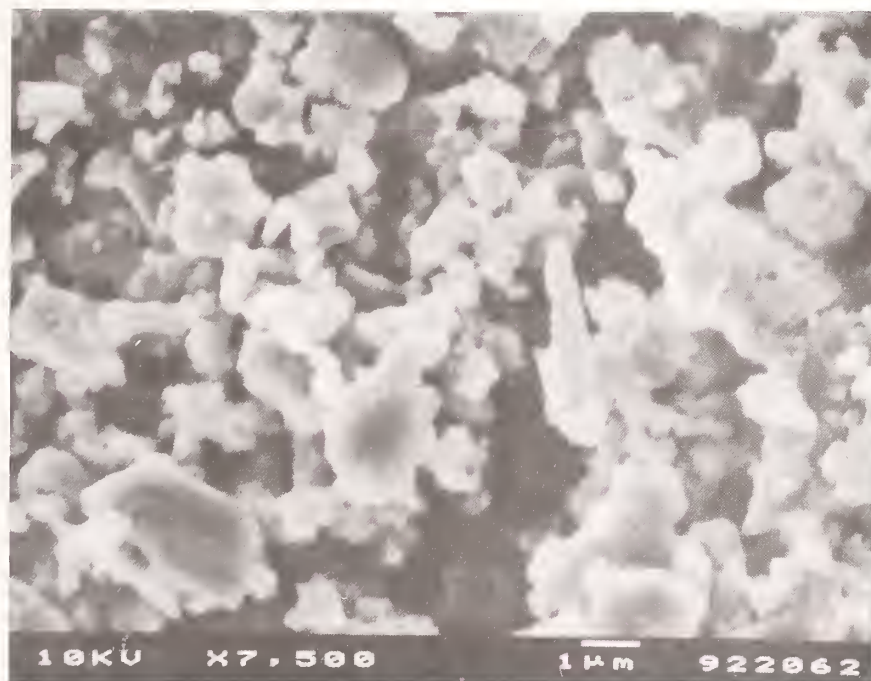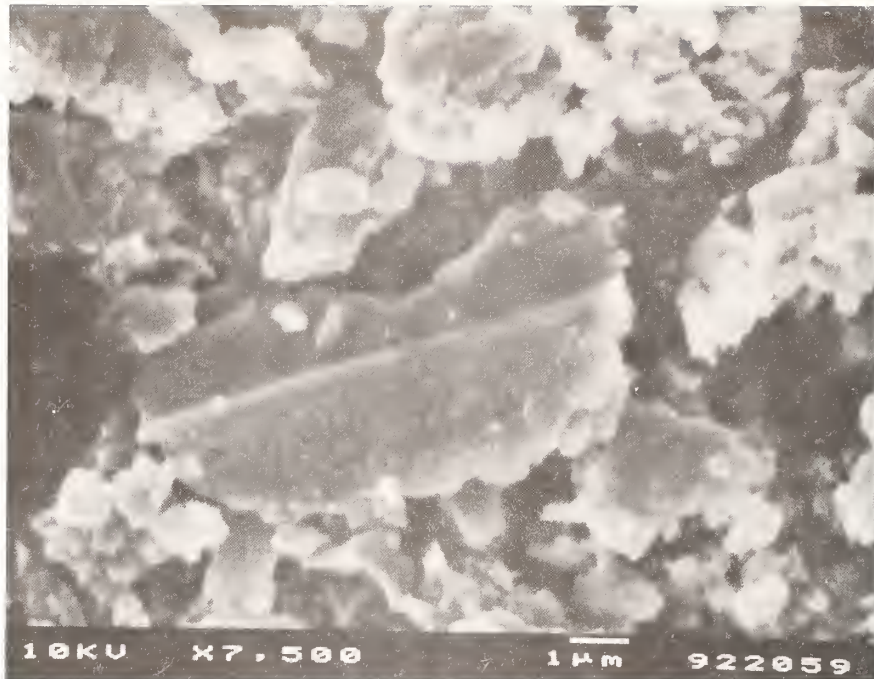
6 (b) Sample B.

Figure 6. Grinding Swarf (102 Micron Diamond Grit Size).

Figure 7. Close-Up View of Grinding Groove (50.8 Micron Diamond Grit Size).
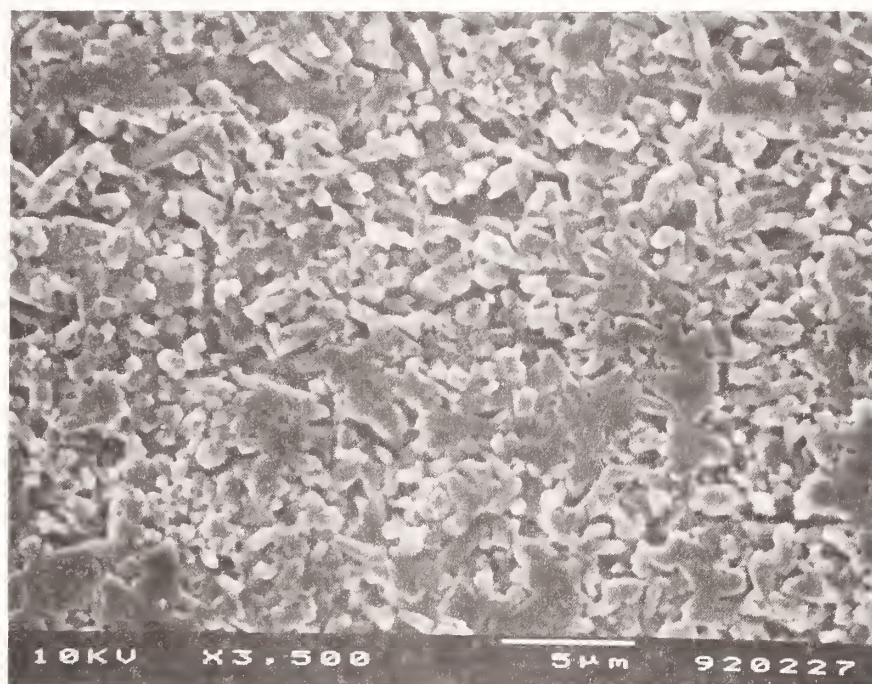
Figure 8. Etched Surface.

A contacting surface profilometer was used to measure the surface finish of the finish ground specimens. The surface finish results are recorded in Table 5, listed by diamond grit size. Ra is the arithmetic mean deviation of the roughness profile from the mean line. All measurements were made perpendicular to the grinding direction. The surface finish is plotted versus grit depth of cut in Figure 9. A plot was also made versus wheel grit size and is shown in Figure 10. These results show, as expected, that the surface finish improves as the wheel grit size and the grit depth of cut become smaller.

Figure 9. Surface Finish, Ra, versus Grit Depth of Cut, t.

Table 5. Surface Finish, Ra

Mean Grit Size		Ra	
microns	inches	microns	μ-in
5.1	0.0002	0.0508	2.0
50.8	0.0020	0.1594	6.28
87.5	0.0035	0.2985	11.75
152	0.0060	0.2864	11.28
249	0.0098	0.4090	16.10

215
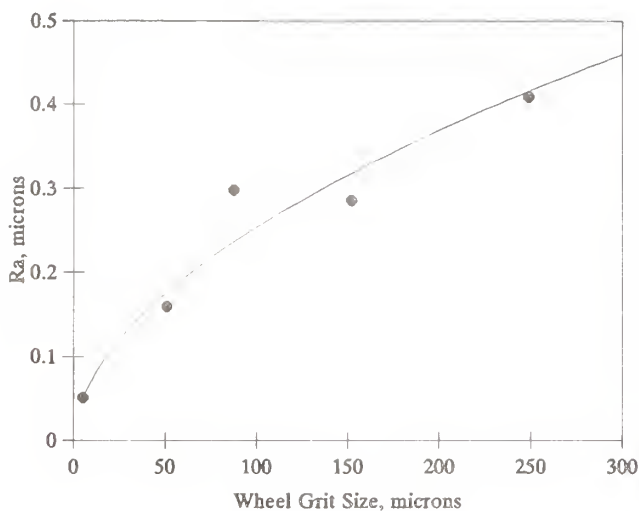
Figure 10. Surface Finish, Ra, versus Wheel Grit Size.

3.3   Strength

Strength data obtained by means of the transverse rupture strength tests on all bars ground in this research is given in Table 6 and is summarized in Figure 11 with strength plotted against wheel grit size, and in Figure 12 plotted versus grit depth of cut, t. The range of strengths obtained for the five test bars at each grinding condition and the Weibull characteristic strength for the five bars are both shown in these figures. Separate plottings are made for the longitudinally ground specimens and those transversely ground. From Figures 11 and 12 it can be seen that for grinding in the longitudinal direction there is no loss of strength as the grit depth of cut, t, increases (or the grit size increases) for the range investigated. Statistical analysis of the data for all longitudinal grinding showed no significant difference in strength. For transverse grinding, there is a decrease in strength as t increases (or the grit size increases) beyond a critical value of t of about 0.160 microns. Statistical analysis of the data for transverse grinding showed that the strengths for the 152 and 249 micron grit sizes are significantly different compared to the strengths for the other grit sizes employed for transverse grinding; they are also significantly different compared to the strengths for all grit sizes employed for longitudinal grinding. Figure 11 agrees with general trends reported previously by Ota (30); however, the strength levels are lower in Ota's work. Ota's maximum strength levels were about 600 to 700 MPa. Additionally, Ota's strengths for transverse grinding never reached those for longitudinal grinding over the 30-160 micron wheel grit sizes explored.   Ota's ceramic workpiece material was sintered silicon

Table 6. Transverse Rupture Strength Test Results

Wheel Grit Size	Microns	5.1	50.8		87.5		152		249	
	Mesh No.	1200	320		180		110		100	
Grind Direction *		T	L	T	L	T	L	T	L	L
Breaking Stress for Individual Bars	MPa	868.6	759.2	962.3	839.6	850.4	857.1	566.8	802.2	604.2
		835.9	856.3	794.0	668.7	545.7	699.1	602.8	667.3	556.8
		731.8	910.8	823.7	880.8	715.1	788.9	507.1	752.9	597.9
		869.7	725.1	812.6	702.1	641.3	881.5	572.0	917.9	683.6
		635.0	688.0	804.4	703.6	691.0	848.2	503.8	884.1	458.9
	Ksi	126.0	110.1	139.6	121.8	123.3	124.3	82.2	116.3	87.6
		121.2	124.2	115.2	97.0	79.1	101.4	87.4	96.8	80.8
		106.1	132.1	119.5	127.7	103.7	114.4	73.6	109.2	86.7
		126.1	105.2	117.9	101.8	93.0	127.9	83.0	133.1	99.1
		92.1	99.8	116.7	102.0	100.2	123.0	73.1	128.2	66.6
Weibull Characteristic Strength	MPa	827.0	826.3	870.9	798.1	732.5	842.8	568.4	844.8	611.9
	Ksi	119.9	119.8	126.3	115.8	106.2	122.2	82.4	122.5	88.8
Weibull Modulus		8.22	7.21	8.48	6.79	5.20	12.27	11.68	7.48	6.57

* Note: L = Longitudinal Grinding, T = Transverse Grinding

216
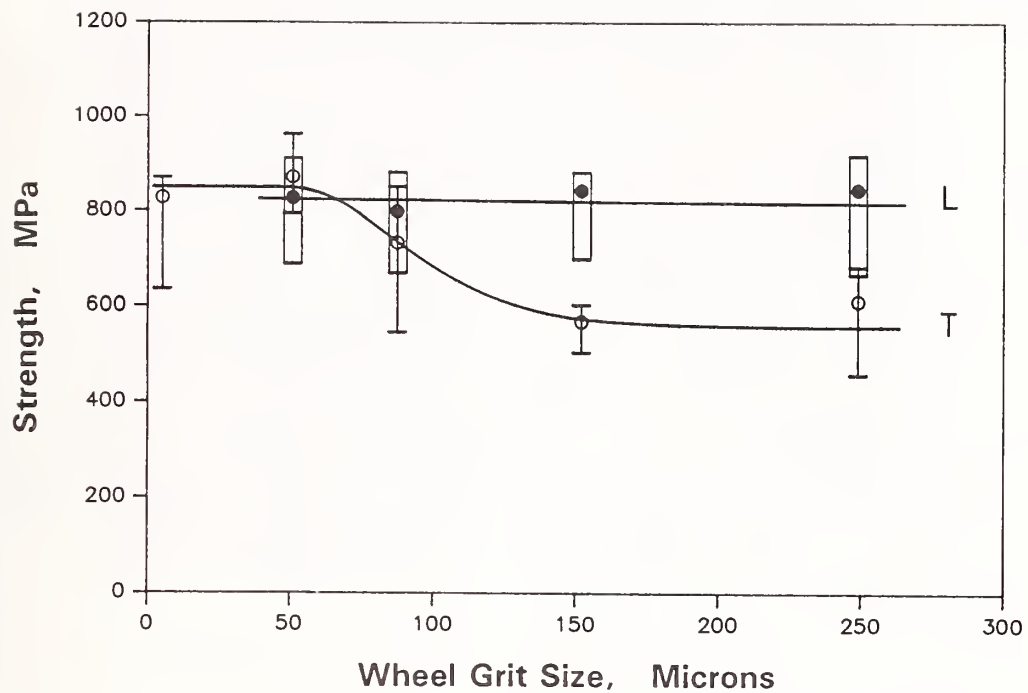
Figure 11.   Transverse Rupture Strength as a Function of Wheel Grit Size in Longitudinal (L) and Transverse (T) Grinding.
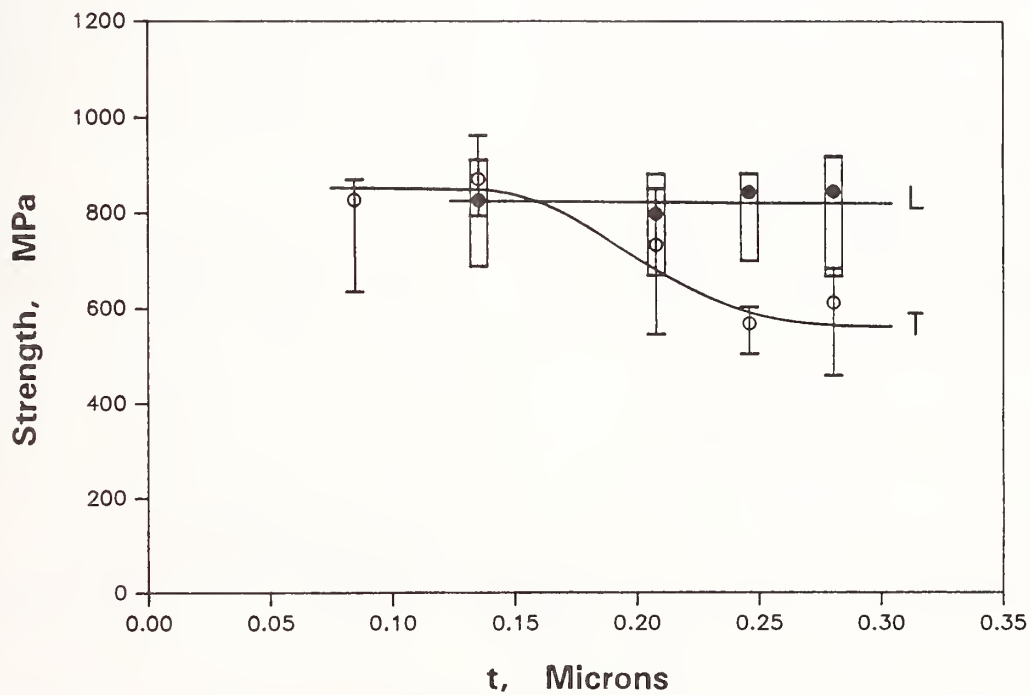
Figure 12.   Transverse Rupture Strength as a Function of Grit Depth of Cut, t, in Longitudinal (L) and Transverse (T) Grinding.

nitride (SSN) which can have lower strength and toughness than hot pressed silicon nitride (HPSN), which possibly explains the differences between the present research and the results of Ota (31).

The work of Bifano (16) suggests that the grit depth of cut, t, for ductile mode grinding of silicon carbide ceramic should be about 0.200 microns or less; above this value the grinding mode changes from a ductile to a brittle mechanism. Additionally, since silicon nitride ceramic has higher toughness than silicon carbide ceramic, it is expected that the critical t value for ductile mode grinding of silicon nitride ceramic will be larger than 0.200 microns. Bifano's definition of ductile mode grinding is based on the relative amount of fractured surface area on the ground surface. He defines ductile mode grinding as grinding which produces 10% or less fractured (damaged) surface area. Looking at Figure 3 and Table 4, it appears that 10% damaged surface area occurs between the 5.1 micron and 50.8 micron diamond grit size wheels (i.e. between Figures 3(a) and 3(b)). Table 3 indicates that this corresponds to a t value of 0.085-0.135 microns, which appears to disagree with the findings of Bifano.

If one defines ductile mode grinding as those grinding conditions where maximum strength is achieved, then from Figure 12 it is seen that the critical t value under this definition is about 0.160 microns. This critical t value is larger than that determined by applying Bifano's definition to this present research, which possibly indicates that the arbitrary percent damaged area in his definition should be larger than 10%. From Table 4, it appears that about 15% might be a more realistic value to employ. Since the real goal is to produce high strength ceramic components, it appears that a ductile

mode grinding definition based on strength is a more appropriate criterion.

During the course of this research, it was observed that the strength of the HPSN employed can vary from one hot pressed billet to another. Strength results for two different billets ground with 50.8 and 87.5 micron grit wheels are shown in Table 7. The results in Table 7 are for test bars ground longitudinally. Statistical analysis of the strength data for Billet AA and Billet BB showed that their strengths are significantly different. Previous results did not show a significant difference in strength from billet to billet (31). This result means that a control set of transverse rupture strength test bars must be ground and tested for each billet in order to make meaningful conclusions when more than one billet is employed in a test series.

3.4   Flaw Detection

The brittle removal process produces microcracks on the surface of the ground ceramic; whereas the surface produced by the ductile removal process should be free of microcracks and thus have higher strength. Thus if cracks on the ground surface can be detected by some non-destructive technique, then it might be possible to employ this technique to determine the extent to which the ductile process exists and the level of strength of the ground surface.

To pursue this possibility, attempts are being made to detect flaws (microcracks) induced by grinding via surface monitoring techniques. Flaws (microcracks) perpendicular to the surface

Table 7. Strength from Billet to Billet

HPSN Material	Transverse Rupture Strength (Weibull Characteristic Strength)			
	50.8 Micron Grit Wheel		87.5 Micron Grit Wheel	
	MPa	Ksi	MPa	Ksi
Billet AA	703.6	102.0	653.4	94.8
Billet BB	826.3	119.8	798.1	115.8
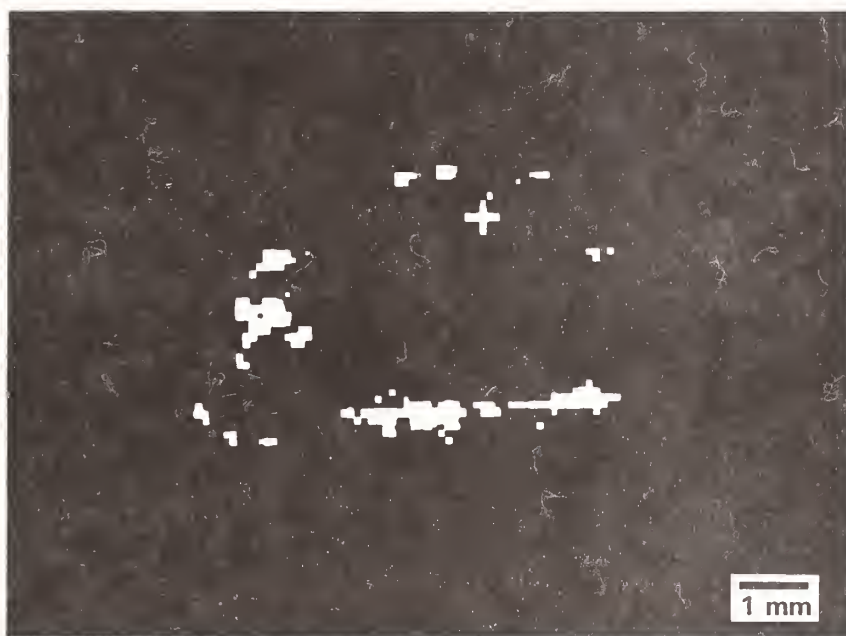
Figure 13.   NMRI (Nuclear Magnetic Resonance Imaging) Image of Cross-Section of Ground Silicon Nitride Specimen.

and in the range of 5-20 microns, which are of typical interest regarding grinding cracks in ceramics (11), are the target size for these techniques. Investigation of the nuclear magnetic resonance imaging (NMRI) technique (31) has shown promise. Figure 13 shows the NMRI image for a ground silicon nitride specimen. The "plus sign" in this figure is an image indicating a flaw. The dots leading down to the "plus sign" are near to the 20 micron range.

Additionally, a technique called Thermal Acousto Photonic NDE (TAP-NDE) is being employed to investigate detection of grinding cracks in ceramics utilizing Rayleigh surface wave and Lamb wave techniques (21-25). This research is in the early stages of investigation. The techniques of thermal wave analysis (imaging) and photothermal microscopy (32) are being studied for possible investigation.

4.   Conclusions

Hot pressed silicon nitride (HPSN) ceramic was ground on a surface grinder with various grit size diamond wheels, and the finished surfaces were observed with SEM and profilometer. Grit depths of

cut were estimated. Transverse rupture strength data was obtained. Additionally, flaw detection methods are being investigated. The following conclusions may be made on the results of this research work.

1.   All finish ground surfaces showed surface damage (pitting) over the range of 5.1 to 249 micron diamond grit sizes investigated (i.e. grit depths of cut, t, ranging from 0.0845 to 0.281 microns). The amount of surface damaged area ranged from 3% to 25% as the wheel grit size ranged from 5.1 microns to 249 microns. None of the surfaces showed evidence of severe fracturing or cracks. The trend was toward less damage and more ductile mode appearance as the grit size became smaller, i.e. as the grit depth of cut became smaller.

2.   It appears that the material removal mechanism in the damaged areas is by fracturing out HPSN grains or clumps of grains.

3.   For grinding in the longitudinal direction along the test bar, there is no loss of strength as the grit depth of cut, t, increases

(or the grit size increases) for the range investigated. For transverse grinding, there is a decrease in strength as t increases (or the grit size increases) beyond a critical value of t. This result is in general agreement with previously published work. The present research provides new information in that it estimates the critical value of t at about 0.160 microns for diamond grinding of hot pressed silicon nitride ceramic. For the grinding conditions employed in this research, this can be achieved with a 50.8 micron grit size (320 mesh number) wheel.

4. It appears that high strength grinding of HPSN occurs when the damaged surface area is less than about 15%.

5. It has been observed that the strength of HPSN can vary from one hot pressed billet to another. This means that a control set of transverse rupture strength test bars must be ground and tested for each billet in order to make meaningful conclusions when more than one billet is employed in a test series.

Acknowledgements

REFERENCES

1. S. Dutta (NASA-Lewis Research Center), "State of the Art in Structural Ceramics Processing for Heat Engine Applications", J. D. Lindsay Lecture Series, Dept. of Chemical Engineering, Texas A&M University, College Station, TX, October 6, 1989.

2. D. W. Lee and J. J. Harwood, "Market Opportunities", A. D. Little, Inc., Cambridge, Mass., pp. 7, 1985.

3. "Technological and Economical Assessment of Advanced Ceramic Materials. Volume 1: Summary and Conclusions.", Prepared by Charles River Associates, Inc. for the National Bureau of Standards, pp. 68, August 1984.

4. Letter from Maxine Savitz, Director, Garrett Ceramic Components Division, Allied-Signal Aerospace Co., Torrance, CA, dated December 17, 1990.

5. A. G. Evans and D. B. Marshall, "Wear Mechanisms in Ceramics", Fundamentals of Friction and Wear of Materials, Edited by D. Rigney, ASME, pp. 439-452, 1981.

6. D. B. Marshall, A. G. Evans, B. T. Khuri-Yakub, J. W. Tien, and G. S. Kino, "The Nature of Machining Damage in Brittle Materials", Proc. Royal Soc. London, Vol. A385, pp. 461-475, 1983.

7. I. Inasaki, "Grinding of Hard and Brittle Materials", Annals of CIRP, Vol.36, No.2, 1987.

8. Y. Jung, I. Ichiro, and S. Matsui, "High-Efficiency Creep-Feed Grinding of Advanced Ceramics", Proceedings of the 27th International MATADOR Conference, pp. 299-304, April 1988.

9. T. W. Liao and G. Sathyanarayanan, "Material Removal Mechanism in Creep-Feed Grinding of Alumina with Resinoid, Vitrified and Electroplated Diamond Wheels", Transactions of the North American Manufacturing Research Institution of SME, 1990.

10. W. Konig, L. Cronjager, G. Spur, H.-K. Tonshoff, M. Vigneau and W. J. Zdeblick, "Machining of New Materials", Annals of CIRP, Vol. 39, No. 2, pp. 673-681, 1990.

11. Private Conversation with Kamal Amin, Norton Company on January 29, 1990.

12. "Flexural Strength of High Performance Ceramics at Ambient Temperature", MIL-STD-1942(MR), Department of the Army, Washington, DC 20310, November 21, 1983.

13. G. D. Quinn, F. I. Baratta and J. A. Conway, "Commentary on U. S. Army Standard Test Method for Flexural Strength of High Performance Ceramics at Ambient Temperature", AD-A160 873, AMMRC 85-21, Army Materials and Mechanics Research Center, Watertown, MA 02172-0001, August 1985.

14. T. Bifano, P. Blake, T. Dow and R. O. Scattergood, "Precision Machining of Ceramic Materials", Intersociety Symposium on Machining of Advanced Ceramic Materials and Components, American Ceramic Society, pp. 99-120, April 1987.

15. P. Blake, T. Bifano, T. Dow and R. O. Scattergood, "Precision Machining of Ceramic Materials", Ceramic Bulletin, American Ceramic Society, Vol.67, No.6, pp. 1038-1044, 1988.

16. T. Bifano, T. Dow and R. O. Scattergood, "Ductile-Regime Grinding of Brittle Materials", Proceedings of the International Congress for Ultraprecision Technology, Ultraprecision in Manufacturing Engineering, pp. 22-40, May 1988.

17. H. K. Tonshoff, R. Telle and P. Roth, "Chip Formation and Material Removal in Grinding of Ceramics", 4th International Grinding Conference, Society of Manufacturing Engineers, Vol.2, Paper No. MR90-539, 1990.

18. T. Bifano, "Ultraprecision Grinding of Glass", Proceedings of the 1991 NSF Design and Manufacturing Systems Conference, Society of Manufacturing Engineers, Dearborn, MI, pp. 193-195, 1991.

19. K. Subramanian and S. Ramanath, "Mechanism of Material Removal in the Precision Grinding of Ceramics", Precision Machining: Technology and Machine Development and Improvement, PED-Vol. 58, American Society Mechanical Engineers, New York, NY, pp. 1-19, 1992.

20. J. E. Mayer, Jr. and C. M. Edwards, "Small Grant for Exploratory Research: Ceramic Machining Flaw Detection", Proceedings of the 1991 NSF Design and Manufacturing Systems Conference, Society of Manufacturing Engineers, Dearborn, MI, pp. 273-274, 1991.

21. C. P. Burger and C. S. Ma, "The Interactions of Ultrasonic Rayleigh Waves with Surface Discontinuities in Steel", Ultrasonic International 85, IPC Science and Technology Press, pp. 61-66, 1985.

22. C. P. Burger, T. D. Dudderar, J. A. Gilbert, B. R. Peters and J. A. Smith, "Laser Excitation Through Fiber Optics for NDE", Journal of Nondestructive Evaluation, Vol.6, No.1, pp. 57-64, 1987.

23. C. P. Burger, J. A. Smith, T. D. Dudderar, J. A. Gilbert and B. R. Peters, "The Use of Fiber Optics Interferometry to Sense Ultrasonic Waves", ISA Transactions, Vol.28, No.2, pp. 51-55, 1989.

24. C. P. Burger, C. Duffer and N. Schumacher, "Non-Contact Evaluation of Quality in FRP Composites", Composite Material Technology 1990, American Society of Mechanical Engineers, PD-Vol.32, pp. 193-196, 1990.

25. N. A. Schumacher, C. Duffer and C. P. Burger, "Non-Contact Non-Destructive Evaluation of Composite Panel with Plate Waves", Composite Material Technology 1991, American Society of Mechanical Engineers, PVP-Vol.37, pp. 219-224, 1991.

26. J. S. Strenkowski and G. D. Hiatt, "A Technique for Predicting the Ductile Regime in Single Point Diamond Turning of Brittle Materials", Fundamental Issues in Machining, PED-Vol.43, American Society

of Mechanical Engineers, New York, NY, pp. 67-80, 1990.

27. G. S. Reichenbach, J. E. Mayer, S. Kapakcioglu and M. C. Shaw, "The Role of Chip Thickness in the Grinding Process", ASME Trans., May 1956.

28. S. Kalpakjian, Manufacturing Engineering and Technology, Addison-Wesley Publishing Co., Reading, MA, pp. 757-758, 1989.

29. Y. Namba, Y. Yamada, A. Tsuboi, K. Unno, and H. Nakao, "Surface Structure of Mn-Zn Ferrite Single Crystals Ground by an Ultraprecision Surface Grinder with Various Diamond Wheels", Annals of CIRP, Vol. 41, No. 1, pp. 347-351, 1992.

30. M. Ota and K. Miyahara, "The Influence of Grinding on the Flexural Strength of Ceramics", 4th International Grinding Conference, Society of Manufacturing Engineers, Vol.2, Paper No. MR90-538, 1990.

31. D. W. Richerson, Modern Ceramic Engineering, Marcel Dekker, Inc., pp. 186, 1992.

32. J. E. Mayer, Jr. and C. M. Edwards, "Small Grant for Exploratory Research: Ceramic Machining Flaw Detection", Proceedings of the 1992 NSF Design and Manufacturing Systems Conference, Society of Manufacturing Engineers, Dearborn, MI, pp. 139-141, 1992.

33. H. K. Tonshoff, W. V. Schmieden, I. Inasaki, W. Konig and G. Spur, "Abrasive Machining of Silicon", Annals of CIRP, Vol. 39, No. 2, pp. 621-635, 1990.

MACHINING OF SILICON NITRIDE: EXPERIMENTAL DETERMINATION OF PROCESS/PROPERTY RELATIONSHIPS

R. L. ALLOR, T. J. WHALEN, and J. R. BAER
Ford Motor Company, Dearborn, MI

K. V. KUMAR
GE Superabrasives, Worthington, OH

Strength controlling flaws in ceramics such as silicon nitride can be introduced during the grinding process. An experimental program was conducted to investigate and improve the efficiency of machining a structural ceramic material, silicon nitride, with diamond abrasives. This paper analyzes the data from two groups of experiments and determines the significant results. The first group of designed experiments, half-factorial, investigated the effects of diamond mesh size and concentration in the grinding wheel, the rate of removal of the ceramic, wheel speed and type of grinding on the strength, surface roughness, power consumption, vertical force and wheel wear. The grinding machine spindle contained air bearings. Two or three significant factors were found to affect each result. For example, the strength of the ceramic was affected by the diamond mesh size when creep-feed grinding was used, whereas diamond concentration and speed of the wheel were found to be significant factors when pendulum-feed grinding was done. The second group of experiments were run on the same grinding machine with a spindle containing steel ball bearings. Results from the second experiment showed that creep or pendulum modes of machining had no effect on strength of machined silicon nitride, nor did removal rates.

INTRODUCTION

Machining of ceramics usually introduces strength controlling features at the surface or in the subsurface region. Allor, Govila and Whalen(1) presented data on the machining of silicon nitride (Si_3N_4) and silicon carbide (SiC) and showed the influence of machining variables on the strength of these advanced ceramic materials. Many other authors have also presented data on machining these advanced ceramics and compilations of papers presented at conferences are available(2-9).
Recently, an experimental program was established to investigate and improve the efficiency of machining hot-pressed silicon nitride with manufactured diamond abrasives. An approach based on statistical design of experiments was used to analyze the effect of grinding parameters on strength of one silicon nitride material.

EXPERIMENTAL DESIGN

The original design was a half factorial 2_V^{5-1} design with five variables at two levels each and two replicates at each experimental condition, totaling 32 experimental runs performed in random order. The five variables were mesh size of diamond (80/100 and 120/140), concentration of diamond in the wheel (75 conc.=3.3cts/cm^3 and 100 conc.=4.4cts/cm^3), specific material removal rate (6 and 12 mm^3/mm-sec), wheel speed (30 and 45 m/s), and type of grinding action (pendulum and creep feed). After noting an error in the rate of removal after several experiments, the 2_V^{5-1} design was redone to form two 2_{IV}^{4-1} blocks, one for pendulum feed and one for creep feed. The block for pendulum feed was performed at rates of 6.0 and 12.0 mm^3/mm-s, while the block for creep feed was performed at 0.6 and 1.2 mm^3/mm-s. Six bars were ground per test condition. The results of the experiments were transverse rupture strength (MPa), average surface roughness (Ra, μm), average power consumption (watt/mm), average vertical force (N/mm) and radial wear on grinding wheel (μm).

The spindle of the grinding machine for the

Table I: Grinding Conditions

Work Material	Hot pressed silicon nitride (NC-132) - Norton
Wheel Specification	
Diamond Type	RVG-880 Diamond
Mesh Size	80/100 and 120/140
Concentration	75 and 100
Bond Type	Phenolic resin
Wheel Size	175ø x 6.3W x 31.75B, mm
Grind Type	Plunge Grind - pendulum and creep feed up cut
Wheel Speed	30 and 45 m/s
Depth of Cut	0.025 and 0.050 mm for pendulum
	0.25 mm for creep feed
Specific Removal Rate	6 and 12 mm^3/mm-s, pendulum (first experiment)
	0.6 and 1.2 mm^3/mm-s, creep feed (first experiment)
	1.2 and 12 mm^3/mm-s (second experiment)
Coolant	HD-90 water soluble, 20:1

above experiment was equipped with air bearings. A second experiment was conducted in which the grinding machine spindle was changed to steel ball bearings. Based on the results from the first experiment, a simple 2^2_{Full} design was used for the second experiment to investigate differences in resulting strength of the material, if any, between samples ground by creep feed mode and pendulum mode at removal rates of 1.2 and 12 mm^3/mm-s. In this case, 8 bar samples were ground per test condition.

Two general references on the design and analysis of these experiments are given(10,11).

EXPERIMENTAL PROCEDURE

A hot pressed silicon nitride (NC132) billet was cut into blank test bars. The dimensions prior to grinding were 60L x 4.5W x 3.5T mm. During the test, approximately equal amounts of material were removed from each side to obtain the finished dimensions. Table I gives the grinding conditions used for the experiment. A phenolic resin bonded wheel was used for all the tests and the choice of RVG°-880 diamond, was based from an earlier study(12). In creep-feed grinding the process used is a large depth of cut with a very slow table feed, as compared to pendulum feed grinding that uses a shallow depth of cut with a fast table feed cutting in

Table II: Results for 1st Experiment/Creep Feed ($2^{4:1}_{IV}$ Matrix with 2 Replicates)

Exp #	Mesh Size	Conc.	Removal Rate (mm^3/mm-2)	Wheel Speed (m/s)	Strength (MPa)	Surface Roughness (μm)	Power (Watt/mm)	Vertical Force (N/mm)	Wear (μm)
1	80	75	0.6	30	848/869	0.50/0.50	58/58	56/103	7.6/7.6
2	120	75	0.6	45	662/717	0.90/0.55	55/55	32/27	25.4/20.3
3	80	100	0.6	45	848/834	0.35/0.45	158/123	88/85	7.6/8.9
4	120	100	0.6	30	696/738	0.35/0.45	78/112	65/49	7.6/8.9
5	80	75	1.2	45	896/800	0.45/0.50	110/100	56/46	6.4/7.6
5	120	75	1.2	30	751/800	0.90/0.70	45/33	15/14	25.4/16.5
7	80	100	1.2	30	814/841	0.50/0.55	78/78	49/49	5.1/6.4
8	120	100	1.2	45	779/676	0.55/0.35	88/110	35/54	7.6/6.4

Table III: Average Effect on Results of Factors in 1st Experiment/Creep Feed

Factor	Strength (MPa)	Surface Roughness (μm)	Power (Watt/mm)	Vertical Force (N/mm)	Wear (μm)
Mesh Size (M)	-116.4	0.12	-23.4	-29.6	7.6
Conc.(C)	-14.7	-0.18	38.9	15.1	-7.3
Removal Rate (R)	18.1	0.06	-6.9	-29.6	-1.6
Wheel Speed (S)	-18.1	-0.08	32.4	3.4	0.6
MC + RS	4.3	-0.16	11.1	13.6	-7.0
MR + CS	30.2	0.01	0.9	15.1	-0.0
MS + CR	-19.9	0.03	-22.4	-2.1	-0.3
Average	786.6	0.53	83.7	51.2	11.0

both directions. In the case of creep feed grind tests, only up cut was used and all of the stock per side was removed in a single pass with the work speed adjusted to obtain the high and low material rates. For pendulum grind tests, the work speed was kept constant and the depth of cut was adjusted to obtain the high and low material removal rates. Following grinding, all the samples were chamfered in the lengthwise direction.

After machining, the bars were broken in four-point bend test to obtain the transverse rupture strength. The baseline strength for the hot-pressed silicon nitride billet used in this study was obtained from bar samples ground according to

reference(13).

FIRST EXPERIMENT: CREEP FEED GRINDING

The data determined in the grinding experiments with creep feed rates of 0.6 and 1.2 mm^3/mm-s are listed in Table II and III.

Strength

The strength data listed in Table II and in Table IV are shown as two values or replicates at each experimental condition. Each value of strength is the average value of six bars.

Only the mesh size variable, of the four variables evaluated, had a significant effect on the

Table IV: Results for 1st Experiment/Pendulum Feed (2_{IV}^{4-1} Matrix with 2 Replicates)

Exp #	Mesh Size	Conc.	Removal Rate (mm^3/mm-s)	Wheel Speed (m/s)	Strength (MPa)	Surface Roughness (μm)	Power (Watt/mm)	Vertical Force (N/mm)	Wear (μm)
1	80	75	6	30	786/676	0.55/0.55	213/190	30/28	3.8/3.8
2	120	75	6	45	696/662	0.75/0.80	113/113	20/19	27.9/25.4
3	80	100	6	45	710/724	0.45/0.60	203/215	37/40	3.8/2.5
4	120	100	6	30	758/765	0.45/0.50	203/203	29/27	2.5/3.8
5	80	75	12	45	662/717	0.65/0.60	333/303	58/52	6.4/8.9
6	120	75	12	30	738/752	0.70/0.80	223/223	28/24	20.3/22.9
7	80	100	12	30	800/738	0.50/0.55	415/460	56/59	3.8/3.8
8	120	100	12	45	772/717	0.60/0.55	370/303	52/46	5.1/8.9

strength of the machined silicon nitride, and these data are shown in Figures 1 and 2. The effect of a variable or factor is the change in response or result produced by a change in the level of the factor. When the level is examined at two levels only, as is the case in these experiments, the effect is simply the difference between the average response of all trials or experiments carried out at the first level of the factor and that of all trials or experiments at the second level. An assumption is made that the distribution of experimental errors is Normal or Gaussian, and this assumption has often been found to hold in practice. Therefore, if the effects are plotted on Normal probability paper, as is done in Figure 2, the effects that fall within experimental error will show a linear relationship and the statistical effects will lie some distance from the line. As in the case shown in Figure 2, the significant effect of mesh size is some distance from the line representing the effects which are included in experimental error. The greater strength was attained in samples machined with 80 mesh diamond abrasive. Diagnostic tools used to determine the significance of the data are the plot of the scaled t-statistic (Figure 1) and the probability plot of the effects (Figure 2). A plot of the probability versus the residuals of a model employing only the effect of the mesh size showed a linear relationship, which indicates that the mesh size variable adequately describes the data.

Surface Roughness

Two significant effects were noted which influenced the surface roughness: the concentration of the diamond in the grinding wheel and the mesh size - concentration two-factor interaction. When an effect of one factor or variable depends on the level of another factor, the two factors are said to interact and these interactions of two factors are called two-factor interactions. The data and plots showing these effects are given in Figures 3, 4 and 5. Since a two-factor interaction is present, one
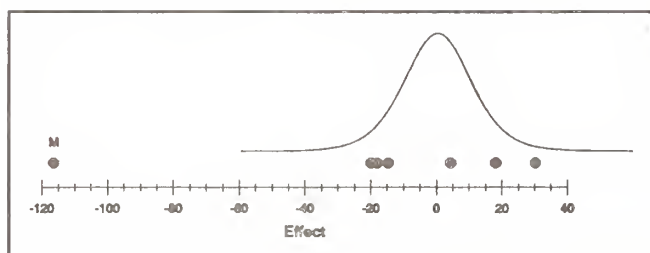
Figure 1: Plot of strength effects and scaled t-statistic shows the region of experimental error, and effect of mesh size is well beyond experimental error.
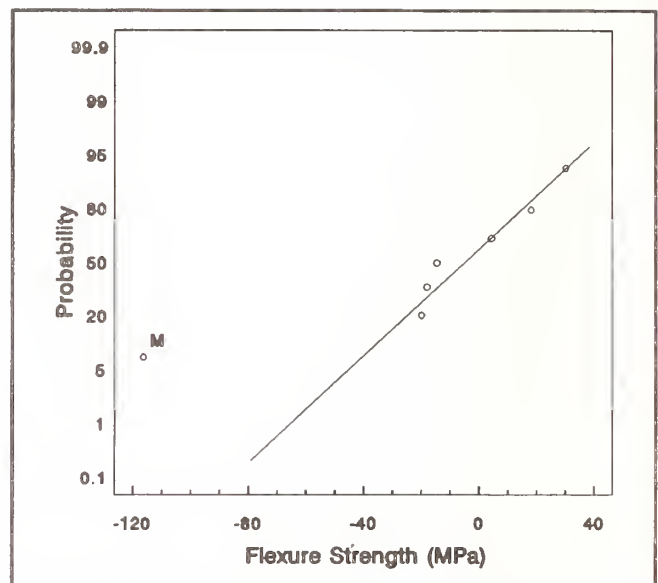
Figure 2: Probability plot of strength effects shows significant mesh size factor separate from other effects which are not significant.
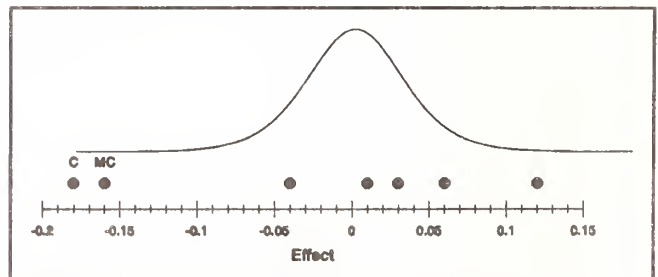
Figure 3: Plot of surface roughness effects and scaled t-statistic shows that concentration and mesh-concentration two-factor interaction are important factors for surface roughness.
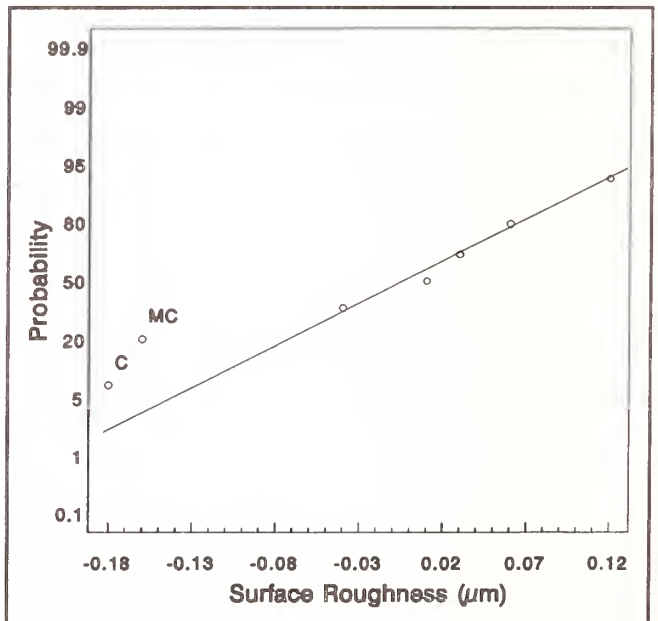
Figure 4: Probability plot of effects of machining variables on surface roughness.

226

sees that the level of the factors influence the results of the experiment. In this case both levels of concentration result in a low surface roughness when 80 mesh diamonds are used in the wheel, but only at the high concentration level does one observe a low surface roughness when a 120 mesh diamond wheel is used. Therefore, low surface roughness was generated with a 80 mesh diamond wheel with either 75 or 100 concentration diamond, and also with 120 mesh diamond wheel with only the 100 concentration (Figure 5).

Average Power

Average power used during grinding was significantly affected by speed, mesh size and concentration. The greater amount of power was used with 80 mesh diamond wheels of 100 concentration at the higher speed of 45 m/s. Figure 6 contains the data for the power results. The best conditions from a power standpoint (lowest power needed) were 120 mesh diamond wheel of 75 concentration at 30 m/s.

Average Vertical Force

The variables of removal rate and diamond mesh size significantly influenced the average vertical force. The effects of removal rate and mesh size on vertical force in Figure 7 are both negative. Therefore, the greater vertical force is found with the lower level of removal rate (0.6 mm³/mm-s) and mesh size (80 mesh size). Since lower vertical force is desired, 120 mesh size and 1.2 mm³/mm-s is preferred.

Wheel Radial Wear

Diamond mesh size, diamond concentration,

and a mesh-concentration two-factor interaction influence the radial wear of the diamond grinding wheel. Figures 8, 9 and 10 contain data which clearly show these effects. The presence of a two-factor interaction requires one to consider the level of each of the significant factors, mesh size and concentration, when one predicts the better operating conditions. In this case, the lower wear rate is obtained for 80 mesh diamond wheels with either 75 or 100 concentration, whereas for 120 mesh wheels, the low wear rate is observed at only 100 concentration.

FIRST EXPERIMENT: PENDULUM FEED GRINDING

The data generated in these experiments with pendulum feed rates of 6 and 12 mm³/mm-s are given in Tables IV and V.
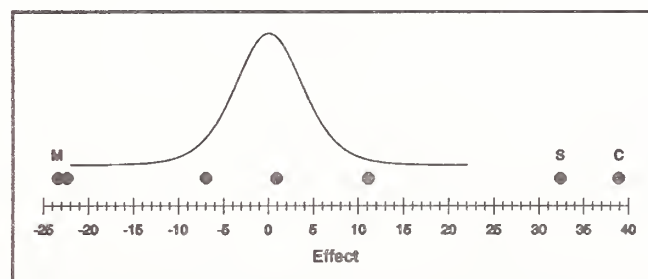
Figure 6: Plot of effects of speed, mesh size and concentration on average power, with scaled t plot to show extent of experimental error.
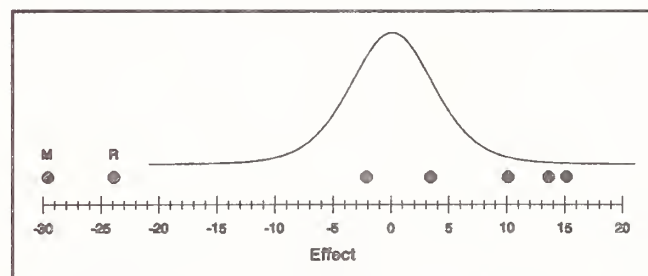
Figure 7: Plot of significant effects of removal rate and diamond mesh size on average vertical force.

Figure 5: Plot of effects of mesh-concentration two-factor interaction on surface finish.
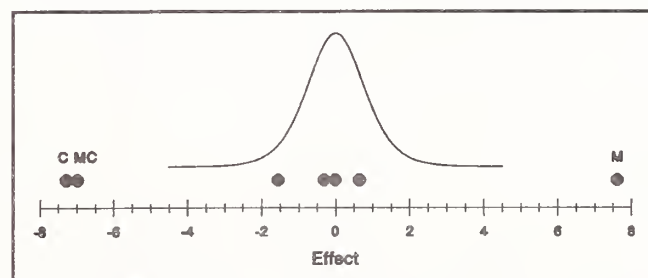
Figure 8: Plot of significant effects of mesh, concentration and a mesh-concentration two-factor interaction on wheel radial wear, with a scaled t plot to show extent of experimental error.

Strength

Both the grinding wheel speed and the diamond concentration were significant factors in influencing the strength of the silicon nitride, as shown in Figures 11 and 12. The higher strength test bars were those machined at the higher speed, 45 m/s, and higher diamond concentration of 100. All other factors fell within the experimental error. The plot of probability versus effects indicates clearly the significance of the two factors, speed and concentration. The linear relationship shown in the plot of probability versus residuals, Figure 13, when the model includes these two factors, enhances our confidence in the interpretation. (See Reference 10, p.333 for discussion of residual analysis.)
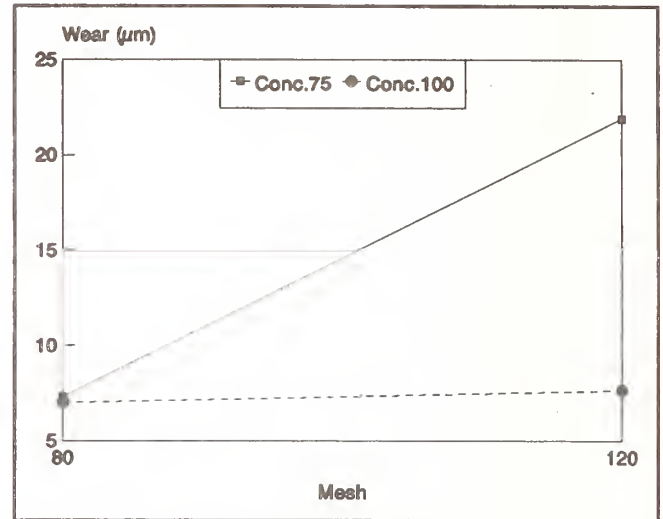
Figure 10: The mesh-concentration two-factor interaction is shown for wheel radial wear.
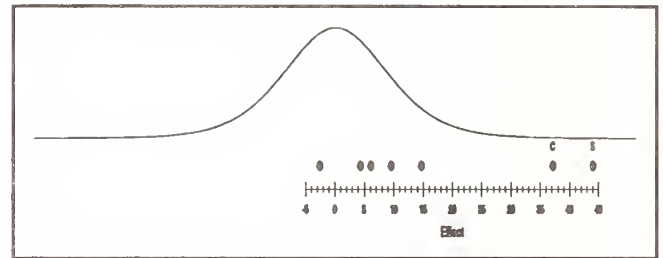
Figure 11: Plot of significant effects of wheel speed and concentration on strength of machined samples, along with a scaled t plot to show extent of experimental error.

Figure 9: Probability plot of factors showing significant factors for wheel radial wear some distance from line representing experimental error.

Table V: Average Effect on Results of Factors in 1st Experiment/Pendulum Feed

Factor	Strength (MPa)	Surface Roughness (μm)	Power (Watt/mm)	Vertical Force (N/mm)	Wear (μm)
Mesh Size (M)	6.1	0.09	-72.6	-14.4	10.0
Conc.(C)	37.1	-0.15	82.6	10.9	-10.7
Removal Rate (R)	14.7	0.04	147.1	18.1	0.8
Wheel Speed (S)	44.0	-0.05	22.1	-5.4	-3.0
MC + RS	4.3	-0.09	19.1	4.9	-8.4
MR + CS	9.5	0.00	-25.4	-4.4	-1.4
MS + CR	-2.6	-0.01	-33.9	-1.9	-1.4
Average	729.5	0.60	255.2	37.8	9.6

Surface Roughness

Identical to the effects observed for the creep-feed grinding, the surface roughness is influenced significantly by the mesh size, the diamond concentration and the two-factor interaction between mesh size and concentration. These results for pendulum feed machining are seen in Figures 14 and 15, which is similar to Figures 3, 4 and 5 for creep feed grinding. The lower surface roughness is observed with either an 80 or 120 mesh diamond wheel with 100 concentration.
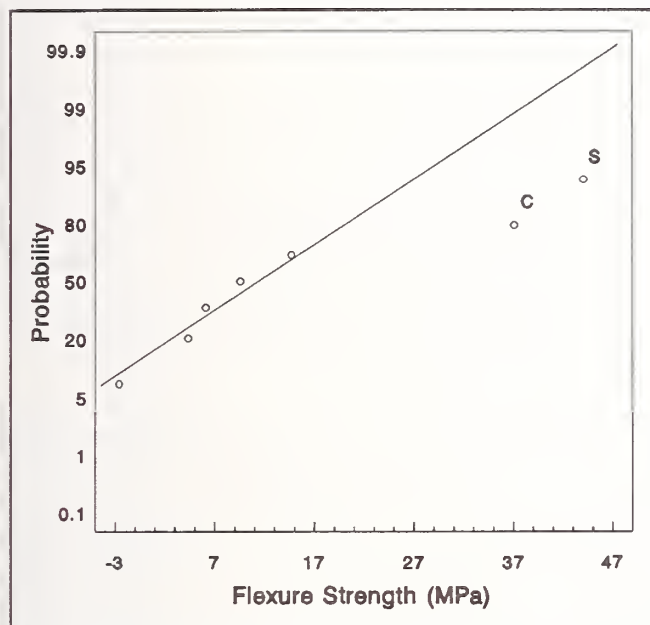
Figure 12: Probability plot of effects showing significant factors of wheel speed and concentration on strength of machining samples.
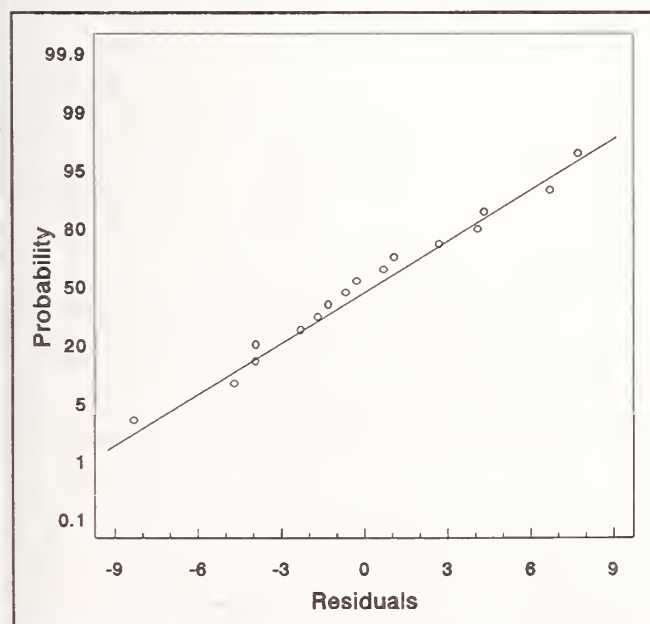
Figure 13: Probability plot of residuals showing linear relationship.

Average Power

Average power recorded during grinding was significantly influenced by removal rate, diamond concentration, and mesh size (Figure 16). A larger amount of power (12 watts/mm) was used for grinding at a high rate, the larger diamond concentration of 100, and the smaller diamond size of 120 mesh. This result is similar to the creep feed grinding in which concentration and mesh size are significant, but wheel speed, and not removal rate, is also influencing the power. The lowest power condition is predicted to be at a material removal
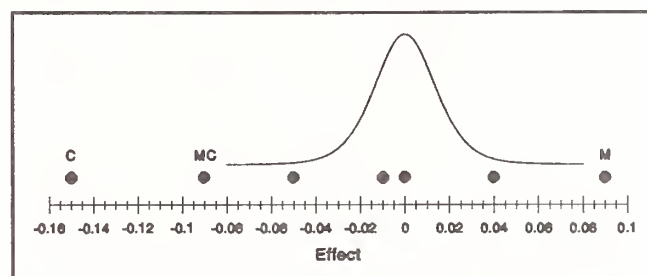
Figure 14: Plot of effects on surface roughness, showing concentration, mesh size of diamond and a mesh-concentration two-factor interaction.
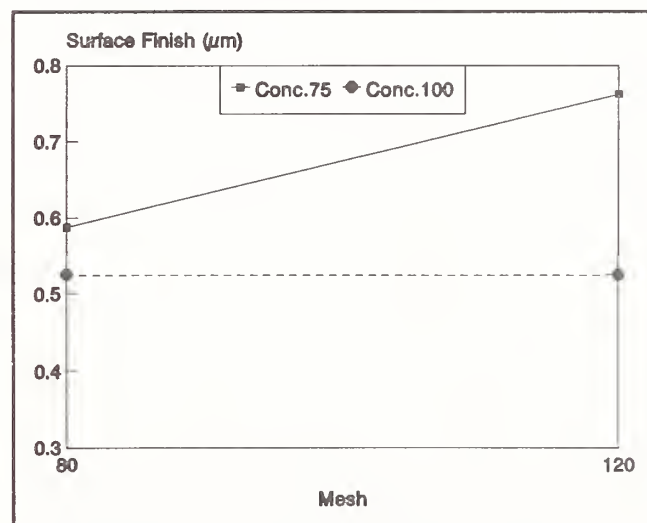
Figure 15: Plot of the two-factor interaction of mesh and concentration for surface finish.
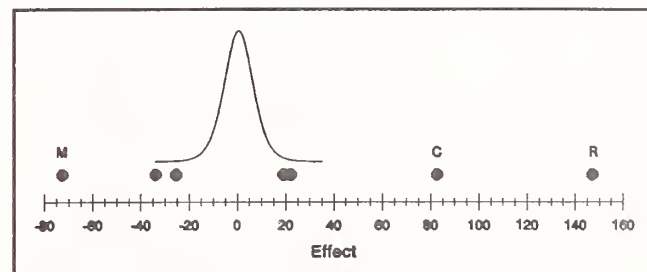
Figure 16: Plot of effects on average power with scaled t distribution to show extent of experimental error.

rate of 6 mm³/mm-s, a 120 mesh wheel with 75 concentration diamond.

Average Vertical Force

The variables of machining rate, diamond concentration in the wheel, and diamond mesh size all influence significantly the vertical force measurement. The data presented in Figure 17 show that a greater force is measured when the rate is 12, the concentration is 100 and the mesh size is 80.

Wheel Radial Wear

The mesh size and the concentration of the diamond, along with the mesh size-concentration two-factor interaction significantly influence the wear of the wheel (Figures 18, 19 and 20). These factors are identical to those observed for the creep feed grinding (Figures 8, 9 and 10). The better

Figure 19: Probability plot shows significant effects of mesh size, concentration and mesh-concentration two-factor interaction on wear.
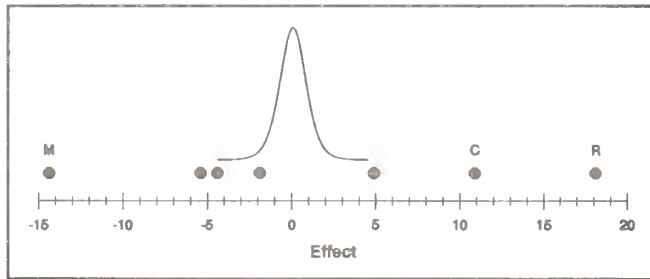
Figure 17: Plot of effects on vertical force with a scaled t distribution plot.
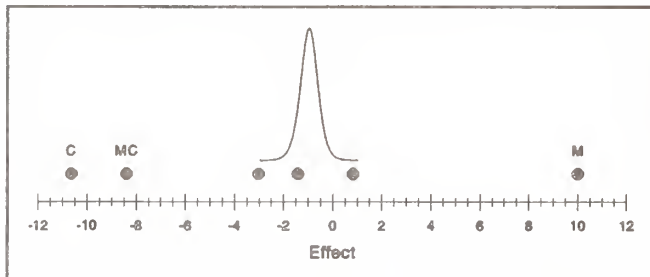
Figure 18: Plot of effects on wheel radial wear with scaled t distribution plot.
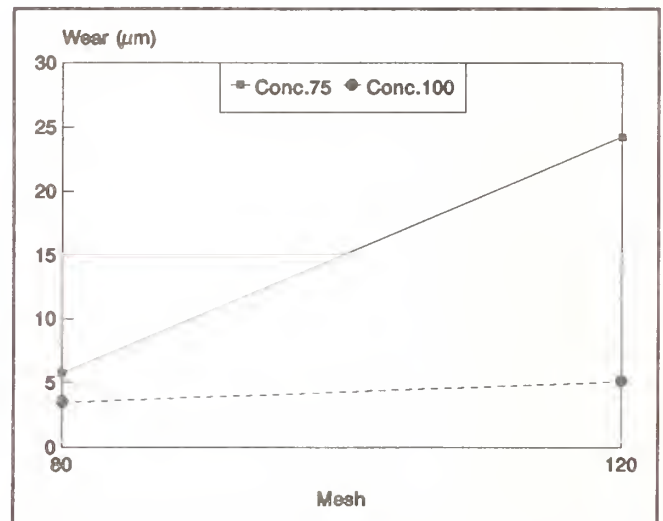
Figure 20: Plot of the two-factor interaction on wear.

Table VI: Comparison of Pendulum & Creep Feed Results (2nd Experiment)

Grind Mode	Cutting Rate (mm³/mm-sec)	Average Strength (MPa)	Surface Roughness (μm)	Average Power (watt/mm)	Vertical Force (N/mm)	Wear (μm)
Pendulum	1.2	800	0.6	48	13	8
Pendulum	12.0	772	0.6	422	66	8
Creep	1.2	827	0.5	74	85	8
Creep	12.0	786	0.5	564	87	3

grinding condition (lower wear) predicted from this study would be either 80 or 120 mesh wheel at 100 concentration level of diamond (Figures 18, 19 and 20).

Second Experiment

The grinding machine dynamics for this experiment were different from the first experiment in that the wheel spindle bearings were changed from air bearings to steel ball bearings. Based on the results of the first experiment, the wheel specification was fixed to a mesh size of 80/100 and 100 concentration. The wheel speed was set to 45 m/s. The results of this 2^2_{Full} design are listed in Table VI. The analysis of variance of the means table is shown in Table VII and Figure 21 and the result is that neither of the factors, mode of machining nor removal rate, had a significant effect on the strength of the machined samples.

Discussion of Results

A summary of the significant effects of the machining variables on the results is shown for the first experiment in Table VIII. One sees that for strength, the mesh size was important for creep feed at the lower removal rate (0.6 and 1.2) whereas the wheel speed and diamond concentration were significant effects for the pendulum feed at the higher removal rate (6 and 12). Roughness is seen to be affected by diamond concentration and mesh size for both types of feed. Power is influenced by concentration and mesh size for both types of feed,

and by speed of the wheel for creep feed, and removal rate for pendulum feed. The average force is affected by rate and mesh size for both types of feed, and the pendulum feed is also influenced by diamond concentration. Wear of the wheel is influenced significantly by mesh size, diamond concentration, and a two-factor interaction of mesh size and concentration for both types of feed.

In the second experiment in which the wheel spindle bearings were changed to steel ball bearings, it was found that the mode of grinding (creep or pendulum) and the machining rate had no significant effect on the strength of the machined samples. This is seen in the analysis of variance of the means table shown in Table VII and Figure 21. The F test listed in the figure indicates that the results could be expected by chance about 50% of the time. Therefore, it is concluded that there are no significant differences in the groups of samples tested.

A summary of the preferred conditions for machining NC132 Silicon Nitride ceramic for improved properties and machining efficiency are

Table VII: Analysis of variance table (second experiment) for comparison of samples machined with ball bearings.

Source	DF	SS	MS	F	p
Factor	3	222	74	0.79	0.509
Error	25	2331	93		
Total	28	2553			
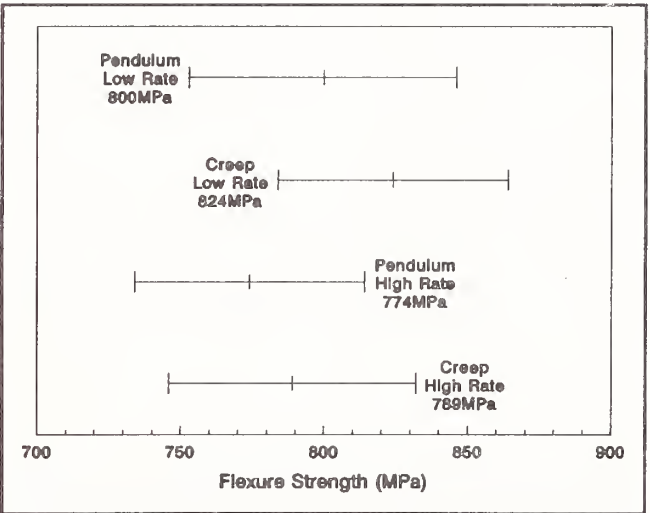
Figure 21: Plot of the 95% confidence intervals for the averages of the four groups.

Table VIII: Significant Machining Factors (1st Experiment)

Results:	Strength (MPa)	Surface Roughness (μm)	Power (Watt/mm)	Vertical Force (N/mm)	Wear (μm)
Creep Feed (0.6 & 1.2 removal rate)	Mesh Size	Conc. Mesh Size-Conc.	Speed Mesh Size Conc.	Removal Rate Mesh Size	Mesh Size Conc. Mesh Size-Conc.
Pendulum Feed (6 & 12 removal rate)	Wheel Speed Conc.	Conc. Mesh Size Mesh Size-Conc.	Removal Rate Mesh Size Conc.	Removal Rate Conc. Mesh Size	Mesh Size Conc. Mesh Size-Conc.

231

listed in Table IX. The table lists only the significant factors and the other factors can be chosen for convenience or economy. One notices that the conditions leading to higher strength will not lead to lower power usage.

A comparison of the strength of samples from all the second experiment (ball bearings) and the baseline data for the billet of silicon nitride from which samples were cut shows that there is no significant difference between these two groups of samples. Table X and Figure 22 have an analysis of variance of the means chart which indicates no difference. However, if we compare the averages from the first and second experiments with the baseline data for the billet material we see in Table XI and Figure 23 that there are significant differences in these comparisons. The data on strength of samples machined with an air bearing spindle are significantly lower than the strengths of samples machined with the ball bearing spindle. However, the averages reflect the diverse machining

Figure 22: Plot of the 95% confidence intervals for strength averages of pendulum and creep feed data (29 samples) with baseline strength data (10 samples).

Table X: Analysis of variance table for comparison of samples machined with air bearings and steel ball bearings.

Source	DF	SS	MS	F	p
Factor	1	319	319	2.81	0.102
Error	37	4200	114		
Total	38	4519			
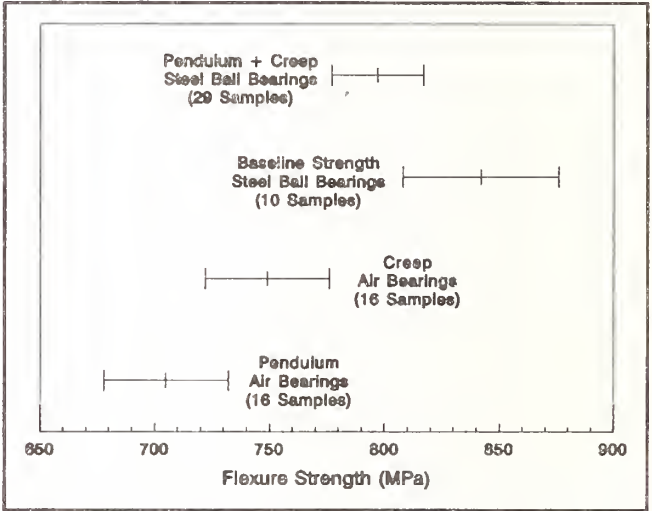
Figure 23: Plot of 95% confidence intervals for strengths of several groups.

Table XI: Analysis of variance table for comparison of all strength data with baseline strength data.

Source	DF	SS	MS	F	p
Factor	3	3069	1023	11.55	0.000
Error	67	5937	89		
Total	70	9007			

Table IX: Best Factor Levels for Machining of NC132 Si_3N_4 Ceramic (1st Experiment)

Results:	Higher Strength	Lower Roughness	Lower Power	Lower Force	Lower Wear
Creep Feed (0.6 & 1.2)	80 Mesh Size	80 Mesh Size 75 or 100 Conc. [OR] 120 Mesh Size 100 Conc.	120 Mesh Size 75 Conc. 30 m/s	120 Mesh Size 1.2 Removal Rate	80 Mesh Size 75 or 100 Conc. [OR] 120 Mesh Size 100 Conc.
Pendulum Feed (6 & 12)	100 Conc. 45 m/s	80 Mesh Size 100 Conc. [OR] 120 Mesh Size 100 Conc.	120 Mesh Size 75 Conc. 6 Rate	120 Mesh Size 75 Conc. 6 Removal Rate	80 Mesh Size 100 Conc. [OR] 120 Mesh Size 100 Conc.

conditions included in the experimental design. Six of the sixteen experiments in the creep feed group were equal in strength to the baseline data, and one of the sixteen experiments in the pendulum feed group was equal to the baseline data.

Machining with the air bearing spindle appears to have a deleterious effect on strength compared to the machine with the steel ball bearing and this may reflect the greater stability available in the steel bearing. It is generally recognized that the grinding of ceramics requires very stable machines.

CONCLUSIONS

1. Designed experiments with a machine using an air bearing spindle showed that there were significant effects of machining variables on the strength and surface roughness of the machined silicon nitride, as well as the power and force observed and the wear on the grinding wheel.

2. Two or three significant variables were observed for each result, with a two-factor interaction of mesh size and diamond concentration observed for surface roughness of the workpiece and wear of the grinding wheel.

3. The second experiment with a machine using ball bearings in the spindle showed that the mode of machining (creep and pendulum) and removal rates (1.2 and 12 mm^3/mm-sec) are not significant factors in the strength of the machined silicon nitride.

4. Baseline strength data generated from samples cut from the NC132 Silicon Nitride billet were the same as strength measured from samples machined in the second experiment using the ball bearings.

5. Averages of strength from the first experiment using the grinding machine with the air bearings were significantly lower than strengths measured in the second experiment using the machine with the ball bearings. Creep or pendulum modes of machining had no effect on strength of machined silicon nitride, nor did removal rates.

REFERENCES

1. R. L. Allor, R. K. Govila, and T. J. Whalen, "Influence of Machining on Strength Properties of Turbine Materials", Ceramic Engineering and Science Proceedings, Vol.3, pp.392, 1982.

2. The Science of Ceramic Machining and Surface Finishing, S. J. Schneider and R. W. Rice (Eds.), Nat.Bur.Standards Special Publication No.348, pp.416, 1972.

3. The Science of Ceramic Machining and Finishing II, R. W. Rice and B. J. Hockey (Eds.), Nat.Bur.Standards Special Publication No.562, pp.518, 1979.

4. W. Konig and J. Wemhöner, "Optimizing Grinding of SiC", Ceramic Bulletin, Vol.68, No.3, pp.545, 1989.

5. W. H. Daniels, A. C. Hawkins, et al, "Superabrasives for Ceramic Grinding and Finishing", Advanced Ceramics Conference, Society of Manufacturing Engineers Paper EM 89-125, Feb.1989.

6. T. N. Farris and S. Chandrasekar, "On the Characterization and Control of Surface Finishing Damage in Ceramics", Journal of Mechanical Working Technology, No.20, pp.69, 1989.

7. K. Subramanian and P. P. Keat, "Parametric Study on Grindability of Structural and Electronic Ceramics-Part I", Machining of Ceramic Materials and Components, American Society of Mechanical Engineers, PED-Vol.17, pp.25, Nov.1985.

8. P. M. Stephan and S. Tuffs, "Machining of High Performance Silicon Nitride Mechanical Face Seal Rings", Machining of Ceramic Materials and Components, American Society of Mechanical Engineers, PED-Vol.17, pp.75, Nov.1985.

9. H. Kawamura, "Study of Grinding Process and Strength for Ceramic Heat Insulated Engine", Society of Manufacturing Engineers Superabrasives '91 Conference Proceedings, June 1991.

10. G. E. P. Box, W. G. Hunter, and J. S. Hunter, Statistics For Experimenters, John Wiley and Sons, New York, New York, 1984.

11. D. C. Montgomery, <u>Design and Analysis of Experiments</u>, 2nd Edition, John Wiley and Sons, New York, New York, 1984.

12. K. Unno and T. Imai, "Performance of Diamond Wheel in Grinding Ceramics", <u>Proceedings of 6th International Conference on Production Engineering, Osaka</u>, pp.26, 1987.

13. G. D. Quinn, F. I. Baratta and J. A. Conway, "Commentary on U.S.Army Standard Test Method for Flexural Strength of High Performance Ceramics at Ambient Temperature", Army Materials and Mechanics Research Center Report AMMRC 85-21, AD A160873, August 1985.

DAMAGE DETERMINATION AND STRENGTH PREDICTION OF MACHINED CERAMICS BY X-RAY DIFFRACTION TECHNIQUES

W. PFEIFFER and T. HOLLSTEIN

Fraunhofer Institute fur Werkstoffmechanik, Freiburg, Germany

The complex relationship between machining parameters and strength-controlling surface properties of high-strength ceramics has been investigated using newly developed x-ray diffraction techniques for the determination of profiles of depth of machining induced plastic deformation and residual stress. The resulting information is compared with results of strength tests performed at different loading conditions and SEM observations. A fracture mechanics approach, which correlates fracture stress and nondestructively determined near-surface properties (residual stress and plastic deformation) is used to evaluate defect size in the surface layer and - as a consequence - to predict fracture strength of machined ceramics. Typical cases of machining like grinding and lapping applied to silicon nitride and alumina are discussed and examples of successfully predicted strength data of machined alumina bars are presented.

Introduction

The high surface quality required for components of structural ceramics can often be achieved only by an additionally applied machining process. This strongly influences the strength and service behaviour of the components and, in addition, causes a considerable increase in manufacturing cost. Therefore, there is a need for non-destructive methods to determine the surface properties of machined components and for models to predict the fatigue and fracture behaviour in order to minimize cost of machining procedures and optimize the quality of components.

Common and easily determinable characteristics of machined surfaces of ceramics like SEM micrographs and roughness values may lead to erroneous assessments of the strength behaviour of the machined parts. This is demonstrated in Fig. 1, where SEM micrographs, roughness values (average peak-to-valley height, R_z) and

characteristic bending strength data for silicon nitride samples lapped with two different grain sizes of boron carbide are compiled: In spite of the 'rougher' and obviously more damaged surface of samples lapped with the coarse grained abrasives (Fig. 1a) these samples show a higher bending strength than those samples which have a smoother surface due to lapping with a fine grained abrasive (Fig. 1b). Similar results were obtained for lapped partially stabilized zirconia [1].

More meaningful methods like fractographic investigations on critical surface flaws or nondestructive observations using, e.g., acoustic or thermal microscopy [2, 3] suffer from conflicting demands for both an utmost global investigation of the surface region relevant for surface behaviour and highest local resolution in order to detect the small machining induced flaws.

235
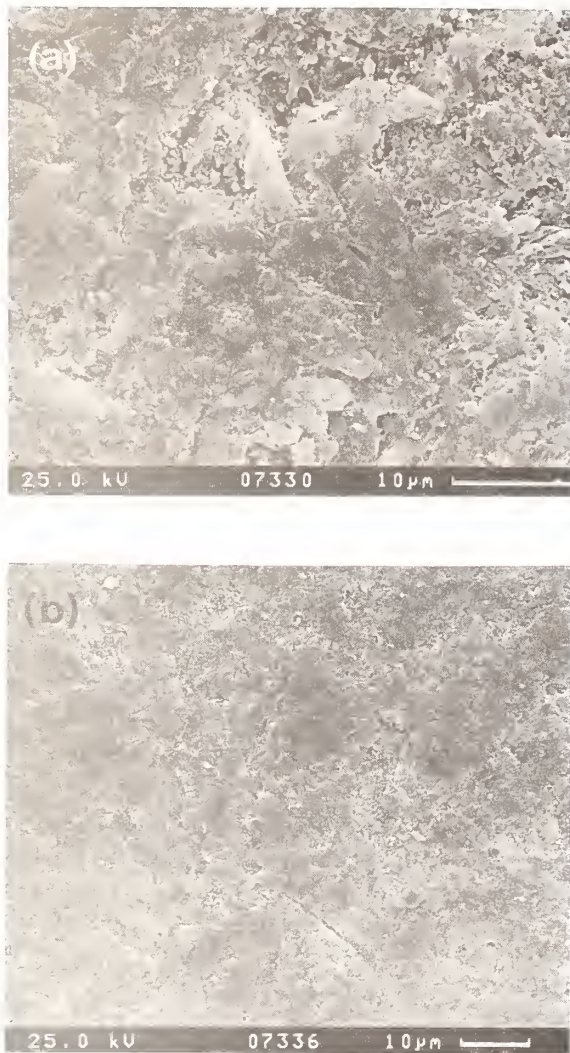
Fig. 1: SEM micrographs and roughness values
of lapped silicon nitride surfaces lead to
erroneous assessments of the strength:
(a): 100μm abrasive, R_Z = 11.5μm,
characteristic bending strength =
587 MPa
(b): 16μm abrasive, R_Z = 7.9μm,
characteristic bending strength =
552 MPa

The aim of the presented investigation was,
therefore, to

i) evaluate and improve nondestructive methods
for determination of machining induced
residual stresses and damage,

ii) quantify the effect of these near-surface
characteristics on the strength, and to

iii) validate these methods by comparison of
experimentally determined strength with
predicted strength data.

Materials and Machining

Flat samples of sintered pure (99.7%) alumina
and Y_2O_3/Al_2O_3 (5%, each) doped sintered
silicon nitride with the dimensions 50x50x3mm
were investigated in lapped and ground condi-
tions. Lapping was performed at different normal
pressures F''_n ranging from 0.02 MPa up to
0.06 MPa and at average surface speeds v_L of
0.9 m/s and 1.8 m/s using boron carbide abrasi-
ves (30 Vol%) with average grain sizes d_K from
9μm up to 100μm. Grinding (up-cut) was per-
formed using a diamond grinding wheel type
D151K+C100 (151 = average grain size in μm)
and infeeds a_e from 0.03mm up to 0.5mm, tan-
gential feed rates v_{ft} from 10mm/s up to
167mm/s and cutting speeds v_s of 25m/s and
50m/s, respectively. The specific material remo-
val rates Q'_w during grinding cover the range
from 10mm^3 /(mm·s) to 40mm^3 /(mm·s).

Additionally, alumina rods (length = 165mm,
diameter = 6mm) were prepared for tensile tests
by cylindrical grinding using three different grin-
ding conditions:

(1) Wheel type=D76K+C75, Q'_w = 0.001mm^3
/(mm·s), a_e = 0.015mm, v_{ft} = 0.08mm/s.
(2) Wheel type=D151V+C100, Q'_w=0.165mm^3
/(mm·s), a_e = 0.025mm, v_{ft} = 6.6mm/s.
(3) Wheel type=D151V+C100, Q'_w = 0.5mm^3
/(mm·s), a_e = 0.025mm, v_{ft} = 20 mm/s.

Strength Tests

Bending strengths of the machined flat samples
were determined using the concentric-ring test
with a loading ring diameter of 8mm and a sup-
porting ring diameter of 40mm. According to the
linear theory of plate bending, a constant maxi-
mum biaxial stress state prevails in the surface

236

within the loading ring. The advantage is, that effects of unproperly prepared edges of the samples can be neglected. Due to the symmetry of the stress state the 'weakest' direction of the surface is expected to lead to failure. Nine samples with identically machined surfaces were broken at stress rates of about 90 MPa/s.

Tension strengths of the alumina rods were determined using a universal testing machine with the so called 'supergrips' for momentum free loading of ceramic specimens with shoulders. Seven to ten samples with identically machined surfaces were broken at stress rates of 90 MPa/s.

The statistical distribution of the measured strength values was evaluated by means of the two-parameter Weibull distribution with the parameters characteristic strength σ_o and Weibull modulus m.

Nondestructive Determination of Machining Induced Residual Stresses

The assessment of defects within the machining influenced surface layer during loading needs the knowledge of the contribution of residual stresses to the overall stress state acting at flaws. Mean values of near-surface macroscopic residual stresses were determined by x-ray diffraction using the well-established $\sin^2\psi$-technique [4]. The distribution of residual stresses versus depth was evaluated using a newly developed application of grazing incident x-ray diffraction techniques [5].

Figure 2 shows the nondestructively determined distributions of machining induced residual stresses for alumina and silicon nitride samples.

They were lapped using different grain sizes of the abrasives: Fine grained abrasives lead to high compressive residual stresses at the surface. Coarse grain abrasives lead to smaller residual stresses at the surface but to thicker surface

layers containing compressive residual stresses (especially for silicon nitride).
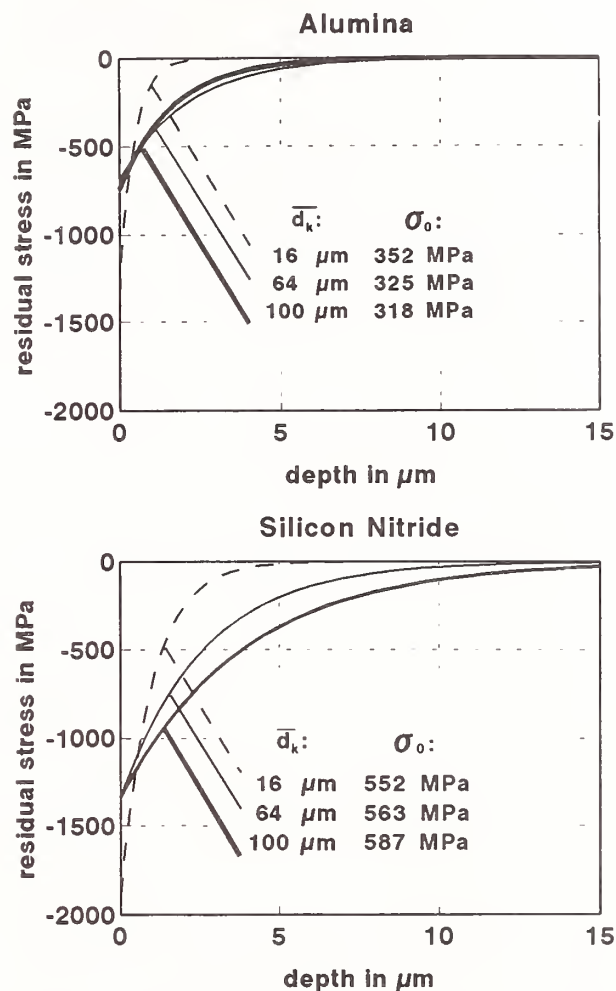
Fig. 2: Lapping of alumina and silicon nitride using abrasives with a large average grain size d_K leads to deep-reaching compressive residual stresses which overcompensate the effect of machining induced damage in the case of silicon nitride (see bending strength data σ_o).

The experimentally determined bending strength data for alumina qualitatively show the expected strength reducing-effect of coarse grained abrasives. In contrast to alumina the compressive residual stresses in silicon nitride obviously overcompensate the effect of machining induced damage on the bending strength.

237

Evaluation of Defect Sizes

The quantitative effect of machining induced residual stress states and the amount of machining induced damage is evaluated by means of fracture mechanics calculations:

The size, distribution and position of strength controlling defects are normally not accessible to direct measurements. Since they are important for the strength, 'effective' flaw sizes were calculated by means of fracture mechanics methods from the bending strength data and the experimentally determined residual stress distributions. These 'flaw sizes' are, of course, affected by the used simplifications but nevertheless they characterize the amount of damage.

The determination of the 'depth' of flaws is based on the equation describing the fracture toughness of brittle materials:

$$K_{Ic} = \sigma_c \cdot f \cdot (\pi \cdot a_c)^{1/2} \qquad (1)$$

The critical fracture stress σ_c is evaluated from the characteristic fracture stress σ_o obtained through the bending test and from the residual stress σ_{res} determined by the x-ray diffraction method. For values of fracture toughness K_{Ic} of the materials tested those values are used, that take into account the absence of 'R-curve effects' in the case of small flaws (Al_2O_3: K_{Ic}=2.4 MPa·m$^{1/2}$ [6], Si_3N_4: K_{Ic} 1.9 MPa·m$^{1/2}$ [7]). The form factor f takes into account the ratio of length/depth of flaws and is 1.12 in case of a surface scratch and $2/\pi$ in case of a half-penny shaped surface flaw. The critical depths of flaws are calculated by numerical integration of the nonlinear loading and residual stress distributions using the weight function method [8].

Figure 3 shows an example of calculated depths for half-penny shaped flaws of lapped alumina and silicon nitride, for two cases:

i) effect of machining induced residual stresses is taken into account, and
ii) effect of machining induced residual stresses is not taken into account.

Especially in the case of silicon nitride the results point out that calculated flaw sizes are larger if the strengthening effect of compressive residual stresses is taken into account. The expected larger flaw sizes (when using coarse grained abrasives) are confirmed by those calculations that include the effect of residual stresses.
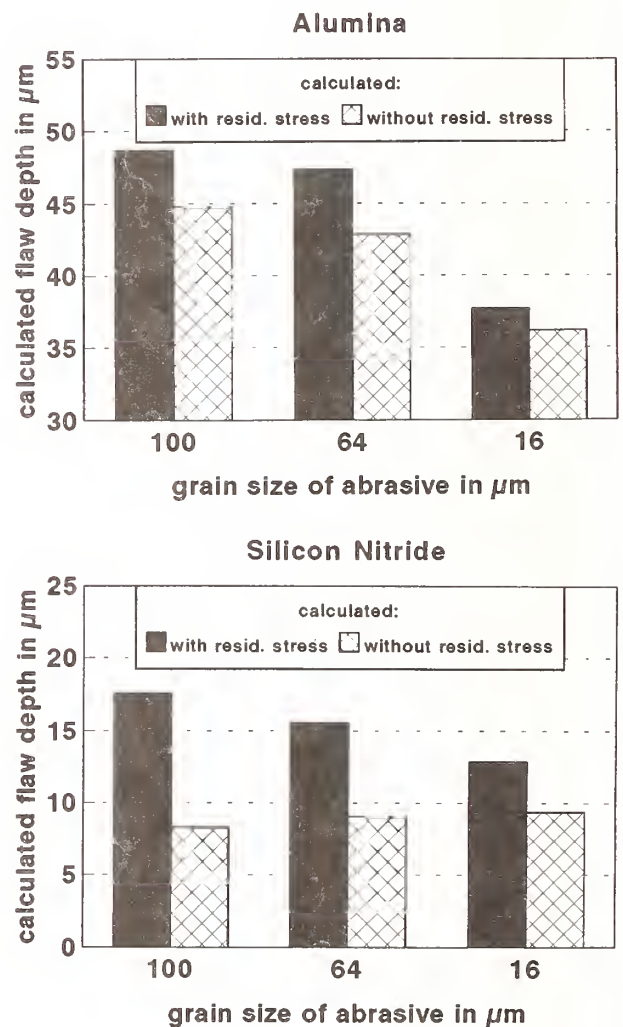
Fig. 3: Lapping induced damage is quantified by calculated depths of flaws only if the influence of residual stresses is taken into account.

The comparison of the depths of flaws detected by SEM fractography (see Fig. 4) with the calculated values additionally shows, that the calculated depths of flaws are of similar magnitude.
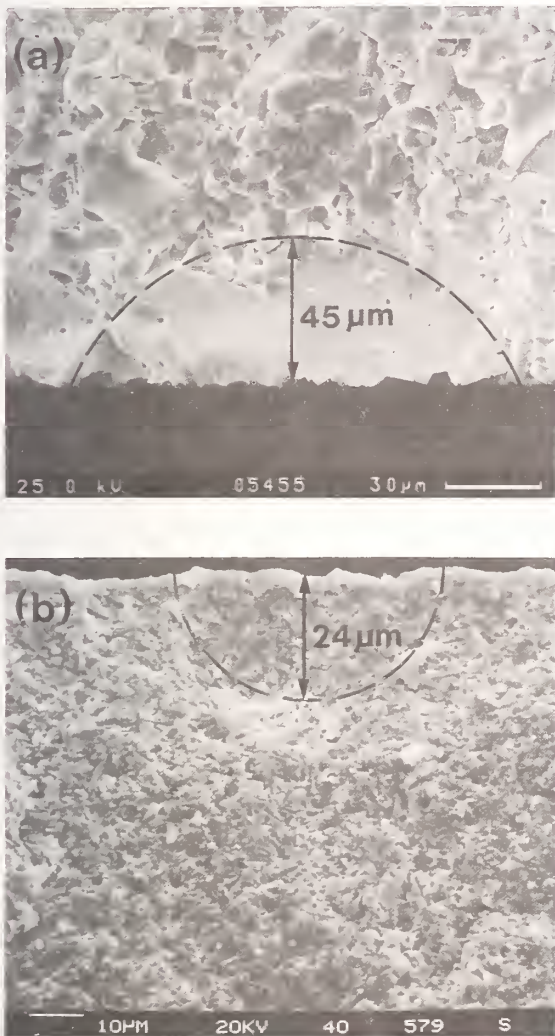
Fig. 4: Micrographs of fracture surfaces with machining induced flaws of alumina (a) and silicon nitride (b). The flaw sizes are estimated on the basis of half-penny shaped cracks.

Nondestructive Determination of Machining Induced Damage

Indentation experiments performed on different brittle materials and theoretical investigations indicate the existence of a (material dependent) relationship between the plastically deformed surface layer and the flaw size (e.g. [9, 10]). The presented method for the nondestructive determination of machining damage is based on the determination of the thickness' a_p of the micro-plastically deformed surface layers and the establishment of correlations between these thickness' and calculated flaw depths a_c.

The thickness of the plastically deformed surface layer can be estimated by a newly developed application of grazing incident x-ray diffraction techniques [5] using the effect of machining induced lattice defects (e.g. dislocations) on microscopic lattice strains.

Figure 5 shows such distributions of microscopic strain within the surface layers of alumina and silicon nitride samples which were ground using different infeeds a_e, different specific material removal rates Q'_w and different cutting speeds v_s.

The effect of different grinding conditions on micro-plastic deformation can clearly be separated by the x-ray diffraction method. The obtained thicknesses of deformed surface layers correspond to the expectations regarding the influence of different grinding conditions on the elementary mechanisms of material removal.

Creep feed grinding conditions (large infeed a_e) as well as high cutting speeds and small tangential feed rates reduce the undeformed chip thickness at the single cutting edge [11]. This, combined with reduced local forces, results in reduced depths of plastic deformation. The bending strength data indicate that the depth of plastic deformation is related to the amount of machining induced damage and that grinding compressive residual stresses (see below) do not significantly influence the bending strength.

In order to validate the relationship between the thickness of plastically deformed surface layers and machining induced damage, the depths of experimentally determined plastic deformation and the calculated flaw depths are compared for alumina and silicon nitride samples in various machined conditions in Fig. 6.

Alumina

a_e:	Q'_w:	v_s:	σ_0:
0.03	5	25	253
0.5	20	25	278
0.5	5	25	341
0.5	10	50	338

Silicon Nitride

a_e:	Q'_w:	v_s:	σ_0:
0.03	5	25	432
0.5	20	25	476
0.5	5	25	513
0.5	10	50	547
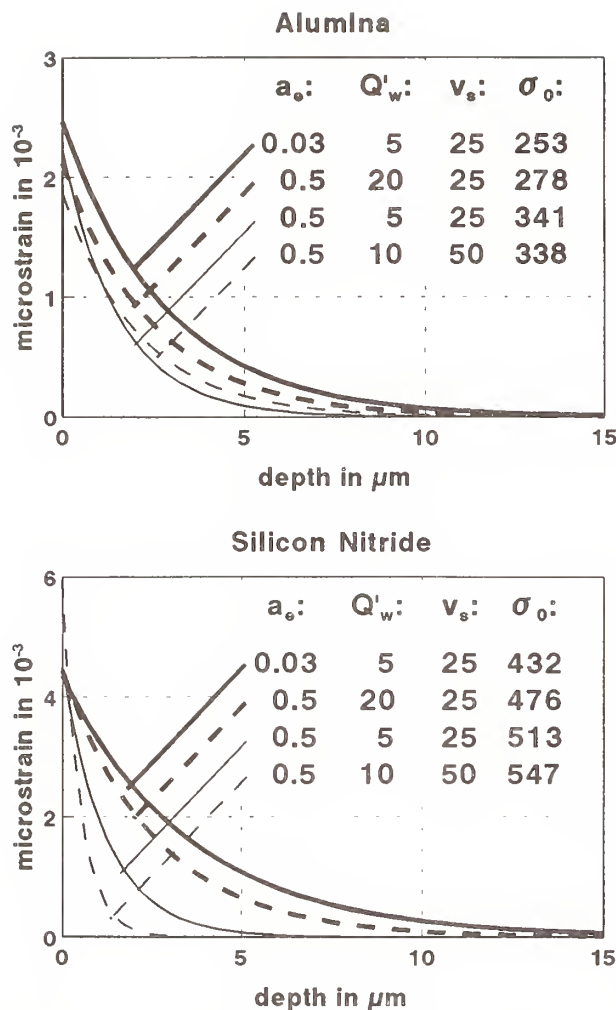
Fig. 5: Grinding using large infeeds a_e (mm), small material removal rates Q'_w (mm³/(mm·s)) and high cutting speeds v_S (m/s) lead to small micro-plastically deformed surface layers and obviously small damage (see characteristic bending strength data σ_o (MPa)).

The depth of plastic deformation was determined at $\varepsilon_p = 10^{-6}$, the flaw depth a_c was evaluated using characteristic bending strength data, experimentally determined residual stress distributions and assuming half-penny shaped flaws.

For alumina, a unique linear dependence between deformation depths and calculated flaw

depths can be established for both lapped and ground samples. Few data points (marked by ↗) do not fit to the regression line: These data points belong to those grinding conditions, where fracture during the strength tests resulted in preferred orientation parallel to the grinding direction.

Alumina

Silicon Nitride

Fig. 6: Correlation between nondestructively determined deformation depths a_p and calculated flaw depth a_c of differently lapped and ground alumina and silicon nitride, half-penny shaped flaws are assumed in all cases.

The more realistic assumption of scratch-like flaws (form factor $f \to 1.12$) in these cases would lead to smaller calculated flaw depths and by this improve the quality of correlation. For machined silicon nitride, different (linear)

dependencies exist for ground and lapped samples: Obviously the ratio of crack depth/ deformation depth is larger in the case of grinding than in the case of lapping or the grinding induced microcracks are more serious (which means more scratch-like). In spite of these uncertainties about the geometry of flaws (which could not be clarified by SEM investigations), the established relationships between deformation depth and crack depth may be used to determine machining damage quantitatively by the advanced nondestructive x-ray diffraction technique.

The determination of the distribution of microscopic strain is a time-consuming experiment, which (due to defocussing effects) is additionally limited to samples with simple geometries. Therefore, a similar relationship between (more easily determinable) mean values of microscopic strains of the surface layer and the calculated flaw depths is established in Fig. 7. This is possible because the mean microscopic strain of surface layers is dominated by the depth of plastic deformation.

Effect of Residual Stresses and Damage on Strength

On the basis of calculated flaw sizes a_c (taking the effect of residual stresses into account) and the appropriate K_{Ic} values, the critical fracture stress values σ_c were calculated. Due to the theoretically given dependence between σ_c and a_c (see eq. 1) the critical fracture stress values σ_c are plotted versus $1/a_c^{1/2}$ and compared with the experimentally determined characteristic bending strength data σ_o (Fig. 8).

The results show that the effects of machining induced damage and residual stresses depend on the type of machining and material:

- For lapped and ground alumina, the contribution of machining induced compressive residual stresses to the bending strength is small, the bending strength is dominated by machining induced damage.
- For ground silicon nitride increasing machining damage is combined with increasing strengthening effects due to compressive residual stresses but these residual stresses do not overcompensate the effect of damage on strength.
- For lapped silicon nitride, the machining induced compressive residual stresses compensate the strength reducing effect of machining induced damage.
- With increasing amount of damage also increasing compressive residual stresses are created due to machining in all cases
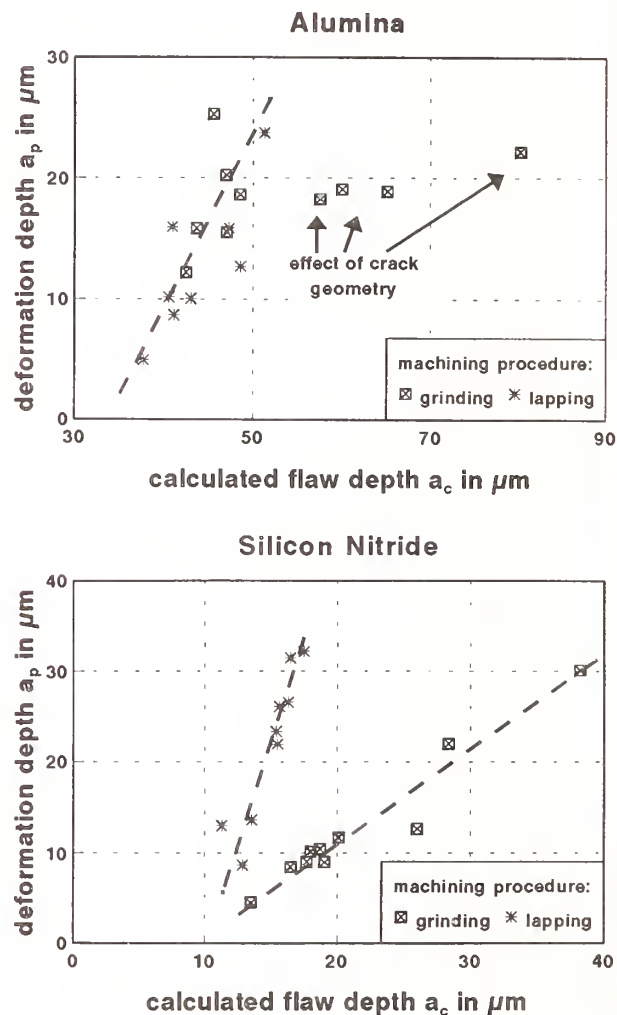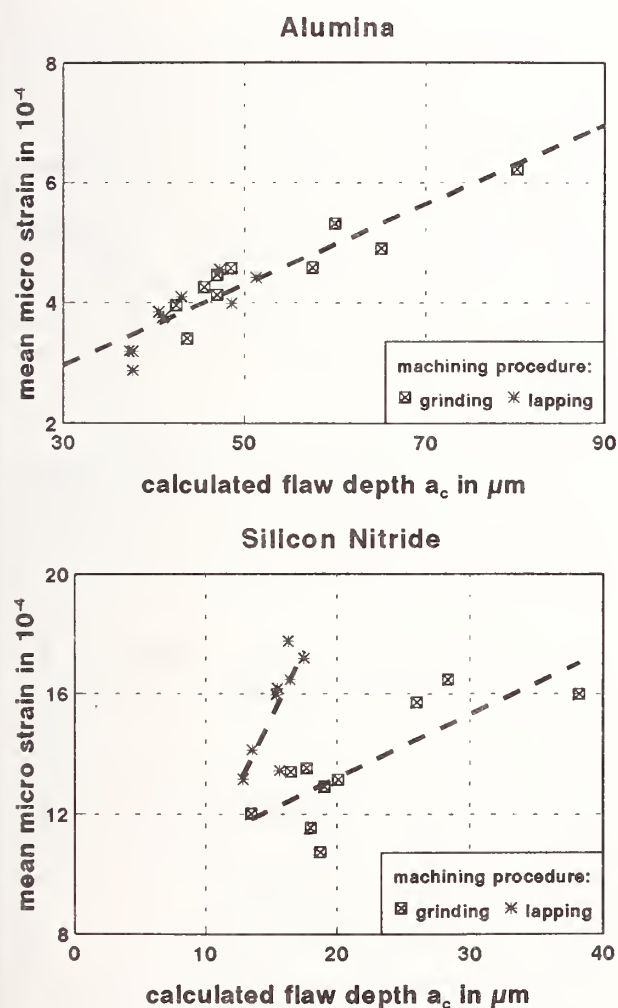

Fig. 7: Correlation between nondestructively determined mean values of deformation and calculated flaw depths a_c of differently lapped and ground alumina and silicon nitride (half-penny shaped flaws are assumed).

investigated. Thus an additional material and machining dependent relationship between micro-plastic deformation and residual stress states can be established [5, 8]. This allows to quantify both the effect of damage and the residual stresses on strength by determination of just one of these surface properties.

Prediction of Strength

It was shown, that the strength dominating properties (residual stresses and flaw sizes) of surface layers of machined ceramics can be evaluated quantitatively by nondestructive x-ray diffraction methods.

Knowing the residual stress distribution within the machining influenced surface layer and using the established relationship between deformation depth and 'crack sizes', it is possible to predict the surface-strength of machined components.

The experimental validation of this thesis is performed using the relation between more easily determinable mean values of microscopic strain and damage (see Fig. 7) and the material and machining dependent relationships between fracture stress, characteristic bending strength and amount of damage (see Fig. 8).
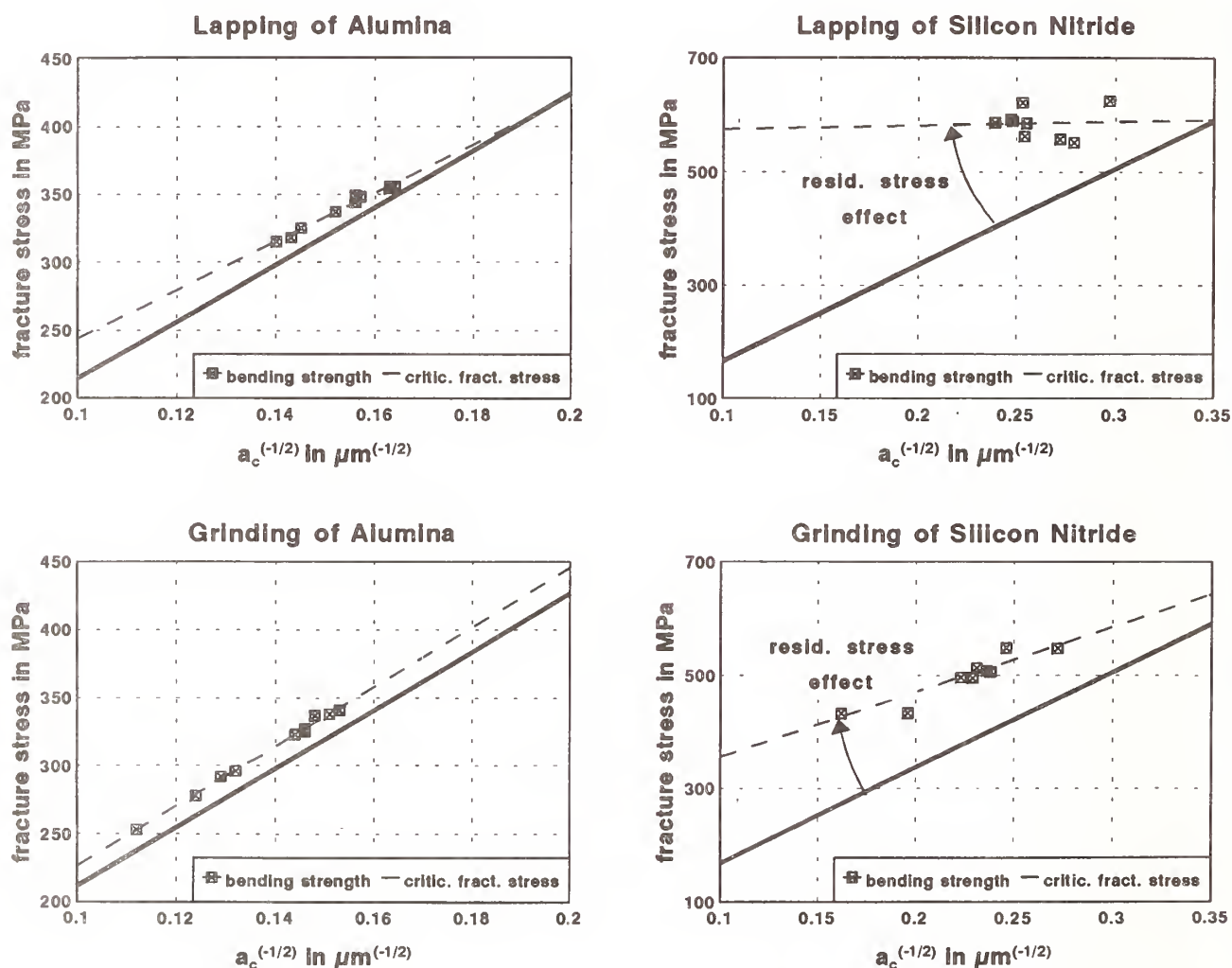
Fig. 8: Strength - damage diagrams showing the effect of machining induced compressive residual stresses on the bending strength of alumina and silicon nitride. σ_c denotes the critical fracture stress which equals the strength in the absence of residual stresses.

The following procedure for the prediction of tension strength of alumina rods which were ground using three different grinding parameters, therefore, consists of two steps:

i) From the mean values of experimentally determined microscopic plastic deformation of the tension rods the corresponding crack depths are derived (Fig. 9a).

ii) From the estimated crack sizes the critical fracture strength σ_c and the additional contribution of compressive residual stresses to the overall characteristic fracture strength σ_o are predicted (Fig. 9b).

The results show that grinding with increasing material removal rates (see $1\rightarrow2\rightarrow3$, Figs.9, 10) leads to increasing flaw depths and reduced strength. The small flaw depths evaluated for the tension rods ground with the smallest material removal rate, (1), are comparable with the calculated flaw depth of bend samples which were lapped with a fine grained abrasive (see Fig. 3).

Fractographic investigations showed, that the fracture causing defects of these samples are 'natural' defects. This means, that the effect of machining induced damage is negligible, whereas grinding at higher material removal rates (2, 3) leads to failure due to machining induced flaws.

The experimentally determined Weibull-distributions of the tensions rods are shown in Fig. 10 and the evaluated characteristic strengths are compared with the predicted values in Fig. 9. The predicted and measured strengths are in good agreement. The small discrepancies between predicted and measured strength data may be due to the effect of the fracture relevant volume on strength. The prediction is based on bend samples with a relatively small fracture relevant volume but applied to tension rods with a larger volume. This leads to a slight overestimation of strength.
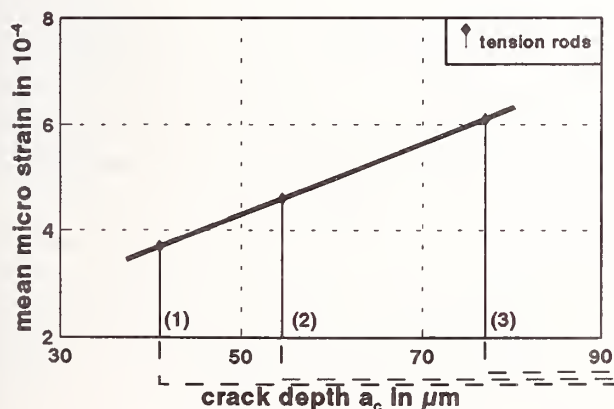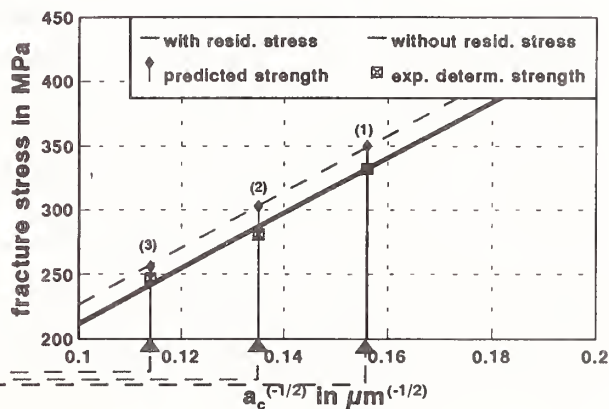
Fig. 9: Prediction of the strength of alumina bars in differently ground conditions:
(a): Evaluation of crack depths by the nondestructively determined plastic deformation.
(b): Assessment of the strength dominating effects of damage and residual stress and comparison with experimentally determined strength data.
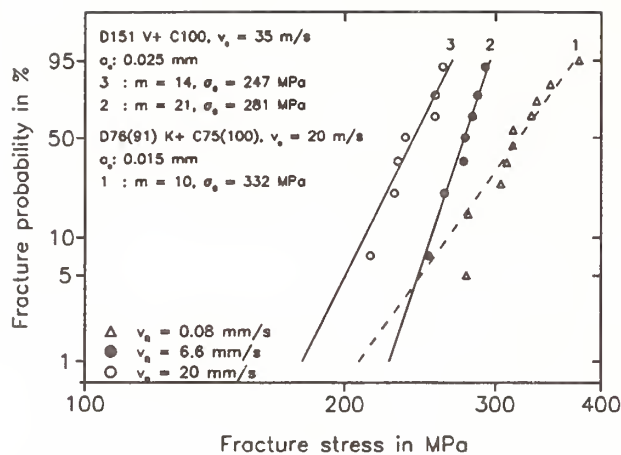
Fig. 10: Weibull distributions of fracture stresses of alumina rods ground with different material removal rates (due to different tangential feed rates v_{ft}). Characteristic tensile strength data (σ_o) and Weibull moduli (m) are indicated.

Summary

The complex relationships between machining parameters and strength-controlling damage and residual stresses of alumina and silicon nitride have been investigated using advanced x-ray diffraction techniques, strength tests and fracture mechanics calculations. Correlations between micro-plastic deformation and amount of damage can be established. They allow to determine nondestructively and quantitatively the amount of machining induced damage. The contribution of machining induced residual stresses to the strength of machined ceramics can be quantified both by calculation of flaw sizes taking the residual stresses into account and by establishing material- and machining-dependent strength - damage - diagrams.

The investigations show that in the case of lapped and ground alumina and of ground silicon nitride bending strength is dominated by machining induced damage. In the case of lapped silicon nitride the effect of damage is compensated by machining induced compressive residual stresses.

Using the established relationships between damage and residual stresses, respectively, and strength, the tension strength of differently ground alumina bars has been predicted with high accuracy.

Acknowledgement

References

[1] W. Pfeiffer, "Influence of Machining-Induced Residual Stresses on the Strength of Ceramics," Proc. of Conf. on Experimental Mechanics, Copenhagen, Denmark, pp. 1237- 1245, 1990.

[2] H. Reiter, M. Maisl, U. Netzelmann and W. Arnold, "Nondestructive Testing of Ceramics by Computed Tomography and High-Frequency Ultrasonics," 4th International Symposium on Ceramic Materials and Components for Engines, Elsevier Science Publ. LTD, London, New York, pp. 880-887, 1992.

[3] H.K. Tönshoff, E. Brinksmeier, and H.G. Wobker, "Randzonenanalyse als Werkzeug zur keramikgerechten Prozeßgestaltung," DKG-Symposium "Bearbeiten von Keramik", Bayreuth, 13.12.1992.

[4] P. Müller and E. Macherauch "Das $\sin^2\psi$-Verfahren der röntgenographischen Spannungsmessung," Z. ang. Phys., Vol. 13, pp. 305-312, 1961.

[5] W. Pfeiffer, "Characterization of Near-Surface Conditions of Machined Ceramics by use of X-ray Residual Stress Measurements," Residual Stress III, Elsevier Science Publ. LTD, London, New York, Vol. 2, pp. 607-612, 1992.

[6] T. Fett and D. Munz, "Evaluation of R-Curves in Ceramic Materials based on Bridging Interactions", KFK-Report 4940, 1991, ISSN 0303-4003.

[7] E. Sommer, R.Mohrmann and M.Rombach, "Lifetime Prediction for Components of Ceramics under Quasistatic and Cyclic Loading," XIth Intern. Colloquium on Mechanical Fatigue of Metals, Kiev, USSR, May 13-17, 1991.

[8] W. Pfeiffer and E. Sommer, "Bewertung der Festigkeitseigenschaften Oberflächenbearbeiteter Keramikbauteile," Werkstoffe, DGM-Informationsgesellschaft mbH, Oberursel, pp. 575-584, 1991.

[9] R.W. Rice, "The Effect of Grinding Direction on the Strength of Ceramics," The Science of Ceramic Machining and Surface Finishing II, B.J. Hockey and R.W. Rice (Eds), National Bureau of Standards Spec. Publ. 348, U.S. Government Printing Office, Washington D.C., pp. 365-376, 1979.

[10] K. Tanaka, "Elastic/Plastic Indentation Hardness and Indentation Fracture Toughness: The Inclusion Core Model," J. of Mater. Sci., Vol 22, pp. 1501-1508, 1987.

[11] W. König and J. Wemhöner, "Optimizing Grinding of SiSiC," Ceram Bull., Vol. 68, No.3, pp. 545-548, 1989.

INFLUENCE OF MICROSTRUCTURE ON GRINDABILITY OF ALUMINA CERAMICS

P. ROTH and H. K. TONSHOFF

University of Hannover, Hannover, Germany

This paper presents the results of grinding experiments with various grades of alumina ceramics. When machined identically, the materials reveal systematical differences in grindability. Grinding forces and energies are controlled by material grain size and toughness. Brittle as well as ductile behaviour of alumina ceramics are identified in grinding. Material removal mechanisms depend strongly on the microstructure of the materials. Grain size is identified as one dominant parameter. With decreasing grain size, plastic deformation becomes more prominent over micro-brittle material removal. With a given material, two parameters determine grit-work interaction: Micro-brittle fracture, ploughing, and cutting action of the grits are observed as a function of (1) grit depth of cut and (2) cutting point density. A thin layer of heavily deformed material is frequently found to cover ground surfaces. Compressive residual stress originates from the plastically deformed sub-surface zone. The magnitude of residual stress is a function of the grit depth of cut. Over a wide range of conventional machining conditions, grain size limits the obtainable surface finish.

Introduction

Modern structural ceramics consist of chemical compounds from the groups of oxides, nitrides, and carbides. In engineering, they are valued for their superior stiffness/weight ratio, high hardness and wear resistance even at elevated temperatures. Yet, it is these very qualities that limit the use of ceramic components in machine design. Prepared from powders by various compaction and sintering techniques, ceramic parts can vary considerably in size and shape. To meet close dimensional tolerances, the more intricate parts have to be finished by grinding, lapping and sometimes polishing with diamond grit. Such abrasive machining is critical in respect of cost and quality control. The surface quality attained by finishing processes can determine the performance of ceramic components. This is a result of the low fracture toughness of ceramics and their sensitivity to surface damage. As modern ceramics are constantly improving in quality, volume defects are reduced in size and number. Thus, it can now be the surface

flaws that determine the mechanical strength of a finished part. In order to determine favourable grinding conditions which retain unimpaired surface integrity, the process of material removal must be investigated systematically.

While in grinding of ceramics the aspects of machining parameters and tool specifications have been examined closely [1-6], it is of equal interest to study the influence of varying microstructure with ceramic materials. As of today, industrial standards such as those for metals do not exist for this rapidly developing group of materials. It is therefore desirable to predict the machinability of a given ceramic from its mechanical properties such as hardness, bending strength, etc. These qualities of a material depend on its chemical composition as well as on its microstructure, i.e. the size and distributions of grains and pores. With multi-phase materials, the interaction between the different phases has to be considered as a further influence.

247

Experimental procedure

The investigations described in this paper have been carried out to determine the influence of ceramic microstructure on grindability. A single-phase alumina ceramic with varied grain size has been chosen for investigation. For the grinding tests, a series of high-purity alumina ceramics were produced under controlled conditions (99.98% Al_2O_3). No additives were used for sintering of five grades at temperatures ranging from 1300°C to 1700°C. In all cases, almost identical densities of at least 98.5% were achieved. Equal in chemical composition, these ceramics differed in microstructure and properties due to the varied sintering cycle. In accordance with the sintering temperatures the alumina grades were designed as TM 30...70. Their mechanical values are given in Table 1 and Figure 1 below.

With rising sintering temperature, average grain size increases from 0.8 to 12 µm. Correspondingly, the hardness of the five alumina grades is found to decrease from 19.4 GPa to 15.8 GPa while fracture toughness rises slightly to remain at a constant level with the larger grained varieties. Bending strength decreases from a maximum at the second finest alumina grade. The important differences in hardness and strength with varying microstructure can be expected to notably influence the grindability of the different alumina varieties.

Table 1: Material properties

Material grade	Sintering temp. T_s [°C]	Grain size d_g [µm]	Hardness HV 10 [GPa]	Fracture toughness K_{Ic} [MPa·m$^{1/2}$]	Bending strength σ_{4b} [MPa]
TM 30	1300	0.83	19.4	3.68	320
TM 40	1400	2.2	19.2	3.80	380
TM 50	1500	4.6	17.7	4.10	340
TM 60	1600	7.8	16.5	4.15	300
TM 70	1700	12.2	15.8	4.07	300

Surface grinding tests were performed using phenolic resin bond diamond wheels with grit sizes ranging from D7 (5-10 µm) to D151 (125-150 µm). Truing was performed by a brake-type rotary truer with silicon carbide wheels. The grinding wheels were then dressed with a porous alumina block at conditions optimized separately for each wheel. Earlier testing had shown that the grinding forces stabilized after an initial phase of rapid wear after dressing. Consequently, each test was carried out until a specific material volume of 300 mm^3/mm had been removed. Throughout the tests, low viscosity mineral oil was used as a coolant.

In existing studies of brittle workpiece materials, the depth of cut of an individual grit, h_{max}, has been demonstrated to determine the transition from micro-brittle to ductile material removal [5]. To study the onset of the different mechanisms, the grit depth of cut was varied via the wheel depth of cut, a_e, the feed speed, v_{ft}, and the grinding speed, v_c. The strongest influence on h_{max} results from the density of cutting edges C in the abrasive process as demonstrated by equation (1) below. Variation of this parameter has been accounted for by the use of different grit size grinding wheels of uniform diamond content.

$$h_{max} = \sqrt{\frac{4}{C \cdot r} \cdot \frac{v_{ft}}{v_c} \cdot \sqrt{\frac{a_e}{d}}} \qquad \text{[7] (1)}$$

The tests encompassed a range from conventional to creep feed grinding conditions. The parameters used in the grinding experiments are summarized in Table 2 below.
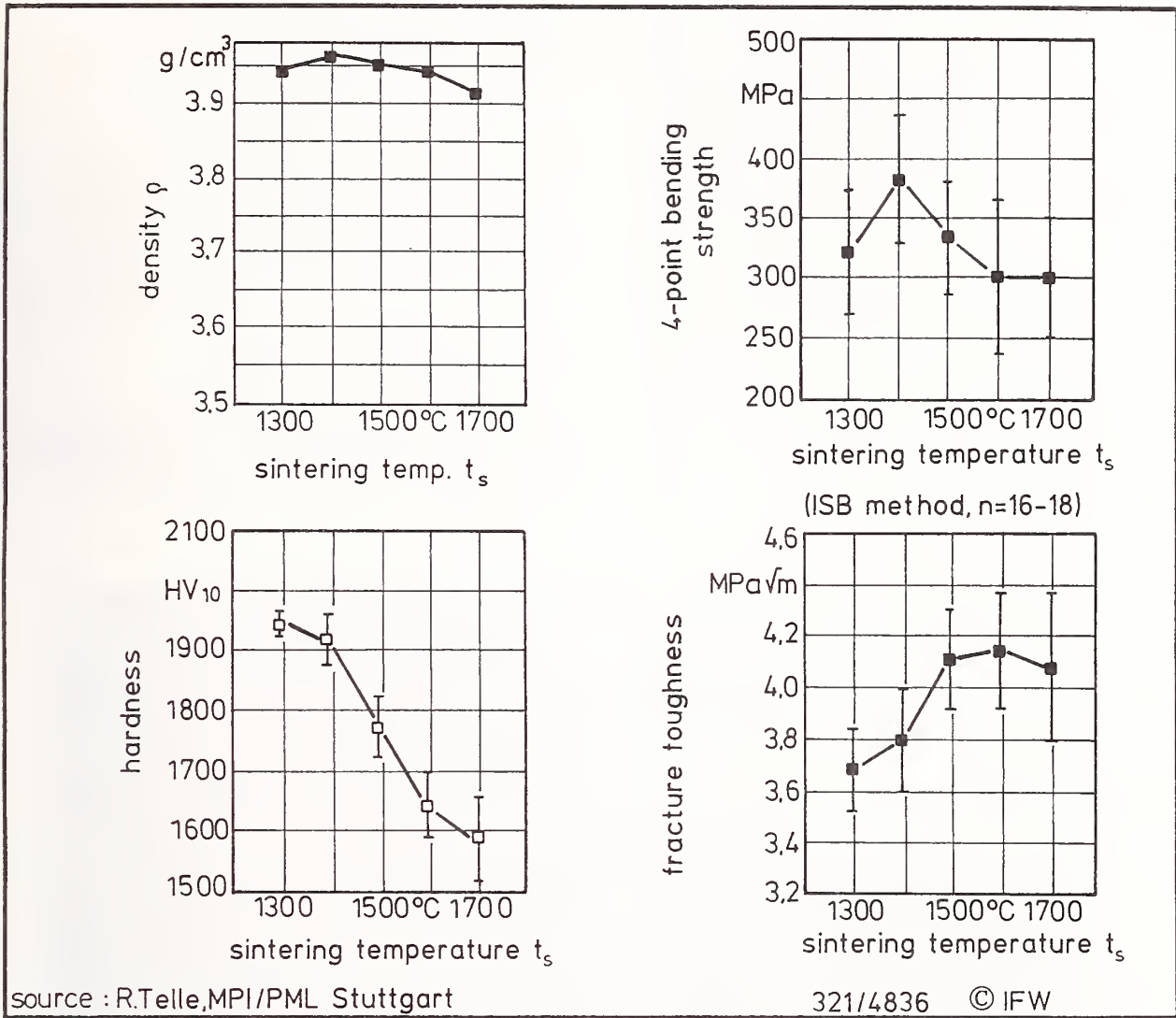
Fig. 1: Mechanical properties of workpiece materials

Table 2: Process settings for the grinding tests

Grinding wheels	1A1-300-10-3 D7...D151 C50, $V_w' = 300$ mm^3/mm (50 mm^3/mm for D20B, 10 mm^3/mm for D7)
Truing	rotary brake type truer; silicon carbide wheels 37 C 60..80 N5V
Dressing	porous alumina block, $Q_{sb}' = 0.5...10$ mm^3/mm·s
Grinding speed	$v_c = 10...25$ m/s, up-grinding
Work feed speed	$v_{ft} = 10...10'000$ mm/s
Wheel depth of cut	$a_e = 0.001...2.0$ mm
Coolant	straight mineral oil ($v = 4.15$ mm^2/s at 40°C), $q = 30$ l/min

In order to analyse the interaction of the grit with the workpiece surface more closely, plane alumina specimens were polished, sputtered with gold, and then ground in a slightly tilted position. By this, the wheel depth of cut increased gradually from zero to a preset maximum and the average grit depth of cut along with it.

During grinding, horizontal and vertical grinding forces were constantly monitored by a piezoelectric dynamometer and recorded by computer. Subsequently, the specific normal and tangential grinding forces were computed off-line. From the tangential grinding force, the specific grinding energy e_c was calculated. It denotes the energy necessary to remove a unit volume of material. It is derived from the tangential grinding force F_t' and the settings of the grinding process by

$$e_c = (F_t' \cdot v_c) / (a_e \cdot v_{ft}). \qquad (2)$$

Surface finish R_z (average peak-to-valley roughness) was measured by stylus tracing to characterize the ground ceramic surfaces. Measurements were performed in several directions relative to the grinding direction. Micrographs of the ground surfaces were prepared by SEM.

To determine residual grinding stress x-ray stress analysis was carried out with Cr-K_α radiation on the (030) plane of alumina. Residual stress $\sigma_\perp$ was measured across the grinding direction.
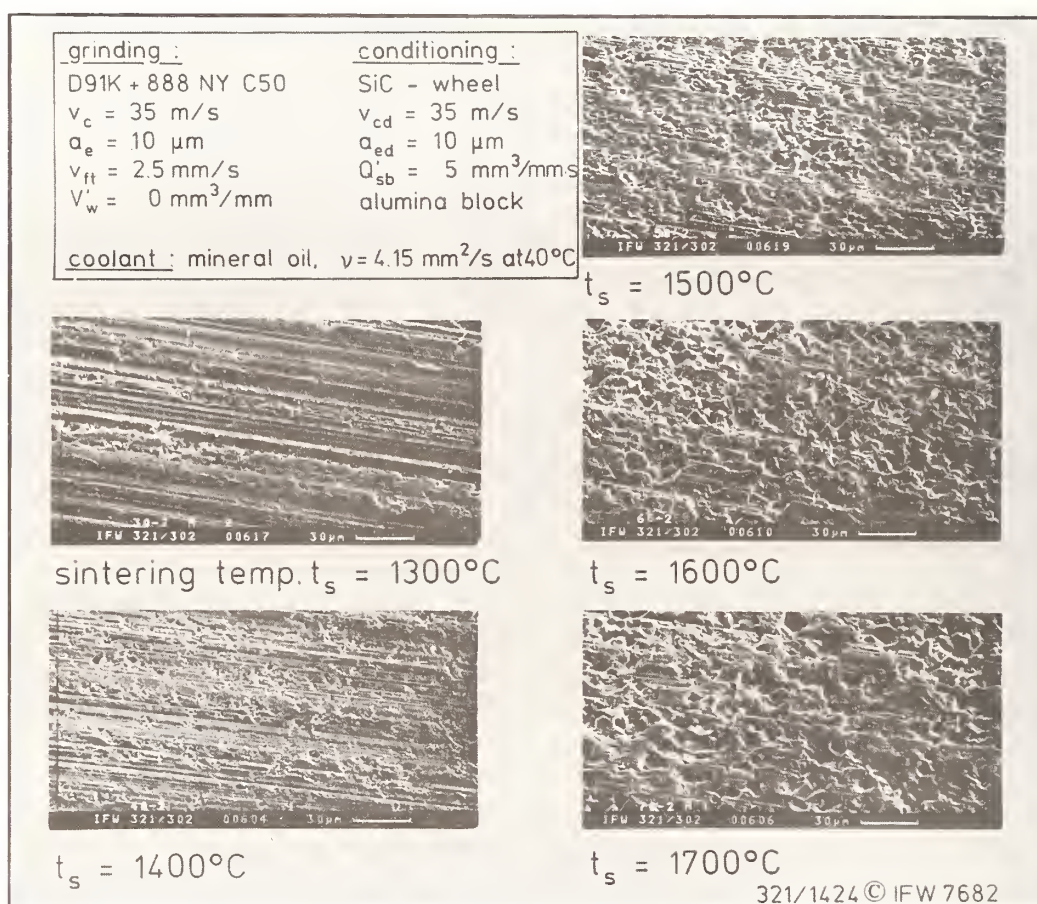
Fig. 2: Surfaces of various alumina ceramics ground at identical conditions

Results

As expected in view of their mechanical values, the five alumina varieties behave very differently in grinding [8]. Figure 2 shows SEM micrographs of ground surfaces. These surfaces were ground identically at a low grit depth of cut in order to facilitate ductile material behaviour. Most importantly, the ground surfaces exhibit different mechanisms of surface formation.

With the fine-grained varieties TM 30 and 40, the ground surfaces appear covered with smooth grooves. Some lateral pile-up of displaced material can be observed. The regular groove pattern is broken by two different types of cavities. Small pores form as grains are broken from the surface under the action of a grit. Larger, flake-like particles are removed by chipping. Some of these have only partly separated from the substrate and remain on the surface close to their original position.

With the increase in grain size, the surfaces become continuosly rougher. The removal of single grains dominates over groove formation. The surfaces of the coarser alumina varieties TM 50 and TM 60 reveal many near-perfect grain facets. Finally with TM 70, transgranular fracture is frequently observed. Some of the remaining plateaus bear traces of plastic deformation as with the fine-grained materials.

In a detail SEM micrograph of a ground TM 30 sample (Fig. 3) the sub-surface structure becomes visible at the edge of a cavity. The top layer is heavily deformed by ploughing and appears unstructured at its broken rim. Its thickness can be estimated at approximately 0.5 µm. Below this layer, the original material microstructure made up of regular sub-micron alumina grains is retained. Visible grain facets suggest that fracture has proceeded predominantly by an intergranular process.

grinding :
D91K + 888 NYB C50

v_c = 30 m/s
a_e = 250 µm
v_{ft} = 2.5 mm/s

dressing :
SiC wheel
v_{sd} = 30 m/s
a_{ed} = 10 µm
Q'_{sb} = 5 mm^3/mm·s
(alumina block)

work material :
high purity alumina,
99.89 %

IFW 321/302   00881   3µm

321/2065   © IFW 7923
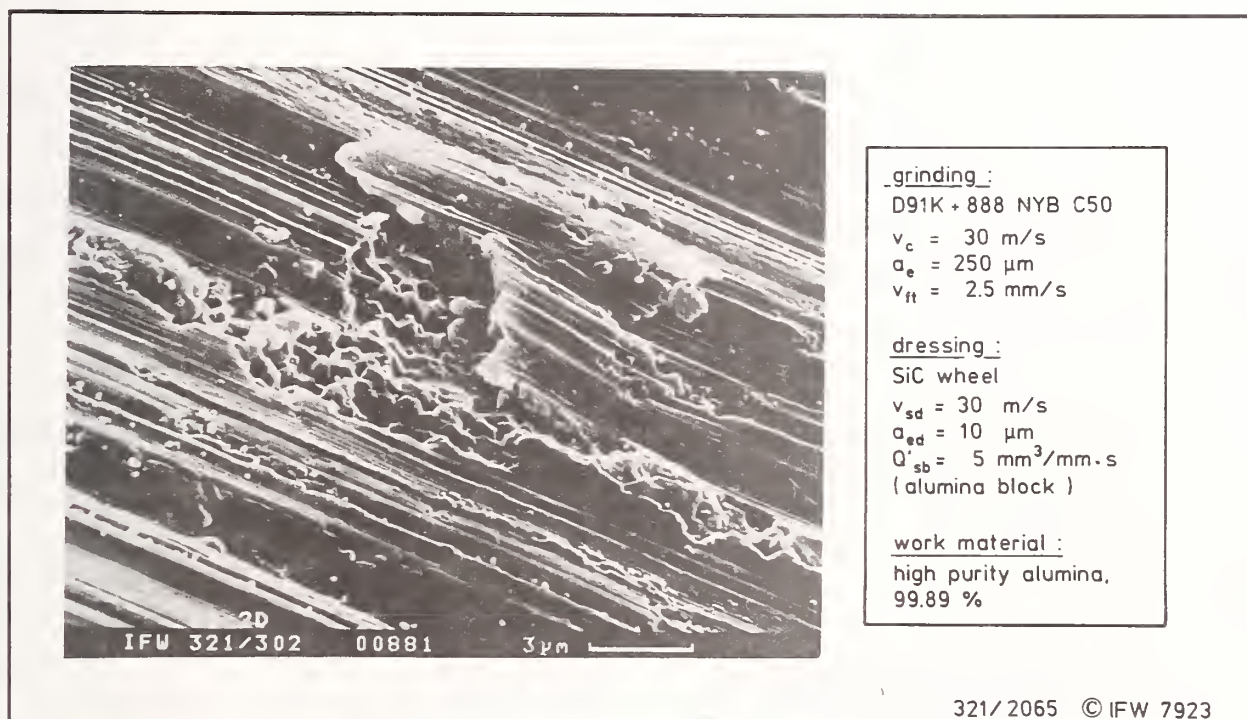
Fig. 3: Ground surface of fine-grained sample

Surface roughness was measured to characterize the ground ceramic surfaces. Figure 4 gives the roughness R_z of the various materials in a polar diagram relative to the grinding direction.

The roughness measurements confirm the visual impression obtained from the SEM pictures in Fig. 2. Roughness increases monotonously with grain size. In TM 30 and TM 40, roughness values are significantly different along and across the grinding direction. This reflects the observed formation of grooves. The directionality of surface roughness gradually disappears with larger material grain sizes to approach isotropic roughness as in a lapped surface with TM 70.

Figure 5 represents the roughness values determined on samples of TM 40 ground under various creep feed and conventional surface grinding conditions. With alumina, unlike ductile work materials, no direct connection exists between the roughness and the grinding conditions. Roughness rises only insignificantly over a wide range of chip cross sections.

251
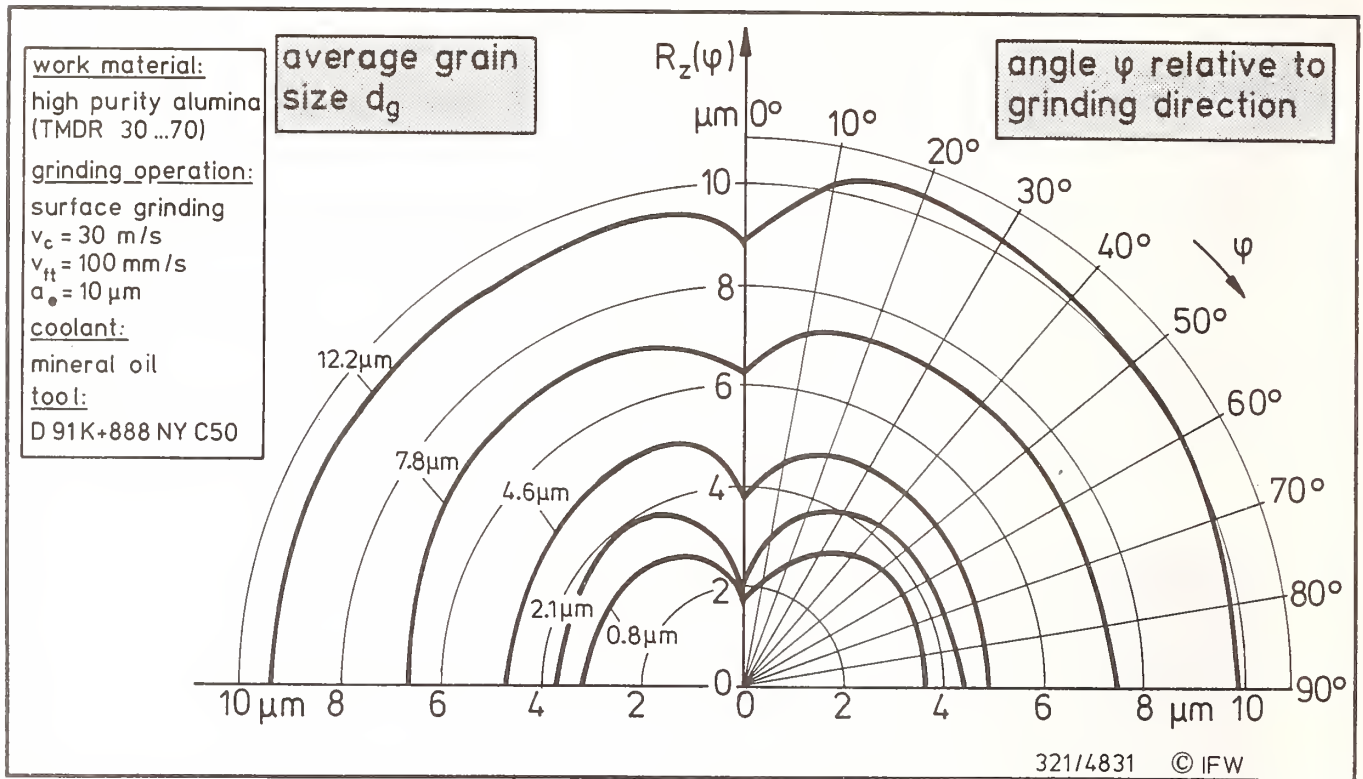
Fig. 4: Directional surface roughness
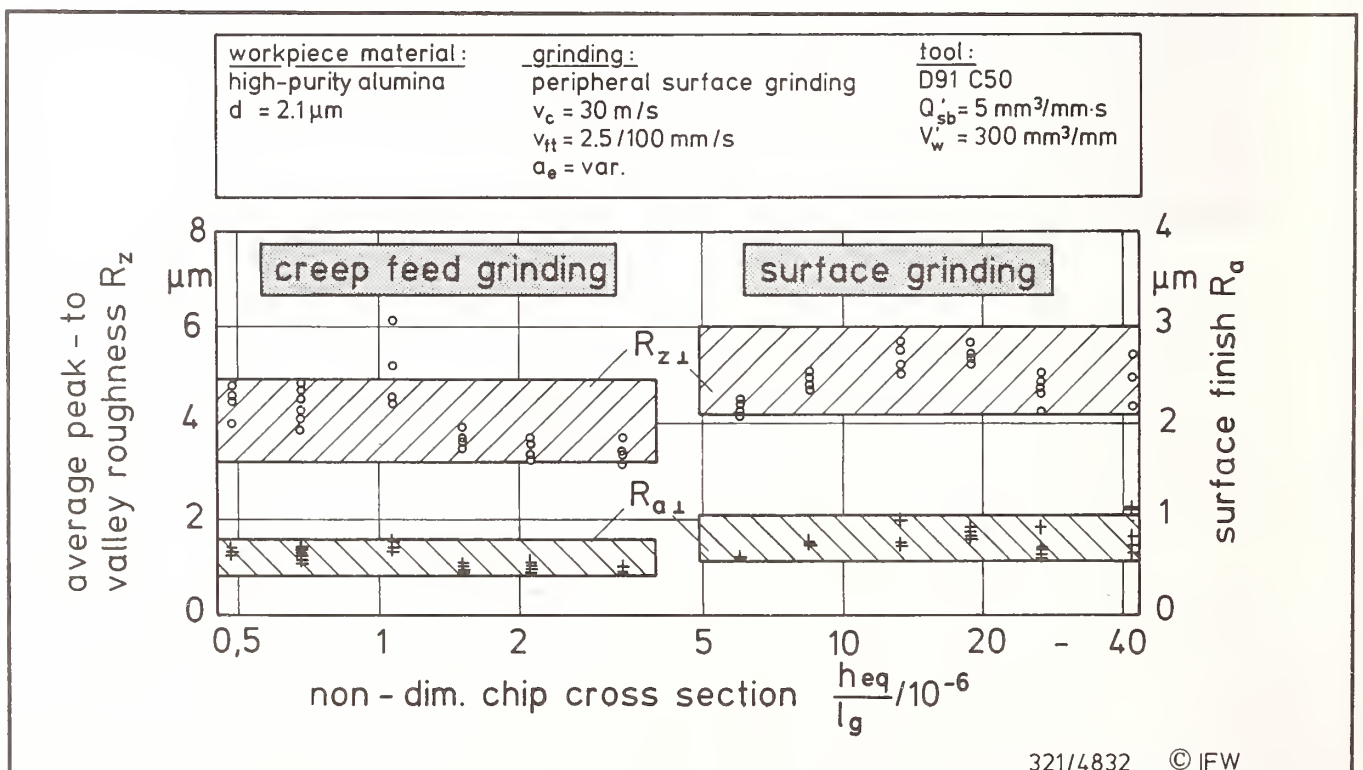
Fig. 5: Roughness as a function of the grinding conditions

252

The grit depth of cut h_{max} has been found useful in metal grinding to predict the roughness of ground surfaces [9, 10]. The parameter of h_{eq}/l_g on the x-axis of Fig. 5 denotes the dimensionless theoretical chip cross section which is closely related to h_{max}. While h_{max} is the truly significant quantity in a kinematic sense, its calculation demands detailed knowledge about the spacial distribution of the cutting edges and about their profiles. To facilitate the comparison of grinding conditions, here the parameter of h_{eq}/l_g is used instead which represents the dimensionless cross section of cut of the individual grit or cutting point.

It is readily derived from the settings of the grinding process by eq. (3) and reqires no experimental input.

$$\frac{h_{eq}}{l_g} = \left(\frac{v_{ft}}{v_c}\right) \cdot \sqrt{\frac{a_e}{d}} \qquad (3)$$

The quantity of h_{eq}/l_g can be used to characterize a set of grinding parameters provided that the spacing of the cutting edges remains constant. For a given grinding wheel and identical dressing conditions, this approximation appears justified. However, different grinding wheels cannot be compared using h_{eq}/l_g.

The specific grinding forces F_n' and F_t' are important quantities to characterize a grinding process. The grinding forces vary strongly between the five alumina grades. The largest forces are found with the smallest grain size materials (Fig. 6).
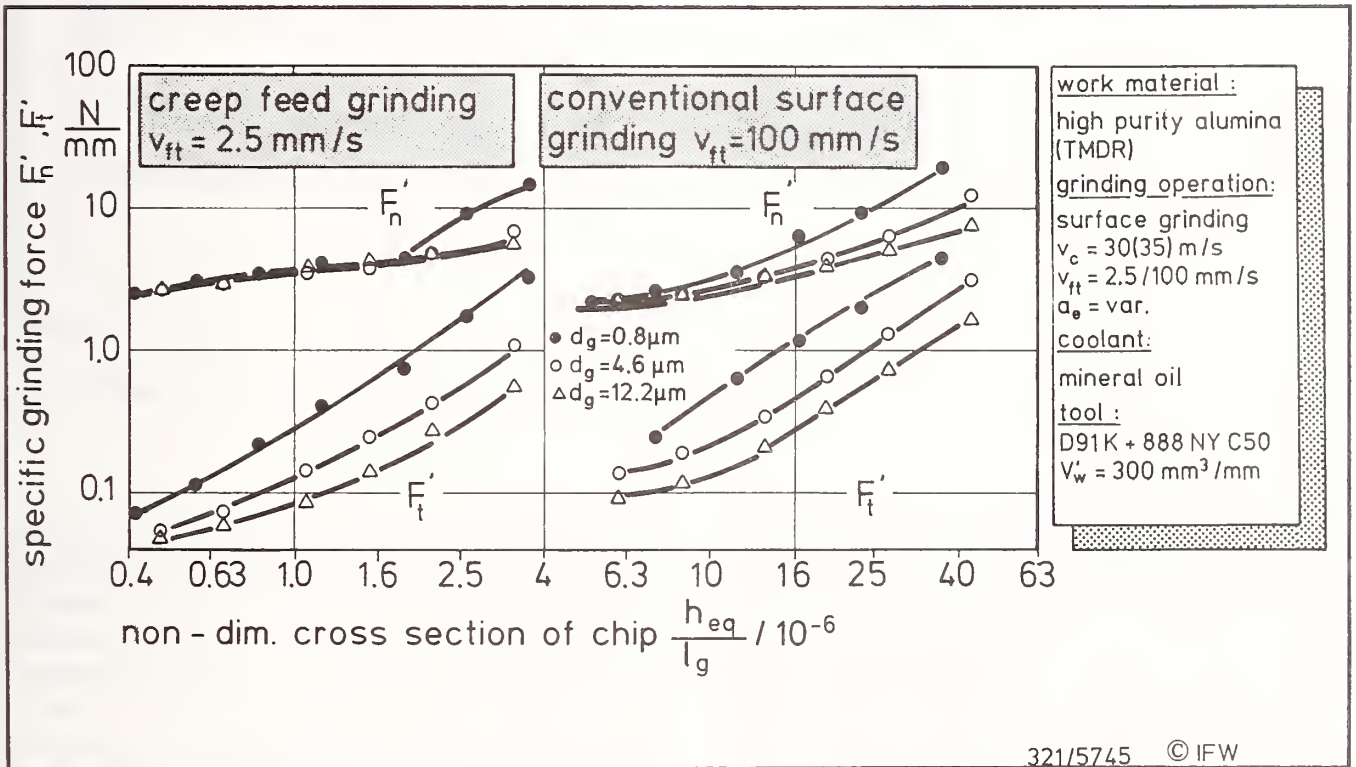
Fig. 6: Normal and tangential grinding forces

In creep feed grinding, the specific normal force F_n' increases only slightly over a wide range. A material influence is hardly detectable. In ordinary surface grinding, the normal forces of the different alumina grades separate systematically with increasing chip cross sections. The larger grain sizes produce lower grinding forces. At the upper end of the range of the tests, the normal forces of the finest and the coarsest alumina grade reach a ratio of three.

Quite similar at low depths of cut, tangential forces F_t' of the various work materials rise at different rates in creep feed grinding. Again, the forces are correlated inversely with grain size. Alumina with a grain size of 0.8 μm requires four to five times the tangential

grinding force of the 12 µm variety. This trend can equally be found in surface grinding over the whole range of cutting depths.

The specific grinding energy e_c derived from the tangential grinding force by eq. (2) depends of the grain size in the same characteristic fashion. In Fig. 7, e_c is plotted versus the dimensionless chip cross section with the grain size included as an additional parameter.
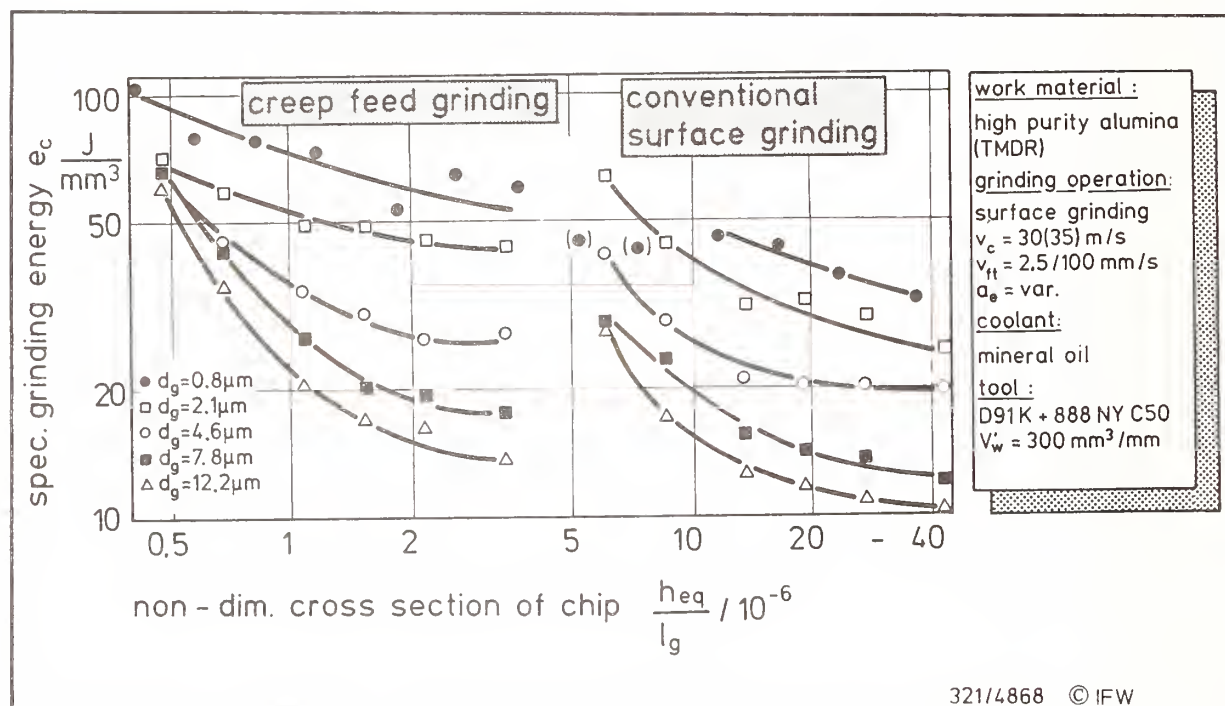
Fig. 7: Specific grinding energy

As in metal cutting, the energy demand for the removal of a unit volume of material decreases with increasing chip thickness. Grain size, however, exerts an even stronger influence on the specific grinding energy than the input parameters of the grinding process. Except for very small material removal rates in creep feed grinding where the curves for the different materials approach an identical value on a high level, specific energy demand varies by as much as a factor of four among the alumina grades with the finest and the coarsest microstructures.

To determine the causes for the strong influence of grain size on grindability, an attempt was made to determine the modes of material removal dominating with each kind of material. For this purpose, grinding tests were performed on tilted ceramic specimens. Figure 8 presents the surface structures obtained in these experiments.

The micrographs demonstrate the results on two different workpiece materials with grain sizes of 0.8 and 4.6 µm respectively for grinding with a constantly increasing grit depth of cut. As the grits contact the polished surface, sharp cutting edges immediately start removing material in the ductile mode (cutting). Duller cutting points first remove the sputtered gold coating in elastic contact (rubbing) and then displace material sideways in plastic deformation (ploughing). With increasing grit depth of cut, cracks begin to form, and material is removed by micro-brittle fracture. The two workpiece materials are clearly distinguished by their different degree of ductility. In the 0.8 µm variety, heavily deformed layers of material are smeared along grooves formed in the surface. Grain breakout and fracture start much earlier in the 4.6 µm alumina grade and thus little deformation can be detected on the the remaining surface.
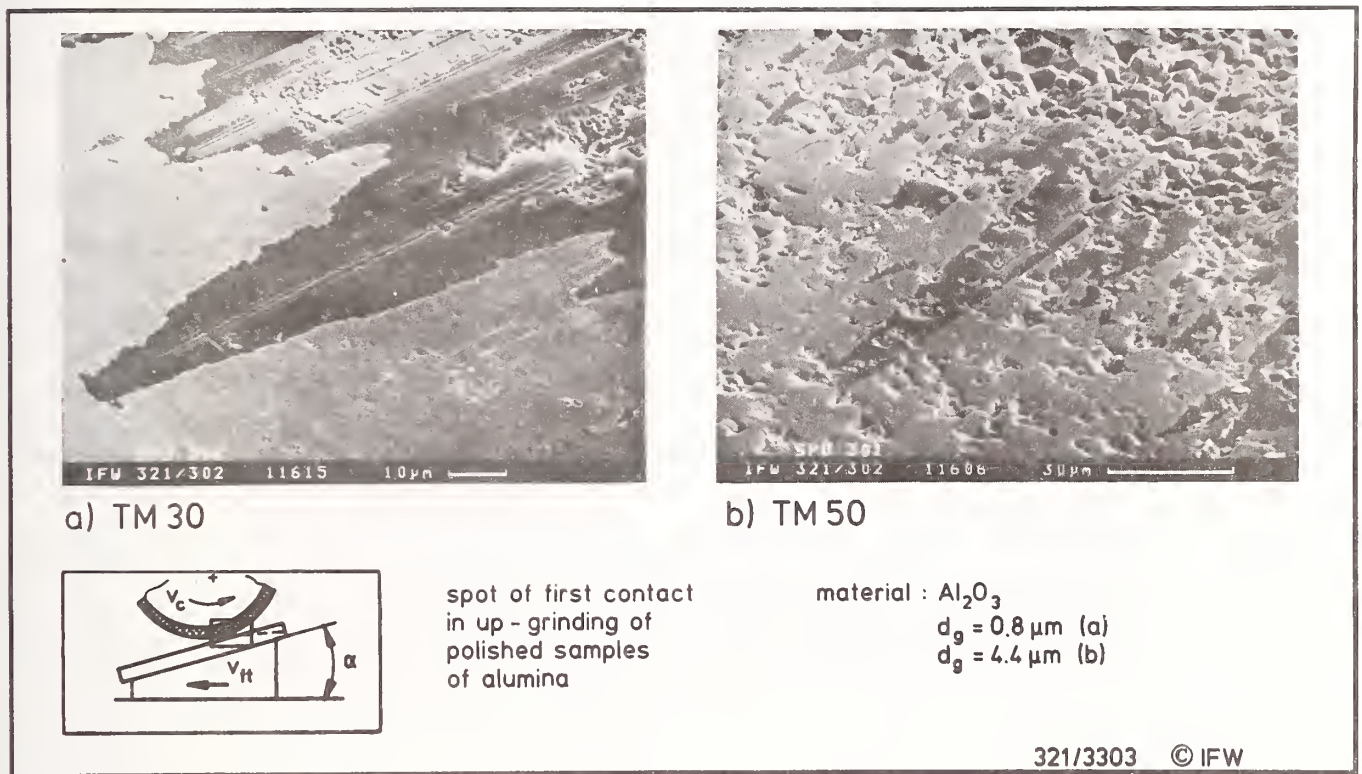
Fig. 8: Traces of rubbing, cutting and ploughing actions of the grit

Figure 9 demonstrates the important influence tool specifications have on the obtainable surface finish. Samples of 0.8 μm alumina were ground with three grinding wheels of grit sizes 65/80 μm (D91), 30/40 μm (D20B) and 5/10 μm (D7) respectively.

With the coarsest grit size wheel part of the sample surface reveals plastic flow but equally a large amount of grain break-out. Flakes of partly-removed material are observed. A D20B wheel at the same settings produces a corrugated surface covered with grinding grooves. A number of smaller cavities from fallen-out grains have not been completely filled up by deformed material. With an extremely fine D7 wheel no fracture is visible at all; the surface is very smooth and completely free of any irregularities.

The measurement of residual grinding stress reflects the amount of sub-surface plastic deformation. Deformation is a function of the load on a single grit as long as no fracture occurs. Due to the difficulty in determining the number of cutting points on a wheel surface, average contact pressures $F_n"$ obtained by dividing the normal grinding force by the contact area are comparable only among results from a single wheel. Figure 10 demonstrates that a correlation exists between the normal grinding force per unit area and residual stress in the workpiece sub-surface.

255
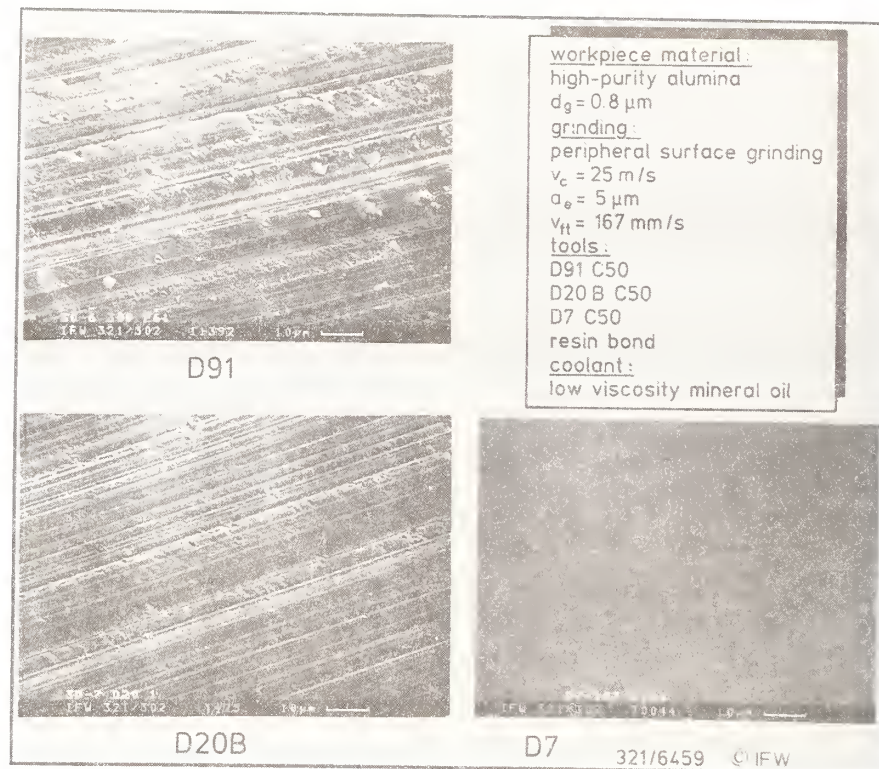
Fig. 9: Tool influence on surface topography
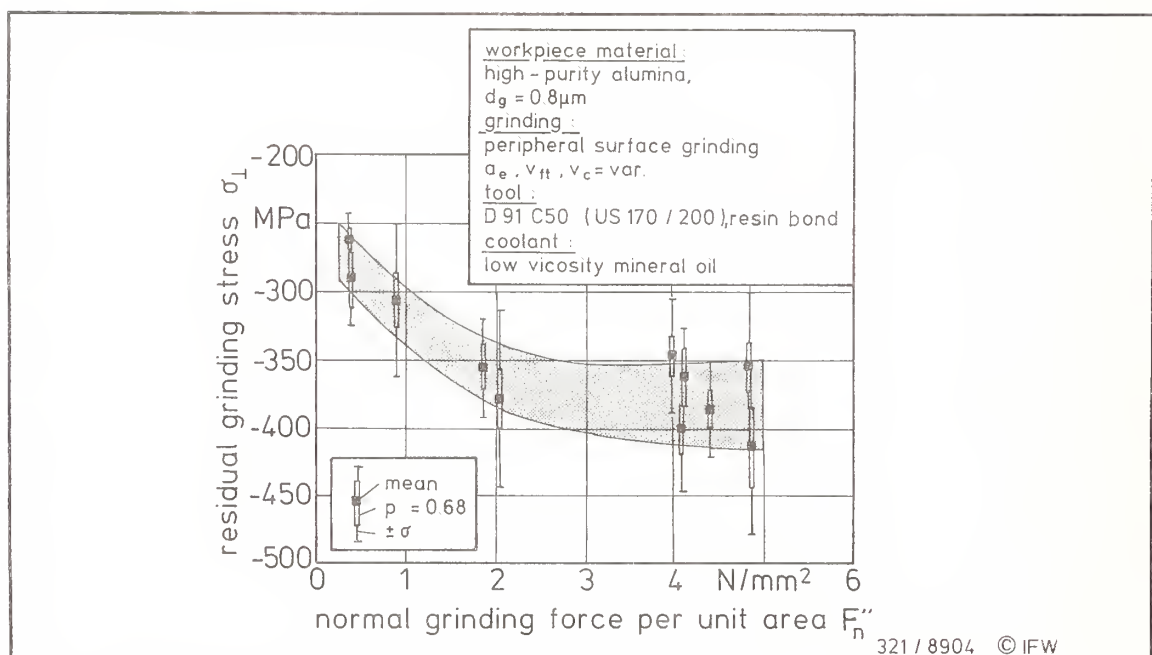
Fig. 10: Residual stress vs. average contact pressure F_n'' in grinding

In Fig. 10 the creep feed grinding tests appear at low F_n'' while surface grinding produces much larger contact pressures. Up to a limit around 2 N/mm², increased grit loads produce increasing values of compressive residual stress. If this limit is exceeded, residual stress remains constant in the range between -350 MPa and -400 MPa. Scatter is somewhat smaller in grinding with small grit loads than at large F_n''.

Discussion

The present study has been conducted on a series of alumina ceramics with varied hardness, toughness, and transverse rupture strength. These aspects of material behaviour originate directly from the grain and pore sizes of the materials. In a brittle material like alumina, the strength of a specimen containing defects is inversely proportional to the square root of the flaw size (GRIFFITH's equation). Most obviously, the grain boundaries themselves act as low-strength imperfections. Their sizes correlate with the respective grain size. Furthermore, the noted segregation of pores in the large grain varieties weaken the material by promoting intergranular crack propagation. Hardness of a ductile material is determined by the resistance toward plastic deformation. As long as no fracture occurs in hardness testing, even brittle ceramics deform plastically in the hydrostatic stress field of the indenter. Deformations are the result of dislocation movement which in a polycrystalline material is obstructed by the grain boundaries. Thus, the hardness will increase with reduced grain size, i.e. higher density of grain boundaries.

Roughness of ground surfaces provides a first indicator of the prevailing mechanism of material removal. Generally, very little influence of machining conditions is found on roughness if machining is carried out in the brittle-fracture domain. Surface finish is only about 20% better in creep feed than in typical surface grinding. Instead, material grain size dominates the roughness of ground surfaces. While the fine-grained aluminas exhibit marked differences in roughness along and across feed direction, the influence of feed direction is almost lost with coarse grain sizes. Grain faces are uncovered by intergranular fracture in micro-brittle material behaviour. As can be gathered from SEM observation, fracture dominates with coarse microstructures while the surfaces of fine-grained aluminas appear covered with a layer of deformed material less than 1 µm thick. In the latter case, the roughness is determined by the traces of the grit. Secondary chip formation with lateral cracking behind the passing grit under the action of residual sub-surface stress is the origin of comparatively large surface defects in surfaces ground with large grit. As grit depths of cut are reduced either via the process input parameters or by the use of finer grit size wheels, the transition from micro-brittle to ductile material removal is passed. Cracking can be avoided completely thus producing surfaces of almost mirror quality. Apart from the grit depth of cut, the density of cutting points plays an important role. To perform a cutting action of the grits and avoid ploughing phenomena as with coarse wheels set at low grit depths of cut, the stress fields of the neighboring grits must overlap. The state of stress created in grinding then forces the workpiece material to be ejected forwards and prevents any groove formation with pile-up of deformed material.

It has been found that both components of the grinding force are linearly dependent of a power function including the equivalent chip thickness h_{eq} and the working engagement a_e at different powers (comp. Fig. 11).

By plotting the specific forces versus this quantity ($h_{eq}^m \cdot a_e^n$), it is possible with a given ceramic to directly predict both force components from the process settings. The exponents determined here are not specific to the grinding of ceramics but turn out identical to those found e.g. in high-efficiency deep-grinding of case hardened steel [11]. At a constant material removal rate, the working engagement a_e determines the contact length and thus the grit depth of cut. Specific forces are higher in creep feed grinding with small grit depths of cut than in conventional surface grinding with much larger grit depths of cut. This principle is a parallel to the decrease of the cutting forces per unit area with increased depth of cut in metal cutting [12].
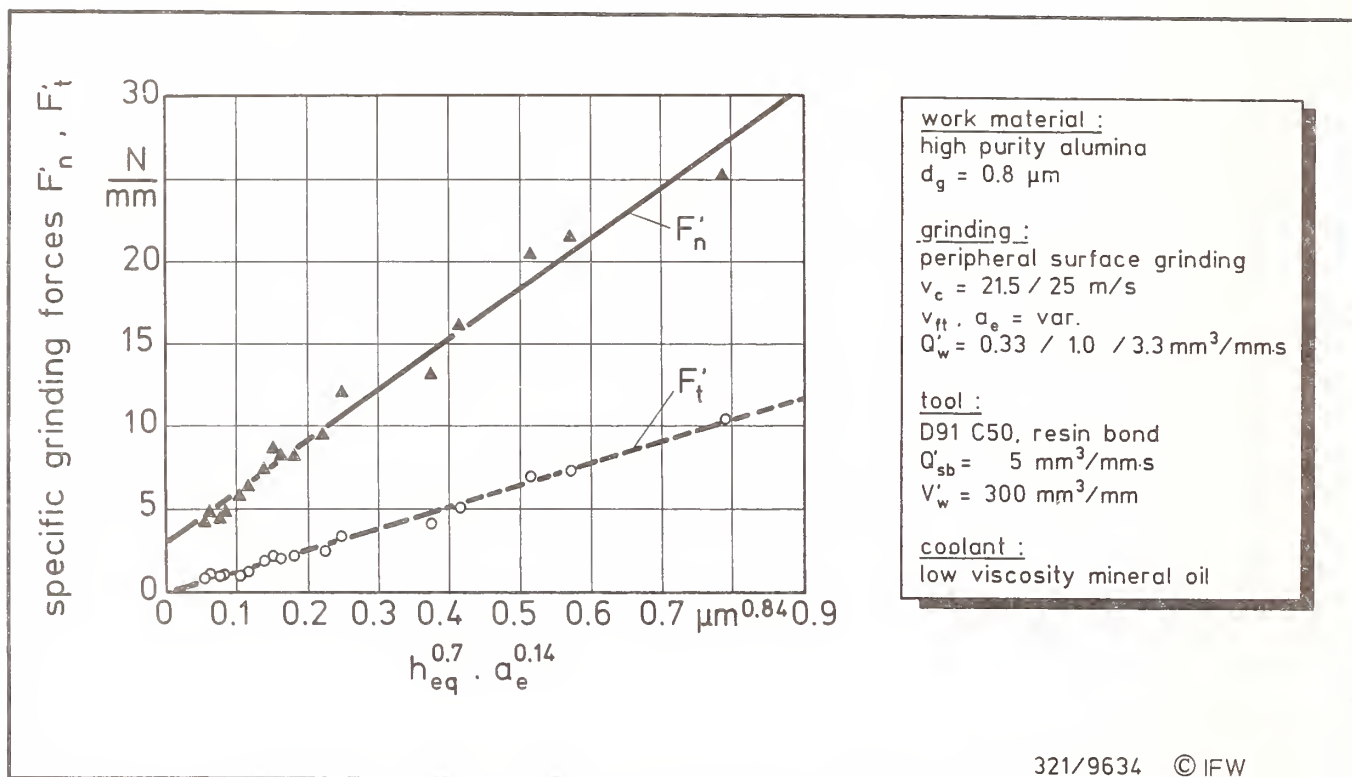
257

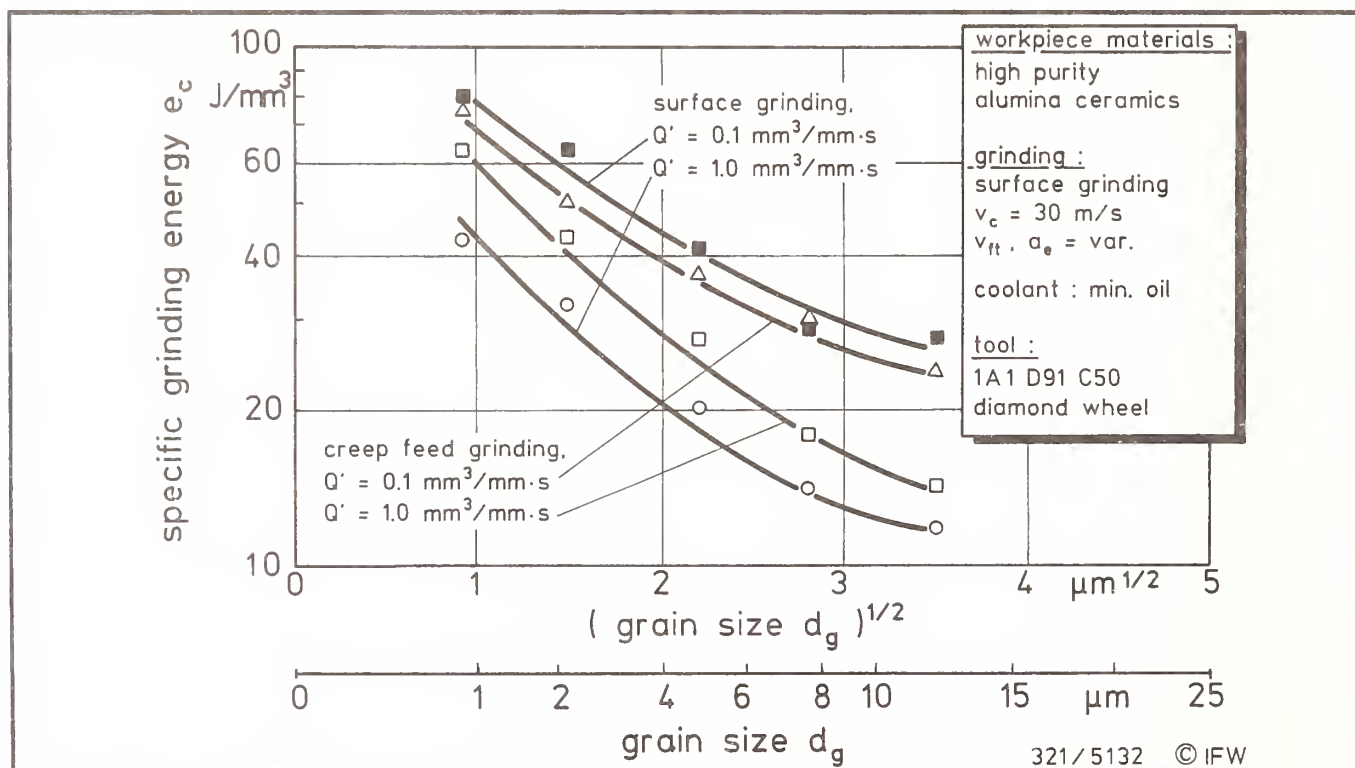Fig. 11: Specific grinding forces as a function of the process settings

Fig. 12: Specific grinding energy e_c vs. workpiece grain size d_g

The specific grinding energy e_c is useful in the assessment of the effectivity of a grinding process [13-15]. It is composed of energy consumed for the formation of new surface in crack propagation, energy necessary for plastic deformation of the work material, and energy dissipated in friction. The specific grinding energy has been shown to vary inversely with the undeformed chip thickness h_{max} or h_{cu} [7, 8, 16]. In grinding of ceramics, e_c indicates the relative importances of brittle and energy-consuming ductile material behaviour. Compared to metals, plasticity is much less important with ceramics. Thus, the grinding energy is composed mainly of the frictional and surface energy terms. The considerable deformation of fine-grained alumina ceramics does not contribute significantly to the measured grinding energy. The results represented in Figure 12 demonstrate the close connection of the grinding energy with workpiece grain size. The two sets of graphs refer to different grinding conditions typical for surface and creep feed grinding. All cases exhibit the same trend, namely an inverse correlation between energy demand and grain size. Between the finest-grained and the coarsest alumina varieties, ratios of up to four in e_c are found. In particular, the specific grinding energy is close to inversely proportional to the square root of the grain size d_g in brittle-domain grinding.

This indicates a significant amount of micro-brittle behaviour in material removal. Fracture mechanics can be used to explain the dependence of grinding force on grain size. The grain boundaries act as defects in ceramic microstructure, especially if, as in the case of coarse grain, rows of pores collect along the grain boundaries. The linear dimension of the individual grain boundaries is a fraction of the grain size. With the boundaries acting as crack origins, the strength of the material in resisting the tangential grinding force is thus directly controlled by grain size. The ratios of measured specific grinding energy among the different workpiece materials agree reasonably well with their grain (flaw) sizes and fracture toughnesses (see Table 3). K_{Ic}^*, d_g^*, and e_c^* refer to the values for the 0.8 μm grain size alumina.

With small grit depths of cut, fracture is avoided and plastic deformation together with friction determines the energy demand for material removal. Again, grain size influences the grinding forces via the grain boundaries' resistance to dislocation movement.

Table 3: Grinding energy demand related to the material properties

Workpiece material (grain size)	$(K_{Ic}/K_{Ic}^*)\cdot\sqrt{d_g^*/d_g}$	$\dfrac{e_c}{e_c^*}$ at $\dfrac{h_{eq}}{l_g}=3\cdot10^{-6}$
0.8 μm	1.00	1.00
2.2 μm	0.63	0.78
4.6 μm	0.48	0.45
7.8 μm	0.37	0.33
12.2 μm	0.29	0.25

Residual stress correlates well with the normal grit load up to a limit where brittle fracture begins to dominate over plastic removal. Residual stress is partly relieved by cracks. Another cause for stagnation at -380 MPa combined with increased scatter is the loss of deformed material from part of the surface which thus no longer contributes to the value of residual stress averaged over the x-ray spot. Further research will have to be directed at measuring the stress levels in surfaces ground in the completely ductile regime at extremely small grit depth of cut.

Conclusions

From grinding tests done on several alumina grades of different grain and pore sizes it is concluded that grain size plays a significant role in material removal. Over a wide range of machining conditions, grinding forces and energies vary inversely with the average grain size of the ceramic. Surface structures give evidence of shear deformation and plastic flow. These are found most markedly with fine-grained material and at low grit depths of cut. While the major part of material removal is probably accomplished by brittle fracture, plastic deformation is held responsible for the final appearance of the ground surfaces. The extent of plastic deformation is determined by material grain size and grain retention in the matrix as machining starts with extremely low grit depths of cut at the beginning of the arc of contact in up-grinding. The brittle/ductile transition takes place at very low grit depths of cut. To produce ground surfaces completely free of chipping, both small grit depths of cut and a high density of cutting points are required.

Residual grinding stress in alumina is found to be compressive in all cases. It is an indicator of the average mechanical loading of each individual grit in the grinding process. With a given wheel, the magnitude of compressive residual stress correlates with the grit depth of cut and with the normal grinding force per unit area. A reduction of load per grit via the use of a finer grit size grinding wheel with a larger number of cutting points will produce reduced compressive stress in the sub-surface zone.

References

[1] H.K. Tönshoff, G. Warnecke, H.-Z. Choi, "Der Beitrag der Forschung zum Sägen von Stein", Internationale Diamanten Rundschau, Vol.11, No.1, pp.5-11, 1977

[2] H.P. Kirchner, J.C. Conway, "Mechanisms of Material Removal and Damage Penetration during Single Point Grinding of Ceramics", Machining of Ceram. Mat.ls and Components, Vol. 17, ASME, New York, pp. 53-61, 1985

[3] H.K. Tönshoff, E. Brinksmeier, "Abrasives and their Influence on Force, Temperature and Surface", Proc. 2nd Internatl. Grinding Conference, Philadelphia, June 10-12, 1988

[4] E. Saljé, H. Möhlen, "Prozeßoptimierung beim Schleifen keramischer Werkstoffe", Internationale Diamanten Rundschau, Vol. 21, No. 4, pp. 243-247, 1987

[5] E. Saljé, H. Möhlen, "Material Removal in Grinding of Advanced Ceramics", SME Techn. Paper MR88-498, pp. 1-19, 1988

[6] P. Blake, T. Bifano, T. Dow, R.O. Scattergood, Precision Machining of Ceramic Materials, Ceramic Bulletin, Vol. 67, No. 6, pp. 1038-1044, 1988

[7] G.S. Reichenbach, J.E. Mayer, S. Kalpakcioglu, M.C. Shaw, "The Role of Chip Thickness in Grinding", Transactions of the ASME, Vol. 78, No. 5, pp. 847-859, 1956

[8] H.K. Tönshoff, R. Telle, P. Roth, "Chip Formation and Material Removal in Grinding of Ceramics", Proc. 4th Internatl. Grinding Conference, Dearborn, October 9-11, 1990, pp. 539-1/539-18

[9] G. Werner, "Kinematik und Mechanik des Schleifvorgangs", Dr.-Ing. Diss., TH Aachen, Germany, 1971

[10] G. Kassen, "Beschreibung der elementaren Kinematik des Schleifvorgangs", Dr.-Ing. Diss., TH Aachen, Germany, 1969

[11] T. Tawakoli, "Hochleistungs-Flachschleifen", Dr.-Ing. Diss., VDI-Verlag, Duesseldorf, Germany, 1990

[12] O. Kienzle, H. Victor, "Spezifische Schnittkräfte bei der Metallbearbeitung", Werkstofftechnik und Maschinenbau, Vol. 47, No. 5, pp. 224/225, 1957

[13]   H.W. Zheng,   G.Q. Cai,   S.X. Yuan,   "An
       Experimental Study on the Mechanism of
       Cermet Grinding", Annals of the CIRP,
       Vol. 38, No. 1, pp. 335-338, 1989

[14]   T.W. Liao,   G.   Sathyanarayanan,   "An In-
       vestigation into Creep Feed Grinding of
       Alumina Ceramic", Transactions North Am.
       Manuf. Res. Inst. of SME (NAMRC XVII),
       Vol. 17, No. 1, pp. 175-184, 1989

[15]   J. Akbari,   Y. Ichida,   K. Kishi,   T. Machida;
       "Grinding Energy of Fine Ceramics", Proc.
       First Internatl. Conference on New Manu-
       facturing Technol., Chiba, 1990, pp. 323-328

[16]   I. Inasaki,   "High   Efficiency   Grinding   of
       Advanced Ceramics", Annals of the CIRP,
       Vol. 35, No.1 , pp. 211-214, 1986

EFFECT OF GRINDING ON STRENGTH AND SURFACE INTEGRITY OF SILICON NITRIDE: PART I

S. JAHANMIR, T. J. STRAKNA*, G. D. QUINN, and H. LIANG**
National Institute of Standards and Technology, Gaithersburg, MD

R. L. ALLOR
Ford Motor Co., Dearborn, MI

R. D. WEST
Therm Advanced Ceramics, Ithaca, NY

Grinding is often the method of choice for machining structural ceramics and has a high potential for large-scale production and automation. Because there are few guidelines available for grinding ceramics, a conservative approach is usually used to minimize the potential grinding-induced damage. With this approach, machining time is high, which increases the cost of machining. The purpose of this paper is to report data and information on the effect of grinding on strength of two types of silicon nitride. The work is part of a study to develop a database that can be used to assist in the optimization of the grinding process to achieve low cost, high reliability, and eventual automation. Standard flexure specimens, made from a reaction-bonded and a sintered reaction-bonded silicon nitride (RBSN and SRBSN), were surface ground in the longitudinal direction under three different conditions. The resulting ground surfaces were characterized with a three-dimensional profiling instrument and a scanning electron microscope. Four-point flexure tests were performed on the specimens and Weibull parameters were calculated to determine the effect of the different grinding conditions on flexure strength. Fractography was performed on the specimens after testing to determine the location and to characterize the fracture origin in each specimen. The results showed that varying the material removal rate by a factor of 20, from 30 to 590 mm³/min, had no significant effect on the characteristic strength or the Weibull modulus of four-point flexure specimens. This implies that material removal rates higher than those currently used for grinding these two types of silicon nitride materials may be possible without strength degradation.

Introduction

Structural ceramics, such as silicon nitride, are attractive for many applications due to their high strength at elevated temperatures, resistance to chemical degradation, wear resistance, and low density. Industry analysts forecast that the market for structural ceramics will grow from $350 million in 1990 to $865 million by 1995 [1,2]. Major market segments for these materials are cutting tools, wear resistant parts, heat engines, and aerospace and defence related applications [1-3]. The high cost of ceramic components versus metallic components, however, has been cited as one of the main problems preventing the automobile manufacturers from employing ceramics in automotive applications [1]. Some studies estimate that of the total production cost machining can account for 30 - 60% and sometimes even up to 90% for high-precision components [4,5]. Therefore, recent reports recommend a coordinated research effort in machining of advanced ceramics [4,6] to reduce machining costs.

Grinding is often the method of choice for machining structural ceramics [4,5] and has a high potential for large-scale production and automation. Because there are few guidelines available for grinding ceramics, a conservative approach is usually used to minimize the potential damage induced by grinding. This involves very low depths of cut and many passes to obtain the desired tolerances, thus increasing the cost of machining. The purpose of this paper is to report data and information on the effect of grinding on the strength of two types of silicon

---

* Graduate Research Assistant, University of Maryland, College Park, MD 20742

** Research Associate, University of Maryland, College Park, MD 20742

nitride. The work is part of a study to develop a database that can be used to assist in the optimization of the grinding process to achieve low cost, high reliability, and eventual automation.

Although many recent papers [6-13] and conference proceedings [14,15] have addressed the issue of machinability for advanced ceramics and provided data, much more data and information are needed on the machinability of specific materials. In Particular, it is important to achieve the maximum possible material removal rate, while minimizing the effect of machining on performance and properties. Previous studies have shown that grinding-induced damage can be detrimental to the strength and performance of ceramic parts [16-22]. Since the process of grinding involves removal of material by deformation and fracture, the machined components often contain residual stress, a deformed layer, surface and subsurface microcracks, phase transformation regions, and other types of damage [23-25]. The extent and the specific nature of the machining-induced damage depend on the type of machining process and the machining parameters. Also, it should be recognized that formation and the influence of machining-induced damage depend on the material type and microstructure, for example, the grain size [23,24].

Flexure testing [26] has proven to be a reasonable, low-cost method for evaluating the effect of machining on strength of ceramic materials [16,17,19,22,23,27-30]. Allor and Baker [27] studied the effect of several grinding parameters on the flexure strength of a hot-pressed silicon nitride. Grinding in the same direction as the maximum tensile stress was found to increase flexure strength, and down feeds up to 0.254 mm/pass had no significant effect on flexure strength. Grinding wheels of grit size between 220 and 600 increased flexure strength, while varying the diamond concentration of the wheel between 75 and 100 on 320 grit wheels had no significant effect on flexure strength. Thomas and West [28,29] studied the effect of grinding parameters on grinding forces, surface finish, and strength of a hot-pressed silicon nitride. The flexure strength of the specimens was found to decrease as the down feed was increased from 0.0254 mm to 0.1778 mm. Higher strengths were obtained, as well as better surface finish, for a 320 grit wheel than for a 150 grit wheel. Miyasato, et al. [30] explored the effect of down feed, different wheel types, and grinding direction on strength, surface finish, and residual stress of a hot-pressed silicon nitride. No significant strength differences were found between different wheel types and down feeds, while grinding normal

to the maximum tensile stress direction decreased strength by 40% compared to grinding parallel to the tensile stress direction.

In the present study, four-point flexure testing was used to assess the effect of grinding on the strength of two commercially available silicon nitride materials, one reaction-bonded and the other sintered reaction-bonded. Weibull statistical analysis [31] was performed on the data. Three grinding conditions were used to achieve a wide range of material removal rates. The surface integrity resulting from the grinding conditions was investigated with a three-dimensional profilometer and SEM. Fractography was performed to identify the location and source of fracture in each specimen.

Experimental Procedure

a) Materials

Two types of silicon nitride materials were used in this study: reaction bonded (RBSN), produced by Eaton Corporation, and sintered-reaction bonded (SRBSN), produced by Ceradyne, Inc. The RBSN was prepared from a mixture of silicon powder with iron oxide, as a nitriding agent, and water [32]. The SRBSN was also processed with silicon powder, but it contained yttria and alumina sintering aides.

The bulk density, crystal structure, and grain size of both materials were determined. Bulk density was measured via fluid displacement. The density of the RBSN was 2.36 g/cm^3 and the density of the SRBSN was 3.22 g/cm^3. The crystal structure of the materials was determined by x-ray diffraction. Both alpha and beta phases were present in the RBSN material with an alpha to beta ratio of 7.7 : 1, whereas the SRBSN primarily contained the beta phase. Grain sizes were measured by direct viewing of polished and etched surfaces of the materials. For the RBSN, the alpha phase was 1 - 2 μm in length and 0.5 - 1 μm in width, while the beta phase was 1 - 3 μm in length and less than 1 μm in width. For the SRBSN, the beta phase was 6 - 8 μm in length and 1 - 3 μm in width. The manufacturers gave the porosity of the materials at approximately 20% for the RBSN and less than 1% for the SRBSN. Both materials contained small inclusions ranging in diameter from 0.1 to 2 μm.

The micrographs in Figure 1 show the microstructure of the RBSN and SRBSN materials as observed in an optical microscope. A distinguishing feature of the RBSN material is the characteristic mottled appearance on a size scale of approximately 50 μm.

The materials were received in billets. The RBSN billets were approximately 86 x 10 x 3.2 mm and were received in three batches. One or two flexure specimens were made from each RBSN billet. The SRBSN billets were 76 x 76 x 13 mm. These billets were sliced into 4 equal size pieces with approximate dimensions of 50 x 25 x 13 mm and the location in the billet of each sliced piece was tracked. A total of 8 to 12 flexure specimens were made from each SRBSN sliced portion. The billet number, location, and batch number from the billets were tracked for each specimen to check the possibility of billet to billet variation and the influence of specimen location within each billet on strength.
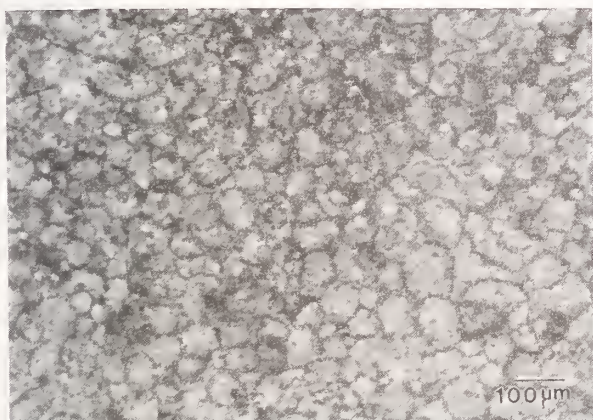
b) Grinding Conditions

A total of 25 to 30 flexure specimens from each material were machined under each set of grinding conditions that will be described shortly. These specimens had dimensions of 3 x 4 x 50 mm, as specified by the ASTM "Standard Test Method for Flexural Strength of Advanced Ceramics at Ambient

RBSN

SRBSN

Figure 1. Optical micrographs of polished surfaces of RBSN and SRBSN.

Temperature" [33]. In order to reduce the possibility of fracture initiation from the edges, all the bars were chamfered as required by the ASTM standard. A sufficient amount of material was removed from the test bars by grinding to reduce effects of surface layers that are often formed during processing and damage caused by slicing. Three sets of grinding parameters, shown in Table 1, were used to finish grind the specimens. In all cases, grinding was performed on a horizontal-spindle surface grinder with resin bonded diamond wheels in the longitudinal direction (parallel to the specimen tensile axis). No spark-out or further surface treatment was performed.

Grinding condition A used a 320 grit wheel, 0.0025 mm/pass down feed, 1.58 mm/pass cross feed, and 7.62 m/min table speed. This resulted in a material removal rate of 30 mm^3/min. During rough grinding, the same parameters were used with the exception of the down feed, which was decreased in the following steps: 0.0127 mm to net dimension +0.2032 mm, 0.0254 mm to net dimension +0.1270 mm, 0.0127 mm to net dimension +0.0508 mm. A total of 0.0508 mm was removed in finish grinding.

Grinding condition B also used a 320 grit wheel. Under this grinding condition, the down feed and the table speed were larger than that of condition A, but the cross feed was smaller. This condition is slightly more aggressive than A, resulting in a material removal rate of 59 mm^3/min. Larger grit wheels

Table 1. Grinding parameters

	A	B	C
Grinding Wheel Grit / Concentration	320 / 100	320 / 75	120 / 63
Grinding Fluid	Synthetic 20:1	Emulsion 50:1	Emulsion 50:1
Wheel Surface Speed (m/s)	28	28	28
Table Speed (m/min)	7.62	12.2	6.10
Cross Feed (mm/pass)	1.58	0.381	0.381
Down Feed (mm)	0.0025	0.0127	0.2540
Volumetric Removal Rate (mm^3/min)	30	59	590

265

(120 grit for RBSN and 150 grit for SRBSN) were used during rough grinding, with a table speed of 6.10 m/min and a down feed of 0.381 mm. A total of 0.254 mm was removed during finish grinding. Conditions A and B represent bench-mark conditions usually used for ceramic materials and recommended as a conservative procedure in the ASTM standard.

Grinding condition C used a 120 grit wheel, 0.2540 mm/pass down feed, 0.381 mm/pass cross feed, and 6.10 m/min table speed. The same set of parameters was used for rough grinding. Condition C is far more aggressive than either A or B, and resulted in a material removal rate of 590 mm³/min.

Other parameters such as diamond concentration and grinding fluid are also listed in Table 1. In addition, each grinding condition was performed on a different machine tool by a different operator. Although these factors may influence the results, this study was mainly concerned with the volumetric removal rate.

c) Surface Integrity Evaluation

The surface topography of the ground samples was evaluated with a three-dimensional stylus profiling system, an optical microscope and a scanning electron microscope (SEM). The profiling system consisted of a stylus profilometer, a moving stage powered by a steppermotor, a personal computer and data acquisition and processing software, and electronics to run the system [34]. Three-dimensional topographical maps were produced on selected test bars of each material and each grinding condition by compiling multiple profile traces taken at fixed intervals on the specimen surfaces. The test bars were mounted in the system such that each trace ran perpendicular to the grinding direction. A total of 200 traces, 3 mm in length and set 10 μm apart, were taken. This corresponds to an area 3 x 2 mm.

A subset of the traced area, approximately 1 x 1 mm, was used to calculate the topographical parameters: root mean square roughness (R_q), average peak to valley roughness (R), and centerline average roughness (R_a). Final leveling of the surface was performed in the software, as well as filtering to remove lower frequency form deviations and system error. The repeatability of the roughness measurements was determined by performing 4 three-dimensional profiles, as described above, on one specimen from each material. The standard deviation about the mean R_q value was 0.02 μm for RBSN and 0.01 μm for SRBSN, representing 7% and 6% of the mean, respectively.

d) Flexure Strength Tests

The flexure strength of the ground test bars was measured in accordance with the ASTM Standard C 1161 for four-point flexure testing [33]. A universal tension/compression testing machine was used at a cross-head speed of 0.5 mm/min to apply a steadily increasing load to each specimen. A load cell was used to measure the load, and an integrated strip-chart recorder was used to record the applied load. A fully articulating steel fixture [35] was used to mount the specimens for testing in four-point flexure position. This fixture has the advantage of articulating during loading to correct for any misalignments due to dimensional errors in the specimens. This ensures a good line-contact between each load-pin and the specimen. The system was calibrated each day before beginning the flexure tests, and checked periodically during the testing sequence.

To perform a test, the width and thickness of each test bar was first measured with a micrometer within 0.0025 mm. It was then placed in the fixture. After mounting, a preload of 5 - 10% of the expected failure load was applied. The specimen and fixture were then inspected and adjusted, if needed, to ensure line-contact between the load-pins and the surface of the specimen. When the mounting was determined to be satisfactory, the contacts of the load-pins were marked on the specimen and the application of load was continued until failure occurred. The fractured specimen was then stored for future examination, and the load at fracture was recorded from the strip-chart.

Following the flexure tests, the strength data were analyzed to determine possible effects of grinding on strength and the variation of strength. In order to identify the location and source of fracture in each test bar, the fracture surfaces were analyzed by stereo optical microscopy. Selected specimens were examined with an SEM. All fractography was performed in accordance with procedures specified in Reference [36].

Experimental Results

a) Surface Integrity

Topographical maps of selected samples ground under the three different conditions are shown in Figures 2 and 3 for RBSN and SRBSN. Differences between the grinding conditions can be seen in these maps as a variation in severity of the grinding striations. It is evident that grinding condition A imparted more severe or deeper striations in both materials. This is more clearly evident in Figure 4,
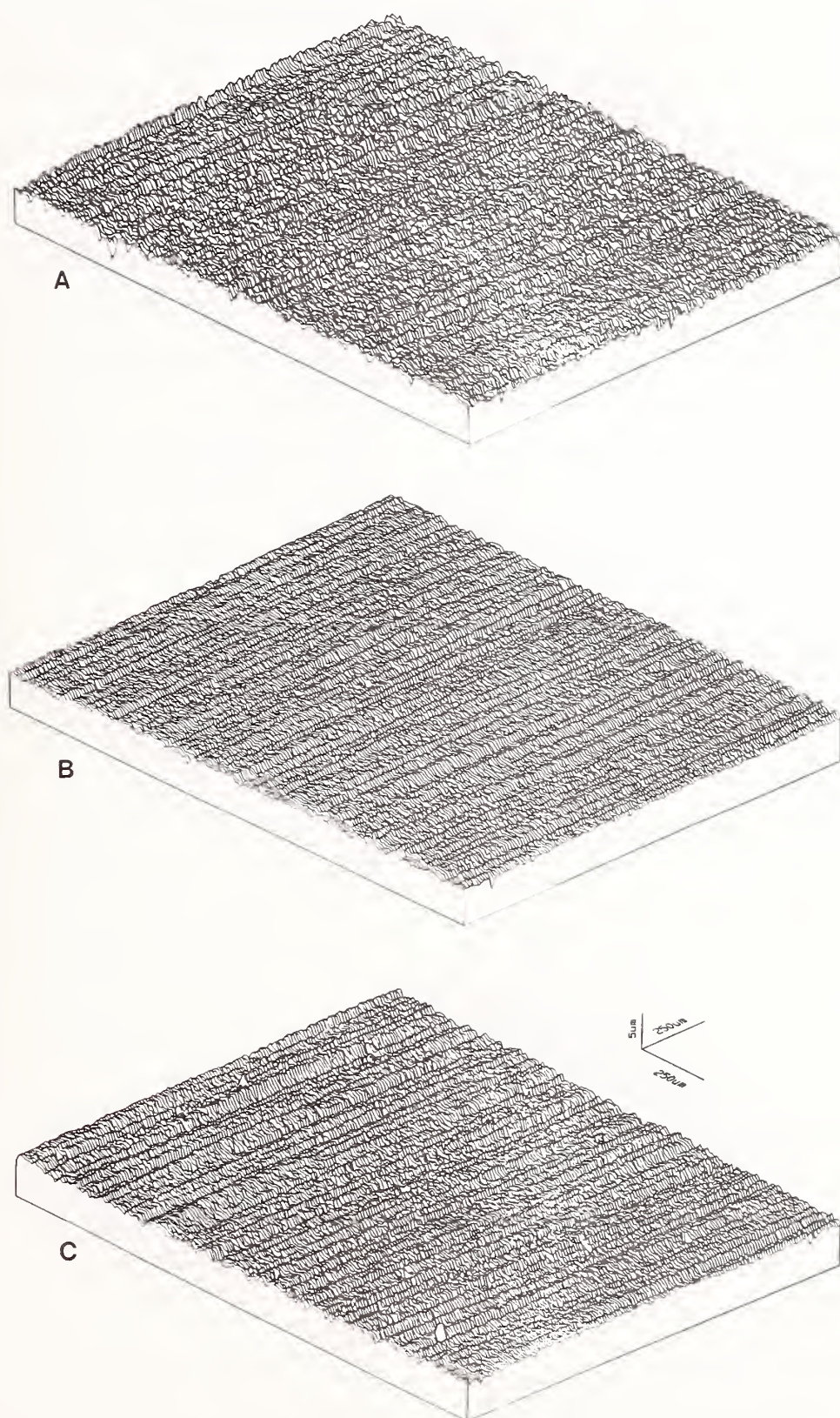
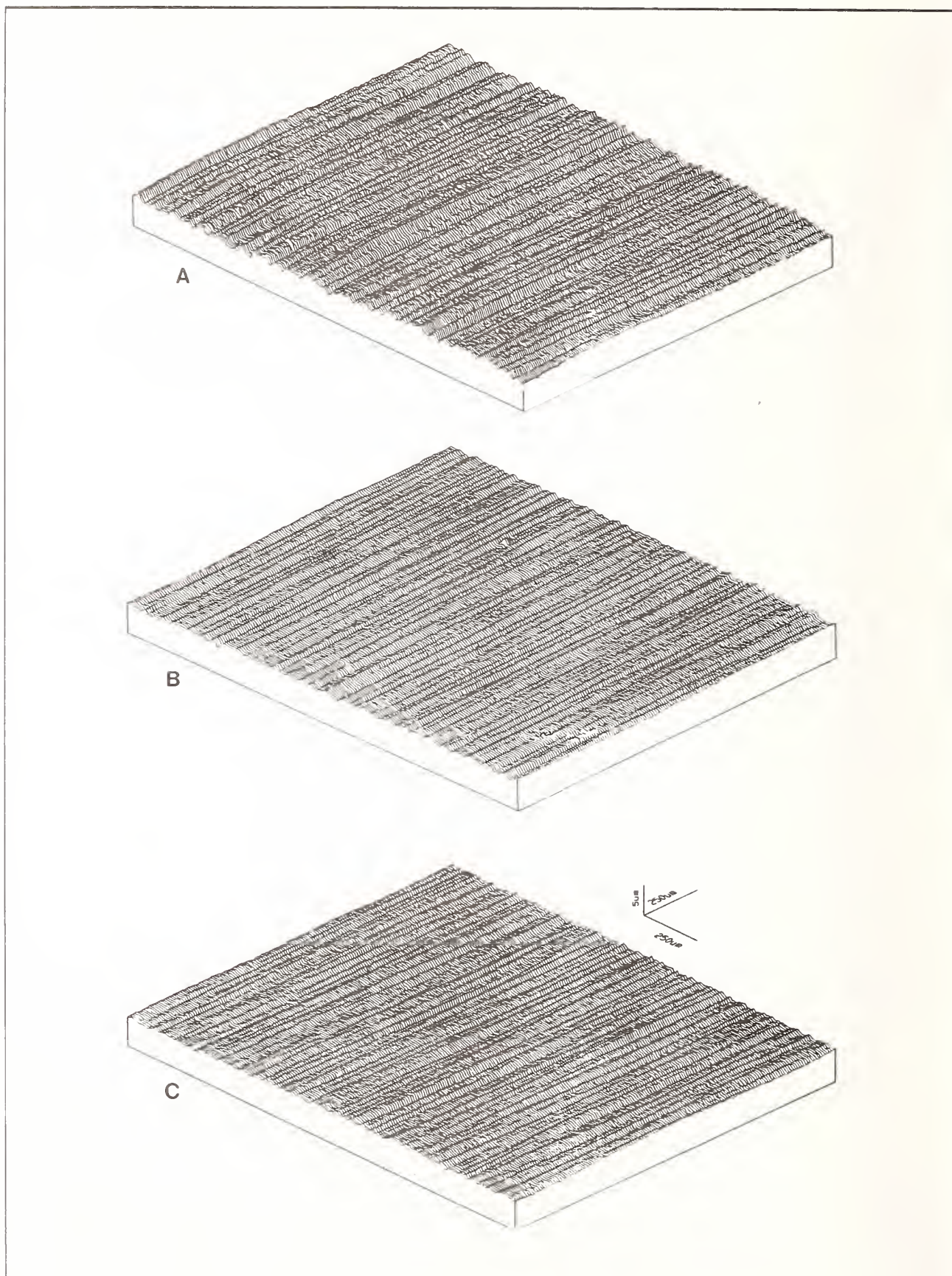Figure 2.   Topography of ground surfaces of RBSN for grinding conditions A, B, and C.

267

Figure 3.   Topography of ground surfaces of SRBSN for grinding conditions A, B, and C.

268

which shows the effect of grinding condition on the R_q roughness of both materials. This figure also shows that the roughness of RBSN is greater than SRBSN for each grinding condition. Grinding condition A produced the largest R_q roughness for both RBSN (0.41 μm) and SRBSN (0.32 μm), followed by C and then B for RBSN (0.38 μm and 0.27 μm), while the R_q roughness of SRBSN surfaces ground under conditions B and C were nearly equal (0.20 μm). The effect of grinding conditions on the other roughness parameters R and R_a were similar to that described for R_q.

As seen in Figures 2 and 3, the two materials display distinct surface characteristics regardless of the grinding conditions used. The RBSN ground surfaces show somewhat random peaks and valleys and relatively obscured grinding striations, though directionality is evident. The ground surfaces of SRBSN, however, display sharp and distinct grinding striations with obvious directionality. These observations exemplify the differences in the mechanical properties and/or microstructure of the two silicon nitrides and may indicate different material removal mechanisms for each in the grinding process.

The SEM micrographs in Figures 5 and 6 are consistent with the topographical maps of the ground surfaces. The SEM micrographs suggest two possible modes, brittle and ductile, for material removal in grinding silicon nitride. The striations in RBSN are not as continuous as those observed for SRBSN. Also, larger pits or pores are seen on the surface of RBSN (Fig. 5) than those on the SRBSN (Fig. 6). The surface structure of these two materials is shown in Figures 7 and 8 at a higher magnification. These figures clearly show that while plastic flow and plowing were the primary material removal mechanisms in SRBSN, these features are less evident in RBSN. This suggests that a brittle fracture process may be the dominant mechanism for grinding RBSN because of its lower strength and higher porosity compared to SRBSN. The difference between the material removal processes of the two materials is a critical issue in determining the extent and nature of possible machining-induced damage.

b) Flexure Strength

Due to the dependance of strength on the flaw population within the specimens, the strength data obtained from the flexure tests is well-fitted by the two-parameter Weibull statistical distribution. The Weibull distribution allows for the fact that failure in a specimen occurs at the largest flaw among a population of flaws existing in the specimen. From this analysis two parameters are obtained: the charac-
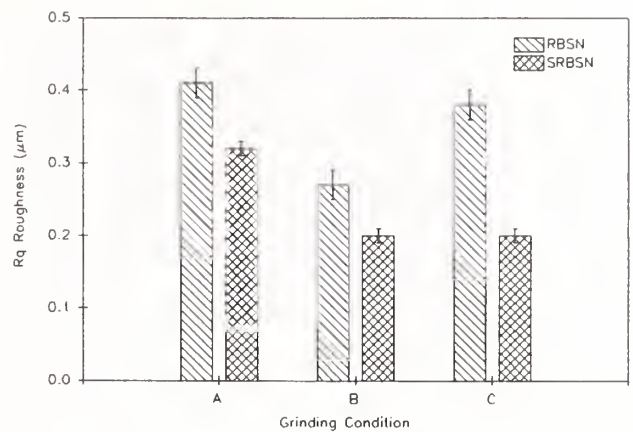
Figure 4. Rq roughness of RBSN and SRBSN for each grinding condition.

teristic strength (scale parameter) and the Weibull modulus (shape parameter). The characteristic strength is the stress at which 63.2% of the specimens failed. The Weibull modulus is an indication of the scatter in the strength data, where the scatter decreases as the Weibull modulus increases. By plotting the probability of failure on Weibull probability axes and the flexure strength on natural log axes (termed Weibull plots) the data can be fitted by a straight line. The least squares fit method was used to fit a line to the data whose slope is the estimate for the Weibull modulus. The stress corresponding to the point on the line where 63.2% of the specimens will fail is the estimate for the characteristic strength.

The 95% confidence intervals for the Weibull modulus and characteristic strength were calculated using the method developed by Ritter, et al. [37]. This analysis is based on the law of propagation of errors and assumes that the scatter in the characteristic strength and Weibull modulus is normally distributed and the coefficient of variation is less than or equal to 10%. This analysis method has been successfully applied to flexure data of ceramics [38].

The Weibull plots for each material and grinding condition are shown in Figures 9 and 10. The data is fitted by a straight line satisfactorily in each case, and thus is well represented by the two-parameter Weibull distribution. The characteristic strength and the Weibull modulus are displayed for each material and grinding condition in Figures 11 and 12 along with the associated 95% confidence intervals. The

269

Figure 5. SEM micrographs of the ground surfaces of RBSN for grinding conditons A, B, and C.

Figure 6. SEM micrographs of the ground surfaces of SRBSN for grinding conditons A, B, and C.
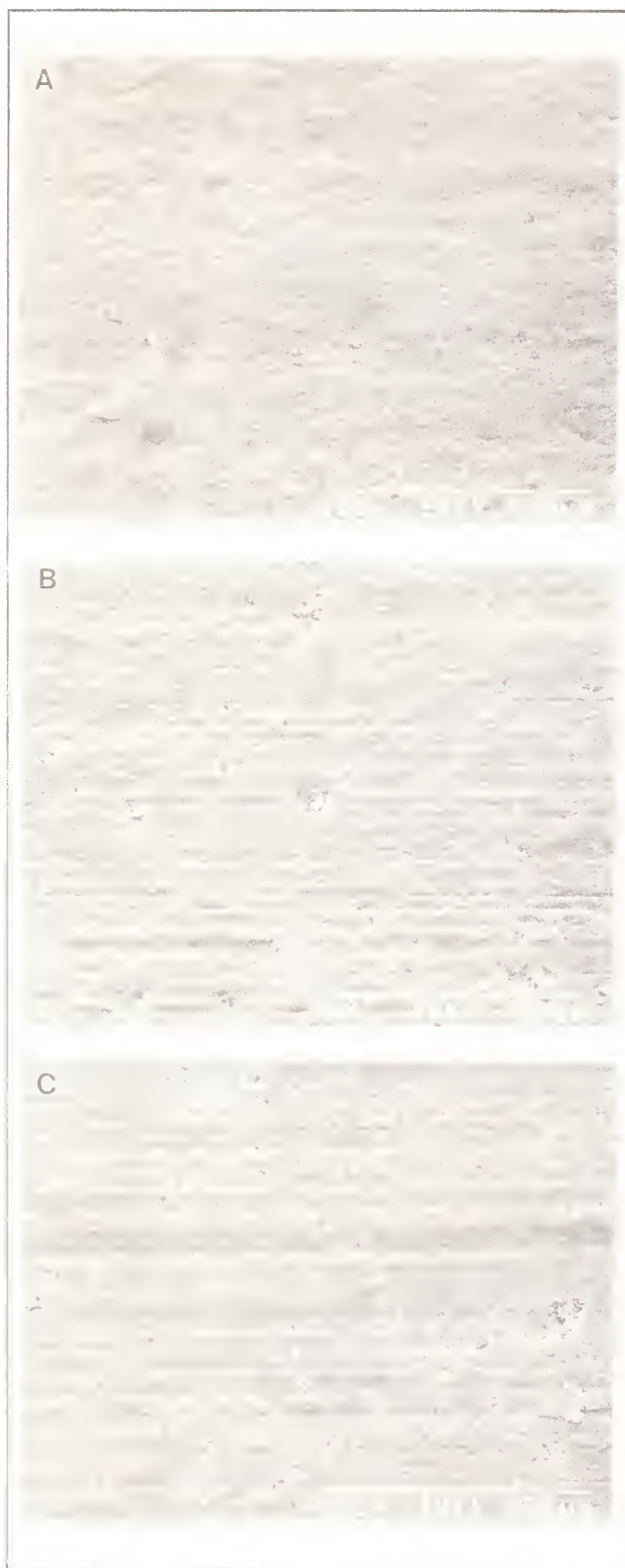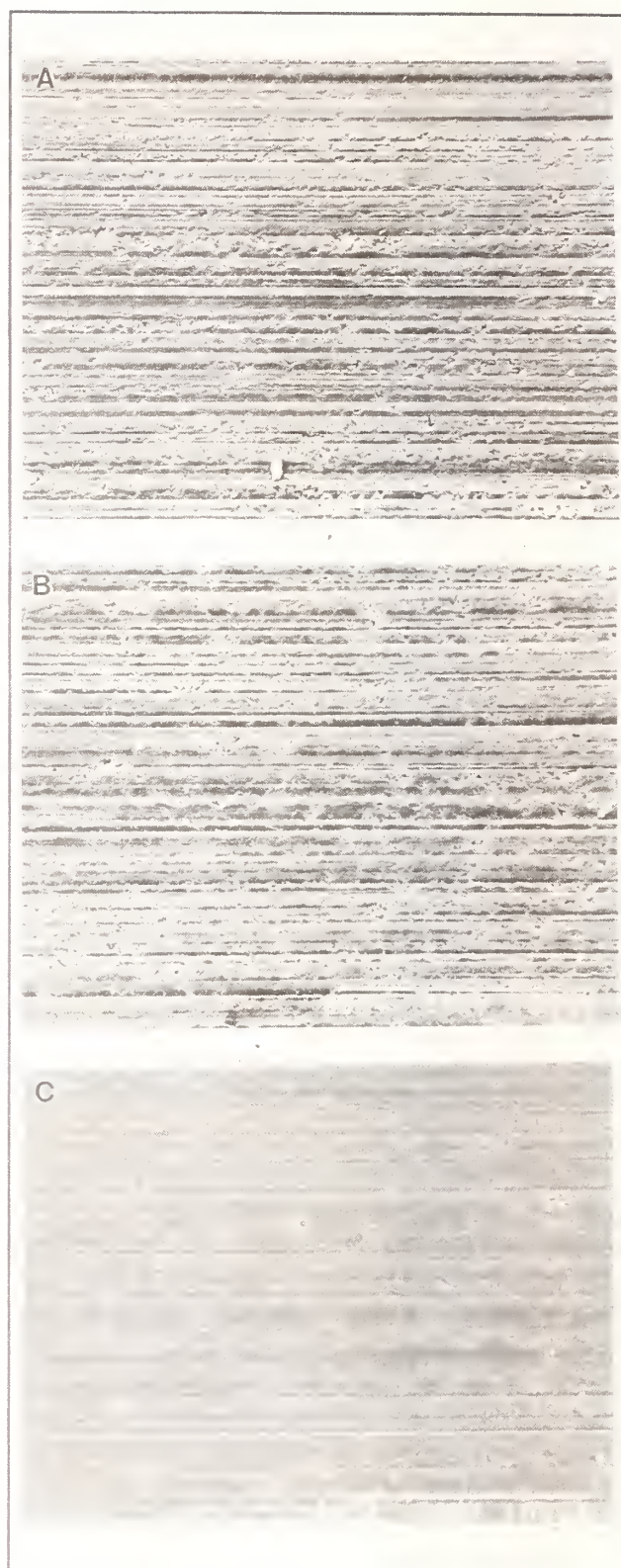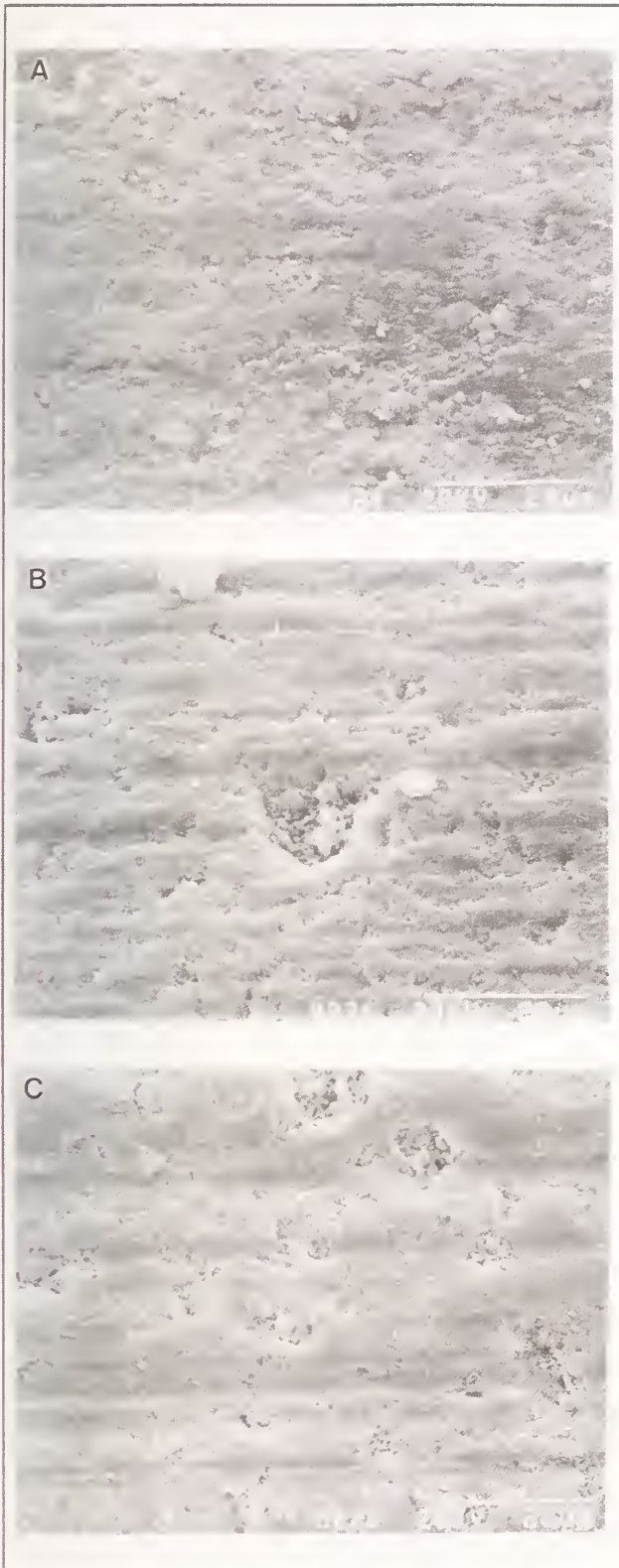
Figure 7. SEM micrographs of the ground surfaces of RBSN for grinding conditions A, B, and C (at a higher magnification than in Figure 5).
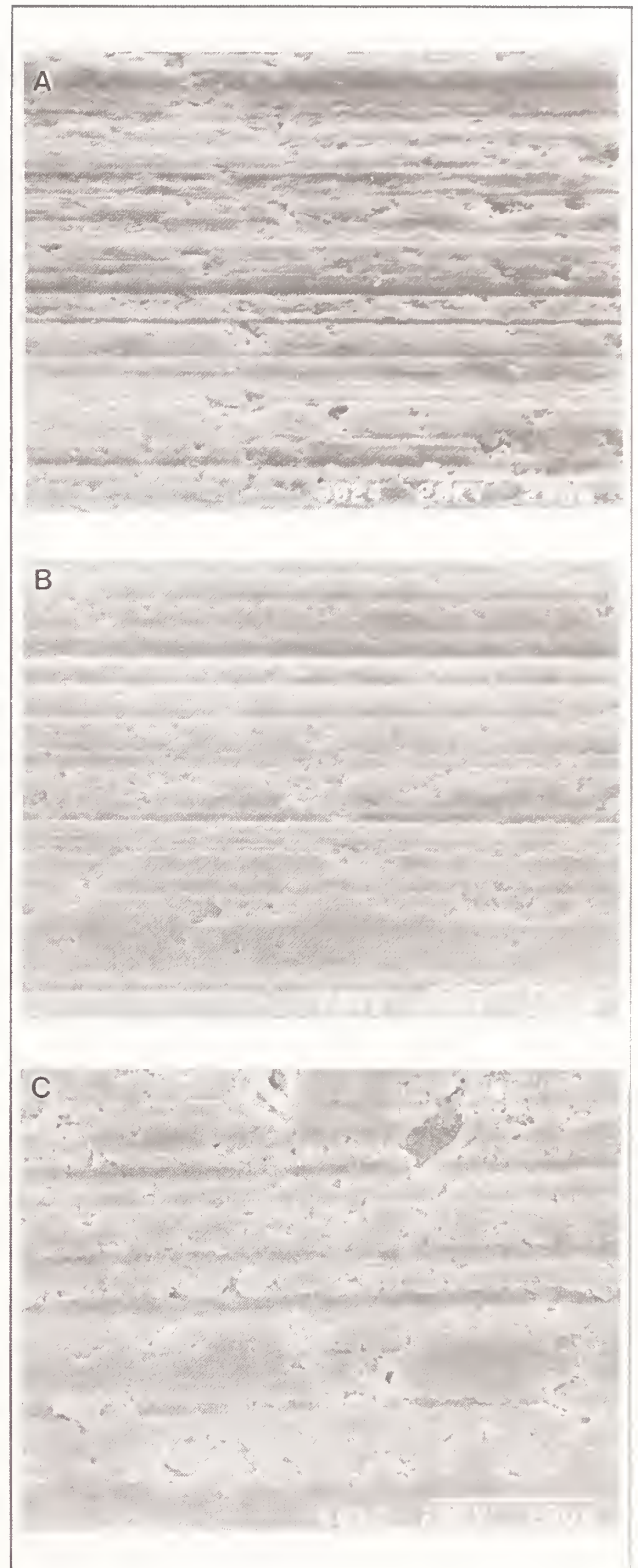

Figure 8. SEM micrographs of the ground surfaces of SRBSN for grinding conditions A, B, and C (at a higher magnification than in Figure 6).
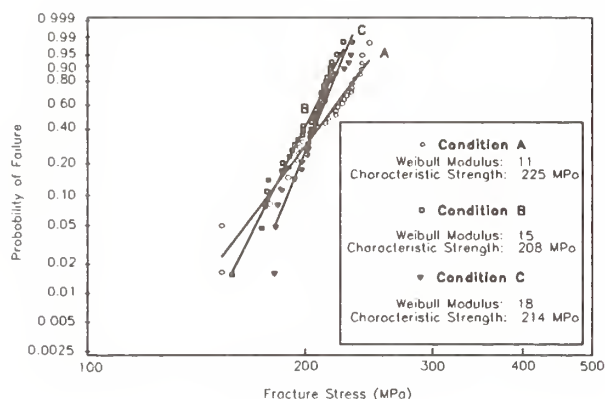
Figure 9 Weibull plot of RBSN samples for each grinding condition.
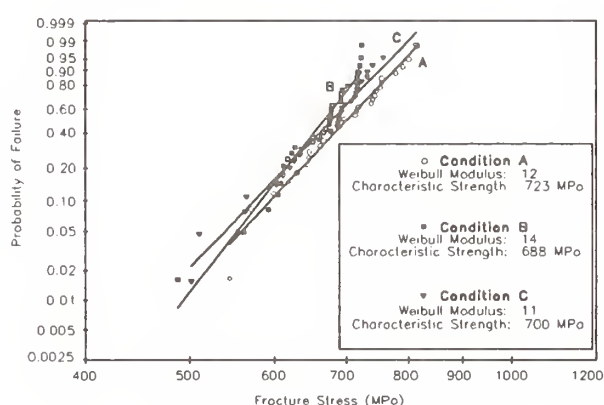
Figure 10. Weibull plot of SRBSN samples for each grinding condition.

characteristic strength varies from 208 to 225 MPa for RBSN and from 688 to 723 for SRBSN. The difference in strength between the two materials is expected due to the different material properties. The characteristic strength for each material, however, does not vary significantly at the 95% confidence level between the grinding conditions. The Weibull modulus varies from 11 to 18 for RBSN and from 11 to 14 for SRBSN. This difference is not statistically significant at the 95% confidence level. The results, therefore, indicate that the three grinding conditions used in this study do not have a significant effect on the characteristic strength and the Weibull modulus of the two silicon nitride materials. Statistical analysis on the characteristic strength and Weibull modulus confirmed that billet to billet variation in SRBSN and batch to batch variation in RBSN had no influence on the fracture results. Since the results are conclusive at the 95% confidence level in showing

no machining effect on the flexure strength, it can be concluded that the testing sequence had no deleterious effect on the results, as well.

c) Fractography

In order to identify the source of fracture initiation and determine the role of machining damage in the fracture, fractography was performed on each specimen using an optical microscope. Fractography provides a practical means for confirming the influence, or lack of influence, of machining procedures. In many advanced ceramics, it is possible to detect and fully characterize the strength limiting flaws, and determine whether the flaws are processing, microstructural, handling, or machining related. Although fractography can be subjective, a recent publication [36] makes the practice much more objective and serves to minimize the subjective factors. The guidelines suggested by this publication were used in the present study to assess the effects of the machining procedures used.

Figure 11. Characteristic strength and Weibull modulus of RBSN for each grinding condition.

Figure 12. Characteristic strength and Weibull modulus of SRBSN for each grinding condition.

272

Fracture of ceramic materials typically induces a set of characteristic features on the fracture surface known as the fracture mirror, mist and hackle. The fracture mirror is a smooth, flat, circular or semi-circular region surrounding the fracture origin. Mist is a border region found along the edge of the mirror and is less smooth than the mirror. Hackle is larger grooves and crack 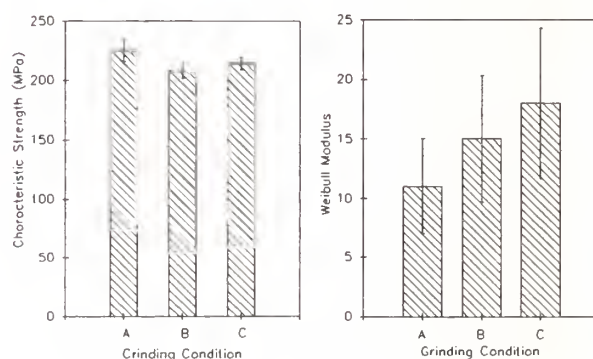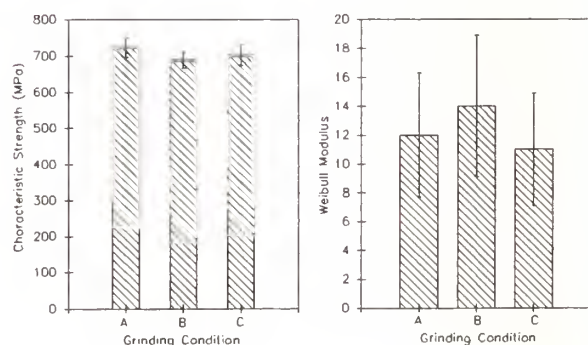lines radiating out from the fracture origin. The approximate origin of fracture can be easily determined by identifying these features.

Often the terms flaw, irregularity, discontinuity, or defect are used to identify the source of fracture initiation. In the present paper, the term flaw is used to identify the fracture origin, and should not be construed to mean that the material has been improperly prepared. This usage is consistent with the recommendation given in Reference [36].

Fracture origins were characterized by identity and location, as recommended by Quinn et al. [36]. *Identity* characterizes the phenomenological aspects of the flaw and identifies the type of flaws. For example, agglomerates, large grains, pores, inclusions, and other microstructural features are volume-distributed flaws, while machining damage, handling damage, and pits from oxidation or corrosion are surface-distributed flaws.

Location of the flaw identifies where the flaw is located in a specific specimen using the three classifications: volume, near-surface or surface, and edge. Classification of the location of the flaws is subjective, and depends on the researchers definition of bulk vs. near-surface. In the present paper, volume-located flaws refer to those fracture origins (fracture mirror centers) observed approximately 100 μm or more below the surface, which correspond to being visibly below the surface when viewed at 50x in an optical microscope. Any fracture origin that appeared closer to the surface was identified as surface or near-surface. Selected specimens were examined in an SEM since, in general, machining damage is very difficult to discern with optical microscopy [23,36,39]. During examination of the fracture surfaces, a simple drawing was made of each fracture surface and notes were taken on points of interest. Examples are shown in Figure 13.

Fractography revealed that the majority of fractures were initiated from near-surface or surface flaws. Fracture origins in the RBSN included 15-40 μm sized pores, agglomerates, and inclusions. The SRBSN origins also were mainly pores and inclusions in the 20-30 μm size range. In several instances, however, the fracture origins were zones of clearly transgranular fracture, whereas the fracture
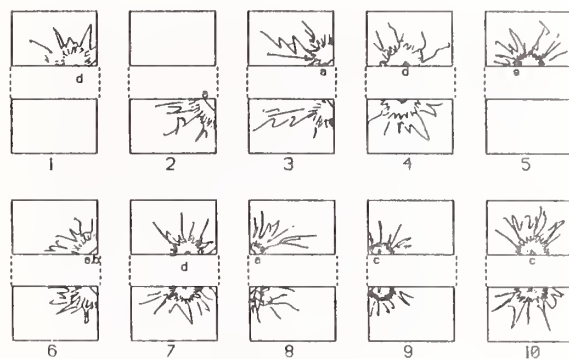
Figure 13. Drawings of fracture surfaces of specimens observed with optical microscopy.

mode of most specimens was highly intergranular. Examples of fracture initiation from volume-distributed and volume-located microstructural features are shown in Figure 14. The fracture origin in the RBSN specimen is identified with a large inclusion, suspected to be iron rich, while a large pore initiated fracture in the SRBSN flexure bar.

The results of the fractographic study are given in Table 2. In some cases, fracture was initiated from the edge and chamfer, and in only a few specimens was machining damage identified as a possible source of fracture initiation. Among the RBSN flexure bars, only those finished under grinding condition A contained fracture origins that were identified as being associated with machining damage. For each grinding condition used on SRBSN, a similar number of fracture origins (9 - 18%) could be associated with possible machining damage. However, the SRBSN specimens had more edge and chamfer fracture origins than the RBSN specimens.

The larger number of possible machining damage and edge and chamfer fractures in SRBSN than in RBSN was not unexpected. Since SRBSN is far more dense than RBSN, the strength of this material is expected to be more sensitive to the effects of machining damage. Machining damage, however, was never absolutely determined to be the cause of failure in any of the specimens. Two examples showing fracture initiation from possible machining damage are shown in Figures 15 for RBSN and SRBSN. In the RBSN specimen, two semi-circular regions extending from the surface can be seen, but they are not sufficiently clear to confirm machining damage as the fracture initiation source. There are other features, as well, such as substantial porosity in the immediate area, leading to uncertainty as to the

273
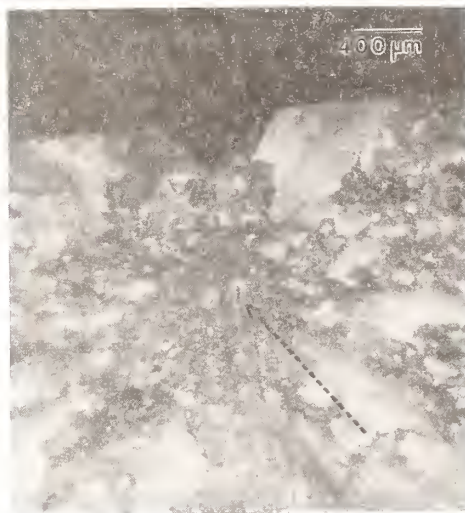
RBSN

SRBSN

Figure 14. Fracture surfaces of RBSN and SRBSN specimens whose fracture origins are both volume-located and volume-distributed microstructural features.

---

source of fracture. In the SRBSN specimen, a semi-circular region extending from the machined surface can readily be seen, but it is certainly interacting with a pore. Thus, machining damage is probably not the sole cause of fracture in this specimen, either.

Discussion

As compared to machining metals, ceramic machining technology is relatively undeveloped. The large foundation of machining data and research that exists for metals does not exist for ceramics. This implies that research in ceramic machining my be

Table 2. Summary of fractography
RBSN

	B	B	C
Volume	32%	3%	7%
Edge and Chamfer	7%	0%	3%
Surface or Near-Surface	61%	96%	90%
Possible Machining Damage	13%	0%	0%

SRBSN

	A	B	C
Volume	10%	3%	7%
Edge and Chamfer	27%	19%	18%
Surface or Near-Surface	63%	78%	73%
Possible Machining Damage	17%	9%	18%

fruitful in improving current methods of machining. The general findings of previous research and experience on the effect of grinding parameters on the strength of ceramics is that a smaller depth of cut may impart less damage, a finer grit size may do the same, and that grinding in the direction of the maximum tensile stress maximizes strength. However, the current procedures may be too conservative in terms of material removal rate; and therefore, the lack of knowledge tends to push machining practice to the "safer" end of the spectrum, i.e., very low material removal rates, and usually, higher cost.

Many of the earlier studies evaluated strength as a function of machining parameters, such as down feed or table speed. The influence of the individual parameters had to be inferred because of the lack of understanding of the grinding process from first principles. In addition, the inherent scatter in the strength results hampered unequivocal interpretation. With the advent of standardized test procedures [33,36] that measure strength accurately to about 1%, and analyses that permit comparison of strength samples, it is now possible to analyze quantitatively the machining influences on strength. In the interest of obtaining narrow confidence intervals in the strength parameters, however, large sample sizes are necessary. The current test standards recommend a

RBSN

SRBSN

Figure 15. Fracture surfaces of RBSN and SRBSN specimens with possible machining damage as the cause of failure.

---

sample size of 30 as a compromise between cost and statistical considerations.
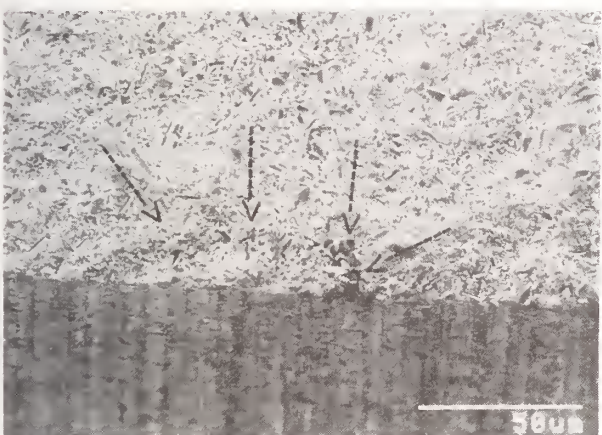
The results of the present study clearly indicate that the grinding conditions used in the study did not have a deleterious effect on the flexure strength and Weibull modulus of the two silicon nitride materials. The implications are that the material removal rate may be increased up to and possibly beyond the values used in this study without strength degradation for RBSN and SRBSN. Because no strength degradation was found when higher removal rates were used and the dominance of pre-existing fracture-initiating flaws in the specimens, it may be stated that the optimal grinding condition in terms of removal rate for these two materials occurs at the maximum removal rate in which the influence of the machining induced flaws is less than the influence of pre-existing flaws in the material. The influence of the pre-existing flaws is, of course, different for each

material and may change as the process used to manufacture the material is improved.

It is thus important to recognize that machinability data is material-specific. The great difference in surface integrity between RBSN and SRBSN resulting from the grinding conditions used in this study demonstrates this. In addition, if it can be accepted that grinding will not degrade strength until the influence of the flaws induced by grinding are more severe than the influence of pre-existing flaws, then it would be expected that the strength of SRBSN would be more sensitive to grinding-induced damage than RBSN because of its lower porosity and greater homogeneity (hence fewer pre-existing flaws). This approach to grinding optimization must be used until the mechanisms of material removal in grinding ceramics are better understood. Trends in the effect of grinding parameters on strength and surface integrity may eventually appear as more machinability data is obtained, thus pointing to underlying mechanisms of material removal.

The material removal rates used in this study are by no means the optimum values. To define the best set of grinding parameters, one must increase the removal rate further and analyze for the effect of grinding on strength and other performance characteristics. This approach has been adopted for the second part of this paper, which follows this paper in the proceedings.

Conclusions

1. Varying the material removal rate by a factor of 20, from 30 to 590 mm^3/min, in the grinding of RBSN and SRBSN did not have a significant effect on the characteristic strength or the Weibull modulus of four-point flexure specimens.

2. Surface roughness and topography were affected by the grinding conditions.

3. The results presented in this paper indicate that higher removal rates than those currently used for the grinding of these two types of silicon nitride may be possible without strength degradation.

Acknowledgments

References

[1] T. Abraham, "The U.S. Advanced Ceramics Industry: The Growth Continues", Journal of Materials, pp. 6-8, January 1992.

[2] Tech Update, "R&D Tackles Ceramics Machining", Manufacturing Engineering, pp. 20-23, October 1992.

[3] R. N. Katz, "Opportunities and Prospects for the Application of Structural Ceramics," Treatise on Materials Science and Technology, Vol. 29, pp.1-25, 1989.

[4] S. Jahanmir, L. K. Ives, A. W. Ruff, and M. B. Peterson, Ceramic Machining: Assessment of Current Practice and Research Needs in the United States, NIST Special Publication 834, U.S. Government Printing Office, Washington, DC, 1992.

[5] L. M. Sheppard, "The Challenges of Ceramic Machining Continue", American Ceramic Society Bulletin, Vol. 71, No. 11, pp. 1590-1610, 1992.

[6] K. Subramanian, "Precision Finishing of Ceramic Components with Diamond Abrasives," Ceramic Bulletin, Vol. 67, No. 6, pp. 1026-1029, 1988.

[7] K. Subramanian, S. Ramanath, and Y. O. Matsuda, "Precision Production Grinding of Fine Ceramics," First International Conference on Manufacturing Technology, Chiba, Japan, 1990.

[8] R. W. McEachron and S. C. Lorence, "Superabrasives and Structural Ceramics in Creep-Feed Grinding," American Ceramic Society Bulletin, Vol. 67, No. 6, pp. 1031-1036, June 1988.

[9] X. S. Li and I. M. Low, "Grinding of Engineering Ceramics with Diamond Wheels," Key Engineering Materials, Vols. 53-55, TransTech Publications, Switzerland, pp. 307-312, 1991.

[10] W. H. Daniels and A. C. Hawkins, "Superabrasives for Ceramic Grinding and Finishing," Technical Paper No. EM89-125, Society of Manufacturing Engineers, Dearborn, MI, 1989.

[11] P. R. Annese, T. Vasilos, and J. S. Annese, "Techniques for Machining Structural Ceramics," Ceramic Industry, pp. 63-65, September 1992.

[12] W. H. Daniels, A. C. Hawkins and A. Antenen, R. Ohnsorg, "Superabrasives for Ceramic Grinding and Finishing," Ceramic Industry, pp. 27-31, April 1992.

[13] J. J. Gagliardi, "Dynamics of Grinding Brittle Materials with Coated Abrasives," American Ceramic Society Bulletin, Vol. 71, No.11, pp. 1641-1646, 1992.

[14] R. Komanduri, and D. Maas (Eds.), "M. C. Shaw Grinding Symposium," The Winter Annual Meeting of the American Society of Mechanical Engineers, Miami Beach, FL, November 17-22, 1985.

[15] K. Subramanian and R. Komanduri (Eds.), "Machining of Ceramic Materials and Components," The Winter Annual Meeting of the American Society of Mechanical Engineers, Miami Beach, FL, November 17-22, 1985.

[16] W. Konig, L. Cronjager, G. Spur, H. K. Tonshoff, M. Vigneau, and W. J. Zdeblick, "Machining of New Materials," Processing of Advanced Materials, Vol. 1, pp. 11-26, 1991.

[17] A. Gallee, M. Nakamura, E. Nagy, D. McGarry, and S. Peteves, "Influence of Machining on the Strength of Hot-Pressed Silicon Nitride, "Proceedings of the 1st European Ceramic Society Conference, Maastricht, The Netherlands, June 18-23, 1989.

[18] H. K. Tonshoff and H. G. Wobker, "Influence of Surface Integrity on the Wear of Ceramic Cutting Tools," Journal of the Society of Tribologists and Lubrication Engineers, Vol. 47, No. 7, pp. 579-583, 1990.

[19] T. Hollstein and W. Pfeiffer, "The Strength and Fracture Behaviour of Engineering Ceramics - Influence of Machining and Residual Stresses," 4th International Symposium on Ceramic Materials and Components for Engines, Goteborg, Germany, June 10-12, 1991.

[20] D. J. Snoha and M. R. Foley, "An Investigation of Residual Stresses in Machined Silicon Nitride," Technical Report 92-46, U.S. Army Materials Technology Laboratory, Watertown, MA, July 1992.

[21] R. Samuel, S. Chandrasekar, T. Farris, and R. H. Licht, "Effect of Residual Stresses on the Fracture of Ground Ceramics," Journal of the American Ceramic Society, Vol. 72, No. 10, pp. 1060-1066, 1989.

[22] R. L. Allor, R. K. Govila, and T. J. Whalen, "Influence of Machining on Strength Properties of Turbine Materials," Proceedings of the 10th Automotive Materials Conference, Ann Arbor, MI, November 12, 1981.

[23] R. W. Rice, S. Freiman, J. Mecholsky, Jr., R. Ruh, and Y. Harada, "Fractography of Silicon Nitride and Silicon Carbide, "Ceramics for High Performance Applications II," J. Burke, E. Lenoe, and R. Katz (Eds.), Chestnut Hill, MA, pp. 669-687, 1978.

[24] R. W. Rice and B. K. Speronello, "Effect of Microstructure on Rate of Machining of Ceramics," Journal of the American Ceramic Society, Vol. 59, No. 7-8, pp. 330-333, 1976.

[25] H. K. Tonshoff, H. Trumpold, E. Brinksmeier, and H. G. Wobker, "Evaluation of Surface Layers of Machined Ceramics," Annals of the CIRP, Vol. 38, No. 2, pp. 699-708, 1989.

[26] G. D. Quinn and R. Morrell, "Design Data for Engineering Ceramics: A Review of the Flexure Test," Journal of the American Ceramic Society, Vol. 74, No. 9, pp. 2037-2066, 1991.

[27] R. L. Allor and R. R. Baker, "Effect of Grinding Variables on Strength of Hot Pressed Silicon Nitride," ASME Paper No. 83-GT-203, 1983.

[28] M. B. Thomas, R. D. West, and W. E. West, Jr., "Grinding Hot Pressed Silicon Nitride for Optimum Surface Finish and Strength," Therm, Inc., Ithaca, NY, Internal Publication, 1987.

[29] M. B. Thomas, R. D. West, and W. E. West, Jr., "Grinding Forces and Grindability of Silicon Nitride and Silicon Carbide Structural Ceramics," American Ceramic Society Meeting, May 1988.

[30] H. Miyasato, H. Okamoto, S. Usui, A. Miyamoto, and Y. Ueno, "The Effect of Grinding on Strength of Hot-Pressed Silicon Nitride," ISIJ International, Vol. 29, No. 9, pp. 726-733, 1989.

[31] W. Weibull, "A Statistical Distribution Function of Wide Applicability," Journal of Applied Mechanics, Vol. 18, pp. 293-297, 1951.

[32] J. P. Edler and B. Lisowsky, "Process for Making Silicon Nitride Articles," U. S. Patent 4,943,401, July 24, 1990.

[33] ASTM Standard C 1161-90, "Standard Test Method for Flexural Strength of Advanced Ceramics at Ambient Temperature," American Society for Testing and Materials, Philadelphia, PA, 1990.

[34] E. P. Whitenton, M. B. Peterson, and L. K. Ives, "Method for Quantitative Measurement of Galling Damage," Metal Transfer and Galling in Metallic Systems, H. D. Merchant and K. J. Bhansali (Eds.), The Metallurgical Society, Warrendale, PA, pp. 155-170, 1987.

[35] G. D. Quinn, "Twisting and Friction Errors in Flexure Testing," Ceramic Engineering and Science Proceedings," Vol. 13, No. 7-8, pp. 319-330, 1992.

[36] MIL-HDBK-790, "Fractography and Characterization of Fracture Origins in Advanced Structural Ceramics," U.S. Department of Defense, July 1992.

[37] J. E. Ritter, Jr., N. Bandyopadhyay, and K. Jakus, "Statistical Reproducability of the Dynamic and Static Fatigue Experiments," Ceramic Bulletin, Vol. 60, No. 8, pp. 798-806, 1981.

[38] G. D. Quinn, "Flexure Strength of Advanced Structural Ceramics: A Round Robin," Journal of the American Ceramic Society, Vol. 73, No. 8, pp. 2374-2384, 1990.

[39] G. D. Quinn, J. Swab, and M. J. Slavin, "A Proposed Standard Procedure for Fractographic Analysis of Monolithic Advanced Ceramics," in Fractography of Ceramics and Glasses, V. Frechette and J. Varner (Eds.), Vol. 22, 1976.

EFFECT OF GRINDING ON STRENGTH AND SURFACE INTEGRITY OF SILICON NITRIDE: PART II

S. JAHANMIR, T. J. STRAKNA*, and G. D. QUINN
National Institute of Standards and Technology, Gaithersburg, MD

R. N. KOPP
Norton Co., Worcester, MA

S. C. Yoon
Cincinnati Milacron, Cincinnati, OH

K. V. KUMAR
GE Superabrasive, Worthington, OH

Standard flexure specimens, made from a reaction-bonded and a sintered reaction-bonded silicon nitride (RBSN and SRBSN), were surface ground in the longitudinal direction under three different conditions involving high material removal rates. The resulting ground surfaces were investigated with a three-dimensional profiling instrument and a scanning electron microscope. Four-point flexure tests were performed on the specimens and Weibull parameters were calculated to determine the effect of the different grinding conditions on flexure strength. Fractography was performed on the specimens after testing to characterize and determine the location of the fracture-initiating flaw in each specimen. Varying the volumetric removal rate in surface grinding from 310 to 516 mm^3/min for RBSN and from 310 to 1737 mm^3/min for SRBSN by employing creep feed grinding conditions was found to have no significant effect on the characteristic strength of these materials. However, one of the grinding conditions, which used spark-out, reduced the Weibull modulus, i.e., increased the variation in flexure strength. The results also showed that surface roughness and topography were affected by the grinding conditions.

Introduction

Grinding is an extensively used technique for machining structural ceramics [1]. There is, however, very little data available on grinding ceramics and cost-effective grinding techniques have yet to be developed [2]. The purpose of the present investigation was to collect data and information on the effect of grinding on strength of two types of silicon nitride. The data will be part of a database being developed to assist in the optimization of the grinding process for low cost, high reliability, and eventual automation. The database will serve to efficiently transfer this information to manufacturers in an effort to make advanced ceramics a practical engineering material.

In Part I of this investigation [3], the effect of three grinding conditions on the strength of a reaction-bonded and a sintered reaction-bonded silicon nitride was investigated. The grinding conditions used encompassed a wide range of material removal

rates. Two of the conditions were bench mark conditions which represented a conservative procedure in terms of material removal rate (30 and 59 mm^3/min) and the amount of damage they may induce, while the third condition was significantly more aggressive, with a removal rate of 590 mm^3/min. Because strength was not affected by these three grinding conditions, the tests were extended using creep feed grinding at higher removal rates. The results of these tests are presented in this paper. The grinding conditions used in this paper and in Part I serve to cover the operational envelope of a typical surface grinder.

Creep feed grinding is characterized by low table speeds and large down feeds [4]. Creep feed grinding of a part is typically completed in one or a few passes and the machining time can be significantly lower than in conventional techniques.

In one of the grinding conditions, spark-out was used for comparison with the others. Spark-out is a technique that is often used in grinding metals to improve surface finish [4]. In this technique, the workpiece is subjected to several passes under the grinding wheel without incrementing the down feed.

---

* Graduate Research Assistant, University of Maryland, College Park, MD 20742

This will allow for material removal at smaller depths of cut, until no further removal takes place (i.e. sparks are no longer generated). Although spark-out is not a high removal rate technique (in fact, it removes very little material), it may have an advantage in obtaining a good surface finish.

Four-point flexure testing was used to determine the effect of grinding conditions on the strength of two commercially available silicon nitride materials. Weibull statistical analysis was performed on the flexure strength data and fractography was performed to identify the location and source of fracture in each specimen. To characterize the surface integrity, surface roughness was measured with a three-dimensional profiling instrument and the ground surfaces were examined in a scanning electron microscope.

Experimental Procedure

a) Materials

In this study, two types of silicon nitride were used -- reaction-bonded (RBSN, produced by Eaton Corporation) and sintered reaction-bonded (SRBSN, produced by Ceradyne, Inc.). Some important material properties of each are shown in Table 1. The composition and microstructure of these materials are detailed in Part I of this investigation [3].

The materials were received in billets. One or two flexure specimens were made from each 86 x 10 x 3.2 mm RBSN billet, which was received in three batches. The SRBSN billets were 76 x 76 x 13 mm and were sliced into 4 equal pieces with approximate dimensions of 50 x 25 x 13 mm. A total of 8 to 12 flexure specimens were made from each SRBSN sliced portion. The billet number, location in the billet, and batch number of the billet were tracked for each specimen to check the possibility of billet to billet variation and the influence of specimen location within each billet on strength.

b) Grinding Conditions

A total of 25 to 30 specimens from each material were machined under each set of grinding conditions used. The specimens were ground to dimensions and tolerances required by ASTM Standard C 1161 Standard Test Method for Flexural Strength of Advanced Ceramics [5] size B specimens (3 x 4 x 50 mm). All edges along the length of the specimens were chamfered to reduce the possibility of fracture initiation from the edges, as prescribed in the standard.

Table 1. Material properties of RBSN and SRBSN

Material	RBSN	SRBSN
Density (g/cm³)	2.36	3.22
Porosity	20%	< 1%
Alpha to Beta Ratio	7.7 : 1	All Beta
Grain Size Length x Width (μm)	1-2 x 0.5-1	6-8 x 1-3

Three sets of grinding parameters were used to finish grind specimens from each material. The grinding parameters are shown in Table 2 (condition D was used on both RBSN and SRBSN). In all cases, horizontal spindle surface grinding was performed in the longitudinal direction of the flexure bars with resin-bonded diamond grinding wheels. These conditions were chosen to be rather aggressive as a continuation of the first part of this investigation [3]. A 320 grit wheel was used for grinding condition D with 15.2 m/min table speed and 0.0051 mm down feed; the cross feed of 4.00 mm/pass represents grinding the full width of a specimen in each pass. In condition D, 1-2 spark-out passes were performed as the final grinding step. Rough grinding was performed at the same conditions with the exception of the down feed, which was incremented in the following steps: 0.0254 mm to net dimension +0.1524 mm and 0.0127 mm to net dimension +0.0635 mm. Conditions E through H represent creep-feed grinding, where typically the table speed is lower and the down feed is larger than in conventional grinding. In conditions E and G, a cross-feed of 1.91 mm/pass was used, whereas, the full specimen width was used in conditions F and H. The resulting volumetric removal rates ranged from 310 mm³/min to 516 mm³/min for the RBSN and 310 mm³/min to 1737 mm³/min for the SRBSN material. In addition, each grinding condition was performed on a different machine tool by a different operator.

In terms of material removal rate, there was some overlap between this study and Part I. However, the high removal rates were obtained by different means than those in Part I. Conditions E through H approach a creep feed grinding mode with high down feeds and low table speeds.

Table 2. Grinding parameters

RBSN	D	E	F
Grinding Wheel Grit / Concentration	320 / 150	150 / 75	80 / 100
Wheel Surface Speed (m/s)	28	33	28
Grinding Fluid	Emulsion 14:1	Emulsion 20:1	Emulsion 20:1
Table Speed (m/min)	15.2	1.52	1.52
Cross Feed (mm/pass)	4.00	1.91	4.50
Down Feed (mm)	0.0051	0.1778	0.0508
Volumetric Removal Rate (mm³/min)	310	516	347

SRBSN	D	G	H
Grinding Wheel Grit / Concentration	320 / 150	150 / 75	80 / 100
Wheel Surface Speed (m/s)	28	33	28
Grinding Fluid	Emulsion 14:1	Emulsion 20:1	Emulsion 20:1
Table Speed (m/min)	15.2	1.52	1.52
Cross Feed (mm/pass)	4.00	1.91	4.50
Down Feed (mm)	0.0051	0.2540	0.2540
Volumetric Removal Rate (mm³/min)	310	737	1737

Notes:
Condition D used 1-2 spark-out passes as a final step. Conditions D, F, and H used Cimperial HD90, whereas E and G used Cimperial 1010 soluble oil grinding fluids.

c) Surface Integrity Evaluation

The surface integrity of the ground specimens was evaluated with a three-dimensional stylus profiling system [6] and scanning electron microscopy. Three-dimensional topographical maps were made of the surfaces of selected test bars of each material for each grinding condition by compiling multiple profile traces taken at fixed intervals on the sample surfaces. Each trace ran perpendicular to the grinding direction. A total of 200 traces, 3 mm in length and set 10 μm apart, were taken. This corresponds to an area of 3 x 2 mm. A subset of the traced area, approximately 1 x 1 mm, was used to calculate the topographical parameters: average roughness (R_a), root mean square roughness (R_q), and average peak to valley height (R).

d) Flexure Strength Tests

The flexure strength of the ground test bars was measured in accordance with the ASTM Standard [5]. A universal testing machine was used at a cross-head speed of 0.5 mm/min to apply a steadily increasing load to each specimen. A load cell was used to measure the load, and an integrated strip-chart recorder was used to record the applied load. A fully articulating steel fixture [7] was used to mount the specimens for testing in four-point bend position. This fixture has the advantage of articulating during loading to correct for any misalignments due to dimensional errors in the specimens. This ensures a good line-contact between each load-pin and the specimen. The system was calibrated before beginning the flexure tests, and checked periodically during the testing sequence. A more detailed description of the test procedure is given in Part I [3].

Experimental Results

a) Surface Integrity

The R_q roughness values corresponding to each grinding condition are shown in Figure 1 for both materials. The observed dependance of R_q roughness on grinding condition and material type was also evident in other roughness parameters such as R and R_a. Figure 1 shows that RBSN has a larger surface roughness than SRBSN for each comparable grinding condition. Even for grinding condition F, where the down feed is lower than condition H by a factor of 5, RBSN exhibits a much higher roughness than SRBSN. The figure also shows that the R_q roughness values for conditions D and E are nearly
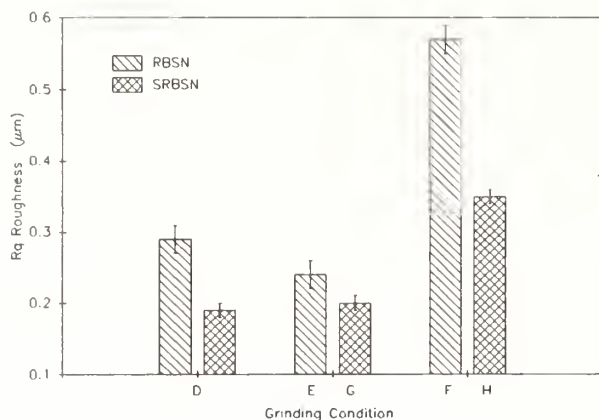
281

Figure 1. R_q roughness resulting from each grinding condition for each material.

equal. This indicates that spark-out with a 320 grit wheel did not produce a finer surface finish than that obtained with a 150 grit wheel at a much higher down feed.

Although it is not possible to establish a correlation between the wheel grit size and surface roughness, because of the variations in grinding parameters, a certain trend is clear. Grinding conditions F and H, which used an 80 grit wheel, also produced the largest surface roughness. It is particularly interesting to note the difference between conditions E and F, where the down feed is larger in the former condition by a factor of 3. Nevertheless, the R_q roughness produced by condition F is approximately twice that produced by condition E. Similarly, the roughness produced by condition H is larger than that produced by condition G. This shows the influence of grit size on roughness.

The topographical maps resulting from the three-dimensional profiling are shown in Figures 2 and 3 for RBSN and SRBSN, respectively. It is important to note the difference in surface characteristics between the two materials. In general, the RBSN surfaces are more random and grinding striations are not so clearly evident. The SRBSN, however, displays distinct and regular grinding striations. In addition, for each material, differences in the severity of grinding striations and the character of the surfaces between each grinding condition are evident. The micrographs of the surfaces in Figures 4-7 confirm the above observations. For RBSN, in Figures 4 and 6, condition D displays semi-flat regions with distinct pits on the surface. The surface generated under condition E is similar to the surface generated by condition D, but lacks much of the smooth regions. The condition F surface is more broken up or crushed, on a small scale, but the peaks

and valleys of the grinding striations are revealed as dark horizontal bands across the surface.

In the SRBSN material, there is little difference in the surface characteristics observed in the micrographs in Figures 5 and 7. Under grinding condition H, however, deeper grinding striations are observed, and the bottom of the deep grooves appear smooth and somewhat featureless.

These observations suggest that considerable plastic flow occurs during material removal in SRBSN, whereas for RBSN, brittle fracture is the dominating process. The spark-out process, however, appears to be associated with plastic deformation or polishing of the surface, especially in RBSN. Although the polishing action produced locally smooth areas, it did not reduce the overall roughness.

b) Flexure Strength

The two-parameter Weibull distribution was used to statistically evaluate the strength data. Weibull plots were used, where the probability of failure, on Weibull probability axis, is plotted against the fracture stress on natural log axis. The slope of the line obtained by least squares fit is the estimate of the Weibull modulus and the strength at which the probability of failure is 0.632 is the estimate of the characteristic strength. The 95% confidence intervals were calculated using the method based on the law of propagation of errors developed by Ritter, et al. [8]. This analysis has been applied successfully to flexure data of ceramics [9].

The Weibull plots of flexure data for each grinding condition are shown in Figure 8 for RBSN and Figure 9 for SRBSN. The data is well fitted by a straight line in each case, thus indicating good representation of the data by the Weibull distribution. The Weibull parameters were calculated without the 3 lowest strength data points in condition E and the lowest data point in condition F. These data were not representative of the population as failure was determined to be caused by the presence of unusually large iron-rich inclusions resulting in extremely low flexure strengths. In the Weibull plots, it is apparent that for both materials condition D stands out with lower slopes.

The Weibull parameters are displayed for each grinding condition in Figure 10 for RBSN and Figure 11 for SRBSN, along with the 95% confidence intervals. As shown by the Weibull plots, the characteristic strengths do not vary significantly among the grinding conditions, ranging from 206 MPa to 216 MPa for the RBSN and from 690 MPa to 703 MPa for the SRBSN. The difference in

282

Figure 2.   Topography of ground surfaces of RBSN for grinding conditions D, E, and F.

283

Figure 3. Topography of ground surfaces of SRBSN for grinding conditions D, G, and H.

Figure 4. SEM micrographs of the ground surfaces of RBSN for grinding conditons D, E, and F.
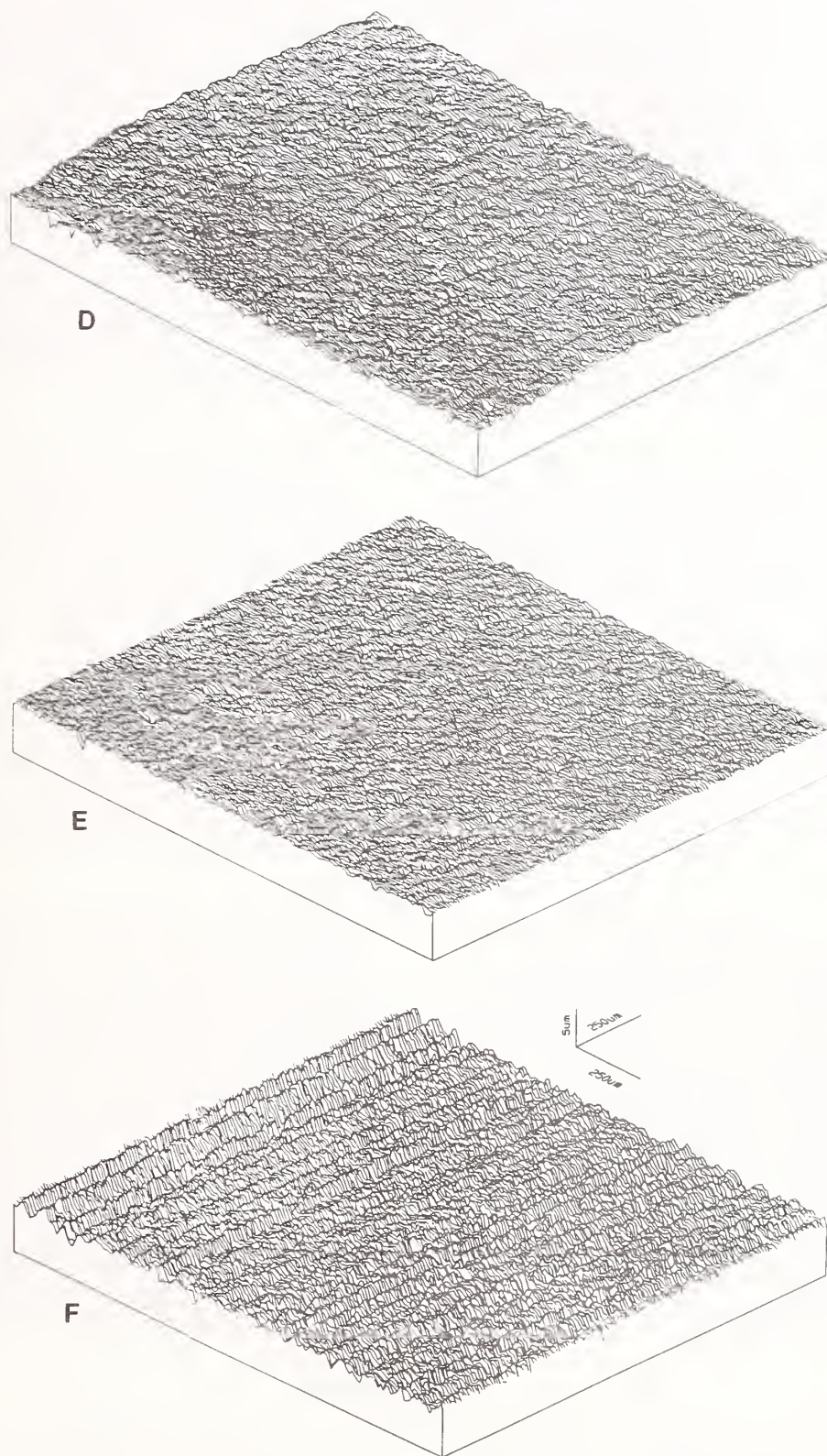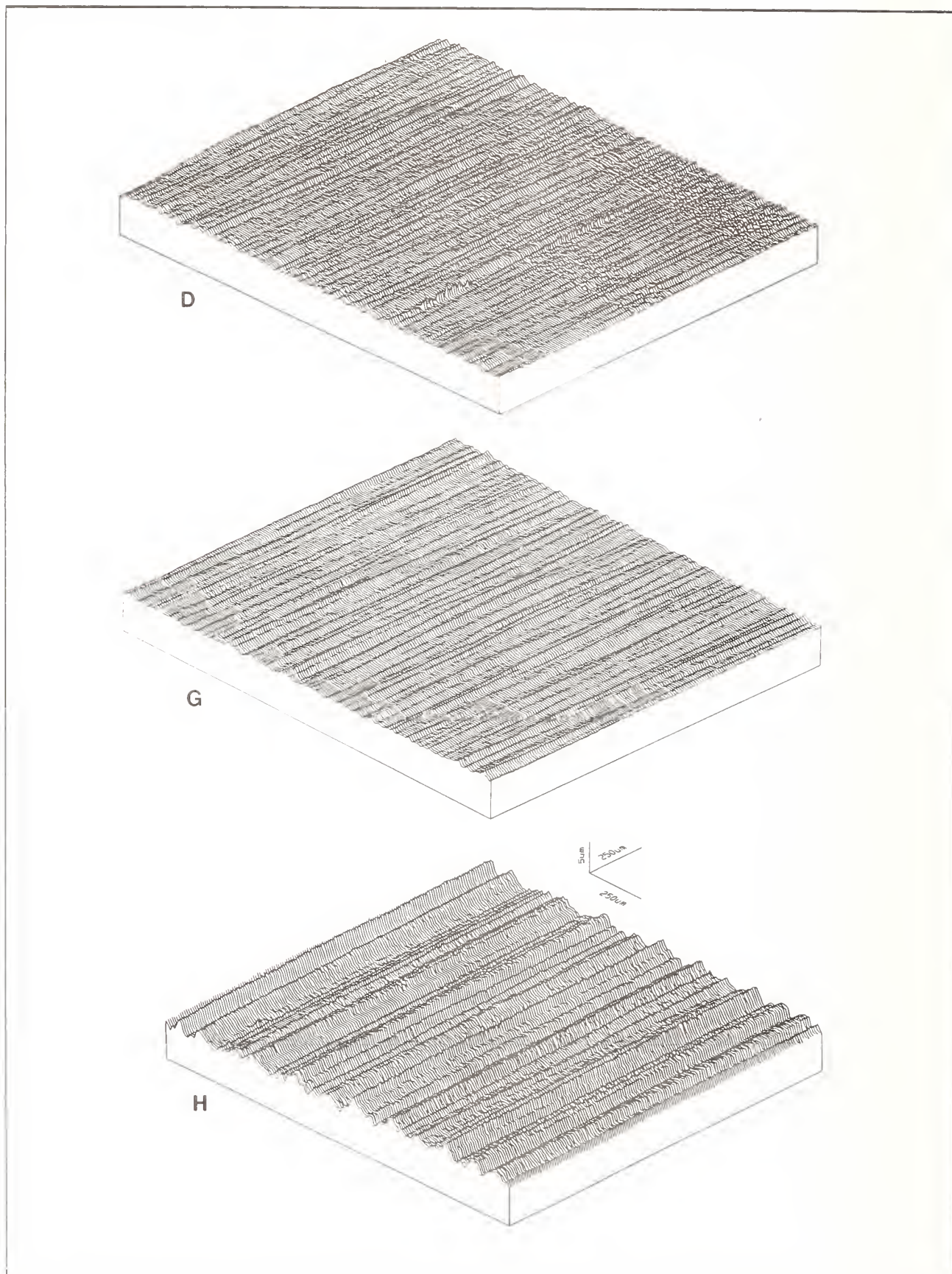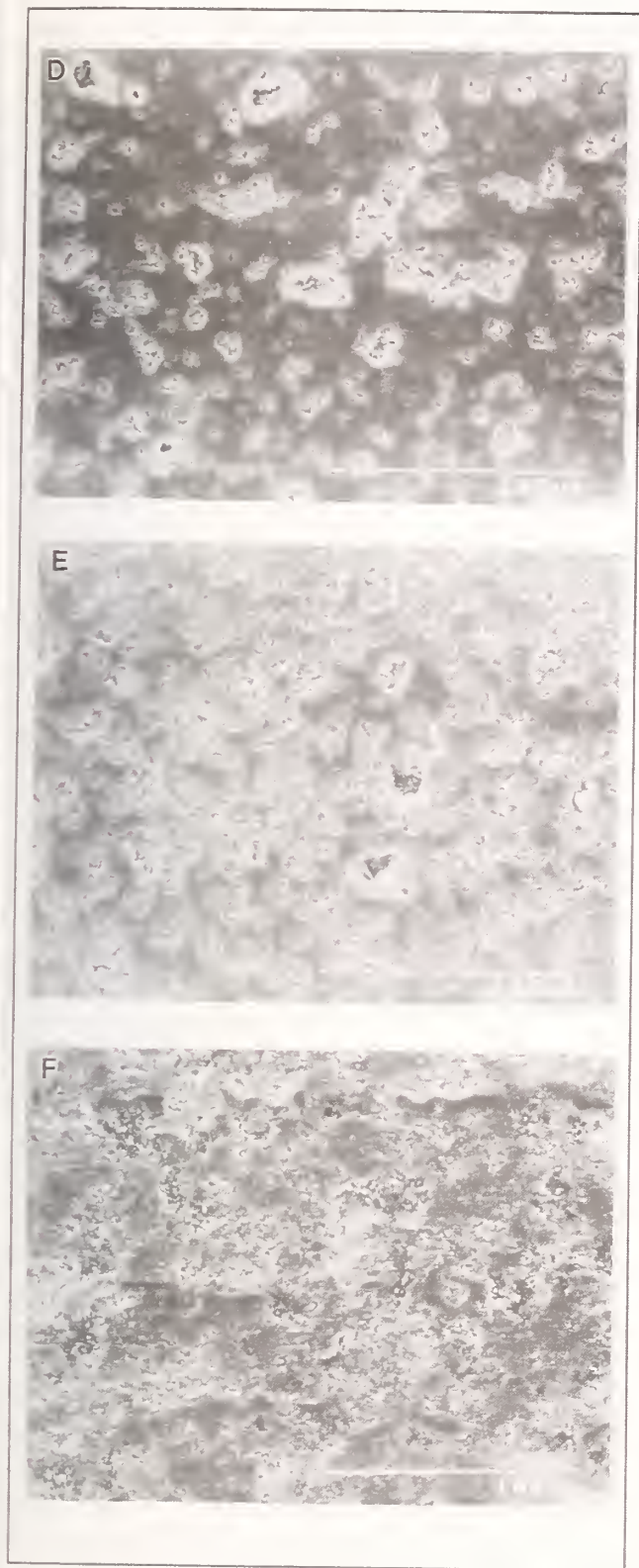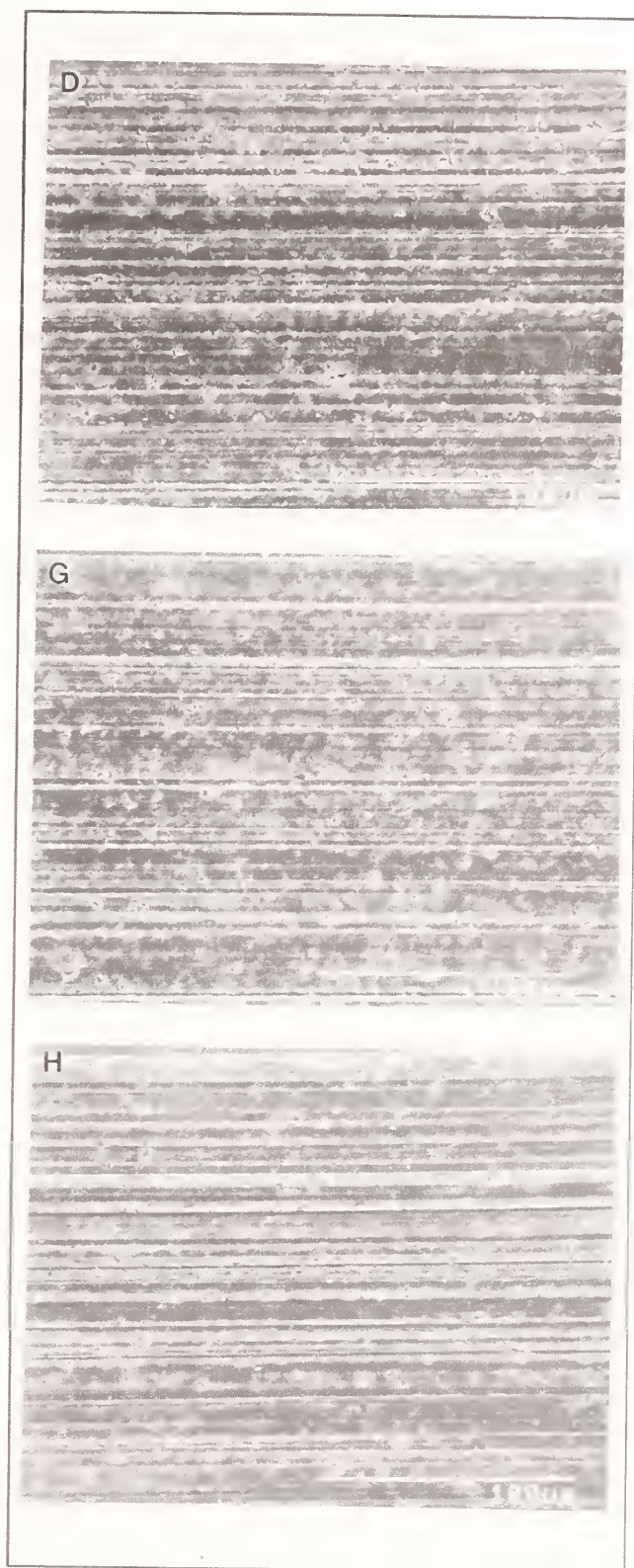

Figure 5. SEM micrographs of the ground surfaces of SRBSN for grinding conditons D, G, and H.
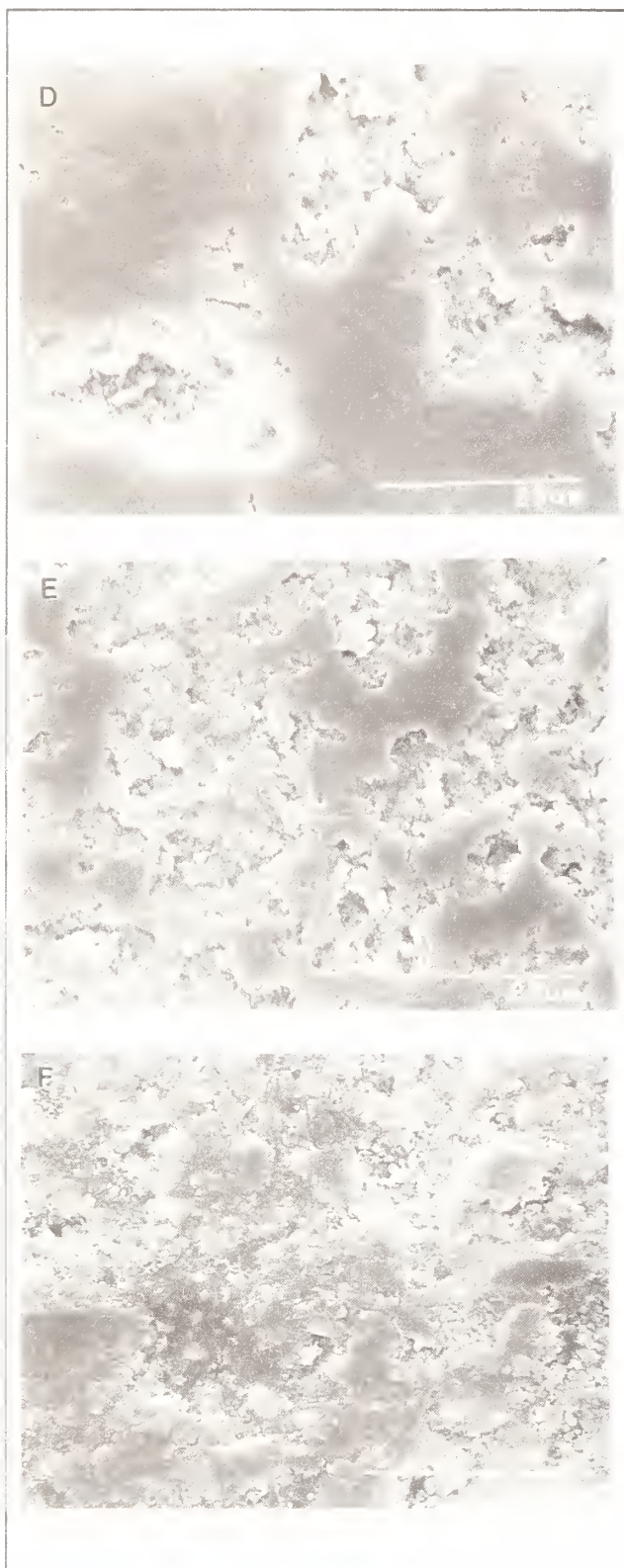
Figure 6. SEM micrographs of the ground surfaces of RBSN for grinding conditons D, E, and F (at a higher magnification than in Figure 4).
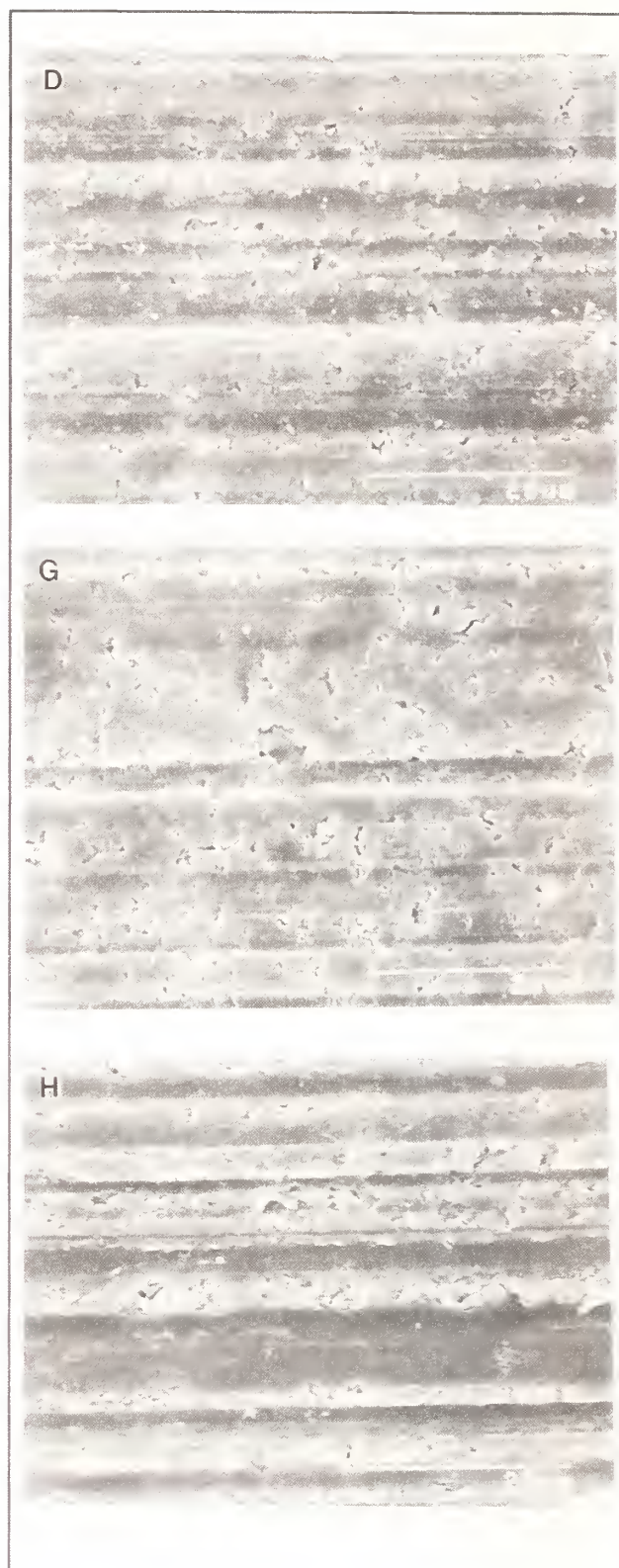

Figure 7. SEM micrographs of the ground surfaces of SRBSN for grinding conditons D, G, and H (at a higher magnification than in Figure 5).
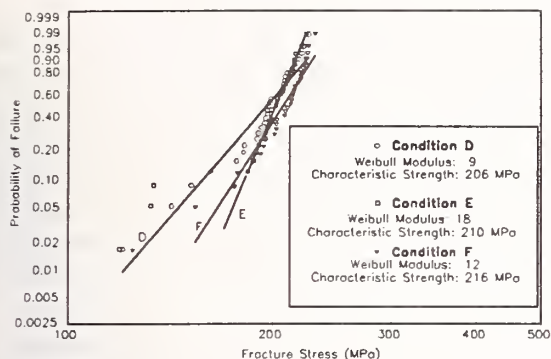
Figure 8. Weibull plot of RBSN samples for each grinding condition.
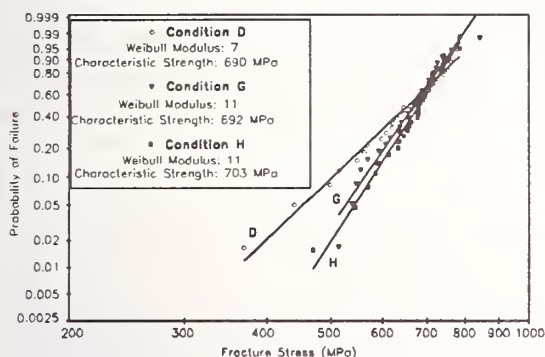
Figure 9. Weibull plot of SRBSN samples for each grinding condition.

strength between the two materials is expected due to their different processing methods and microstructures. In terms of the 95% confidence intervals, a statistically significant difference is observed only for the Weibull modulus between conditions D and E in RBSN in Figure 10. The data in Figures 8 and 9, however, indicate that the variation in strength for both materials is increased by grinding condition D, since the Weibull modulus is lower for this grinding condition.

c) Fractography

Fractography was performed, according to the published guidelines in Reference [10], on each specimen to identify the location and source of fracture initiation and to determine if machining damage played a role in fracture. Fracture origins were characterized by identity and location, as recommended by Quinn et al. [11]. The procedure used in this study was identical to that used in Part I.

Identity characterizes the phenomenological aspects of the flaw and identifies the type of flaws. For example, agglomerates, large grains, pores, inclusions, and other microstructural features are usually volume-distributed flaws; machining damage, handling damage, and pits from oxidation or corrosion are usually surface-distributed flaws.

Location identifies where the flaw is located in a specific specimen. The three classifications used are volume, near-surface or surface, and edge. Classification of the location of the flaws is subjective and depends on the researchers definition of bulk vs. near-surface. In the present paper, volume-located flaws refer to those fracture origins observed in the examination of the fracture surfaces by optical microscopy to be approximately 100 μm or more below the surface. Any origin that appeared closer to the surface was identified as surface or near-surface. The latter specimens were considered to be candidates having possible machining related fracture origins if no obvious flaw, such as an inclusion, was observed at the fracture origin.

Figure 10. Characteristic strength and Weibull modulus of RBSN for each grinding condition.

Figure 11. Characteristic strength and Weibull modulus of SRBSN for each grinding condition.

287

Table 3. Summary of fractography

RBSN

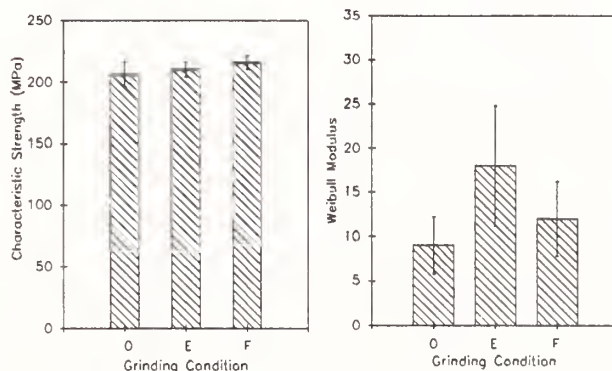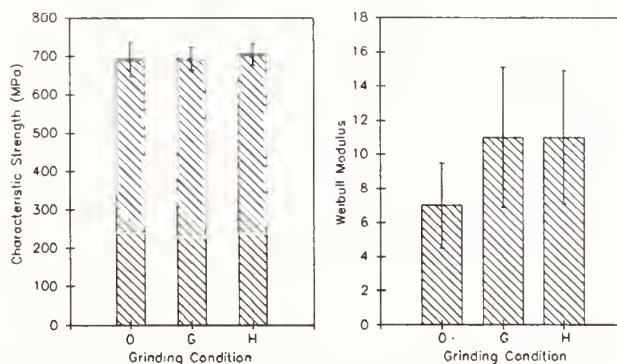|	D	E	F
Volume	4%	17%	13%
Edge and Chamfer	11%	13%	13%
Surface or Near-Surface	85%	70%	74%
Possible Machining Damage	0%	0%	0%

SRBSN

	D	G	H
Volume	10%	29%	21%
Edge and Chamfer	28%	13%	3%
Surface or Near-Surface	62%	58%	76%
Possible Machining Damage	0%	0%	0%

Selected specimens were examined in an SEM since, in general, machining damage is very difficult to discern with optical microscopy [10,11,12].

A summary of the fractography results is shown in Table 3. Some of the flexure specimens fractured from flaws located in the volume and near the edge and chamfer. Examination of the fracture surfaces in the SEM did not reveal any evidence for fracture initiation from machining damage. Associated with the majority of failures were near-surface or surface flaws. The fracture origins were associated with pores, agglomerates, and inclusions in RBSN and with inclusions, pores, and regions of incomplete densification in SRBSN. For example, the fracture surface of an SRBSN specimen is shown in Figure 12. Although the fracture origin is very close to the surface, there is little evidence of machining damage. Because a region of porosity can be readily identified at the fracture origin, it can be assumed that machining damage did not play a significant role in the fracture of this specimen.

Discussion

As stated in the introduction, the goal of our research program is to obtain data and information for the optimization of the grinding process for ceramics. To achieve this objective, grinding should be performed at the highest possible removal rates consistent with maintaining the desired strength of the part. A wide range of removal rates have been explored in this investigation (in both Parts I and II). The results clearly indicate that the fracture strengths of the two materials are relatively unaffected by the grinding conditions, although material removal rates were varied by a factor of 60.

Since a broad range of grinding conditions were used, it was expected that a wide range of machining damage would be introduced. However, characteristic strength was not significantly affected by any of the grinding conditions used. This indicates that the pre-existing flaws in the two materials had a larger influence on characteristic ′strength than the flaws produced in grinding. The implications of these findings is that the optimum grinding conditions have not yet been obtained. Therefore, further testing is warranted at even higher removal rates.
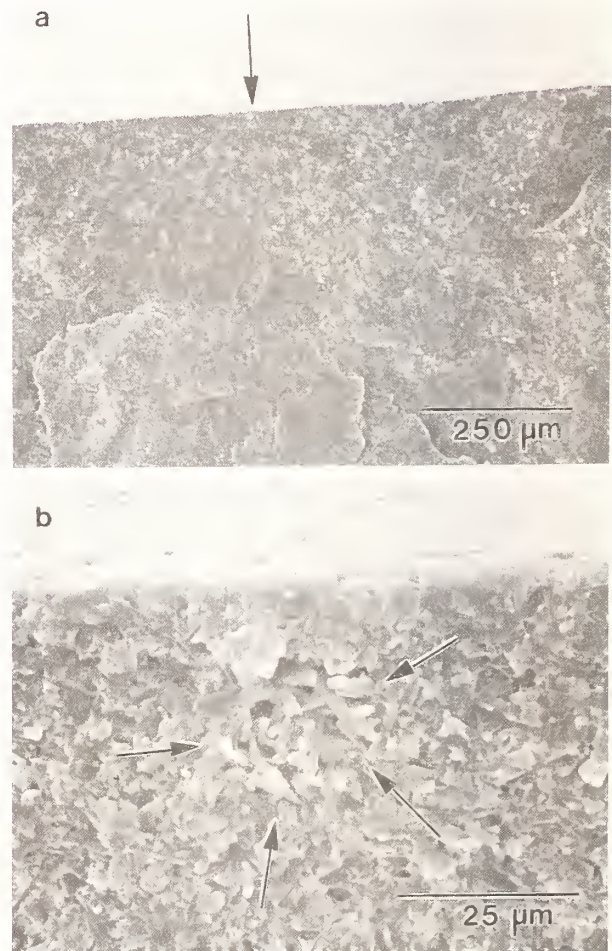

Figure 12. Fracture surface of an SRBSN specimen at a) low magnification and b) high magnification.

288

A key requirement for a production viable grinding process is a high material removal rate [13]. Creep feed grinding has this characteristic and may be the technique of choice for grinding advanced ceramics. Creep feed grinding techniques can produce parts with higher strength and better surface finish than conventional grinding [14]. Normal forces, however, are much higher for creep feed grinding and may require machine tools with higher stiffness.

Surface roughness measurement and evaluation of ground surfaces in the SEM indicated that surface integrity is influenced by the grinding condition. In particular, creep feed grinding with coarse grit wheels produced a rougher surface in both materials. In SRBSN, there did not appear to be any grinding damage. However, the brittle fracture process, which dominated the removal process in RBSN, could have resulted in the formation of microcracks. Nevertheless, a detrimental effect on strength was not observed.

It must be emphasized that the data presented in this paper are only applicable to the two types of silicon nitride materials tested in the present investigation. Application of these results to other types of silicon nitride materials could be erroneous. For example, silicon nitride materials with a reduced flaw population, compared with the RBSN and SRBSN, are expected to be more sensitive to machining damage. Recent studies [15,16] have shown that grinding related surface damage can be detrimental to the strength of hot isostatically pressed silicon nitride, even on longitudinally ground tensile specimens.

A question of the sensitivity of the flexure experiments to machining damage may also be brought up by these results. Previous studies have shown that strength is reduced by 30-60% when the specimens were ground in a direction perpendicular to the long axis of the flexure specimens [17]. This reduction in strength is attributed to the formation of median cracks by grinding, such that the crack plane is perpendicular to the tensile axis during flexure testing [18,19]. It is then possible that specimens ground in the transverse direction are more sensitive to grinding damage, particularly, at high removal rates.

Although the results in this paper showed that the strength was not affected by the grinding conditions used, the variation in strength was increased by the grinding condition in which spark-out was used. During spark-out passes, the diamond particles slide on the workpiece without removing much material. This added abuse may have amplified some of the damage from previous grinding, therefore, randomly

introducing machining flaws that reduce strength in some specimens. Another concern in using spark-out is that the stiffness of the machine tool must be sufficiently high to allow very low (and therefore precise) down feeds [20]. Otherwise, dynamic instability can result and produce undesirable surface integrity. A possible explanation for the observed variation in strength with the spark-out passes is an increased level of machining damage and interaction of this damage with the pre-existing flaws. Such interactions would obscure identification of the cause of fracture when using fractography. Nevertheless, since the surface roughness was not improved, the spark-out passes did not provide a beneficial effect.

Conclusions

1. Varying the volumetric removal rate in surface grinding from 310 to 516 mm^3/min for RBSN and from 310 to 1737 mm^3/min for SRBSN by employing conventional and creep-feed grinding conditions had no significant effect on the characteristic strength of four-point flexure specimens made from these materials.

2. The grinding condition that used spark-out reduced the Weibull modulus of the flexure specimens, i.e., increased the variation in flexure strength.

3. Surface roughness and topography were affected by the grinding conditions. A coarse grit wheel used in creep-feed grinding generated a rougher surface than surfaces produced with finer grit wheels.

Acknowledgments

Information on product names, manufacturers, or suppliers are included in this report for clarification. This does not imply endorsement of the products or services by NIST.

References

[1] K. Subramanian and S. Ramanath, "Mechanism of Material Removal in the Precision Grinding of Ceramics," Precision Machining: Technology and Machine Development and Improvement, PED-Vol. 58, ASME Winter Annual Meeting, November 8-13, pp. 1-19, 1992.

[2] S. Jahanmir, L. K. Ives, A. W. Ruff, and M. B. Peterson, Ceramic Machining: Assessment of Current Practice and Research Needs in the United States, NIST Special Publication 834, U.S. Government Printing Office, Washington, DC, 1992.

[3] S. Jahanmir, T. J. Strakna, G. D. Quinn, H. Liang, R. L. Allor, and R. D. West, "Effect of Grinding on Strength and Surface Integrity of Silicon Nitride: Part I," Proceedings of the International Conference on Machining of Advanced Materials, Gaithersburg, MD, July 20-22 1993.

[4] S. Malkin, Grinding Technology, New York, NY, pp. 188, 1989.

[5] ASTM Standard C 1161-90, "Standard Test Method for Flexural Strength of Advanced Ceramics at Ambient Temperature," American Society for Testing and Materials, Philadelphia, PA, 1990.

[6] E. P. Whitenton, M. B. Peterson, and L. K. Ives, "Method for Quantitative Measurement of Galling Damage," Metal Transfer and Galling in Metallic Systems, H. D. Merchant and K. J. Bhansali (Eds.), The Metallurgical Society, Warrendale, PA, pp. 155-170, 1987.

[7] G. D. Quinn, "Twisting and Friction Errors in Flexure Testing," Ceramic Engineering and Science Proceedings," Vol. 13, No. 7-8, pp. 319-330, 1992.

[8] J. E. Ritter, Jr., N. Bandyopadhyay, and K. Jakus, "Statistical Reproducability of the Dynamic and Static Fatigue Experiments," Ceramic Bulletin, Vol. 60, No. 8, pp. 798-806, 1981.

[9] G. D. Quinn, "Flexure Strength of Advanced Structural Ceramics: A Round Robin," Journal of the American Ceramic Society, Vol. 73, No. 8, pp. 2374-2384, 1990.

[10] MIL-HDBK-790, "Fractography and Characterization of Fracture Origins in Advanced Structural Ceramics," U. S. Department of Defense, July, 1992.

[11] G. D. Quinn, J. Swab, and M. J. Slavin, "A Proposed Standard Procedure for Fractographic Analysis of Monolithic Advanced Ceramics," in Fractography of Ceramics and Glasses, V. Frechette and J. Varner, (Eds.), Vol. 22, 1976.

[12] R. W. Rice, S. Freiman, J. Mecholsky, Jr., R. Ruh, and Y. Harada, "Fractography of Silicon Nitride and Silicon Carbide, "Ceramics for High Performance Applications II," J. Burke, E. Lenoe, and R. Katz, (Eds.), Chestnut Hill, MA, pp. 669-687, 1978.

[13] K. Subramanian, S. Ramanath, and Y. O. Matsuda, "Precision Production Grinding of Fine Ceramics," First International Conference on Manufacturing Technology, Chiba, Japan, 1990.

[14] W. Konig, L. Cronjager, G. Spur, H. K. Tonshoff, M. Vigneau, and W. J. Zdeblick, "Machining of New Materials," Processing of Advanced Materials, No. 1, pp. 11-26, 1991.

[15] M. R. Foley and V. K. Pujari, "Tensile Testing in the Development of Processing Methods for High Strength/High Reliability Silicon Nitride," Ceramic Engineering and Science Proceedings, 16th Annual Conference on Composites and Ceramics, Fall 1992.

[16] R. H. Licht, M. R. Foley, L. C. Sales, and D. M. Tracey, "Surface Integrity in Advanced Structural Ceramics," Presented at the Workshop on Super-abrasives and Grinding Wheel Technology for Machining Ceramics, Oak Ridge National Laboratory, Oak Ridge, TN, May 1992.

[17] H. Miyasato, H. Okamoto, S. Usui, A. Miyamoto, and Y. Ueno, "The Effect of Grinding on Strength of Hot-Pressed Silicon Nitride," ISIJ International, Vol. 29, No. 9, pp. 726-733 1989.

[18] R. W. Rice and J. J. Mecholsky, "The Nature of Strength Controlling Machining Flaws in Ceramics," The Science of Ceramic Machining and Surface Finishing II, National Bureau of Standards SP562, U. S. Government Printing Office, Washington, DC, pp. 351-378, 1976.

[19] B. R. Lawn, A. A. Evans, and D. B. Marshall, "Elastic/Plastic Indentation Damage in Ceramics: The Median/Radial Crack System," Journal of the American Ceramic Society, Vol. 63, No. 9-10, pp. 574-581, 1980.

[20] K. Subramanian, Personal Communication, 1993.

PRECISION MACHINING

TOOL FLANK WEAR IN SINGLE POINT DIAMOND TURNING

J. S. STRENKOWSKI and W. C. LARSON
North Carolina State University, Raleigh, NC

In this paper, wear mechanisms on the flank of diamond tools are investigated. In particular, wear due to solid state diffusion of carbon atoms from the tool into the workpiece and abrasion wear are studied for their relative contribution to overall flank wear. Flank wear in single point diamond turning is of particular importance because degradation of the flank can lead to surface roughness and damage in the machined workpiece surface.

The wear of diamond tools during machining is highly influenced by the temperature and velocity of the chip/tool interface. Using a 2-D Eulerian model of orthogonal cutting, the chip velocity and the temperature distribution in the chip and the tool is determined. By coupling this information with a model of wear, the relative contributions of diffusion-controlled wear and abrasion effects can be assessed.

It is found that flank wear is due to solid-state diffusion. Computed tool temperatures are consistent with temperatures required for producing a prescribed level of observed wear from experimentally-measured worn tools.

1. INTRODUCTION

Diamond tools can wear in a variety of ways including mechanical attrition and thermal degradation. Mechanical attrition is the abrasive removal of material from the tool by the workpiece. Wear due to abrasion is a function of the relative hardness of the workpiece and the tool, which is a function of the crystal orientation of the tool. It is negligible when machining soft materials, but it is the dominant mechanism for tool material removal for hard materials (1) such as during diamond lapping of a diamond tool. Thermal degradation occurs at elevated temperatures when the diamond crystal oxidizes and/or turns into graphite (graphitization). These reactions occur at high temperatures and are dependent on the crystal structure of the diamond, the presence of oxygen, and pressure. Diamond tools begin to oxidize and graphitize at 1500 °C in an inert environment (2). In the presence of oxygen this reaction can start to occur at 500 °C (3). However, experimental observations and theoretical cutting models indicate that temperatures of this magnitude are not reached in single point diamond turning (SPDT) of copper (4), so that thermal degradation is an unlikely wear mechanism.

Diamond tools exhibit wear on both flank and rake faces during single point turning. Wear on the rake face is characterized by crater patterns along the rake and almost negligible wear near the cutting edge. In contrast, flank wear is characterized by the appearance of a wear land on the tool flank parallel to the surface of the workpiece, which is relatively smooth. Flank wear is of particular interest because it can lead to surface damage and roughness in the machined workpiece.

The two most common forms of diamond tool wear include abrasion and chemical wear. In chemical wear, solid state diffusion of carbon atoms from the tool occurs directly into the workpiece. This can be seen in the machining of materials such as steel in which carbon is highly soluble. For these materials, diamond tools wear

very quickly (5) and it is suspected that solid state diffusion is the dominant wear process. Because solid state diffusion depends exponentially on the temperature, small changes in temperature can have large effects on the wear rate. This has been observed experimentally in wear patterns of diamond tools, in which deep wear pits occur in regions of high temperature, which are adjacent to unworn areas of low temperature (6). Therefore, there is some basis for diffusion as the dominant chemical wear mechanism for diamond tool wear.

The temperature must be accurately predicted in order to predict the wear due to diffusion. There have been numerous attempts to evaluate the temperature in diamond turning. The average temperature in SPDT was directly measured by Iwata (4), but a discrete temperature distribution along the rake and flank faces has yet to be determined by experiment. The temperature distribution can be evaluated using advanced numerical techniques, such as the finite element method. A model of orthogonal cutting has been developed by Strenkowski and Carroll (7), (8) and by Strenkowski and Moon (9) for chip geometry and temperature prediction. These models can be applied to micromachining in single point diamond turning with additional refinement. Specifically, modifications must be made to the boundaries because they are close to the cutting zone so that the temperatures within the workpiece and tool are extremely sensitive to the thermal boundary conditions. This sensitivity can be eliminated by incorporating a reduced thermal conductivity along the tool boundary that accounts for the remaining portion not included in the tool model.

This paper focuses on the understanding of diamond tool wear mechanisms for cutting of copper. In particular, wear due to solid state diffusion and abrasion wear are investigated for their relative contribution to the overall flank wear. Predicted flank wear is compared with measured wear rates for cutting of copper, and excellent agreement was found. Temperature contours in the tool confirm that flank wear is largely a diffusion-controlled mechanism.

2. FORMULATION OF A VISCOPLASTIC CUTTING MODEL

An Eulerian finite element technique can be used to simulate the complex interaction between the workpiece and the tool in terms of basic engineering quantities such as strain, strain-rate, flow stress, pressure, temperature, and tool forces. In this technique, the grid is spatially fixed and the workpiece behavior is treated as viscoplastic. The governing equations can be derived as follows. For a body undergoing plane strain steady-state

deformation, the equations of equilibrium can be written in the form:

$$[L]\{\sigma\} + \{f\} = 0 \quad \text{in } V \tag{1}$$

where $\{\sigma\}$ is a vector of stress components, $[L]^T$ is a matrix of first-order differential operators in x and y, and $\{f\}$ is a vector of applied body forces. Because the workpiece undergoes large deformations, it is more appropriate to describe its behavior in terms of strain-rate and particle velocity, rather than strain and displacement as in conventional solid mechanics problems.

For extremely large strain-rates, the workpiece deforms in a viscous manner. In general, the deviatoric stress $\{\sigma'\}$ is linearly related to the strain-rate $\{\dot{\varepsilon}\}$ as:

$$\{\sigma'\} = [\overline{D}]\{\dot{\varepsilon}\} \quad \text{and} \quad [\overline{D}] = \mu \begin{bmatrix} 2 & 0 & 0 \\ 0 & 2 & 0 \\ 0 & 0 & 1 \end{bmatrix} \tag{2}$$

where μ is the viscosity of the workpiece and is given by

$$\mu = \frac{\overline{\sigma}}{\sqrt{3}\,\dot{\varepsilon}} + \overline{\mu} \tag{3}$$

where $\dot{\varepsilon}$ is the second invariant of the strain-rate tensor or the effective strain-rate, $\overline{\sigma}$ is the effective flow stress, and $\overline{\mu}$ accounts for work hardening of the workpiece. For the special case of ideal plasticity, $\overline{\mu}$ becomes zero.

The stress can be written in terms of the deviatoric stress $\{\sigma'\}$ as:

$$\{\sigma\} = \{\sigma'\} - \{m\}p \quad \text{and} \quad \{m\}^T = \{1 \ \ 1 \ \ 0\} \tag{4}$$

The pressure p can be eliminated by recognizing that it is related to the rate of volumetric strain $\dot{\varepsilon}_v$ by

$$p = \alpha\dot{\varepsilon}_v = \alpha\{m\}^T[L]\{u\} \quad \text{where} \quad \alpha = 10^k\mu \tag{5}$$

where E is Young's modulus, and $\{u\}$ represents the particle velocity components. This is the so-called penalty function formulation (10) which is widely used for dealing with incompressible or nearly incompressible problems. The advantage of using a penalty function method is that the pressure can be expressed in terms of the strain-

296

rates and eliminated from the governing equations. This reduces the number of degrees of freedom to only nodal velocities. However, a drawback of this approach is that a suitable value for the penalty number a must be chosen. The value of k will vary depending on the application and the size of the computer word. Note that a very large value for k will lead to ill-conditioning or over-constraint of the governing equation. In contrast, a small value for k does not satisfy the incompressibility constraint. For the cutting model, it was found that a k equal to 5 was suitable.

The equations of equilibrium may now be written in terms of the particle velocities by substituting equations (2), (4), and (5) into equation (1), which gives

$$-[L]^T\{m\}\alpha\{m\}^T[L]\{u\} + [L]^T[\overline{D}][L]\{u\} + \{f\} = 0 \quad (6)$$

which is applicable for steady-state cutting. The finite element equations may be derived by using a Galerkin approach (11). In this method, the governing differential equation for the flow field is satisfied over the domain, where the weighting functions are chosen to be the same shape functions used for discretizing the velocity,

$$\{u\} = [N]\{U\} \quad (7)$$

where [N] is the shape function matrix and {U} is the vector of nodal velocities. Substituting equation (7) into (6), multiplying the resulting equation by $[N]^T$, and integrating over the volume results in the discretized equations:

$$[[K] + [K^p]]\{U\} = \{F\} \quad (8)$$

where $[K^p]$ contains the penalty term α. In solving equation (8), a penalty function formulation must be used in which α is identified as the penalty number. Because α approaches infinity for an incompressible material, reduced integration techniques must be used to evaluate $[K^p]$ as compared to [K] to eliminate element locking. Note that the viscosity can become very large and exceed the allowable real number range of the computer. Therefore, a suitable cut-off value must be supplied to avoid numerical error. For the cutting model described above, a cut-off in the range of 10^8 - 10^{10} was found to be suitable.

Thermal Model

During metal cutting, a significant amount of heat is generated due to the plastic work in the primary shear zone and frictional sliding along the tool/chip interface along the rake and flank faces. The high temperature generated during cutting

can directly influence the resulting quality of the machined parts and the life of the cutting tool. For example, crater wear and flank wear are greatly effected by the temperature.

The highest temperature and temperature gradients occur in a small region close to the cutting edge. A two-dimensional finite element thermal model can be coupled to the cutting model described in the previous section. The resulting velocity, strain-rate, stress, and chip/tool contact length as calculated by the cutting model are used as input data for the thermal model. The thermal model for a two-dimensional, steady-state, heat conduction-convection problem is governed by the following partial differential equation:

$$k\left(\frac{\partial^2 T}{\partial x^2} + \frac{\partial^2 T}{\partial y^2}\right) - \rho C_p\left(u\frac{\partial T}{\partial x} + v\frac{\partial T}{\partial y}\right) + \dot{Q} = 0 \quad (9)$$

where k is the thermal conductivity, ρ is the mass density, C_p is the specific heat, and $\dot{Q}$ is the volumetric heat generation rate defined as:

$$\dot{Q} = \tau\dot{\gamma} + \tau_f V_s \quad (10)$$

where τ is the effective flow stress, $\dot{\gamma}$ is the effective strain-rate, τ_f is the interfacial shear stress, and V_s is the sliding velocity of the chip along the rake face. The first term in this equation is the heat generated due to the plastic work in the entire workpiece, and the second term is the heat generated due to the frictional sliding along the tool/chip interface. Because only a small portion of the workpiece and the tool is modeled, the thermal boundary conditions must be chosen very carefully. In particular, the boundary of the tool in the model is actually an internal boundary. Therefore, prescribing a room temperature condition on this boundary is not realistic. However, this problem can be overcome by reducing the thermal conductivity of the elements along the boundary of the tool to account for the portion of the tool that is not included in the model.

The thermal finite element equations can be derived from the temperature equation (9) by using a standard Galerkin approach. Expressing the temperature in terms of the same shape functions as in equation (7) leads to

$$[K]^e\{T\}^e = \{F\}^e \quad (11)$$

where $\{T\}^e$ is the nodal temperature vector and

$$[K]^e = \int_{x,y} k\left(\frac{\partial[N]^T}{\partial x}\frac{\partial[N]}{\partial x} + \frac{\partial[N]^T}{\partial y}\frac{\partial[N]}{\partial y}\right) dxdy$$

297

$$+ \int_{x,y} \rho C_p [N]^T (u \frac{\partial [N]}{\partial x} + v \frac{\partial [N]}{\partial y}) \ dxdy \quad (12)$$

and

$$\{F\}^e = \int_{x,y} [N]^T \dot{Q} \ dxdy \quad (13)$$

Note that the workpiece, chip, and tool are included in the thermal model, so that a complete mapping of the temperature field in the workpiece and tool can be determined.

3. DIAMOND TOOL WEAR MECHANISMS

In the next two sections, the relative contribution of abrasion and diffusion-controlled wear to flank wear will be investigated.

3.1 Abrasion Wear

The high speed flow of workpiece material across the flank of the tool provides an ideal condition for abrasive wear. Abrasive wear is governed by Archard's wear law:

$$W = K_1 PS \quad (14)$$

where W is the wear volume, P is the normal load, S is the sliding distance, and K_1 is the wear volume per unit load per unit sliding distance, or wear constant. This equation can be used to find the wear rates by replacing the sliding distance S by the relative sliding velocity.

To investigate the contribution of abrasive wear to overall flank wear, previously reported diamond turning experiments with worn tools were carried out in which changes along the cutting edge and clearance face were measured (12). A straight edge tool with a 0° rake angle and a 6° clearance angle was used to plunge cut a plated copper workpiece to a depth of 1 mm. The width of the cut was normalized to 1 mm. The wear was determined by directly measuring the wear land and indirectly determining the tool edge radius from the measured tool forces. The worn tool geometry can be determined from the wear land length, tool edge radius, rake angle, and clearance angle, which can then be used to compute the wear volume. Table 1 summarizes the changes in the tool geometry as a function of the cutting distance for diamond turning of copper. The change in tool geometry is shown schematically in Figure 1.

The volume worn away can be converted to wear rate $\dot{W}$ by:

$$\dot{W} = AwV/d \quad (15)$$

Table 1: Worn tool geometry variation.

Distance (Km)	Edge Radius (mm)	Wear Land (mm)
10	0.10	0.9
20	0.18	1.2
40	0.59	1.8
70	0.84	2.7
100	0.95	3.3

where A is the measured wear area, w is the width of cut, V is cutting velocity, and d is the distance cut between measurements. Using this equation for a 10 m/s cutting speed and cutting width of 1 mm, the wear rates for various elapsed distances can be calculated, which are summarized in Table 2. The last column of Table 2 shows the wear rate divided by the average wear land length. Note that the relatively constant normalized wear rate implies a wear process that is dependent on the area of contact.

Values of K_1 of 1.4 to 4.1 $* 10^{-12}$ mm^3/Nm have been determined using slow speed rubbing tests of diamond on copper (1). Using these values and the measured thrust forces, abrasive wear rates of 6.02 to 17.6 x 10^{-12} mm^3/s are predicted by equation (14). The range of values of K_1 are due to the uncertainty in the crystal orientation of the diamond tool. Note that these computed wear rates are much lower than the measured wear rates. Therefore, abrasion is not the dominant wear mechanism and the bulk of the wear must be accounted for by another mechanism.
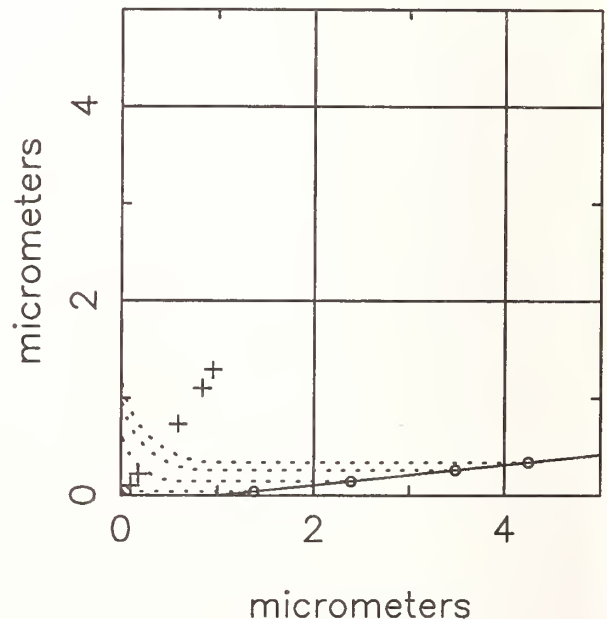

Figure 1: Worn tool profile.

298

Table 2: Tool wear rates.

Case (Km)	Total Area (mm^2)	Wear Rate (10^{-12} mm^3/s)	Norm'lzed. Wear Rate (10^{-9} mm^2/s)
10 - 20	0.0536	54	45
20 - 40	0.315	158	84
40 - 70	0.698	233	79
70- 100	0.964	312	83

3.2 Diffusion-Controlled Wear

Solid state diffusion of carbon atoms from the diamond tool to the workpiece is governed by Fick's First Law, which is given by

$$J = \left(-D\frac{\partial C}{\partial x} \right) \qquad (16)$$

where J is the diffusion flux, C is the concentration of carbon atoms, and D is the diffusion coefficient. In this equation, the diffusion coefficient depends on the temperature T as,

$$D = D_0 \exp\frac{-\Delta E_D}{RT} \qquad (17)$$

where D_0 is the frequency factor, ΔE_D is the activation energy, and R is the universal gas constant. These equations are coupled to the thermal analysis through the temperature dependence of the diffusion coefficient. Once the temperature distribution has been determined in the tool, the temperature dependent diffusion coefficient along the tool/chip interface can be found. Solving Fick's First law gives the diffusion flux, which is directly related to diffusion wear of the tool.

The previous equations can also be used to calculate the temperature required to produce an experimentally observed wear pattern due to diffusion. The carbon concentration gradient can be estimated by setting the separation between the tool and the workpiece to be equal to the atomic lattice parameter. The concentration of carbon atoms in the tool is fixed and the concentration of carbon atoms in the chip is zero, so that the concentration gradient can be approximated as:

$$\frac{\partial C}{\partial x} = \frac{C_{tool}}{l_{dia}} \qquad (18)$$

where C_{tool} is the concentration of carbon atoms in the tool and l_{dia} is the lattice parameter of diamond. Note that the carbon concentration in the chip remains essentially zero due to the short time of contact with the tool. The flux required to produce a given wear depth is :

$$J_{req} = \frac{d_{wear}C_{tool}}{t_{mach}} \qquad (19)$$

where J_{req} is the required flux, d_{wear} is the depth of wear damage, and t_{mach} is the machining time. Equations (16) through (19) can then be solved for the temperature (T_{req}) necessary to account for the observed wear:

$$T_{req} = \frac{\dfrac{-\Delta E_D}{R}}{\log\left(\dfrac{d_{wear}\, l_{dia}}{t_{mach}}\right) - \log D_0} \qquad (20)$$

where l_{dia} is the lattice parameter of diamond, d_{wear} is the depth of wear damage, and t_{mach} is the machining time. For the interstitial diffusion of carbon atoms into copper, $D_0 = 74. \times 10^{-6}$ m^2/s and $\Delta E_D = 37.9$ kcal/mole (13). This equation can be applied to the previous wear experiments by setting R = 1.98 cal/mole K, $t_{mach} = 9000$ sec, and $l_{dia} = 0.35$ nm. Using equation (20), a temperature of 254 $^{\circ}$C along the flank of the tool is required to account for all of the observed wear for a distance of 10 to 100 Km.

4. PREDICTION OF TOOL TEMPERATURES

Diffusion-controlled wear depends exponentially on the temperature in the tool. Therefore, an accurate assessment of the role that diffusion plays in flank wear is highly dependent on accurate determination of the tool flank temperatures. Tool temperatures can be determined with the finite element model described in a previous section. Figure 2 shows the finite element model of the workpiece, chip, and tool. An enlarged view of the region near the cutting edge is shown in Figure 3 in which the predicted temperature contours are also shown. Note that the maximum temperature of the tool is 175 $^{\circ}$C and it occurs near the cutting edge.
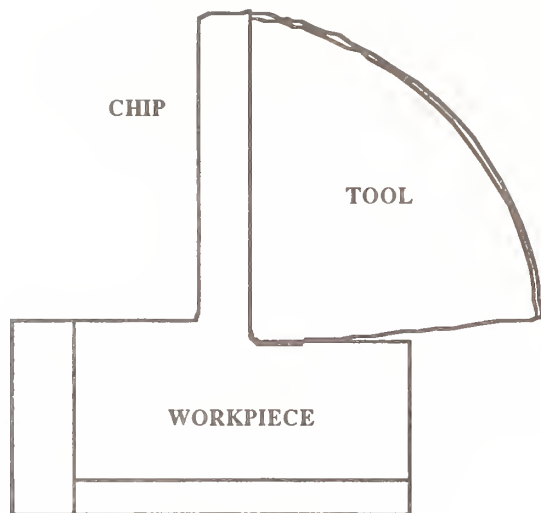
Figure 2: Finite element model of tool and workpiece (with flank).

Figure 4: Predicted temperature contours ($^{\circ}$C) near tool edge (with flank).
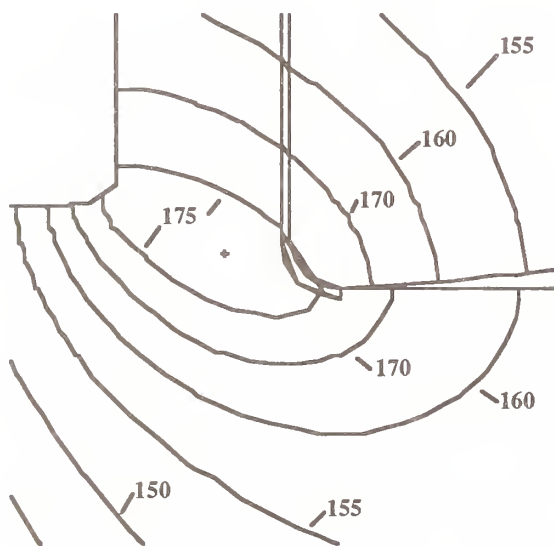

Figure 3: Predicted temperature contours ($^{\circ}$C) near tool edge (without flank).

Figure 4 shows the temperature contours with a tool flank included. Note that this figure corresponds to an edge radius of 0.59 mm and a flank land length of 1.6 mm. The inclusion of the flank in the model results in a 75 $^{\circ}$C increase in temperature along the flank to 250 $^{\circ}$C. This is in good agreement with the required temperature of 254 $^{\circ}$C for the observed wear due to diffusion.
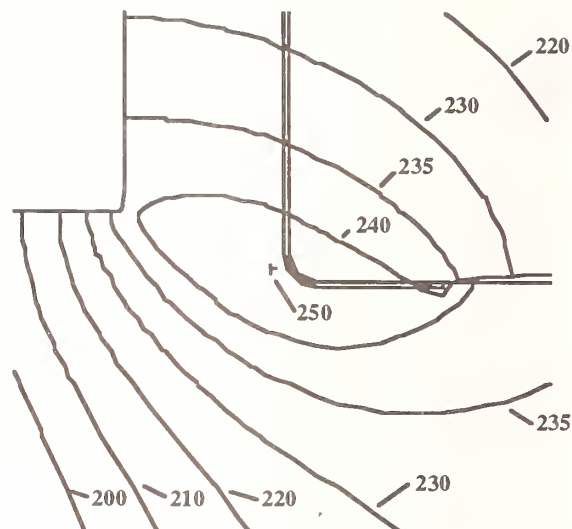
The temperatures predicted by the finite element model can be verified by calculating the temperature rise along the flank of the tool due to friction as follows. The energy due to frictional heating on the flank $\dot{E}_{flank}$ is given by:

$$\dot{E}_{flank} = B_2 F_{ff} V_c \qquad (21)$$

where F_{ff} is the measured frictional force on the flank and V_c is the cutting speed. Assuming that the average temperature rise in the workpiece and tool are equal, the fraction of frictional heat along the flank face that flows into the workpiece is given by Jaeger (14) as:

$$B_2 = \frac{k_{wp}}{k_{wp} + k_t} \qquad (22)$$

where k_{wp} and k_t are the thermal conductivities of the workpiece and tool, respectively. For a thermal conductivity of 7.03 W/cm $^{\circ}$C for type 1 diamond, and 3.95 W/cm $^{\circ}$C for the copper workpiece, this fraction equals 36%. Note that because of the large thermal conductivity of diamond as compared to copper, the majority of the heat (64%) flows into the tool, which is the opposite of what occurs in conventional cutting where the bulk of the heat flows into the workpiece.

The bulk temperature rise due to frictional heating along the flank can now be calculated using the energy balance:

$$\Delta T = \frac{\dot{E}_{flank}}{m \dot{C}_p \rho} \qquad (23)$$

where ΔT is the temperature rise, C_p is the specific heat, and ρ is the density. The mass flow rate $\dot{m}$ is found by assuming that the workpiece can be modeled as two strips of material. One strip represents the chip with a depth equal to the depth of cut, and the other is imbedded in the workpiece subsurface. This strip carries heat into the flank region of the workpiece. Because of the short duration that the workpiece is in contact with the tool flank, it is reasonable to assume that this portion of the heat is confined to only the subsurface region of the workpiece.

This equation can now be used to determine the temperature rise due to frictional heating along the flank. Using a measured frictional force on the flank of 0.71 N/mm for a 10 m/s cutting speed gives a temperature rise of 74 $^{\circ}$C for a mass flow rate based on a strip of material equal to the depth of cut. Note that the incoming temperature of the workpiece in the flank area is predicted from the finite element model with no flank to be 175 $^{\circ}$C, as shown in Figure 3. Therefore, the total temperature of the tool flank is 250 $^{\circ}$C, which agrees with the required temperature calculated in equation (20) for the observed wear and the temperature predicted by the finite element model with a flank, as shown in Figure 4. Therefore, diffusion-controlled wear is a likely mechanism of flank wear for a diamond tool.

5. CONCLUSIONS

Wear due to solid state diffusion and abrasion wear have been investigated for their relative contribution to overall flank wear. A finite element model of the cutting process was used to determine the temperatures in the tool. In addition, a thermal analysis was conducted to determine the temperature rise due to friction heating along the flank of the tool. By coupling this temperature information with a model of wear, the relative contributions of diffusion-controlled wear and abrasion effects were assessed.

It was found that computed tool temperatures were consistent with temperatures required for producing a prescribed level of observed wear from experimentally-measured worn tools. Because the required temperatures were based on a diffusion-controlled model of wear, it can be concluded that solid-state diffusion of carbon from the diamond tool is a plausible mechanism for flank wear.

REFERENCES

1. D. Crompton, W. Hirst, M.G.W. Howse, "The Wear of Diamond", Proc. R. Soc. Lond. A, 333, pp. 435-454, 1973.

2. G. Davies, T. Evans, "Graphitization of Diamond at Zero Pressure and at a High Pressure", Proc. R. Soc. Lond. A, 328, pp. 413-427, 1972.

3. J. Wilks, E. Wilks, Properties and Applications of Diamond, (Butterworth-Heinemann Ltd, Oxford), 1991.

4. K. Iwata, T. Moriwaki, K. Okuda, "A Study of Cutting Temperature in Ultra-High Precision Diamond Cutting of Copper", 15TH North American Manufacturing Research Conference Proceedings, 1987 SME Manufacturing Technology Review, 2, pp. 510-515, 1987.

5. C.J. Evans, R.L. Lundin, E.S. Paul, R.S. Polvani, D.D. Stewart, E. Whitendon, Proceedings of the Seventh Annual Meeting of the American Society for Precision Engineering, pp. 57-60, 1992.

6. J. Drescher, T.A. Dow, in Precision Engineering Annual Report (North Carolina State University, Raleigh, NC), Vol. VIII, 1990.

7. J.T. Carroll III, J.S. Strenkowski, "Finite Element Models of Orthogonal Cutting With Application to Single Point Diamond Turning,", International Journal of Mechanical Sciences, Vol. 30, pp. 899-920, 1988.

8. J.S. Strenkowski, J.T. Carroll III, "An Orthogonal Metal Cutting Model Based on an Eulerian Finite Element Method," Manufacturing Processes, Machines and Systems, Proceedings of the 13th NSF Conference on Production Research and Technology, pp. 261-264, 1986.

9. J.S. Strenkowski, K.J. Moon, "Finite Element Prediction of Chip Geometry and Tool/Workpiece Temperature Distributions in Orthogonal Cutting", ASME Journal of Engineering for Industry, Vol. 112, pp. 313-318, 1990.

10. O.C. Zeinkiewicz, P.N. Godbole, "A Penalty Function Approach to Problems of Plastic Flow of Metal with Large Surface Deformations", J. of Strain Analysis, Vol. 10, p. 180, 1975.

11.   R.C. Cook, D.S. Malkus, M.E. Plesha,
       Concepts and Applications of Finite
       Element Analysis, (John Wiley & Sons,
       New York, New York), 1989.

12.   J.D. Drescher, PhD Dissertation, North
       Carolina State University, 1992.

13.   D. Bergner, "Diffusion of Heavy
       Interstitials in Metals", Metallurgia I
       Odlewnictwo, Vol. 12, No. 4, pp. 379-400,
       1986.

14.   J.C. Jaeger, "Moving Sources of Heat and
       the Temperature of Sliding Contacts", Proc
       of the Royal Society, NSW, Vol. LXXVI,
       pp. 203-224, 1942.

DEPTH PROFILING OF RESIDUAL STRESS ALONG INTERRUPTED TEST CUTS IN MACHINED GERMANIUM CRYSTALS

R. G. SPARKS
Alcoa Technical Center, Alcoa Center, PA

M. A. PAESLER
North Carolina State University, Raleigh, NC

Residual stress profiles in machined germanium have been determined by measuring the longitudinal optical phonon spectra using micro-Raman spectroscopy. Lateral spatial resolution of 1 μm results from this direct non-destructive technique. By measuring the Raman spectra with several probe wavelengths, axial resolution of 10 nm is obtained through differential absorption profiling, or DAP. The stress field in these machined brittle semiconductors is characterized by a surface layer under compression, an abrupt compressive-to-tensile transition, and a deeper-lying region of tension which ultimately relaxes in the unstressed bulk. The abrupt transition is indicative of a change from plastic to elastic deformation. The DAP technique has been applied to interrupted test cuts in diamond-turned germanium to reveal that fractured regions of the machined surface possess higher tensile stress that occurs at shallower depths than unfractured regions. A qualitative mechanism of the machining process consistent with these residual stress data is presented.

Introduction

Previous Raman investigations of residual stresses in thin films have assumed that the stress field is contained only in the film with very little penetration of the stress into the sample substrate. Such studies also generally assume that the magnitude of the stress is constant throughout the film with no variations occurring axially. (1 - 4) Stress in these films will result in Raman spectra that are shifted by an amount which is indicative of the changes in the frequencies of the normal modes of vibration in the crystal. Since the stress is constant throughout the depth of the film there is little or no evidence of asymmetry in the shifted Raman peaks and the analysis of the stress magnitude is straightforward. In samples that display a continual variation in the stress field such as that occurring in a polished or single point diamond turned material, the above assumptions can no longer be made.(5, 6) The stress in this case is again contained in a thin surface region analogous to the case of a grown or deposited film but there is no distinct boundary for the termination of the stress field. In such cases the stress field may also be a continuously varying quantity with respect to depth into the sample. In such cases the Raman peaks are not only observed to be shifted, but are also seen to be asymmetrically broadened by the superposition of a continuum of stress states occurring axially in the material. The observed lineshape of the resulting Raman signal can be quantitatively analyzed by mechanisms based on the convolution of the penetration depth of the light and the depth of the stress field.(5 - 9)

The occurrence of asymmetrically broadened Raman peaks can be understood if one assumes that the residual stress field varies continuously with depth. By probing greater and greater depths in the material through the use of successively

longer wavelengths of light one obtains stress information from a broad overlying region of the sample. This leads to a superposition of a continuum of Raman peaks, with each infinitesimal peak shifted by the stress field. A Raman spectrum obtained in such a material measures this superposition of Raman signals. The resulting spectrum displays a broadening of the features. Superposition broadening can be exploited to obtain high axial resolution depth profiles of residual stress by computer profiling of the stress based on the broadened and shifted Raman features.(5 - 7)
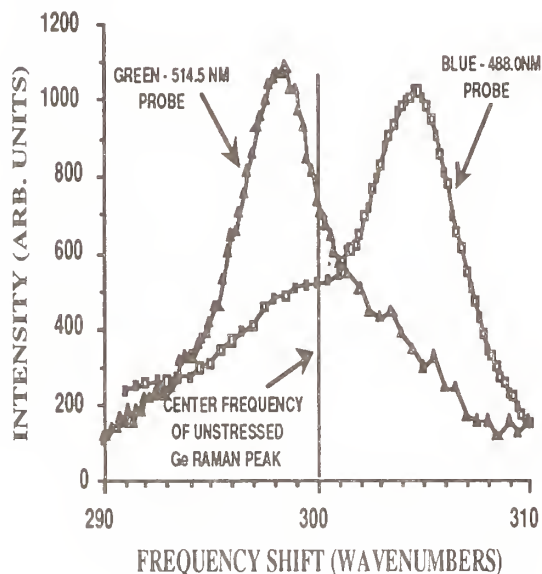

Figure 1. Asymmetrically Broadened Raman Spectra. Micro-Raman spectra obtained using 514.5 and 488.0 nm probe wavelengths are displayed for a single point diamond turned Ge crystal. Note the respective shifts of the resulting peaks from the unstressed position of 300 cm^{-1} as well as the asymmetric broadening induced in each case.

Figure 1 shows micro-Raman spectra obtained in the ductile region of a feed cut in germanium for both 514.5 and 488.0 nm probe wavelengths.(5, 6) The asymmetric broadenings of the Raman lines are clearly seen. An important detail of the spectra is the evidence of a shift of the peak position towards compressive stress in the 514.5 nm (green) data and a shift of the peak in the opposite direction (tensile stress) for the

488.0 nm (blue) data. Both green and blue spectra show clear evidence of asymmetry. The asymmetry is also clearly seen to be wavelength dependent since the green peak broadens toward lower <u>absolute</u> wavenumbers (tensile stresses) while the blue data broadens toward higher <u>absolute</u> wavenumbers (compressive stresses). If the broadening were due to spectrometer error one would expect both green and blue data to show asymmetries that were similar to one another toward either higher or lower wavenumber. Figure 1 clearly indicates that this is not the case.(5, 6, 10)

Differential Absorption Profiling of Residual Stresses

When light of intensity I_0 penetrates a solid, the intensity, I, at any depth z will be determined by an exponential decay of the incident field. In the case of Raman scattering, the light must penetrate to a depth z before being scattered and it must return to the surface in order to be collected; therefore, the intensity of the Raman signal from any depth, z, will be proportional to $e^{-2\alpha z}$. The absorption coefficient for the scattered light is actually very slightly different from that of the incident light but these slight variations do not affect the analysis and will not be considered. The value of the absorption coefficient, α, depends on both the material of interest and the energy of the incident light.(11) The exponential decay of the intensity of the Raman signal with depth combined with the variation of the absorption coefficient with photon energy makes determination of stress profiles from Raman spectra in opaque semiconductors possible. Other investigations of polish induced surface strain in semiconducting materials such as InP and GaAs have assumed that the stress field is an exponentially decaying function of depth.(8, 9) While such an assumption may be valid for stress induced damage occurring at the surface of a polished sample it is not valid, in general, for the process of single point diamond turning, which typically displays little or no surface damage in regions of ductile material removal.(5, 6, 10) The stress fields generated are thus qualitatively different

from those produced in samples with polish induced surface damage only.

In our analysis of Raman spectra, we found that in test cases, the stress profiling was not a function of the choice of the analytical lineshape chosen for the Raman spectrum at a given depth. That is, both a Lorentzian and a Gaussian assumption resulted in essentially the same stress profile for a given set of input data. The lack of response of the differential absorption profiling technique to the changes in lineshape may be attributed to the similarity of both Gaussian and Lorentzian lineshapes near the peak position. Significant variations between these lineshapes occur at positions more widely separated from the peak location where the effects of instrument noise may be expected to dominate any slight effects from the lineshape differences. The convergence of the DAP analysis is much slower when using the Lorentzian, thus in order to expedite convergence a Gaussian lineshape was used in this analysis.(10) The analytical expression for the intensity of the Raman signal, $R(\omega)$ is then given by;

$$R(\omega) = A \int \exp(-2\alpha z) \exp\left[\frac{-(\omega-\omega_z)^2}{2\sigma^2}\right] dz$$

where $\omega_z = \omega_0 + S(z)$ This expression consists of an integral over all depths and contains an exponential decay which modifies the assumed Gaussian lineshape. The Gaussian is located at angular frequency ω_z and has an associated natural line width $2\sigma^2$. The amplitude factor, A, is included to scale the integral to the measured Raman data. The depth dependence, z, enters expression in the exponentially decaying intensity factor and in ω_z. The term ω_z consists of the location of the unshifted Raman signal, ω_0, plus the shift induced due to the stress at each incremental depth dz. This shift function, $S(z)$, will hereafter be referred to as the stress profile and is the quantity of interest in this investigation.

A depth, z_0, is chosen such that beyond this depth the stress may realistically be presumed to vanish. The integral in the Raman function is naturally divided into two regions, greater and less than z_0. Where the stress is zero $(z > z_0)$, the Gaussian lineshape can be taken outside the integral and the remaining integral can easily be solved analytically. For $0 < z < z_0$, the stress is changing and the integral can only be solved numerically. Numerical integration involves dividing the interval into dz elements and evaluating the function at each incremental depth dz. Therefore the stress function, $S(z)$, must be evaluated at each dz regardless of its functional form. The stress at each depth can be made a parameter that is free to vary. The function to be fitted becomes

$$R(\omega) = \sum_j \exp(-2\alpha z_j) \exp\left\{\frac{-(\omega-[\omega_0+S(z_j)])^2}{2\sigma^2}\right\} dz + \frac{A}{2\alpha} \exp[-2\alpha z_0] \exp\left\{\frac{-(\omega-\omega_0)^2}{2\sigma^2}\right\} + bk$$

The first term is the integral over a depth of zero to z_0 of the assumed Gaussian lineshape. The second term is the integral of the Gaussian lineshape from a depth z_0 to infinity and is constant for a given value of z_0. An additional term, bk, allows for a background correction. This correction amounts to removal of a constant number of dark counts from the Raman spectra. The only parameters free to vary are the $S(z_j)$'s, the residual stresses at each depth; thus the stress profile can assume any form, even if it is discontinuous.

Least squares data analysis involves minimization of the sum of the squares of the differences between the experimental, Y_{exp}, and the calculated data, Y_{fit}. This sum of squares is referred to as χ^2, and

$$\chi^2 = \sum \frac{(Y_{exp}-Y_{fit})^2}{\eta^2}$$

where η^2 is the experimental uncertainty associated with each data point. Since the Raman data are collected in a photon

counting mode, the data follow Poisson statistics and the uncertainty, η is equal to the reciprocal of the square root of the number of counts (typically $\eta \leq 0.01$ near the Raman peak).(12) The interval from zero to z_0 is divided into an appropriate number of intervals, each having width dz. The Raman function is approximated by the above sum, and the stress at each depth is varied until the calculated Raman signal corresponds to the one obtained experimentally by minimization of χ^2.

χ^2 is a function of the experimental uncertainties and the parameters $S(z_j)$. These parameters span a j dimensional parameter space. There are a number of standard methods for minimizing the function χ^2, which involve searching parameter space for the smallest value of χ^2.(12) A grid search least squares technique is employed which involves the independent variation of each parameter, $S(z_j)$, until χ^2 is minimized. The next parameter is adjusted, following a grid in parameter space. The above procedure is repeated until the incremental change in χ^2, that is $\Delta\chi^2$, is less than some specified value (typically 1%). The disadvantage of this method is that convergence is very slow since each parameter is adjusted independently while holding all the others constant. It is also implicitly assumed that the various χ^2's are optimal, or near optimal. In the initial stages of the fit (i.e. far from the minimum χ^2), this is not the case and this effect contributes to the slow convergence of this method. The criterion for a good fit is determined by minimizing χ^2. If data are taken with green and blue laser lines, it, is possible to define a χ^2_{blue} and χ^2_{green} to measure the deviations from the blue and green data respectively. The simplest solution to this problem is to minimize the total χ^2 defined as the sum of χ^2_{blue} and χ^2_{green}, or

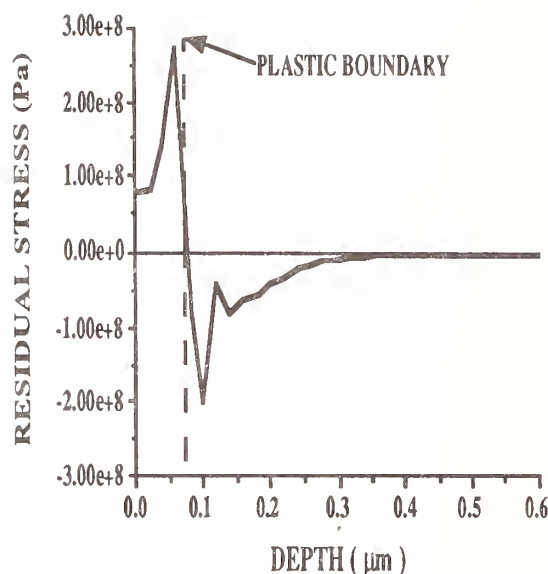$$\chi^2_{tot} = \chi^2_{blue} + \chi^2_{green}$$

Figure 2. A depth profile of residual stress in machined Ge. The depth profile was obtained using 514.5 and 488.0 nm probe wavelengths from the spectra shown in Figure 1. The surface displays a zone of compression with a counterbalancing region of tension beneath. The abrupt change from compressive to tensile stress is indicative of the plastic/elastic boundary.

A typical stress profile obtained from machined Ge using the technique described above is shown in Figure 2. The single crystal of Ge was prepared by single point diamond turning the surface of the crystal via a facing cut in the form of a flat region. The facing cut was performed using a -10° rake angle, 6° clearance angle diamond tool with a maximum depth of cut of 240 μm. The infeed rate utilized was 2.5 μm/rev, with a spindle speed of 6.28×10^3 rad/sec. The depth resolution of this technique is determined by the distance between the $S(z_j)$'s. A value of 10 nm is typically used for this spacing and changes in the residual stress have been observed over this scale, indicating that this value is a good upper-bound for the depth resolution in this system. The maximum depth resolution for this technique is determined by the value of the absorption coefficient for the light used, with higher absorption coefficients giving greater depth resolution. Since the stress is changing over the volume sampled, it is inappropriate to

determine the magnitude of the stress from the peak value of the Raman signal alone. Initial depth profiles were generated using only 514.5 and 488.0 nm wavelengths. Though this procedure resulted in reasonable depth profiles the convergence time of this method was extremely slow. In an effort to decrease the convergence time as well as provide more reproducible data the number of light wavelengths used to probe the stress field was increased. The use of 514.5, 496.5, 488.0 and 457.9 nm excitation wavelengths decreased the convergence time of the deconvolution routine tenfold. Stress profiles generated using a greater number of wavelengths usually display fewer signs of numerical instability than do those obtained using the 514.5 and 488.0 nm wavelengths alone.

Residual Stresses Along Tool Shoulders in Interrupted Test Cuts

The fabrication of optical quality or precision surfaces in materials is of prime interest in both the electronics and optics industries. Classical techniques of grinding and polishing have allowed many ductile materials such as metals to be formed into figures with complex profiles. Recent advances in materials fabrication have used diamond crystals in either a grinding or turning mode for the production of high quality surfaces in materials such as ceramics and glasses as well as metals. In the process of single point diamond turning a diamond crystal is used like a conventional lathe tool to form surfaces of optical quality. The process of single point diamond turning has also allowed a number of otherwise brittle materials such as semiconductors and glasses to be machined in a ductile mode. In such cases the diamond turning technique can produce surfaces of optical quality with complex figure profiles such as aspheres (e.g off-axis paraboloids) with the introduction of little surface damage into the workpiece.(10)

The process of material removal via the technique of single point diamond turning in brittle materials, however, introduces stresses into the workpiece that can in some instances lead to undesirable effects such as figure deformation,

subsurface damage, or fracture. The fabrication of an optical quality surface with significant residual stress fields and/or subsurface damage is, therefore, counterproductive to the manufacture of a useful device. A non-destructive probe of residual stress states and subsurface damage in machinable brittle materials is thus indicated as an important tool for the evaluation of the quality of such machined surfaces. There exist a limited number of suitable non-destructive methods for characterizing the residual stress states in such machined materials. The technique of laser Raman spectroscopy has been proven to be useful for the non-destructive determination of stresses in thin films where the region of stress is typically contained in the film only. Brittle semiconductors such as silicon and germanium are easily measured using Raman spectroscopy and the Raman spectra are sensitive to the residual stress in such samples. In addition a non-destructive probe of residual stresses may be used to confirm the validity of various theoretical mechanisms of the machining action.(5, 6, 10)

The relation of the residual stress field to the transition between ductile and brittle fracture can play a significant role in understanding the physics of the material removal process in the machining of brittle materials such as germanium. It is hypothesized that a region of high compressive stress indicative of plastic deformation should exist at the leading edge of the diamond tool used to machine brittle materials such as germanium. The extent of this plastic deformation is expected to be much greater in magnitude than the stress field present in the finished surface due to the excessive deformation that must accompany material removal in the process of single point diamond turning. A further factor which can play an important role in the fabrication of smooth surfaces is also the depth and magnitude of the compensating zone of residual tension occurring in the machined sample. Although one might expect the stress field to display increasing surface tensile stress in regions of fracture, the results of this investigation have proven that this is not necessarily the case. Variations in the

magnitude and depth of the residual stress field might also expected for different machine parameters. High negative rake angle tools, for instance, have been found to result in stress fields of greater magnitude than tools with lower negative rake angle.(13)

An important method for the evaluation of the residual stress fields as well as the surface induced damage occurring during the process of single point diamond turning has been the formation of interrupted test cuts. Interrupted test cuts are made by rapidly removing the diamond tool during the process of machining. The rapid removal of the tool leaves behind a profile of the tool in the surface of the machined sample. The behavior of the remaining machined surface may then be studied as a function of position along the resulting profile. Such profiles typically display a range of behavior from purely ductile removal at the base of the profile at the level of the finished surface to a region of pure brittle fracture at the upper regions of the profile where no material removal has taken place. The profile remaining in the sample surface is often referred to as a tool shoulder and should not be confused with the actual diamond tool used in the machining process.

Depth profiles of the residual stress states as the probe spot is moved up the tool shoulder (toward the uncut portion) remaining in the machined sample after rapid removal of the diamond tool in interrupted test cuts were obtained using four wavelengths (476.5, 488.0, 496.7, 514.5 nm) at each probe location. The depth profiles of the residual stress remaining in the sample were investigated using the differential absorption profiling technique that was previously discussed. The depth of penetration of the compressive stress field as well as the depth of the plastic/elastic boundary has also been investigated as a function of position on the tool shoulder. The penetration of this stress field can then be related to the transformation from ductile to brittle material removal in single point diamond turning.
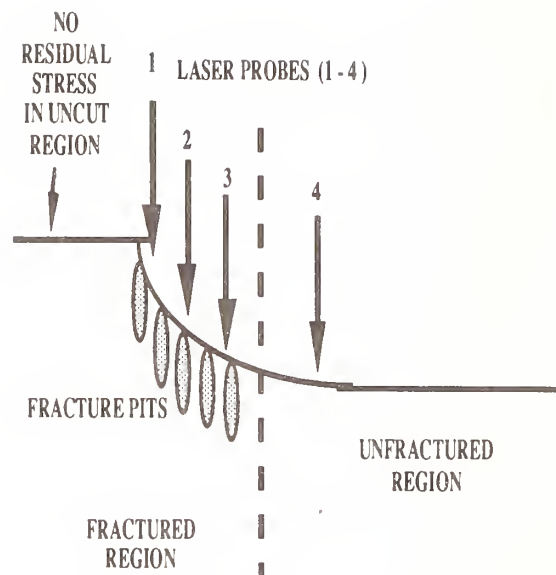

Figure 3. Probe positions for investigation of residual stress fields along interrupted test cuts remaining in the Ge sample after removal of the diamond tool. The laser probe positions are indicated by the arrows. The relative dimensions of the depth of the tool shoulder to horizontal position are not drawn to scale. In this case the diamond tool was moving from right to left (cross-feed direction) before being removed from the Ge workpiece. The workpiece motion due to spindle rotation is in a direction normal to the plane of the page.

The investigation of residual stresses in the interrupted test cuts remaining in the machined germanium samples were undertaken by locating the microscopic probe spot at various positions along the shoulder as shown in Figure 3. The probe spot was located at an indicated position and a micro-Raman spectrum was obtained using the longest wavelength (514.5 nm) probe. The laser was then tuned to the next wavelength without moving the probe position to ensure that each wavelength probed the same microscopic spot. The laser probe position was then moved to the next probe location where the process was repeated. All spectroscopic data were analyzed using the differential absorption profiling algorithm that has been previously discussed. The depth profiles which were
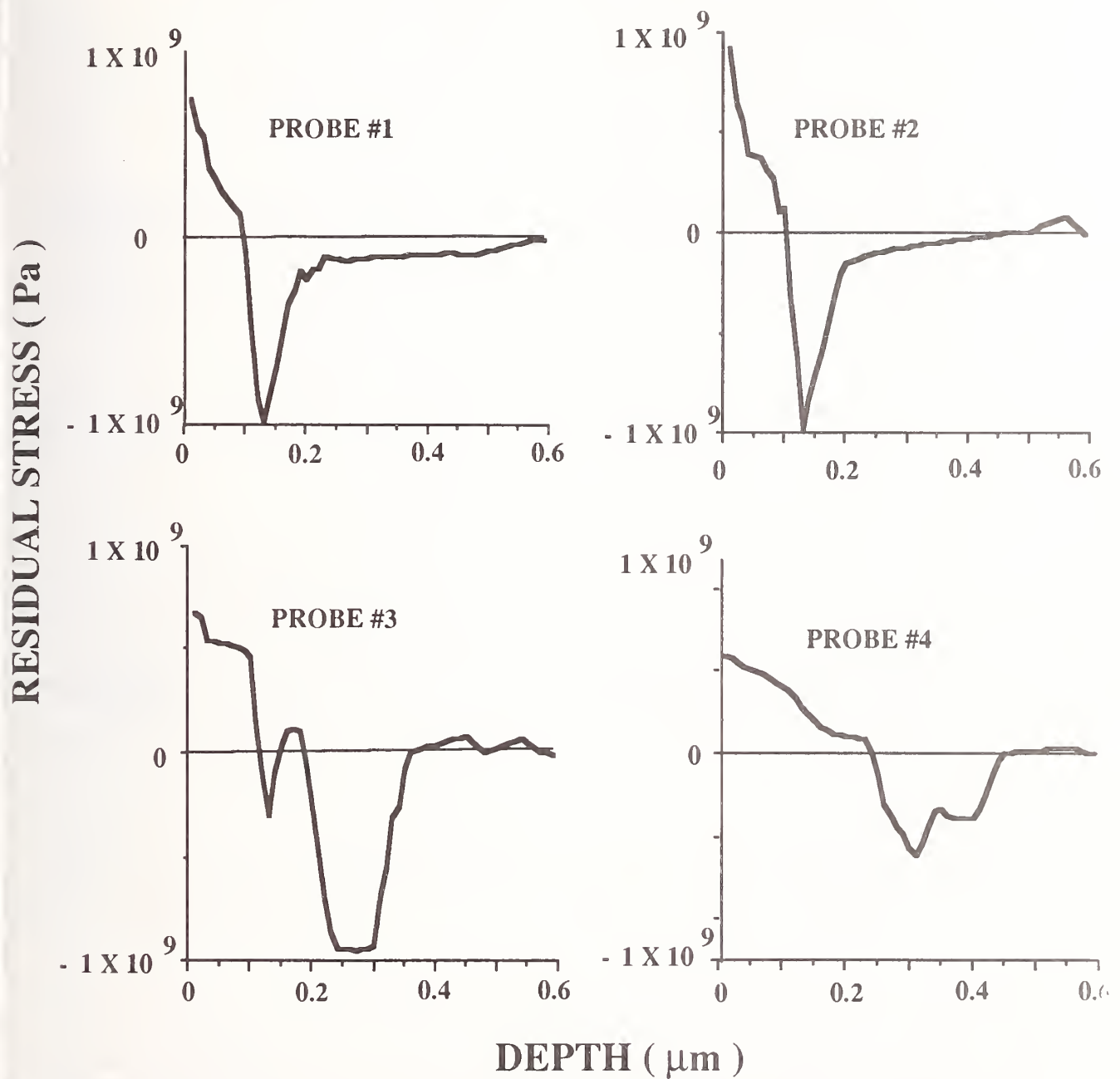
Figure 4. Depth profiles generated for -45° rake angle tool with low cutting speed. The profiles are shown in order of increasing distance from the uncut region. The bottommost profile was thus obtained in the ductile cut region with no surface damage evident. The displayed stresses can be considered to be accurate to within ± 10.0 MPa.
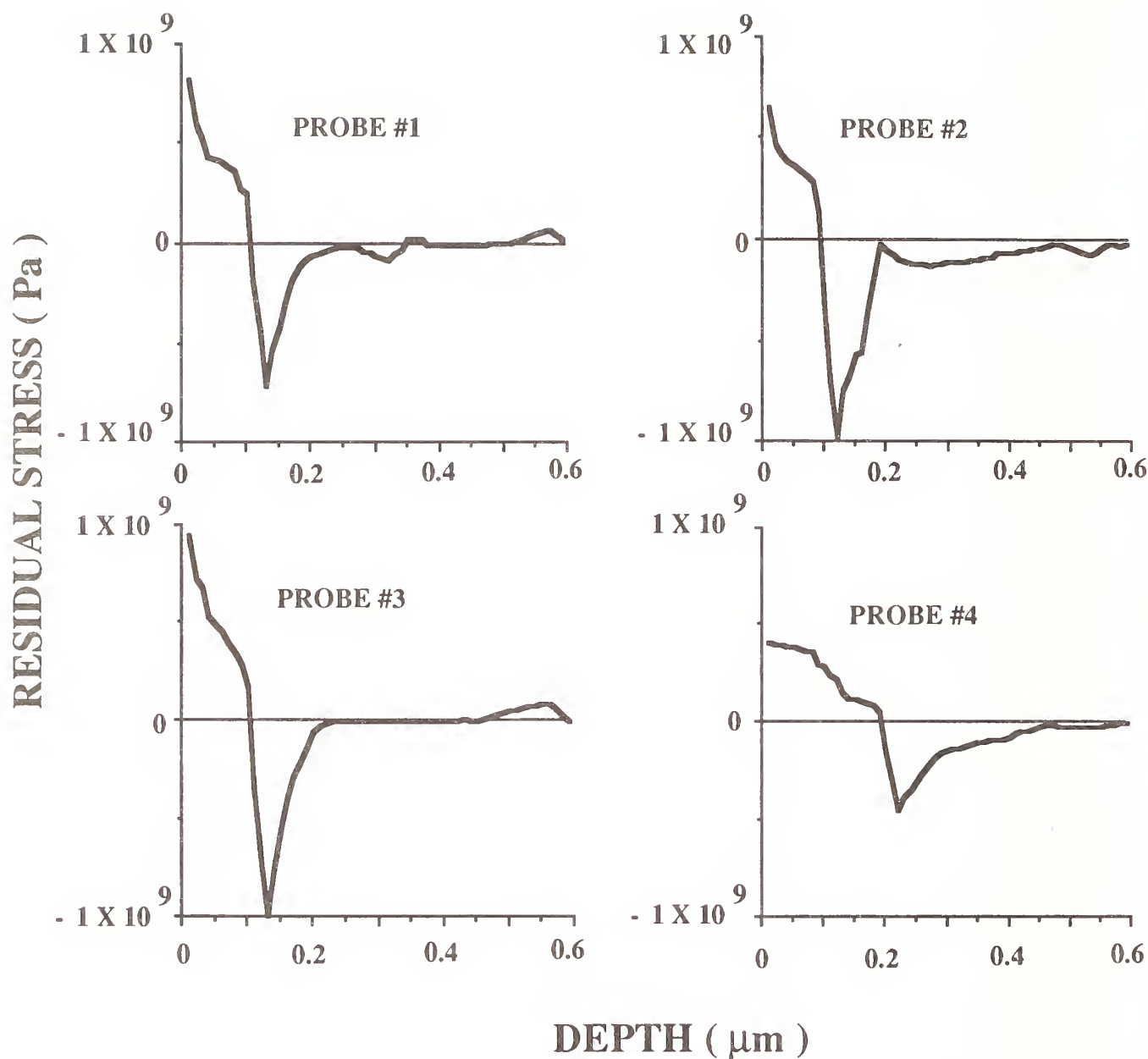
Figure 5. Depth profiles generated for the -30° rake angle tool. The profiles again are shown in order of increasing distance from the uncut region. Though similar to the case of the -45° rake angle tool several differences are evident in both the magnitude and depth of the resulting stress field. The displayed stresses can again be considered to be accurate to within ± 10.0 MPa.

generated from this data are reproducible to a high degree, i.e subsequent runs of the deconvolution program with small changes in background and amplitude parameters resulted in insignificant changes in the resulting depth profiles.

Several samples which were machined using several different rake angle tools (-45° and -30°, 2.5 µm/rev infeed rate, 240 - 500 µm depth of cut, 6° clearance angle) were investigated using this technique. The germanium wafer machined using the -45° rake angle tool was probed in two test cuts of different cutting speed (6.28 X 10^3 rad/sec, 15.7 X 10^3 rad/sec). The depth profiles resulting from these cutting speeds are approximately equivalent. The depth profiles generated for interrupted test cuts remaining after cutting by a -45° rake angle tool shown in Figure 4 show similarities to those generated for the -30° case shown in Figure 5. In both cases a general region of compressive stress is found at the sample surface. In the ductile cutting regime where there is little evidence of surface fracture the magnitudes of the compressive stress field for the -30° rake angle tool are ≈ 4.0 X 10^8 Pa. Significant differences in the maximum magnitude of the surface compressive field are evident as one moves up the tool shoulder into the visibly fractured region as shown in Figure 6. The compressive surface stress increases in magnitude until the average compressive component has roughly doubled the value found in the absence of fracture.

The maximum value of compressive stress is seen to occur at approximately the middle of the tool shoulder where the frequency of pitting and fracture is highest. The compressive field then diminishes as the probe position is moved toward the transition region where no cutting has taken place. A significant difference between the -30° and -45° rake angle tools is seen to be the relative magnitudes of the compressive surface stresses. In the fractured regions the higher negative rake angle tool is seen to produce a stress field of greater magnitude than the lower negative rake angle tool. In the absence of an applied force the total integrated stress must vanish

in the surface regions. The existence of a surface compressive stress field thus implies the existence of a counterbalancing tensile field lying beneath the compressive zone.(14, 15) The magnitude of the tensile field is directly proportional to the magnitude of the compressive surface zone. The maximum magnitude of the tensile field typically occurs at the approximate depth of the boundary between plastic and elastic deformation as illustrated in Figure 4. The magnitudes of the tensile stress field are plotted as a function of probe position in Figure 7 for the three cases studied. The same general trend as evidenced in Figure 6 for the surface compressive stress is again present in the deeper tensile field. Regions of high fracture possess a high tensile stress field which accompanies the greater surface compressive stress.
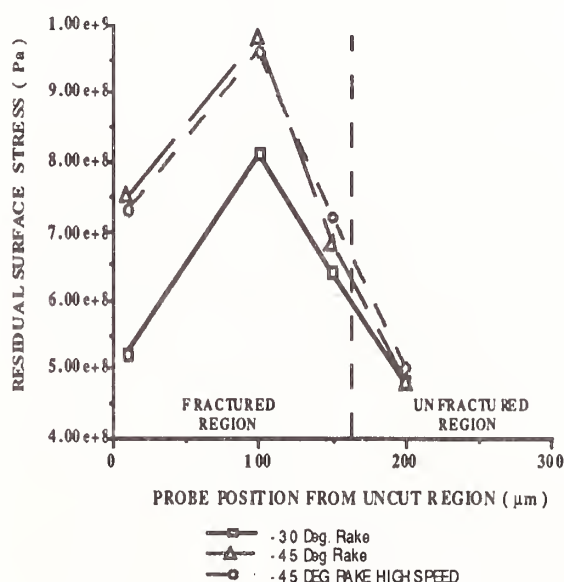

Figure 6. Surface compressive stress as a function of position from the uncut region. The approximate transition from ductile to brittle material removal is indicated by the vertical line. The compressive surface stress is seen to reach a maximum in the center of the fractured region. The displayed stresses are accurate to within ± 0.1 X 10^8 Pa.

Fractured regions are further characterized by the depth at which the transition from compressive to tensile stress occurs. In the regions which display

no fracture the transition from compressive to tensile stress occurs at a depth of 0.2 μm beneath the sample surface as indicated in Figure 8. Fractured regions typically display transitions that occur at shallower depths of 0.1 μm. The depth of transition is approximately constant for all probe positions measured in fractured regions. The transition from ductile cutting to fracture is thus characterized by two distinct features. The first is the magnitude of the stress fields (both compressive and tensile), the second being the depth at which the transition from plastic (compressive stress) to elastic (tensile stress) deformation has occurred.
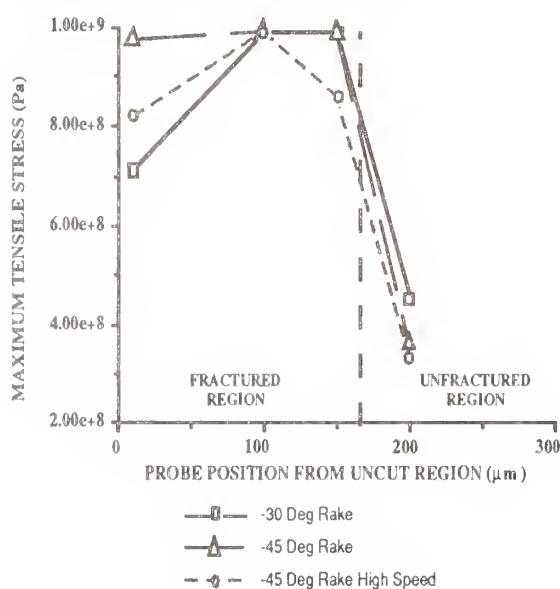

Figure 7. Maximum tensile stress as a function of probe position. The maximum magnitude of the tensile stress filed occurring beneath the compressive zone is plotted as a function of position from the uncut region. The stress is seen to follow the same general pattern of the compressive stress shown Figure 4. The vertical line indicates the transition form brittle to ductile material removal. The displayed stresses are accurate to within ± 0.1 X 10^8 Pa.

Surface Failure from Crack Nucleation at the Plastic/Elastic Boundary

The behavior of the residual stress field in the region of transition from ductile to brittle material removal suggests that the formation of a smooth surface with little or no evidence of surface fracture depends directly upon two important considerations. The first factor to be considered in the evaluation is the relative magnitudes of the compressive and tensile stress fields encountered in the sample. It has been well established by other researchers that machining, grinding and polishing processes give rise to a radially compressive residual field with a region of tangential tension outside the plastic zone which surrounds the contact site.(15) Our depth profiling investigations have confirmed these results, and it is suggested from the study presented in this section that if the magnitudes of the stress field reach a certain critical value then fracture ensues. Such a conclusion is consistent with the Griffith criterion for crack growth i.e when the critical value of stress is reached a crack will begin to propagate in an unstable manner.(16)

The depth at which the plastic/elastic boundary occurs is also demonstrated as an important factor in the formation of surface damage in a machined part. The process of plastic deformation, as discussed previously, relies on the motion of dislocations and defects through the crystal structure. At the transition from plastic to elastic deformation it has been noted by many researchers that the maximum values of the tensile stress in the elastic field occur at this transition. It has, in addition, long been known that dislocation density increases with increasing stress. The presence of high stress gradients in the vicinity of the plastic/elastic boundary thus give rise to a high defect and dislocation concentration in this region.(17,18) As previously discussed the fracture thresholds for median and lateral cracks (both subsurface varieties) are found to be nucleation limited because of the lack of preexisting flaws to serve as nucleation sites. The presence of dislocations and defects at the plastic/elastic boundary can then provide nucleation sites for microcracking to occur in either the median or lateral system.(19) The existence of microcracks alone, though adding to the degree of subsurface damage, does not in itself constitute a sufficient condition for

the propagation of cracks into the finished surface. The additional presence of a tensile stress field which lies at a sufficiently shallow depth, however, may serve to further open these microcracks and provide a driving mechanism for their unstable growth.(15)
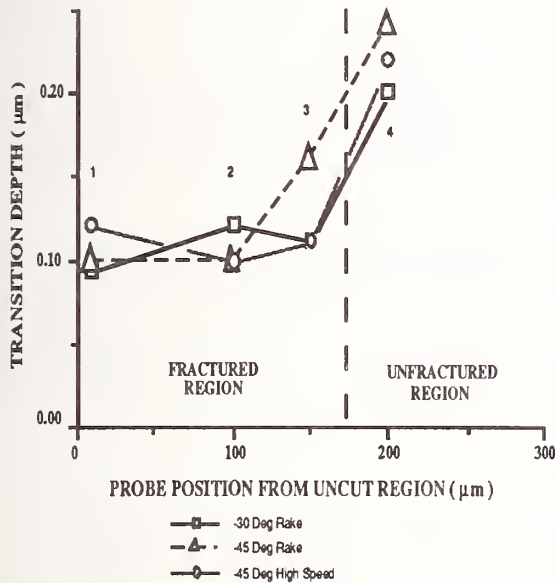

Figure 8. Transition depth versus probe position. The depth of transition from compressive to tensile stress is plotted as a function of position from the uncut tool shoulder edge. The vertical line again divides regions of fracture and non-fracture. The depth resolution in this case is ± 5 nm.

The investigations of residual stress fields occurring in interrupted test cuts points to the following mechanism for the transition from ductile to brittle material removal in the process of single point diamond turning. Ductile material removal takes place due to the large plastic deformations occurring in the material which accommodates plastic flow. The portion of material that is removed in this fashion is concentrated in a small region in the vicinity of the tool tip. The majority of material is removed high on the tool shoulder in a brittle fashion due to radial cracking which is activated from preexisting surface flaws in the material. Since the region of this brittle material removal is subsequently subjected to the high plastic deformation of the tool tip the

regions of brittle fracture are removed leaving a surface formed by plastic flow. If the compressive field arising from the plastic zone at the tool penetrates deeply enough, the effect of the residual tensile field as a crack opening force is counterbalanced. Microcracks may nucleate from dislocations and defects at the plastic/elastic boundary but will not derive sufficient driving force from the tensile field for their subsequent growth and propagation into the finished surface. If however the zone of plastic deformation penetrates to a more shallow depth the underlying tensile field will serve to drive the microcracks nucleated from the high defect and dislocation concentration at the plastic elastic boundary into the finished surface.

This mechanism provides a qualitative explanation for the improvement of surface finish and allowed depths of cut with increasing negative rake angle tools. Tools of large negative rake angle result in plastic deformation zones which penetrate more deeply than those of tools of lower rake angle. Since the resulting plastic/elastic transition lies more deeply in the sample than the transitions associated with lower negative rake angle tools the formation of microcracks lies more deeply beneath the surface which increases the ability of the surface to resist fracture formation. This trend may only be expected to apply for a range of negative rake angle tools since the accompanying stress magnitudes also increase with increasing negative rake angle. If a sufficiently large tensile stress magnitude is produced in the surface a point will eventually be reached at which the stress will result in unstable crack growth even though the transition boundary is relatively deep.

Summary
Micro-Raman spectroscopy has been used to measure the residual stresses in machined surfaces with a lateral resolution near the diffraction limit. We have extended this technique to incorporate axial resolution (i.e. depth into the sample) by using several excitation wavelengths, which, by virtue of their differing penetration depths, allow determination of

313

stress profiles as a function of depth into the sample. Greater depths in the material may be probed by using longer wavelengths of light thus leading to a superposition of a continuum of Raman peaks. Depth profiles of residuals stress can then be obtained using computer analysis of the resulting Raman spectra.

Surface fracture is characterized by high residual stresses as well as a shallow plastic/elastic transition depths. The high residual stress fields typically occur with a layer of compression at the surface with an underlying tensile region beneath. The transition depth from compressive to tensile stress is indicative of the transition from plastic to elastic deformation. The presence of high defect and dislocation concentrations in the vicinity of the plastic/elastic transition serve as nucleation sites for microcracks of the lateral and/or median system. When the plastic/elastic transition lies at a sufficiently shallow depth the residual tensile field will act to further open these microcracks resulting in their propagation and growth into the finished surface. If the stress fields are of low magnitude the constraints on the necessary penetration depth may be relaxed somewhat, i.e low stress fields may allow the plastic/elastic boundary to occur at shallower depths without surface failure than would higher stress fields.

REFERENCES

1. S. Lyon, R. Nemanich, N. Johnson, and D. Biegelsen, "Microstrain in laser recrystallized silicon islands on fused silica," Appl. Phys. Lett., **40**, 316 (1982)

2. Th. Englert, G. Arbstreiter, and J. Pontcharra, "Determination of Existing Stress in Silicon Films on Sapphire Substrate using Raman Spectroscopy," Solid State Elect., **23**, 31 (1980)

3. Y. Cheong, H. Marcus, and F. Adar, "Raman microprobe measurements of residual strains at the interfaces of Si on quartz," J. Mater. Res., **2**, 902 (1987)

4. S. Brueck, B. Tsaur, J. Fan, D. Murphey, T. Deutsch, and D. Silversmith, "Raman measurements of stress in silicon-on-sapphire device structures," Appl. Phys. Lett., **40**, 895 (1982)

5. R. G. Sparks and M. A. Paesler, "Micro-Raman analysis of stress in machined silicon and germanium," Prec. Eng. **10**, 191 (1988)

6. R. G. Sparks, W. S. Enloe, and M. A. Paesler, "Development of a high axial resolution Micro-Raman Technique for studying the effects of machine parameters in machined semiconductors," Microbeam Analysis 1989, 149 (1989)

7. W. Enloe, *Masters Thesis*, North Carolina State University, unpublished

8. H. Shen and F. Pollack, "Raman study of polish-induced surface strain in <100> GaAs and InP," Appl. Phys. Lett., **45**, 692 (1984)

9. Z. Hang, H. Shen, and F. Pollack, "Comprehensive investigation of polish-induced surface strain in <100> and <111> GaAs and InP," J. Appl. Phys, **64**, 3233 (1988)

10. R. G. Sparks, *Ph. D Thesis*, North Carolina State University, unpublished

11. S. Sze, *Physics of Semiconductor Devices*, pp. 40-44, (John Wiley & Sons, New York, 1981)

12. P. R. Bevington, *Data Reduction and Error Analysis for the Physical Sciences*, pp. 189-194, (McGraw-Hill, New York, 1969)

13. H. R. Philipp and E. A. Taft, "Optical Constants of Germanium in the Region 1 to 10 eV," Phys. Rev., **113** (4), 1003 (1959)

14. J. I. Pankove, *Optical Processes in Semiconductors*, pp. 34-87, (Dover, New York, 1971)

15. D. Johnson-Walls, A. Evans, D. Marshall and M. James, "Residual Stresses in Machined Ceramic Surfaces," J. Am. Ceram. Soc., **69** (1), 44 (1986)

16.   S. Chaing, D. Marshall and A. Evans, "The response of solids to elastic/plastic indentation, II. Fracture Initiation,"J. Appl. Phys., **53** (1), 298 (1982)

17.   C. Barrett, W. Nix and A. Tetelman, *The Principles of Engineering Materials*, pp. 226-236, (Prentice-Hall Inc., Englewood Cliffs, 1973)

18.   F. Mclintock, A. Argon, *Mechanical Behavior of Materials*, (Addison-Wesley, Reading, 1966)

19.   S. Chaing, D. Marshall and A. Evans, "The response of solids to elastic/plastic indentation, I. Stresses and residual stresses," J. Appl. Phys., **53** (1), 312 (1982)

DESIGN OF ULTRAPRECISION GRINDING MACHINES FOR DUCTILE MODE GRINDING OF BRITTLE MATERIALS

H. SHIMURA
Tokyo Metropolitan College of Aeronautical Engineering, Tokyo, Japan

F. HASHIMOTO
The Timken Co., Canton, OH

J. YOSHIOKA
NUTR K. K., Chiba, Japan

The field of ductile mode grinding of brittle materials using grinding wheels with a grain size larger than the ductile-brittle transition value d_c is defined as nano-grinding technology. In the present paper, new design concepts are introduced for a vertical spindle surface grinding machine, aiming at developing an ultraprecision and high stiffness machine tool for finishing of silicon wafer with 8 inch diameter. This concept is also applied to develop an ultraprecision centerless grinding machine. Both ultraprecision grinding machines have been built and evaluated through grinding tests. Effects of application of these concepts on motion accuracies and stiffness are shown by experimental results.

1. Introduction
(1) Technical problems in ductile mode grinding

In the case of mass production, ultraprecision grinding technology for brittle materials is principles of motion copying, ductile mode grinding with high copying accuracy and crack-free machining (grain size $>$ d_c), predictability of wheel wear in ductile mode, and programming of grinding processes in brittle mode and ductile mode for improving cost performance.

(2) Development of ultraprecision grinding machines and trueing cut grinding machines

The motion accuracies and system stiffness required for the machine tools and the trueing accuracies of grinding wheels for achieving the criteria of the ductile mode grinding are specified, and the following trial targets can be derived using the measure :
feed resolution : $d_c/10$,
straightness of carriage : d_c/travel range,
work and wheel support stiffness : no more deformation than the feed resolution under grinding load,
vibration level of work and wheel support system : d_c,
trueing accuracies : $< d_c$,
height distribution of cutting points : $< d_c$. ———— these items by M. Miyashita[1]

2. The applied design concepts
2.1 Force compensated hydraulic linear actuator

Two types of force compensated hydraulic linear actuator units are applied.

(A) Positioning system of wheel head with dual hydraulic linear actuators
Figure 1 shows the positioning servo system with dual force operated hydraulic linear actuators[2]. In Figure 2, a pressure difference between two cavities of the positioning actuator (p_1-p_2) corresponding to difference between command input and output of feedback displacement transducer actuates the piston of the positioning actuator to the place at the command position. Grinding wheel head slide is fed directly by a couple of actuators without any lead screws or gears in order to eliminate backlash. This system is one of multi-points drive.[2] The actuators face each other and they have their shares
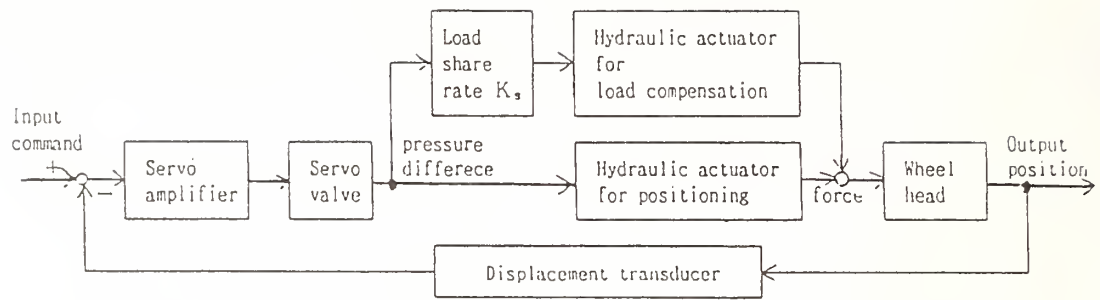
Figure 1 Block diagram of positioning servo system with dual hydaraulic linear actuators
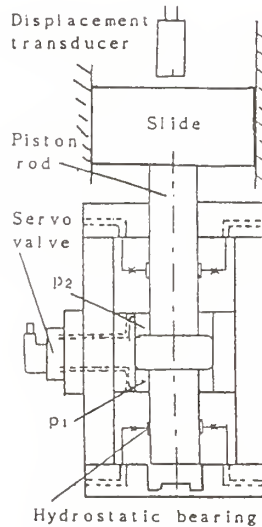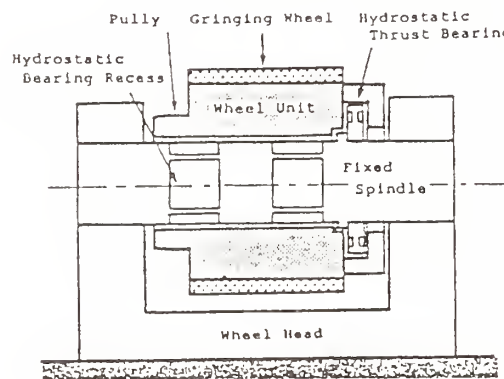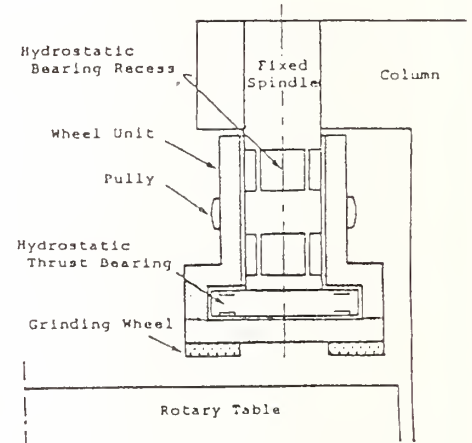

Figure 2 Hydraulic
linear actuator

(a) Construction of both
end fixed spindle

(b) Construction of one
end fixed spindle

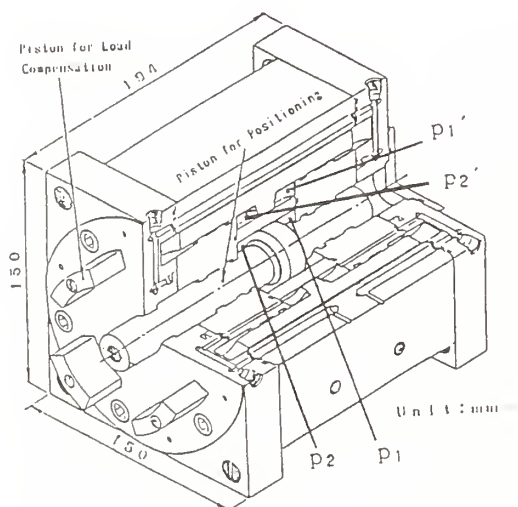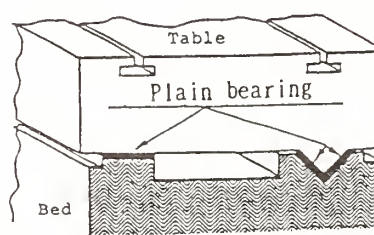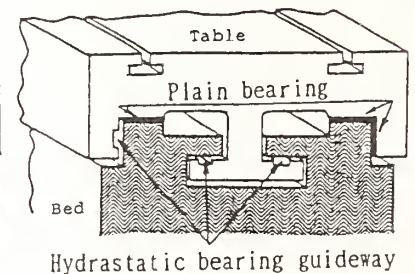Figure 4 Construction of wheel unit on stationary spindle

Figure 3 Hyraulic actuator with
L. C. unit — Nanoact —
(Designed by F. Hashimoto)

(a) Conventional guideway

(b) Composite bearings
geideway

Figure 5 Construction of composite bearings
guideway

318

in load of the wheel head. One of them is for positioning and the other is for load compensation in order to reduce load of the positioning actuator. A pressure difference between two cavities of the positioning actuator (p_1-p_2) is measured with pressure sensors, and its output signal is input to servo amplifier for the load compensation. A pressure difference $(p_1'-p_2')$ is supplied to the actuator for load compensation. Load share rate K_s is ratio of load shared by the actuator for load compensation to load of the positioning actuator. The actuator for load compensation shares load of $K_s/(1+K_s)$ and load of the positioning actuator is reduced to $1/(1+K_s)$. It is expected high resolution and high repeatability in positioning under heavy friction load. This system is applied to the surface grinding machine.

(B) Nanometer positioning actuator with load compensation unit

Figure 3 shows the nanometer positioning actuator with load compensation unit referred to as Nanoact. It has two pistons. The inner piston is for positioning and the outer piston is for load compensation. They are coaxial, and the piston for positioning is built in the piston for load compensation. Therefore, Nanoact can be be very compact. Both pistons are supported by hydrostatic bearing. They are connected to the connecting plate at each front end. A pressure difference between two cavities of the inner positioning actuator (p_1-p_2) is picked up with pressure sensors and its output signal is input to the servo amplifier for load compensation. A pressure difference $(p_1'-p_2')$ equal to a pressure difference of the positioning actuator (p_1-p_2) is supplied to the outer actuator for load compensation. The effective sectional area of outer piston is K_s times as wide as one of inner piston. K_s is 2.4 in Figure 3. The piston for load compensation shares load of $K_s/(1+K_s)$. Load of positioning piston is reduced to $1/(1+K_s)$. High resolution of positioning is expected. Nanoact is used for the ultraprecision centerless grinding machine.

2.2 Stationary spindle structure

Figure 4 shows a construction of stationary spindle structure.[3] One or both ends of the spindle is fixed on the housing. Stationary spindle structure is a closed force flow system and gives high structural stiffness.

2.3 Composite bearings guideway

In Figure 5, a composite bearings guideway is composed of a couple of plain bearing guideway and hydrostaic bearing guideway.[4] It enables to build a uniform distribution of oil film thickness and to eliminate any play between the guideways. It is expected to improve dynamic stiffness and motion accuracies.

2.4 Hydrostatic support of wheel unit

A wheel unit is hydrostatically supported on a stationary spindle, and a high accuracy and repeatability of runout are expected.

3. Design of ultraprecision vertical spindle surface grinding machine

The ultraprecision vertical spindle type surface grinding machine for ductile mode grinding of brittle materials has the following characteristics:
1) positioning system of grinding wheel head with dual force operated linear actuators as shown Figure 1,
2) stationary spindle structure, which is fixed at one end of spindle on wheel head,
3) composite bearings guideway is applied to the guideway between column and wheel head slide. Also it is applied to the guideway between X slide and bed,
4) grinding wheel unit hydrostatically supported on the stationary spindle.

Figure 6 shows the schematic of ultraprecision vertical spindle rotary table type surface grinding machine.[5] In Figure 6, the hydraulic actuator for positioning is fixed upon the bottom of the column, and the actuator for load compensation is fixed on the top of the column in order to reduce load of the positioning actuator. Each piston rod is connected directly with wheel head without any lead screws or gears. Displacement transducer for position feedback is fixed on the column. Wheel head is fed by a tandem drive system. Wheel unit which is supported hydrostatically on the stationary spindle is driven with a belt. The rotary table is supported on the X slide with hydrostatic bearings.
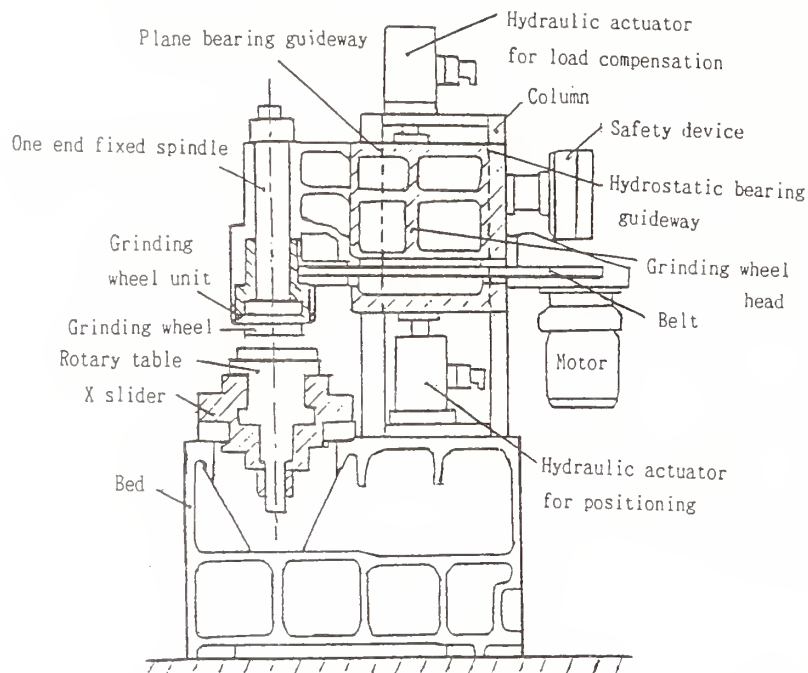
319

Figure 6 Scheme of the vertical spindle
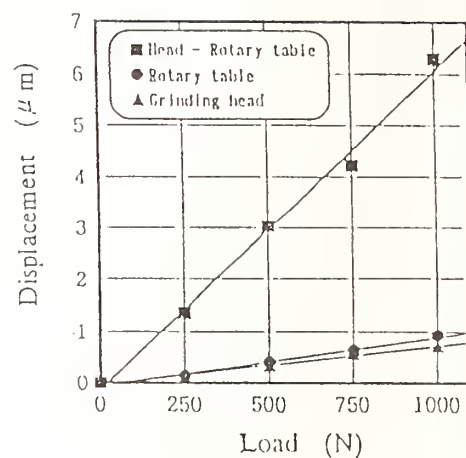surface grinding machine

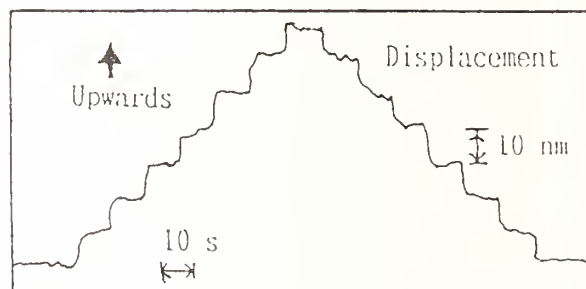Figure 7 Stiffness record of
the surface grinding machine

Figure 8 Record of wheel head
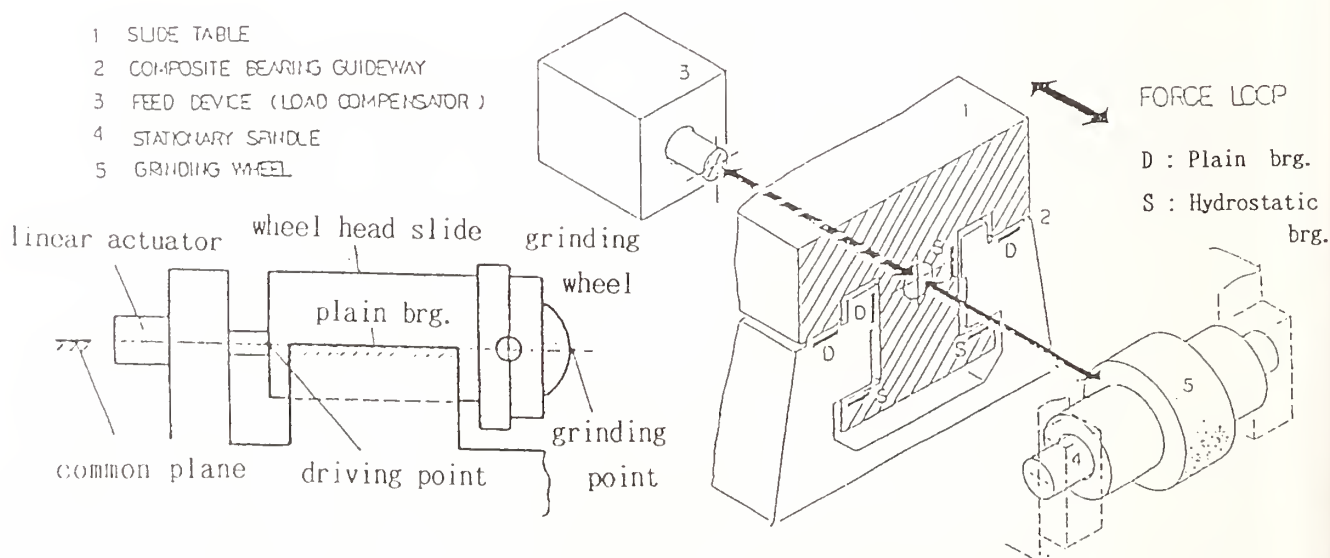displacement on the surface grinding
machine for stepwise feed of 10 nm

1 SLIDE TABLE
2 COMPOSITE BEARING GUIDEWAY
3 FEED DEVICE (LOAD COMPENSATOR)
4 STATIONARY SPINDLE
5 GRINDING WHEEL

FORCE LOOP

D : Plain brg.

S : Hydrostatic
brg.

Figure 9 Kinematic drive of grinding head slide

320

Figure 7 shows the stiffness record between the wheel head and the rotary table of the surface grinding machine for loads up to 1000 N. The stiffness at a radius of 100 mm from the center of spindle is higher than 160 N/μm. Figure 8 is the record of grinding wheel head displacement for stepwise feed of 10 nm. It shows the positioning resolution of 10 nm and little generation of lost motion at reversing point of feed direction.

4. Design of ultraprecision and high stiffness centerless grinding machine

The ultraprecision and high stiffness centerless grinding machine for ductile mode grinding of brittle materials was designed based on the following[6]:

  (1) Guidelines of design
1) High stiffness and high precision
2) Stability of thermal deformation characteristics
3) Minimum outside diameter of ground workpiece 0.1 mm
4) Full automatic centerless grinding machine with auto-setup function
  (2) Applied new technology
1) Use of low thermal expansion materials and a symmetric structure
2) Kinematic drive of grinding head slide (shown in Figure 9)
3) Hydraulic actuator with load compensation unit —— Nanoact ——
4) Composite bearings guideway
5) Fixed spindle structure
6) Controlled 2-axes work support blade with auto-lock mechanism.
    Table 1 shows the specification of the centerless grinding machine.

5. Motion accuracy and stiffness of the centerless grinding machine

The experimental test results on the motion accuracies and stiffness are summarized as follows:
(1) Performances of the positioning servo cntrol system of the force operated hydraulic linear actuator (Nanoact)
    Nanoact is applied to feed the grinding wheel head slide. The total stiffness is about 180 N/μm as shown in Figure 10. The resolution of positioning servo control system feeding the grinding wheel head slide is 8 nm/step under Coulomb's friction of 784 N, as shown with

experimental result of Figure 11.
(2) Trueing accuracies and remountability
    The diamond wheel was trued on a specialized grinding machine equipped with the hydrostatically supported wheel on the stationary spindle for trueing cut to an accuracy of 100 nm runout and was remounted on the centerless grinding machine to the same accuracy.

6. Grinding test results

Through-feed centerless grinding tests were carried with diamond wheels on cylindrical test pieces of ZrO_2, BK7, SIALON and HP-Si_3N_4 shown in Table 2. Typical records of the roundness and the surface roughness are shown in Figure 12. Size of the test pieces, grain size of diamond wheels, and the resulted grinding accuracies of roundness and surface finish are listed on the Table 3. Figure 13 shows that ductile mode grinding is superior to lapping in shape generation. Surface grinding tests for silicon wafers were carried out by the newly designed surface grinding machine and conventional machines. Damaged layer on the test pieces ground by the designed machine was thinner than one by conventional machines.[6] The flatness of ground 6 inch silicon wafer was less than TTV 0.6 μm.

7. Summary

(1) The surface grinding machine
    The designed machine has feed resolution of the order of 10 nm. The loop stiffness more than 160 N/μm were obtained. Grinding tests of silicon wafers revealed that
1) the subsurface damage was in the order of a half micron.
2) The flatness of a 6 inch silicon wafer was less than TTV 0.6 μm.
(2) The centerless grinding machine
    The designed machine has feed resolution of 8 nm. The total stiffness is about 180 N/μm. Through-feed centerless grinding tests were carried with diamond wheels for cylindrical test pieces of ZrO_2, BK7, SIALON and HPSN. The roughness for ground test pieces of ZrO_2 was 10 nmRa, and the roundness was 10 nm.
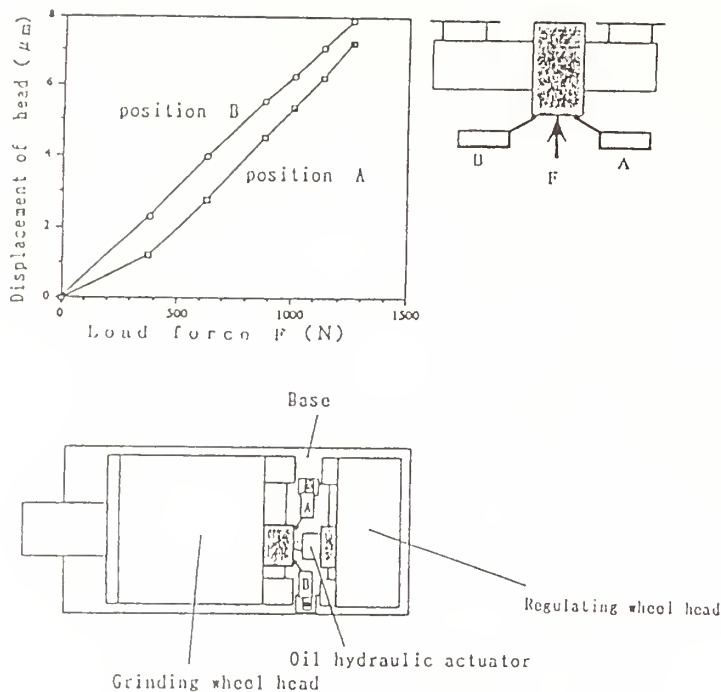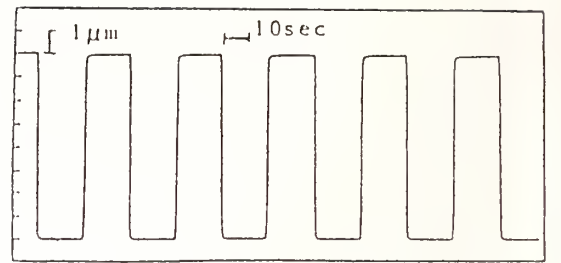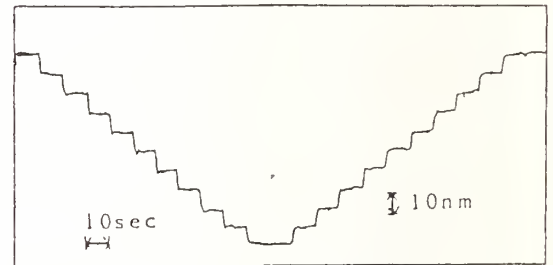
Figure 10 Total stiffness of the centerless grinding machine

(a) Repeatability of positioning for stroke of 8 μm

(b) Positioning for stepwise feed of 8 nm

Figure 11 Positioning characteristics of the slide table driven by Nanoact

Table 1 Design specification of the centerless grinding machine

Name	NANOTRON
Dimensions	$1085^L \times 460^W \times 450^H$
Materials	Ultra-Low Thermal Expansion Castiron
Grinding Wheel	Diamond Wheel or CBN Wheel $150^D \times 50^W$
Regulating Wheel	Ceramics or Steel Wheel $150^D \times 50^W$
Wheel Support	Hydrostatic on Fixed Spindle
Work Support Blade	2-Axes Controled Work Support Blade with Auto-Lock Mechanism
Workpiece	Brittle Materials, $\phi 0.1 \sim \phi 20mm$
Machine Stiffness	Total Stiffness of Grinding System about 160 N/μm
Slide Feed	Resolution of Positioning 0.001 μm provided with NANOACT

Table 2 Vickers hardness of the test pieces

Material	Hardness
ZrO_2	HV 1200
BK7 (glass)	HV 700
SIALON	HV 1900
HP-SN	HV 1700

Table 3 Grinding accuracies

Material	Size	Roundness	Roughness
ZrO_2	$\phi 2.5 \times 10^L$	10 nm	10 nm Ra
BK7	$\phi 0 \times 11^L$	34 nm	15 nm Ra
SIALON	$\phi 4.1 \times 29^L$	15 nm	28 nm Ra
HPSN	$\phi 10 \times 10^L$	34 nm	55 nm Ra

ZrO2, BK7 : 3000 resined bonded wheel
SIALON: D4/8 vitrifieded bonded wheel
HPSN : 800 vitrifieded bonded wheel
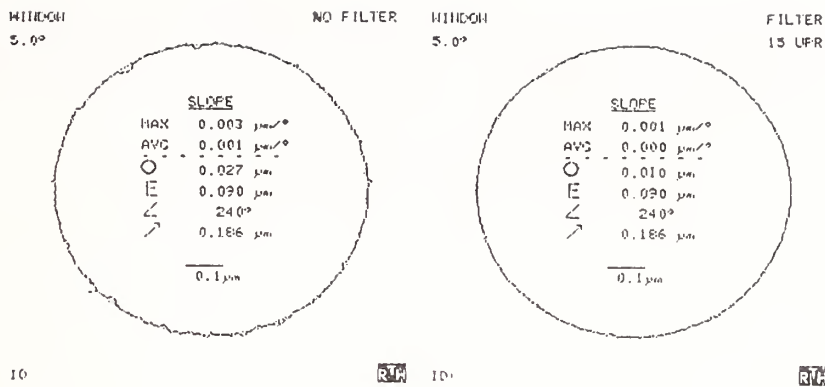
Roughness of 11nmRa
(a) No filter

Roughness of 10nmRa
(b) Filter 15 UPR

Figure 12　Typical records of the roundness for test
piece of ZrO_2　(size: $\phi2.5*10.5^L$)

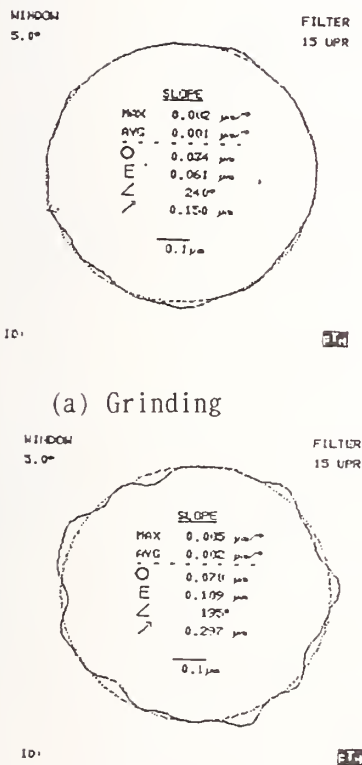(a) Grinding

(b) Lapping

Figure 13　Roundness records for grinding
and lapping　(material: ZrO_2)

Reference

1　M. Miyashita, "The Way to Nanogrinding
　Technology", SPIE Proc., Vol. 1333, p. 13,
　1990.
2　H. Shimura, J. Yoshioka, M. Takahashi,
　F. Hashimoto, and M. Miyashita,
　"Ultraprecision Grinding — Construc-
　tion of Positioning System of Wheel
　Head — ", Autumn Meeting of JSPE,
　pp. 55-56, 1986. (in Japanese)
3　J. Yoshioka, F. Hashimoto, M. Miyashita,
　A. Kanai, T. Abo, and M. Daito,
　"Ultraprecision Grinding Technology for
　Brittle Materials: Application to
　Surface and Centerless Grinding
　Processes", M. C. Show Grinding Symposium
　ASME, PED-Vol. 16, pp. 209-227, 1985.
4　J. Yoshioka, K. Koizumi, M. Shimizu,
　H. Yoshikawa, M. Miyashita, and A. Kanai,
　"Surface Grinding with a Newly
　Developed Ultra Precision Grinding
　Machine", SME Mfg. Eng. Trans., pp. 18-
　28, 1983.
5　K. Abe, N. Yasunaga, M. Miyashita,
　J. Yoshioka, and M. Daito, "Study on
　Ultraprecision Grinding Technology for
　Brittle Materials (1)", Autumn Meeting
　of JSPE, pp. 551-552, 1992. (in Japanese)
6　J. Yoshioka, M. Miyashita, A. Kanai,
　M. Daito, and F. Hashimoto, "Ductile Mode
　Grinding of Brittle Materials with
　Newly Designed Centerless Grinding
　Machine", Proc. of ASPE Annual Conf.,
　pp. 143-144, 1990.

323

PRECISION FORM TRUING AND DRESSING FOR ASPHERIC CERAMICS MIRROR GRINDING

T. KURIYAGAWA, K. SYOJI, and L. ZHOU
Tohoku University, Sendai, Japan

The goal of this paper is the development of a precision truing and dressing device for an extremely fine-grit round-profile diamond wheel. A new and compact truer is designed and built to achieve the desired profile without detachment of the diamond wheel from the grinding machine. This "Arc Truer" has a rotation unit consisting of a silicon carbide cup wheel, and a swing/infeed mechanism for the cup wheel. The truer has the advantage that dressing after truing is not necessary, and that sharp cutting edges protrude from the wheel surface. The profiled wheel is for ductile-regime grinding of aspheric ceramic mirrors. As the wheel is wider than conventional ones for form generation grinding, it is expected that the wheel wear and grinding characteristics will be uniform widthwise. In this paper, a resin bonded diamond wheel is used, and truing tests are carried out with a CNC ultra-precision surface grinding machine. A new grinding method for form generation is proposed and truing characteristics and accuracy of the Arc Truer are investigated.

1. Introduction

Hot isostatic processed silicon carbide (HIP-SiC), which has high heat conductivity and a small coefficient of linear expansion, is the material normally used for constructing mirrors for reflecting short wavelength radiation (e.g. X-ray, etc.). Advanced technologies for both mirror surface finishing and aspheric machining are demanded in the field of mirror grinding.

Many trials of mirror grinding or ductile-regime grinding have been made. Analyses of ductile behavior of brittle materials, and development of CNC ultra-precision grinding machines and diamond wheels have been useful in this regard [1]-[10]. Recently, several attempts of grinding of aspheric ceramics mirrors have been made [11]-[13]. In mirror grinding, wheel life is usually short, and it is difficult to keep a grinding characteristic of the wheel constant. Furthermore, truing and dressing are the most important processes which affect the wheel performance. However, there are few studies of precision truing and dressing for mirror grinding.

This paper proposes a new grinding method for aspheric mirrors that uses an extremely fine grit diamond wheel with a round profile. A precision truing and dressing device, called the Arc Truer, is developed to obtain a wheel having round cross-sectional profile on a surface grinding machine. The truer demonstrated excellent truing characteristics.

2. Principle of Form Generation with a Round Profile Wheel

In the field of three-dimensional ultra-precision mirror grinding, form generation of a workpiece is carried out with a 4- or 5- axis controlled grinding machine as shown in Fig. 1. With this grinding method, form accuracy of a ground workpiece depends on the total accuracy of the grinding machine. If an ideal precision grinding machine can be developed, three-dimensional ultra-precision machining can be realized in which part accuracy is proportional to the machine accuracy. When grinding a mirror of a difficult-to-grind material such as silicon carbide, loading and dulling of a wheel can easily occur, decreasing both the machining accuracy and the wheel life, since the
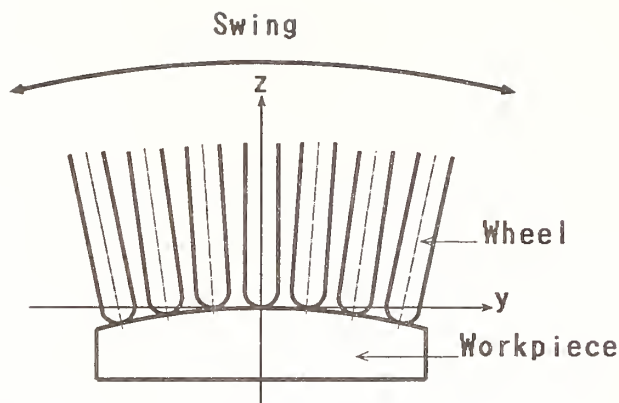
Fig. 1   Conventional method of form generation

Fig. 2   New method of form generation

same part of the diamond wheel is used in grinding.

In this paper, a new method for form grinding is proposed by means of a diamond wheel with a curved profile. Since the workpiece profile generated by this method is an envelope of a family of arcs as shown in Fig. 2, any convex or concave profile can be produced. As the grinding point is changed along the wheel profile with every grinding pass, the entire width of the wheel can be effectively used and wheel life is expected to increase. In this method, form accuracy of a ground workpiece depends on the accuracy of not only the grinding machine but also the wheel profile. Therefore, a device capable of precisely truing an arc profile on a wheel is required.

3. Wheel Design and Accuracy of Ground Surface

As shown in Fig. 3, the xyz coordinate system (x axis is perpendicular to the plane of paper and in the direction of the table feed) is fixed on the table of the grinding machine. The workpiece is symmetric with respect to the xz–plane ($y = 0$), and b is the width. The cross section of the workpiece is expressed by the equation $z = f(y)$, where $(y, z) = (0, 0)$.

B is the wheel width and R is the radius of the arc cross section. When grinding a convex workpiece with the wheel, the following restrictions apply between R and B:

$$2R \geq B \tag{1}$$
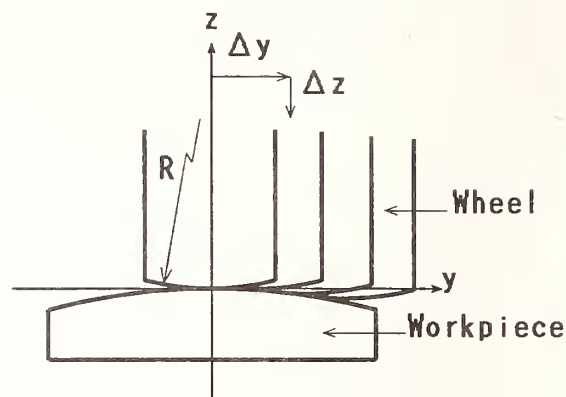
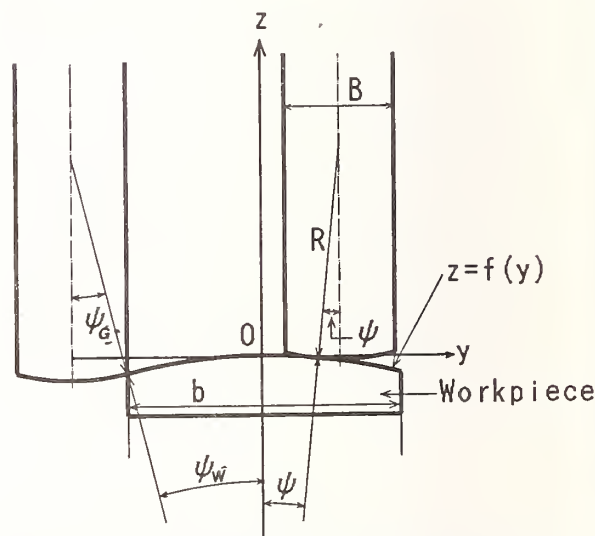$$0 < R < \infty \tag{2}$$

$$\psi_G \geq \psi_W \tag{3}$$

Fig. 3   Arc profiled wheel and workpiece

where

$$\psi_G = \arcsin\left(\frac{B}{2R}\right), \quad \psi_W = \left|\arctan\left(f'\left(\frac{b}{2}\right)\right)\right| .$$

When grinding a concave workpiece, one further restriction must be added:

$$R \leq \rho_{min} \tag{4}$$

where ρ_{min} is the minimum value for the radius of curvature $\rho = \dfrac{(1+f'(y)^2)^{3/2}}{f''(y)}$.

The accuracy with which a workpiece can be ground by a wheel that satisfies the above conditions was then considered. This accuracy can be expressed in terms of the profile error, surface roughness and waviness of the workpiece. The profile error and surface roughness depend on the grinding machine used and the grit size of the
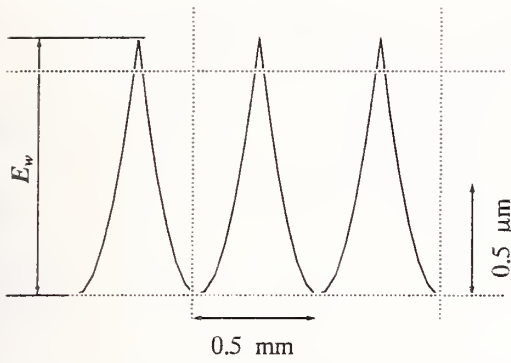
Fig. 4 Waviness E_w generated on workpiece (R=40mm, B=20mm, r=100mm, b=50mm)

Fig. 5 Relationship between waviness E_w and increment $\Delta\psi$

wheel. For example, in our surface plunge grinding tests, we achieved a surface roughness of $R_{max} \approx$ 0.25 μm ($R_a \approx$ 25 nm) in the case of SD1500 diamond wheel, and $R_{max} \approx 0.05$ μm ($R_a \approx$ 5 nm) in the case of SD3000 diamond wheel. Therefore, we will discuss the waviness on the yz plane only. The following assumptions were used: The wheel profile was ideally trued into an arc and the profile was transcribed to the workpiece during grinding. The cross feed, Δy, is given in such a manner that the density of grinding points along the wheel profile is uniform, namely the increment of $\Delta\psi$ in the center angle ψ is constant. For simplicity, the shape of the workpiece is limited to a cylinder with radius r and width b as shown in Fig. 3. In this case, condition (3) is $R \le rB/b$. Profile generated on the yz cross section of the workpiece ($r = 100$ mm, $b = 50$ mm) can be calculated as shown in Fig. 4. Peak–to–valley height of the profile is defined as the waviness, E_W. Figure 5 shows the influence of $\Delta\psi$ and R on the value of E_W. It is clear that the value of E_W decreases as R increases or as $\Delta\psi$ becomes smaller.

In designing a wheel, R is taken to be as large as possible in the range of conditions (1) through (4) keeping in mind the general consideration of grinding machine table size and wheel manufacture.

4. Arc Truer

An Arc Truer for a cylindrical grinding machine was developed and its truing accuracy investigated [14]. The stiffness of the truer, the infeed accuracy of the green silicon carbide (GC) cup wheel, and the control method all exert a great influence on truing accuracy. The Arc Truer in this experiment is an improved one, and trued an extremely fine grit diamond wheel precisely.
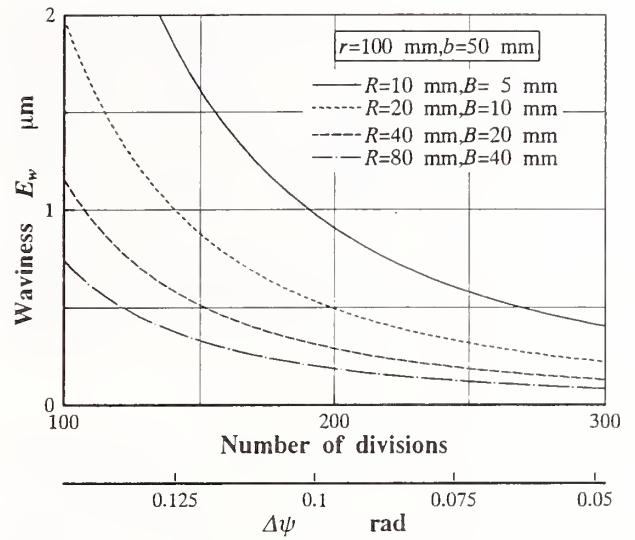
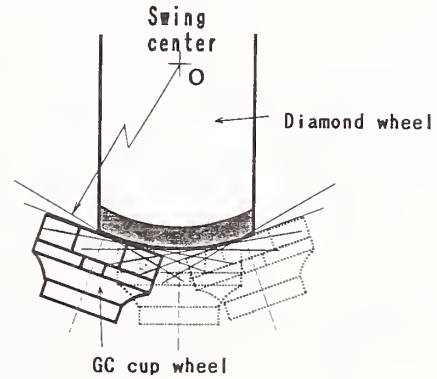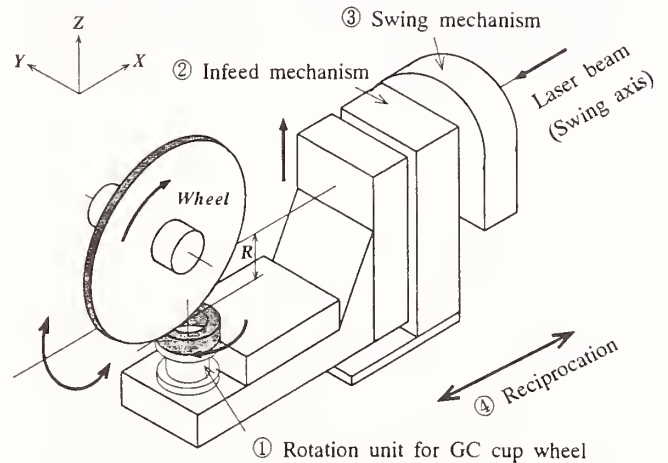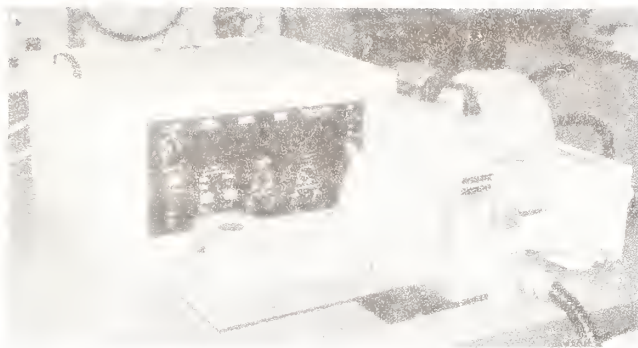The principle of arc truing is shown in Fig.

(a) Truing principle

(b) Schematic drawing of Arc Truer

Fig. 6 Arc Truer

6(a). The rotating GC cup wheel reciprocates in a direction vertical to the plane of the paper and

(a) Arc Truer and its controller

(b) Swing during truing

Fig. 7   Photographs of the Arc Truer

Table 1   Specifications of the Arc Truer

① **Rotation unit for GC cup wheel**	
• GC cup wheel	6A2, $90^D \times 10^W$
• Rotational speed	60~600 rpm
• Peripheral speed	17~170 m/min (ϕ90)
• Camming of wheel surface	0.005 mm / ϕ90
• Perpendicularity of wheel axis and swing axis	0.002 mm / 90 mm
• Intersection of wheel axis and swing axis	0.01 mm
② **Infeed mechanism**	
• Drive	Stepping motor (direct)
• Stroke	40 mm
• Distance between wheel surface and swing axis	10~50 mm
• Minimum infeed	0.001 mm
• Feed speed	150 mm/min
• Straightness of infeed	0.003 mm / 40 mm
• Perpendicularity of infeed and swing axis	0.005 mm / 40 mm
• Thrust stiffness	10 N/μm
③ **Swing mechanism**	
• Drive	Stepping motor + Worm
• Maximum swing angle	±60 deg
• Minimum swing angle	0.0072 deg/step
• Swing speed	0.2~1.2 rpm
• Parallelism of swing axis and grinding machine table	0.01 mm / 40 mm

$\overset{50\ \mu m}{\vdash\!\!\!-\!\!\!-\!\!\!\dashv}$
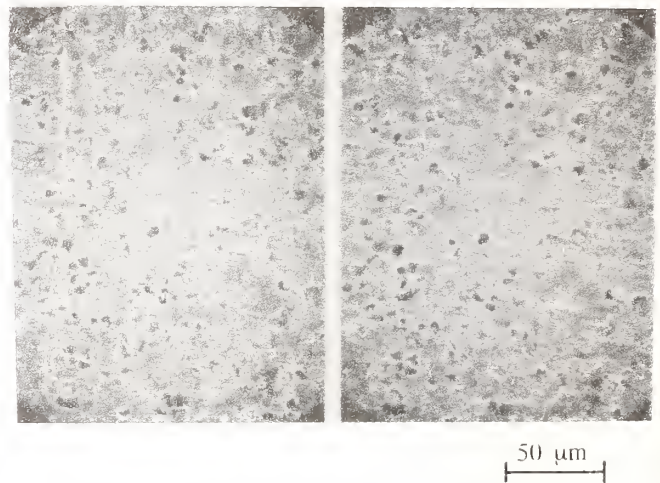
Fig. 8   Typical stereo SEM photograph
(Truing conditions are shown in Table 2)

swings around the center O. Fig. 6(b) shows a schematic drawing of the Arc Truer. It is composed of a rotation unit for a GC cup wheel ①, an infeed mechanism ② and a swing mechanism ③. The arc profile of the wheel is trued in combination with the above three motions and the table reciprocation of the grinding machine ④. The radius, R, of the trued profile can be changed from 10 mm to 50 mm. Fig. 7(a) is a photograph of the Arc Truer and its control unit. Table 1 shows its specifications. Fig. 7(b) is a photograph of the Arc Truer truing a wheel on the grinding machine. Fine adjustment of the relative position of the Arc Truer and the diamond wheel is needed during set up on

the table. In this experiment, the adjustment is made using a laser beam with an axis that coincides with the swing axis. Since truing and dressing occur simultaneously during truing with a GC cup wheel, the process offers a significant advantage that dressing is not necessary after truing.

5. Truing Tests

5.1 Grain Density

Truing tests for a straight wheel were carried out to determine optimal conditions. An extremely fine grit diamond wheel (SD1500R125BRC, 1A1, diameter: 205 mm, width: 15 mm, diamond layer depth: 5 mm) and an ultra-precision surface
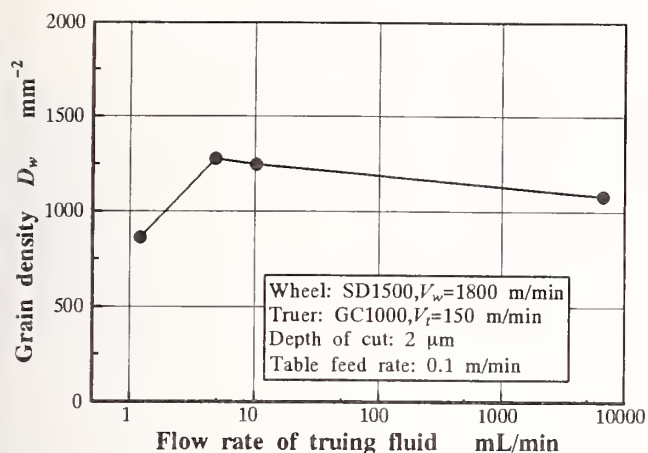
Fig. 9   Relationship between flow rate of truing fluid and grain density
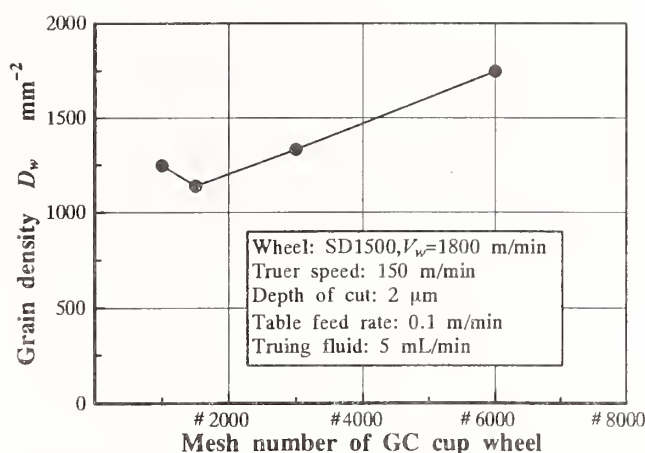

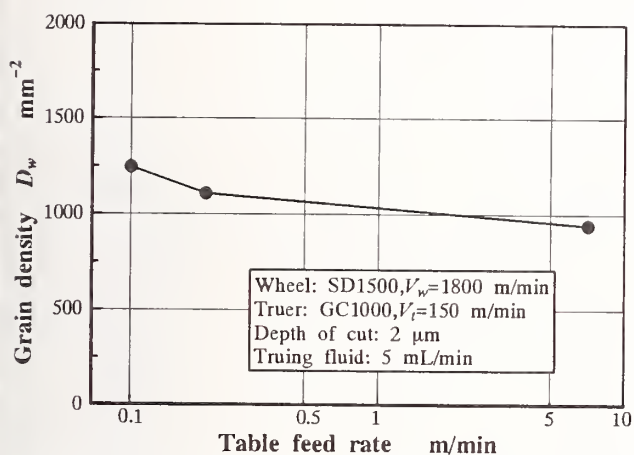Fig. 11   Relationship between mesh number of GC cup wheel and grain density

Fig. 10   Relationship between table feed rate and grain density
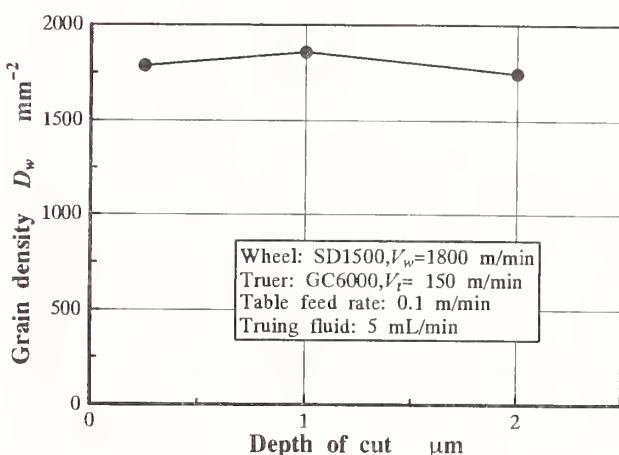

Fig. 12   Relationship between depth of cut and grain density

grinding machine were used. Synthetic fluid was sprayed on a GC cup wheel as truing fluid. The wheel was prepared so that a piece could be partially removed and its working surface was observed by stereo SEM. Figure 8 shows a typical stereo SEM photograph of the wheel surface just after truing. In this photograph, a number of diamond grains can be seen protruding from the wheel surface. At the same time, holes from which diamond grains were released can be observed. Grain density on the wheel surface was measured and used as an estimate of truing performance.

Fig. 9 shows the influence on grain density of various truing fluid flow rates. In the case of an extremely small flow rate, loading of loose GC abrasive occurred not only into the GC cup wheel, but also into the diamond wheel and many diamond grains were pulled off, thus lowering grain density. At a flow rate of 5 mL/min or more, however,

loading did not occur and grain density was increased. Grain density was almost constant throughout this range.

Figs. 10 and 11 show the influence of table feed rate and grain size of the GC cup wheel on grain density. It is clear from the figures that slower table feed rate and finer grain size result in higher grain density. Fig. 12 shows the influence of depth of cut on truing, Δ_t. Grain density was almost constant in the range of $\Delta_t < 2$ μm. In the case of $\Delta_t = 0.25$ μm, however, the volume of loose GC abrasive was too small to true the wheel efficiently. In contrast, at $\Delta_t > 2$ μm, chatter marks occurred on the wheel periphery. In light of the above results, optimal truing conditions were as shown in Table 2.

5.2 Truing Accuracy

Arc truing tests were carried out by an Arc

329

Table 2 Optimal truing conditions

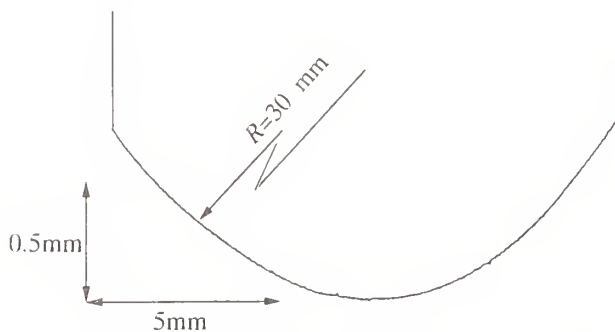|	
Diamond wheel peripheral speed	1800 m/min
GC cup wheel speed	600 rpm
Flow rate of truing fluid	5 mL/min
Table feed rate	0.1 mm/min
Grain size of GC cup wheel	#6000
Depth of cut	1 μm

**Fig. 13** Cross−sectional profile of trued wheel

Truer and a CNC ultra−precision surface grinding machine. In this truing test, an arc profile (R = 30.700 mm) was generated from a straight profile. The tested wheel was a SD1500R125B (diameter: 305 mm, width: 15 mm, diamond layer depth: 5 mm) and the truing conditions in Table 2 were applied. First, rough truing was performed using GC cup wheels whose mesh numbers are #400, #800, and #1000, in that order. Finally, finish truing was performed using a #1500, #3000 or #6000 GC cup wheel.

Fig. 13 shows the arc cross sectional profile of the trued wheel. Profile measurement was carried out through a transcription method. Fig. 14(a) shows the parameters used to evaluate truing accuracy. The difference between the value of the expected radius and the value of the approximated radius of the measured cross section is defined as the radius error, E_r. The deviation from the approximated arc is defined as the profile error, E_s, and the difference between the maximum and minimum values of E_s is defines as the maximum profile error, E_{sm}.

Fig. 14(b) shows a typical trace of the profile error, E_s, along the wheel profile. It is clear that the truing accuracy widthwise is within ±0.4 μm (E_{sm} = 0.8 μm). Fig. 15 shows the influence of depth of cut Δ_t and mesh number of GC cup wheel on the maximum profile error, E_{sm}, in finish truing. In the case of Δ_t = 2 μm, finer grain size (larger mesh number) resulted in smaller value of E_{sm}. In the case of Δ_t = 1 μm, however, truing with GC6000 cup wheel was a little unstable, because it
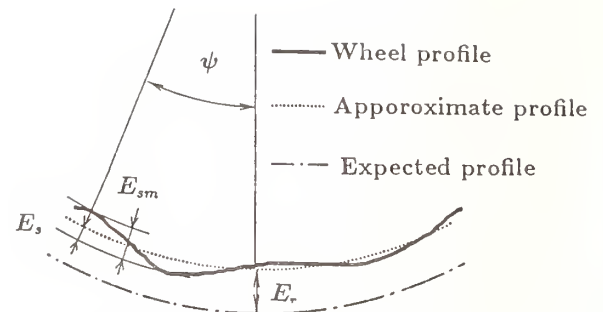
(a) Profile error E_s and radius error E_r
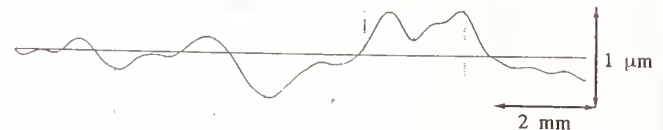
(SD1500, V_w=450 m/min, GC1500, V_t=150 m/min, Δ_t=1 μm, v_t=0.1 m/min)

(b) Profile error E_s

Fig. 14 Truing accuracy

Wheel: SD1500,V_w=450 m/min
Truer speed: 150 m/min
Table feed rate: 0.1 m/min
Swing speed: 0.6 rad/min
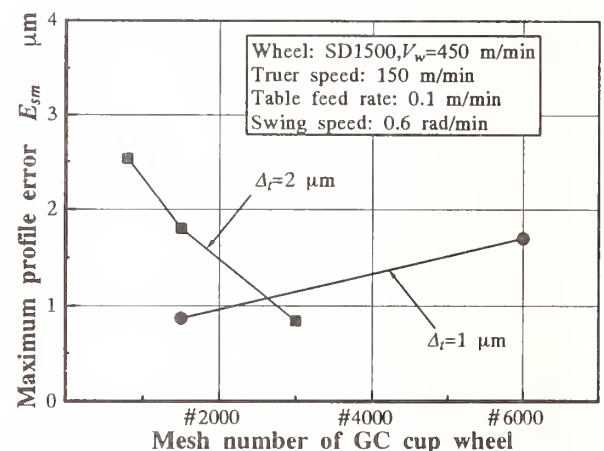
Fig. 15 Influence of depth of cut and mesh number of GC cup wheel on maximum profile error

was difficult to supply truing fluid uniformly on the swinging GC cup wheel. Therefore, E_{sm} value of GC6000 cup wheel became larger than that of GC1500.

Measured values of R were in the range of 30.627 mm to 30.711 mm. As the set up value of R was 30.700 mm, an E_r of less than ±0.08 mm could be achieved. In the actual grinding of an aspheric mirror surface, it is necessary to compen−sate for the wheel depth of cut by inputting data regarding the measured wheel profile to the CNC controller.

330

6. Conclusion

A new grinding method was proposed for aspheric mirrors that uses an extremely fine-grit round-profile diamond wheel. A precision truing and dressing device called an "Arc Truer" was also developed to obtain a curved profile wheel cross section. An examination of truing accuracy of the Arc Truer revealed that profile and radius errors were within ±0.4 μm and ±0.08 mm, respectively.

References

1. T.G.Bifano, T.A.Dow, and R.O.Scattergood, "Ductile-Regime Grinding: A New Technology for Machining Brittle Materials," Trans. of the ASME, Vol. 113, May, pp.184-189, 1991.

2. T.A.Dow, and R.O.Scattergood, "Ductile/Brittle Transition and Development of Ductile Mode Grinding Technology," J. of the JSPE, Vol. 56, No. 5, pp.794-798, 1990.

3. T.G.Bifano, and S.C.Fawcett, "Specific Grinding Energy as an In-Process Control Variable for Ductile-Regime Grinding," Precision Engineering, Vol. 13, No. 4, pp.256-262, 1991.

4. M.Miyashita, "Ductile mode Grinding Technology for Brittle Materials: The Way to Nanogrinding Technology," J. of the JSPE, Vol. 56, No. 5, pp.782-787, 1990.

5. W.S.Blackley, and R.O.Scattergood, "Ductile-Regime Machining Model for Diamond Turning of Brittle Materials," Precision Engineering, Vol. 13, No. 2, pp.95-103, 1991.

6. K.E.Puttick, and A.Franks, "The Physics of Ductile-Brittle Machining Transitions: Single-Point Theory and Experiment," J. of the JSPE, Vol. 56, No. 5, pp.788-792, 1990.

7. N.J.Brown, "Lapping: Polishing and Shear Mode Grinding," J. of the JSPE, Vol. 56, No. 5, pp.800-804, 1990.

8. P.A.McKeown, K.Carlisle, P.Shore, and R.F.J.Read, "Ultra-Precision, High Stiffness CNC Grinding Machine for Ductile Mode Grinding of Brittle Materials," J. of the JSPE, Vol. 56, No. 5, pp.806-813, 1990.

9. K.Carlisle, and P.Shore, "Experience in the Development of Ultra Stiff CNC Aspheric Generating Machine Tools for Ductile Regime Grinding of Brittle Materials," Proc. of the 6th IPES, Braunschweig, pp.85-94, 1991.

10. H.Ohmori, I.Takahashi, and T.Nakagawa, "Mirror Surface Grinding by Metal Bonded Super-Abrasive Wheel with Electrolytic In-Process Dressing," Proc. of the 6th IPES, Braunschweig, pp.153-165, 1991.

11. H.Suzuki, "Development of CNC Ultra Precision Aspheric Grinder and 3-Dimensional High Precise Machining of Brittle Materials," J. of the JSPE, Vol. 56, No. 5, pp.815-819, 1990.

12. T.Osaka, K.Unno, A.Tsuboi, Y.Maeda, and K.Takeuchi, "Development of High-Precision Aspheric Grinding/Turning Machine," Proc. of the 6th IPES, Braunschweig, pp.95-102, 1991.

13. Z.Zhong, and T.Nakagawa, "New Grinding Methods for Aspheric Mirrors with Large Curvature Radii," Annals of the CIRP, Vol. 41, No. 1, pp.335-338, 1992.

14. L.Zhou, K.Syoji, and T.Kuriyagawa, "Truing of Super-abrasive Wheel for Form-grinding," Proc. of 7th IPES., in press, 1993.

ELECTROCHEMICAL DRESSING OF BRONZE BONDED DIAMOND GRINDING WHEELS

E. WELCH, Y. YI, and T. BIFANO
Boston University, Boston, MA

An experimental apparatus was constructed to study electrolytic dressing on bronze-bonded diamond grinding wheels. An EDM power supply was used to drive the electrolysis. Experiments were performed to explore the qualitative microstructural features of the dressing, and to evaluate the quantitative rates of oxide film formation and wheel erosion. For one choice of the relevant process parameters (open circuit electrode voltage, electrode gap size, electrolyte, and pulsed voltage duty cycle) it was found that an oxide film extended both out of and into the wheel surface. The rate of growth into the wheel of the electrolytically affected layer was found to be approximately constant (1.5 nm/s). Other combinations of the relevant electrolysis parameters are currently under investigation.

INTRODUCTION

It has been demonstrated that ceramics can be fabricated using fixed-abrasive grinding without generating sub-surface damage (1-3). The absence of damage, a requirement in many structural and optical applications, demands sufficient control of the machine tool that a critical load (or depth of cut) is not exceeded by the diamond grains in the grinding wheel.

A problem encountered in such fine grinding is that the wheel is not generally found to be *self-dressing*. That is, the grinding process itself does not erode the grinding wheel bond at a rate sufficient to expose new diamonds before old diamonds become worn out. As an example, Figure 1 shows the progression of specific grinding energy as a function of material removed for a particular ultraprecision grinding process. In the experiment from which this graph was obtained, a 4-8 μm grit wheel was first dressed to expose new diamond edges, then used to blanchard-grind CVD silicon carbide under conditions that would ensure a damage-free surface on the ceramic work piece(4).

After a total removal volume of 3 cubic millimeters, the specific grinding energy began to rise rapidly, indicating that the diamond grains were no longer effectively removing material. Scanning Electron Microscope (SEM) photographs of the wheel surface suggested three possible contributors to increased grinding energy: dulling of the diamond grains, loading of the wheel with grinding swarf, and loss of diamonds from the wheel surface. Under such conditions, the wheel must be re-dressed to restore its original cutting capability.

There are various techniques available for dressing, which can be divided into two categories: intermittent and in-process. *Intermittent* dressing occurs while the wheel is not grinding, typically at the end of a grinding pass across the work piece. A common method of intermittent dressing involves pressing a porous ceramic "dressing stick" against the wheel surface. The porous ceramic erodes the wheel bond without significantly affecting the cutting edges of the newly exposed diamonds. *In-process* techniques have witnessed recent progress involving

glass-fiber dressing media bonded to the work piece surface (5), and electrolytic in-process dressing (ELID) (6-8). ELID has been found to be an effective tool for production-level machining of ceramics to optical quality finishes using cast iron fiber bonded wheel (6).

Currently, such wheels are available from only one source. In the US, the most common bond material used in precision grinding of ceramics is bronze. Our research is aimed at exploring the applicability of the ELID process to bronze-bonded diamond grinding wheels.
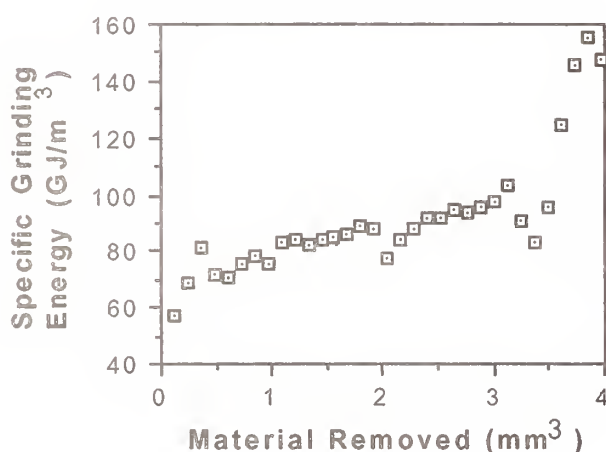

Figure 1: Specific grinding energy as a function of total material removed in a blanchard-style micro-grinding operation on CVD silicon carbide. The sharp increase in specific energy is a result of diamond wear.(6)

BACKGROUND

In the ELID process, an electrolytic cell is created with the rotating grinding wheel as the anode, immersed in a flowing electrolyte and opposed by a fixed, graphite cathode. The basic theoretical equation governing wheel recession rate as a function of electrolysis parameters can be derived from Faraday's Laws of electrolysis and Ohm's Law (9):

$$\dot{x} = \frac{MVA_c}{zFl\rho_a\rho A_w}$$

where M is the molecular weight of the anode material, V is the applied voltage across the gap, A_c is the active surface area of the cathode, z is the valence of the anode material, F is Faraday's constant, l is the inter-electrode gap distance, ρ_a is the density of the anode, ρ is the resistivity of the electrolyte, and A_w is the surface area of the wheel. Often, instead of simple stock removal according to this equation, the electrolysis generates an oxide film on the anode. If the conductivity of the film is low, it may act to retard the electrolytic material removal rate.

ELID techniques have been under development for ceramic microgrinding for about five years (10). Most of the early work in this field was performed on cast iron fiber bond grinding wheels. It has been proposed that the mechanism of ELID consists of the formation of a passivated oxide film on the surface of the cast iron wheel, followed by a gradual removal of the oxide layer due to abrasive wear between the oxide and the work piece (6). As the non-conductive oxide layer is removed, the electrical resistance between the fixed cathode and the rotating anode (i.e. the grinding wheel) is reduced, causing increased electrolysis and a rebuilding of the oxide layer. The oxide layer acts as a feedback controller in the dressing process. Without it, electrolytic erosion would take proceed at a nearly constant rate for a particular set of ELID conditions. The formation of a passivated oxide layer inhibits further electrolysis, linking the wheel erosion rate to the abrasive wear rate of the oxide.

In practice, ELID is accomplished using a DC, AC, or pulsed DC power supply. While all three have been used, the relative merits or deficiencies of the selected type of power source are not well understood (10).

ELECTROLYSIS FOR BRONZE-BONDED GRINDING WHEELS

In 1992, we initiated an investigation of electrolytic in-process dressing of bronze-bonded diamond grinding wheels for ceramic micro-grinding. We began with a phenomenological study designed to provide insight into what occurs on the surface of the wheel during electrolysis. Using scanning electron micrography, we examined the surfaces of bronze-bonded grinding wheels subjected to electrolysis. A second series of experiments were directed at quantifying electrolysis processes on bronze wheels in terms of the *rate of growth of the electrolytically affected layer*. These experiments were conducted on a rotating grinding wheel, without any grinding taking place (i.e., no work piece contact). The results will serve as input for a planned set of experiments involving electrolysis analysis during actual grinding.

Surface Features in Bronze-Bonded Wheel Dressing

In our initial qualitative study, a bronze grinding wheel was cut into eight segments that could each act as an anode (these small anodes were sized for viewing under the SEM). A block of graphite was used as the cathode. The two electrodes were positioned parallel to one another, spaced apart by non-conducting shims, in an electrolyte bath (a 1 Molar NaCl solution). A 20 watt power supply was used to provide the current across the electrode gap. A digital storage oscilloscope was used to measure both voltage and current. The anode was subjected to electrolysis for a brief period, and was then inspected under the SEM. This cycle was repeated several times. A series of fiducial markings engraved into the anode surface prior to the beginning of the experiment permitted re-viewing of a particular location at various stages of the experiment.

Figure 2 shows the surface of one of the small anodes at 500X magnification, prior to any electrolysis. Figure 3 shows the same location after 2.5 minutes of

electrolysis at 4 volts, with a 380 µm gap. It was observed that etching did not occur uniformly. Rather, the electrolytic process appeared to cause localized pits on the bronze surface.

Dynamics of Film Formation and Wheel Recession

Figure 4 is a schematic of the experimental set-up used to evaluate electrolysis dynamics. The bronze bonded grinding wheel is rotated by a servo-controlled DC motor. The bottom third of the wheel is immersed in the electrolyte bath. A steady flow of new electrolyte is continually added to the bath, and the overflow is discarded. Temperature and conductivity probes in the electrolyte bath are continuously monitored. The anodic wheel is maintained at ground potential using a contacting graphite brush. The graphite cathode is positioned with its surface parallel to the face of the cup-shaped grinding wheel. The electrode gap is adjusted using a micrometer-driven linear ball-bearing stage. Electrode power is provided by a pulsed EDM power supply, with specifications outlined in Table 1.

Table 1: Specifications of the EDM power supply.

Voltage	150 Volts (max)
Current	35 Amps (max)
Pulse On Time	0.1 to 1000 µs
Pulse Off Time	0.1 to 1000 µs
Duty Cycle	0.1 to 99.9%

Before mounting the wheel on the test apparatus, it was trued and two 6 mm wide, 20 µm deep grooves were cut into its cup face, using a separate ultraprecision grinding machine. These grooves serve as reference surfaces for measuring oxide film thickness and the electrolytically affected depth. Before each electrolysis test, the wheel face was returned to its original condition by chemically etching it with a three-part solution of distilled water, hydrogen peroxide (3%), and ammonium hydroxide (30%), mixed in equal proportions. Subsequently, a capacitive displacement
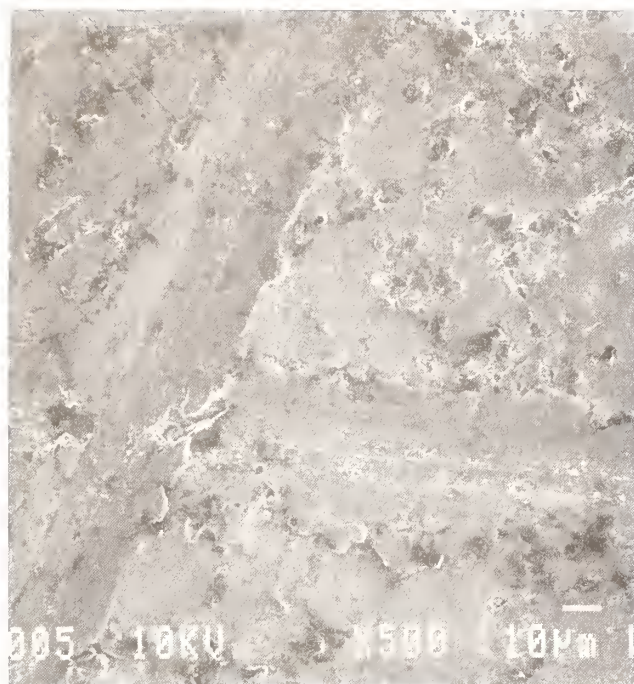
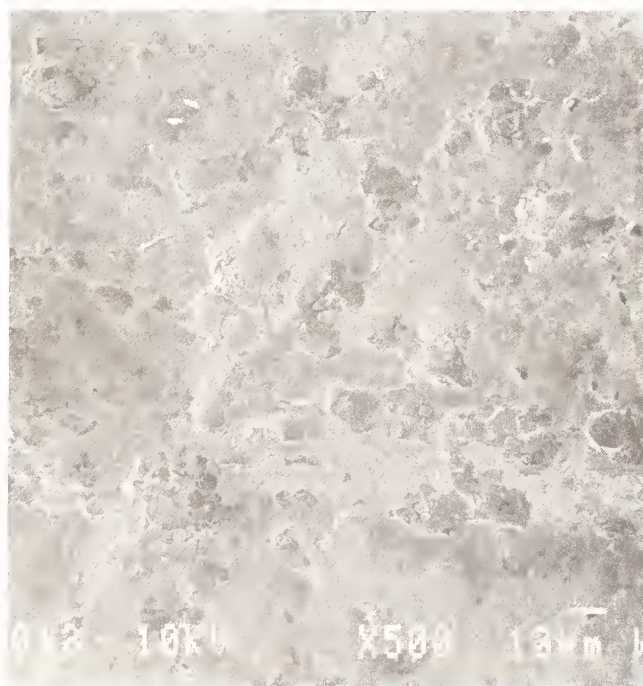Figure 2: SEM photo of bronze surface prior to electrolysis.

Figure 3: SEM photo of bronze surface showing pitting brought about by electrolysis.
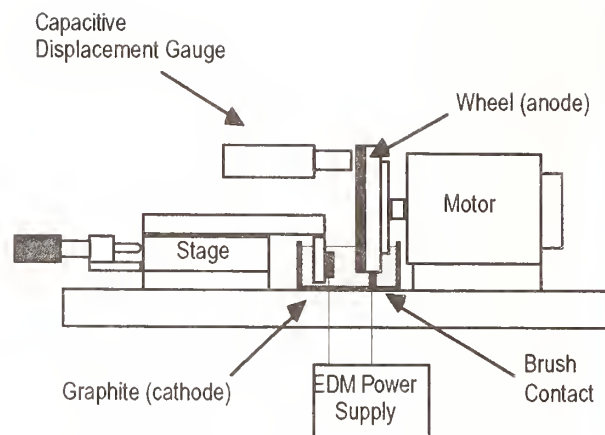

Figure 4. Experimental Set-up

gauge, with 10 nm resolution, 40 kHz bandwidth, and 50 μm range, is used to measure the face of the cup wheel. The gauge records a profile of the rotating wheel face; this profile, which includes the grooves, serves as a reference against which future profiles can be compared.

To protect the grooves during a test, a hard, removable film was applied to the grooves. Cellulose nitrate (clear finger nail polish) was found to be non-conducting, rugged, transparent, and soluble in acetone, making it ideal for this masking operation.

After masking the grooves, the trough built around the lower third of the grinding wheel was flooded with electrolyte from a large reservoir using a constant flow-rate, one-pass coolant delivery system. The wheel was then rotated at 200 rpm, and the entire apparatus was allowed to run for 10 minutes without applied voltage before the beginning of each test.

The electrolysis tests were conducted using the parameters shown in Table 2. A total of thirteen tests were made, varying only the duration of the test, up to 180 minutes. Conductivity and temperature, which generally remained constant in all tests, were recorded at one-minute intervals.

Maximum and minimum values of the voltage and current waveforms were mea-

Table 2. Settings for electrolysis tests

Parameter	Setting
Voltage	130 Volts
Electrode Gap	250 μm
Duty Cycle	50 %
Cathode Area	55 mm^2
Electrolyte	0.0002 M NaCl
Flow Rate	140 ml/min.
Wheel Speed	200 rpm
Wheel Type	Bronze, 10-20 Concentration 100
Wheel Geometry	101 mm outer diam. 89 mm inner diam.
Test Duration	0-180 minutes

sured and stored at three second intervals. After the test was completed, the electrolyte was drained from the system. At this point, a hard oxide film had built up on the wheel surface (A film forms even in the absence of electrolysis, due to surface oxidation in the 10 minute warm-up period). The wheel was then rinsed with methanol and allowed to air dry, after which the protected grooves were uncovered using acetone. The displacement gauge was then used to measure a profile of the wheel. When the original profile was subtracted from this new profile, a measure of the oxide film thickness could be made. A problem with this technique is that, in principle, the oxide film should not be conductive, and would not permit accurate profile measurement using the capacitance gauge. In fact, measurements of resistance across the film consistently showed that the film continued to be conductive, even when it had grown to considerable thickness. After storing a profile of the oxidized wheel, the reference grooves were again protected with cellulose nitrate. The film on the surface of the wheel was removed by a two-step application of acids. The acids were applied to the rotating wheel with a sponge. The first application used 7% HCl for two minutes. The second application used 2% H_2SO_4, also for two minutes. After each acid application, methanol was applied to the wheel to rinse residual acid and dry the wheel. HCl and H_2SO_4 were chosen because they are used in industrial pickling solutions that remove oxide films

from bronze without attacking the metal itself. Resistance of the bronze bond to chemical attack by the acid solutions was confirmed experimentally.

After removal of the oxide film, the protective coating on the reference grooves was again removed, and another profile of the wheel face was measured and stored. From this new profile, the original profile was subtracted, and the difference was displayed on an oscilloscope. Figure 5 shows one of these "difference profiles" in the vicinity of a reference groove. The peak of the difference profile corresponds to the reference groove on the grinding wheel. Since this area was unaffected by the electrolysis process, the difference profile is set to zero at this peak. From this zero level, the distance to the to the base of the difference profile is a measure of the *electrolytically affected depth*. With the oxide film removed, it is also a measure of the *recession of the bronze*. Our estimate of the probable measurement error in calculating the depth of the electrolytically affected depth is +/- 1 micrometer. This includes errors due to: non uniformity of the oxidation and acid etching processes, gauging/fixturing errors, and setting the electrode gap.
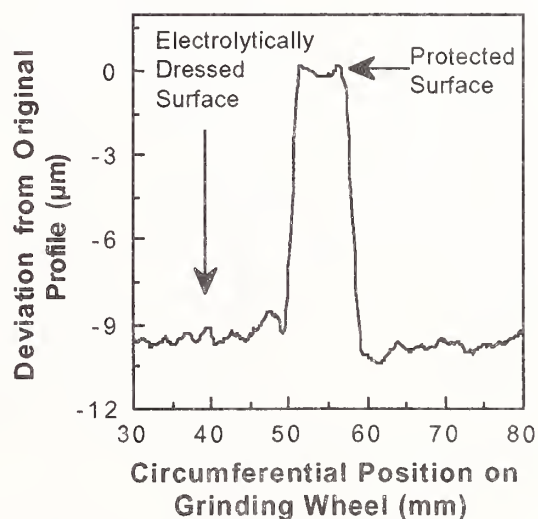

Figure 5: Difference profile, resulting from subtraction of final wheel profile (with the oxide film removed) from reference profile. Data is for a 70 minute electrolysis test.

RESULTS AND DISCUSSION

Figures 6 and 7 display data for the series of timed electrolysis tests. Figure 6 shows the electrolytically affected layer as a function of time, while Figure 7 shows the height of the oxide film above the original surface of the wheel, again as a function of time.

Figure 8 shows a representative plot of voltage and current from one our tests. Unlike the results reported by others for cast iron grinding wheels, the voltage and current remain relatively constant throughout the electrolysis test. This is due to the fact that our oxide film is conductive, and does not inhibit the electrolysis process. Also, at <50 micrometers in thickness, the oxide film is much thinner than the 3-4 mm oxide layer reported for cast iron wheels (10).

At the same time, the film advances into the bronze binder in the wheel, convert-
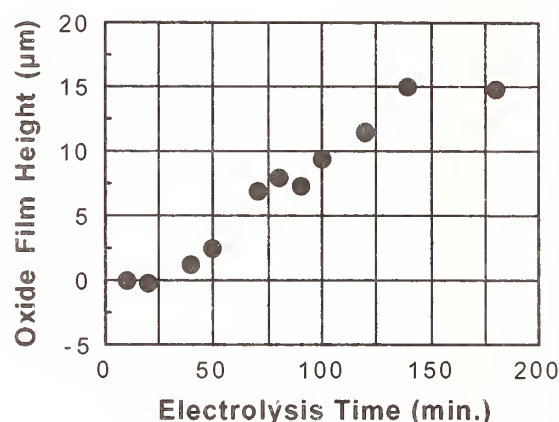
Figure 7. Oxide film height (above original surface) as a function of time.
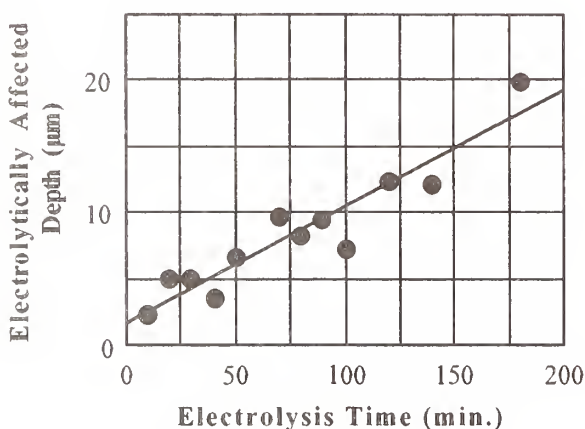
Figure 6: Electrolytically affected depth versus time for electrolysis tests. The electrolytically affected depth is a measure of the recession of the bronze bond. In this graph, the solid line is a linear regression of the data, indicating a slope of 1.5 nm/second.

From Figure 7 one can see that the oxidized surface of the wheel does not recede with electrolysis. Because of the growth of an oxide film both into and out of the original surface, the film on the wheel face actually advances toward the cathode.

Figure 8: Maximum voltage and maximum current as a function of time for a 30 minute electrolysis test.

ing bronze into oxide. The depth to which this oxide film extends is a parameter that we label the "electrolytically affected depth." In the absence of work piece abrasion of the oxidized film, the film might eventually grow thick enough to obscure the diamonds in the wheel. Thus,

338

the rate at which the oxide film wears in an actual grinding process is a critical parameter.

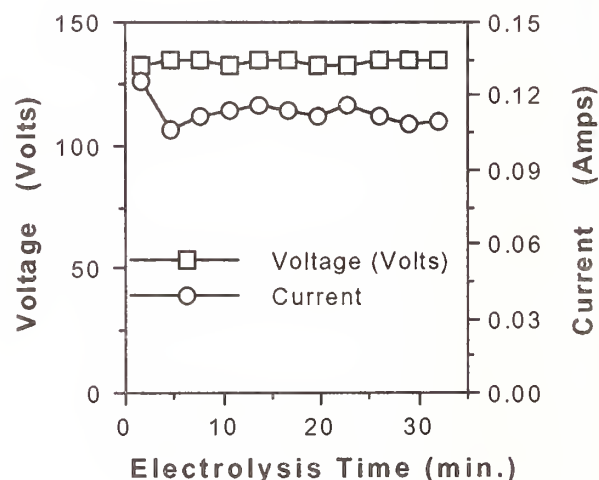For the conditions chosen in our electrolysis experiments, the rate of oxide film growth *into* the wheel is approximately constant at 1.5 nm/s. If the grinding process is such that the erosion rate of the oxide film due to abrasion is greater than the rate of oxide film formation, one would expect the film generation rate (1.5 nm/s) to be equal to the dressing rate (or rate of wheel recession). As the abrasion wears through the oxide layer, the work piece will contact the bronze sub-layer, which is difficult to further abrade. Gradual rebuilding of the oxide layer through electrolysis would allow continued dressing at a rate equal to the film growth rate. Currently, it is unclear to us whether the oxide film will be more or less abrasion resistant than the underlying bronze bond.

If, however, the grinding process is such that the removal rate of the oxide film due to abrasion is less than the rate of oxide film formation, one would expect the rate of growth of the film to outpace the rate of wheel recession. In this case, the oxide abrasive wear rate will determine the rate of wheel recession, independent of the growth rate of the electrolytically affected layer.

The film observed on the surface of the wheel does not prevent, nor even slow down the electrolytic process; rather the boundary between the bronze and the electrolytically affected layer on a bronze-bonded wheel continues to advance into the wheel at a constant rate with dressing time. The rate for the particular combination of factors investigated here 1.5 nm/s. It is expected that this rate will be decrease linearly with decreasing cathode voltage magnitude and will decrease inversely with electrode gap. Our plan is to alter the test parameters systematically to determine if these relationships will hold, and to install this system on an ultraprecision grinding apparatus.

CONCLUSIONS

A relatively simple test procedure for analyzing electrolysis dynamics has been described. In a series of experiments, we have found that electrolysis results on bronze-bonded grinding wheels are quite different than those reported for cast iron grinding wheels. We have found that a thin, conductive oxide film forms on the surface of the wheel for the conditions tested. The rate of growth of this film into the grinding wheel is remarkably constant for up to three hours of electrolysis. The dressing process may be controllable using this constant film growth rate, depending on the abrasive wear characteristics of the film in actual grinding conditions. Further work varying the electrolysis parameters and including the effects of actual grinding are planned in the near future.

REFERENCES

1. T. G. Bifano, T. A. Dow, and R. O. Scattergood, "Ductile-Regime Grinding: A New Technology for Machining Brittle Materials," **ASME J. Eng. for Industry,** [113], pp. 184-189, 1991.

2. T. G. Bifano, Y. Yi, and W. K. Kahl, "Ductile-Regime Grinding of Ceramic Mirrors," in review, **J. Precision Engineering,** 1993.

3. T. G. Bifano and S. C. Fawcett, "Specific Grinding Energy as an In-Process Control Variable for Ductile-Regime Grinding," **Precision Engineering,** [13]:4, pp. 256-262, 1991.

4. T. G. Bifano, Y. Yi, and W. K. Kahl, "Fixed Abrasive Grinding of CVD SiC Mirrors", Accepted for publication, **J. Precision Engineering,** 1993.

5. K. Abe and N. Yasunaga, "Cleaning Technique for Super Abrasive Grinding Wheel with FRP Cleaner", *Proceedings of ASPE 1992 Annual Meeting*, pp. 83-86, 1992.

6. H. Ohmori and T. Nakagawa, "Mirror Surface Grinding of Silicon Wafers with

Electrolytic In-Process Dressing", Annals of CIRP, 1990.

7.   R. Polvani and C. J. Evans, "Preparing Ultraprecision Grinding Wheels", *ASPE 1992 Annual Meeting*, October, 1992.

8.   R. Polvani and C. J. Evans, "Electrical Assisted Grinding of Precision Glass and Ceramic Parts", *Optical Fabrication and Testing Workshop*, **OSA Technical Digest Series Volume 24**, pp. 120/WB2-1, 1992.

9. J. A. McGeough, Principles of Electro-chemical Machining, Chapman and Hall, 1974.

10.   K. L. Blaedel and P. J. Davis, Foreign Trip Report, (Visit to Japan), Lawrence Livermore National Laboratory, June 1990.

EFFECT OF DUCTILE-REGIME GRINDING ON THE STRENGTH OF HOT-ISOSTATICALLY-PRESSED SILICON NITRIDE

L. K. IVES, C. J. EVANS, S. JAHANMIR, R. S. POLVANI,
T. J. STRAKNA*, and M. L. MCGLAUFLIN
National Institute of Standards and Technology, Gaithersburg, MD

Hot isostatically pressed silicon nitride was surface ground in the ductile regime. The specimens were in the form of standard flexure test bars thereby permitting the evaluation of both the surface finish and the influence of grinding on fracture strength. A high precision grinding machine equipped with air-bearing spindles was employed for ductile-regime grinding. In-process electrochemically assisted dressing of the 2000 grit diamond metal-bond wheel permitted the simultaneous grinding of multiple specimens. For comparison, similar specimens were also ground by conventional means employing 400 grit and 900 grit wheels. Specimens ground in the ductile regime exhibited improved characteristic strength and superior surface finish.

Introduction

Silicon nitride ceramics, along with a number of other advanced ceramics, are increasingly important materials for applications which demand high hardness, high strength, excellent wear resistance, and extreme chemical inertness. These materials become even more attractive when exposure is at elevated temperatures. Unfortunately, the properties that make advanced ceramics so useful, coupled with very limited ductility, render them difficult to machine. In general, abrasive machining methods are employed with diamond grinding being the most flexible for achieving complex parts geometries, high precision, and satisfactory removal rates [1,2]. The finish and integrity of conventionally diamond-ground surfaces are suitable for many applications. For rolling-element bearing components and other highly critical applications the as-ground surface may not be adequate. When surfaces must be extremely smooth and the presence of machining damage minimized, an additional finishing step, abrasive polishing, is required. Conventional polishing methods, however, usually involve different fixturing, give relatively low material

removal rates and have considerable difficulty in maintaining specified tolerances for other than the simplest geometries.

Ductile-regime grinding is an attractive alternative finishing method which can minimize or perhaps entirely eliminate the need for final polishing [3, 4]. With this grinding method it is possible to create components having extremely precise geometric form and at the same time produce surface finishes on a nanometer scale of roughness. In addition, near surface and subsurface damage is expected to be comparable with that achieved by fine abrasive polishing. The success of ductile-regime grinding has been demonstrated in the fabrication of aspheric glass optical components [5]. Ductile-regime grinding has also been demonstrated in the case of semiconductors [6] and several ceramic materials [3,4,7].

In practice, ductile-regime grinding is accomplished by limiting grit penetration to a depth less than that at which fracture is initiated. While grit penetration in polishing is controlled largely by using abrasive media of a sufficiently small grit size, in grinding, control is a result of achieving and maintaining extremely precise displacement of the tool with respect to the workpiece.

To operate within the ductile regime, grit penetration must not exceed a threshold depth, about

0.1 μm or less, determined primarily by the hardness and toughness of the material being ground [4]. Material removal is confined to the extent of grit penetration and is described by the cross sectional profile of the grit in the direction of motion. Plastic flow is considered to play a critical role and the chip formation process is likened to that which occurs with ductile materials. When the ductile threshold depth is exceeded, microcracks are introduced into the surface and material removal occurs by brittle fracture processes that may extend far beyond the grit penetration profile [8].

The purpose of the present investigation was threefold: 1) to show that ductile-regime grinding of a high strength, hot-isostatically-pressed silicon nitride material could be achieved; 2) to assess the influence of ductile grinding on the strength of this material; and 3) to compare ductile-regime grinding to two more-or-less conventional grinding methods with respect to influence on strength and surface finish.

The experimental approach was similar to that taken in two related investigations [9,10] concerned with the effect that grinding might have on the strength of different types of silicon nitride and on the influence of grinding parameters on strength and surface finish. In those investigations and similarly in the present study, the workpieces or specimens were four-point flexure test bars. By applying the grinding condition of interest to the critical tensile surface of the flexure bar, the influence on strength of that grinding condition was determined by conducting a flexure test. Subsequently, fractography, carried out by means of light microscopy and scanning electron microscopy (SEM), was used to locate and examine the fracture origin, the intent being to determine if the originating flaw could be associated with grinding induced damage. The surface topography was evaluated by means of SEM, stylus profilometry, and light optical methods.

Experimental Procedure

a) Specimen Material

The material employed in this investigation was a bearing grade, hot-isostatically-pressed silicon nitride (Noralide NBD-200, a product of Cerbec, Inc.**). Specifications provided by the manufacturer are given in Table 1. To minimize the possible influence of processing related variations, the specimens were cut from the same production lot of

Table 1. Properties of NBD-200 silicon nitride*

COMPOSITION	1 wt.% MgO, bal. Si_3N_4
DENSITY (g/cm³)	3.16
ELASTIC MODULUS (GPa)	320
POISSON'S RATIO	0.26
HARDNESS, VICKERS 10 kg, (GPa)	16.6
STRENGTH PROPERTIES @ 20°C -FLEXURAL, 4-point bend, (MPa) -WEIBULL MODULUS -TENSILE (MPa) -COMPRESSIVE (GPa) -HERTZ COMPRESSIVE (GPa) (ball on flat)	800 9.7 400 3.0 28
FRACTURE TOUGHNESS, K_{Ic} (MPa.m$^{1/2}$)	4.1
THERMAL PROPERTIES -THERMAL EXPANSION COEF. (10^{-6}/°C) 170°C - 20°C 20°C - 1000°C -THERMAL CONDUCTIVITY (W/m.K) 100°C 500°C 1000°C -MAXIMUM USE TEMPERATURE (°C)	0.43 2.9 29.3 21.3 15.5 1000

*Manufacturers data

** Certain trade names and company products are identified in order to adequately specify the experimental procedure. In no case does such identification imply recommendation or endorsement by the National Institute of Standards and Technology, nor does it imply that these products are necessarily the best available for the purpose.

material. The starting material consisted of 5 tiles, each having dimensions of 9 x 58 x 59 mm. Flexure bar specimens for each grinding condition were distributed equally among all tiles to minimize variations that might be associated with differences among the tiles.

b) Grinding Methods

Grinding was carried out to obtain flexure test bars with final dimensions of 4.0 x 3.0 x 50 mm in compliance with configuration B of ASTM C1161-90 Standard Test Method for Flexural Strength of Advanced Ceramics at Ambient Temperature [11]. The tensile surface of each flexure bar was ground: 1) under conditions resulting in a ductile removal mechanism, 2) using a conventional grinding method employing a 400 grit wheel that satisfied the requirements of ASTM C1161-90 designed to minimize or eliminate the effect of surface preparation on flexure strength, and 3) under carefully controlled conditions with a 900 grit wheel to produce a smooth surface, and also thought to minimize grinding damage. The conditions for each of these grinding methods (designated ductile, 400 grit, and 900 grit) are summarized in Table 2. In all cases grinding was parallel to the long axis of the bar.

Initial preparation was the same for all bars. Preparatory grinding was done on the five tiles to obtain flat surfaces and appropriate starting dimensions. A relatively coarse 150-180 grit resin-bond diamond wheel was used for this purpose. Eighteen bars were then cut from each tile with a resin-bond diamond saw to a size of approximately 4 mm thick, 6 mm wide, and 51 mm long. This oversize (0.5 mm on each face) was sufficient that the effects of process-related variations at the original tile surface and damage introduced by preliminary grinding and cutting could be eliminated by subsequent surface grinding.

One set of 30 bars was then surface ground in compliance with ASTM Standard C1161-90. The standard requires that grinding on each face be conducted in two stages. In the first stage material is to be removed at a rate of no more than 0.03 mm/pass and that at least 0.06 mm remain for removal in the final finishing stage at a rate not to exceed 0.002 mm/pass. The same requirements also apply to the chamfers which must be placed on the long edges of each bar. Grinding is to be carried out with a wheel having diamond grit in the 320-500 size range. In this investigation, a nominally-400 grit resin-bond diamond wheel was employed. Additional grinding parameters are listed in Table 2. Finished in this way, the 30 specimens were then

Table 2. Grinding parameters used to finish flexure bar tensile surface

PARAMETER	METHOD		
	400 GRIT	900 GRIT	DUCTILE-REGIME
WHEEL -TYPE -BOND -GRIT -CONCENTRATION	Periphery Resin 400 100	Periphery resin 900 -	Cup Bronze 2000 50
DRESSING METHOD	Powered SiC grinding wheel	-	In process electrochemical
COOLANT	Water-base synthetic 20:1	Water-base synthetic 20:1	Water-base emulsion 80:1
WHEEL SURFACE SPEED (m/s)	29	-	16
FEED RATE (cm/min.)	-	-	0.2
DEPTH PER PASS (mm)	0.0025	-	0.0001
DEPTH REMOVED (mm)	0.05	0.005	

ready for flexure strength measurement and surface finish characterization.

Except for what would be the tensile face, the above grinding procedure was also used for the two other sets of 30 bars. For the thirty bars finished by means of the 900 grit method, final grinding of the tensile face employed wheels of progressively finer grit size, with the last 0.005 mm removed by means of a 900 grit resin-bond diamond wheel.

For the bars to be finished by ductile-regime grinding, the thickness was reduced only to 3.076 mm with the final 0.076 mm to be removed from the tensile face according to the various steps associated with the ductile-regime grinding method described below.

Ductile-regime grinding was performed on a Moore M-18 Aspheric Generator retrofitted with an integral, AC motorized, Professional Instruments Co. BlockHead 4R air bearing grinding spindle. The machine configuration is shown schematically in Figure 1. The axes of rotation of the grinding and main work spindles lie in a plane parallel to the machine's xz-plane. The grinding spindle axis was tilted at an angle of about 10° from the work spindle axis. Bronze-bond cup wheels, 100 mm in diameter, were employed for grinding.
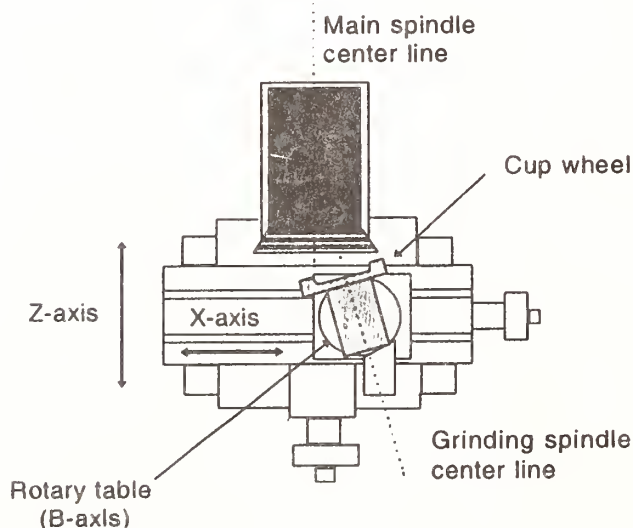

Figure 1. Machine configuration for ductile-regime grinding (top view).

To minimize the possible effects of process variability between flexure bars and to emulate, to some extent, practical grinding approaches, all 30 bars were machined simultaneously. This was accomplished by mounting the bars to an interface plate attached to a face plate on the M-18 spindle. Prior to mounting the bars, the interface plate was single point diamond turned to eliminate run-out and obtain a flat, parallel surface. A low-temperature melting-point wax was used for mounting the bars.

Fifteen bars were arranged in three groups of five, 120° apart, such that the groups effectively formed the sides of an equilateral triangle. Thus, the central portion of each bar, where the stress is highest in the four-point bend test, had its machining-lay parallel to the axis of the bar. The remaining fifteen bars were also arranged in three groups of five. However, they were oriented parallel to the medians of the equilateral triangle formed by the first three groups of bars and were effectively ground perpendicular to the long axis of the bar. At the completion of grinding, these bars were set aside for a separate study, not part of the present investigation.

As an initial step, preliminary experiments were performed to identify parameters which would ensure grinding within the ductile regime. Based on these experiments, the following conditions were found to be suitable: a 2000 grit (6-10 μm) 50 concentration diamond wheel, grinding spindle speed of 3000 rpm (5 m/s wheel surface speed), work spindle speed of 10 rpm, 0.1 μm nominal depth of cut, and 2 mm/min feed rate. Satisfactory results were obtained using both a mineral oil coolant and a water-base emulsion coolant. Initial machining experience suggested that wheel wear would be relatively rapid, requiring frequent dressing, so it was decided to grind exclusively in water-base coolant. This allowed the use of electrochemical in-process dressing [12].

Initial truing of the wheel was done with a 400 grit (40-50 μm) metal-bond diamond wheel. In the grinding configuration used, i.e. the face of the cup wheel at an angle of ~10° to the face plate, there was nominal line contact between the workpiece and the outer edge of the freshly trued wheel. Wear, however, produced a conical shaped wheel and an accompanying increase in contact area. This resulted in a higher contact force and increased machine deflection, adversely affecting grinding precision and finish. Thus, retruing was required at intervals throughout the grinding process.

In grinding such hard ceramics as silicon nitride, especially with metal-bond wheels, maintaining the wheel in a well-dressed condition is of critical importance. Rapid grit wear requires that the dressing procedure be applied frequently, or better,

344

continuously by means of an in-process method. Electrochemical dressing, employed in this investigation, is not only an effective means of dressing metal-bond wheels but also has the advantage that no mechanical contact is required with the wheel. Moreover, the rate of dressing can be controlled by adjusting the applied current. Compared to abrasive dressing methods, electrochemical dressing also avoids the introduction of abrasive particles and the damage that these particles might cause to the workpiece.

The dressing apparatus itself consisted of a flat metal electrode positioned parallel to the face of the cup wheel. The electrode mounting fixture was attached to the housing of the grinding spindle.

As-mounted, the flexure bar blanks were non-planar by over 10 μm. Preliminary grinding was performed using a 400 grit wheel to level the bars. A semi-finishing cycle using a 1200 grit (15-20 μm) wheel produced a surface with some residual fine fractures which were removed in the final ductile grinding mode using the parameters previously described.

The 400 grit and 900 grit grinding methods employed conventional horizontal-spindle, reciprocating-table grinding machines. The grinding was done by a commercial shop experienced in machining ceramic materials. Operational parameters are summarized in Table 2. Only limited information was available for the 900 grit method which was considered to be proprietary.

d) Flexure Test Procedure

Flexure tests were conducted using a four-point bending configuration. The steel flexure fixture was fully articulating to facilitate accurate alignment. Load was applied by means of a screw driven universal tension / compression test machine. The applied force was sensed with a load cell and the amplified signal monitored by means of a strip-chart recorder. Load was applied at a constant cross-head speed of 0.5 mm/min. An initial preload of 5 to 10% of the expected failure load was first applied and displacement halted while inspection was made for proper specimen alignment. If the alignment was not satisfactory (this rarely occurred) the load was released and the needed adjustments made. With proper alignment in the preload condition, the displacement was resumed and continued until failure. The load at failure, specimen width and thickness, and flexure span were used to calculate the failure stress, i.e., the fracture strength of the specimen. A Weibull statistical analysis was carried

out on the data. The resulting Weibull modulus and characteristic strength (defined as the stress at which 63.2% of the specimens failed) were used to assess the influence of the grinding method. A more detailed description of the test procedure and data analysis approach can be found in the paper by Jahanmir et al. [9].

The fracture surfaces of each specimen were examined by means of light optical microscopy and in selected cases by means of SEM to identify the location and possible nature of the fracture origin.

Results and Discussion

a) Surface Finish

Scanning electron micrographs displaying the typical finish of surfaces ground by the ductile, 400 grit, and 900 grit methods are shown in Figure 2-4. Apart from a few pits and an occasional scratch, the ductile ground surface, at least in the central region of the bars, was nearly indistinguishable from that produced by careful polishing. A representative SEM micrograph of the central region is shown in Figure 2a. At the edges of the bars, however, there was a band of fine pits. This indicated that grinding was to some extent in the brittle regime at that location. Figure 2b shows the pitted region adjacent to the chamfered edge of the bar.

The surface prepared with the 400 grit method, Figure 3, is seen to consist of a relatively high concentration of pits distributed over a pattern of parallel grooves lying along the direction of grinding. The pits are a consequence of microfracture that occurred during material removal. The smooth areas between pits suggest that plastic flow and perhaps ductile removal also had occurred.

The finish of the surface ground with the 900 grit method, Figure 4, differs from that prepared by the 400 grit method in that grinding grooves are very shallow and are barely detected in this SEM micrograph (the grooves are more apparent in the topographic map, Fig. 6b). Pits similar to those associated with the 400 grit method are present, however. Complete details of the 900 grit grinding method were unavailable precluding the development of additional conclusions regarding the appearance of the surface.

The shape of the ductile ground surfaces was evaluated by means of a phase measuring interferometer. Along their central long axes, the bars were flat to approximately 1 μm. Lateral traces also showed that the bars were flat near their ends.
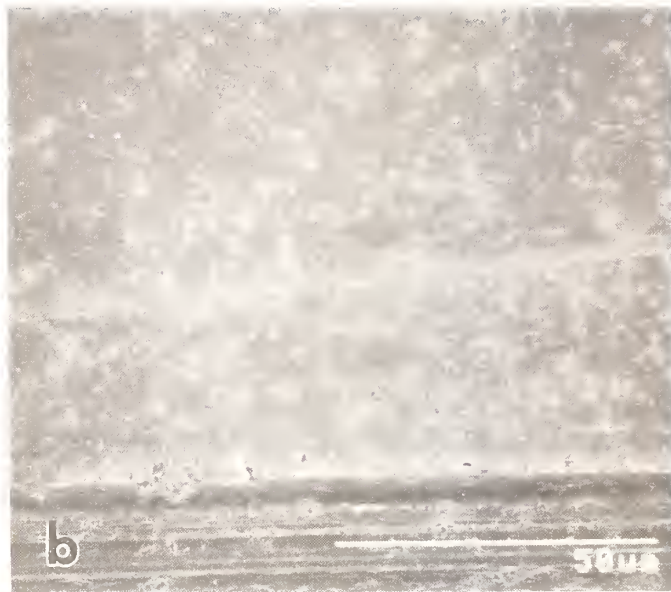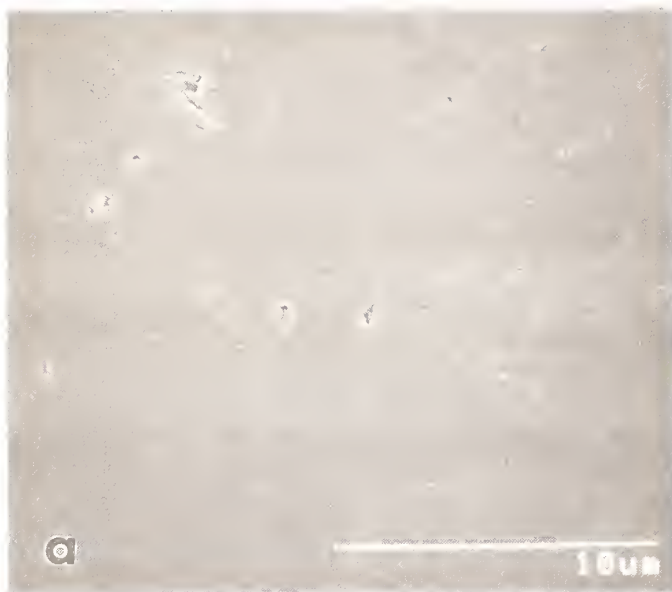
Figure 2. SEM micrographs of surfaces ground by ductile-regime method. a) near center of bar, b) adjacent to chamfer edge showing evidence of micro-fracture.
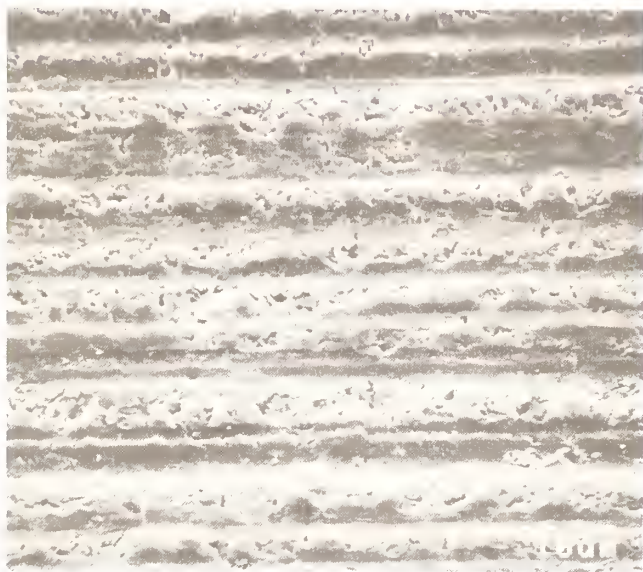

Figure 3. SEM micrograph of surface ground by means of the 400 grit method.

Figure 4. SEM micrograph of surface ground by means of the 900 grit method.

The centers of the bars, however, were crowned laterally by about 3 μm. This surface geometry can be explained by the fact that the M-18 was not designed to be a stiff production grinding machine. Thus, because of machine defection, stock removal will not equal nominal infeed. At the center of the bar, this causes no problem, nor at the ends of the bar where the grinding direction is at an angle relative to the bar axis so that the wheel contact bridges several bars. As the wheel approaches an edge – particularly at the mid span of the bar at the gap between adjacent bars caused by the chamfers – the situation changes. The wheel contact area decreases resulting in a higher contact pressure, and more material is removed causing the crowning.

The surface finish of the ductile ground bars was measured with a phase measuring microinterferometer using a 20X objective. This gave a 0.5 mm square aperture and a spatial resolution of approximately 2 μm per pixel. A representative example of a ductile ground surface is shown in Figure 5. The indicated roughness of the ductile ground surfaces was found to be approximately 3 nm R_a.

Stylus profilometry was employed to generate three-dimensional maps of surfaces prepared with the 400 grit and 900 grit methods and to determine roughness values. Representative examples of surface maps are shown in Figure 6. Surface roughness values are given in Table 3. These values were determined by averaging over a 1 mm by 1 mm area of the surface.
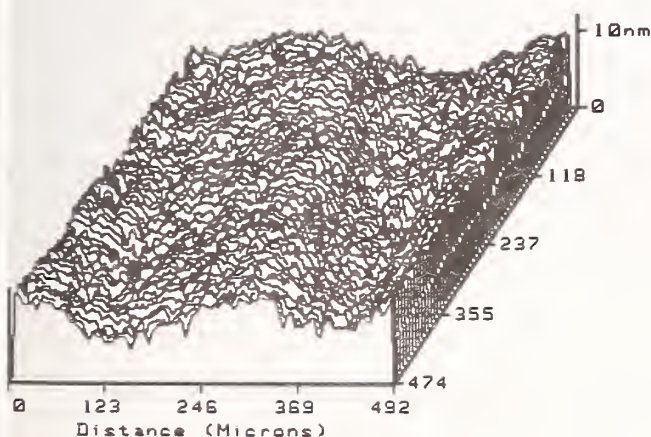
Table 3. Surface roughness values

GRINDING METHOD	SURFACE ROUGHNESS, R_a (μm)
400 GRIT	0.30
900 GRIT	0.018
DUCTILE REGIME	0.003

The grooved topography of the surface ground with the 400 grit method is quite apparent in Figure 6a. As mentioned previously, only shallow grooves can be distinguished on the surface prepared with the 900 grit method shown in Figure 6b. The pits observed in the SEM micrographs result only in small local variations in the surface maps due to the relatively low lateral resolution employed (10 μm between traces), and the limited capability of the stylus (10 μm tip radius) to trace such features. The surface ground with the 900 grit method is significantly smoother (0.018 μm R_a) than the surface ground with the 400 grit method (0.30 μm R_a).

b) Fracture strength

Weibull plots displaying probability of failure vs. fracture stress are shown in Figure 7 for the three grinding conditions. Straight lines representing a linear least square fit for each data set are shown. The slope of each line gives the corresponding Weibull modulus, and the point on the line at which 63.2% of the specimens fail defines the characteristic strength. Figure 8 compares the characteristic strength and Weibull modulus values for each condition. Within the 95% confidence limits indicated in Figure 8, it is clear that the ductile-regime grinding method resulted in a higher characteristic strength compared to the 400 grit and 900 grit methods. Statistically, the 400 grit and 900 grit methods resulted in about the same characteristic strengths. It is interesting to note that the strength values in the range 900-1000 MPa obtained here are significantly higher than the value of 800 MPa given by the manufacturer in Table 1. Although detailed information was not available, the lower strength is apparently the result of greater damage introduced during specimen preparation.

As seen in Figure 8, there is no statistical difference in Weibull modulus values determined for the different grinding conditions. That is, the spread

Figure 5. Three-dimensional interferometry representation of ductile ground surface.
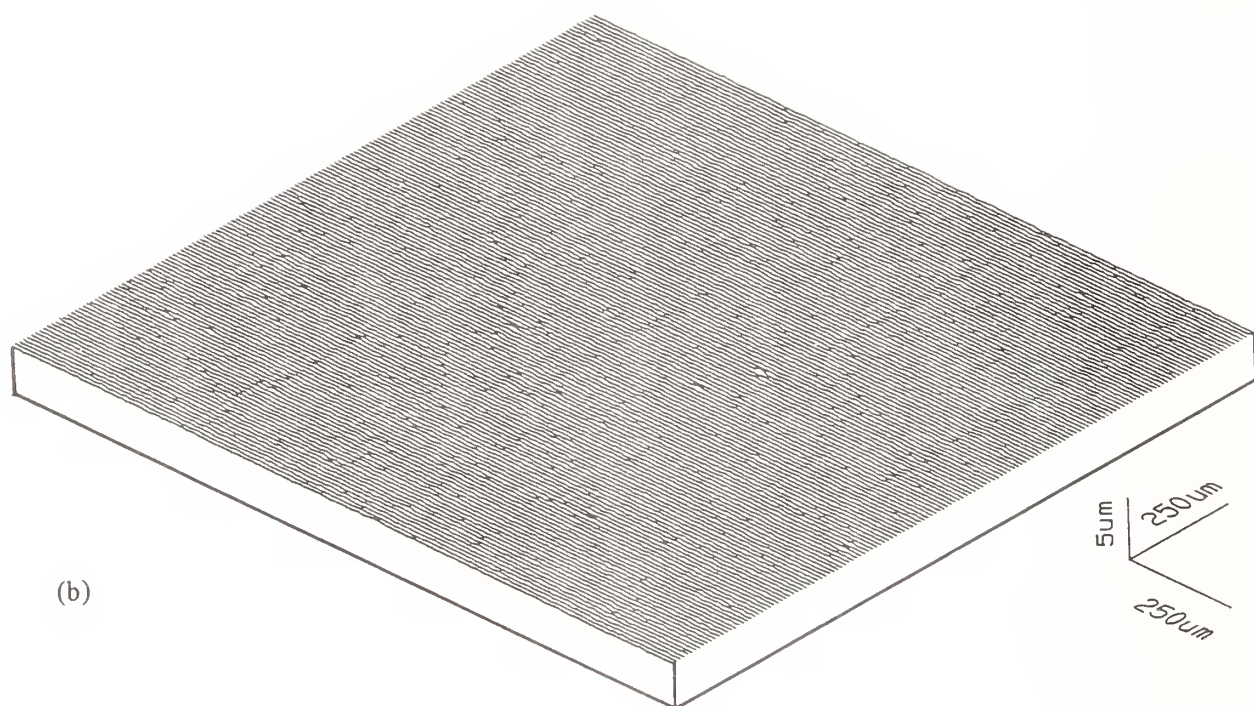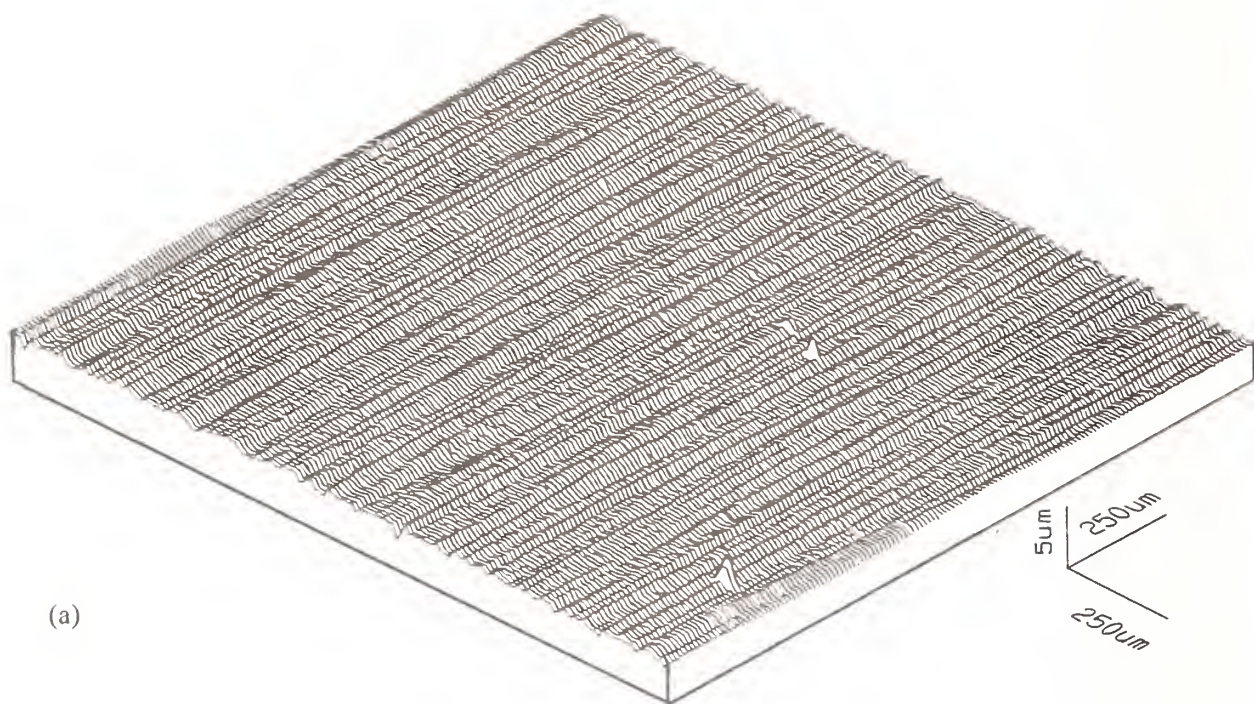
Figure 6. Surface roughness maps generated by stylus profilometry. a) 400 grit method. b) 900 grit method.
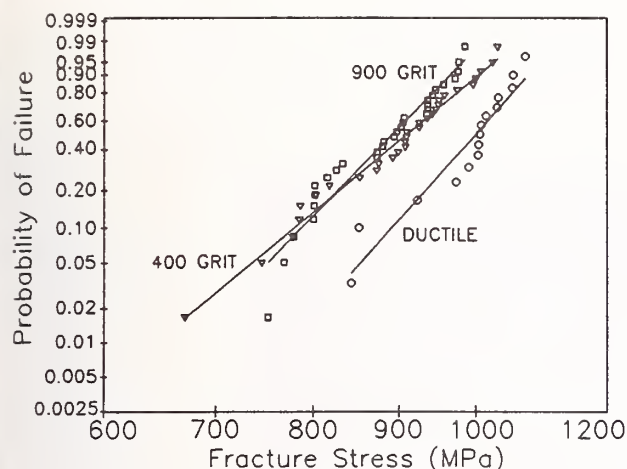
Figure 7. Weibull plots of flexure strength comparing 400 grit, 900 grit and ductile-regime methods.

in the distribution of fracture stress values was approximately the same for the three grinding methods.

There are four factors which could contribute to the greater strength of the ductile ground specimens. These are 1) the lack of grinding induced flaws, 2) smaller flaws at the ductile ground surface compared to the other grinding methods, 3) a smoother surface from ductile grinding and consequently the elimination of notch effects, and 4) a more favorable residual stress state at the ductile ground surface. Examination of the fracture surfaces in the immediate vicinity of the fracture origin was employed to assess the influence of factors 1), 2), and 3) above. Analyses were not carried out to determine the possible influence of the fourth factor, the surface residual stress state. The identification of a larger compressive residual stress at the ductile ground surface, for example, might be regarded as providing greater resistance to failure.

Scanning electron micrographs of a mating pair of fracture mirrors obtained on one of the fractured, ductile ground specimens are shown in Figure 9. The mirrors intersect the ground surface in a nearly semicircular shape. This is a good indication that the fracture origin was at the surface of the specimen. The centers of the mirrors at their intersection with the ground surface are shown at higher magnification in Figure 10. The specimens were tilted so that both the fracture surface and ground surface could be imaged simultaneously. The presence of an inclusion, large grain, or

evidence of a pre-existing pore could not be identified. By a process of elimination, this suggests a microcrack or pit in the surface, perhaps introduced by machining, might have acted as the fracture origin. The geometry of the fracture surface, shown in Figure 10, could indicate that the microcrack or pit was oriented at an angle to the tensile axis.

Of the 15 ductile ground specimens tested, all had fracture mirrors that were similar in appearance, apart from size and small geometric variations, to that shown in Figure 9. All were semicircular in shape
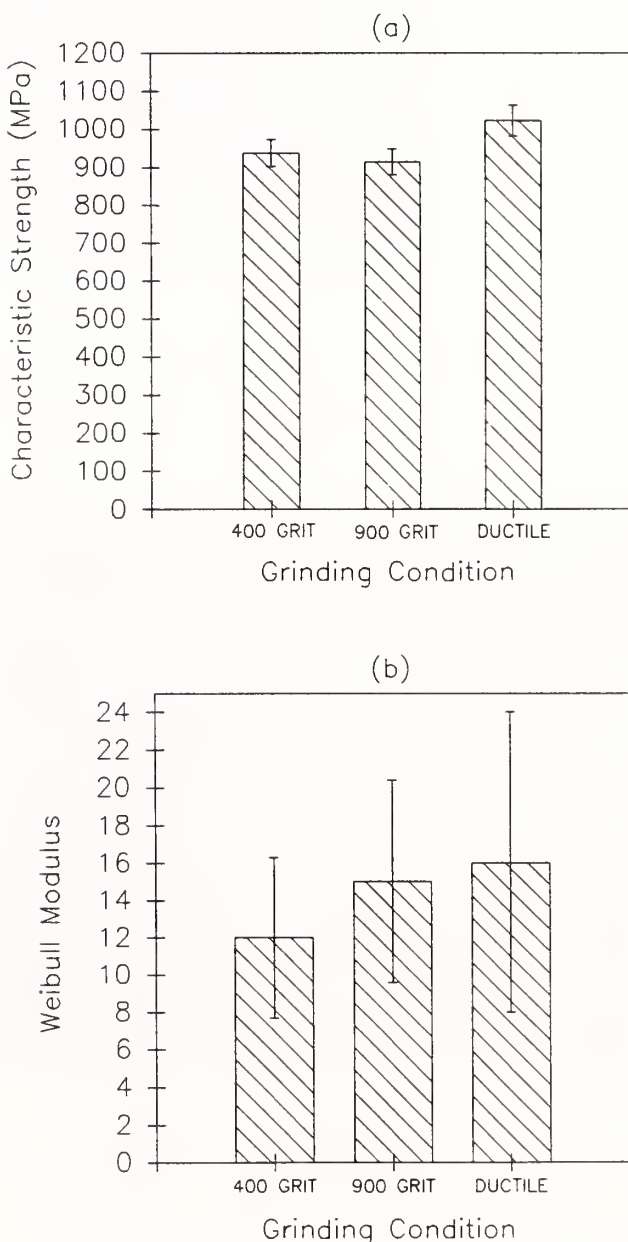

Figure 8. Influence of grinding method on a) characteristic strength and b) Weibull modulus.

349

Figure 9. SEM micrographs of mating fracture mirrors on ductile ground specimen.
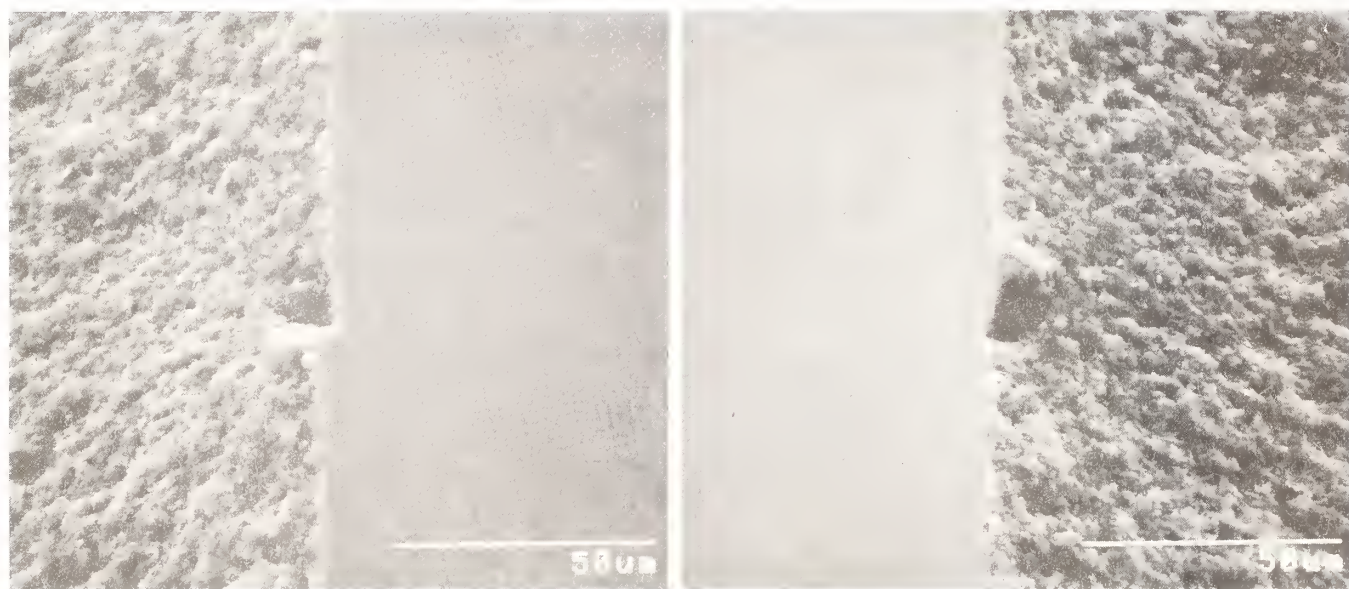

Figure 10. SEM micrographs of fracture origins in Figure 9 at higher magnification. Specimens are tilted at 45° to show ground surface.

indicating an origin in the immediate vicinity of the ground surface. In two instances the fracture mirror was at the specimen chamfer. In no case was there conclusive evidence that the initiating flaw was an inclusion, large grain, or pore, nor was it possible to associate a machining related surface scratch or pit with the origin. As was noted previously, a few scratches and pits were present in the ductile ground surfaces. Moreover, the pitted zone near the edge of the bar was not a preferred location for fracture initiation. Therefore, the obvious pits and scratches were not necessarily the sources of fracture initiation. It is possible that large cracks that are closed or lie slightly below the surface, and therefore not detected in the SEM, are the predominant source of failure.

Examination of fracture surfaces of specimens prepared with the 400 grit and 900 grit methods was similarly indeterminate with respect to associating the fracture origin with a specific flaw. The fracture mirrors were similar in appearance to those on the ductile ground specimens. However, the fact that the average strength of specimens prepared with the 400 grit and 900 grit methods was less than that of the ductile ground specimens suggests that machining related flaws did have an adverse effect on failure. The only alternative, as mentioned previously, is that a more favorable surface residual stress state of the ductile ground specimens resulted in the higher strength.

Conclusions

(1) By utilizing a high precision grinding machine, ductile-regime grinding of a high-strength hot-isostatically-pressed silicon nitride was demonstrated. Moreover, simultaneous grinding of multiple specimens was achieved by employing in-process electrochemical dressing of the metal-bond grinding wheel. Insufficient machine axial stiffness, however, did lead to a brittle zone near the edge of the specimens.

(2) Ductile-regime grinding led to a higher flexure strength than conventional grinding with a 400 grit resin bond wheel, where the conventional method met the requirements of ASTM Standard C1161-90. A grinding method employing a 900 grit wheel produced a smoother surface than the 400 grit method; however, the flexure strength was not improved. Approximately the same Weibull modulus was obtained for the three grinding methods.

(3) Fractographic analysis of the failed flexure test specimens was not able to identify the nature of the originating flaws. All of the examined fractures originated in the immediate vicinity of the surface. Even though a few pits and scratches were present on the ductile ground surface, these visible defects did not act as preferential sites for failure.

References

[1] S. Jahanmir, L. K. Ives, A. W. Ruff, and M. B. Peterson, Ceramic Machining: Assessment of Current Practice and Research Needs in the United States, NIST Special Publication 834, U.S. Government Printing Office, Washington, DC, 1992.

[2] R. W. McEachron and S. C. Lorence, "Superabrasives and Structural Ceramics in Creep-Feed Grinding," Ceramic Bulletin Vol. 67, pp. 1031-1036, 1988.

[3] K. Mitzutani, T. Kawano, and Y. Tanaka, "A Piezoelectric-Drive Table and Its Application to Micro-Grinding of Ceramic Materials," Precision Engineering, Vol. 12, pp. 219-226, 1990.

[4] T. G. Bifano, T. A. Dow, and R. O. Scattergood, "Ductile-Regime Grinding: A New Technology for Machining Brittle Materials," Trans. ASME Vol. 113, pp. 184-189, 1991.

[5] I. F. Stowers, R. Komanduri, and E. D. Baird, "Review of Precision Surface Generating Processes and Their Potential Applications to the Fabrication of Large Optical Components," Proc. SPIE Vol. 966 in Advances in Optical Fabrication and Metrology Including Large Optics, J. B. Arnold and R. E. Parks, eds., pp. 62-73, 1988.

[6] P. N. Blake and R. O. Scattergood, "Ductile-Regime Machining of Germanium and Silicon," J. American Ceramics Soc., Vol. 73, pp. 949-957, 1990.

[7] P. Blake, T. Bifano, T. Dow, and R. O. Scattergood, "Precision Machining of Ceramic Materials," Ceramic Bulletin, Vol. 67, pp. 1038-1044, 1988.

[8] A. G. Evans and D. B. Marshall, "Wear Mechanisms in Ceramics," in Fundamentals of Friction and Wear of Materials, D. A. Rigney, ed., ASME Press, New York, NY, pp. 439-452, 1981.

[9] S. Jahanmir, T. J. Strakna, G. D. Quinn, H. Liang, R. L. Allor, and R. D. West, "Effect of Grinding on Strength and Surface Integrity of Silicon Nitride, Part I," in Proceedings of the International Conference on Machining of Advanced Materials, Gaithersburg, MD, July 20-22, 1993.

[10] S. Jahanmir, T. J. Strakna, G. D. Quinn, R. N. Kopp, C. S. Yoon, and K. Kumar, "Effect of Grinding on Strength and Surface Integrity of Silicon Nitride, Part II," in Proceedings of the International Conference on Machining of Advanced Materials, Gaithersburg, MD, July 20-22, 1993.

[11] 1992 Annual Book of ASTM Standards, Vol. 15.01, Refractories; Carbon and Graphite Products; Activated Carbon, ASTM, Philadelphia, PA, pp. 333-339, 1992.

[12] H. Ohmori and T. Nakagawa, "Mirror Surface Grinding of Silicon Wafers with Electrolytic In-Process Dressing," Annals of the CIRP, Vol. 39, pp. 329-332, 1990.

INFLUENCE OF DUCTILE MODE GRINDING ON THE STRENGTH OF SILICON BASED CERAMICS

J. M. BOETTGER
United Technologies Research Center, East Hartford, CT

M. K. KER
Cranfield Institute of Technology, Bedford, England

P. SHORE
Cranfield Precision Engineering, Ltd., Bedford, England

D. J. STEPHENSON
Cranfield Institute of Technology, Bedford, England

Test bars of silicon carbide and silicon nitride were diamond ground with various machining conditions. Ultra fine "nanometric" surface textures were obtained using particular machining methods.

Three and four point bend tests were carried out to reveal any improvement of fracture strength through the precision grinding trials. A method of predicting any potential increase in fracture strength of a ceramic through precision grinding was verified.

Work described in this paper further illustrates that good quality surface texture is no indication of high strength or reliability of a ceramic component.

INTRODUCTION

Manufacture of precise ceramic components often involves some finish machining. This finish machining is commonly carried out by diamond grinding. Previous research in this field (1,2) has shown that the strength properties of ceramics components can be greatly affected by any finish grinding. It has also shown that the direction of the grinding is influential when using conventional grinding practices. Higher strengths were found when the direction of "lay" was parallel to the tensile stress axis.

More recent research (3) has proposed that a significant increase in fracture toughness and Weibull modulus can be obtained by using "ductile regime" or "ductile mode" grinding methods. Using this mode of grinding, the dependence on the direction of machining is considered to be less influential. Ductile regime grinding of ceramics is described as a machining process which does not introduce or propagate microcracking into the ceramic surface. This ductile mode of material removal is possible only if the stressed volume of material and the associated forces arising from individual grains interacting with the ceramic are controlled and remain below critical levels.

In order to ensure that the mode of material removal is maintained in a ductile regime it is necessary to accurately control the machining forces. This can be achieved by use of controlled force grinding or, by using highly stiff and precise machine tools.

Generally, research into ductile mode grinding of glasses and ceramics has involved the use of fine grain size grinding wheels (4). It is well understood that difficulties in achieving a stable process are encountered with such wheels. Much reliance is placed on the dressing technique and recent developments in dressing technology have ensured that long term stability can be assured when using fine grain abrasive wheels (5). The electrolytic in-process dressing (ELID) method allows the use of fine grain hard metal bond wheels for ductile mode grinding.

In addition to ductile grinding, there are other possible methods to modify the surface of ceramics and therefore influence mechanical properties. The

effect of a flash oxidation treatment on the strength of engineering ceramics has been well documented (6). The fracture strength and Weibull modulus can both be improved considerably by the appropriate thermal exposure and this is generally believed to result from a crack blunting mechanism. If this is the case, then the level of strength enhancement could provide an indication of the possible improvements resulting from ductile grinding assuming that the surface defects can be minimized.

EXPERIMENT

Ceramic test bars (7) were initially produced using a conventional grinding machine and grinding technology. Various types of silicon nitride and silicon carbide were evaluated, as listed in Table 1.

Table 1. Silicon Based Ceramics

Material Name	Supplier	Type	Grain Size	Density
NT 230	Norton/ TRW	SiSiC	5μm	>99%
UF 15	T&N Technology	SSiC	5μm	>99%
Issue 4 Si_3N_4	T&N Technology	HIP'ed Si_3N_4	1μm	>99%
SiSiC – Siliconized SiC SSiC – Sintered SiC				

A number of the test bars were assessed for fracture strength and Weibull modulus in the Mil specification condition.

The remaining test bars were either;

1) Precision ground using a high precision and highly stiff grinding machine.

Or

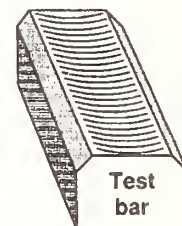2) Heat treated using flash oxidation conditions to oxidize the surface.

These test bars were subsequently tested for fracture strength.

Precision grinding methods.

The test bars were initially prepared to the Mil specification using a standard Jones & Shipman 540 peripheral wheel surface grinding machine. The direction of the "lay" for this initial machining was parallel to the length of the bars, see Figure 1.
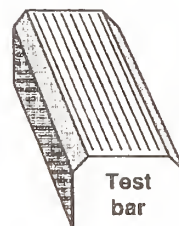
Longitudinal lay (Parallel to length)   Transverse lay (Perpendicular to length)

Figure 1. Lay of grinding on test bars.

Subsequent precision grinding carried out in the ductile regime was undertaken using a CPE CNC cup wheel grinding machine, shown in Figure 2. The specification of the grinding wheels used are listed in Table 2.
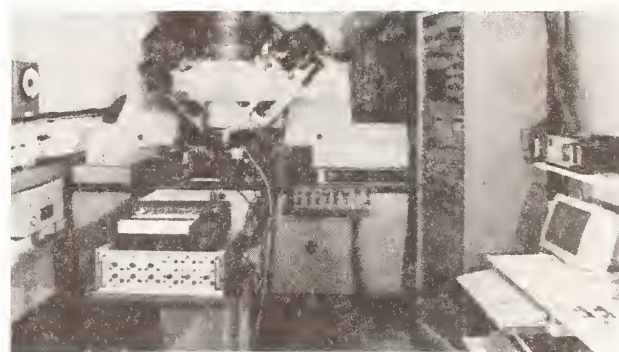

Figure 2. CPE precision grinding machine.

Table 2. Grinding Wheel Specification.

Type of Grind- ing	Grit Size Spec. (µm)	Wheel Spec.	Bond Type	Supplier
Conven- tional	46	D46/C40 /X53	Metal (brass)	Diamant Boart
Preci- sion	3−6	D3/6/C75 /FX3	Metal (cast iron)	Sintobrator
Preci- sion	3−6	D3/6/C75 /B912	Resin	Diamant Boart

Fine grain grinding wheels, 3−6 µm, were necessary to produce nanometric quality surfaces. These wheels are often difficult to use and require frequent dressing to maintain adequate "openness" and prevent "loading". Two methods of dressing were used. An aluminium oxide abrasive stick was used for the resin bonded wheel, and ELID (5) was employed with the fine metal bond wheel.

Due to the configuration of the CPE grinding machine the precision "ductile" mode grinding was carried out with the "lay" perpendicular to the length of the test bars.

Oxidation tests.

To investigate the influence of a flash oxidation treatment on fracture strength, batches of silicon nitride and silicon carbide test bars were oxidized in air at 1000°C for 25 hours and 100 hours respectively. These conditions were established to provide the optimum improvement in properties for each batch of material.

RESULTS & DISCUSSION

Previous studies reported in the literature concerning the grinding of engineering ceramics have suggested that there is a good correlation between surface finish and fracture strength (8−10). It has also been proposed that although strength increases as the surface finish improves, there is little benefit in producing surfaces to better than 1 µm R_{max} (8−11). The preliminary results in this study also

show similar trends as summarized in Figure 3. This figure illustrates the change in fracture strength as the surface finish improves for HIP'ed Si_3N_4 and SSiC. Each batch of ceramic exhibits only a small or no increase of strength even though ultrafine surfaces (0.02 µm R_{max} as measured on a Wyko TOPO 3D, 40LX head) were produced by ductile mode grinding on all three materials.
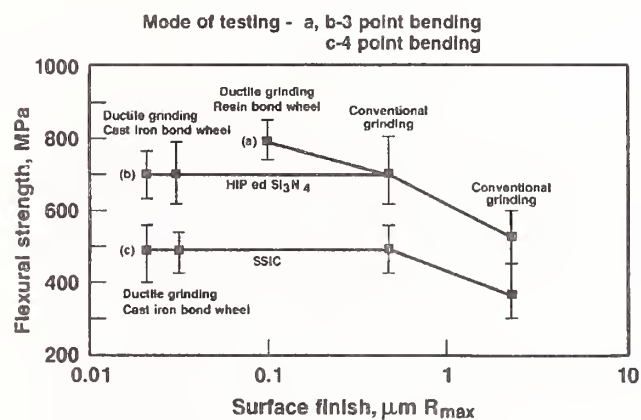

Figure 3. Strength as a function of surface finish.

Examination of the fracture surfaces revealed that almost all test pieces had failed from surface defects consistent with machining damage even though the ultrafine surfaces had been produced under ductile conditions which were known not to initiate surface or subsurface damage (12,13). This clearly indicated that critical surface defects were still present at the surface after ductile grinding.

This was further demonstrated by the large improvement in strength obtained by the flash oxidation treatment. Table 3 shows that strength increases between, 16% and 53% are possible for the conventionally ground test bars, and that the increase in strength is highest for the Si_3N_4. This increase in strength due to oxidation has been associated with a crack tip blunting mechanism which minimizes the effect of surface defects. As shown in Figures 4 and 5, the majority of failures for this batch were from internal defects within the bulk material rather than from machining damage at the surface. The Weibull modulus also increased typically from 6 in the ground condition to 14 after oxidation.

Table 3. Influence of Oxidation on the Strength of Silicon Based Ceramics
(four point bend testing)

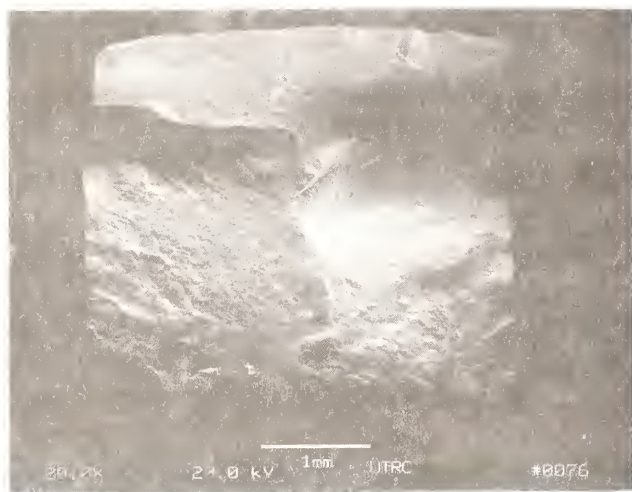| Material	Oxidation Time at 1000°C (hours)	Strength in Mil Spec. Condition (MPa)	Strength in Mil Spec. Condition (after oxidation)	% Increase in Fracture Strength (MPa)
NT 230	100	254	295	16
UF 15	100	245	338	38
Si₃N₄	25	360	550	53

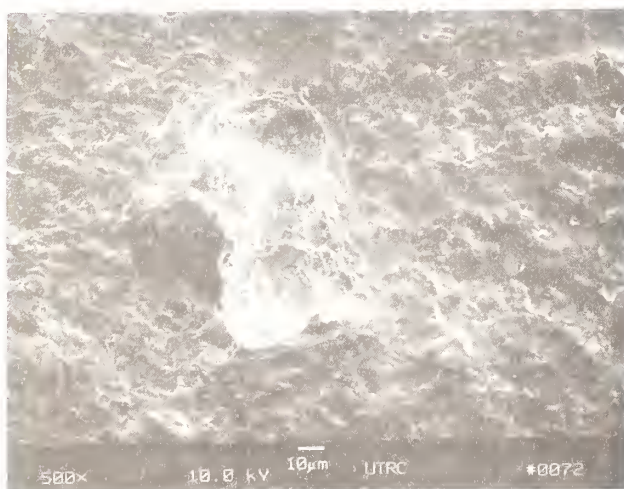Figure 4.   Failure from internal defect in SiSiC.

Figure 5.   Higher magnification of defect in Fig. 4.

The modest improvement in strength resulting from the ductile grinding and the significant benefit of a flash oxidation treatment both point to the presence of surface damage which was identified as microcracks and a heavily deformed layer produced during the conventional grinding process (12). The poor improvement in strength following ductile grinding clearly results from the presence of surface damage introduced during previous grinding operations. As the depth of cut required for effective ductile grinding is small, typically 1 μm or less ,the total stock removed to produce an ultrafine surface finish is relatively low. Hence, although a high quality surface finish may be obtained, this does not guarantee the removal of surface and subsurface damage which will control mechanical behavior.

To illustrate this effect the influence of stock removal on strength enhancement has been studied. It was considered that the Si₃N₄ was the most appropriate for this work since the flash oxidation treatment had resulted in the highest increase in strength suggesting that this material would be most sensitive to stock removal. The depth of damage following conventional grinding can be estimated from detailed structural and residual stress measurements. (12). The depth of damage in the form of microcracks and the level of residual stress varies from surface to surface depending on the prior grinding history. For the 0.5 μm R_{max} and the 2.5 μm R_{max} surface finishes considered here, the total depth of subsurface damage was determined to be $40-50$ μm and $80-90$ μm respectively.

The crack length at failure can be estimated from the fracture strengths. For a beam subjected to bending, (14),

$$K_{1C} = 2.4\sigma_C \frac{\sqrt{a_C}}{\pi}$$

356

The fracture toughness of the Si₃N₄ was estimated to be 4.7MPa $\sqrt{m}$ from indentation tests (12). Using the average strength values given in Figure 6 for 2.5 μm and 0.5 μm R_{max} surfaces, critical crack lengths of approximately 90 μm and 50 μm are obtained.

This suggests that the magnitude of subsurface damage produced by conventional grinding is of the same order as the critical defect size and therefore determines the strength of the ceramic. Thus, to ensure optimum strength, the layer of damaged material must be removed by ductile grinding. Figure 6 illustrates the strength enhancement obtained for both surface finishes as more material is removed by use of "ductile" mode grinding. The fracture strengths for these tests were measured under 3 point bending to maximize the number of data points obtainable from the batch of test bars. Two tests per bar were possible for the three point testing, whereas only one test per bar was afforded with four point testing. The optimum strength increase was obtained following the removal of about 90 μm and 50 μm for the 2.5 μm and 0.5 μm R_{max} surface finishes respectively, this is the same as predicted from the fracture mechanics approach.

Firstly, surface roughness gives no indication of the strength of the ceramic, this is determined more by the level of subsurface damage introduced or remaining from the conventional grinding.

Secondly, material removal by ductile grinding can be undertaken without initiating or propagating microcracks. The fact that the fracture stresses for the two surface finishes shown in Figure 6 approach a similar value is to be expected since the optimum strength is now determined by the intrinsic defect size in the material. Following the complete removal of the original layer of surface/subsurface damage by ductile grinding, new surface defects will be produced which were originally present in the bulk of the material. Thus, failures should be expected to result from either surface or internal locations depending on the probability of finding a critical defect. Indeed, examination of the fracture surfaces indicated that the majority of failure were from internal sources.

These observations demonstrate the potential benefits of ductile grinding but also show that there is an upper strength, limited by the intrinsic properties of the ceramic rather than the processing of the surface. Clearly, the greatest benefits from ductile grinding will only be realized for high quality ceramics which exhibit high intrinsic strength.

A measure of the potential benefits attainable by ductile grinding can be obtained from a flash oxidation treatment which minimizes the influence of surface defects and should provide a simple means of estimating the upper strength level of the material.

CONCLUSIONS

1. Ductile mode grinding can enhance the strength of engineering ceramics by reducing the size of surface defects. The maximum level of strength enhancement is determined by the incidence of internal defects which will ultimately arrive at the surface as material is removed.

2. Although ultrafine surface finishes are possible by ductile mode grinding, surface finish has little effect on strength. Rather, it is the level of surface/subsurface damage introduced by conventional grinding that determines mechanical behavior.
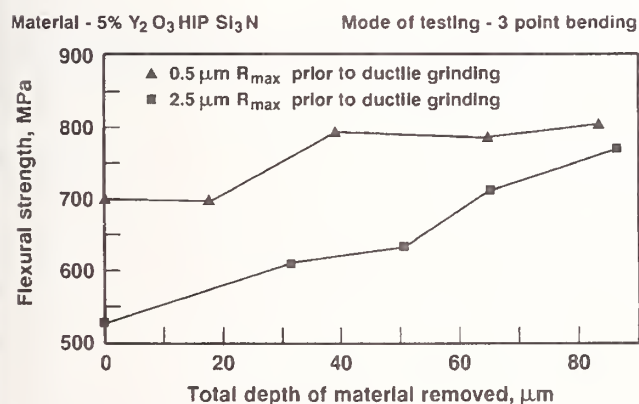

Figure 6. Strength as a function of material removed in a ductile mode (using resin bond wheel).

This improvement in strength as a function of the depth removed by ductile mode grinding highlights two important conclusions.

3. A simple fracture mechanics approach can be used to estimate the level of stock removal required in order to remove the original grinding damage.

4. A flash oxidation treatment, used to minimize the effect of surface defects, gives a good indication of the possible improvements in strength attainable by ductile grinding.

REFERENCES

1. I. Inasaki. "Grinding hard and brittle materials," Annal of CIRP, Vol. 36, No. 2, 1987.

2. T. J. Whalen, L. L. Terner, "Surface condition and strength of silicon carbide−silicon materials," The Science of Ceramic Machining and Surface Finishing II, NBS Special Publication 562, 1978.

3. P. Shore. "State of the art in "damage free" grinding of advanced engineering ceramics," British Ceramics Proc., Vol. 46, 1990.

4. T. G. Bifano. "Ductile regime" grinding of brittle materials, Ph.d Dissertation, North Carolina State University, 1988.

5. H. Ohmori, T. Nakagawa, "Mirror surface grinding by metal bonded super abrasive wheel with electrolytic in−process dressing," Progress in Precision Engineering, IPES6, 1991.

6. D. W. Richerson, Modern Ceramic Engineering, Marcel Dekker, 1982.

7. U. S. Department of Defense, "Flexural strength of high performance ceramics at ambient temperature," MIL-STD-1942A, 1990.

8. T. Kubo. Conf. Proc., Japan Ceram. Soc., 1978, p. 114.

9. S. Ito, M. Nakamura, and W. Kanematsu, "Machining of high performance ceramics," Bulletin Japan Soc. of Prec. Engrg., 1987, p. 167.

10. M. Ota, and K. Miyahara, "Influence of grinding on flexural strength of ceramics," SME 4th Intl. Grinding Conf., Dearborn, Michigan, 1990, p. 538.

11. P. Hancock, T.N. Ho, M−K Kerr, D.J. Stephenson. Processing Adv. Mat., 1991, 1, 145.

12. M−K. Ker, Phd Thesis, School of Industrial and Manufacturing Science, Cranfield Institute of Technology, 1992.

13. M. J. Ball, N. A. Murphy, P. Shore, "Electrolytically assisted "ductile" mode diamond grinding of BK7 and SF10 optical glasses," SPIE, Vol. 1573, No. 30 ,1991.

14. F. W. Smith et al., ASME J. Appl. Mech, Vol. 34, 1967, p. 953.

EFFICIENT AND PRECISION GRINDING TECHNIQUE FOR CERAMICS WITH ELECTROLYTIC IN-PROCESS DRESSING (ELID)

H. OHMORI
The Institute of Physical and Chemical Research, Tokyo, Japan

Research on efficient and precision grinding technique for ceramics is stimulated by the necessity for mass – production of ceramic parts. The establishment of new grinding technique for ceramics realizing high efficiency and quality has been expected by the employment of tough metal bonded superabrasive wheels and rigid grinding machines. However, the maintenance of the grindability of ceramics could not be achieved because of its hardness and toughness. The author together with coresearchers has proposed the new grinding technique utilizing electrolytic in – process dressing (ELID), and applied this technique to ceramics grinding successfully. Mirror surface quality was obtained by using a #4000 cast iron fiber bonded diamond (CIFB – D) wheel for representative ceramics. Stabilization and reduction of grinding forces have been achieved even in rough grinding operations of ceramics with efficiency of 6000 mm³/min by using a #140 CIFB – D wheel and an ordinary surface grinder. Applications of ELID technique on ceramics grinding such as cylindrical grinding, aspheric generation, grooving and cutting were also realized.

1. Introduction

Application of advanced materials such as fine ceramics is spreading widely for replacement of con – ventional materials. Ceramic parts are machined by grinding and are finished by lapping or polishing processes. However, recent develop – ments of advanced ceramics are making its effective machining processes more and more difficult. For rapid production of high pre – cision ceramic parts, new machining

techniques, realizing efficiency and quality simultaneously, is needed. High reduction of grinding costs must be done.

The author has proposed the mirror surface grinding technique with electrolytic in − process dressing for silicon wafer (1), and later applied the technique to ceramics successfully (2). This technique was proved to be effective for both finish grinding and rough grinding of ceramics (3). This paper describes an advanced grinding technique for ceramics utilizing electrolytic in − process dressing (ELID).

2. Problems in Grinding of Ceramics

Grinding of ceramics is becoming more difficult, because of increasing toughness of the new advanced ceramics. In ordinary grinding op − erations, utilizing resinoid or vitrified bonded super abrasive wheels, lower grinding ratios and unstable grindabilities have been inevitable for ceramics machining (4). Efficient grinding, utilizing a rigid machining center and metal bonded diamond wheels, has been proposed for ceramics machining; but its reliability and adaptability in practical appli − cations for ceramic parts manufac − turings have not been established (5).

This is attributed to the lack of adequate dressing technique. A possible solution for the above − mentioned problems is utilization of a new grinding technique known as "ELID − Grinding" which can control abrasive protrusions before and during grinding of ceramics.

3. Electrolytic In − Process Dressing (ELID) Technique

1) Principle

The ELID − grinding method is not a complex machining process, but an efficient grinding technique where electrolytic in − process dressing is used to maintain the abrasive protrusions during grinding. This phenomenon is not continuous; it is rather "adaptive" to wear of the abrasives. Figure 1 shows the principle of the proposed ELID − grinding process (1). The grinding wheel is connected to the positive terminal of a power supply with a smooth brush contact; and a fixed electrode is made negative. In the small clearance of approximately 0.1mm between the negative and the positive poles, electrolysis occurs upon supply of a suitable grinding fluid and an electrical current.

2) Behavior

Figure 2 shows the electrical

behavior during dressing and ELID grinding. At the time pre – dressing starts, the surface of the trued wheel has a good electrical conductivity. Therefore, the current is as high as has been set on the power source, and the voltage between the positive pole and the negative pole is low (denoted by ①). For several minutes, the bond material (mainly iron in cast iron) is removed by electrolysis. It is mostly ionized into Fe^{2+}, forming hydroxides, Fe $(OH)_2$ or Fe $(OH)_3$. Next, these substances change into oxide substances such as Fe_2O_3. After these reactions occur, the electro – conductivity of the wheel surface is reduced with the growth of the insulating substances. Thereby, the current decreases, and the working voltage becomes as high as that which has been set as the open voltage (denoted by ②).

3) Mechanism

Figure 3 shows a schematic illustration of the mechanism of the ELID – grinding process. After grinding with the predressed wheel begins, the protruding grains grind the workpiece. Accordingly, as the grains are worn, the oxide layer on the bond is removed. The wear of the oxide layer causes an increase in the electro – conductivity of the wheel surface. Thus electrolysis in –

creases (denoted by ③ in Fig.2) and the oxide layer can be recovered. The protrusion of the grains, therefore, remains constant in a general sense. The cycle described can be changed according to the grain size of the employed wheel. ELID works most effectively if the thickness of the oxide layer and the depth of the etched layer on the wheel surface are balanced.

4) Advanced Construction of ELID

The ELID – system is composed of such elements as a wheel bond material, a power supply, and a grinding fluid. The selection of elements determines the properties that can be realized by ELID. Electrical dressing itself is not a new technique; it is said that the history started in the 1960's in the USA (6). Among many electrical dressing techniques, ELID is the only one that utilized a non – linear electrolyzing phenomenon with an insulating layer on the wheel surface. Therefore, the standard ELID – system is composed of a cast iron bonded wheel, a direct current pulse generator as a power supply, and an ordinary chemical solution type grinding fluid diluted by water as an electrolyte, which upon combination generates an in – sulating layer easily. For rough grinding, the composition of the

361

elements for ELID which makes the oxide layer thinner is better from the viewpoint of higher dressing rate.

4. ELID – Grinding for Mirror Surface Machining of Ceramics

1) Experimental Equipments

Mirror surface grinding experi – ments were conducted by utilization of the equipments shown in Table 1. A rotary surface grinder with an ELID – system and cast iron fiber bonded diamond (CIFB – D) wheels were employed. Grinding chips of cast iron by #80 electroplated wheel are used as the "fiber" for the bond material of the employed wheel (7). The machine has oil hydrostatic bearings for the wheel spindle and the rotary table. Figure 4 shows a schematic of the ELID – grinding type and a close – up view of the machine. For ELID – power supply, a pulse generator was employed. Represent – ative ceramics such as SiC, Si_3N_4, ZrO_2, Al_2O_3 – TiC were selected. Table 2 shows the properties of the employed ceramics.

2) Characteristics

All wheels were trued by a car – borundum wheel. Figure 5 shows changes of ground surface roughness with and without ELID using a #4000 (the distribution of the grit size is $2 - 6 \mu$ m, the average grit size is 4μ m) CIFB – D wheel. When ELID is applied, surface roughness was improved during the grinding operation, and becomes a mirror quality at approximately Rmax40 – 50nm, where Rmax means maximum peak to valley of the surface roughness. On the other hand, surface roughness could not be improved without ELID. This is because ELID enables the fine dia – mond particles to protrude and engage in fine removal of the ground surface. Without ELID, the bond material of the CIFB – D wheel made the ground surface rougher by rubbing caused from the strong friction between the wheel bond surface and the work surface. Figure 6 shows that a stable grinding forces was maintained during the ELID – grinding operation using a #4000 CIFB – D wheel.

3) Examples

Several types of ceramics have been finished by using the ELID technique with fine grit CIFB – D wheels. Figure 7 shows examples for SiC, Si_3N_4, ZrO_2 and Al_2O_3 – TiC ceramics finished by ELID with a #4000 grit wheel. Difference of surface rough – ness among the examples is very small. High surface quality of Rmax

30 – 50nm, Ra 5 – 6 nm (Ra means average value of peak to valley in surface roughness) has been ob – tained. Roughness patterns of the ground surfaces as in Figure 8 suggest fine grinding marks on the finished surfaces.

4) Ductile Mode Grinding

Figure 9 shows the ground surfaces observed at high magnifications. In mirror surface grinding of Si_3N_4 and ZrO_2 ceramics, mostly ductile mode ground surfaces were obtained with the #4000 wheel. In SiC ceramics, a mixed ductile and brittle fracture modes was observed. In $Al_2O_3 – TiC$ ceramics, a fine brittle fracture ground surface was obtained. It is important to recognize the differences in removal modes in ground surfaces finished at similar surface roughness values. By the employment of ELID in fine grinding of ceramics, ground surface characterization is easier and more reliable than by conventional grinding, because a fine surface finish can be maintained.

5. ELID – Grinding for Rough Machining of Ceramics

1) Experimental Equipments

Rough and efficient grinding ex – periments were conducted by util – ization of the equipments shown in Table 3. A reciprocal surface grinder with an ELID – system and cast iron fiber bonded diamond (CIFB – D) wheels with a coarse grit were employed. Figure 10 shows the ELID – grinding principle of the appli – cation and the close – up view of the grinding machine. For ELID – power supply, a specialized pulse generator was employed. Representative ceramics such as SiC, Si_3N_4, Sialon, WC were selected for the grinding tests. Table 4 shows the properties of the employed ceramics.

2) Characteristics

Figure 11 shows the normal grinding force in grinding of Si_3N_4 ceramics with and without ELID. When ELID was not applied, the normal grinding force increased gradually to approximately 450N. On the other hand, ELID reduced the normal grinding force to about 200N.

Table 5 is a summary of several typical ELID – grinding conditions. In traverse grindings as in Fig. 11, the material removal rate of 1800mm^3 ⁄min is not high compared with ordinary grinding operations. But, in plunge grinding conditions such as in Table 5, a removal rate as high as 6000mm^3⁄min could be achieved with ELID – technique. Figure 12 shows an effect of ELID in reduction of the normal grinding force. Even

when ELID started to be supplied during grinding operation, grinding force could be reduced in the course of the operation. Figure 13 shows the effect of grinding conditions and the grinding direction on the grinding force for SiC.

Figure 14 shows an influence on grinding force by working current of ELID. Higher working currents reduces the grinding force. But Fig. 14 suggests that the differene of the grinding forces will be smaller after large stock removal. This is because CIFB wheel has a non − linear electrolyzing feature, and so dressing rate was decreased by a small amount.   Modification of the fluid for ELID will be effective in increasing the dressing rate.

3) Difference on Materials

Table 6 shows the normal grinding force obtained in ELID grinding of different work materials. The hardest material is SiC, and the toughest material is WC. WC tends to load the wheel surface with chips. Even when ELID is applied, the grinding force is higher than that of other ceramics. SiC ceramic is the most brittle material among the employed ceramics, and its grinding force is the lowest.

6.Application of ELID −

Grinding for Ceramics

1) Cylindrical Mirror Surface Grinding with ELID

Figure 15 shows application of ELID for cylindrical external surface grinding. Figure 16 is an example of cylindrical surface grinder equipped with an ELID − system. Cup wheels can be used for cylindrical grinding if the wheel spindle rotates vertical to the work spindle. But the application shown in Fig. 16 is popular in production shops. Figure 17 shows examples finished by a CIB − D (Cast Iron Bonded) and a CIB − CBN straight wheel of # 4000 with ELID on a cylindrical grinder. The surface roughness of Si_3N_4 ceramic cylinders was approximately Rmax40nm, and the roundness of the finished cylinder of ϕ 50mm was $0.1 − 0.2$ μ m.

2) Curved Mirror Surface Grinding with ELID

Figure 18 shows a schematic diagram for spherical and aspherical ELID − grinding. A straight wheel is used in order to obtain desired geometry with a CNC grinding machine.   Figure 19 shows an example of surface roughness of finished aspherical lens [BK − 7 glass]. Good mirror surface quality has been achieved   by using ELID and a

#8000 CIFB − D wheel. Figure 20 shows machined and finished spherical and aspherical mirrors of ceramics with ELID − grinding technique. Even on a conventional machining center, good mirror surface quality has been obtained. Figure 21 shows stability of the grinding force on spherical mirror machining. An ultraprecision aspheric generator which had airspindles and high positioning resolution of 10nm was recently employed, and an excellent surface accuracy was achieved.

3) Efficient Shape Grinding with ELID

Figure 22 shows an effectively machined ceramic sample with ELID − plunge grinding using a #140 CIFB − D wheel. Blades of 0.3mm width could be made without chipping at a high removal rate of 6000mm³／min.

With respect to another application of rough grinding with ELID, high speed cutting using ELID − grinding has been tried. Figure 23 shows the schematic diagram. Figure 24 is an example cut by a #120 CIFB − D blade wheel of 1mm width and ELID. Figure 25 shows the stability and the reduction of normal grinding force in cutting operation using ELID.

7.Conclusions

This paper described ELID − grinding technique and its effects and characteristics in efficient and precision machining of ceramics. Mirror surface quality was esta − blished with fine grit wheels and ELID. Moreover, grindability and stability in rough grinding of ceramics were greatly improved with coarse grit wheels and ELID − system. Finally, the author applied ELID − technique to curved surface mach − ining such as cylindrical, spherical or aspherical, and grooved surface successively. Practical manufacturing of ceramics parts is expected to become effective widely from rougher to finer or ultrafine processes.

TOPCON Corp. for their support and cooperation.

References

[1] H. Ohmori and T. Nakagawa : Grinding of Silicon using Cast IronFiber Bonded Wheel (3rd report), Preprint for Autumn Conference of JSPE, (1987) 687.(In Japanese)

[2] H. Ohmori and T. Nakagawa : Mirror Surface Grinding of Hard and Brittle Materials Using Cast Iron Fiber Bonded Wheel, Preprint for Autumn Conference of JSPE,(1988) 355.(In Japanese)

[3] I. Takahashi, H. Ohmori and T. Nakagawa : Highly Efficient Grinding of Hard and Brittle Materials (2nd report) , Preprint for Spring Conference of JSPE,(1989) 355.(In Japanese)

[4] K. Takahashi and Y. Sekiya : Characteristics in Matching of Diamond Wheel − Influence of Filler Type in Resinoid Bond −, Preprint for Spring Conference of JSPE,(1988) 657.(In Japanese)

[5] T. Uematsu, K. Suzuki, T. Narita and T. Nakagawa : Grinding of Hard and Brittle Materials Utilizing Machining Center (9th report), Preprint for Spring Conference of JSPE, (1987) 589.(In Japanese)

[6] K. Okano : Electro − chemical and Electro − discharge Dressing of Super − abrasive Wheel, Journal of JSPE, Vol.55, No.6, (1989) 998.(In Japanese)

[7] T. Nakagawa, M. Kimura and K. Suzuki : Manufacturing of Diamond Wheel with Matrix Using Fiber Obtained by Grinding , Preprint for Spring Conference of JSPE,(1985) 633. (In Japanese)

[8] H. Ohmori and I. Takahashi : Rough and Efficient Grinding of Electrolytic In − Process Dressing (ELID), Preprint for Autumn Con − ference of JSPE, (1992) 543 . (In Japanese)

[9] H. Ohmori and T. Nakagawa : Mirror Surface Grinding of Silicon Wafers with Electrolytic In − Process Dressing, Annals of the CIRP Vol. 39,1,(1990) 329.

[10] H. Ohmori, I. Takahashi and T. Nakagawa : Mirror Surface Grinding by Metal Bonded Super − abrasive Wheel with Electrolytic In − Process Dressing , Progress in Precision Engineering (IPES6/UME2),(1991) 152.

[11] H. Ohmori and T. Nakagawa : Electrolytic In − Process Dressing (ELID) for Mirror Surface Grinding, Proceedings of the 10th International Symposium for Electro − machining, (1992) 553.

[12] H. Ohmori : Electrolytic In − Process Dressing (ELID) Grinding Technique for Ultraprecision Mirror Surface Machining, Int. J. JSPE, Vol. 26, No.4, 273.
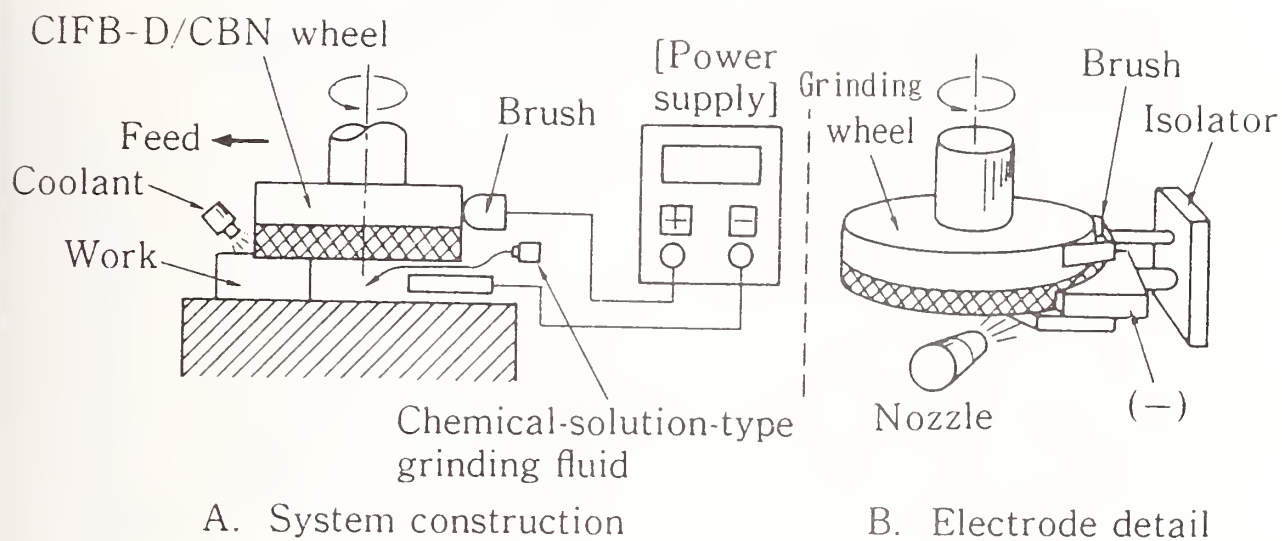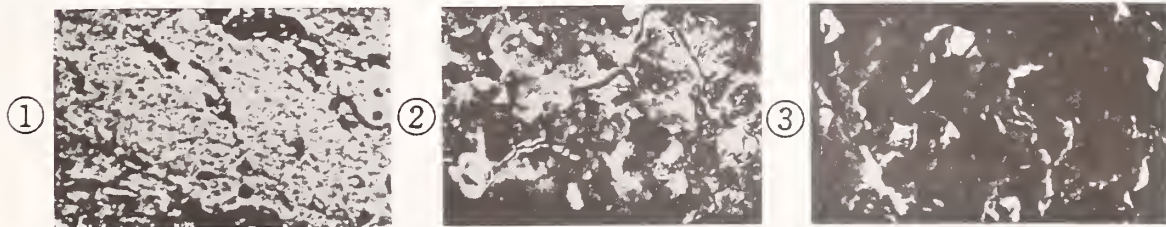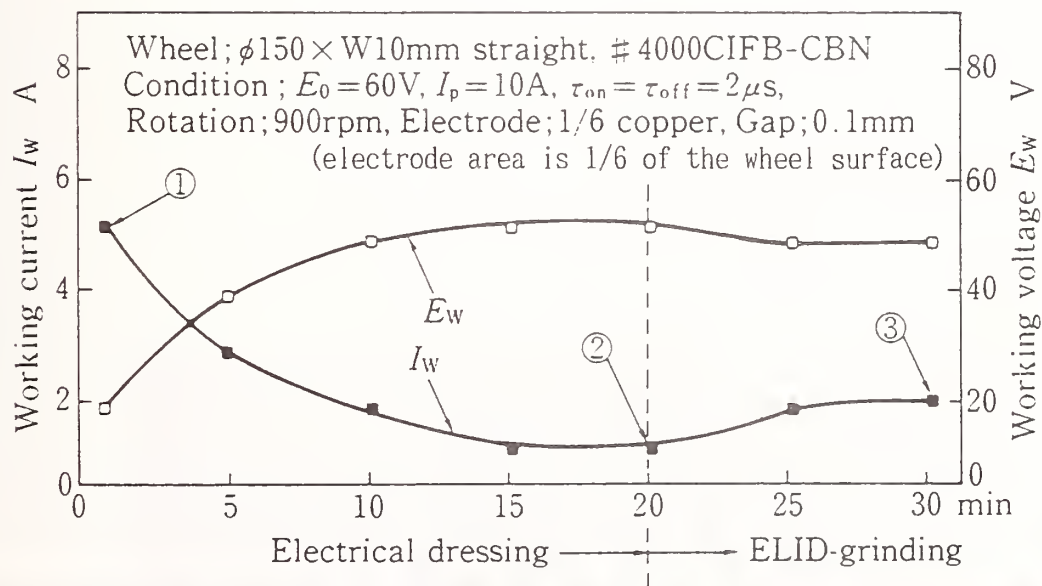
A. System construction   B. Electrode detail

Fig. 1 Principle of ELID-grinding

Wheel; $\phi150 \times W10mm$ straight, $\sharp4000$CIFB-CBN
Condition; $E_0 = 60V$, $I_p = 10A$, $\tau_{on} = \tau_{off} = 2\mu s$,
Rotation; 900rpm, Electrode; 1/6 copper, Gap; 0.1mm
(electrode area is 1/6 of the wheel surface)

Electrical dressing ⟶ ELID-grinding

Fig. 2 Behavior of electrolytic dressing and ELID

① Dressing started (3A ~)   ② Dressing completed (~1A)

Fe²⁺ ions   Protruding grain

Elid-cycle

(Hydroxide, oxide)
Insulating layer

④ ELID stabilized (~2A)   ③ ELID started (~1.5A)

Worn   Oxide layer removed   Contacted   Scraped oxide   Chip
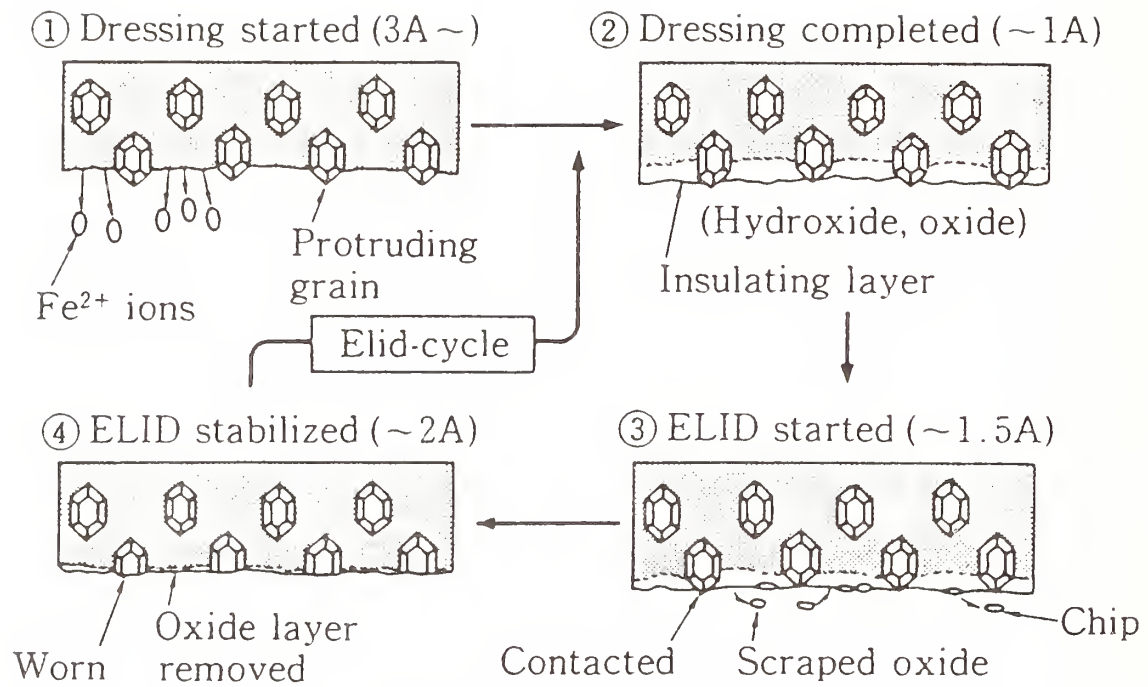
Fig. 3 Mechanism of ELID-grinding

Table1 Specification of equipments

Grinding machine	Vertical rotary surface grinder *Both the wheel spindle and the rotary table are oil hydrostatic bearings.
Grinding wheel	#600CIFB-D wheel (for rough grinding), Conc. 100, #4000CIFB-D wheel (for fine grinding), Conc. 50 Dimentions: ϕ200×W5 Cup
Power supply	Direct current pulse generator *Open voltage:60V (square wave) *Peak current:30A *Pulse width:1-5μs (on-time, off-time) *Duty factor:maximum 50%
Fluid	Chemical solution type grinding fluid (×50 dilutin by water)
Truer	#100 Carborundam wheel (ϕ80×W20) and brake truer
Measurement	Surface roughness measuring instrument using 5μmR diamond stylus

368

Table 2 Properties of ceramics workpieces

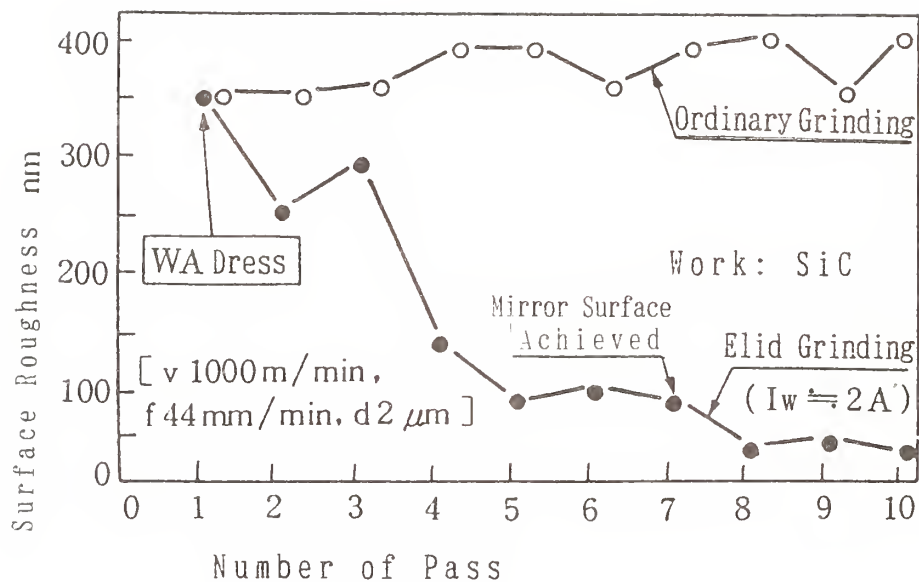|	SiC	Si_3N_4	ZrO_2	Al_2O_3-TiC
Vickers hardness H_v	2700	1700	1350	1900
Fracture toughness K_{1C} MPam$^{1/2}$	3.0	7.0	6.8	5.0
Remark	—	—	PSZ	TiC 30%
Sintering	normal			
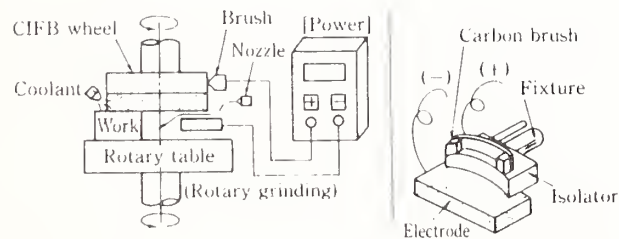
A)ELID-Grinding application
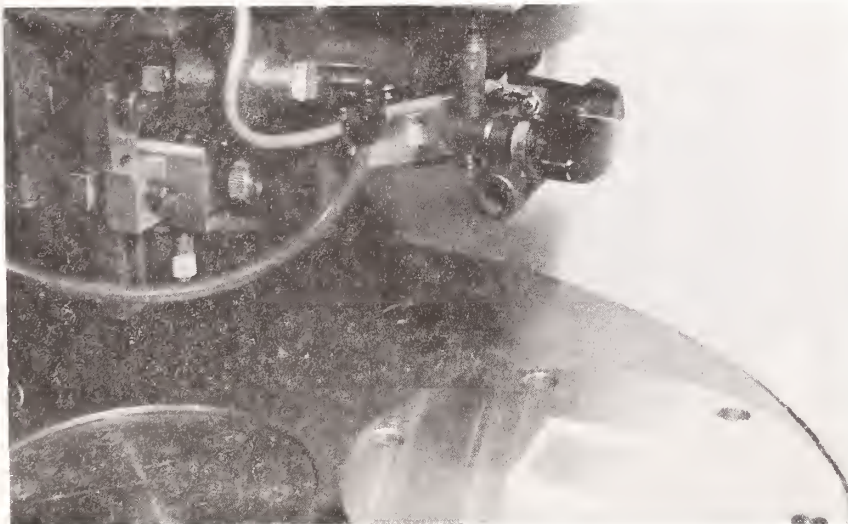
B)Close-up view of grinding machine
Fig.4 Rotary ELID-grinding principle and the employed machine

(v, f and d mean wheel velocity, feed rate, and depth of cut)
Fig. 5 Changes of ground surface roughness for SiC workpiece
using #4000CIFB-D grinding wheel
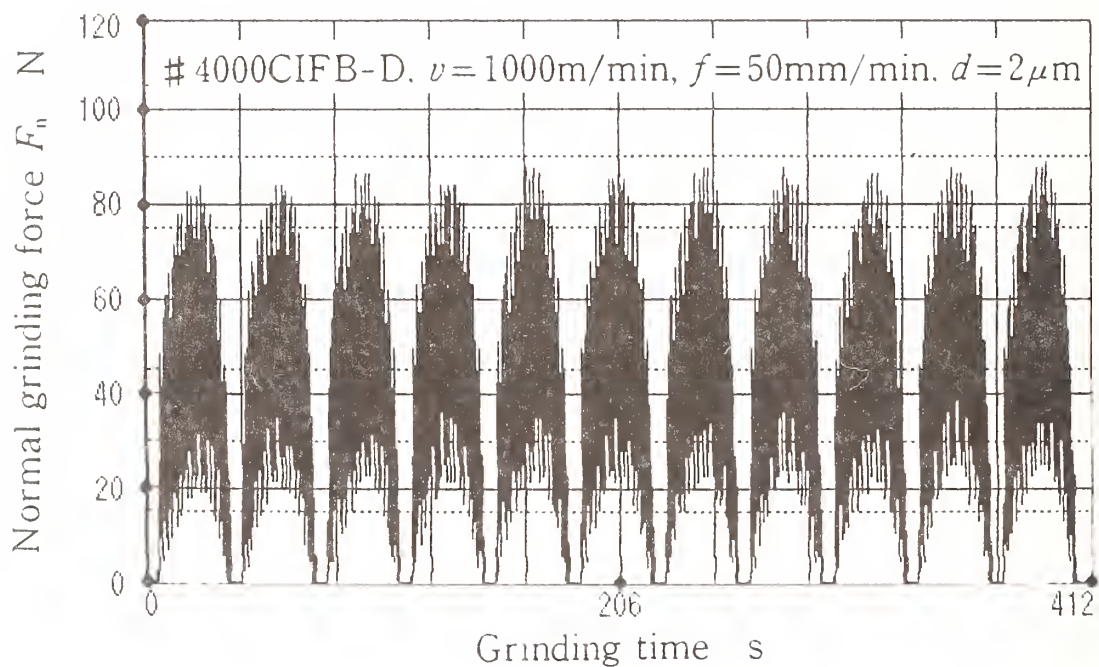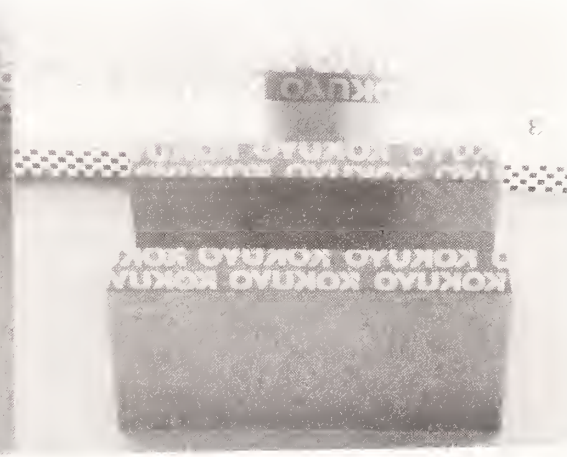

Fig. 6 Change of grinding force with ELID for WC
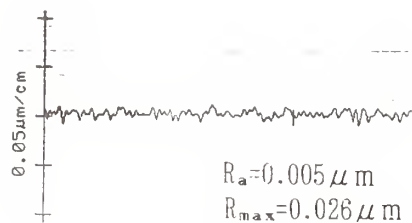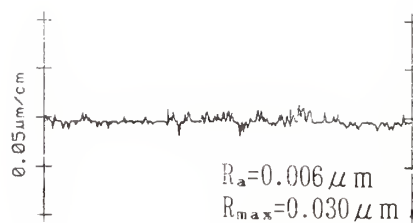
370

A)SiC

B)Si_3N_4

C)ZrO_2

D)Al_2O_3-TiC

Fig.7 Examples of finished ceramics

A)SiC
$R_a = 0.005 \mu m$
$R_{max} = 0.026 \mu m$

B)Si_3N_4
$R_a = 0.006 \mu m$
$R_{max} = 0.030 \mu m$

C) ZrO_2
$R_a = 0.005 \mu m$
$R_{max} = 0.034 \mu m$
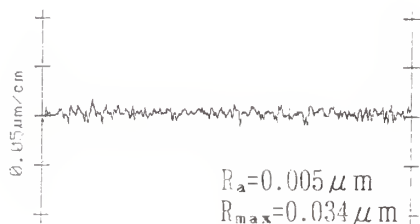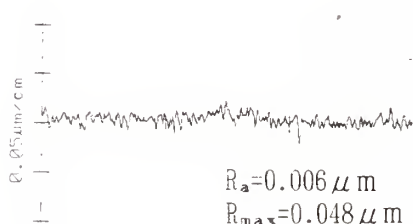
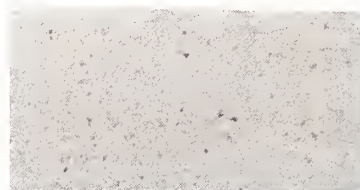D)Al_2O_3-TiC
$R_a = 0.006 \mu m$
$R_{max} = 0.048 \mu m$

Fig. 8 Surface roughness obtained by ELID-grinding

A)SiC

B)Si_3N_4

C) ZrO_2

D)Al_2O_3-TiC

(Optical microscopic photographs)

50 μm

Fig. 9 Surface quality by ELID-grinding

Table 3 Specification of equipments

Grinding machine	Reciprocal surface grinder 　*Maxumin table speed is 25m/min, and maximum 　　spindle rotation is 2550rpm. 　*The spindle motor capacity is 2.2kW.
Wheel	#140, #170CIFB-D straight wheel, Conc. 100 Dimentions: ϕ150×W10
Power supply	Direct current pulse generator 　*Open voltage:60, 90V 　*Peak current:10, 30A 　*Pulse width:1.5-5.5μs(on-time, off-time) 　*Maximum duty factor:50%
Fluid	Chemical solution type grinding fluid (×50 diluted by water)
Truer	#100 Carborundam wheel(ϕ80×W20) and brake truer
Measuring instrument	2-axes dynamometer for measuring grinding forces and analizing system of grinding forces on a personal computer

Table 4 Properties of ceramics workpieces

	SiC	Si_3N_4	Sialon	WC
Vickers hardness H_v	2700	1700	1740	1200
Fracture toughness K_{1c} MPam$^{1/2}$	3.0	7.0	7.7	12
Remark	—	—	—	Co 12 %
Sintering	normal			
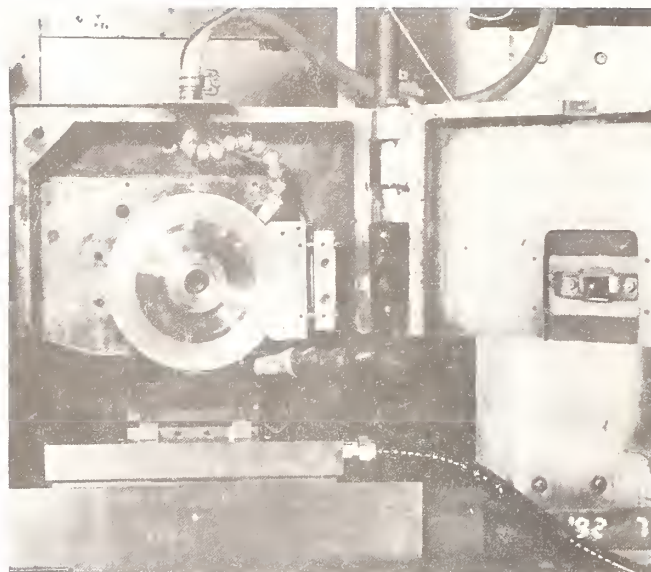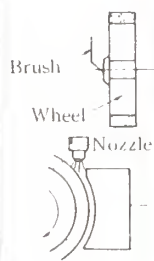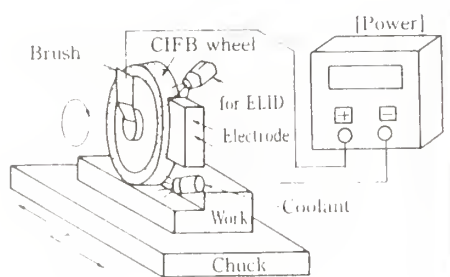
A)ELID-grinding application   B)Close-up view of grinding machine
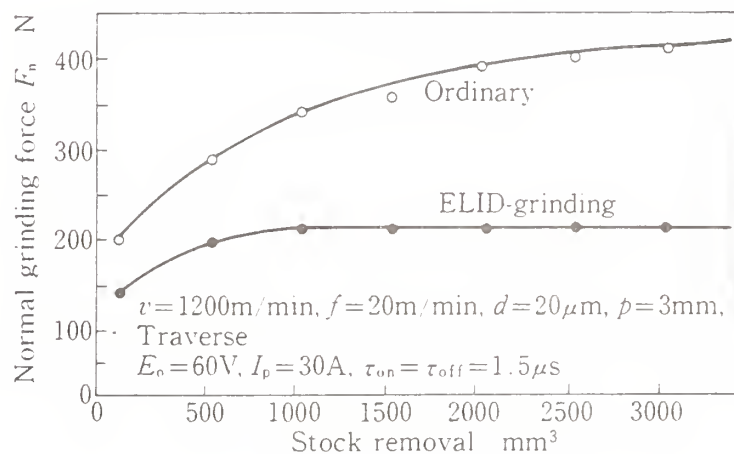Fig.10 Reciprocal ELID-grinding principle and the employed machine

Fig.11 Changes of normal grinding force;
Wheel:#170CIFB-D, Work:$Si_3N_4(50\times50)$

Table 5 Plunge grinding condition

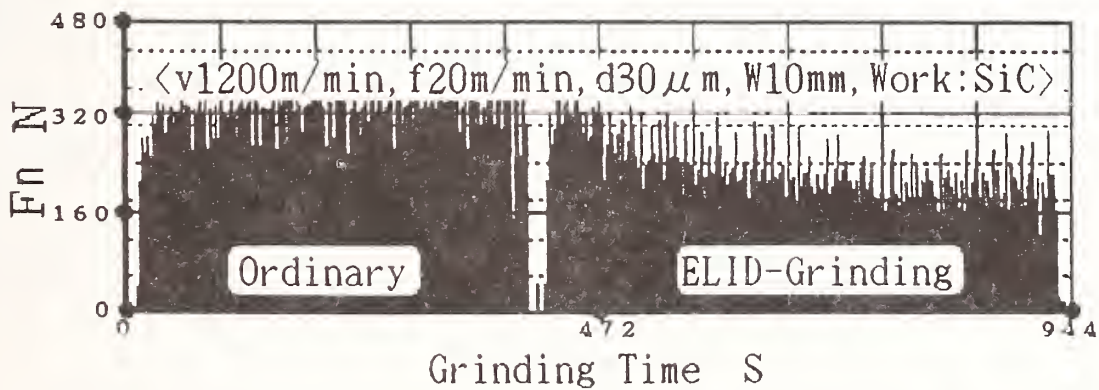| Work material / Conditions		SiC	Si$_3$N$_4$	Sialon	WC
Grinding conditions	Wheel velocity:v m/min	1200			
	Feed rate :f m/min	20			
	Grinding width:B mm	10			
	Depth of cut:d μm	30			10
Removal rate mm³/min		6000			2000
ELID conditions	Open voltage:Eo V	90			
	Peak current:Ip A	10			
	On-time :τon μs Off-time :τoff μs	2 2			

Fig. 12 Reduction of grinding force due to ELID for SiC
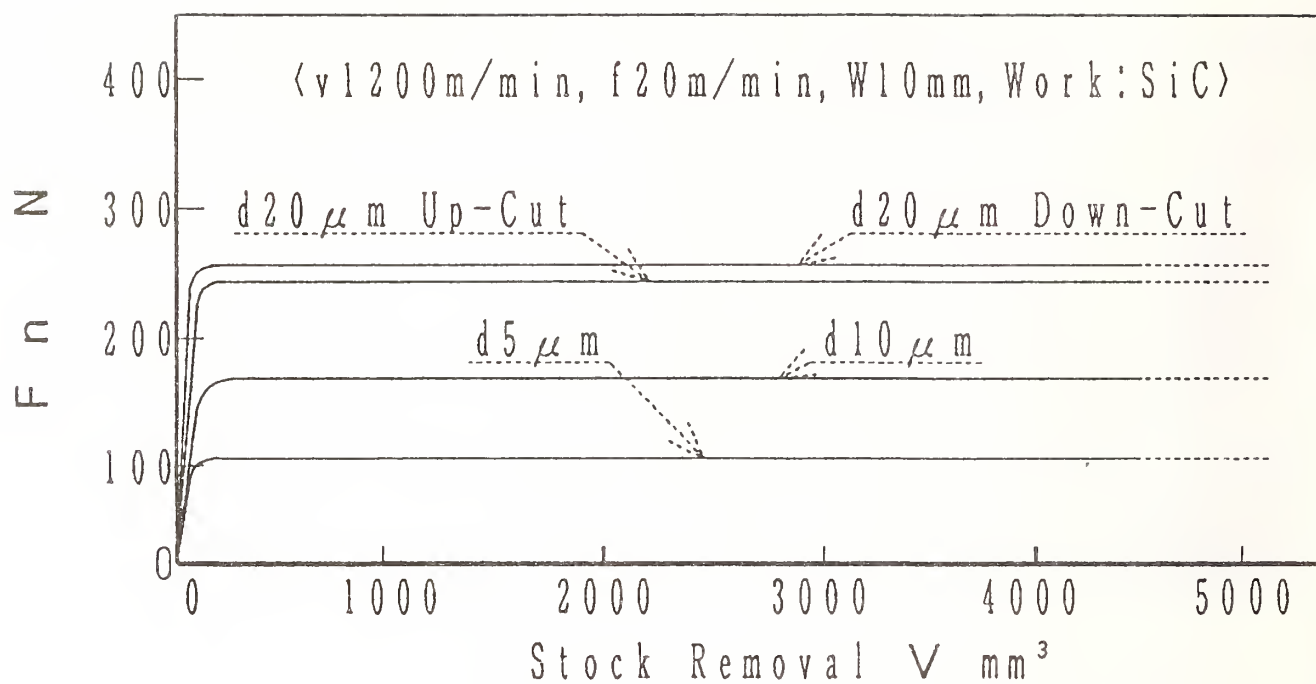
Fig. 13 Influence of grinding condition and grinding direction for SiC
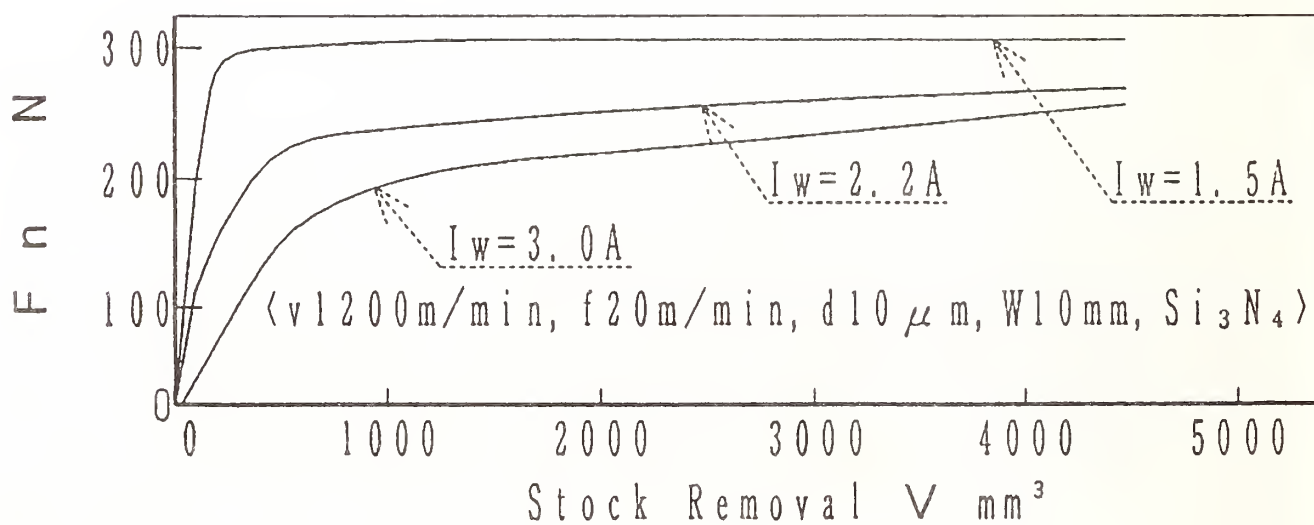
Fig. 14 Influence of current on grinding force for Si₃N₄

Table 6 Normal grinding force and working current for ELID
grinding of different work materials

Removal Rate	SiC		Si₃N₄		Sialon		WC	
mm³/min	Fn N	Iw A	Fn N	Iw A	Fn N	Iw A	Fn N	Iw A
2000	170	2.2	280	2.2	300	2.2	450	6.0
4000	250	3.0	500	6.0	500	4.2	—	—
6000	350	4.0	650	7.5	650	5.0	—	—
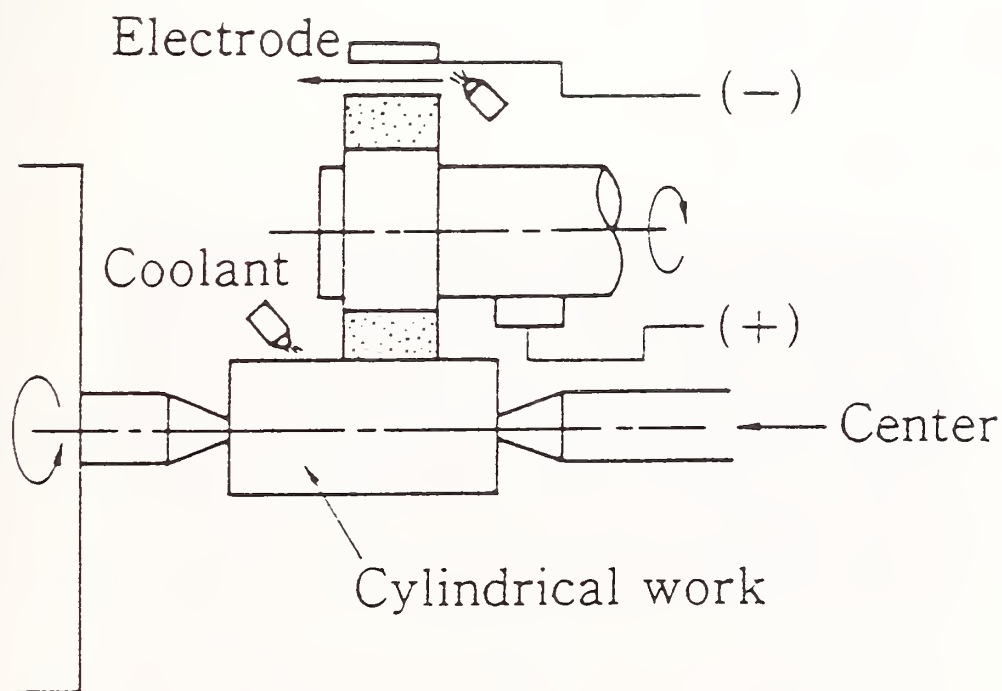
Fig.15 Application of ELID for cylindrical external surface grinding
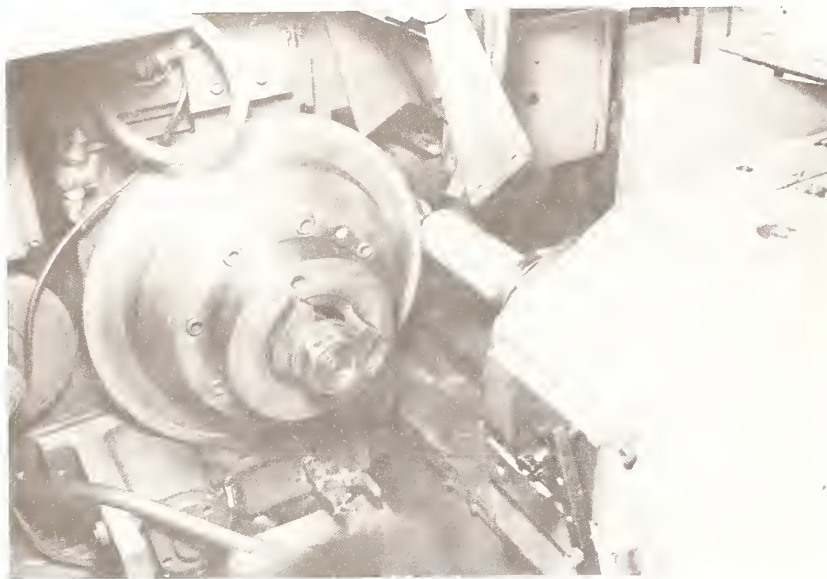
Fig. 16 Example of cylindrical surface grinder with ELID
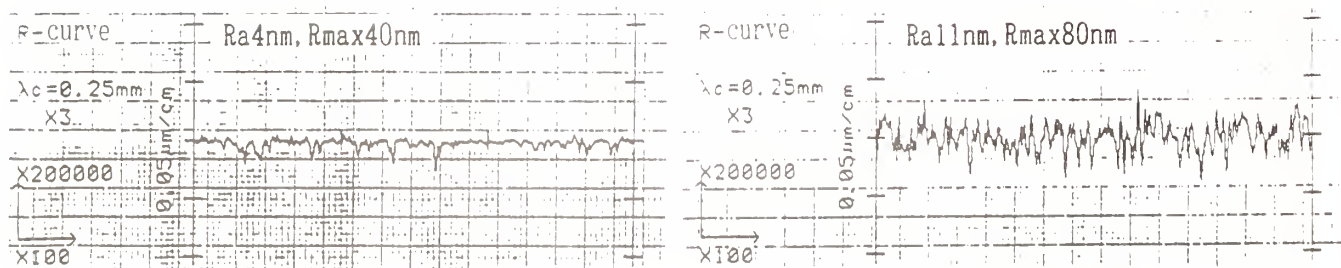
Si$_3$N$_4$ (#4000CIB-D, ELID)　　　　Steel (#4000CIB-CBN, ELID)

A) Surface roughness
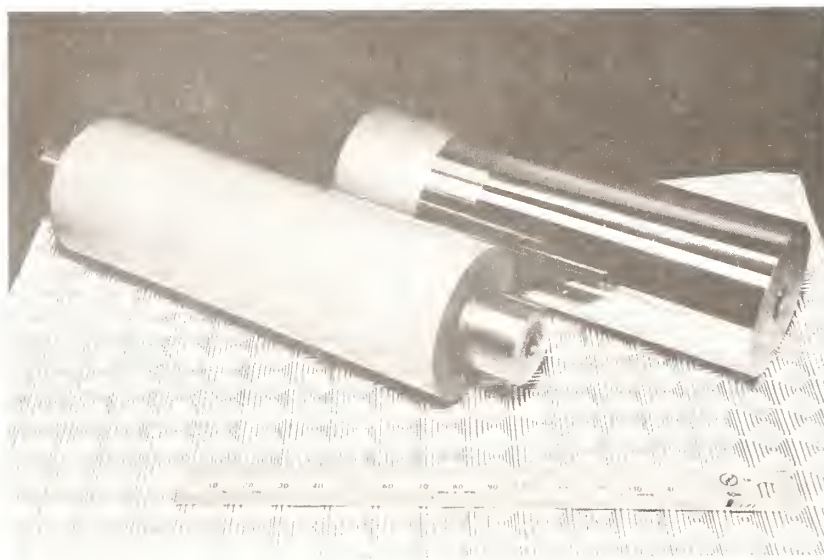
B) Finished workpices

Fig. 17 Examples finished by cylindrical grinder with ELID

Fig. 18 Schematic diagram for spherical and aspherical ELID-grinding

A) Surface roughness

B) Ground surface
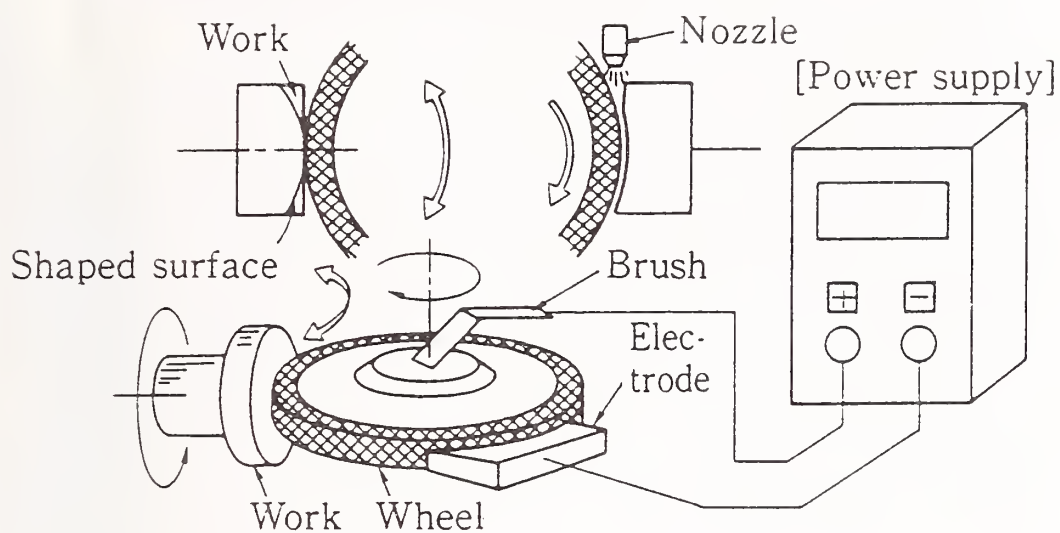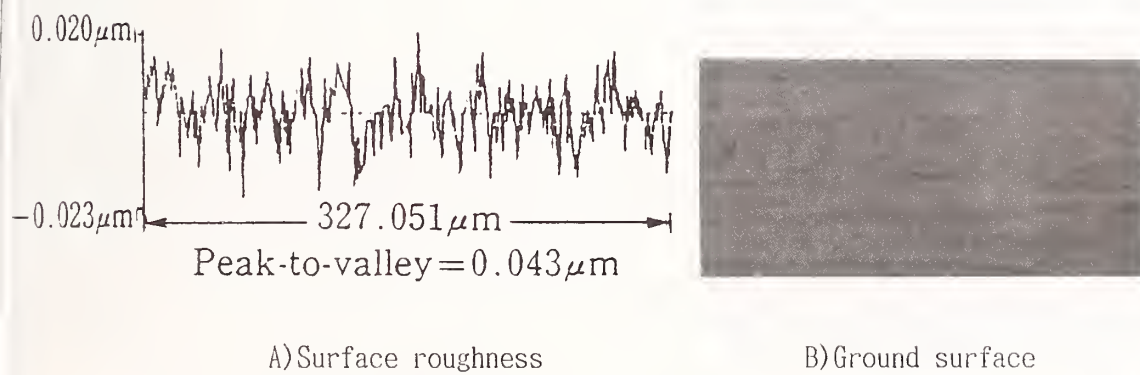
Fig. 19 Surface quality of finished aspherical lens (BK-7)

A)WC mirror (speherical)   B)SiC mirror (aspherical)

Fig. 20 Finished spherical and aspherical ceramics mirrors

Grinding Conditions : v_t 1500 m / min, f 100 mm / min, d 2 μm, v_w 500 rpm, R 100 mm, work : ϕ 50 mm Si
ELID Conditions : E_o 140 V, I p 5 A, τon 5 μs, τo ff 1. 7 μs
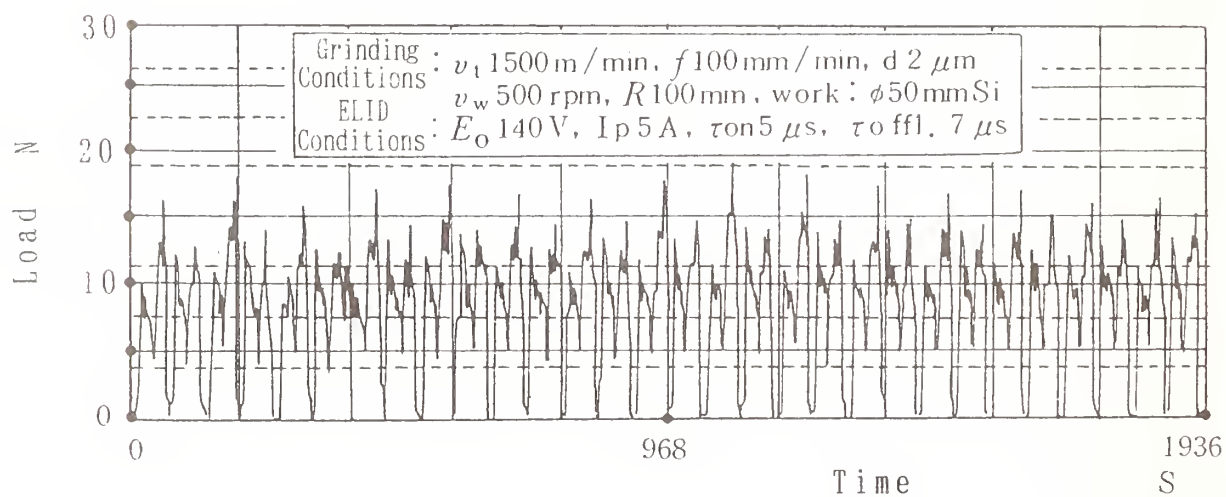
Fig. 21 Stability of grinding force on spherical mirror machining
for silicon
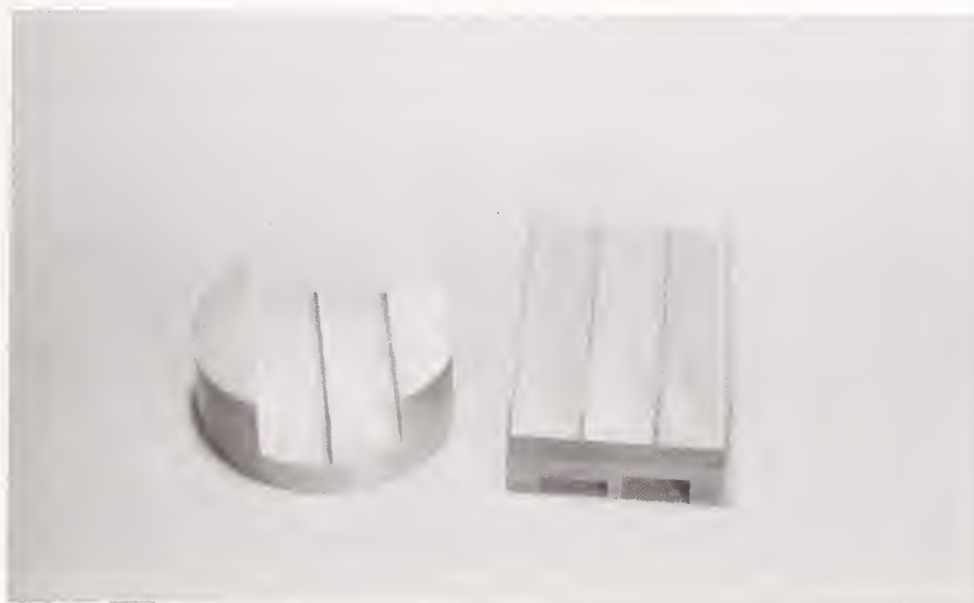
A)Sialon   B)Si$_3$N$_4$

Fig. 22 Ceramics specimens machined with ELID-plunge grinding
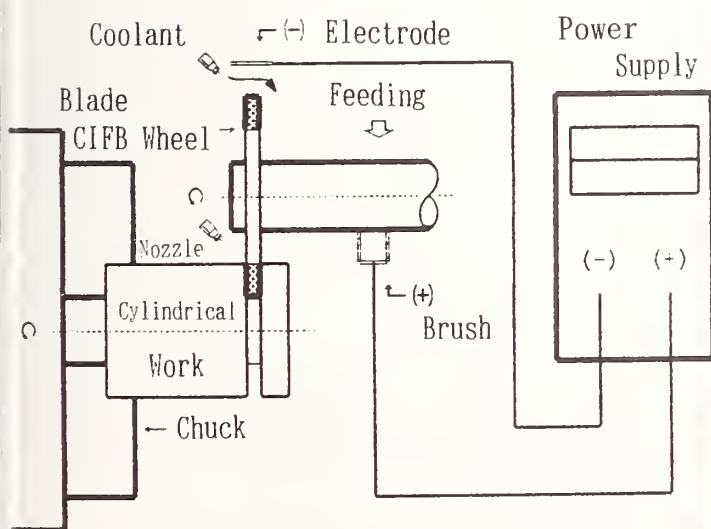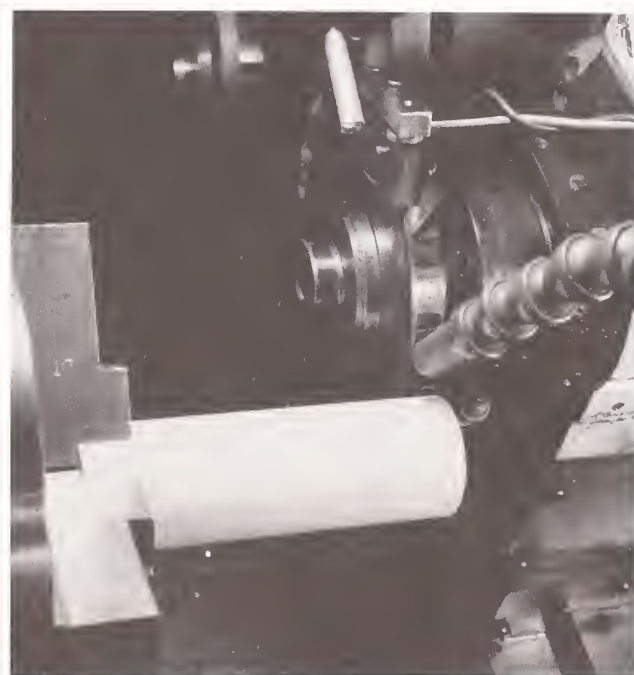
A)Cutting with ELID   B)Near view of machine

Fig. 23 Schematic of high speed cutting with ELID
and the employed machine
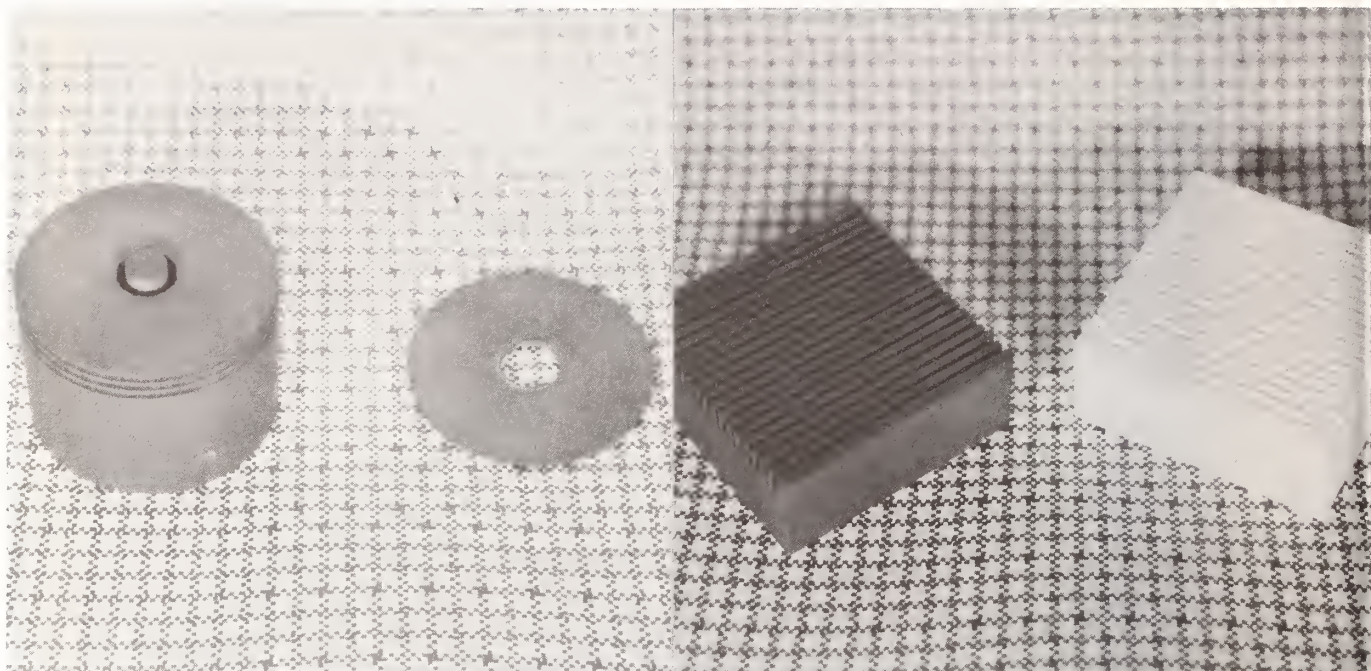
A) Al_2O_3

(Cylindrical cutting sample)

B) Si_3N_4 C) Al_2O_3

(Groove shaping samples)

Fig. 24 Examples cut by #100/120 CIFB-D blade wheel with ELID
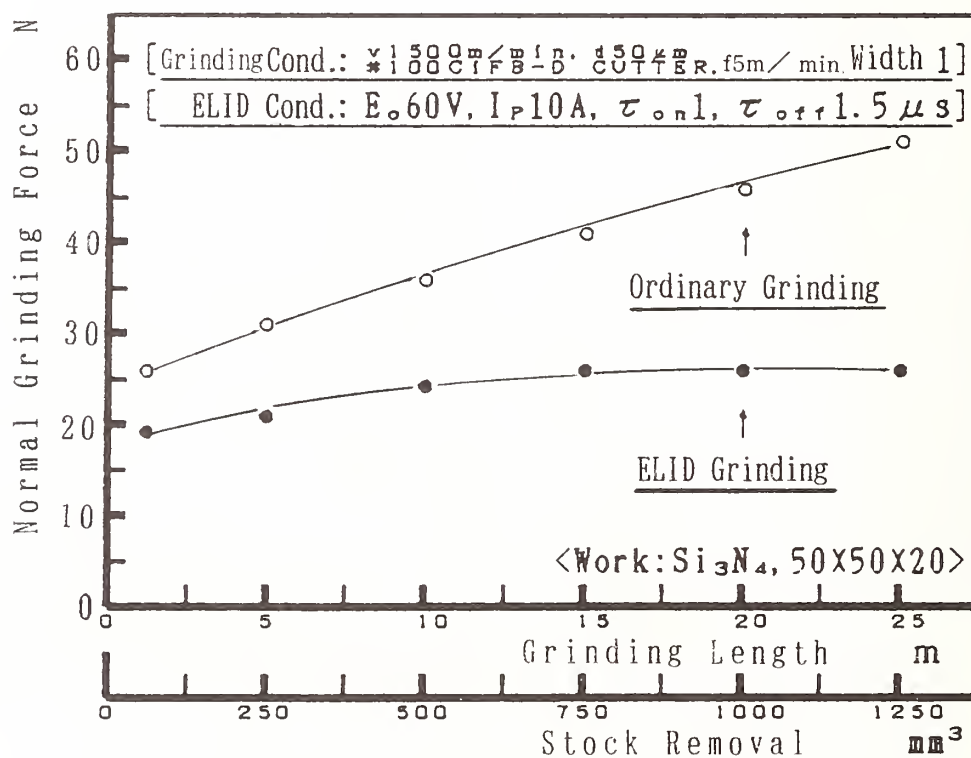
Fig. 25 Stability and reduction of normal grinding force
in cutting operation with ELID for Si_3N_4

FREE ABRASIVE MACHINING

ULTRASONIC SHAPING: AN ECONOMICAL PROCEDURE TO MACHINE COMPLEX CERAMIC COMPONENTS

R. HAHN and C. LOST
University of Tubingen, Tubingen, Germany

P. SCHULZE
Erosonic AG, Wattwil, Switzerland

A new technique is presented to fabricate complex ceramic components using a multipart tool system for ultrasonic machining. Mechanical oscillation combined with an abrasive slurry causes the vibrating sonotrode to reproduce its shape into the hard and brittle material. The result of this machining operation is an accurate component of almost any geometry.

In this study, the influence of the ultrasonic shaping procedure on the surface quality, bending strength and fatigue behaviour of a feldspatic porcelain and an experimental monolithic alumina was investigated. It was found that diamond grinding of porcelain yielded a rough surface and a decrease in bending strength and fatigue. In contrast, ultrasonic shaping resulted in a smoother surface. However the smoothest surfaces were achieved by lapping, although, bending strength and fatigue behaviour of the conventional feldspathic porcelain were significantly increased by ultrasonic machining. The influence of the work gap to the process is discussed as an effective instrument to control the material removal mode, either for shaping or for finishing in the same operation.

Introduction

Due to the dimensional distorsions during firing, complex ceramic components have to be (re-) machined to control shapes, tolerances and surface finish. Material removal rates, surface quality and subsurface integrity depend on the microstructure and toughness of the machined ceramics (1).

Conventional diamond coated grinding instruments are suitable for grinding porcelains efficiently (2). However, for the most high toughness monolithic ceramics, ceramic matrix composites and single crystals, efficient removal rates can hardly be achieved by diamond grinding (3). Additionally, accurate geometrically complex shapes, such as prototypes, unique medical implants or tooth restorations, and close dimensional tolerances can not be realized (4, 5).

Alternatively, honing and lapping are efficient refinishing procedures for polishing flat surfaces with diamond slurries (6). Chemical etching is a slow process, which is hard to control for vertical removal, although future development of laser induced etching may increase the applications.

Laser or elektron beam machining of brittle ceramics yield thermal gradients and explosively induce internal stress, wich may cause spontaneous damage (7). In addition, shaping three-dimensional surfaces is almost impossible (8). Electron discharge machining requires an electrical conductive material or the addition of conductive elements (9), which yields a black color and decreases the original strength behaviour. Both ultrasonic machining and ion milling, using ionized argon in a high vacuum, are suitable for shaping ceramics gently (10, 11). However, because ion milling requires expensive machinery, it is not economical for shaping unique components or small volumes, such as medical implants or tooth restorations. Thus, ultrasonic shaping remains as the only technology

particularly suited for shaping high toughness ceramics i.e. for tooth restorations (12).

The presented processing technique is based on an accurate wax or resin model of the target component (10). Using an adjusting device the positive model is favourably orientated to the z-axis of the machine, unilaterally fixed and contralaterally coated with a special polymer up to the widest circumference (equator). The resin die is then locked at a tool holder, which is aligned parallel to the z-axis of the machine. After hardening and insulating of the polymer, the remaining model surfaces are completely resin embedded and also fixed to a contralateral aligned tool holder. The obtained polymer presonotrodes can be separated and the original model removed completely. A mould form is made enclosing the presonotrodes with a refractory investment material and conventionally prepared to casting. The actual sonotrode patterns are directly cast onto the tool holders using a tough metal (13).

For ultrasonic machining, as detailed below, the sonotrodes are axially aligned, spatially locked and unilaterally coupled to the oscillating unit of the machine, in succesion. In polyphase operations the tools are sunk into both sides of the preform, thereby the surface properties of the component can be characterized by using defined anisotropic blanks and modelling the sinking depth of the first operation (Figs. 1, 2).

The aim of this study was to compare the surface quality, bending strength and fatigue behaviour of ultrasonically shaped ceramics to that after conventional grinding and lapping.

Test Procedure

In this study the machining induced influences on a feldspatic porcelain and an experimental monolithic aluminium oxide ceramic (ISO 6474 standard) were compared. Seventytwo rectangular porcelain test bars of size 3.0 mm x 5.0 mm x 22.0 mm were fabricated following ISO 6872 standard. Twentyfour randomly selected specimens each were alternatively surface treated by lapping, diamond grinding or ultrasonic machining.

A vertical standardized device served to cut the surface plan-parallel to 2.00 mm in thickness. The lapped samples were preground to a thickness of 2.30 mm, followed by diamond lapping to 2.00 mm, using water based diamond slurry with decreasing abrasive grain sizes to 3 μm.

For grinding, an experimental set up was used, mounting a conventional D 91 diamond wheel to a high-speed electromotor. The cutting speed was constant at 35 m/s. A standardized normal force of 20 N (linear spring) was applied acting the sample against the rotating tool. For the aluminium oxide ceramic the wear of the diamond wheel was extremly high, which made grinding of the particular test bars almost impossible. Consequently, diamond ground or lapped alumina specimens could not be evaluated.

For ultrasonic machining a prototype machine was used as detailed below. Another twentyfour ultrasonically shaped alumina test bars (ISO 6474) of equivalent dimensions served as controls.

Evaluating the critical bending strength and fatigue behaviour, two subgroups of 12 specimens each were randomly divided from the porcelain and alumina test bars. Using a compression testing machine, a three-point bending test was applied in air at room temparature (cross head speed = 0.05 mm/min, span between bearers = 15.00 mm, roller bearing surfaces = 1.6 mm in diameter) measuring the applied load over the flexion of the sample (ISO 6872 standard). Following the fracture, the machined porcelain surfaces were investigated using profilometry. Rmax (maximum peak-to-valley height), Rz (mean peak-to-valley height) and Ra (arithmetric mean roughness value) were measured following DIN 4768 (mesured length = 4.8 mm, diamond cone 2 mm, 60°). Additionally, Rk (core height of the profile excluding the highest peaks and deep valleys) and the affiliated bearing ration curves (Abbott-Plots) were quantified in accordance with DIN 4776 to show the ratio between the bearing surfaces and the profile depths. Six spots of all specimens were analyzed to calculate median and percentiles.

Each surface of the test samples was measured twice, arranging a 90° angle between the measured length which was located parallel to the edges.

For fatigue, cyclic load was applied to the remaining 12 samples (50 000 cycles, 60% of the critical bending stress, stress ratio = 0.1), followed by

critical fracturing as detailed above. The data were analyzed with a statistical software. The median and corresponding quartiles of the roughness values are summerized in Table 1, and bending strength data are displayed as a box plot (Fig. 7). An ANOVA was used to prove for significance (95%).

Ultrasonic shaping

The machining process (as specified in DIN 8589 part 15) uses ultrasonically induced vibrations (f = 20 ± 0.5 kHz) amplified by a booster and delivered to a designed tool (sonotrode). This, combined with an abrasive slurry, causes the tooling to reproduce its shape into any hard and brittle material, in negative (12). The material removal process is based on an indirectly applied mechanical energy made by defined longitudinal strokes of the form sonotrode coupled with a slurry, such as boron carbide (F 280) suspended in water (1:10). The fast motion of the tool works the abrasive into the face of the workpiece, thus microscopically chipping and grinding away the material (Fig. 3a). Moving down the tool, the abrasive filled fluid causes an elastic-plastic distortion of the sonotrode face and creates flat microcracks in the surface of the work-piece (Fig. 3b). Swinging the sonotrode up, the work gap is rinsed with slurry, supplying the abrasive and removing the chips (Fig. 3c). Because the carrying fluid is successively compressed and expanded between sonotrode and workpiece, a cavitational erosion also occurs.

The process can be controlled by varying the gap between the tool and the workpiece. During the actual shaping period, the distance between the sonotrode and the ceramic is kept constant by tuning the vertical pressure (p = 0.5 - 1.5 bar) and the amplitude (A_{max} = 5 - 20 μm) of the master sonotrode to an optimum, which is specific for each individuell sonotrode and material. Thereby the material removal rate can be raised to a maximum, decreasing the process time and the wear of the tool surface. Exceeding a critical vertical pressure, a sufficient acceleration of the abrasive is impossible, limiting an economic removal performance.

Increasing the gap between the tool and the machined surface by tuning the vertical pressure to 10 % of the individuell applied maximum, immediately before achieving the target shape, the energy adaption becomes even more indirect by visco-elastic muffling of the abrasive movement in the slurry suspension. Thereby refinishing can be applied to the machined surfaces (Fig. 3d).

Results

The diamond ground surfaces revealed superficial chipping, such as acute indents, spallings and sharp incisions, which yielded a rough porcelain surface microstructure (Fig. 4). On the other hand the ultrasonic machining provided a leveled surface microrelief (Fig. 5), although diamond lapping decreased the porcelain roughness values the most (Table 1, Fig. 6).

When compared to diamond grinding and lapping, ultrasonic machining resulted in a significantly increased bending strength of the porcelain test bars (Fig. 7). However, this particular effect of the ultrasonic treatment on porcelain significantly decreased after applied fatigue. There were no significant differences in the critical bending strength of the lapped and the ground porcelains, although after applying fatigue the ground specimens were weakened (Fig. 7). The experimental alumina revealed significantly the highest bending strength (Fig. 7).

Discussion

The functional performance of ceramic components is based on the surface structure and their specific chemical or physical properties. The influence of applied surface treatment or machining procedure on the surface microrelief was recently investigated. Thus, SEM studies, as well as profilometry, exposed glazing and conventional polishing, i. e. using fine-grained finishing diamonds suitable for achieving smooth surfaces, although overglazing revealed the smoothest microrelief (14). However, the surface quality was dependent on both, the microstructure of the ceramic and the applied surface treatment. Fracture mechanic studies and stress analysis experiments exposed surface and subsurface defects of ceramic components, such as initial microcracks, acute indents, sharp incisions or delamination as the most crucial factors limiting strength and fatigue behaviour (15, 16, 17).

As a characteristic feature of ceramic surfaces, the small indents, pinholes and microcracks are not accessible for conventional profilometry using the diamond stylus technique (5 μm in tip, 90°) (18). The translucency of feldspathic porcelains complicates optical profilometry such as laser scanning systems (19). Therefore, a special diamond cone (2μm in tip; 60°) and a filter system following DIN 4768 were found as being compatible for ceramic surface analysis.

Applied diamond grinding induces a rough surface and subsurface damage resembling delamination (20). While refinishing using conventional diamond lapping, the delaminated layer can be removed and the surface relief leveled, although deep radial microcracks which were induced during diamond grinding are retained.

On the other hand, ultrasonically machined ceramics show a rougher surface than lapped specimens, however the rounded microrelief is favourable for carrying applied load (21). Additionally, the oscillating hammering of the boron carbide against the ceramic cause surface inherent residual stresses. Thus, the fracture resistance can be increased by offsetting the applied stress (22), even though fatigue partly decreases this effect during cyclic loading.

Due to their low tenacity, this effect is favourably featured when ultrasonically machining fragile glass matrix composites, such as feldspathic dental porcelains. In contrast, high tough ceramics, including monolithic alumina are primarily more resistant to crack growth, fatigue and fracture (4).

However, the principle to reinforce ceramic materials by inducing inherent residual stresses is well known from tetragonal zirconia polycrystals which are used for reinforcing alumina (23, 24).

In conclusion, applied load can be statistically concentrated on surface inherent flaw tips, such as superficial sharp indents or subsurface damage, on machined ceramic components. Depending on the crack growing energy, a blind fissure or a critical progressing crack can be initiated leading to fatigue or fracture (4, 25). Networking surface and structurally inherent flaws by statistically growing microcracks, the fracture resistance may decrease, leading to fatigue failure (26).

Conclusions

1. The described ultrasonic shaping procedure facilitates the machining of almost any geometry and provides an economical removal rate, while treating the surface layer gently.
2. Bending strength and fatigue behaviour of ultrasonically treated porcelain test bars are significantly better than the ground or lapped controls.

References

1. I. Inasaki, "Grinding of Hard and Brittle Materials," CIRP Annals, Vol. 36, pp. 463-471, 1987.
2. W. Mörmann and M..Brandestini, "Verfahren zur Herstellung medizinischer und zahntechnischer alloplastischer, endo- und exprothetischer Paßkörper," Patent, EPA 0054785, 1981.
3. O. W. Richardson, "Modern Ceramic Engineering," Marcel Decker Inc., New York, 1982.
4. R. Hahn and C. Löst, "Konventionelle Dentalporzellane versus bruchzähe Hochleistungskeramiken," Dtsch. Zahnärztl. Z., Vol. 47, pp. 659-664, 1992.
5. M. Weck, R. Hartel and U. Böttger, "Anforderungsprofile an Fertigungseinrichtungen zur Ver- und Bearbeitung von keramischen Werkstoffen," VDW Forschungsbericht 0150, Aachen, 1987.
6. G. Spur, "Keramikbearbeitung," Hanser, München, 1989.
7. C. Emmelmann and H. Semraw, "Keramikbearbeitung mit dem Laser," Laser Magazin, Vol. 3, pp. 8-14, 1987.
8. R. F. Firestone, "Lasers and other Nonabrasive Machining Methods for Ceramics," Mat. Science Comp., Vol. 32, pp. 133-138, 1987.
9. U. Panten, "Funkenerosive Bearbeitung von elektrisch leitfähigen Keramiken," Tech Diss, TH Aachen, 1990.
10. R. Hahn, "Verfahren zur Herstellung von Zahnersatzteilen mit Hilfe zweier Sonotroden, Vorrichtung zum formgebenden Bearbeiten von Werkstücken unter Verwendung einer Sonotrode und Verfahren zur Herstellung einer in der Zahntechnik verwendbaren Sonotrode," Patent, DE 39 28 684, 1989.

11. J. Orloff, "Focused Ion Beams," Sci. Am., Vol. 10, pp. 96-101, 1991.

12. R. Hahn and C. Löst, "Sonoerosive Fertigung keramischer Zahnrestaurationen," Dtsch. Zahnärztl. Z., Vol. 47, pp. 734-739, 1992.

13. R. Hahn and C. Löst, "Sonoerosive Fertigung keramischer Einlagefüllungen," Quintessenz, accepted for publication, 1992.

14. C. J. Patterson, A. C. McLundie, D. R. Stirrups and W. G. Taylor, "Refinishing of Porcelain by Using a Refinishing Kit," J. Prosth. Dent., Vol. 65, pp. 383-388, 1991.

15. S. E. Brackett, J. M. Leary, K. A. Turner and R. D. Jordan, "An Evaluation of Porcelain Strength and the Effect of Surface Treatment," J. Prosthet. Dent., Vol. 61, pp. 446-451, 1989.

16. W. Pfeiffer, W. Berweiler and T. Hollstein, "Optimierung ausgewählter keramischer Hochtemperaturwerkstoffe hinsichtlich Festigkeit, Ermüdung und Oberflächenzustand," IWM-Bericht, W 10/90, Fraunhofer Inst. für Werkstoffmechanik, Freiburg, 1990.

17. Y. Sano, M. Fujisawa, K. Shinohara, T. Uetani, H. Tadano, H. Horiguchi, M. Adachi, N. Wakamatu, T. Goto and I. Sekine, "Influence of Surface Properties on the Bending Strength of Optec Porcelain," Gifu Shika Gakkai Zasshi, Vol. 16, pp. 577-581, 1989.

18. G. Henzold, "Rauheitsmessung mit elektrischen Tastschnittgeräten," DIN Normenheft, Vol. 12, Beuth, Berlin, 1971.

19. R.-J. Ahlers, "Optische Verfahren zur Oberflächenprüfung," Z. Ind. Fertig., Vol. 74, pp. 465-468, 1984.

20. H. Siemer and H.-G. Wobker, "Randzonenanalyse an keramischen Werkstoffen," Sprechsaal, Vol. 123, pp. 282-293, 1990.

21. T. Hollstein, D. Meyer and W. Pfeiffer, "Fertigungseinfluß auf Festigkeit und Bruchverhalten von Hochleistungskeramik," Materialprüf., Vol. 33, pp. 332-337, 1991.

22. D. Johnson-Walls, A. G. Evans, D. B. Marshall and M. R. James, "Residual Stresses in Machined Ceramic Surfaces," J. Am. Ceram. Soc., Vol. 69, pp. 44-47, 1986.

23. N. Claussen, "Umwandlungsverstärkte keramische Werkstoffe," Z. Werkstofftech., Vol. 13, pp. 138-147, 1982.

24. F. Wakkai, T. Iga and T. Nagano, "Effect of Dispersion of ZrO_2 Particles on Creep of Fine-Grained Al_2O_3," J. Ceram. Soc. Jpn. Inter., Vol. 96, pp. 1176-1178, 1988.

25. K. Jakus, D. C. Coyne and J. E. Ritter, "Analysis of Fatigue Data for Lifetime Predictions for Ceramic Materials," J. Mater. Sci., Vol. 13, pp. 2071-2080, 1978.

26. H. Richter, "Langsame Rißausbreitung und Lebensdauerbestimmung - Vergleich zwischen Rechnung und Experiment," Ceram. Forum Int., Vol. 57, pp. 10-12, 1980.

Table 1:
Surface quality of a variably treated feldspatic porcelain. Median ($\overline{x}$), minimum (x_{min}) and maximum (x_{max}) of the measured roughness values (Rmax, Rz, Ra and Rk) in relation to the applied surface treatment.

		x_{min}	x_{max}	$\overline{x}$
Ground Surfaces	Rmax	14.27	36.26	22.80
	Rz	13.09	21.79	16.03
	Ra	2.10	2.65	2.33
	Rk	7.12	8.72	7.60
Lapped Surfaces	Rmax	0.20	0.47	0.32
	Rz	0.17	0.28	0.22
	Ra	0.018	0.022	0.019
	Rk	0.062	0.067	0.064
Ultrasonically Machined Surfaces	Rmax	8.19	15.78	11.94
	Rz	7.13	10.36	8.64
	Ra	1.08	1.23	1.14
	Rk	3.40	3.87	3.54
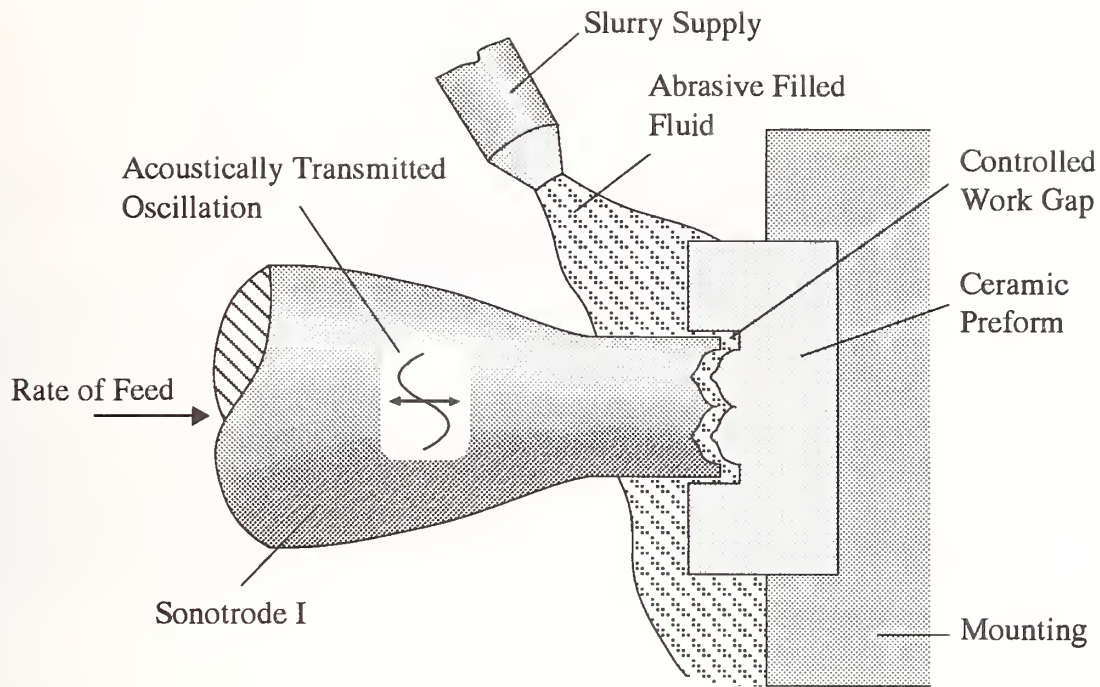
Fig. 1: Operation 1
Diagrammatic view of the first operation ultrasonically shaping an artificial ceramic tooth crown, as an example of a very involved geometrical component.
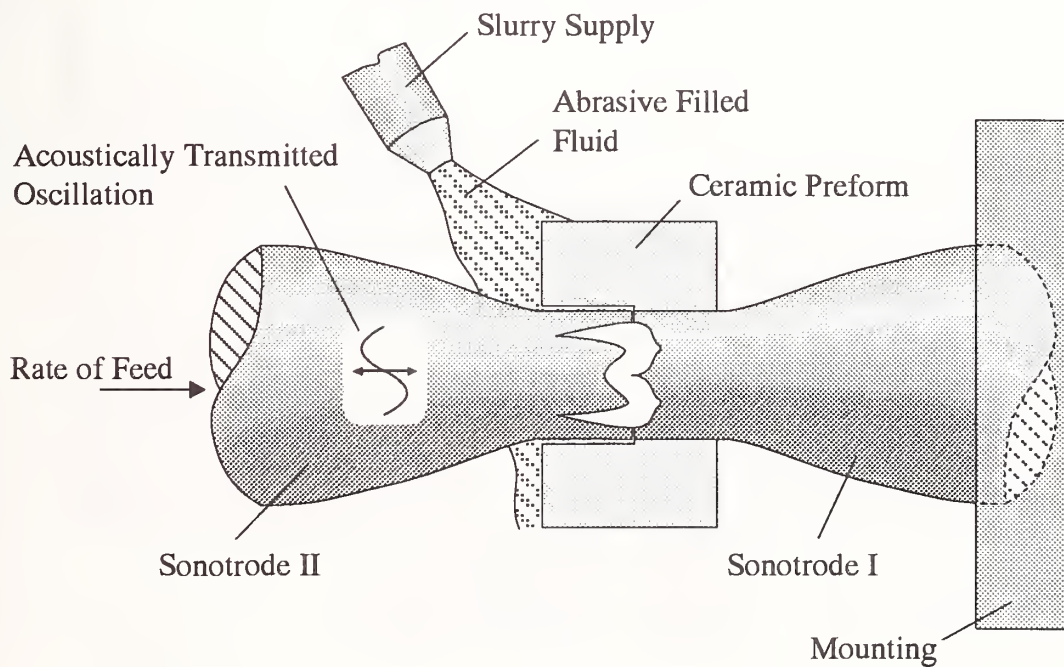
Fig. 2: Operation 2
By sinking the second sonotrode into the contralateral surface of the unilaterally machined preform, the actual component is shaped (diagrammatic). In this operation the first sonotrode acts as a shaped seat for the ceramic blank. The spatial relation of the sonotrodes is clearly defined by the exact alignement of the length axis and the square position.

391
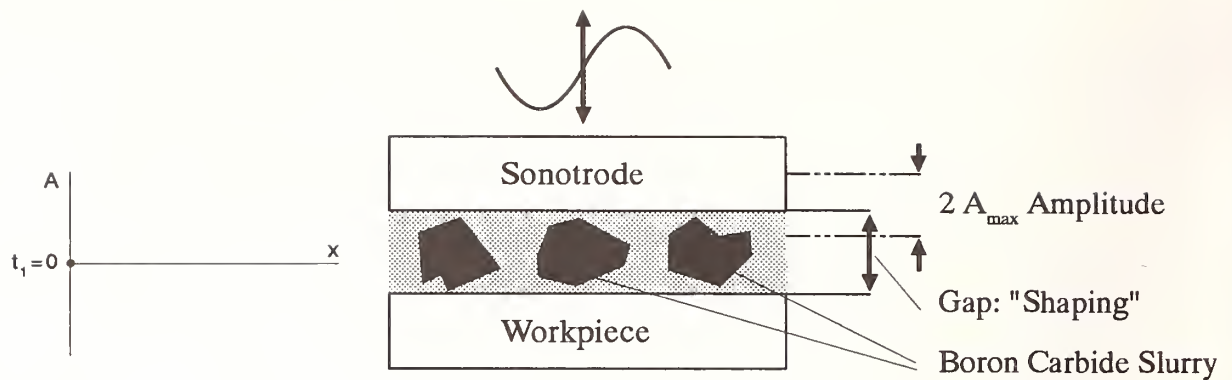
Fig. 3a:
Schematic description of the ultrasonically machining operation. The transmission of the linear oscillation to the master tool results in a physical stroke of the sonotrode of a few microns at a rate of 20 kHz. During the actual shaping period, the tooling never touches the ceramic surface. The abrasive grains are propelled indirectly by the mechanical motion of the oscillating tool and pummel the surface of the workpiece.
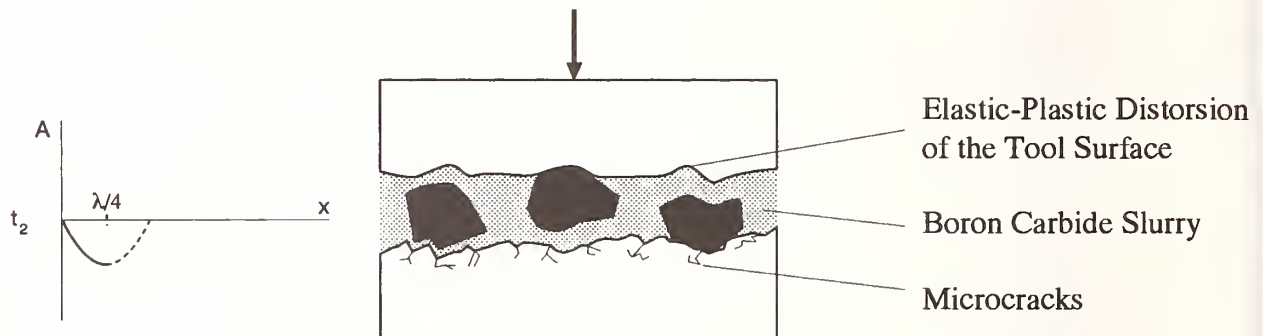
Fig. 3 b:
Because of the contrasting elastic properties of the tool surface and the ceramic, the abrasive is indirectly hammered onto the machined surfaces.
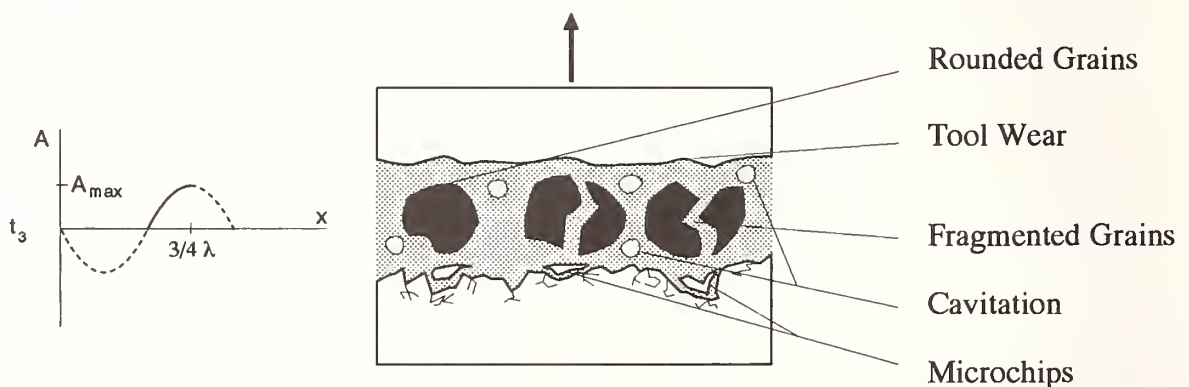
Fig. 3c:
Material is removed by erosion and grinding as they are created by the abrasive grains, the carrying fluid and additional cavitation.
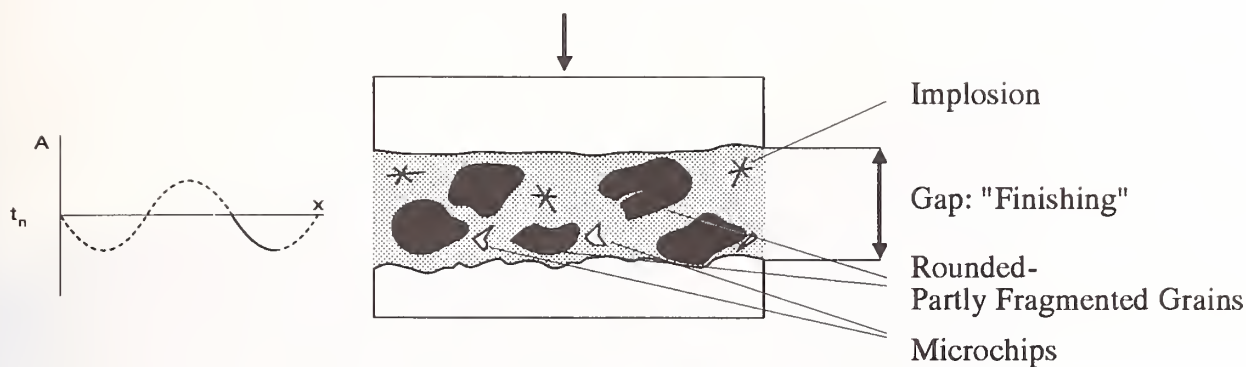
Fig. 3d:
Expanding the work gap between the sonotrode and the ceramic results in a increasingly indirect energy adaption, refinishing the machined surfaces.
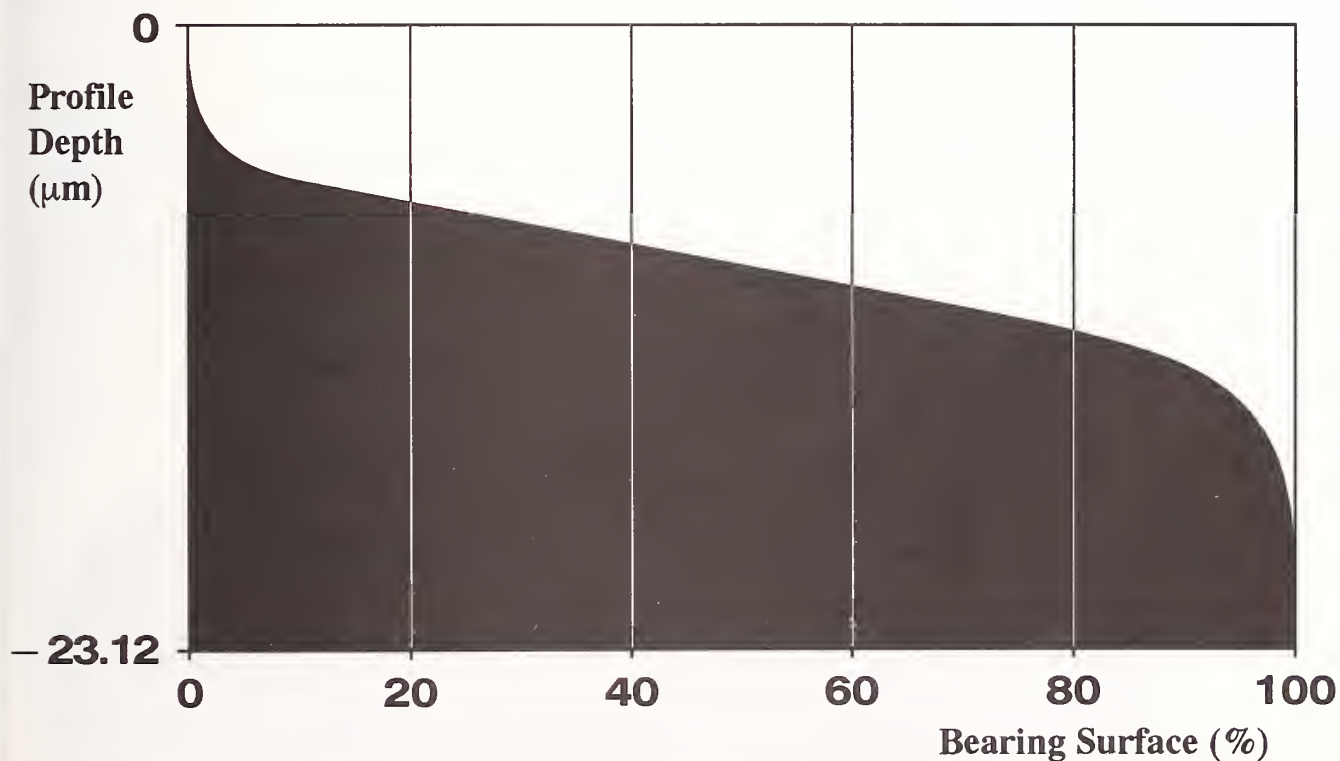
Fig. 4:
Surface density of a representative diamond ground porcelain specimen. The Abbott-Plot relates specifically to the applied surface treatment. This ground sample showed a "total" surface of 100 % in a depth of -23.12 microns.

393
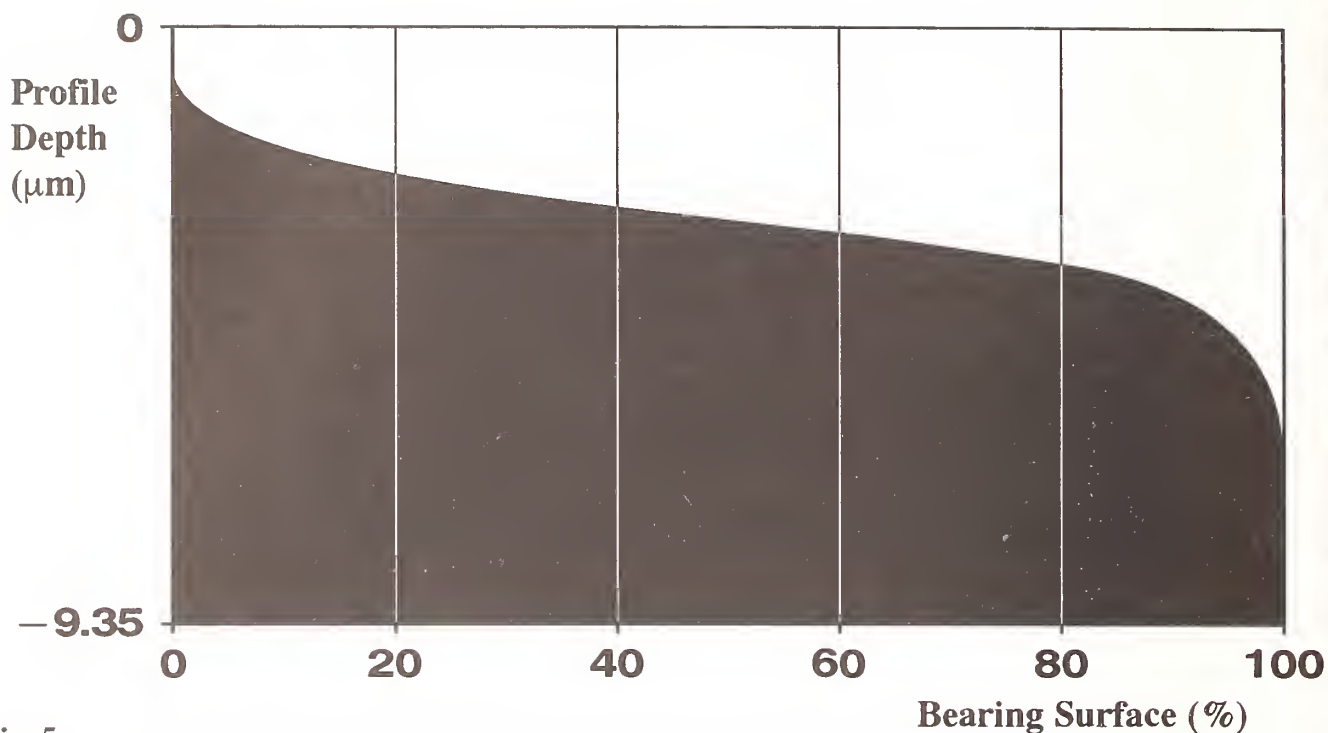
Fig. 5:
Surface density of a representative ultrasonically machined porcelain specimen. The almost symmetrical coarse of the Abbott-Plot indicates a leveled microrelief with a maximum roughness of -9.35 μm in this specimen.
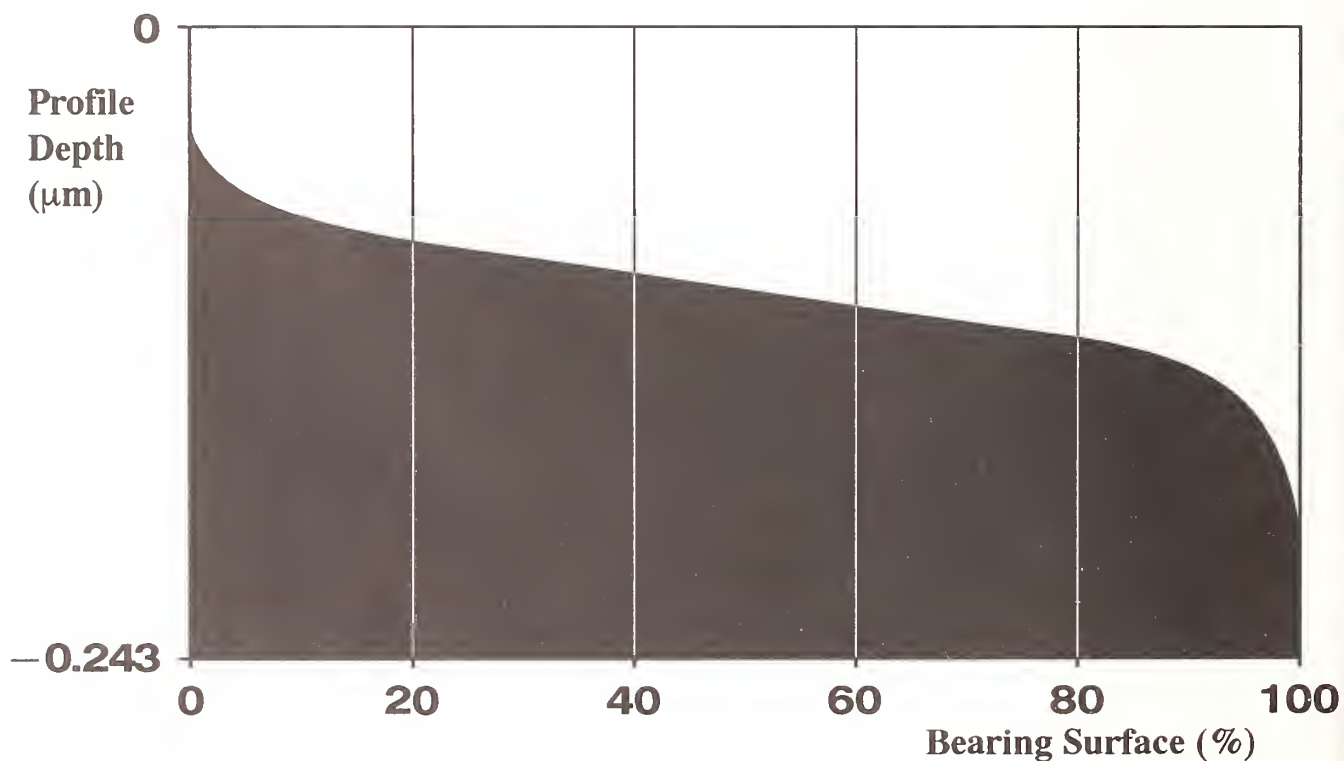
Fig. 6: Surface density of a representative diamond lapped porcelain specimen (Abbott-Plot). The used lapping procedure reproducibly maintained flat microsurfaces (-0.243 μm).
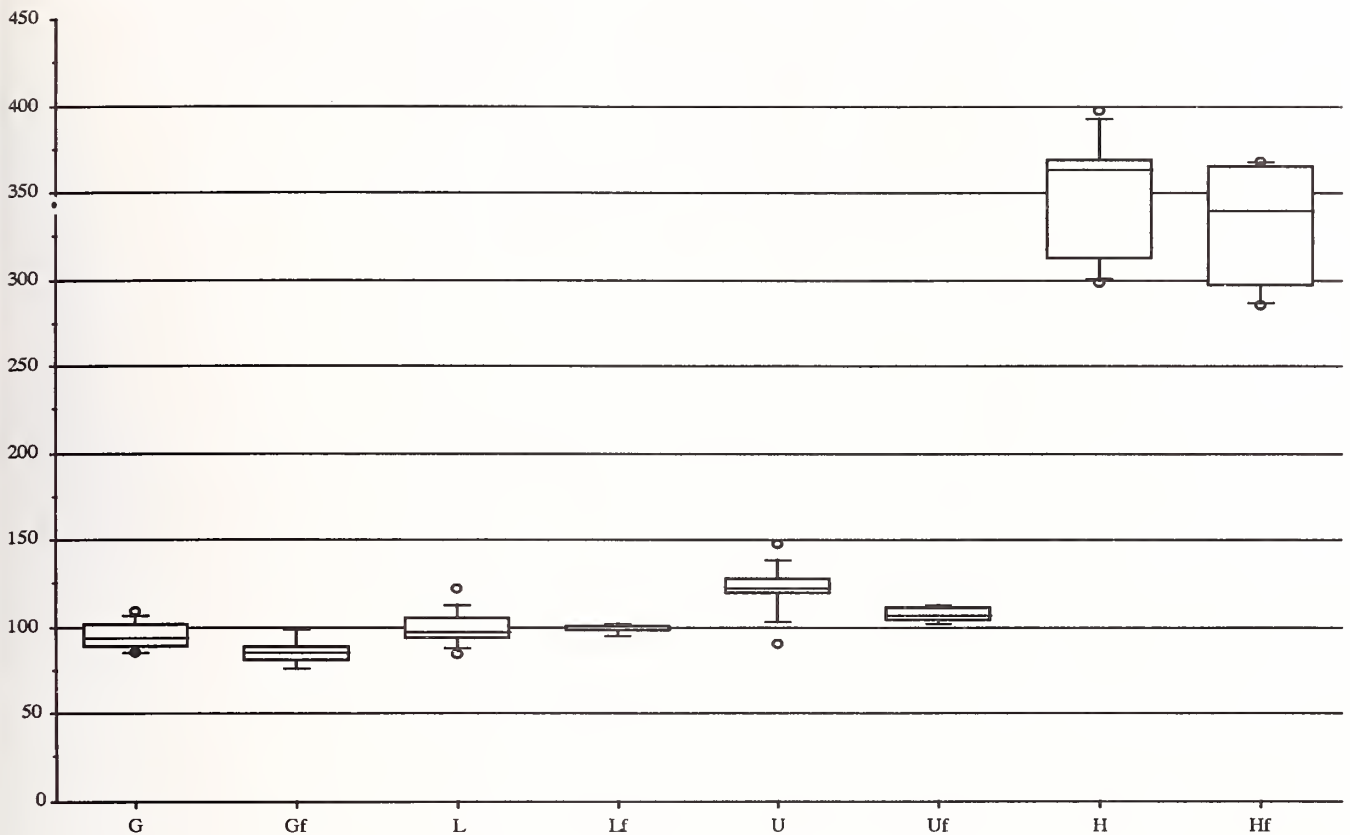
Fig. 7:
Box-Plot of bending strength of porcelain (Biodent Inlay Ceramic) and experimental alumina test bars in relation to the applied surface treatment, before and after cyclic loading. The box displays the median as well as the 25% and the 75% quartile as the belonging scattering value. The whiskers show the 10% and the 90% quantile; values far outside are plotted as empty circles. For both critical bending strength and fatigue behaviour, the ultrasonically machined specimens show the highest values.

G = ground porcelain
Gf = ground porcelain after cyclic loading
L = lapped porcelain
Lf = lapped porcelain after cyclic loading
U = ultrasonically machined porcelain
Uf = ultrasonically machined porcelain after cyclic loading
H = ultrasonically machined experimental alumina
Hf = ultrasonically machined experimental alumina after cyclic loading

A MODEL FOR HYDRO AND HYDRO-ABRASIVE JET MACHINING OF CARBON FIBER REINFORCED PLASTIC COMPOSITES

R. GROPPETTI and A. CATTANEO

Universita degli Studi di Perugia, Perugia, Italy

Hydro Jet Machining (HJM) and Hydro-Abrasive Jet Machining (HAJM) have demonstrated high effectiveness and potential for multilayer Carbon Fibre Reinforced Plastic (CFRP) composites. A deep understanding of the material removal mechanism for machining is needed for prediction of productivity and quality, and for prediction and avoidance of machining damage. The problem of the quality of the cut in the kerfing area of a CFRP workpiece is of great interest, because functional behaviour highly depends on the level of damage and defects along the edge of the workpiece, due to delamination, spalling and surface roughness.

This paper presents and discusses a theoretical global energetic model and its experimental validation, that is a contribution to the study of the mechanism of delamination occurring during multilayer CFRP composite machining by means of HJM and HAJM. A predictive model of edge damage caused by HJM and HAJM can be useful in order to evaluate machining conditions, to predict the machining results in terms of kerfing conditions without time-consuming and expensive experiments.

1. INTRODUCTION

Among the machining processes for Carbon Fibre Reinforced Plastic (CFRP) multilayer composites, Hydro Jet Machining (HJM), or briefly Water Jet, and Hydro-Abrasive Jet Machining (HAJM), or Abrasive Water Jet, have demonstrated high effectiveness and potential. Many efforts are devoted both in industry and in research institutions to study these processes in order to get a deep understanding of the material removal mechanism, to predict machining results in terms of productivity and quality, and to predict and to avoid machining damage.

HJM and HAJM processes are based on a high speed jet of water or water and abrasive particles, focused, mixed and accelerated, to impinge on the workpiece in a restricted area. The material removal mechanism is complex and involves erosion, abrasion, cavitation, deformation, and fracture. The problem of the quality of the cut in the kerfing area of a CFRP workpiece is of great interest, because functional behaviour highly depends on the level of damage and defects along the edge of the workpiece, due to delamination, spalling and surface roughness. Both HJM and HAJM offer virtually net shape and finished workpieces without heat affected zone. But, when machining conditions are not set properly, delamination, spalling and low surface finish can take place. While many results have been published regarding structural analysis and synthesis methods based on theoretical and experimental mechanics of composites, rather few studies analyse CFRP multilayer composite machining problems.

Multilayer Carbon Fibre Reinforced Plastic (CFRP) composites are widely used as structural components because they offer high performance and cost effectiveness. Many efforts have been done in order to define design rules and methodologies for an optimal design, in terms of number and orientation of plies, their relative

positions, or the thickness of the boundary between two plies, etc. [1, 3, 10, 17]. It has been demonstrated also that the optimal design of the CFRP structural components depends on many factors and decisions, that have to be taken into consideration concurrently, because they are highly coupled, particulary functional requirements and factors relevant to their manufacturing process. Therefore new approaches, methodologies and techniques have to be followed to execute this decision process, as concurrent engineering, sensitivity analysis, design of the experiments etc. [3, 9, 17, 21, 23]. Many results have been published regarding structural analysis and synthesis methods based on theoretical and experimental mechanics of composites. Rather few studies analyse composite manufacturing problems, particulary machining, piercing and cutting of composite materials [10, 11, 15]. Because multilayer CFRP composite products have to be finished and trimmed by piercing and cutting, some undesirable effects may occur as a low surface finish or high roughness of the edge of the part, i. e. of the side of the kerf, delamination and spalling [1,20,21,23]. The quality of the cut is particulary important for the behaviour of CFRP structural components because delamination may also take place due to edge effects, as stress concentration near the edge [3] when the part is in operation.

HJM and HAJM are processes, based on a high speed jet, for HJM a water jet only, for HAJM a hydro abrasive jet formed by a stream of abrasive particles focused by a secondary nozzle or focuser, mixed and accelerated by the high speed hypersonic jet of water, obtained by the output from a primary nozzle of water highly pressurized usually up to 400 MPa. The hydro or hydro-abrasive jet impinges on the workpiece in a restricted area, giving origin to complex micro-machining interactions with the material, as erosion, abrasion, cavitation and brittle fracture of the material. The paper presents a theoretical analysis and experiments of the mechanism of delamination, occurring when CFRP multilayer composite cutting and piercing by means of HJM and HAJM. A delamination predictive model of the dependence of delamination on the cutting process variables, based on a global energetic approach [4,10], is discussed and the main results of this validation are analysed as a contribution to the study of the mechanism of delamination due to the machining process. A suitable model of the edge damage due to machining can be useful in order to predict and optimize kerfing conditions, without time-consuming and experiments, when cutting and piercing CFRP laminated composites.

2. HJM / HAJM DELAMINATION MODELLING

When cutting and piercing CFRP by means of HJM and HAJM the principal structural damage is delamination [5,10,11,15]. Hydro and hydro-abrasive jet stability perpendicular to its own axis is limited and it can be disturbed within the cutting kerf easily. The cutting surface shows the characteristic bundles of parallel visible grooves, which are bent opposed to the fibre direction. The fibres embedded in the matrix act as obstacles, therefore HJM jet is deflected and erodes the soft component of the material first. That leads to the typical appearance of washed-out matrix protuding fibres [15]. This occurs mainly at the upper end of the cut. The jet erodes the matrix material only, whereas the fibres remain as solid links across the kerf. The main action of the jet is in the direction of the fluid flow and generally perpendicular to the surface. The more the jet penetrates into the material, the less is the force, due to the absorption of jet energy during penetration, and delamination appears at the exit side. Water pressure between the layers is a cause of material damage of CFRP with HJM. An increase of the pressure gives origin to a higher feed rate and an improvement of the surface quality. CFRP surfaces machined by HAJM show a much higher uniformity than workpieces machined at lower feed rate by HJM and no washed-out single fibres had been obtained [10,14].

Cut surface is usually smoother in the upper part of the kerf than in lower part, that presents waviness.

For the piercing process it is demonstrated that at high pressures, depending on material thickness, the jet loading close to the bottom of the hole causes delamination in the bottom layers. A failure analysis of HJM piercing of multilayer

composite has been performed to study the process of delamination [5]. With the help of energy balance, a simple analytic equation is proposed in order to choose the water pressure in such a way that no delamination occurs. In the following section this model will be summarized and considered critically. The jet impinges on the laminae and each layer is penetrated by the jet. The model assumes that the jet thrust force acts in the centre of a circular plate and the single laminae responds to the acting force with flexible bending. During the kerfing process the uncut material thickness becomes thinner, and the force distributes on a decreased number of laminae connections. A first delamination stage occurs when the laminae bending forces are exceeded by the jet thrust force and the laminae starts to come off and a first crack arises. During a second delamination stage, water penetrates into this crack and due to water pressure crack propagates. According to this model, delamination can be avoided if crack initiation is suppressed, and delamination occurs when the strain exceeds the critical value of the laminae bonding force at the crack initiation site or at the tip of the crack.

A critical water jet pressure can be determined, that should not be exceeded to avoid delamination, following an approach of linear elastic fracture mechanics [19], based an energy balance equation. This equation relates the energy release rate with the thrust force of the jet, the displacement and the stored strain energy, using the classic plate bending theory and the assumption of a concentrated load on a circular plate with clamped ends. The phenomenon can be led to an erosion, loading and impact of the impinging jet on the workpiece surface, with matrix cracking and erosion into the laminae, delamination, fiber breakage and erosion. However from the analysis of the experimental results, considering the nature of this phenomenon, the plastic energy dissipated in the contact zone is a good parameter to measure the degree of damage received by the laminae [20]. Moreover from this analysis it was noticed that delamination occurs mainly cutting by pure water jet. Therefore a semi-empirical predictive model, based on an energetic approach has been defined [10], in order to correlate the extent of the

delamination extent to the energy of the jet at a defined depth inside the kerf, corresponding to the bottom layer, where delamination takes place.

The istantaneous energy can be expressed as a function decreasing at the different depth inside the multilayer composite and a proportional relation can be assumed between the instantaneous energy applied to the part and the material volume removal rate, as demonstrated in [2] and [10]. Using the Levenberg-Marquardt Method for the estimation of the parameters of nonlinear models [18], the specific energy E, or residual energy on the bottom ply, for unit length and width equal to d_j at the kerfing depth, can be expressed by the following semi-empirical equation:

$$E = \left(1 - \frac{h}{z_{max}}\right)\frac{\dot{m}(V - V_o)^2}{2ud_j} \qquad (2.1)$$

The average extent Del of the delamination damage, expressed into length unit, can be evaluated along a direction orthogonal to the kerf, i.e. to the feed of the cutting operation. The specific energy, expressed by the previous equation (2.1), can be correlated to this average delamination damage extent Del. A single negative exponential relation between Del and E can be assumed as follows, where β and γ are suitable parameters:

$$Del = \gamma e^{-\beta E} \qquad (2.2).$$

This simple equation, that represent a delamination avoidance model suitable for practical applications, has been justified with a good correlation factor by a regression analysis on experimental results, as it will be discussed in the following section.

Equations (2.1) and (2.2) allow the definition of the domain of HJM process variables that do not arise delamination damage. While this energy approach seems to have a general validity, because experimental validation has been executed on different materials, the validity of equations (2.1) and (2.2), as semi-empirical models, is restricted to the domain of the experiments. The analysis of the results of the

experiments has demonstrated a good correlation among the average delamination damage extent and the main process variables, as water pressure, feed rate, standoff distance of the nozzle from the workpiece surface and the residual energy.

3. MODEL VALIDATION AND DISCUSSION

Experiments were designed to understand the mechanism of structural damage in HJM and HAJM piercing and cutting of CFRP and validate the proposed delamination avoidance model. The results of these experiments were correlated with the process variables and analysed in order to validate the proposed models.

3.1 Experimental Procedure

The experimental setup was based on an advanced HJM/HAJM cell installed at Dipartimento di Meccanica, Politecnico di Milano [4, 8].
The test parts were made by a composite that consists of cloth prepreg carbon fibre laminae, which are stacked one upon the other and embedded in a conventional epoxy matrix. The carbon fibres are united in bundles and crosswisely woven with each other within the layer. The structure of the laminae is similar to texile tissues at which the fibre boundles are interwoven rectangularly (90°). The fabrication was performed while curing laminae and matrix by using the autoclave method with standard process conditions. The main specifications of the test parts are summarized in Table 1. The specimens were fabricated in rectangular plates with a length of 200 mm and a width of 100 mm. For the various experiments three thicknesses were used, respectively 1.6, 2.2, 4.4 mm. The surfaces are different on both sides of the material: one side is rough and without recognizable pattern, whereas the other one is smooth and the cloth weave design can be detected. The rough side has been used as the jet entrance side. When HAJM was investigated, natural garnet (mesh 80) was chosen as abrasive material.

The experiments have been designed for both HJM and HAJM, cutting and piercing. To warrant a time optimized execution of the experiments, a meaningful cut and hole partition on the specimens as well as a time planning of the single experiments were adopted. Every edge of the specimen possesses 12 cuts. In Table 2 the process parameters adopted during the HJM experiments have been reported. These values have been chosen to study the behaviour in limit conditions. During the experiments water pressure, feed rate, standoff distance and primary nozzle diameter were considered as parameters.

The specimens for the piercing experiments has been prepared in a particular way. A protection layer on the surface has been necessary, in order to avoid the impact of the jet on the workpiece surface when the high pressure valve is actuated, which effects like a shock. The arrangement for the piercing experiment was different from the cutting experiment arrangement: three different nozzle diameters were used.
These experiments were executed with HJM, because HAJM did not produce delamination under standard experimental conditions.

3.2 Results and Discussion

The investigation of the delamination behaviour for HJM is meaningful, in general, for small material thicknesses, because for higher material thicknesses the cutting ability of jets without added abrasives is not sufficient. The processed material is not cut through perfectly and resulting surface is often very rough. However, the knowledge about the possibility to avoid delamination damage, HJM offers alternatives, compared to the relatively more expensive HAJM .

Beside delamination other damage arises during the machining process which influence the quality of the cut, e. g. spalling formation or kerf shape and conicity. Although all these damages have been fully analysed, here only delamination is reported. The area of delamination along the cuts, i. e., where adjacent laminae separate from each other, are recognizable due to a dent formation on the bottom layer. As a rule the visible delamination is greater at fibres bundles crosswisely orientated to the cutting direction than at bundles in parallel arrangement. Therefore, the extent of the separated layers is not constant and fluctuates along the entire kerf

length. However, these observations exclusively refer to the outer layer at the jet exit side. The test-cuts demonstrate that delamination is always connected with the appearance of spalling. The experiments have made clear that every cut crosses three bundles of the bottom laminate layer which are oriented perpendicularly to the feed rate direction. At these places the extent of the delamination is always wider than at bundles that run parallel to the cutting direction. Therefore, for each cut there are six maximum delamination zones. Since for the usage of a machined workpiece only the largest extent of the damage is crucial, these six areas of the largest lamina separation have been measured. In order to record a width of delamination, the recognizable border of lamina separation has been marked and, using a microscope with linescale, the width of delamination has been measured. Due to the observed fluctuations of six measured values for the extent of delamination, a medium width of delamination *Del* as the arithmetic average values of these six measurements has been defined. The consideration of the complete cuts shows that delamination never occurs between laminates at the jet entrance side. The cutting surface at the upper zone of the kerf is rather smoother without any protrusion of fibre or cavities. With growing penetration depth of the jet, the cutting surface becomes increasingly rougher .

The measurement of the damage of piercing takes place similar to the one of cutting. For the maximum extent of delamination the maximum radius of delamination was registered and for spalling the largest distance between hole rim and damage border. The technical execution and devices used for the value recording were generally the same as the ones used for the cutting experiments.

The produced holes were generally of very poor machining quality. Nearly every hole can be insufficient concerning the chosen criteria for delamination, spalling, and hole shape. Properly no piercing experiments exist that gives a satisfactory and usable hole. The poor quality of the pierced holes appears in the delamination formation most clearly. For all pierced holes damage in form of delamination occurs at a great extent. The boundary between separated and non-separated layers runs not circulary. Delamination takes place at a rim of the hole, whereas at the other no damage occurs.

The maximum extent of damage was very large for each hole and did not start for less than 2 mm. All the delamination layers of the piercing tests were connected with the workpiece body. This behaviour was also observed during the cutting tests. Hence no tipped up separated material layers appear, and it looks as if the width of crack is rather narrow between the loose laminae.

A dependence of delamination on the arrangement of the fibre bundles was not observed. Therefore, it is not necessary for the direction of maximum delamination radius to be identical with the orientation of the fibre bundles, which surround a hole.

The delamination problem is exclusively confined to the specimen surface at the jet exit side. Due to the small diameter, it is not possible to cut open the hole. Therefore, an investigation of the occurrence of delamination between the laminae within the material cannot be executed. Despite the great dispersion of the measured values for the maximum delamination radius, two fundamental tendencies can be observed: on one side, for all three nozzle diameters an increase of the delamination extent with growing working pressure is to be observed. On the other side, the maximum radius of delamination arises with a larger nozzle diameter.

An influence of the standoff distance on the delamination behaviour was not observed in the beginning for the executed piercing tests. The great dispersion of the maximum delamination radius does not give the possibility to observe a principle tendency.

Also, spalling and hole shape were analysed in order to validate the proposed model [5], demonstrating a dispersion of the results. The analysis demonstrated that the experimental results concerning the influence of the nozzle diameter on the delamination correspond to the model in principle. Therefore, the critical pressure decreases with increasing nozzle diameter so that the delamination starts at lower pressures. In this way, the prerequisite is created that the laminate separation increases with greater nozzle diameter and constant pressures which are above the critical value. This behaviour was observed in the

experimental results, but a discrepancy between the experimental results and the theory was observed, probably due to the fact that jet diameter was assumed to be equal to nozzle diameter. In fact considering the measured hole diameter at the jet entrance side of the specimen instead of the nozzle diameter, the predicted values approach the experimental results in a better way.

Systematical experiments were executed also for HAJM, and demonstrated to remove the two limitations of HJM, i. e., the maximum workpiece thickness that can be cut and the need of a careful selection of cutting conditions to avoid delamination.

Suitable parameters were used for HAJM tests and the analysis was carried out in the same manner as for HJM. The results showed that all specimens were completely cut through for all parameter combinations. But in contrast to the former HJM experiments, there is no delamination damage for any of the cuts. A limited spalling was observed. The cuts were very clean and showed an equally smooth surface and the width of the kerf presented a small variation along the whole cut length. No delamination was recognizable within the domain covered by the experiments [10].

From the energetic point of view the HAJM results are an accordance with the HJM results, when at the higher energy level of the hydro jet, delamination does not take place. However due to the intrinsicly higer complexity and cost of HAJM, when low thickness CFRP components have to be cut, HJM is generally adopted if suitable cutting conditions can be used to avoid delamination damage.

The results of the experiments, executed by means of HJM, were analysed in order to validate the proposed energetic model (eqs. (2.1) and (2.2)) and to correlate the average delamination extent damage with the main process variables, as water pressure, feed rate, standoff distance of the nozzle from the workpiece surface, and with the residual energy. Four main variables were adopted in the HJM cutting experiments on specimens at three different thickness (see Table 2). An analysis of variance was executed using the Yates Method [12]. Factorial experiments were designed with five factors at two levels

(A=water pressure, B=feed rate, C=specimen thickness, D=standoff distance, E=nozzle diameter). Table 3 shows the HJM delamination experimental data in factorial form. The experimental variance was estimated, assuming that third order interactions among factors are negligible or unimportant. A suitable significance level was set equal to 2.5% . Table 4 shows the Yates Method on HJM delamination experimental data. A pressure increase from 270 MPa (A0) to 350 MPa (A1) causes a decrease of delamination in all the experimental conditions (average value= 1.32 mm). A feed rate increase from 500 mm/min (B0) to 1000 mm/min (B1) always causes a delamination increase (average value= 0.52 mm). A specimen thickness increase from 1.6 mm (C0) to 2.2 mm (C1) causes the increase of the delamination (average value= 0.69 mm).

From this analysis all the effects were significant for the single factors, except E, and the CD, AE, CE, DE double interactions. An increase of pressure reduces delamination, while an increase of feed rate and thickness increases also delamination. Double interactions suggest that the effect of C is influenced and reduced by the effect of D. It is interesting to observe that, even if E alone is not significant, it has an influence on A, C, D. The AE and ED interactions mean that the influence of A and D factors is limited by a superior level of E, that enhances C factor. With the remark that these results are restricted to the domain of these experiments, it can be noticed that pressure and feed rate have a great influence on the average delamination extent. This conclusion can be seen as a justification of the dependence of delamination on the absorbed energy, that is mainly increases with the velocity of the jet, i. e. with its kinetic energy, and with the supply pressure, while this energy decreases when feed rate increases.

A regression analysis of the experimental results for specimen thickness equal to 1.6 mm demonstrates, with a good correlation, that delamination increases when pressure decreases and feed rate increases: e.g. Fig. 1 shows the dependence on feed rate of the average extent *Del* of the delamination damage, expressed into length unit, along a direction orthogonal to the kerf, at constant supply pressure. Also a multiple

regression analysis on the two variables pressure and feed rate has confirmed this behaviour. The analysis of the results on specimens of larger thickness demonstrates that delamination increases for the same process conditions.

Finally a systematic analysis was executed of the experimental results in order to validate the proposed energetic model. By means of the Levenberg-Marquardt Method [18] the parameters of the proposed model were estimated. Therefore the residual energy E at the bottom ply was evaluated (eq.(2.1)) and correlated with the average extent Del of the delamination damage, expressed into length unit, along a direction orthogonal to the kerf, i.e. to the feed of the cutting operation. Assuming for the kerf depth of the bottom ply the specimen thickness reduced by the ply thickness, the parameters of eq. (2.2) were estimated with good correlation.

The regression analysis function curve of the Del average delamination versus the E residual energy is shown in Fig. 2. From the observation of this behaviour it can be inferred that, at a low energy level, bending stresses occur related to flexural deformation causing delamination, and, in order to avoid delamination, cutting conditions have to assure a high residual energy level on the bottom ply, in order to allow localized net fiber breakage and matrix cracking due to high transverse shear stresses without delamination [10,20].

4. CONCLUSIONS

The residual energy of the impinging jet on the bottom plies presents a fundamental role on the delamination mechanism of multilayered Carbon Fibre Reinforced Plastic (CFRP) composite during a cutting process by means of Hydro Jet Machining (HJM). A semi-empirical delamination avoidance model has been defined that identifies suitable machining conditions that assure a certain minimum energy level during operation. While Hydro Abrasive Jet Machining (HAJM) allows generally results without structural damage to CFRP laminated workpieces with both low and high thickness, the less expensive and simpler Hydro Jet Machining (HJM) can be applied advantageously to low thickness, provided that these suitable machining conditions are selected.

The energetic model, that has been proposed and validated, can be applied in order to predict and avoid delamination when HJM is adopted for CFRP cutting in order to obtain composite parts of high quality. This model not only provides a better understanding of this phenomenon but also allows a concurrent engineering of CFRP laminated composite structural components, and it is suitable to be implemented in a CAD/CAE/CAM tool for multilayer CFRP composite components.

REFERENCES

1. P. W. R. Beaumont, "The failure fibre composites: on overview", The Journal of strain analysis for engineering design, Vol.24, no.4, pp.189-205, October, 1989.
2. Blickwedel, H., Guo, N.S., Haferkampf, H., Louis, H., "Prediction of Abrasive Jet Cutting Efficiency and Quality", 10th Int. Symposium on Jet Cutting Technology, Amsterdam, pp. 688-707, 1990.
3. E. Capello, R. Groppetti, "On an energetic semi-empirical model of hydro-abrasive jet material removal mechanism for control and optimization", Proc. of the 11th Int. Conf. on Jet Cutting Technology, St Andrews, pp.101-120, 1992.

4. C. C., Chamis, "Design concepts / parameters assessment and sensitivity analyses of select composite structural components", Int. J. of Materials and Product Technology, Vol. 1, no. 2, pp. 211-229, 1986.

5. H. Ho. Cheng, "A Failure Analysis of Water Jet Drilling in Composite Laminates", Int. J. Mach. Tools. Manufact., vol. 30, no. 3, pp.423- 429, 1991.

6. J. L. Davet, P. H. Destuynder, T. H. Nevers, "Some Theoretical Aspects on the Modelling of Delamination for Multilayered Plates", in Local Effects in the Analysis of Structures, Elsevier Science Publ., Amsterdam, pp. 181- 197, 1985.

7. K. Faber, H. Oweinah, "Influence of process parameters on blasting performance with abrasive jet", Proc. 10th Int. Symposium of Jet Cutting Technology, Amsterdam, pp. 571- 593, 1990.

8. R. Groppetti, G. Comi, "Contribution to Computer Control and Optimization of Hydro Abrasive Jet Machining Process", Proc. of the International Conference on Computers in Industry, ASME, Santa Clara, pp. 530- 549, 1991.

9. Groppetti, R., Arpino, F., "Assyst : A consultation system for the integration of product and assembly system design", in Design For Manufacture Strategies Principles and Techniques, Addison Wesley Publ. Co., Wokingham, pp. 246-257, 1991.

10. R. Groppetti, A. Armanni, A. Cattaneo, G. Franceschini,"Contribution to the Study of the Delamination of Carbon Fibre Reinforced Plastic (CFRP) Laminated Composites during Piercing and Cutting by Hydro Jet Machining (HJM) and Hydro Abrasive Jet Machining (HAJM)", Computer Aided Design in Composite Material Technology III, Computational Mechanics Publications Southampton Boston and Elsevier Applied Science London, pp. 189-209, 1992.

11. M. Hashish, "Machining of Advanced Composites with Abrasive- Waterjets", ASME, Manufacturing Review, vol. 2, no. 2, pp. 142-150, 1989.

12. C. R. Hicks, "Fundamental Concepts in the Design of Experiments", Holt, Rinehart and Winston, New York, pp. 102-106, 1964.

13. T. Isobe, H. Yoshida, K. Nishi, "Distribution of Abrasive Water Jet and Acceleration Mechanism", Proc. of the 9th International Symposium on Jet Cutting Technology, Sendai, pp. 341-348, 1988.

14. W. Koenig, C. H. Wulf, "The Influence of the Cutting Parameters on Jet Forces and the Geometry of the Kerf", Proc. of the 7th International Symposium of Jet Cutting Technology, BHRA, pp. 355- 368, 1984.

15. W. Koenig, C. H. Wulf, P. Grass, H. Willerscheid, "Machining of Fibre Reinforced Plastics", CIRP Annals, Vol.34/2,pp.537-548,1985.

16. S. Matsui, H. Matsumura, Y. Ikemoto, K. Tsukita, H. Shimizu, "High Precision Cutting Method for Metallic Materials by Abrasive Waterjet", Proc. of the 10th Technology, Amsterdam, pp. 343-350, 1990.

17. P. Pedersen, "On sensitivity Analysis and optional design for Laminates", in Mechanical Behaviour of Composites and Laminates, Elsevier Applied Science, London, pp. 274-283, 1987.

18. W.H. Press, B.P. Flannary, S.A. Teukosky, W.T. Vetterling, Numerical Recipes in Pascal, The Art of Science Computing, Cambridge University Press, Cambridge, pp. 574-580, 1988.

19. H. Saghizade, C.K.H. Dharan, "Delamination Fracture Toughness of Graphite and Aramid Epoxy Composites", Transations of ASME, Vol. 108, pp. 290-295, October 1986.

20. C.T. Sun, T. Wang, "Impact Wave Response and Failure in Composites Laminates", in Mechanical Behaviour of Composites and Laminates, Elsevier Applied Science, London, pp. 19-31, 1987.

21. R. Talreja, "Damage development in composites: mechanism and modelling", The Journal of strain analysis for engineering design, Vol. 24, No. 4, pp. 215-222, 1989.

22. D. J. Wilkins, V.M. Karban, "Cuncurrent engineering for composites", Int. J. of

Materials and Product Technology, Vol. 6, no. 3, pp. 257-268, 1991.

23. J. G. Williams, "The fracture mechanics of delamination tests", The Journal of strain analysis for engineering design, Vol. 24, No. 4, pp. 207-214, 1989.

NOMENCLATURE

$\dot{m}$ Water jet mass flow rate
P Water pressure
V Impinging jet velocity
V_o Threshold velocity
d_j Primary nozzle diameter
z_{max} Maximum kerf depth for quasi-static feed rate
h Workpiece thickness
E Residual energy on the bottom ply
u Feed rate
Del Average delamination damage
β, γ Delamination avoidance model parameters

Prepreg Weight [g/m^2]	345
Elastic Modulus [GPa]	63
Ultimate Strength [MPa]	643
Elongation [%]	1.05
Fibre Content [%V]	52.4
Cured Ply Thickness [mm]	0.23
Specimen Thicknesses [mm]	1.6 , 2.2 , 4.4

Table 1 - Test part CFRP specifications.

Water Pressure [MPa]	150 , 190 , 230 , 270 , 310 , 350
Feed Rate [mm/min]	500 , 1000 , 2000 , 4000 , 6000 , 8000
Standoff Distance [mm]	1 , 2 , 4 , 8
Nozzle Diameter [mm]	0.08 , 0.12 , 0.16 , 0.20
Specimen Thickness [mm]	1.6 , 2.2 , 4.4

Table 2 - HJM experimental conditions.

		E0				E1			
		C0		C1		C0		C1	
		A0	A1	A0	A1	A0	A1	A0	A1
D0	B0	1.32	0.1	2.76	0.5	0.78	0	2.72	1.82
	B1	2	0.53	3.13	1.82	1.38	0.11	3.68	2.85
D1	B0	1.8	0	1.88	0.2	0.7	0	1.25	0
	B1	2.06	0.58	2.15	0.52	1.18	0	1.76	0.35

Table 3 - HJM delamination damage experimental data in factorial form [mm]
(A=water pressure, B=feed rate, C=specimen thickness,
D=standoff distance, E=nozzle diameter).

Comb.							Effetti	Sigma	Fsper	5%	2.5%
(1)	1,32	1,42	3,95	12,16	21,35	39,93	2,495625	49,8252	1158,304	1	1
a	0,1	2,53	8,21	9,19	18,58	-21,17	-1,323125	14,0053	325,5858	1	1
b	2	3,26	4,44	13,34	-12,85	8,27	0,516875	2,13728	49,68609	1	1
ab	0,53	4,95	4,75	5,24	-8,32	0,01	0,000625	3,1E-06	7,26E-05	0	0
c	2,76	1,8	2,27	-6,26	4,23	14,85	0,928125	6,89133	160,2052	1	1
ac	0,5	2,64	11,07	-6,59	4,04	-1,37	-0,085625	0,05865	1,363531	0	0
bc	3,13	2,08	1,88	-3,78	1,07	1,99	0,124375	0,12375	2,876934	0	0
abc	1,82	2,67	3,36	-4,54	-1,06	1,81	0,113125	0,10238	2,380022	0	0
d	1,8	0,78	-2,69	2,8	4,57	-11,07	-0,691875	3,82953	89,02644	1	1
ad	0	1,49	-3,57	1,43	10,28	-1,09	-0,068125	0,03713	0,863131	0	0
bd	2,06	4,54	-3,28	2,7	-0,91	-2,73	-0,170625	0,2329	5,414384	0	0
abd	0,58	6,53	-3,31	1,34	-0,46	-0,55	-0,034375	0,00945	0,21976	0	0
cd	1,88	0,7	-2,05	0,7	0,33	-11,27	-0,704375	3,96915	92,27236	1	1
acd	0,2	1,18	-1,73	0,37	1,66	-0,25	-0,015625	0,00195	0,045405	0	0
bcd	2,15	1,25	-1,88	-0,42	0,93	-1,73	-0,108125	0,09353	2,174283	0	0
acbd	0,52	2,11	-2,66	-0,64	0,88	-1,71	-0,106875	0,09138	2,124301	0	0
e	0,78	-1,22	1,11	4,26	-2,97	-2,77	-0,173125	0,23978	5,57421	0	0
ae	0	-1,47	1,69	0,31	-8,1	4,53	0,283125	0,64128	14,90803	1	1
be	1,38	-2,26	0,84	8,8	-0,33	-0,19	-0,011875	0,00113	0,026226	0	0
abe	0,11	-1,31	0,59	1,48	-0,76	-2,13	-0,133125	0,14178	3,295968	0	0
ce	2,72	-1,8	0,71	-0,88	-1,37	5,71	0,356875	1,01888	23,68623	1	1
ace	1,82	-1,48	1,99	-0,03	-1,36	0,45	0,028125	0,00633	0,147112	0	0
bce	3,68	-1,68	0,48	0,32	-0,33	1,33	0,083125	0,05528	1,285071	0	0
abce	2,85	-1,63	0,86	-0,78	-0,22	-0,05	-0,003125	7,8E-05	0,001816	0	0
de	0,7	-0,78	-0,25	0,58	-3,95	-5,13	-0,320625	0,8224	19,11871	1	1
ade	0	-1,27	0,95	-0,25	-7,32	-0,43	-0,026875	0,00578	0,134326	0	0
bde	1,18	-0,9	0,32	1,28	0,85	0,01	0,000625	3,1E-06	7,26E-05	0	0
abde	0	-0,83	0,05	0,38	-1,1	0,11	0,006875	0,00038	0,00879	0	0
cde	1,25	-0,7	-0,49	1,2	-0,83	-3,37	-0,210625	0,3549	8,250563	1	0
acde	0	-1,18	0,07	-0,27	-0,9	-1,95	-0,121875	0,11883	2,762441	0	0
bcde	1,76	-1,25	-0,48	0,56	-1,47	-0,07	-0,004375	0,00015	0,00356	0	0
acbde	0,35	-1,41	-0,16	0,32	-0,24	1,23	0,076875	0,04728	1,099092	0	0

Table 4 - Yates Method on HJM delamination damage data.

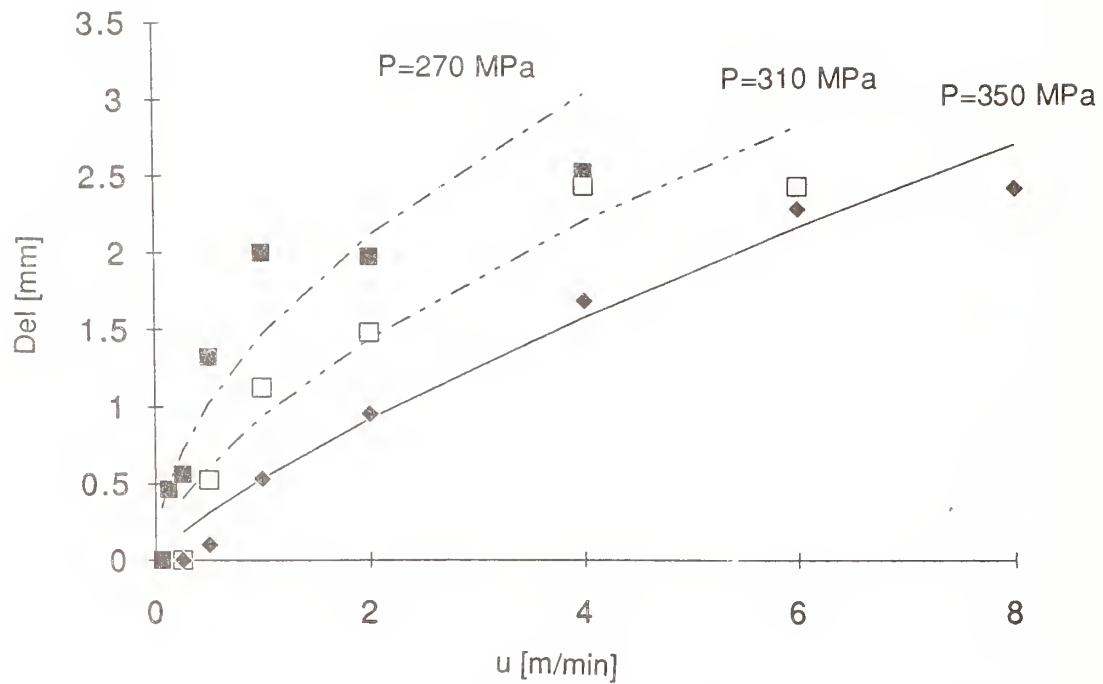Fig. 1 - Dependence of delamination damage on feed rate and water pressure (HJM, primary nozzle diameter=0.15 mm, CFRP thickness=1.6 mm).
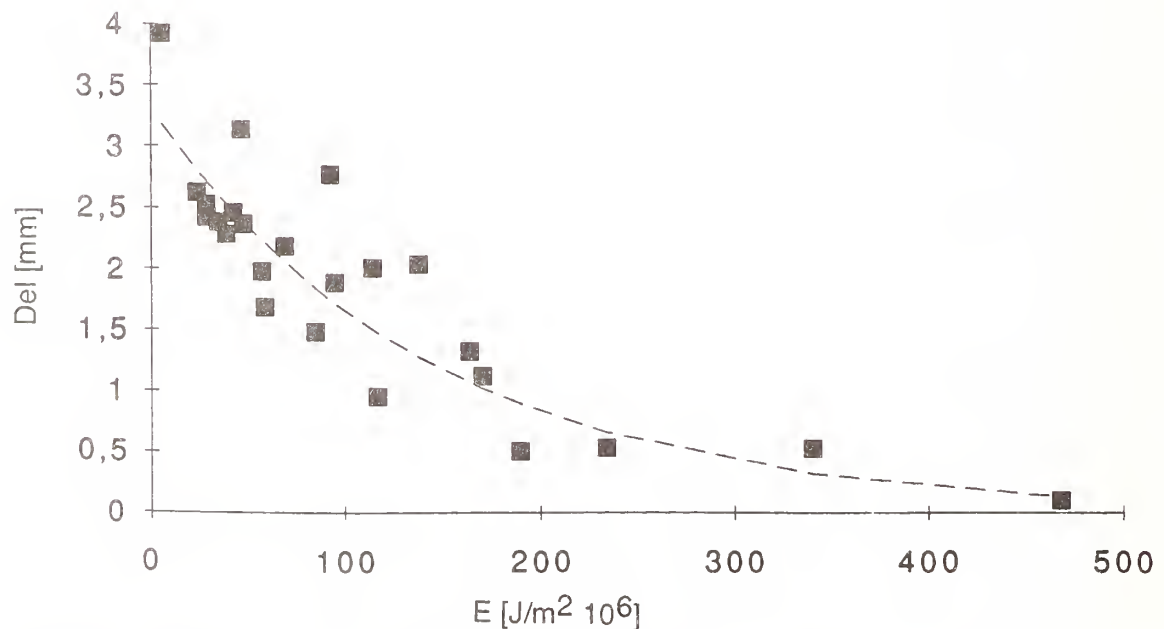

Fig. 2 - Dependence of delamination damage on jet residual energy at kerf bottom ply (HJM, primary nozzle diameter=.15 mm, CFRP thicknesses=1.6,2.2 mm, standoff distance=2 mm, water pressure=270/310/350 MPa,feed rate=500, 1000,2000,3000,4000,6000,8000 mm/min).

EFFICIENT MECHANOCHEMICAL POLISHING FOR SILICON NITRIDE CERAMICS

T. UEMATSU
Toyama Prefectural University, Toyama, Japan

K. SUZUKI and M. H. WU
Nippon Institute of Technology, Saitama, Japan

K. SUZUKI
Toyama Prefectural University, Toyoma, Japan

O. IMANAKA
Gunma Polytechnic College, Gunma, Japan

Instead of conventional loose abrasive mechanochemical polishing, a fixed abrasive tool or a polishing disc for mechanochemical polishing was used here for obtaining a high polishing efficiency and a better working environment.

In experiments, Si_3N_4 disc workpieces were polished with a polishing disc made of Cr_2O_3 on a vertical spindle surface grinding machine. By choosing an appropriate polishing pressure and rather high rotating speeds of the tool and the workpiece, initial surface roughness of Rmax=0.17μm(maximum peak to valley height) was improved to Rmax=40nm only within 30 seconds. Even for initial surface of Rmax=0.7μm, surface finish of better than Rmax=50nm was obtained in about 30 seconds.

1. INTRODUCTION

Adoption of ceramic parts into actual products has been restricted because of poor grindability of these materials. But the application of ceramic parts has already started because of the fact that mechanical properties, especially the toughness, reliability, and homogeneity of ceramics have improved, and new grinding methods(1) have been developed.

Requirements of obtaining better surface quality of ceramic materials for mechanical use are increasing. But in many cases conventional grinding methods can not cope with these requirements. In order to improve surface finish, lapping or polishing with very fine diamond abrasives is usually applied. But it is not possible to obtain satisfactory surfaces free from scratches and/or damaged layer.

Mechanochemical polishing method(MCP in short, Fig.1)(2) utilizes mechanochemical reaction between soft abrasive grains and harder work material for providing smooth surface finish. Accordingly, the method extends the benefit of solving various problems
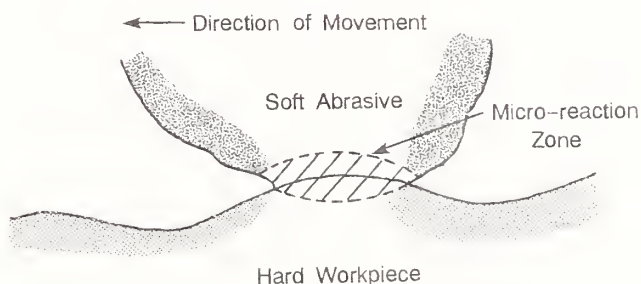
Fig.1 Model of mechanochemical reaction(2).

such as damaged work surface layer and appearance of scratches found in lapping or polishing with hard diamond abrasives.

This method has been used as an important one in the field of precision finishing of electro-magnetic and optical materials. But there still remain problems to be solved such as poor productivity, insufficient working environment, and restriction in geometry of engineering ceramic parts to be finished, especially with complex shapes and of rather

409

large size. This paper describes a new mechanochemical polishing method proposed by the authors to solve these existing problems.

2. PROBLEMS IN EXISTING MCP AND THEIR SOLUTIONS

2.1 MCP with a Fixed Abrasive Tool

Problems in the existing MCP method are rather poor working environment, low finishing efficiency and restriction in geometry to be applied. These problems are caused mainly by using loose abrasives in MCP. Some of these problems can be solved by the development of a fixed abrasive tool for MCP by T.Suga(3). The polishing tool consists of chromic oxide abrasives with a resinoid bond.

In order to apply the MCP method to ceramic components of rather large size, it is essential to develop a highly efficient MCP method by investigating polishing conditions, polishing tools and polishing machines(4).

2.2 Conditions for High Efficiency MCP

Figure 2 shows a schematic illustration for high efficiency MCP of a silicon nitride ceramic disc with a resinoid Cr_2O_3 polishing disc on a specially designed machine. It is essential to find suitable conditions for promoting mechanochemical reaction between the tool and the workpiece, leading to high removal rates. For example increasing the working pressure and the relative peripheral speed of the tool and the workpiece may increase the temperature at micro-reaction zones and increase the polishing distance, resulting in a high removal efficiency. But an upper limit of working pressure is restricted by the strength of the polishing disc. If the rotational speed is too high, accumulation of heat in the workpiece and the polishing disc may damage both the tool and the workpiece.

3. EXPERIMENTAL APPARATUS AND CONDITIONS

A vertical spindle surface finishing machine was used instead of an existing lapping machine to rotate a polishing disc and a disc type workpiece with a rather high speed(Fig.3).
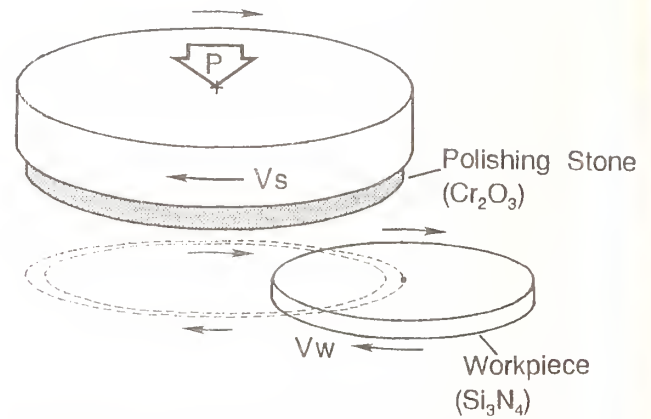
Fig.2 Schematic MCP method for disc type workpiece.
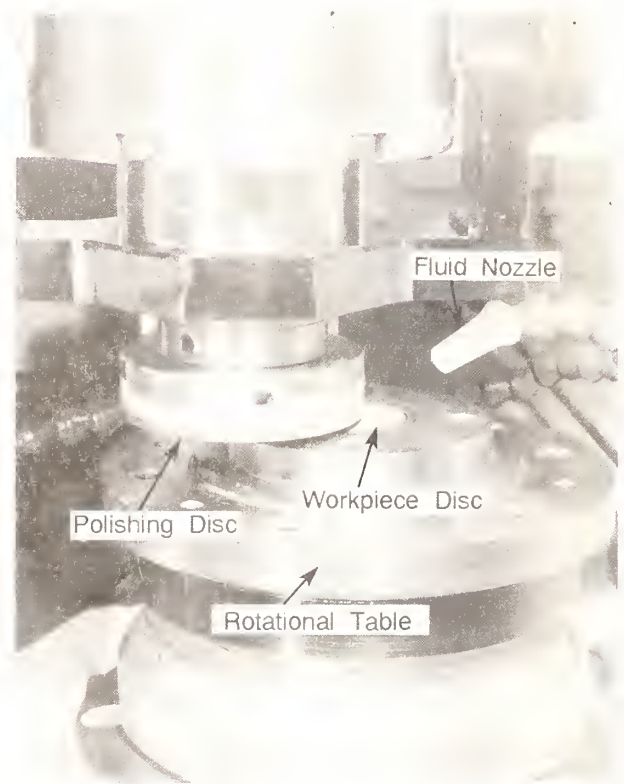
Fig.3 Set-up for high efficiency MCP.

Table 1 Experimental devices and conditions.

Machine	:Vertical surface finishing machine (Air controlled constant pressure polishing machine)
Polishing tool	:Cr_2O_3 polishing disc(D=80mm,b=5mm)
Workpiece	:(1)Si_3N_4 disc(D≒34mm,t=1.5mm,Rmax=0.17-0.8μm) (2)SiC disc (D=34mm,t=2mm,Rmax≒0.6μm) :Pre-grinding: Cup wheel(SD2500), Plunge grinding
Measurement	:Surface roughness profilometer(stylus radius=5μm)
Conditions	:Tool peripheral speed : Vs=0.42-8.3 m/s :Work peripheral speed: Vw=0.83-5.0 m/s :Normal pressure : P =0.70-2.5 MPa :Fluid : Chemical soluble type

A polishing disc with 80 mm diameter was rotated at a peripheral speed of Vs=0.42 – 8.3 m/s. A sintered silicon nitride workpiece with a diameter of 34 mm and a thickness of 2 mm was rotated by a sub–spindle installed in the machine bed at a peripheral speed of Vw=0.83 – 5.0 m/s. The maximum values of these speeds are several times higher compared to existing lapping machines. The normal pressure was varied from P=0.7 – 2.5 MPa, this being rather high compared to existing methods on conventional lapping machines. Chemical solution type coolant was used to cool the polishing disc and the workpiece. Table 1 lists the experimental devices and conditions.

4. EXPERIMENTAL RESULTS
4.1 MCP Conditions for Silicon Nitride Disc Workpiece

Effects of normal pressure and rotational speeds of the polishing disc and the workpiece on the improvement of surface finish were investigated.

(1)Effect of Normal Pressure

Effect of normal pressure was investigated under constant tool peripheral speed Vs and work peripheral speed Vw at a polishing time of t=30s (Fig.4). When low normal pressure, such as P=0.7 MPa was adopted, surface finish was not improved in a short polishing time of t=30s. But rather high normal pressure, larger than P=1.3 MPa was used, surface finish improved from the initial roughness Rmax=170nm to Rmax=55nm.

(2)Effect of Tool and Work Peripheral Speeds

Figure 5 shows a relation between tool peripheral speed Vs and the surface roughness attained at t=30s. Figure 6 shows a relation between work peripheral speed Vw and the surface roughness attain at t=30s. It is clear from these diagrams that both Vs and Vw do not influence the surface finish so much. But the smoothest surface, having Rmax=25nm, was obtained when a high work speed of Vw=5.0 m/s and a low tool speed of Vs=2.1m/s were adopted.

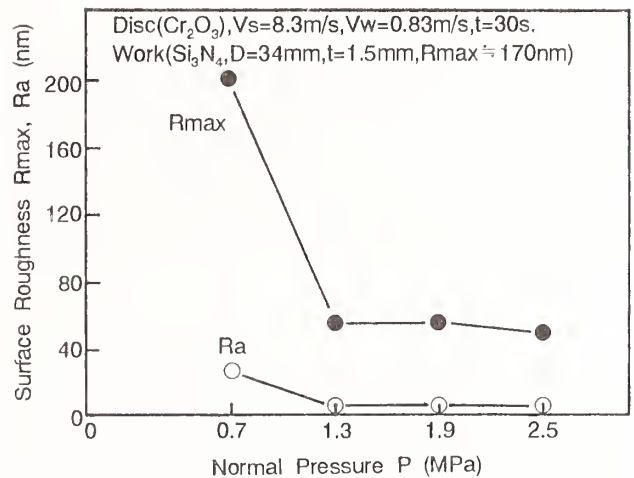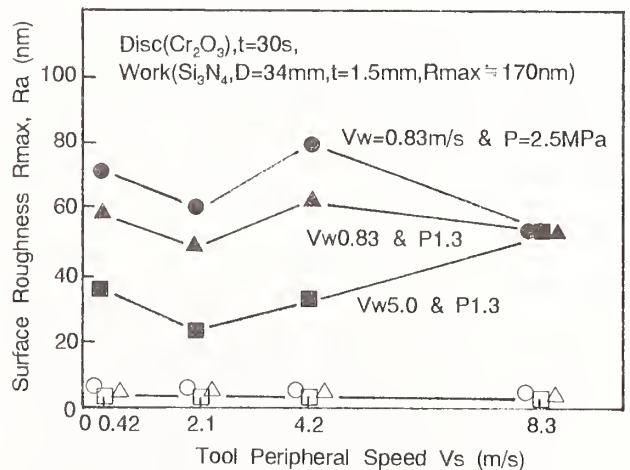Fig.4 Effect of normal pressure on surface finish.

Fig.5 Effect of tool peripheral speed.
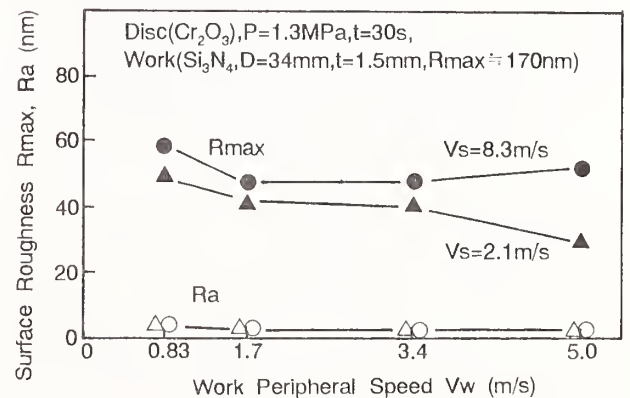
Fig.6 Effect of work peripheral speed.

411

(3)Effect of Polishing Time

The change of surface roughness as a function of polishing time was investigated for three combinations of tool and work peripheral speeds(Fig.7). Surface finish was improved rapidly during initial 20 seconds, and the initial surface of Rmax=170nm was improved to Rmax=35 – 60 nm at t=60s.

(4)Effect of Pregrinding Conditions

Two workpieces having almost the same surface roughness value(Rmax=0.7 – 0.8μm), one of which was pre-ground with a straight wheel on a surface grinding machine and the other was pre-ground by plunge grinding with a cup wheel on a vertical spindle grinding machine, were polished. In both cases surface roughness was improved rapidly at the initial stage of MCP as shown in Figure 8. The roughness of the surface pre-ground with a straight wheel improved from Rmax=0.8μm to Rmax=60nm within t=90s, in spite of a rough initial surface; but it required a long time to
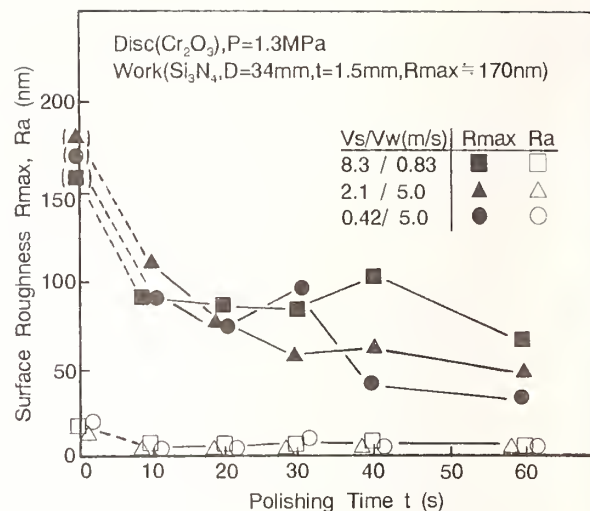
Fig.7 Effect of polishing time.

Fig.8 Effect of pre-grinding conditions.

[Initial,Rmax=0.17μm]   [MCPed,Rmax=40nm]
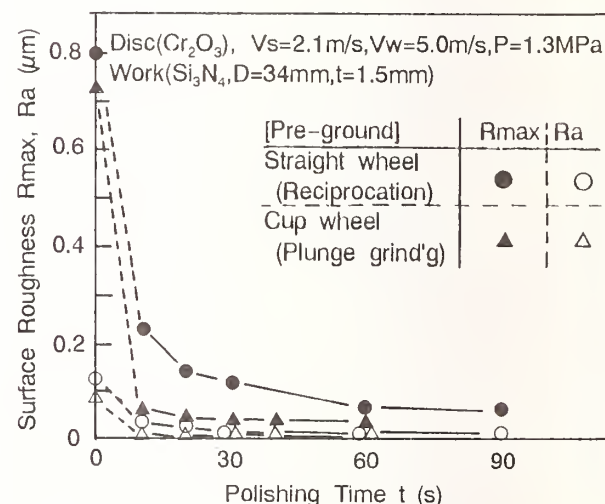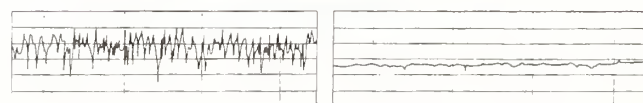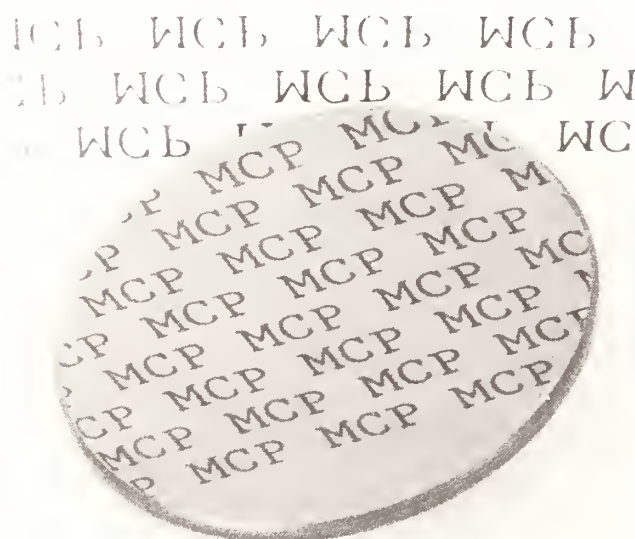
Fig.10 Mirror finished sample MCPed under optimum conditions.

Disc(Cr_2O_3), Vs=2.1m/s,Vw=5.0m/s,P=1.3MPa,t=30s,
Work(Si_3N_4,D=34mm,t=1.5mm,Initial Rmax=0.17μm)

(a)Pre-ground by reciprocation grinding with a straight wheel

(b)Pre-ground by plunge grinding with a cup wheel

Fig.9 Change of surface profiles for different pre-ground workpieces.

412

remove scratches completely. On the other hand the roughness of the surface pre-ground by plunge grinding with a cup wheel became less than Rmax=50nm within only t=30s. Figure 9 shows the change of the surface profile in both cases. It is found from the Figures 8 and 9 that the rate of improvement of surface roughness depends not on the initial surface roughness but on the initial profile of the pre-ground surface.

4.2 Effect of Optimum Conditions

By adopting appropriate polishing conditions such as Vs=2.1 m/s, Vw=5.0 m/s, and P=1.3 MPa, surface finish was improved within a very short time: for example, from Rmax=0.17μm to Rmax=40nm, only in 30 seconds as already shown in Figure 7. Figure 10 shows a mirror finished sample and surface profiles of the initial and the finished surfaces after 30 seconds of polishing. This result indicates that a very high finishing efficiency can be realized by MCP, which has been thought to be poor in polishing efficiency, if optimum finishing conditions and an appropriate method are adopted.

4.3 Application of MCP Method to Silicon Carbide Workpiece

The above-mentioned MCP method was also applied to sintered silicon carbide workpieces under almost the same conditions as silicon nitride discs. Figure 11 shows that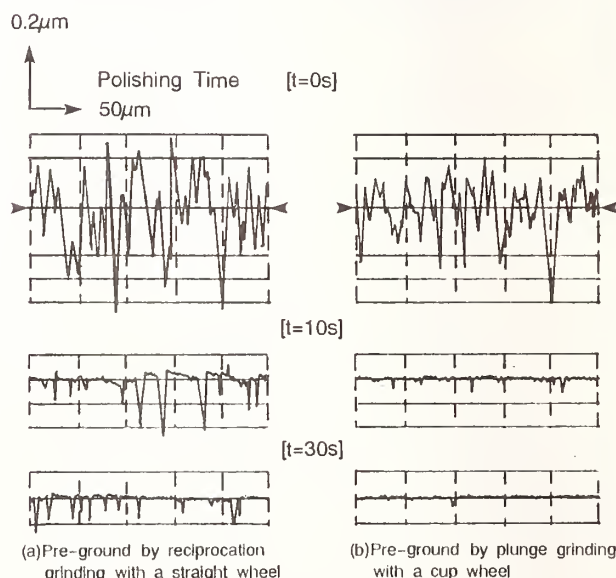 surface finish was improved to Rmax=0.1μm from the initial surface roughness of Rmax=0.6μm. It was found in the MCP of silicon carbide discs that it takes longer, attainable surface roughness is rougher, and scratch marks in pre-grinding are left on the finished surface. This indicates that finishing of silicon carbide material by MCP is more difficult than silicon nitride workpieces, and more investigations concerning polishing conditions in MCP, polishing disc materials and so on should be conducted.

5. CONCLUSIONS

In order to solve problems in existing mechanochemical polishing, a highly efficient
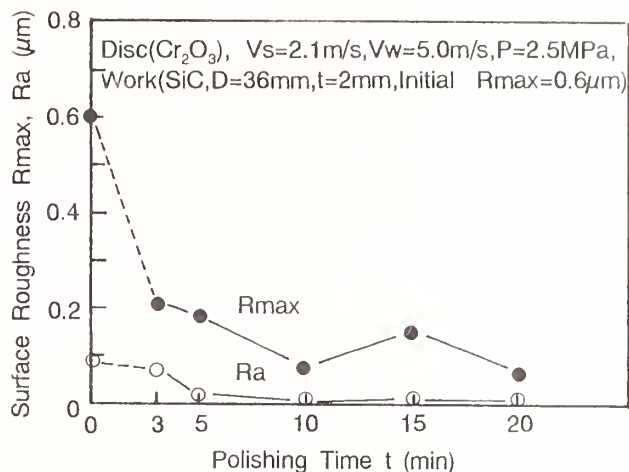
Fig.11 MCP for SiC workpiece.

MCP method has been developed. By applying this method to flat portion of a silicon nitride ceramic product, satisfactory results were obtained. This method has potential for use in finishing ceramic components.

ACKNOWLEDGEMENTS

REFERENCES

(1)T. Nakagawa, K. Suzuki and T. Uematsu, "Highly Efficient Grinding of Ceramics and Hard Metals on Grinding Center,"Annals of the CIRP 35/1, pp.205-210,1986.
(2)N. Yasunaga, A. Ohara and O. Imanaka, J. of JSPE, Vol.44, p.77, 1978(in Japanese).
(3)T. Suga, S. Suzuki and K. Miyazawa, "Mechanochemical Polishing of Sintered Silicon Nitride," J. of JSPE, Vol.55, p.2247, 1989(in Japanese)
(4)K. Suzuki, T. Uematsu, et al., "Development of a New Mechanochemical Polishing Method with a Polishing Film Method for Ceramic Round Bars," Annals of the CIRP 42/1, pp.339-342, 1992.

MAGNETIC ABRASIVE FINISHING OF WC-CO CURVED SURFACES

M. ANZAI and E. KAWASHIMA
University of Tokyo, Tokyo, Japan

H. OTAKI
Nihon University, Narashino, Japan

T. NAKAGAWA
University of Tokyo, Tokyo, Japan

Summary

Most of mold manufacturing procedures have been automated by the introduction of NC machine tools and CAD/CAM systems. But the surface finishing of the mold must be still done manually by well-skilled workers. Though many attempts were made to eliminate this hand work, automatic finishing of mold surface with 3-dimensional curvature has not been achieved yet. A new magnetic abrasive finishing process is proposed as a potential method for the automation of surface finishing. In order to improve the grindability of magnetic abrasive process for WC-Co alloys, a new magnetic abrasive and finishing procedure was developed. This magnetic abrasive and finishing procedure was experimentally confirmed to have a sufficient grindability to finish EDMed surface of WC-Co alloys into mirror surfaces. This magnetic abrasive finishing may contribute to the automatic finishing of WC-Co alloy.

1. Introduction

Generally, EDMed mold surfaces are finished by skilled manual labor. In this study, magnetic abrasive finishing process was used to polish the surface of WC-Co alloy. New types of magnetic abrasives were developed by sintering, and were confirmed to have remarkably high grindability in comparison with existing abrasives.[1] This study aims at investigating the grindability of these magnetic abrasives for a WC-Co alloy and confirming the possibility of automatic surface finishing using a NC machine tool.

2. Experimental

2.1 Magnetic Abrasive Finishing Machine

The outline of the magnetic abrasive finishing machine is shown in Fig.1.[2] This set up includes an NC milling machine, a steel rod(0.45%C), a coil and a D.C. electric source. The diameter of copper wire covered with phenol resin is 1 mm and the number of turns in the coil is 3500. The gap between the rod and the surface of workpiece can be easily changed. The abrasives are attracted to the magnetized rod. The workpiece is finished by the force of attraction between the rod and the workpiece. As is evident from Fig.1, the finishing set up is so simple that this might be employed on any kind of machine tools. Magnetic abrasive finishing experiments were performed with this machine using newly developed magnetic abrasives. The stock removal was checked by measuring the difference in weights of unfinished and finished workpieces. The surface

roughness and the line profiles were checked by a surface profilometer,while the surface properties were observed with scanning electron microscope(SEM).

2.2 Magnetic abrasives
2.2.1 Finishing Method using Diamond Paste and Magnetized Iron Powder

The method for the preparation of magnetized iron powder + diamond paste

Fig.2 Principle of new finishing method using diamond paste and magnetized iron powder brush

which uses a brush and slurry abrasives is shown in Fig. 2.[3] The iron powder particles are attracted to the magnetic rod and also the workpiece which is magnetized by this rod. Slurry abrasives are held by the pores between iron powder and other particles. The slurry abrasives are attracted towards the workpiece due the magnetic force which results in polishing of the workpiece. As the diamond paste has high grindability in comparison with conventional slurry abrasives,this finishing method is suitable for polishing of hard materials like WC-Co alloy. But the abrasive life is short and this is not suitable for polishing of 3-dimensional shapes. Therefore iron bonded diamond magnetic abrasives were developed by sintering process.

2.2.2 Iron Bonded Diamond Magnetic Abrasives Prepared by Sintering

Figure 3 shows the preparation process for iron bonded diamond magnetic abrasive by sintering method. [4] At first,iron and graphite powders are mixed in a stainless steel pot and balls for 10 min.Then these powders and diamond particles and 1 Wt% of zinc

Fig.1 Outline of magnetic abrasive finishing machine and it's finishing priciple

416

stearate are mixed in the stainless steel pot and balls for 10 min. These raw materials for magnetic abrasives are formed into the deep cup with a wall thickness of 2.5 mm under a compacting pressure of 490 MPa. Then the green compact is sintered at 1423K for 30 min in NH₃ cracking gases. Finally, sintered product is pulverized by hammer and whose powders are passed through sieves.

3. Results and discussions

3.1 Fundamental Finishing Characteristics of Diamond paste + Magnetized Iron Powder Brush

The effect of increasing revolution of magnetic tool on the stock removal using diamond paste and iron powder is shown in Fig.4. Workpiece used for polishing is WC-Co alloy (8-16%Co) which could not be finished by conventional slurry abrasive. The stock removal increases lineally with the rotational speed of the tool. This value is higher than the value of stock removal using conventional slurry abrasive on carbon steel workpiece under similar finishing conditions.[5]

The effect of finishing gap and magnetic flux density on the stock removal using diamond paste and magnetized iron powder is shown in Fig.5. The stock removal increases with

Fig.3 Preparation of iron bonded diamond magnetic abrasives by sintering

the finishing gap, but the stock removal under finishing gap of 1.2 mm is low. In the finishing conditions of smaller gap, the pores between iron powder and particles which hold the diamond paste decreases according to increasing of magnetic flux density. On the other hand, the stock removal decreases in the
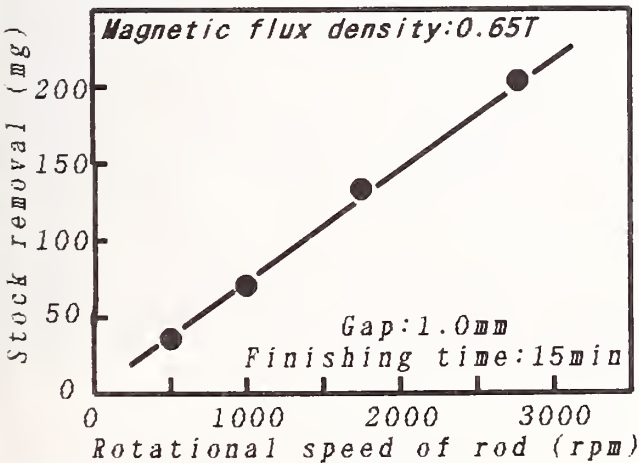
Fig.4 The effect of rotational speed of rod on the stock removal / workpiece: WC-Co alloy / Abrasive:iron powder(2g) +diamond paste(0.7g)+stearic acid(0.3g)
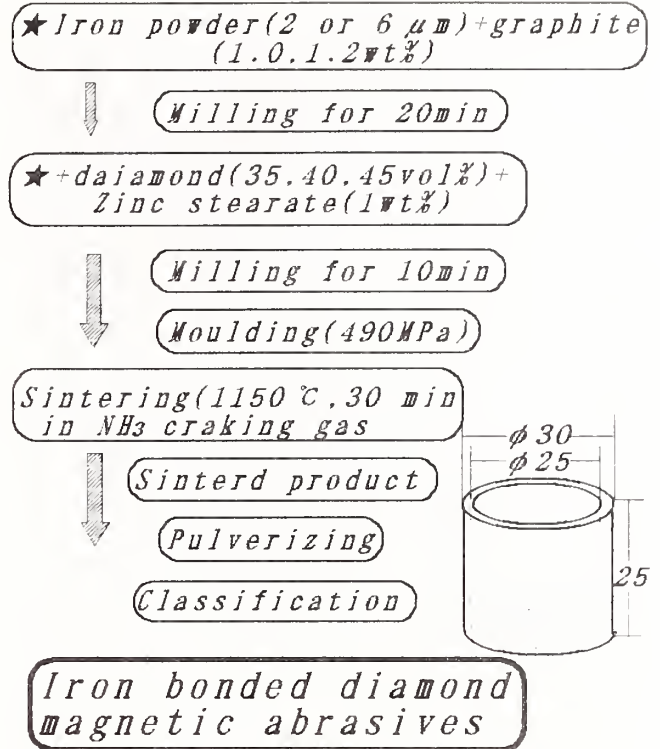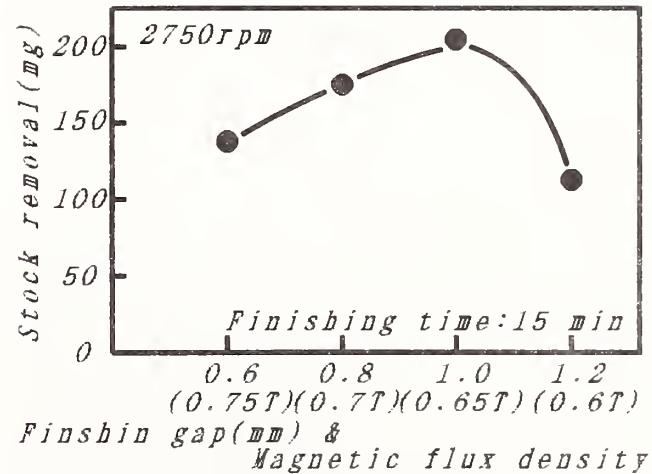
Fig.5 The effect of gap and magnetic flux density on the stock removal /workpiece:WC-Co alloy /Abrasive: ironpowder(2g)+diamond paste(0.7g)+ stearic acid(0.3g)

finishing conditions of larger gap. This is caused by weak force of attraction between the iron powder and workpiece with decrease in magnetic flux density.

The effect of diamond paste content on the stock removal is shown in Fig.6. The stock removal increases lineally with the diamond paste content. However, the stock removal may be saturated with 70 vol% of diamond paste content.

Figure 7 shows the relationship between surface roughness(Rmax:maximum surface roughness,Rz:10 point average surface roughness,Ra:center line average surface roughness) and diamond paste content. The surface roughness after finishing is under Rmax=0.1μm on the workpiece of WC-Co alloy using diamond paste including sub-micron diamond particles. The best surface roughness was obtained at about 50 to 65 vol% of diamond paste. Original roughness remained on the workpiece under 50 vol% of diamond paste content. In the volume content of over 65%, surface roughness was not good which is caused by the over polishing of workpiece surface.

The effect of feed speed of workpiece on the surface roughness is shown in Fig.8. The feed speed of 3 mm/min is suitable for giving an acceptable surface roughness.
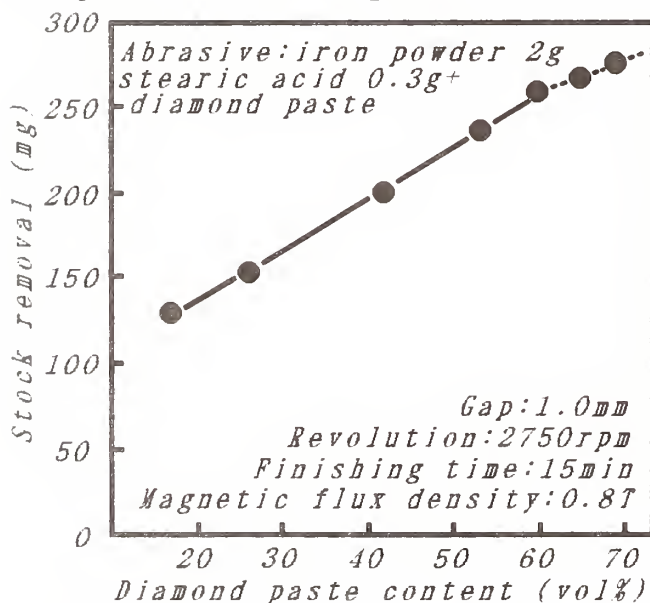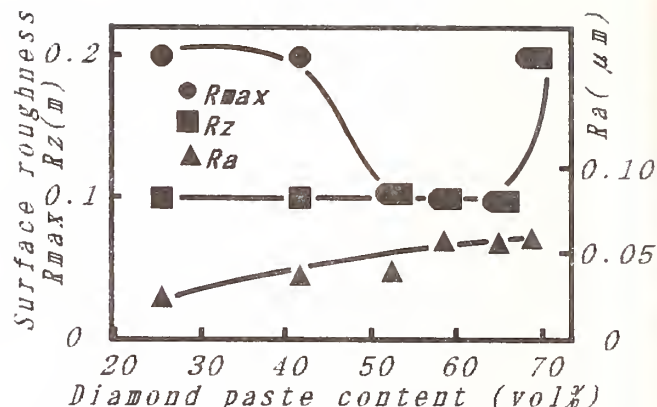
Fig.7 The effect of diamond paste content on the surface roughness/ Workpiece:WC-Co alloy/Abrasive:iron powder(2g)+stearic acid(0.3g)+diamond paste/Magnetic flux density:0.8T/2750 rpm/Gap:1.0mm/Finishing time:15min/ Original roughness:4μmRmax,3μmRa, 0.5μmRa
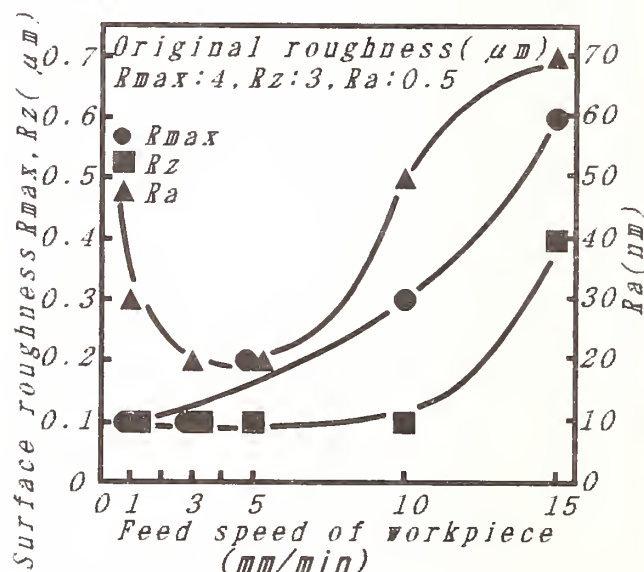
Fig.8 The effect of feed speed of workpiece on surface roughness/ Workpiece:WC-Co alloy/Abrasive:iron powder(2g)+stearic acid(0.3g)+diamond paste(0.4g)/Magnetic flux density:0.8T /2750 rpm/Gap:1.0mm

Figure 9 shows the SEM images of surface of WC-Co alloy and it's surface roughness profiles.(A) is as fabrication and (B) is after finishing using diamond paste and magnetized iron powder brush.

The finishing conditions are :
  *composition of abrasives = iron
    powder(KIP300AS:2.0g) +diamond paste
    (0.4g) + stearic acid(0.3g)
  *finishing gap between rod and
    workpiece = 1.0 mm

Fig.6 The effect of diamond paste content on the stock removal / workpiece:WC-Co alloy

418

*rotational speed of rod = 2750 rpm
*magnetic flux density = 0.8 T
*finishing time = 15 min
The surface with the original roughness of Rmax=4μm was finished in 15 min operation to Rmax=under 0.1μm as is evident from Fig. 9.

Figure 10 shows the external appearance of WC-Co alloy plate and finished one.

The finishing conditions are:
*composition of abrasives = iron powder(KIP300AS:2.0g)+diamond paste (0.4g) + stearic acid(0.3g)
*finishing gap between rod and workpiece = 1.0 mm
*rotational speed of rod = 2750 rpm
*feed speed of workpiece = 3 mm/min
*magnetic flux density = 0.8 T
*finishing time = 15 min
As is evident from Fig.10,the surface of finished sample shows the mirror surface. Unfortunately the finishing method has several weak points that are responsible for a short abrasive life and it is too expensive. It is well known that diamond has the highest hardness among all the abrasives, but when used in paste form the life is short. Therefore, iron bonded diamond magnetic abrasives by sintering was developed.
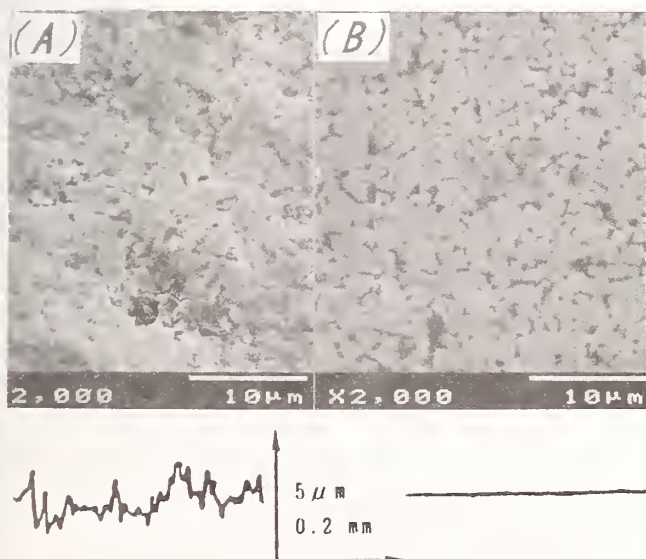
Fig.9 SEM images of surface of WC-Co alloy and surface roughness profiles /(A):as fabricated (B):after finishing
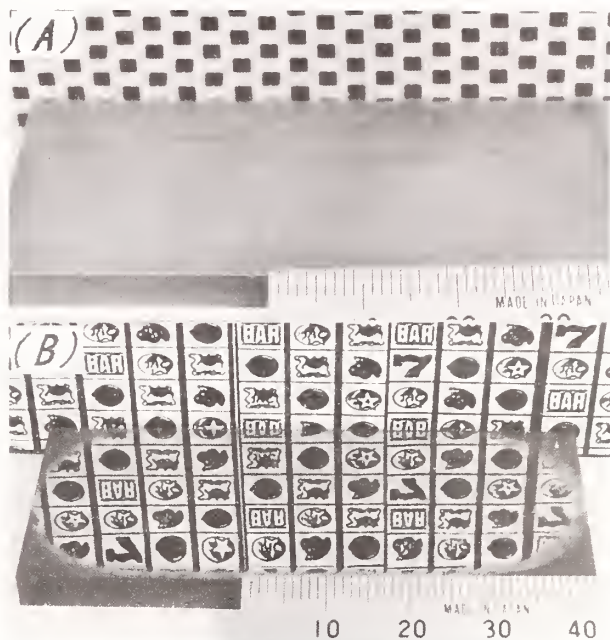
Fig.10 External appearance of WC-Co plate /(A):as fabricated (B):after finishing

3.2 Finishing Characteristics of Iron Bonded Diamond Magnetic Abrasive for WC-Co Curved Surfaces

The effect of finishing gap and magnetic flux density on the stock removal using iron boned diamond magnetic abrasive, which consisted of 35 vol% diamond particles is shown in Fig. 11. The average diameter of diamond particles is 11.5 μm. The workpiece of WC-Co alloy machined by wire-cut EDM, and whose radius curvature of concavo-convex was 40 or 80 mm.

The finishing conditions were :
*magnetic abrasives = iron bonded diamond / grain size = 214-425 μm
*abrasive weight = 1.5 g
*rotational speed of rod = 1000 rpm
*feed speed of workpiece = 5 mm/min
*moving of finishing tool= stroke for 3 times with 1 mm pitch
*shape of rod top = radius curvature 8 mm with slit
The stock removal decreases lineally with the finishing gap for any radius of curvature. This is caused by the decreasing magnetic flux density.
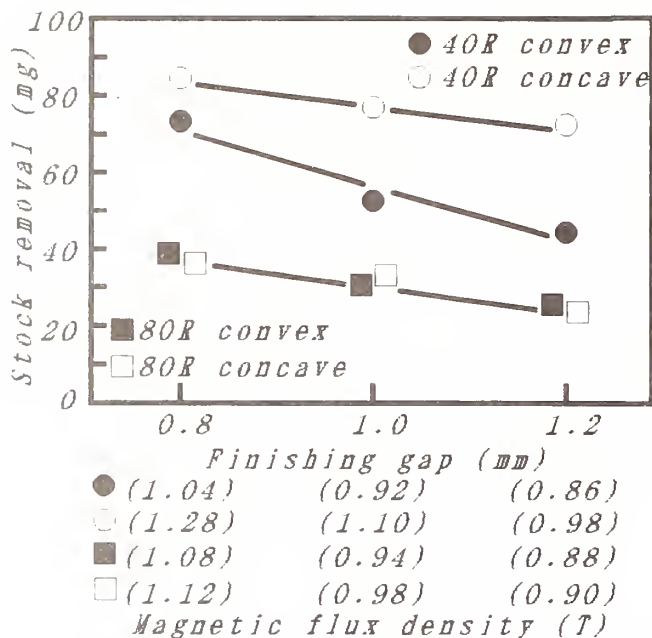
419

Fig.11 The effect of finishing gap and magnetic flux density on the stock removal Workpiece:wire-cut EDMed WC-Co alloy with curvature

Fig.12 The effect of rotationl speed on stock removal /workpiece:wire-cut EDMed WC-Co alloy with curvature

Fig.13 The effect of feed speed of workpiece on the stock removal/workpiece:wire-cut EDMed WC-Co alloy with curvature

The effect of increasing rotational speed of rod on stock removal is shown in Fig. 12. The finishing conditions of this experiment were based on the one of Fig.11 except a finishing gap of 0.8 mm was used.The stock removal increases linearly with the rotational speed at any radius of curvature. The difference in stock removal for different radius of curvature may be due to the addition of mechanical force which was generated by the mass of abrasives closely attached at the point of the smallest gap. This problem can be solved by the moving finishing tool(rod) to a normal line.

The effect of feed speed of workpiece on the stock removal is shown in Fig.13.

The finishing conditions are :
 *magnetic abrasives = iron bonded
  diamond / grain size = 214-425 μm
 *abrasive weight = 1.5 g
 *finishing gap = 0.8 mm
 *rotational speed of rod = 1750 rpm
 *moving of finishing tool = stroke for
  3 times with 1 mm pitch
 *shape of rod top = radius curvature
  8 mm with slit
The stock removal decreases linearly

with the feed speed of workpiece for any radius of curvature. This result is reasonable because of the finishing time per unit area become short according to increase of feed speed of workpiece.

The effect of rotational speed of rod on the surface roughness is shown in Fig.14.

The finishing conditions are :
 *magnetic abrasives = iron bonded
  diamond / grain size = 214-425 μm
 *moving of finishing tool = stroke for
  3 times with 1 mm pitch
 *shape of rod top = radius curvature
  8 mm with slit
 *abrasive weight = 1.5 g
 *finishing gap = 0.8 mm
 *radius curvature of workpiece =40 mm
  / convex
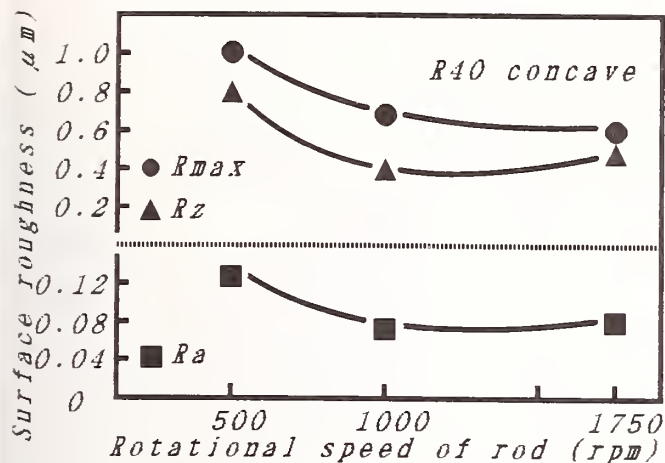
Fig.14 The effect of rotationl speed of rod on the surface roughness workpiece:wire-cut EDMed WC-Co alloy with curvature

Fig.15 External appearance of wire-cut EDMed s-shape WC-Co alloy /(A):as machined (B):after finishing

The roughness value of Rmax = 0.5 μm was obtained under finishing condition of 1000 rpm. But this roughness value is worse than the value for using diamond paste and magnetized iron brush. It is possible to solve this problem using finer diamond particles in the magnetic abrasives like a sub-micron order in the diamond paste.

Figure 15 shows the external appearance of s-shape WC-Co alloy which was machined by wire-cut EDM and it's roughness profiles. (A) is as machined and (B) is after finishing with iron bonded diamond magnetic abrasive using NC program.

The finishing conditions are :
*moving of finishing tool = stroke for 3 times with 1 mm feed pitch
*magnetic abrasives = iron bonded diamond / grain size = 300–425 μm
*radius curvature of workpiece = 100 mm / concavo-convex
*shape of rod top = radius curvature 8 mm with slit (Figure 16)
*finishing gap between rod and workpiece = 1.4 mm
*average diameter of diamond particle = 60–70 μm
*diamond content in abrasive = 35 vol%
*feed speed of workpiece = 10 mm/min
*rotational speed of rod = 2750 rpm
*magnetic flux density = 0.8 T
*abrasive weight = 2.0 g

Fig.16 External appearance of rod top

3.3 Polished Example of WC-Co Alloy Punch

Figure 17 shows an outline of the magnetic finishing apparatus for WC-Co alloy punch using Sm-Co magnet and also the external appearance of finished sample. The diamond paste and iron powder brush were used as abrasives in the finishing of hard metal. It was possible to finish the WC-Co alloy punch to a surface finish under Rmax = 0.1μm.

However,magnetic abrasive finishing is not suitable for polishing of non-magnetic ceramics like a SiC in comparison with WC-Co ally. Moreover, this finishing method has geometric limitations for corner of cavity or groove. But, this magnetic abrasive finishing has the advantage of cost reduction using conventional NC machine tools and this method is suitable for magnetic substances like a steel.

421

4. Conclusions

Based on the facts described above, the authors can conclude that magnetic abrasive finishing process may be considered as one of the potential methods for the flat or curved surface finishing of wire-cut EDMed WC-Co alloy. In this finishing, the most important factors are development of magnetic abrasives according to materials and design of optimum magnetic circuit. The magnetic abrasive finishing will be used in practice in the field of automation of WC-Co alloy mold or punch surface finishing with the development of a suitable magnetic abrasives and new magnetic finishing process by the authors.

Outline of finishing form

Fig.17 External appearance of WC-Co alloy punch after finishing with Sm-Co magnet and compund of diamond paste and iron powders

References

[1] T.Shinmura:Tool Engineer,40,10 (1988) 48

[2] M.Anzai,T.Sudo and T.Nakagawa: Proceedings of the 2nd International Conference on Die and Mould Technology,(1992) 145

[3] M.Anzai, T.Sudo , H.Otaki ,Takuya Obana and T.Nakagawa:Journal of the Japan Society of Powder and Powder Metallurgy,39(1992) 510

[4] M.Anzai,Hisanori Otaki,Toru Sudo and T.Nakagawa: Paper being for publication in International Journal of the Japan Society Precision Engineering, (1992)

[5] M.Anzai,K.Masaki and T.Nakagawa: Journal of the Japan Society of Grinding Engineers,33,4(1989) 34

TURNING AND MILLING

MACHINING CERAMIC MATERIALS FOR DENTAL RESTORATIONS

E. D. REKOW
University of Maryland at Baltimore, Baltimore, MD

G. M. ZHANG
University of Maryland at College Park, College Park, MD

V. P. THOMPSON
University of Maryland at Baltimore, Baltimore, MD

Ceramic dental restorations must perform in a demanding environment including dynamic loading with high-stress in a wet and corrosive environment. Patient expectations for a restoration include both esthetics and long life. In this regard, ceramics are appealing but their brittle nature is a significant limitation. All of the fabrication techniques for creating dental restorations damage the ceramic. However, the smoother the surface produced, the less likely it is damaged sufficiently to compromise its clinical performance. The objective of this investigation is to determine the interaction between machining parameters and machining environments on surface finish. Additionally, an overview of the oral environment and design specifications for dental restorations as well as a brief review of clinical failures of current ceramic restorations are presented.

Dentistry provides a demanding environment in which to investigate ceramic materials, their properties, and their performance. Patient are no longer satisfied with gold restorations, particularly for their front teeth. Increasing numbers of patients are demanding esthetic restorations for both the front and back teeth. In this regard, ceramics are appealing for dental restorations because of their esthetics as well as their strength, wear resistance, chemical durability, and biocompatibility. Unfortunately, the brittle nature of current esthetic materials is a significant limitation for widespread use in dentistry. All fabrication techniques damage the ceramic surfaces. In the wet and corrosive environment of the mouth, microscopic damage from fabrication can propagate, resulting in clinical failure. For any given ceramic, the smoother the surface produced, the less likely it contains damage and the more probable it will survive in the clinical application. This paper presents results of investigations to elucidate the influence of machining parameters and machining environment on surface finish. Additionally, it provides an outline of the oral environment and design specifications for dental restorations as well as a brief review of clinical failures of current ceramic restorations.

Design Requirements for Dental Ceramics.
The oral environment to which these materials are subjected is demanding. The teeth (and any restorations associated with them) are continually bathed in saliva - a composite of secretions of a number of salivary and mucous glands, the gingival crevice, and fluid transudate from the oral mucosa. It contains epithelial and blood cells, bacteria, and food debris in water (1). The average flow rate is approximately 0.3 ml/minute but this value rises considerably during eating or salivation. In a normal person, between 700 and 800 ml of saliva is secreted daily.

Instantaneous temperature ranges of 65°C (150°F) degrees are common during the

course of an average meal (2). Thermal conductivity and the coefficient of thermal expansion for restorative materials are important properties to be considered in preserving the pulp of the tooth and minimizing thermal changes in the restorative material (which can cause tooth sensitivity and/or open gaps between the restorative material and the tooth which can induce decay). The pH ranges typically experienced during a normal day may range from 0.5 (when drinking soda, for instance) to 8 (with some toothpastes) (3).

Forces generated during normal chewing functions are typically 77 kgm (170 pounds) but these vary markedly from one area of the mouth to another. In the molars, the range is from 40-90 kgm (90-200 pounds) but only 9-25 kgm (20-55 pounds) in the incisors, the most anterior teeth. Biting forces are generally higher in males than in females and are usually greater in young adults than in children. A force of 75-80 kgm (160-190 pounds) applied to a tooth cusp with area of approximately 0.039 cm^2 (0.006 in^2) generates a compressive stress of 193 MPa (28,000 psi) (2). Instantaneous forces may be substantially higher than the values reported from these studies.

Loading occurs on a cyclic basis with an average of 1400 cycles per day (4). For people who grind their teeth, however, that value is 5-10 times this amount per day.

Wear of restorative materials in the mouth is an important and complex phenomenon (5). Wear of a restorative material must be measured against enamel, as well as against other restorative materials in other teeth. Normal enamel to enamel wear is approximately 30-40 microns/year depending upon the region of the mouth; it is highest for posterior teeth (6,7). Excessive wear of a restorative material may cause a tooth to supererupt causing interferences during function. Supereruption also accelerates breakdown of the restorative material. An often overlooked aspect of wear is the wear that occurs between adjacent teeth. This occurs because teeth are free to move independently

Parameter/Characteristic	Values
Oral Environment:	
Temperature Range[2]	65°C (150°F)
Load[2]	70 kgm (170 lbs)
Cycles/day[4]	1400
pH Range[3]	0.5 - 8
Tooth Properties:	
Modulus of Elasticity	
Molar (dentin)[2]	1.2 X 10^4 MPa
	17 x 10^5 psi
Molar (enamel)[2]	4.6 X 10^4 MPa
	67 x 10^5 psi
Proportional Limit	
Molar (dentin)[2]	148 MPa (21,000 psi)
Molar (enamel)[2]	224 MPa (32,500 psi)
Strength	
Molar (dentin)[2]	305 MPa (44,200 psi)
Molar (enamel)[2]	79 MPa (37,800 psi)
Coeff. of Linear Expansion[2]	11.4 Kx10^{-6}
Density[27]	2.9 gm.cm^{-3}
Specific Heat[27]	0.18 (cal/gm . C)
Conductivity[27]	0.0022 (cal.cm/ cm^2.sec.C)
Diffusivity[27]	0.0042 (cm^2.sec^{-1})
Color (Munsell scale)	
Hue[2]	7.5 YR - 2.7Y
Brightness[2]	5.8/ to 8.5/
Chroma[2]	1.5-5.6
Restoration Requirements:	
Surface Roughness[8]	<2 micrometers
Fit[9]	<60 microns
Expected Life[10]	10+ years

Table 1.   Oral Environmental Conditions and Tooth Properties

during function. If excessive wear occurs between two teeth, the posterior teeth move forward causing disruptive changes in the bite.

Because of their relatively high hardness when compared to enamel, roughness in ceramics can cause very high wear rates on any opposing tooth structure. To minimize wear, surface roughness must be less than 2 microns (8). Wear effects are moderated, to some degree, by saliva and adsorbed proteins. However, this effect is not yet well understood.

Fit of any restoration is critical for its success. If a restoration projects over the edge of the tooth, especially near the gumline, it will entrap food debris. The by-products of the breakdown of this debris by the microflora in the mouth can result in both potential damage to tooth supporting tissues through inflammation and in decay of the tooth itself.

If the restoration does not adapt well creating a gap between the tooth and the restoration, leakage beneath the restoration is likely to occur. Again, food debris is likely to be trapped or imbedded in the area of improper fit. The breakdown of that debris will result in decay. For long term clinical success, the adaptation at the edge between the tooth and the restorative material must be to within 60 micrometers (0.002 inches) (9). If this criterion is met, most ceramic restorations are expected to last at least 10 years (10).

Color is paramount for reestablishing esthetics of a tooth that is to be restored. In general, the Munsell data for hue range is from 7.5YR to 2.7Y, brightness from 5.8/ to 8.5/, and chroma from 1.5 to 5.6 (2)

Biocompatibility and toxicity are also critical to the long term success of any restorative materials to be used in the mouth. Few if any dental materials are totally inert from a physiological standpoint. Ideally the material should be harmless to the pulp of the tooth and to the soft tissues surrounding the tooth. It should contain no toxic diffusible substances that can be absorbed into the circulatory system. It must be free of potential sensitizing agents that could lead to allergic reactions. And it must have no carcinogenic potential. The American Dental Association has developed a specification for evaluating the toxicity of any materials to be used for dental restorations (ANSI/ADA Document 41, Recommended Standard Practices for Biologic Evaluation of Dental Materials and Devices).

Table 1 summarizes the oral environmental conditions and provides information regarding the physical properties of human teeth and restorative materials.

Clinical Performance of Dental Ceramics.
Dental ceramics have been around for decades, provided excellent esthetics in the anterior regions of the mouth. Restorations for posterior regions of the mouth, fabricated from the same materials, failed almost immediately. Higher strength ceramics with aluminous cores or cast ceramics were introduced to eliminate the problem. Unfortunately, the clinical failure rates remain high. This is especially true in the high stress posterior regions of the mouth.

Malamut et al. reported a failure rate of 2.9% in 616 restorations with up to 4 years of service life, 13.5% in 369 restorations with up to 7 years of service life (11). Christensen et al. found failure rates as high as 80% for multi-unit all ceramic bridges (12). Little data is yet available on clinical failures of machined ceramic restorations. However intracoronal machine-ground glass ceramic and feldspathic porcelain restorations are vulnerable to fracture at the edges in 0.5% of the restorations as well as bulk fracture in 1-2.5% of the restorations within three years (13).

The primary clinical failure mode is fracture. The initiation site of the fracture is generally on the internal surface of the restoration. The internal surface is fabricated to fit a prepared (ground) tooth. When cast ceramics are used, the surfaces are sandblasted or ground to remove refractory materials. (The external surface is then polished but the internal surface is left unpolished to improve the mechanical advantage of the adhesives which hold the restoration to the tooth.) The sandblasting and/or grinding processes introduce defects and/or expose porosities which function as nucleation sites for fracture. Machining, while less widely used until now, is likely to induce similar defects. The microcracks initiated during fabrication, grow to a critical size when exposed to the oral environmental effects of repeating loading, wear, and saliva. When this critical size is reached, fractures occur (14).

Fractography of failed cast all-ceramic (Dicor) restorations suggests that failures are caused by surface defects located, primarily, on their internal surface (15-18). Most of the effects of loads delivered during damaging surface contact (fabrication-related processes, chewing, and wear) take place below the ceramic surface. Micro-cracks extending normal to the contact surface have been

identified as being the failure origin for both structural ceramics (19,20) and for dental ceramics (21). Finite element analyses have demonstrated similar failure mechanisms (17).

Machining Ceramic Dental Restorations.
Recently, CAD/CAM systems have been introduced to speed the production of dental restorations (22). The primary fabrication technology used by these systems is machining (either grinding or milling). Dental restorations have an extremely complex three-dimensional shape. Milling rather than grinding offers advantages for rapid shaping. To be economically sound, machining time for a crown should be under 20 minutes. For comparison, a typical crown for a posterior tooth can be approximated as a cylinder with diameter of 10 mm and height of approximately 5-7 mm. Both the internal and external surfaces must be shaped. As discussed above, not only is the speed of material removal important, the resulting surface roughness and degree of damage are critical to the success of the restoration.

Ceramic materials currently used for dental restorations are predominantly either feldspathic or reinforced porcelains and glass ceramics (23). Two new materials are the primary focus of investigations for CAD/CAM produced dental restorations: (1) Dicor-MGC (Dentsply) which is a two-phase micaceous glass and (2) Vita Porcelain which is a feldspathic porcelain (24).

Unfortunately, machining of ceramics is generally application dependent (25). Almost nothing has been reported addressing the effects of milling parameters on surface finish for any dental CAD/CAM ceramic materials. What has been published has generally related to grinding (21,25).

The objective of this investigation was to establish a preliminary empirical relationship between surface finish and milling parameters (spindle speed, depth of cut, and feed rate) and the machining environment. The investigation reported here utilizes the factorial design (26).

The results of this effort provide an important basis for more in-depth investigation of a very complex problem.

Method and Materials.
To investigate the effects of machining parameters on surface finish, a 2^3 factorial design was selected. This approach uses orthogonal arrays to provide insight into the relationship between surface finish and machining parameters. The three parameters under investigation were feed, depth of cut, and cutting speed. Additionally, different machining environments were investigated in a second 2^3 factorial design.

Cylinders of Dicor MGC (Dentsply) with diameter of 16 mm and length of 12 mm were mounted on a metal base plate using an epoxy resin (figure 1). A Matsuura MC-510
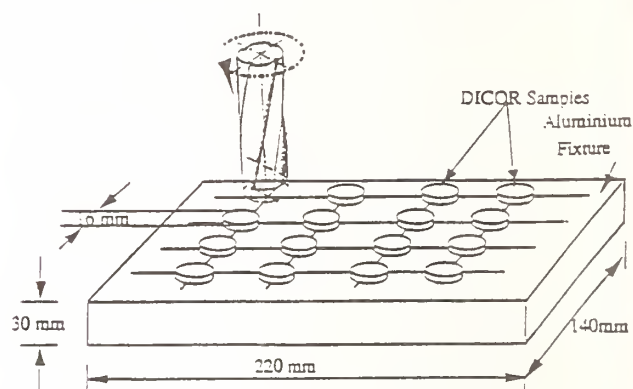
Figure 1.   Dicor MGC in Machining Fixture

machining center was used to perform the milling operations. High-speed steel end mills were used for the machining because of their ease of availability and cost. Machining was done with the cutting fluid introduced at the cutting tool-Dicor interface. Two different fluids were used: distilled water and distilled-water with a chemical additive. Machining parameters (summarized in Table 2) were selected based on previous machining experience with Dicor MGC as follows: feed rate: 10-20 mm/minute, depth of cut: 0.05-0.10 mm, spindle speed: 200-400 rpm. Surface roughness was measured using a Taylor-

Test Number	Feed Rate (mm/min)	Depth of Cut (mm)	Spindle Speed (rpm)	Cutting Fluid Type
1	10.0	0.05	200	water
2	20.0	0.05	200	water
3	10.0	0.10	200	water
4	20.0	0.10	200	water
5	10.0	0.05	400	water
6	20.0	0.05	400	water
7	10.0	0.10	400	water
8	20.0	0.10	400	water
9	10.0	0.05	200	chemical
10	20.0	0.05	200	chemical
11	10.0	0.10	200	chemical
12	20.0	0.10	200	chemical
13	10.0	0.05	400	chemical
14	20.0	0.05	400	chemical
15	10.0	0.10	400	chemical
16	20.0	0.10	400	chemical

Table 2.   Machining Parameters

Horbson profilomter (resolution 0.01 micron). Surfaces were also qualitatively evaluated under scanning electron microscopy.

The factorial design permits generation of an empirical formula quantifying the relative effects of the machining parameters - both alone and in combination. For this investigation, the parametric equation is given by the following equation which considers the linear effects:

$$R_a = ME + 1/2(FMEx_1 + DMEx_2 + SSMEx_3 + IFDx_1x_2 + IFSSx_1x_3 + IDSSx_2x_3 + IFDSx_1x_2x_3)$$

where:

R_a = Surface roughness
ME = Mean effect = average of all surface roughnesses
FME = Main effect of feed rate
x_1 = Feed rate
DME = Main effect of depth of cut

x_2 = Depth of cut
SSME = Main effect of spindle speed
x_3 = Spindle speed
IFD = Interaction between feed and depth of cut
IFSS = Interaction between feed and spindle speed
IDSS = Interaction between depth of cut and spindle speed
IFDS = Interaction between feed, depth of cut, and spindle speed

It should be noted that such equations are conditional on the choice of test setting and cannot be extrapolated beyond the range of tested parameters. Also, the parameters x_1, x_2, and x_3 are normalized with respect to the mean and the range of parameter settings.

Results and Discussion. Results are summarized in table 3 and figures 2 and 3.

429

Test Number	Measured Value Ra			Avg
1	2.71	2.80	2.63	2.7
2	5.64	5.42	5.80	5.6
3	8.36	8.41	7.86	8.1
4	4.42	4.58	4.27	4.4
5	3.92	3.70	3.81	3.8
6	6.14	6.28	5.98	6.1
7	1.90	1.85	1.74	1.8
8	7.93	7.30	7.61	7.6
9	0.97	1.02	1.08	1.0
10	4.35	4.21	4.06	4.2
11	3.16	2.90	3.04	3.0
12	2.81	2.70	2.93	2.8
13	0.76	0.79	0.85	0.8
14	4.40	4.05	4.22	4.2
15	3.71	3.90	4.08	3.9
16	5.40	5.82	5.61	5.6

Table 3.   Average Surface Roughness for Dicor MGC

Figure 4 presents representative sets of profiles taken from tests numbers 1 and 9 (feed rate 10.0 mm/min, depth of cut 0.05 mm, spindle speed 200 rpm, and cutting fluids water and water with a chemical additive respectively). Figure 5 is a three-dimensional reconstruction of a 30 micron by 30 micron section of surfaces machined under identical conditions in water and in water with a chemical additive.

Figure 2.   Surface roughness for machining in water only
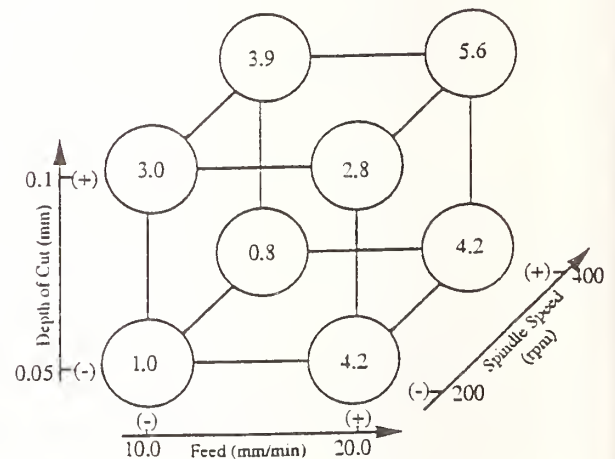
Figure 3.   Surface roughness for machining in water with a chemical additive

	ME	FME	DME	SSME	IFD	IFSS	IDSS	IFDS
Water only	4.96	4.52	-1.07	-0.37	0.93	-1.78	0.28	1.43
Water plus	3.39	1.23	1.13	2.08	-0.73	-0.23	2.08	1.43

Table 4.   Main and Interactive Effects

Main effects and interaction values for the test conditions were determined using a table of contrast coefficients (26) (table 4). For samples machined in water spray only, surface roughness (R_a) ranged from 1.8 microns (test 7: feed=10 mm/min, depth of cut=0.10 mm, spindle speed=400 rpm) to 8.1 microns (test 3: feed=10 mm/min, depth of cut=0.10 mm, spindle speed=200 rpm). At first glance, it would appear that spindle speed is the greatest determinant in surface roughness. However, when other comparisons where only the spindle

430

Ra=1.2μm

Ra=0.9μm

Ra=0.8μm

Ra=0.8μm

Ra=1.1μm

Ra=0.7μm

Ra=0.9μm
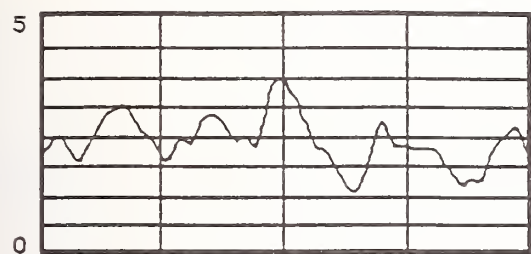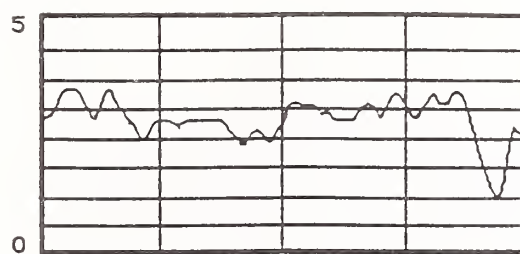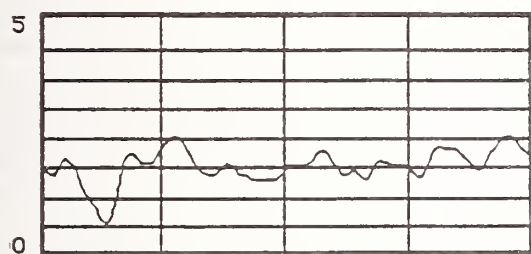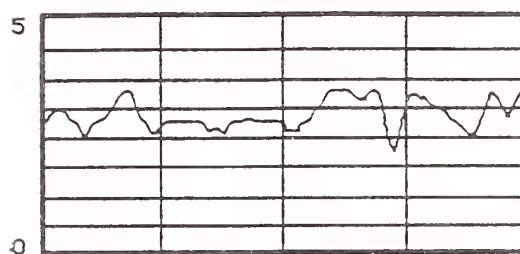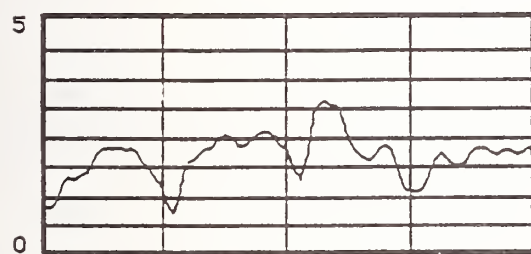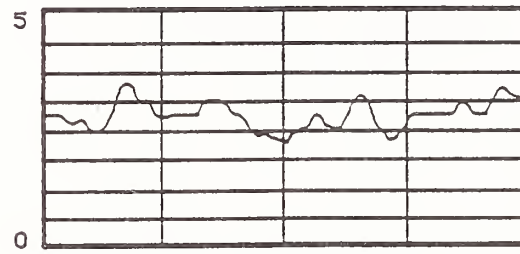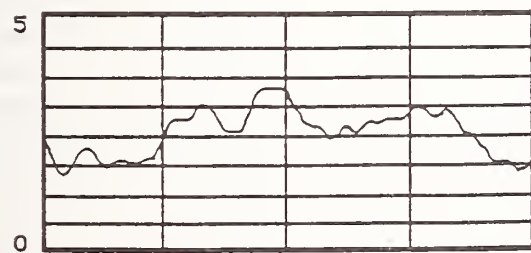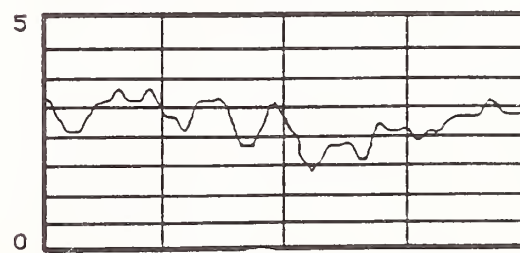
Ra=0.8μm

(a)   Distilled Water Only   (b)   Chemical Additive Used

Figure 4.   Representative Surface Roughness Profiles

431
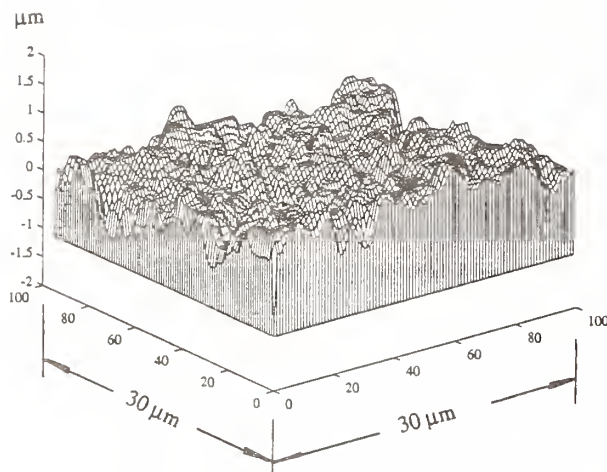
(a)   Surface Topography (Distilled Water Only)
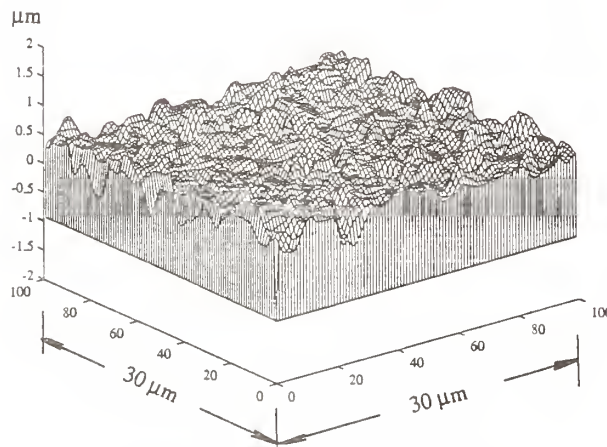
(b)   Surface Topography (Chemical Additive Used)

Figure 5.   3-D Reconstruction of Surface Topographies (feed rate 10 mm/min, depth of cut 0.05 mm, spindle speed 200 rpm)

speed is changed are investigated, the differences in roughness are quite small: 1.1 micron between test 1 and test 5, 0.5 microns between tests 2 and 6. For test 4 and 8, however, surface roughness difference is 3.2 microns. Obviously, the relationship between surface finish and machining parameters is not dependent upon only a single variable.

Calculating main and interactive effects gives the values summarized in Table 3. Using these variables, the equation for machining Dicor MGC in a water-only environment becomes:

$$R_a = 4.96 + 2.26x_1 - 0.54x_2 - 0.19x_3 + 0.47x_1x_2 - 0.89x_1x_3 + 0.14x_2x_3 + 0.72x_1x_2x_3.$$

This empirical model provides an estimate for surface roughness as a function of machining parameters. The negative values of the main effects associated with depth of cut and spindle speed indicate that increasing these parameters will reduce the surface roughness. On the other hand, increasing the feed rate will make the surface rougher. Small changes in feed rate will impact the surface finish more quickly than changes in either the depth of cut or feed rate. The numerical values associated with two-factor interactions elucidate the interplay between the three machining parameters on surface finish. The interplay between feed rate and spindle speed is far more important than the interplay between the other combinations of parameters. However, even this interaction has less of an influence on surface finish than feed rate.

For samples machined in water with a chemical additive, surface roughness (R_a) on average was less than for water-only samples. The average surface roughness for all tests with water only was 4.96 microns vs 3.39 microns with water plus a chemical additive.

With the additive, roughness ranged from 0.8 microns (test 13: feed = 10 mm/min, depth of cut = 0.05 mm, spindle speed = 400 rpm) to 5.6 microns (test 16: feed = 20 mm/min, depth of cut = 0.10 mm, spindle speed = 400 rpm). Note that the parameter yielding maximum and minimum surface roughness are not the same as for maximum and minimum roughness with the water-only spray. This implies that changing the cutting environment alters the material removal mechanism. Other investigations indicate that, with chemical additives, the most prominent change is the ratio of the tangential cutting force component to the feed force component of the cutting force; the ratio changes significantly, without any change in the resultant cutting force[24].

Calculating main and interactive effects

gives the values summarized in table 3. Using these variables, the equation for machining Dicor MGC in water with a chemical additive becomes:

$$R_a = 3.39 + 0.62x_1 + 0.57x_2 + 1.04x_3 - 0.37x_1x_2 - 0.12x_1x_3 + 1.04x_2x_3 + 0.72x_1x_2x_3.$$

It is interesting to note that with the chemical additive, the relative contributions of the various parameters change dramatically. For instance, with water only, feed rate has the greatest impact of single factors on the surface finish (FME=2.26). For water plus chemical additive, spindle speed makes the greatest impact on finish (SSME=1.04). Additionally, for water only, the main effects of depth of cut and spindle speed are significantly less than for feed. With water plus additive, however, feed and depth of cut make nearly equal contributions, and they are much more nearly equal to the effect of changes in spindle speed than with water only.

With water plus chemical, the major interactions is between depth of cut and spindle speed (vs. feed rate and spindle speed for water only). Another difference is that not only do the values of the main effects and interaction coefficients change, the signs of some of them reverse. For instance, in water only, increasing the depth of cut improves the surface (DME<0) whereas with water plus the chemical additive, increasing the depth of cut roughens the surface (DME>0). Similarly, increasing the spindle speed will improve the surface in water; whereas, the same change will make the surface rougher in water plus a chemical.

Contour maps were created from the surfaces presented in figures 5a and 5b. The average roughness was calculated. Then a map was created for all areas of the surface with surface roughness of +1.0 micron, +0.5 micron, the average roughness (0.0), -0.5 micron, and -1.0 micron. Only two areas (both for the water-only environment) were found to have a profile roughness of +1.0 micron. In

figure 6, all surfaces with roughness of at least +0.5 microns is shown as black areas. For a dental restoration, these represents the first points of contact with the opposing tooth or restoration. The more peaks at a given height, the less likely there will be wear; the forces of occlusion during jaw function will be more evenly distributed. Obviously the environment in which a dental restoration is machined can have a significant impact in the likelihood for clinical success.
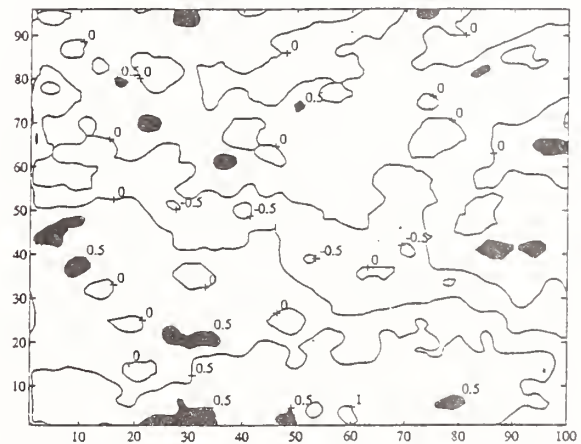
(a)   Contour Map (Distilled Water Only)
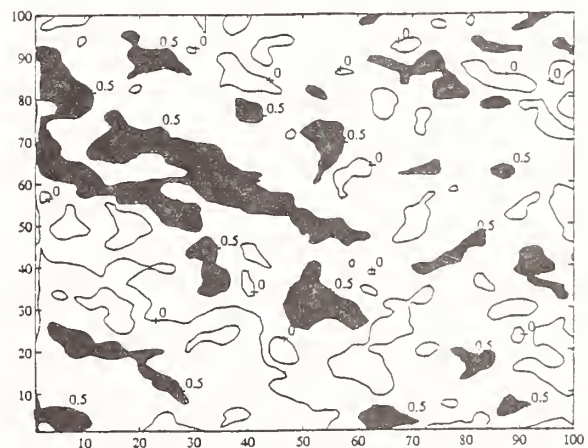
(b)   Contour Map (Chemical Additive Used)

Figure 6.   Contour Maps of Surfaces in Figure 5.

Summary. The factorial design technique provides insight into the interplay between machining parameters and surface finish within the range of variables investigated for one machinable dental ceramic. In a water-only cutting environment, feed rate is the major factor influencing surface finish. For water with a chemical additive, spindle speed becomes the most important single factor. However, within the range of the parameters tested, both feed rate and depth of cut will make significant differences on surface finish and the interaction between the depth of cut and spindle speed is critical.

The empirical model provides a method to select machining parameters which will produce a required surface finish. It also defines subsequent investigations. For water-only machining, there is little need to investigate large numbers of samples created with different spindle speeds since little if any change is likely to result from even substantial changes in this speed. Alternatively, for machining with water plus the chemical additive, major emphasis must be placed on fully characterizing the influence of spindle speed on surface finish. Additionally, the interplay between depth of cut and spindle speed is important and warrants further investigation.

Further elucidation of the most important coefficients of the interplay between machining parameters and surface finish must continue. Other ceramic materials and cutting tools need to be investigated. The empirical equation needs to be made more robust by extending the range of variables. The impact on clinical performance needs to be established. The long range objective of our investigations is to develop an empirical equation powerful enough to establish a basis to efficiently establish machining parameters as a function of material properties. This will provide a method to achieve a specified surface finish for an array of ceramics which could be used for dental restorations.

References.

1. G. Nikiforuk, Understanding Dental Caries: Etiology and Mechanisms, Karger, 1985.
2. R. Phillips, Skinner's Science of Dental Materials, WB Saunders, 1991.
3. J.F. McCabe, Anderson's Applied Dental Materials, Blackwell Scientific Publications, 1985.
4. R.G. Craig, Restorative Dental Materials, CV Mosby, 1980.
5. J.M. Powers, S.C. Bayne, "Friction and Wear of Dental Materials", ASM Handbook, Volume 18: Friction, Lubrication and Wear Technology, PJ Blau, Volume Chairman, ASM, pp. 665-681, 1991.
6. P. Lambrechts, M. Braem, M. Vuylsteke-Wauters, G. Vanherle, "Quantitative in vivo Wear of Human Enamel", J Dent Res, Vol. 68, pp. 1752-1754, 1989.
7. F. Roulet, P. Mettler, U. Friedrich, "Ein klinischer Vergleich dreier Komposits mit Amalgam für Klass II Füllungen unter besonderer Berücksichtigung der Abrasion, Resultate nach 2 Jähren", Schweiz Monatsschr Zahnkeilkd, Vol. 90, pp. 18-30, 1983.
8. P. Lambrechts, G. Willems, M. Braem, G. Vanherle, "Composites in the 21st Century", J Dent Res, Vol. 72, Abstract 686, 1993.
9. J.C. Holmes, "Marginal Fit of Castable Ceramic (Dicor) Crowns", MS Thesis, University of North Carolina, 1986.
10. K.J. Anusavice, "Criteria for Selection of Restorative Materials: Properties vs. Technique Sensitivity", Quality Evaluations of Dental Restorations, K.J. Anusavice (ed), Quintessence, 1989.
11. K.A. Malament, D.G. Grossman, "Bonded vs Non-Bonded Dicor Crowns: A Four Year Report", J Dent Res, Vol.

71 (AADR Abstracts), Abstract 1720, 1992.

12. R. Christensen, G. Christensen, "Service Potential of All-Ceramic Fixed Prostheses in Areas of Varying Risk", J Dent Res, Vol. 71 (AADR Abstracts), Abstract 1716, 1992.

13. E.D. Rekow, "A Review of the Developments in Dental CAD/CAM Systems", Current Science: Current Opinion in Prosthodontics, Vol. 2, pp. 25-33, 1992.

14. B.R. Lawn, Fracture of Brittle Solids, Second Edition, Cambridge University Press, in press.

15. J.R. Kelly, S.D. Campbell, H.K. Bowen, "Fracture-Surface Analysis of Dental Ceramics", J Prosth Dent, Vol. 62, pp. 536-541, 1989.

16. J.R. Kelly, R. Giordano, R.L. Pober, M.J. Cima, "Fracture Surface Analysis of Dental Ceramics: Clinically Failed Restorations", Int J Prosthodont, Vol. 3, pp. 430-440, 1990.

17. K.J. Anusavice, S. Hu, B. Hojjatie, "Tensile Stress in Glass-Ceramics Crowns Effect of Flaws and Cement Voids", J Dent Res, Vol. 70 (IADR Abstracts), Abstract 1343, 1991.

18. S. Scherrer, W.G. deRijk, "Factors in the Fracture Resistance of Posterior All-Ceramic Crowns", J Dent Res, Vol. 70 (IADR Abstracts), Abstract 1342, 1991.

19. R.W. Rice, "Ceramic Fracture Features, Observations, Mechanisms, and Uses", Fractography of Ceramics and Metal Failures, ASME STP 827, AM Soc for Testing and Materials, pp. 5-103, 1984.

20. R.W. Rice, J.J. Mecholoski Jr. "The Nature of strength Controlling Machining Flaws in Ceramics", The Science of Ceramics Machining and Surface Finish II, MBS 526, pp. 351-378, 1979.

21. J.R. Kelly, H. Lüthy, A. Gougoulakis, R.L. Pober, W.H. Mörmann, "Machining Effects on Feldspathic Porcelain and Glass Ceramics: Fractographic Analysis", Proceedings, International Symposium on Computer Restorations, WH Mörman (ed) Quintessence, pp. 253-274, 1991.

22. E.D. Rekow, "Dental CAD/CAM Systems - What is the State of the Art?", JADA, Vol. 122, No. 13, pp. 42-48, 1991.

23. R van Noort, "Dental Materials: 1990 Literature Review, J Dent, 19, 327-351, 1991.

24. D.G. Grossman, "Structure and Physical Properties of Dicor-MGC Class-Ceramics", Proceedings, International Symposium on Computer Restorations, W.H. Mörmann (ed), Quintessence, pp. 103-117, 1991.

25. S. Jahanmir, L.K. Ives, A.W. Ruff, M.B. Peterson, Ceramic Machining: Assessment of Current Practice and Research Needs in the United States, NIST Report SP-834, 1992.

26. G.E.P. Box, W.G. Hunter, J.S. Hunter, Statistics for Experimenters: An Introduction to Design, Data Analysis, and Model Building, J Wiley & Sons, 1978.

27. M. Braden, "Heat Conduction in Normal Human Teeth", Arch Oral Biol, Vol. 9, pp. 279-486, 1964.

TURNING OF FIBER AND PARTICLE REINFORCED ALUMINUM

K. WEINERT and D. BIERMANN
University of Dortmund, Dortmund, Germany

The main problem for the conventional machining of metal matrix composites (MMC) is the tool wear which is caused by hard and abrasive reinforcements. To find suitable cutting tool materials, several aluminium matrix composites have been machined with different tools: cemented carbides, coated cemented carbides, polycrystalline diamond (PCD) and a CVD-diamond coating on cemented carbide and on Si_3N_4-ceramic. The analysis of tool wear has shown that there are some basic rules concerning wear rate and the relationship between hardness and grain size of the reinforcement and the hard phases of the cutting tool material. Cutting tool materials which are suitable for different aluminium matrix composites have been tested with a variation of cutting parameters.

1   Introduction

In comparison to conventional materials metal matrix composites have many advantages, for example excellent strength-to-weight ratios, increased stiffness and wear resistance. With continuing improvements in process technology MMCs, particularly short fibre and particle reinforced aluminium alloys, have become cost competitive with conventional materials. But to expand the application of these materials cutting and finishing operations also have to be investigated. For conventional machining like turning, milling, drilling etc., extensive tool wear is the main problem.

2   Test Materials and Cutting Tools

During the investigations several composites with a matrix of aluminium (AlMg3, AlMgSi1Mn,

AlMg1SiCu, AlSi12CuMgNi) and a reinforcement of SiC- and B_4C-particles or δ-Al_2O_3-short fibres, were machined (Table 1).

An important point for the machinability of MMCs is to find suitable cutting tool materials. Therefore cemented carbide with different grain sizes and coatings, polycrystalline diamonds (PCD) and a CVD-diamond coating on cemented carbide and on Si_3N_4-ceramic have been investigated. For all turning tests a neutral tool holder with inserts of the geometry TPUN 1603 (clearance angle $\alpha = 11°$, rake angle $\gamma = 0°$ and $6°$, entering angle $\chi = 90°$, nose radius r = 0.4 and 0.8 mm) have been used. The turning tests have been carried out on a CNC-lathe. Figure 1 shows the hardness of the reinforcement materials and the cutting tool materials. It shows that SiC and B_4C particles are harder than all cutting tool materials excluding PCD.

Table 1: Test materials

Matrix	Reinforcement	Volume fraction [vol. %]	Particle size/ fibre size
AlSi12CuMgNi	δ-Al_2O_3	20	d=3µm l=0,05-0,1mm
AlMgSi1Mn	SiC	20	d(50)=13µm
AlMg1SiCu	SiC	25	d(50)=21µm
AlMg3	B_4C	10	d(50)=13µm

d: diameter; l: length; d(50): mean grain size
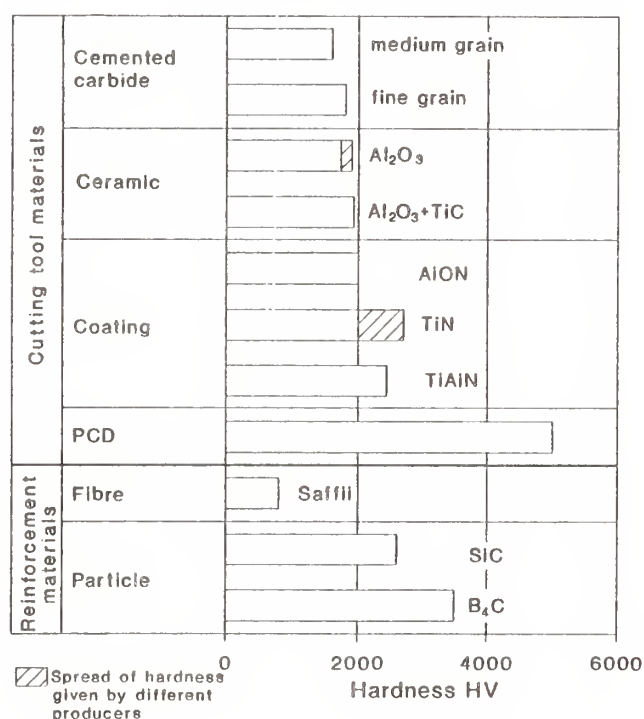
Fig. 1: Hardness of cutting and reinforcement materials

3 Tool Wear

Selection of the cutting tool material is fundamental in determining the extent and type of wear to be expexted. The wear processes can be divided into four main wear mechanisms: adhesion, abrasion, surface fatigue and tribochemical reaction (1). The relative importance of these mechanisms for the tool wear of a machining process depends on many factors: work material, machining operation, cutting conditions, tool geometry etc.. From a tribological point of view figure 2 shows a schematic representation of the elements and parameters of a cutting process. Solid bodies are the different cutting materials which have been used. Counter bodies are the metal matrix composites. The surrounding medium is air. But in the cutting zone and in the contact area of chip and tool vacuum can be assumed (2). Interfacial medium can be particles from the solid body or counter body or particles of a chemical reaction between solid body, counter body and surrounding medium. Because of the thermal and mechanical activation during the cutting process chemical reactions are possible.

The wear process at the rake face and clearance face of the tool can be classified as sliding wear. It can be two-body wear, where the particles or short fibres are fixed in the metal matrix of the workpiece. Also possible is three-body wear, where the particles are trapped between the contact surfaces of solid body and counter body (figure 3).

The reasons for tool wear when machining metal matrix composites are the direct contact between the particles or fibres and the cutting edge and their relative motion to the rake and clearance face. Therefore, the hardness of the reinforcements is a dominant factor for tool wear.

438
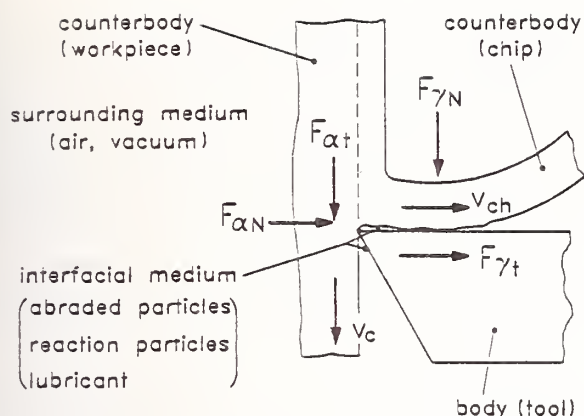
Fig. 2: Schematic representation of a cutting process

Fig. 4: Tool wear when machining reinforced aluminium
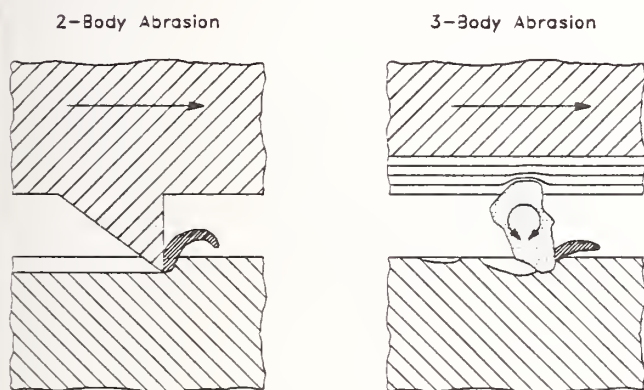
Fig. 3: Two-body and three-body wear (1)

3.1 Tool Wear of Cemented Carbides

Figure 4 shows the effect of cutting time on flank wear of a cemented carbide with medium grain when turning different reinforced aluminium alloys. The wear rate increases with hardness of the reinforcement material. Although the volume fraction of B_4C-particles is only 10 vol.% the wear rate is extremely high. When machining δ-Al_2O_3 short fibre reinforced aluminium the wear is relativly low although the matrix consist of an eutective aluminium alloy.

The topographies of the worn cutting edges lead to the conclusion that the main wear mechanism is abrasion (figure 5). But there is a great difference between the tool wear when machining δ-Al_2O_3
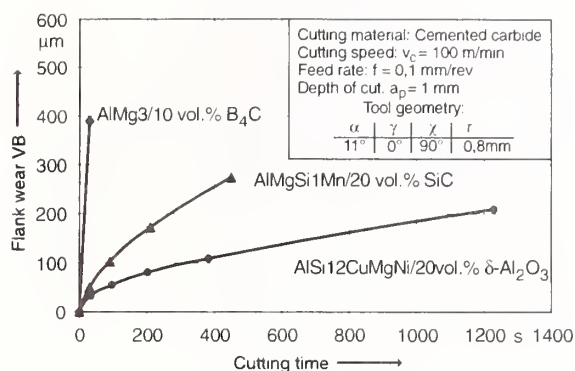
reinforced aluminium or SiC and B_4C reinforced aluminium. In the first case the hardness of the reinforcement is lower than the hardness of the WC-grains of cemented carbides. Therefore the δ-Al_2O_3 fibres or fractions of them cannot abrade the cemented carbide by microcutting. But free WC-particles which are seperated by micro-cracking and fatigue from the cemented carbide insert can act like a polishing compound between the chip, workpiece and the cutting tool. In the case of SiC and B_4C the hardness is higher than the WC-grains of cemented carbides. Therefore the cemented carbides are abraded by micro-cutting which is indicated by the grooves at the clearance face. For the machining of δ-Al_2O_3 rein-forced aluminium the wear resistance of fine grained cemented carbide is improved against the standard medium grain. The reason for this result is the higher toughness of the fine grained cemented carbide by which the resistance against microcracking and fatigue can be improved. In the case of SiC or B_4C reinforced aluminium the influence of the grain size of cemented carbide on the flank wear rate is reversed. The main wear mechanism is abrasion by microcutting. Therefore, wear rate can be decreased by using coarse grained cemented carbide (3).

439

AlSi12Cu MgNi/
20 vol.% δ-Al$_2$O$_3$

AlMgSi1Mn/
20 vol.% SiC

AlMg3/10 vol.% B$_4$C
10 μm

Cutting material: Cemented carbide
(medium grain)

Cutting speed: v_c= 100 m/min
Depth of cut: a_p= 1 mm
Feed rate: f = 0,1 mm/rev

Tool geometry:

α	γ	χ	r
11°	0°	90°	0,8mm
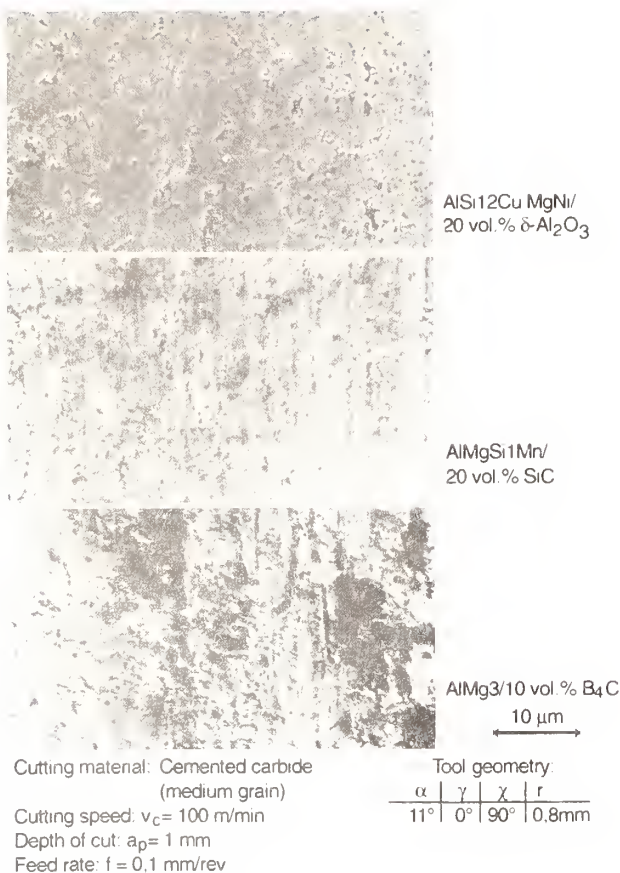
Fig. 5: SEM photographs of the flank wear of cemented carbides used for cutting reinforced aluminium

3.2 Tool Wear of TiAlN-Coated Cemented Carbides

The investigation for machining reinforced aluminium alloys with different cutting tool materials has shown that for turning SiC or B$_4$C particle reinforced aluminium neither ceramics nor the different coatings on cemented carbide (AlON, TiN, TiAlN) offer advantages in relation to uncoated cemented carbides (4). But for turning δ-Al$_2$O$_3$ short fibre reinforced aluminium TiAlN-coated cemented carbides are suitable. Corresponding to the results when turning δ-Al$_2$O$_3$ reinforced aluminium with uncoated cemented carbides, the wear rate of the TiAlN-coated fine grained cemented carbide is lower than for the medium grained material (4, 5). Because of the

good results of TiAlN-coating for machining δ-Al$_2$O$_3$ reinforced aluminium additional experiments with various cutting parameters have been carried out. As to the wear rate, the results of these investigations are summarized in figure 6. The increase of feed rate and use of a coolant have almost no influence on the tool wear. But the wear rate increases rapidly with an increase in cutting speed. For turning with cutting speeds up to v_c = 250 m/min, the wear rate is relative low and a cutting tool life of 15 minutes for a flank wear limit of VB = 0.2 mm is reachable. Although the tool life of TiAlN-coated cemented carbide at these cutting conditions is lower than for PCD, the application of this coating can be suitable because of the cost of PCD tools, particularly for geometrically complex tools like drilling tools.
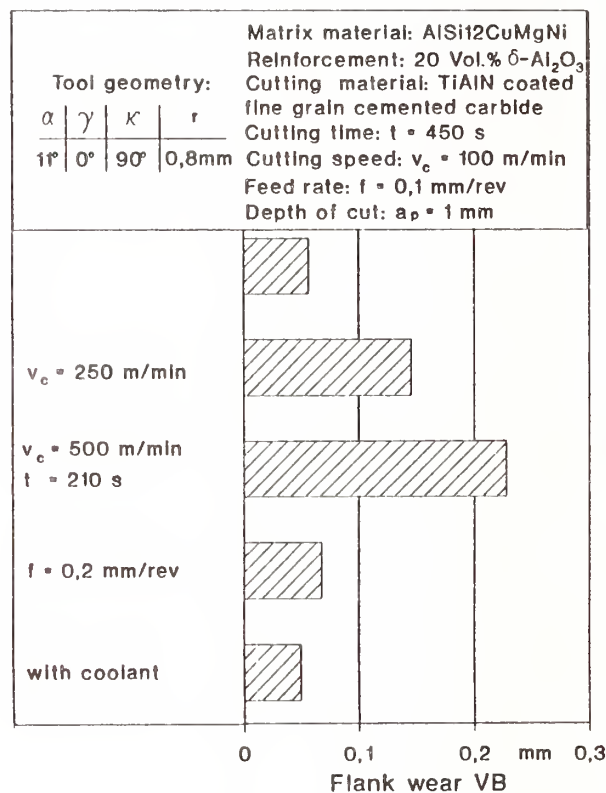
Fig. 6: Tool wear when machining δ-Al$_2$O$_3$ reinforced aluminium with TiAlN-coated fine grained cemented carbide

3.3   Tool wear of PCD

With regard to the wear rate the best results for machining different reinforced aluminium alloys have been achieved with PCD (5). Some modifications of PCD inserts, different grain sizes (PCD 010: 10 µm; PCD 025: 25 µm), polished insert and a positive rake angle $\gamma = 6°$ have been tested to optimize the application of PCD tools for turning operations. Figure 7 shows the development of wear rate of different PCD tools for the machining of SiC and B_4C reinforced aluminium.

When turning SiC or B_4C reinforced aluminium the wear rate decreases with the application of coarse grained PCD 025. Also the positive rake angle and the polishing of the PCD insert reduce the wear rate. The lowest wear rate can be achieved with PCD inserts including all above mentioned modifications. The influence of polishing and positive rake angle on tool wear can be explained by the reduction of friction that leads to lower cutting temperatures and cutting forces. Therefore, the thermal and mechanical load on the PCD tool is reduced.

Figures 8 and 9 show SEM photographs of the worn cutting edges. The PCD inserts used for cutting SiC reinforced aluminium exhibit rough surfaces at the worn rake and clearance face. The wear of the PCD 025 insert shows no grooves and at the rake face of the PCD 010 tool there are only weak grooves visible. After the machining of B_4C reinforced aluminium the topography of the wear land shows grooves especially at the rake face.

The fact that tool wear is less when using coarse grained PCD corresponds to the results for turning an aluminium alloy with 18% silicon and quartz reinforced epoxy (6). Also an investigation for grinding PCD tools has shown that the abrasion of PCD increases with the decrease of the PCD grain (7). Because there is only a small difference in hardness and toughness between PCD 010 and PCD 025 the explanation for the results cannot be given by the properties of the PCDs. In the following two mechanisms are proposed:
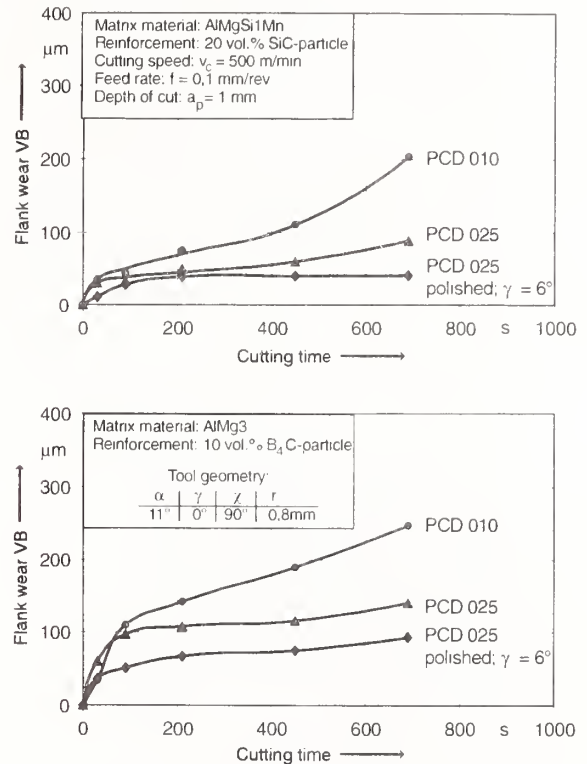
Fig. 7:   Tool wear when turning SiC and B_4C particle reinforced alumminium with different PCD inserts

a)   The wear mechanism corresponds to the observed mechanism for cutting SiC and B_4C reinforced aluminium with cemented carbide. The wear resistance of PCD 025 is improved compared to PCD 010 because the grains are larger than the reinforcement particles of the composites. Therefore, the wear resistance of PCD 025 is improved against an abrasion wear by microcutting. This argument is supported by the results of the investigations about the wear mechanisms when machining unreinforced aluminium (AlSi12) with PCD (8). In this case the main wear

441

mechanism is abrasion which produces grooves on the PCD tools. This is refered to the formation of alumina at the tool which could be hard enough to produce grooving wear.

b) Because of the lower hardness of SiC and B_4C compared to PCD, formation of the wear is produced by microcracking and fatigue. Free PCD particles lead to grooves at the inserts. This is underlined by the different dimensions of the grooves depending on the PCD grain size (compare figure 9).
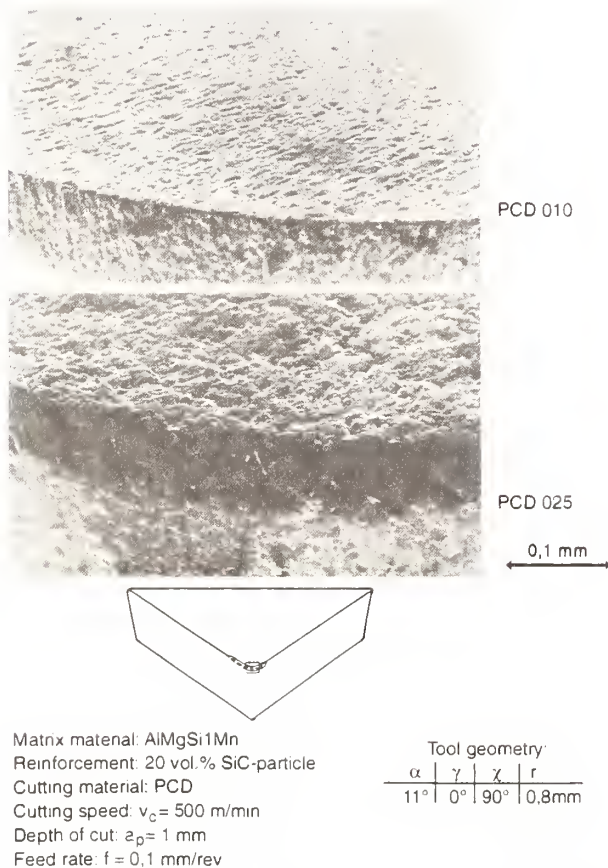
PCD 010

PCD 025

0,1 mm

Matrix material: AlMgSi1Mn
Reinforcement: 20 vol.% SiC-particle
Cutting material: PCD
Cutting speed: v_c = 500 m/min
Depth of cut: a_p= 1 mm
Feed rate: f = 0,1 mm/rev

Tool geometry:			
α	γ	χ	r
11°	0°	90°	0,8mm

Fig. 8: SEM photographs of PCD inserts used for cutting SiC reinforced aluminium

PCD 010

PCD 025

0,1 mm

Matrix material: AlMg3
Reinforcement: 10 vol.% B_4C-particle
Cutting material: PCD
Cutting speed: v_c = 500 m/min
Depth of cut: a_p= 1 mm
Feed rate: f = 0,1 mm/rev

Tool geometry:			
α	γ	χ	r
11°	0°	90°	0,8mm
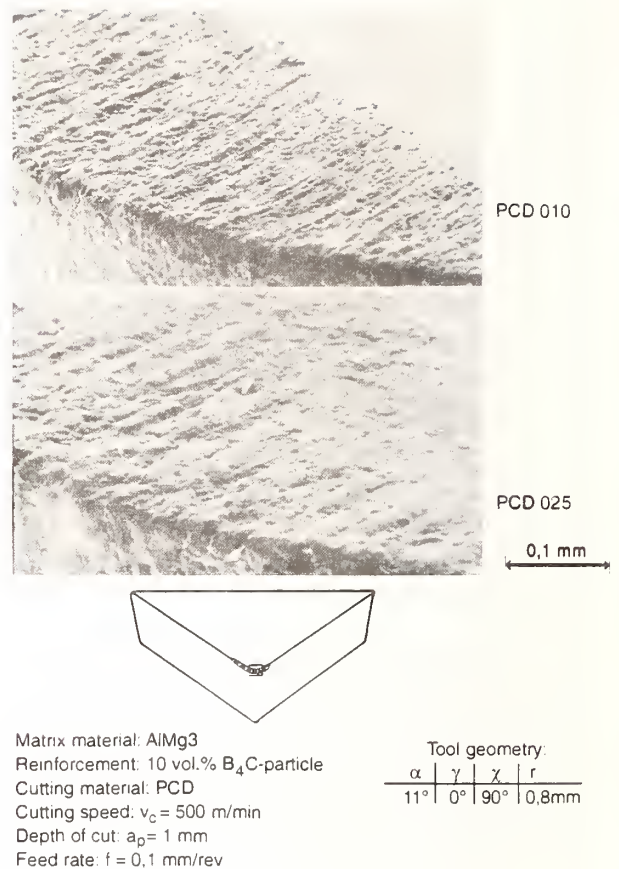
Fig. 9: SEM photographs of PCD inserts used for cutting B_4C reinforced aluminium

3.4 Tool Wear of CVD-Diamond Coated Tools

The development of CVD-diamond coatings for cutting tools leads to promising applications for machining extremely abrasive materials of low structural coherence, such as carbide and ceramic green compacts, but also plastics and certain types of Al-Si alloys (9). Also machining of MMCs could be an field of application for diamond coated tools. Especially for geometrically complex tools this coating could be a viable alternative to PCD tools. Substrate materials should contain carbide forming elements like tungsten, tantalum, titanium and zirconium to support the formation of diamond crystals. Si_3N_4-

ceramic is suitable as substrate material for diamond coating (10).

First investigations for the inset of CVD-diamond coated cemented carbides and Si_3N_4-ceramics have been carried out in cooperation with a producer of diamond coatings. Figure 10 shows a SEM photograph of the CVD-diamond coating on Si_3N_4-ceramic substrate. Because of the crystallization during the coating process the surface of the diamond coating is rough. Single diamond crystals are visible.
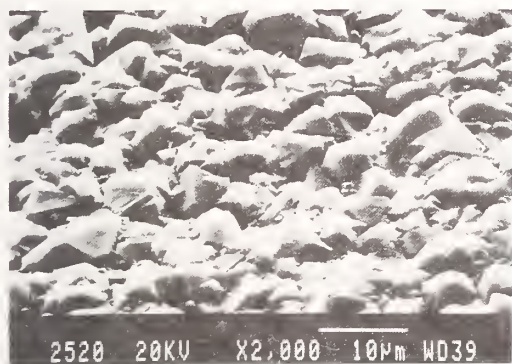
Fig. 10: SEM photograph of a CVD-diamond coating on Si_3N_4-ceramic

Compared to the machining of δ-Al_2O_3 or SiC reinforced aluminium with uncoated cemented carbide, tool wear is reduced by the CVD-diamond coating (figure 11). Particularly, the diamond coating on a Si_3N_4-ceramic substrate leads to a very low tool wear when machining SiC reinforced aluminium. For turning B_4C reinforced aluminium the diamond coating is unsuitable, because the coating has been abraded after a few seconds cutting time.

Figure 12 shows SEM photographs of the worn diamond coated Si_3N_4-ceramic inserts used for turning δ-Al_2O_3 and SiC reinforced aluminium. The flank wear is very low for both inserts. Although δ-Al_2O_3 reinforced aluminium produces a lower wear rate with uncoated cemented carbides than SiC reinforced aluminium, the results for turning with diamond coated Si_3N_4-

ceramic are reversed. The flank wear at the worn cutting edge after machining δ-Al_2O_3 reinforced aluminium is very smooth and shows only polishing of the diamond coating. But at the transition of rake to clearance face there are some cracks and particularly bursts at the rake face. At the insert used for cutting SiC reinforced aluminium there is almost no wear after a cutting time of t = 11.5 min. Only a slight abrasion of diamond crystals at the cutting edge is visible.
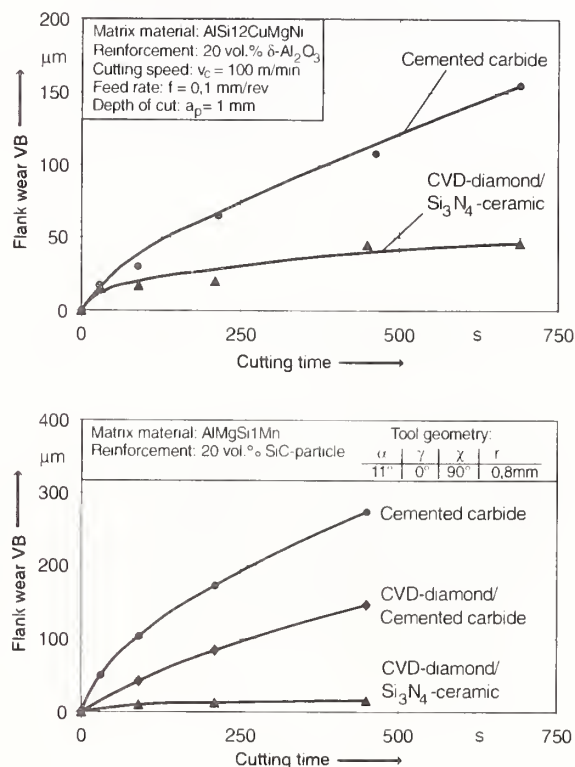
Fig. 11: Tool wear when machining reinforced aluminium with CVD-diammond coated tools

The results for turning MMCs with diamond coated tools are very promising and there are still possibilities to improve the wear resistance of the diamond coating, for example by increasing of the coating thickness or by polishing the diamond coating.

AlSi12CuMgNi/
20 vol.% δ-Al$_2$O$_3$

AlMgSi1Mn/
20 vol.% SiC

50 μm

Cutting material: CVD-diamond/
Si$_3$N$_4$-ceramic
Cutting speed: v$_c$ = 100 m/min
Depth of cut: a$_p$ = 1 mm
Feed rate: f = 0.1 mm/rev

Tool geometry			
α	γ	χ	r
11°	0°	90°	0.8mm
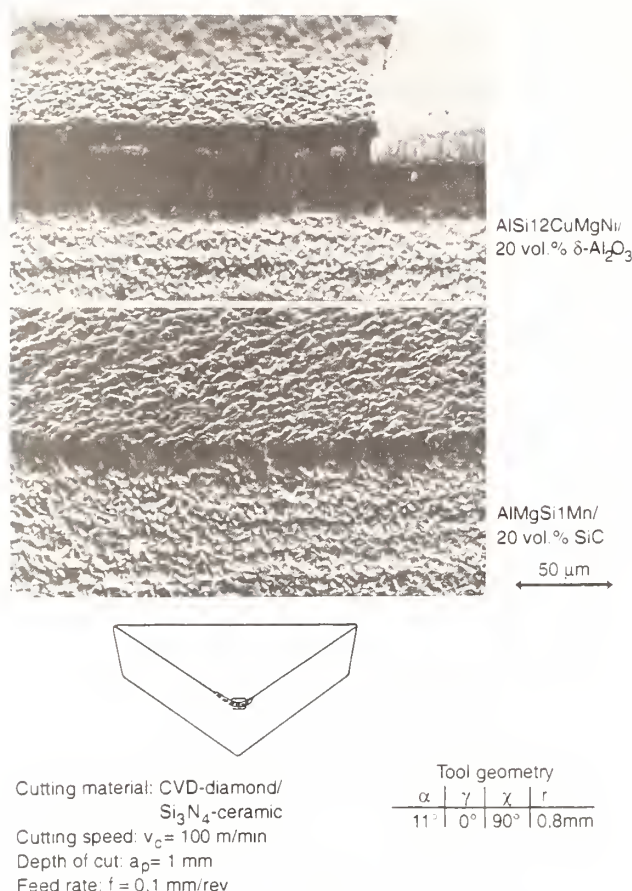
Fig. 12:   SEM photographs of CVD-diamond coated Si$_3$N$_4$-ceramic used for cutting reinforced aluminium

wear decreases with an increase of toughness of the cemented carbides.

Using a TiAlN-coating on cemented carbide tool wear can be reduced for cutting δ-Al$_2$O$_3$ reinforced aluminium. When turning at cutting speeds up to v$_c$ = 250 m/min wear rate is relative low. Although, the tool life of the TiAlN-coated cemented carbide is lower than for PCD, the use of this coating can be suitable because of the cost of PCD tools, particularly for geometrically complex tools like drilling tools.

For the application of PCD to machining SiC or B$_4$C reinforced aluminium this study has shown that tool wear rate decreases with increasing the grain size of PCD. Also a positive rake angle and the polishing of the PCD insert reduce the wear rate. The lowest wear rate can be achieved with PCD inserts which include all three modifications.

The results for turning MMCs with diamond coated tools are very promising. Compared to the machining of δ-Al$_2$O$_3$ or SiC reinforced aluminium with uncoated cemented carbide, the tool wear is seriously reduced by using CVD-diamond coating, particularly the diamond coating on a Si$_3$N$_4$-ceramic substrate led to a very low tool wear when machining SiC reinforced aluminium.

References

(1)   K.-H. Zum Gahr, "Microstructure and Wear of Materials", Tribology Series, Vol. 10, Elsevier Amsterdam, 1987.

(2)   K.-H. Kloos, "Technische Verschleißvorgänge in tribologischen Systemen und deren Simulation", Reibung und Verschleiß bei metallischen und nichtmetallischen Werkstoffen, DGM Informationsgesellschaft Verlag, 1990, publisher Prof. K.-H. Zum Gahr.

4   Conclusions

This investigation has shown that different cutting tool materials should be used for turning MMCs depending on the hardness of the reinforcement. When machining SiC or B$_4$C particle reinforced aluminium with cemented carbides, the tool wear is produced by microcutting, because the reinforcements are harder than the hardphases of cemented carbide. To reduce the tool wear, the grain size of the hardphases should be larger than the size of the reinforcement. The tool wear is caused by microcracking and fatigue for turning δ-Al$_2$O$_3$ reinforced aluminium. Therefore, tool

(3)   D. Biermann, A. Fischer and D. Meister,
        "Verschleißerscheinungsformen bei der
        spanenden Bearbeitung von Verbundwerk-
        stoffen auf Aluminiumbasis", Tagungs-
        band zu dem Fachgespräch "Neue Werk-
        stoffe -Anforderungen an die Schneide",
        Universität Dortmund, 09-12 June 1992.

(4)   L. Cronjäger and D. Biermann, "Turning
        of Metal Matrix Composites", Proceedings
        of Euromat 91, European Conference on
        Advanced Materials and Processes, Uni-
        versity of Cambridge, 22-24 July 1991.

(5)   L. Cronjäger, D. Meister and D. Bier-
        mann, "Spanende Bearbeitung von faser-
        und partikelverstärkten Leichtmetall-Ver-
        bundwerkstoffen", Metall, Vol. 46, No.
        10, pp. 1010-1017, 1992.

(6)   P.J. Heath and M.E. Aytacoglu, "Erzeu-
        gung und Beurteilung von Schneidkanten
        an Syndite PKD-Werkzeugen", Diamant
        Information M38, De Beers, Düsseldorf,
        1985.

(7)   I.M. Kenter, "Einfluß der Prozeßparameter
        auf den Materialabtrag beim Schleifen
        von PKD", IDR, No.4, pp. 246-252, 1991.

(8)   W. König and A. Bömcke, "Verschleiß-
        mechanismen beim Zerspanen mit PKD",
        IDR, No. 2, pp. 78-87, 1990.

(9)   T. Leyendecker, O. Lemmer, A. Jürgens
        and S. Esser, "Industrial Application of
        Crystalline Diamond Coated Tools", Sur-
        face and Coatings Technology, Elsevier
        Sequoia, Lausanne, No. 48, pp. 253-260,
        1991.

(10)   E. Lugscheider and U. Müller, "Kristalline
        Diamantschichten auf Schneidwerkzeu-
        gen", Ingenieur-Werkstoffe, Vol. 4, No.
        7/8, pp.42-44, 1992.

TURNING OF CARBON AND GLASS FIBER HYBRID CLOTH COMPOSITE MATERIAL

N. L. CUPINI
UNICAMP/FEM/DEF, Campinas, Brazil

J. R. FERREIRA
EFEI/IEM/DPR, Itajuba, Brazil

Experiments were carried out to study the performance of different tool materials, like ceramics, SIALON, whisker-reinforced ceramic, cemented carbide, cubic boron nitrite (CBN), and diamond (PCD). They were tested in turning of carbon and glass fiber reinforced fenolic resin composite. Two different workpiece shapes were used: laminated plate and filament wound tube. During the experiments, tool wear, surface roughness, and feed force were measured, under several cutting lengths, cutting speed, and fiber directions in composite. Experimental results showed that, due to the great influence of tool wear on workpiece surface roughness, only diamond tools are suitable for use in finish turning. In rough turning, the cemented carbide tools showed to be the best solution. Although, it showed larger wear than diamond, the cost/benefit ratio is much lower and special precautions are not necessary.

INTRODUCTION

The use of composite materials based on fiber reinforced plastics (FRP) is increasing, specially in aeronautic, aerospace, and automotive industries (1). As a consequence, new processes must be developed to ensure high precision and good surface quality of the components (2).

The FRP are mold mainly in plates, laminated and sheet shapes. Because of this, drilling and cutting with abrasive discs and diamond saws are more frequent among the large number of machining operations that can be used (3). Only a few number of papers and reports on turning, milling and grinding of FRP can be found. The main goal of this work is to contribute with alternative applications of FRP, particularly for the case of turning (4).

This work presents some turning experiments carried out in carbon and glass fiber reinforced fenolic resin (CGFRR). Laminated plates and filament wound tubes were used as samples, as shown in Figure 1. The experiments were carried out to evaluate tool wear, surface roughness, and feed force during several cutting lengths (cutting times) for different tool materials. The influence of the relative fiber direction and cutting speed were also evaluated.

EXPERIMENTAL PROCEDURE

TOOLS, MATERIALS AND EQUIPMENT

The properties of the CGFRR tested were: carbon fiber (70%) and glass fiber (30%) hybrid cloth; fenolic resin (35 to 40% weight); 1,4 to 1,5 g/cm^3 density.

Cemented carbide (ISO K10), ceramic $(Al_2O_3 + ZrO_2)$, ceramic $(Al_2O_3 + TiC)$, whisker-reinforced ceramic $(Al_2O_3 + SiC)$, SIALON $(Al_2O_3 + Si_3N_4)$, cubic boron nitrite (CBN), and diamond (PCD) tools were used. The carbide, CBN, and diamond tools had the geometry ISO SNUN 120412. The geometry of the ceramic tools was SNGN 120712.

Experiments were conducted in a CNC lathe with 30 HP power. The feed force were measured by a dynamometer. Tool wear and surface roughness were evaluated using conventional equipment, and a vacuum cleaner was used to remove the chip from the environment.

EXPERIMENTAL METHODS

Two sets of experiments were carried out:

a) FILAMENT WOUND TUBE

SECTION A-A

b) MACHINED TUBE SAMPLE OF LAMINATED PLATE

SECTION A-A
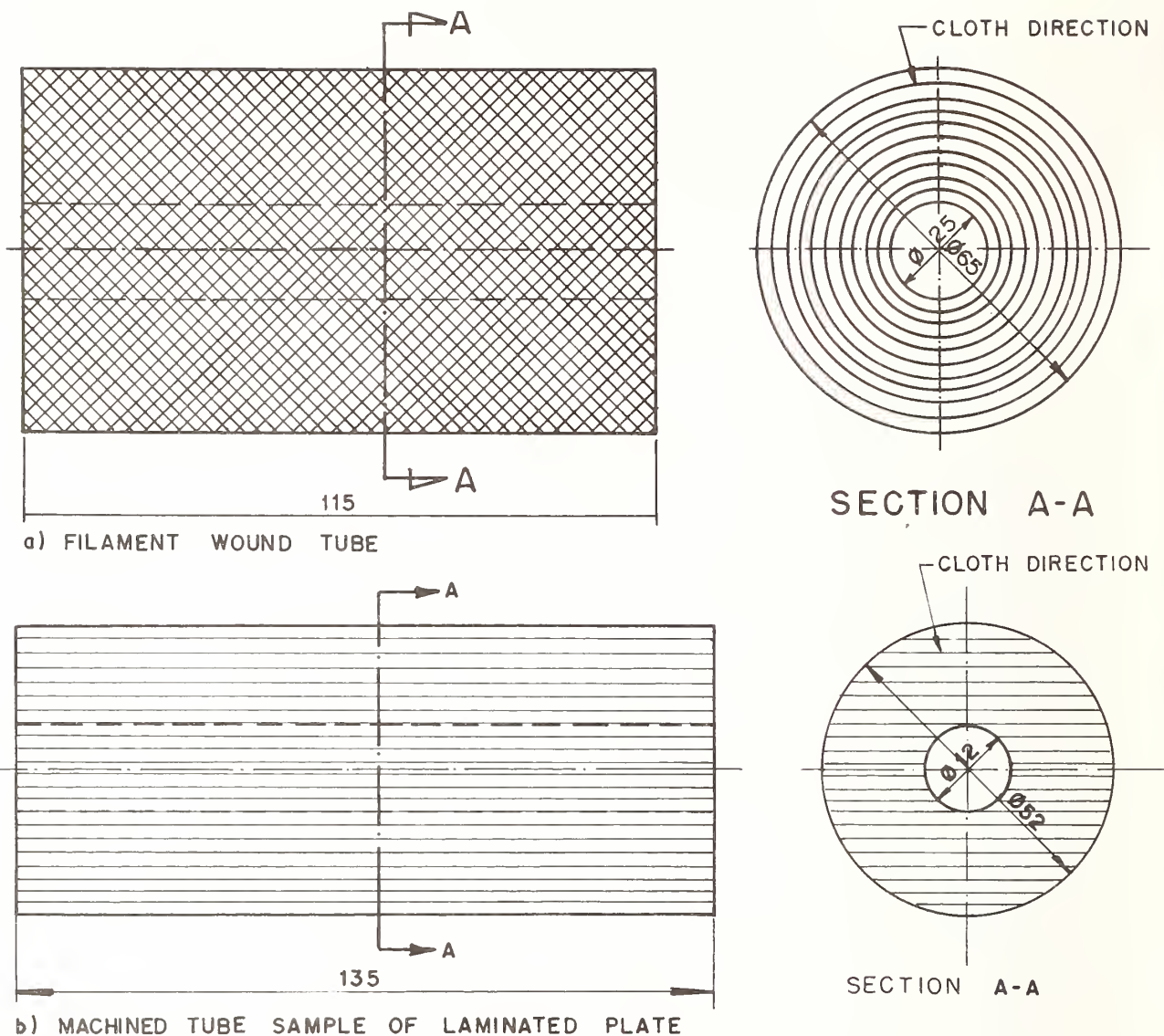
Figure 1 - Workpiece

wounded cloth with cutting conditions larger than those usually used, and laminated plate with usual cutting conditions (Figure 1).

In the first case, all tool materials were used to evaluate tool wear, surface roughness, and feed force for the following cutting conditions: cutting speed 320 m/min, feed 0.1 mm/rev, and depth cut 1.0 mm. This set of experiments was used only to classify the tool materials based on their cutting behavior.

In the second case, diamond and cemented carbide tools chosen in the first set of experiments were tested. The cemented carbide tool wear growth was observed for the following cutting conditions: cutting speeds 25, 100, 200, 320, and 450 m/min, feed 0.1 mm/rev, and depth of cut 1.0 mm. The obtained surface roughness after diamond tool tests was observed for the following cutting conditions:

cutting speed 200 m/min, depth of cut 1.0 mm, and three different feeds 0.1, 0.2, and 0.3 mm/rev.

RESULTS AND DISCUSSIONS

The tool wear growth for several cutting lengths are shown in Figure 2 for the first set of experiments. For all the ceramic tools, a very high tool wear rate was observed. The SIALON presented the highest wear rate and the whisker-reinforced ceramic the lowest one. The CBN presented a better behavior compared with ceramics and cemented carbides. On the other hand, diamond showed to be better then CBN. If the cost/benefit ratio is considered only for rough turning, the cemented carbide shows to be the best among all the tool materials tested.

In finish turning operation, the behavior of the tested tool materials varies as shown in Figure 3. As

448
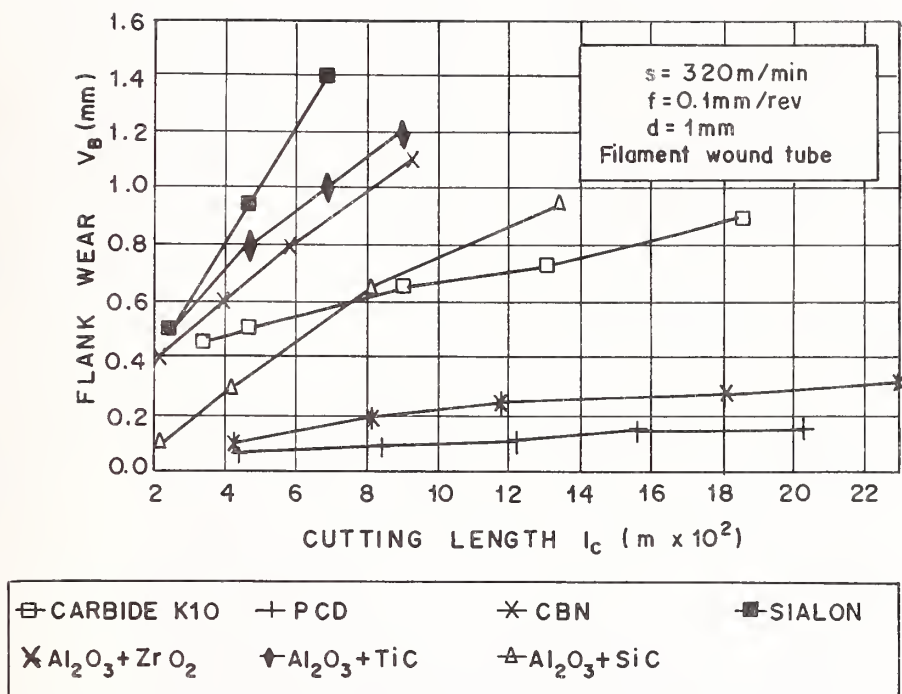
Figure 2 - Tool flank wear against cutting length.
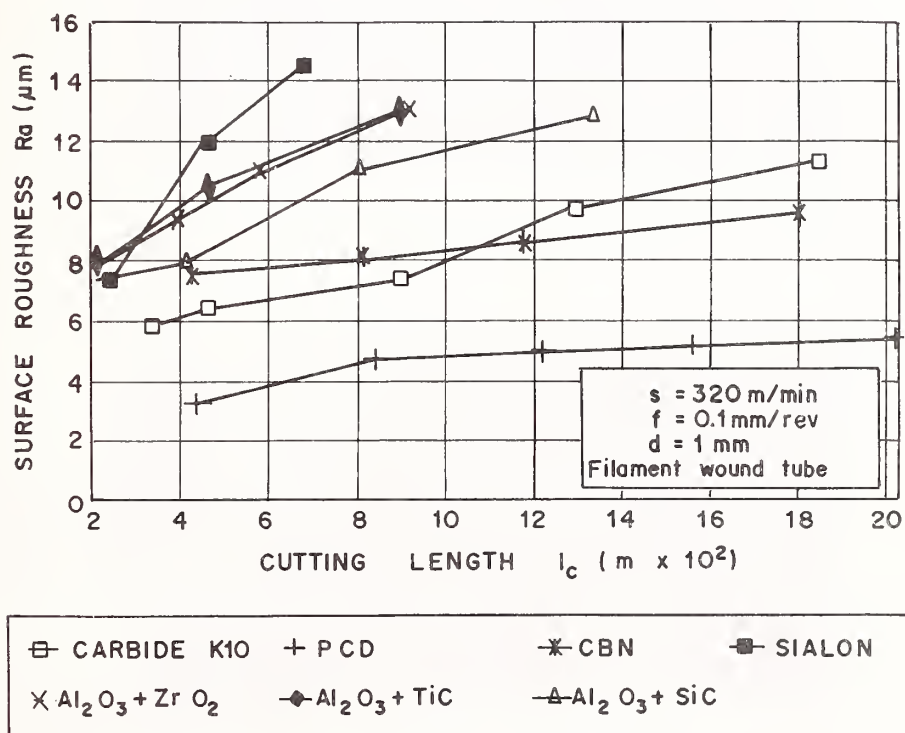
Figure 3 - Surface roughness (Ra) against cutting
          length.

449

the composite material presents fiber delamination and groove formation because of resin presence in FRP, the larger amount of wear larger incidence of fiber delamination and groove formation on the FRP resin and larger the influence on surface roughness. Because of this, the more wear resistant is the tool, the better is its behavior related to surface roughness. The results presented in Figure 3, shows that the best tool material in finish turning operation is the PCD.

It was also observed for all tool materials, that the average surface roughness (Ra) varies rather linearly with the cutting length. This could be explained by the fact that the abrasion is the only tool wear mechanism present. The polished flank surface, the absence of crater wear and, mainly the absence of groove wear, denotes that the active wear mechanism is mainly based on the high abrasivity of the composite material (Figure 4a). For ductile steels, where other wear mechanisms are present during machining, the resulting surface roughness is normally influenced by the groove wear variation (Figure 4b).
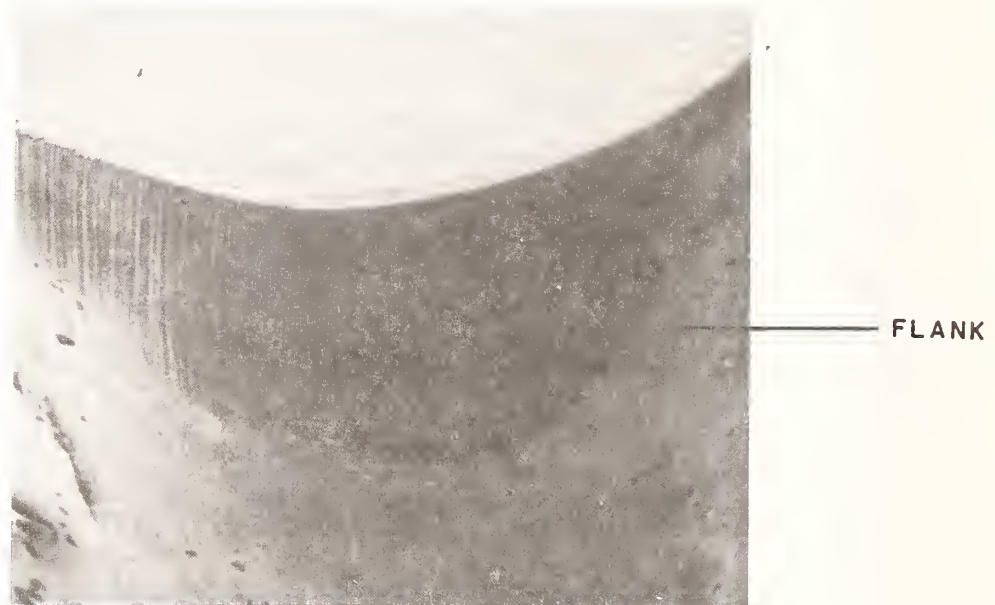
a) Composite material turning
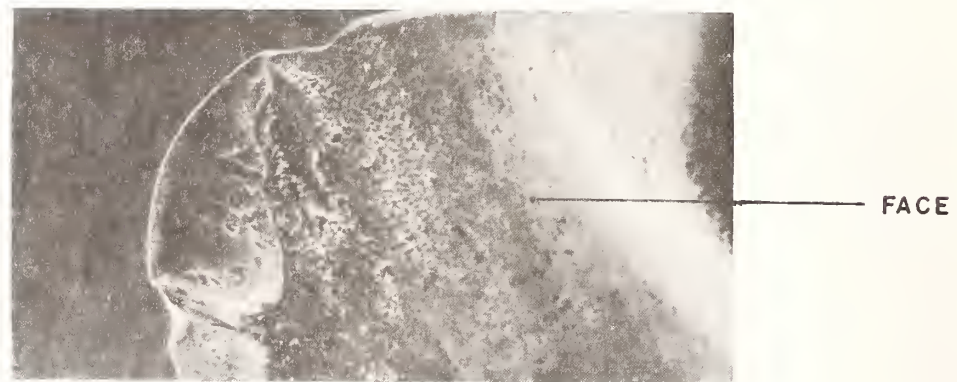
b) Ductile steels (SAE/AISI 1045) turning.

Figure 4 - Mechanism of tool wear

450

Figure 5 shows how the feed force increases with cutting length. For some tool materials the rate of increase of feed force is remarkable (SIALON and ceramics). For PCD and CBN, the feed force remains almost constant. On the other hand, it had been shown in Figure 2 how the flank wear varies with the cutting length. So, the variation of feed force could be explained by increasing of the flank wear with cutting length, and the absence of crater wear as shown in Figure 4a.

The feed force intensity for fresh tools, considered for PCD, was found to be close to 50 N. This level of feed force is in the range obtained for steels (5). It means that, despite of the low density of CGFRR, it require large forces for machining, probably because of its good mechanical properties.

For the second set of experiments, during the turning of laminated plate, the cemented carbide evaluated, and the influence of fiber direction on surface roughness for the case of PCD tools was tool wear growth during several cutting speeds was investigate.

Figure 6 shows how the cemented carbide tool wear vary with cutting speed. It can be observed that up to a cutting speed of 325 m/min, the flank wear increases slowly. For higher cutting speed, at least for 450 m/min, the flank wear increases morerapidly, because of lower tool wear heat resistence (5).

In Figure 7, it is possible to see that the surface roughness is maximum when the fibers have 45 and 225 angles with the cutting direction. This fact occurs because, due to the relative fiber position, the possibility of delamination increases as cutting time elapses. Also in Figure 7, it can be seen that there isa strong influence of feed, similar to turning of conventional materials.
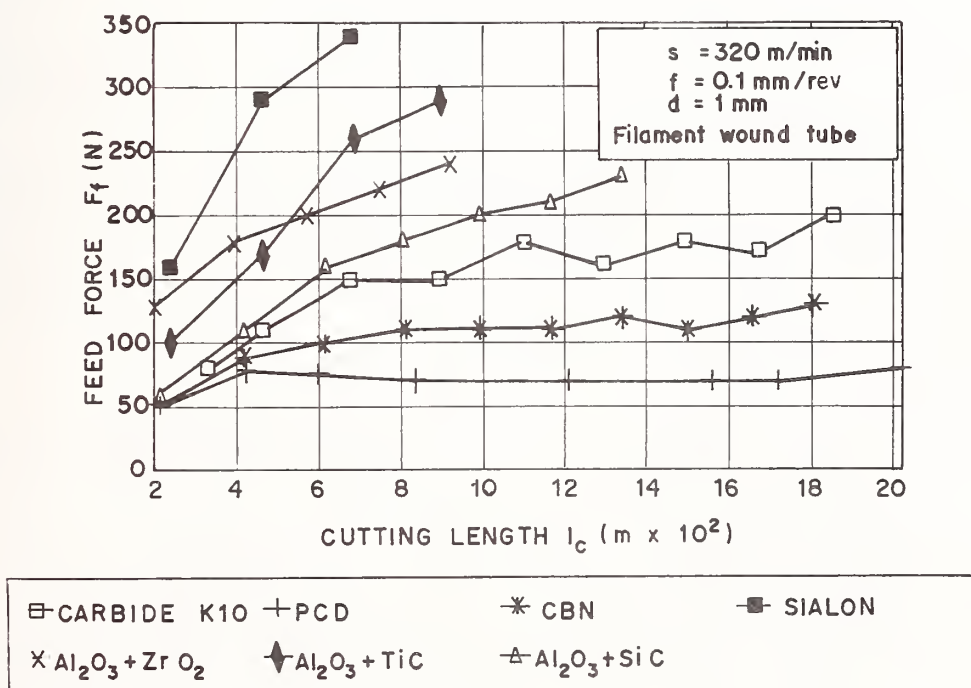
Figure 5 - Feed force against cutting length.
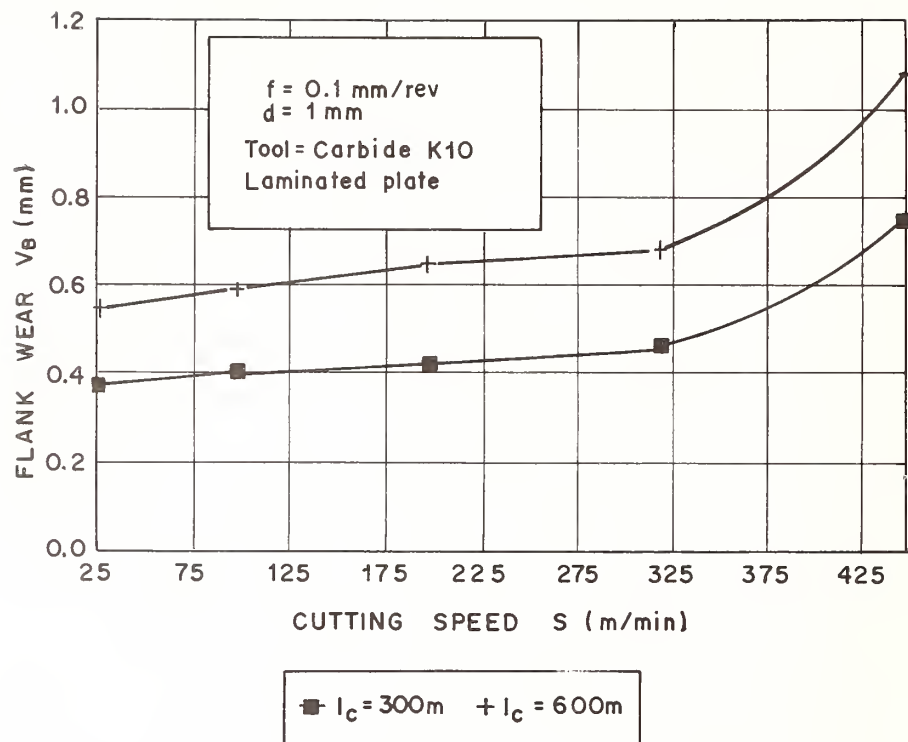
Figure 6 - Flank wear against cutting speed.
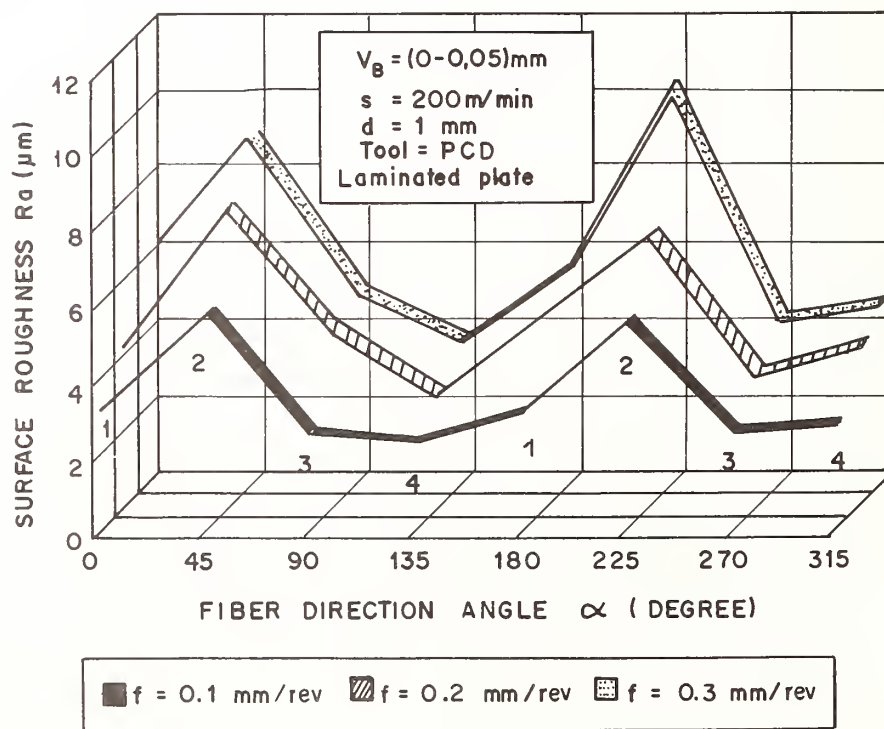
Figure 7 - Surface roughness (Ra) against fiber
direction angle.

452

CONCLUSIONS

Based on the results, it can be concluded that:

- The use of CBN and ceramic tools in the turning of composite materials is not feasible based on a technical and economical point of view.

- The workpiece surface roughness increases with the tool flank wear until the fiber delamination.

- A large scatter in surface roughness measurements was found, because of a great number of defects caused by delamination and groove formation. The origin of these is related to the relative direction of fibers with respect to the cutting directions.

- In finish turning operations, only the diamond tool can ensure a surface roughness in the range of 2.5 to 5.0 μm (Ra).

- For rough turning with cemented carbide tools, the optimum cutting speed is between 320 m/min and 450 m/min. For cutting speeds less then 320 m/min, the wear evoluton is not so different. For cutting speed higher then 450 m/min, large values of wear occurs very rapidly.

- In rough turning operations the use of carbide tools showed to be the best solution. In spite of presenting bigger wear when compared to diamond tool, it results in a better cost/benefit ratio; and when it is used, there is no necessity of special care.

- Despite of low density of CGFRR, it requires higher levels of cutting forces in the range of cutting forces used for steels.

- Because of flank wear and absence of crater wear, feed force increases remarkably with the wear evolution. Only for PCD and CBN tools, that are very wear resistant, no remarkably variation of feed force was observed.

REFERENCES

1. T. J. Reinhart, "Engineering Materials Handbook, Composites", ASM International, Vol.1, Ohio, 1987.

2. H. Takeshita, K. Wehara, "Cutting Mechanism of Some Composite Materials", Second International Metal Cutting Conference, Tokio University, Japan, 1985.

3. S. K. Malhotra, "High Steel Tool Wear Studies in Machining of Glass Fiber Reinforced Plastics", Wear, vol. 132, 1989.

4. U. E. Wunsch, G. Spur, "Turning of Fiber-Reinforced Plastics", Manufacturing Review, vol. 1, june of 1988.

5. D. Ferraresi, "Fundamentos da Usinagem dos Metais", Editora Edgard Blücher, São Paulo-Brasil, 1977.

6. Y. Hasegawa, "Characteristics of Tool Wear in Cutting GFRP", 5th International Conference on Production Engineering, Tokio, 1984.

7. A. Koplev, A. Lystrup, "The Cutting Process, Chips, and Cutting Forces in Machining CFRP", Composites, Vol. 14-4, 1983.

LASER-ASSISTED HOT MACHINING OF CERAMICS AND COMPOSITE MATERIALS

W. KONIG and A. K. ZABOKLICKI

Fraunhofer Institute of Production Technology, Aachen, Germany

Laser-assisted turning of ceramic contributes to the expansion of the range of methods which can be used to machine ceramic materials. It offers a greater degree of flexibility than grinding in terms of the geometry of functional surfaces of the part.

Parts and tools which are subjected to high levels of wear are clad with hard alloys such as stellite 6 for protection. The only options currently available to machine these hard alloys are grinding and electrical discharge machining (EDM). Laser-assisted milling thus offers a very promising complement and alternative.

The basic principles of laser-assisted hot machining processes will be explained in this contribution. Experimental results obtained during operations involving laser-assisted turning of ceramic (silicon-nitride), and laser-assisted milling of composites material (hot-work tool steel/stellite 6) will be compared and discussed and potential areas of application will be highlighted.

Introduction

Hot machining technology is enjoying a renaissance, thanks to progress in laser techniques. The flame-, friction- and resistance-heating media were used in this field at the beginning of the 20th century (1). Recently, tests have been carried out using plasma jet heating (1, 2). One disadvantage which these methods of heating have in common is that the power density of the heat source is generally insufficient to heat parts of the workpiece adequately. If the heat source is required to provide a pre-set power level, the heat transfer area must be large enough to heat the zone in front of the tool cutting edge to the appropriate temperature. The requirements for hot machining are fully met by the laser beam. The power density of the laser beam can reach values in excess of 10^6 W/cm^2. Additional benefits to be gained are the handling flexibility offered by the CO_2-laser and the Nd:YAG-laser which are equipped with a focusing-optical system and an optical fiber, respectively, and the ability to form the laser beam with the use of appropriate focusing optics (mirrors or lenses) onto different spot shapes of the point being machined.

Initial investigations into laser-assisted turning of various materials were undertaken a few years ago (3, 4). These studies indicate that laser-assisted turning of materials such as titanium- and nickel-base alloys decreases the cutting forces and the tool wear by 20% - 50%.

The results of preliminary investigations into laser-assisted turning of ceramic materials such as silicon-nitride are also available (5, 6, 7, 13).

In milling operations, in contrast to turning, the cutting edge is subjected to mechanical and thermal alternating stress. The highly dynamic stress is caused by the interrupted cut and by the changing chip thickness during the cutting operation. Thermally induced plastification of the material, using laser power, appears in reducing mechanical stress in machining to offer decisive advantages (8, 9).

455

Basic Principle of Laser-Assisted Hot Machining

Laser-assisted hot machining is carried out using a laser beam to heat the workpiece material selectively, i.e. heating only the chip cross-section, during the cutting operation, _Figure 1_.
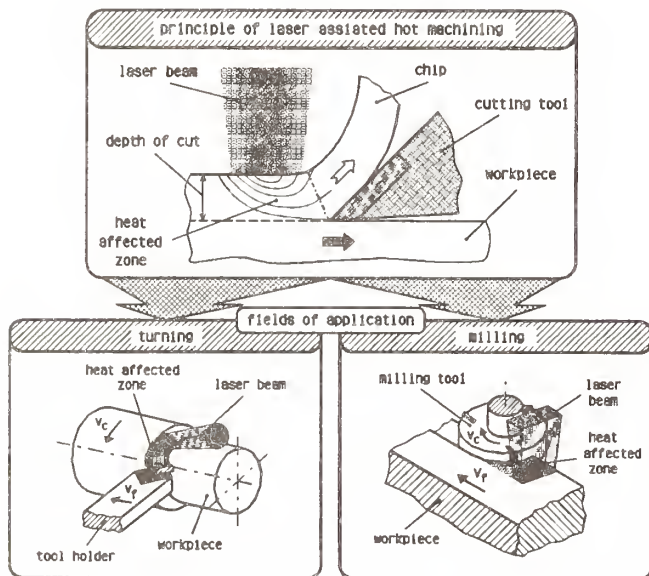
Figure 1: Principle and fields of application of laser-assisted hot machining

The feed movement of the workpiece causes a certain area to be continuously heated and subsequently removed by a tool cutting edge. The laser beam energy absorbed by the workpiece surface is converted into thermal energy and results in rapid heating and often, in localized melting of the outer layer, resulting in a steep temperature gradient. The temperature balance throughout the workpiece is effected by thermal conductivity. Knowledge of the local and temporal temperature progression at the surface and in the depth of cut is essential for the determination of the optimal cutting and, above all, of the laser beam parameters for the material removal rate required. The formation of isothermal areas in the workpiece can be determined using mathematical simulation models containing the solution of the thermal conductivity equation (4). The temperature of the surface produced and of the laser interaction point are of practical significance for hot machining. The process parameters such as laser beam intensity and interaction time must be selected so as to ensure that the temperature at a defined depth of cut

does not result in damage to the outer layer of the functional surface produced.

The two laser types now in common industrial use, CO_2- and increasingly Nd:YAG-laser can be used as heat sources.

Depending on the kinematics of the cutting operation, the workpiece moves with the cutting or feed rate in the same way as in, for example turning or milling operations in relation to the stationary or oscillating laser beam focal spot which has a defined geometry on the surface of the workpiece in front of the tool cutting edge (Figure 1). The temperature of the chip cross section directly in advance of the cutting edge is dependent on the volume removed and the energy introduced via the laser beam. The total cutting energy is converted largely into heat, due mainly to plastic strain in the shearing zone and to friction between the cutting edge and chip (10). The increase in total temperature in the area around the cutting edge, causes changes in the physical-mechanical properties of the material.

Metallic alloys and the silicon-nitride ceramics listed in _Figure 2_ are examples of materials which are particularly difficult to cut.
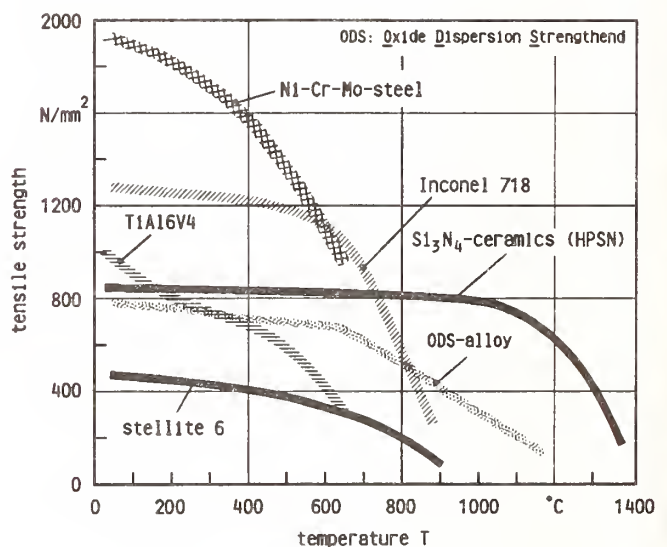
Figure 2: High-temperature strength of materials which are difficult to machine. (source: DIN, WL, AFNOR, Knotek)

However, tensile strength decreases with increasing temperature, which result in the plastification of the material, and consequently making the material considerably easier to cut by hot

machining operations.

Hot machining technology has the following advantages:

- decrease of cutting forces,
- reduction of tool wear,
- avoidance of tool breakage,
- use of inexpensive tool materials,
- decreased dynamic excitation (chatter vibration) and
- higher material removal rates.

Laser-Assisted Turning of Silicon-Nitride Ceramics

Silicon-nitride ceramics, by virtue of their combination of favourable characteristics such as low density, high level of hardness, good high-temperature strength at temperatures above 1000°C, as well as thermal and chemical resistance, are increasingly being used in mechanical applications.

Finish machining is necessary in most cases due to distortion, contraction and limited formability in hot-pressing or hot-isostatic-pressing operations carried out on silicon-nitride ceramics. Machining operations with geometrically undefined cutting edge, such as grinding or lapping are currently applied on an industrial scale in the manufacture of ceramic parts. These machining operations, however, are very time-consuming and are limited with respect to the range of geometries that can be produced. Attempts are, therefore, under way to improve other technologies such as laser-assisted turning to a sufficient degree to permit their use in the machining of ceramics, in order to obtain higher removal rates and to increase flexibility in terms of part geometry.

Machining silicon-nitride ceramics at room temperature with a defined cutting edge involves high tool wear; this process variant is consequently of little practical significance (11). When due account is taken of the temperature-dependent strength behaviour of silicon-nitride ceramics, material-oriented machining technology is, however, conceivable even for tools with a defined cutting edge (c.f. Figure 2). Since amorphous areas exist at the grain boundaries of the crystalline structure of silicon-nitride (12), partial plastifica-

tion of the material is to be expected; thereby providing the conditions necessary for chip formation (7, 13).

Test Procedure

The turning tests were carried out on machinery consisting of a two-carriage lathe and integrated 2.5 kW-CO_2- and 1.5 kW-Nd:YAG-laser beam source. One of the tool carriages on the lathe guides the beam, the other holds the tool, _Figure 3_.

Figure 3: Experimental set-up for laser-assisted turning.

The guidance system consists of a deflection and focusing optic. In contrast, the Nd:YAG-laser beam is guided to the machining point by a flexible optical fibre. The positioning of the focused laser beam directly in front of the cutting edge is variable in both cases. Two types of silicon-nitride were used for the turning tests:

- HPSN-ceramics (hot-pressed silicon-nitride) with a sample diameter of 30 mm and
- HIPSN-ceramics (hot-isostatic-pressed silicon-nitride) with a sample diameter of 10 mm.

The cutting tool materials in the turning tests were two polycrystalline tool materials: polycristalline diamond (PCD) and cubic born nitride (CBN) with negative tool cutting edge geometry.

Results and Discussion

The results of the turning experiments carried out

457

on silicon-nitride ceramics will be presented and discussed in the following.

Cutting Forces

The value of the cutting force components is an important measure by which to evaluate the behaviour of a material during a cutting operation. The cutting forces in laser-assisted turning operations are influenced to a great extent not only by process parameters such as cutting speed, feed rate and depth of cut but also by the temperature of the workpiece at the cutting zone.
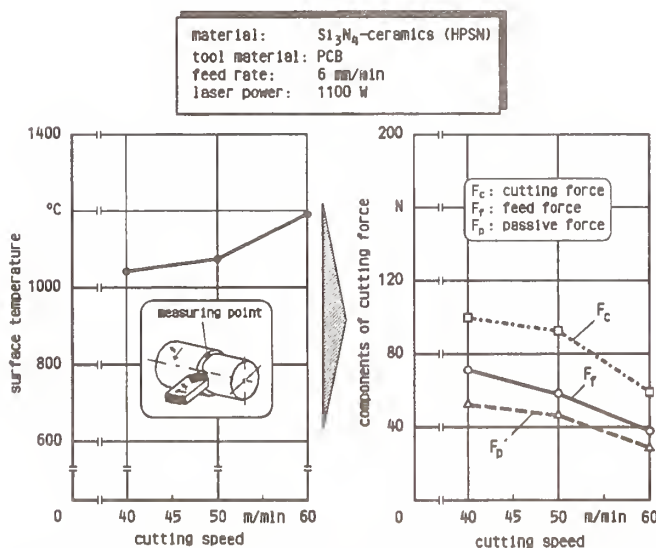
Figure 4: Machining temperature and cutting force components in dependence on cutting speed.

Figure 4 shows surface temperature and cutting force components (F_c: cutting force/direction of primary motion, F_f: feed force/direction of feed motion and F_p: passive force/perpendicular to the directions both of primary motion and of feed motion) as a function of cutting speed at constant CO_2-laser power. The workpiece surface temperature on the chamfer, at an angle of 90° in front of the tool cutting edge was measured by the two-color-pyrometer (temperature measuring range: 800-3000°C). The results shown are mean values of the temperature at the beginning and at the end of the turning process. The machining operation begins with a pre-heating phase during which the workpiece is heated to a surface temperature of approximately 1100°C in the area

around the first tool contact. The turning process begins once the initial temperature has been reached.

As shown in Figure 4, the surface temperature rises with increasing cutting speed. Both the laser interaction time and the time in which the same point of the workpiece surface is reached by the focal point of the laser drop as cutting speed is increased. This results in higher workpiece temperatures in the machining zone. The temperature gradient is likely to be steeper in the direction of chip thickness.

The cutting forces diminish as a result of the rise in temperature (Figure 4). This change in force (e.g. in the case of cutting force F_c by approximately 50 %) is attributed to increased temperature in the chip cross section and to sufficient softening of the workpiece.

The second important process parameter in turning operations is the feed rate. The influence exerted by this parameter on the surface temperature and the cutting force components is shown in *Figure 5*.
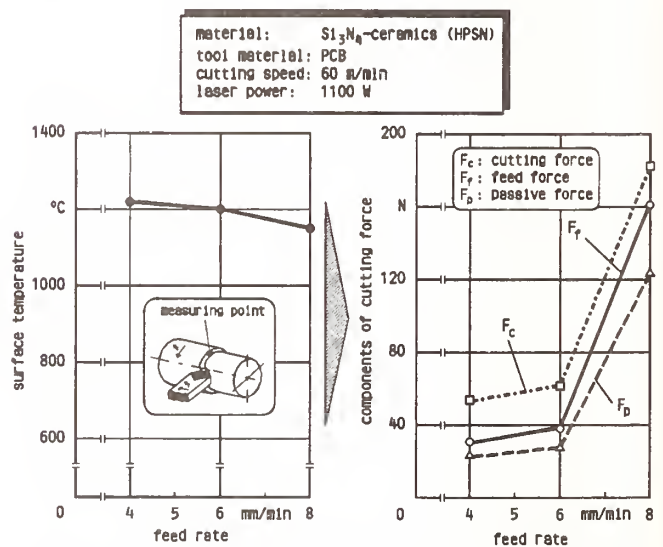
Figure 5: Machining temperature and cutting force components in dependence on feed rate.

At constant CO_2-laser power, the surface temperature is observed to fall with rising feed rates. Increasing of feed rate results in higher cutting forces. This is attributed to insufficient temperature (<1200°C) throughout the chip cross section.

458

The dependence of cutting force components on feed rate and cutting speed at constant Nd:YAG-laser power is shown in *Figure 6*.

Figure 6 info box:
material : Si_3N_4 – ceramics (HPSN)
tool material: CBN
depth of cut : 1 mm
laser power : 700 W (Nd:YAG-laser)
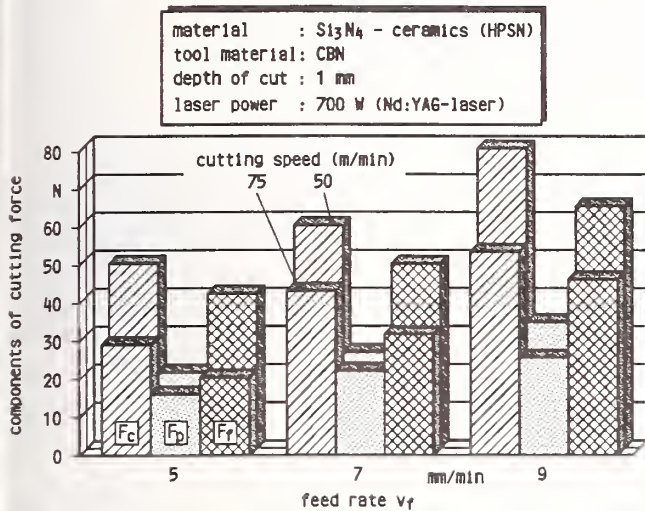
Figure 6: The cutting force components in dependence on feed rate and cutting speed.

Here too, cutting forces are observed to rise with increasing feed rate and fall with higher cutting speed.

It emerges too, that the power requirement when a Nd:YAG-laser (laser power: 700 W, Figer 6) is used as a heat source is approximately 35 % lower than when a CO_2-laser (laser power: 1100 W, Figer 5) is used.

Cutting Tool Wear

The forces acting on the cutting edge and the temperatures in the workpiece and cutting tool generated by the two heat sources - the self-induced heat as a result of friction and strain at the machining point and the external heating by the laser beam - cause various wear mechanisms.
The progression of flank wear on a PCD-tool cutting edge as a function of the turning length is shown in *Figure 7*.
After turning length of 100 mm, the maximum flank wear is 0.08 mm.

Figure 7 info box:
material : Si_3N_4 – ceramics (HPSN)
tool material : PCD
cutting speed : 50 m/min
feed rate : 6 mm/min
depth of cut : 1 mm
laser power : 1 – 1,1 kW (CO_2-laser)
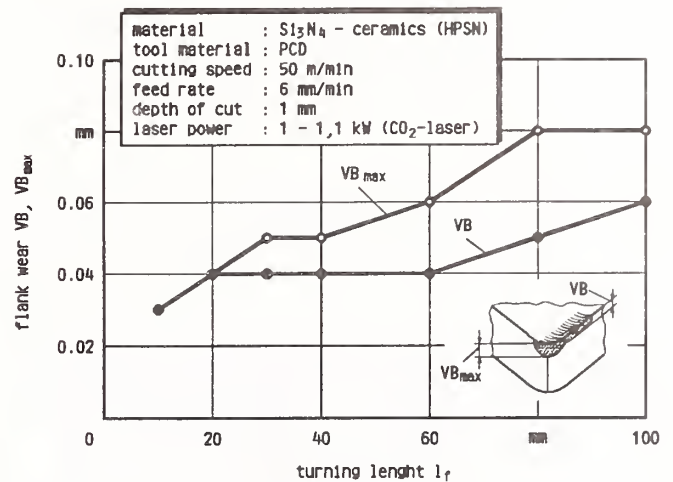
Figure 7: The flank wear of tool cutting edge in dependence on turning length.

Figure 8 shows SEM photos (scanning electron microscope) of the face and cutting edges of a PCD-tool cutting edge.

Figure 8 info box:
tool material: PCD
machining parameters:
l_f = 20 mm
v_c = 50 m/min
v_f = 6 mm/min
a_p = 1 mm
P_L = 1100 W
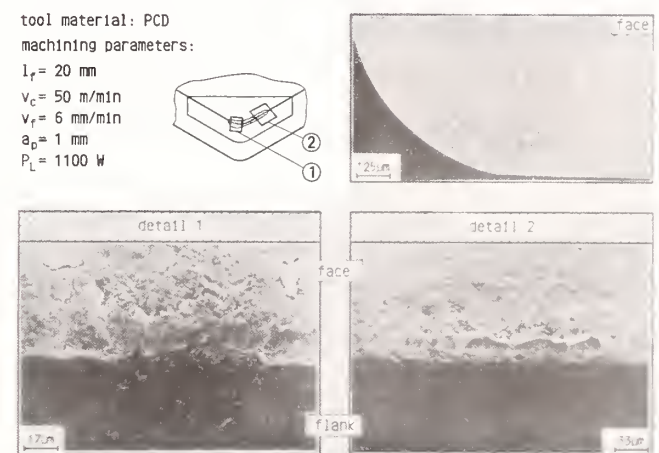
Figure 8: Types of tool wear (PCD-tool cutting edge).

The PCD-tool cutting edge demonstrates flank wear of 0.07 mm after turning length of 20 mm. The two detailed photos (at the bottom of Figure 8) illustrate the tool cutting edge wear as results of thermal-mechanical stress during turning operation. New cutting edges are formed by a deposit of ceramics material on the flank and the face cutting edge.
The tool wear of PCD and CBN by laser-assisted turning of silicon-nitride ceramics can be classified as:

☐ flank wear,

□ crater wear on the tool face,
□ rounding of the cutting edge.

Chip Formation

Figure 9 provides information concerning the shape and type of chips removed during turning operations carried out on silicon-nitride ceramics.

Figure content includes labels:
- shape of chip (general view) — 200μm
- lower side of chip (detail 1) — 7μm
- upper side of chip (detail 2) — 7μm

material:	Si_3N_4-ceramics (HPSN)
tool material:	PCB
cutting speed:	50 m/min
feed rate:	0.01 mm/rev.
depth of cut:	1 - 1.5 mm
laser power:	1.35 kW
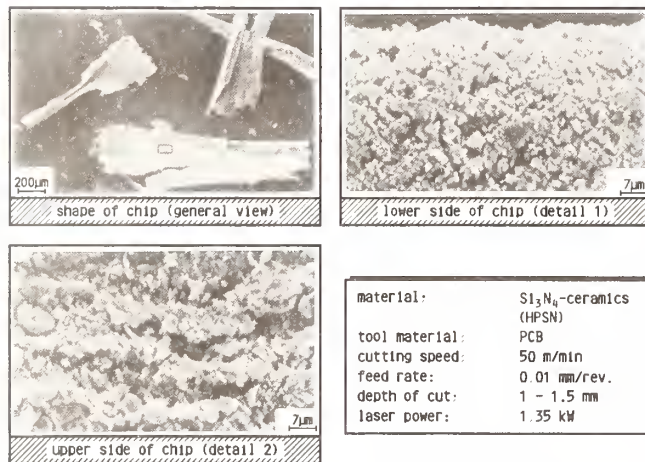
Figure 9: Shape and type of chips produced in laser-assisted turning of HPSN-ceramics.

The chip morphology illustrate, that plastic deformation controls the chip formation process in hot machining. The rod-shaped Si_3N_4-grains loosened from their original cohesion by intercrystalline sliding are visible on the surfaces (Figure 9, detail 1). In detail 2, a segmented structure is visible indicating dynamics in the shearing plane.

Surface Quality

The amount of thermal energy involved in laser-assisted turning raises the question as to the extent of surface damage. The surfaces were, therefore, evaluated using roughness measurements, SEM-photos and X-ray examination (for determination of residual stress and micro-extension levels). *Figure 10* shows surface topology and surface roughness. The surface turned demonstrates the uniform structure which characterizes a visible feed marks (Figure 10, top). The values of the surface roughness measurement (R_a: the arithmetic mean of the departures of the profile

from the mean line, R_z: the average height difference between the five highet peaks and the five lowest valleys within the sampling length, R_t: the maximum peak to valley height of the profile assessment length) are comparable with those achieved in grinding processes (Figure 10, bottom).

Figure content includes labels:
- workpiece
- machined surface
- topology of surface — 25μm

machining parameters	
material:	Si_3N_4-ceramics (HIPSN)
tool material:	PCB
cutting speed:	75 m/min
rate of feed:	6 mm/min
depth of cut:	0,8-1,2 mm
laser power:	330-380 W

surface roughness: 1,32 ... -1,67 ... 0,0 ... 1,25

R_z=2,47 μm R_t=3,09 μm R_a=0,48 μm
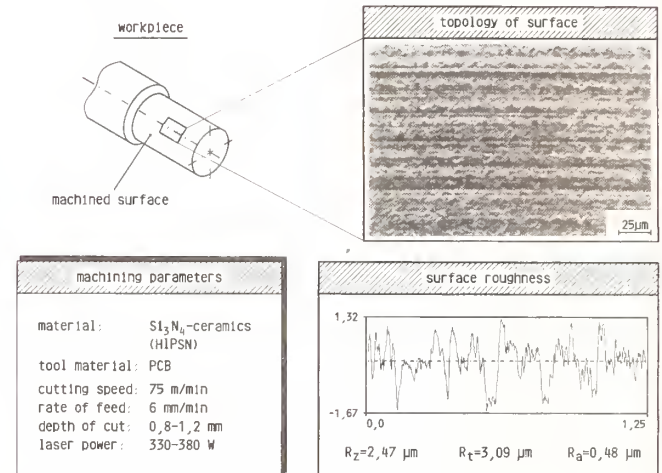
Figure 10: Surface quality.

Diffraction analysis:
□ components of residual stress:
  - laser-assisted turning: cross to the turning direction
  - traverse grinding: parallel to the grinding direction
□ penetration depth: 8 μm

laser-assisted turning	
tool material	: CBN
depth of cut (a_p)	: 1 mm
feed rate (v_f)	: 6 mm/min
laser power (P_L)	: 330-380 W

traverse grinding	
feed rate (v_{fa})	: 100 mm/min
number of revolutions (n_w)	: 250 rev/min
infeed/stoke (q_e)	: 0.02 mm
infeed ($a_{e,ges}$)	: 1 mm

material: Si_3N_4 - ceramics (HIPSN)
compressive residual stress
width of diffraction line
cutting speed v_c: 50 m/min 75 m/min 25 m/s 50 m/s

Figure 11: Comparison of the compressive residual stress and the width of diffraction line of machined surface in laser-assisted turning and grinding. (source: FhG-IPT/IWM)

Recent investigations (14, 15) show that micro-extension visible only on X-ray images which is

460

caused by lattice faults arising in the course of the machining operation, permits the state of damage to be reliably characterised. *Figure 11* shows the compressive residual stress and the width of diffraction line shown on X-ray images (micro-extension is proportional to the width of difraction line) of two surfaces which had been turned with laser assistance and ground.

Both samples were prepared to obtain the same levels of surface roughness. Lower compressive residual stress and micro-extension values are obtained in laser-assisted machining operations than in grinding operation. The difference between these two operations could be due to laser heating, or annealing by laser heating. Additional tests are necessery to substantiate these results.

Machining Examples

Figure 12: Machining example (HPSN-ceramics).
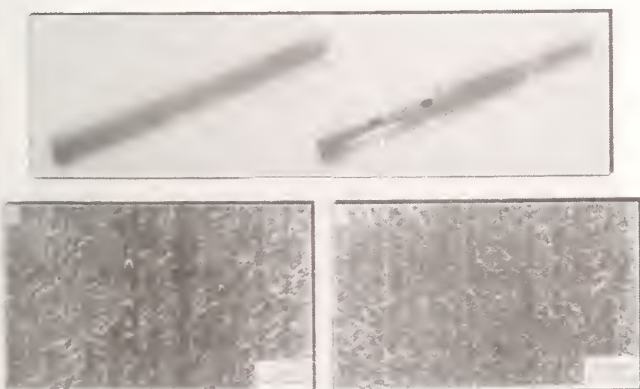
Figure 13: Machining   example   (HIPSN-ceramics).

Figure 12 and *Figure 13* show examples of the machining of HPSN- and HIPSN-ceramics (sintered, rough sample and machined part) with SEM-photos of the machined surface.

Laser-Assisted Milling of Composite Materials

Functional surfaces are coated with hard iron, nickel or cobalt (e.g. stellite) based alloys to enhance the wear and corrosion characteristics of tools and parts subjected to high stress levels. The coating, which is carried out using surface welding or laser beam technology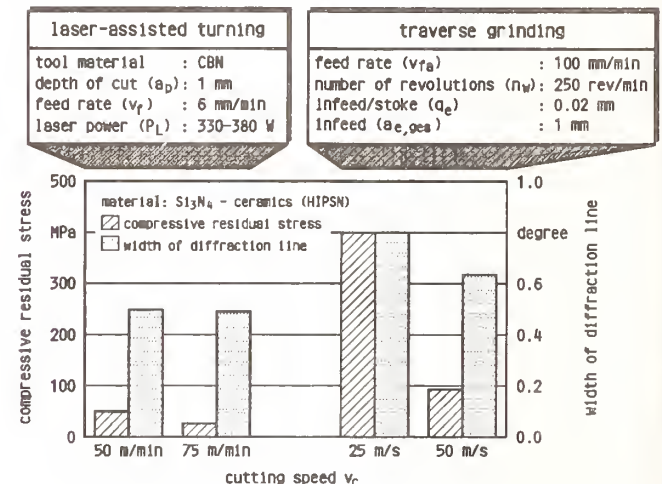, is applied during initial manufacture and repair operations. Such composite materials, consisting of a simple base material and high quality coating are becoming increasingly important as effective cost saving measures.

The Co-base alloy (stellite 6) was used as the work material for milling investigations. Appropriate flat samples were genereted by multi-layer laser beam cladding up to a thickness of approximately 5 mm.

Hard alloys are usually machined in time-consuming and costly grinding or electro discharge operations because of their poor machineability. Their high levels of hardness, strong local variations in hardness and structural inhomogeneity of the layers and irregular coating pose a number of problems. External heat supply via laser beam during turning or milling operations on these materials results in reduced material strength (c.f. Figure 2), thereby facilitating cutting (8).

Test Procedure

Milling tests were carried out using a plane-milling machine with a drive power of 8 kW and a maximum spindle speed of 4000 min^{-1} and an integrated CO_2-laser. A CO_2-high-performance laser with a maximum output of 5 kW was used to generate the beam. As shown in *Figure 14* the beam was deflected onto the workpiece and focused on the surface into an elliptical focal spot in front of the milling tool via a focusing optic attached to the spindle box on the machine.

CBN (cubic boron nitride) was used as a tool

material in both the conventional and laser-assisted milling operations under examination. The milling tool selected was a toroidal end mill with negative cutting edge geometry and a diameter of 32 mm.

Figure 14: Experimental set-up for laser-assisted milling.

Results and Discussion

The aim of the investigations was to determine the degree to which the machinability of the material can be improved by laser-heating. The results obtained from the milling tests will be presented and discussed in the following. Attention will focus on the cutting forces and on tool wear in the evaluation of the cutting process.

The force components (F_f: feed force, F_{fN}: feed perpendicular force and F_p: passive force) are compared in *Figure 15* for machining length of 70 mm.
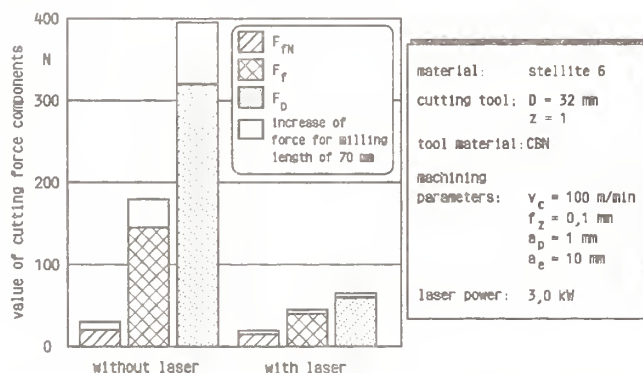
Figure 15: Comparison of the process forces in conventional and laser-assisted milling.

In the case of laser-assisted machining, there is a significant reduction in force. This change in force is due to a temperature increase in the entire chip cross section and the resultant material plastification. As a result of the high wear levels sustained by CBN-tool cutting edges during conventional machining operations ($VB_{max} = 1$ mm after 70 mm machining length), the cutting force components rise steeply and finally cause cutting edge failure. In comparison, significantly less tool wear occurs in laser-assisted milling operations. The flank wear of cutting edge (VB_{max}) is only 0.06 mm.

Conclusions

To recapitulate, it can be said that the results of the investigations presented, indicate that laser-assisted hot machining technology offers a number of advantages.

The investigations into laser-assisted turning of silicon-nitride ceramics show that surfaces with good grinding quality ($R_z < 3$ μm and $R_a < 0.5$ μm) can be obtained. The low cutting forces permit parts with small diameters to be machined. As the machining examples show, flexible part geometry is an additional benefit to be gained from this technology.

Preliminary investigations into the laser-assisted milling of stellite 6 coatings have resulted in a reduction by approximately 70 % in the cutting forces occurring during the process and by approximately 90 % in tool wear in comparison with conventional machining operations.

Additional investigations will be undertaken in order to evaluate the technological and economic viability of laser-assisted hot machining. One of the main objectives of these investigations will be to determine the optimum process parameters for the minimization of process forces and tool wear as well as of the influence exerted on surface layers.

462

References

1. R. Clausen, "Untersuchungen zur Bearbeitung metallischer Werkstoffe durch Warmzerspanen und Plasma-Abtragen", Dissertation Technische Universität Berlin (TU), 1969.

2. W. L. Weingaertner, "Plasmerunterstützte Warmzerspanung", Dissertation Rheinisch-Westfälische Technische Hochschule Aachen (RWTH), 1983.

3. B.M. Jau, S.M. Copley, M. Bass, "Laser Assisted Machining", 9th North American Manufacturing Res. Conf. Proc., SME, Vol. 19-22, Nr.5, pp.12-15, 1981.

4. B. M. Jau, "Laser Assisted Machining of Hard to Machine Materials", Dissertation University of Southern California, 1981.

5. W. König, A. Wagemann, H.-G. Mayrose, "Laserunterstütztes Drehen von heißgepreßtem Siliziumnitrid", Industrie Anzeiger, Vol.111, Nr.99, pp.34-36, 1989.

6. W. König, F. Ferlemann, C. Hermanns, A. Zaboklicki, "Machining of New Materials with Advanced Machining Processes - Laser-Assisted Machining", 25th ISATA Conference, Florence-Italy, pp.435-456, 1992.

7. W. König, A. Zaboklicki, "Laserunterstützte Drehbearbeitung von Siliziumnitrid-Keramik", be published: VDI-Z, No. 6/July, 1993.

8. W. König, F. Treppe, A. Zaboklicki, "Laserunterstütztes Fräsen", VDI-Z, Vol. 134, No. 2, pp.43-48, 1992.

9. A. Zaboklicki, "Laserunterstützte Zerspanung von Verbundwerkstoffen", VDI-Berichte, Nr.965.2, VDI-Verlag, 1992.

10. W. König, "Fertigungsverfahren, Band 1: Drehen, Fräsen, Bohren", VDI-Verlag, 1990.

11. H. Kiso, T. Taguchi, M. Fukuhara, T. Kimuro, "Machining of Advanced Ceramics by Turning with Polycrystalline Diamond Tool", Bull. Japan Soc. of Prec. Eng., Vol.21, Nr.2, pp. 142-143, 1987.

12. H. Salmang, H. Scholze, "Keramik", Springer-Verlag, 1983.

13. K. Uehara; H. Takeshita, "Cutting Ceramics with Technique of Hot Machining", Annals of the CIRP, Vol.35, Nr.1, pp.55-58, 1986.

14. W. Pfeifer: "Influence of Machining-induced Residual Stresses on the Strength of Ceramics", Proceed. of the 9th Intern. Conf. on Exper. Mech., Vol.3, pp.1237-1245, 1990.

15. W. Pfeifer, E. Sommer: "Bewertung der Festigkeitseigenschaften oberflächenbearbeiteter Keramikbauteile", DGM Informationsgesellschaft mbH, Oberursel 1991.

STUDY OF THE FORMATION OF MACRO- AND MICRO-CRACKS DURING MACHINING OF CERAMICS

G. M. ZHANG, D. K. ANAND, S. GHOSH, and W. F. KO
University of Maryland, College Park, MD

This paper presents an experimental study on the formation of macro- and micro-cracks during machining of ceramic materials. In this study, Aluminum oxide (Al_2O_3) was the test material and polycrystalline diamond tipped carbide inserts were used. The cutting forces were recorded during each turning process and the surface finish was measured after machining. An environmental SEM was used to obtain high-magnification images of macro- and micro-cracks induced by machining. With the assistance of a computer-based vision system, quantification of fracture surfaces with respect to crack nucleation, growth, and cleavage was attempted. Results from this research provide an insight into the prevailing mechanisms of material removal during machining of ceramics, and suggest the development of microcrack-controlled machining technologies.

1.   Introduction

The need for high-strength materials has led to the development of advanced ceramics. Advantages that ceramics have over other materials include superior heat resistance, wear resistance, and corrosion resistance. Increasing applications for ceramic materials are being found in industries such as aircraft, automobile, and micro-electronics.

Although most of the ceramic parts are manufactured to near net shape by pressing and sintering processes, precision machining is required to achieve a high degree of geometrical accuracy. Consequently, machining of ceramics has been a rapidly growing field. A traditional ceramics machining process is grinding where ceramic material is removed by the fine cutting edges of abrasives particles. In general, productivity of the grinding process is low, and micro-cracks are formed on and beneath the machined surface that often cause premature failure of ceramic components during service due to brittle fracture. With the ever increasing number of ceramic materials, new and innovative processing methods are needed to achieve cost reduction and quality assurance.

Many attempts have been made in this regard. As reported in (1), a "laser lathe" was developed where the dual beam principle was applied to remove ceramic materials in a molten form. However, the thermal damage induced on the surface and the sub-surface during laser machining is one of the drawbacks of the technique. Another processing method is abrasive jet machining, which uses a stream of high pressure fluid with abrasives insdes to pierce and wash ceramic materials away (2). But, the availability of the advanced equipment and the associated economic factors have limited its application on the shop floor. Recently, a new method, called "heat assisted machining," which integrates laser machining and grinding to remove ceramic materials in a ductile regime, is being developed. Product quality and productivity is expected to be significantly improved. However, with the wide selection of abrasive grains in the market to high levels of performance and dimensional accuracy, grinding is still widely used in machining ceramics (3).

465

This paper presents a research focused on basic understanding of the material removal mechanisms during machining of ceramic materials. Aluminum oxide (Al_2O_3) was the test material and Polycrystalline diamond tipped carbide inserts were used. All machining tests were performed on a CNC turning center. Cutting forces were recorded during machining and surface finish was measured after machining. An environmental SEM was used to examine both macro- and micro-cracks formed on the sample surfaces. With the assistance of a computer-based vision system, 3-dimensional images of the fracture surfaces were reconstructed and quantified with respect to the micro-crack formation during machining. Contour plots are used to characterize the size and shape of cracks and their orientation. Effects of three basic machining parameters, namely cutting speed, feed, and depth of cut, on the crack formation were investigated using a factorial design technique. Results from this research provide an insight into the micromechanisms of material removal during machining of ceramics, and suggest the development of crack-controlled machining technologies.

2. Procedures of Experimental Investigation

Research results over the last few years have shown that material removal in machining ceramics is dominated by brittle fracture (4-6). Evans and Marshall investigated the cutting mechanisms of grinding ceramics. They pointed out that the cutting mechanisms (or wear mechanisms) are due to plastic flow and lateral cracking (7). They predicted a lateral fracture threshold loading limit. When the force developed during machining is below the loading threshold, plastic cutting occurs. On the other hand, lateral cracking occurs when the developed force is above the loading threshold. The interplay between the dynamic characteristics of a machining process and the micro-fracture mechanisms of the workpiece material at molecular level calls for a systematic study of the physics behind the material removal process during machining of ceramics. This research focuses on an experimental investigation, which consists of three major components:

1. Machining of ceramic material for sample preparation.
2. Profilometric measurements of machined surfaces.

3. SEM examinations of microstructural and fractographic feature of the material being machined.

2.1 Machining of Ceramic Material

Figure 1 shows the experimental setup for machining aluminum oxide (Al_2O_3). A CNC lathe was used. The machined Al_2O_3 is a cylindrical bar with initial diameter = 16 mm and length = 60 mm. The purity is 99.8% and the grain size is 10 - 12 μm. The material is a strong, dense recrystalized high-alumina ceramic material. Some material properties related to machining are listed below.

Hardness	1100-1200 kg/mm^2
Modules of Elasticity	380 GPa
Compressive Strength	3000 MPa
Fracture Toughness	4.0 MPa*$\sqrt{m}$
Melting Point	2050 ^{o}C
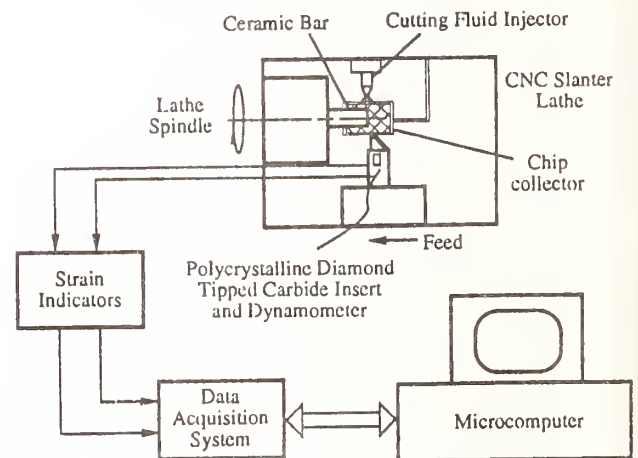
Figure 1 Experimental Setup for Machining Alumina

A dynamometer was attached to the toolpost and the tool holder was fixed on the dynamometer. During machining, polycrystalline diamond tipped carbide inserts, with nose radius 0.25 mm and -7 ^{o} rake angle, were used to machine the alumina bars. In order to absorb the heat generated during machining, distilled water was used as cutting fluid during machining. Chips are collected in a funnel shaped device with a built-in filter to separate chip from the cutting fluid. The dynamometer measured the cutting

466

force in both the cutting speed and feed directions. The data were recorded and stored in a PC-based data acquisition system.

For setting the machining conditions, or selecting feed, depth of cut, and cutting speed, a factorial design method with duplicates was used (8) Table 1 lists the eight combinations of the three machining parameter settings and the measured cutting force data in both the cutting speed and feed directions. For example, the row listed as Test 5 in Table 1 means:

(1) Three machining parameter settings are feed = 0.05 mm/rev, depth of cut = 0.77 mm, and cutting speed = 67m/min;

(2) The average measured cutting force component in the feed direction is 15.4 N (an average of two measurements, 13.9 N and 16.5 N), and the average measured cutting force component in the cutting speed direction is 6.5 N (an average of two measurements, 6.2 N and 6.7 N); and

(3) The measured roughness average value from the machined surface, R_a = 2.30 μm.

2.2 Surface Finish Measurements

After machining, surface profiles were traced for the machined surfaces on a Talystep Stylus Instrument. In this research, the roughness average, R_a, was used as the characterization index for the finish quality evaluation. The eight measured R_a values are listed in Table 1. The best finish quality, R_a = 1.05 μm, was achieved at a combination of feed = 0.012 mm/rev, depth of cut = 0.26 mm, and cutting speed = 67 m/min. The worst finish quality, R_a = 2.30 μm, was at a combination of feed = 0.05 mm/rev, depth of cut = 0.77 mm, and cutting speed = 11 m/min. These results are in agreement with the established metal machining theory. Figure 2 presents surface profiles along the feed direction and taken from four different samples. It is interesting to note that all the four patterns of height variation displayed in Fig. 2 are of random nature. No detectable effects of the tool nose radius and the tool motion pattern can be found with respect to the surface profile formation. However, these profiles display

Table 1 Machining Parameters Settings and Results

Test No.	Parameters Settings			Force Measurements, N				Resultant Force	Surface Roughness, R_a
	Feed	Depth of Cut	Cutting Speed	Feed Force		Tang. Force		Force	
	mm/rev	mm	m/min.	Run 1	Run 2	Run 1	Run 2	N	μm
Test 1	0.012	0.772	67.	8.36	8.47	3.56	3.60	9.14	1.35
Test 2	0.012	0.772	11.	22.46	22.68	4.98	4.93	23.11	1.92
Test 3	0.012	0.264	67.	3.83	3.71	2.16	2.05	4.32	1.05
Test 4	0.012	0.264	11.	3.24	5.03	1.47	1.99	4.48	1.15
Test 5	0.051	0.772	67.	13.94	16.49	6.16	6.67	16.51	2.17
Test 6	0.051	0.772	11.	21.34	23.99	8.72	8.75	24.29	2.30
Test 7	0.051	0.264	67.	4.24	3.93	3.08	2.91	5.07	1.51
Test 8	0.051	0.264	11.	5.76	5.14	2.61	2.20	5.96	1.70

several deep valleys along the feed direction. The deepest valleys are found in the case of high feed and large depth of cut (Fig. 2d). These narrow and deep valleys suggest occurrence of brittle fracture during the chip formation.

Ra = 1.05 μm
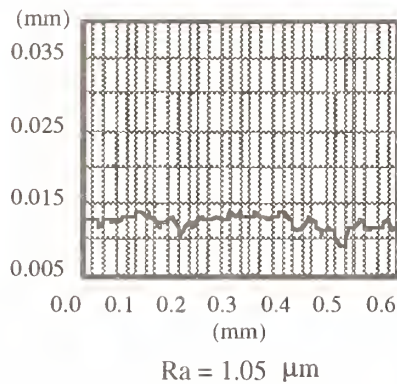
(a) Test 3:   f=0.012 mm/rev,
    d = 0.264 mm, v= 67 m/min

Ra = 1.35 μm
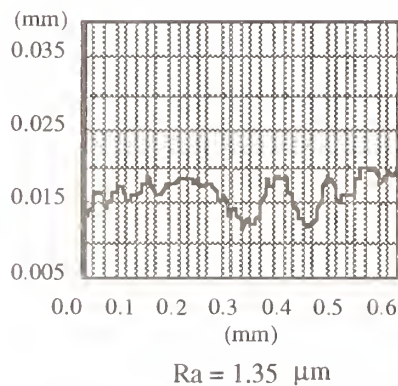
(b) Test 1:   f=0.012 mm/rev,
    d = 0.772 mm, v= 67 m/min

Ra = 1.70 μm

(c) Test 8:   f=0.051 mm/rev,
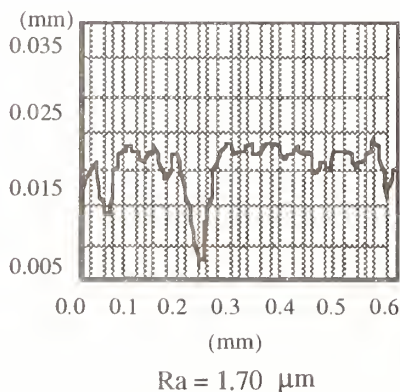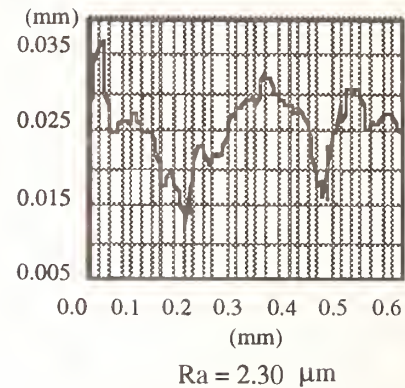   d = 0.264 mm, v= 11 m/min

Ra = 2.30 μm

(d) Test 6:   f=0.051 mm/rev,
    d = 0.772 mm, v= 11 m/min

Figure 2 Surface Profiles Measured from the Machine Surface

2.3   SEM Examination

To understand the process of chip formation during machining and identify the relationship between the fracture mode and the microstructure of the materail, a detailed examination and analysis of the fracture surface is required. In this research, an environmental scanning electron microscope (ESEM) was used to obtain high-magnification images that provide details about the geometry of the formed chips and the topography of the machined surfaces. Another advantage of using ESEM is that no conductive coating is required as in the case of ordinary SEM. This allows a direct identification of macro- and micro-cracks induced by machining without the influence of applied coating.

Figure 3 presents a set of electron micrographs of the chips collected during machining.   Figure 4 presents a set of micrographs of the surfaces machined under the eight combinations of depth of cut, feed, and cutting speed settings at two levels.

3.   Analysis of Experimental Results

The basic philosophy applied for data analysis is first to identify if there are similarities between the machining of ceramic materials and the machining of metals. Afterwards, focus will be given to analyzing new and important findings. It is expected that there exist significant differences in the micromechanisms of material

468

removal between the two types of machining process.

3.1 Cutting Force Generated during Machining

Following observations are made by examining the cutting force results listed in Table 1:

1.   The cutting force produced during machining is proportional to the cutting area. The small cutting forces, such as 4.32 N and 4.48 N, are associated with the combinations of low feed and depth of cut settings, and the largest cutting forces, such as 24.3 N and 23.1 N, with the combinations of high feed and depth of cut settings. This observation follows the law of material strength, i.e., force is proportional to the applied area at a given stress level, or at a given loading threshold.

2.   As a first approximation, the unit cutting force, calculated as a ratio of the measured cutting force to the cutting area, ranges from 650 N/mm² to 2500 N/mm². The low limit of the unit cutting force happened during machining at a high cutting speed setting, a phenomenon that could be interpreted as the effect of high temperature on the material removal. However, such a wide variation of unit cutting force can only be contributed to the fact that the fracture strength of a brittle material fluctuates. The fluctuation can be as much as an order of magnitude (5). In fact, this characteristic indicates that ceramic materials can be removed at a low unit cutting force if the machining condition is preferred, pointing out great promise to search new and innovative machining technologies.

3.   The magnitude of the tangential cutting force component is much smaller than that of the cutting force component along the feed direction, a phenomenon just opposite to what has been observed during the machining of metals where the magnitude of the tangential force is much larger than that of the feed force.

3.2 Mechanisms of Material Removal

The analysis presented in this section includes a detailed examination and analysis on fracture mechanisms for clarification of the role of the microstructure, or understanding the metallurgical factors that control the material removal process. The analysis is first divided into two parts for examining the chip formation and surface topography formation, respectively. Then we combine the results from these analyses and propose a model to describe the mechanisms of material removals including the chip formation process. Special efforts are made to illustrate a developed computer vision system for visualizing and quantifying the fracture surface formed during machining.

3.2.1 Mechanisms of Chip Formation

Information on the chip formation mechanisms can be obtained through the examination of the four micrographs of chips shown in Fig. 3:

1.   The chip fragments shown in Fig. 3a and Fig. 3b were formed during two machining processes with depth of cut settings at 0.77 mm and 0.26 mm, respectively. It is not surprising to conclude that a high material removal process, such as the one with a large depth of cut, will produce large chip fragments. However, the size of chip fragments formed during a single machining process varies significantly. For example, the chip fragments shown in Fig. 3b are significantly different in size. This phenomenon indicates that special attention must be paid to the investigation of chip formation during machining of ceramic materials.

2.   The two chip fragments shown in Fig. 3d were taken at a high magnification. They represent two types of chip observed in this experimental study. The unique feature among the two types of chips is their lateral surfaces, which are formed by brittle fracture. This feature indicates that the chip formation during machining is a macro-scale fracture process, or cleavage fracture

(a) Test 6 f=0.05 mm/rev. d=0.77 mm, v=11 m/min

(b) Test 8 f=0.05 mm/rev. d=0.26 mm, v=11 m/min

(c) Crack Trapped in the Cleavaged Chip (Test 6)

(d) Machined Chip with Plowing Marks (Test 6)

Figure 3 SEM Micrographs of the Chips Formed during Machining

Feed = 0.012 mm/rev.
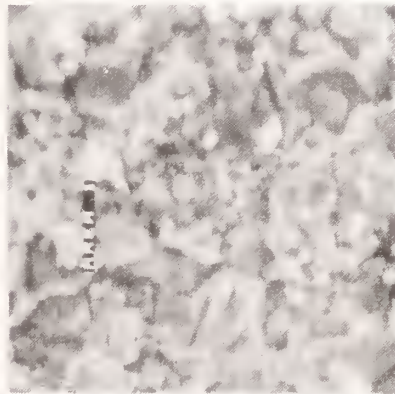
(a) d = 0.772 mm
     v = 67. m/min.
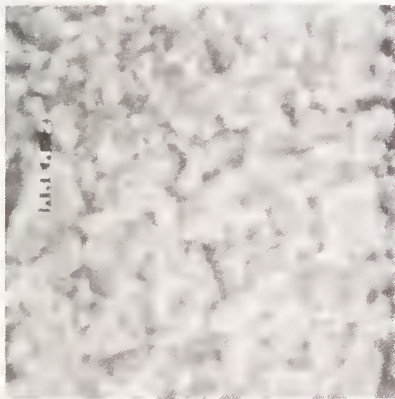
(b) d = 0.772 mm
     v = 11. m/min.
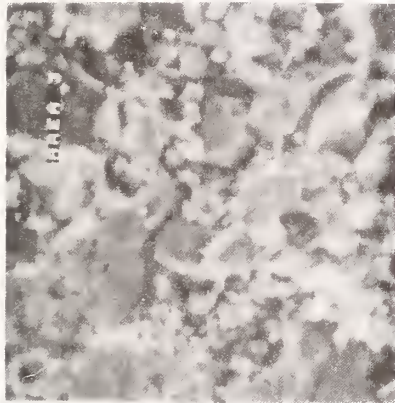
(c) d = 0.264 mm
     v = 67. m/min.
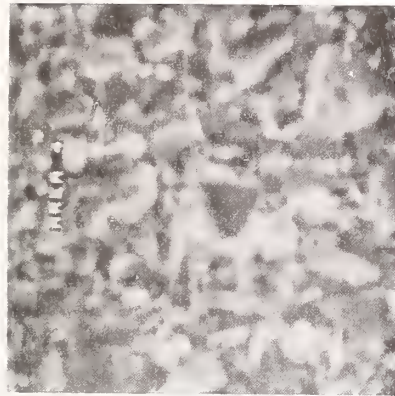
(d) d = 0.264 mm
     v = 11. m/min.

Feed = 0.051 mm/rev.
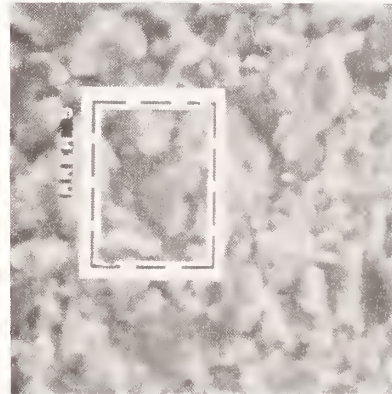
(e) d = 0.772 mm
     v = 67. m/min.

(f) d = 0.772 mm
     v = 11. m/min.
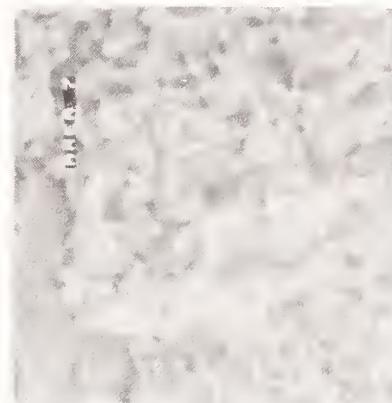
(g) d = 0.264 mm
     v = 67. m/min.
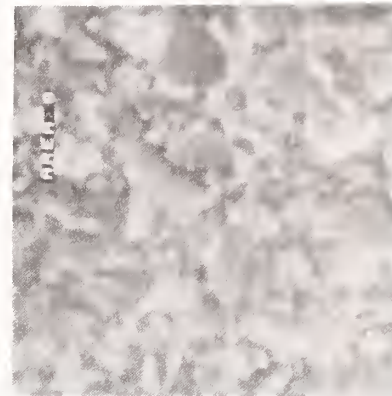
(h) d = 0.264 mm
     v = 11. m/min.

Figure 4 SEM Micrographs of the Machined Surfaces under the 8 Combinations   (x 500)

471

mode. However, there exists a unique difference between these two types of chip. The chip on the right side of the figure has a smooth flat surface. The parallel lines, or the plowing marks, on the smooth surface resemble the chip flow over the rake face of a cutting tool, a phonomenon routinely observed during machining of metals. Note that this chip was formed under a machining condition where the temperature measured in the cutting zone was about 750°C. This suggests that formation of this type of chip could start from plastic deformation in the cutting zone, then progress into plastic flow over the rake face, and end with separation from the machined part due to fracture. This suggestion can be interpreted as the existence of deformation mode in a fracture process for brittle materials (5, 8). Research in the future direction should pursue applying the elastic-plastic fracture mechanics to characterize the crack tip field in the chip formation process. Figure 5 illustrates the proposed formation process of the two types of chip, namely, the machined chip and the fractured chip during machining. The fractured chip is defined as those chip fragments formed without direct contact to, or flow over, the tool rake face. This may provide an explanation to the random nature of the height variation pattern observed in taking surface profiles from the machined surface.
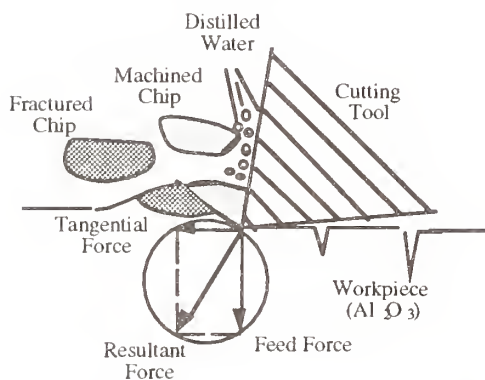

Figure 5 Two Types of Chip Formed during Machining of Alumina

3. The micrograph at a high magnification shown in Fig. 3c depicts the intergranular fracture

developed within a fractured type of chip formed during machining. The location of the crack with respect to the chip as a whole is marked in Fig. 3a. It shows that the crack is about 5 μm in width and 120 μm in length. It is intersting to note that this crack was trapped when a fractured chip was formed, indicating that the formation of fractured chip fragments is due to the catastrophic failure of the ceramic material under high stresses (above the loading threshold), developed during machining.

3.2.2 Mechanisms of Surface Topography Formation

One of the ultimate objectives of machining engineering ceramics is to achieve a high degree of the geometrical accuracy of a designed part. The topography formed on a machined surface plays a key role in this regard. Based on the previous discussion, the machined surface is an assemblage of fracture surfaces left by the chip formation. Reliability of a machined part during its service period is directly related to the status of macro- and micro-cracks formed on the machined surface as well as the region just beneath the machined surface. A new approach, which integrates profilometry, microscopic analysis and image processing, is developed to investigate the mechanisms of surface topography formation (9).

1. Macro- and microscopic examination of the fracture surface. The eight micrographs shown in Fig. 4 are the images taken from the surfaces machined under the eight machining conditions with a magnification of 500. The intergranular fracture along the grain boundaries can be clearly identified on these machined surfaces, indicating their preferred, river-like crack paths, as depicted in Fig. 4. An important observation is that almost all of the intergranular cracks initiated at triple point junctions (intersections of the grain boundaries) and dislocation pile-ups at the grain boundaries. Figure 6 is a micrography of a chip fragment collected during machining. A magnification of 4,500 is used to reveal both microstructural and fractographic
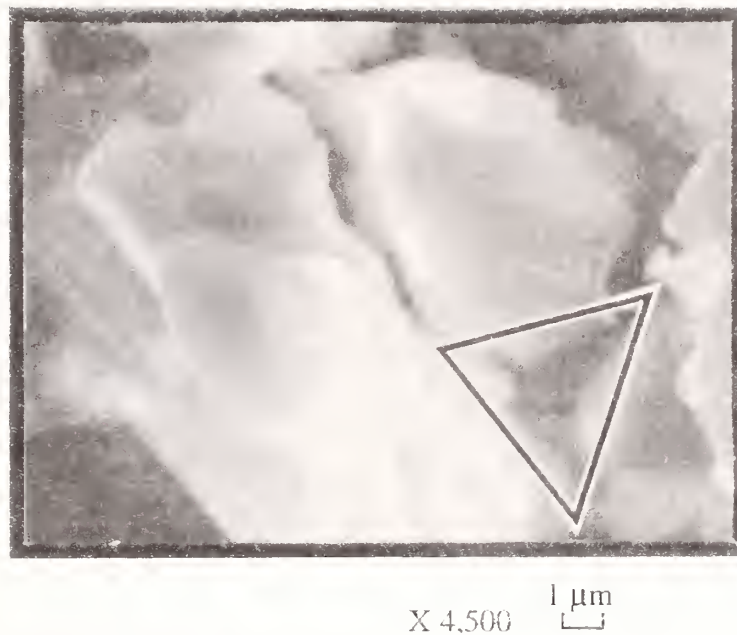
472

X 4,500 ⊔—⊔ 1 μm

Figure 6   Microstructural and Fractographic feature around a Single Grain
           (A Triple Point Junction Is Indicated)

feature around a single grain. The picture depicts the three pairs of contacting points between the neighboring grains. It is very likely that the cutting force induces local residual tensile stresses at these triple points during machining. In combination with stresses from deformation generated within the grains due to the cutting action, crack nucleation is initiated at these locations. As the machining process goes on, the progressive development of grain boundary microcracking leads to crack growth, or propagation. Figure 6 also illustrates the cleavages due to microcracking at the triple point junctions. The progression of intergranular cracks causes an entire grain to dislodge from the machining area, leading to intergranular fracture or cleavage fracture. The process of grain dislodging forms micro-cracks, and then macro-cracks, and finally, the topography of a machined surface.

2.   Profilometric examination. By examining Fig. 2 and Table 1 jointedly, a small Peak-to-Valley value is associated with a machining process with a small cutting force. It indicates that most of the crack initiation, growth, and cleavage were confined with a very limited local areas, or "short-crack" regions (5), when the cutting force was rather small. As these "short-cracks" extended, the toughness of alumina built up and resisted extension of these developed cracks. Figure 7 illustrates a steadily increasing toughness with expanding crack size for alumina (5). On the other hand, the profile with a large Peak-to-Valley value is associated with a machining process generating a large cutting force. This indicates that the induced local residual tensile stresses exceeded a critical value, but the toughness keeps at a constant level because the crack length has reached a critical value, say 10 μm illustrated in Fig. 7 for alumina. Under such circumstances, accelerated crack propagation will lead to the occurrence of catastrophic failure of alumina. During machining, this could imply the increase of formed fractured chip fragments. An excessive amount of fractured chip fragments could introduce large irregularities on the

473

machined surface, as illustrated in Fig. 2d.
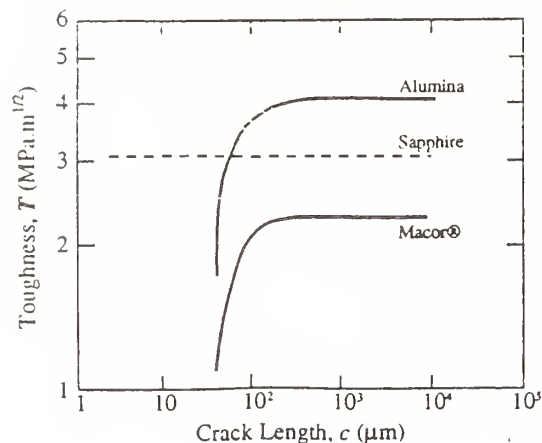
Figure 7 Fracture Toughness as a Function of Crack Length (5)

3. Stereophotogrammetric examination through image processing. Stereoscopy offers a direct and nondestructive procedure for determining the elevation of a fracture surface at selected regions (10-12). In this research, a software package, which integrates image processing, profilometry, and computer graphics, was developed to visualize the surface topography formed during machining, display patterns of crack propagation, and quantify the size and shape of intergranular and transgranular cracks from the ESEM micrographs. Figure 8 presents a visualized surface topography in three-dimensional space and an associated contour map. The corresponding area of the surface topogarphy is marked in the micrograph shown in Fig. 4e(area 5). The reconstructed fracture surface topography vividly depicts the surface texture formation during machining. It visualizes the appearance of surface cracks and quantifies the relative positions between the surface roughness and the surface cracks. For example, the distance 4.2 μm marked in Fig. 8a, obtained through calibration using the profilometric measurements, provides a valuable information for post-machining, such as grinding and polishing, as well as reliability assessment of the machined parts. By
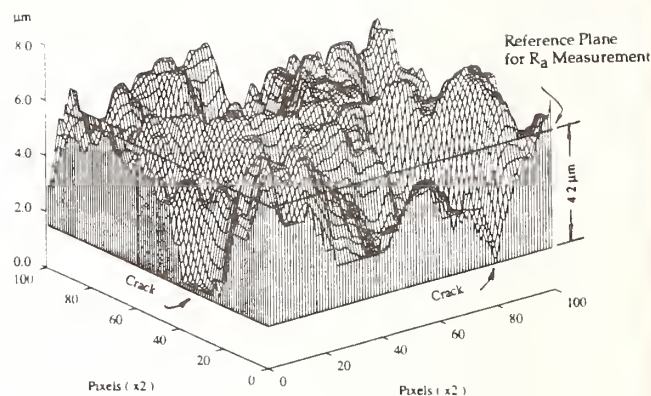
(a) Visualization of Surface Topography and Crack Indications
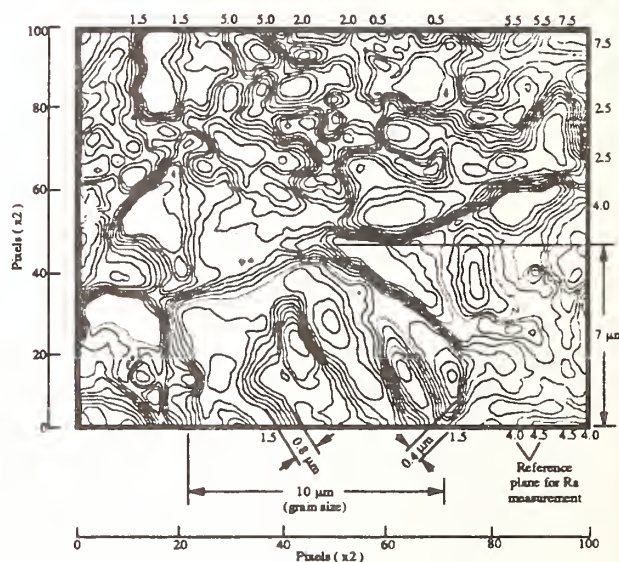
(b) Contour Map for Quantifying the Formed Cracks

Figure 8 Fracture Surface Reconstruction and Crack Closure

examining the deduced contour map shown in Fig. 8b where the interval between the contour lines is 0.5 μm. The numbers shown outside the frame are the heights of the location, the

474

lowest point of the surface topography being taken as 0.0 μm. On the other hand, the pixel number, as illustrated in Figs, 8a and 8b, provides a scale for calculating dimensions in a horizontal plane. By adding the width between two contour lines, a quantitative information about the size and shape of a crack can be estimated. For example, the width marked as 0.4 μm in Fig. 8b covers 6 contour lines. The information provides the size of a V-shape crack having an angle of $7.6^o$ with its vertex 4.2 μm away from the reference plane for R_a measurements. It is interesting to note that the contour map could assist us in identifying transgranular cracks. For example, the boundaries of a grain sized 10 μm can be identified on the map, as shown in Fig. 8b. Within the grain, a crack path is also identified. It is marked 0.8 μm. If further investigation on this spot is pursued, we might be able to have information about transgranular cracks developed by machining. The principal objective of modern quantitative fractography is to express the geometric characteristics of the features on the fracture surface in quantitative terms. The stereophoto-grammetric examination through image processing developed in this research may provide a powerful tool to establish the quantitative relationships between the crack formation and machining conditions.

3.3 Material Removal Mechanisms during Machining

From the above discussion, as a material removal process, machining of ceramic materials shares certain common characteristics with what we have observed from machining of metals. Both machining processes involve cutting force generation, chip formation, and surface topographical generation. However, machining of ceramic materials possesses unique characteristics. Based on our experimental work,

we present a model to describe the material removal process with emphasis on the relationships between the macroscopic and microscopice fracture behaviors. Figure 9 illustrates the five essential stages in this basic physical process:
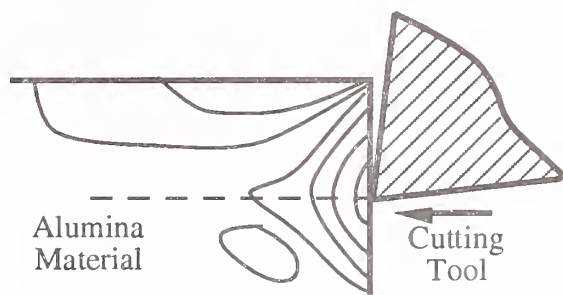
(a) Dynamic Loading and Induced Stress Field
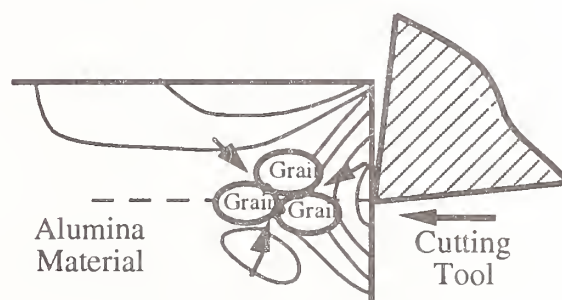
(b) Crack Initiation
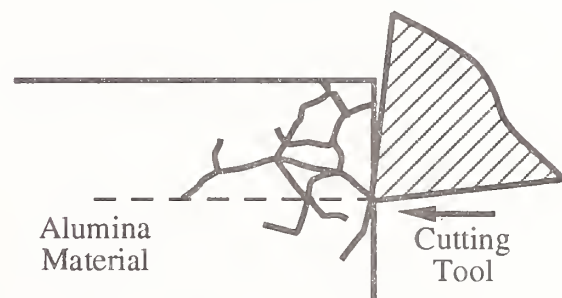
(c) Crack Propagation

(d) Chip Formation

475
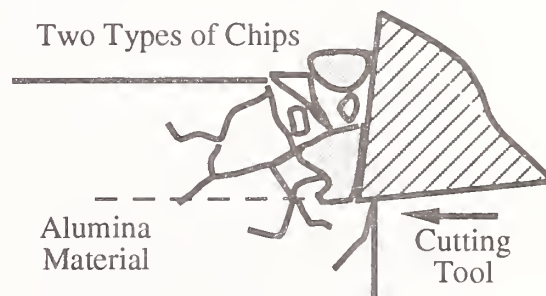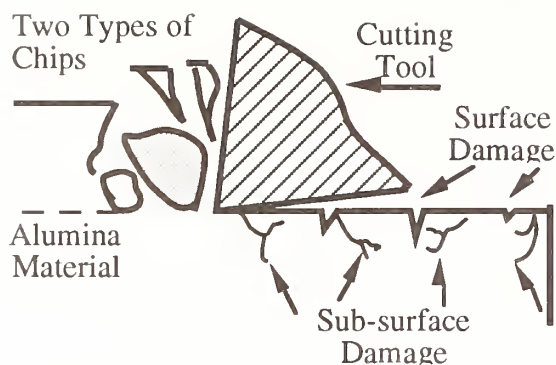
(e) Formation of Surface and
Sub-surface Damage

Figure 9 Five Essential Stages in the Material
Removal

1. Dynamic Loading. When a machining process starts, the tool approaches to the part material. At the instant when the tool touches the part material, the impact between them induces stresses in the material and a stress field is formed (Fig. 9a).

2. Crack Initiation. When subjected to the induced stresses, crack nucleation begins immediately. Their sites are locations of stress singularities where high internal tensile stresses build up. These locations can be triple-point junctions, dislocation pile-ups at grain boundaries, and second-phase particles. All of these flaws could initiate micro-cracks (Fig. 9b).

3. Crack Propagation. As the machining process goes on and stresses continue to develop in the material, the formed microcracks grow in the material immediately surrounding them. Both intergranular and trangranular cracks are developed and advanced obstacles are encountered (Fig. 9c).

4. Chip Formation. The process of crack propagation is terminated when more micro-cracks propagate and produce unstable fracture. The material separated by fracture can be in a position either contacting with the rake face of the cutting tool or away from the cutting zone, depending on the pattern of crack propagation. Consequently, two types of chip will be formed. The type of machined chip (shadow areas)

represents the fractured material directly under the tool action and also subjected to the temperature influence. On the other hand, the type of fractured chip depends on the pattern of crack propagation, which is governed by the material microstructure (Fig. 9d).

5. Formation of Surface and Sub-surface Damage. Due to brittle fracture, chip fragments are formed during machining. At the same time, surface texture is formed on the machined surface with cracks because brittle fracture. These cracks are called surface damage and, in general, unavoidable during machining of ceramic materilas. In addition, the residual effects of brittle facture near the surface layer bury numerous micro-cracks to a certain depth, leading to sub-surface damage (Fig. 9e).

3.4 Development of Crack-controlled Machining Technologies

Based on the comprehensive under-standing of material removal mechanisms, we should have gained guidelines for developing new and innovative machining technologies to control the crack formation. The following suggestions are made in this regard.

1. Control of Microstructure of Ceramic Material. It has been recognized that machinability can be significantly improved by controlling microstructure of metals through heat treatment. The same philosophy applies to the machining of ceramic materials as well. The microstructure of ceramic materials is central to strength and toughness properties. By controlling the size and shape of individual grains, or the volume fraction of incorporated second phases, we may be able to balance the need for avoiding structure failure from design point of view and the need for degrading short-crack toughness from the viewpoint of improving machina-bility. A typical example would be the development of Dicor/MGC, a glass-ceramic material designed for use in dental restorations (14). The material has a unique microstructure consisting of mica flakes of approximately 70 volume percent dispersed in a non-

476

porous glass matrix. The cleavage along the literal planes of mica flakes functions as stress concentration, a situation similar to the stress concentration around the inclusions in free-machining steels, offering an excellent machinability.

2. Control of Machining Parameters. It is certain that the tool geometry will play a key role in determining the distribution of induced stresses in the material being machined. By limiting the volumetric ratio of fractured chip to machined chip, we may be able to manage surface and sub-surface damage. The ductile region grinding is a typical example of keeping at a low level or eliminating the formation of fractured chip during machining. Proper selections of the three cutting parameters (feed, depth of cut, and cutting speed) may render an optimal machining performance possible. In the study of environmental effects on fracture mechanics, it has been well recognized that stress-corrosion cracking causes intergranular or cleavage separation by a loss of cohesion (15). Therefore, use of cutting fluids can improve machining efficiency. In fact, chemical-assisted machining has been studied intensively, showing great promise for crack-controlled machining (16-17).

3. New Processing Methods. Laser-based heat assisted machining is being developed. By controlling the temperature of the cutting zone, an increase of pre-fracture plastic deformation could reduce brittle fracture significantly, leading to a full control of machining process. On the other hand, crack arrest through post-processing would be a typical example to improve surface quality after machining.

4. Conclusions

In this research, a fundamental study related to machining of alumina is conducted. It consists of cutting force measurement, assessment of surface finish quality, and analysis of micromechanisms of material removal during machining. The results are summarized as follows.

1. Machining of ceramic materials is characterized by crack initiation and propagation, leading to chip formation. There are two types of chip, i.e., machined chip and fractured chip. nd cleavage fracture are the three key elements in the machining process. A model is proposed to describe the material removal process.

2. By integrating image processing, profilometry and computer graphics, a computer-based vision system is developed for expressing the geometric characteristics of features on the fracture surface through three-dimensional visualization and contour mapping.

3. Collaboration between shop floor machinists and material processing engineers is needed. to 1). optimize ceramic microstructures, that provide required resistance to the initiation and propagation of brittle cracks while maintaining an acceptable machinability; and 2). develop new and innovative machining technologies for effectively controlling the crack formation during machining.

References

1. G. Chryssolouris, J. Bredt, S. Kordas, and E. Wilson, "Theoretical Aspects of a Laser Machine Tool," ASME Winter Annual Meeting Proceedings, PED 20, pp. 177-190, December 1986.

2. M. Mazurkiewicz, "Understanding Abrasive Waterjet Performance,"

Machining Technology, Vol. 2, No.1, pp. 1-3, 1991.

3. K. Subramanian, S. Ramanath, and Y. O. Matsuda, "Precision Production Grinding of Fine Ceramics," Proceedings of the First International Conference on Manufacturing Technology, Chiba, Japan, 1990.

4. R. C. Bates, "Micromechanical Modeling for Prediction of Lower Shelf, Transition Region, and Upper Shelf Fracture Properties," Part 3, in Fracture Mechanics: microstructure and micromechanisms," Edited by Nair, et al, ASM International, pp. 131-168, 1989.

5. B. R. Lawn, "Fracture of Brittle Solids," Second Edition, Cambridge University Press, Cambridge, in press.

6. J. Cagnoux, and A. Cosculluela, "Influence of Grain Size on Triaxial Dynamic Behavior of Alumina," Part 6 in Dynamic Failure of Materials: Theory, Experiments, and Numbers," Eds. H. Rossmanith, and A. Rosakis, Elsevier Applied Science, pp. 73-84, 1991.

7. A. G. Evan, and D. B. Marchall, "Wear Mechanisms in Ceramics," In Fundamentals of Friction and Wear, Ed. D. A. Rigney, Metals Park, Ohio, American Society of Metals, pp. 439-452, 1980,.

8. G. Box, W. Hunter, and J. Hunter, "Statistics for Experimenters, An Introduction to Design, Data Analysis, and Model Building," John Wiley & Sons, Inc., 1978.

9. J. Landes, and R. Herrera, "Micromechanisms of Elastic/Plastic Fracture Toughness," Part 4, in "Fracture Mechanics: microstructure and micromechanisms," Edited by Nair, et al, ASM International, pp. 111-130, 1989.

10. K. Komai, and M. Noguchi, "Fracture Surface Reconstruction Technique and Crack Closure," Part 5, in "Fractography", Edited by Koterazawa, et al., Elsevier Applied Science, pp. 161-186, 1990.

11. E. E. Underwood, "Recent Advances in Quantitative Fractography," Part 2, in Fracture Mechanics: microstructure and micromechanisms," Edited by Nair, et al, ASM International, pp. 87-109, 1989.

12. E. E. Underwood, "Quantitative Fractography", Chapter 8, in Applied Metallography, G. F. Vander Voort, Ed., Van Nostrand Reinhold, pp. 101-122, 1986.

13. J. E. Hilliard, Quantitative Analysis of Scanning Electron Micrographs," Journal of Microscience, 95, Part 1, pp. 45-58, 1972.

14. D. Grossman, "Structure and Physical Properties of Dicor/MGC Glass-Ceramic," Proceedings of the 1991 International Symposium on Computer Restorations, Regensdort-Zurich, Switzerland, pp. 103-115, 1991.

15. W. Gerberich, "The Micromechanics and Kinetics of Environmentally Induced Fractures," Part 3, in "Fracture Mechanics: microstructure and micromechanicsms," Edited by Nair, et al, ASM International, pp. 201-208, 1989.

16. G. Zhang, T. Hwang, D. Anand, and S. Jahanmir, "Tribological Interaction in Machining Aluminum Oxide Ceramics," Proceedings of the Navy Tribology Workshop, Annapolis, Maryland, May 11-13, pp. 9-13, 1992.

17. G.M. Zhang, T.W. Hwang, and D.K. Anand, "Chemo-Mechanical Effects on the Efficiency of Machining Ceramics," Proceedings of 1993 National Science Foundation Design and Manufacturing Systems Conference, Charlotte, NC, January, pp. 421-428, 1993.

THE MACHINABILITY OF DIFFERENT DENTAL MATERIALS FOR CAD/CAM SYSTEMS

K. H. KUNZELMANN and R. HICKEL
University of Munich, Munich, Germany

In spite of increased machinability and optimized physical properties, presently available materials for dental CAD/CAM restorations suffer from chipping at machined edges. The aim of this study was to compare glass ceramic materials, sintered leucite reinforced ceramic, dental hybrid composites and an experimental hydroxiapatite with regard to the amount of chipping at machined edges. Samples in shape of a computer generated test-inlay with rectangular edges were machined using a dental CAD/CAM machine (disc diameter: 4 cm, average grain size: 64 μm, unloaded surface speed: 45 m/s). The machined samples were evaluated with both SEM and profilometer. Samples with a fine microstructure (hot-pressed, fine grain size of the sinter particles) had smaller margin defects. Increasing crystallite contents improved margin quality, too. <u>The average chip size at machined egdes of the tested materials was: phlogopite containing glass ceramic: 60 μm, leucite reinforced ceramic: 60 μm, tetrasilicic fluormica glass ceramic: 80 μm, feldspathic porcelain: 105 μm.</u>

Introduction

The increasing esthetic demands of patients and excellent biocompatibility have led to growing interest in using ceramics as restorative materials in dentistry. Usually the restorations are fabricated by slip-casting, controlled crystallization of glass or hot-pressing of precrystallized glasses. A lost-wax process is used to shape the molten glasses or glass-ceramics. The properties of these materials are highly dependent on the skills of the dental technician. In addition process-dependant microdefects reduce the fracture toughness and increase the time-dependant failure probability of restorations [1].
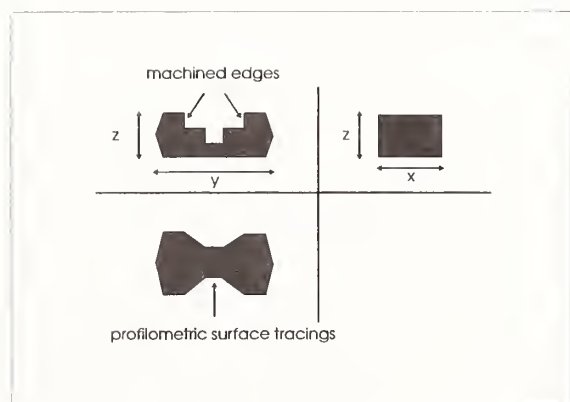

Figure 1:
Computer generated 3D-data set for the CAD/CAM-unit.

Efforts to automate the production of dental restorations have induced the developement of CAD/CAM-units to process dental ceramics [2, 3, 4]. Computer-aided manufacturing of dental restorations helps to reduce the above mentioned limitations by using optimized ceramic materials with little variation in microstructure. With already commercially available devices the prefabricated ceramic blocks are milled with diamond coated grinding discs to fit into tooth cavities. In spite of increased machinability and physical properties presently available materials for CAD/CAM purposes suffer from chipping at machined edges. The chipping defects do not only reduce the accuracy of fit of the restorations but may be the predominate cause of catastrophic failure [5].

The aim of the present study was to optimize ceramic materials for better stability of machined edges in presently available CAD/CAM milling devices for dental restorations. For this purpose experimental ceramic materials reinforced with leucite were compared with commercially available machinable ceramics. In addition a conventional dental hybrid composite and an experimental hydroxiapatite material were included to evaluate the amount of chipping at machined edges of other materials which are commonly used for dental restorations.

Materials and Methods

The tested materials were machined with a dental CAD/CAM milling device driven with a high-speed motor. The cutting tool is a diamond coated grinding disk with a diameter of 4 cm (average grain size: 64 μm). The unloaded surface speed of the grinding disc is 45 m/s. Ceramic blocks complete one rotation per second around the axis and against the grinding disc. The samples were machined to the shape of a computer generated test-inlay with rectangular edges (Fig. 1). The samples were water cooled during the milling process. To reduce surface tension a combined detergent and lubricant was added to the cooling water.

The experimental ceramic materials were prepared by a dental ceramics manufacturer. The raw materials were fused at 1450°C to molten glass. For increased homogeneity the melt was quenched, dried, crushed and molten for a second time. In a following tempering process the amorphus glass was converted to a partially crystalline glass ceramic which was crushed and ground to particles [6]. The particles ware shaped in a sinter process to the material blocks used in our study. The variables which were investigated were different crystallisation conditions, cooling rates after sintering to the final shape, sinter conditions and grinding sizes of the sinter particles.

The materials were coded and all experiments were done without knowing the composition or the properties of the coded samples. The machined samples were evaluated in the SEM.

The investigation of the experimental materials was done in four test series. In a first screening series the influence of different crystallite contents on machinability was examined qualitatively with the SEM. Seven materials with varying leucite contents and varying sinter conditions were used. Table 1 summarizes the linear thermal expansion coefficients of the experimental materials and their sinter conditions. With increasing leucite content the thermal expansion coefficient also increased. According to the manufacturer A - D are highly crystalline glass ceramics, E is semicrystalline, F is amorphus glass and G is a feldspathic porcelain for enamelling to metals.

In the second series the influence of internal stress caused by the contraction mismatch of the glassy phase vs. the crystal phase leucite on the defect size at machined edges was studied. For this purpose two highly crystalline materials, E-ST and E-MT, with the composition summarized in Table 2 but with identical sinter conditions were compared [6]. One half of the specimen were cooled with the furnace switched-off and the other half at a cooling rate of less than 5°C per minute.

Table 1:
Thermal Expansion Characteristics and Sinter Conditions of
the Experimental Ceramics

Material (external code)	α_0 (10^{-6}/°K) [-500°C]	α_0 (10^{-6}/°K) [500-600°C]	Pressure to form greenware [MPa]	Sinter temperture [°C]
A	18.8	24.9	2.1	820
B	18.8	24.9	3.3	820
C	18.8	24.9	2.1	850
D	18.8	24.9	3.3	850
E	20.0	23	3.3	920
F	8.3	7.9	3.3	920
G	14.5	14.2	3.3	880

Table 2:
Composition (wt %) of the basic glasses for E-MT and E-ST

Oxide	SiO_2	Al_2O_3	K_2O	Na_2O	B_2O_3	CeO_2	CaO	BaO	TiO_2
Basic glass of E-MT	63.0	17.7	11.2	4.6	0.6	0.4	1.6	0.7	0.2
Basic Glass of E-ST	64.0	14.3	10.1	8.0	0.6	0.9	3.3	1.5	0.3

In the third series, the influence of microstructure on machinability was studied. To obtain a finer microstructure the samples were hot-pressed. The sinter process took place at a temperature of 1050°C and simultaneously applied pressure of 0.5 MPa. The quality of the machined edges was compared to the samples of series 1.

Further improvement of the sinter process was achieved in the fourth series by a finer grain size of the sinter particles and hot-pressing. During the preceeding experiments the average grain size of the particles was between 30 - 40 μm, whereas the materials in series 4 had an average grain size of 7 μm. To validate the influence of the crystallite phase a highly crystalline material (PK-MT) was compared with a material with a higher content of glassy matrix (BS-PK).

The results of these optimized materials were compared with already commercially materials which were optimized for machinability. Two of them were developed for dental application whereas the third one is widely use in medical implant technology.

In the last series, materials with different micro structure were tested for their feasibility as machinable restorative materials. Dental composites are successfully used either as plastic materials which are light-cured in the oral cavity or as inlay systems which are fabricated extra-orally and bonded to the teeth with a composite bonding system. A conventional dental hybrid composite (20 wt% bifunctional methacrylate, 79 wt% anorganic filler particles with an average diameter < 1,5 μm, 1 wt% photoinitiator and pigment) was formed in cylindrical shape for milling and then light cured as recommended

in vacuum with intensive light. As teeth consist predominately of hydroxiapatite the restoration of teeth with the same material would be the most natural way to treat carious lesions. An experimental hydroxiapatite from bovine bones (theoretical density: 99,5 %) served as screening sample.

The surface roughness was measured with a profilometer (diamond stylus, tip angle 90°, 5 μm tip radius, ISO 4287/1, $\lambda = 0,8$). The roughness of the machined edges, the width and the depth of the defects at the edges of the specimen were recorded with a diamond knife (3 mm broad, tip angle 120°, 5 μm tip radius, DIN 4768 and DIN 4768/1, $\lambda = 0,8$).

Results

Specimens with a higher crystallite contents exhibited less surface roughness than materials with a higher glassy matrix contents (Table 3). SEM evaluation of the samples with a high leucite contents shows regions with surface defects of brittle fracture mode besides plastically deformed areas without substantial micro-cracking (Fig. 2) while samples with little or no crystallite contents showed only brittle fractures on the surfaces.

All materials suffer from chipping at the machined edges (Fig. 3). The sizes of the shell-shaped defects at the machined edges range up to 300 μm with increasing values for higher contents of glassy matrix. The cooling rates had no influence on the size of the defects. All samples of series 2 exhibited defects up to 200 μm along the machined edges. Hot-pressing of the samples in series 3 resulted in a more homogenous surface and less machining damage along the edges with flaws of only 60 μm. An additional gain in margin stability was achieved in series 4 by finer grain sizes of the hot-pressed materials. The PK-MT samples had defect sizes up to 50 μm and the BS-PK samples up to 100 μm.

The marginal defects of the commercially available dental ceramic materials ranged from 80 to 100 μm. The phlogopite containing glass-ceramic samples had the smallest defect sizes of the commercially available materials with defect sizes at the edges up to 60 μm (Fig. 4). Both the dental hybride composite material and the experimental hydroxiapatite showed defects up to 150 μm. The fracture mode of the defects of both materials was of plastic in nature. The composite had a fine surface structure whereas the hydroxiapatite was characterized by a porous, fine-grained surface with smooth islands of highly condensed material (Fig. 5).

The result of the measurements with the surface roughness analyser are given in Table 4, using the parameters R_z and R_{max}. The R_z-value is the mean of the maximum peak-to-valley values from 5 consecutive sampling lengths, while R_{max} is the maximum peak-to-valley value of all 5 sampling lengths.

Table 3:
Surface roughness of test specimen with different leucite contents. (R_a = average surface roughness according to ISO 4287/1 ($\lambda = 0,8$), SD = standard deviation).

Material	R_a [μm]	SD [μm]
A	1.47	0.07
B	1.66	0.08
C	1.62	0.08
A	1.58	0.1
E	1.58	0.11
F	1.76	0.11
G	1.80	0.18

Figure 2:
Machined surface of material A. The Surface exhibits brittle fracture mode are besides plastically deformed areas (right window).
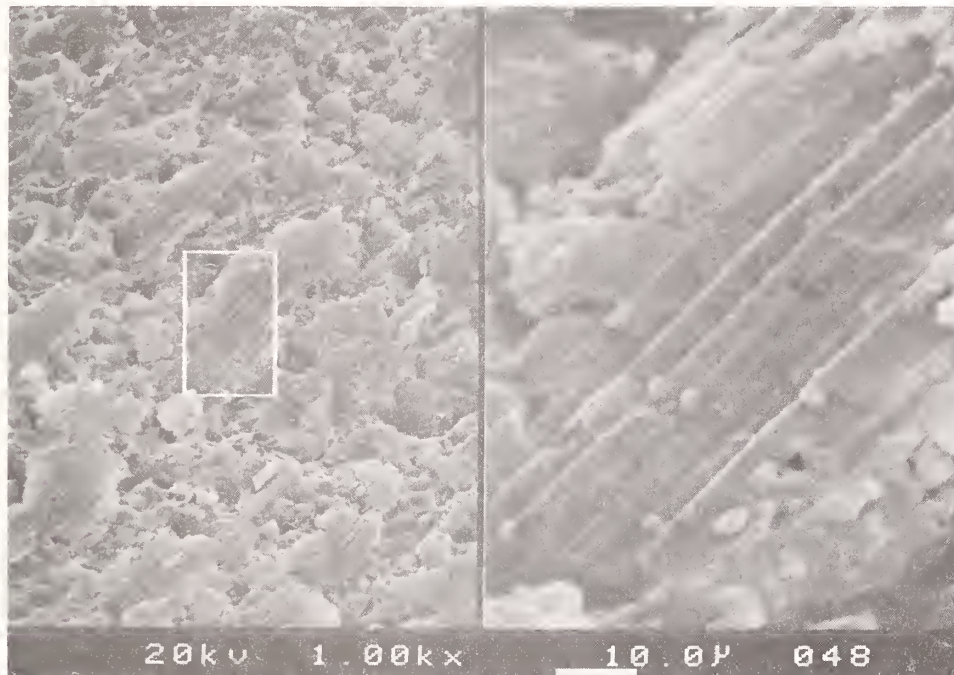

Figure 3:
Large defects at the machined edge of material D.
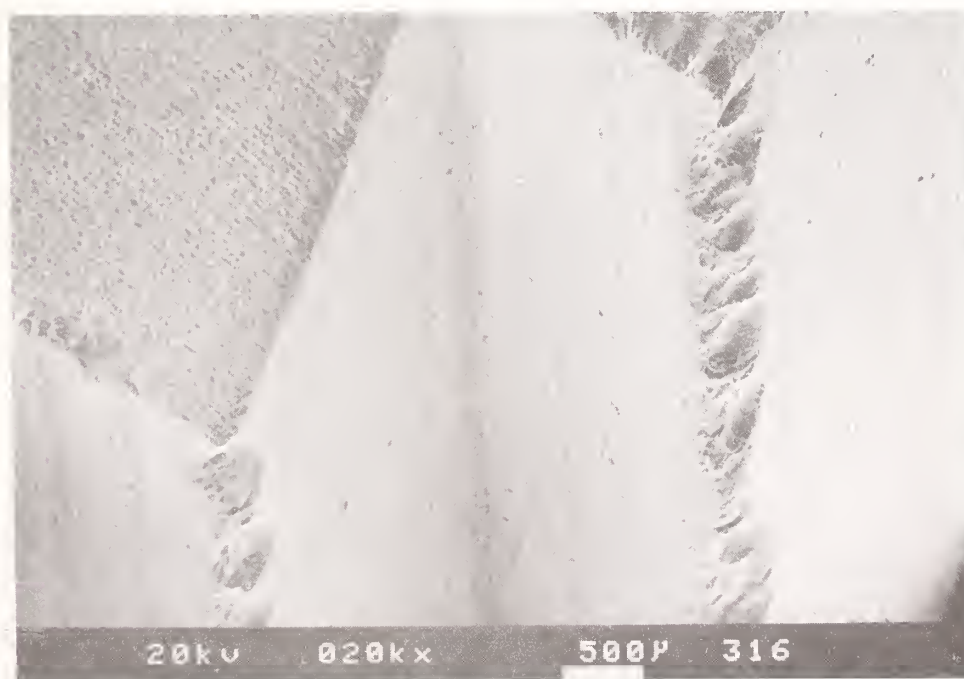
Figure 4:
Small defects at the machined edge of the optimized experimental
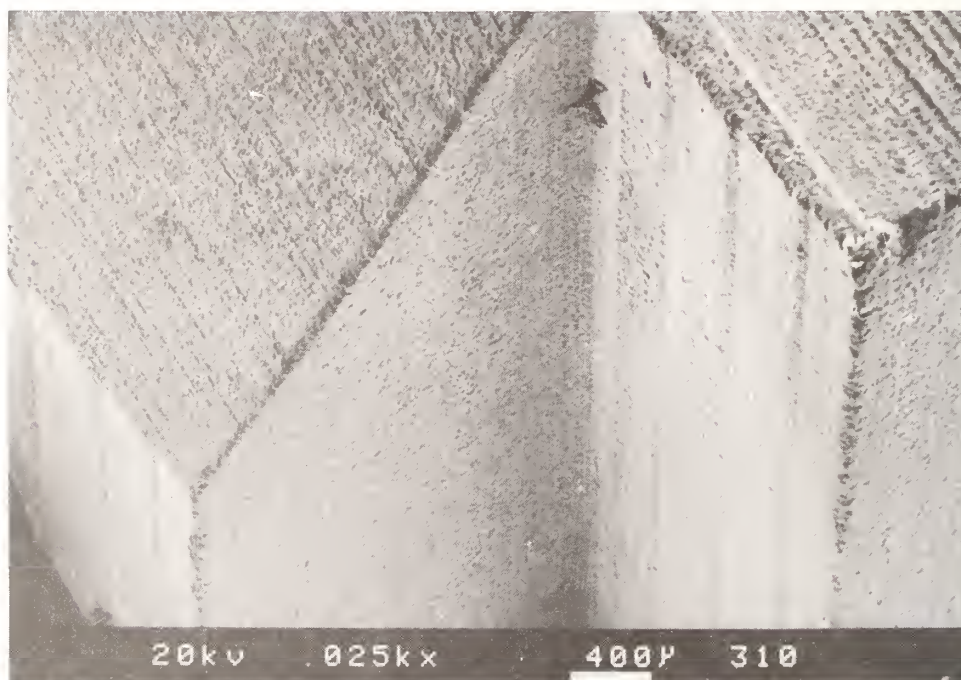material PK-MT.

20kv .025kx 400μ 310

Figure 5:
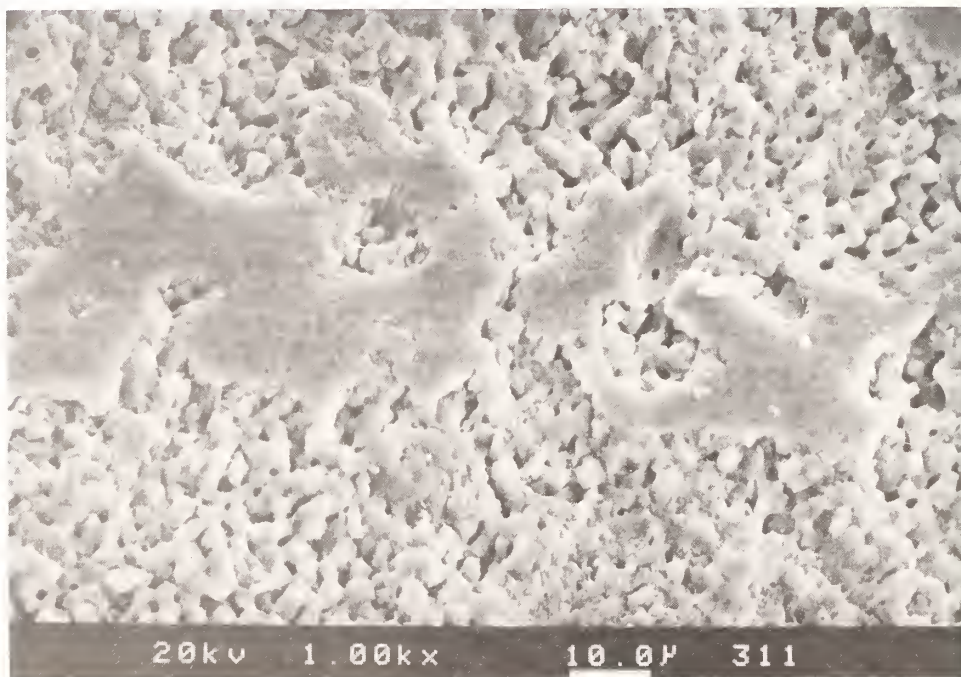SEM picture of the surface structure of an experimental hydroxiapatite.

20kv 1.00kx 10.0μ 311

Table 4:
Roughness of the machined edges recorded with a diamond knife (DIN 4768 and DIN 4768/1).

Material	$R_z[\mu m]$	$R_{max}[\mu m]$
A	6,67	7,33
B	5,51	5,86
D	6,58	9,1
F	6,67	8,73
F	9,11	11,96
G	6,67	9,59
E-MT (cooling rate: < 5°C)	9,16	14,35
E-MT (cooling with furnace characteristic)	6,06	8,44
E-MT (hot-pressed, conventionally ground)	6,51	7,51
PK-MT (hot-pressed, fine ground)	6,06	6,58
BS-PK (hot-pressed, fine ground)	5,98	7,09
feldspathic porcelain	5,55	7,19
phlogopite containing glass ceramic	5,98	6,18
tetrasilicic fluormica glass ceramic	7,13	8,28

Discussion

Material removal under the load of the cutting tools takes place by microcracking and chipping of the surface. The induced microcracks result in larger chips if the crack is not deflected and branched by crystallites. This is confirmed by the increased surfaces roughness of materials with a higher portion of glassy matrix and the SEM pictures. With raised leucite contents plastically deformed areas can be observed with nearly indistinguishable grain boundaries (Fig. 2). Kelly [5] attributes this as "polishing wear" resulting in declined wear rates with the number of grinding cycles. This is in accordance with the reduced working times of the grinding tools for tetrasilicic fluormica glass ceramic compared to feldspathic porcelain [7].

Although chipping at machined edges was less for materials with a higher leucite contents other factors seemed to influence the dimension of the defects. The contraction mismatch between the thermal expansion of the leucite cystallites and the glassy matrix can result in stabilizing internal stress [6, 8]. At machined edges, however, the internal stress can increase the size of the defects. A slower cooling rate after firing the samples can reduce the inner tensions leading to increased margin quality. The different tempering methods, however, had no influence on the margin stability of the edges. Another possible explanation of the large margin defects was breaking of the margin corners along the grain boundaries of the frit particles. This was verified by series 3 with the improved sinter technique, i. e. hot-pressing of the sinter particles, and series 4 with the finer grain size of the frit particles. Both series resulted in improved margin quality. Series 4 additionally confirmed the findings of series 1 that a higher crystallite contents results in less margin defects, because material BS-PK, which showed larger flaws, had a lower leucite contents than material PK-MT. The margin quality of the fine ground and hot-pressed experimental material is comparable to the phlogopite containing glass ceramic.

The differences between the phlogopite containing glass ceramic material, the experimental material PK-MT and the tetrasilicic fluormica glass ceramic may be explained through their microstructure. The phlogopite containing glass ceramic, which shows the smallest defects at machined edges, is a glass ceramic material with spherical crystallites. The

experimental materials are leucite reinforced. Leucite crystallites are cubical or tetragonal in shape [9]. In both cases only small edge defects are observed whereas the tetrasilicic fluormica glass ceramic had larger defects (Table 4) because of the interlocking nature of the flat plate-like crystals [10]. Instead of single crystallites, crystallite agglomerates broke away from the machined edges. Further investigations may show the influence of the cristallite shape on fracture toughness, fatigue strength and chipping at machined edges, because on the one hand it can be expected that the interlocked, plate-like crystallites give better fracture or fatigue data while on the other hand the machinability of fine structures may be better with the less interlocked spherical, cubical or tetragonal cystallites.

Esthetic appearance also needs to be considered in the dental context. While the tetrasilicic fluormica glass ceramic or PK-MT are tooth colored and can be processed to dental restoration in a one step procedure, the phlogopite containing glass ceramic is too opaque for esthetic restorations. Better esthetic results can be obtained with non-tooth-colored materials in a two step procedure if they are used as copings which can be individually characterized in consecutive firing processes. This technique could be transfered even to high-strength alumina ceramic containing at least 70 % pure alumina in the body. Here the greenware from aluminum oxid could be shaped to a coping with the CAD/CAM-unit, reinforced with the glassy matrix and color-characterized afterward leeding to a highly fracture resistant and esthetic dental restoration.

Both, composite and hydroxiapatite samples, demonstrate that they have potential as machinable materials. With these materials the working time of the grinding tool is nearly tenfold compared to the ceramic materials. Composites can be used now for small, non-stress bearing restorations. Further experiments are needed however, to optimize these materials for larger restorations.

Conclusion

The first step to optimize ceramic materials for milling conditions similar to the available dental CAD/CAM-systems should be to minimize structural defects. The influence of the reinforcing crystallite system can be determined in a second step. In dentistry improving of the esthetic appearance is the third step in the development of new machinable materials. Since the used CAD/CAM-unit represents only a fixed set of tribosystem variables, the development of future systems should be more flexible regarding their milling devices in order to adapt to the requirements of new materials.

References

[1]   J. W. McLean, "The Science and Art of Dental Ceramics", Oper Dent, Vol. 16, pp. 149 - 156, 1991.

[2]   D. Rekow, T. M. Speidel, and A. G. Erdman, "Computer-Aided System to Automate Production of Posterior Dental Restorations", Abstract 1336, J Dent Res, Vol. 65, p. 317, 1986.

[3]   F. Duret, J. L. Blouin, and B. Duret, "CAD-CAM in dentistry. J Am Dent Ass, Vol. 117, pp. 715 - 718, 1988.

[4]   W. H. Mörmann, M. Brandestini and F. Lutz, "Das Cerec-System: Computergestützte Herstellung direkter Keramikinlays in einer Sitzung", Quintess Zahnärztl Lit, Vol. 38, pp. 457 - 462, 1987.

[5]   J. R. Kelly, H. Lüthy, A. Gougoulakis, R. L. Pober, and W. H. Mörmann, "Machining Effects on Feldspathic Porcelain and Glass Ceramic: Fractographic Analysis", Proceedings of the International Symposium on Computer Restorations, pp. 253 - 273, 1991.

[6]   G. Beham, " IPS-Empress: Eine neue Keramik-Technologie", IVOCLAR/VIVADENT Report #6, 1990

[7]   W. Mörmann, and O. Furrer, "Efficiency of an Electric Drive in the CEREC CAD-CAM Unit", J Dent Res, Vol. 71, Spec. Issue, Abstr. # 3, p. 516, 1992.

[8]   K. J. Anusavice, P. H. Dehoff, B. Hojjatie, and A. Gray, "Influence of Tempering and Contraction Mismatch on Crack Development in Ceramic Surfaces", J Dent Res, Vol. 68, No. 7, pp. 1182 - 1187, 1989.

[9]   H. Claus, "Die Bedeutung des Leuzits für die Dentalkeramik", Zahnärztl Welt/Reform, Vol. 90, No. 6, pp. 44 - 46, 1981

[10] D. G. Grossman, "Structure and Physical Properties of DICOR MGC Glass-Ceramic", Proceedings of the International Symposium on Computer Restorations, pp. 103 - 115, 1991.

MECHANICS OF TOOL WEAR DURING MACHINING OF ADVANCED FIBROUS COMPOSITES

G. SANTHANAKRISHNAN, R. KRISHNAMURTHY, and
S. K. MALHOTRA
Indian Institute of Technology, Madras, India

Advanced fibrous composites, owing to higher specific strength , elastic modulus and also impact and corrosion resistance find wide range of applications in aerospace, automobile and other industrial sectors. To obtain dimensional tolerance and also to maintain certain functional features, composites are usually machined. Owing to their heterogeneous nature and also depending upon the orientation and nature of reinforcing fibre used, the composites pose considerable problems in machining. Pulsating cutting forces, higher order cutting temperature and chip clogging encountered during machining of composites result in thermo-mechanical stress induced spalling, abrasion and chip notching modes of tool wear. Different types of tool wear and the associated mechanisms, observed during machining of carbon fibre reinforced plastics (CFRP) and Kevlar fibre reinforced plastics (KFRP) composites with plain and coated cemented carbides are presented in this paper.

INTRODUCTION

Rapid developments in composites including resin, metal and ceramic based composites have opened their application range. This is largely due to their high specific strength, elastic modulus, corrosion resistance and good fatigue resistance. Though composites are usually moulded, for obtaining close fits and tolerances and also for achieving near-net shape, certain amount of machining has to be carried out. Due to their non-homogeneity, composites pose considerable problems in machining. The data available for machining of homogenous metallic materials cannot be used for composite machining. Further each composite differs in its machining behaviour since its physical and mechanical properties largely depend on type of fibre, fibre content, fibre orientation and variabilities in the matrix material. Among the resin based composites, carbon fibre reinforced plastics(CFRP) and Kevlar fibre reinforced plastics(KFRP) find the wider application in aerospace industries. In FRP composites, which is an assemblage of plastics and fibres in different orientations, it is difficult to investigate the mechanism of material removal during machining[1,2], since the action of each fibre encountered by the
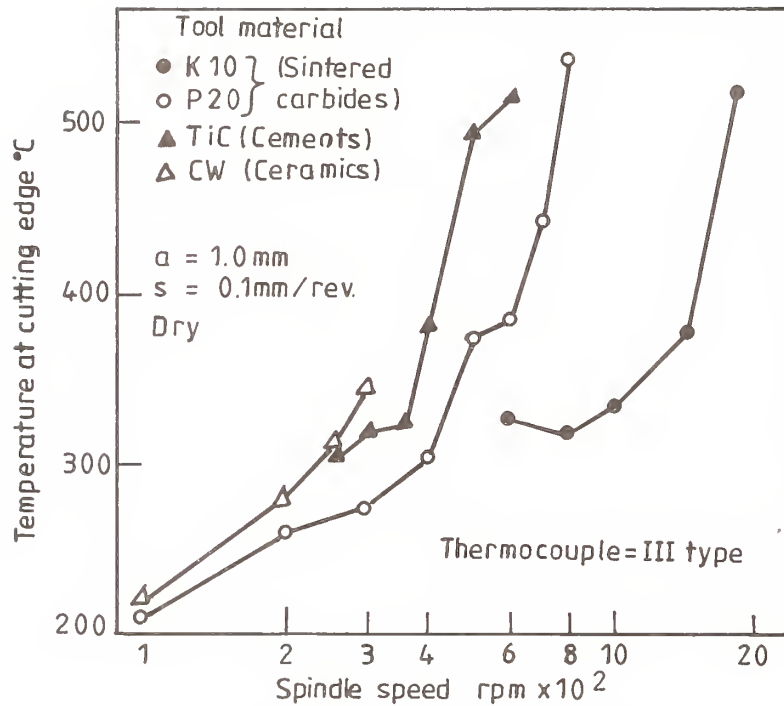
Fig. 1   Relation between spindle speed and
temperature at cutting edge [3]

cutting tool will be varying from moment to moment. Thus, a cutting tool in machining a FRP composite will experience an environment of pulsating load, apart from load fluctuation. The cutting edge will also experience higher order cutting temperatures[3] during machining. Figure 1 illustrates the influence of cutting speed and type of cutting tool on cutting temperature during machining of composites. It is seen that the cutting temperature increase with cutting velocity. For each tool, there exists a critical velocity around which there is a rapid increase in cutting temperature. Since composites have poor thermal conductivity, the cutting tools must dissipate major part of the heat generated; thereby experiencing higher cutting temperatures.

Apart from pulsating forces, and higher temperatures the cutting edge will also experience large scale abrasion due to the rubbing of the fibres on the machined work surface over the flank portion of the cutting tool. Thus, a cutting tool will be subjected to impact fatigue, thermal degradation and abrasion; thereby experiencing different forms of tool wear. Figure 2 [4] illustrates the influence of cutting temperature on wear and associated causes for tool wear. From this figure, it can be seen that most of wear mechanisms reported become operational during machining of composites. Observations on tool wear during machining of composites have illustrated mixed modes of tool wear.

EXPERIMENTAL

Machining trials have been carried out on filament wound CFRP and KFRP tubes in a precision, rigid and high speed
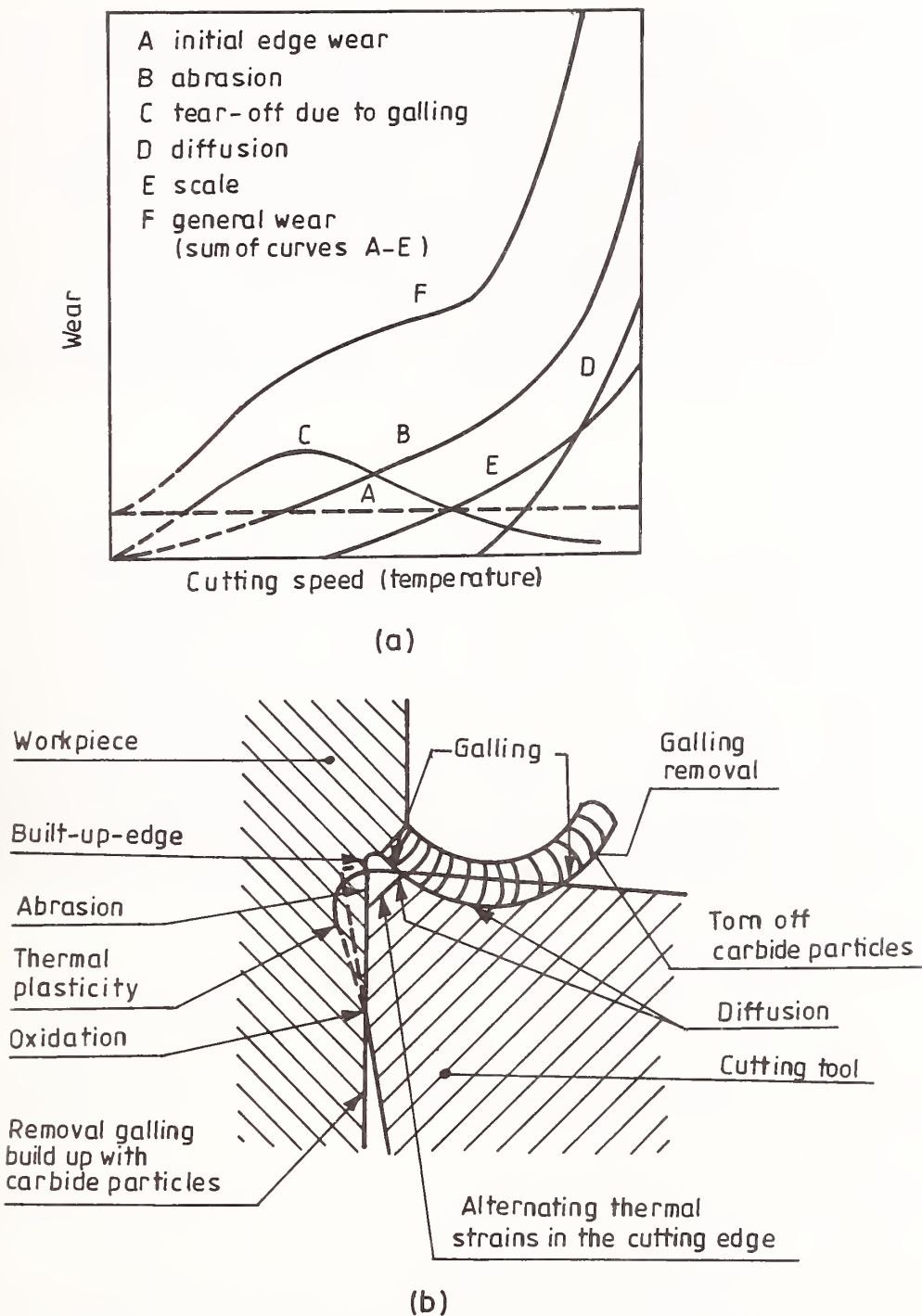
Fig. 2 Schematic representation of (a) Wear as a function
of cutting speed.(b) Causes of Wear [4]

VDF lathe using plain and coated cemented carbides as detailed in Table 1. Work piece material and dimensional specifications and layup sequence are detailed in Tables 2,3 & 4. Apart from measurement of cutting forces and surface finish, tool wear was also observed using optical and scanning electron microscopes. Typical observations are presented in the following sections.

491

TABLE 1. MACHINING CONDITIONS

```
----------------------------------------------------------------
Cutting direction          Right hand turning
Cutting speed              V, m/min      -      50  to 200
Feed rate                  s, mm/rev.    -     0.025 to 0.150
Depth of cut               a, mm         -      1 and 1.5
Tools                      12.7mm    square   inserts - Sintered
                           carbides(P30,K20),Coated    carbides
(TiN/TiC coated on K-type substrate)
Tool nomenclature :
```

-6	6	-6	75	90	0.8

```
Coolant                    Dry
----------------------------------------------------------------
```

TABLE 2. WORK PIECE - MATERIAL SPECIFICATIONS

```
----------------------------------------------------------------
```

<u>Fibres</u>
a. Carbon rovings - BESFIGHT, 6.4 μ filament dia, 6000 fibres/tow.
b. Carbon cloth - 0.017 inch (0.432mm) thick, 7.4 oz./yd^2. (230gm/m^2)
c. Kevlar-49 roving - 4560 DEINER-969, 546 $\pm$ 16 Tex.
d. Kevlar-49 cloth - 0244, 4 end satin weave, 0.3mm thick, 220 gm/m^2.

<u>Resin</u>
a. Epoxy Resin   Ciba Geigy   LY 556
b. Epoxy Hardner   Ciba Geigy   HT 972
```
----------------------------------------------------------------
```

TABLE 3. WORK PIECE -DIMENSIONAL SPECIFICATIONS

```
----------------------------------------------------------------
```

MATERIAL	INNER DIAMETER(m)	OUTER DIAMETER(m)
CFRP	0.0975	0.1200
KFRP	0.1020	0.1226

```
----------------------------------------------------------------
```

TABLE 4. LAY UP SEQUENCE FOR CFRP AND KFRP COMPOSITE TUBES

```
----------------------------------------------------------------
```

I Layer   : one layer of cloth with warp placed parallel to the axis of the tube.
II Layer   : One layer of cloth with warp placed at 45° to the axis of the tube.
III Layer : Hoop winding (90°) with roving
(This layer sequence was repeated till the required thickness was achieved.)
```
----------------------------------------------------------------
```
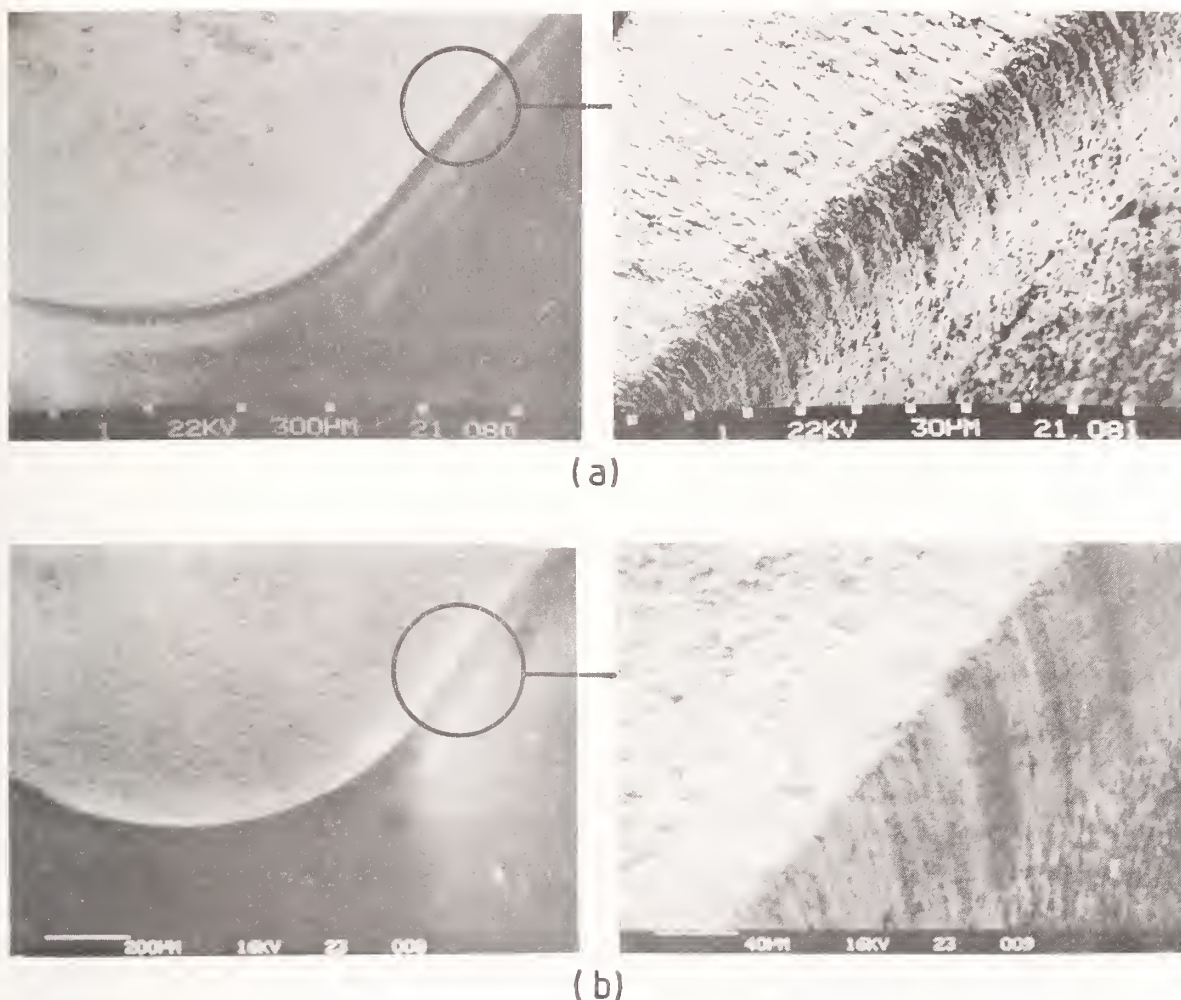
Fig. 3 Typical observation of flank wear on (a) P30 and
(b) K 20 Cemented carbide tools (CFRP Machining)

RESULTS AND DISCUSSION

Machining of CFRP Composites

Flank wear of plain cemented carbides

During machining, the cutting tool flank experiences severe adhesion due to sliding against the fibre in the work surface. This results in the generation of flank wear. Figure 3 illustrates typical observation of flank wear on tool grades P30 and K20 (Table 5) in machining CFRP composites. It is seen that while P30 tool experiences abrasive flank wear, K20 tool exhibit relatively smoother wear surface. The hardness of P30 tool was 14500 MPa (HV30), while it was 16000 for K20 tools. Despite the marginal difference in the hardness, K20 tool exhibited a fairly smooth and broader flank wear. During machining, TiC particles in the P30 tools can be dislodged [5] and transferred to the work surface. On further sliding, this loosely held TiC partricles could abrade the tools, in addition to the plowing and grooving of the tool by the carbon fibres. K20 tools,

493

TABLE 5. TOOL AND COATING MATERIALS PROPERTIES

PROPERTIES	P-30	K-20	TiN coating	TiC coating
Hardness(HV30) MPa	14500	16000	26000	32000
Comp.Strength MPa	4700	5000	-	-
Conductivity W/m- K	45	80	46.1	25
Coeff.of Thermal Expansion 10^{-6}m/m- K	6.7	5	-	-

which are plain cemented carbides without the hard TiC particles, exhibited smoother flank land associated with localised small scale deformation of the contacting asperities, resulting in smoother flank wear. This situation is analogous to machining of cast iron, where K20 performs better than P30.

Flank wear of coated carbides

CFRP composites have been machined with TiN coated (K type sub-strate) tools. A typical observation on flank wear of coated carbide tool is presented in Figure 4. It is seen that the continuous sliding of the machined work-surface over the tool flank has displaced the coating material down to the flank wear boundary, presenting typical tear-drop projections. Tear-drop projections represent material wiped down to the wear boundaries by sliding contact. When the just machined work-surface slides past the secondary flank of the coated carbide, localised attrition between the coating material and work surface will occur, resulting in higher contact temperatures over such spots. This can facilitate transport of the coating material experiencing attrition down to the flank land boundary.

Comb-cracking during flank wear

During machining of CFRP composites, the coated carbide tools exhibited a pattern of comb cracking over the flank land. Figure 5 presents a typical observation of comb-cracking on TiN coated tools. A number of parallel cracks running in a direction normal to the cutting edge can be seen on the flank-land. The occurrence of comb-cracking can be attributed to alternate thermo-mechanical stressing of the tool material during machining of composites. During machining, a cutting tool usually experiences higher temperatures at three distinct zones: depth of cut line (dcl) zone, nose, and secondary grooving zone (Figure 6). The zones farther away from the cutting nose undergo rapid heating and cooling, experiencing quenching stresses and cracking [6]. Apart from this, the orientation of fibres with respect to the cutting edge induces force fluctuations. Thus, the coated carbide would have experienced thermo-mechanical stresses, resulting in cracking of the coating in a section over the dcl zone. Once originated subsequent cracks occurred in zones closer to the cutting nose. With continued machining, comb cracking running parallel to the cutting edge
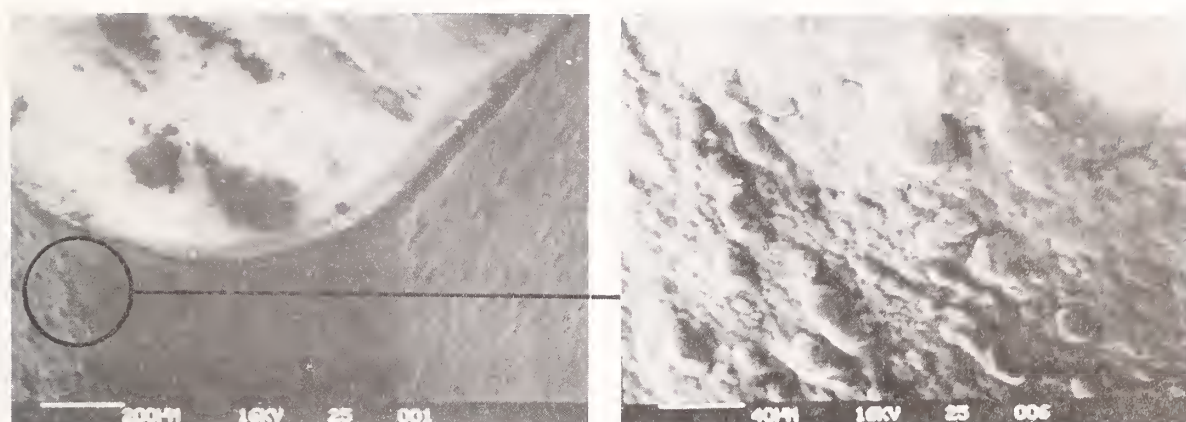
Fig. 4   Tear drop projections on the secondary flank of TiN
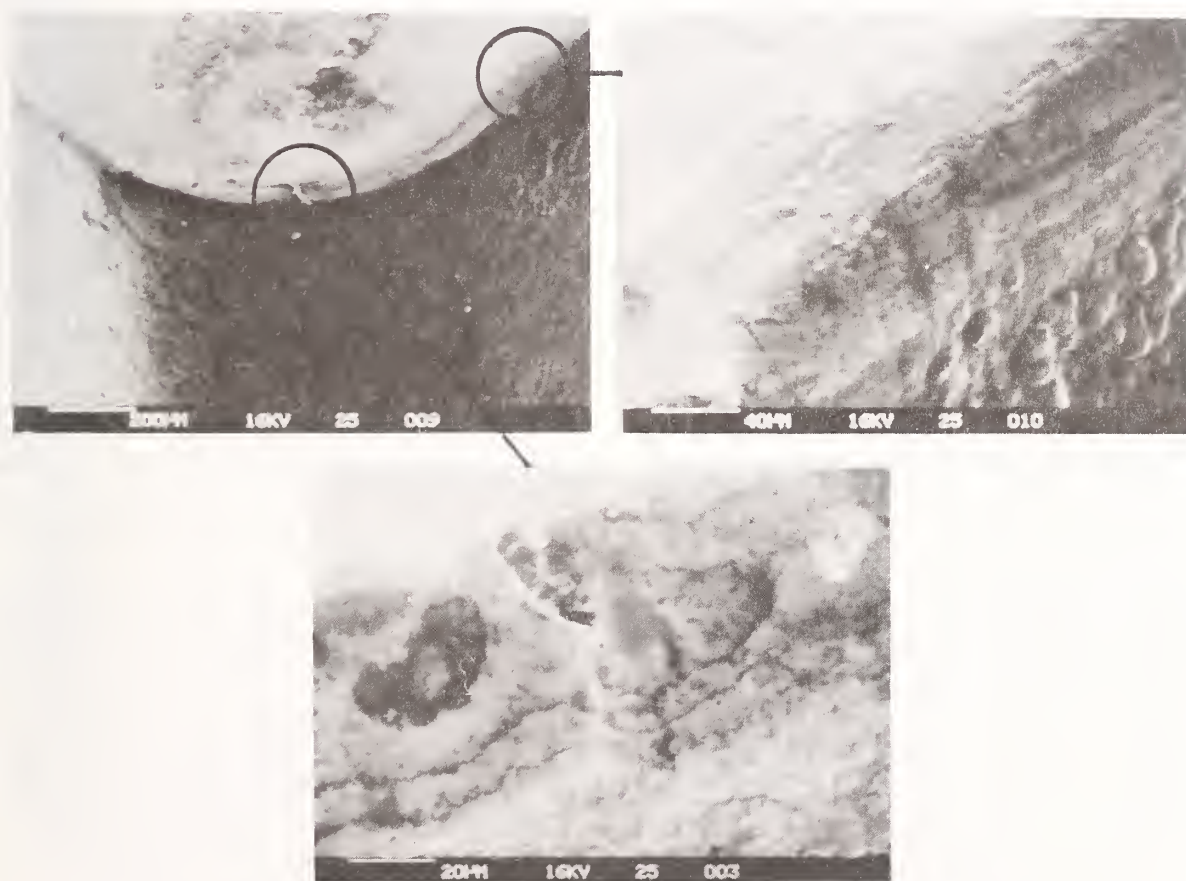coated K - type substrate tool (CFRP Machining)

Fig. 5   Comb - cracking observed on TiN coated K - type
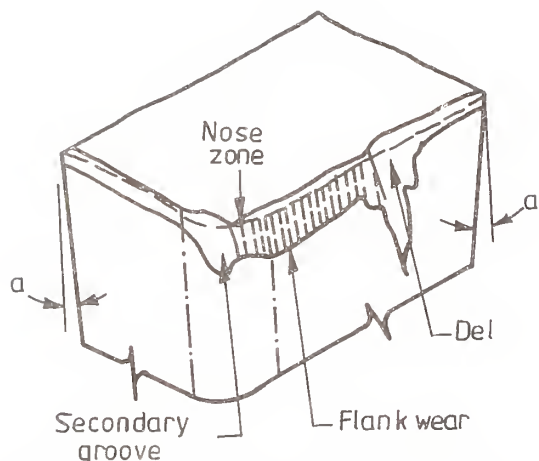substrate tools (CFRP Machining)

Fig.6 Schematic illustration of
tool wear

also occurred, weakening the
tool-flank and spalling of the
coating. This can be seen in
Figure 5. Spalling of hard and
brittle material is due to de-
cohesion failure and usually
results in sharp spall-boundary.
The occurrence of de-cohesion
failure and consequent spalling
is illustrated in Figure 7.

**Flank wear asssociated with
fatigue**

Cyclic loading of cutting
zone can promote fatigue of
hard materials of the cutting
tool. Continuation of machining,
even after occurrence of

localised spalling resulted in
higher order chipping of the
coated tool. The observed
chipping of the TiN coated
tools, associated with a dimpled
fracture of the substrate is
presented in Figure 8. The load-
reversal during machining of
CFRP composites could have
induced low-cycle fatigue of the
tool material over the cutting
zones resulting in chipping of
the flank portion.

Machining of KFRP Composites

Machining of KFRP was
observed to be more hazardious
severe, owing to the clogging
and chipping of the cutting
edges by the fussy chip produced
during KFRP machining. This has
resulted in sudden chipping of
the cutting edge, making it
difficult to predict the tool
performance. Figure 9 presents
the types of chips produced
during CFRP and KFRP machining.
Short segmented chips with
broken carbon fibres were
produced during CFRP machining;
while continuous tenacious and
fussy chip in lumps were
produced with KFRP machining.
This has resulted in clogging of
the cutting edge and consequent
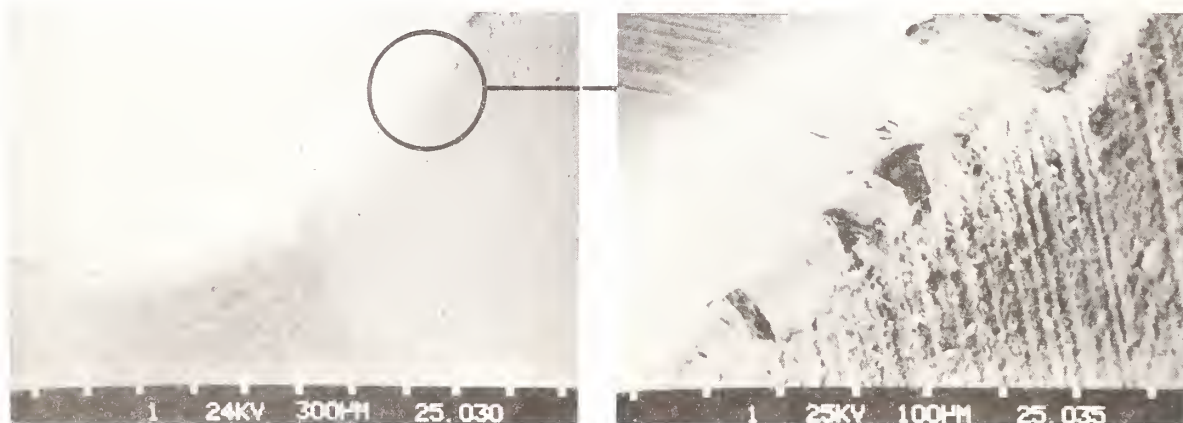chipping. Chipping of P30 tools

Fig.7   Cohesion failure and consequent spalling of TiN
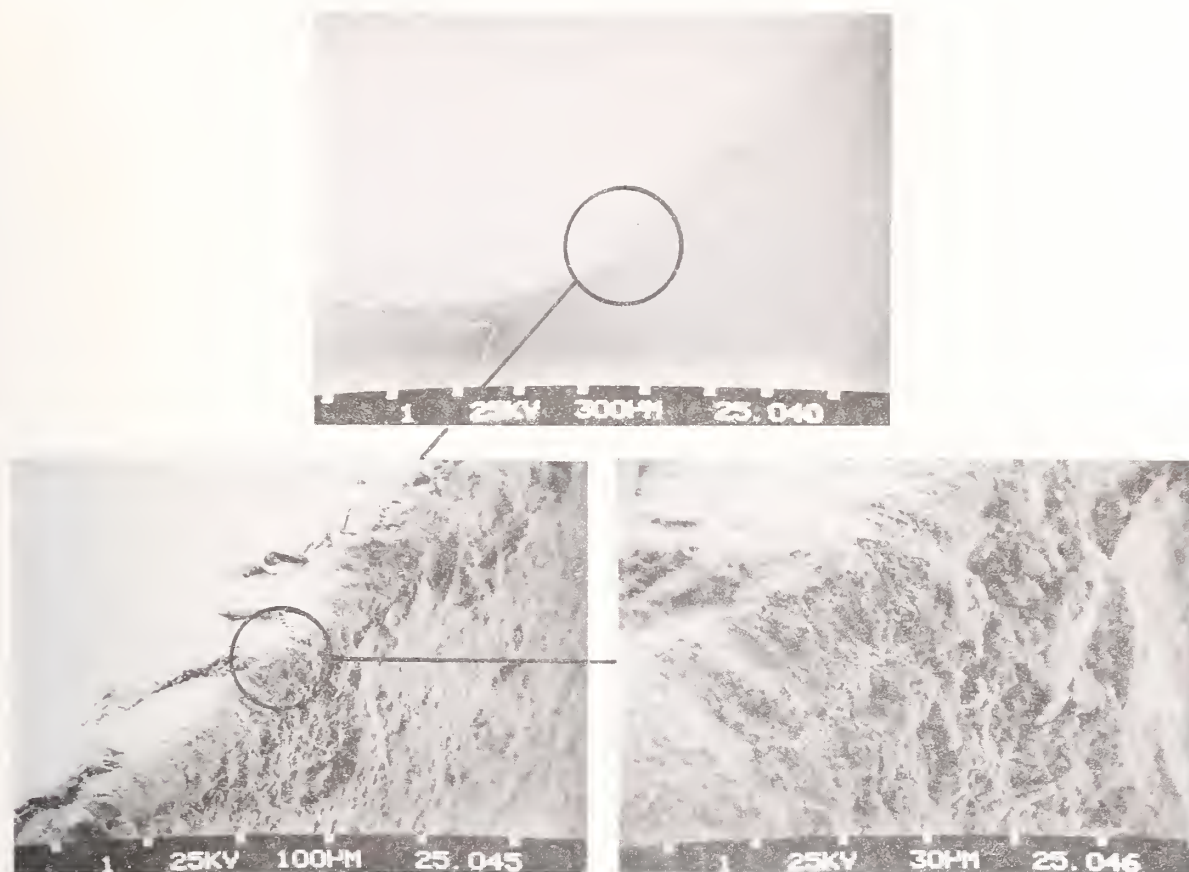coated K-type substrate tools (CFRP Machining)

496

Fig. 8 Chipping of TiN coated K-type substrate tool
associated with a dimpled fracture of substrate
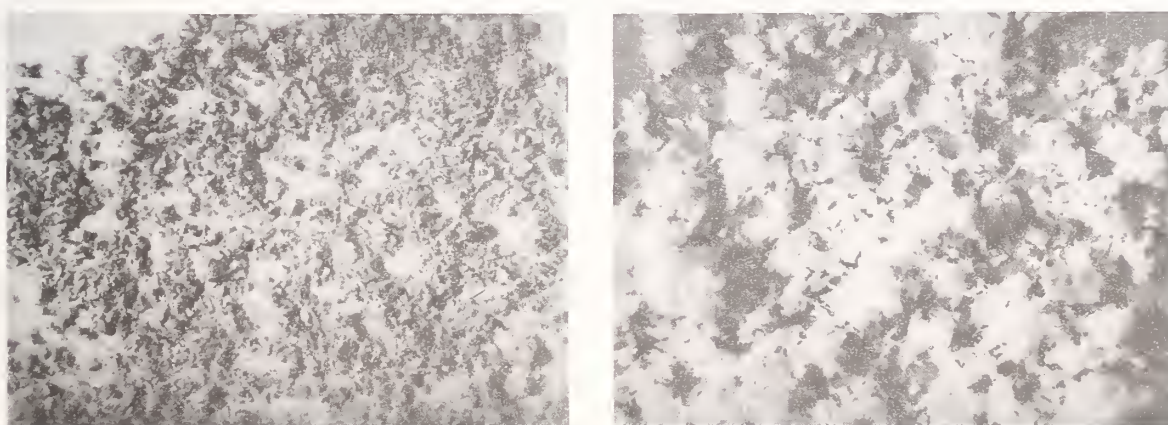
Fig. 9 Type of chips produced during FRP machining
(a) CFRP and (b) KFRP
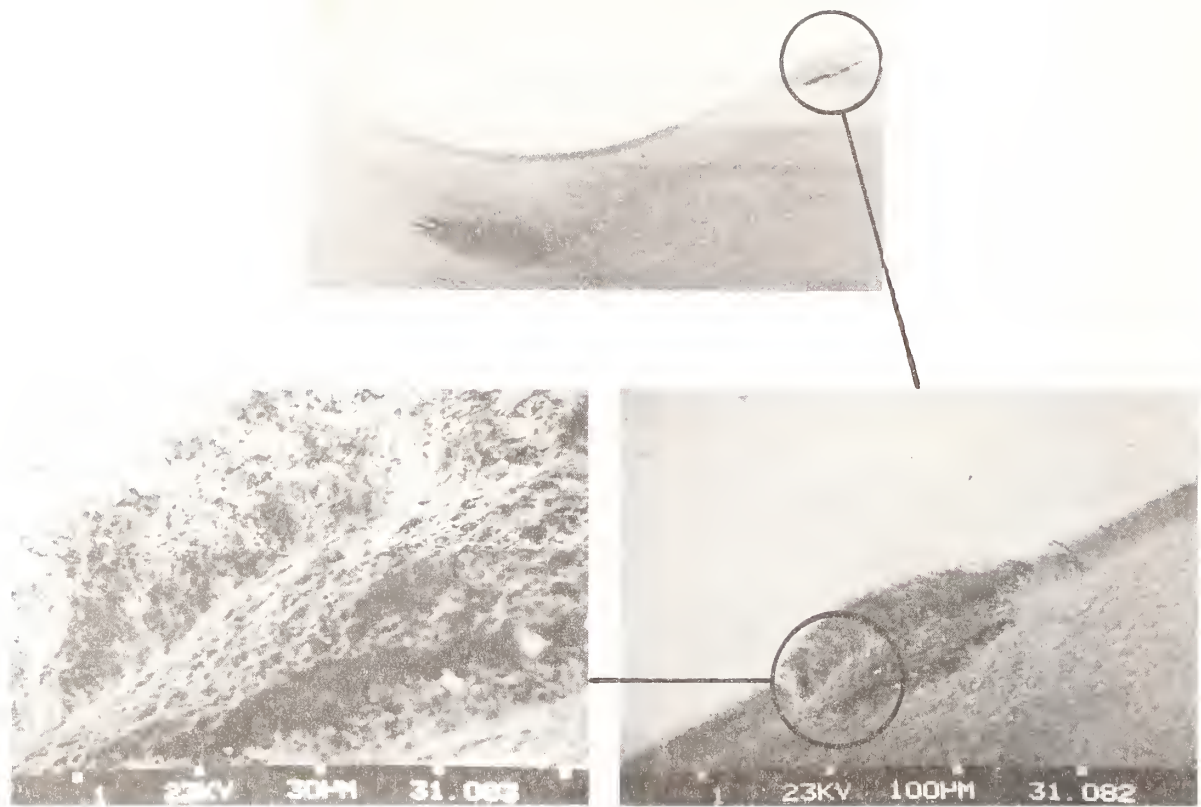
Fig. 10 Notchining over dcl zone - P30/KFRP Machining

over dcl during machining of KFRP composite is presented in Figure 10. Unlike the case of carbon fibre, Kevlar is tenacious and cannot be cut easily, resulting in producing fussy chip in lumps. Figure 11 presents bending stress strain characteristics of reinforcing fibres [7]. It is seen that, while carbon is relatively brittle Kevlar is tenacious, production of fussy chip in lumps and continuous rubbing of chip over the tool material resulted in spalling of coating with TiN coated tools as well. Typical spalling of coating observed on TiN coated tool is presented in Figure 12. Continuous rubbing of fussy chip in lumps over the cutting zone, might have caused localised galling and removal of material resulting in spalling.

CONCLUSIONS

Observations on machining of CFRP and KFRP composites have shown two distinct tool wear mechanisms; 1) thermo-mechanical and stress induced tool wear with CFRP, and 2) dominant chip notching with KFRP composites.

- Comb-cracking and consequent spalling by de-cohesion failure was the dominant cause of flank wear of TiN coated carbides.

- P30 carbides experienced abrasion dominant flank wear, while K20 carbides exhibited relatively wider, but smoother flank wear while machining CFRP composites.

- All the cutting tools used for machining of KFRP composites

498
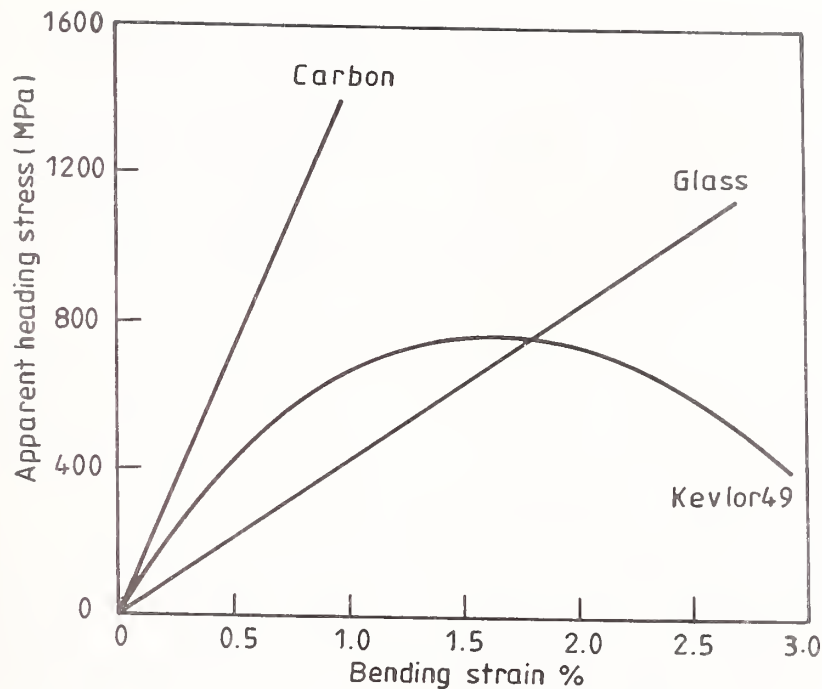
Fig.11 Bending stress-strain characteristics of Reinforcing fibres [7]
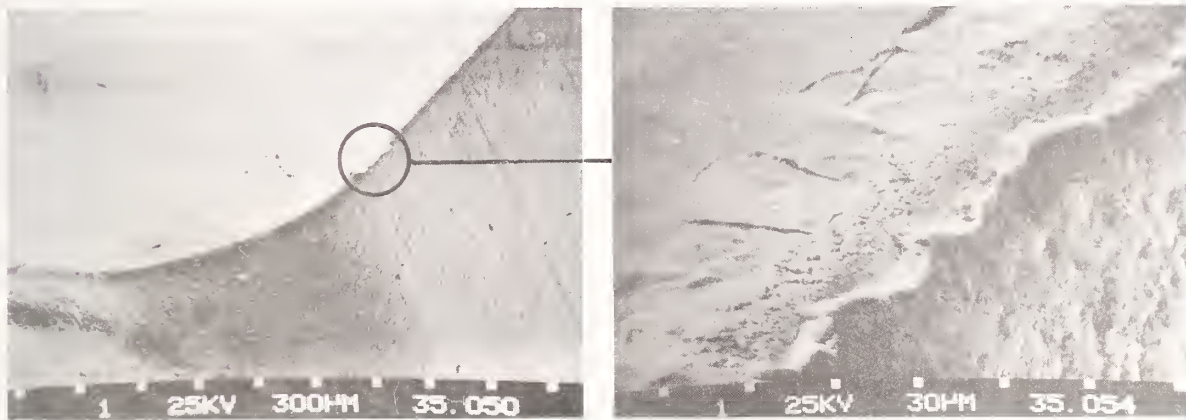
Fig. 12 Typical spalling of coating observed with TiN coated K-type substrate tool (KFRP machining)

experienced severe chip notching and galling over the dcl zone.

- From the types of chips produced it can be concluded that for machining of KFRP composites, a cutting tool having sharp cutting edge with as small a nose radius as possible may be recommended for effectively cutting the chip,

thereby minimising the tendency for chip clogging and notching.

REFERENCES

1. K.Sakuma and M.Seto, "Tool Wear in Cutting Glass Fibre Reinforced Plastics (The Relation Between Fibre Orientation and Tool Wear)",

Bull.of JSME, Vol.26, No.218, pp.1420-1427, Aug. 1983.

2. K.Sakuma and M.Seto, "Tool Wear in Cutting Glass Fibre Reinforced Plastics (The Effect of Physical Properties of Tool Materials)", Bull.of JSME, Vol.22, No.163, pp.107-114, Jan.1979

3. K.Sakuma and M.Seto, "Tool wear in Cutting Glass Fibre Reinforced Plastics (The Relation Between Cutting Temperature and Tool Wear)", Bull.of JSME, Vol.24, No.190, pp.748-755, April 1981.

4. W. Schintlemeister, "Cutting Tool Materials Coated by Chemical Vapour Deposition",

WEAR, Vol.100, pp. 153-163, 1984.

5. G.Santhanakrishnan, "Investigations on Machining of FRP Composites and Their Tribological Behaviour", Ph.D. Thesis, IIT Madras, India, June 1990.

6. R.Krishnamurthy, and A.S. Choudhyury, "Comb Cracking of Cemented Carbides", Proc.13th AIMTDR Conference, Jadavpur University,India, pp.99-B103, 1988.

7. K.Friedrich, "Ultra High Strength Materials", Fotschritt Berichte Der VDI, Zeitschriften, Vol.5, No.82, 1984/1.

THE METALLURGY OF CBN AND ITS WEAR IN HIGH SPEED MACHINING OF FERROUS MATERIALS

G. RAI

Smith Megadiamond, Provo, UT

Cubic boron nitride (CBN) tools are increasingly being used in high-speed machining of materials due to many advantages when using CBN tooling as an alternate to tungsten carbide or to grinding operations. These are: excellent high-temperature strength, required to maintain its shape at cutting temperatures; high melting temperature; relative chemical inertness towards most materials; and a hardness second to only diamond. However, use of CBN in machining of some ferrous-containing materials, which include ferritic steels and some forms of cast iron, is limited due to higher than expected tool wear. This paper describes, in general terms, the high-pressure process of synthesizing polycrystalline CBN tool blanks, the role of second phase material in the microstructure, and its interaction with CBN grains. The results of an Auger electron microscopy study on diffusion couples comprising a CBN layer in contact with ductile cast iron, exposed to 1000°C for extended periods of time, is described. It was found that the concentration of boron in the cast iron decreased with increasing sputtering time, whereas the nitrogen concentration remained virtually unchanged. In the CBN layer, however, the carbon concentration at the interface was higher than the bulk concentration in the CBN layer.

INTRODUCTION

The trend toward higher productivity places a premium on reducing manufacturing time by use of high speed, precision machine tools. A cutting tool used for these systems must be resistant to fracture and to plastic deformation in order to maintain its integrity. If these requirements are met, then resistance to wear becomes the primary concern. The maximum cutting speed for the cemented carbides is limited by their inability to resist plastic deformation in the machining of steel and other alloys. The carbide family of tools starts melting around 1250°C and the strength of carbide falls off rapidly with increasing temperature. Peak machining temperatures of about 1000°C are easily attained in practice[1], resulting in severe plastic deformation at the cutting edges. The advent of a superabrasive family of cutting tools, comprising essentially polycrystalline diamond (PCD) and polycrystalline cubic boron nitride (PCBN) materials, has made it possible to further increase the speeds and feeds.

The use of polycrystalline diamond cutting tools is somewhat limited to non-ferrous materials and ceramics due to the affinity of carbon with most metallic materials, particularly iron based engineering materials. On the other hand, PCBN cutting tools have found wide acceptance in machining a variety of materials ranging from cast iron to superalloys because of their relative chemical inertness. Many advances have been made in the development of grades of CBN-based tools to further reduce the chemical affinity of tool material with the work piece. The purpose of this paper is to briefly describe the manufacturing process, the microstructural constituents of PCBN

and its chemical interaction with nodular cast iron as evaluated by a diffusion couple study.

SYNTHESIS OF POLYCRYSTALLINE CUBIC BORON NITRIDE

The polycrystalline CBN blanks with a tungsten carbide substrate are synthesized by a high-pressure, high-temperature process. The starting material, generally, is CBN crystals which have been cleaned, classified and reduced. The feed powder, which is a mixture of CBN crystals and sintering aids, is placed onto a WC-Co disc, then encapsulated using refractory metals. This capsule is placed in a heater tube which, in turn, is surrounded by pyrophyllite, a pressure transmitting media used in high-pressure systems.

Among the many technologies for achieving ultra high pressures, cubic press technology has been found to favor PCD products having curved surfaces[2]. The cubic press employs the use of six anvils, as shown in a schematic diagram (Figure 1), to apply pressure simultaneously on all six faces of a pyrophyllite cube, which houses the heater tube and the encapsulated CBN material for sintering. The pressure applied is in the range of 50 to 70 Kbars (5 to 7 GPa) above the determined critical pressure for HBN to CBN transformation, as shown in Figure 2. In some instances hexagonal boron nitride (HBN) is used along with cubic boron nitride crystals and catalysts, which could be metals or metal nitride. Hexagonal boron nitride, in this case, is dissolved into the solvent or catalyst within the high-temperature, high-pressure CBN stability region. Cubic boron nitride then very likely nucleates heterogeneously on the existing CBN sites and grows. Control of the nucleation and growth processes is used to vary the physical properties of the polycrystalline composite. The sintering process utilizes liquid phase to promote intercrystalline CBN bonding. The liquid phase is provided by melting of the carbide substrate at the CBN-carbide interface. This seems to be achieved by the extensive alloying effect of boron and nitrogen[3] with the pseudo-eutectic phase of tungsten carbide cobalt, which is reported to wet CBN crystals extremely well. The liquid phase infiltrates the CBN powder bed by capillary action and fills interstitial positions.

In liquid phase assisted sintering some shrinkage occurs as a result of particle rearrangement, which is facilitated by the lubricating action of liquid and driven by its surface tension, which pulls the particles together. In addition, regions of forced contact between CBN particles are under mechanical stress, which locally increases the particles' chemical potential[4]. This results in more rapid solution of those particle regions into liquid phase, with matter being transported by diffusion in the liquid to be deposited elsewhere. Therefore, the particle centers approach each other and the pores shrink just as in the solid state sintering process.

MATTER TRANSPORT IN ULTRA HIGH PRESSURE SINTERING

Densification by solution-precipitation in liquid phase sintering is largely governed by diffusion of material through the liquid phase. The diffusion of matter can be accomplished by lattice or grain boundary diffusion, as shown in Figure 3. Since CBN crystals are the closest packed structures and are comprised of atoms of different chemical nature, the lattice diffusion contribution to sintering is very limited. On the other hand, atom transport by grain boundary diffusion is the more dominant mechanism for sintering. The role of pressure in sintering of CBN grains is essentially to provide a stable region in which back conversion of CBN to HBN is prevented. Its effect on the diffusion constant, whether for boundary or lattice diffusion, is not well understood, but can lead to very high compressive stresses at grain contacts. According to the Gibbs-Thompson equation[5], the increase in chemical potential or solid solubility due to stress is given as:

$$\Delta C = C_o [\exp (\sigma_{appl} \, v \, /kT) - 1] \qquad (1)$$

where ΔC is the solubility increase, σ_{appl} is applied stress, C_o is the solubility under no applied stress, v is the molecular volume of the solid, T is temperature, and k is the Boltzman constant. For a two to three times increase in effective stress, solubility can easily be increased by 50 to 70% at 1300°C. The effect of ultra high pressure, therefore, appears to be two fold: it increases the solubility of CBN particles in the liquid metal and

502

increases the diffusion rate. Both of these tend to enhance the sintering rate.

DEVELOPMENT OF CBN MICROSTRUCTURE

During the sintering process, the initially separate CBN crystals are transformed into grains of a polycrystal that contact their neighbors on nearly all sides. The void space between particles is filled with the liquid pool of metal infiltrating from the molten tungsten carbide interface. At first these are long channels that extend to the surface, but later develop more defined shapes. Sometimes these channels are quite thick and are devoid of any CBN grains. Figures 4a and 4b show features of these channels, also called metal "rivers", that are found in the high-pressure sintering process. Figure 4b is a higher magnification microphotograph showing details of precipitation of tungsten carbide grains from the metal pool formed during cooling. It is necessary to control formation of these metal rivers, as these constitute weak regions in the cutting tool leading to excessive wear.

The microstructure of polycrystalline cubic boron nitride essentially comprises CBN grains of 1 to 3 micron in size. The metallic second phase is found along the triple points and also along grain boundaries, as shown in Figures 5a and 5b at two magnifications. The size of the metal pool is larger at the triple points compared with the metal pool size on the grain boundaries. Figures 5c and 5d are scanning electron micrographs of specimens subjected to leaching for one hour in a mixture (50% by volume) of nitric and hydrofluoric acids. The figures show extensive intercrystalline bonding of CBN crystals, with voids representing prior presence of metallic catalyst material. A qualitative energy dispersive analysis suggested that the metal pools are essentially W-Co alloys with smaller amounts of Al. The amount of metal as determined by density measurement generally varies between 20 to 24% by weight of the CBN layer.

WEAR OF CBN TOOLS DURING MACHINING

Non-catastrophic tool wear (viz., gradual wear) during machining or turning operations can be grouped into two regions:

1. Low Speed or Mechanically Activated Wear. The primary mode of wear in most ceramic and hard materials falls under this category, where removal of tool material occurs by scouring action of hard phase inclusions or protruding asperties in the work piece[6]. Thermal and mechanical fatigue may also play some role in abrasion wear[7]. While hardness of the tool material is the most obvious and significant consideration in abrasive wear, the role of toughness of the tool material is not so well defined. In brittle materials, at a critical load, a sub-surface median vent crack is formed on the plane of the applied stress. With additional loading this sub-surface crack grows to a critical size, at which point it becomes unstable and a catastrophic failure ensues[8]. In tool materials such as CBN, abrasion can be assumed to take place when two adjoining cracks intersect. The removal volume is then related to the length of cracks in the tool. Laboratory research shows that abrasion wear of tool materials involves microfracturing of grains, indicating that toughness of grains plays a major role in their wear resistance. The wear rate (W) is found to relate to fracture toughness (K_{IC}) by the following equation[9,10], where A is a constant:

$$W = A/(K_{IC})^4 \qquad (2)$$

This seems to have been found true for carbide cutting tools also. It is quite clear that for similar physical properties of cutting tool material, a tougher tool material will show better abrasion resistance.

2. High Speed or Thermally Activated Wear. The physical mechanisms that are responsible for producing gradual wear depend on cutting temperature. For each combination of tool and work piece materials, the transition temperatures between wear regimes are determined by the chemical and mechanical properties of the tool-work piece system. In low speed operations, chemical interaction between the tool and work piece is insignificant. In high speed machining, where temperatures[11] can rise in excess of 1000°C, the chemical stability of the

tool material with respect to the work piece becomes a very important contributor to wear. The chemical solubility of the tool material in the work piece increases exponentially with temperature. In essence, the tool material dissolves in the hot flowing chips and the transport of material from the tool cutting edge to hot chips can be visualized to occur in two steps, namely: transfer of tool material by solid state diffusion across the interface and transport of dissolved tool material from interface to chip bulk[12].

The wear of PCBN tools in the machining of ferritic materials has been studied. Heath[13] observed the reactivity of PCBN with soft non-martensitic phases of iron at relatively higher speeds. There are evidences in literature[14] indicating that machining non-hardened steels with PCBN was not economical due to "diffusion wear" resulting from high solubility of boron and nitrogen atoms in ferrite. Aspinwal, et al[15] reported that wear of PCBN tools is larger when cutting ferritic, as opposed to pearlitic, cast iron with surface speeds in excess of 90 m/min. They also found that relatively small changes in chemical composition of the work piece may produce very large changes in wear rate.

The flow of chips across the tool face is reported to produce peak temperatures of 1000°C in the vicinity of the cutting edge. The peak temperature seems to be governed by the nature of chip formation which could change from continuous to discontinuous. It was reported that crater wear in PCBN tools machining hardened M2 steel was lower than in its soft condition. Soft M2 steel exhibited continuous chip formation which became discontinuous when steel was hardened. In the milling of cast iron at speeds of 1,800 surface meters per minute, the PCBN wear rate for pearlitic steels was significantly lower than for ferritic steels. The segmentation of the pearlitic chips was more pronounced than ferritic steel[16]. It seems very likely that wear of PCBN in machining at high speeds is governed by a chemical dissolution process where tool constituents, namely the tungsten carbide-cobalt binder phase and boron and nitrogen atoms, interact mechanically and chemically with the work piece. It appears, however, that chemical interaction characterized by solid state diffusion of

atoms is a more dominant wear mechanism of PCBN tools.

DIFFUSION COUPLE EXPERIMENTS

Since both B and N exhibit solid solubility in ferrite, a diffusion study involving PCBN and ferrite is very useful in understanding the extent of matter transport across the interface. For this purpose, ferritic cast iron and PCBN tools of the same size were polished and pressed using an Instron machine to provide an intimate contact. These were held together tightly with the help of a vice. The diffusion couple was then annealed under pure hydrogen in a furnace maintained at 1000°C for 40 hours. The sample was allowed to cool in the furnace.

AUGER ELECTRON SPECTROSCOPY (AES) OF CAST IRON AND PCBN

The extent of inter-diffusion of CBN and ferritic cast iron constituents was analyzed using Auger electron spectroscopy (AES). Both the cast iron and CBN pieces were first cleaned and then sputtered to remove the outer layer to a depth of approximately 40 to 50 Å. The sputtering rate was determined to be 5 Å per second. The elemental analysis of both the cast iron and CBN pieces was continued as a function of sputtering time until no changes in the atomic concentration of elements could be detected. The atomic concentration profiles as a function of sputtering time for different elements in cast iron and CBN are shown in Figures 6 and 7, respectively. From these figures the following inferences can be drawn:

1. The atomic concentration of B and N does not change after about 2 minutes of sputtering, indicating that diffusion is limited to a depth of less than approximately 0.05 micron.

2. The B to N atomic ratio decreases from the bulk of the tool material to the interface of the diffusion couple. This indicates a faster rate of B diffusion into cast iron as compared to nitrogen.

3. The atomic concentration of C changes significantly from the diffusion interface to the bulk of tool material and remains approximately constant after a depth of approximately 0.08 micron.

4. The Fe atomic concentration in the CBN material does not significantly change with sputtering time, indicating a lack of Fe diffusion in the tool material.

5. The atomic concentration of nitrogen in the cast iron piece does not change with sputtering time, suggesting that nitrogen is probably lost at the interface in the form of gas and only B diffuses into cast iron.

Since the AES system analyzes constituents over an area of 1 mm x 1 mm, it also includes the light element analysis in the second phase (WC-Co) of the PCBN structure. It is, therefore, quite likely that diffusion of elements such as carbon into the tool material may also have occurred through the WC-Co phase of the structure. During machining using PCBN cutting tools, the moving chip provides a most efficient sink for diffusion of tool constituents. Since the tool is always in contact with the newly formed surface of the work piece, the diffusion rates can be faster than predicted by the static diffusion couple study.

SUMMARY

PCBN cutting tools provide an excellent combination of hardness, toughness and relative chemical stability to most work piece materials. However, chemical interaction between tool material and some forms of cast iron appears to be a major cause of wear. Interdiffusion between the tool and work piece materials could take the form where B and N essentially dissolve into the work piece; the work piece constituents, on the other hand, dissolve into the tool material mainly through the second phase (WC and Co).

ACKNOWLEDGEMENT

REFERENCES

1. M. C. Shaw, "Temperatures in Cutting," Proceedings of the Special Prod. Engineering Conference, ASME, Special Volume, Nov. 1988.

2. H. T. Hall, "High Pressure-Temperature Apparatus," Metallurgy at High Pressures and High Temperatures, edited by K. A. Gaschneider and M. T. Hepworth, Gordon and Breach Science Publishers, NY, 1964.

3. G. Rai, "Microstructure and Mechanical Properties of CBN Twinserts," Proceedings of the Int'l Conference on New Diamond Science and Technology, pp. 1069-1079, 1991.

4. J. H. Rosolowski and J. E. Burke, "Sintering," General Electric Corporate R & D Technical Report, 1988.

5. O. H. Kwon and G. L. Messing, "HIP of Liquid Phase Sintered Ceramic Composites: Tailoring Multiphase and Composites Ceramics," Materials Science Research, edited by R. E. Tressler, G. L. Messing, C. G. Pantano, and Robert E. Newnham, Vol. 20, pp. 41-53, 1985.

6. J. G. Baldoni and S. T. Buljan, "Ceramics for Machining," Ceramic Bulletin, Vol. 67, pp. 381-387, 1988.

7. E. Rabinowicz, Friction and Wear of Materials, NY: John Wiley, 1966.

8. A. Misra and I. Finnie, "A Review of the Abrasive Wear of Metals," trans. ASME, Vol. 104, pp. 94-101, 1982.

9. S. T. Buljan and V. K. Sarin, "Machining Performance of Ceramic Tools," Cutting Materials, edited by F. W. Gorsler, AIME, Metal Park, OH, pp. 335-348, 1981.

10. J. G. Baldoni, S. F. Wayne, and S. T. Buljan, "Cutting Tool Material: Mechanical Properties - Wear Resistance Relationship," trans. ASME, Vol. 29, pp. 347-352, 1986.

11. B. M. Kramer and N. P. Suh, "Tool Wear by Dissolution: A Quantitative Understanding," trans. ASME, J. Engg, for Industry, Vol. 102, pp. 303-312, 1979.

12. P. J. Heath, <u>Ultra Hard Materials</u>, ASM handbook, 9th ed., Vol. 16, pp. 333-352, 1987.

13. P. Hancock, "Coated Cutting Tools - Influence of Composition and Surface Integrity in High Speed Machining," <u>Final Technology Report</u>, Cranfield Institute of Technology, 1978.

14. D. K. Aspinwal and W. Chen, "Report on CBN Tooling Applications in Machining of Iron," University of Birmingham, 1987.

15. P. A. Dearnley, "A Metallurgical Evaluation of Tool Wear and Chip Formation When Machining Pearlitic Grey Cast Irons With Dissimilar Graphite Morphologies," <u>Wear</u>, Vol. 101, pp. 33-68, 1985.

16. Z. Palamii, "Cutting Temperature in Intermittent Cutting," <u>Int'l J. of Machine Tools and Manufacture</u>, Vol. 27, pp. 261-274, 1987.
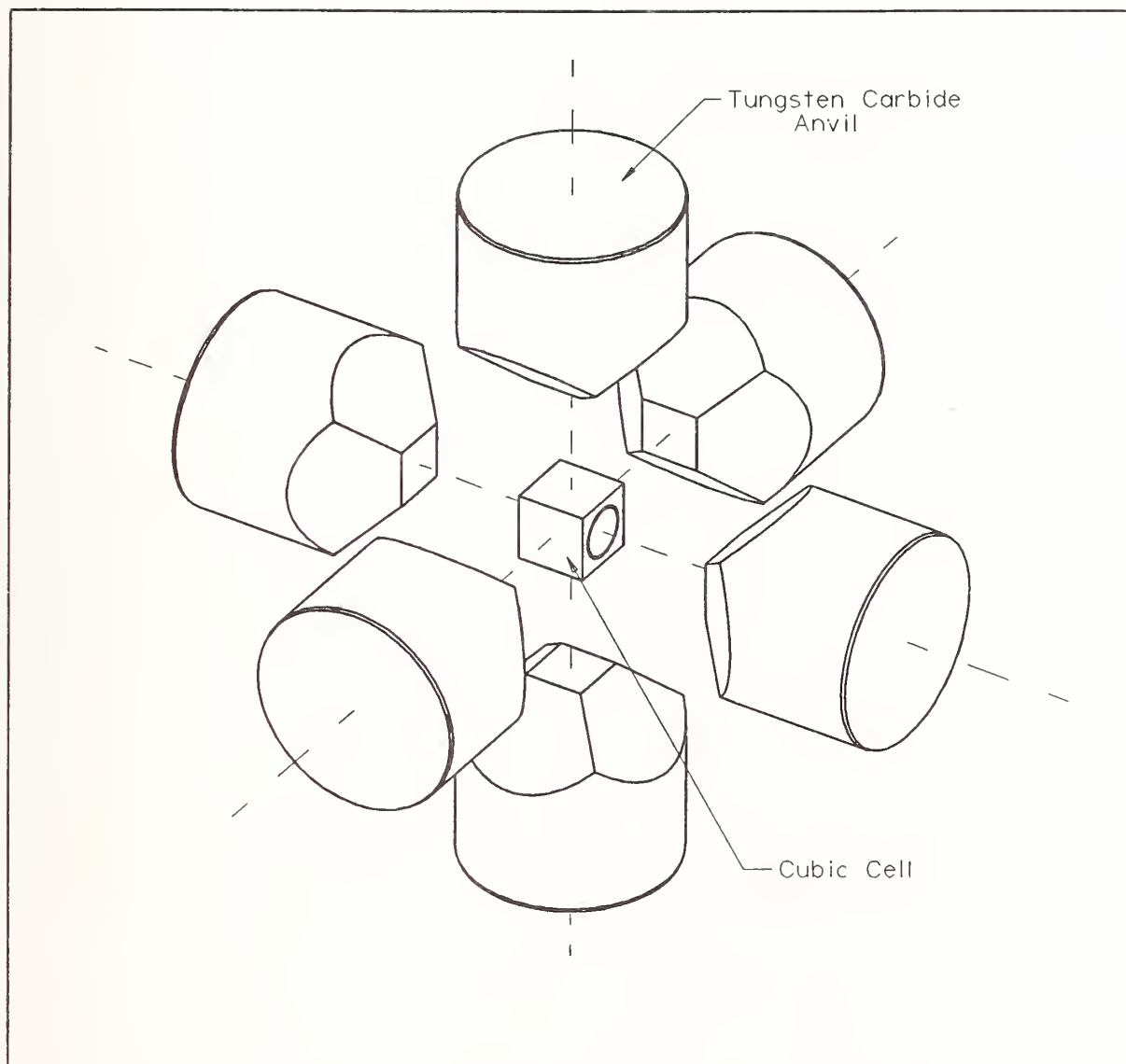
Fig. 1. Anvil configuration of Cubic Press
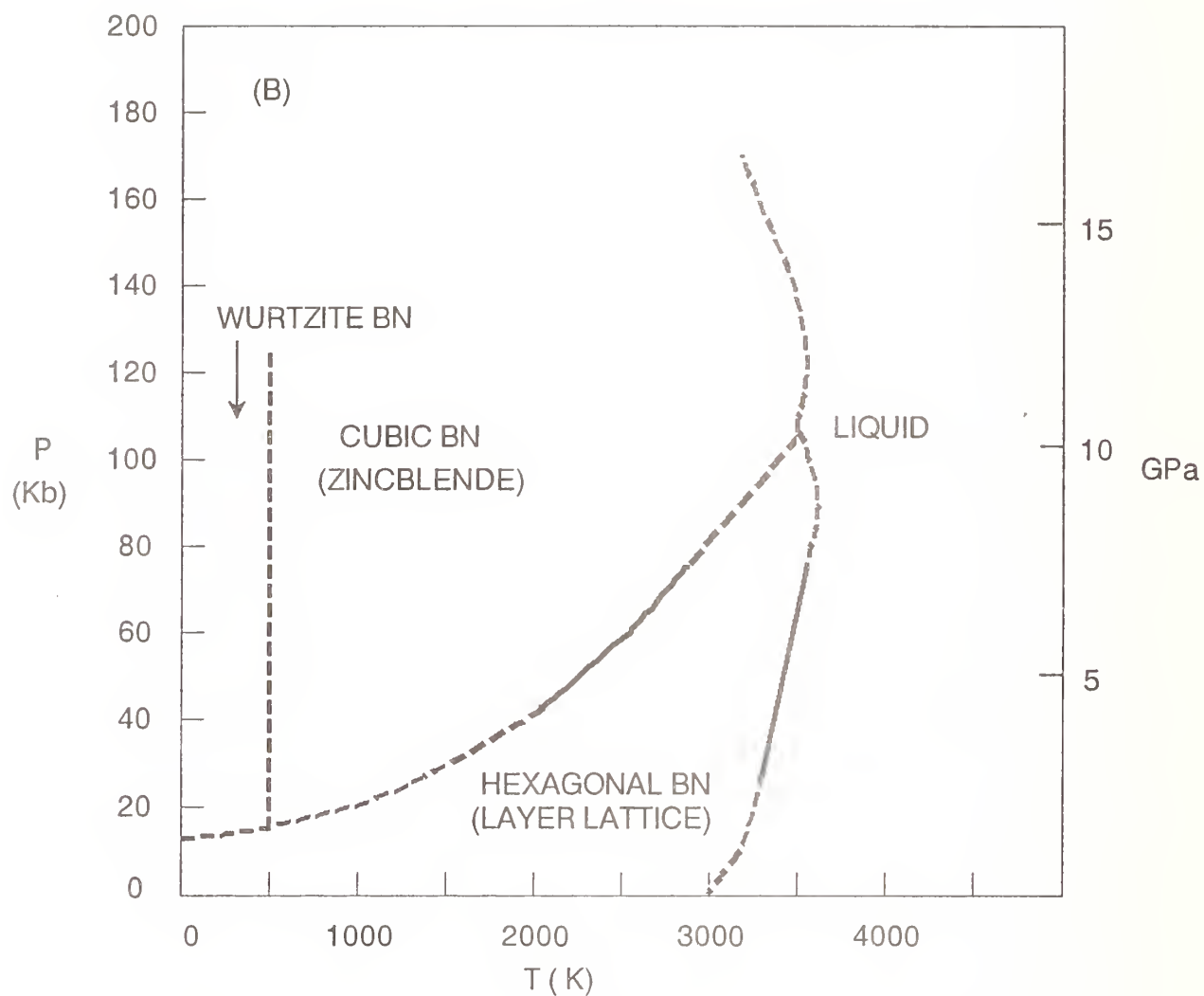
Fig. 2   Thermodynamic stable regions for conversion and growth
of cubic boron nitride.
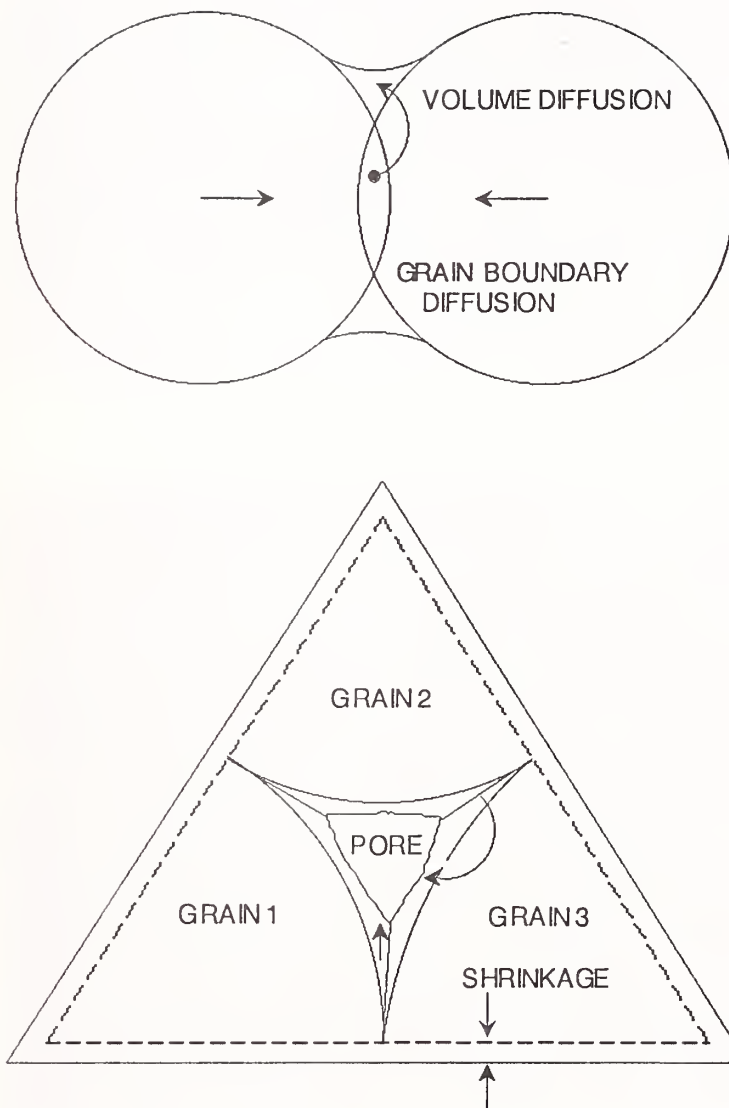
Fig. 3   Transport of matter between cBN particles through grain boundaries
and bulk diffusion. Pores disappear when they are touching grain
boundaries.
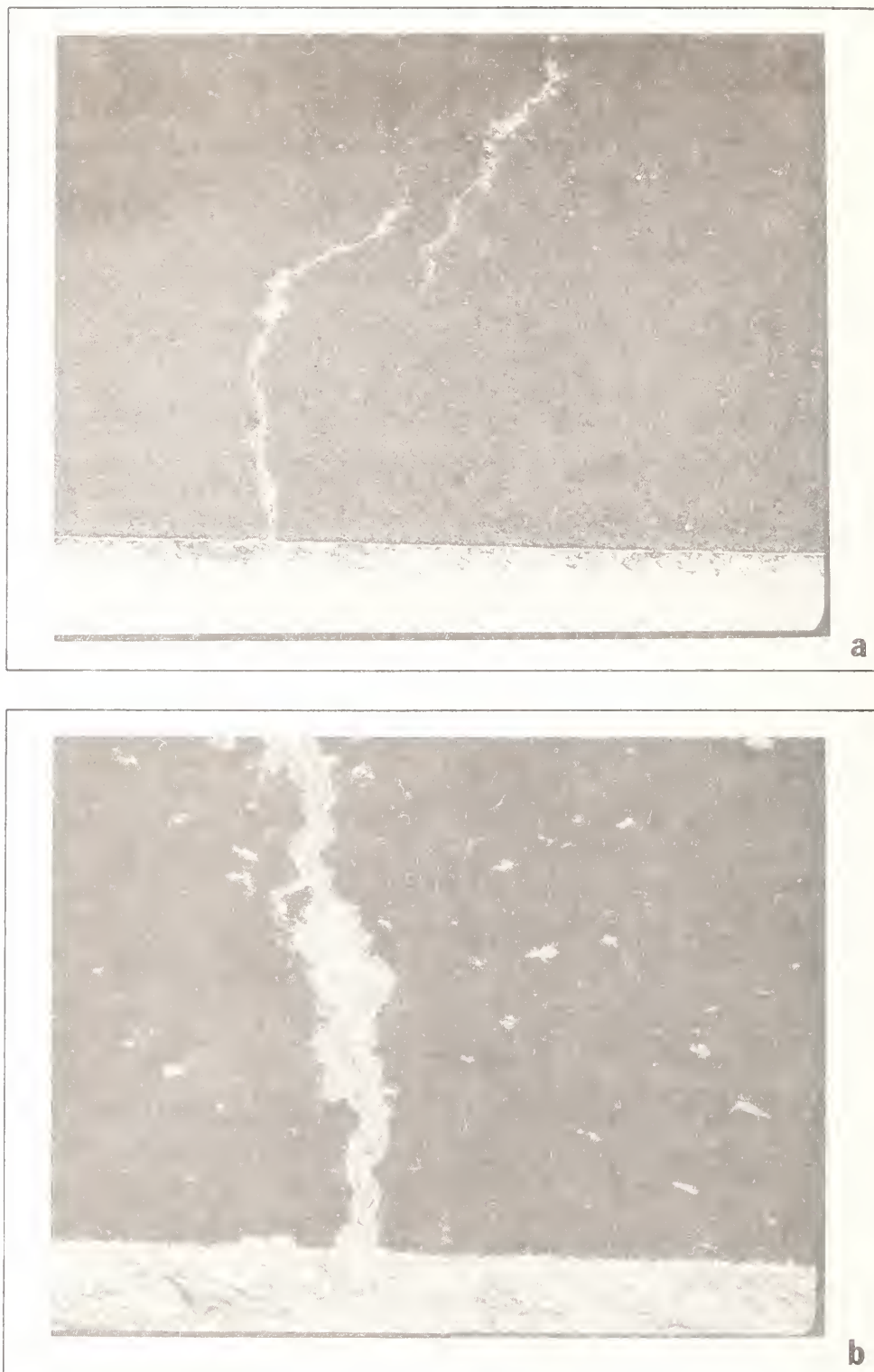
Fig. 4 Optical photomicrographs of cBN sintered under ultra high pressure
conditions showing (a) channels or rivers of metallic liquid which have formed
(100x), and higher magnification view (b), of the same showing WC precipitation
from liquid upon cooling. (500x).
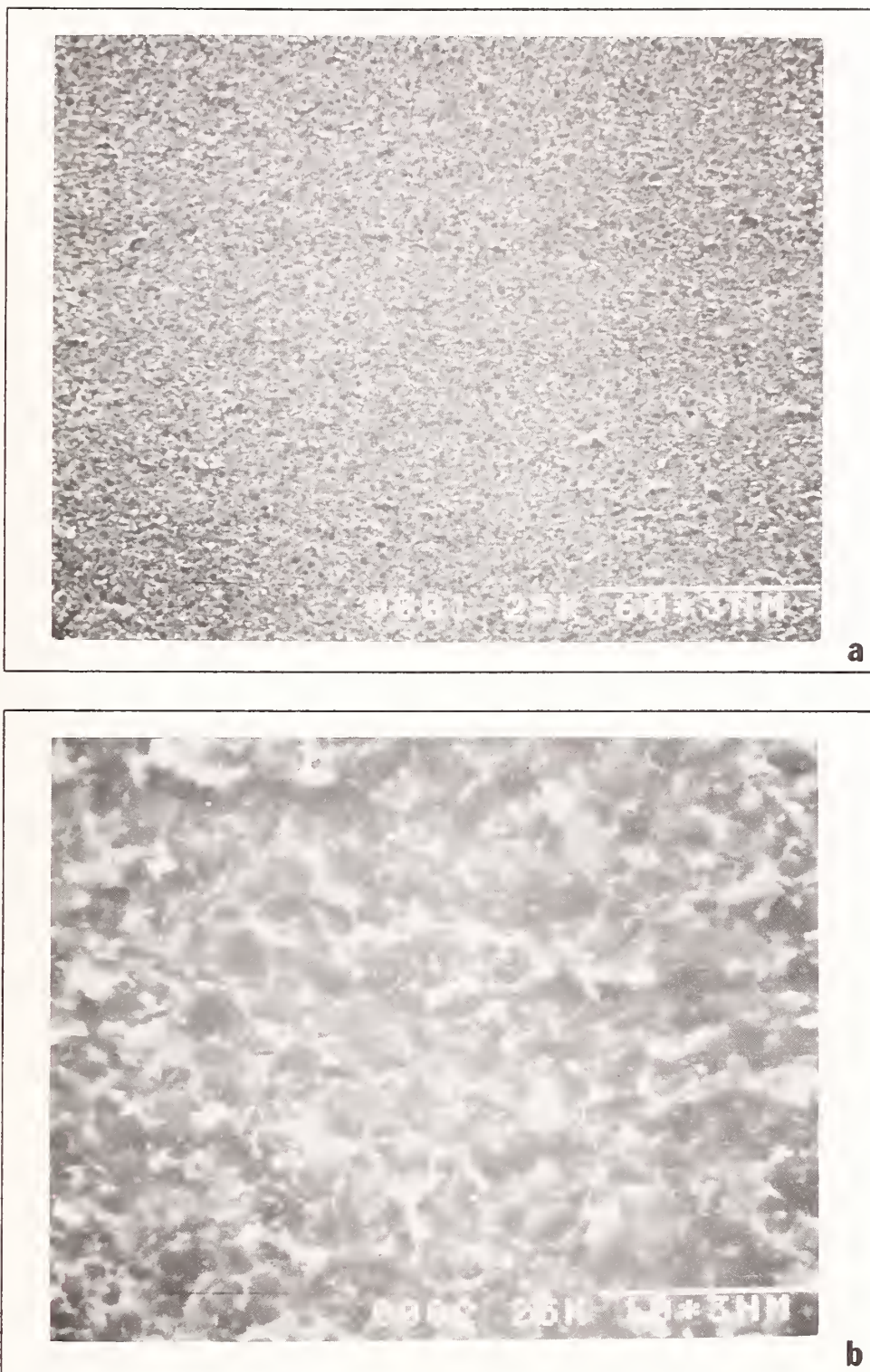
Fig. 5 Scanning electron micrograph (a) at 500x of polycrystalline cubic boron nitride sintered using ultra high pressure technology. Micrograph (b) at 1000x shows catalyst material which can be seen at grain boundaries and at triple points.

Fig. 5 Scanning electron micrograph (c) of polycrystalline cubic boron nitride sintered using ultra high pressure showing etched structure at 500x. Micrograph (d) is of the same structure now at 3000x showing intercrystalline cBN bonding.
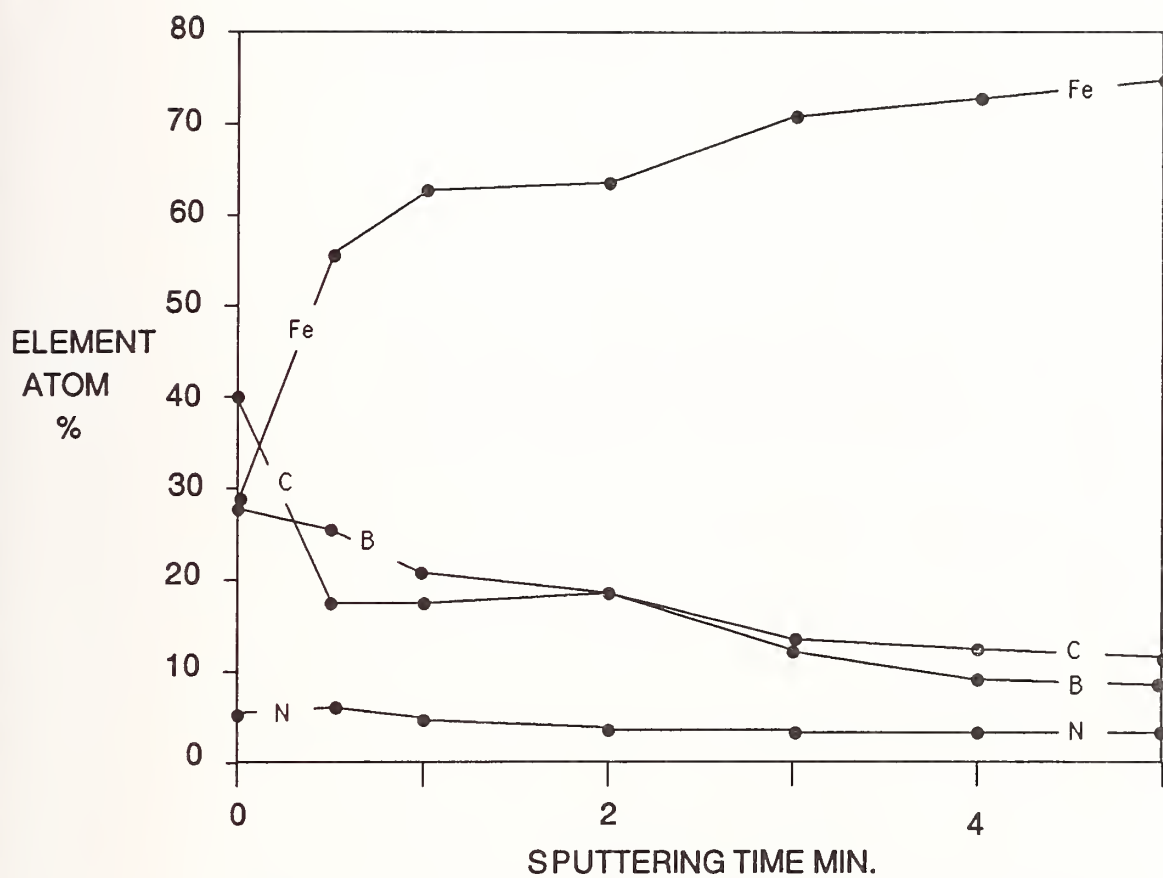
Fig. 6 Concentration profile of elements in cast iron as determined by AES after diffusion.

Fig. 7 Concentration profile of elements determined by AFS
in the PcBN tool material after diffusion.

LASER AND ELECTRICAL DISCHARGE MACHINING

CRACK-FREE PROCESSING OF HOT-PRESSED SILICON NITRIDE CERAMICS USING PULSED YAG LASER

N. MORITA
Chiba University, Chiba, Japan

This paper describes the effect of crack-free laser processing of hot-pressed silicon nitride ceramics on fracture strength and residual stress. The fracture strength of the processed test pieces was determined by three-point bending tests. 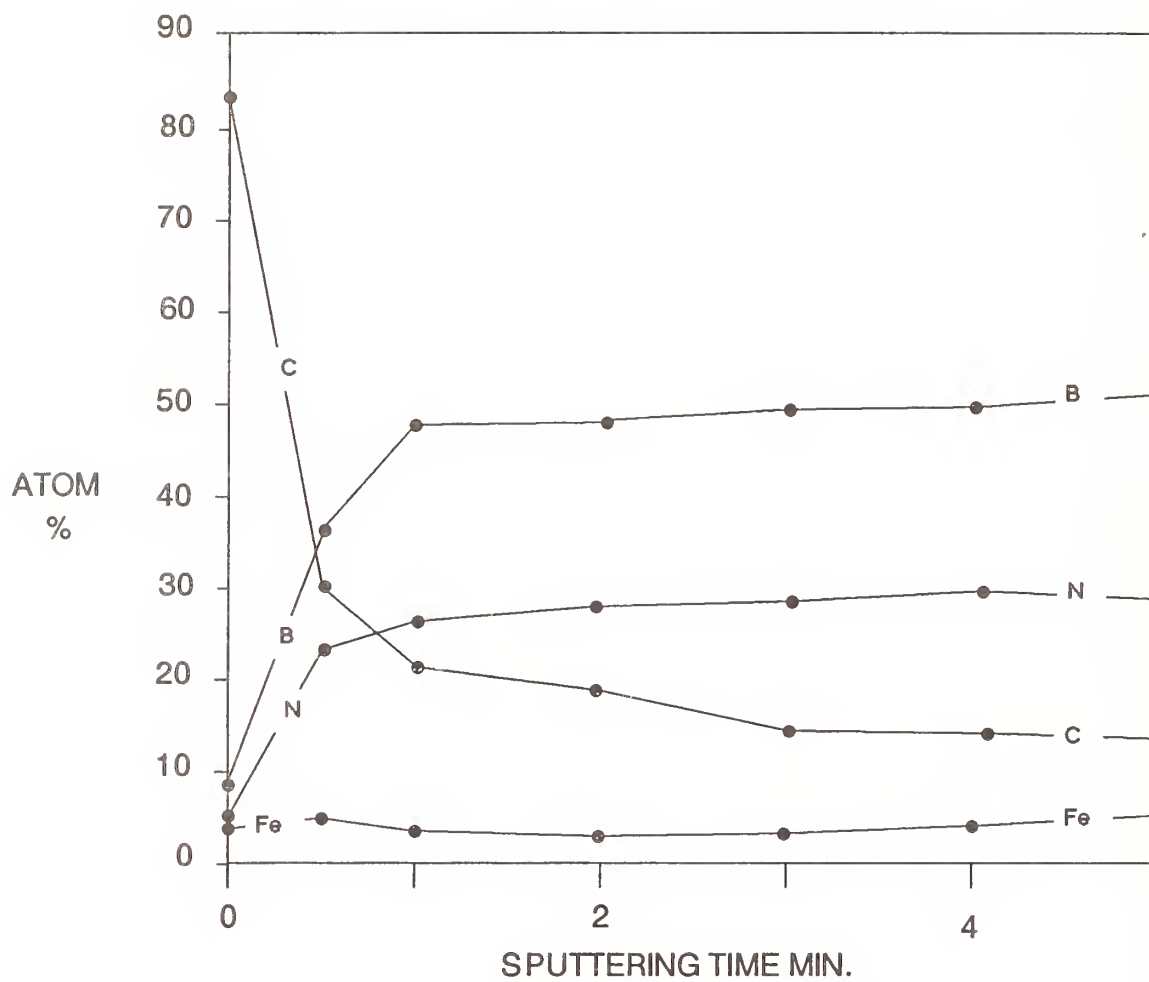The residual stress in the processed surface was characterized by X-ray diffraction measurement. The strength of the laser-processed workpieces was reduced to 90-80% compared with that of the ground workpieces because of subsurface layer damage, which included the heat-affected layer and the residual stress layer. In particular, the latter greatly affected the fracture strength because the higher compressive residual stress layer generated during grinding was released by laser processing. It is concluded that the newly developed crack-free processing technique has great industrial possibilities.

1. Introduction

Advanced fine ceramics have many excellent physical and chemical properties. However, their hardness and brittleness make them difficult to machine. The focused laser beam is one of the tools which can be used to machine fine ceramics[1]~[4]. However, the laser machining method has some dissdvantages such as the generation of recast layers[5] and the development of thermal-stress-induced cracks[6]. These defects decrease the fracture strength of ceramics, and also worsen other good characteristics[7]. This is probably the primary reason why laser applications for machining ceramics have been limited[8],[9].

This paper describes the feasibility of a crack-free processing method for hot-pressed silicon nitride (Si_3N_4) ceramics using an yttrium aluminum garnet (YAG) laser. The influences of the laser waveforms, such as pulse duration, peak output power and pulse repetetion frequency on the generation of cracks and recast layers during laser drilling are evaluated. The fracture strength and the residual stress are measured for the purpose of evaluating the crack-free surface.

2. Influences of Laser Waveforms on the Generation of Cracks and Recast Layers

2.1 Experimental procedure

Two types of YAG laser oscillators, a pulse-pumped YAG laser with pulse durations of 120 μs to 7 ms and a continuous-pumped YAG laser, were used in the present experiments.

Moreover, in order to obtain the laser pulses with durations in the order of magnitude of 10 μs, we set up a 100 mm-diameter aluminum disk with a slit, as illustrated in Fig. 1, and rotated it at 10 000 revolutions per minute using a DC motor so that the pulsed YAG laser beam was partly chopped by the slit through which it passed. The chopped laser beam with durations of 20 μs, 65 μs and 110 μs can be obtained by using disks with slit widths of 1 mm, 3 mm and 5 mm,

respectively.

In addition, the laser pulses with durations of 160 ns to 700 ns were oscillated by switching the AO (acoustooptic)-modulators mounted on the continuous-pumped YAG laser. These short pulses generated by AO-modulator operation are generally called Q-switched pulses.

The pulsed laser waveforms which were obtained in the manner described above are shown in Fig. 2. Table 1 shows combinations of laser parameters examined in the experiment, such as pulse duration (t), output energy per pulse (E), the number of irradiated pulses (N), and the peak output power (P). The number of irradiated pulses was controlled so that the total output energy $E_t (= E \times N)$ was maintained constant at 24.4 J, which was based on the energy of the longest pulse duration of 7 ms. The peak output powers were made nearly fixed at 4 kW, regardless of pulse durations, except that of the Q-switched pulse.

The hot-pressed silicon nitride ceramics (Si_3N_4), which were sintered using Y_2O_3 and Al_2O_3 as sintering aids, were investigated. They were ground into $10 \times 15 \times 5$ mm size by the resin-bond diamond wheel of #400 grains. The properties of Si_3N_4 ceramics are indicated in Table 2. Si_3N_4 ceramics are one of the ceramic materials which are very sensitive to constructive defects such as cracks and voids. In the observation of recast layers and cracks, a scanning electron microscope (SEM) and an X-ray microanalyzer (XMA) were used.

2.2 Results
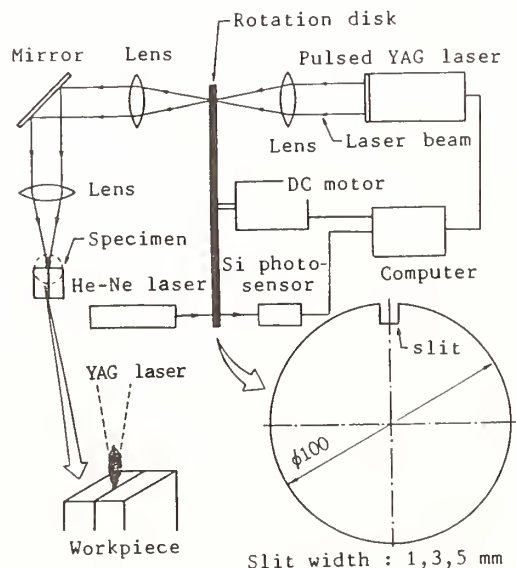
Si_3N_4 ceramics decompose into silicon vapor and nitrogen gas directly at about 2 150 K under the condition of slow heating at atmospheric pressure. Rapid laser heating and vaporizing may very possibly produce the liquid silicon phase around the laser-processed surface. Figure 3 shows the state of the crack development in the laser-drilled hole. The crack propagates from a recast layer (which looks white in the SEM photograph) into the matrix.

Table 1 Combinations of laser parameters examined in the experiment

t	160ns	500ns	20μs	65μs	110μs	120μs	800μs	7ms
E	10mJ	3.7mJ	75mJ	230mJ	380mJ	670mJ	3.2J	24.4J
P	15.4	4.0	3.6	3.6	3.5	5.6	4.0	3.5

Energy : E
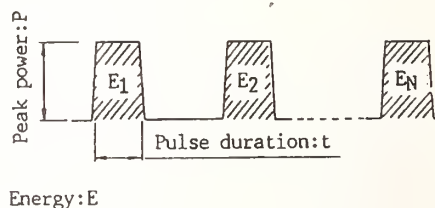
Table 2 Properties of Si_3N_4 ceramics.

Specific heat (J/kg·K)	712.3
Density (kg/m³)	3260
Thermal conductivity (W/mK)	29.3
Poisson's ratio	0.27
Young's modulus (GPa)	303.9
Thermal expansion coefficient ($\times 10^{-6}$/K)	3.2

Fig. 1 Experimental equipment to obtain laser pulses with durations of the order of 10 μs

(a) Q-switching pulse   (b) Pulse chopped by rotation disk

t=160ns   t=20μs

0.2μs/div.   20μs/div.

(c) Normal pulse

t=0.8ms

0.2ms/div.

Fig. 2 Typical pulsed laser waveforms

518

Figure 4 shows the characteristic X-ray photographs of the recast layer. The recast layer contains richer silicon and yttrium elements than dose the matrix. Figure 5 illustrates the silicon $K\beta$ X-ray emission spectrum observed in the recast layer. X-ray analyses identified the recast layer as Si, not as Si_3N_4 or SiO_2. From these observations, we see that the recast layers are mainly composed of silicon.

We believe that the recast layer is formed because the silicon vapor generated by decomposition of Si_3N_4 is saturated in the hole and condenses into liquid during laser heating.

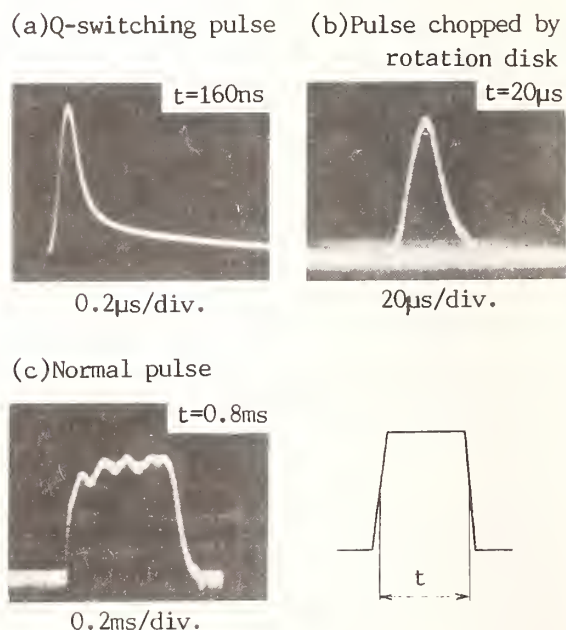Figure 6 shows the dependence of the crack length and the recast layer thickness on the peak output power. The increase in the peak output power causes the crack propagation and thick recast layer formation. It is necessary to maintain the peak output power as low as possible for crack-free machining ceramics.
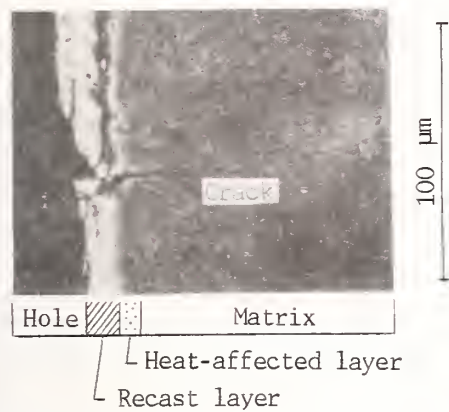

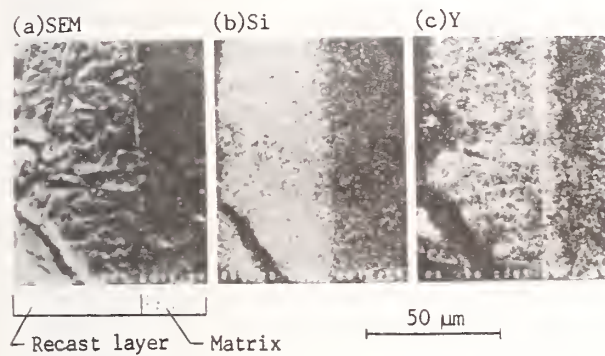Fig. 3 State of the crack development in the laser-drilled hole

Fig. 4 Characteristic X-ray photographs of the recast layer

Fig. 5 Silicon $K\beta$ X-ray emission spectrum observed in the recast layer

Fig. 6 Dependence of the crack length and the recast layer thickness on the peak output power

Total pulse energy E_t: 25 J

t	160ns	500ns	20μs	65μs	110μs	120μs	800μs	7ms
E	10mJ	3.7mJ	75mJ	230mJ	380mJ	670mJ	3.2J	24.4J
N	2500	6600	326	106	65	37	8	1
P	15.4	4.0	3.6	3.6	3.5	6.9	4.0	3.8

Fig. 7 Influences of the pulse duration on the crack length and the recast layer thickness

519

Figure 7 illustrates the influences of the pulse duration on the crack length and the recast layer thickness. The crack length and the recast layer thickness are reduced with a decrease in the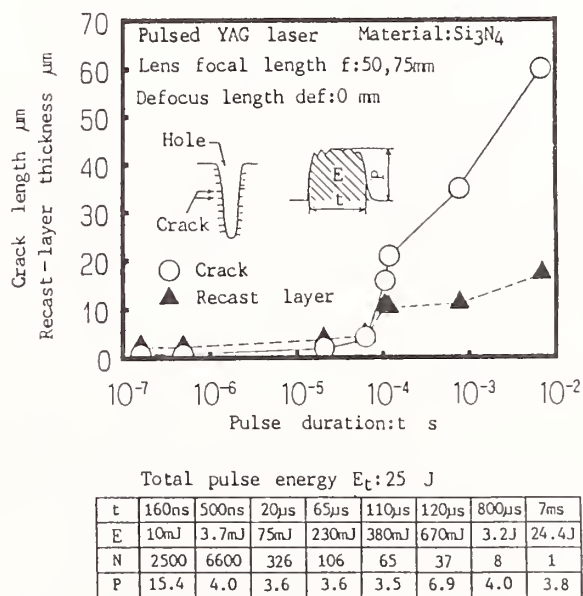 pulse duration. The crack length is smaller than the recast layer thickness when the pulse duration is less than 65 μs. This indicates that shallow cracks are developed within the recast layer without the growth of cracks into the matrix. In particular, no cracks were observed in the recast layer when Q-switched pulses with a duration shorter than 500 ns were used. This suggests that the thermal stress distribution induced by a short laser pulse is only localized in the laser-heated shallow area.

Figure 8 shows the dependence of the crack length and the recast layer thickness on the pulse repetition frequency. Repetition frequency higher than 10 kHz thickens the recast layers and propagetes the cracks suddenly into the matrix. This result suggests that the short laser pulses with high repetition frequency establish a thermal stress distribution similar to that induced by a long laser pulse. The critical repetition frequency for crack-free processing shifted to the side of frequency lower than 10 kHz when the higher peak output power was used.

Therefore, in order to achieve crack-free machining of Si₃N₄ ceramics, it is necessary to process them using a laser beam pulsed for a duration of under 500 ns at a repetition frequency of less than 10 kHz. It appears that the crack development results from the thermal shock and the thermal expansion mismatch between the recast layer and matrix.

3. Fracture Strength and Residual Stress of Crack-Free Surface

3.1 Experimental procedure

Two techniques were applied to the evaluation of laser-processed surface integrity. One technique involved measurement of the fracture strength by the bending method, and another was residual surface stress measurement by an X-ray diffraction technique. The X-ray method has previously been successfully used to measure surface stress in Si_3N_4 ceramic material[10].

Hot-pressed silicon nitride (Si_3N_4) ceramics, which were mixed and sintered with yttria (Y_2O_3) and alumina (Al_2O_3) as sintering aids, were examined in the experiments. The properties of the Si_3N_4 ceramics are shown in Table 2.

Standard test pieces were prepared for the three-point bending tests provided in JIS R-1601. They were finished to $3 \times 4 \times 40$ mm size and 0.8 μm surface roughness (R_{max}) by a surface grinding process under

the conditions shown in Table 3 with resin-bond diamond wheels.

In the next process, one side of the standard test pieces was finished by a crack-free laser milling process[11] under the conditions shown in Table 4 using a continuous-pumped and Q-switched YAG laser beam. The laser milling process is illustrated in Fig. 9. The removal depth of the laser milling was fixed at
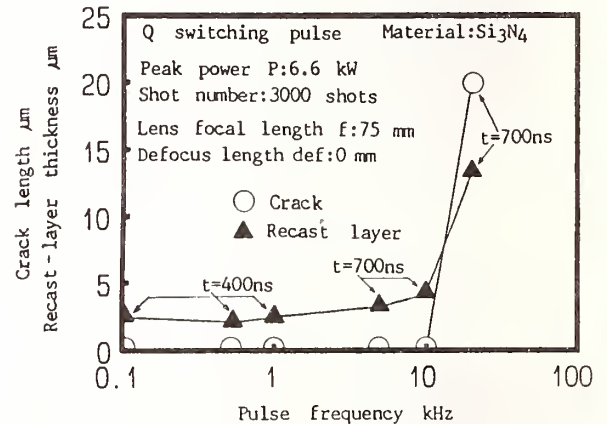
Fig. 8 Dependence of the crack length and the recast layer thickness on the pulse repetition frequency

Table 3 Surface grinding process conditions

Process		Machining conditions	
Rough grinding 1st	Wheel	φ200 10ᵗ mm,#200,Resin	
	Depth of cut	12 μm	
	Feed rate	15 m/min(X),4 mm/pass(Y)	
Rough grinding 2nd	Wheel	φ200 10ᵗ mm,#400,Resin	
	Depth of cut	5 μm	
	Feed rate	8 m/min(X),2 mm/pass(Y)	
Finish grinding	Wheel	φ200 10ᵗ mm,#600,Resin	
	Depth of cut	2 μm	
	Feed rate	5 m/min(X),0.5mm/pass(Y)	
Wheel rotation rate : 2850 r.p.m.			

Table 4 Crack-free laser milling process conditions

Laser machining conditions		
Depth of cut (mm)	0.1	0.3
Pulse repetition frequency (kHz)	320	1000
Surface roughness Rz (μm)	3	5
Feed rate (mm/s)	2.80	
Scan width (μm/pass)	50	
Assisting gas (kgf/cm²)	Air(2.5)	

Fig. 9 Laser milling process

0.1 mm and 0.3 mm by controlling the pulse repetition frequency to keep it at the levels of 320 Hz and 1 000 Hz, respectively. Under these conditions, no cracks were observed in the very thin recast layers which were formed as a reduction product on the laser-milled surface. The bending strengths of the standard test pieces and laser-milled ones were analyzed by the Weibull statistics method.
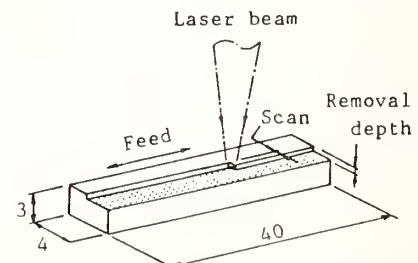
The test pieces were ground into $10 \times 15 \times 5$ mm size for the X-ray residual stress measurement under the same conditions shown in Table 3. The residual stress in the ground and laser-milled surface was measured under the X-ray diffraction conditions given in Table 5. In the present experiments, strain normal to the (411) lattice planes of β-Si$_3$N$_4$ was measured using Cr-Kα radiation. In this case, high resolution against depth is attained because the X-ray penetration depth for the (411) lattice planes is small, $6 \sim 11$ μm[12]. We used the $\sin^2 \psi$ method for the determination of residual stress.

3.2 Influences of crack-free laser processing on fracture strength

It is necessary to investigate the influences of crack-free laser processing on fracture strength to determine its practicability. Figure 10 shows the

Table 5 X-ray residual stress measurement conditions

X-ray diffraction conditions	
X-ray diffraction method	Parallel beam method
Characteristic X-ray	Cr Kα spectrum
Diffraction plane	β-Si$_3$N$_4$ (411)
Diffraction angle (deg)	125.58
Filter	Vanadium foil
X-ray-irradiated area (mm^2)	15×(2~3)
Tube voltage (kV)	50
Tube current (mA)	40
Divergent angle (deg)	0.5
Scanning speed (deg/min)	0.45

Table 6 Average fracture strength and Weibull modulus obtained from the results shown in Fig. 2

Machining method	Average fracture strength(kgf/mm^2)	Weibull modulus
(A) Grinding (#600)	93.9	18.7
(B) Laser machining (0.1mm depth) after (A)	82.6	17.2
(C) Laser machining (0.3mm depth) after (A)	74.1	24.8

Table 7 Annealing conditions

Test piece	Annealing condition
Ground (Standard)	in Ar gas at 1000℃ for 12 hours
Laser milled	in N$_2$ gas at 1000℃ for 10 hours

Weibull plots of fracture strengths of the three-point bending test pieces with various depths of laser milling. Table 6 shows the average fracture strength and Weibull modulus obtained from the results shown in Fig. 10. The average fracture strength of laser-milled test pieces is smaller than that of the ground ones, 88% for 0.1-mm-depth milled test pieces and 79% for 0.3-mm-depth milled ones, respectively. The strength reduction of 10 to 20% seems to depend on both the heat-affected layer and residual stress layer.

In the next step, lapping tests and annealing tests were carried out to determine the reason for the
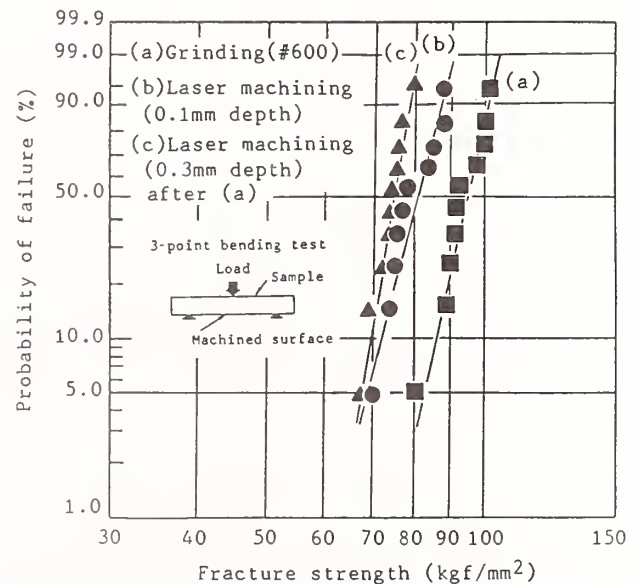

Fig. 10 Weibull plots of fracture strengths of the three-point bending test pieces with various depths of laser milling
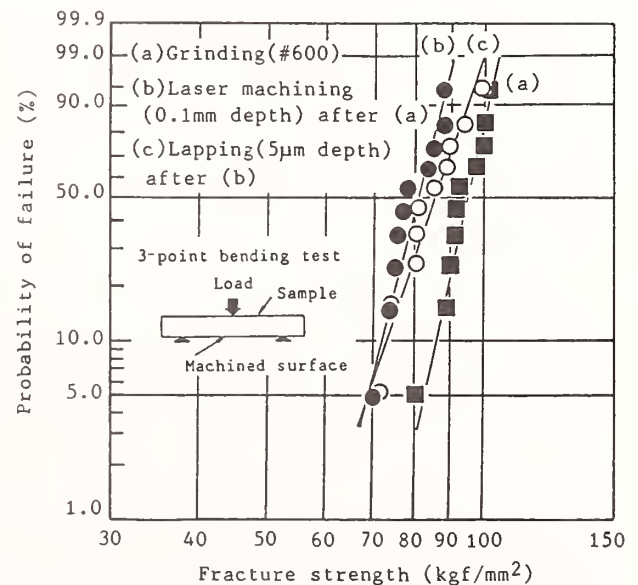

Fig. 11 Weibull plots of fracture strengths of laser-milled test pieces and lapped ones

521

strength reduction after laser-milling. Annealing conditions are shown in Table 7. Figure 11 shows the Weibull plots of fracture strengths of laser-milled test pieces and lapped ones. The increase in fracture strength after lapping, which was about 20 MPa (2 kgf/mm²), was very small. Also, the strength of sufficiently lapped test pieces did not recover to the previous level. The small increase in strength by lapping shows the existence of subsurface damage layers such as brittle thin recast layers with microcracks. The difference in fracture strength between the ground test pieces and lapped ones suggests that compressive residual stress is generated in the test-piece surface after grinding.

It is well known that the residual compression stress layer established by diamond grinding, which is about 20 μm thick, improves mechanical properties such as fracture strength and toughness[6]. Figure 12 shows the Weibull plots of fracture strengths of the ground testpieces and annealed ones after grinding. The decrease in strength by annealing explains the release of residual compression stress because the lapping treatment after annealing did not make the strength recover.

It seems that not only the recast layers, but also the removal of the residual compression stress layer causes the decrease in fracture strength in laser milling. Figure 13 shows the Weibull plots of fracture strengths of the laser-milled test pieces and annealed ones after laser milling. The average strength is almost constant after annealing. This means that residual stress does not develop in laser processing.

3.3 Influences of crack-free laser processing on residual stress

The residual stress after machining has direct effects upon the mechanical properties of materials. Table 8 shows the results of the experiment on the effect of surface finishing on residual stress. A negative value of stress means compression. The residual stress is compression independent of the nature of the finished surface. The residual stress at any laser-milled depth is smaller than that of the ground surfaces.

Table 9 shows the results of the experiment on the effect of surface finishing on both average fracture strength and Weibull modulus. The difference in strength between the ground test pieces and annealed ones after grinding is about 48 MPa (4.9 kgf/mm²). This value reflects the residual stress in the ground surface, as shown in Table 8, (A). This proves that the decrease in strength after annealing depends on the release of residual surface compression stress. The difference in strength between the laser-milled

test pieces and annealed ones after laser milling is close to the residual stress in the laser-milled surface, as shown in Table 8, (B) and (C).

Table 8 Results of the experiment on the effect of surface finishing on residual stress

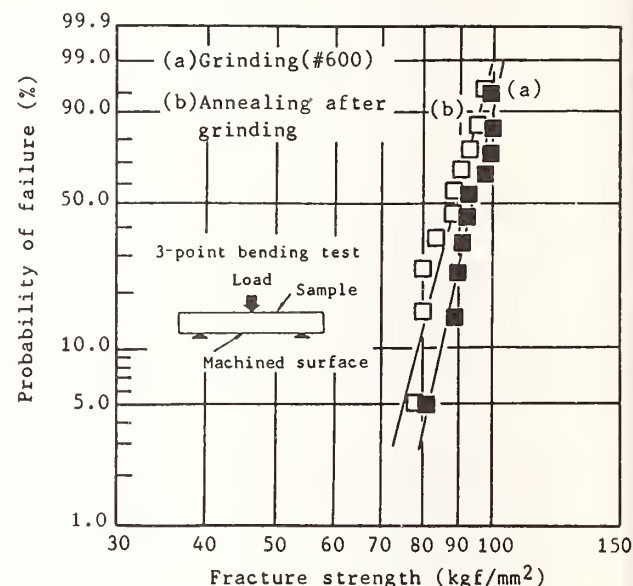| Measured surface	Residual stress (kgf/mm²)
(A) Ground (#400)	-9.82±1.14
(B) Ground (#400) & laser machined (0.1mm depth)	-2.34±0.98
(C) Ground (#400) & laser machined (0.3mm depth)	-1.19±0.98

Fig. 12 Weibull plots of fracture strengths of the ground test pieces and annealed ones after grinding
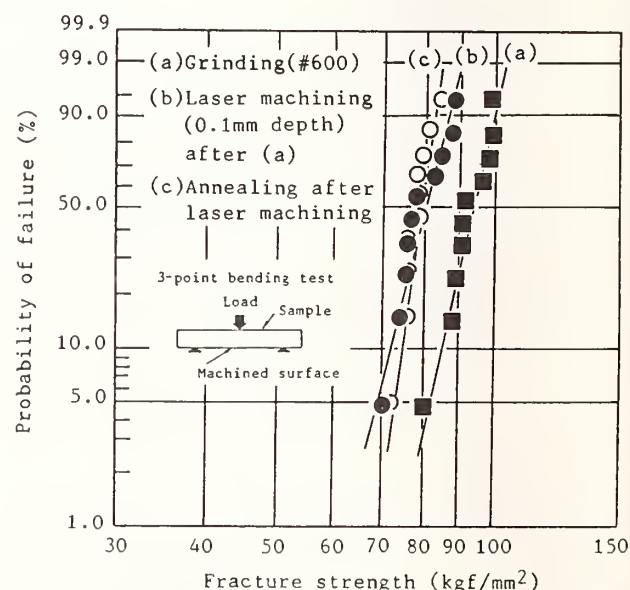

Fig. 13 Weibull plots of fracture strengths of the laser-milled test pieces and annealed ones after laser milling

522

Table 9 Results of the experiment on the effect of surface finishing on both average fracture strength and Weibull modulus

Machining method	Average fracture strength(kgf/mm^2)	Weibull modulus
(A) Grinding (#600)	93.9	18.7
(B) Annealing in Ar gas after (A)	89.0	16.1
(C) Laser machining (0.1mm depth) after (A)	82.6	17.2
(D) Annealing in N_2 gas after (C)	78.7	29.3
(E) Lapping (5μm depth) after (C)	84.9	12.2

Figure 14 shows the results of the SEM observation of the laser-processed and ground surfaces. It was found that the recast layers are mainly composed of porous silicon oxide (SiO_2) on the laser-processed surface, with no cracks. The surface roughness value was smaller than 6 μm R_{max}.

From the experimental results described above, we may conclude that crack-free processing using a Q

-switched YAG laser makes the fracture strength 10 to 20% lower because of the brittle recast layer and the release of residual surface compression stress after grinding. The combination of crack-free processing and diamond grinding will be more effective in the improvement of surface integrity.
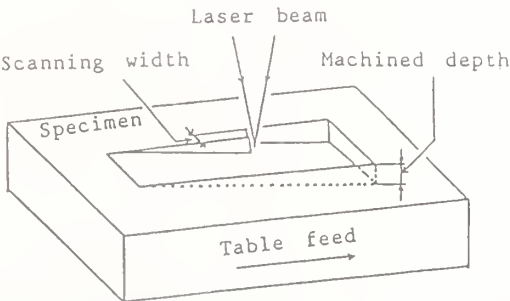
Fig. 15 Schematic illustration of the laser-milling process

a) Slope shaping

b) Sinusoidal plane shaping

Fig. 16 Cross sections of samples which were milled by controlling the pulse repetition frequency (a) linearly and (b) sinusoidally.
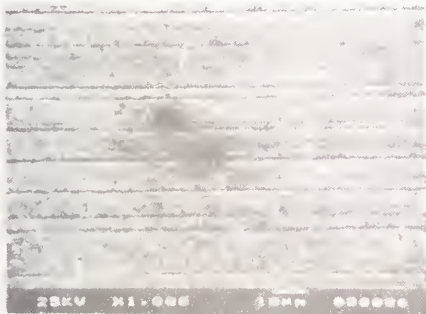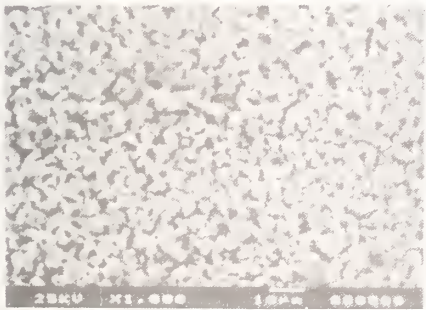
(a) Ground surface

(b) Laser-milled surface
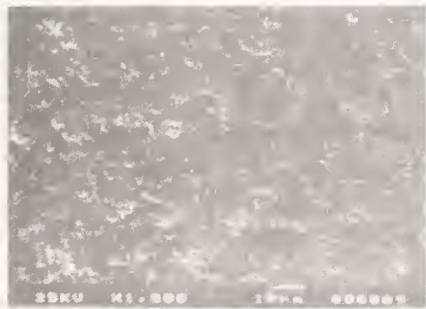
(c) Lapped surface

Fig. 14 Results of the SEM observation of the laser-processed and ground surfaces

4. Applications

We have applied crack-free laser processing to three-dimensional shaping. Figure 15 shows a schematic illustration of the laser-milling process[7]. The pulsed laser beam is scanned on the test piece surface by NC-controlled stage feed. The pulse repetition frequency was changed for the required machined depth on each position of the test pieces. Figure 16 shows cross sections of samples which were milled by controlling the pulse repetition frequency (a) linearly and (b) sinusoidally[7].

The laser-turning process was developed for cylindrically shaped test pieces. Figure 17 illustrates the laser-turning process. The laser beam was
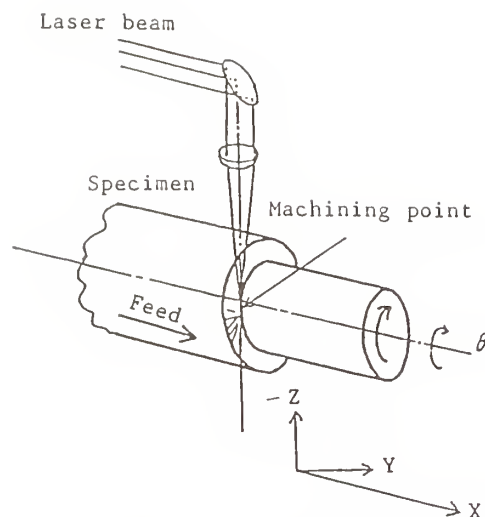
Fig. 17 Laser-turning process.
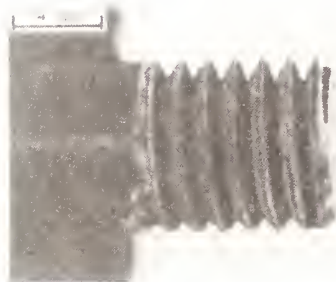
Fig. 18 Screw-cutting sample with 8 mm diameter

irradiated in a tangential direction to the rotational axis to facilitate control of the machining depth. Figure 18 shows a screw-cutting sample of which the diameter was 8 mm[15].

5. Conclusions

We have investigated the influences of heat-affected layers and residual stress on fracture strength for the purpose of evaluating the practicability of our newly developed crack-free processing technique for ceramic materials. The conclusion reached is that the 10 to 20% decrease in fracture strength after laser processing depends on both brittle recast layers and the release of residual compression surface stress. The residual compression surface

stress induced by diamond grinding improves the fracture strength. Therefore, the removal of residual compression stress after laser milling causes the decrease in fracture strength. We think that this crack-free processing method has great industrial possibilities in combination with the traditional machining process.

References

(1) Chryssolouris, G., Bredt, J. and Kordas, S., The Winter Annual Meeting of ASME, PED - Vol. 17 (1985), p.9.

(2) Chryssolouris, G. and Bredt, J., Proceeding of International Symposium on Machining of Advanced Ceramic Material (1987), p. 1.

(3) Chryssolouris, G. and Bredt, J., Interceram, Vol.37. No. 2(1988), p. 43.

(4) Wallace, R. J., Bass, M. and Copley, S. M., J. Appl. Phys., Vol. 59, No. 10(1986), p. 3555.

(5) Wallace, R.J. and Copley, S.M., Advanced Ceramic Materials, Vol. 1, No. 3(1986), p. 277.

(6) Paek, U. C. and Gabliano, F. P., IEEE Journal of Quantum Electronics, Vol.QE-8, No.2(1972) p.112.

(7) Sakamoto, H., Morita, N., Watanabe, T. and Yoshida Y., Proceedings of the First International Conference on New Manufacturing Technology Chiba(1990), p. 571.

(8) Morita, N., Watanabe, T. and Yoshida Y., Trans. Jpn. Soc. Mech. Eng., (in Japanese), Vol. 56, No.522-C(1990), p. 498.

(9) Morita, N., Ishida, S., Fujimori, Y. and Ishikawa, K., Pulsed Laser Processing of Ceramics in Water, Applied Physics Letter, Vol. 52, No. 23(1988), p. 1965.

(10) Walls, D. J., Evans, A. G., Marshall, D. B. and James, M. R., J. Am. Ceram. Soc., Vol. 69, No. 1(1986), p. 44.

(11) Morita, N., Sakamoto, H., Watanabe, T. and Yoshida Y., The Winter Annual Meeting of ASME, MD-Vol. 16(1989), p. 9.

(12) Tanaka, K., Kurimura, T., Matsui, E. and Akiba, Y., Materials (in Japanese), Vol. 36 (1987), p. 817.

(13) Lange, F. F., James, M. R. and Green, D. J., J. Am. Ceram. Soc., Vol. 66, No. 6 (1983).

(14) Morita, N., Watanabe, T. and Yoshida, Y., Crack-Free Processing of Hot-Pressed Silicon Nitride Ceramics using Pulsed YAG Laser, JSME Int. J., Ser. lll, Vol. 34, No. 1 (1991), p. 149.

(15) Morita, N., Watanabe, T. and Yoshida, Y., Crack-Free Processing of Hot-Pressed Silicon Nitride Ceramics using Pulsed YAG Laser, JSME Int. J., Ser. lll, Vol. 3 , No. 1 (199), p.

ELECTRICAL DISCHARGE MACHINING OF ADVANCED CERAMICS

N. M. FAULK

Tennessee Technological University, Cookeville, TN

Finishing advanced ceramic materials into intricate shapes with the required tolerance is often extremely difficult using traditional machining methods. This has led to the development of more sophisticated machining methods which do not depend on mechanical contact. Electrical discharge machining (EDM) is such a techniques and it successfully overcomes many of the difficulties faced by other techniques. Since there is no direct contact, this method is ideal for hard, brittle, and refractory materials. There are a few material requirements, such as a minimum electrical conductivity, but for machinable materials very good tolerances of below 1 μm have been achieved.

Research has successfully demonstrated that several ceramics such as TiB_2, B_4C, and several composites containing nitrides, carbides, and borides can be shaped to an ultra-smooth finish. Cut and uncut surfaces were examined, indicating the cutting mechanism, the surface quality, and contaminants.

Introduction to EDM

Electrical Discharge Machining (EDM) is derived from conventional diesinking, first developed as a practical metalworking method by Lazarenko and Lazarenko (1) after World War II. Much theoretical and experimental work has been conducted since that time in order to identify the basic processes involved. Recent research has started to extend this metal-finishing technique to processing ceramics and composites (2-3). These studies have shown that EDM can be successfully applied to ceramics, including monoliths, cermets, and ceramic-matrix composites (CMCs) if the electrical resistivity is below 300 $\Omega \bullet$ cm (4).

Electrical discharge machining has been developed into an outstanding technique for precision machining. Diesinking and wire EDM machines allow intricate cutting and shaping of appropriate solid materials to nearly any three-dimensional size or shape. Tolerances below 1 μm (40 μin.) have been achieved (4,5); EDM can produce a mirror finish, even on ceramics, giving a surface roughness of less than 0.3 μm (12 μin.) (6,7). This technique is especially important for machining hard, brittle, and high-melting-point materials, which cannot be machined by conventional techniques such as grinding.

The rate of material removal is influenced mainly by the electrical and thermal properties of the workpiece (the metal or other material), but not at all by the hardness of the material. This is an advantage for ceramics, which are often limited by their hardness and/or low toughness. In EDM, the workpiece and the shaping tool are the electrodes separated by a liquid dielectric. Because there is no direct physical contact between the electrodes, no mechanical stress is placed on the workpiece.

Depending on the application, there are two types of machines used for EDM operation. The diesinking machine, also known as the ram-type, plunge, or vertical erosion machine (Fig. 1), can be used for tapping, cutting holes, and helical machining, and is capable of cutting or sinking very complicated shapes into a workpiece. The workpiece is the cathode and the shaping tool (die) is the

anode in this type of machine. It is desirable to remove material from the workpiece, but not from the tool, in order to use the die repeatedly for the same application. Heavy hydrocarbons and kerosene are most commonly used as the dielectric fluid in this conventional form of EDM.
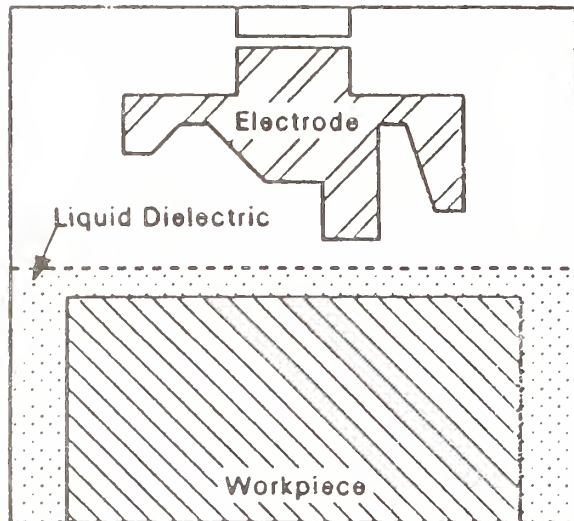
Before EDM
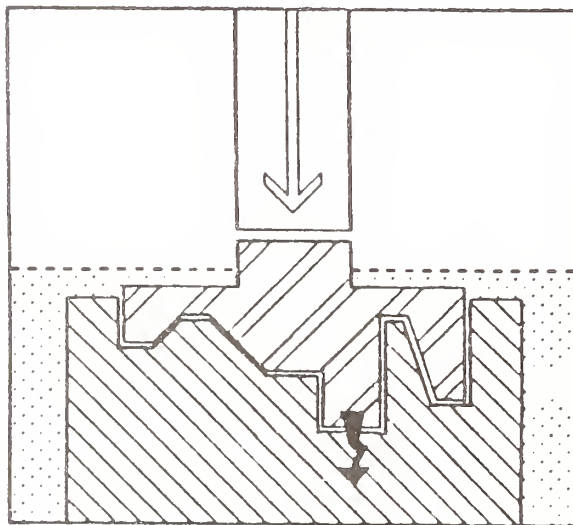
After EDM

Figure 1. Schematic diagram of the die-sinking machine.

Wire-cutting machines (Fig. 2) evolved from research on diesinking machines (5). Instead of using a shaped electrode as the tool, wire-cutting

machines use a thin metallic wire under tension to cut like a jigsaw. Some erosion of the wire is allowable because the wire is continuously wound between spools as it travels through the material, but excessive wire erosion can cause wire breakage. This breakage is the dominant practical and economic problem of wire-cut EDM. In this type of machining, water is the usual dielectric, and brass-, steel-, or molybdenum-based wire is used for the electrode. The polarity is switched for wire-cutting machines: The workpiece is the anode, and the wire is the cathode. Since the early 1980s, most of the research and development work in the EDM area has focused on wire-cutting (5). Refinements include increased cutting speeds, extended taper angles, and independent programming of the upper and lower wire guides so that operators can cut shapes that have different geometries at the top than at the bottom. Also in very limited use as an attachment to the wire machine is a rotary spinning or indexing fixture. This process, also referred to as rotary EDM, allows for better flushing and for cutting circular parts that would otherwise be impossible to cut.
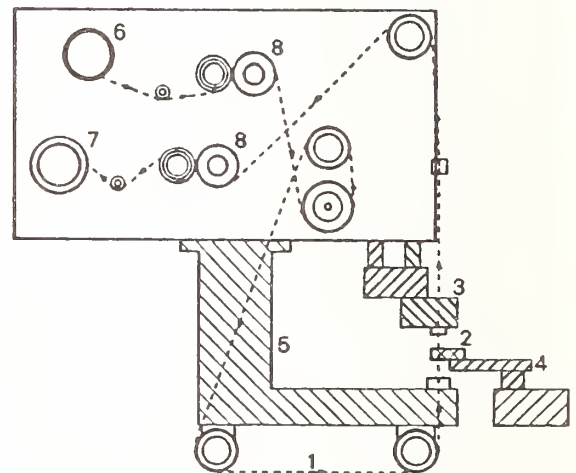
1.	Wire (cathode)
2.	Workpiece (anode)
3.	Wire Guide Table
4.	Workpiece Table
5.	Machine Body
6.	Wire Spool
7.	Used-Wire Spool
8.	Wire Tension Adjusters

Figure 2. Schematic diagram of the wire-cutting machine.

The Electrical Discharge Process

Electrical discharge machining is based on electric discharge erosion. Figure 3 illustrates how this discharge process works, with discussion following the work of Lee and Feick (8), Foster (5,9), and Eubank and coworkers (10,11). The three necessary components, that is, the two electrodes and the dielectric fluid flowing in the gap between them, can be seen in Fig. 3. Note that the dielectric field contains ultrafine solid impurities. An electric field generated by applying approximately 200 volts DC across the gap, with an average width of 40 μm (1.6 mils), generates a magnetic field between the workpiece and the electrode. At first, the two pieces are insulated by the dielectric, so no current flows across the gap. The resulting electric field, however, causes the micron-size particles to be suspended and to form a bridge. This causes the breakdown, or deionization, of the dielectric. The voltage (V) falls to about 25 V, and the current (I) rises to a constant value set by the operator. The plasma channel, seen forming in panel 3 of Fig. 3, grows during the pulse time (t), or "on-time". The intense heat produced causes a vapor bubble to form around this channel. The surrounding liquid dielectric restricts plasma growth, thus concentrating the input energy, V•I•t, into a very small volume. Energy densities up to 3 J/mm³ (50 Btu/in.³) result, which cause the plasma temperature to reach nearly 40,000 K (72,000°F), and the plasma pressure to rise as high as 300 MPa (2700 atm) due to inertial and viscosity effects (10).

During this on-time, the high-energy plasma affects both electrodes in different ways, depending on the properties of the materials involved. For most applications, the plasma melts both electrodes (9), as explained below. As the current flow halts, the bubble implodes, drawing the molten material into the gap. The dielectric fluid flushes and solidifies this molten material and then carries it away, while also cooling the electrode surfaces. The cycle is then repeated.

The pulse duration is one operating condition that greatly influences the material removal rate (MRR). The optimum pulse duration depends on which type of EDM machine is being used. For diesinking machines, optimum times of 10 to 100 μs are common, whereas for wire-cutting machines, times are less than 2 μs (3). The difference is explained by the following discussion.

Because of bombardment of fast-moving electrons at the start of the pulse, the anode melts rapidly first, but then begins to resolidify after a few microseconds. Recall that for the diesinking machine the anode is the shaping tool. This resolidification is believed to be due to the rapid expansion of the plasma radius at the anode, which causes a decrease in the local heat flux at the anode surface. This expansion is referred to in the literature as channel widening (12) or expanding circle heat source (11). Melting of the cathode occurs one to two orders of magnitude later because of the lower mobility of the positive ions. Thus, for the diesinking machines, time must be allowed for the resolidification of the die, but for the wire-cutting machine, much lower times may be used to allow high erosion rates of the anodic workpiece.

Mechanisms Involved

Two mechanisms for ceramic erosion have been reported during EDM: melting and evaporation, and thermal spalling. Each mechanism is discussed below, along with examples of the materials that each erodes.

Melting and evaporation of the electrodes is the most common method for erosion and the one traditionally explained and modelled (9-14). For metals and most ceramics, the plasma melts both electrodes. As the current flow ceases, a violent collapse of the plasma channel and vapor bubble causes superheated, molten liquid on the surfaces of both electrodes to explode into the gap, where the liquid dielectric resolidifies the molten material. Analysis of the debris was carried out on a WC-Co system by Gadalla and Tsai (15-16), and they concluded that, in some cases, the plasma temperature causes evaporation of material from the electrode. Their studies clearly show that material is removed in both the liquid and gaseous state; perfectly spherical particles are apparently resolidified particles from the gaseous state, whereas irregularly shaped particles are solidified from the liquid state (17).

Not all the molten material can be removed after the spark due to surface tension, tensile strength, and bonding forces between the liquid and solid. Crosby reports that for carbides cut with a combination of diesinking and wire-cutting EDM, the recast layer has a depth of about 5 μm (0.2 mil) (18).
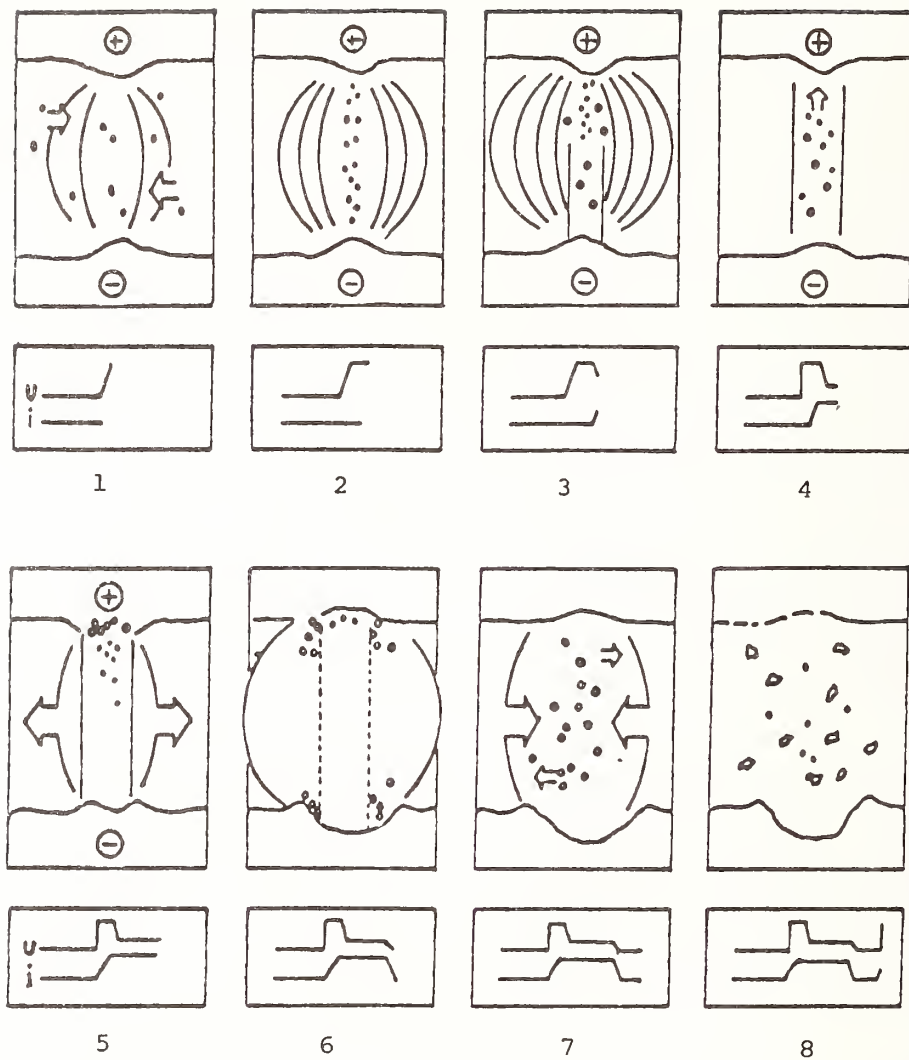
1. Build-up of an electric field.
2. Formation of a bridge by conductive particles.
3. Beginning of discharge due to emission of negative particles.
4. Flow of current by means of negative and positive particles.
5. Development of discharge channel due to a rise in temperature and pressure. Formation of vapor bubble.
6. Reduced heat input after drop in current. Explosion-like removal of material.
7. Collapse of vapor bubble.
8. Residues: material particles, carbon, and gas.

Figure 3. A sequential set of eight panels showing how EDM works

Pure ceramics eroded by melting include B_4C, SiC, and graphite; CMCs such as Al_2O_3-TiC, Sialon-TiN, Si_3N_4-TiN and SiC-TiB_2, and cermets, including WC-Co and Si-SiC (15,19). Table 1 contains information on most of these materials. Many of the CMCs listed in this table have a conductive phase added to decrease the resistivity (2). Consider Al_2O_3-TiC; its polished surface can be seen in Fig. 4, where the light phase is the TiC. The EDM surface with resolidified melt-formation droplets is shown in Fig. 5. Surface roughness measurements show the roughness to be <30 μm (<120 mils) (19). This reflects, in part, the large grain size of the material.

Table 1. Materials Used in This Study

Material	Composition*	Resistivity Ω-cm
1. TiB_2	N/A	1.8e-7
2. B_4C	N/A	0.5
3. Al_2O_3-TiC	70/30	3.5e-3
4. Al_2O_3-TiC	70/30	1.0e-2
5. Si-SiC	5/95	1.43e-4[†]
6. Si-SiC	2/98	1.47e-4[†]
7. Sialon-TiN	80/20	7.0e-4
8. Si_3N_4-TiN	75/25	1.5e-3
9. SiC-TiB_2	80/20	1.0
10. BN-TiB_2	65/35	1.2e-3[†]
11. BN-TiB_2	75/25	1.4e-3[†]

[*] First value corresponds to first phase listed.
[†] Resistivity calculated assuming linear change with composition.

Thermal spalling is usually defined as the mechanical failure of a material, without melting, due to the internal stresses created by heating and/or cooling, which overcome the bond strength. This occurs as a material expands and contracts during the sudden temperature changes associated with EDM, resulting in tension and compression sufficient to cause tensile or compressive failure, respectively.

To calculate the spalling temperature, equations that show the thermal stress, created due

to a temperature gradient can be used (20). During heating, the specimen is exposed to high temperatures in the plasma; fluxes on the order of 10^{10} to 10^{11} W/m² (3.2 x 10^9 to 3.2 x 10^{10} Btu/h/ft²) are reported for EDM (21). Due to heat transfer from the plasma to the workpiece, a compressive force perpendicular to the surface of the workpiece is created. Moreover, because the surface attempts to expand, but cannot, due to the constraint from the bulk of the specimen, compressive stress is created parallel to the surface. When the stress exceeds the ultimate compressive strength of the material, failure by thermal stress is assumed. During cooldown (flushing), the reverse occurs; quench rates of 10^5 to 10^9 K/s are observed (21). The compressive forces created by the plasma disappear and tensile forces are created in the specimen as the surface attempts to contract. Failure occurs if the stress exceeds the tensile strength.

Materials with high thermal expansions and low thermal conductivity are subjected to higher stresses due to more severe gradients. If a material has a low strength or Young's modulus, as well, the tendency to spall is enhanced. When the sparks are localized in the same spot, the material may also break by fatigue after a limited number of cycles. An additional property that plays a role in whether or not a material spalls is the melting point. If the melting point is low enough, the material simply melts or evaporates, as discussed above, and no stresses build up to cause fracture. Petrofes (19) reports that materials with melting points below 2800°C (5100°F) are cut by the melting mechanism.

An example of a ceramic that erodes by spalling is pure TiB_2. Figure 6 shows the polished, uncut surface of this material, whereas the cut surface is seen in Fig. 7. Note the absence of melt droplets or a recast layer as was seen in Fig. 5. Instead, fracture of crystals and flaking are observed in this high-melting-point ceramic. The liquid droplets seen on the surface are not from the surface melting but rather from the brass wire (2). Energy-dispersive x-ray spectrometry (EDS) proves that these droplets contain copper and zinc only. Other than these droplets, there is no recast layer on the machined surface. The small holes present in the grains themselves are due to dislocations initially present in the crystals, which the thermal process of EDM revealed by thermal etching.

529

Figure 4. Polished surface of Al_2O_3-TiC (Material 4, Table 1).

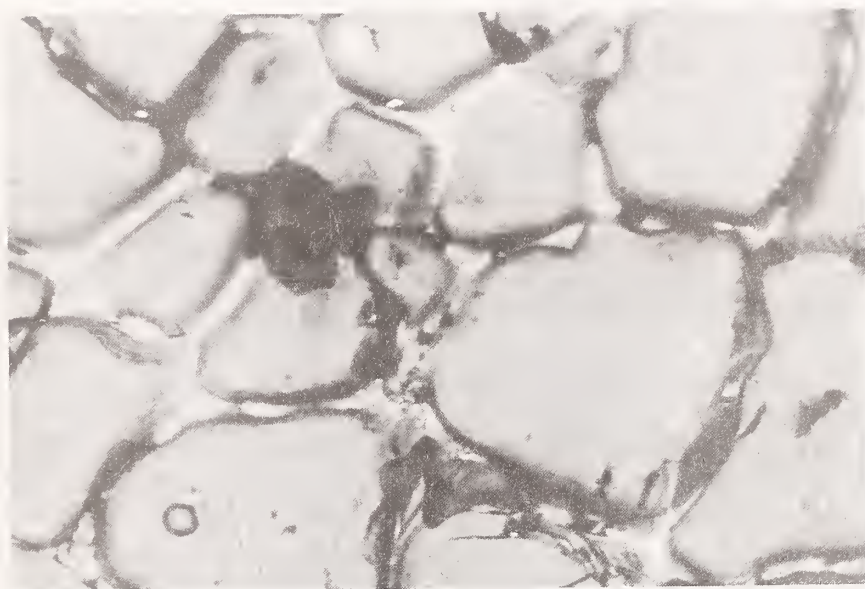Figure 5. EDMed surface of Al_2O_3TiC.

Figure 6. Polished surface of TiB$_2$ (Material 1, Table 1).
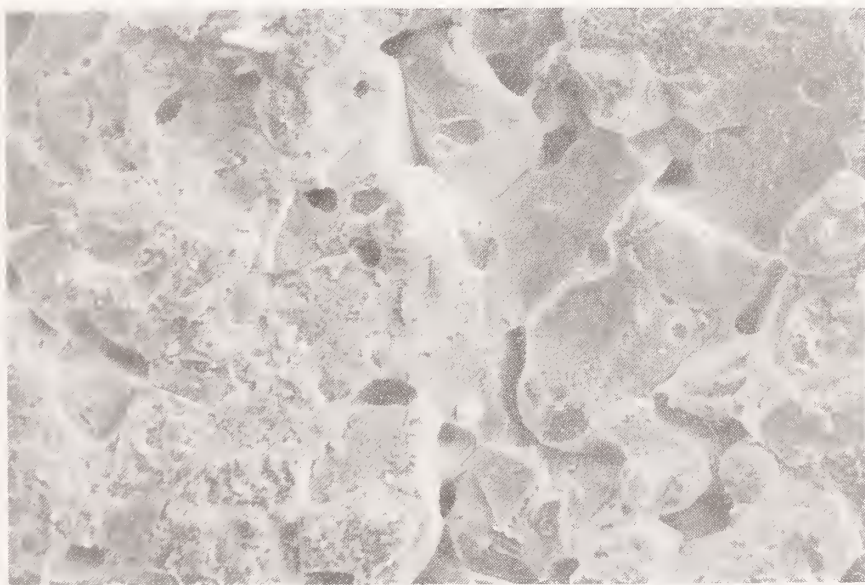

Figure 7. EDMed surface of TiB$_2$.

Application of EDM to Advanced Ceramics

Studies have been performed to answer several questions that are important from an industrial point of view, such as the degree of contamination of the surface; the effects of EDM on the hardness, surface stresses, and strength; the material removal rate attainable; and the effect of the grain size of the material. These are considered separately below and summarized in Tables 2 and 3.

Table 2. Summary of EDM on Materials Studied

Material	Melting Temperature (°C)	Cutting Mechanism	Material Removal Rate (mm³/min)
1	2920(m)	Spall	8.28
2	2450(m)	Melt	0.60
3	2018(m)	Melt	2.42
4	2018(m)	Melt	2.52
5	1415(m)	Melt	3.15
6	1415(m)	Melt	2.00
7	1878(d)	Melt	4.40
8	1878(d)	Melt	2.33
9	2700(s)	Melt	3.52
10	3000(m)	Spall	12.2
11	3000(m)	Spall	10.4

m = melting, d = decomposition, s = sublimation

I. Gadalla and Petrofes studied the surfaces created by applying EDM to several samples of advanced ceramics (22). Elemental mapping was performed on many of the samples in order to determine the extent of contamination on the surface by the material or impurities in the dielectric, which in the cited case was tap water. The brass wire that was used (63/37% copper/zinc) caused some contamination. Copper alloy resolidified droplets with a lower concentration of zinc and a fine dispersion of zinc exist over the entire surface. The zinc dispersion is expected due to its higher vapor pressure. Viewed by EDS, the surface subjected to EDM showed traces of sodium, potassium, and chlorine from the tap water added to the deionized water (the dielectric fluid used) to adjust its conductivity.

II. The Vicker's microhardness of surfaces prepared by EDM was compared to that of diamond sawn and polished surfaces (19); see Table 3. It was concluded that for those materials that were machined by the melt mechanism, EDM produced surfaces with lower hardnesses than those obtained with a diamond saw. This conclusion implies that the internal stresses created by EDM on quenching the liquid phase are less than those created by mechanical erosion. On the other hand, the hardness obtained for spalled materials by EDM was greater than that obtained by a diamond saw. This indicates that the hardness obtained by the spalling mechanism is comparable to mechanical erosion. In some cases, regardless of the erosion mechanism, polished surfaces gave the highest hardness due to the high mechanical stresses created, capture of debris by a softer matrix material, and/or possible redistribution of phases.

III. Surface residual stresses were determined by Gadalla and Tsai for surfaces of WC-Co composites subjected to EDM and were found to be anisotropic (15). In another study (10), it was found that flaking due to spalling causes residual compressive stresses, but the contracting due to solidification of melted surfaces causes residual tensile stresses.

IV. The decrease in strength of a ceramic machined by EDM is its biggest drawback. Saito (23) reports that even when no cracks are observed on the machined surface, the value of the bending strength is between 40 to 50% of its initial value for several ceramics and CMCs. Nakamura does report, however, that when no cracks are observed on the surface, the bending strength can be recovered by removing entirely the roughness with a fine diamond grinding wheel of 400 grit or more (24).

Table 3. Vicker's Microhardness Testing†
for Machined Surfaces

Material	Diamond Saw*	EDMed	Polished
	HV	HV	HV
1	1366 ± 200	3253 ± 210	2971 ± 240
2	2569 ± 680	1995 ± 600	2800 ± 100
3	1734 ± 300	1306 ± 330	2163 ± 110
4	2193 ± 270	1521 ± 280	2349 ± 220
5	2111 ± 510	1633 ± 680	N/A‡
6	2914 ± 120	2341 ± 210	N/A‡
7	1099 ± 70	1197 ± 310	1721 ± 240
8	1737 ± 210	1353 ± 350	2373 ± 420
9	2700 ± 490	1672 ± 460	2598 ± 450
10	265 ± 70	561 ± 200	630 ± 200
11	300 ± 70	343 ± 70	375 ± 180

† All tests performed at 1kg load 30 sec, except materials 10 and 11. Softness of these materials required 300 g load 15 sec.

* Low-speed diamond saw: 300 rpm, 300g load, low diamond concentration blade.

‡ Material too porous to get a reading on the indentation.

V. For a wide variety of advanced ceramics, including pure ceramics, cermets, and CMCs, Petrofes reports cutting rates of 10 to 50 mm²/min (0.02 to 0.08 in.²/min), but does not claim that these numbers are optimum (19). Saito reports rates of 100 to 200 mm²/min (0.2 to 0.4 in.²/min) for conductive Sialon (contains TiN) and Si_3N_4 using optimum cutting conditions (23).

VI. Gadalla and Petrofes report that larger grain sizes of the nonconductive phase (for composites) cause higher roughness and a higher removal rate because the loss of a single grain leaves a large crater and removes more material, compared to a small grain (22). They also report the case of an Al_2O_3--TiC composite of grain sizes

20 and 30 μm (0.8 and 1.2 mils), respectively, in which the x-ray diffraction pattern of the machined surface showed much broader peaks than did its polished surface. This indicated that the melted material produced by EDM precipitated finer crystals with high residual stresses on quenching.

Expanding Use of EDM for Ceramics

Advanced materials that are difficult or impossible to machine by conventional abrasive methods can be machined into complex shapes using EDM, it they have low enough electrical resistivity (< 300 Ω•cm). Because the tool and the workpiece are separated by a dielectric field, extremely hard and brittle materials can be cut. The EDM process takes place by melting, evaporating, or fracturing the surface, depending on the melting point of the material.

Several materials have been successfully cut, and as awareness of the requirements for EDM grows, more ceramics manufacturers are adding conductive phases to their products to make them machinable. Use of this technique is expected to grow as operators begin to see ways to incorporate EDM into production.

References

1. B. R. Lazarenko and N. I. Lazarenko, "Machining by Erosion," American Mach., Vol. 91, No. 26, p. 120-121, 1947.

2. N. F. Petrofes and A. M. Gadalla, "Electrical Discharge Machining of Advanced Ceramics," American Ceramics Soc. Bull., Vol. 67, No. 6, p. 1048-1052, 1988.

3. N. F. Petrofes and A. M. Gadalla, "Processing Aspects of Shaping Advanced Materials by Electrical Discharge Machining," Adv. Mater. Manuf. Proc., Vol. 3, No. 1, p. 127-153, 1988.

4. R. F. Firestone, "Abrasionless Machining Methods for Ceramics: The Science of Machining and Surface Finishing II," National Br. Stand. Spec. Publ., No. 562, B. J. Hockey and R. W. Rice, Ed., p. 261-281, 1979.

5. R. F. Foster, "Evolution of Wire EDM," Tool. Prod., Vol. 47, No. 12, p. 90-93, 1982.

6. J. C. Quinlan, "What's New in EDM," Tool. Prod., Vol. 52, No. 12, p. 40-49, 1987.

7. L. Houman, "EDM Surfaces: The Persistent Problem of Measurement," Carbide Tool J., Vol. 14, No. 4, p. 24-26, 1982.

8. D. W. Lee and G. Feick, "The Techniques and Mechanisms of Chemical, Electro-chemical, and Electrical Discharge Machining of Ceramic Materials;" The Science of Machining and Surface Finishing, National Bur. Stand. Spec. Publ., No. 348, p. 197-211, 1972.

9. R. F. Foster, "Advanced Wire Cutting EDM," Carbide Tool J., Vol. 14, No. 4, p. 22-23, 1982.

10. D. DiBitonto, M. R. Patel, and P. T. Eubank, "Theoretical Models of the Electrical Discharge Machining Process, Part I: A Simple Cathode Erosion Model," J. Appl. Phys., Vol. 66, No. 9, p. 4095-4103, 1989.

11. M. R. Patel, M. A. Barrufet, P. T. Eubank, and D. D. DiBitonto, "Theoretical Models of the Electrical Discharge Machining Process. Part II: The Anode Erosion Model," J. Appl. Phys., Vol. 66, No. 9, p. 4104-4111, 1989.

12. C. van Osenbruggen, "High-Precision Spark Machining," Philips Tech. Rev., Vol. 30, No. 6, 7, p. 195-208, 1969.

13. S. M. Pandit and K. P. Rajurkar, "A New Approach to Thermal Modelling Applied to Electro Discharge Machining," No. 81-WA/HT-3, American Society of Mechanical Engineers, 1981.

14. A. Erden, "Effect of Materials on the Mechanism of Electric Discharge Machining (E.D.M.)," Trans. ASME, Vol. 105, No. 2, p. 132-138, 1983.

15. A. M. Gadalla and W. L. Tsai, "Machining of WC-Co Composites," Adv. Mater. Manuf. Proc., Vol. 4, No. 3, p. 411-423, 1989.

20. R. W. Davidge, Mechanical Behavior of Ceramics, Cambridge University Press, p. 118-122, 1979.

21. A. E. Berkowitz and J. L. Walter, "Spark Erosion," J. Mater. Res., Vol. 2, No. 2, p. 277-288, 1987.

22. A. M. Gadalla and N. Petrofes, "Surface of Advanced Ceramic Composites Formed by Electrical Discharge Machining," Mater. Manuf. Proc., Vol. 5, No. 2, p. 253-271, 1990.

23. N. Saito, "A Review of Special Machining of Fine Ceramics," Sumitomo Elect. Tech. Rev., Vol. 25, p. 1-19, 1986.

24. M. Nakamura, K. Kubo, and S. Hirail, Electr. Mach. Tech., Vol. 8, No. 2, p. 1-12, 1984.

EFFECT OF GRAIN SIZE ON WIRE ELECTRICAL DISCHARGE MACHINING OF POLYCRYSTALLINE DIAMOND

S. Z. WANG, K. P. RAJURKAR, and J. KOZAK
University of Nebraska-Lincoln, Lincoln, NE

Application of ultra-hard cutting tool materials such as polycrystalline diamond (PCD) is continuously expanding. However, shaping of PCD blanks is a long, labor-intensive and costly process. Wire electrical discharge machining (WEDM) has the potential to be an effective and economical technique for the production of tools from PCD blanks. This paper reports the effect of grain size of PCD, discharge frequency and discharge energy of WEDM on machining feed rate and quality of machined surfaces of PCD blanks. Surface roughness and notch depth (which is often observed at the diamond WC interface) were measured to study the cutting edge quality of the PCD blanks.

INTRODUCTION

Polycrystalline diamond (PCD) tool blanks have been developed to machine special alloys, composites, and abrasive nonmetallic materials. Due to the unique properties of PCD tool blanks, they are widely used in the automotive industry (for machining pistons, brake cylinders, transmission cases, and engine blocks), in the aerospace industry (for machining engine components), the jewelry industry (for flycutting and engraving), in the woodworking industry (for machining particle board, fiberboard, and composite materials), and in the textile industry (for machining water jet cutting nozzles) (1). PCD is essentially a synthesized, extremely tough, and intergrown mass of randomly orientated diamond crystals. It is produced by sintering together the carefully selected diamond particles at a very high temperature (approx. 1500 °C) and ultra-high pressures (about 6 GPa). PCD materials are extremely tough and strong. They can be regarded as a composite material which combines the hardness, abrasion resistance, compressive strength, and high thermal

conductivity of diamond with the toughness of tungsten carbide. They are available in several grades, based on the average diamond grain size in the PCD layer (2).

Shaping of PCD tool blanks is challenging due to inherent properties of high strength and high toughness. Diamond grinding is one of the most commonly used techniques (3). The structure of the PCD layer is very homogeneous, and the pertinent high wear-resistance causes problems even in grinding. In order to remove the material from the PCD blank, the diamond layer of the grinding wheel must be renewed by a trueing or dressing operation frequently, resulting in rapid wear of the wheel. During grinding, depending on the PCD grade and contact force machining rates are 0.5 to 2.0 mm³/min and the G ratio (ratio of workpiece removal volume and grinding wheel wear volume) is 0.005 to 0.02 (4). Thus, the grinding wheel wear rate is 50 to 200 times higher than the workpiece removal rate. Hence, grinding is suitable only to a limited extent for the production of PCD profile tools. Although diamond in the PCD layer is not electrically

conductive, PCD sintered material manufactured with cobalt as a solvent catalyst has adequate electrical conductivity suitable for electrical discharge machining (EDM).

The removal of material in EDM is achieved with the erosive effect resulting from electric sparks between two electrodes. Sparks of short duration (0.1 - 2000 µs) are generated in a liquid dielectric gap separating tool and workpiece. In wire electrical discharge machining (WEDM) a wire of diameter ranging from 0.05 to 0.25 mm is used as a tool electrode and the dielectric (deionized water) is injected into the machining gap. WEDM produces complex 2- and 3-dimensional shapes in hard materials with a high degree of accuracy (0.005 - 0.05 mm), without the use of a complicated and expensive EDM profile electrode. Because of the use of relatively inexpensive tool (wire) and non-contact nature of the process, WEDM offers a lower cost alternative with inherent higher accuracy.

Although EDM are becoming an attractive alternative for PCD cutting, the relevant published information is extremely limited. The machining feed rate and the surface roughness are influenced by wire speed. The machining rate has been found to be maximum for a wire speed of 4 - 5 m/sec (5). The surface roughness also increases as the wire speed increases. One study (6) indicates that higher removal rates can be achieved with a high generator voltage and pulse frequency. The optimum cutting edge waviness is apparently achieved with a discharge current of 4 - 6 A and a low generator voltage of 120 V. Recently, authors have reported the effect of pulse frequency, charge current, and pulse on-time on erosion rate and the machining performance of cutting blanks with different layer thicknesses of PCD and tungsten carbide (7). The influence of frequency and energy of electric discharge on the material removal rate (i.e., cutting speed) of PCD blanks, and the mechanism of removing diamond grains from the matrix based on the effect of thermal stresses on the diamond grains and cobalt phase during electrical erosion have also been studied (8). The machining feed rate has been found to increase

with discharge frequency and discharge energy. The wire electrical discharge machining rate of the PCD layer is almost 3 - 5 times lower than that of the tungsten carbide substrate. The difference in values of thermal expansion of diamond and cobalt plays an important role in the diamond grain removal during WEDM of PCD.

This paper reports the result of an investigation of WEDM of PCD blanks with different grades. The goal of this research is to study the influence of different diamond grain sizes on the material removal rate (i.e., cutting speed). The surface roughness and "notch" depth have also been measured to study the cutting edge quality of the PCD layer.

EXPERIMENT

PCD blanks of three different grades were machined by a 5-axis CNC wire electrical discharge machine. The three grades correspond to 2 µm, 10 µm, and 25 µm diamond grain sizes in the PCD layer. The blank consists of a 0.7 mm thick PCD layer and a 2.48 mm thick tungsten carbide substrate.

The discharge energy with a transistor-controlled RC relaxation circuit is determined by the value of the capacitor which is in parallel with the machining gap and the value of discharge voltage. The no-load operating voltage is adjustable from U = 80 to 200 V with variable current of I = 0.5 to 128 A and a pulse frequency f = 1 to 250 kHz. The manually set value of pulse frequency controls the pulse off-time by means of transistors and relative trigger circuits. Because of the RC circuit, the discharge period is very short (usually less than 4 µs), and therefore, stable arcing does not occur during machining with this system.

A stratified (zinc coated brass) wire of 0.25 mm diameter was used as the negatively polarized tool electrode. The wire speed and the wire tension were kept at 6 m/min and 1.5 N respectively. The operating voltage (U) was set at 120 V, charge current (I) was set at 48 A, and

pulse on-time (t_p) was set at 3.2 μs. The capacity (C) and pulse frequency (f) were varied between 1 - 3.3 μF and 8 - 20 kHz respectively.

An on-line data acquisition system and a trigger circuit were used to record the machining feed rate and the actual number of sparks. The collected on-line data was used to obtain the average machining feed rate and the average discharge frequency. The discharge frequency which indicates the actual number of sparks on the workpiece surface is a more realistic parameter than the pulse frequency which is the setting parameter of the machine (9). The material removal rate (MRR) was determined by weighing the workpiece before and after machining during each experiment and calculating the result based on the period of machining time. The machined surfaces were studied by scanning electron microscopy (SEM) and surface roughness profilometer. A toolmakers microscope was used to measure the "notch" depth between the PCD layer and tungsten carbide substrate.

EXPERIMENTAL RESULTS AND ANALYSIS

Machining Rate

The experimental results of the machining feed rate (V_f) as a function of discharge frequency (f_d) and capacitance (C) are shown in Figure 1.
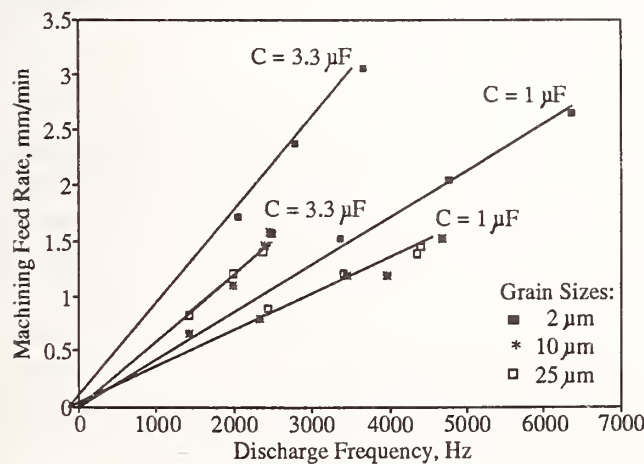

Figure 1 Feed Rate of Machining (V_f) vs. Discharge Frequency (f_d)

For all three grades of PCD, higher capacitance and higher discharge frequency result in higher values of machining feed rate. The linear trend of increase of machining feed rate (V_f) with discharge frequency can be explained on the basis of the following relations developed in (7,8).

The average feed rate of machining (V_f) (shown in Figure 2) in mm/min and/or the cutting speed (V_c) in mm²/min defined as $V_c = V_f \cdot H$ are a function of discharge frequency (f_d) and capacitance (C),

$$V_f = A f_d \tag{1}$$

and,

$$V_c = A H f_d \tag{2}$$

where

$$A = k \frac{30 U_d^2}{H (d_w + 2s_b)} C$$

k = constant of proportionality
U_d = peak voltage, V
H = height of workpiece, mm
d_w = diameter of wire, mm
s_b = gap between wire and workpiece, mm

Thus, the discharge frequency (f_d) and capacitance (C) seem to be the parameters influencing the erosion rate and, therefore, the
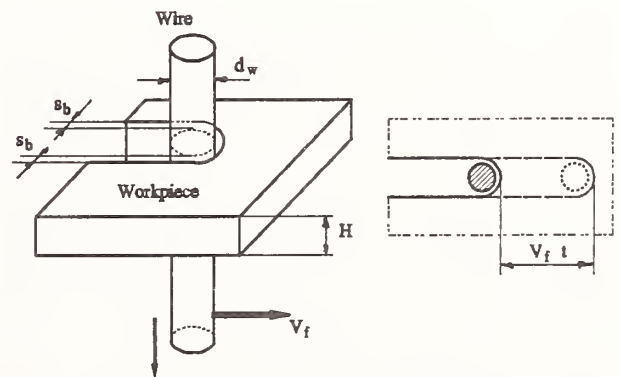

Figure 2 WEDM Operation [8]

quality of the machined surface.

The higher machining feed rate of 2 μm grain size as compared to 10 μm and 25 μm grain sizes may be due to a finer and more uniform distribution of electrically conductive cobalt binder (6), and lower bond strength between particles and the binder. The large grain sizes seem to result in a better diamond intergrowth under high pressure and high temperature synthesis process. The difference in coefficients of thermal expansion of diamond grain and cobalt may also be contributing to easier dislodging of smaller grains than larger grains (8). The increase of machining feed rate (for all grades) with discharge frequency is due to the lower off-time (i.e., non-productive or non-machining time) corresponding to higher discharge frequency. The spark generated crater size depends on the discharge energy including pulse on-time. The off-time provides a pause between two successive discharges for removing the debris and flushing the dielectric fluid.

The experimental results also indicate that there is no significant difference between machining feed rates of 10 μm and 25 μm grain sizes. The regression equations corresponding to lines shown in Figure 1 for the different grades of PCD blanks are,

Grain Sizes:

$$
\begin{aligned}
2\ \mu m \qquad & V_f = 4.33 \cdot 10^{-4} C^{0.56} f_d \\
10\ \mu m \qquad & V_f = 3.29 \cdot 10^{-4} C^{0.51} f_d \qquad (3) \\
25\ \mu m \qquad & V_f = 3.41 \cdot 10^{-4} C^{0.48} f_d
\end{aligned}
$$

where C is in μF, f_d is in Hz, and V_f is in mm/min. For parameter values: U_d = 110 V, C = 1 - 3.3 μF, H = 3.18 mm, s_b = 0.25 mm, and d_w = 0.25 mm.

The volume of material removal (V_m) per discharge can be estimated using the following relation (7),

$$
V_m = \frac{V_f \, H \, (d_w + 2s_b)}{f_d} \qquad (4)
$$

The calculated values of the volume of material removal (V_m) for different grades PCD blanks are shown in Figures 3 and 4.
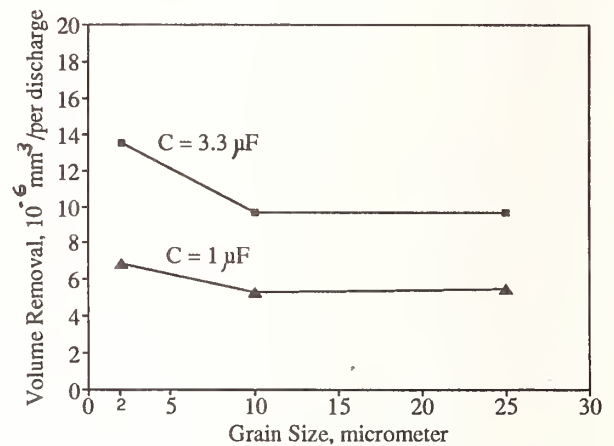

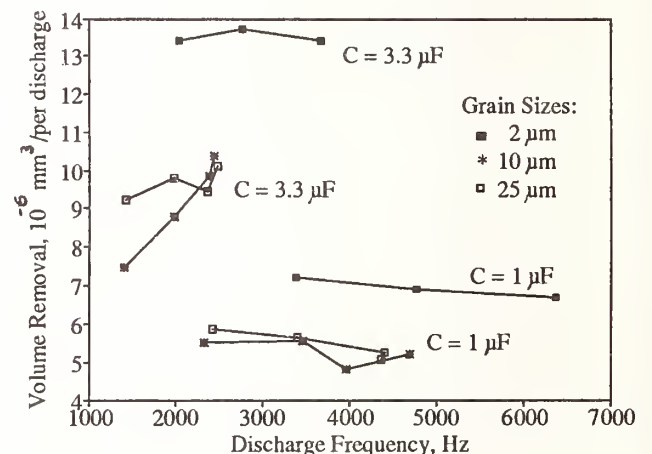Figure 3   Volume Removal (V_m) vs. Grain Sizes (2, 10, and 25 μm)

Figure 4 Volume Removal (V_m) vs. Discharge Frequency (f_d)

The material removed or eroded per discharge is a function of the discharge energy which in turn depends on the value of the capacitance. Hence, a higher capacitance value results in higher volume of PCD removed per discharge. The grain size as mentioned earlier plays an important role in the erosion process. However, it seems that the change in volume eroded per discharge is insignificant beyond a critical value of grain size.

538

The off-time represented by discharge frequency plays a less dominant role in WEDM erosion mechanism than in die-sinking erosion mechanism. The stability and dielectric deionization phenomenon and the avoidance of arcing are greatly influenced by the duration of the off-time in die-sinking EDM. In wire EDM, the motion of wire, the flow path of dielectric fluid and the additional effect of gravity in removing debris result in more or less uniform effect of off-time on the erosion process. Therefore, it is expected that the off-time or discharge frequency will have an insignificant effect on erosion per discharge. Results shown in Figure 4 seem to confirm the above mentioned physical phenomena. However, a slight decrease in erosion per discharge with higher discharge frequency or lower off-time similar to die-sinking EDM can be seen for all results except the blanks with 10 µm and 25 µm grain sizes at 3.3 µF. The results for 25 µm grain size PCD blank show a consistent distribution around an average value of 9.5×10^{-6} mm^3/per discharge, where as a rapid increase in the erosion rate per discharge with discharge frequency is evident in case of 10 µm grain size PCD blank. The wire broke at discharge frequency values higher than 2.5 kHz at 3.3 µF with 10 µm and 25 µm grain sizes PCD blanks. A further investigation of 10 µm grain size PCD blank erosion under different machining parameters needs to be carried out to understand this behavior.

Quality of Machined Surface

The quality of the cutting edge and corresponding microgeometrical features influence the overall performance and economy of the cutting process. A longer tool life, lower cutting forces and vibrations, and better surface finish require a properly finished and micro-defect free PCD cutting tool edges. Therefore, the effects of discharge frequency (f_d), discharge energy (capacitance C), and grain size on surface roughness and notch depth have been investigated.

The measurement of average surface roughness values over the entire PCD surface layer revealed no consistent trend with machining parameters. It seems that machining parameters used in this investigation did not affect the surface roughness values. The PCD layer was not large enough for recommended 0.762 mm cut-off (wavelength) for which the traverse length is 5.08 mm and, therefore, a cut-off of 0.254 mm (a traverse length of 1.524 mm) was used in measuring the roughness values. This constraint on the cut-off may have contributed to the lack of emergence of any specific trend of surface roughness values.

Therefore, two separate sets of measurement were taken. The first set corresponds to the zone 1 at the entry of the wire in the cutting region. The second set corresponds to the zone 2 extending from the approximately middle of the workpiece cutting length to the exist of the wire (Figure 5). The results of surface roughness (R_a) are shown in Figure 6.
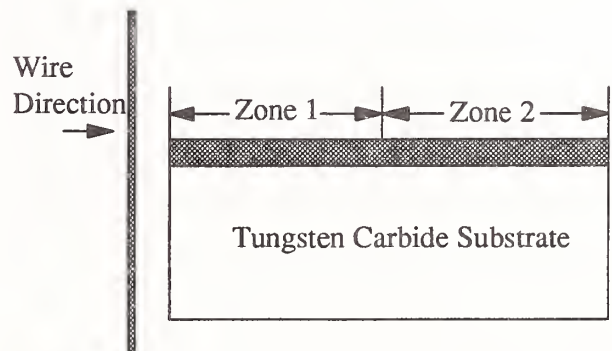

Figure 5 Surface Roughness Measurement Zones

Figure 6 shows that the surface roughness of the PCD layer with 2 µm grain size is slightly less than with 10 µm and 25 µm grain sizes. From the calculations, the average roughness for 2 µm grain size is 2.5 µm and 3.1 µm for 10 µm grain size. There seems to be a definite difference between surface roughness values of the two zones. The surface roughness (R_a) of the first zone of the PCD layer is approximately 50% times more than that of the second zone. The difference in surface characteristics may be
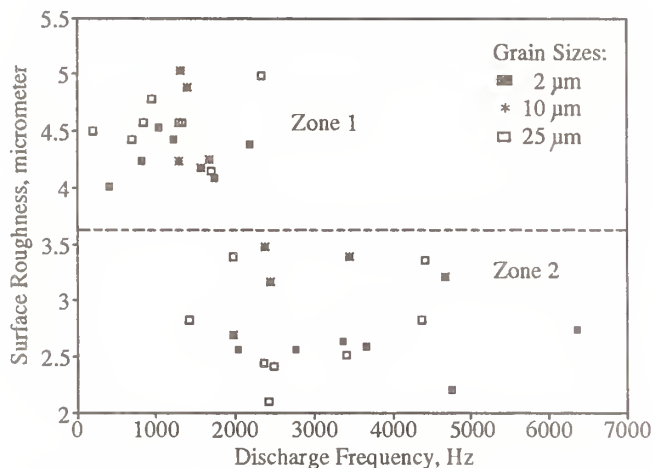
Figure 6 Surface Roughness (R_a) vs. Discharge Frequency (f_d) on Two Zones

explained by analyzing the change of discharge frequency during machining. A typical discharge frequency record is shown in Figure 7.

Initially when the wire enters the cutting region, the process is unstable and following a transition zone becomes fairly stable. The initial instability, longer off-time providing sufficient time for resolidification of molten but not ejected workpiece material, and the movement of wire (i.e., non-uniform distribution of sparks and related energy) tend to generate a rougher surface in the first zone. The stability of the process as well as shorter off-time (higher discharge frequency) helps in continuous and uniform
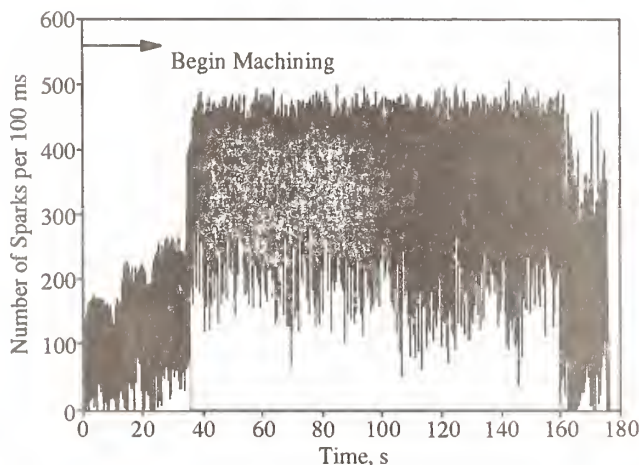

Figure 7 Discharge Frequency (f_d) of Machining Workpiece (10 µm grain size)

distribution of sparking which results in better surface roughness in zone 2.

The machined surfaces were also studied by scanning electron microscope. The SEM photographs (Figure 8) show the significant differences among the three grades of PCD blanks. The machining conditions were set at I = 48 A, t_p = 3.2 µs, C = 3.3 µF, and f = 12 kHz. The discharge frequency values corresponding to 2 µm, 10 µm, and 25 µm grain sizes PCD blanks are 2773 Hz, 2388 Hz, and 2370 Hz respectively. The smoother surface generated by WEDM of 2 µm grain size workpiece shown in Figure 8(a) as compared to that of 10 µm and 25 µm grain size workpieces shown in Figure 8(b,c) may be due to a finer and more uniform distribution of electrically conductive cobalt binder and higher discharge frequency or lower off-time as mentioned above. A comparison of Figures 8(a), 8(b), and 8(c) also shows that the larger voids (cavities) are left on the surface of PCD layer with large grain size. These grains are either removed during the erosion process due to the difference in coefficient of thermal expansion of diamond and cobalt and/or subsequent shock wave impact resulting from the collapse of the plasma channel.

A "notch" formation at the transition zone between the PCD layer and the tungsten carbide substrate during WEDM process can be seen in Figure 9, similar to observations have been reported in (8). It is believed that processes taking place during the production of PCD composites lead to a higher cobalt concentration in this transition or interface zone. The cobalt being electrically conductive is eroded easily from this high cobalt density region. The grain size has a significant effect on the notch depth and surface characteristics of PCD composites as shown in Figure 9(a-c). The notch depth is smaller for 2 µm grain size PCD composite than that of either 10 µm or 25 µm grain size composites. Figure 10 shows the variation of notch depth measured by a toolmakers microscope (accuracy 0.001 mm). The uniform and relatively smaller density of cobalt in the PCD composite transition zone seems to result in

540
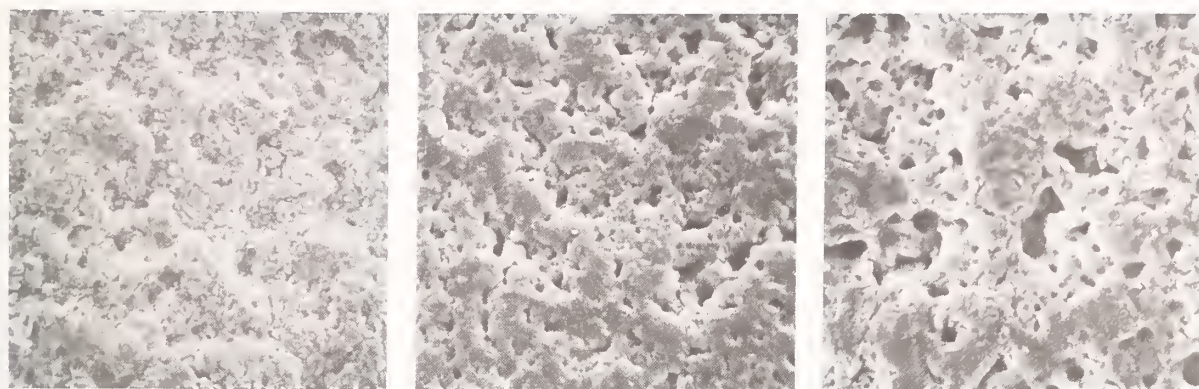
(a) 2 µm   (b) 10 µm   (c) 25 µm

Figure 8 SEM Photograph for the Three Grades of the PCD Layer (×750)

(a) 2 µm   (b) 10 µm   (c) 25 µm

Figure 9 SEM Photograph Showing the Difference in the Notch Depths (×150)

lower notch depth with 2 µm grain size as compared to those of 10 µm and 25 µm grain sizes. The higher energies (i.e., large capacitance values) expectedly lead to a deeper notch. The pulse frequency does not seem to have a significant effect on notch depth, although the trend at 12 kHz with a capacitance of 3.3 µF is not consistent with the rest of the results.
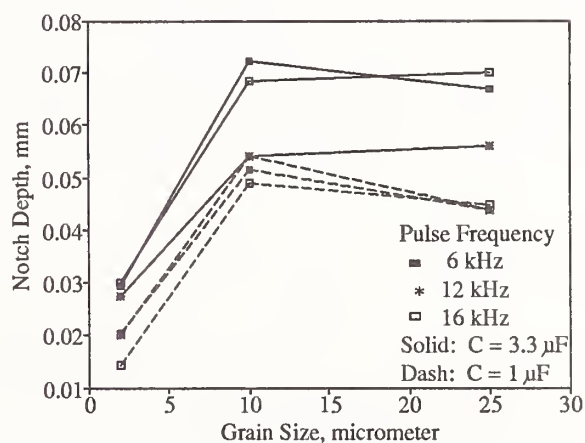

Figure 10 Notch Depth (K_t) vs. Grain Sizes (2, 10, and 25 µm)

541

SUMMARY

This paper reports the investigation of the effect of discharge frequency and discharge energy (i.e., capacitance) on the machining feed rate, the volume of material eroded per discharge, and cutting edge quality during wire electrical discharge machining of polycrystalline diamond blanks of different grain sizes. The machining feed rate and the volume of material removed per discharge decrease as the diamond grain size increases from 2 µm to 10 µm and have no significant change between 10 µm and 25 µm diamond grain size. The surface roughness and the notch depth were measured to investigate the quality of the PCD layer. The average roughness of 2 µm grain size is slightly less than that of 10 µm and 25 µm grain sizes. No significant difference between the surface roughness values of the PCD layer with 10 µm and 25 µm grain sizes was observed when the discharge frequency and the discharge energy are changed. However, it was observed that the surface at the entry of the wire is rougher (by almost 50% more) than the surface near the exit of the wire. The notch depth shows that 2 µm grain size as better cutting edge quality than 10 µm and 25 µm diamond grain sizes.

REFERENCES

1. "J & M Diamond Tool Makes Great Strides in Machining Polycrystalline Diamond," EDM Digest, Vol. XIII, N. 1, 1991, pp. 14-15.

2. Jennings, M., "Wire Drawing with Natural Diamond and PCD," Diamonds in Industry, DeBeers Industrial Diamond Division, 1991, pp. 3-5.

3. Kenter, M., "Effect of Process Parameters When Grinding PCD-3" Industrial Diamond Review, Vol. 52, N. 553, June 1992, pp. 313-318.

4. Wyss, R., and Pollak, E., "Machining Concept for PCD Tools," Swiss Quality Production, 1990, pp. s70-s75.

5. Fengguo, C., Yansheng, M., Yuanfang, W., and Jinjuan, F., "A Machining Technique of Superhard Materials PCD & CBN Using Wire EDM," Proceeding of International Symposium for Electro-Machining (ISEM-10), 1992, pp. 359-363.

6. Spur, G., Puttrus, M., and Wunsch, U. W., "Wire EDM of PCD," Industrial Diamond Reviews, Vol. 48, June 1988, pp. 264-266.

7. Wang, S. Z., Kozak, J., and Rajurkar, K. P., "Study of Wire Electrical Discharge Machining of Polycrystalline Diamond," To be published in Transaction of the NAMRI/SME, May 1993.

8. Kozak, J., Rajurkar, K. P., and Wang, S. Z., "Material Removal in WEDM of PCD Blanks," Submitted to Journal of Engineering for Industry, 1993.

9. Rajurkar, K. P., and Wang, W. M., "On-Line Monitor and Control for Wire Breakage in WEDM," Annals of the CIRP, Vol. 40/1, 1991, pp. 219-222.

LASER MACHINING OF SILICON NITRIDE CERAMICS

A. G. SOLOMAH

SAC International Ceramics Ltd., Mississauga, Ontario, Canada

Silicon nitride ceramic materials were machined using a high power CO_2 laser beam. The laser beam was operated under continuous or pulsed mode at different power levels. Argon, oxygen and nitrogen were used as assist gases. The as-cut surfaces of silicon nitride materials were found to possess different surface flaws, mainly porosity, which affect the subsequent surface grinding processes. It was concluded that oxygen is the most suitable assist gas during laser cutting under continuous or pulsed mode operation. Laser cutting of silicon nitride can not be used alone to finish such ceramic materials, however it can be used as a complementary process to conventional diamond grinding especially in high speed cutting of complicated shapes and geometries.

INTRODUCTION

Silicon nitride and carbide are prime candidate materials for ceramic components in advanced heat engines due to their superior properties, such as strength, toughness, wear resistance, light weight and oxidation resistance at high operating temperatures, e.g. 1300 C (1). However, manufacturing components from such hard and tough ceramic materials requires sophisticated processing techniques to produce "near-net" shapes after densification. The final product must be machined to achieve the required dimensional tolerance and acceptable surface finish to increase the reliability of such components under anticipated operating conditions.

Diamond tooling and machining are the accepted techniques to machine such hard ceramic materials (2). However, diamond machining is very expensive and it is a very slow process, especially when complex shapes are required. Machining ceramics with diamond tooling accounts for about 60-70% of the cost of the final product. Cutting and drilling are considered the most time consuming steps in diamond machining of advanced ceramic materials, especially when complex geometries are required.

Laser machining can be a very cost-effective technique to reduce the cost of ceramic machining, especially for line cutting, drilling and profile cutting. Several researchers in Japan and Europe have investigated the use of high power CO_2 lasers to cut silicon nitride, zirconia and alumina ceramics (3-7). Success has been achieved in machining these ceramic materials under controlled conditions. The economics of such a new machining process are not available yet. However, we have performed a preliminary energy savings analysis comparing diamond tooling and the laser in cutting silicon nitride materials, which showed a saving of 60% (see Appendix).

MATERIALS AND EXPERIMENTAL WORK

Hot-pressed silicon nitride ceramic materials containing about 3 wt% MgO and other non-

specified amounts of different sintering additives were used to carry out the preliminary work to investigate the feasibility of cutting with a high power (1.5 kW) carbon dioxide laser. The density of the hot-pressed billets was > 99% of the theoretical density. The hardness, H, and fracture toughness, K_{IC}, were determined using indentation techniques and their values were 16 GPa and 4.5 MPa.m$^{1/2}$, respectively. The flexural strength, σ, was 560 Mpa, as measured using a three point bending test.

The laser was a single mode CO_2 laser which has the capability of producing a high quality continuous output beam at 10.6 µm over a power range of 50 to 1500 W. A lens focussed the output to a spot as small as 100 µm, corresponding to a maximum power density of more than 10^7 W/cm^2. The laser could also be pulsed at a repetition rate up to 5 kHz. Motion of the workpiece under the focussed laser beam was accomplished by means of an x-y positioning table together with a programmable motion controller. Speeds of up to 15 cm/s were achievable with travel of 30 cm in each direction. In the present study, the laser beam was operated in two different modes, continuous wave and pulsed; the power ranged from 600 to 900 W in each case, while the frequency in pulsed operation varied from 150 to 900 Hz. The focal length was fixed at 12.7 cm and the working distance between the nozzle and workpiece was 150 µm. Oxygen and argon were used as assist gases. The thickness of the silicon nitride workpiece was 6 mm and the cutting speed was 0.25 cm/s.

The as-cut surfaces were characterized using visual inspection for colour changes and macrocracking, while their microstructure and microcracking were examined using scanning electron microscopy (SEM) provided with an energy dispersive x-ray analyzer (EDAX).

Conventional diamond grinding was utilised to remove the as-cut surface in order to achieve a surface finish quality similar to that produced by diamond machining. A 220 grit diamond wheel was used to remove the damage layer followed by 320 grit to remove aa additional depth of 40 µm to reach the bulk material.

RESULTS AND DISCUSSION

1. Cutting using continuous wave laser

Surface quality changed drastically when the power level changed from 1200 to 600 W. With oxygen assist gas, smoother surfaces were achieved when lower power levels were utilized, especially near the bottom of the workpiece. High power levels caused severe shattering and fracture, which can be explained on the basis of thermal shock due to the lower heat conductivity of Si_3N_4 generating high levels of differential thermal strains between the top and the bottom of the workpiece. Lowering the power level reduced this problem and produced a smoother surface. The cutting mechanism responsible for this process is the oxidation of Si_3N_4 according to:

$$2Si_3N_4 + 7O_2 ---->6SiO + 8NO \qquad (1)$$

$$6SiO + 3O_2 ----> 6SiO_2 \qquad (2)$$
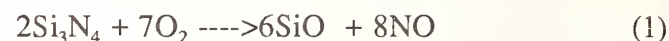
The thickness of the oxidised layer, or silica scale, was measured as 150 to 350 µm, using optical microscopy.

Microstructural examinations using SEM revealed that the porosity changed as the laser beam penetrated throughout the thickness. Figures 1(a) and 1(b) show that the porosity decreases in density and in pore size with penetration depth. The shiny spots shown in the bottom of Fig. 1(a) are metallic silicon inclusions, as revealed by EDAX analysis. It is thought that at the top layer of the workpiece oxidation takes place rapidly, generating SiO and NO gases which are further converted into higher oxygen content, thus consuming more oxygen. This situation can reduce the oxygen content of the gas mixture which would then be less oxidising in the deeper layers, thereby producing fewer gas bubbles and a lower porosity. This is in agreement with the presence of metallic silicon inclusions deeper in the workpiece which do not exist in the top layers.

544

Fig.1(a) SEM micrograph showing the morphology of the silicon nitride edge as cut with 600 W continuous laser power and oxygen assist gas.
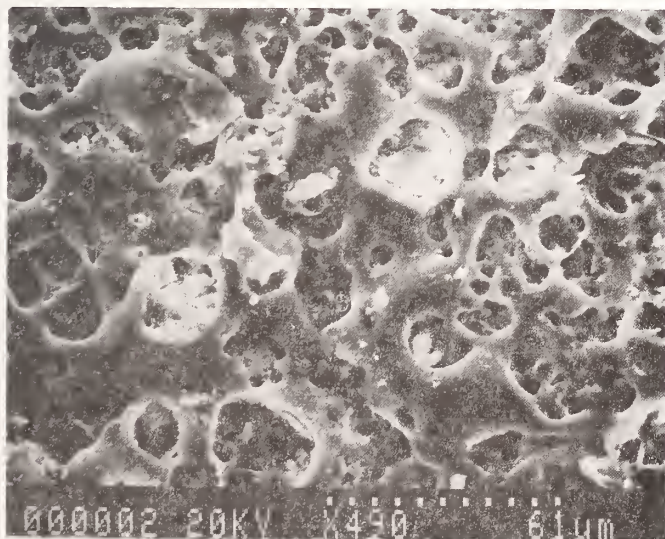

Fig.1(b) Porous layer in Fig.1(a) shown under higher magnification (490X vs 60X).

Under an argon atmosphere, metallic shiny surfaces were produced but fracture occurred at all laser power levels. Since argon is an inert gas, cutting was carried out by a decomposition/evaporation process, according to the following reaction:

$$Si_3N_4 \text{ --------> } 3Si + 2N_2 \qquad (3)$$

The temperature of the above reaction is > 1785 C.

The penetration of molten silicon was impeded through the entire thickness and therefore fracture occurred. Visual and optical examination have confirmed that the first three mm of the thickness has the best surface finish achieved by the laser beam under any of the experimental conditions. It is expected that such laser cutting can be utilized to produce a high quality surface finish, which require no further finishing, for thin silicon nitride materials, e.g. wafers and substrates of thickness less than three mm.

2. Cutting using pulsed laser

When a thermal pulsing mode was utilized, significant reduction in fracturing was observed due to the diminished thermal shock compared to continuous mode laser operation. Under oxidizing cutting conditions, surface finishes similar to those of the continuous mode were obtained. No significant differences in surface finish were noticed with changing frequency (150 to 900 Hz). However, microstructural examinations using SEM have revealed that porosity is more uniform and finer in pore size than that found during the continuous cutting mode. Figure 2 shows such topographical features which are distinct from those shown in Figure 1.

545

Fig.2 SEM micrograph showing the morphology of the cut edge for silicon nitride cut with 600 W of pulsed laser power and oxygen assist gas.

CONCLUSIONS

1. High power CO_2 laser cutting of silicon nitride ceramic materials can be successfully achieved under oxidising conditions using either continuous wave or pulsed operation.

2. The oxidised surface layer has a thickness of 150 to 350 μm, which requires further grinding using conventional diamond tooling.

3. Thin wafers or substrates made of silicon nitride ceramic materials can be successfully machined using inert assist gases, e.g. argon, yielding a surface finish requiring no further grinding.

4. The mechanisms involved in the laser cutting of silicon nitride ceramics depend on the assist gas, which controls the cutting and surface finish quality.

REFERENCES

1. R.N. Katz, " Recent Development in High Performance Ceramics," in Materials Technology - 1976, A.G. Chynoweth and W.M. Walsh, Jr., Eds., Am. Inst. Phys., Pub., pp. 236-252 (1976).

2. R.H. Chand, K.P. Castello and T.M. Payne, " Finish Machining of Technical Ceramics - An Engineering Approach," in Proc. of SME Conference on Advanced Ceramics '90, Rosemont, Illinois (1990).

3. J. Yamamoto and Y.Yamamoto, "Laser machining of Silicon Nitride," in Proc. LAMP '87, Osaka, Japan, pp. 297-303.

4. M. Naeem, M.E. Preston and J.R.Tyrer, "Machining of Engineering Ceramics With A High Power CO2 Laser," Adv. Manuf. Eng., Vol. 2, 27-31 (1990).

5. R.F. Firestone, "Laser and other non-abrasive machining methods for ceramics," in Advanced Ceramics '87 Conference, 17-19 February 1987, MR87-112-6.

6. I.J. McColm and N.J. Clark, Forming, shaping and working of high-performance ceramics, Chapter 5, Chapman and Hall Publisher, London, England (1986).

7. T. Araya and T. Umino, "Present Status of CO2 Laser Processing," J. Mater. Eng., 15, 299-306 (1991).

APPENDIX

Energy Consumption of Laser vs Diamond Machining

To demonstrate that laser cutting of ceramic materials is an energy efficient process compared to conventional diamond machining, tests were performed on the cutting of a 6 mm thick plate (100 mm diameter) of silicon nitride using both techniques.

With diamond cutting, a total cut length of 144 cm was made in 128 min using a surface grinder, which consumed 2.3 kW of electrical power. Thus the electrical energy consumed is 4.9 kW-hr. Using the carbon dioxide laser at a power level of 600 W, the same length of cut was made in 9.45 min. Such a laser consumes 12.5 kW of electrical power, giving electrical energy consumption of 1.97 kW-hr. Therefore, the laser machining would require only 40% of the energy consumed by diamond maching.

TECHNOLOGY IN PULSED ND:YAG LASER DRILLING OF AN AL-LI BASED/SIC METAL MATRIX COMPOSITE

T. M. YUE and W. S. LAU
Hong Kong Polytechnic, Hong Kong

C. Y. JIANG
Nanjing Aeronautical Institute, Nanjing, China

The behavior of laser micro-drilling of an Al-Li/SiC metal matrix composite was studied using a pulsed Nd:YAG laser. The concept of critical intensity was employed to predict the profile and the diameter of the drilled hole. The dimension of the hole was found to be related to the relative position of the laser focal spot to that of the workpiece. In the case of through hole drilling of thin sheet material, the diameter of the hole can be best controlled by the beam intensity. Moreover, a moving laser source, by nature of its tunnelling action, can improve on the uniformity of the dimension of the processed hole, this is particularly valid for thick materials.

1. INTRODUCTION

The unique properties of Al-based/SiC metal matrix composites (MMCs) are, undoubtedly, of great attractions to many engineering applications. However, they have not been widely utilized until quite recently because of the high production cost and technical difficulties encountered in their manufacture. To-day even with the advanced manufacture routes, though they can be produced in a wide variety of grades and forms (1-4), most of these materials are not produced to finished net shapes. Thus post-production shaping becomes essential to generate usable engineering components.

It is well accepted that Al-based/SiC composites are difficult to machine; and apparently the only sensible tooling material for this kind of exotic materials is polycrystalline diamond(PCD) (5,6). Nevertheless, in the realm of micro-machining, laser technology seems to provide the best alternative. The "non-contact" nature and the extreme high intensity of the beam precludes the problem of tool wear and also minimizes any unacceptable microstructural changes.

At present, information uncovered in the open literature concerning laser machining of MMCs are scarcely available. Previous study has shown that pulsed Nd:YAG laser can offer a real possibility in cutting Al-Li/SiC composites in that the quality of the cut was largely dictated by the beam intensity (7).

This research aimed to deepen the knowledge on the behavior of laser drilling of Al-Li/SiC materials so as to establish a model capable of predicting the profile of the "machined" hole.

2. MATERIAL

The material subjected to the present investigation was a newly developed Al-Li(8090)/SiC MMC which has already attracted much attentions in the aerospace industry owing to its extremely high specific mechanical properties. The material was in 2.2mm sheet supplied in the annealed condition. The nominal composition of the matrix material is presented in Table 1. The matrix is reinforced with 17%(wt.) SiC particles having an average size of 3μm. Figure 1 shows a typical microstructure of the composite material.

Table 1 Major elements in 8090 alloy

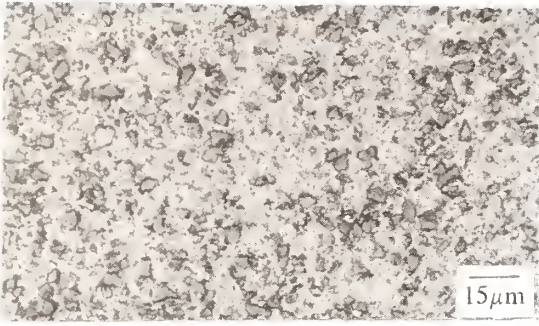| Element	Weight(%)
Li	2.2-2.7
Mg	0.5-1.2
Cu	1.0-1.6
Al	balance

Fig.1 Typical microstructure of the MMC material

3. THEORETICAL BACKGROUND

In spite of the complex and unsteady conditions exist during laser processing in that the material is melted, vaporised, and expelled in a very short time span. It has been shown that in laser drilling of various materials the depth of the "machined" hole is strongly related to the critical intensity(I_c)[*] of the laser beam and for the 8090/SiC composite material the I_c was found to be 7.5×10^9 W/m^2 (8).

Assuming a Gaussian TEM$_{00}$ mode condition I_c is given by:

$$I[r_t(z),z] = I(0,z)\exp[-\frac{2r_t^2(z)}{R^2(z)}] = I_c \qquad (1)$$

The notations of the various parameters are defined as shown in the following diagram:
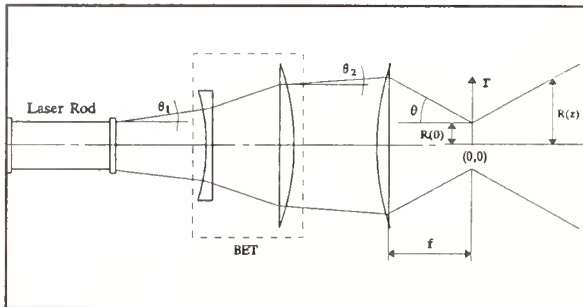
Schematic diagram of the Laser optic system

---

[*]I_c is the threshold intensity which initiates vaporization

Since,

$$R(z) = \sqrt{R^2(0) + (\theta z)^2} \qquad (2)$$

and

$$\frac{I(0,z)}{I(0,0)} = \frac{R^2(0)}{R^2(z)} \qquad (3)$$

Now the threshold radius which describes a circle of $r = r_t(z)$, having its intensity $= I_c$, can be written as:

$$r_t(z) = \sqrt{[R^2(0) + (\theta z)^2]\ln\sqrt{\frac{I(0,0)R^2(0)}{I_c[R^2(0) + (\theta z)^2]}}} \qquad (4)$$

where,

$$I(0,0) = \frac{2P_{LP}}{\pi R^2(0)} = \frac{2E}{\pi R^2(0)t_i} \qquad (5)$$

(P_{LP} = the pulse power; E = pulse energy; t_i = pulse duration)

According to equation 4 the profile of the machined hole will depend on E and t_i provided the physical parameters of the laser are fixed. And from equation 4 both the maximum value of $r_t(z)$, i.e. r_{max}, and its corresponding position, Z_{max}, can be obtained by taking the derivative of equation 4 with respect to z:

$$z_{max.} = \pm\sqrt{\frac{I(0,0)R^2(0)}{I_c \, e} - R^2(0)/\theta} \qquad (6)$$

4. EXPERIMENTAL PROCEDURES

Laser micro-drilling was conducted on a pulsed Nd:YAG laser with a maximum time-average power of 120W. The beam parameters were varied in the experiment with the pulse energy(E) ranging from 1 to 5J/pulse; pulse duration(t_i) = 1ms; with the pulse

550

frequency(f_p) fixed at 23Hz. All of the experiments were carried out using argon as the flushing gas operating at a pressure of 0.2 MPa.

To validate equation 1, i.e., the profile of the machined hole, blind-holes were drilled in the plane of the rolling direction using five different beam intensities: 1000W/cm^2, 1500W/cm^2, 2000W/cm^2, 2500W/cm^2 and 3000W/cm^2. Based on the outcome of these results, the relationship between the maximum diameter of through holes that can be achieved with different beam intensities was studied by a defocusing method (locating the surface of the material at the position corresponding to Z_{max}).

5. RESULT

The blind-holed specimen was sectioned using the EDM wire-cut and the profiles are revealed in Figure 2. Figure 3 compares some of these results to those as predicted by equation 3. In general, the experimental results agreed well with the theory, except at the position near the entrance of the blind holes; the results will be discussed in a later section. As in the case of through hole drilling, the relationship between the beam intensity and the hole diameter at the beam entrance and exit surfaces are presented in Figure 4 and Figure 5 respectively and the top surface of the drilled specimen is shown in Figure 6. The measured diameter at the entrance side was significantly larger than the predicted value, whereas for the exit surface they were reasonably in good agreement.
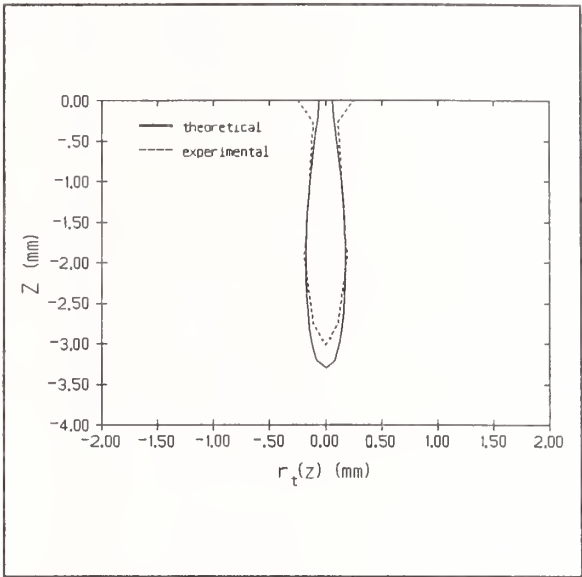

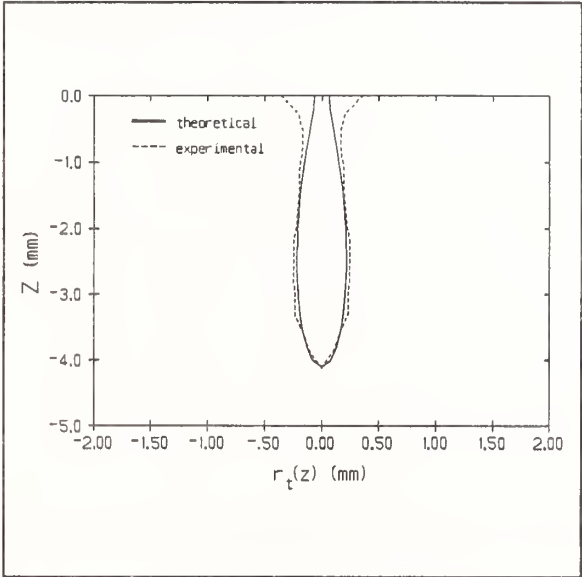Fig.3a Blind hole profile at intensity=2000W
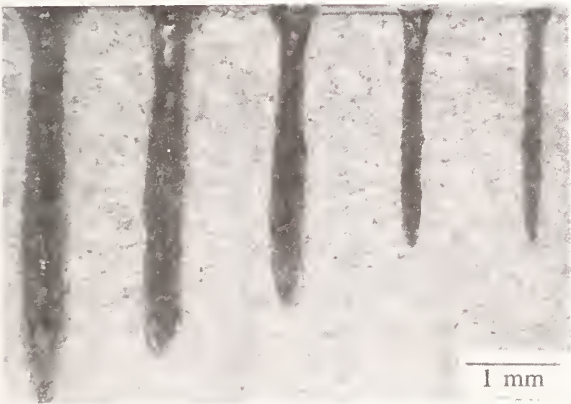

Fig.3b Blind hole profile at intensity=3000W

Fig.2 Blind hole profile as a function of intensity
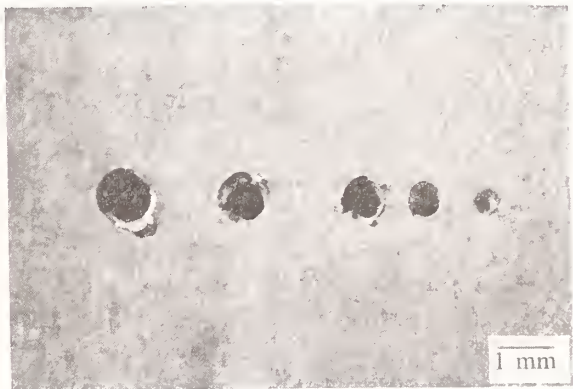(I$_t$ from right to left: 1000-3000W, steps 500W)

Fig.6 Through hole diameter as a function of intensity
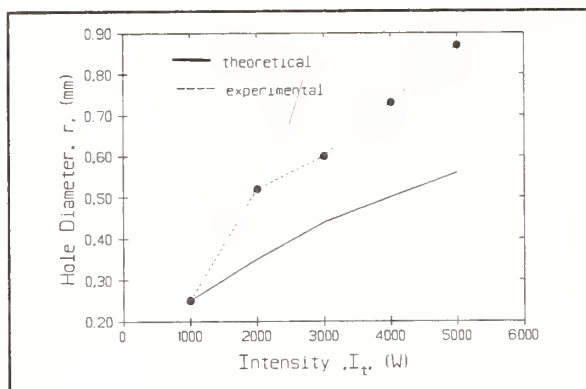(I$_t$ from left to right: 1000-5000W steps 1000W)
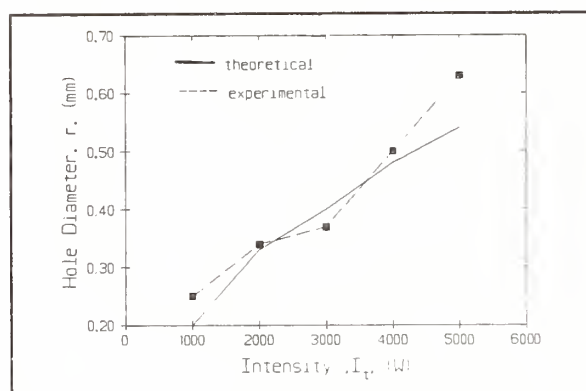
Fig.4 Intensity vs. top surface hole diameter

Fig.5 Intensity vs. exit surface hole diameter

6. DISCUSSION

(a) Blind hole drilling

The good agreement between the experimental profile and that as predicted by equation 2 suggests that in blind hole drilling the contour of the hole can be best described by a single parameter namely, the critical intensity, I_c. The results, both theoretical and experimental, also show that a spear-head profile is obtained in the absence of relative movement between the workpiece and the laser beam along the Z-direction. The fact that the dimension at the entrance of the hole is larger than the predicted value is possible due to the melting effect occurring at the surface. As the laser beam reaches the surface of the specimen, areas next to the vaporized zone would be melted and expelled with the aid of the argon jet. Such skin effect is also time dependent, i.e. if more pulses are required to accomplish the hole then the surface regions next to the vaporized zone would be exposed longer to sufficiently high radiation to melt the material. As a consequence, the tapered entrance would become larger and deeper. However, such effect was much less pronounced inside the blind hole because of the shielding effect of the top surface stopping most of the laser radiation of less than that of the critical intensity from entering the hole. In addition to this, due to the geometry of the hole any melted phases would be less likely to escape. Built on this argument, the profile of the blind hole at the surface could be better described by the melt zone contour based on calculations of heat conduction models rather than using the critical vaporizing criterion.

(b) Through hole drilling

In theory, through hole drilling is possible provided the thickness of the sheet does not exceed the overall length of the profile. But again the shape of the hole would not be uniform and will depend on the position of the workpiece relative to the focal point of the laser beam according to equation 4. For instance, if the bottom surface of the workpiece is at the corresponding $Z_{max.}$ position then an inverted-taper hole would form (Figure 7). Nevertheless, it is possible to improve the uniformity of the hole by a moving laser source travelling in and out of the specimen. Figure 8 presents the result of such a case, apparently the profile of the hole machined with the laser tunnelling action was better than the one without. Therefore, for thick materials if a moving laser source is employed or as in the case of thin sheets, by placing the top surface of the material at the Z_{max} position the diameter of the hole can be estimated using equations 6 and 4. Results shown in Figures 4 and 5 confirmed that the size of the hole was related to the intensity of the beam and it is believed that by further refinement of the theory of co-operating with the melted boundary condition a more representative solution can be obtained.

Based on equation 4, it is also possible to control the dimension of the through hole by a defocusing technique, in that the position of the specimen can be placed at different levels along the beam path. However, when using such technique to machine thin specimens, corrections must be made to account for the melted regions.

The idea of employing the concept of critical beam intensity to predict the profile of the "machined" hole can, certainly, offer some practical information on laser micro-machining of MMC materials. The approach is unique in the sense that it alleviates many of the uncertainties such as metal reflection, laser-gas-material interactions, etc. which arise during laser processing.

552

laser drilling direction

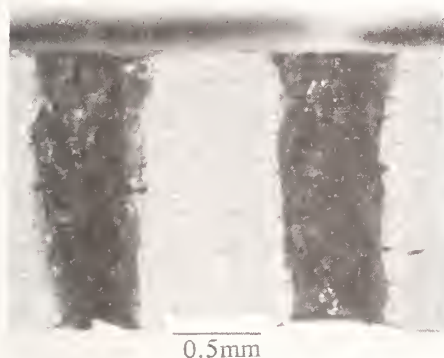Fig.7 Specimen placed at $Z_{max.}$ resulted an inverted taper hole

Fig.8 Left:with a stationary laser source;
Right: with a travelling laser source

CONCLUSIONS

(1) The profile of the laser machined holes can be determined using the critical intensity criterion; however, the model required modification when applied to the entrance region.

(2) The profile of the hole would vary depending on the relative position of the workpiece to that of the laser focal spot.

(3) The maximum diameter of the machined through holes was related to the critical intensity.

(4) In using a moving source technique, the uniformity of the through hole can be improved.

REFERENCES

1. A.Niklas, L.Froyen and L.Delaey, "Comparative Evaluation of Extrusion and Hot Isostatic Pressing as Fabrication Techniques for Al-SiC Composites", Materials Science and Engineering, A135 pp.225-229, 1991.

2. A.R.E.Singer, "Metal Matrix Composites Made by Spray Forming" Materials Science and Engineering, Vol.A135, pp.13-17, 1991.

3. T.M.Yue and G.A.Chadwick, "Squeeze Casting of Light Alloys and Their Composites-A Review", Proceedings of the 6th International Manufacturing Conference with China, 10-12 March 1993, Hong Kong.

4. D.R.Pank, J.J.Jackson, "Metal Matrix composite Processing Technologies for Aircraft Engine Applications", ASM/TMS Materials Week '92, 2-5 November 1992, Chicago, Illinois USA.

5. M. Brun, M. Lee and F. Gorsler, "Wear Characteristics of Various Hard Materials for Machining SiC-Reinforced Aluminium Alloy", General Electric Corporate Research & Development, Report No.84CRD327, 1984.

6. G.A. Chadwick and P.J. Heath, "Machining Metals Matrix Composites", Metals and Materials, Feb., pp.73-76, 1990.

7. W.S. Lau, T.M. Yue, C.Y. Jiang and S.Q. Wu, "Pulsed Nd:YAG Laser Cutting of SiC/Al-Li Metal Matrix Composite", Proceedings of the Machining of Composite Materials Symposium, ASM/TMS Materials Week, Chicago USA, 2-5 Nov. 1992, pp.29-34.

8. C.Y. Jiang, W.S. Lau, T.M. Yue and L. Chiang, "On the Maximun Depth and Profile of Cut In Pulsed Nd:YAG Laser Machining", to be published in the CIRP Annals 1993.

NIST Technical Publications

Periodical

Journal of Research of the National Institute of Standards and Technology—Reports NIST research and development in those disciplines of the physical and engineering sciences in which the Institute is active. These include physics, chemistry, engineering, mathematics, and computer sciences. Papers cover a broad range of subjects, with major emphasis on measurement methodology and the basic technology underlying standardization. Also included from time to time are survey articles on topics closely related to the Institute's technical and scientific programs. Issued six times a year.

Nonperiodicals

Monographs—Major contributions to the technical literature on various subjects related to the Institute's scientific and technical activities.

Handbooks—Recommended codes of engineering and industrial practice (including safety codes) developed in cooperation with interested industries, professional organizations, and regulatory bodies.

Special Publications—Include proceedings of conferences sponsored by NIST, NIST annual reports, and other special publications appropriate to this grouping such as wall charts, pocket cards, and bibliographies.

Applied Mathematics Series—Mathematical tables, manuals, and studies of special interest to physicists, engineers, chemists, biologists, mathematicians, computer programmers, and others engaged in scientific and technical work.

National Standard Reference Data Series—Provides quantitative data on the physical and chemical properties of materials, compiled from the world's literature and critically evaluated. Developed under a worldwide program coordinated by NIST under the authority of the National Standard Data Act (Public Law 90-396). NOTE: The Journal of Physical and Chemical Reference Data (JPCRD) is published bimonthly for NIST by the American Chemical Society (ACS) and the American Institute of Physics (AIP). Subscriptions, reprints, and supplements are available from ACS, 1155 Sixteenth St., NW, Washington, DC 20056.

Building Science Series—Disseminates technical information developed at the Institute on building materials, components, systems, and whole structures. The series presents research results, test methods, and performance criteria related to the structural and environmental functions and the durability and safety characteristics of building elements and systems.

Technical Notes—Studies or reports which are complete in themselves but restrictive in their treatment of a subject. Analogous to monographs but not so comprehensive in scope or definitive in treatment of the subject area. Often serve as a vehicle for final reports of work performed at NIST under the sponsorship of other government agencies.

Voluntary Product Standards—Developed under procedures published by the Department of Commerce in Part 10, Title 15, of the Code of Federal Regulations. The standards establish nationally recognized requirements for products, and provide all concerned interests with a basis for common understanding of the characteristics of the products. NIST administers this program in support of the efforts of private-sector standardizing organizations.

Consumer Information Series—Practical information, based on NIST research and experience, covering areas of interest to the consumer. Easily understandable language and illustrations provide useful background knowledge for shopping in today's technological marketplace.

Order the above NIST publications from: Superintendent of Documents, Government Printing Office, Washington, DC 20402.

Order the following NIST publications—FIPS and NISTIRs—from the National Technical Information Service, Springfield, VA 22161.

Federal Information Processing Standards Publications (FIPS PUB)—Publications in this series collectively constitute the Federal Information Processing Standards Register. The Register serves as the official source of information in the Federal Government regarding standards issued by NIST pursuant to the Federal Property and Administrative Services Act of 1949 as amended, Public Law 89-306 (79 Stat. 1127), and as implemented by Executive Order 11717 (38 FR 12315, dated May 11, 1973) and Part 6 of Title 15 CFR (Code of Federal Regulations).

NIST Interagency Reports (NISTIR)—A special series of interim or final reports on work performed by NIST for outside sponsors (both government and non-government). In general, initial distribution is handled by the sponsor; public distribution is by the National Technical Information Service, Springfield, VA 22161, in paper copy or microfiche form.